Keizo Ugai
Hiroshi Yagi
Akihiko Wakai

Editors

Earthquake-Induced Landslides

Proceedings of the International Symposium
on Earthquake-Induced Landslides,
Kiryu, Japan, 2012

Springer

Earthquake-Induced Landslides

Keizo Ugai · Hiroshi Yagi
Akihiko Wakai
Editors

Earthquake-Induced Landslides

Proceedings of the International Symposium on Earthquake-Induced Landslides, Kiryu, Japan, 2012

Springer

Editors
Keizo Ugai
Department of Civil
    and Environmental Engineering
Gunma University
Kiryu, Gunma
Japan

Akihiko Wakai
Department of Civil
    and Environmental Engineering
Gunma University
Kiryu, Gunma
Japan

Hiroshi Yagi
Faculty of Education, Art and Science
Yamagata University
Yamagata
Japan

Preface

It is our great honor and pleasure to hold the International Symposium on Earthquake-induced Landslides (ISEL) in Kiryu, Japan, on November 7–9, 2012. This symposium was organized by the Japan Landslide Society (JLS).

Since ancient times, there have been an enormous number of landslides and debris flows caused by earthquakes and post-earthquake rainfall in earthquake-prone regions and countries in the world. These phenomena have induced catastrophic disasters and damages to the people and the society. Therefore, it is very important for people interested in this field to gather and exchange ideas and information on the mechanism of the phenomena and methods of the disaster mitigation. We believe that this symposium will provide the experts with such an opportunity.

The 2011 Great East Japan Earthquake disaster was recorded on the greatest scale that we have ever experienced in Japan. We have to learn from this experience and adopt it to our future disaster prevention managements. During the symposium, the scientific reports on the recent activities by the Earthquake-induced Landslides Research Project (ELRP) in the JLS will also be made and it will provide us with fruitful information on the related topics. The project was established in 2009 and it has been all completed until April 2012. In the project, altogether eight working groups, which are carrying out concrete investigations and analyses on individual items, were organized to cover the all objectives of the task force. Some of the results of the activities based on each working group are also included in the chapter for "JLS WG Report" in this book.

Main topics of interest in this symposium are the following:

1. Investigation of recent and historical earthquake-triggered landslides and their impacts
2. Characteristics, processes, and mechanisms of earthquake-triggered landslides
3. Physical and numerical modeling of earthquake-triggered landslides
4. Instrumentation and monitoring technologies for earthquake-related landslides
5. Risk assessment and management of earthquake-related landslides
6. Stabilization and disaster mitigation of earthquake-related landslides

7. Earthquake-related landslide dams and their risk assessment and management
8. Monitoring, prediction, and early warning systems for post-earthquake landslides and debris flows
9. Other relevant topics concerning earthquake-related landslides.

In launching this event, we are particularly grateful to Kiryu City Office and Highland Kanto Liaison Organization for their cooperation and strong support. The financial aid from the Tokyo Geographical Society is also greatly appreciated.

Japan, 2010–2011   Keizo Ugai

Contents

Part II   JLS-ELRP WG Report

Part III   Case Study

Part IV   Mechanism

Part V   Simulation

Part I

Keynote Lecture

Formation and Risk Reduction of Landslide-Dammed Lakes Resulted by the M_s 8.0 Wenchuan Earthquake: A Brief Review and a Proposal

Peng Cui, Zhi-man Su, Xiao-qing Chen and Jia-wen Zhou

Abstract

The M_s 8.0 Wenchuan earthquake produced 257 landslide lakes along the faults and rivers. The outburst risk of the lakes was successfully relieved by emergent risk analysis and response treatments. This paper briefly reports the activities of risk reduction based on remote sensing data and field surveys in the study area. For the purpose to recognize and reduce the risk of landslide dammed lake, the formation process of landslide dam has been analyzed using the method of numerical simulation. Four indexes were chosen to perform a quick evaluation of risk, including dam structure, dam height, maximum water storage capacity, and size of the population in potentially affected area. The evaluation results have been successfully applied to emergency treatment of dammed lakes such as the Tangjiashan dammed lake, the largest landslide-dammed lake resulted from the earthquake that has the highest risk of outburst and various scenarios of potential failure were analyzed. From the success of risk reduction of Tangjiashan dammed lake, lessons have been learnt to farther understand the risk management and develop effective countermeasures for risk reduction, based on which a research proposal is suggested.

Keywords

Landslide-dammed lake · Risk assessment · Risk reduction · Wenchuan earthquake · Tangjiashan dam

P. Cui (✉) · Z. Su · X. Chen J. Zhou
Key Laboratory of Mountain Hazards and Surface Process, Institute of Mountain Hazards and Environment, Chinese Academy of Sciences, #.9, Block 4, Renminnanlu Road, Chengdu 610041, China
e-mail: Pengcui@imde.ac.cn

J. Zhou
State Key Laboratory of Hydraulics and Mountain River Engineering, Sichuan University, Chengdu 610065, China

1 Introduction

The M_s 8.0 Wenchuan earthquake occurred at 14:28 local time (Beijing time) on 12 May 2008, in Wenchuan Country, Sichuan Province of China, triggering large numbers of rock falls, landslides, rock avalanches, and landslide dams (Cui et al. 2009; Xu 2009). These earthquake dams posed serious threats to upstream people as

the impounded lake water level rise. A potentially worse situation can be the potential downstream flooding due to dam breach and rapid release of the impounded water.

Analyzing 73 cases of landslide dam failures, Costa and Schuster (1988) found that 27 % failed in the first day after formation, 41 % failed in 1 week, 50 % failed within 10 days, 80 % in 6 months and 85 % within 1 year. Thus, nearly all such dams would eventually fail. It was therefore critical and urgent to recognize and evaluate the risk of failure and take emergency treatment.

Our research team travelled to the landslide dam sites right after the earthquake and conducted consultant researches for the government in the following days (Cui et al. 2009, 2011, 2012; Chen et al. 2011). Due to the lack of data, special analysis methods were developed and adopted to support the decision-making by authorities. More concern was given to the Tangjiashan dammed lake, which is the largest landslide-dammed lake. The earthquake disaster relief office used all of our risk evaluation results and successfully took the emergency treatment. To understand the dynamic process of the formation of landslide dammed lake, a numerical modeling method was proposed to simulate the dynamic process of the formation. This paper makes a brief review of the risk reduction of the landslide-dammed lakes and puts forwards a proposal for further studies.

2 Numerical Analysis of the Formation of Landslide Dam

To understand the formation and process of landslide dammed lake is the precondition to recognize and reduce the risk of landslide dammed lake. The formation process of landslide dammed lake can be cognizant of four steps, the initiation of slide on unstable slope, the motion of sliding mass from original location to down slope, the pileup of delivered debris and blockage river channel in donga, the impoundment water and lake level rise. As the formation process of landslide lake is hard to be monitored and recorded, numerical models are used to simulate the dam formation and the subsequent failure and runoff of materials (Cui and Zhou 2012).

The simulation process was divided into two steps: the landslide step and the river-blocking step. The landslide dam in Yangjiagou gullyed was selected as example. Firstly, two-dimensional discrete element method (PFC2D) was adopted to simulate the dynamical process of the landslide. And then the shallow-water equation and finite difference method was used to analyze the hydrodynamic mechanisms of the river-blocking process of the landslide dammed lake.

The impounded water level varies in time as shown in Fig. 1.1. Knowledge about the overflow of the landslide dam, appeared under different water flow conditions, was obtained. The result is help for the design of mitigation measures.

3 Landslide-Dam Recognition and Risk Assessment

Both field investigation and remote sensing inspection were carried out soon after the earthquake. The remote images with 2 m resolution were taken by Aerial Digital Senso 40 (ADS40) from 16 to 28 May 2008 (Cui et al. 2009). It revealed that there were 257 landslide lakes along the fault rupture zone and river channels (Fig. 1.2).

Under the emergency circumstances, the dam height, structure, and the lake capacity were selected as the main indices to assess the hazard of dammed lake (Table 1.1) (Cui et al. 2009). Out of the 257 lakes, 33 were highly potential to outburst flooding, and 12 collapsed before 25th May. The Tangjiashan dammed lake was in the highest risk,
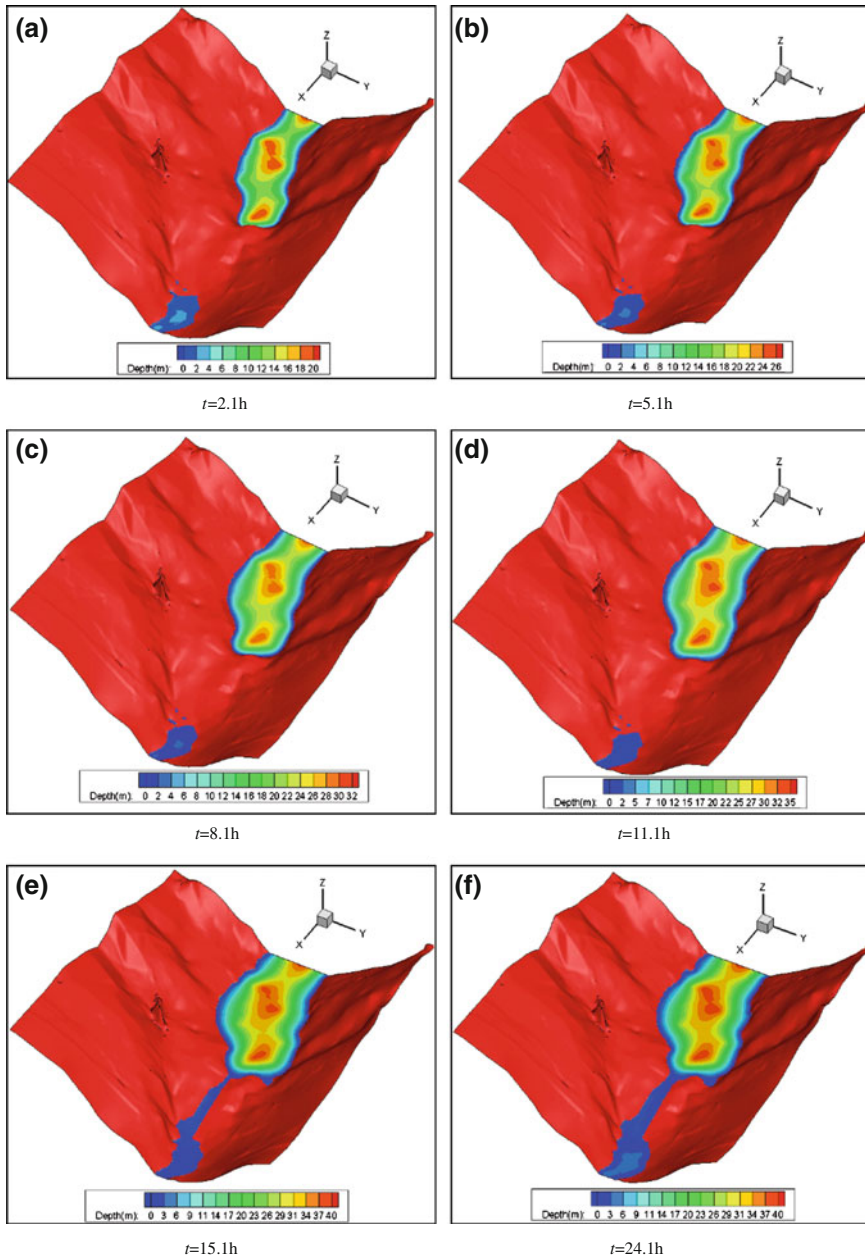
Fig. 1.1 Water levels of Yangjiagou landslide lake in different moment (Cui and Zhou 2012)

while 7 lakes were high, 5 lakes were medium and 8 lakes were low. Four modes of failure were assumed for each dam, including instantaneous full collapse, partial instantaneous collapse, progressive collapse, and gradual collapse.

By taking potential inundation are as into account, risk assessment levels were presented as follows: 17 debris dams were evaluated as dangerous (1 very high risk, 7 high risk, 5 medium risk, and other 4 immediately below high risk dams).
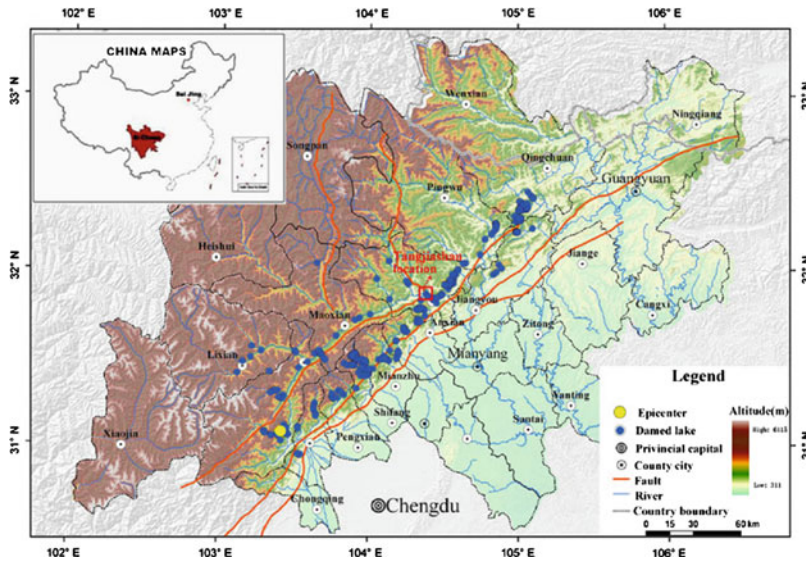
Fig. 1.2 Distribution of landslide-dammed lakes caused by Wenchuan earthquake (Cui et al. 2009)

Table 1.1 Hazard grading of dammed lakes

Grading of hazard	Indices		
	Dam height/m	Dam structure	Lake capacity/$\times 10^4$ m^3
Extremely high	>100	Mainly composite by soil	>10^4
High	50–100	Soil composited with little amount of block	10^3–10^4
Medium	25–50	Block composited with little amount of soil	10^2–10^3
Low	<25	Mainly composite by block	<10^2

Note at least two in three of the indices must be satisfied

4 Emergency Response in the Tangjiashan Dammed Lake

4.1 General Information and Survey Data

The Tangjiashan dam is the largest landslide dams produced by the Wenchuan earthquake, blocking the Tongkou river (a tributary of the Fujiang river). The dam consisted of 2.04×10^7 m^3 of landslide debris, 803 m in length along the river, 611 m in width across the river, and 83–124 m in thickness. The lake had a volume of 3.15×10^8 m^3, potentially inundating 8.92 km^2 upstream (Fig. 1.3). It posed a serious threat to at least 1.3 million people downstream.

4.2 Rapid Risk Analysis

Hazard assessment of the dam indicated that it was unlikely to collapse suddenly. Scenarios equivalent to 20, 25, 33, and 50 % were chosen to analyze the flood and its variations along the channel and the potential inundation areas.

Corresponding to the four cases, the flood was estimated to be in depth of 4.6, 5.1, 5.7, and 6.2 m, respectively, when it reached Mianyang, the second largest city in Sichuan Province, 48 km downstream the dam (Cui et al. 2012). The inundation area was designated as low risk (3.35 km^2), medium risk (3.84 km^2), high risk (4.22 km^2), and very high risk (4.65 km^2), which provided the basic information for planning emergency evacuation.

Fig. 1.3 View of the Tangjiashan landslide and blockage. River flows from *left* to *right* (Photo from Ministry of Land and Resources)

4.3 Emergent Risk Mitigation

The most common method of stabilizing a landslide dam is to construct an erosion-resistant open-channel spillway across the dam or across an adjacent abutment (Schuster 2006). For the Tangjiashan dam, a trapezoidal spillway was designed at the right side of the natural barrier because of the lower position and small excavation. The cross-section has an initial bottom width of 13 m, and a side slope of 1:1.5; the mid-portion of the channel has a bottom width of >7 m and side slope of 1:1.45. The entrance elevation is 740.0 m; the exit elevation is 739.0 m. The depth is 10 m, and the total length is 475 m. The designed discharge was 1,160 m^3/s (Liu and Yang 2009).

The impounded water level reached 740.37 m, the level of the spillway, at 8:00 h on June 7. By 1:00 h on June 10, the level reached its highest elevation, 743.1 m, and by 7:00 h flow in the sluiceway was 497 m^3/s. By 8:00 h, with the sluiceway eroding, the lake level had dropped to 742.8 m, and the discharge rosed to 940 m^3/s. Peak discharge of 6,500 m^3/s in the sluiceway

occurred at 12:30 h, with the water level reduced to 735.8 m. Thereafter, discharge fell rapidly, and by 20:00 h, the discharge was 290 m^3/s; the water level had dropped to 719 m, and the lake volume was reduced to 1.12×10^7 m^3. By 7:00 h on June 11, discharge had declined to 56 m^3/s in sluiceway, near the mean flow of the Tongkou River (Liu and Su 2012).

The sluiceway enlarged to a channel 800 m in length, and 145–235 m in width (80–100 m wide at the bottom). Inlet elevation is 710 m; outlet elevation 690 m. The peak outflow discharge of 6,500 m^3/s was larger than a flood of 1 % probability, of 6,040 m^3/s, and slightly less than the historical flood of record at Beichuan of 6,720 m^3/s (Yang 2008). The remaining portion of the dam, armored by significant proportions of boulder-size (>256 mm) debris, will resist further erosion, and the channel cut through it will continue to stabilize by progressive armoring. Risk of renewed blockage failure will also decline as the downstream channel of the barrier fills with sediment. No injuries or destruction resulted from the discharge. The risk mitigation was successful.

5   Lesson Learned

Among the 33 landslide lakes regarded as dangerous, 12 dams have naturally overtopped, and 17 dams with a higher level of risk had been treated with engineering measures safely. The remaining four dams no longer existed after the artificially overtopping of the Tanjiashan lake. Those dams composed of large boulders and masses of intact rock may be able to resist erosion and maintain stability for long time. The risk of outburst of the lakes was successfully released through the emergent risk analysis and response actions mentioned above. However, in retrospect we can see that improvements were possible.

(1) The risk evaluation for potential outburst flooding from the debris dam break or collapse is still incomplete. Special attention should be paid to the Peak flood discharge at the toe of a dam. We should determine much exactly about the mode of dam breach in different conditions to get more precise results in calculating the flood parameters in each control section.

(2) In the case of the Tangjiashan lake, although initial breach erosion was slow, later erosion was uncontrollably rapid. Increased slope of the engineered channel and adoption of a compound, trapezoid–triangular cross-section can be considered. And other measures to control the rate of breach incision can be investigated.

(3) Although emergency treatment is successful in general, the evacuation from potential risky area lasted for an unnecessarily long period. Also take the Tangjiashan lake emergency response for example. If evacuation began after dam overtopping, the duration of the stay in tents for Mianyang City refugee would be minimized to less than 1 day, but not 12 days. Therefore, precise risk management planning can reduce this time in the future after improving knowledge of breach process of natural barrier.

6   A Proposal for Future Researches

For more effectively risky management of the dammed lakes, the authors suggest that further attention should be paid to following scientific and technical issues in the future.

(1) Prediction of formation of landslide lakes. Study the formation mechanism and conditions of landslide lakes through statistical analyses and physical model experiments based on the collected data about the formation of landslide lakes and the knowledge of geomorphology, soil mechanics, hydrology, hydraulics, etc. The formation conditions include material condition, spatial (geometry) condition and dynamic condition. It is expected to establish formation models to quantitatively describe the material movement and the transfer of energy and to identify the places prone to landslide lakes.

(2) Hazard assessment of landslide dam breaching. Conduct field investigations and modeling experiments to reveal the relationship between the stability of landslide dam and its influencing factors, including factors on dam material and structure, and to judge the modes of dam failure, such as partial collapse, dam failure due to internal erosion ("piping"), dam failure due to overtopping. These works will contribute to develop hazard assessment methods, supporting the decision-making of government offices.

(3) Breaching mechanism of landslide lakes. Study the effect of influencing factors on dam breaching, including dam height, geometry shape, material type, structure, erosion-resistant, and so on. Then study the dynamic process and mechanism of dam breaching through physical modeling experiments, field experiments and case studies. Based on these work, breaching models are wished to be improved and served to develop a software with general

applicability, high-precision and high-reliability.

(4) Computational method of flood routing resulted from dam breaching. Study flood hydrograph at the toe of a dam during breaching process, as well as its influencing factors, through prototype and experimental data. And then improve the flood routing computing formula to incorporate different breaching modes of possibly appeared dam types and thus exactly predict the flood hydrograph and the key parameters of flood in downstream, including the time of arrival, the flood discharge and the water level.

(5) Risk analysis and risk management. Based on the work mentioned above, propose assessment index system and method of potential loss with RS and GIS techniques and set up a software platform on risk analysis. Meanwhile, put forwards risk mitigation measures and emergency plan corresponding to the results of risk analysis. Furthermore, establish a landslide lake risk management system through combining the risk mitigation measures with land-use planning and other hazard mitigation engineering of river basins.

(6) Emergent risk mitigation technique. It is necessary to systematically study the practical applicability of different emergent risk mitigation technique for the better engineering design of emergent treatment, improve the technical regulations and establish a technique system of risk reduction of landslide lakes with different types of dam under different regional hydrology conditions.

(7) Treatment for the remains of landslide dams. There are many probably events in near future which may induce the instability of the dam remains, such as the rapid rising up of water level or a surge in the lakes, newly blockages on the artificial channels on the top of the dams, suddenly sliding along the potential weak layer of the dams. In the long term, significantly attention should be paid to the establishment of premise conditions to preserve dam remains and develop persisting treating countermeasures.

(8) Evolution of landslide lakes. Not only the stability of the dam and influencing factors ought to be monitored, but also the evolution of the river channel both upstream and downstream. It will provide valuable information for the long term treatments on the landslide dammed lake and for the researches in the evolution of geomorphology and environment of river with nature dams.

(9) Development and utilization of landslide lakes. If a landslide lake could be retained for a long time, it would become valuable for development and utilization. However, it is necessary to study how to exploit the resource of landslide lakes in a safe and sustainable way, such as how to transform the landslide lake into a tourist spot combining with locally cultural background and how to utilize the landslide lakes to provide hydroelectric power. It is meaningful to settle the scientific and technical problems aroused from the long-term preserving and utilizing, which would contribute to the harmonious relationship between human beings and nature.

References

Chen X, Cui P, Li Y et al (2011) Emergency response to the Tangjiashan landslide-dammed lake resulting from the 2008 Wenchuan earthquake, China. Landslides 8:91–98

Costa JE, Schuster RI (1988) The formation and failure of natural dams. Geol Soc Am Bull 100:1054–1068

Cui P, Zhou J (2012) Formation mechanism of landslide lakes. In: Liu N, Chen Z, Cui P et al (eds) Barrier lakes and risk reduction. Science Publishing House, Beijing (in Chinese)

Cui P, Zhu Y, Han Y et al (2009) The 12 May 2008 Wenchuan earthquake lakes: distribution and risk evaluation. Landslides 6:209–223

Cui P, Han Y, Chao D et al (2011) Formation and treatment of landslide dams emplaced during the 2008 Wenchuan earthquake, Sichuan, China. In: Evans SG, Hermanns RL, Strom A et al (eds) Natural and artificial rockslide dams. Springer, Berlin, pp 295–321

Cui P, Dang C, Zhuang J et al (2012) Landslide-dammed lake at Tangjiashan, Sichuan province, China (triggered by the Wenchuan earthquake, May 12, 2008): risk assessment, mitigation strategy, and lessons learned. Environ Earth Sci 65(4):1055–1065

Liu N, Su Z (2012) Case study of risk reduction of barrier lakes. In: Liu N, Chen Z, Cui P et al (eds) Barrier lakes and risk reduction. Science Publishing House, Beijing (in Chinese)

Liu N, Yang Q (2009) The emergency handling technique and practice of Tangjiashan barrier lake. China Eng Sci 11(6):74–81 (in Chinese)

Schuster RL (2006) Risk-reduction measures for landslide dams. Italian J Eng Geol Environ (Special Issue) 1:9–13

Xu Q, Fan X-M, Huang R-Q et al (2009) Landslide dams triggered by the Wenchuan earthquake, Sichuan Province, south west China. Bull Eng Geol Environ 68:373–386

Yang Q (2008) Key technologies of emergency treatment of Tangjiashan dammed lake. China Water Resour 16:8–11 (in Chinese)

Local Scale Seismic Landslide Susceptibility Assessment Based on Historic Earthquake Records Combined with Accelerometer Monitoring and Ambient Noise Data

2

Janusz Wasowski, Vincenzo Del Gaudio, Domenico Casarano, Piernicola Lollino and Sandro Muscillo

Abstract

Uncertainty in the quantification of earthquake loading poses one of the major difficulties in local scale seismic landslide susceptibility assessments. This problem can be exacerbated for slope settings that are likely to produce considerable amplifications of seismic shaking. We address this issue by examining the case of a historic landslide triggered by the 1627 Apulian (southern Italy) earthquake (epicentral intensity X on the MCS scale) in the peri-urban area of Caramanico (central Italy), distant ∼120 km from the epicenter. The failure caused a large downslope displacement and destroyed several buildings. The slope seismic response is assessed using data from long-term accelerometer monitoring of the hillslope and from recent ambient noise measurements. This provided evidence of significant directional amplifications, e.g., by a factor of approximately 4 and 20, respectively in terms of peak horizontal acceleration and Arias Intensity during the 2009 Mw 6.3 L'Aquila earthquake that occurred 60 km NW of Caramanico. Then taking into account the site amplification, permanent displacements are calculated by applying a rigorous Newmark approach. This study shows that historical information on landslides triggered at apparently anomalously large distances from an earthquake epicentre can help to identify hillslopes influenced by site effects and that reconnaissance-type measurements of ambient noise can be useful to reveal directional amplifications. The importance of accurate assessments of other relevant input parameters (e.g., material properties, slip surface geometries, groundwater conditions) used in seismic slope modeling is also recognized.

J. Wasowski (✉) · D. Casarano · P. Lollino
CNR-IRPI (National Research Council—Istituto di
Ricerca per la Protezione Idrogeologica),
via Amendola 122 i, 70126 Bari, Italy
e-mail: j.wasowski@ba.irpi.cnr.it

V. D. Gaudio · S. Muscillo
Dipartimento di Scienze della Terra
e Geoambientali, Università di Bari, Bari, Italy

1   Introduction

Although the occurrence of high magnitude (>7) earthquakes in Italy seems very rare according to the historical records, weak to moderate seismic shaking is relatively common (Boschi et al. 2000) and known to have triggered many slope failures. Many potentially unstable areas of Italy are also densely populated and research on seismically-induced landsliding deserves high priority.

In this context, one of the major difficulties in seismic landslide hazard assessments is linked to the uncertainty in the quantification of earthquake loading (e.g. Wasowski et al. 2011 and references therein). This problem can be exacerbated especially for slope settings that are likely to produce considerable amplifications of seismic shaking. Site effects may often result from a combination of amplifications caused by slope litho-stratigraphic (soil) and topographic responses (e.g. Paolucci et al. 1999; Del Gaudio and Wasowski 2011) and their quantification is not simple. We address this issue with reference to the study area of Caramanico Terme, a thermal spa center and tourist resort located in the central Apennine Mountains, one of the most seismically active regions of Italy (Fig. 2.1).

The area is prone to landsliding and several examples of historically documented failures induced by earthquakes were discussed by Wasowski and Del Gaudio (2000). While this earlier work was focused mainly on rockfalls, with hazard being assessed by identifying susceptible areas and defining temporal occurrence in terms of seismic threshold exceedance probability, here we re-examine the case of a historic landslide triggered by an earthquake of epicentral intensity X on the MCS scale, occurred on 30 July 1627 in the Apulian region (southern Italy). The failure affected the peri-urban area of Caramanico, causing destruction of several buildings. This case is also of interest, because the 1627 landslide affected a hillslope that is now traversed by a 1.5 km long tunnel.

A preliminary study of the landslide indicated that despite the large epicentral distance (∼120 km) the 1627 earthquake triggering could be compatible with general magnitude-distance relations (Keefer 1984). However, the slope stability analysis also showed that the seismic input inferred by using common attenuation relationships would have been insufficient to produce the failure (Wasowski et al. 2004).

In this work the seismic response of the slope failed in 1627 is re-assessed by considering the new data from the ongoing long-term accelerometer monitoring of the Caramanico area (Del Gaudio and Wasowski 2007, 2011) and from recent ambient noise measurements, which provided evidence of significant site amplifications, including directional effects (Del Gaudio et al. 2008; Del Gaudio and Wasowski 2012). We first provide background information on the geological setting of the area. This is followed by a reconstruction of the 1627 landslide event. Then the characteristics of the 1627 earthquake and ground motion estimates are provided. Finally, constrained shaking parameters are used to calculate permanent displacement (Dn) by applying the rigorous Newmark approach.

2   Background Information

The causes of landsliding in the area of Caramanico are related to the interaction of climatic, seismic and human factors. The environmental factors leading to slope instability have already been discussed (Wasowski 1998; Wasowski and Del Gaudio 2000), hence only a brief description of the local geological setting is presented here.
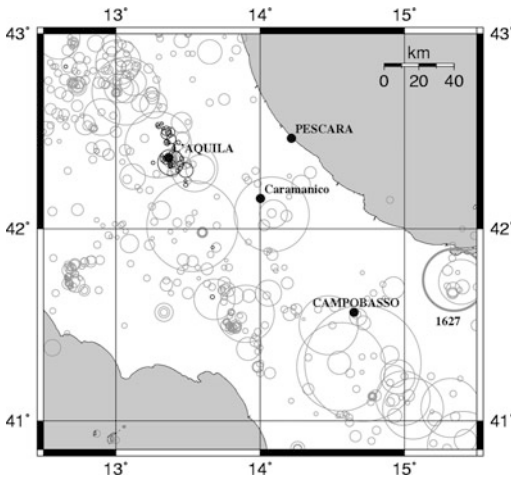
Fig. 2.1 Seismicity of south-central Italy: *circles* represent the focal volumes (according to Bath and Duda 1964) of earthquakes of magnitude >4 occurred from 1000 to 2011. *Grey circles* are mainshocks of historical earthquakes (data from Catalogue CPTI11, Rovida et al. 2011), including the Apulian 1627 earthquake. *Black circles* are instrumentally detected events occurred from 2007 to 2011 (data from the database of the ISIDe Working Group 2010). Note the event cluster corresponding to the 6.3 Mw 2009 L'Aquila earthquake

Three main lithological units are present in the study area (Fig. 2.2):

1. Quaternary/Holocene age sediments, which can be classified as soils. They include variably thick (from few to tens of meters) colluvial materials. These materials mantle large portions of the hillslope areas and include different sized carbonate clasts with or without a clayey-silty-sandy matrix.
2. A several meters thick deposit of carbonate megabreccia which forms the caprock of the Caramanico hillslopes (Quaternary?).
3. Marly mudstones, including rare sandstone intercalations (Early Pliocene), which form the local substratum.

The widespread instabilities of the Caramanico hillslopes can be broadly related to the spatial distribution of these three main lithotypes and their hydrogeological properties. The stability of the slopes is influenced by the presence of: (i) a low hydraulic conductivity mudstone substratum; (ii) a highly permeable megabreccia slope caprock which acts as an aquifer; and

(iii) medium to low hydraulic conductivity colluvial soils, which overlie the mudstone aquiclude and can locally also act as an aquifer.

Limited piezometric measurements from sites covered by thick colluvia indicated groundwater levels at considerable depths, often close to the mudstone substratum interface (Wasowski et al. 2004).

3   Reconstruction of the 1627 Earthquake-Induced Landslide

Wasowski and Del Gaudio (2000) quoted several historical records to demonstrate the case of earthquake triggering for the 1627 Caramanico landslide. They also indicated that seismic trigger could be compatible with the magnitude-source distance threshold proposed by Keefer (1984).

3.1   Topographic Site Conditions

The descriptions reported by Almagià (1910) indicate that the 1627 event resulted in significant downslope displacements of a monastery built in 1448. The historical source quotes that the monastery "descended from the nearby mountain together with the ground, from the first level and ran to another site even farther, as did the walls and other houses, without however being dismembered or falling apart entirely". The movement caused overthrowing of several buildings in the area occupied today by the Caramanico cemetery. This area represents the accumulation zone of the 1627 landslide, because the frescos in the cemetery chapel built in 1756 contain the description stating that the monastery "funded on the nearby hill…was pushed down here by the impetus of the 1627 earthquake".

On the basis of the above considerations and taking into account the present morphology of the slope we infer that the detachment area of the 1627 landslide was located more than 100 m upslope from the cemetery site and speculate that the failure involved the slope area mantled by thick colluvia (Fig. 2.2). However, at present
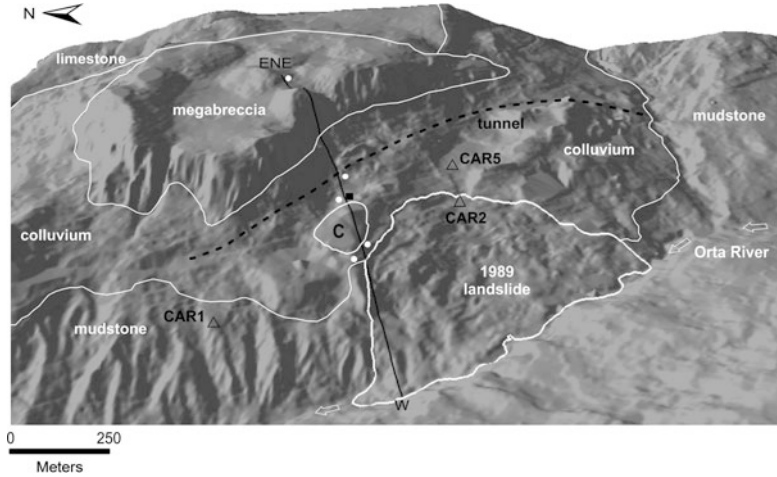
Fig. 2.2 DEM of the study area showing lithological units and measurement sites. *White lines* mark lithological contacts, approximate limits of the 1627 landslide deposit at the cemetery site (C) and the 1989 landslide. CAR1,2,5 mark the location of the accelerometric stations (reference station CAR4, located 2.5 km SE of Caramanico, is not shown). *Black rectangle* and *white dots* indicate, respectively, the site of HVNR measurement and borehole locations. Note also positions of the road tunnel and the profile shown in Fig. 2.3

it is difficult to pinpoint the exact location of the detachment area of the 1627 landslide.

3.2 Geological Site Conditions

A simplified geological profile across the failed hillslope is shown in Fig. 2.3. Local topographic and geologic complexities enhanced by landslide processes make the reconstruction of the sub-surface conditions uncertain. Nevertheless, the overall hillslope morphology and the litho-stratigraphic relations inferred from borehole information are compatible with the occurrence of deep-seated landsliding. The presence of thick colluvium and the fact that despite a significant downslope translation the monastery was not destroyed, further suggest the occurrence of a deep and more or less coherent failure.

The uncertainty regarding the depth and geometry of the failure surface and the presence of the colluvium including abundant, more or less cemented coarse limestone detritus causes difficulties in the assessment of realistic in situ effective shear strengths. Thus some simplifying assumptions are adopted with reference to the geological material properties. Considering that

the 1627 earthquake occurred in the middle of the summer (hot and typically dry season in Italy), "dry" conditions are assumed for the stability analysis. We also hypothesize that the failure surface developed within the colluvium.

4 The 1627 Earthquake and Constraints on Ground Motion Input Data

The 1627 Apulian earthquake occurred within the southern Apennine foreland which is char-acterised by major strike-slip sources (e.g. Del Gaudio et al. 2007). Historical macroseismic data (e.g. Boschi et al. 2000) indicate that the 1627 seismic sequence was characterised by four strong shocks (between 30 July–6 September), with epicentral intensity ranging from VIII-IX to X; the mainshock and the first strong aftershock occurred on July 30, only 15 min apart. The application of well established algo-rithms to the spatial distribution of intensity values (Gasperini et al. 1999) and the large amount of the macroseismic data allowed con-straining the magnitude estimates to a value of 6.7 ± 0.2 for the mainshock (Rovida et al.,
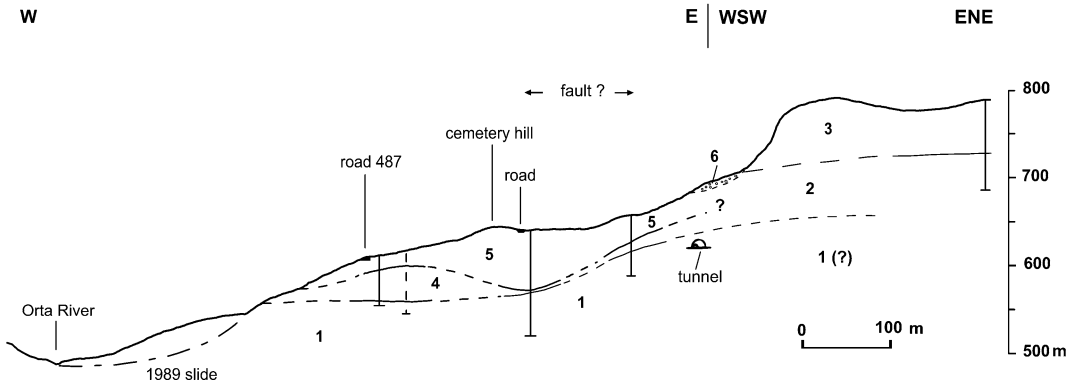
Fig. 2.3 Simplified geological profile of the hillslope, site of the 1627 earthquake-induced failure (after Wasowski and Del Gaudio 2000). Symbols: *1* mudstone substratum; *2* clay-rich silty sandy deposits with variable admixtures of carbonate debris; *3* carbonate megabreccia (caprock); *4* remoulded clay-rich materials with variable amounts of angular carbonate clasts; *5* variably cemented carbonate debris; *6* recent carbonate detritus of rock fall origin

2011). With the epicentre of the 1627 event distant about 120 km from the landslide site, the shaking felt in Caramanico would be expected much attenuated. In fact, the application of Italian attenuation relationships (Sabetta and Pugliese 1996; Bindi et al. 2009) results in low PGA and Ia values. In particular, under the deep soil conditions, the Ia values are below the median shaking intensity of 0.32 m/s, a threshold indicated by Harp and Wilson (1995) for triggering coherent-type landslides.

Obviously the uncertainties regarding the choice of seismic input data are large in case of historic events, which lack instrumental records. We address the problem by applying Ground Motion Prediction Equations (GMPE) calibrated on data from accelerometer sites on rock/stiff soil and by taking into account the local site effects revealed by the accelerometer monitoring at Caramanico.

4.1   Indications from Accelerometer Monitoring at Caramanico

The data acquired by an accelerometer monitoring network, established in 2002–2005 in Caramanico to study the dynamic response of slopes characterized by different topographic and geologic conditions, revealed the presence of significant site amplifications (Del Gaudio

and Wasowski 2007, 2011). For the present study of interest are three accelerometer stations located on the hillslope affected by the 1627 landslide (Fig. 2.2):

(a) CAR1, on a slope in Pliocene mudstones, dipping 18° to WSW;

(b) CAR2, 600 m to SSE of CAR1, within the same hillslope locally dipping 11° to WSW, but on the head of a landslide that in 1989 mobilized a 30–40 m thick colluvium overlying the same mudstone formation cropping out at CAR1;

(c) CAR5, about 200 m east of CAR2, on the same colluvium unit as in CAR2, but upslope from the 1989 landslide crown, in gently inclined (<7°) area.

An additional station (CAR4) located 2.5 km SE of Caramanico, on limestones forming a gentle slope, was used as reference.

Given the similarities of the subsurface geology (thick colluvia overlying the mudstones), one can infer the dynamic response of the slope that failed in 1627 from the accelerometer records of CAR1 and CAR5. An evaluation of the potential amplification was carried out by considering peak values of horizontal acceleration (PHA) and Arias Intensity measured along horizontal directions (Ia_{max}) registered at CAR1 and CAR5 during the same events. The relative amplification factors are plotted in Fig. 2.4. The comparison of the

PHA CAR5/CAR1

Ia$_{max}$ CAR5/CAR1
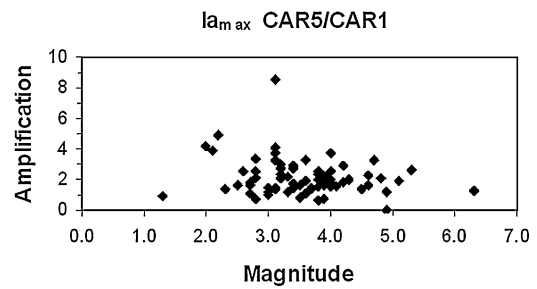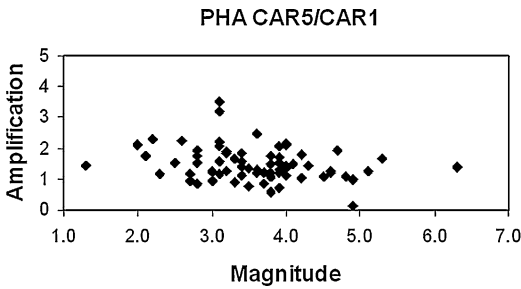
Fig. 2.4 Relative amplification factors at station CAR5 with respect to CAR1 for peak horizontal acceleration (PHA) and maximum Arias intensity measured along

horizontal directions (Ia$_{max}$), as a function of event magnitude

recordings demonstrated that the ground motions at CAR5 are consistently amplified with respect to CAR1. The relative amplification factors average around 1.5–2.2 for PGA and Ia, respectively (with maxima of 4.5 and 8.5). Del Gaudio and Wasowski (2011) documented the presence of very similar relative amplifications between CAR2 and CAR1as well.

It is also of interest to compare time series of horizontal acceleration registered at CAR1 and CAR5 (Fig. 2.5) for the mainshock of the 6 April, 2009 l'Aquila Mw6.3 earthquake, with epicentre located about 60 km NE of Caramanico (Fig. 2.1). The comparison reveals that, even though the peak value at CAR5 was only 40 % larger than at CAR1, for several shaking cycles (along directions different from N–S) ground acceleration was up to 2–3 times higher at CAR5. At site CAR2 ground accelerations were even larger, especially along WSW directions (Del Gaudio and Wasowski 2011).

Notably, in comparison to the reference station on rock (CAR4), the observed amplification factors were considerably higher, especially for the events of magnitude larger than 4. In terms of PGA, amplification factors between 2 and 6 were observed at CAR2 and CAR5 (with a value of 4 for the strongest Mw 6.3 L'Aquila event); in terms of Ia, CAR5 was characterized by amplifications of 9–32 (but with the minimum of 9 just for the strongest earthquake), whereas even larger values (15–35) were found at CAR2.

The observations at site CAR2 provided evidence of site response directivity phenomena that can occur on some slopes along potential sliding

2009.04.06 01:32:26 (L'Aquila, M$_W$ 6.3)
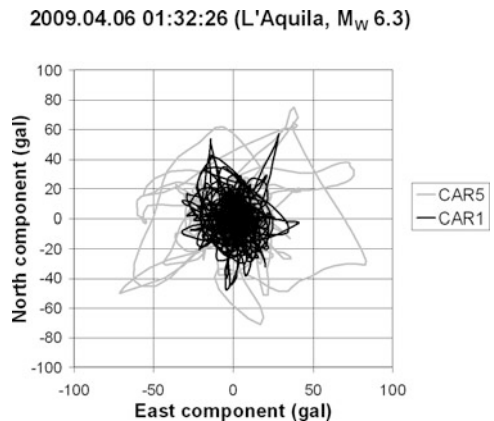
Fig. 2.5 Times series of the horizontal acceleration registered for the mainshock of 2009 L'Aquila earthquake at stations CAR1 and CAR5

directions as an effect of directional resonance affecting deep-seated landslides (Del Gaudio and Wasowski 2007). As shown by Del Gaudio et al. (2008), the presence of resonance conditions (and, possibly, its directional character) can be detected via seismic noise analysis, according to the Nakamura technique (Nogoshi and Igarashi 1971; Nakamura 1989); directivity can be inferred by calculating spectral ratios between horizontal and vertical components of noise recording (HVNR values) along different azimuthal directions. Importantly, resonance conditions, with HVNR peak values close to 4, i.e. similar to the values of 4–5 observed at CAR5 and CAR2, respectively, were identified through recent measurements carried out in the 1627 landslide area (Del Gaudio and Wasowski 2012).

Table 2.1 Summary of ground motion input data and corresponding Newmark displacement estimates

	PGA (g)	Dn (cm)		
		$a_c = 0.01$ g	$a_c = 0.02$ g	$a_c = 0.05$ g
Caramanico				
Bedrock	0.038	6.7	1.9	0
Amplified conditions MIN	0.054	8.2	2.2	0
Amplified conditions INTERM	0.061	11.1	3.9	0.2
Amplified conditions MAX	0.066	12.3	4.2	0.6
El Centro (NS component)				
Bedrock	0.033	4.9	0.3	0
Amplified conditions MIN	0.052	6.4	1	0
Amplified conditions INTERM	0.060	10	2.1	0
Amplified conditions MAX	0.064	10.6	2.4	0
El Centro (EW component)				
Bedrock	0.051	15	2.4	0
Amplified conditions MIN	0.062	18.4	4.6	0
Amplified conditions INTERM	0.073	25.8	8.4	0.2
Amplified conditions MAX	0.088	29.9	10.3	0.4

Minimum (MIN), intermediate (INTERM) and maximum (MAX) PGA values are derived from "bedrock" accelerograms amplified using software STRATA

4.2 Ground Motion Input Data

To estimate the shaking conditions at Caramanico during the 1627 earthquake we first used a procedure proposed by Sabetta and Pugliese (1996), which allows obtaining artificial accelerograms representative of the ground motion expected for the Italian events of defined magnitude and distance at a site characterised by the presence of thick (>20 m) and relatively stiff soil-type lithologies (S-wave velocities > 400 m/s). This is done using GMPE's calibrated on the Italian accelerometer data to define median characteristics of time-dependent ground motion spectra, in order to calculate non-stationary time series simulating realistic accelerograms.

To take into account site amplification effects, the artificial accelerograms were used as input to a 1D layering model to perform a site response analysis in the frequency domain through the code STRATA (Kottke and Rathje 2008), which is available at http://www.gnu.org/licenses/. The program conducts equivalent-linear site response analysis in the frequency domain using time

domain input motions or random vibration theory methods, and allows for randomization of the site properties.

To define the non-linear soil shear behaviour under seismic loading, we followed the empirical correlations of Vucetic and Dobry (1991) describing the variation of shear stiffness and damping ratio with shear strain for PI = 0. The soil thickness (30 m), constrained by the boreholes, and a unit weight of 20 kN/m3 were used. The applied shear wave velocity (Vs) values (600 m/s for soil and 1300 m/s for the bedrock) are based on the results of the Refraction Microtremor (ReMi) investigation at Caramanico (Coccia et al. 2010).

For the local bedrock (mudstones) a unit weight of 24 kN/m3 was adopted. The values of damping refer to the results of laboratory tests (G. Lanzo, University of Rome La Sapienza) conducted on one undisturbed mudstone sample obtained from a borehole drilled in the vicinity of the 1627 landslide site.

The amplified accelerograms generated with software STRATA were used for subsequent slope stability analysis. Significantly, the

Fig. 2.6 Variation of the seismic critical coefficient (k_c) with respect to: (*upper figure*) friction angle φ, with c = 3 kPa) and (*lower figure*) cohesion c ($\varphi = 27°$), for different values of the slope angle (β)
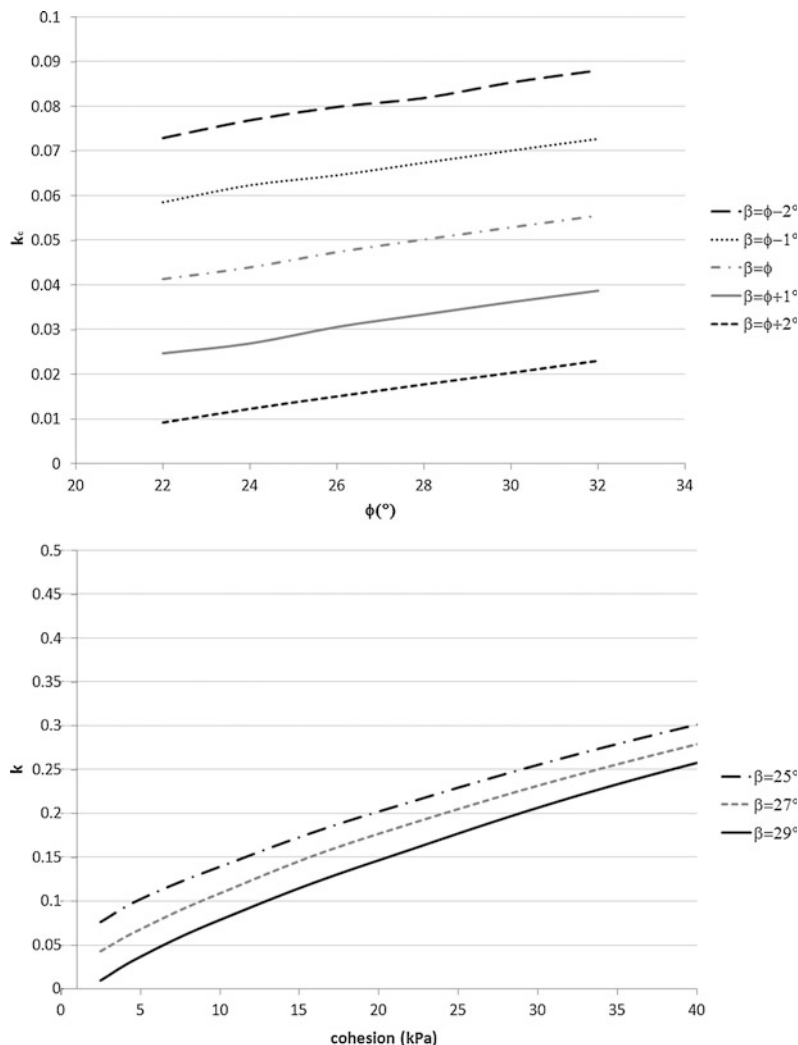
amplifications (up to $\sim 100~\%$, Table 2.1) obtained are closely comparable to the amplification factors identified from accelerometer monitoring at Caramanico.

5   Dynamic Slope Stability Analysis Based on Newmark Model

First the assessment of the critical or yield seismic coefficient value k_c (value of seismic acceleration expressed in g that produces a pseudostatic factor of safety = 1) was carried out by applying the upper-bound pseudo-static limit analysis and assuming a logspiral failure mechanism representative of a local slope failure (Chang et al. 1983). Plane strain conditions were assumed for isotropic and homogeneous soil mass (e.g. colluvium) sliding on a failure surface characterised by a rigid-plastic Mohr–Coulomb constitutive law. There is a lack of accurate information on the original, pre-failure slope inclination (β), as well as on the mobilised values of cohesion (c) and soil friction angle (φ) along the failure surface. Therefore, a parametric

analysis was carried out with respect to both c (ranging between 3 kPa and 40 kPa; $\varphi = 27°$) and φ (ranging between $22°$ and $32°$; c = 3 kPa), for prescribed values of the slope inclination β. According to the upper-bound limit analysis, for each pair of $[\varphi, \beta]$ and $[c, \beta]$ values, the k_c value was derived by imposing the minimization of k_c with respect to the geometrical parameters. The results of the analysis in terms of k_c values against φ and c are shown in Fig. 2.6 and the corresponding critical acceleration values ($a_c = k_c \cdot g$) were selected for the calculation of the earthquake-induced permanent displacements.

The rigorous permanent-displacement (Dn) analysis, with double integration of the soil mass acceleration over the time intervals characterised by $a > a_c$ (Newmark 1965), was performed using a software developed by Jibson and Jibson (2003). Three amplified accelerograms characterized by the minimum, intermediate and maximum values of PGA, as well as a non-amplified synthetic accelerogram representative of the slope bedrock conditions were used in the Dn analysis. In addition, for comparative purposes we used an accelerogram from a strike-slip event of similar magnitude to that of the 1627 earthquake, (the 1956 M 6.8 El Alamo Baja, California earthquake), registered at El Centro station (with flat ground, deep, stiff soil conditions) positioned at an epicentral distance (121 km) that is about the same as the distance between Caramanico and the 1627 earthquake epicentre.

The results show that significant displacements, that is close to 10 cm, a threshold assumed by Wilson and Keefer (1985) for the occurrence of coherent slide type failures, are obtained by imposing very low k_c values (within 0.02) and amplified conditions (Table 2.1). Such low k_c values are derived if similar values of slope geometry (β) and friction angle (φ) are assumed, along with low values of the soil cohesion (cf. Fig. 2.6). We speculate that by breaking the cementation bonds within the colluvium rich in carbonate clasts, the mainshock might have drastically reduced the cohesion and caused the failure during the strong aftershock that followed 15 min later.

6 Concluding Remarks

This study illustrates how historical earthquake information can be combined with present day in situ accelerometer monitoring for seismic landslide susceptibility assessments. The Caramanico accelerometer monitoring data show that on hillslopes with bedrock covered by thick colluvia, local litho-stratigraphic amplification can generate seismic shaking much higher (one order of magnitude in terms of total shaking energy) than that estimated by ordinary attenuation relationships (with calibration relying on accelerometers typically located on flat ground). This is consistent with the Newmark analysis of the 1627 seismic landslide at Caramanico, which indicates that significant site amplification would have been necessary to trigger the failure.

However, evaluations of seismic stability of slopes relying on Dn estimates require the integration of different types of input data (topographic, geotechnical, hydrogeological, seismological), which are characterized by a certain degree of natural dispersion (e.g. seasonal temporal variability), as well as variable resolution, quality, and reliability (cf. Murphy et al. 2002). The application of Newmark displacement analysis to the 1627 case shows that without accurate knowledge of slope material properties the reconstruction of mechanisms of seismically triggered deep slope failures could be difficult. We also recognize that the Dn results linked to low critical coefficient values (<0.05) can be affected by considerable degree of uncertainty (cf. Strenk and Wartman 2011).

References

Almagià R (1910) Studi geografici sulle frane in Italia. Mem Soc Geogr Italy 13:431

Bath M, Duda SJ (1964) Earthquake volume, fault plane area, seismic energy, strain, deformation and related quantities. Ann Geofis 17(3):353–368

Bindi D, Luzi L, Pacor F, Sabetta F, Massa M (2009) Towards a new reference ground motion prediction equation for Italy: update of the Sabetta–Pugliese (1996). Bull Earthq Eng 7:591–608

Boschi E, Guidoboni E, Ferrari G, Mariotti D, Valensise G, Gasperini P (2000) Catalogue of strong Italian earthquakes from 461 B.C. to 1997. Ann Geofis 43(4):609–868

Chang C, Chen WF, Yao JTP (1983) Seismic displacements in slopes by limit analysis. J Geotech Eng Div ASCE 110(7):860–874

Coccia S, Del Gaudio V, Venisti, N, Wasowski J (2010) Application of Refraction Microtremor (ReMi) technique for determination of 1-D shear wave velocity in a landslide area. J Appl Geophys 71:71–89. doi: 10.1016/j.jappgeo.2010.05.001

Del Gaudio V, Wasowski J (2007) Directivity of slope dynamic response to seismic shaking. Geophys Res Lett 34:L12301. doi:10.1029/2007GL029842

Del Gaudio V, Wasowski J (2011) Advances and problems in understanding the seismic response of potentially unstable slopes. Eng Geol 122:73–83. doi: 10.1016/j.enggeo.2010.09.007

Del Gaudio V, Wasowski J (2012) Application of ambient noise analysis for investigating site amplification properties of slopes susceptible to seismically induced failures. In: Proceedings 11th international and 2nd North American symposium on landslides, Banff (Canada), 2–8 June 2012

Del Gaudio V, Coccia S, Wasowski J, Gallipoli MR, Mucciarelli M (2008) Detection of directivity in seismic site response from microtremor spectral analysis. Nat Hazards Earth Syst Sci 8:751–762

Del Gaudio V, Pierri P, Frepoli A, Calcagnile G, Venisti N, Cimini G (2007) A critical revision of the seismicity of Northern Apulia (Adriatic Microplate—Southern Italy) and implications for the identification of seismogenic structures. Tectonophysics 436(1/4):9–35. doi:10.1016/j.tecto.2007.02.013

Gasperini P, Bernardini F, Valensise G, Boschi E (1999) Defining seismogenic sources from historical earthquake felt reports. Bull Seismol Soc Am 89:94–110

Harp EL, Wilson RC (1995) Shaking intensity thresholds for rock falls and slides: evidence from 1987 Whittier narrows and superstition hills earthquake strong-motion records. Bull Seismol Soc Am 85:1739–1757

ISIDe Working Group (INGV 2010) Italian seismological instrumental and parametric database: http://iside.rm.ingv.it

Jibson RW, Jibson MW (2003) Java programs for using Newmark's method and simplified decoupled analysis to model slope performance during earthquakes. U.S. Geological Survey Open-File Report 03-005, version 1.1

Keefer D (1984) Landslides caused by earthquakes. Geol Soc Am Bull 95:406–421

Kottke AR, Rathje EM (2008) Technical manual for strata. Pacific Earthquake Engineering Research Center Report 2008/10, University of California, Berkeley, California

Nakamura Y (1989) A method for dynamic characteristics estimation of subsurface using mi-crotremor on the ground surface. Q Rep Railw Tech Res Inst 30(1):25–30

Newmark NW (1965) Effects of earthquakes on dams and embankments. Géotechnique 15(2):137–160

Nogoshi M, Igarashi T (1971) On the amplitude characteristics of microtremor (part 2) (in Japanese with English abstract). J Seismol Soc Jpn 24:26–40

Murphy W, Petley DN, Bommer J, Mankelow JM (2002) Uncertainty in ground motion estimates for the evaluation of slope stability during earthquakes. Q J Eng Geol Hydrogeol 35:71–78

Paolucci R, Faccioli E, Maggio F (1999) 3D response analysis of an instrumented hill at Matsuzaki, Japan, by a spectral method. J Seismol 3:191–209

Rovida A, Camassi R, Gasperini P, Stucchi M (eds) (2011) CPTI11, the 2011 version of the parametric catalogue of Italian earthquakes. Milano, Bologna http://emidius.mi.ingv.it/CPTI

Sabetta F, Pugliese A (1996) Estimation of Response spectra and simulation of nonstationary earthquake ground motions. Bull Seismol Soc Am 86(2):337–352

Vucetic M, Dobry R (1991) Effect of soil plasticity on cyclic response. J Geotech Eng Div ASCE 117:89–107

Strenk PM, Wartman J (2011) Uncertainty in seismically induced slope deformation model predictions. Eng Geol 122:61–72

Wasowski J (1998) Understanding rainfall-landslide relationships in man-modified environment: a case history from Caramanico Terme (Italy). Environ Geol 35:197–209

Wasowski J, Del Gaudio V (2000) Evaluating seismically induced mass movement hazards in Caramanico. Eng Geol 58(3–4):291–311

Wasowski J, Lee C, Keefer D (2011) Toward the next generation of research on earthquake-induced landslides: current issues and future challenges. Eng Geol 122(1–2):1–8. doi:10.1016/j.enggeo.2011.06.001

Wasowski J, Lollino P, Del Gaudio, V, Casarano D (2004) Unraveling the case of a historic seismic slope failure—implications for local hazard assessments (abstract). EGU General Assembly (Nice, 24–30 April, 2004)

Wilson RC, Keefer DK (1985) Predicting the areal limits of earthquake–induced landsliding. In: Ziony JI (ed) Evaluating earthquake hazards in the Los Angeles region—an earth science perspective. U. S. Geological Survey Professional Paper 1360, pp 316–345

Use of Indirect Evidence for the Prehistoric Earthquake-Induced Landslides Identification

3

Alexander Strom

Abstract

Presence of large and/or long runout prehistoric rockslides is often equalized with an evidence of strong past earthquakes without providing any additional reasons in favor of such assumption—just due to enormous size and surface expression of these features. The erroneous assumption on seismic origin of a particular landslide or group of landslides would cause not only an overestimation of seismic hazard, but, also, underestimation of an overall landslide hazard due to much longer recurrence period of large earthquakes in comparison with other triggering phenomena like rainstorms. Examples of reliable substantiation of seismic origin of large rockslides based on identification of spatially distributed sedimentary features in the lacustrine environment closely timed to river damming event are presented and discussed.

1   Introduction

Presence of large and/or long runout prehistoric rockslides is often equalized with an evidence of strong past earthquakes without providing any additional reasons in favor of such assumption—just due to enormous size and surface expression of these features.

Indeed, many high magnitude earthquakes were accompanied by large bedrock landslides and rock avalanches. The 1911 Sarez earthquake (M ∼ 7.4) in the Pamirs triggered the 2.2 km³ Usoi landslide (Gaziev 1984; Schuster 2002; Ischuk, 2011; Ambraseys and Bilhamn 2012), the 1949 Khait earthquake (M7.5) in the Tien Shan—the 7.5-km long rock avalanche (Leonov 1960; Evans et al. 2009b), the 1959 Hebgen Lake earthquake (M7.1) in Montana, USA—the Madison Canyon landslide (Hadley 1964), the 1970 Ancash earthquake (M8.0) in Peru produced the Huascaran ice-rock avalanche (Plafker and Eriksen 1978), the 2002 Denali Fault earthquake (M7.9) in Alaska—several

A. Strom (✉)
Head of Seismic Hazard Assessment Department, Geodynamics Research Center—Branch of JSC "Hydroproject Institute", Volokolamskoe Shosse 2, 125993, Moscow, Russia
e-mail: a_strom2002@yahoo.co.uk

spectacular rock avalanches (Jibson et al., 2006), the 2008 Wenchuan earthquake (M8) triggered the giant Daguangbao rockslide 0.75–1.1 km^3 in volume and numerous smaller landslides and rockslides (Wu et al. 2010; Yin et al. 2011). The list can be expanded.

At the same time numerous large bedrock landslides had occurred without seismic triggering—the 1903 Frank rockslide 30 Mm^3 in volume in Canada (Krahn and Morgenstern 1976), the 1964 Aini landslide $\sim$20 Mm^3 in volume in Tajikistan (Fedorenko 1988), the 1962 Huaskaran ice-rock avalanche—the aseismic predecessor of the larger 1970 event (Evans et al. 2009a), the 1974 Mayunmarka rockslide 1.6 billion cubic meters in volume in Peru (Hutchinson and Kojan 1975), the 1987 Val Pola rock avalanche $\sim$40 Mm^3 in volume in Italy (Crosta et al. 2011), the 2000 Yigong landslide 300 Mm^3 in volume and about 10 km long in Tibet, China (Shang et al. 2003), etc. Thus, neither size of slope failure nor its abnormally long runout can prove its seismic origin itself.

If, however, the assumption on seismic origin of a particular landslide or group of landslides is erroneous, it would cause not only an overestimation of seismic hazard, but, also, underestimation of an overall landslide hazard. Direct linking of large-scale rock slope failures' formation with strong earthquakes only, which are relatively rare events with typical recurrence intervals at a particular causative fault varying from several hundred to several thousands of years, means that large bedrock landslides should occur with same recurrence. However, other natural phenomena that can trigger such slope failure (e.g. rainstorms, hurricanes, and abnormal snowmelt) are much more frequent. For example, 3 typhoons hit Taiwan annually on average (Jan et al. 2005) while large earthquake occur at this island several times per century only (Hung 2000; Cheng 2007). In the area where the 1999 M7.6 Chi–Chi earthquake induced large Tsao-Ling landslide, 5 large-scale slope failures occurred since 1862, but only three of them—in 1862, 1941, and 1999—were triggered by earthquakes. Two others—in 1942 and in 1979 were rain-induced phenomena (Hung 2000).

No doubts that seismicity, strong earthquakes in the first place, is one of the main factors leading to slopes' instability. But such large-scale bedrock landslides origin should be not just postulated, but substantiated somehow. This is especially important for the regions where historical data on various natural phenomena are available for a short time, much less than the recurrence period of large earthquakes. Several examples of such substantiation from the Tien Shan mountains are described and discussed hereafter.

2 Spatially Distributed Sedimentary Features Closely Timed to Slope Failure Event

Reliable and well-grounded assumption on seismic origin of a particular large-scale bedrock landslide could be based on the analysis of minor slope failures or liquefaction-induced features located at some distance from the master event but closely related to it in time. This can be exemplified by the Late Pleistocene Kokomeren rockslide and by the Holocene Lower-Aral rocks avalanche in Central Tien Shan, Kyrgyzstan (Fig. 3.1) both of which caused river damming.

2.1 The Kokomeren Rockslide and Dammed Lake

Rockslide about 1 km^3 in volume occurred on the 1600-m high northern slope of the Kokomeren River valley, formed a dam with maximal height up to 400 m that was deeply eroded subsequently, and a lake that impounded river valley for at least 14 km (Fig. 3.2).

Judging from the uppermost level of lacustrine sediments that have been identified (4 and 5 on Fig. 3.2), water rose at least up to 1820 m a.s.l., indicating the dams' effective height not less than 130 m. Since the river had cut a new bypass gorge through the bedrock and there are indications that the lake had been significantly

Fig. 3.1 Location of the case studies described. *1* the Kokomeren rockslide, *2* the Lower-Aral rockslide, *3* liquefaction site in the past Lower-Aral lake sediments
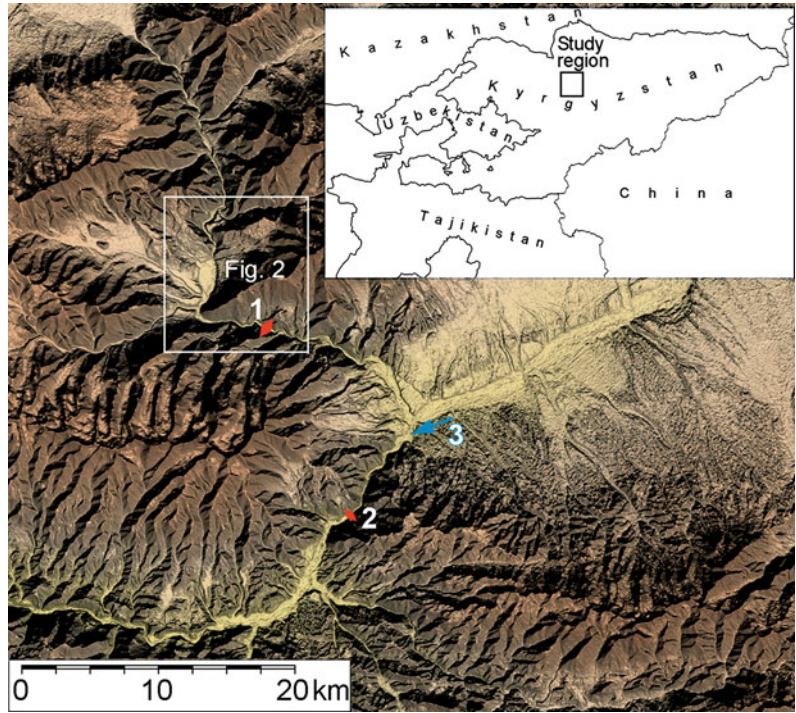
Fig. 3.2 Past lake dammed by the Kokomeren rockslide at minimal water level of 1820 m a.s.l. Hatched areas—landslide deposits; red lines with short teeth—headscarps; yellow numbered dots—outcrops mentioned in the text
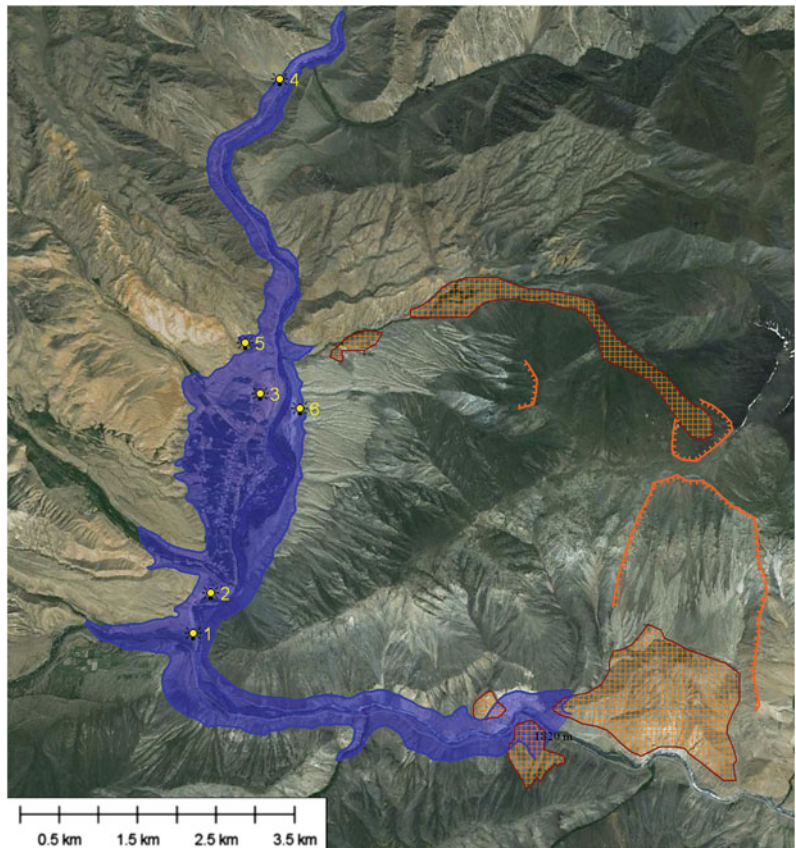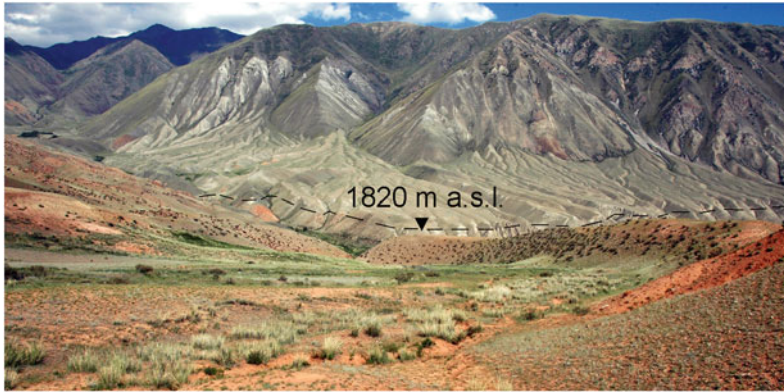
Fig. 3.3 The Kyzyl-Oi intermountain depression, whose lower part was submerged by the lake. Neogen red beds at the foreground; Paleozoic ridge with coalescing debris flow fan at the background. Active fault passes at the foot of the ridge. Elevation marks point 6 on Fig. 3.2

filled by lacustrine sediments, it was hypothesized that the water body had existed for about 1000 years (Hartwich et al. 2008).

Features that had originated simultaneously with master event should be imbedded in the stratigraphic sequence immediately bellow or within the basal layer of the lacustrine sediments. Such units were found out about 5 km upstream from the dam (from 1 to 2 on Fig. 3.2), where the lake had occupied small intermountain neotectonic Kyzyl-Oi depression. Between this site and the dam the lake had filled deep narrow gorge (see Fig. 3.2) that was impounded, most likely, shortly after damming. Considering present-day mean discharge of the Kokomeren River of about 80 m³/sec [State Water Inventory 1987], water probably appeared at this site less than in 5 days after river damming. Such time span is much less than the precision of any numerical dating method (Walker 2005).

West bank of the lake within the depression was composed of Neogene red beds and characterized by rather smooth terrain, while its east bank lies at the foot of high ridge composed of Paleozoic dark gray metasediments (Fig. 3.3). Here the main part of the lacustrine succession is represented by "classical" laminated silt (1 on Fig. 3.4), locally interbedded by alluvial gravels and debris flow sediments with semi-rounded granite clasts brought by ephemeral streams from the west.

Fig. 3.4 Lacustrine sediments in the Kyzyl-Oi depression. This exposure is between sites marked by 1 and 2 on Fig. 3.2. Here *1* laminated silt unit; *2* basal matrix supported breccia unit

This unit is underlain by 1–1.5 m thick unsorted, poorly bedded matrix-supported breccia with up to 5 cm clasts of east-bank metasediments "floating" in red matrix that originated from the reworked Neogene clay and silt brought from the west (2 on Figs. 3.4, 3.5). Besides dark-gray angular clasts there are some semi rounded "boulders" of Neogen siltstone or mudstone (at 65–80 cm on Fig. 3.5) whose roundness indicates that they were transported from a more distant zone. At some locations this

Fig. 3.5 Sedimentary features of the coarse bedded basal breccia underlying laminated silt layers

breccia is mixed with well-rounded alluvial cobbles and boulders that could be brought here from the adjacent river terrace. Basal breccia is exposed in several outcrops at a distance of about three kilometers (from point 1 to point 3 on Fig. 3.2).

It is evident that basal unit reflects initial reworking of the surficial sediments by rising water. However, presence of large amount of unrounded clasts of metasediments at a rather large distance from their source slope could be due to abnormally intensive entry of debris from the high east-bank slope caused by strong motion of the main shock and, likely, aftershocks. Most probably they were brought here by debris flows that originated on the steep opposite slope of the valley (see Fig. 3.3). Pure gravitational collapse of scree would not be able to bring debris 200–300 hundreds meters far from the slope foot.

At the southern end of this outcrop (point 1 on Fig. 3.2), which is at a closest distance from the high opposite slope, the basal breccia is replaced by chaotic clast-supported dump of angular blocks up to 30–50 cm, rarely 1 m in size (Fig. 3.6). Blocks at the upstream part of this outcrop are partially mixed with well-rounded granite boulders typical of stream facies of alluvium. This unit is a typical rockfall from the opposite—east bank of the river that collapsed, likely, directly in the stream just before the site was submerged by rising water. Similarly to the matrix-supported basal breccia it had been overlaid by laminated silt layers visible at a right upper part of Fig. 3.6.

Later on the entire succession resting within the active fault zone was tilted northward and, again later on—displaced by significant (up to several meters) right-lateral strike-slip offset along NE-SW-trending rupture, proving the recurrent style of tectonic deformations along this fault zone (Strom and Stepanchikova 2008). It can not be excluded that the Kokomeren rockslide itself could be triggered by the earthquake at the same fault. However, the surficial manifestation of that event is masked by rockfall and stream alluvium.

Lake sediments on the opposite—east bank of the river are represented by coalescing debris flow fans (can be seen on Fig. 3.3 at the background) overlying alluvial gravels. The elevation at which these fans' surface remains now shows that they were deposited at the level much higher than the level of the west-bank basal unit (compare Figs. 3.3 and 3.4). It should be noted that debris flows did not erode the top of the alluvial gravelly sediments. All this indicate that distal parts of debris flows had entered into the lake that was impounded less than in one year [volume of the lake is roughly estimated from 5 to 7×10^8 m^3, while Kokomeren present-day mean annual discharge is $2,5 \times 10^9$ m^3/year (State Water Inventory 1987)].

There is also some not very clear evidence that these fans had buried deposits of several minor rock avalanches, similar to a larger one that had collapsed from the northern side of the same ridge where the Kokomeren rockslide had originated (see Fig. 3.2). Ambiguity of such

Fig. 3.6 Accumulation of
angular blocks of
metasediments mixed at
the right side with alluvial
granite boulders. Site is
about 70–100 m
downstream from the
outcrop shown on Fig. 3.4

interpretation comes from the fact that both rock avalanches and subsequent debris flows had exactly the same source zone and, thus, are composed of very similar material. I want to point out that formation of debris flows is typical of the epicentral zones of strong earthquakes, which could be exemplified by the events following the 2008 Wenchuan earthquake (Tang et al. 2011).

Additional evidence in favor of the Kokomeren landslide seismic origin are: (A) it fell on the terrace about 100 m high above that time riverbed, which excludes slope undercutting by erosion as possible alternative triggering factor; (B) active fault displacing river terraces few hundreds meters downstream from the dam site stretches directly toward the headscarp area (Strom and Stepanchikova 2008).

2.2 The Lower-Aral Rock Avalanche and Dammed Lake

One more case study allowing some speculations on the simultaneity of the master landslide and of minor sedimentary features could be found in the same valley, 13 km downstream from the Kokomeren landslide. Here, immediately south from the Aral village, in the road cut one can observe laminated lacustrine silt overlying thick unsorted and poorly bedded mixture of coarse arkose sand and detritus representing the reworked granite talus (Fig. 3.7).

This site is located at the distal part of the past lake dammed about 10 km downstream by the Holocene Lower-Aral rock avalanche that had blocked the Kokomeren River by a 70-m high dam (2 on Fig. 3.1).

The most interesting peculiarity of this outcrop is the presence of liquefaction-induced features—the lowermost layers of laminated silt had sank into the underlying basal coarser unit, while younger laminae are not subjected to such deformations. It means that both units—massive poorly sorted basal layer and overlying laminae were in liquefiable state and, thus, liquefaction occurred soon after these units deposition.

The observed features could be explained as follows. The main shock of an earthquake (of course not of the same that, likely, triggered the Kokomeren rockslide) caused rock avalanche that blocked the valley. The narrow gorge was impounded rather soon after the event—less than in one month approximately, judging from the $2{,}5 \times 10^9$ m^3/year mean discharge of the river (State Water Inventory 1987) and lake volume of about 1.2×10^8 m^3. Slope reworking by rising water caused formation of the basal unsorted unit (1 on Fig. 3.7), and, later on, gave place to deposition of overlying initial laminated silt

Fig. 3.7 Lacustrine sediment accumulated at the tail-end of the past lake dammed by the Lower-Aral rockslide. *Above*—an overview. *Below*—marked part photographed in the shadow. *1* basal massive coarse arkose sand; *2* lower part of silt unit affected by liquefaction, whose portion in the center sank in the basal sand; *3* upper part of silt unit (boundary is marked by beheaded arrows) represented by nearly horizontal laminated layers

layers (2 on Fig. 3.7). Liquefaction of loose water-saturated sediments and formation of liquefaction-induced features could have been caused by strong aftershock(s) that occurred after the primary earthquake. Subsequent lake sedimentation was not disturbed by any dynamic effects and resulted in accumulation of undisturbed laminated silt layers (3 on Fig. 3.7).

Quite limited extent of the outcrop (practically the entire site can be seen on the upper part of Fig. 3.7), and absence of other similar exposures do not allow such sound conclusion on seismic origin of the features described as, for example, in the Issyk-Kul basin, where liquefaction-induced features were observed in the numerous kilometers-long exposures of Quaternary lacustrine sediments (Korjenkov 2000). Nevertheless, this case study demonstrates another type of the phenomena distant from the master event in space but closely linked with it in time, which allows assumption of seismic origin of both.

3 Discussion

According to Malamud et al. (2004) strong earthquakes and other energetic triggering phenomena like typhoons and snowmelt usually produce one or few large and extra-large landslides along with numerous medium and minor features. Indeed, the 1911 M7.4 Sarez earthquake triggered only one gigantic Usoi landslide without anything else comparable (Ischuk 2011), the same year M ~ 8.2 Kemin earthquake—four large bedrock landslides up to several tens of million m^3 in volume and hundreds small and medium-size landslides and rockfalls (Bogdanovich et al. 1914), the 2005 M7.6 Kashmir earthquake—one extra-large Hattian Bala rockslide ~85 Mm^3 in volume and numerous smaller events (Owen et al. 2008), the 2008 M7.9 Wenchuan earthquake—one gigantic Daguangbao bedrock landslide 0.75–1.1 km^3 in volume (Wu et al. 2010; Yin
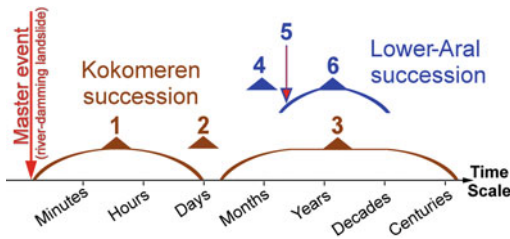
Fig. 3.8 Succession of events that occurred after formation of large-scale Kokomeren landslide (*brown*) and Lower-Aral landslide (*dark-blue*). Large *red arrow*—master event likely triggered by strong earthquake. *1* rockfalls and abnormal talus formation; *2* deposition of poorly sorted breccia at the base of the dammed lake sediments; *3* laminated lacustrine silt accumulation; *4* deposition of poorly sorted coarse arkose sand at the base of the dammed lake sediments; *5* formation of the liquefaction-induced features likely triggered by strong aftershock; *6* laminated lacustrine silt accumulation

et al. 2011), several much smaller landslides—one-two orders less in size and more than 60,000 medium and small slope failures (Yin et al. 2009; Huang and Li 2009), etc.

It is evident that hundreds and thousand years after the event it would be difficult to proof that several large-scale slope failures occurred simultaneously, though it is one of the most widely used criteria, allowing seismically triggered landslides identification (Crozier 1992). This criterion is often used for landslides located close to a large active fault (e.g. Belousov et al. 1994, Bull 1996). Such approach requires extensive dating, which is not always easy to perform and whose precision could be not as high as necessary.

Case studies described above allow sufficiently sound conclusion on very close timing of master events—large-scale slope failures and of other phenomena that occur at a rather large distance from the former ones. In the Kokomeren case these are rockfalls and increased talus accumulation that could occur within few days between rockslide formation and rise of water in the reservoir. In the Lower-Aral case liquefaction of loose lake sediments could take place shortly (likely from months to years) after river-damming landslide (Fig. 3.8). Close timing, in turn, along with sound reasoning that spatially distributed minor sedimentary features could be triggered by seismic shaking,

provide strong, though indirect argument of seismic triggering of master events.

Back analysis of slope stability can be very useful to discriminate between seismic and non-seismic origin of the master landslide. In the above cases, however, one can not reconstruct the pre-sliding topography and structural pattern of the detachment zone with relevant accuracy. This prevents reliable estimate of safety factor leaving us with indirect evidence only.

In the two landslide cases discussed, the "classical" silt laminae are underlined by unsorted or poorly sorted unit up to 1–1.5 m thick. This reflects the initial stage of the impoundment when rising water reworks the local slope materials. It could be hypothesized that abnormally intensive material reworking was supported by additional drift of debris or by its loosening caused by strong seismic shaking. Confirmation or disproof of this assumption requires more studies of the sediments accumulated in the existing and past lakes dammed naturally or artificially.

4 Conclusions

Careful analysis of basal units of sediments from landslide-dammed lakes allows identification of spatially distributed sedimentary features closely timed to the main landslide occurrence even if we have no possibility to date them precisely. Time span between phenomena that produced both master and accompanying events could be much less than the precision of most of modern dating methods (Walker 2005).

Convincing evidence that spatially distributed minor sedimentary features closely timed to master event could be triggered by seismic shaking, provide additional, though indirect argument of seismic triggering of the river damming landslide itself.

References

Ambraseys N, Bilhamn R (2012) The Sarez-Pamir earthquake and landslide of February 1911. Seismol Res Lett 83:294–314

Belousov TP, Skobelev SF, Strom AL (1994) On estimation of the recurrence period of strong earthquakes of the central Tien Shan (according to the data of absolute geochronology). J Earthquake Pred Res 3:226–236

Bogdanovich KI, Kark IM, Korolkov BYa, Muchketov DI (1914) Earthquake of the 4th January 1911 in the northern districts of the Tien Shan. Tr Geol Com Ser 89 (in Russian)

Bull WB (1996) Prehistorical earthquakes on the alpine fault, New Zealand. J Geophys Res 101(B3):6037–6050

Cheng C-T, Chiou S-J, Lee C-T, Tsai Y-B (2007) Study on probabilistic seismic hazard maps of Taiwan after Chi–Chi earthquake. J GeoEng 2(1):19–28

Crosta GB, Frattini P, Fusi N, Sosio R (2011) Formation, characterisation and modeling of the Val Pola Rock-Avalanche Dam (Italy). In: Evans SG, Hermanns R, Scarascia-Mugnozza G, Strom AL (eds), Natural and artificial rockslide dams. Lecture Notes in Earth Sciences 133:347–368

Crozier MJ (1992) Determination of paleoseismicity from landslides. In: Bell DH (ed) Landslides (Glissements de terrain). Proceedings of the 6th international symposium, Christchurch, New Zealand 2:1173–1180

Evans SG, Bishop NF, Smoll LF, Murillo PV, Delaney KB, Oliver-Smith A (2009a) A re-examination of the mechanism and human impact of catastrophic mass flows originating on Nevado Huascarán, Cordillera Blanca, Peru in 1962 and 1970. Eng Geol 108:96–118

Evans SG, Roberts NJ, Ischuck A, Delaney KB, Morozova GS, Tutubalina O (2009b) Landslides triggered by the 1949 Khait earthquake, Tajikistan, and associated loss of life. Eng Geol 109(3–4):195–212

Fedorenko VS (1988) Rockslides and rockfalls and their prediction. Moscow State University Publishing House (in Russian)

Gaziev E (1984) Study of the Usoi landslide in Pamir. In: Proceedings of 4th international symposium on landslides, Toronto, 1:511–515

Hadley JB (1964) Landslides and related phenomena accompanying the Руипут Lake earthquake of August 17, 1959. USGS Professional Paper 345-K:107–138

Hartvich F, Mugnai F, Proietti C, Smolková V, Strom A (2008) A reconstruction of a former rockslide-dammed lake: the case of the Kokomeren river valley (Tien Shan, Kyrgyzstan), Geophysical research abstracts 10 EGU general assembly 2008

Huang RQ, Li WL (2009) Analysis of the geo-hazards triggered by the 12 May 2008 Wenchuan earthquake, China. Bull Eng Geol Environ 68:363–371

Hung J–J (2000) Chi–Chi earthquake-induced landslides in Taiwan. Earthquake Eng Eng Seismol 2(2):25–33

Hutchinson JN, Kojan E (1975) The Mayunmarca landslide of 25th April 1974, Peru, Report Ser. No. 3124/RMO. RD/SCE, UNESCO, Paris

Ischuk AR (2011) Usoi rockslide dam and lake sarez, Pamir mountains, Tajikistan. In: Evans SG, Hermanns R, Scarascia-Mugnozza G, Strom AL (eds.), Natural and artificial rockslide dams. Lecture Notes in Earth Sciences 133:423–440

Jan C-D, Chen C-L (2005) Debris flows cased by Typhoon herb in Taiwan. In: Jacob M, Hungr O (eds) Debris-flow hazards and related phenomena. Praxis. Springer, Heidelberg, pp 539–556

Jibson RW, Harp EL, Schulz W, Keefer DK (2006) Large rock avalanches triggered by the M 7.9 denali fault, Alaska, earthquake of 3 November 2002. Eng Geol 83:144–160

Korjenkov AM (2000) Seismogenic convolutions in soft lacustrine sediments of the Issyk-Kul Lake, Tien Shan, Kyrgyzstan—initial report. J Earthquake Pred Res 8:514–519

Krahn J, Morgenstern NR (1976) Mechanics of the frank slide. In: Rock engineering for foundations and slopes, American Society of Civil Engineers 1:309–331

Leonov NN (1960) The 1949 Khait earthquake and geological conditions of its occurrence. In: Proceedings of Russian academy of sciences, Geophysical series, No 3:409–424 (in Russian)

Malamud BD, Turcotte DL, Guzzetti F, Reichenbach P (2004) Landslides, earthquakes and erosion. Earth Planet Sci Lett 229:45–59

Owen LA, Kamp U, Khattak GA, Harp EL, Keefer DK, Bauer MA (2008) Landslides triggered by the 8 October 2005 Kashmir earthquake. Geomorphology 94:1–9

Plafker G. Eriksen GE (1978) Nevados Huascaran avalanches, Peru. In: Voight B (ed) Rockslides and avalanches 1:277–314

Schuster RL (2002) Usoi landslide dam, southeastern Tajikistan. In: Proceedings of International Symposium on landslide risk mitigation and protection of cultural and natural heritage, Kyoto 489–505

Shang Y, Yang Z, Li L, Liu D, Liao Q, Wang Y (2003) A super-large landslide in Tibet in 2000: background, occurrence, disaster, and origin. Geomorphology 54:225–243

State Water Inventory (1987) Perennial data on the mainland superficial water regime and resources. IX, Kyrgyz SSR. Leningrad, Gidrometeoizdat Publishing House. (In Russian)

Strom AL, Stepanchikova P (2008) Seismic triggering of large prehistoric rockslides: Pro and Con case studies. In: Proceedings of the international conference on management of landslide hazard in the Asia-Pacific region (Satellite symposium of the first world landslide forum) 202–211

Tang C, Zhu J, Ding J, Ciu Xchen L, Zhang J (2011) Catastrophic debris flows triggered by a 14 August 2010 rainfall at the epicenter of the Wenchuan earthquake. Landslides 8:485–497

Walker M (2005) Quaternary dating Methods. John Willey & Sons Ltd, Chichester

Wu S, Wang T, Shi L, Sun P, Shi J, Li B, Xin P, Wang H (2010) Study on catastrophic landslides triggered by 2008 great Wenchuan earthquake, Sichuan. China J Eng Geol 18(2):145–159

Yin Y, Wanf F, Sun P (2009) Landslide hazards triggered by the 2008 Wenchuan earthquake, Sichuan, China. Landslides 6:139–151

Yin Y, Zheng W, Li X, Sun P, Li B (2011) Catastrophic landslides associated with the M8.0 Wenchuan earthquake. Bull Eng Geol Environ 70(1):15–32

Bhedetar Landslide, Eastern Nepal: Aftermath of the Sikkim Earthquake (18th September 2011)

4

Vishnu Dangol, Hiroshi Yagi and Daisuke Higaki

Abstract

The Bhedetar Landslide is one of the numerous landslides in Eastern Nepal that were triggered by the 18th September 2011 Sikkim earthquake (M: 6.9). The landslide is a rock avalanche type which caused serious damages to the 69+000 and 69+500 chainages of the Koshi Highway. Huge boulders were fallen down from the hill slope and rolled down hitting and sweeping the road surface at 69+000 chainage and damaging the road surface at 69+500 chainage located just below the 69+000 chainage. The road was fully blocked for the traffic movement and pedestrians for two and half days. Even at the time of our study (first week of April, 2012), the road sections at 69+000 and 69+500 chainages were single lane temporary track with earthen surface and huge rock blocks were in both sides of the road. This present paper describes the general condition of the Bhedetar Landslide and attempts to decipher causes of sliding besides the main trigger.

1   Introduction

Due to the 18th September 2011 Sikkim earthquake (M: 6.9), several "new" and "reactivated" landslides have occurred in Eastern Nepal and India right from the Himalayan foot-hill region up to the higher Himalayan range. The destructive earthquake caused serious damages on various civil structures in the eastern part of Nepal.

It is also pertinent to mention here that moderate to heavy monsoon rainfall prior to the occurrence of the earthquake, during and post

V. Dangol (✉)
Department of Geology, Tri-Chandra Campus,
Tribhuvan University, Kathmandu, Nepal
e-mail: vdangol@yahoo.com

H. Yagi
Faculty of Education, Art and Science, Yamagata
University, 1-4-12 Koshirakawa machi,
Yamagata 990-8560, Japan

D. Higaki
Faculty of Agriculture and Life Science,
Hirosaki University, 1 Bunkyo-cho,
Hirosaki 036-8561, Japan
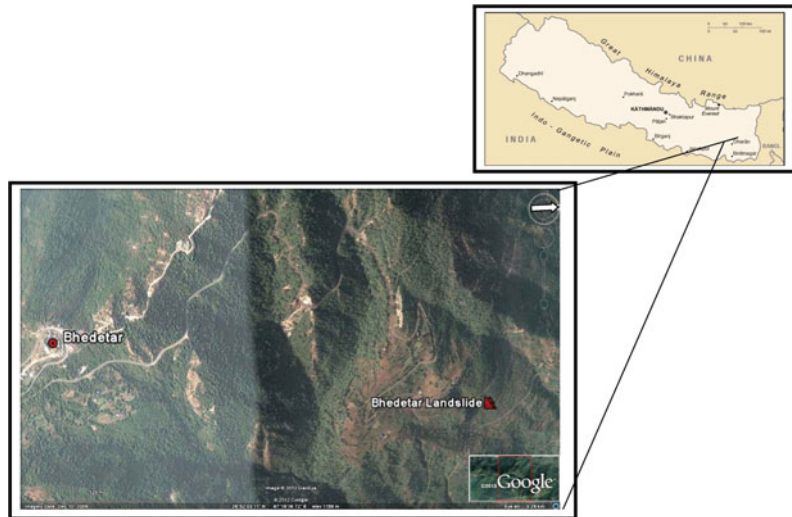
earthquake event is reported from the area. The rainfall contributed to some extent in lowering the shearing strengths of already-loosened (due to earthquake shaking) slope forming mass and ultimately triggered the landslide just immediately after the earthquake shock.

The road sections at 69+000 and 69+500 chainages of the Koshi Highway is completely destroyed by the earthquake induced Bhedetar Landslide. The landslide is a rock avalanche type and is located at approximately 6 km from Bhedetar along the Koshi Highway (Fig. 4.1). Huge boulders were fallen down from the hill slope and rolled down hitting and sweeping the road surface at 69+000 chainage and damaging the road surface at 69+500 chainage located just below the 69+000 chainage (Fig. 4.2).

The road was fully blocked for the traffic movement and pedestrians for two and half days. By concentrated efforts of the Department of Roads, District Administration Offices of Dhankuta and Sunsari, Nepal Army, Nepal Police, Armed police and all other concerned authorities, the highway was successful opened by 15:00 of 21st September, 2011. Due to various problems and emergency conditions, temporary tracks are made such that they are single lane with rough (earthen) surface. Original track at 69+000 chainage needs to be reconstructed by replacing the existing damaged retaining structures and that at 69+500 chainage is required to be rehabilitated by removing/

breaking the huge boulders on the road surface and maintaining it (DoR 2011).

2　Geology of the Study Area

The study area falls within the Lesser Himalayan region. Regionally, the area belongs to the Midland Group of Precambrian age (PEPP 2009), which is further subdivided into four formations, namely Dubbidanda Formation (Dbd), Sulikot Formation (Sl), Chiuribas Formation (Cb) and Bhedetar Formation (Bl). The Dubidanda Formation is represented by greenish grey quartzite with chloritic phyllite and augen gneiss. The Sulikot Formation (Sl) is composed of fine- to medium-grained grey quartzite and grey phyllite, whereas the Chiuribas Formation (Cb) contains green phyllite with grey, purple slate and grey quartzite. The Bhedetar Formation is made up of pink quartzite with purple slate and grey quartzite. The Bhedetar Landslide lies within the Dubbidanda Formation (Dbd).

3　Earthquake Event

The **2011 Sikkim earthquake** (Event ID usc0005wg6) was a magnitude 6.9 (M_w) earthquake centered within the Kanchenjunga Conservation Area (27.723°N, 88.064°E), near

Fig. 4.2 An overview of Bhedetar landslide

Table 4.1 Casualties by country (http://en.wikipedia.org/wiki/2011_Sikkim_earthquake)

Country		Deaths
	India	97
	China	7
	Nepal	6
	Bhutan	1
	Bangladesh	0
Total		111
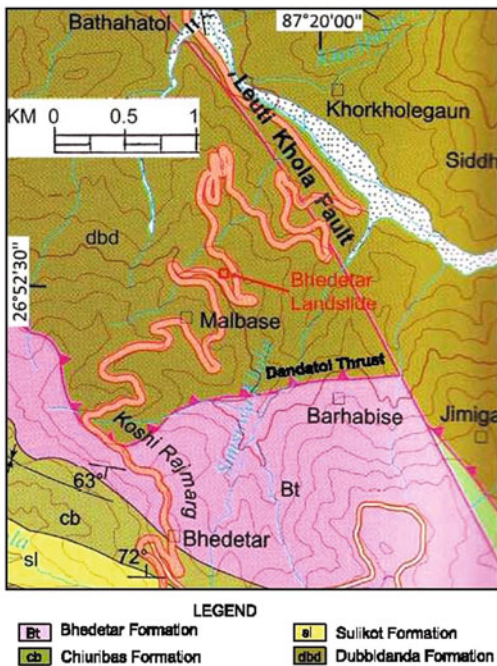
Fig. 4.3 Geological map of study area (modified after PEPP 2009)

the border of Nepal and the Indian state of Sikkim, at 18:10 IST (12:40 UTC) on Sunday, 18th September 2011 (http://earthquake.usgs.gov/earthquakes/recenteqsww/Quakes/usc0005wg6.

php) The earthquake was felt across northeastern India, Nepal, Bhutan, Bangladesh and southern Tibet.

The earthquake struck near a mountainous, albeit very populous region near the Sikkim–Nepal border; most of the structures were reported to be highly vulnerable to earthquake shaking. Upon impact, tens of thousands of residents evacuated their homes, and many areas suffered from communication and power outages. The strong shaking caused significant building collapse and mudslides; at least 111 people were confirmed killed by the effects of the earthquake, and hundreds of others sustained injuries. As the earthquake occurred in the monsoon season, heavy rain and landslides rendered rescue work more difficult (Fig. 4.3).

Initial analyses suggest the earthquake was complex, likely a result of two events occurring close together in time at depths of 19.7 km beneath the Earth's surface. At the latitude of the September 18 earthquake, the India plate converges with Eurasia at a rate of approximately 46 mm/year towards the north-northeast. The broad convergence between these two plates has resulted in the uplift of the Himalayas, the world's tallest mountain range. The preliminary focal mechanism of the earthquake suggests strike slip faulting, and thus an intraplate source within the upper Eurasian plate or the underlying India plate, rather than occurring on the thrust interface plate boundary between the two.

USGS ShakeMap : SIKKIM, INDIA
Sun Sep 18, 2011 12:40:48 GMT M 6.9 N27.72 E88.06 Depth: 19.7km ID:c0005wg6

Map Version 2 Processed Sun Sep 18, 2011 08:57:05 AM MDT − NOT REVIEWED BY HUMAN

PERCEIVED SHAKING	Not felt	Weak	Light	Moderate	Strong	Very strong	Severe	Violent	Extreme
POTENTIAL DAMAGE	none	none	none	Very light	Light	Moderate	Moderate/Heavy	Heavy	Very Heavy
PEAK ACC.(%g)	<.17	.17-1.4	1.4-3.9	3.9-9.2	9.2-18	18-34	34-65	65-124	>124
PEAK VEL.(cm/s)	<0.1	0.1-1.1	1.1-3.4	3.4-8.1	8.1-16	16-31	31-60	60-116	>116
INSTRUMENTAL INTENSITY	I	II-III	IV	V	VI	VII	VIII	IX	X+

At least 111 people were killed in the earthquake (Table 4.1). Most of the deaths occurred in Sikkim, with reports of fatalities in and near Singtam in the East Sikkim district (http://en.wikipedia.org/wiki/2011_Sikkim_earthquake). Several buildings collapsed in Gangtok. Eleven are reported dead in Nepal, including three killed when a wall collapsed in the British Embassy in Kathmandu. Elsewhere, structural damage occurred in Bangladesh, Bhutan, and across Tibet; another seven fatalities were confirmed in the latter region.

Sikkim experienced three aftershocks since the earthquake, occurring at magnitudes of 5.7, 5.1, and 4.6 (M_w) within 30 min of the initial earthquake. Kathmandu experienced two aftershocks that both had a magnitude of 4.8 M_w. The aftershocks had no serious impact in the region. At least 20 aftershocks back-to-back throughout the night created panic in the Gangtok. On 19th September, tremors shook some parts of Maharashtra measuring 3.9 (Mw) at around 06:30 IST including Latur, Osmanabad and Solapur districts. However, no loss of life or property was reported (Fig. 4.4).

4   Bhedetar Landslide

The Bhedetar Landslide is located at approximately 6 km from Bhedetar along the Koshi Highway (Latitude: N 26° 52′ 33′, Longitude: E 87° 19′ 31″). It is one of the numerous landslides in Eastern Nepal that were triggered by the 18th September 2011 Sikkim earthquake (M: 6.9). The landslide is a rock avalanche type which

Fig. 4.5 Slicken side planes on quartzite with stations

completely destroyed the road sections at 69+000 and 69+500 chainages of the Koshi Highway. Huge boulders were fallen down from the hill slope and rolled down hitting and sweeping the road surface at 69+000 chainage and damaging the road surface at 69+500 chainage located just below the 69+000 chainage.

The landslide zone from crown to toe is almost bare and is covered by debris. Around the landslide zone, the slopes are covered by small trees and bushes. Some of the boulders are fairly large (more than 8 m in length) with striation marks on slicken side planes (Fig. 4.5). The average size of boulders is 1.5 m.

The length of Bhedetar Landslide is nearly 150 m and the width is approximately 40 m. The width is less than 30 m at 69+000 chainage, whereas it is more than 50 m at 69+500 chainage. The natural slope at the landslide zone is N 65° E, which is also the movement direction of the masses detached from hill side. Towards the hill side the slope is steeper ($\sim 60°$) than on the valley side ($\sim 40°$).

The rock in the landslide zone is represented by light grey to white quartzite belonging to the Dubbidanda Formation (Dbd) of Precambrian Midland Group. The rock is massive, but with open cracks/joints. The discontinuity planes especially the foliation planes are iron stained indicating good water movement. They are slightly to moderately weathered.

The landslide (rock avalanche) was triggered by the 18th September 2011 Sikkim earthquake (M: 6.9). The main causes of the avalanche was open joints and cracks along the discontinuity planes, some of which probably had infilling materials. At the same time the joint planes exposed at surface were weakened by weathering. There was moderate to heavy monsoon rainfall prior to the occurrence of the earthquake, during and post earthquake event. The rainfall also contributed to some extent in lowering the shearing strengths of already-loosened (due to earthquake shaking) slope forming mass and ultimately triggered the just immediately after the earthquake shock.

5   Conclusions

1. The Bhedetar Landslide triggered by the 18 th September 2011 Sikkim earthquake (M: 6.9) is a rock avalanche. The hill side slope of the landslide is steeper ($\sim 60°$) than the valley side slope ($\sim 40°$).
2. Huge boulders averaging in length of 1.5 m (some more than 8 m in length) were fallen down from the hill side and rolled down sweeping the road surface and destroying retaining structures at 69+000 chainage and blocking the road at 69+000 and 69+500 chainages. The road was completely blocked for two and half days.
3. The moderate to heavy monsoon rainfall prior to and during the occurrence of the earthquake might have lowered the strength of slope forming mass, making it easy to slide down.
4. Besides the major triggering factor, i.e. 18th September 2011 Sikkim earthquake, rock structures, weathering and infilling materials in open discontinuities are underlying causes of the landslide.

References

DoR (Department of Roads, Nepal) (2011) Report on earthquake damaged road (Koshi Highway), Unpublished Report, Kathmandu, Nepal, p 3

PEPP (Petroleum Exploration Promotion Project, Department of Mines and Geology, Nepal) (2009) Geological map of parts of Sunsari, Morang and Dhankuta districts, Eastern Nepal, Scale 1:50,000, Kathmandu, Nepal

http://earthquake.usgs.gov/earthquakes/recenteqsww/Quakes/usc0005wg6.php

http://en.wikipedia.org/wiki/2011_Sikkim_earthquake

Classification of the Geomorphology, Geology and Movement Types of Earthquake Landslides

5

Daisuke Higaki and Shinro Abe

Abstract

Various types of landslides have been induced by the past earthquakes in Japan and outside of the country. This study aims to classify the geomorphology, geology, and types of movement at the sites of earthquake landslides including those of the 2011 Tohoku Earthquake. Earthquake landslides show common movement types with similar geological properties. They are (1) translational slides in ridges and cuestas with Tertiary–Quaternary well-bedded sedimentary rocks, (2) flows in areas with unconsolidated Quaternary volcanic sediments, (3) shallow rotational slides at ridges in areas of volcanic rocks, and (4) rock failures and toppling in areas of granite, accompanied by the flow of weathered granite. Many of the earthquake landslides occur within a 30 km distance of the epicenter for earthquakes up to magnitude 7. A magnitude of 8 and above can often induce rock slides at locations over 100 km away. Flow of unconsolidated volcanic sediment and rock failures of consolidated bedrock occurred at locations 200–300 km away. These indicate that magnitude 8 is the line of demarcation at which the relationship between the distance from the epicenter to landslide sites and the movement types changes significantly. The scale of the earthquake fault may be the cause of it. Many recent earthquake landslides have also been observed at residential embankments in Japan.

1 Introduction

Large-scale onshore earthquakes, inducing landslides of various types have occurred continuously, for the past 10 years in Japan. Abe and Hayashi (2011) previously reported on the relationship between the types of earthquake-induced landslides (henceforth, earthquake landslides) in Japan and the geomorphological

D. Higaki (✉)
Hirosaki University, 3 Bunkyo-cho, Hirosaki-shi, Aomori-ken, 036-8561, Japan
e-mail: dhigaki@cc.hirosaki-u.ac.jp

S. Abe
Okuyama Boring Co. Ltd, 10-39 Shinmeicho, Yokote-shi, Akita-ken 013-0046, Japan
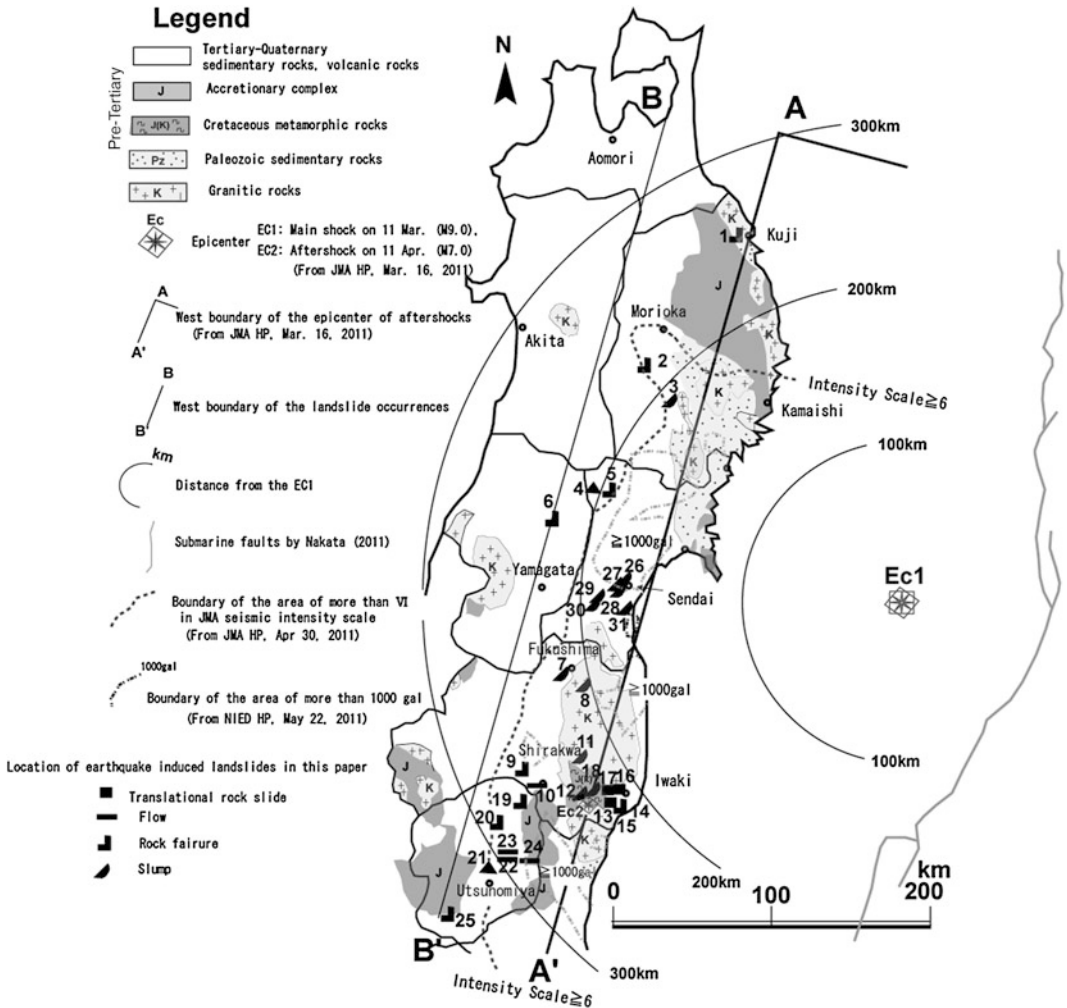
Fig. 5.1 Locations of the landslides by the 2011 off the Pacific Coast of Tohoku Earthquake and geological distribution

and geological properties of the landslide sites. Many earthquake landslides occurred across the Tohoku and northern Kanto regions following the 2011 large-scale Tohoku earthquake (*M*9.0) that occurred in the oceanic trench. This study analyzes the geomorphology, geology, and types of movement at the sites of earthquake landslides, including those triggered by the Tohoku earthquake.

The results of this study confirmed that earthquake landslides share common movements (with respect to the distance from the earthquake fault, i.e., epicenter) in areas with certain geomorphological and geological properties.

2 Overview of the Landslides that Occurred During the 2011 Tohoku Earthquake

Landslides that occurred during the 2011 Tohoku earthquake and its aftershocks were distributed along a belt extending from the Tohoku region to northern Kanto; many of which belong to the Tertiary and Quaternary geological system. The aftershock on April 11 (*M*7.0) was an onshore earthquake whose focus was located directly above the earthquake fault. This aftershock triggered landslides in the pre-Tertiary metamorphic rocks and Tertiary mudstone
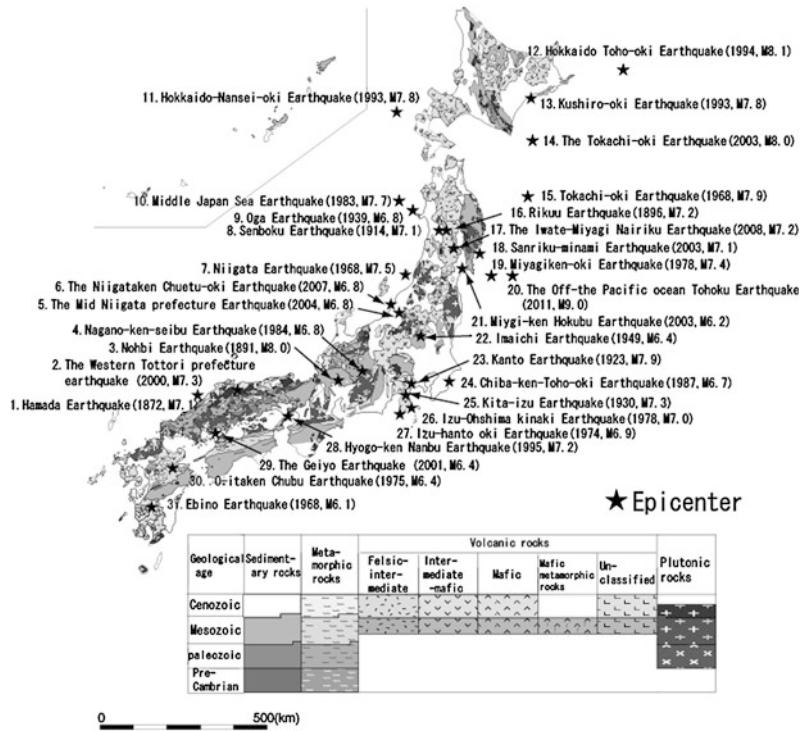
bedrocks. The area of landslide occurrence was approximately 600 km in length and 70 km inland from the western edge of the aftershock area. Tertiary pumice tuff bedrock failed, and a flow of Quaternary unconsolidated volcanic deposits occurred over 300 km inland from the epicenter. Slope movements also occurred in numerous hilly residential-area embankments in Sendai, Fukushima, and Iwaki. The intensity of the earthquake at these landslide sites was over 6 according to the Japanese Meteorological Agency (JMA) scale, and earthquake acceleration was in the range of 500–1,000 gal (Fig. 5.1).

3 Movement Types and Geomorphological and Geological Properties of Recent Earthquake Landslides in Japan

Many large-scale earthquakes have been recorded historically in Japan. Thirty-one scientific articles have chronicled earthquake landslides—

from the 1872 Hamada earthquake up to the 2011 earthquake off the Pacific Coast of Tohoku (Abe and Hayashi 2011) (Fig. 5.2). Many of these recorded magnitudes of over 6. Of these, earthquakes with magnitudes over 8 included the 1994 Eastern Hokkaido Coastal earthquake (M8.1) and the 2011 Tohoku earthquake (M9.0). Many earthquake landslides occur at magnitudes above 5 on JMA scale (Usami 1996; Japan Meteorological Agency 2008) about half of these are on shore earthquakes.

On the basis of the work of Abe and Hayashi (2011), the geomorphological and geological characteristics and the movement types of earthquake landslides are summarized below.

3.1 Areas of Quaternary Unconsolidated Volcanic Deposits

In earthquake landslides caused by offshore earthquakes (e.g., the 1974 Izu Peninsula Coastal earthquake and the 1968 Tokachi-Oki earthquake) and onshore earthquakes (e.g., the 1949 Imaichi

earthquake and the 1984 Western Nagano earthquake), shallow disintegrative slides and flows of unconsolidated volcanic sediment (volcanic ash, pumice, scoria, etc.) have been known to occur (Okusa et al. 1978). In the Western Nagano earthquake, a large-scale landslide from Mt. Ontakesan evolved into a debris flow, reaching 12 km downstream (Inokuchi 1985). During the 2011 Tohoku earthquake, flow type landslides also occurred along hillsides and terrace cliffs of southern Fukushima Prefecture and northeastern Tochigi Prefecture.

3.2 Areas of Tertiary–Quaternary (Pleistocene) Sedimentary Rocks

Landslides during the 1914 Northern Akita Prefecture earthquake (Abe and Takahashi 1997) and the 2004 Chuetsu earthquake (Abe et al. 2006; Takahashi et al. 2005), and landslides on Okushiri Island during the 1993 Hokkaido Southwestern Offshore earthquake (Tanaka 1994), occurred as translational slides in well-bedded sedimentary rocks such as Tertiary mudstone and siltstone. These landslides include both primary and re-activated types (e.g., The Japan Landslide Society, 2007). During the 2008 Iwate and Miyagi inland earthquake, a large-scale translational slide moved ignimbrite cap rocks 350 m over alternate layers of sandstone, mudstone, and siltstone from Pleistocene volcanic caldera deposits (Moriya et al. 2010). These translational slides often occur in cuesta and mountain ridges, with a sandstone–mudstone–siltstone alternating layer as the sliding surface. Translational slides were observed to occur during the 2011 Tohoku earthquake in areas of Tertiary mudstone in places such as Iwaki, Fukushima and Matsushima, Miyagi.

3.3 Areas of Pre-tertiary Metamorphic and Sedimentary Rocks

Examples of earthquakes that induced landslides in areas of pre-Tertiary metamorphic and sedimentary rocks include the 1891 Nohbi earthquake, the 1994 Hokkaido Eastern Offshore Earthquake, and the 2011 Tohoku earthquake.

The Nohbi earthquake caused toppling along the earthquake fault over entire mountain slopes, with disintegrative slides occurring in many places from the head to the end of the slope (Tabata and Hara 1999). After the 1994 Hokkaido Eastern Offshore Earthquake, primary large-scale translational slides were reported to have occurred in the alternating layers of Cretaceous hard shale and fine-grained sandstone (Tajika 2009). During the April 11 aftershock of the 2011 Tohoku earthquake, slumps were confirmed in pre-Tertiary crystalline schists that were fractured near the earthquake fault.

3.4 Granite Belt

Earthquake landslides occurred in granite belts during the 1923 Kanto earthquake, the 2000 Western Tottori earthquake, and the 2001 Geiyo earthquake. Such cases were generally not found in relation to the 2011 Tohoku earthquake, except for a few small-scale shallow slides in the Abukuma Mountains. Many of the earthquake landslides in granite belts occurred due to disintegrative slides and flow of arenaceous granite.

3.5 Distributional Area of Volcanic Rock Types

Shallow surface slides in the distributional area of Lower Miocene andesite and rhyolite during the 1896 Rikuu earthquake (Abe and Takahashi 1997) and toppling of molten basalt rocks during the 2000 Western Tottori earthquake (Yamashita 2002) are some of the reported cases in volcanic rock areas. Rock failures of pumice tuff also occurred in various parts of Fukushima Prefecture during the 2011 Tohoku earthquake.

3.6 Residential Embankments

Slope movement of residential embankments occurred at numerous sites. Both the 1978 Miyagiken-oki Earthquake and the 2011 Tohoku earthquake damaged such embankments in Sendai and Shiroishi in Miygai Prefecture.

Figure 5.3 classifies the geomorphology, geology, and movement types of the landslides reported by Abe and Hayashi (2011) on the basis
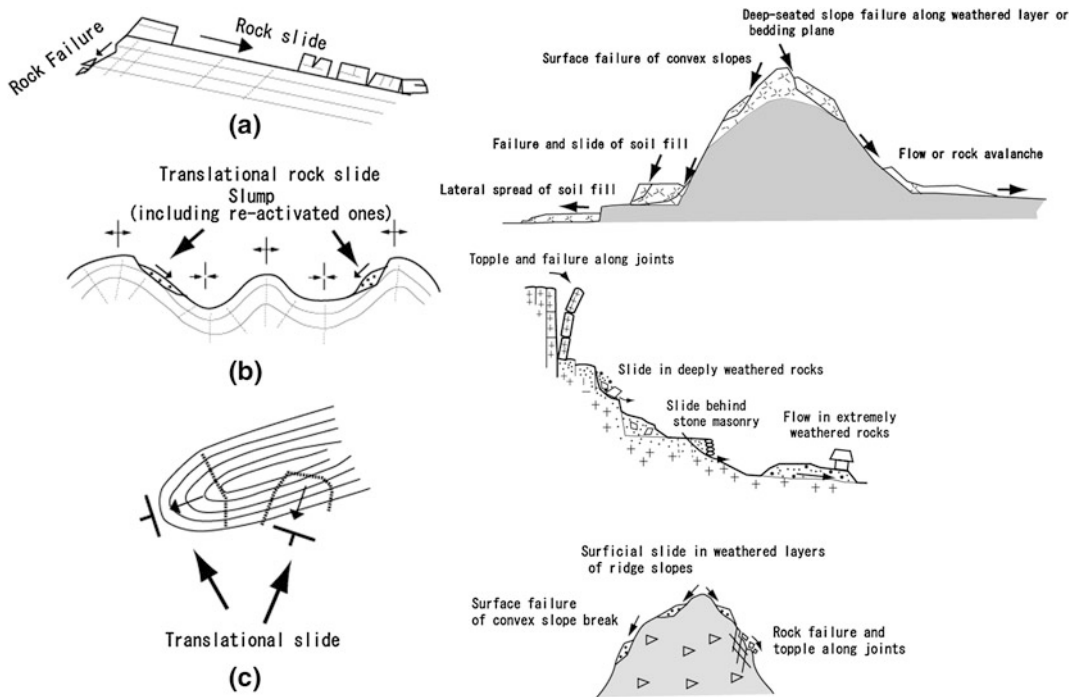
Fig. 5.3 Geology, movement type of earthquake landslides and their distance from the epicenter

of their similarities. The classification does not contradict the properties of landslides from the 2011 Tohoku earthquake.

4 Distance from Epicenter, Geological Properties, and Movement Types of the Earthquake Landslides

Landslides discussed in Sect. 5.3 typically occur within 30 km of the epicenter. However, flow often occurs over 100 km away from the epicenter in unconsolidated volcanic sediment. Landslides also occurred in embankments over 100 km away from the epicenter, thus extending the damage area. Figure 5.4 shows the relationship between the distance from the epicenter to the site of the landslide and the geology and movement types of the slides. In cases with earthquakes of magnitude 8 and larger, bedrock slides, rock failures and flows, and slope movement of embankments have occurred 200–300 km away from the epicenter. Examples include the 1994 Hokkaido Eastern Shore earthquake, the 2003 Tokachi-Oki earthquake, and the 2011 Tohoku earthquake.

Figure 5.5 shows the same relationships as Fig. 5.4, but for earthquake landslides in regions outside Japan, on the basis of literature available from the 1971 San Fernando earthquake (M6.9) (Abe 2012). As for the Japanese earthquakes, landslides were most likely to occur within a 30 km range from the epicenter, many slides were translational slides in well-bedded sedimentary rock, and flow of unconsolidated volcanic sediment was found at locations 150–250 km away.

At the site of China's onshore Wenchuan earthquake, where a magnitude of 8 was recorded, limestone and pre-Tertiary sedimentary rock slides were discovered more than 60 km away from the epicenter, verifying that the relationship between the distance from the epicenter and the form of landslide outbreak becomes different when the earthquake is of magnitude 8 or above.

Thus, for the 2011 Tohoku earthquake, cases of rock failures and flow that occurred several hundred kilometers away from the epicenter were compared with past earthquake landslides
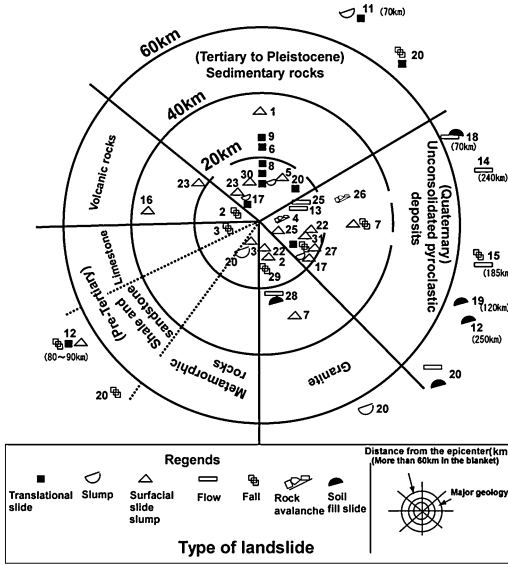
Fig. 5.4 Geology, movement type of earthquake landslides and their distance from the epicenter (outside of Japan)
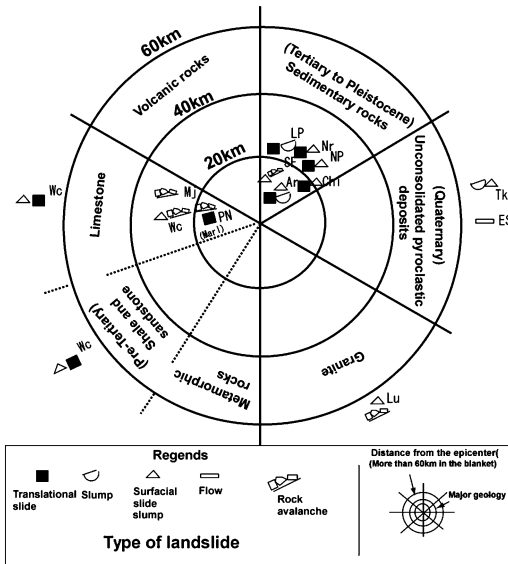
Fig. 5.5 Typical types of earthquake-induced landslides and their geological and topographical settings outside Japan. (1) Tertiary to Quaternary well-bedded sedimentary rocks (A) Cuesta, (B) Folding (C) Crest slope. (2) Quaternary unconsolidated pyroclastic deposits. (3) Granitic rocks. (4) Volcanic rocks
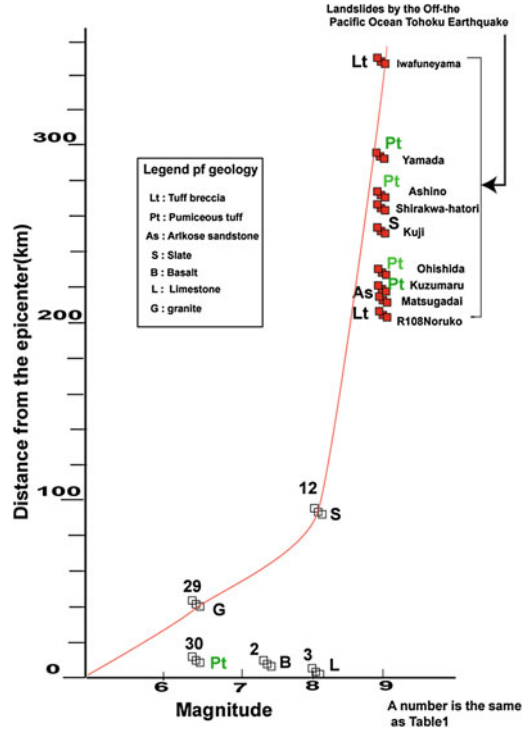
Fig. 5.6 Magnitude and distance from the epicenter of earthquake-induced landslides in unconsolidated pyroclastic deposits

(Fig. 5.6 and 5.7). It was found that rock failures occurred at a distance of over 100 km away from magnitude 8 earthquakes, especially for pumice tuff rock failures and at undercut slopes along rivers. Flows also occurred in unconsolidated volcanic sediments at locations over 100 km away from the epicenter for earthquakes of magnitude 7 and beyond.

As noted before, there is a difference in distance between the fault and the earthquake landslide as well as their morphology from magnitude 8 and beyond.

5   Conclusion

Earthquake landslides show common movements in landslide sites with similar geological properties. The movement types can be summarized as follows: (1) translational slides in ridges and cuestas with Tertiary–Quaternary
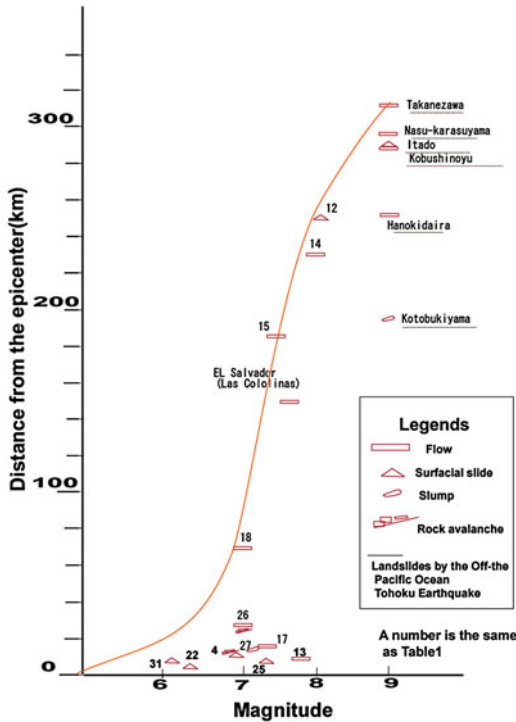
Fig. 5.7 Magnitude and distance from the epicenter of earthquake-induced rock failures

well-bedded sedimentary rocks, (2) flows in areas with consolidated Quaternary volcanic sediments, (3) shallow rotational slides at ridges in areas of volcanic rock, and (4) rock failures and toppling in areas of granite, accompanied by the flow of granite soil.

This study has evaluated the relationship between the distance from the epicenter and the type of earthquake landslides. Research has revealed that many of the earthquake landslides occur within a 30 km distance of the epicenter for earthquakes up to magnitude 7. However, it was also revealed that a magnitude of 8 and above can often induce rock slides at locations over 100 km away, and flow of unconsolidated volcanic sediment and rock failures of consolidated bedrock at locations 200–300 km away, indicating that magnitude 8 is the line of demarcation at which the relationship between the distance from the epicenter to sliding sites and the movement types of the slides changes significantly. This is possibly because of a significant difference in the location and epicenter of the earthquake as the

scale of the earthquake fault becomes larger. Upon evaluating the distance between the landslides and the faults, determining the position under the earthquake fault or under the seabed would become important.

Many recent earthquake landslides have also been observed at residential embankments.

Further research is needed to evaluate various issues, including the relationships between the location of the fault and that of the earthquake landslides, the physical and mechanical characteristics of unconsolidated volcanic sediment that cause flow to be induced far from the epicenter, the characteristics of the pumice tuff that lead to rock failures, and the relationship between earthquake movement and landslides in embankments.

References

Abe S (2012) Locations of landslides-distance from the epicenter, Jishin-Jisuberi (Earthquake Induced Landslides). The Japan Landslide Society, Tokyo, pp 110–112

Abe S, Hayashi K (2011) Morphologic features of landslides induced by recent large-scale earthquakes and their geomorphologic and geologic features. J Jpn Landslide Soc 48(1):52–61

Abe S, Takahashi A (1997) Landslide processes during earthquakes in the "Green Tuff" area in the Tohoku District—The Rikuu earthquake and Senboku earthquake in Akita Prefecture. J Jpn Soc Eng Geol 38(5):265–279

Abe S, Takahashi A, Ogita S, Komatsu J, Moriya H, Yoshimatsu H (2006) Seismic intensity and geomorphological/geological features of landslides due to earthquakes in the area of Tertiary strata in Japan. J Jpn Landslide Soc 43(3):27–34

Inokuchi T (1985) The large-scale landslide and rock avalanche along the Denjo River, Investigation Report of the Nagano-ken Seibu earthquake in 1984. National Center for Earth Science and Disaster Prevention, pp 45–62

Japan Meteorological Agency (2008) http://www.jma.go.jp/jma/kishou/books/ saigaiji/saigaiji_200801.pdf

Moriya H, Abe S, Higaki D (2010) Structure of the large-scale landslide at the upstream area of Aratozawa Dam induced by the Iwate-Miyagi Nairiku earthquake in 2008. J Jpn Landslide Soc 47(2):1–7

Okusa S, Tatsuoka F, Taniguchi E et al (1978) The report on the landslides in the Mitakairitani area caused by the Izu-Oshima-Kinkai Earthquake in January 1978. Bull Public Works Res Inst, Minist Constr 1432:34

Tabata S, Hara Y, Inoue K (1999) Real circumstances of sediment movements caused by the 1891 Nohbi earthquake. J Jpn Soc Eros Control Eng 52(3):24–33

Tajika J (2009) Landslide in Shikotan Island, induced by Hokkaido-Toho-oki earthquake, October 4, 1994. J Jpn Landslide Soc 45(6):29–32

Takahashi A, Ogita S, Yamada T, Moriya H, Abe S, Haraguchi T (2005) Rock slide due to the 2004 Niigataken Chuetsu earthquake in Hitotumine-zawa, Japan. J Jpn Landslide Soc 42(2):19–26

Tanaka K (1994) Landslides triggered by earthquakes, in regards to Okushiri Island in Hokkaido's Southwestern Offshore Earthquake, Japan Landslide Society Kansai Symposium "Landslides triggered by Earthquakes" 27–38

The Japan Landslide Society (2007) Earthquake-induced landslide disaster in middle mountains-Study Report on the 2004 Mid-Niigata earthquake. Part I: Geomorphology and Geology. Jpn Landslide Soc 172

Usami T (1996) New comprehensive list of Japan damage earthquake. University of Tokyo Press, Tokyo, p 493

Yamashita Y (2002) Characteristics of rockfall in Tottori Prefecture caused by an earthquake and effect of rockfall prevention work. J Jpn Landslide Soc 39(2):70–74

The Collapse Process of Granular Slopes Under Seismic Forcing

6

Hsien-Ter Chou, Ching-Fang Lee and Su-Chin Chen

Abstract

The relaxation processes of dry granular slopes under horizontal shakings are experimentally examined in this study. The experiments show that the reduction of slope angle is mainly controlled by seismic acceleration amplitude, but also depends on particle arrangement and boundary effects. The proposed scaling law with an exponential decay well represents the relaxation process of surface slope in all experiments. Maximum velocities occur near the free surface. Three possible failure patterns such as the plane failure, arc-shape failure, and surface fluidization with standing waves are examined. The results can be of help to back calculate the seismic forcing upon granular piles in the field studies.

1   Introduction

The geological phenomena such as sand piles, pyroclastic levees, and debris-flow deposition exist widely in common geomorphologic processes. While the pile is forced by an additional vibration (*ex.* vertical or horizontal shaking), the granular assembly will start to deform, collapse, or fluidize as a liquid state. For a mountainous area where earthquakes occur frequently, the horizontal seismic acceleration is commonly greater than the vertical one. The effect of vertical vibration on slope angle decay is not significant according to experimental results performed by Ichii and Ohmi (2004). Although the horizontal seismic acceleration is generally lower than the gravitational

H.-T. Chou (✉)
Department of Civil Engineering,
National Central University, Chung-Li,
32001 Taiwan, Republic of China
e-mail: htchou@cc.ncu.edu.tw

C.-F. Lee
Disaster Prevention Technology Research Center,
Sinotech Engineering Consultants, INC, Taipei 105,
Taiwan, Republic of China

S.-C. Chen
Department of Soil and Water Conservation,
National Chung Hsing University, Taiwan,
Republic of China
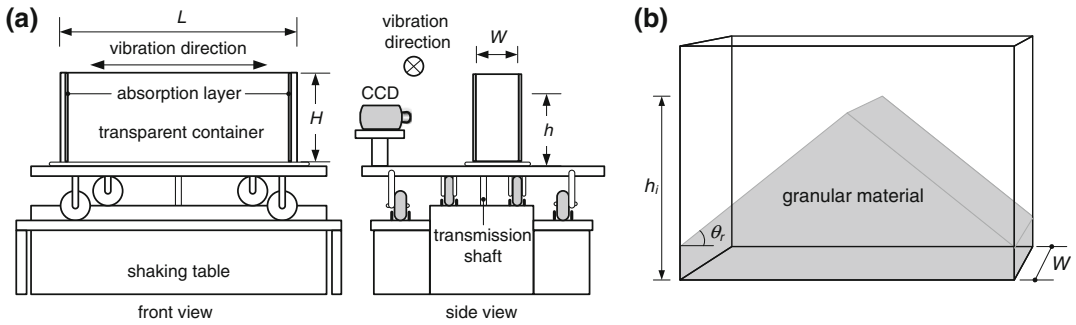
Fig. 6.1 **a** The schematic sketch of the experimental setup; **b** confined boundary configuration

acceleration (g) in the field, slope failure and rock avalanches are commonly observed.

The effects of vertical and horizontal vibrations on different granular material were widely evaluated. Seed and Goodman (1963) noticed the relation between the deposition angle of dry soil and horizontal (vertical) acceleration. The study pointed out while the inclined angle between horizontal plane and shaking direction equals to final equilibrium angle of soil pile, the inclined angle of the pile has a maximum decay. Evesque et al. (1989) observed that the acceleration threshold of granular collapsing is a constant which is independent of particle size. Jaeger et al. (1989; Jaeger and Nagel 1992) noted that a linear relationship between angle of deposits and collapse time is valid for greater vibrations, but this correlation doesn't work at lower shaking. Ristow et al. (1997) found the vibrating acceleration is a major factor controlling the phase transition (solid phase into liquid phase) of granular assembly under horizontal shaking. The angle of deposition obeys Coulomb friction law, which depends on the convective pattern and acceleration under both vertical and horizontal vibrations (Sarath and Behringer 1998). Chou and Chang (2004) studied the stable angle of the 2D and 3D granular piles under horizontal shakings. They found the shaking magnitude, particle arrangements, and the relative strokes are three predominant controlling factors on final slope

angle. The relation of angle decay, δ_e, is defined as

$$\delta_e = \phi - \theta_e = \tan^{-1}\left(\frac{a_h}{g - a_v}\right) \qquad (6.1)$$

where ϕ is the angle of repose of material and θ_e is the residual angle of repose at equilibrium; a_h and a_v are corresponding horizontal and vertical accelerations, respectively.

The sand motions under vibrations can be classified into two distinct regimes according to experimental observations (Medved et al. 2000; Nadler et al. 2009; Raihane et al. 2009; Debayle et al. 2009). A closed-packing bottom layer follows the container motion (like solid phase), and a highly fluidized layer near the upper surface characterized by violent motions (like gaseous and liquid phases). Experimentally, the convectional and simple harmonic motions are observed, and the shear characteristic length scales follow a similarity rule during the shaking process. In addition, Metcalfe et al. (2002) proposed that the increase of the shaking acceleration will gradually enhance the flow pattern from the quasi-static regime into the liquid phase.

In this study, the relaxation process of surface slope under horizontal shakings for different dry granular materials is examined. Firstly, the effects of the shaking conditions and granular properties (*ex.* amplitudes of vibration, frequency, and coefficients of friction) on the slope stability in the laterally confined walls were explored. The difference between active and

passive dynamic behaviors, such as velocity contour and flowing region was also investigated. Finally, the relationship between the collapsing magnitude and vibrating processing is proposed.

2   Experimental Apparatus and Material

The experimental setup is shown in Fig. 6.1. It consists of a horizontal shaking table and an upper transparent rectangle container filled with granular material (the internal dimension of the box: $L = 40$ cm, $H = 20$ cm, and $W = 10$ cm). The sinusoidal vibration is generated by an electronic motor with operation frequencies of 0–250 rpm. The sinusoidal displacement $x(t)$ of the shaker can be expressed as

$$x(t) = \lambda \sin(2\pi f t) \qquad (6.2)$$

where λ and f denote the vibrating stroke and frequency ($\omega = 2\pi f$). The dimensionless acceleration magnitude Γ can be derived as follows

$$\Gamma = \frac{\lambda (2\pi f)^2}{g} = \frac{a_h}{g} \qquad (6.3)$$

where a_h and g are horizontal and gravity acceleration (9.81 m/s^2), respectively. The vibrating amplitude is adjustable and set to be 0.75, 1.45, and 1.88 cm in the experiments. The granular materials include glass beads (particle size: $d = 2.0 \pm 0.1$ mm, density: $\rho = 2.44$ g/cm^3, angle of repose: $\theta_r = 18.1^\circ$), mill stones ($d = 3.5 \pm 0.2$ mm, $\rho = 2.45$ g/cm^3, $\theta_r = 25.3^\circ$), and polystyrene beads ($d = 5.8 \pm 0.1$ mm, $\rho = 2.10$ g/cm^3, $\theta_r = 20.8^\circ$). A high-speed camera (CASIO, EX-F1) was fixed synchronously on the shaking table to obtain a series of successive images. The camera lens is perpendicular to the shaking direction. The sampling rates depend on the operation acceleration which vary from 30–200 fps. The image resolutions are 1920 (W) × 1080 (H) pixels and 640 × 480 pixels at 60 and 200 fps, respectively.

The experimental setup of a triangle granular pile with two symmetrical inclined slopes (Fig. 6.1b) was used to explore the dynamic behaviors. The shock absorption layers were placed on both lateral boundaries to reduce the wall effect. The initial pile deposition in the container is formed by the free fall from a hopper before starting the vibration. The initial static angle of granular pile is slightly greater than angle of repose due to the wall friction. Besides the original width ($W = 10$ cm), one also reduces the widths of container ($W = 7.5$ and 5 cm) to observe the side wall effect for the experiments. Before the experiment was carried out, the initial height (h) and slope angle (θ) have to be recorded first. Subsequently, one adjusted the operation frequency then turned on the shaking table to generate slope avalanching. The vibration stops when the grains on the inclined slope either remains static (for smaller Γ) or the granular slope reaches a dynamic equilibrium (for greater Γ). Each run of experiment repeats twice and the average value was taken. The successive and final equilibrium of slope angles are acquired from package ImageJ, an image processing and analysis software in Java code. The measured angle accuracy is up to 10^{-2} in degree. Before each velocity measurement, the geometrical deformation of the obtained images has to be corrected by spatial transformation in Matlab. In this preprocess, one takes a pair of control points and uses them to infer a spatial transformation. For selecting the transformation type of 'projective', it needs four pairs of control points on images for calibration at least. Input points form an m-by-2 double matrix containing both x and y coordinates of designated control points in the image. The points of reference are also in the form of an m-by-2 double matrix containing x and y coordinates of control points specified in the base image. After finishing the geometrical calibration, the velocity of processed images would be measured with the corresponding computing process. The collapsing velocities of grains at the transparent side-wall are determined from a sequence of images with PTV approach (Capart et al. 2002). The approximate root-mean-squared error on velocity is 1.69–4.24 cm/s in this work. As far as the concern of measurement accuracy, the relative displacement vector and velocity filed for any analysis is analyzed according to the averaged values of latest 50 frames.
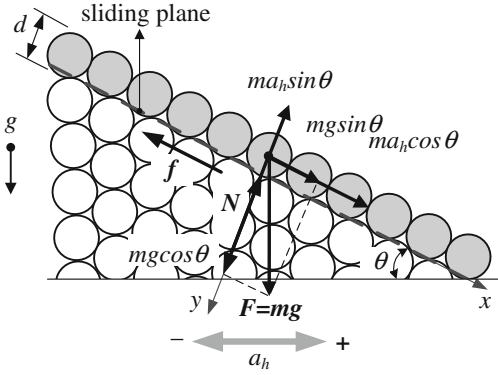
Fig. 6.2 The inclined surface sliding due to the horizontal shaking. *Upper gray* surface grains are assumed to be slipping along the sliding plane (*black dashed line*)

3 Mechanics of Seismic Sliding

The dry slope failures often occur during the seismic forcing. Considering a granular pile is lied on a horizontal plane under the gravity acting (see Fig. 6.2). The initial slope of the pile is close to the angle of repose (φ). The cohesion is ignored here since the dry granular material is used. One assumes a thin granular layer ($h{-}1d$, see Fig. 6.2, surface gray grains) slips down to the inclined pile; the normal force (N) and driven force (T_d) are as follows

$$N = m(g \cos \theta - a_h \sin \theta) \qquad (6.4)$$

$$T_d = m(g \sin \theta + a_h \cos \theta) \qquad (6.5)$$

where m is the mass of the sliding layer. According to the Coulomb failure criterion, the slipping condition can be written as: $\mu N < T_d$ with $\mu = \tan \phi$,

$$\Gamma > \frac{\tan \phi - \tan \theta}{1 + \tan \phi \tan \theta} = \tan(\phi - \theta) \qquad (6.6)$$

where $\Gamma = (a_h/g)$. The critical condition exists under F.S. = 1, which corresponds to $\Gamma = \tan(\phi - \theta_e)$. The final angle of the granular pile under seismic forcing reads.

$$\theta_e = \phi - \tan^{-1}(\Gamma) \qquad (6.7)$$

Similarly, Evesque and Rajchenbach (1989) suggested the shaking acceleration is the sole control factor governing the final deposition angle and independent of magnitude of vibration. Chou and Chang (2004) proposed the angle defect under seismic forcing is also related to the seismic displacement amplitude λ and particle-size arrangement as follows.

$$\delta_e = \tan^{-1} \left(k / (1 + 0.243 (\frac{1}{f_s} \frac{k}{\lambda/d_b})^{0.853}) \right)$$

$$\text{with } f_s = \sqrt{1 + 2d_b/d_t} / [(1 + d_t/d_b) \\ (\sqrt{1 + 2d_b/d_t} - 1)] \qquad (6.8)$$

where $k = a_h/g$; d_t and d_b are the diameters of upper (top) and lower (bottom) particles. f_s–1.18 for $d_t/d_b = 1$ for 3D case. It is valid in the range of maximum angle of repose of material ($\delta_{max} {\cong} \phi$). The prediction of Eq. (6.8) has been verified by experiments. For uniform particles under moderate seismic forcing, the difference between Eqs. (6.7) and (6.8) is negligible.

4 Experimental Observations of Collapse Process

4.1 Variations of Surface Angle Decay

Figure 6.3a, b depict a series of digital images for various relative shaking accelerations. The evolution of slope avalanching depends on the shaking magnitude. The great a_h/g directly causes a flat surface pattern in an initial short period (~ 6 s; see Fig. 6.4b), whereas the initial heap holds for a long time under a very small seismic forcing a_h/g (Fig. 6.3a).

As shown in Fig. 6.4, the granular motion with the angle $\theta_i(t)$ at any time can be either in the active (the acceleration of particles are opposite to the down slope direction) or the passive states (the acceleration of particles follows the down slope direction). Depending on the shaking magnitude, the unstable particles usually collapse at the onset of maximum

Fig. 6.3 Selected digital frames for slope decay under various horizontal shaking accelerations. **a** $a_h/g = 0.051$; **b** $a_h/g = 0.321$ (mill stone; $d = 3.5$ mm, $W = 10$ cm, $\lambda = 1.45$ cm)

(a)   (b)

t=0 s

t=6 s

t=18 s
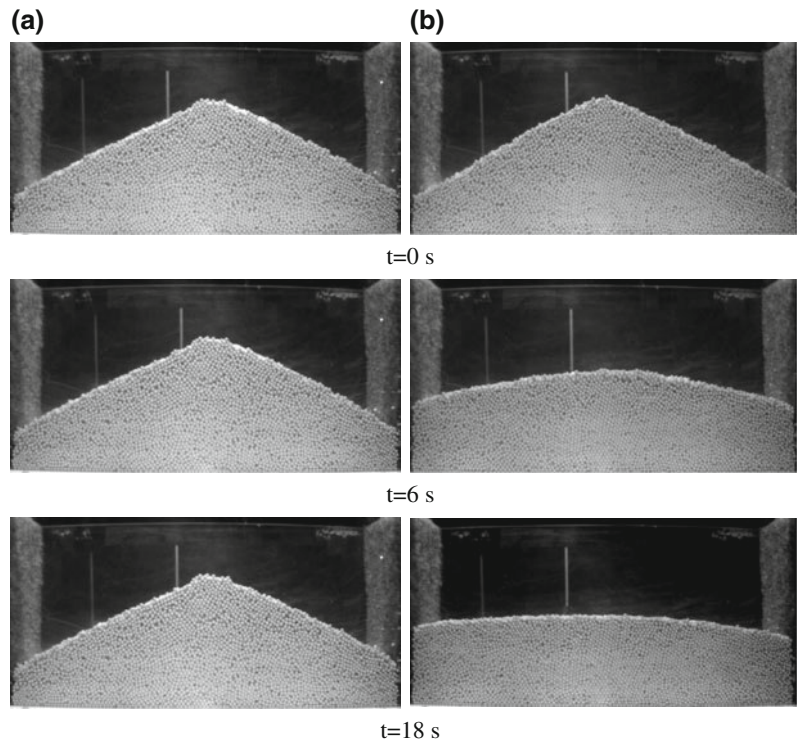
Fig. 6.4 The relaxation process of surface slope decay ($W = 10$ cm, $d = 5.8$ mm, $\lambda = 1.45$ cm, $a_h/g = 0.310$)
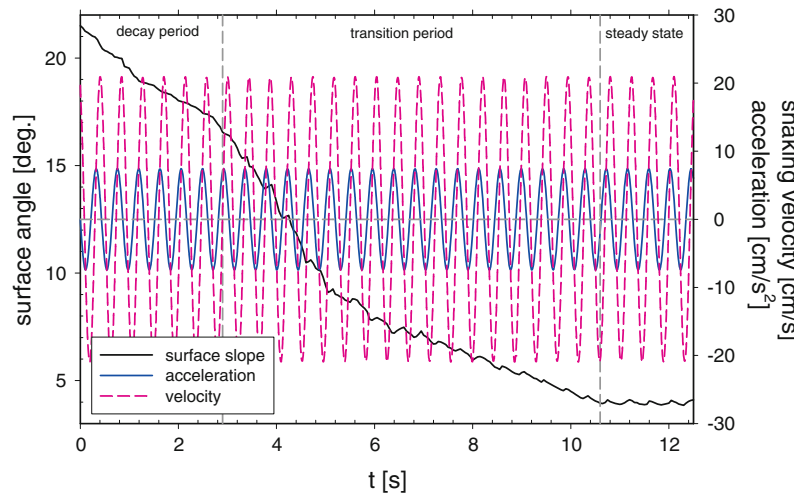
acceleration in the active state, then the surface slope decays and approaches to a lower stable angle. One observes the upward movement of particles along the free surface in the passive state as long as the surface angle is lower than the specific threshold. So the dynamic angle of granular slope is not solely a monotonous decay during the whole shaking process.

The relaxation of surface slope consists mainly of (1) the fast decay period, (2) transition period, and (3) steady state with a dynamic undulation. The influence of passive state can be ignored at the first stage since the inertia force acting on the particles is less than gravitational avalanching. The great surface avalanching takes place mostly at the active state. The stairway-like shape of
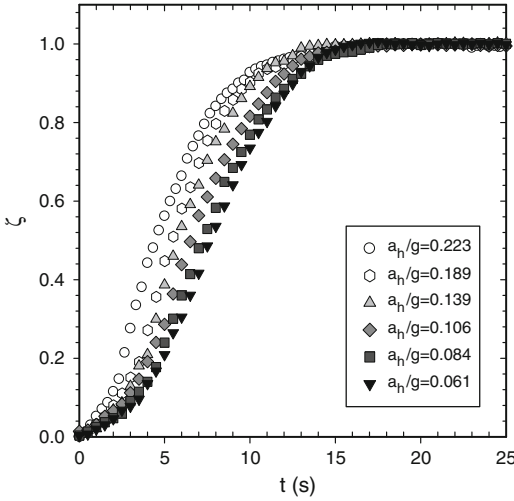
Fig. 6.5 ζ as a function of time scale (mill stone, $d = 3.5$ mm, $\lambda = 0.75$ cm, $W = 10$ cm)

curve is evidently observed from the experimental measurements. However, a reverse upslope appears while the slope is less than a critical angle. The slope raised in the passive state occurs at certain specific surface slope ranges. After the transition period, two different patterns are observed on the granular surface. One is a stable slope for the low a_h/g values, and the other is a dynamic oscillating surface slopes which profiles vary between the active and passive states for high a_h/g values (Fig 6.5).

4.2 Scaling Law of Slope Relaxation

The initial angle of granular pile is defined as θ_o and its difference between the angle at any time $\theta_i(t)$ is then called $\delta(t)$. The surface angle relaxation is observed to obey an exponential decay law, which is related to the time and vibration acceleration.

$$\zeta = \frac{\delta(t)}{\delta_e} = \left(1 - e^{-t/b}\right)^n \qquad (6.9)$$

where δ_e is the difference between initial and equilibrium angles ($= \theta_o - \theta_e$). b and n are fitting parameters. Thus ζ is a dimensionless angle describing the evolution of angle decay ($\zeta = \delta_d/\delta_e$)

during the seismic forcing, n is a coefficient relative to shaking magnitude.

Figure 6.6 shows how dimensionless angle ($\zeta = \delta_d/\delta_e$) varied with time ($t$) and scaled time ($t/t_e$) for various material and amplitudes of vibration ($\lambda = 0.75$ cm). The relative shaking acceleration, a_h/g, ranges between 0.061 and 0.223. Greater relative shaking accelerations, a_h/g cause higher slope decay and approach the equilibrium condition more quickly. The fitting parameter b seems to be a constant in all cases ($b = 0.16$–0.18), but n increases with coefficient of internal friction of granular media (θ_r) instead of the particle size (d). As shown in Fig. 6.6a–c, the best fitting curves for different λ in all experiments read as

$$\zeta = \left(1 - e^{-(t/t_e)/b}\right)^n \qquad (6.10)$$

Despite the inherent properties of particles, the scaling law presented here is applicable to different granular media. (3) The influence of λ on avalanching period is not obvious in higher θ_r of material (e.g. mill stones), but it has a slight effect on the smooth grains. For glass and polystyrene beads, ζ is inversely proportional to the shaking magnitude at the same time. It implies that increasing λ may affect the final equilibrium slope angle. To compare the results of the final equilibrium time with different granular material, one follows above experiments to plot t_e/T against a_h/g in Fig. 6.7. The equilibrium time decreases as the λ/d increases. In addition, t_e/T tends to approach a constant (25-28) while a_h/g is up to 0.2–0.3.

4.3 Effect of Side Walls

The variations of scaled final angle and relative shaking magnitude are shown in Fig. 6.8. The solid line is a critical borderline between stable and unstable regions according to Eq. (6.7).

The lower shaking magnitude keeps the stability of granular assembly on a steeper inclined slope, whereas the higher one will collapse quickly to a more gradual slope. The final angle in the stable state also indicates the evidence of side wall effect. The final scaled angle at low a_h/g presents a tendency above the theoretical prediction in spite of the material used. Additional
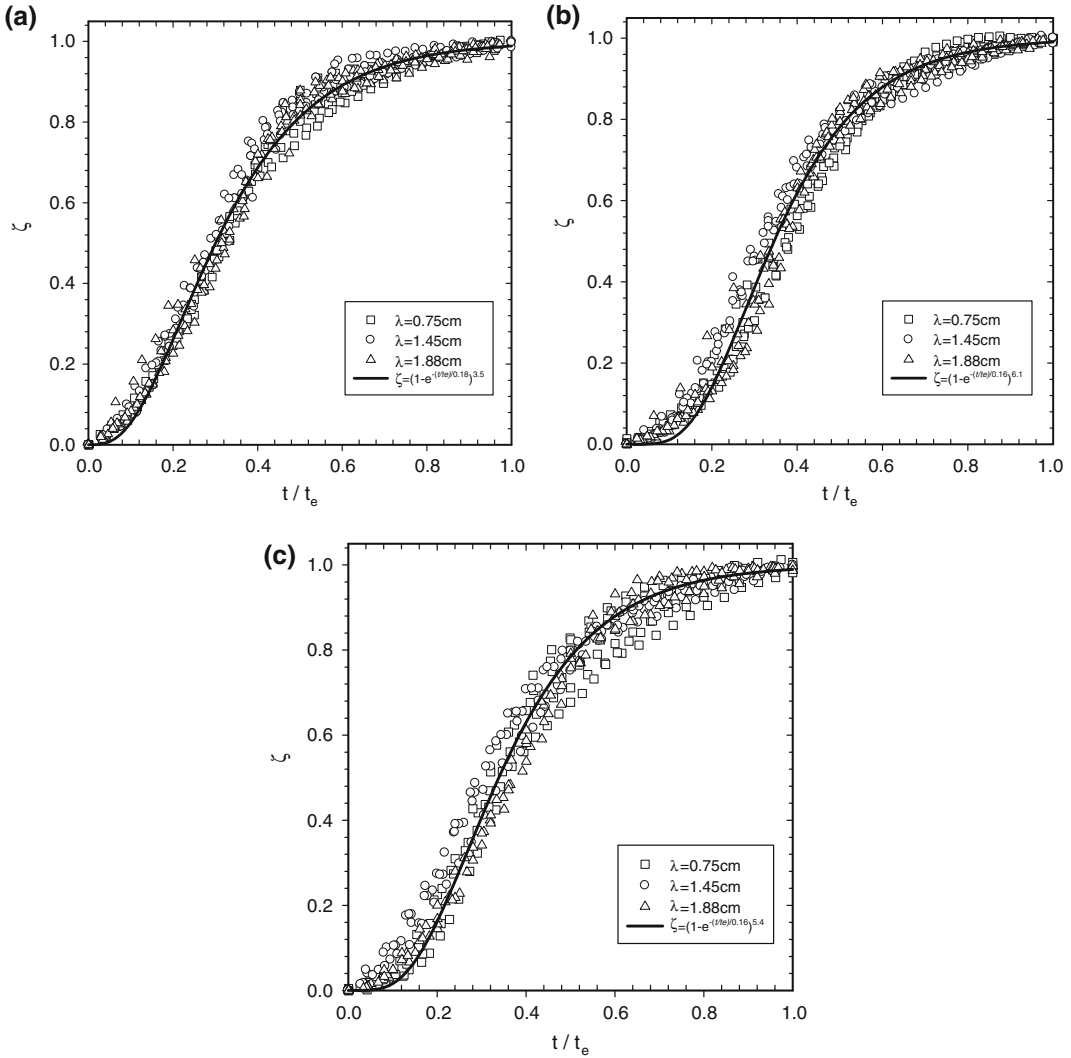
Fig. 6.6 ζ as a function of dimensionless time for **a** $d = 2.0$ mm, **b** $d = 3.5$ mm, and **c** $d = 5.8$ mm; $W = 10$ cm

friction acting on the lateral walls promotes a steeper surface angle. However, the final angle falls below the border line while the relative shaking magnitude is greater than a particular threshold. This tendency is similar to the findings of Ichii and Ohmi (2004).

Wall friction also affects the flowing dynamic evidently such as velocity profile, density fraction, and surface angle. In contrast with the shaking cases, the wall effect is unclear and seldom discussed in the literatures. We investigate the variations of equilibrium slope for the cases with three gap widths. Figure 6.9a–c present the

wall effect on slope decay during the shaking forcing for 5 min. Systematical features exist in all experimental runs. The slope decay of granular pile, δ, increases linearly with the increasing a_H/g and the decreasing gap width (W). The narrow gap shows a stronger wall effect on the inside medium than the wide one. The inconsistent results derive from the difference of the initial deposition slope before the shaking acting—a granular heap can be piled a steeper stable slope in a narrow gap. Consequently, the greater slope decay is then measured in the cases of narrow width. One may also discover the disagreement

Fig. 6.7 Dimensionless time of the final equilibrium angle against the scaled shaking amplitude for different granular material ($W = 10$ cm)
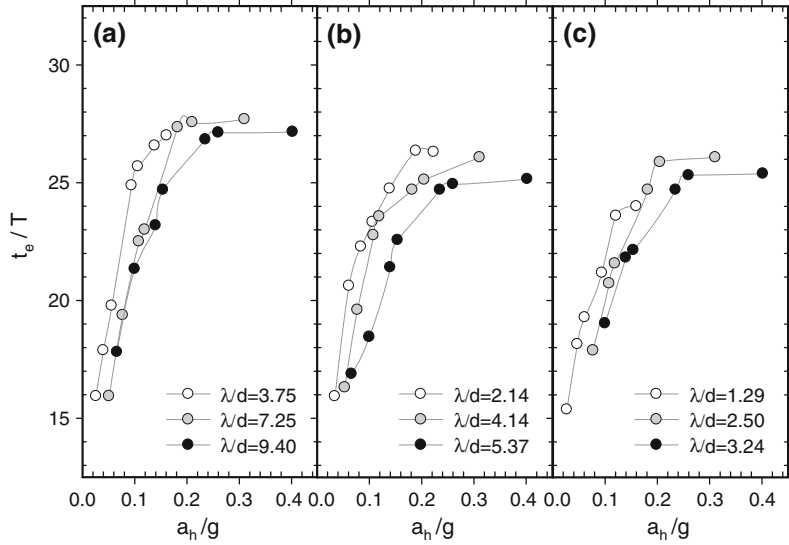
Fig. 6.8 Scaled equilibrium surface angle (θ_e/ϕ) as a function of a_h/g for three granular material. θ_e is the residual angle of repose at equilibrium. *Solid lines* are the critical condition of the slope sliding under seismic force action ($W = 10$ cm)
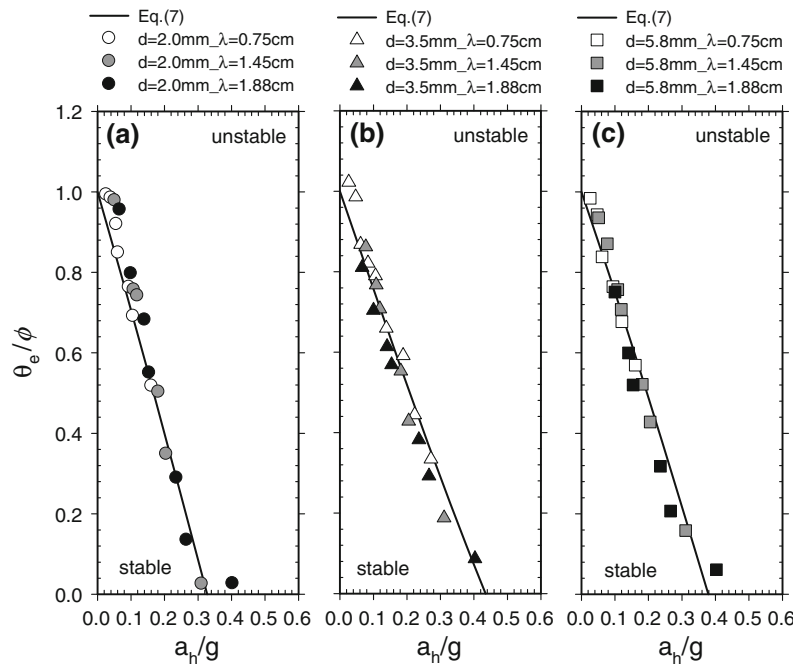
between experimental observations and predictions based on Eqs. (6.1) and (6.8).

The driving force on particles must exceed the frictional resistance among the particles and adjacent walls, and then it starts to bring the surface avalanching. The critical a_h/g depends on the width of container—the narrow gap needs a higher critical value of a_h/g than that in wide channel since the particle has a lower freedom in motion. As the relative shaking magnitude increases, the disagreement for both predictions and experiments are more remarkable due to ignoring the wall effect
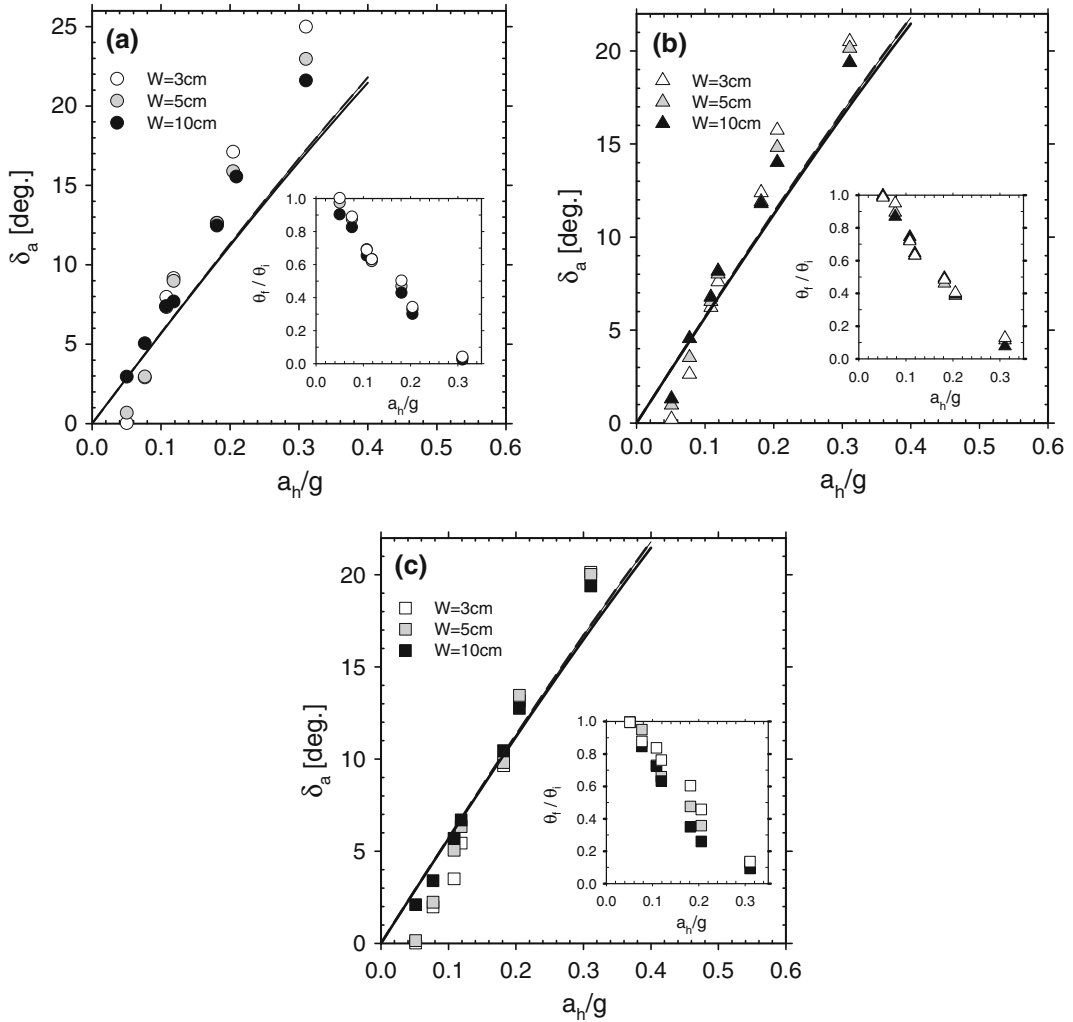
Fig. 6.9 δ as a function of a_h/g for three granular material (**a** $d = 2.0$ mm, **b** $d = 3.5$ mm, and **c** $d = 5.8$ mm) and widths of the container ($W = 3$, 5, and 10 cm). *Black dashed* and *solid lines* are derived form Eqs. (6.1) and (6.8). Inset presents the corresponding scaled final angle varying with a_h/g for three granular material and widths of the container ($\lambda = 1.45$ cm)

in Eqs. (6.1) and (6.8). The insets in Fig. 6.9 show the dimensionless final equilibrium angles, θ_e/ϕ, for the corresponding a_h/g. A slight dependence on variation of W depicts the appearance of wall friction especially in the case of large particles diameter (d). The coarse particles sometimes form a local hump when the downward avalanches occur on the surface slope. The inclined slope collapses to a near horizontal surface just at $a_h/g = 0.3$. Two important features can be noted: (1) the effect of side-wall friction is reduced by increasing relative shaking acceleration (a_h/g) or increasing gap width; (2) the critical relative shaking acceleration depends strongly on variation of W, but it is irrelevant to the property of particles in this work.

4.4   Dynamic Characteristics of Granular Collapse

As shown in Fig. 6.10a–d, the particle trajectories are compared with different time interval obtained from a sequence of experimental images. The data are averaged at least over a full shaking period, *i.e.*,
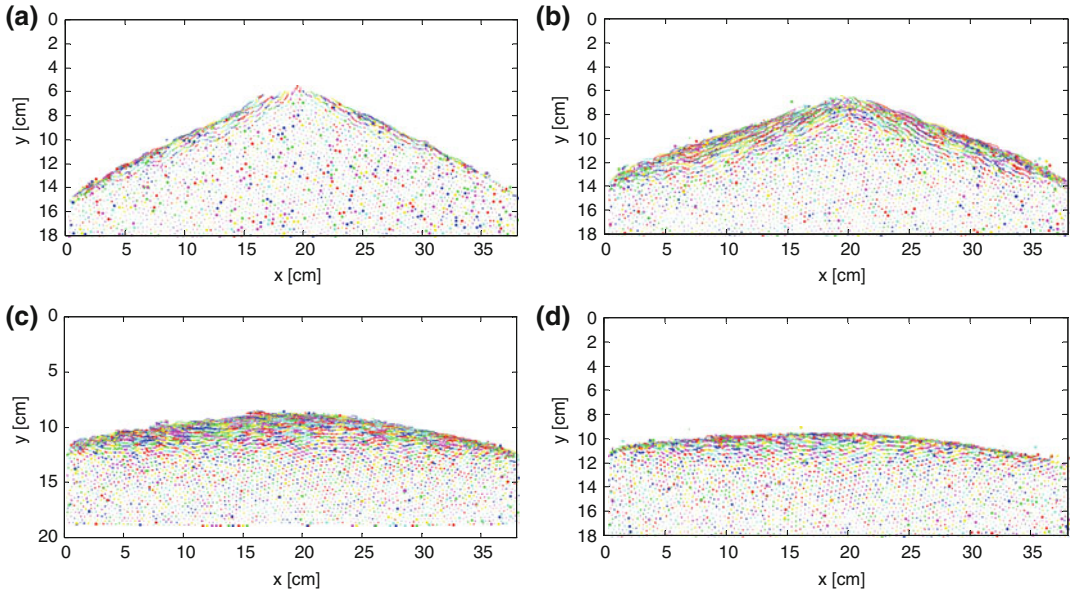
Fig. 6.10 Trajectory reconstruction at different time: **a** $t = 1$–2.1 s; **b** $t = 3$–4 s; **c** $t = 5.5$–6.5 s; **d** $t = 11$–12 s. The unit in velocity fields: cm/s ($d = 3.5$ mm, $a_h/g = 0.310$, $\lambda = 1.45$ cm, $W = 10$ cm)

including both the active and the passive states. From the flowing image analysis, two phenomena are evident: Firstly, the initial collapse is characterized by a shallow surface flows until the slope approaching to a stable state. For a homogeneous slope, Katz and Aharonov (2006) concluded that the failure type consists primarily of the isolated surface flows while $a_h/g < 0.6$ (wet sand with containing 1 % water). According to their study, the large slumps and sill slides usually occurs when the higher shaking acceleration ($a_h/g > 0.8$) are applied. At the beginning of granular collapse, the horizontal shaking induces a significant surface slope failure in the active state (Fig. 6.10a). The faster movements occur both sides of the inclined surface, whereas the inside particle velocities are almost null. After the first decay period, the surface movements are replaced by the deep sporadic avalanches (Fig. 6.10b). Secondly, in contrast to the initial surface collapse, the flowing layer near the surface expands gradually with time, while the surface slope is further reduced. Once the surface slope of the pile is less than the specific critical angle, the horizontal failure surface is then emerged. Consequently, the faster shaking acceleration will cause a fluidized layer at the convex

slope above the failure plane (Fig. 6.10c, d). Therefore, the surface pattern will not remain a constant shape despite the granular pile is either in the active or passive states. The surface oscillation with a reciprocating motion here can be regarded as dynamic equilibrium which resembles a standing wave.

Figure 6.11 shows the thickness of the fluidized layer at the centerline of the granular pile for various shaking magnitudes. It is analogous to the results of Debayle et al. (2009) (the inset of Fig. 6.11b). The thickness of the fluidized layer, h_f/d, is obtained form 200 successive particle trajectories (Fig. 6.11a). As shown in Fig. 6.11b, there is a critical threshold of relative shaking acceleration, $(a_h/g)_c$, for surface fluidization. Comparing with different granular material used in this study, the dimensionless thickness of fluidized layer is almost unchanged. The critical relative shaking acceleration inducing the surface fluidization appears at $a_h/g = 0.123$. It means that the fluidized layer occurs on the surface slope of granular pile when a_h/g is great than 0.123 in the study. While $a_h/g < 0.123$, only the granular falling and shallow sliding can be observed on the surface

Fig. 6.11 **a** 200 successive particle trajectories which included the active and passive states ($d = 5.8$ mm, $a_h/g = 0.310$, $\lambda = 1.45$ cm, $W = 10$ cm); **b** Evolution of the thickness of fluidized layer with different shaking magnitude for a granular pile in the lateral confined container. The initial height of the pile, $h_i = 9.4$–9.6 cm, $\lambda = 1.45$ cm, and $W \times H = 10 \times 38$ cm. Inset indicates the experimental result of Debayle et al. (2009) for dry sand grains, $d_{ave} = 0.6$ mm, $h_i = 6$ cm, and $W \times H = 4 \times 8$ cm
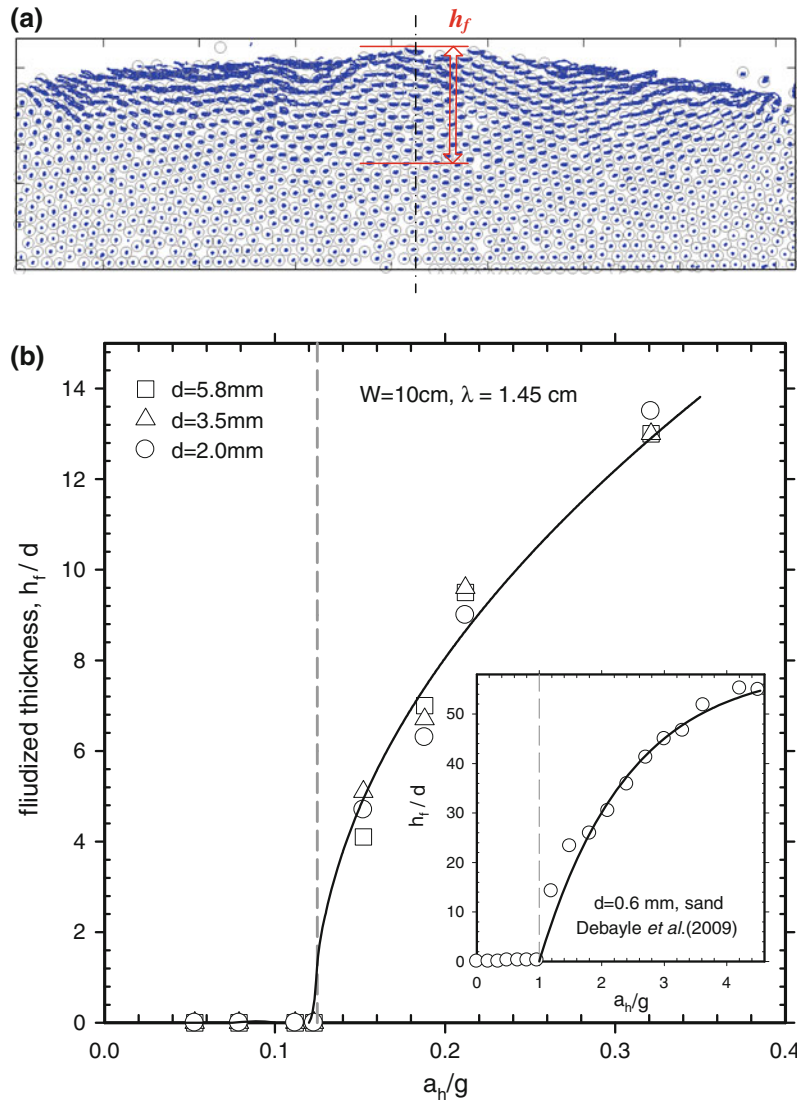
slope. A noticeable difference exists in $(a_h/g)_c$ between spherical particles and irregular shape. The shape of grains and surface friction coefficient are the predominant parameters controlling the onset of the surface fluidization.

Three failure patterns appear when a granular slope is under the horizontal shaking (Fig. 6.12a–c). At first, the collapsing grains slides from the surface to the slope foot. The failure pattern is analogous to the plane failure and is consistent with the experimental observation by Katz and Aharonov (2006). The surface flow in a vibrating box is determined by the failure depth and area for

homogenous granular material. The slope failure takes place mainly in the active state and remains its stable surface in the passive state for a slow a_h/g (<0.11); nevertheless, the slope failure keeps avalanching despite of the shaking state for a moderate a_h/g (<0.3; Fig. 6.12a). Since both ends are fixed, the collapsing particles don't expand along the shaking direction. As a consequence, the failure plane develops at the slope foot while the surface slope angle is lower than the critical angle ($\sim \tan^{-1}(a_h/g)$). This slip plane is near convex shape called the circular failure. The direction of particle motion begins to divide into different
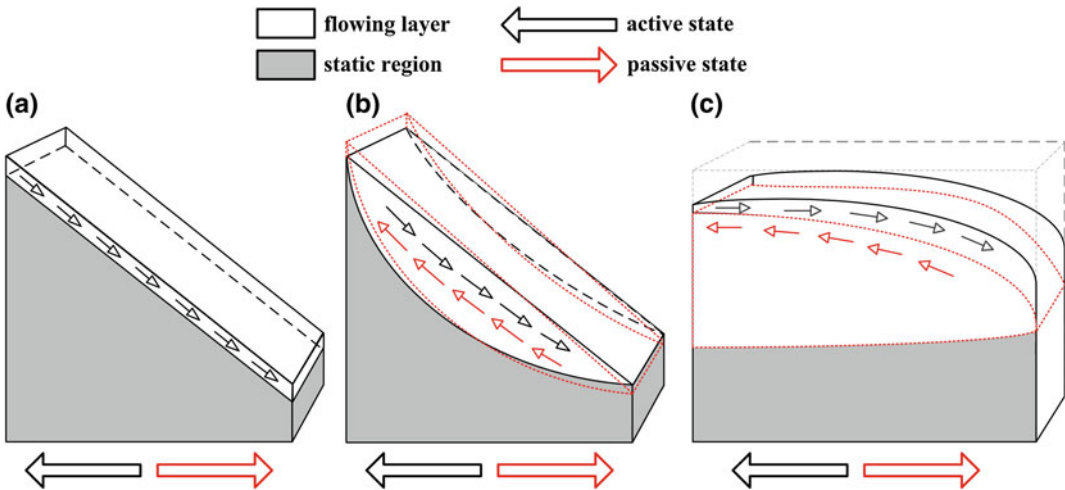
Fig. 6.12 The conceptual failure mechanisms for granular slope under the horizontal shaking: **a** plane failure-shallow surface flows; **b** arc-shape failure; **c** surface fluidization-standing wave pattern

routes depend on the shaking phase during this stage: one is the downward avalanches and another is an upward reverse angle increase (Fig. 6.12b). Indeed, the flowing depth is also enhanced with contrast to the previous failure pattern. For the experiment with a greater a_h/g, the surface pattern will become a dome-shape surface with a concave slip plane (Fig. 6.12c). The long-term observation shows that the wavy-shape surface swings back and forth with the bottom shaking even though it is vibrated after 5 min. The thickness of surface fluidized layer above the borderline is directly proportional to the horizontal shaking acceleration.

5   Conclusions

The slope relaxation of the granular pile with confined boundaries has been explored experimentally in this study. A proposed scaling law with an exponential decay is capable of describing the slope relaxation process. The narrow width needs a great critical relative shaking acceleration to trigger the slope avalanches. As the seismic forcing increases, three failure patterns such as the plane failure, arc-shape failure, and surface

fluidization with standing waves are observed accordingly.

References

Capart H, Young DL, Zech Y (2002) Vorono imaging methods for the measurement of granular flows. Exp Fluids 32(121):121–135

Chou HT, Chang YY (2004) Relaxation of angle of repose for three dimensionless granular material under horizontal vibrations. J Chin Inst Civ Hydraul Eng 16(1):145–154 (in Chinese)

Debayle J, Raihane A, Belhaoua A, Bonnefoy O, Thomas G, Chaix JM, Pinoli JC (2009) Velocity field computation in vibrated granular media using an optical flow based multiscale image analysis method. Image Anal Stereol 28:35–43

Evesque P, Rajchenbach J (1989) Instability in a sand heap. Phys Rev Lett 62:44–46

Ichii K, Ohmi H (2004) Slope stability of cohesionless material under large seismic shakings. In: 11th international conference on soil dynamics and earthquake engineering and the 3rd international conference on earthquake geotechnical engineering proceedings, vol 2(2), pp 388–395

Jaeger HM, Liu C, Nagel SR (1989) Relaxation at the angle of repose. Phys Rev Lett 62:40–43

Jaeger HM, Nagel SR (1992) Physics of the granular state. Science 255:1523–1531

Katz O, Aharonov E (2006) Landslides in vibrating sand box: what controls types of slope failure and frequency magnitude relations? Earth Planet Sci Lett 247:280–294

Medved M, Jaeger HM, Nagel SR (2000) Modes of response in horizontally vibrated granular matter. Europhys Lett 52(1):66–72

Metcalfe G, Tennakoon SGK, Kondic L, Schaeffer DG (2002) Granular friction, Coulomb failure, and the fluid-solid transition for horizontally shaken granular materials. Phys Rev E 62:031302–031315

Nadler S, Bonnefoy O, Raihane A, Chaix J-M, Gelet J-L, Thomas G (2009) Numerical simulation of granular media under horizontal vibrations. In: 6th international conference on micromechanics of granular media, Golden, Colorado, United States

Raihane A, Bonnefoy O, Nadler S, Gelet JL, Chaix JM, Thomas G (2009) Convective flow in a horizontally vibrated 3D granular packing. In: 6th international conference on micromechanics of granular media, Golden, Colorado, United States

Ristow GH, Straßburger G, Rehberg I (1997) Phase diagram and scaling of granular materials under horizontal vibrations. Phys Rev Lett 79:833–836

Sarath GKT, Behringer RP (1998) Vertical and horizontal vibration of granular materials: coulomb friction and a novel switching state. Phys Rev Lett 81(4):794–797

Seed HB, Goodman RE (1963) Slope stability in cohesionless materials during earthquakes. Soil Mechanics and Bituminous Materials Research Laboratory, Berkeley

Slope Motion Response and Failure Under Strong Earthquakes: Recording, Monitoring and Modeling

Runqiu Huang

Abstract

About 56 thousand landslides were induced by the Ms 8.0 Wenchuan earthquake on May 12, 2008. Field survey revealed that a majority of the landslides occurred in the transition parts from the middle to upper portions of deep valley slopes, on the thin ridges and especially parts of prominent terrains. Those positions have evident topographic amplification effects to seismic loading. An analysis of the spatial distribution of PGAs demonstrates that the directivity effect and the hanging wall effect in the near-fault ground motion occurred in this earthquake. Monitoring of the aftershocks has shown that the micro-relief is one of the key factors for topographic amplification and site conditions have an important effect on slope ground motion response. Large scale shaking table test was used to analyze the ground motion response of the slopes with different lithologies and structures. Both dip slopes and anti-dip slopes have significant PGA amplifications at the upper top region. Results of numerical simulation and fracture mechanics based calculation show that failure development parts of the dip slopes and anti-dip slopes are different.

Keywords

Ground motion · Topographic amplification · Wenchuan earthquake · Peak ground acceleration · Shaking table modelling · Landslide

1 Introduction

The Wenchuan earthquake (Ms = 8.0; at 31.021°N, 103.367°E), with a focal depth of about 14 km, occurred beneath the steep eastern margin of the Tibetan Plateau in Sichuan, China on May 12, 2008. The earthquake caused 69,227 fatalities and 374,643 injured, and also triggered over 56,000 landslides, over a total area of 811 km² (Dai et al. 2010), produced about 5–15 km³ of loose materials (Parker et al. 2011). Field survey further revealed that the most serious damage occurred in the transition parts from the middle to upper portions of deep valley slopes, thin ridges and especially parts of prominent terrain. Those positions have evident topographic amplification effects.

R. Huang (✉)
State key Laboratory of Geo-hazards Prevention and Geo-environment Protection, Chengdu University of Technology, Chengdu, 610059, China
e-mail: hrq@cdut.edu.cn

Topographic relief has a profound influence on the propagation of seismic waves, giving rise to distinct zones of amplification or damping of ground acceleration in specific topographic locations (Benites and Haines 1994; Bouchon and Baker 1996). Topographic amplification effects on seismic waves are known to cause important gradients in ground acceleration in individual mountain ridges (Meunier et al. 2008). Seismic accelerations cause short lived disturbances in the balance of forces within hill slopes that may induce slope failure (Youd and Perkins 1978; Keefer 1984, 2000). Peak ground acceleration (PGA) is simply the amplitude of the largest peak acceleration recorded on an accelerogram at a site during a particular earthquake. It is often used as a parameter to describe strong ground motion although it is only useful for analysis of short period structures (Douglas 2003).

In most cases, seismic slope failure potential is assessed by traditional pseudo-static methods that consider the seismic shaking as an additional force. Such techniques are limited in their capacity to simulate the propagation of seismic waves within the slope. In particular, the interactions of the incoming waves with the local topography are not taken into account in these methods. (Bourdeau and Havenith 2008).

In the context of the 2008 Wenchuan earthquake, we analysed the strong-motion recordings of the main shock, monitored the aftershocks, and carried out large scale shaking table modelling and numerical simulations. So, the topographical amplification effects of slope ground motion response and failure under seismic shaking are studied thoroughly in the present paper.

2   Strong-Motion Recordings During Earthquake

During the Wenchuan Earthquake, over 1,400 components of acceleration records were obtained from 460 permanent free-field stations and three arrays for topographical effect and structural response observation in the network system from the main shock (Li et al. 2008). Figure 7.1 shows the distribution of the stations along the co-

seismic ruptures. Among the records from the main shock, there are more than 560 components with PGA larger than 10 Gal, 226 larger than 50 Gal, 115 larger than 100 Gal, 42 larger than 200 Gal, 16 larger than 400 Gal, and 7 larger than 600 Gal (Li et al. 2008). The largest PGA was recorded at Wolong station (E103.2°, N31.0°) in Wenchuan County. PGAs in the EW, NS, and UD directions are 957.7 Gal, 652.8 Gal and 948.1 Gal, respectively (Table 7.1). Besides, the relatively high PGAs were recorded in Qingping station in Mianzhu City and Bajiao station in Shifang City near the seismic fault (Table 7.1).

We extracted the acceleration peaks of seismic waves of all stations and set the threshold value as PGA > 200 Gal, and drew the peak contour graph as shown in Fig. 7.1. It can be observed that surface acceleration peak contour line is distributed in elliptic type around the seismic fault. The peak acceleration is higher as the area become nearer to the seismic fault. If the rupture process is considered as a series of seismic energy release events from the southwest to the northeast and the surface rupture caused by earthquake spread to the northeast at extremely fast speed (the average rupture speed is 4.8 km/s), Doppler effect in the transmission process can cause the seismic wave to make bigger impacts in the northeast end.

On the whole, the area with horizontal PGAs exceeding 200 Gal is wider than the distribution area of vertical PGAs. In this earthquake, the vertical PGAs decreased faster as the distance increases to the seismic fault. The horizontal seismic waves along the fault spread farther than the waves perpendicular to the fault (Figs. 7.1, 7.2).

From Figs. 7.1, 7.2, it can be observed that, in the hanging wall of the fault in the segment from Wolong of Wenchuan to Tashui of Anxian County, the vertical components of acceleration peaks of seismic waves are usually high. In the areas such as Wolong in Wenchuan and Qingping in Mianzhu, vertical accelerations exceed 600 Gal sometimes. Figure 7.3 shows the contours of the ratios of the PGA on EW direction over the PGA on UD direction. It can be seen from Fig. 7.3 that within the range of around 30 km from the surface rupture zone of central

Fig. 7.1 PGA isoline map of horizontal direction (EW) recorded from the main shock of the Wenchuan earthquake
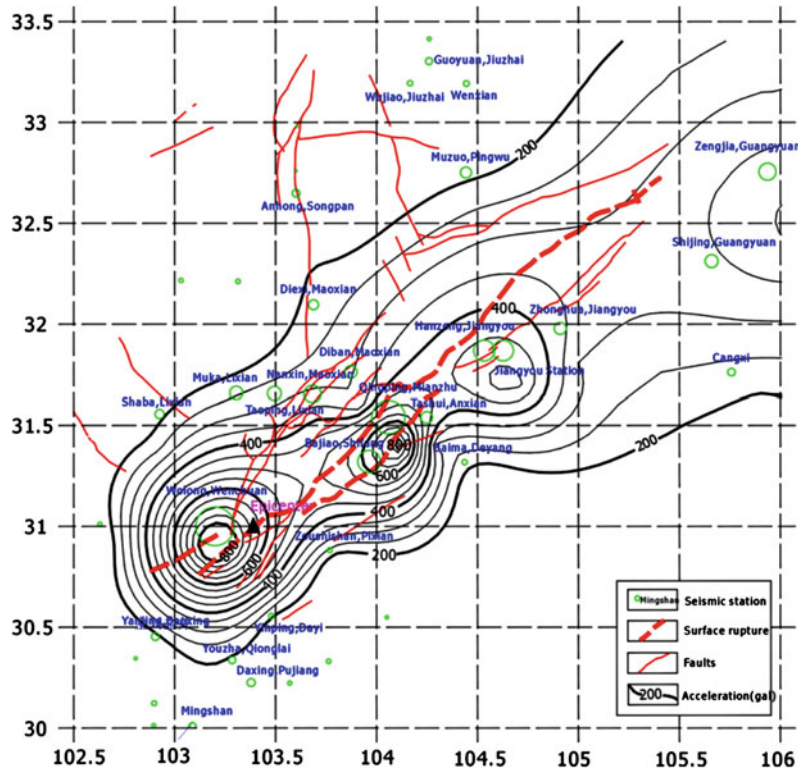
Table 7.1 Strong-motion records (PGA) of the Wenchuan earthquake near the seismic fault

Station	Location	PGA(Gal)		
		EW	NS	UD
Wolong, Wenchuan	E103.2°, N31.0°	957.7	652.8	948.1
Qingping, Mianzhu	E104.1°, N31.5°	824.1	802.7	622.9
Bajiao, Shifang	E104.0°, N31.3°	556.1	581.5	633
Tashui, Anxian	E104.3°, N 31.5°	289.5	203.5	179.9
Shijing, Guangyuan	E105.8°, N32.2°	310.4	273.9	143.7
Zengjia, Guangyuan	E106.1°, N32.6°	424.4	410.4	143.7
Jiangyou	E104.7°, N31.8°	511.3	458.6	198.2
Hanzeng, Jiangyou	E104.6°, N31.8°	519.4	350.1	444.3
Taoping, Lixian	E103.5°, N31.6°	339.7	342.3	379.5
Nanxin,Maoxian	E103.7°, N31.6°	421.2	349.2	352.4

fault in the hanging wall of segment from Wolong in Wenchuan to Qingping in Mianzhu, between which and the front fault, the horizontal and vertical acceleration peaks are quite close. The ratio approaches 1.0. However, in the areas near the seismic center, especially in the range from Lixian County to the north of seismic center and Bajiao of Shifang to the south in the hanging wall of fault, the ratio between horizontal and vertical acceleration values is lower than 1, namely, the vertical acceleration is higher than the horizontal acceleration.

During the earthquake, when the horizontal and vertical accelerations of the same order appeared in the same time in the mountain slope, as the vertical acceleration point upwards, the
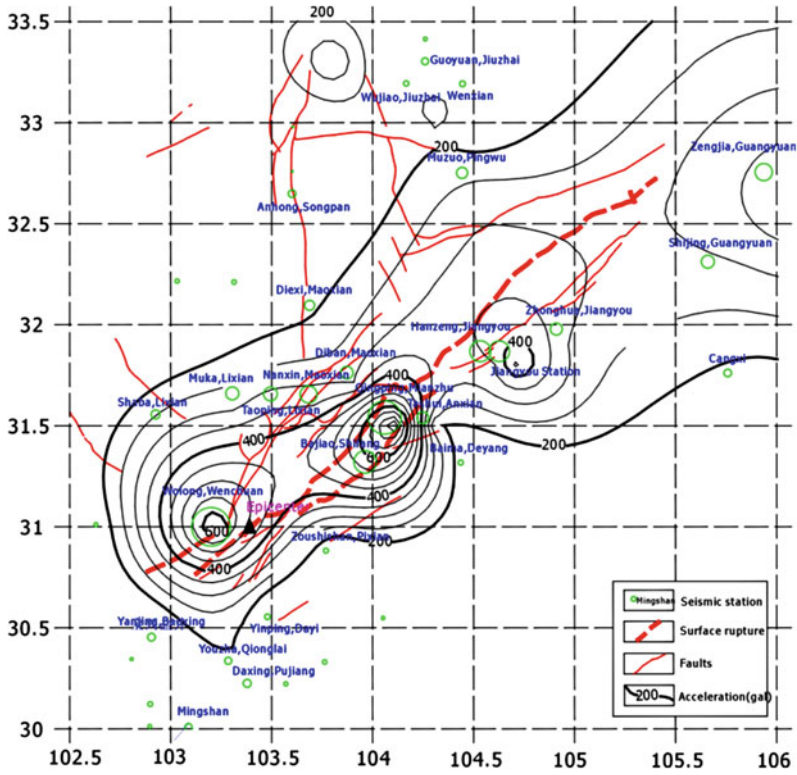
Fig. 7.2 PGA isoline map of vertical direction (UD) recorded from the main shock of the Wenchuan earthquake

Fig. 7.3 Contours of the ratio of the horizontal PGAs (EW) over the vertical PGAs (UD) recorded from the main shock of the Wenchuan earthquake
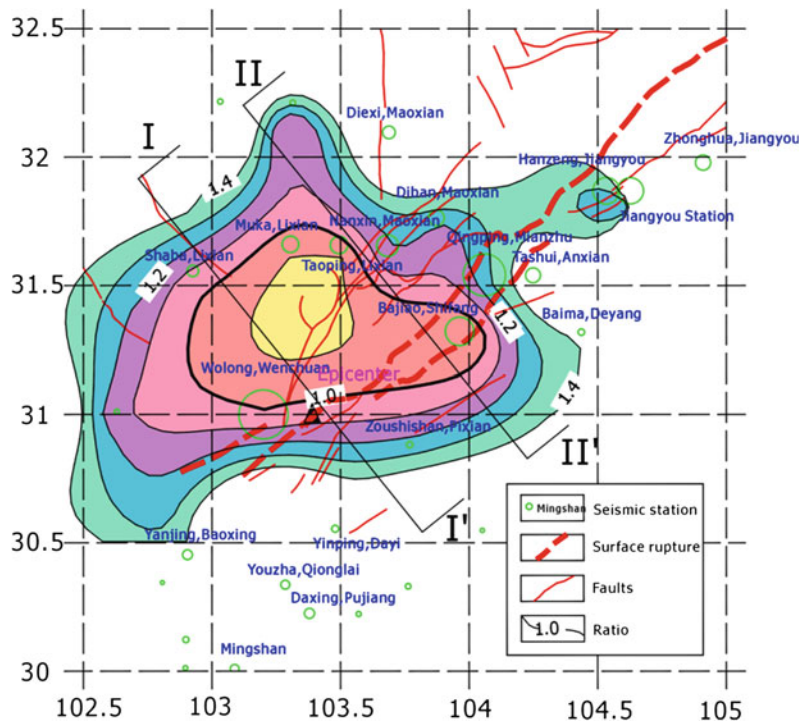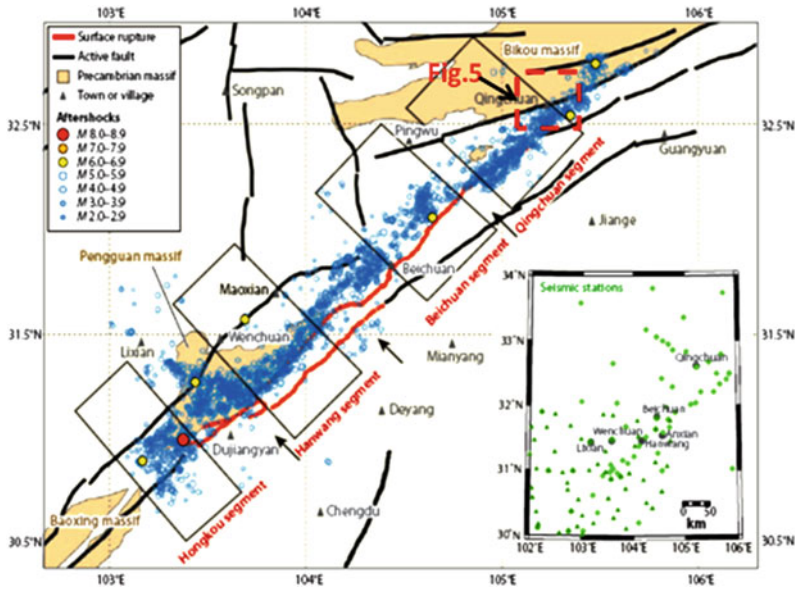
Fig. 7.4 Relocated aftershock distribution of the Wenchuan earthquake (after Zhang et al. 2010). The lower-right inset shows distribution of seismic stations used for the aftershock relocations. Triangles are stations affiliated with the Western Sichuan Seismic Array deployed since 2007; diamonds are from the Sichuan Seismic Network and some temporary stations deployed after the main shock

mountain body had a certain weightless effect that is objectively reduced the spatial constraint on the rock body and made it incline towards free face. In the hanging wall of segment of the central fault from Wenchuan to Qingping and in the segment from Bajiao of Shifang to Qingping of Mianzhu between the front fault and the central fault, the horizontal acceleration was quite high in the slope and the vertical acceleration was close to that or higher, which would result in more slope destruction. This result was proved by the remote-sensing interpreted data of the area.

3 Monitoring of the Aftershocks

3.1 Monitoring Program

As of February 10, 2010, 311 major aftershocks with magnitude Ms ≥ 4.0 in Wenchuan earthquake area were recorded. The strongest was Ms 6.4 on May 25, 2008 in Qingchuan County, as shown in Fig. 7.4 (Dai et al. 2010; Zhang et al. 2010). In order to obtain the ground motion response of the real slopes under strong quakes, a monitoring profile composed of five stations was deployed in Dongshan and Shiziliang mountains, Qingchuan County on September 1, 2009 to observe motions of aftershocks of the Wenchuan earthquake, as shown in Figs. 7.5, 7.6. Until January 24, 2010, 60 aftershock events were detected.

3.2 Monitoring Results

Dongshan Slope

Taking the recorded PGA values of 1# station (788) as a standard, the ratio of PGA values in different directions of 2# (871 m) and 3# (962 m) stations to 1# station are shown in Fig. 7.7 and Table 7.2.

The above figures and table suggested that:

(1) Horizontal peak: the horizontal ground motion response was bigger than 1.0 in the main in the slope hillside of Dongshan (871 m), while it was lower than 1.0 in the mountain top (962 m). In the hillside, the amplification effect was stronger in the

Fig. 7.5 Location map of the monitoring profile
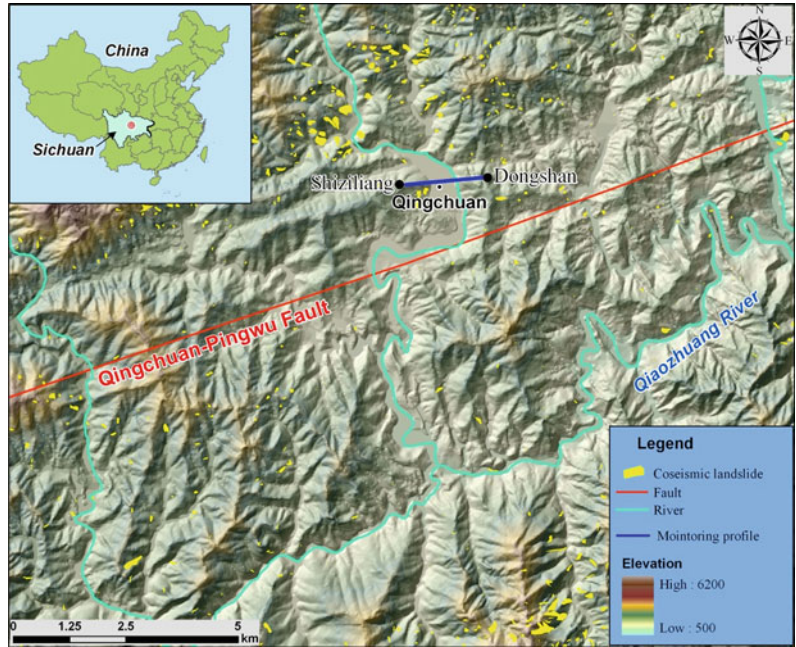
Fig. 7.6 The monitoring profile
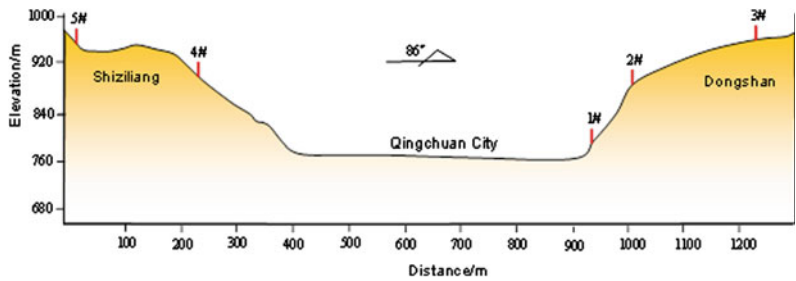
Fig. 7.7 The ratio of PGA values at 4# (893 m) and 5# (962 m) station to those at 1# station. **a** East–West direction, **b** North–South direction, **c** Vertical direction
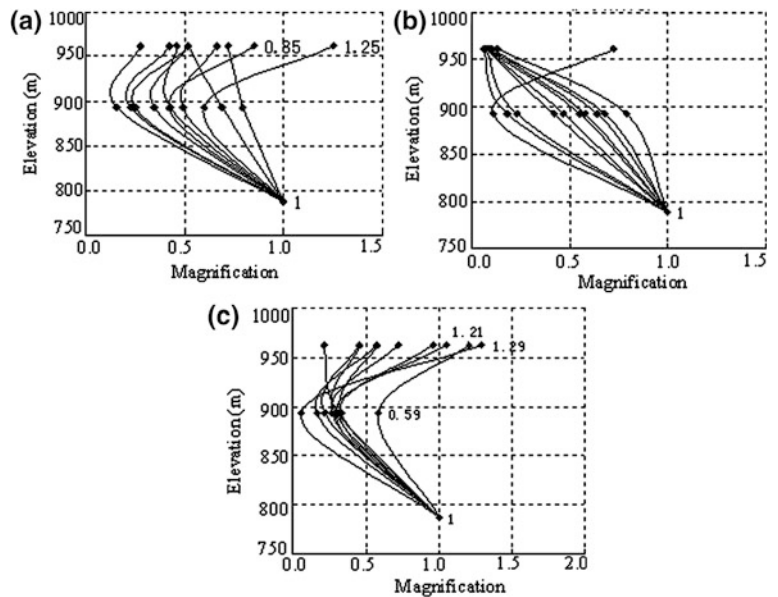
Table 7.2 The ratio of PGA values at 2# and 3# station to those at 1# station

Elevation (m)	EW		NS		UD	
	≥1.0 (%)	<1.0 (%)	≥1.0 (%)	<1.0 (%)	≥1.0 (%)	<1.0 (%)
3# (962 m)	5	95	19	81	48	52
2# (871 m)	38	62	76	24	0	100

south-north direction than in the East–West direction, and the amplification coefficient was 1.0–2.48 times; in the mountain top, the amplification effect was slightly stronger in the south-north direction than in the east–west direction and the amplification coefficient was 1.0–1.48 times.

(2) Vertical peak: in the slope hillside of Dongshan (871 m) the vertical ground motion response was decreasing, whereas amplification phenomenon appeared in the mountain top (962 m) and the coefficient was 1–1.84 times.

(3) Vector peak: in the slope hillside of east mountain (871 m) the dynamic amplification effect of horizontal and three-directional vector peak accounted for a certain proportion and the amplification coefficient was 1.0–1.58, but in the mountain top (962 m) the horizontal and three-directional vector peaks were decreasing.

(4) In the same earthquake, with the increase of elevation of monitoring point, the number of horizontal response coefficient being higher in the hillside slope of Dongshan than in the mountain top accounted for 95 % of the statistical number. The response was protruding with the increase of elevation, implying that the horizontal peak response in the hillside slope of Dongshan was stronger than that in the mountain top.

(5) In the same earthquake, with the increase of monitoring elevation, the number of vertical response coefficient being higher in the mountain top than in the hillside accounted for 65 % of the statistical number. The response was concave with the increase of elevation, demonstrating that the vertical

peak in the mountain top of Dongshan was stronger than that in the hillside.

With the increase of monitoring station elevation, the dynamic amplification effect should be stronger in the hillside than in the mountain top, and the SN amplification coefficient was more evident. Based on the thin feature of Dongshan, it is deducted that SN dynamic vibration is more striking, and the amplification effect is affected by topography. However, in the slope hillside of Dongshan, the number of horizontal EW peak being bigger than SN peak accounted for 64 % of the statistical number, so it is inferred that the free-face in the EW direction of the observing point has more obvious influence on the horizontal peak. Meanwhile, the horizontal peak is bigger than the vertical peak, indicating that the ground motion response in the monitoring point of 871 m was dominated by horizontal force.

When the elevations were equal or close, the dynamic amplification in Dongshan slope was obviously stronger than that in Shiziliang slope. Based on the thin feature of mountain body, it is inferred that dynamic sloshing of Dongshan slope should be stronger than that of Shiziliang mountain body, but in the outstanding ridge of mountain top, the topographic amplification feature may be the same. Through the monitoring to the slopes on both sides of Dongshan and Shiziliang, it is found that under seismic loads, the slope ground motion response to the earthquake doesn't just increase with the increase of elevation, but has a close relation with the micro-relief of slope, local free-face condition, physical features of rock body, and characteristics of fracture development.

Table 7.3 Similarity Constants of the model

Quantities	Similarity ratio	Constants
Geometry size (L)	$C_L = 100$ (controlled quantity)	100
Density (ρ)	C_ρ (controlled quantity)	1
Acceleration (a)	$C_a = 1$ (controlled quantity)	1
Weight (γ)	$C_\gamma = C_\rho$	1
Elastic modulus (E)	$C_E = C_\rho C_L$	100
Poisson's ratio (μ)	$C_\mu = 1$	1
Cohesion (C)	$C_C = C_\rho C_L C_a$	100
Friction angle (Φ)	$C_\Phi = 1$	1

4 Large Scale Shaking Table Modeling

Due to wide distribution of the sedimentary rocks in the Longmenshan zone, landslides in the stratified rock slopes are easy to be found in the disaster area. In order to figure out the failure mechanism and ground motion responds of these slopes under earthquake shaking, two types of typical lithology slope with dip and anti-dip structures have been used for the shaking table test.

(1) Hard rock slope: They are usually limestone or dolomite rock slope. As the main perforating joint, rock formation plane is usually developed orthogonal with other joints.

(2) Soft rock slope: They are usually phyllite, shale and slate rock slope. The rock formation plane is the controlling preferred plane.

Four typical stratified slope types are selected to test on the shaking table:

Hard rock dip slope (HD)
Hard rock anti-dip slope (HAD)
Soft rock dip slope (SD)
Soft rock anti-dip slope (SAD).

4.1 Set Up of the Modeling

In order to compare these different structures, a linear type and "U" shape valley (Fig. 7.8) are built for analysis, with a geometry scale 1:100. The similarity ratios are given in Tables 7.3 and 7.4.

Using the above similarity relationship, proportion experiments are proceeded to determine the ratio law. Final ratios are as following Table 7.5.

Considering the different structural features between hard rock slope and soft rock slope, the constructions of these two types are different. The hard rock slope is built with prefabricated solid blocks (Fig. 7.9), and the soft rock slope is built by layer (Fig. 7.10).

Constructed slopes are put into 2 rigid structure model cubes with 20 cm cushioning layer to avoid boundary effect. 42 acceleration monitor devices are installed inside these slopes (Fig. 7.8). The built model is shown in Figs. 7.11 and 7.12.

4.2 Results

Actual seismic wave from Wolong station are used to apply on shaking table, and the PGA value are improved gradually from 0.1 g to 0.6 g, the responsive PGA are extracted from every sensor inside slopes and made comparison with A8 (table sensor). PGA amplification coefficients are acquired and the distribution is shown in the following figures.

Dynamic response of hard rock slope is shown in Fig. 7.13, and the PGA amplification relationship with input signal amplitude of the slope shoulder is in Figs. 7.14, 15.

(1) Both dip slope and anti-dip slope have significant PGA amplification on the upper top region. In dip slope, such amplification

Fig. 7.8 Model layout in shaking table test
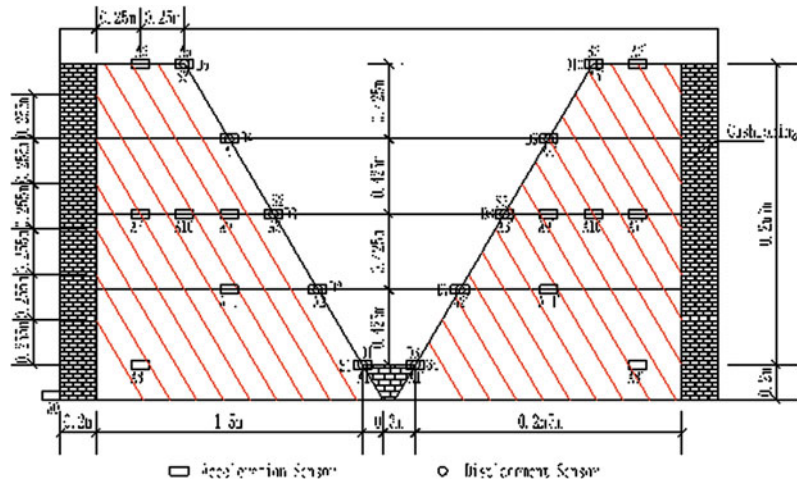
Table 7.4 Model Material parameter table

Lithology	Hard rock		Soft rock	
Type	Prototype	Model	Prototype	Model
Density (KN/m^3)	26.5–27.5	27	26–27	26
Elastic modules (MPa)	6000–9000	73.7	1000–3000	24.1
Poisson's ratio	0.25	0.25	0.28	0.28
Cohesion (MPa)	5–50	0.12	0.5–5	0.043
Friction angle(°)	38–45	43	30–38	35
Joint Cohesion (MPa)	0.5–1.0	0.006	0.05–0.5	0.001
Joint Friction angle (°)	35–40	37	25–30	25

Table 7.5 Similarity material ratio

Material (%)	Barite	Sand	Plaster	Glycerol	Water	Motor oil
Soft rock	51.3	32.1	9.0	6.4	1.3	0
Hard rock	43.2	30.9	12.3	8.6	1.2	3.7

developed in the upper half top, the 1/2 slope height is about 2 times, while the slope shoulder up to 3–6 times. While in the anti-dip slope, superior amplification start at 2/3 slope height, with 2 times amplification, and the slope shoulder is up to 3–4.5 times.

(2) In the dip slope, 1/4 is a sensitive region to seismic wave. The PGA amplification coefficient can reach up to 3 times, higher than the anti-dip slope, which means that such position is an easily failure area during the earthquake.

(3) In the dip slope, PGA amplification has little difference between the surface and the inside, both increasing rapidly under acceleration higher than 0.4 g. While in the anti-dip slope surface, when input acceleration is higher than 0.2 g, the PGA amplification coefficient maintained 4 times, even is slightly decreased.

Such phenomenon does not mean PGA amplification coefficient reducing with input acceleration rising while higher than 0.2 g in HAD slope, judging from the phenomenon

Fig. 7.9 Building with solid blocks
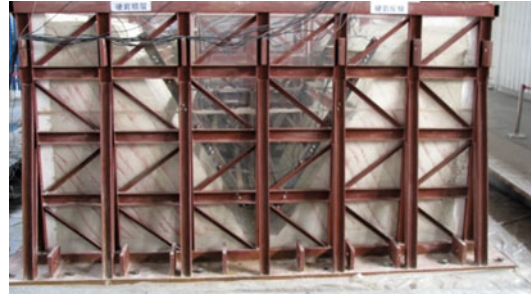
Fig. 7.11 Hard rock slope model

Fig. 7.10 Building layer by layer
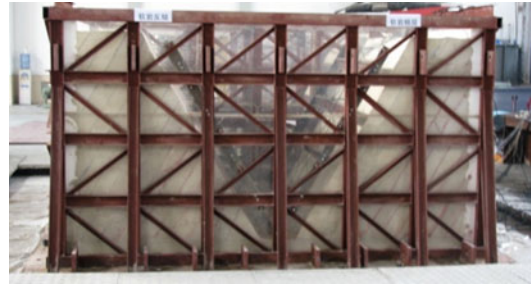
Fig. 7.12 Soft rock slope model

Fig. 7.13 Hard slope with horizontal seismic wave (*Blue* is 0.1 g, *Purple* is 0.2 g, *Green* is 0.4 g, *Red* is 0.6 g)
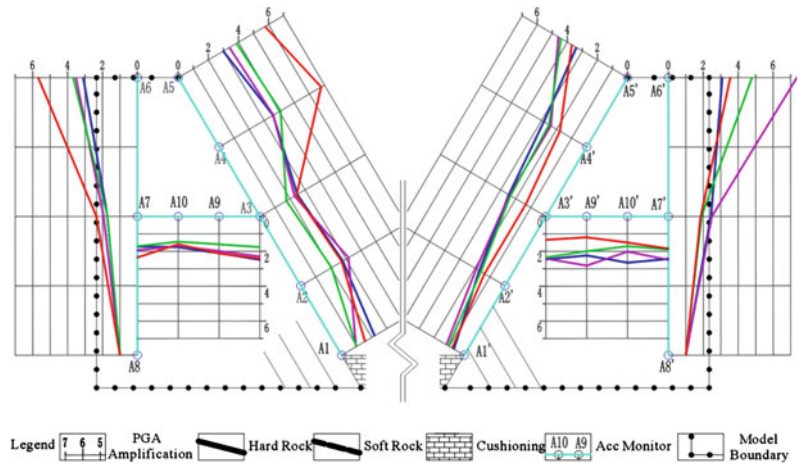
in experiments. HAD slope has crack and relaxed rock mass developed at the slope shoulder, which influences the ground motion response of this position.

(4) While higher than 0.2 g, HAD slope has more PGA amplification inside the slope than the surface, both being higher than HD

slope (Figs. 7.14, 7.15). It means that HAD slopes are easy to crack at the rear edge of slope top, which fits the field investigation well.

(5) The ground motion response characteristic of the HD slope top is opposite to HAD slope, which means in the former ones. It is
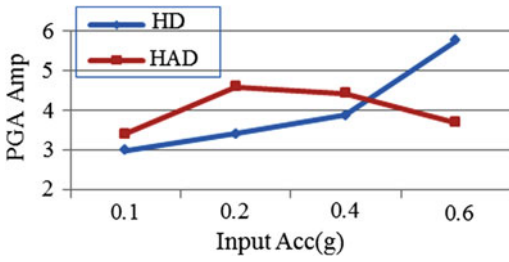
Fig. 7.14 Acceleration response at the hard slope shoulder (A5)
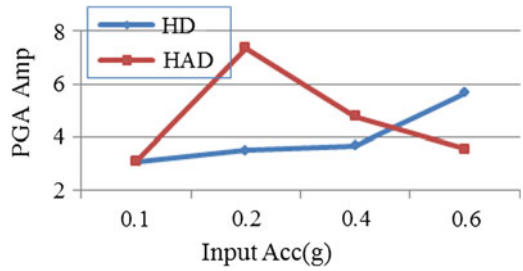
Fig. 7.15 Acceleration response at the rear edge of hard slope top (A6)

Fig. 7.16 Soft slope with horizontal seismic wave (*Blue* is 0.1 g, *Purple* is 0.2 g, *Green* is 0.4 g, *Red* is 0.6 g)
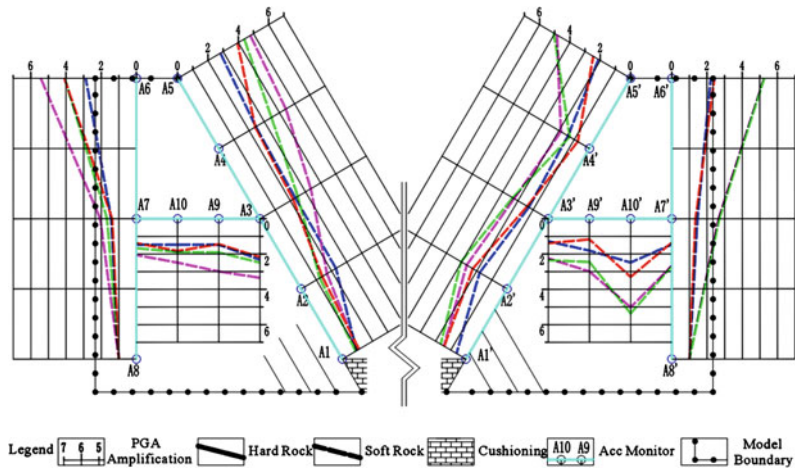
easy for them to be damaged in the shallow surface during earthquake.

Figure 7.16 is PGA amplification of the soft rock slope, the PGA amplification vary with input signal PGA shown as Figs. 7.17, 7.18.

(1) Biggest PGA amplification is apparent at 0.2 g, which is higher than other values. Means PGA amplification will not increase with the input signal, even decrease.

(2) On the slope surface, PGA amplification has been significantly increasing while higher than 0.2 g at 1/2 slope height, up to 3–5, after that elevation, PGA amplification has little variation.

(2) In SAD slope, starting with 1/4 slope height, PGA amplification in slope surface maintains about 2 times until slope shoulder, which has a rapid growth up to 5 times. The slope surface PGA amplification coefficient of SD and SAD slope shows the dynamic failure mechanism difference of these two slopes. SD slope has common deformation characteristic in the surface, while SAD slope is easy to be damaged at slope toe or slope shoulder.

(3) 0.2 g seems to be a boundary between significant ground motion response of the soft rock slope shoulder. And it is not clear between dip and anti-dip both in surface and inside of the slope.

5 Numerical Modeling

5.1 Theory Background

Generally, franc2D/L (Cornell Fracture Group) is used to analyze the crack propagation
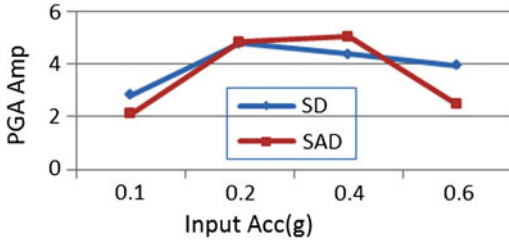
Fig. 7.17 Acceleration response at the hard slope shoulder (A5′)
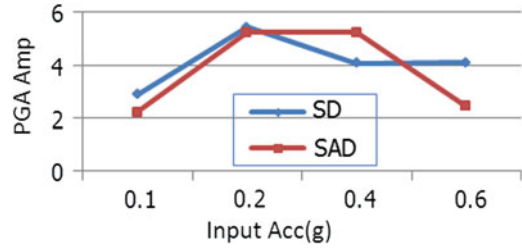
Fig. 7.18 Acceleration response at the rear edge of hard slope top (A6′)
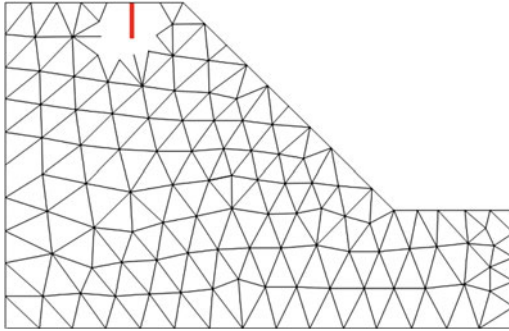
Fig. 7.19 FEM model of crack at rear edge of slope top
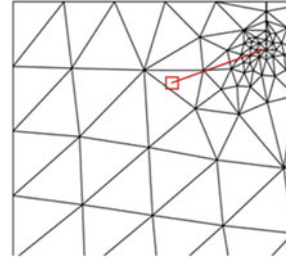
Fig. 7.20 Crack propagation direction while acceleration points to slope inside

behavior, which is based on strain energy density theory (S criteria) and energy release rate theory (G criteria) of the fracture mechanics.

(1) Griffith Crack:

When curvature of the crack tip

$$0 \le \rho \le \frac{8}{\pi} b_0$$

where corresponding critical stress is

$$\sigma_c = \sqrt{\frac{2E\gamma}{\pi a}}$$

where, E *is* elastic modulus, γ is surface energy density, and a is length of crack.

(2) G criteria:

Type I crack can be expressed as:

$\mathbf{K}_1 = \alpha\sigma\sqrt{\pi n}$

where, a is stress without crack, σ is size of crack, and n is shape coefficient (relative to crack size and location).
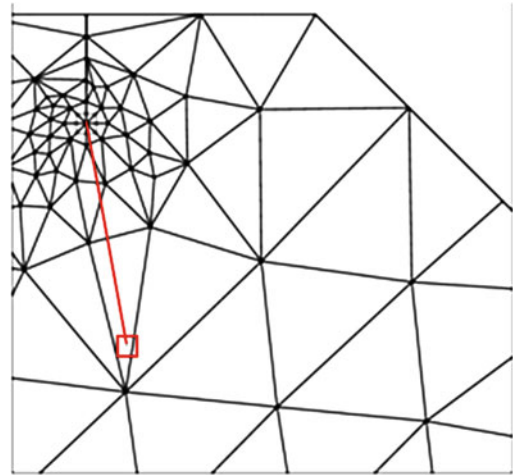
Fig. 7.21 Crack propagation direction while acceleration points to slope outside

5.2 Simulation Results

Assume the crack propagation in a slope is started with surface rupture. Such behavior is close to the variation stress field of the slope. A

Table 7.6 Crack propagation direction of different acceleration combination

V H	0 g	0.2 g	0.3 g	0.4 g	0.6 g	0.8 g	0.9 g	1.0 g	1.2 g
0.2 g	70.53	70.53	70.53	70.53	70.53	70.53	70.53	70.53	70.53
0.3 g	70.53	70.53	70.53	70.53	70.53	70.53	70.53	70.53	70.53
0.4 g	22.68	64.23	70.53	70.53	70.53	70.53	70.53	70.53	70.53
0.5 g	11.24	11.24	27.35	42.57	70.53	70.53	70.53	70.53	70.53
0.6 g	7.99	7.99	13.74	17.30	31.37	64.23	70.53	70.53	70.53
0.7 g	6.48	8.36	9.63	11.24	16.15	20.08	34.83	49.08	70.53
0.8 g	5.56	6.88	7.69	8.65	11.24	15.36	18.44	22.68	37.79
0.9 g	5.04	5.99	6.56	7.22	8.89	11.24	12.82	14.79	20.61
1.0 g	4.64	5.39	5.83	6.33	7.52	9.09	10.08	9.26	14.36
1.1 g	4.23	4.98	5.32	5.71	6.62	7.77	8.46	9.26	11.24
1.2 g	4.64	4.46	4.93	5.26	5.99	6.88	7.41	7.99	9.40

typical slope FEM model with a crack on the rear edge of slope is shown in Fig. 7.19, with a height 300 m and a gradient of 45°, and the elastic modules is 20 GPa, Poisson's ratio is 0.25, unit weight is 2650 kg/m³. The stresses and strains are calculated by the linear-elastic finite element method. Different acceleration combinations are used to calculate the crack propagation direction.

The crack propagation direction during earthquake has two opposite results: when instantaneous acceleration point to outside slope, the propagation direction point to slope leading edge (Fig. 7.20), or else point to the inside slope (Fig. 7.21).

Different PGA combinations are used to calculate the crack propagation, as the crack which point to the inside slope doesn't have significant influence to the stability of slopes and relative calculation is ignoring. The results are shown in Table 7.6 and Fig. 7.22.

As shown above, the direction of crack propagation (include angle with crack itself) is generally deflected with large angle in nature acceleration environment (both vertical and horizontal accelerations are zero). Without vertical acceleration, as horizontal acceleration increasing, the angle decreases rapidly. While higher than 0.4 g, the angle became an acute one, which means the crack will extend along itself. Increasing vertical acceleration will lead

to corresponding higher horizontal acceleration for the angle deflection. The needed horizontal acceleration value is always lower than the vertical value.

When horizontal acceleration is higher than 0.6 g, it is easy to develop a small angle based on previous calculation. That is the reason that in the strong seismic zone, high and steep rear edge after landslide is very common.

5.3 Discussion

A typical slope has its height and gradient, within specific earthquake intensity, the PGA value in slope surface is generally different due to elevation amplification effect. So it is a convenient way to acquire PGA amplification coefficient variation with altitude by the finite element method. With different input seismic wave PGA, previous results can be used to estimate the failure patterns by crack propagation direction.

Following slope is 300 m high, has a 45° dip angle. The input accelerations are 0.2 g and 0.5 g. The crack pattern is as following.

Generally, in 0.2 g horizontal acceleration area, after PGA amplification, the upper top of the slope will acquire an acute crack angle, leads to steep slide surface, and gradually deflects into

Fig. 7.22 Relationship between acceleration combination and crack propagation direction
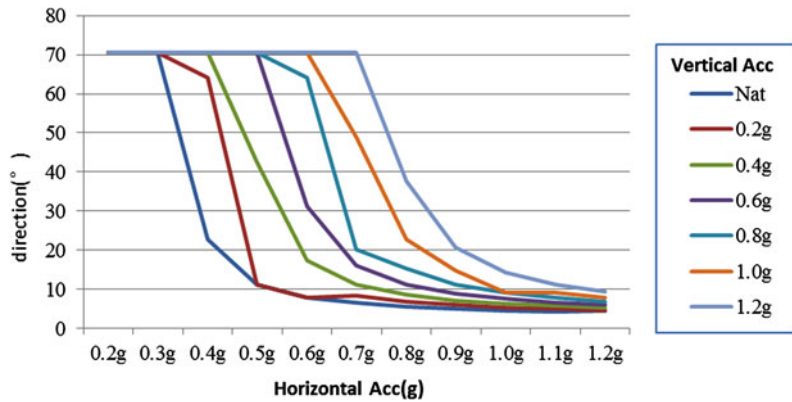
Fig. 7.23 Horizontal acceleration 0.2 g
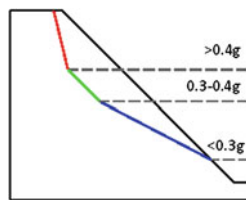
Fig. 7.24 Horizontal acceleration 0.5 g

a gently gradient with elevation decreases (Fig. 7.23). With higher acceleration such as 0.5 g, the crack will extend to bottom of the slope directly (Fig. 7.24). That is why high and cliffy slide surface in rear edge of landslides is very common in the strong earthquake zone.

6   Conclusions

Through analysing the strong-motion recordings of the main shock, monitoring results during the aftershocks, large scale shaking table modelling and numerical simulations, the topographical amplification effects of slope ground motion response under seismic shaking were studied thoroughly. The main results and conclusions are reached as follows:

(1) A preliminary analysis of the spatial distribution of PGAs demonstrates that the directivity effect and the hanging wall effect in the near-fault ground motion as observed from past large earthquakes around the world also occurred in the Wenchuan earthquake. PGAs are relatively large in the fault rupture propagation direction, and also roughly larger on hanging wall. In the near-

fault records, the PGA is generally larger in the EW direction than the NS direction. A comparative analysis of the horizontal and vertical components of the main shock records displays that the PGA is larger in the vertical direction than in one or two horizontal directions for some near-fault records.

(2) A monitoring profile composed of 5 stations was deployed in Dongshan and Shiziliang Mountain, to obtain the ground motion response of the real slopes during aftershocks. It was found that micro-relief is one of the key factors for topographic amplification and site conditions have an important effect on seismic response. The monitoring to the slopes on both sides of Dongshan and Shiziliang showed that under seismic loads, the slope ground motion response to the earthquake doesn't just increase with the increase of elevation, but has close relations with the micro-relief of slope, local free-face condition, physical features of rock body, and characteristics of fracture development.

(3) Large scale shaking table tests were used to analyze the ground motion response of the

slope with different lithology and structure. Both dip slope and anti-dip slope have significant PGA amplification on the upper top region. In dip slope, such amplification developed in the upper half top, the 1/2 slope height is about 2 times, while the slope shoulder up to 3–6 times. While in the anti-dip slope, superior amplification start at 2/3 slope height, with 2 times amplification, and the slope shoulder is up to 3–4.5 times.

(4) Numerical simulation and fracture mechanics based calculation were used to explain the unique phenomenon of the landslides triggered by the quake. Based on stress increase magnitude results, failure development parts of the dip slope and anti-dip slope are different. The dip slope is in the foot section, while the anti-dip slope is in the middle section.

References

Benites RA, Haines AJ (1994) Quantification of seismic wave field amplification by topographic features. Research Report to the Earthquake Commission, New Zealand 108

Bouchon M, Baker J (1996) Seismic response of a hill: the example of Tarzana California. Bull Seismol Soc Am 86:66–72

Bourdeau C, Havenith H-B (2008) Site effects modelling applied to the slope affected by the Suusamyr earthquake (Kyrgyzstan 1992). Eng Geol 97:126–145

Dai FC, Xu C, Yao X, Lu L, Tu XB, Gong QM (2010) Spatial distribution of landslides triggered by the 2008 Ms 8.0 Wenchuan earthquake, China. J Asian Earth Sci 40(4):883–895

Douglas J (2003) Earthquake ground motion estimation using strong-motion records: a review of equations for the estimation of peak ground acceleration and response spectral ordinates. Earth Sci Rev 61:43–104

Keefer DK (1984) Landslides caused by earthquakes. Bull Geol Soc Am 95:406–421

Li XJ, Zhou ZH, Yu HY (2008) Strong motion observations and recordings from the great Wenchuan Earthquake. Earthq Eng and Eng Vib 7:235–246

Meunier P, Hovius N, Haines JA (2008) Topographic site effects and the location of earthquake induced landslides. Earth Planet Sci Lett 275:221–232

Parker RN, Densmore AL, Rosser NJ, de Michele M, Li Y, Huang RQ et al (2011) Mass wasting triggered by the 2008 Wenchuan earthquake is greater than orogenic growth. Nat Geosci 4:449–452

Youd TL, Perkins DM (1978) Mapping liquefaction-induced ground failure potential. J Geotech Eng. Div ASCE 104:433–446

Zhang PZ, Wen XZ, Shen ZK et al (2010) Oblique, high-angle, listric-reverse faulting and associated development of strain: the Wenchuan earthquake of May 12,2008, Sichuan China. Annu Rev Earth Planet Sci 38:353–382

Part II

JLS-ELRP WG Report

Secondary Hazards Associated with Coseismic Landslide

8

Takashi Okamoto, Masaaki Sakurai, Satoshi Tsuchiya, Hiroyuki Yoshimatsu, Kiichiro Ogawa and Gonghui Wang

Abstract

Landslide hazards induced by earthquakes are classified into a primary hazard and a secondary hazard from temporal and spatial viewpoints of damages. Working Group 3 (WG-3) of the Earthquake-induced Landslides Research Projects comprehensively investigated the secondary hazards associated with coseismic landslide. First of all, we provided a definition of them as the landslide hazard occurred with a delay in time and over a wider area, which triggered by post-seismic rainfall, snowmelt and transportation of debris. Then we collected past cases of the secondary landslide disasters, classified them by time scale and disaster type. This paper reports on some major secondary landslide disasters according to our classification as follows: (1) Formation and break of

T. Okamoto (✉)
Tohoku Research Center, Forestry and Forest
Products Research Institute, Nabeyashiki 92-25,
Simo-kuriyagawa, Morioka, Iwate 020-0123, Japan
e-mail: okataka@ffpri.affrc.go.jp

M. Sakurai
Forest Conservation Research Institute Co., Ltd,
Sibukawa, Japan

S. Tsuchiya
Faculty of Agriculture, Shizuoka University,
Shizuoka, Japan

H. Yoshimatsu
Kawasaki Geological Engineering Co., Ltd,
Tokyo, Japan

K. Ogawa
Asia Air Survey Co., Ltd, Kawasaki, Japan

G. Wang
Disaster Prevention Research Institute, Kyoto
University, Kyoto, Japan

landslide dams, (2) Post-seismic landslides, (3) Long-term degradation of mountainous forest watershed, (4) Isolated districts due to traffic disruption and functional decline of countermeasure works.

Keywords

Secondary coseismic landslide · Landslide dam · Post-seismic landslide · Long-term degradation · Isolation

1 Introduction

In Japan, major earthquakes have induced various types of landslides. Most of coseismic landslides are occur during seismic ground shaking, but some of them are actually induced with a delay in time and over a wider area; these are called secondary coseismic landslides. The Working Group 3 (WG-3) of the Earthquake-induced Landslides Research Projects, organized in the Japan Landslide Society, comprehensively investigated the hazards of secondary coseismic landslides. In this paper, we define secondary hazards associated with coseismic landslide and classify them by time scale and disaster type, then explain some cases of them.

2 Definition and Classification of Secondary Hazards Associated with Coseismic Landslide

WG-3 discussed issues concerning various aspects of secondary hazards associated with coseismic landslide. Firstly, we defined the hazards as follows: "Landslide hazards that were induced by post-seismic factors such as rainfall, snowmelt and aftershock with a delay in time and over a wider area". Here, direct hazards caused by the coseismic landslide are not taken into the definition. According to the definition, the secondary hazards are shown diagrammatically in Fig. 8.1 by phenomenological aspect, and in Fig. 8.2 in respect of social impact.

Next, we classified the secondary hazards into four groups based on time scale and disaster type as follows: (1) Formation and break of

landslide dams, (2) Post-seismic landslides, (3) Long-term degradation of mountainous forest watershed and (4) Isolation of districts due to traffic disruption and functional decline of countermeasure works. (1) to (3) are direct hazards and (4) is an indirect hazard. Social unrest, economic concerns and psychological anxiety of victims are not considered since they are also affected by other disasters such as fire and tsunami.

3 Cases of Secondary Disasters Associated with Coseismic Landslide

3.1 Formation and Break of Landslide Dams

Coseismic landslides sometimes deposit debris in a river and obstruct its flow (called a "landslide dam"). Earthquake has almost the same number of triggers for landslide dam as rainfall (Fig. 8.3). A landslide dam may submerge houses and farms by the accumulation of water above the dam. Furthermore, breakage of the landslide dam often cause flooding, debris flow, and considerable damage in the downstream basin. Therefore, landslide dam is a serious mass movement that should be investigated with priority compared with other coseismic hazards.

In the Nikko Earthquake (AD 1683), a landslide occurred on the slope of Mt. Katsurou, and its debris formed a landslide dam in the Oga River in the upper basin of the Kinu River. Ikari village, which is located upstream of the dam, was submerged after 90 days, and the main road along the river was also submerged. In 1704, the
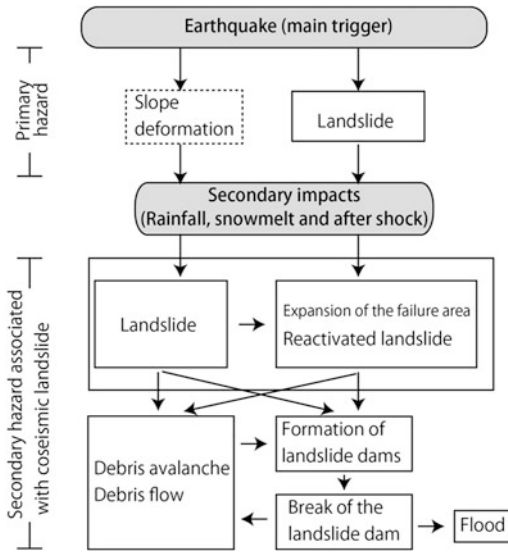
Fig. 8.1 Overview of the secondary hazards associated with coseismic landslide
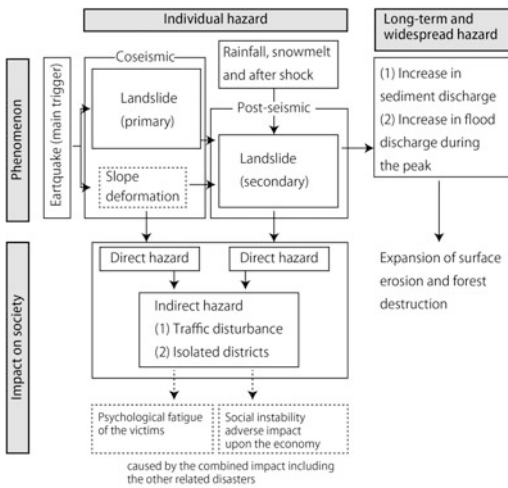
Fig. 8.2 Social impacts by the secondary hazards associated with coseismic landslide

Fig. 8.3 Trigger for landslide dam formation (Schuster 1986)
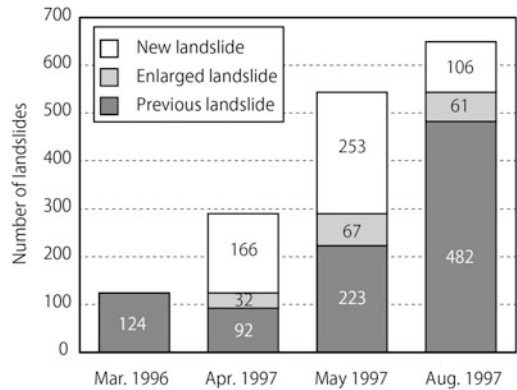
Fig. 8.4 Temporal variation in number of landslides after the earthquake in the northern part of Kagoshima Prefecture (1997) (Matsumoto et al. 1998)

landslide dam broke by heavy rain and the resulting floodwater reached the town of Utsunomiya (Sato 1983).

In the Zenkouji Earthquake (1847), more than 60,000 landslides were induced and 51 landslide dams were formed in the Matsushiro domain. One of the largest landslides at Mt. Iwakura dammed the Sai River, and a dammed lake of up to 70 m depth and 23 km length formed. This

lake broke after 19 days, causing flood damage in the lower reaches (Akahane 1998).

In the Mid Niigata Prefecture Earthquake (2004), 55 landslide dams were formed along the Imo River. The largest dam at Higashi-Takezawa village was 30 m high and submerged upper villages and roads (Photo 8.1). As an emergency measure, the water was drained by pumps and a temporary channel, then the dam was stabilized by check dams and channel works (Ministry of Land, Infrastructure and Transport Yuzawa Office 2005).

In the Iwate-Miyagi Nairiku Earthquake (2008), some landslide dams submerged a hot spring hotel and some houses along the river (Photo 8.2). Many landslide dams were also formed by the Wenchuan Earthquake (2008): the largest dam created a lake more than 6 km long

Photo 8.1 Submerged village and road by landslide dam caused by the Mid Niigata Prefecture Earthquake in 2004 (Higashi-Takezawa village, Niigata Pref., Japan) (Sakurai and Goto 2005)

Photo 8.2 Submerged houses by landslide dam caused by the Iwate-Miyagi Nairiku Earthquake in 2008 (Yunokura village, Miyagi Pref., Japan) (taken by Okamoto T.)

Photo 8.3 Landslide dam caused by the Wenchuan Earthquake (2008) in China (taken by Sakurai M.)

Photo 8.4 Debris flow disaster at Oyama village, Kanagawa Pref., Japan caused by heavy rain two weeks after the Kanto Earthquake (1923) (Editional committee of Isehara municipal census 1963)

along the river (Photo 8.3) (Chigira et al. 2010). Although channel works have been constructed, long-term sediment discharge is still a concern.

3.2 Post-Seismic Landslides

At an unstable slope due to strong ground shaking, post-seismic landslides are sometimes induced by the subsequent rainfall, snowmelt and aftershock. In this section, we describe cases of post-seismic landslides including debris flows.

In the Kanto Earthquake on September 1 (1923), many landslides occurred in the Tanzawa mountainous district, and large amounts of debris were deposited on unstable slopes. Between September 12 and 15, heavy rains (200–300 mm in 4 days) during a typhoon induced many landslides including some serious debris flows. At Oyama village, one person was killed and 140 houses were destroyed by a large debris flow (Photo 8.4), and other villages were also damaged by other debris flows. Some post-seismic landslides also occurred in the Hakone volcanic mountainous area near Tanzawa (Nakamura et al. 2000). There was heavy rainfall throughout the Tanzawa district from north to south, including part of the Hakone area. These debris flows occur in the areas with strong ground shaking by the Kanto Earthquake.

In the Hyogo-ken Nanbu Earthquake (1995), many landslides were induced around the fault of Mt. Rokko. Four months later, a newly-induced landslide and expansion of collapsed areas were found by interpreting aerial photographs. Furthermore, landslides after the earthquake were caused by less rainfall than before the earthquake (Tomita et al. 1996).

After the Mid Niigata Prefecture Earthquake (2004), a secondary failure was found at the Higashi-Takezawa landslide area during the subsequent snowmelt season. In addition, many small landslides were also found on the slopes by airborne laser survey along the Imo River after the snow-cover season.

3.3 Long-Term Degradation of Mountainous Forest Watershed

When many landslides or a large landslide are caused by an earthquake, a large amount of debris is rapidly supplied to mountainous slopes. The landslides destroy the forest soil and forest floor plants which prevent surface erosion of the slope, and so the damaged mountainous area remains degraded for a long time.

In March 1997, earthquakes with magnitude 6.5 occurred in the northern part of Kagoshima Prefecture, and many landslides were induced where granitic rocks are distributed near the epicenter. In this area, new landslides and the expansion of landslides increased due to the magnitude 6.3 aftershock in May 1997 and subsequent rainfall during the rainy season. The number of landslide gradually increased from 124 before the earthquake to 649 after the earthquake (Fig. 8.4) (Matsumoto et al. 1998).

After the Kanto Earthquake (1923), the ratio of landslide area was estimated to be 21.4 % in the Nakagawa river basin and 25.3 % in the Kurokura river basin (Kanagawa Prefecture 1930). However 22 % of the degraded area was restored, the degraded area remained for a long time after the North-Izu Earthquake (1930) and heavy seasonal rains in 1937 and 1938 (Ozawa

Photo 8.5 Landslide close to the Omigawa railway Station caused by the Niigata-ken Chuetsu-oki Earthquake (2007) (Niigata Pref., Japan) (taken by Sakurai M.)

1998). In recent years, the basins were finally stabilized by continuous countermeasure works (Ishigaki et al. 2007).

In the Western Nagano Prefecture Earthquake (1984), 36 million m^3 of collapsed soil traveled down the slope of Mt. Ontake as debris flow, and degraded forested area covering 6 million m^2. Even though countermeasure works such as check dams and revegetation were carried out, a debris flow occurred in 1987 (Nagano Regional Forest Office 1991).

3.4 Isolation of Districts due to Traffic Disruption and Functional Decline of Countermeasure Works

Roads and railways are sometimes disrupted by coseismic landslides, thus they often isolate some districts. In addition, loss of infrastructure such as electrical power and communication means makes isolation more serious. Particularly, traffic may be easily disrupted and cause the isolation of mountainous and island villages where the traffic system is sparse.

In the swarm earthquakes of the northern Izu Island chain (2000), Wakagou village on Niijima Island was isolated when a coseismic landslide blocked a road (Furukawa 2001), showing how easily a depopulated district may become isolated.

In the Mid Niigata Prefecture Earthquake (2004), 41 roads were damaged and 17 routes were closed by coseismic landslides, and 61 villages were isolated (Hokuriku Regional Development Bureau 2005). Furthermore, coseismic landslides destroyed many fences for snow avalanche control and reduced their effect during winter (Sakurai and Goto 2005).

In the Niigata-ken Chuetsu-oki Earthquake (2007), a landslide of 20 m width, 40 m height and 5 m depth occurred, blocking the railway track close to Omigawa Station (Photo 8.5) (JSEG Research Mission of the Niigataken Chuetsu-oki Earthquake Disaster 2007). As a result, a section of the railroad was closed for 2 months.

References

Akahane S (1998) The Zenkoji earthquake and sediment disasters, 150 years after the Zenkoji earthquake, Damages and measures in the Matsumae domain, pp 1–4 (in Japanese)

Chigira M, Wu X, Inokuchi T, Wang G (2010) Landslides induced by the 2008 Wenchuan earthquake, Sichuan, China. Geomorphology 118:225–238

Editional committee of Isehara municipal census (1963) Isehara municipal census report, pp 431–433 (in Japanese)

Furukawa H (2001) Disasters and emergency countermeasures of roads and steep slope by the swarm earthquakes at Niijima and Kozusima. JSCE Mag Civ Eng 86(4):63–66 (in Japanese)

Hokuriku Regional Development Bureau (2005) The Mid Niigata prefecture earthquake—the record of the past year, http://www.hrr.mlit.go.jp/saigai/H161023/chuetsu-jishin/. Accessed on 6 April 2012) (in Japanese)

Ishigaki I, Hiruma N, Matsuzaki N, Uchiyama Y (2007) Feature of landslide generation in Nisitanzawa Mountainous district after 1923, Results of the Scientific Research on the Tanzawa Mountains, pp 432–438 (in Japanese)

JSEG Research Mission of the Niigataken Chuetsu-oki Earthquake Disaster (2007) Urgent report of the 2007 Niigataken Chuetsu-oki earthquake disaster. J Jpn Soc Eng Geol 48(4):192–202 (in Japanese)

Kanagawa Prefectural Government (1930) The 1923 Kanto Earthquake landslide disaster map of forest devastation in Hakone area (in Japanese)

Matsumoto M, Simokawa M, Jitosono T (1998) Landslides on granitic slopes caused by earthquakes in 1997 in northwestern Kagosima, Kyusyu. Res Bull Kagoshima Univ 26:9–21 (in Japanese with English abstract)

Ministry of Land, Infrastructure and Transport Yuzawa Office (2005) Disasters and countermeasures of the Mid Niigata prefecture Earthquake (2004), p 13 (in Japanese)

Nagano Regional Forest Office (1991) Annual report on the forest conservation works, pp 271–300 (in Japanese)

Nakamura H, Tsuchiya S, Inoue K, Ishikawa Y (2000) Jisin Sabo (Earthquake and sediment control), Kokon Syoin, pp 60–70 (in Japanese)

Ozawa M (1998) The 1923 great Kanto Earthquake and forest conservation works in the Kanagawa Prefecture, disasters in mountainous area due to earthquakes and their countaimeasure works, pp 111–136 (in Japanese)

Sato K (1983) The Tenna Earthquake and the Ikari flood. Geography 28(4):20–26 (in Japanese)

Sakurai M, Goto S (2005) Natural slope failure and the sediment disaster. The Foundation Engineering and Equipment, Monthly, vol 33(10), pp 66–69 (in Japanese)

Schuster RL (1986) Landslide dams, process, risk and mitigation, Geotechnical special publication. ASCE 3:111–130

Tomita Y, Sakurai W, Naka N (1996) Study on the extension of collapse caused by rainfall after the earthquake in Rokko mountain range. J Jpn Soc Eros Control Eng 48(6):15–21 (In Japanese with English abstract)

Effects of Existing Prevention Works on Earthquake-Induced Landslides

9

Akira Nakamura, Tomoyuki Noro, Kiyoteru Maruyama, Bateer Hasi, Yasuo Ishii and Nobutoshi Ikeda

Abstract

We investigated the effects of existing drainage work on earthquake-induced landslides, in the areas of seismic intensity larger than 5-plus of the Mid Niigata prefecture Earthquake in 2004, the Niigataken Chuetsu-oki Earthquake in 2007 and the Iwate-Miyagi Nairiku Earthquake in 2008. The results showed that earthquake-induced landslides on the areas where countermeasures had been conducted were located within 12 km from the epicenter and 10 km from the source fault. Moreover, results revealed lowering of the groundwater level was less than 1.8 m after control works.

Keywords

Earthquake · Landslide · Landslide prevention works · Groundwater drainage works

A. Nakamura (✉)
Nippon Koei Co., Ltd. (former Snow Avalanche and Landslide Research Center, PWRI), Tokyo, Japan
e-mail: a4066@n-koei.co.jp

T. Noro · K. Maruyama
Snow Avalanche and Landslide Research Center,
PWRI 2-6-8 Nishiki-Cho, Myoko-shi, Niigata
Prefecture 944-0051, Japan

B. Hasi
Asia Air Survey Co., Ltd. (former Snow Avalanche and Landslide Research Center, PWRI), Tokyo, Japan

Y. Ishii
University of Tsukuba (former Snow Avalanche and Landslide Research Center, PWRI), Tsukuba, Japan

N. Ikeda
KOWA, Co., Ltd, Niigata, Japan

1 Introduction

Many landslides have been reported in inland reverse fault earthquakes with a seismic intensity of 5-plus or higher which have occurred mostly in the eastern part of Japan in recent years, such as the Mid Niigata prefecture Earthquake in 2004 and the Iwate-Miyagi Nairiku Earthquake in 2008 (The Japan Landslide Society established a Special Research Committee of the Mid-Niigata Earthquake-induced Landslides 2007; Hasi Bateer et al. 2009; Geographical Survey Institute 2009). More earthquakes with a high seismic intensity are expected to occur according to a report (The Headquarters for Earthquake Research Promotion 2009; The Headquarters for Earthquake

Research Promotion 2010) from the Earthquake
Research Committee of the Headquarters for
Earthquake Research Promotion, and it is feared
that such earthquakes will trigger landslides.

Meanwhile, investigations were conducted
after the Southern Hyogo prefecture earthquake
in 1995 to examine the earthquake resistance of
landslide prevention works (Ministry of Con-
struction River Bureau Sabo (Erosion and Sedi-
ment Control) Department Slope Conservation
Division 1996). The investigations found that the
landslide prevention works retained their func-
tion even after the earthquake, and that facility
designs which were not based on earthquake
resistance could withstand earthquakes. Also,
Ikeda et al. (Ikeda Nobutosi et al. 2006) investi-
gated the effects of earthquakes on landslide
prevention works after the Mid Niigata prefecture
Earthquake in 2004. They reported that visible
movements, such as cracks, were rarely found at
slopes where landslide prevention works had
been in place. At areas where landslide move-
ment was observed, they were mostly small.

Yet, the effects of seismic motion on landslide
slopes where landslide prevention works are
installed are not necessarily clear. For example,
slope movements is not usually observed at areas
where landslide prevention works are in place.
Also, there have been no studies that evaluated
the relationship between earthquake-induced
landslides and factors such as the lowering of
groundwater levels caused by landslide preven-
tion works at landslide blocks where counter-
measures are in place (hereinafter referred to as
"landslide blocks on which countermeasures
have been conducted") and safety factors after
countermeasures are taken. Therefore, for the
purpose of clarifying how seismic motions affect
landslide blocks with countermeasures, this study
investigated the lowering of ground water levels
before and after the installation of landslide pre-
vention works, and examined the relationship
between these aspects and landslide conditions.
This study covered the Mid Niigata prefecture
Earthquake in 2004 (hereinafter "the Mid Niigata
Earthquake"), the Niigataken Chuetsu-oki
Earthquake in 2007 ("the Chuetsu-offshore
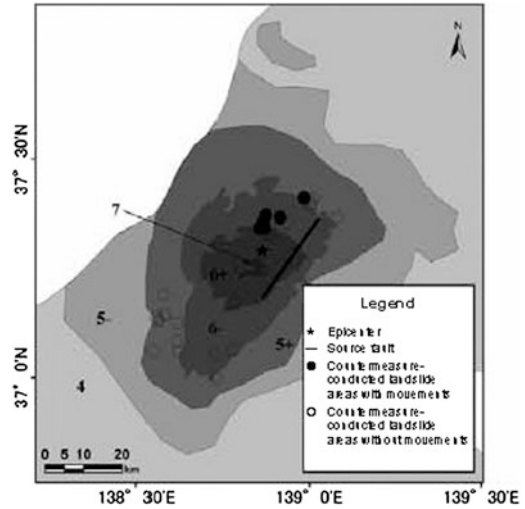
Fig. 9.1 Estimated seismic intensity distribution of the
chuetsu earthquake modified from JMA 2004(Japan
Meteorological Agency 2004)

earthquake"), and the Iwate-Miyagi Nairiku
Earthquake in 2008 ("the Iwate-Miyagi Nairiku
Earthquake").

Part of this report was presented at the 49th
conference of the Japan Landslide Society
(Nakamura Akira et al. 2010).

2 Investigation Methods

The study was conducted targeting the Mid Nii-
gata Earthquake (M 6.8), the Chuetsu-oki Earth-
quake (M 6.8), and the Iwate-Miyagi Nairiku
Earthquake (M 7.2). Figures 9.1 9.2, 9.3 show the
distribution of the estimated seismic intensities of
these earthquakes. Figures 9.1, 9.2, 9.3 separately
show landslide prevention zones with counter-
measures are conducted. Figures 9.1, 9.2, 9.3
indicate that landslides occurred at areas where the
seismic intensity was higher than 5-plus during
reverse fault earthquakes of about M 7.0 (Hasi
Bateer et al. 2011). Therefore, the range of
investigation was set at areas where the seismic
intensity was larger than 5-plus as shown in
Figs. 9.1 9.2, 9.3. The investigations were then
conducted targeting landslide blocks with no by
countermeasures.
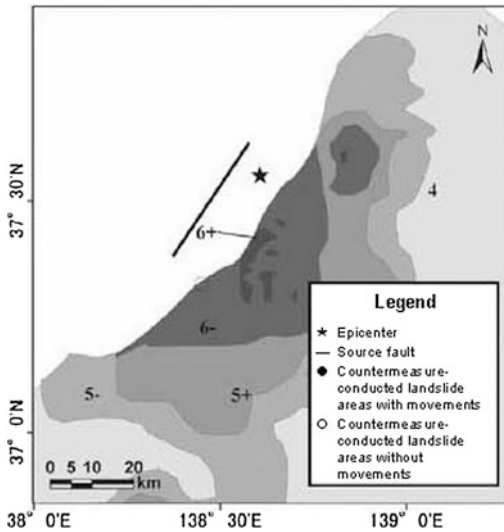
Fig. 9.2 Estimated seismic intensity distribution of the chuetsu—offshore earthquake modified from JMA 2007(Japan Meteorological Agency 2007)
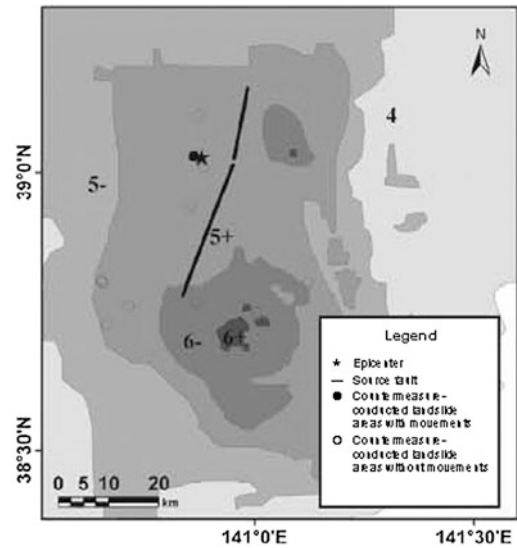
Fig. 9.3 Estimated seismic intensity distribution of the Iwate/Miyagi—inland earthquake modified from JMA 2008(Japan Meteorological Agency 2008)

The earthquake-induced landslide blocks were categorized by landslide damage investigation reports (Snow Avalanche and Landslide Research Center, PWRI 2009; Snow Avalanche and Landslide Research Center, PWRI 2010; Hokubu Engineering Works Office Kurihara Area Office, Miyagi Prefecture 2009). The construction methods of landslide prevention works and the conditions of movements were also investigated and their relationships were examined.

Baator, et al. (2010) (Hasi Bateer et al. 2011) studied the distributions of earthquake-induced landslides in the Mid Niigata Earthquake and the Iwate-Miyagi Nairiku Earthquake and the relationship with the distances from epicenters or sources of faults. He indicated a high correlation between areas with many earthquake-induced landslides and distances from source faults. Therefore, this study also examined the relationship between distances from epicenters and source faults and movements in landslides.

In addition, this study examined the groundwater levels before and after installing landslide prevention works using documents such as landslide damage investigation reports (Snow

Avalanche and Landslide Research Center, PWRI 2009; Snow Avalanche and Landslide Research Center, PWRI 2010; Hokubu Engineering Works Office Kurihara Area Office, Miyagi Prefecture 2009) and studied relationships with the investigated damages.

3   Investigation Outcomes

3.1   Conditions of Earthquake-Induced Movements

As shown in Table 9.1, there were 388 landslide blocks with countermeasures in the investigation area. Earthquake-induced landslides examined in this study are those where cracks, faulting, or collapse were observed in surveys(Snow Avalanche and Landslide Research Center, PWRI 2009; Snow Avalanche and Landslide Research Center, PWRI 2010; Hokubu Engineering Works Office Kurihara Area Office, Miyagi Prefecture 2009) conducted after the earthquakes. Small-scale collapses which the widths and lengths were up to about three meters were regarded as no movement.

Table 9.1 Number of landslide blocks in each earthquake

Name of Earthquake	(1) Number of studied blocks where counter measures were conducted	Number of blocks where movements were observed among (1)
The Chuetsu earthquake	300	15
The Chuetsu-offshore earthquake	9	0
The Iwate Miyagi inland earthquake	79	2
Total	388	17

Table 9.2 Number of landslide blocks in each earthquake

No movement	
Full movement	
Movement in upper parts	
Movement in lower parts	
Partial movement	

Among the three earthquakes covered in this study, there was overlap of some parts of the investigation areas of the Mid Niigata Earthquake and the Chuetsu-oki Earthquake. The study targeted earthquakes in which the distance to the epicenter was shorter in blocks where overlapping zones were located.

Among all 388 blocks, movements were observed at 17 blocks (hereinafter "blocks with movements"), and the incident rate was about 4 % (Table 9.1). The study covered 300 blocks at the site of the Mid Niigata Earthquake, and 15 of them were blocks with movements. At the site of the Chuetsu-oki Earthquake, the study covered nine blocks, and there were no blocks with movements. The study covered 79 blocks at the site of the Iwate-Miyagi Nairiku Earthquake, and two of them were blocks with movements. Yet, there is the possibility that earthquake-induced movements may vary depending on precipitation before the earthquake and conditions of groundwater during the earthquake, but this study was conducted without taking these aspects into account.

3.2 Categories of Movements

As shown in Table 9.2, blocks with movements are categorized into four types: full movement;

Fig. 9.4 Example of movement in whole lanslide

movement in upper parts; movement in lower parts; and partial movement. "Full movement" means that movements or collapses were observed at most of the landslide blocks designated before the earthquake as shown in Fig. 9.4. "Full movement" is the category where landslide stability fell during the earthquake and triggered a relatively large movement. "Movement in the upper part" is the category where earthquake-induced movements such as cracks were
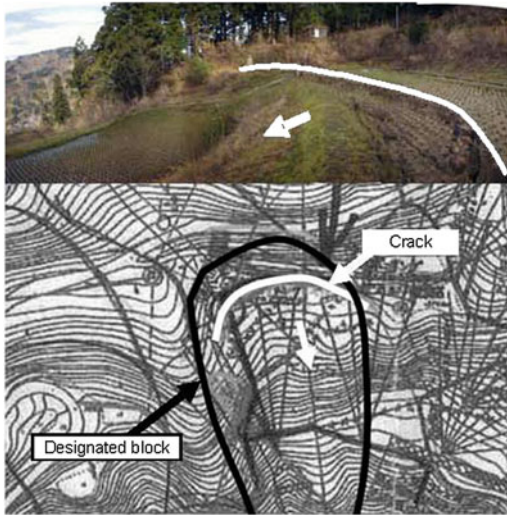
Fig. 9.5   Example of movement in upper parts
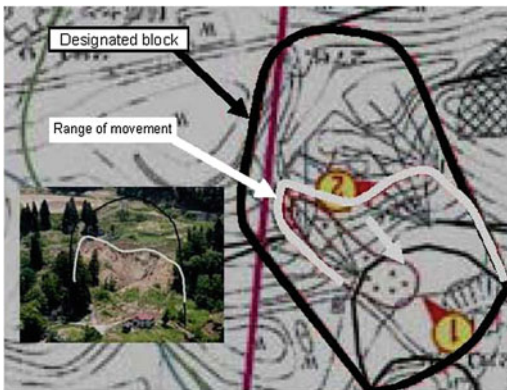
Fig. 9.6   Example of movement in lower parts

Fig. 9.7   Example of partial movement

that a movement occurred by sharing some of the sliding surface of a landslide when the stability at lower parts of the landslide fell. As shown in Fig. 9.7, "partial movement" is the category where a movement might have occurred at some sections, such as the side of blocks designated before the earthquake, or movement might have occurred in unison with areas outside a designated block. "Partial movement" means there is the possibility that the stability of some part of a soil mass on a landslide or slopes around a block fell and triggered a movement.

3.3   Relationship Between Landslide Prevention Works and Movements

Multiple landslide prevention works were used together in the landslide blocks with countermeasures that were studied. Therefore, the relationship with landslide prevention works and movements was studied by categorizing landslide prevention works as shown in Table 9.3. For example, in blocks where horizontal boring and an infiltration well are in place, the infiltration well is considered the main facility of the block. Meanwhile, in blocks where an infiltration well and topsoil removal or counterweight fill are in place, the topsoil removal or the counterweight fill is considered the main facility. In blocks where prevention works and

observed only at the upper parts of blocks designated before the earthquake, and new, continuous cracks and faulting were observed at an upper slope near blocks designated before the earthquake as shown in Fig. 9.5. "Movement in upper parts" means there is the possibility that the stability of a landslide fell during the earthquake and triggered a relatively small movement. As shown in Fig. 9.6, "movement in lower parts" is the category in which a movement or a collapse which is about the same size as the width of the landslide occurred at the lower part of blocks designated before the earthquake. "Movement in lower parts" means that there is the possibility

Table 9.3 Classification of landslide prevention facilities

	Category of Preventive faciliities	Components of actual Preventive faciliities
Control Works	Horizontal boring	Horizontal boring
	InfiIteration well	InfiIteration well InfiIteration wel + Horizontal boring
	Counter weight fill, soil removal	Counter weight fill soil removal Counter weight fill + InfiIteration well soil removal + InfiIteration well Counter weight fill + InfiIteration well + soil removal soil removal + InfiIteration well + Horizontal boring
Prevention Works	Pilling	Pilling Pilling + infilteration well Pilling + infilteration well + Horizontal boring
	Anchoring	Anchoring Anchoring + Infilteraion well Anchoring + Infilteraion well + Horizontal boring
	Other (channel, soil retaining)	Surface Channel Soil retaining wall,etc.
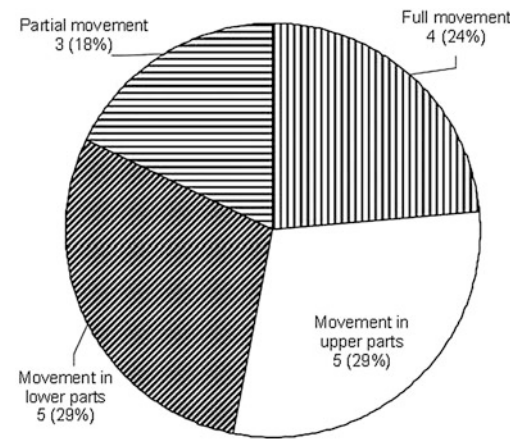
Fig. 9.8 Status of occurence of moving areas

Fig. 9.9 Number of moving bloks in facilities

control works are in place, the restrain work is considered the main facility. The relationship between the construction types of landslide prevention works and movement categories were examined based on such categorization.

Categories shown in Table 9.2. There were five blocks each in "movement in upper parts" and "movement in lower parts," accounting for 29 % of all the blocks, four blocks or 24 % in "full movement," and three blocks or 18 % in "partial movement."

Figure 9.8 shows the conditions of movements by type of facility for landslide prevention. According to Fig. 9.9, movements were observed at 12 of 163 blocks with horizontal boring, and the ratio of blocks where movement occurred with this construction type (hereinafter "movement ratio") was 7 %. Movements were observed at three out of 94 blocks with infiltration wells, and the movement ratio was 3 %. Movements were observed at one block with a counterweight fill or soil removal and one block

with anchoring. Yet, no movements were observed at blocks with piling or other construction works (ditches or sheathing).

The results of examining the relationship between landslide prevention works and movements as described above showed that earthquake-induced movements occurred at a slightly higher rate at blocks where only horizontal boring was in place compared to blocks with other construction methods.

We found that blocks with movements were mostly located within 12 km from the epicenters and about 10 km from the source faults.

3.4 Relationship Between the Groundwater Level Lowering and Movements

In terms of the lowering of the groundwater level caused by the existing landslide prevention works, the highest water levels before and after installing prevention facilities were studied based on the groundwater level observations(Snow Avalanche and Landslide Research Center, PWRI 2009; Snow Avalanche and Landslide Research Center, PWRI 2010; Tookamachi Promotion Bureau and Niigata Prefecture 2003; Osaki Engineering Works Office, Miyagi Prefecture 1997; Hokubu Engineering Works Office Kurihara Area Office, Miyagi Prefecture 2009; Miyagi Prefecture 1997) and the difference of the two levels was obtained. When multiple observation holes for groundwater levels are located within one study block, the lowest water level at each observation hole was obtained, and the average of all water levels was used as the value of groundwater level lowering.

Figure 9.10 shows the relationship between lowering value of the groundwater level and movement categories. The value of groundwater level lowering was 1.8 m or less at a total of ten blocks, including four blocks where "full movement" was observed, three blocks with "movement in upper parts," and three blocks with "movement in lower parts." Meanwhile, the groundwater level fell 10 m or more at one
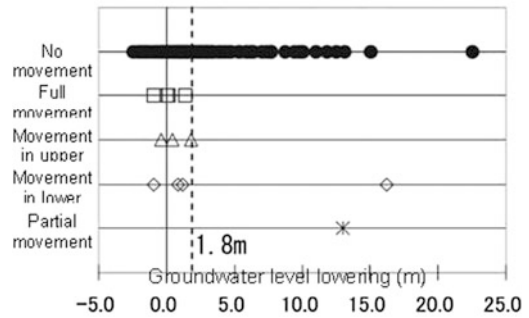
Fig. 9.10 Relationship between ground water lowering and type of moved area
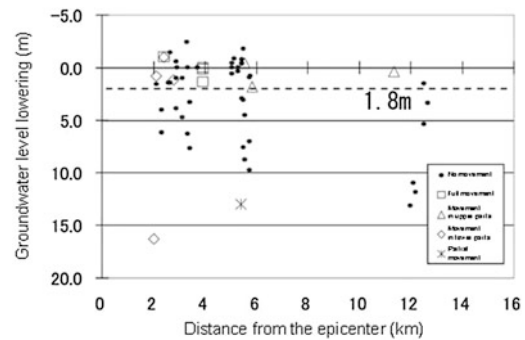
Fig. 9.11 Relationship between ground water lowering and distance from epicenter

block with "movement in lower parts" and one block with "partial movement," while movements were also observed.

Figure 9.11 shows the relationship between the lowering value of the groundwater level and the distance between epicenters and blocks. Figure 9.12 shows the relationship between the lowering of the groundwater level and the distance between source faults and blocks. Based on Figs. 9.11 and 9.12, no clear correlation between the lowering of the groundwater level and the distance between epicenters/source faults and blocks was found in blocks with movements. Two blocks in which 10 m or more of groundwater level lowering was recorded and which were categorized into "movement in lower parts" and "partial movement" were not especially close to epicenters and source faults compared to the other blocks.
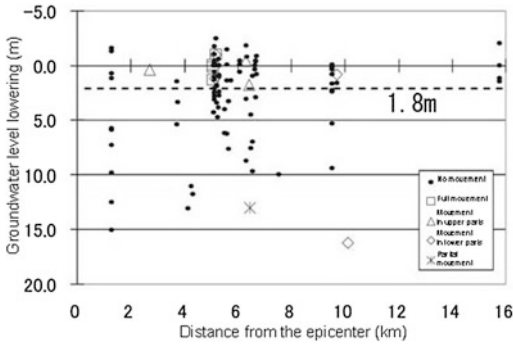
Fig. 9.12 Relationship between ground water lowering and distance from Source fault
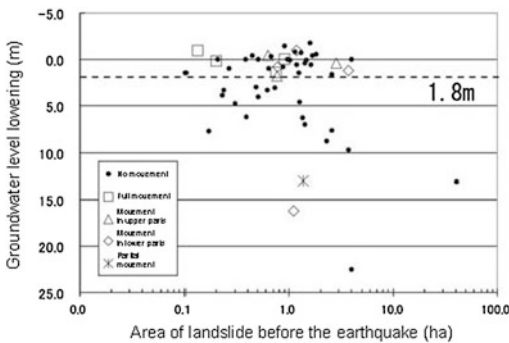
Fig. 9.13 Relationship between ground water lowering and landslide size

Even with the same degree of groundwater level lowering, levels of contribution toward stability improvement differ depending on the size of the landslide. Thus, the areas of the landslides are obtained to indicate the sizes by multiplying the landslide's length by its width, and their relationship with the lowering of the groundwater level. The results are shown in Fig. 9.13. Based on Fig. 9.13, no correlation between the lowering of the groundwater level and landslide size was found in blocks with movements. There is no clear difference between the sizes of the two blocks where 10 m or more of groundwater level lowering was recorded and which were categorized as "movement in lower parts" and "partial movement" and the sizes of other blocks with movements.

Groundwater observation holes were located on main traverse lines in two blocks where 10 m or more of groundwater level lowering was

observed. The movement categories at these two blocks are "movement in lower parts" and "partial movement," and the cause of the movement might be partial instability. Examination of the plan views of these two blocks revealed that movements occurred away from locations where horizontal boring and infiltration wells had been installed. No groundwater observation holes are installed at areas where movements occurred, and the groundwater level conditions are unknown. Yet, it is possible that the effects of landslide prevention works on lowering groundwater levels were small at areas where movements occurred.

4 Summary

The study examined the relationship among the lowering of the groundwater, the safety factors of slopes, and the conditions of earthquake-induced movements, targeting landslide blocks with countermeasures at areas hit by earthquakes with a seismic intensity of 5-plus or higher which occurred during the Mid Niigata Earthquake, the Chuetsu-oki Earthquake, and the Iwate-Miyagi Nairiku Earthquake, which are earthquakes of about 7.0-magnitude. The study found the following.

(1) Landslide blocks with countermeasures where only horizontal boring is in place showed the trend that earthquake-induced movements occurred at a slightly higher frequency than with other construction types.

(2) Most of the values of groundwater level lowering at landslide blocks with countermeasures where earthquake-induced movements were observed were 1.8 m or less, except at two blocks.

The findings of this study are based on the analysis of limited cases; however, the study estimates that there are many landslides where no earthquake-induced movement occurs as long as the landslide prevention works function as initially designed, even when earthquakes with similar intensities occur at the studied areas. Also, the effects of seismic motion on landslide slopes with landslide prevention works can be

further revealed if cases of earthquake-induced movements are accumulated in the future by continuously measuring groundwater levels and landslide displacement at slopes where landslide prevention works are installed.

References

The Japan Landslide Society established a Special Research Committee of the Mid-Niigata Earthquake-induced Landslides (2007) Distribution of landslides in Higashiyama hills. Earthquake-induced Landslide Disasters in middle Mountains-Study Report on the 2004 Mid-Niigata Earthquake Part I-Geomorphology and Geology:85 (in Japanese)

Hasi B, Ishii Y, Maruyama K, Suzuki S, Terada H (2009) Relationship of source fault and earthquake-induced landslide distribution -cases of the Chuetsu and Chuetsu-offshore earthquake, Niigata Prefecture, Japan. The General Meeting of Japan Landslide Society Proceedings 199–200(in Japanese)

Geographical Survey Institute (2009) Geographical Survey Institute research data D•1-No.541 1:25,000 Active Fault Map of the 2008 Iwate-Miyagi Nairiku Earthquake (Active Faults Landslide and Earthquake Induced Geomorphic Features). (in Japanese)

The Headquarters for Earthquake Research Promotion (2009) National Earthquake Prediction Map; (in Japanese) http://www.jishin.go.jp/main/chousa/09_yosokuchizu/index.htm

The Headquarters for Earthquake Research Promotion (2010) National Earthquake Prediction Map,Map2010 version; (in Japanese)http://www.jishin.go.jp/main/chousa/10_yosokuchizu/index.htm

Ministry of Construction River Bureau Sabo (Erosion and Sediment Control) Department Slope Conservation Division(1996) Examination Committee report Summary about the Earthquake Resistance such as Prevention of Landslide Institutions. 24 (in Japanese)

Ikeda N, Shinbo N, Sakai S (2006) Damages Condition of the Facilities Landslide Prevention caused by Nigata Prefecture Chuetsu Earthquake. Journal of Japan Landslide Society 43(4):16–24(in Japanese)

Nakamura A, Maruyama K, Hasi B, Hara Y, Ishii, Y (2010) Effect of the landslide prevention works at the time of the earthquake. Japan. The General Meeting of Japan Landslide Society Proceedings 130–131(in Japanese)

Japan Meteorological Agency (2004) Japan Meteorological Agency Natural Phenomenon Report 2004 Earthquake Breaking News No.7 Chuetsu Earthquake, Niigata Prefecture, 2004.3(in Japanese)

Japan Meteorological Agency (2007) Japan Meteorological Agency Natural Phenomenon Report 2007 Earthquake and Tsunami Breaking News No.3 Chuetsu offshore Earthquake, Niigata Prefecture 2007.10 (in Japanese)

Japan Meteorological Agency (2008) Japan Meteorological Agency Natural Phenomenon Report 2008 Earthquake Breaking News No.1 Iwate-Miyagi Inland Earthquake Prefecture, 2008.10(in Japanese)

Hasi B, Ishii Y, Maruyama K, Suzuki S, Terada H, Nakamura A (2011) Distribution and scale of landslides induced by recent reverse-fault earthquakes in Japan. Journal of Japan Landslide Society 48(1):23–38(in Japanese)

Snow Avalanche and Landslide Research Center, PWRI (2009) Report of Organizing Research Data. Landslide prevention works which was broken by the Chuetsu Earthquake. 38(in Japanese)

Snow Avalanche and Landslide Research Center, PWRI (2010) Report of Organizing Research Data, Scale of Landslides (in Japanese)

Tookamachi Promotion Bureau, Niigata Prefecture (2003) Nonaka Area, Construction for Landslide Preservation Report. 21 (in Japanese)

Osaki Engineering Works Office, Miyagi Prefecture (1997) Monitoring Report of Mitenohara Landslide (1997). 21(in Japanese)

Hokubu Engineering Works Office Kurihara Area Office, Miyagi Prefecture (2009) Report of Research and Analysis. Shuku Landslide. 58 (in Japanese)

Miyagi Prefecture (1997) List of Potential Landslide Site. 118(in Japanese)

An Examination of the Stability of an Earthquake-Induced Landslide and Landslide Dam

10

Ryoichi Ohno, Satoshi Niwa, Hideya Iwata and Sachihiko Ozawa

Abstract

The Masuzawa landslide was triggered by the Iwate–Miyagi Earthquake in 2008. The landslide ran almost 30 m and crushed the opposite side of the slope. The lower part of the sliding mass covered the riverbed and formed a landslide dam that was 23 m high. If the dam body eroded, the landslide could possibly become destabilized and move again. A heavy rainfall or large seismic aftershocks could make the landslide unstable.Two important points must be considered regarding the stability problem. One problem is how to estimate the deformation process of the dam, and the other is how much seismic force the landslide might experience during a possible aftershock. Three numerical methods were used for these estimates: a one-dimensional riverbed calculation model for the dam-erosion process, a three-dimensional finite difference method (FLAC®) for the estimation of seismic forces acting on the slide, and a Newmark method to estimate the sliding distance.Following the two-stage seismic design used in Japan, level-1 and level-2 earthquakes were tested. The landslide was stable during a level-1 earthquake, which has a typical magnitude of shaking. Also, in the future, the landslide might become unstable during a level-2 earthquake, which represents the strongest possible shake. The Newmark method was used to estimate the sliding distance during the level-2 quake. The sliding distance was calculated as 0.1 m, which was too small to trigger a big slide.

R. Ohno (✉) · S. Niwa · H. Iwata · S. Ozawa
Japan Conservation Engineers, Co., Ltd, Sannomiya
International Building, 2-1-30 Hamabe-dori, Chuo-
ku, Kobe City, Hyogo Prefecture, Japan
e-mail: r-ohno@jce.co.jp

1   Introduction

The Iwate–Miyagi Earthquake in Japan (2008)
caused a number of slope failures and landslides
in the inland region of the Eastern Tohoku area.[1]
The scale and number of earthquake-induced
landslides cannot be compared with those that had
occurred in Japan in the past. The Masuzawa
Landslide (Kurokawa et al. 2010, Fig. 10.1) was
located in the upstream area of the Koromo River
near Oshu City in the Iwate Prefecture. The
landslide ran almost 30 m and crushed the oppo-
site side of the slope. Fortunately, it caused no
human or material loss, but the main slide body
dammed up the center of the stream and formed a
landslide dam that was 23 m high. The water flow
near the dam was checked, and a pond had
appeared on the upstream side of the dam.

If the water flow gradually eroded the dam
body, the landslide could possibly be destabilized
due to the removal of the lower part of the dam's
mass. In the future, a heavy rainfall or a large
seismic aftershock could make both the dam and
the landslide unstable. If the slide is moved again,
it might run down the stream, create a debris flow,
and harm the residents down below.

In this study, three types of numerical methods
were used to estimate the stability problem of the
dam and the landslide. First, a riverbed calcula-
tion for the deformation process of the dam
occurred. Second, a three-dimensional seismic
analysis model, 500×500 m width in top view,
was prepared, which calculates the seismic force
acting on the mass during a possible aftershock in
the future. Third, to evaluate the safety level of
the landslide during a quake, the Newmark (1965)
method was used to calculate the deformation of
the sliding mass. The stability problem of land-
slide and landslide dam is discussed in this paper.

2   Methods and Results

Three different numerical methods were applied
to estimate the stability problem.

---

[1] Activities in WG 4 of JLS-ELRP.
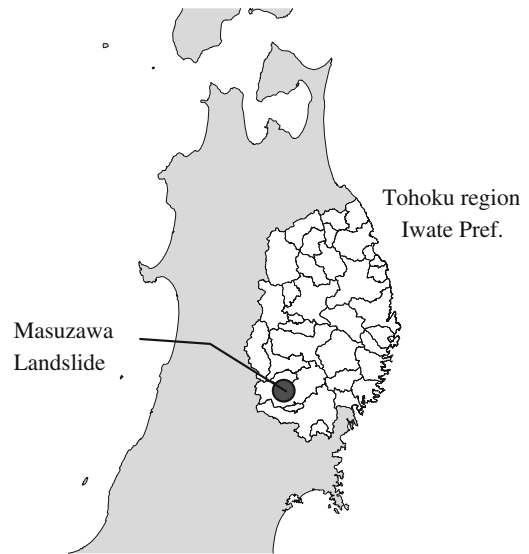
Fig. 10.1 Map of Masuzawa landslide, Japan

2.1   Deformation of Dam: Riverbed Calculation

The sliding mass formed a landslide dam at the
center of the streamline that is 23 m high. If the
dam eroded, the slide could possibly be
destabilized.

To estimate the eroding process in advance,
the rainfall intensity should be evaluated. Using
observed daily rainfall data from the Matsurube
station, the rainfall extreme value (100-year
probability) was evaluated as 340 mm/day.
Using this value, the flow rate was estimated and
then applied to the riverbed calculation.

There are not many tools we can utilize to
estimate the deformation process of the dam.
However, one- or two-dimensional riverbed
calculations can be used. In this case, the
streamline can be approximated in a one-
dimensional form, and one-dimensional analysis
is adopted for the calculation.

One-dimensional riverbed calculation is
composed of those equations below.

Continuity equation of total flow:

$$\frac{\partial A_t}{\partial t} + \frac{\partial Q_t}{\partial x} = s_t B + 2 s s_t h_t \qquad (10.1)$$

Continuity equation of debris flow:

$$\frac{\partial A_c}{\partial t} + \frac{\partial Q_c}{\partial x} = c_*(Bs_t + 2Bss_t h_t) \qquad (10.2)$$

Equation of motion:

$$\frac{\partial Q_t}{\partial t} + \beta_t \frac{\partial}{\partial x}\left(\frac{Q_t^2}{A_t}\right) = -gA_t \frac{\partial \eta_t}{\partial x} - B\frac{\tau_b}{\rho_t} \quad (10.3)$$

Temporal change of riverbed elevation:

$$\frac{\partial z_b}{\partial t} = -s_t \frac{B}{B + \Delta B} \qquad (10.4)$$

Temporal change of river width:

$$\frac{\partial B}{\partial t} = 2ss_t \frac{h_t}{H} \qquad (10.5)$$

Temporal change of side slope height:

$$\frac{\partial H}{\partial t} = s_t \frac{B}{B + \Delta B} \qquad (10.6)$$

Each symbols are defined as below:

A_t cross-sectional area of total flow [m^2]
A_c cross-sectional area of debris flow [m^2]
Q_t discharge of total flow [m^3/s]
Q_c discharge of debris flow [m^3/s]
B river width [m]
H side slope height from riverbed [m]
η_t surface elevation of total flow [m]
g gravitational acceleration [m/s^2]
ρ_t bulk density of total flow [kg/m^3]
τ_b shear stress at riverbed [kN/m^2]
β_t correction coefficient [-]
c_* debris concentration at riverbed [-]
z_b riverbed elevation [m]
s_t erosion velocity of riverbed [m/s]
ss_t erosion velocity of side slope [m/s]

The relations between each symbols are shown in the schematic Fig. 10.2. The shear stress at the riverbed, τ_b is estimated by the Manning's roughness equation. As the dam-erosion begins with either one side slope or from both sides simultaneously (Fig. 10.3), the estimation of the erosion velocity s_t and ss_t is very important to express the erosion process. The detailed calculation method of those velocity are
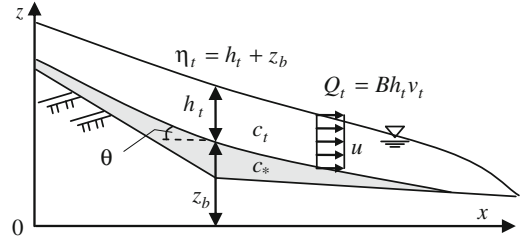
Fig. 10.2 Schematic of one-dimensional riverbed calculation
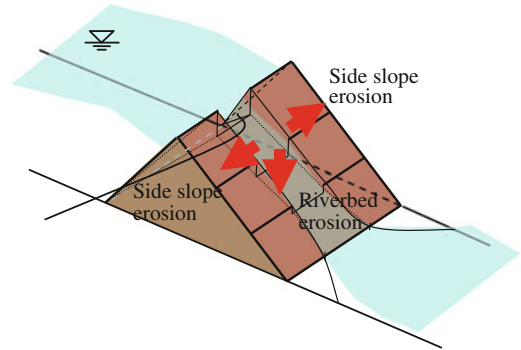
Fig. 10.3 Schematic of the dam-erosion process
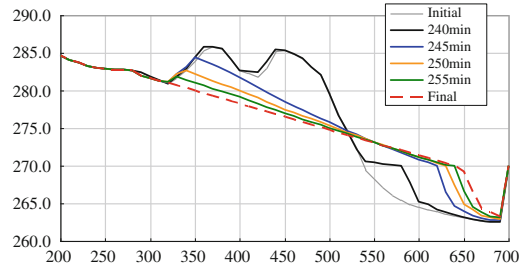
Fig. 10.4 Longitudinal section view of dam-erosion

shown by Satofuka et al. (2007), Takahashi and Nakagawa (1992).

Figure 10.4 shows the results of the riverbed calculation and dam-erosion process using a longitudinal section view. The dam body is almost eroded in the upper zone, and conversely, in the lower zone, the suspended sediment settled down, and the riverbed increased.

According to this result, the topography of the ground surface was revised. Surface revising was performed in the following manner: the upper zone of the riverbed was decreased based on the
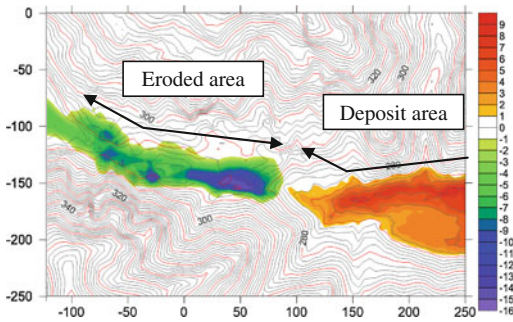
Fig. 10.5 Contour map of the difference between the revised and original ground surface

assumption that the side slope would be cut 35 degree in the cross section, and the lower zone of the riverbed was increased based on the assumption that riverbed surface is horizontally flat from the surface level of settled sediment. The revised ground surface was used for the seismic analysis described in the next section. Figure 10.5 shows the difference between revised surface and original surface.

2.2 Seismic Analysis

For the estimation of the seismic force acting on the dam and the landslide, the simplest approach adopts the maximum wave acceleration recorded near the slide. However, with such a strong quake, the maximum acceleration value easily exceeds 1000 gal, which is too strong to use as static an external force; which means, once it slides, it never stops. In addition, the sliding body over the 100 m slope length is too big to assume the slide has a uniform seismic spatial and temporal force. To evaluate the spatial and temporal variance of the seismic force acting on the slide, a three-dimensional finite difference method (FLAC®) is adopted for the calculation. FLAC is a commercially base computing code; for more detail, refer to the distributer's website: http://www.itascacg.com/.

Prepare Level-1 and Level-2 Quake
Following the 2-stage seismic design used in Japan, level-1 and level-2 earthquakes, supplied to inspect the stability problem, were prepared.

A level-1 earthquake has a typical magnitude of shaking that might occur during the next few decades. The Iwate Prefecture surveyed possible earthquakes and predicted the supposed scale of quakes and damages from the quakes. They released the results, such as ground acceleration, velocity, and housing damages, to the public so that disaster prevention preparations would be improved. One of the predicted quakes is suitable for a level-1 quake, which was evaluated with a horizontal seismic coefficient value of 0.13.

A level-2 earthquake represents the strongest possible shake in the future; for example, the Tohoku Earthquake in 2011 is recognized as a general level-2 earthquake. Masuzawa, located far from the epicenter of the Tohoku Earthquake, was not as strong as the Iwate–Miyagi Earthquake in 2008. So, we adopt the Iwate–Miyagi Earthquake as a level-2 quake.

The Ishibuchi Dam, located 3.1 km from Masuzawa in the northwest, has a record of the seismic wave from the Iwate–Miyagi Earthquake in 2008. This is the nearest seismic record to Masuzawa. Using a multiple reflection method in one-dimension, the observed wave at the Ishibuchi Dam was transformed to a wave equivalent to the Masuzawa's seismic bedrock's S-wave velocity. The transformed wave was adopted as a level-2 input quake for seismic analysis by FLAC.

Seismic Analysis for Level-1: Janbu
A level-1 quake is represented by a seismic coefficient value of 0.13. This value can be directly entered into the Janbu equation for stability analysis. The safety factor (F_S) obtained from Janbu is 1.065, so the landslide is stable against a level-1 quake.

Seismic Analysis for Level-2: FLAC
With the seismic wave prepared from Ishibuchi Dam, the seismic force acting on the slide body was evaluated using a three-dimensional finite difference code, FLAC. Figure 10.6 illustrates the prepared model view. It has 93,994 nodes and 93,104 elements, which are mainly in the shape of a box, but some are in the shape of a prism or tetrahedron. The model has five different layers, and the parameter values are

Table 10.1 Parameters used in seismic analysis

Layer			w1	w2	w3	w4	w5
Bulk density	ρ	[g/cm^3]	1.906	2.041	2.234	2.243	2.127
S-wave velocity	v_s	[km/s]	0.152	0.453	0.762	1.076	1.441
P-wave velocity	v_p	[km/s]	0.337	1.309	1.849	2.320	3.081
Shear modulus	G	[MN/m^2]	44	419	1,297	2,597	4,417
Elastic modulus	E	[MN/m^2]	121	1,200	3,626	7,079	12,014
Poisson ratio	v	[–]	0.372	0.432	0.398	0.363	0.360
Reference strain	γ_r	[%]	0.302	0.099	0.183	0.067	0.183
Shear strength	c	[kN/m^2]	199.1	536.2	930.1	1503.6	3264.4
	ϕ	[deg]	28.6	31.5	33.1	34.5	36.8
Tensile strength	q_t	[kN/m^2]	176.3	354.8	523.6	735.5	1273.8
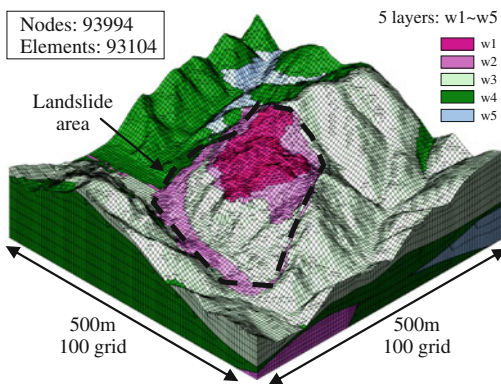
Fig. 10.6 Bird's-eye view of model

Fig. 10.7 Plastic zone elements indicated at the peak time of a level-2 quake

shown in Table 10.1. Hyperbolic curves are used to represent the nonlinear property of the soil constitutive law.

Figure 10.7 illustrates the elements in the plastic condition at the quake's peak time of input during the shear deformation process. There are many plastic elements around and inside the landslide. FLAC calculates every element's moment (by calculation time step, Δt), so the acceleration of the slide body elements can be identified. Watanabe and Baba (1981) showed that the seismic force acting on the slide body could be approximated using an averaged value of acceleration inside the slide body (Fig. 10.8). Following Watanabe and Baba's method, seismic force was calculated using the average acceleration just inside the slide body. By conducting this calculation repeatedly throughout the quake, time-series data of a seismic force wave was

Fig. 10.8 Schematic of horizontal acceleration vector acting on the slide body

produced. The ratio of seismic force versus the self-weight of the sliding mass is defined as a seismic coefficient and is prepared as time-series
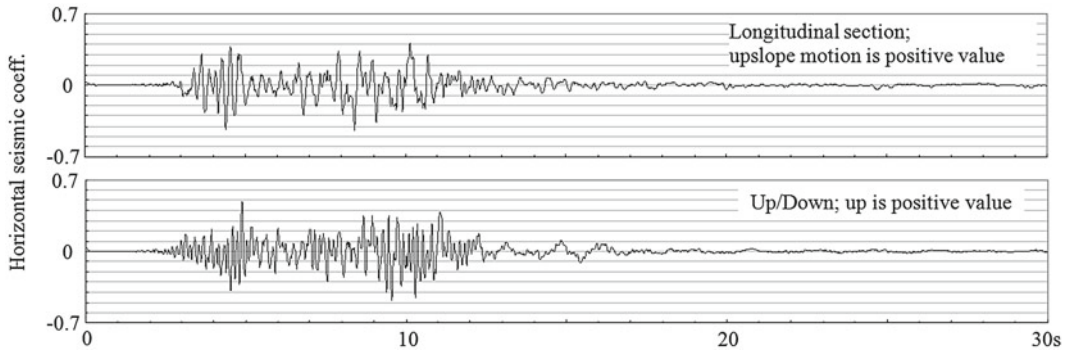
Fig. 10.9 Seismic coefficient wave acting on the slide mass calculated from FLAC

data, which is the input wave for the Newmark method described in the next section. Figure 10.9 shows the obtained horizontal seismic coefficient wave acting on the slide mass calculated from the FLAC analysis result.

Sliding Distance: Newmark Method

The Newmark (1965) method was used to estimate the sliding distance during a level-2 quake. The critical seismic coefficient, which is the maximum threshold for the slide's initial movement, is defined as a constant using the Janbu equation. Given the level-2 seismic coefficient wave described in the previous section, the sliding distance could be computed by summing up the differences between the critical and level-2 seismic coefficients in the time-series data.

The sliding distance calculated by Newmark was 0.11 m. It looks like a small value for the slide body, which has a 224 m slope length. Further discussion was conducted in the following section.

3 Discussion

3.1 Criterion for Sliding Distance

Moriwaki (2001) stated that the critical sliding distance, which is a threshold for the landslide to break and move a long distance, depends on its slope length. That is;

$$D_C = 0.0135 L_C^{0.919} \qquad (10.7)$$

where D_C is the critical sliding distance [m] and L_C is the slope length [m]. If the landslide slides more than D_C, then it might start moving faster and rush down the slope. The D_C of the Masuzawa 224 m slope length was calculated as 1.95 m. Taking account of the D_C length along slope, D_C in the horizontal length was calculated as 1.76 m, given the slope angle of 25°.

The seismic analysis results showed that the Masuzawa landslide would slide 0.11 m. Considering that the critical slide distance (D_C) is 1.76 m, the sliding distance, 0.11 m, is too small to trigger a big slide. So, in this case, the Masuzawa Landslide is stable against a level-2 quake.

3.2 Effect of Topography and Water Level

Using seismic analysis, the effects of the topography and water level differences were examined. Two different water levels were prepared: the mean water level (MWL) and the high water level (HWL) (Fig. 10.10). Both were treated as water pressure in the Janbu equation, and the high water level generally lowers the safety factor of the slide.

Table 10.2 shows the results of the seismic analysis. A high water level decreases the safety factor by 0.05, but the safety factor still remains higher than 1.0, and the slide remains stable. In the case of an earthquake, a mean water level is
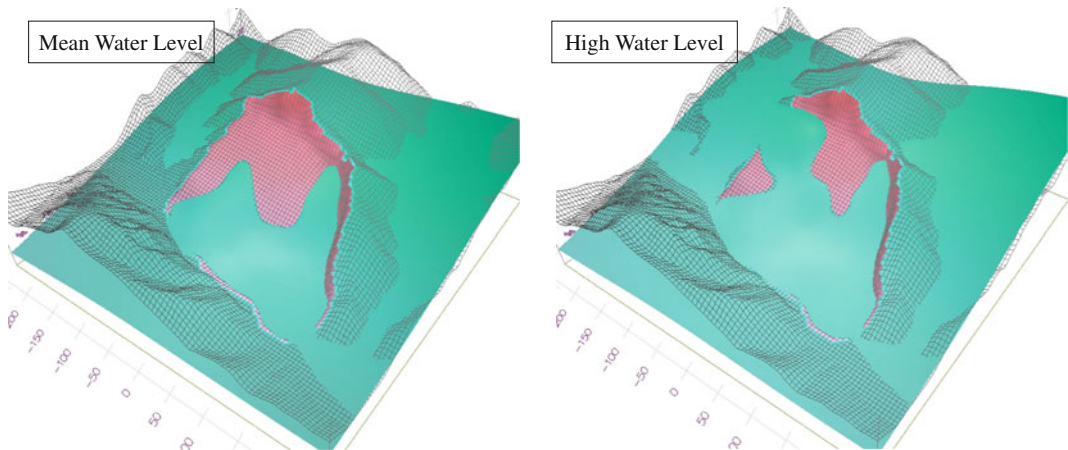
Fig. 10.10 Two different levels of water

Table 10.2 Result of seismic analysis

Topography	Water level	Quake	Seismic coefficient	Minimum safety factor during quake (sliding distance)
Dam not eroded	MWL	None	–	$F_s = 1.482$
	HWL	None	–	$F_s = 1.430$
	MWL	Level-1	0.130	$F_s = 1.065$
	MWL	Level-2	Max 0.444	(0.11 m)
Dam eroded	MWL	None	–	$F_s = 1.364$
	HWL	None	–	$F_s = 1.313$
	MWL	Level-1	0.130	$F_s = 0.983$
	MWL	Level-2	Max 0.444	(0.20 m)

assumed because both an earthquake and heavy rainfall rarely occur simultaneously.

The case "Dam not eroded" means that the landslide dam is not eroded by stream water, and the ground surface is original. In this case, the slide is relatively stable because the dam itself supports the slide. The case "Dam eroded" means that the slide loses its lower support, and the ground surface is revised. In this case, the safety factor gets smaller (1.065–0.983) and the sliding distance grows (0.11–0.20 m). A level-1 quake makes the landslide unstable and level-2 makes move a slight distance of 0.20 m. Although the landslide moves slightly when it is hit by a level-1 or level-2 quake, the sliding distance is small in comparison to the critical sliding distance and the dam located at the lower

part of the slide plays important role in keeping the slide stable.

4   Conclusion

Using three different types of analysis tools, the stability problem of the Masuzawa landslide was thoroughly inspected. If the water flow erodes the landslide dam, the slide loses its support, and the stability of the slide decreases, even during a level-1 earthquake. The sliding distance when the dam is by hit a level-1 or level-2 quake is small compared to the critical sliding distance of the Masuzawa, and the landslide remains stable. Although, protecting the dam from erosion is an important factor for landslide stability.

References

Kurokawa M, Iwata H, Shibasaki T, Ohno R, Ozawa S, Teramura T (2010) Investigation report of Masuzawa landslide and landslide dam in Iwate Prefecture, induced by The Iwate–Miyagi Nairiku Earthquake in 2008. J Jpn Landslide Soc 47(6):33–40

Moriwaki H (2001) A risk evaluation of landslides in use of critical surface displacement. J Jpn Landslide Soc 38(2):11–18

Newmark NM (1965) Effects of earthquakes on dams and embankments. Geotechnique 15(2):139–160

Satofuka S, Yoshino K, Ogawa K, Mizuyama T (2007) Prediction of flood peak discharge at landslide dam outburst. J Jpn Soc Eros Control Eng 59(6):55–59

Takahashi T, Nakagawa H (1992) Prediction of flood hydrograph due to collapse of a natural dam by overtopping. Bul Disaster Prev Res Inst 35(B-2):231–248

Watanabe H, Baba K (1981): A study of stability analysis method using dynamic analysis of filled dam (writen in Japanese). J Jpn Natl Comm Large Dams 97:25–38

Warning/Evacuation and Monitoring Methods for Earthquake-Induced Landslides

11

Michiya Irasawa, Akira Suemine and Yuichi Ueno

Abstract

Phenomena related to earthquake-induced landslides are diverse and include debris flows, floods, and overflowing due to breaching of landslide dams. They are also characterized by diversity in timing of occurrence, in changes in various phenomena and in the scope or scale of impact. We focus on diverse time-series changes as a characteristic of earthquake-induced landslides. On the basis of these characteristics, the main warning and evacuation measures and monitoring approaches for earthquake-induced landslides are divided into three stages in terms of time elapsed. The warning/evacuation and monitoring methods applicable to each stage are described as below. Stage 1: For several hours starting immediately after the earthquake (short term). People may voluntarily evacuate the area to avoid danger; alternatively, the local mayor may issue an evacuation advisory or order. Because quantitative monitoring with instruments is hard to conduct owing to the unavailability of equipment, warning/evacuation measures at this stage are usually determined by individuals (mayors), depending largely on these individuals' experiences of sediment disasters. Stage 2: For several hours to several days after the earthquake (medium term). Government assistance and recovery efforts begin with a search for

M. Irasawa
Department of Forest Resources Science,
Iwate University, 3-18-8 Ueda,
Morioka, Iwate 020-8550, Japan

A. Suemine
Research Center on Landslide, Disaster Prevention
Research Institute, Kyoto University, Gokasho, Uji,
Kyoto 611-0011, Japan

Y. Ueno (✉)
Disaster Prevention Division, Nippon Koei Co., Ltd,
4–2 Kojimachi, Chiyoda-ku,
Tokyo 102-0083, Japan
e-mail: ueno-yc@n-koei.jp

missing persons and efforts to rescue survivors. Monitoring equipment and warning equipment can be installed. On the basis of the results of field investigations and data from equipment, major warning and evacuation measures are put into practice. Monitoring at this stage is directed at (i) warning and evacuation and safety management, and (ii) understanding landslide behavior. Stage 3: For several days to several months after the earthquake (long term). Full recovery efforts are underway. Several days after the earthquake, the evacuation advisory or order may be lifted, depending on the results of observations of landslide behavior and on whether sensors are installed. The purposes of monitoring at this stage are the same as before, namely to understand landslide behavior, secure work safety. Disbanding warning and evacuation systems is added as an additional purpose. We also describe advance preparation for warning/evacuation, and educational activities.

1 Contents

2 Warning and Evacuation in the Event of Earthquake-Induced Landslides

2.1 Information Gathering/Transmission and Warning/Evacuation

The purpose of warning and evacuation at the time of earthquake-induced landslides is to avoid or reduce human damage. Information gathering/transmission and communication systems are indispensable to carry out appropriate warning and evacuation measures.

In the short term, the first priority is to collect information so as to understand where the landslide has occurred and its scale and immediate danger (urgency and priority). Only after such information is collected can organized lifesaving efforts and warning/evacuation activities become possible. In the medium term, information is gathered through monitoring on the danger posed by the landslide, and warning and evacuation information is distributed. In the long term, permanent measures and recovery plans are put into practice in an order of priority determined from the collected monitoring information.

Because aftershocks frequently occur for a while following earthquakes and climate factors such as heavy rains and melting snow can cause sediment disasters, understanding changes in disaster phenomena is also important.

As described above, warning and evacuation are closely linked with information gathering/transmission; however, if important infrastructure such as traffic, communication, and power systems is damaged by a large-scale earthquake, then the collection and transmission of hazard information may be substantially restricted. Such restriction is one of the characteristics of

earthquake warning and evacuation activities, although infrastructure may gradually recover over time.

2.2 Phenomena for Which Warning and Evacuation Should Be Considered (Earthquake-Induced Landslides for Which Warning and Evacuation May Be Necessary)

The current technology does not yet allow us to predict the time, place, and intensity of an earthquake with a precision sufficiently useful for warning and evacuation (except in the case of the Tokai Earthquake, for which a certain level of monitoring is in place). Therefore, with the current level of technology it is also impossible to conduct warnings and evacuations for fast-moving phenomena such as a sediment disaster due to a main quake because of the short time lag between the occurrence of the earthquake and such a disaster.

For secondary disasters following an earthquake, conventional monitoring methods used for rainstorm-triggered disasters can basically be applied to individual phenomena, and warning and evacuation are possible. Monitoring methods for specific phenomena are listed below.

(1) Landslide dam
   As discussed (Chap. 8 Characteristics of Secondary Disasters), the secondary disasters with the largest disaster potential are debris flows and floods due to the breaching of landslide dams.
   Standing water level monitoring is the basic monitoring method, but quantification of dam shape and the amount of water in the dam by using wide-area measurements such as airborne laser scanning survey is more effective for large-scale hazards. In areas with large seismic ground motions, more river channels are likely to be blocked. There have been cases where data from water level gauges and debris flow sensors located along a river from upstream to downstream have been collected and integrated for warning purposes; examples are in the Imo River basin in the Mid Niigata prefecture Earthquake and the Hasama River basin in the Iwate-Miyagi Nairiku Earthquake.

(2) Landslides, soil collapse, and rockfalls
   Many cases have been observed whereby a surface failure or landslide induced by an earthquake (main quake) has expanded because of aftershocks, rainfall, or melting snow. In the case of the Southern Hyogo prefecture earthquake in 1995, many surface failures and rockfalls that had occurred near the fault in the Mt. Rokko area caused new surface failures and expanded the existing failure areas over a 4 month period. In the case of a landside in Higashi-takezawa that blocked water channels as a result of the Mid Niigata Prefecture Earthquake 2004, secondary failure of the hillside slope occurred during the snowmelt season, and many failures in the Imo River basin occurred after snowfall.
   As described above, expansion of failures and landslides attributable to aftershocks, rainfall, or melting snow is typically observed over time in the case of earthquake-induced landslides. In many cases, conventional landslide observation using expansion gauges is applicable to monitoring and warning/evacuation for such phenomena.

(3) Debris flows
   Examples of earthquake-induced landslides, failures, or rockfalls resulting in debris flows due to heavy rain include sediment runoff after the Western Tottori Prefecture Earthquake in 2000 and the Tanzawa debris flow following the Great Kanto Earthquake in 1923. As shown in the cases of the Sichuan Earthquake in China and the Chichi Earthquake in Taiwan, the amounts of rainfall that triggered debris flows were 1/4 to 1/3 of those before the earthquakes. Therefore, the rainfall levels at which weather forecasts or warnings (e.g. heavy rain advisory information and warnings) are issued are generally lowered after an earthquake occurs.

Warning and evacuation in the case of debris flows are usually based on direct monitoring with debris flow sensors, and particularly wire sensors. However, to provide sufficient time for evacuation, warning and evacuation based on rainfall levels are more effective.

(4) Increase in sediment production and runoff due to combined disasters

Not only landslides and slope failures but also loosening of slopes or cracks as a result of earthquakes increase sediment production. Down-flow or accumulation of the sediment produced may increase sediment runoff and cause debris flows at times of heavy rain or snow melting. Cases have been reported where the amounts of sediment have tended to increase for several years following an earthquake.

2.3 Diversity of Time-Series Changes in Earthquake-Induced Landslides

Phenomena related to earthquake-induced landslides are diverse and include debris flows, floods, and overflowing due to breaching of natural dams. They are also characterized by diversity, as described in Table 11.1.

On the basis of the characteristics of the cases described above, the main warning and evacuation measures and monitoring approaches for earthquake-induced landslides and related phenomena are summarized in Fig. 11.1 in terms of the time elapsed.

Figure 11.1 is divided into three parts in terms of time elapsed. The warning/evacuation and monitoring methods applicable to each part are described as below.

(1) For several hours starting immediately after the earthquake (short term)

At this stage, because the main causes of landslides are the main quake or aftershocks, quantitative monitoring with instruments is hard to conduct owing to the unavailability of equipment. Therefore, monitoring is conducted mostly by visual observation of damage from helicopters.

Table 11.1 The diversity of earthquake-induced landslides

Diversity in timing of occurrence	Phenomena do not occur all at once immediately after an earthquake. They occur over several hours, days, or months afterward
Diversity in changes in various phenomena	Sometimes phenomena change over time, and this may result in other disasters. For example, collapsed soil may become debris flows or block river channels and create landslide dams as a result of rainfall after an earthquake
Diversity in the scope or scale of impact	Some landslides affect only discrete areas, whereas some affect wide areas

(2) For several hours to several days after the earthquake (medium term)

At this stage, government assistance and recovery efforts begin with a search for missing persons and efforts to rescue survivors. If the aftershocks have stopped, monitoring equipment such as cameras and sensors and warning equipment such as sirens can be installed. On the basis of the results of field investigations, camera footage, and data from sensors, major warning and evacuation measures are put into practice. The scope of the impact of landslide dam can be predicted by simulating overflows so that more detailed measures can be taken in consideration of the affected areas and the arrival time of the water.

Monitoring at this stage is directed at (i) warning and evacuation and safety management, and (ii) understanding landslide behavior. Monitoring to achieve the first objective is done by using, for example, wire sensors and cameras in order to secure the safety of personnel who need to enter hazardous areas for short periods of time. Monitoring to achieve the second objective is done mainly by observing ground-surface displacement with timber piles and extensometer in order to identify the scale and mechanism of the hazard and the precise
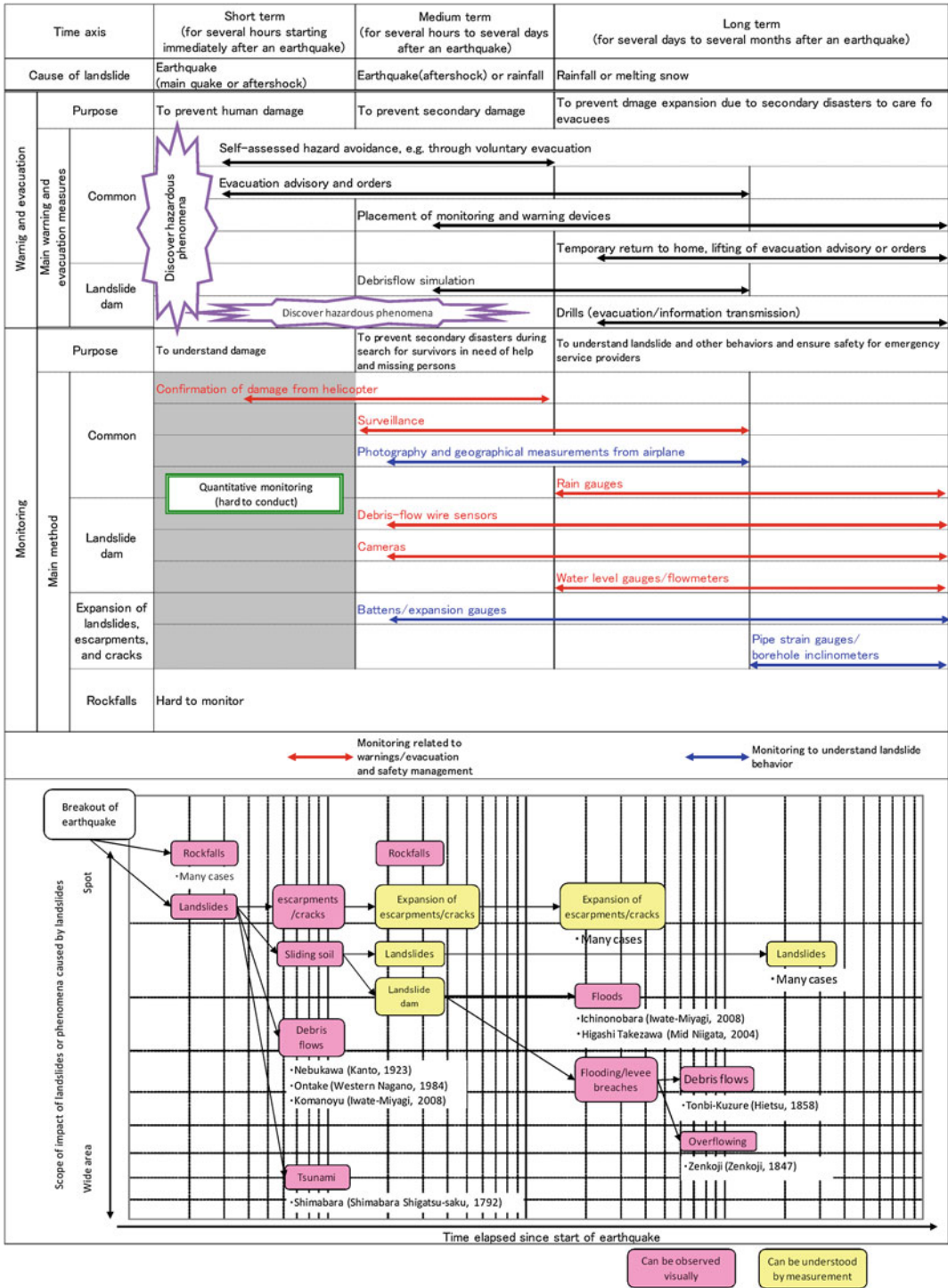
Fig. 11.1 Time series changes in phenomena related to earthquake-induced landslides and warning/evacuation and monitoring

hazardous areas. Geographical measurement is also conducted by aerial photography or laser scanning survey to understand the whole picture of landslides and gather data for use in the overflow simulation.

(3) For several days to several months after the earthquake (long term)

At this stage, full recovery efforts are underway. Several days after the earthquake, residents may be allowed to return home temporarily or the evacuation advisory or order may be lifted, depending on the results of observations of landslide behavior and on whether sensors are installed. Evacuation drills may also be conducted to prevent damage from secondary disasters such as debris flows attributable to the blockage or breaching of river channels.

The purposes of monitoring at this stage are the same as before, namely to understand landslide behavior, secure work safety, and measure standing water levels in blocked river channels; disbanding warning and evacuation systems is added as an additional purpose. Sufficient equipment would already have been installed for monitoring and ground displacement measurement using devices such as pipe strain gauges for general landslide behavior observation.

2.4   Basic Warning/Evacuation and Monitoring Policy for Earthquake-Induced Landslides

As discussed above, summaries of the phenomena associated with earthquake-related landslides in the past have revealed that the nature and scope of impact of such phenomena change with time.

Generally, appropriate warning/evacuation and monitoring methods should be selected to suit the events under consideration and their scope of impact and purpose. We need to apply different purposes and methods to warning/evacuation and monitoring in response to the changing status of earthquake-induced landslides.

3   Advance Preparation for Warning/Evacuation, and Educational Activities

3.1   Residents

As Japan has entered a period of brisk seismic activity in recent years, there is growing concern about warning and evacuation measures in the event of earthquakes; however, what experts think about warning and evacuation is not necessarily the same as what the public thinks about it, owing to differences in knowledge levels and approaches. Because residents themselves need to take warning and evacuation action once an earthquake occurs, discussions among experts alone cannot achieve the effective warning and evacuation of residents. Residents themselves need to perform drills for effective warning and evacuation in hypothetical situations. With this in mind, this section focuses on residents.

3.2   Current Warning and Evacuation Activities

Because warning and evacuation situations vary widely according to the time and place of the landslide and the nature of the earthquake (e.g. trench or inland type), the effectiveness of warning and evacuation activities cannot be enhanced solely by improving the accuracy of estimated scenarios.

To make warning and evacuation activities more effective in the post-earthquake stage of self- and mutual help, disaster-prevention community leaders who can respond to different situations should play an important role. Such leaders are required to have knowledge of earthquakes and the landslides induced by them so that they can take flexible action appropriate to the situation during the period when the entire picture of the disaster has not yet emerged. Furthermore, because several days may be required before mutual help among residents can function in areas susceptible to earthquake-induced landslides, knowledge of how to externally dispatch information, negotiate, and procure necessities

such as food to sustain life is also required. These actions should not depend merely on leaders' individual abilities; a system in which residents help each other is also very important. More specifically, leaders should know who has what knowledge in their community.

Although education and training are important for establishing a system of mutual help, they tend to become routine. To continue education and training for a long period of time and prevent them from becoming routine, in addition to map training, elements that make residents enjoy training are necessary, and training methods that include game-like elements have been developed. Besides the acquisition of knowledge, one of the main purposes of training is to establish a common understanding among residents of the geographical characteristics of their communities. Therefore, not only map training but also field workshops are now conducted. In education, in addition to the teaching of new technology, sharing of local history of the disaster after which an area has been named, as well as the ancient wisdom of how to survive (e.g. how to make drinking water from natural materials and cook wild herbs) may sometimes be useful.

With these measures, local community groups should be established and a system of mutual help should be put in place. In recent years, the relationship between heightened needs for privacy and declining vitality of local communities has been pointed out. We need to foster future leaders through local activities with the common goal of disaster prevention.

4   Conclusion

Warning and evacuation measures for earthquake-induced landslides differ according to local conditions, and there is no single solution that works for all situations. The solution best suited to each community should be established through dialog between residents and experts. It is often said that a disaster prevention plan is a living document; it should therefore be amended and improved as necessary, and the improvement process should be ongoing. In this sense, local engineers and universities need to play important roles.

Historical and Prehistoric Earthquake-Induced Landslides in Japan

12

Subcommittee for Historical Earthquake Landslide Studies in the Earthquake-Induced Landslide Program, the Japan Landslide Society (JLS-ELRP)

Abstract

Japanese historical documents mentioning natural disasters such as earthquakes and landslides in the Japanese islands date from as early as the 5th century. Our subcommittee reviewed a large number of these historical documents and extracted information on the topographical and geological features of earthquake-induced landslides. The resulting database includes 130 landslide-events that occurred from the late prehistoric period to the 20th century. The subcommittee statistically analyzed those landslides and found that the landslide-slope gradient mode is between 30 and 35°, that 61 % of the landslides have gradients between 25 and 40°, and that almost all occurred in and around the larger landslide topography which is identified by air-photo interpretation. Landslides consisting of convex ridge and/or convex plain, which together account for about 30 %, are the most characteristic of earthquake-induced landslides. About half of the listed landslides formed a landslide dam, suggesting either that earthquake-induced landslides frequently create landslide dams, or that those that create landslide dams have been recorded because of their causative role in disasters during the historical era.

Subcommittee for Historical Earthquake Landslide Studies
in the Earthquake-Induced Landslide Program, the Japan Landslide Society (JLS-ELRP)
1-1-1, Higashi, Tsukuba, Ibaraki 305-8567, Japan

1 Introduction

The Japanese islands are located in an active mobile belt, and many earthquakes occur in and around Japan. As the islands are mountainous and densely populated, earthquakes often cause landslide disasters, and people have recorded the

Table 12.1 Summary of prehistoric and historic earthquake-induced mass sediment movements in the Japanese islands

No.	Name	Date Yr.(AD).Month.Day	Magnitude	Type	Latitude	Longitude	Distance from Epicenter (km)	Area (m2)	Volume of debris (m3)	Length (m)	Width (m)	Slope topography	Gradient (°)	Relative height (m)	Geology	Landslide Dam?
0-1					36.33	138.85		3.5E+06	3.5E+08	1500	2800	convex valley	11	300	Neog. Normal sediments	
0-2					37.08	137.62		6.5E+06	2.0E+08	3600	1000	concave valley	5	320	Neog. Normal sediments	No
0-3					34.51	136.38		1.4E+06	7.7E+07	2200	700	concave valley	24	1000	Accretionary complex	Yes
0-4					36.53	137.18		9.4E+05	1.3E+07	1000	1000		15	200	Neog. Volcanics	Yes
0-5		8090 ±60 BP			36.53	137.17		3.3E+05	3.7E+07	900	700		7	170	Neog. Volcanics	Yes
0-6					35.16	134.65		8.8E+05	3.0E+07	1100	800	convex plain	23	450	Neog. Volcanics	Yes
0-7					38.35	141.09				9000	11000		1		Neog. Normal sediments	n.d.
1-1	Wado Totomi	715.7.4	6.5~7.5	Intraplate	36.32	137.97				820	730	convex valley			Accretionary complex	No
2-1	Kanto Shokoku	818.8.-	≧7.5	Intraplate	36.48	139.18	29	4.9E+05	6.3E+06	750	1300	straight plain	40	300	Quat. Volcanics	No
2-2															Quat. Volcanics	No
3-1	Goki Shichido	887.8.22	≧7.5	Interplate	36.01	138.37		6.0E+06	3.5E+08	3500	2250	convex	30	350	Quat. Volcanics	Yes
4-1	Echigo-nanseibu	1502. 1.28	6.5~7.0	Intraplate	36.88	137.88		1.4E+06	5.0E+07	1200	1200	convex	31	820	Accretionary complex	Yes
5-1	Tensho	1586. 1.18	7.8±0.1	Intraplate	36.22	136.91	25	5.0E+05	2.5E+07	750	500	convex ridge	35	900	Meso~Paleoz. Volcanics	Yes
5-2					36.17	136.87	19	3.6E+05	2.4E+06	700	600	straight valley	35	700	Paleog. Volcanics	Yes
5-3					36.17	136.86	19	4.4E+05	3.0E+06	1000	800	straight valley	35	700	Paleo. Volcanics	Yes
5-4					36.56	137.00		7.0E+04	3.0E+07	1000	1000	convex valley	14	250	Neog. Volcanics	Yes
5-5					35.32	137.58		2.6E+05	1.7E+07	550	650	convex ridge	25	260	Plutonic rocks	Yes
6-1	Keicho Bungo	1596.09.01	7.0±1/4	Intraplate	33.29	131.43		1.0E+05	4.5E+06	400	300	convex to straight	27	210	Quat Volcanics	n.d.
8-1	Kanbun	1662. 6.16	7 1/4~7.6	Intraplate	35.25	135.88	13	6.0E+05	2.4E+07	1000	800	convex ridge	43	650	Accretionary complex	Yes
9-1	Tnenna	1683.6.18	6.0~6.5	Intraplate	36.81	139.55		n.d.							Quat Volcanics	n.d.
9-2		1683. 6.18	6.0~6.5		36.76	139.50	15	7.0E+05	2.8E+07	2500	400	convex ridge	30	1400	Quat Volcanics	No
9-3		1683.10.20	7.0±1/4		36.92	139.69	3	1.3E+05	3.8E+06	450	400	convex ridge	40	220	Neog. Volcanics	Yes
10-1	Hoei Ugo	1704. 5.27	7.0±1/4	Intraplate	40.56	139.99		3.6E+06	1.1E+08	800	2800	straight plain	35	620	Neog. Volcanics	Yes
11-1	Hoei	1707.10.28	8.6	Interplate	35.31	138.31		1.2E+06	1.2E+08	1000	1800	concave valley	30	1100	Accretionary complex	Yes
11-2					35.21	138.54		1.0E+05	5.0E+06	950	350	straight plain	25	450	Neog. Normal sediments	Yes
11-3					33.47	134.15		4.7E+05	8.5E+06	1000	500	convex	31	470	Accretionary complex	No
11-4					34.36	134.14		n.d.							Neog. Volcanics	No
11-5					33.57	133.23		1.3E+05	4.4E+06	450	250	convex ridge	35	270	Accretionary complex	Yes
12-1	Shotoku Shinano	1714. 4.28	6.5	Intraplate	36.74	137.90	6.5	n.d.		400	500		45	250	Neog. Normal sediments	Yes
13-1	Mikawa・Ina	1718.8.22	7.0±1/4	Intraplate	35.32	137.93		4.0E+04	8.0E+05	285	310	convex ridge		230	Accretionary complex	Yes
14-1	Oshima Oshima	1741.8.17	6.9	Intraplate	41.52	139.35		1.7E+07	2.4E+09	5000	7000	straight to convex ridge	23	1850	Quat. volcanics	No
15-1	Horeki Takada	1751.5.21	7.0~7.4	Intraplate	37.17	138.09	12	n.d.	9.0E+06	450	850	convex ridge	70	160	Neog. Normal sediments	No
15-2					37.10	138.05	11	n.d.		2130	370	concave valley	43	410	Neog. Normal sediments	No
15-3					37.12	138.13	6	n.d.		950	860	straight plain	45	200	Neog. Normal sediments	No
15-4					37.16	138.15	7.5	n.d.							Neog. Normal sediments	No
16-1	Kansei Shimabara	1792.5.21	6.4	Intraplate	32.76	130.36	6	1.4E+06	3.3E+08	2000	1000	convex ridge	35	600	Quat. Volcanics	No

Rows 0-1 through 0-7 are labelled "Prehistoric Events".

Table 12.1 Continued

No.		Date Yr.(AD).Month.Day	Magnitude	Type	Latitude	Longitude	Distance from Epicenter (km)	Area (m2)	Volume of debris (m3)	Length (m)	Width (m)	Slope topography	Gradient (°)	Relative height (m)	Geology	Landslide Dam?
17-1	Koka Zenkoji	1847.5.8	7.4	Intraplate	36.65	138.04	17	1.4E+05	3.0E+06	1200	500	concave valley	35	300	Neog. Normal sediments	No
17-2					36.65	138.01	18	1.8E+05	2.6E+06	1050	250	concave valley	40	200	Neog. Normal sediments	No
17-3					36.65	138.09	11	1.3E+05	2.7E+06	650	300	concave valley	30	500	Neog. Normal sediments	No
17-4					36.59	138.06	18	8.4E+05	8.4E+07	1300	750	convex plain	15	320	Neog. Normal sediments	Yes
17-5					36.60	138.06	17	1.3E+05	2.0E+06	650	300	convex plain	15	220	Neog. Normal sediments	Yes
17-6					36.56	137.96	26	1.2E+05	1.5E+06	600	300	convex plain	25	180	Neog. Normal sediments	Yes
17-7					36.62	138.06	15	8.0E+04	1.2E+06	800	150	concave valley	30	250	Neog. Volcanics	Yes
17-8					36.71	137.95	22	8.5E+04	1.2E+06	200	400	convex plain	35	230	Neog. Normal sediments	Yes
17-9					36.81	138.62	41	4.0E+05	2.0E+07	1000	900	convex plain	20	350	Neog. Volcanics	Yes
18-1	Ansei Tokai	1854.12.23	8.4	Interplate	35.37	138.36	162	7.0E+05	6.6E+07	1400	750	straight valley	40	1300	Accretionary complex	No
18-2					35.21	138.54	152	3.8E+04	6.0E+05	250	200	straight plain	35	250	Neog. Normal sediments	No
19-1	Ansei Hietsu	1858.4.9	7.0～7.1	Intraplate	36.53	137.56	40	1.3E+06	1.3E+08	1500	1200	concave valley	30	860	Quat. Volcanics and Plutonic	Yes
19-2					36.34	137.17	40	4.0E+05	3.6E+06	350	550	straight plain	40	250	Metamorphic rocks	Yes
19-3					36.28	137.03	40	1.5E+05	2.2E+06	540	320	convex	35	260	Metamorphic rocks	Yes
19-4					36.30	137.07	40	8.0E+04	9.4E+05	420	250	convex	35	190	Metamorphic rocks	Yes
19-5	aftershock	1858.9?	7.1	Intraplate	36.57	137.68			7.2E+06	1250	575				Plutonic rocks	Yes
20-1	Hamada	1872.3.14	7.1	Intraplate	35.06	132.42	34	n.d.							Neog. Volcanics	No
21-1	Teshio	1874.2.28	5.5	Intraplate	44.64	141.80		3.2E+04	9.7E+05	360	360	straight plain	80	30	Neog. Normal sediments	No
22-1	Nobi	1891.10.28	8.0	Intraplate	35.61	136.62	3	surficial slope failure							Accretionary complex	Yes
22-2					35.57	136.65	6	debris flow							Accretionary complex	No
22-3					35.69	136.56		6.0E+04	1.5E+06	320	235	concave valley	39	150	Accretionary complex	Yes
22-4					35.63	136.35	23	1.6E+05	1.6E+06	580	420	concave valley			Accretionary complex	Yes
22-5					35.71	136.52	14	7.5E+04	1.8E+06	200	250	straight plain	37	170	Accretionary complex	Yes
22-6					35.68	136.54	10	8.5E+04	1.1E+07	1150	425	concave valley	39	500	Accretionary complex	No
23-1	Meiji Shonai	1894.10.22	7.0	Intraplate	38.93	139.97		3.0E+04	1.0E+05	500	100	concave valley	7	60	Quat. Normal sediments	No
23-2					38.94	139.97		4.0E+04	1.0E+05	400	100	concave valley	14	100	Quat. Normal sediments	No
23-3					38.93	140.13		2.3E+02							Neog. Normal sediments	n.d.
23-4					38.93	140.13		1.0E+03							Neog. Normal sediments	Yes
23-5					38.94	140.15		3.0E+02							Neog. Normal sediments	n.d.
23-6					38.92	140.20									Neog. Normal sediments	No
23-7					38.93	140.19	25								Neog. Normal sediments	No
23-8					38.95	140.21									Neog. Normal sediments	n.d.
23-9					38.92	140.21									Neog. Normal sediments	n.d.
24-1	Rikuu	1896.8.31	7.2	Intraplate	39.44	140.67	8	7.0E+04		350	200	concave			Neog. Volcanics	Eisit
25-1	Anegawa	1909.8.14	6.8	Intraplate	35.42	136.41	10								Accretionary complex	n.d.
25-2					35.47	136.46									Accretionary complex	n.d.
26-1	Akita Senpoku	1914.3.15	7.1	Intraplate	39.51	140.26	10	3.0E+03	2.3E+05	50	60	straight plain	38	40	Neog. Normal sediments	No
26-2					39.49	140.31	7	1.0E+03	1.5E+04	30	35	convex ridge	30	15	Neog. Normal sediments	Yes
26-3					39.48	140.31	7	1.8E+03	2.3E+04	30	65	straight ridge	30	20	Neog. Normal sediments	Yes
26-4					39.47	140.30	9	1.0E+04	2.6E+05	110	95	convex ridge	28	55	Neog. Normal sediments	Yes

Table 12.1 Continued

	Features of Earthquake				Features of Large Sediment Movement											Landslide Dam?
No.	Date Yr.(AD).Month.Day	Magnitude	Type	Latitude	Longitude	Distance from Epicenter (km)	Area (m2)	Volume of debris (m3)	Length (m)	Width (m)	Slope topography	Gradient (°)	Relative height (m)	Geology	
26–5 Akita Senpoku	1914.3.15	7.1	Intraplate	39.47	140.31	8	3.2E+03	3.2E+04	40	80	straight plain	25	23	Neog. Normal sediments	No
26–6				39.46	140.30	24	4.5E+03	n.d.	50	90	convex ridge	40	40	Neog. Normal sediments	No
26–7 Ugo Hiraga	1914.3.28	6.1	Intraplate	39.30	140.43	10	n.d.								
27–1 Taisho Kanto	1923.9.1	7.9	Interplate	35.18	139.09	18								Quat. Volcanics	No
27–2				35.20	139.10	18	1.4E+05	1.0E+06	500	800	concave valley		250	Quat. Volcanics	No
27–3				35.20	139.14	15	2.5E+05		250	500	convex valley		30	Quat. Volcanics	No
27–4				35.22	139.14	18	n.d.							Quat. Volcanics	No
27–5				35.31	139.19	15	n.d.				straight ridge			Quat. Normal sediments	Yes
27–6				35.36	139.21	19	2.0E+04	2.3E+05	100	200	straight ridge		20	Quat. Normal sediments	Yes
27–7				35.43	139.23	26	n.d.						20	Neog. Normal sediments	No
27–8				35.41	139.20	25	n.d.						20	Neog. Volcanics	Yes
27–9				35.41	139.08	30	6.3E+04	3.0E+05	350	250	concave valley	30	200	Neog. Volcanics	Yes
27–10				35.40	139.00	35	n.d.						200	Neog. Volcanics	Yes
27–11				35.36	139.04	28	n.d.						200	Quat. Normal sediments	Yes
27–12				35.37	139.04	29	n.d.						200	Quat. Normal sediments	Yes
27–13				35.55	139.23	39	4.0E+04	5.0E+05	200	200	concave ridge	35		Neog. Volcanics	Yes
27–14				35.43	139.24	26	n.d.						200	Neog. Volcanics	No
27–15				35.44	139.25	44	n.d.						200	Neog. Volcanics	No
29–1 Kitaizu	1930.11.26	7.3	Intraplate	35.15	139.00	6	3.0E+04	2.0E+05	150	200	plain	50	100	Quat. Volcanics	Yes
29–2				35.03	138.99	8	n.d.	3.0E+04						Quat. Volcanics	No
29–3				35.00	138.98	11	2.4E+04	1.5E+05	160	150	convex	40	60	Quat Volcanics	Yes
29–4				34.97	139.01	14	n.d.		150	180			30	Quat Volcanics and Neog. Normal sediments	Yes
29–5				34.95	138.95	18	4.7E+04	4.0E+05	150	150		20	100	Quat. Volcanics	Yes
29–6				35.18	139.03	10	8.0E+03	2.0E+05						Quat. Volcanics	n.d.
30–1 Oga	1939.5.1	6.8	Intraplate	39.89	139.85	38	3.8E+03		100	75		22	40	Neog. Normal sediments	No
30–2				39.97	139.78	28	5.1E+04		150	340				Neog. Normal sediments	No
30–3				39.96	139.79	30	6.9E+04		230	600		12		Neog. Normal sediments	No
30–4				39.96	139.80	30	2.9E+04	4.3E+05	100	300	straight ridge	17	30	Neog. Normal sediments	No
30–5				39.95	139.86	35	2.5E+03		100	50	concave valley	23	38	Neog. Normal sediments	No
30–6				39.97	139.85	33	2.2E+04		160	360	concave ridge			Neog. Normal sediments	No
32–1 Imaichi	1949.12.26	6.2	Intraplate	36.72	139.68		3.4E+06	2.0E+07	4300	1000	straight plain	1	70	Alluvium	No
33–1 Niigata	1964.6.16	7.5	Interplate	38.50	139.30	13	8.0E+04	1.2E+06	250	450	straight plain			Quat. Normal sediments	No
34–1 Matsushiro	1965.8.3		Intraplate	36.55	138.23			4.0E+05	200	150	straight plain	12	40	Quat. Normal sediments	No
36–1	1984.9.14	6.8	Intraplate	35.87	137.49	7	4.1E+05	3.4E+07	1300	430	straight ridge	26	650	Quat. Volcanics	Yes
36–2 Naganoken–nanseibu				35.81	137.46	9	2.2E+04	2.4E+05	110	200	concave valley	35		Quat. Volcanics	No
36–3				35.81	137.55	3	1.9E+04	2.3E+05	250	150	convex valley	35	50	Quat. Volcanics	No
37–1	1993.7.12	7.8	Interplate	42.18	139.52	50	8.5E+03	1.5E+05	225	100	straight plain	28	120	Neog. Normal sediments	No
37–2 Hokkaido–nanseioki				42.17	139.50	50	1.3E+04	1.0E+05	80	160	convex ridge	35	60	Neog. Normal sediments	No
37–3				42.20	139.45	50	5.4E+04	8.0E+05	300	180	concave valley	15	80	Neog. Normal sediments	No

occurrence of such disasters, for example, in documents or on monuments.

Historical documents mentioning earthquake disasters in Japan date from as early as the 5th century, and many documents, as well as memorial monuments, describe the damage caused by earthquake-associated landslides. We compiled historical records of earthquake-induced large sediment movements and built a database in which we compiled the reconstructed general features of the described landslides (Table 12.1). In this paper, we report the results of our statistical analysis of the features of these landslides.

2 Background and Study Method

Japanese historical earthquake research started in the late 19th century, and numerous documents mentioning earthquakes have been systematically compiled and published since the last quarter of 20th century [e.g., Usami 1980]. These documents, which include local histories as well as documents recorded by the central government, describe not only the earthquake shaking but also damage and ground deformation caused by landslides, tsunamis, and other earthquake-related phenomena, and the information that they contain is very useful for reconstructing individual earthquake-induced landslide events.

Published geomorphological research is an important adjunct to historical document interpretation. Areas in which landslides have occurred in the last 1,000 years are often characterized by undissected landslide topography, and other geological evidence, such as the presence of landslide-dam deposits or fractured rocks dated by the radiocarbon method or by using included archaeological relics, can also be used to identify sites of landslides or other large-scale mass transportation.

The subcommittee integrated and comprehensively interpreted data obtained from historical, geomorphological, and other geological investigations and recorded each event on a chart, based on the documents published by the Public Works Research Institute, Ministry of Construction (1997). The data on the charts, including the general features of each earthquake (date, magnitude, type of fault, etc.) and landslide (location, area, volume, length and width, slope shape and gradient, relative height, local geology, whether landslide dam was formed, etc.) and references, were then entered into the database.

3 Character of Documents in Each Period and Location

Japanese historical documents are unequally distributed with regard to their location of origin and age. Moreover, they reflect the author's social situation and interest. Therefore, it is essential to consider the nature of each document.

During the earliest period (from the 5 to the late 12th century), almost all extant documents were written in Kinki district, where the capital cities of the central government of the time were located. However, the official histories from the seventh to the 9th century, the central government recorded large regional events, from which we can identify major events of the period. In the Middle Ages (late 12 to late 16th century), the central government was weak and as a result official government documents are few and do not cover the entire period, but regional traditions, noblemen's diaries, and temple documents partly compensate for the lack of official records. We were able to identify only one event from this period. In the early modern period (late 16 to late 19th century), the number of official and private documents increased explosively by growth of production. Moreover, these documents include many contemporary maps and pictures of major events that allow us to precisely identify their locations. About one-third (40) of the events that we identified date to the early modern period. Since the 19th century, numerous scientific investigations have been carried out, increasing the accuracy and certainty of records in Japan. About half of the included events (63) are from the modern period.
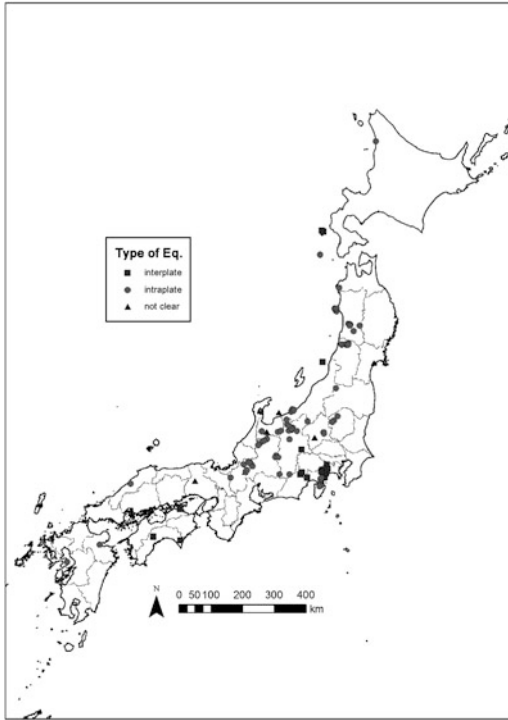
Fig. 12.1 Distribution of historical and prehistoric earthquake-induced landslides in Japan

Fig. 12.2 Distribution of the gradients of earthquake-induced landslides
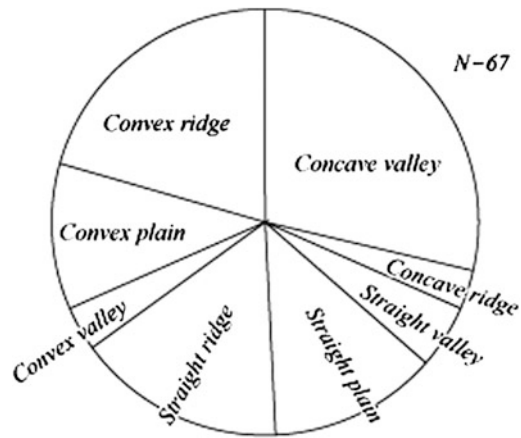
Fig. 12.3 Topographical types of earthquake-induced landslides

4 Distribution of Earthquake-Induced Landslides

The identified sediment movements are distributed throughout the Japanese islands (Fig. 12.1), but they tend to be concentrated in the inner zone (i.e., on the Japan Sea side). This distribution probably reflects the combined influences of geology and seismicity. Soft rocks of Neogene-to-Quaternary age, which are found mainly in the inner zone and in central Honshu (Japanese main island) tend to slide during earthquakes. The frequency of large intraplate earthquakes and the density of inland active faults are both higher in the inner zone than in the outer zone (i.e., the Pacific Ocean side), whereas most earthquake-induced landslides in the outer zone are related to the great interplate earthquakes that occur at relatively long time intervals along the Japan Trench and the Nankai Trough.

5 Geomorphological Features

One goal of our study was to clarify the geomorphological characteristics of earthquake-induced landslides, for example, by examining the distribution of slope gradients and landslide morphology. The distribution of longitudinal gradients of the 74 landslides in the database for which gradient data were available (Fig. 12.2) showed that the mode lay between 30 and 35°, and 61 % of the landslides had gradients between 25 and 40°. This result is consistent with reported gradients of recent earthquake-induced landslides, which tend to be steeper than those of non-earthquake-related landslides [e.g.,

Fig. 12.4 Geologic settings of earthquake-induced landslides
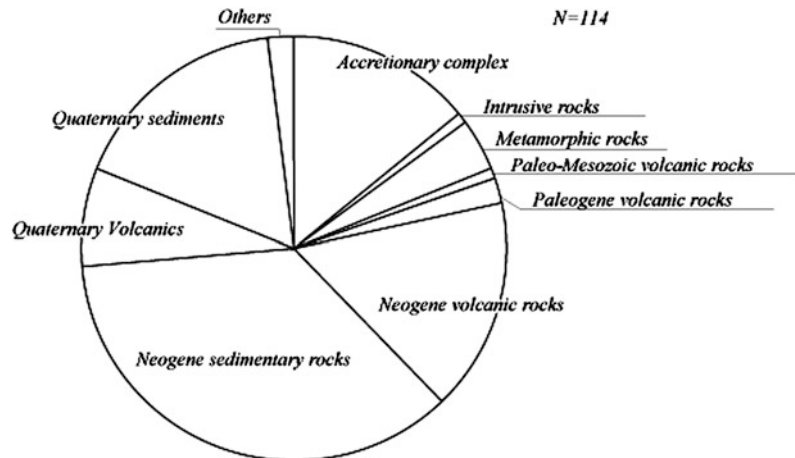
Yagi et al. 2007; Has et al. 2011], although the gradients of the landslides in the database are a little gentler than reported gradients of recent earthquake-induced landslides. This result suggests that earthquake-induced landslides generally occur on steeper slopes than those caused by rainfall and snowmelt. However, larger landslides were more likely to be recorded in historical documents than small, steep landslides.

We classified each landslide into nine topographical types on the basis of its longitudinal (concave, straight, or convex) and cross-sectional (valley, plane, or ridge) shape (Fig. 12.3). Concave–valley landslides, which account for about 30 % of the total, are topographically similar to rainfall-induced landslides, whereas concave–, straight–, and convex–ridge landslides, which together account for about 30 % of the total, are the most characteristic of earthquake-induced landslides.

Nearly all of the landslides in the database occurred in and around areas where landslide geomorphology is identified by air-photo interpretation. The remainder (about 10 %) were small landslides such as might be caused by rock falls or gully erosion. This finding suggests either that most earthquake-induced landslides occur on or near the previous landslides or that most areas of showing geomorphological evidence of large-scale, recent landslide activity are a result of earthquake-induced landslides. Some earthquake-induced landslide areas are associated

with Quaternary volcanoes. For example, in 1984, an earthquake centered beneath Mt. Ontake in central Honshu triggered the Ontake Denjo landslide, with a relative height of 650 m and a debris volume of 3.4×10^7 m³. The largest known earthquake-induced mass sediment movement associated with a volcano is the collapse of Oshima volcano in 1741. During this event, an estimated debris volume of 2.4×10^9 m³ slid into the Japan Sea, generating locally high tsunami waves.

6 Geologic Features

We summarize the general geologic features of earthquake-induced sediment movements as follows. Rocks of Neogene or Quaternary age underlie about 80 % of the landslide sites, and rocks of Paleozoic and Mesozoic accretionary complexes account for nearly all of the rest (Fig. 12.4). In contrast, Doshida and Inokuchi (2011) studied the geology associated with both earthquake-induced and non-earthquake-related landslides in the Japanese islands and found that the older rocks were, the more densely distributed landslide geomorphic features were. This high percentage of landslide sites on Neogene or Quaternary rocks in our database suggest that earthquake-induced landslides tend to occur under different geologic conditions than other landslides, or that our database is not sufficient to

be used to assess the general geology of earthquake-induced landslide sites.

It was difficult to distinguish clear relationships between geologic structure and the direction of landslide slip from the information in the documents. Consequently, we could reconstruct these relationships for only 28 events. Of these, 12 (about 40 %) were dip-slope events.

7 Landslide Dams

About half of the landslides in the database formed landslide dam, that means earthquake-induced landslides frequently create landslide dams, or landslide dams were disproportionately recorded in the historical documents. Our data are inconclusive as to whether earthquake-induced landslides are closely related to landslide dams.

8 Future Studies

Our database of earthquake-induced landslides in Japan is not sufficient. In the future, we plan to improve this catalog by additional geologic and geomorphological investigations, as well as by extracting more information from historical documents. Nevertheless, the present database is useful for examining the locations, geomorphological features, and geologic settings of earthquake-induced landslides, and for shedding light on potential locations of future landslides and on landslide mechanisms.

9 Appendix

Members of the subcommittee for Historical Earthquake Landslide Studies in Earthquake-induced Landslide Program, Japan Landslide Society (JLS-ELRP) are as follows:

Takashi, Inokuchi (National Research Institute for Earth Science and Disaster Prevention)

Kimio, Inoue (Sabo Frontier Foundation)

Taku Komatsubara[*](Geological Survey of Japan)

Shinro Abe (Okuyama Boring Co., Ltd.)

Takamasa Imamura (Geographical Survey and Photography Co., Ltd.)

Noriya Kamihara (Eight Japan Consultants Inc.)

Satoshi Kojima (Gifu University)

Masaaki Sakurai (Forest Conservation Research Institute Co., Ltd.)

Yoji Sawa (Asia Air Survey Co., Ltd.)

JingCai Jiang (Tokushima University)

Jun Tajika (Geological Survey of Hokkaido)

Hidehisa Nagata (Fu Sui Do Co., Ltd.)

Hiroomi Nakazato (National Institute for Rural Engineering)

Yoichi Hasegawa (Japan Conservation Engineers & Co., Ltd.)

Tamotsu Nozaki (Nozaki EG Consulting)

Takahiko Furuya (Prpfessor Emeitus of Chiba University and Senior Adoviser of Nissaku Co., Ltd.)

Shoji Doshida (National Research Institute for Earth Science and Disaster Prevention)

Hinako Suzuki (National Research Institute for Earth Science and Disaster Prevention)

References

Doshida S, Inokuchi T (2011) Assessment of landslide susceptibility using landslide maps. Abstracts of 50th meeting of the Japan landslide society, pp 206–207. in Japanese

Has B, Ishii Y, Maruyama K, Terada H, Suzuki S, Nakamura A (2011) Distribution and scale of landslides induced by recent reverse-fault earthquakes in Japan. J Jpn Landslide Soc 48:23–38 in Japanese with English abstract

National Research Institute for Earth Science and Disaster Prevention (2010), Landslide distribution maps. http://lsweb1.essbosai.go.jp/

Public Works Research Institute, Ministry of Construction (1997) A study report on actual state phenomena of large sediment movement and sediment-related disasters caused by earthquakes, Technical Memorandum of the Public Works Research Institute #3501, 261 p. in Japanese

Usami T (ed.) (1980) Japanese historical earthquake documents (new edn), vol. 1. Japan Power Electric Association. in Japanese

Yagi H, Yamasaki T, Atsumi M (2007) GIS analysis of geomorphological features and soil mechanical implication of landslides caused by the 2004 Niigata Chuetsu Earthquake. J Jpn Landslide Soc 294–306. in Japanese with English abstract

The Classification and Features of Earthquake-Induced Landslides in the World

13

Masao Yamada, Gonghui Wang and Keiji Mukai

Abstract

In the subcommittee of the overseas earthquake-induced landslides of the Japanese Landslide Society, the investigation of landslides triggered by earthquakes in the world was performed through mining the case studies from published literatures and documents. The sampled landslides triggered by big earthquakes (say, $M > 6.0$) since 1900 exceeds 70, and most of them are located in China, Japan, Iran, Indonesia, India, Pakistan, the United States, Chile, Peru, Italy, and Turkey etc. The type of these coseismic landslides extends to a wide range. These landslides were normally catastrophic, not only due to their direct damage, but also due to their resultant effects (such as tsunami, landslide dam, debris flow during post-quake heavy rainfall, and so on). In order to brief understanding on these coseismic landslides, we extracted several cases among the sampled landslides in the world and analyzed the landslides with extensive damage. We outlined the features of differing types of landslides based on their geomorphologic and geological characteristics, and also on the magnitude of the earthquake.

Activities in WG 7 of JLS-ELRP.

M. Yamada (✉)
Information Conservation Engineers Co.,Ltd,
Tokyo, Japan

G. Wang
Disaster Prevention Research Institute Kyoto
University, Kyoto, Japan

K. Mukai
Sabo & Landslide Technical Center, Tokyo, Japan

1   Introduction

To have a basic idea on the features of different types of landslides triggered by earthquake, the subcommittee of the overseas earthquake-induced landslides of the Japanese Landslide Society sampled those landslides triggered by earthquakes with their magnitude $M > 6.0$ all over the world since 1900. From the literatures and documents off the Internet, we sampled more than 70 landslides. Table 1 shows the list of these landslides, where the occurrence day of the earthquake, the disaster-affected country and region, the magnitude of the earthquake, the damage and fatalities (missing person is included), geographical and geological feature, the movement type of the landslide, the secondary disaster, and special note are presented.

The movement type of the landslide due to the earthquake in the world extends to a wide range such as cliff crumble, rock fall, slide, bedrock collapse, surface failure, rock sliding, flowslide, marine landslide, the slump, and rock avalanche etc. Through the information obtained from internet, it is normally difficult to identify the types of those coseismic landslides occurred in the past accurately. Here, we classified landslides by their movement into four types: fall/topple/collapse, slide, mixture of fall and slide, and flow/spread in order to understand the overall landslides realities.

2   The Classification of Coseismic Landslides

According to our statistics, the landslides triggered by inland earthquakes are almost three times of those triggered by the earthquakes at interplate. Fig. 13.1 shows the frequency distribution of landslide against the magnitude of the earthquake, from which we can see that a large number of landslides were triggered by the earthquakes with their magnitude greater than 7.5.

We also classified those landslides by their geological features (Fig. 13.2). The Quaternary period, the Neocene mudstone and sandstone, volcanic rocks such as granite and basalt account for 80 % of the whole landslides. Coseismic landslides had also been triggered in the Paleogene or older sedimentary rocks, limestone although the number is small.

Seeing the moving types of these landslides, we found that the the first 3 types, i.e., fall/topple/collapse type, the slide type, and the mixture type, occupied most of the landslides. The flowslides with long traveling distance occurred a little in wide areas (Fig. 13.3).

The 2011 off the Pacific Coast of Tohoku Earthquake, Japan, also triggered some landslides, although the damage by the resultant tsunami was devastating. These landslides caused severe damages to the properties and loss of lives.

Moreover, marine landslides had also been triggered in the sea or the lakes. Also glacier landslides can be triggered in some high mountains, causing devastating damages to the downstream area.

3   Typical Cases of Different Types of Landslides

As shown in Table 13.1, there are various types of coseismic landslides. Here we introduce some typical cases of differing types of landslides.

3.1   Mixture of Surface Failure and Slide Type

1994/1/17 San Fernando Valley, California, USA

The Northridge Earthquake (Mw6.7) occurred in San Ferrnando Valley of Southern California on 17 January, 1994. This is a typical inland one occurring along a blind fault. The slip displacement of fault plane due to this earthquake reached 3 m and the St. Susana Mountain has raised 70 m.

Geological settings are crushed Tertiary sedimentary rock in unconsolidated and poorly consolidated states. Almost no precipitation had been observed for 3 months before the

Table 1 List of the earthquake-induced landslides in the world

Earthquake occurrence day	Disaster-affected country and region	Magnitude of earthquake	Damege situation	Geography and geology	Movement type	Special note
1906/4/18	USA, California, SanFrancisco	7.8	About 3,000 dead	Stratum of opposite dip	Slide type	Deep landslide, landslide dam
1908/12/28	Southern part of Italian peninsula and northern part of Sicilian island	7.2	About 100,000 dead	Volcanic topography(Sicilian island: rhyolite, obsidian)	Slide type	Tsunami, submarine landslide
1915/1/13	Central part of Italian peninsula	7.0	About 30,000 dead		Slide type	
1920/12/16	China, Gansu, Ningxiahuizu(haiyuanxian)	Ms8.5	About 240,000 dead	Silty sand, loess, mudstone and red clay	Slide type	
1927/5/23	China, Gansu, Gulangxian	8.0	About 40,000 dead	Slip surface is Tertiary sand stone under loess	Slide and fall type	
1931/8/11	China,xinjiang, Uygur Autonomous Region	8.1	About 15,000 dead		Slide and fall type	
1932/12/25	China, Gansu, Mabao	7.6	About 70,000 dead		Fall type	Avalanche
1933/8/25	China, Sichuan, Moxian, Xizhen	7.5	More than 20,000 dead		Slide and fall type	Landslide dam
1934/1/15	India and Nepal, Bihar	Ms8.3	Uncertainty			
1949/7/10	Tajikistan, Khait	7.6	About 20,000 dead	Loess	Flow type	Flow type, debris flow
1950/8/15	China, Tibet, Chayu	8.5	About 4,800 dead		Slide type	Avalanche, iceberge collapse, landslide dam
1950/8/15	India, Assam	Ms8.6–8.7	About 4,000 dead		Slide type	
1958/7/10	USA, South-East part of Alaska	7.7	3 dead	Surface deposit in Pleistocene or Holocene age. Geology around the landslide region is Pyramid Peak layer (limestone)	Slide type	Tsunami

(continued)

Table 1 (continued)

Earthquake occurence day	Disaster-affected country and region	Magnitude of earthquake	Damege situation	Geography and geology	Movement type	Special note
1959/8/18	USA, Montana, Hebgen Lake	7.3	Uncertainty	The upper zone of the slope is gneiss or schist and the base of the slope is dolomite.	Slide, fall and flow type	Rock landslide, rock avalanche, slump type
1960/5/22	Chile	8.3-8.5	About 1743 dead (directly victim)	Tuff and moraine		
1962/9/1	Iran, North-West area	Ms8.3–8.5	About 12,000 dead		Slide and fall type	
1964/3/28	USA, Alaska, Anchorage	9.2	128 dead(113 victim by tsunami)	Tsunami, Upper Pleistocene	Slide type	Translational landslide
1966/3/8,22	China, Hebei, Xingtai	6.8,7.2	8182 dead		Fall type	
1968/5/31	New Zealand, Inanghua	7.2	2 dead	Granite and limestone		Landslide dam
1970/5/31	Peru, North area	Ms7.8	About 70,000 dead	Franite in Tertiary age and gracier		Landslide with gracier
1970/10/31	Papua New Guinea, Madang	7.0	Uncertainty	Miocene -Pleiocene volcanic hard rock		Debris flow, flow type
1973/2/6	China, Sichuan, Luhuoxian and Ganzixian	7.6	2175 dead		Slide type	
1974/5/11	China, Yunnan	7.1	1,423 dead		Slide and fall type	Landslide dam
1976/2/4	Guatemala	Ms7.5	About 23,000		Fall type	Debris flow
1976/5/29	China, Yunnan	7.3,7.4	98 dead		Fall type	Surface collapse
1976/7/27	China, Tianjin-Tangshan	Ms7.7–8.0	About 242,000 dead		Fall and slide type	
1976/8/16,23	China, Sichuan, Songpan, Pingwu, Nanping and Wenxian	7.2,2⟹	41 dead		Fall and slide type	Sector collapse, debris flow

(continued)

Table 1 (continued)

Earthquake occurence day	Disaster-affected country and region	Magnitude of earthquake	Damege situation	Geography and geology	Movement type	Special note
1977/3/21	Iran, Khurgu	6.9	152 dead		Slide and fall type	
1978/6/12	Japan, Miyagi offshore	7.4	28 dead	Andesite mudstone/sandstone/tuff, loam, gravel	Fall and slide type	
1988/11/6	China, Yunnan, Lincan city	7.6	748 dead	Limestone	Fall type	
1988/12/7	Armenia	6.9	About 41,000 dead		Flow type	Slump type
1990/6/21	Iran, North-West area	7.7	About 41,000 dead	Tuff, agglomerate and limestone, Quaternary deposit and shale/sandstone	Fall and slide type	
1994/1/17	USA, California, San Fernando Valley	Mw6.7	About 60 dead	Pliocene sand stone and silt stone	Rock slide	Rock landslide
1995/1/17	Japan, South part of Hyougo	7.2	6,434 dead	Granite, marine deposit and Kobe layer	Fall type	
1999/9/21	Tiwan, Nantouxian, Jijizhen	Ms7.7	2,496 dead	Pliocene, Miocene sedimentary rock	Slide type	
2003/12/26	Iran, South-East area	6.6	About 40,000 dead	Loose sand	Fall type	
2004/10/23	Japan, Niigata, Cyuetsu	6.8	68 dead	Mudstone, sandstone and mudstone-sandstone alternative	Slide type	
2005/3/20	Japan, Fukuoka west offshore	7.0	1 dead	Basalt	Fall type	
2005/10/8	Pakistan, Kashmir	7.6–7.8	More than 90,000 dead		Slide type	Landslide dam
2007/3/25	Japan, Noto peninsula offshore	6.9	1 dead	Mudstone, coast terrace	Fall type	
2008/5/12	China, Sichuan	8.0	87,150 dead	Dolomite, sand shall, silt stone and limestone	Fall and slide type	Rock avalanche
2008/6/14	Japan, Iwate and Miyagi	7.2	23 dead	Lacustrine deposit, pumice tuff	Slide, flow and fall type	Topple

(continued)

Table 1 (continued)

Earthquake occurence day	Disaster-affected country and region	Magnitude of earthquake	Damege situation	Geography and geology	Movement type	Special note
2009/9/30	Indonesia, Indonesia island, Padang	Mw7.6	More than 1,100 dead	Scoria	Fall type	
2010/2/23	Indonesia, West part of Java	7.3	44 dead		Flow type	
2010/2/27	Chile	Mw8.8	550 dead	Coast terrace, Tertiary sedimentary rock	Fall type	Tsunami, surface collapse
2010/4/14	China, qinghai, Yushu	7.1	2,968 dead	Colluvial deposit, diluvium soil	Fall and slide type	
2011/3/11	Japan, East-north area	9.0	About 19,000 dead	Loam	Slide type	Tsunami, flow type
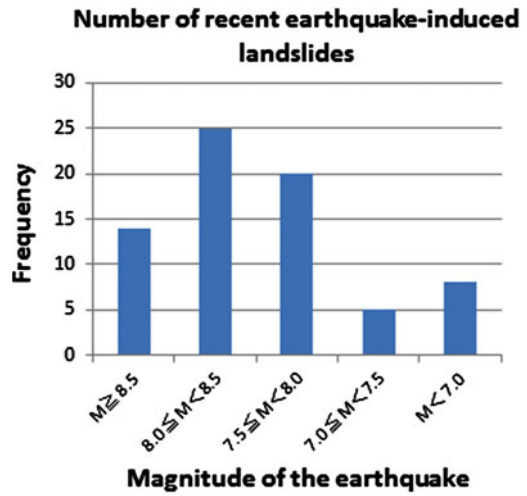
Fig. 13.1 Frequency of landslides against earthquake magnitude
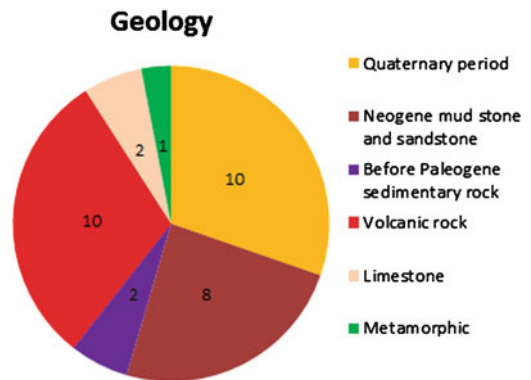
Fig. 13. 2 Geology of earthquake-induced landslides
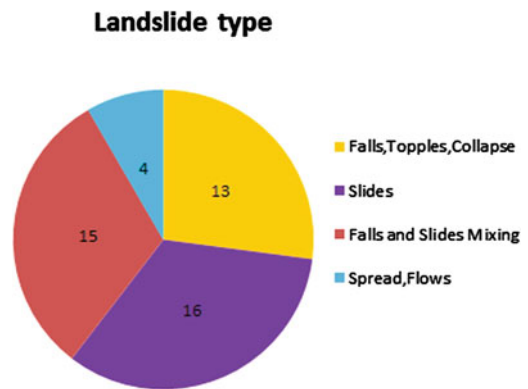
Fig. 13.3 Moving type of earthquake-induced landslides

earthquake. Many of the landslides occurred here are surficial failures (fall type) with their depth less than 5 m. There are also some re-activated rotational/translational slides with their sliding depth > 5 m.

3.2   Slide/fall Mixture Type and Landslide Dam

1999/9/21 Jijizhen, Nantou, Taiwan

An earthquake (Ms7.7) occurred in Jijizhen, Nantou prefecture, Taiwan, on 21 September, 1999, along the fault of Chelongpu. Maxmum slip displacement of Chelongpu fault is 8.5 m in horizontal direction and 9.8 m in vertical direction. This earthquake triggered a lot of landslides in the mountainous areas and the cliffs of plain region. There are two large landslides occurred in Caoling and Jiufenershan distinct. Caoling landslide is a bedrock (sandstone-shale alternative layer) slide with its length being 1.7 km. While Jiufenershan landslide is a collapse type with its length being 1.6 km, and its bedrock being shale layer of the Miocenein. Two landslide dams were formed by Jiufenershan landslide. A clay layer 3–5 cm thick was identified as the sliding surface for these two landslides.

2005/10/8 Kashmir, Pakistan

An earthquake (Mw7.6) occurred in Kashmir region, Pakistan on 8 October, 2005, which triggerd a large-scale collapsed landslide in Dandbeh area. This landslide has a length of 1.8 km and depth of 50 m. The geology is sandstone-mudstone alternative layer of the Neogeneary Murree formation, and the sliding surface was formed along several bedding planes. A landslide dam was formed with the dam length along the river being 1.3 km, and a depth of 250 m in maximum. There are also many shallow landslides occurred on the slopes along the national road of Jhelum River and Neelum River. It is thought that the displaced landslide materials originated mostly from the stratum near the ridge of the opposite slopes

where the bedrock had been loosened due to the rock creep of the topple type.

3.3   Fall and Rock Avalanche Type

2008/5/12 Sichuan, China

A massive earthquake (Ms8.0) occurred in Sichuan, China on 12 May, 2008, which is also known as Wenchuan earthquake, after the location of the earthquake's epicenter. Three faults of the Longmenshan fracture zone located in the north-northwest part of Chengdu City moved. The slip displacement reached 8.5 m in vertical direction.

The geology is limestone and sandstone-shale alternative layer of the Mesozoic-Paleozoic age. Many fall and rock avalanche type of landslides were triggered. In some cases, the velocity of the rock avalanche was even faster than 40 m/s, and more than 20,000 people were directly killed by different types of landslides. Among those catastrophic rock avalanches, a giant one occurring in Daguangbao area has a traveling distance of 4.5 km and a depth of about 300 m with a displaced debris of about 700×10^6 m^3.

3.4   Shallow Landslide and Debris Flow

2009/1/8 Cinchona, Costa Rica

An earthquake (M6.2) occurred in the north area in Costa Rica on 8 January, 2009. Many shallow landslides were triggered by the earthquake, and most of them originated from the vicinity of the mountain ridges. The geology is volcanic ash soil (loam), and the mineral compositions of the loam are allophane and halloysite. The property of the loam is similar to that of the Kanto loam in Japan. The collapse morphology is the shallow landslide occurred along the river and the debris flow. The background of the collapse is the steep valley topography and the river erosion. Because many landslides were triggered along the river, many landslide dams were formed after the earthquake.

Some of the landslide dams collapsed soon after the earthquake, resulted in catastrophic outburst debris flow and floods.

3.5 Roch Avalanche and Flowslide After Earthquake

2009/9/2 Bandung, Indonesia

A strong earthquake (M7.3) occurred in Tasikmalaya offshore, the Java island, Indonesia on 2 September, 2009. Due to this earthquake, some rock avalanches were triggered in West Java State, resulting in many fatalities and great damages to houses and roads. The geology is andesite volcanic rock of the Tertiary, and deep weathering of the slope is remarkable. This region is high rainy area where the annual precipitation exceeds 3000 mm. Therefore, big rock lump come off easily due to the earthquake. It is thought that the saturated part on the toe of the slope enabled the occurrence of the landslide, and then collapse failure occurred on the upper part of the slope, resulting commenced rock avalanche.

Moreover, some landslides due to the heavy rainfall after the earthquake occurred in the Bandung prefecture and also in same West Java State on 23 February, 2010. It is reported that a lot of cracks might have been triggered by the Tasikmalaya earthquake, and these cracks enabled the infiltration of precipitation, and then lead to the occurrences of landslides. A big landslide has fluidized with a traveling distance of about 900 m.

3.6 Flow and Topple Type Landslide

2011/3/11 Tohoku area, Japan

A giant earthquake (Mw9.0) occurred in the Pacific Ocean offshore of Tohoku area in Japan on 11 March, 2011. The earthquake is a typical one locating on the plate boundaries. The fault destruction distance is 500 km and the fatalities

by the tsunami disaster and others (such as landslides) have reached about 19,000.

Some landslides occurred in Shirakawa district, Fukushima prefecture by the earthquake on 11 March, and then some additional landslides were triggered in Iwaki district by the aftershock on 11 April again. The geology in Shirakawa district is volcanic deposit consisted of pumice, scoria and loam layer. The soil layers on the slope had very high water content (~ 150 %). On the other hand, the landslide in Iwaki district occurred in the mountain ridge and was a topple type landslide reflecting the terrain effect of the earthquake.

References

Ito T, Utomo EP (2009) Rock fall avalanche triggered by Tasikmalaya Earthquake in Indonesia. J. Jpn Landslide Soc 46(3):76–78

Keefer DK (1984) Landslides caused earthquakes. Geol Soc Am Bull 95:406–421

Keefer DK (2002) Investigating landslides caused by earthquakes-a historical review. Surveys Geophys 23:473–510

The third mission of the Japan Landslide Society (2006) Report of the field reconnaissance and inspention on landslides induced by the 2005 Northern Pakistan Earthquake. J Jpn Landslide Soc 43(2):48–51

The Japan Landslide Society (2012) Earthquake-induced landslides

Wang F, Muhammad W, Zhang F, Takeuchi A (2011) Tandikek and Malalak rapid and long runout landslides triggered by West Sumatra Earthquake 2009(M7.6) in Indonesia. J Jpn Landslide Soc 48(4):29–33

Yamada M, Cai F, Wang G (2010) Wenchuan earthquake and mountain disaster. Rikou Tosho, Tokyo

Relationship Between Geological Structure and Landslides Triggered by the 2007 Mid-Niigata Offshore Earthquake

14

Tamotsu Nozaki and Baator Has

Abstract

Compared with the case of the 2004 Mid-Niigata Earthquake, by which so many large and middle-scale landslides were triggered, only a few middle-scale ones occurred with many small-scale ones by the 2007 Mid-Niigata Offshore Earthquake in spite of their similar geology and topography [landslide-scale with apparent volume (the Japan Landslide Society, 2004); small-scale: 10^2–10^4 m^3, middle-scale: 10^4–10^6 m^3, large-scale: 10^6–10^8 m^3]. Some of them, however, caused serious damage to the infrastructures. Around the Hijirigahana cape in Yoneyama town located at about 30 km south of the epicenter, some middle to small-scale landslides occurred as a group. Geology of the study area is composed of sedimentary rocks simply dipping to the sea. An open anticline gently plunges to north, and the study area is just located on and around its axial part. Due to the topography 'cuesta', both of translational and rotational slides occurred on the cataclinal and orthoclinal slope, respectively. It had been thought that mechanism of those landslides was not so complicated because of the simple structure. During the excavation for the countermeasure of those landslides, however, a vertical fault, which looked like a tectonic one, with some others including bedding faults were found behind the affected area. Although the most hazardous slide occurred on the cataclinal slope was a simple translational one, rotational slide occurred on the orothoclinal slope was a little complicated, and non-tectonic structure due to the pre-historical event was found behind the new slide.

1 Introduction

This paper is one of our case-studies on the landslides triggered by large earthquakes which occurred within the last decade in Niigata Prefecture.

T. Nozaki (✉)
Nozaki EG Consulting, Niigata, Japan
e-mail: nozakit@kb3.so-net.ne.jp

B. Has
Asia Air Survey, Co., Ltd, Tokyo, Japan

Fig. 14.1 Location map
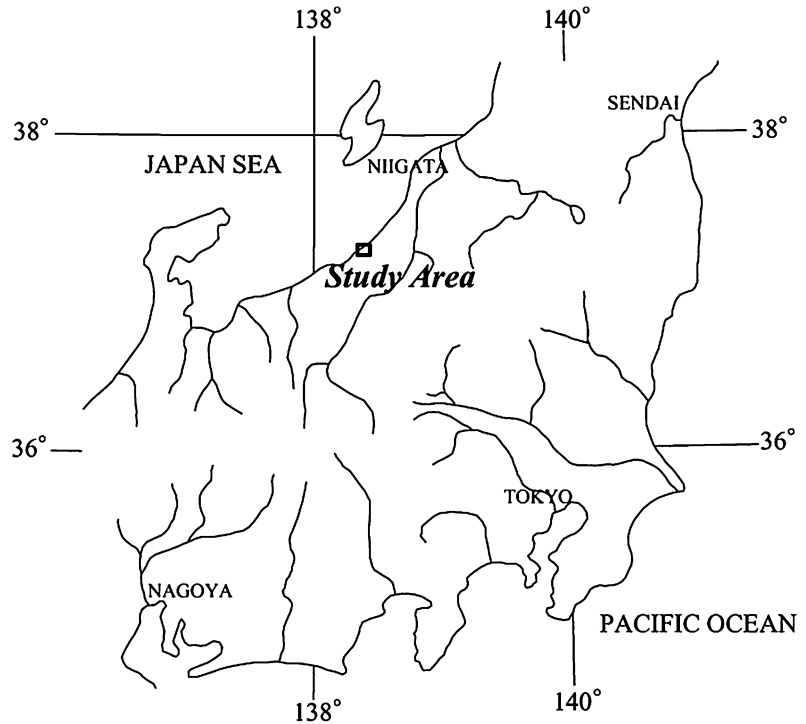
Tragically, on July 16, 2007 only 3 years after the Mid-Niigata Earthquake (Mj = 6.8) in 2004, the Mid-Niigata Offshore Earthquake (Mj = 6.8) occurred. Both of the ravaged areas were partly overlapped, because both the epicenters were only 25 km away, and many residents in the affected area of the preceded earthquake, who had just rebuilt or were the halfway to repair their houses, were miserably suffered with liquefaction and slope movement again (Fig. 14.1).

Compared with the case of the 2004 Earthquake, by which so many large and middle-scale landslides were triggered, only a few middle-scale ones occurred with many small-scale ones by the 2007 Earthquake in spite of their similar geological and topographical conditions. Some of them, however, caused serious damage to the highways and the railroad lines. Around the Hijirigahana cape in Yoneyama town located at about 30 km south of the epicenter, some middle to small-scale landslides occurred as a group (see Fig. 14.2). These landslides blocked a local road at two places, and accidentally a car passing along was trapped between them (see Photo. 14.1), fortunately the driver and his car were safe. Geology of the study area is composed of sedimentary rocks simply dipping to the sea. An open anticline gently plunges to north, and the study area is just located on and around its axis. Due to the topography 'cuesta', both of translational and rotational slides occurred on the cataclinal and orthoclinal slope, respectively. It had been thought that mechanism of those landslides was not so complicated because of the simple homoclinal structure. During the excavation for the counter measure of those landslides, however, a vertical fault, which looked like a tectonic one, with some others including bedding faults were found behind the new slides. In this paper, we described the hazard of landslides, and discussed the mechanism of the new and old rockslides with the issue of non-tectonic geological structure.

Fig. 14.2 Distribution of landslide units triggered by the earthquake
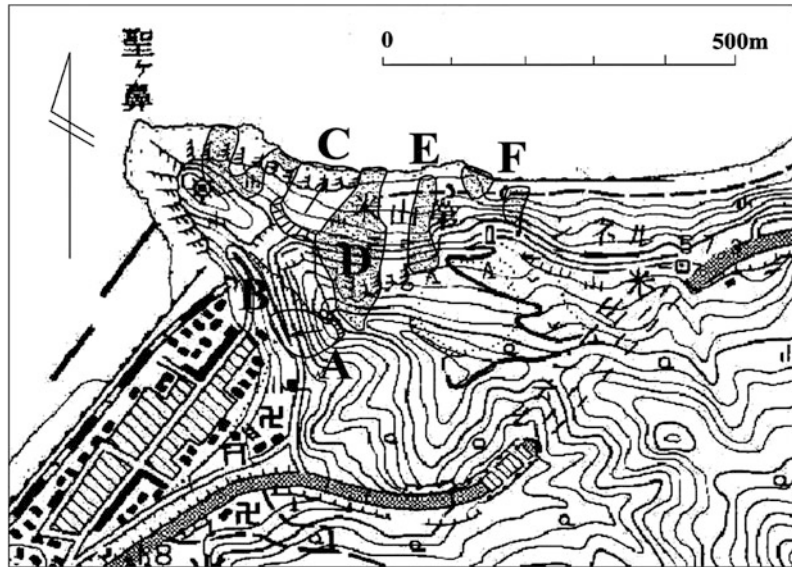
2　Geology

A late Miocene member of sandstone-rich alternating beds of sandstone and siltstone, part of which was beautifully outcropped along the local road passing through the cape (see Photo 14.2), is conformably overlain by the volcanic rocks, and disconformably underlain by the member of siltstone intercalated with thin beds of sandstone and a thick pumice tuff at its upper horizon (see Fig. 14.3). Both of the upper and the lower members of sedimentary rocks were named Hijirigahana Formation by the Yoneyama Research Group (Yoneyama Research Group, 1973). The disconformity between both members, however, was found during our investigation of this disaster. These strata gently dip (25–30°) toward sea making cataclinal and orthoclinal slopes on north and west side of the cape respectively. This cape is located just on the axis of broad open anticline, of which the axis plunges to north. That is the reason why the aspect of bedding plane in the study area trends EW and dips north in spite of NS trend of the anticlinal axis. Although vertical joints, which were slightly tilted to SW, tend to develop in NW–SE and less other directions, there was no noteworthy tectonic fault except for some bedding-plane slips which were found on a part of new and old sliding surfaces.

3　Landslides Triggered by the Earthquake

Two units of the landslide A and B rotationally moved without clear boundary between them on the western side of the cape, where is rather steep orthoclinal slope. On the other hand, four units of landslides C, D, E, F and small others occurred on northern side, where is gentle and typical cataclinal slope (see Figs. 14.2, 14.3).

3.1　Rotational Slides on the Orthoclinal Slope

On the western side of the cape, the slope looks toward west or southwest, and the strata dip to
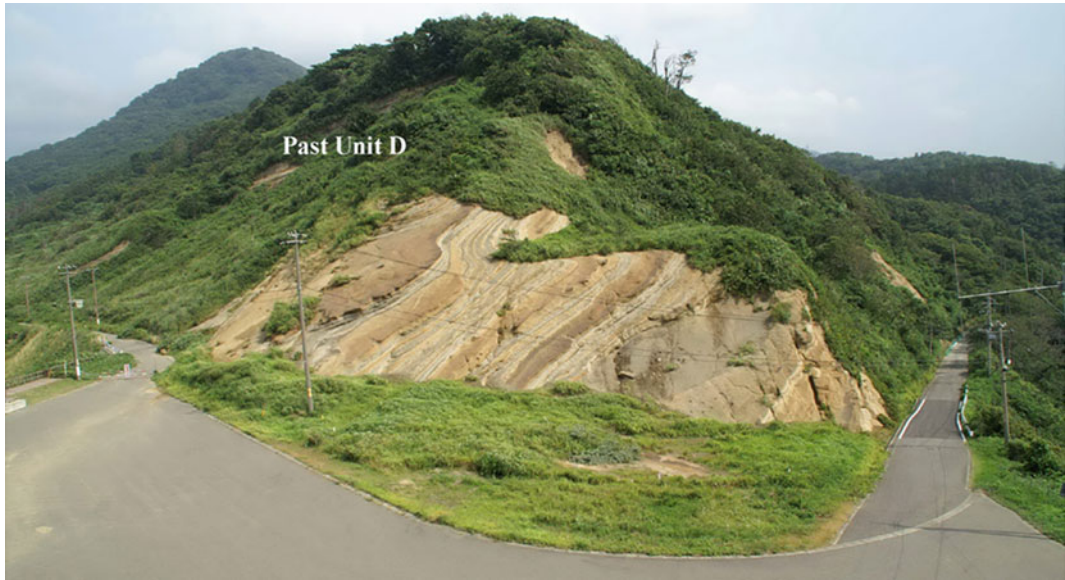
Photo. 14.1 View of the study area before the earthquake (Photograph taken on Aug. 10, 2005 by Atsuo Ueki, Kashiwazaki city education center)
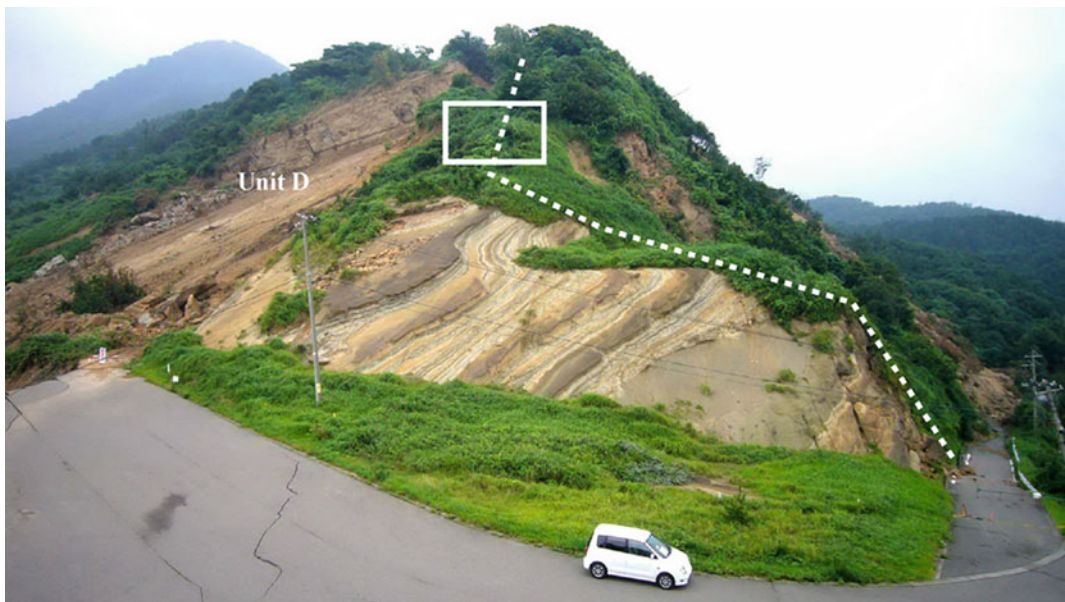
Photo. 14.2 View of the study area after the earthquake (Photograph taken on Aug. 4, 2007. *Dotted line* is trace of the fault observed at the *box*, location of Photo 14.3)

north forming orthoclinal structure. Except for the upper part of the slope, where the rock consists of alternating beds of sandstone and siltstone, basement rock consists of siltstone member intercalated sparsely with thin layers of loosely indurated sandstone and a thick soft pumice tuff at its upper part.

About 5 m high head-scarp was created below the crown of Unit A along the ridge associated with parallel cracks, and the vertical
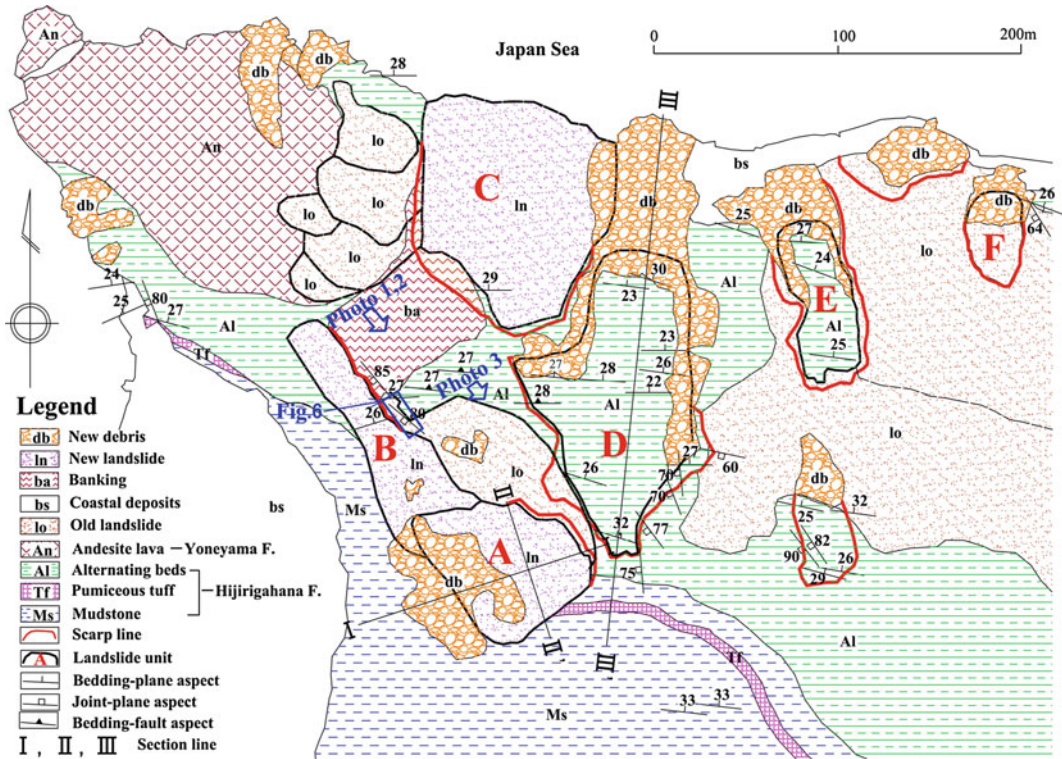
Fig. 14.3 Geological map of the study area

crack which was 0.3–0.7 m high at the head area of Unit B obliquely run across the road. No clear boundary appeared between Unit A and B. Although displacement of Unit B was less than 0.7 m at the head, its width was transversely elongated more than 100 m along the lower part of the slope, and the southern flank was buried beneath the debris of Unit A. The affected area of Unit B was unknown in detail because of the short displacement, and the relationship between the two units was not able to be clarified because of the way of complicated displacement at the boundary. However, the tip of the sliding surface of both units even the toe of the debris of Unit A did not apparently reach to the foot of the slope, and the JR tunnel located just under the landslides had no damage. Although slightly gentler slope than the other part was created at the head of Unit A, the gradient of this orthoclinal slope was more than 40 degrees as a whole. Magnitude of the Unit A was approximately 90 m wide, 120 m long and 10 m thick.

On the outcrop of alternating beds located at the northern end of the ridge which meets with the road, a few consistent vertical joints directed to NW were observed. New open spaces associated with small debris were observed along these joints and bedding-planes, and those sedimentary rocks were evidently loosened by the tremor of earthquake. However, it was clear that some of them had been already loosened by the pre-events because of the evidence of sealing cracks with asphalt on the road and the grass roots invaded into some of those open cracks.

3.2 Translational Slides on the Cataclinal Slope

The most hazardous unit D, which pre-existed before the earthquake, extended mainly to the upper slope, and only thin strata must have been ripped off on the central to lower part of the unit (see Fig. 14.4), because a part of the road, which

Fig. 14.4 Longitudinal section of Unit D
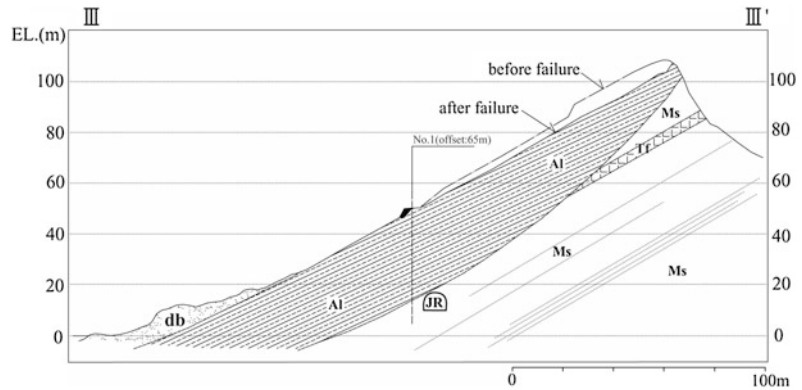
Fig. 14.5 Changing dip of strata along longitudinal section of Unit D
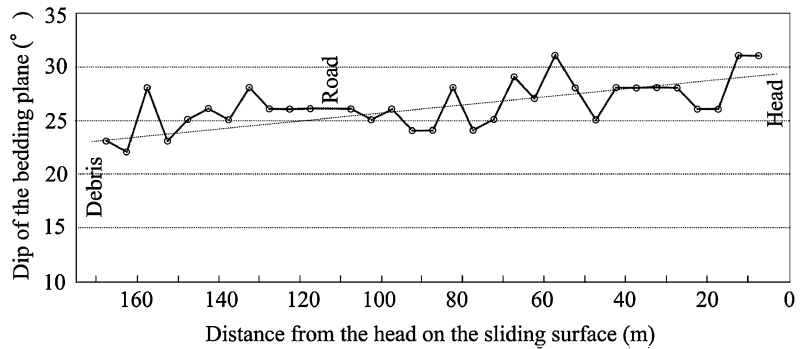
had run across the central part of the unit, remained intact. The maximum width is about 100 m, the length is about 200 m, the head was a little more than 100 m above sea level, and the volume accumulated at the foot of the slope was evidently less than 10,000 m^3. The upper end of the sliding surface reached beyond the ridge along a bedding-plane, hence no head-scarp remained. On the eastern side of the slide, however, "detached scarp" rose sheer more than 10 m, and the sequence of alternating beds of sandstone and siltstone was well-observed there. On the western side of the slide, 5–8 m high side-scarp was created, and a part of it toppled as rock-panels separated by high-angle joints trending NW. Almost entire sliding mass reached to the beach, and the sliding surface was widely exposed.

On the higher portion of the sliding surface, a large number of slicken lines, which was directed approximately to the dip of the strata, were

extensively curved on a bed of siltstone. Slicken lines found on the sliding surface at the foot of the western scarp, however, were approximately parallel to the strike of the strata. It means that these slicken lines had evidently occurred as a bedding-plane slip during the past folding : tectonic movement, and functioned as a potential sliding surface. The sliding surface, however, did not occur along only one bedding-plane, but occurred along bedding planes connected in a stepwise manner making a micro-staircase (see Fig. 14.4). This means that the sliding surfaces shifted to the lower sequence of the strata downslope. The whole sliding surface, therefore, looked a little steeper than the dip of the strata.

Figure 14.5 shows the changing dip of strata at intervals of every 5 m along the center line of Unit D. The attitude of the bedding plane was approximately EW25–30°N, and it became gentler little by little descending from the head to the

Photo. 14.3 Fault appeared on the cut-slope

foot of the slide with undulation. As a result, the configuration of the sliding surface drew a very gentle arc as a whole due to this changing dip and the micro steps.

Unit C was exceptionally rotational making a typical head scarp on the cataclinal slope. The sliding mass had consisted of old debris derived from JR tunnel which run across just under the ravaged area. This unit did not run so long, and stopped on the slope. It is inferred that the sliding surface did not exceed 5 m in depth at most considering on its configuration and dip slope. Unit E occurred adjacently on the eastern side of Unit D was also a translational type, and the sliding surface was exposed in the same manner. Gravelly soil outcropped on its head scarp, however, was evidently old landslide debris; 2–3 m in thickness. Much smaller unit F was located at the east entrance of the old tunnel. Although this unit was

also translational, it obliquely cut across the bedding-plane, and the sliding surface of an old landslide unit was observed on the side scarp.

4   Unexpected Structure Found During Excavation Work

A fault tilted with high angle toward SW direction appeared during excavation work for one of the countermeasures at the northern part of the ridge between Unit A and B (see Photo 14.3). Although its precise direction of the separation and the throw was not known, it was evidently a normal dip separation fault. The right side of the fault in the photo was hanging wall; both sides of the wall looked intact. Incidentally, the upper central bushy part in Photo 14.2 was the cut slope in Photo 14.3. On its

Fig. 14.6 Sketch of outcrop located on the western side slope
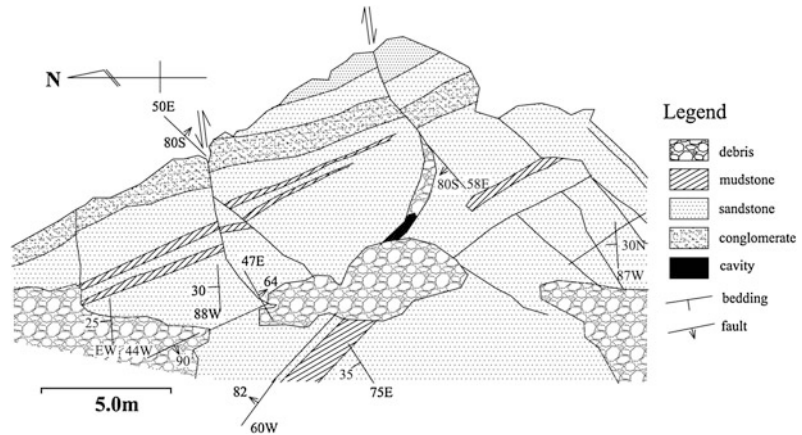
extension line on the outcrop in the foreground of Photo 14.2, however, no such a fault was seen. It means that the fault did not extend there. Figure 14.6 shows the sketch of the outcrop observed from west (right hand side), where was right-end portion of this outcrop (see Fig. 14.3). Although this part was loosened a little, and some tiny failures and/or peeling off occurred in places by the tremor, some high-angle faults were observed as shown in Fig. 14.6. We had thought at first, therefore, this outcrop had been a part of the intact rock before the earthquake. However, it was clarified that only a central part of the rock was intact and surrounded by the displaced masses after our detail observation.

Figure 14.7 is the sketch map of the cut-slope observed during the excavation work of the unstable debris, which was made for the stabilization of Unit A. Unfortunately, this sketch had not been schemed before the work, some parts of this map, therefore, were analyzed from the photos taken during the cut-work. We observed, however, all the cores drilled just after the earthquake at this site, and draw this map and geological sections (Fig. 14.8) with reference to those data. Although landslide debris moved by the earthquake had been completely excavated, a high angle fault dipping to west appeared at the head of the cut slope, and thick crush zones along bedding-planes and/or bedding-plane-slip faults also appeared at the middle and lower part of the slope, hence the original scheme had to be changed (Niigata Branch of the JLS 2008). As a

result, the excavated volume reached to 70,000 m^3, much larger than the original plan of 20,000 m^3.

5 Mechanism of Landslides

5.1 Landslides on Orthoclinal Slope

It was not discernible during excavation whether the fault shown in Photo 14.3 was tectonic or non-tectonic, because both walls of the fault looked utterly intact. Beautiful alternating beds had widely cropped out around its northern extension line, and sliding surface and/or bedding plane had been widely bared stripping off the mass of Unit D on its southern extension line: no evidence of fault was there on both sides. It is impossible that tectonic fault dies out in such a short distance. On the other hand, throw of the normal fault found behind the head scarp of Unit A was about 10 m tilting with high angle toward west, and it became abruptly gentle and made an arc at the intersection with the bedding-plane-slip fault. In addition, the strata of hanging wall were apparently disintegrated or crushed at random in places, and thick crush zones along bedding-plane-slips were observed (see Fig. 14.8). Therefore, it was clear that this fault was a part of old sliding surface. Although its extension to north was not traceable because of covering of debris or soil, it must be the identical one described above. It reasonably
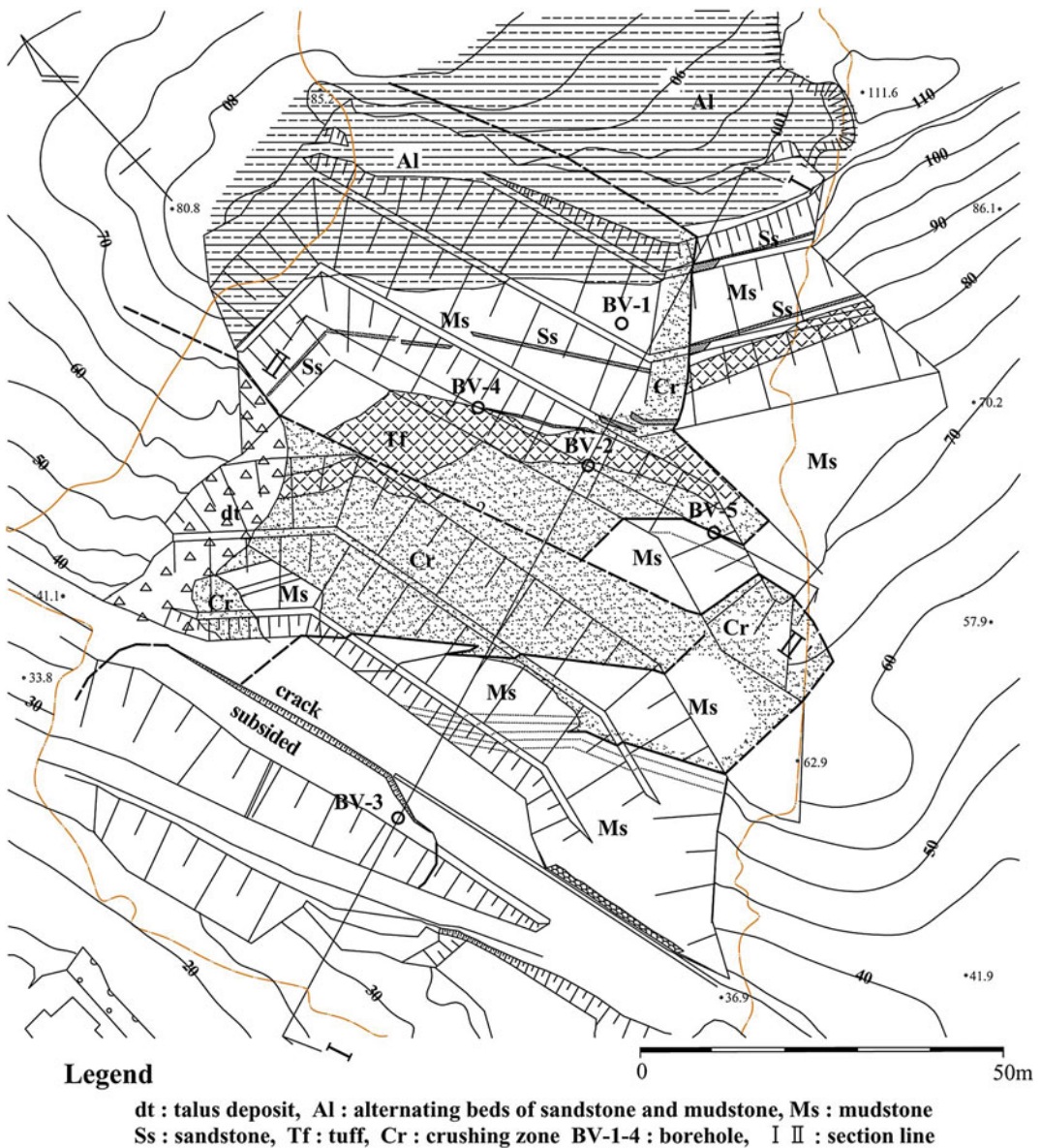
Fig. 14.7 Sketch map of cut-slope during excavation work of Unit A

extends turning to west toward the natural outcrop shown in Fig. 14.6. It means that the whole structure was non-tectonic created by the old gravitational movement except for some bedding-slip faults.

Although the head area of Unit A started to move west, that displacement was deflected from west to north at the lower part. This movement is well-explained with the structure above-mentioned, that is, the head area displaced creating the head scarp along the non-tectonic fault or vertical joints, then the sliding mass was deflected along pre-existed bedding-plane-slip associated with crush zone at the lower slope. Mechanism of Unit B is unknown the detail, because the visible displacement was

Fig. 14.8 Geological sections of Unit A
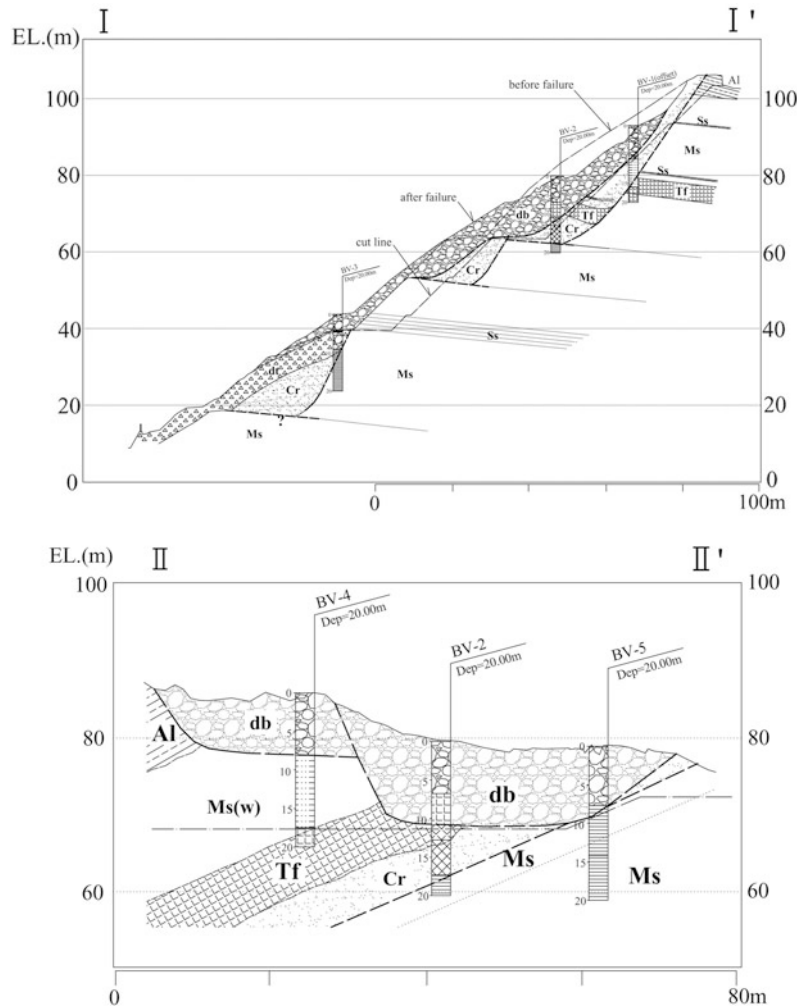
limited at the head area and the almost entire area was covered with soil and vegetation. We believe, however, it must be basically same with the mechanism of Unit A, because of the same geological structure.

5.2 Landslides on Cataclinal Slope

As shown in Photos, cataclinal slope consists of beautiful alternating beds of sandstone and silt-stone, which are easily sheared off along bed-ding planes. Moreover, the bedding-plane-slips observed in places also must have fostered the development of gravitational sliding as potential sliding surface. These slips must have occurred with flexural slip on the axial part of anticline, because the slicken lines and the dip of the bedding-plane crossed each other at almost right angles, each of those slips was not so long extended though. The sliding surface of Unit D drew a very gentle arc making micro steps, and this configuration made it a little steeper at its upper part. Therefore, it might have been one of the reasons why the sliding mass was not so disintegrated and reached to the foot of the slope, or might have helped it at least.

Along the ridge located between the catacli-nal and orthoclinal slope, vertical joints had developed with NW–SE trend, and the west-side

scarp of Unit D was controlled by them. The almost entire slope including Unit C, D, E and F were located in a bigger old landslide area, and it is reasonably inferred that translational slides had been repeated on this slope in the past. In comparison between Photos 14.2, 14.1, we found that extents of Unit D and past Unit D were almost same. Therefore, it is inferred that Unit D must have occurred on the same slope of the past slide extending a little to the head area, and only 2–3 m thick veneer of alternating beds on the upper slope slid down to the beach as a new rockslide including a little old debris, because the volume of the debris was less than 10,000 m^3.

Same type of rapid translational rockslides as Unit D, represented by Yokowatashi landslide (Nagata and Nozaki 2007), were triggered at many places by the 2004 Mid-Niigata Prefecture Earthquake.

6   Conclusions

It looked landslides induced by the 2007 Mid-Niigata off shore earthquake on the cataclinal slope were extensive and more hazardous than those on orthoclinal slope. However, they did not so extend over the limit of the pre-existed slide and those sliding masses were shallow except only the upper part of Unit D. The sliding surface of Unit D made a micro-staircase, and the dip of the strata increases toward the head. This kind of structure might have helped the long travel of the sliding mass.

On the other hand, the mechanism of land-slides on the orthoclinal slope was rather complicated and interesting. During the excavation for the countermeasure of those landslides, a vertical fault with some others including bedding faults were found behind the earthquake-induced failure zone. Even after the counter-measure including excavation work, it had been believed that those structures were tectonic or synsedimentary disturbance happened under the sea water. However, the authors clarified that those structures were limited around and/or under the affected area, and they had not reached to the extending nor underlying strata. There-fore, we concluded that those complicated structures must have been created by preceded slope movement, probably induced by the pre-historic earthquake.

References

The Japan Landslide Society (2004) Landslides. geo-morphological and geological recognition on land-slides and their technical terms. p.17 (written in Japanese)

Nagata T, Nozaki T (2007) Fracture surface markings on landslide scarps and movement of the landslide induced by the Mid Niigata Prefecture Earthquake in 2004. The Japan Landslide Society, Earthquake-induced Landslide Disasters in middle Mountains. "Study Report on the 2004 Mid-Niigata Earthquake PartI", Geomorphology and Geology, pp 160–167

Niigata Branch of the JLS (2008) Mid-Niigata offshore earthquake and landslides "Yoneyama-cho landslide" (written in Japanese)

Yoneyama Research Group (1973) On the Neogene tertiary system in the Yoneyama District, Niigata Prefecture, Japan. Earth Science, 27,1, pp 1–18 (written in Japanese)

Part III
Case Study

Catastrophic Landslides of Pyroclastics Induced by the 2011 off the Pacific Coast of Tohoku Earthquake

Masahiro Chigira, Akito Nakasuji, Shinya Fujiwara
and Masayuki Sakagami

Abstract

The 2011 off the Pacific coast of Tohoku Earthquake induced 4 soilslide-avalanches of pyroclastic fall deposits with volumes from 500 m^3 to 30000 m^3 in Shirakawa and Nakagawa, where 6+ and 6− seismic intensities of JMA scale were recorded, respectively. These landslides occurred on rather gentle slopes with 13° to 23° with sliding surfaces in the depths of 3 m to 9 m but had a high mobility, which is shown by apparent friction angles ranging from 10° to 16°. Trees on slopes have been transported on debris in a standing position. The causal factors of these landslides were slope-parallel bedding of pyroclastics that include very weak paleosol, in which a sliding surface was made, and that the beds that slid had been undercut to have lost the support from lower slope. The paleosols were rich in halloysite, which is a weathering product of volcanic ash and pumice. Soil slide-avalanches like those described above have been induced also by previous earthquakes, including 1949 Imaichi, 1968 Tokachioki, and 1978 Izu-Oshima-Kinkai earthquakes. Among these, the landslide numbers of the Tohoku Earthquake were much less than those of the other earthquakes, which could be related to less amounts of preceding rainfall before the Tohoku Earthquake than the others. The Tohoku Earthquake occurred during a dry season in Japan and had only 94 mm during 60 days before the earthquake, while the other earthquakes had 250–400 mm antecedent

M. Chigira (✉)
Disaster Prevention Research Institute, Kyoto
University, Gokasho, Uji, 611-0011Japan
e-mail: chigira@slope.dpri.kyoto-u.ac.jp

A. Nakasuji · S. Fujiwara · M. Sakagami
Kokusai Kogyo Co. Ltd, 2-24-1 Harumi-cho,
Fuchu-shi, Tokyo, 183-0057, Japan
e-mail: akito_nakasuji@kk-grp.jp

S. Fujiwara
e-mail: shinya_fujiwara@kk-grp.jp

M. Sakagami
e-mail: masayuki_sakagami@kk-grp.jp

rainfalls. Pyroclastic fall deposits generally are distributed widely, so if much more rainfall had preceded the earthquake, more landslides could have been induced.

1   Introduction

The 2011 Off the Pacific Coast of Tohoku Earthquake (hereinafter, the Tohoku Earthquake) is the strongest seismic event (Mw 9.0) ever recorded in Japan by modern methods. It struck on March 11, 2011, at 14:46:18.1, with an epicenter 24 km deep off the Sanriku coast at 38°06.22′N, 142°51.6′E (Japan Meteorological Agency 2011a, b). The quake was particularly destructive because of its tsunami; damage from landslides and avalanches, by comparison, was limited. This said, soil-slide avalanches did occur on gentle slopes at Shirakawa (Fukushima Prefecture; seismic intensity of 6+ on the JMA scale) and Nakagawa (Tochigi Prefecture; 6−) (see Figs. 15.1 and 15.2). We investigated these occurrences through geological field examinations, laser surveying, X-ray mineralogical analysis, various physical property measurements, and geomorphic analysis by means of aerial photographs taken before the earthquake. In this manner, we examined the various geological characteristics of these slides for comparison against similar occurrences in past earthquakes.

2   Landslide Distribution and Characteristics

Notable soil-slide avalanches occurred at five locations, four in Shirakawa, Fukushima Prefecture (Hanokidaira, Shirasawa, Shirasawa NE, and Okanouchi) and one in Nakagawa, Tochigi Prefecture (Oshino). As will be described in more detail later, the Okanouchi slide involved a colluvium of weakly welded tuff. The other four were avalanches of pyroclastic fall deposits. We directly examined four of the five; a summary of their characteristics is presented as Table 15.1.

We did not directly examine the Shirasawa NE slide and thus do not include it within the table.

The areas of Shirakawa and Nakagawa are widely covered by Quaternary pyroclastic fall deposits from the Nasu volcano and other sources (Suzuki 1993).

2.1   Landslide at Hanokidaira (Shirakawa, Fukushima Prefecture)

Casualties: 12 dead, 1 missing

Extent: horizontal length 251 m; height 47 m; volume ((60 m long × 50 m wide × 5 m deep) + (50 m long × 70 m wide × 4.5 m deep)) = 30,000 m³

Apparent friction angle: 10.0°

Geology: paleosol, pumice, scoria, weathered ash

Geological structure: bedded texture roughly parallel to slope surface; some weathered ash present in thick drifts.

Morphology before the event: Aerial photographs taken in 1975 by the Geospatial Information Authority of Japan showed a cup-shaped gully head at the location that later marked the bottom of the avalanched slope. We infer that the gully eroded the slope from its bottom, thus undercutting the upper portion from its bedding.

2.2   Landslide at Shirasawa (Shirakawa, Fukushima Prefecture)

Damage: forest and paddy

Apparent friction angle: not measureable (calculated to be 15° from horizontal length and height)

Extent: horizontal length 330 m; height 70 m (estimated with 1/25,000 map); volume (95 m long × 30 m wide × 3 m deep) = 9,000 m^3

Geology: paleosol, pumice, weathered ash

Geological structure: bedded roughly parallel to slope surface

Morphology before the event: gully head. Debris came down from head to southeast and then south. A clear knickpoint exists midway up the gully, and the avalanche occurred above it. As was the case with the Hanokidaira landslide, the bedding had been undercut at the knickpoint.

2.3   Landslide at Okanouchi (Shirakawa, Fukushima Prefecture)

Casualties: 1 dead, 1 house completely destroyed
Apparent friction angle: 16°

Extent: horizontal length 143 m; height 40 m; volume (76 m long × 41 m wide × 5 m deep) = 16,000 m^3

Geology: colluvium of weakly welded tuff (brown soil mixed with rock fragments)

Geological structure: bedded texture roughly parallel to slope surface; strong weathering at deeper depths; high moisture; exposed weakly welded tuff alongside slope base; spring water observed flowing from cracks within it.

Morphology before the event: ridgetop; a road runs across the bottom of the slope. The slide surface is exposed at the road cut.

2.4   Landslide at Oshino (Nakagawa, Tochigi Prefecture)

Damage: forest, paddy, house (partially destroyed but no injuries)
Apparent friction angle: 13°

Extent: horizontal length 330 m; height 75 m; volume (55 m long × 25 m wide × 4 m deep) = 5,500 m^3

Geology: paleosol, pumice, weathered ash

Geological structure: bedded texture roughly parallel to slope surface
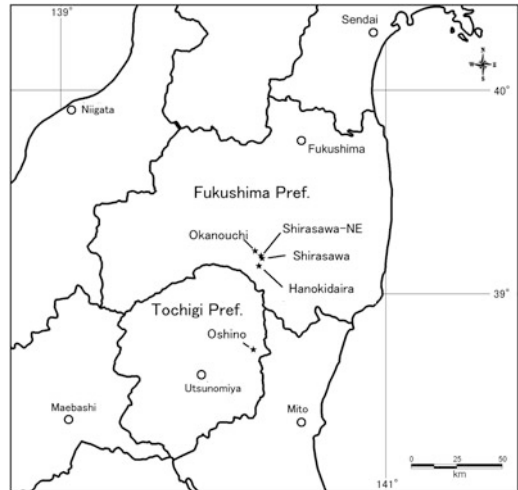
Fig. 15.1 Index map of the landslides

Morphology before the event: Aerial photographs taken in 1975 by the Geospatial Information Authority of Japan show the northern half of the lower slope to extend to what was once the head of a steep gully. The gully apparently eroded the slope from its bottom, thus undercutting the upper portion.

3   Characteristics of Sliding-Surface Paleosols

Paleosols constituting the sliding surfaces of landslides induced by the 2011 Tohoku Earthquake were very moist and weak, with density measurements ranging from 1.6 g/cm^3 to 2.1 g/cm^3 and gravimetric moisture contents ranging from 0.4 to 0.6 (Table 15.2). All the paleosols contained fine pores of a diameter of up to 1 mm. Similarly, their mineralogy can be characterized as quartz, halloysite, cristobalite with tridymite. Halloysite is widely known to be a weathered product of volcanic glass (Aomine and Wada 1962). Cristobalite has been reported to be a weathered product of ignimbrite within the Shirakawa pyroclastic flow (Chigira et al. 2002). As for the Hanokidaira landslide, a layer of pumice resting above paleosol was found to be soft, easily crushable within one's fingers, and readily liquefiable; however, no halloysite was detected
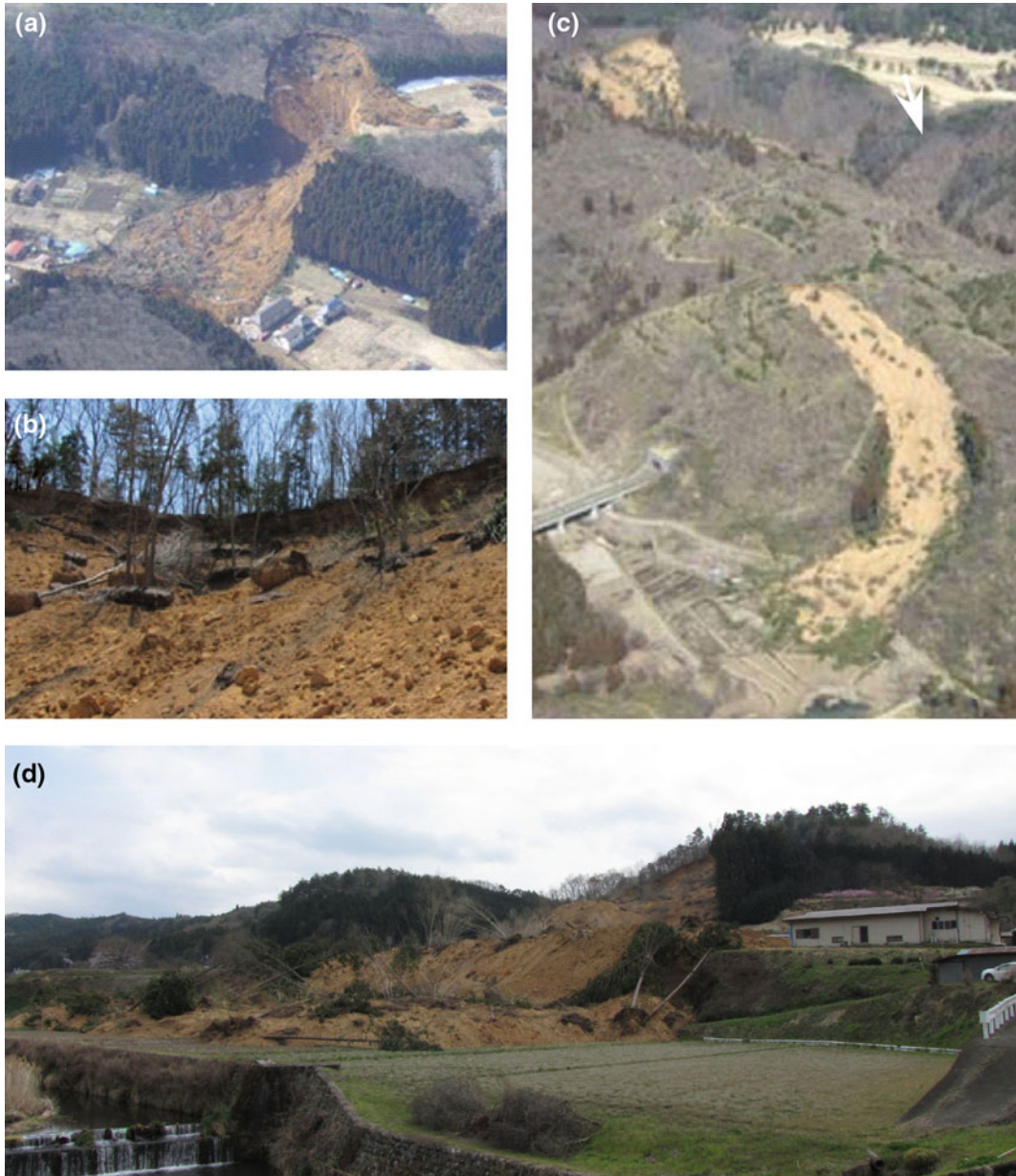
Fig. 15.2 Photographs of the landslides we studied. **a** Aerial view of the Hanokidaira landslide. **b** Source area of the Hanokidaira landslide. **c** Aerial view of the Shirasawa landslide. **d** the Oshino landslide. Photoes a and c were taken by the Ministry of Land, Infrastructure, Transportation, and Tourism

within it. Sliding surfaces have been confirmed to be made in the top part of the paleosol and not in the pumice bed at the foot of the peripheral cliff of the Hanokidaira landslide. Soil hardness values obtained by using Soil Hardness Tester (Yokota and Iwamatsu 1999; Chigira and Yokoyama

Table 15.1 A list of soil-slide avalanches induced by the 2011 Tohoku earthquake. Only Okanouchi landslide occurred on a colluviums slope, while others on pyroclastic slopes

Locality	Damage	Appearent friction angle (°)	Horizontal length (m)	Height (m)	Volume (m³)	Goelogy	Sliding surface	Depth (m)	Slope angle (°) of a source area	Morphology before the event	Slope direction
Hanokidaira	12 dead missing	10	251	47	30,000	Paleosol, pumice, scoria, weathered ash	Paleosol	5 ~ 9	22	Undercut?	N45°E
Shirasawa	Forest and paddy	15	330	70	9,000	Paleosol, pumice, weathered ash	Paleosol	3	13	Undercut	S60°E
Okanouchi	1 dead	16	143	40	16,000	Collivum of weakly welded tuff	Paleosol	5	18	Undercut	S
Oshino	Forest and paddy	13	330	75	5,500	Paleosol, pumice, weathered ash	Paleosol	4	23	Undercut	N56°E

2005) suggested that the sliding surface was formed in the weakest layer in the Hanokidaira landslide.

Pyroclastic fall avalanches of the 1986 Off Tokachi Earthquake and the 1978 Izu-Oshima-Kinkai Earthquake all entailed a sliding surface within paleosol (Inoue et al. 1972; Chigira 1982; Chigira 1995; Yoshida and Chigira 2011). The 1949 Imaichi Earthquake produced sliding surfaces in a pumice bed that had transformed into a whitish clay and were rich in halloysite (Morimoto 1951). The halloysite in a landslide induced by the 1978 Iu-Oshima-Kinkai earthquake is interpreted to be the reaction product of gibbsite with silica in the percolating water from above beds after the burial of the paleosol (Chigira 1982), which is resilicification of gibbsite (Kleber et al. 2007). The surface soil in the Hanokidaira landslide site are dominated by gibbsite without halloysite and the paleosol is dominated by halloysite, which suggests that the halloysite may be made by the resilicification of gibbsitic soil.

Examinations of paleosol structures in the vicinity of the sliding surfaces reveals that in all cases the structures had lost their original pores down to a depth of 1–2 cm below the slide surface and that plagioclase/pumice particles have been crushed out of shape. This comes as a result of strong shear deformation, to which paleosol on the bottom of the slide surface was exposed upon the physical transport of the material. Chigira (1982) examined pyroclastic fall landslides occurring during the 1978 Izu-Oshima-Kinkai Earthquake. By means of soft X-ray photography of slide-surface paleosols, he found that plastic deformation of paleosol occurred from a depth of several centimeters directly below the surface down to 10 cm, with essentially all pores eliminated through crushing. This result indicates that deformation within a landslide is concentrated at the slide surface and its environs. Also inferred is that the paleosol, being clay, had low moisture permeability, such that pore pressure within the area of shear deformation, unable to be released, remained at a high level. This suggests that surface liquefaction like that reported by Sassa et al. (1996) may have occurred.

Table 15.2 Physical properties of the paleosols

Place	Material	Moisture density(g/cm^3)	Dry density (g/cm^3)	Gravimetric water content	Gravimetric water-soil ratio
Oshino	Paleosol (Halloysite)	1.66	0.75	0.55	1.20
Hanokidaira	Paleosol (Halloysite)	2.03	1.20	0.41	0.68
Shirasawa	Paleosol (Halloysite)	1.90	1.05	0.44	0.80
Okanouchi	Paleosol (Halloysite)	–	–	–	–
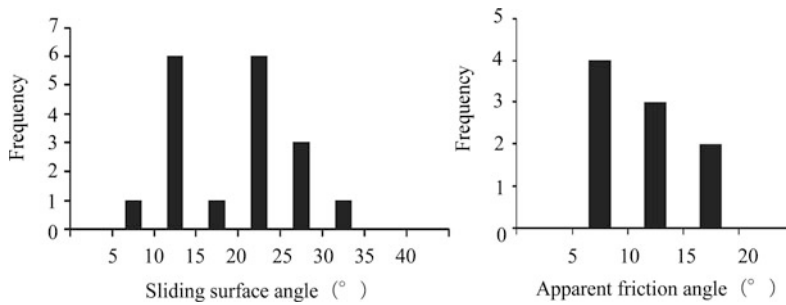
Fig. 15.3 Slope angles and apparent friction angles of soil-slide avalanches of pyroclastic fall deposits. Data: 1923 Kanto earthquake (Kamai 1990), 1968 Off Tokachi earthquake (Inoue et al. 1972), 1978 Izu-Oshima-Kinkai earthquake (Chigira 1982), 1984 West Nagano prefecture earthquake (Oyagi 1987; Kawakami et al. 1985), and 2011 Tohoku earthquake

4 Geological and Morphological Factors to Earthquake-Induced Landslides

Pyroclastic fall avalanches very similar to those of the 2011 Tohoku Earthquake occurred with considerable frequency within the 1949 Imaichi Earthquake (Morimoto 1951), the 1968 Off Tokachi Earthquake (Inoue et al. 1972; Yoishida and Chigira 2011), and the 1978 Izu-Oshima-Kinkai Earthquake (Chigira 1982; Chigira 1995). In this section, we compare the geological and morphological characteristics of these landslides, and comment on the qualitative assessment of slope stability under seismic loading. Of the earthquakes mentioned above, the 1978 Izu-Oshima-Kinkai Earthquake produced relatively few landslides (7 occurrences) but, as they were all within a 1 km^2 area, their geographical density was high. A related factor behind their paucity was the monogenetic volcanic nature of the avalanched material, which itself was very narrowly distributed. Conversely, with regard to the 1949 Imaichi

Earthquake, maps from Morimoto (1951) indicate landslides in 88 locations. Similarly, for the 1968 Off Tokachi Earthquake, landslides are reported to have occurred in approximately 150 locations (Inoue et al. 1972; Yoshida and Chigira 2011) for an average geographical density of four landslides per square kilometer. The landslides that occurred within the 2008 Iwate-Miyagi Inland Earthquake were dominated by the collapse of pumice tuff and welded ignimbrite. In other words, those slides were of a different nature than the ones discussed in this report (Hashimoto et al. 2009).

4.1 Surface-Parallel Bedding Structure and Slope Undercutting

Almost all the pyroclastic fall landslides induced by the four abovementioned earthquakes (Imaichi, Tokachi, Izu-Oshima, and Tohoku) occurred within a bedded structure parallel to the original slope. Also, the slopes were fairly gentle, ranging from 8°to 34° (Fig. 15.3). With regard to the

Imaichi Earthquake and the Off Tokachi Earthquake, no detailed examinations were made to determine whether or not the lower portion of the slopes had been undercut. With regard to the Izu-Oshima-Kinkai Earthquake, however, it was found that all avalanced slopes had been undercut (Chigira 1982). Similarly, all avalanched slopes examined in relation to the Tohoku Earthquake were also determined to have been undercut; and, in the case of the 2004 Mid-Niigata Prefecture Earthquake, all primary landslides having an sliding surface in tuff were observed to have been undercut dip slopes (Chigira and Yagi 2005). These experiences suggest that undercut dip slopes are in a peculiar condition with respect to seismic action at the undercut and that the presence/absence of an undercut is a critical factor for the assessment of slope stability during earthquakes.

4.2 High Mobility

The degree of landslide/avalanche mobility is typically indicated by the apparent friction angle or the equivalent coefficient of friction (Hsu 1975), which themselves are expressed as the angle of a line tying the crown of a landslide to its toe or as the tangent of that angle. A compilation of apparent friction angles for pyroclastic fall avalanches within various earthquakes, including the 2011 Tohoku Earthquake, the 1923 Kanto Earthquake (Kamai 1990), the 1968 Off Tokachi Earthquake (Inoue et al. 1972; Yoshida and Chigira 2011), the 1978 Izu-Oshima-Kinkai Earthquake (Chigira 1982), and the 1984 West Nagano Earthquake (Oyagi 1987; Kawakami et al. 1985), produces a range of 7° to 17° (Fig. 15.3), which in all cases is indicative of a high degree of mobility. These indicate a low degree of resistance at not only the source of the avalanche, but also along the transport path (main track). Experience from the Izu-Oshima-Kinkai Eearthquake (Chigira 1982) and the Tohoku Earthquake shows that there is little erosion on the bottom surface of the deposited material at either the transport path or the depositional area, suggesting that the material encounters little resistance along its bottom surface as it travels. While it is possible that some surface liquefaction occurred along the sliding surface as mentioned earlier, the transport mechanism over the transport path remains unknown.

4.3 Slope Directionality

The avalanches that occurred in the 2011 Tohoku Earthquake all faced from northeast to south, which suggests a relation between these landslides and the direction of seismic action. A high degree of directional alignment was also noted for pyroclastic fall landslides within the 1978 Izu-Oshima-Kinkai Earthquake and the 1968 Off Tokachi Earthquake, and here as well researchers have pointed to the possibility that a relation exists between such alignment and the direction of seismic action (Inoue et al. 1972; Chigira 1982). Further research is needed to examine the behavior of undercut slopes exposed to seismic forces.

4.4 Preceding Rainfall

Making use of AMeDAS and other rainfall data from the Japan Meteorological Agency, we compiled the cumulative rainfalls during the preceding 10 days, preceding 30 days, and preceding 60 days at sites that subsequently avalanched during various earthquakes (Fig. 15.4). Preceding 10 day rainfall was heavy before the Off Tokachi Earthquake and the Iwate-Miyagi Inland Earthquake and light before the Imaichi Earthquake, the Izu-Oshima-Kinkai Earthquake, and the Tohoku Earthquake. Similarly, the preceding 30 day rainfall was relatively light before the Imaichi Earthquake and the Tohoku Earthquake, and the preceding 60 day rainfall was extremely light (less than half that of any other earthquake) before the Tohoku Earthquake. The slide surfaces of avalanches occurring within these earthquakes consist of clayey weathered material or paleosol, all of which have a high degree of moisture retention. Such water retention appears to exert a deleterious effect on
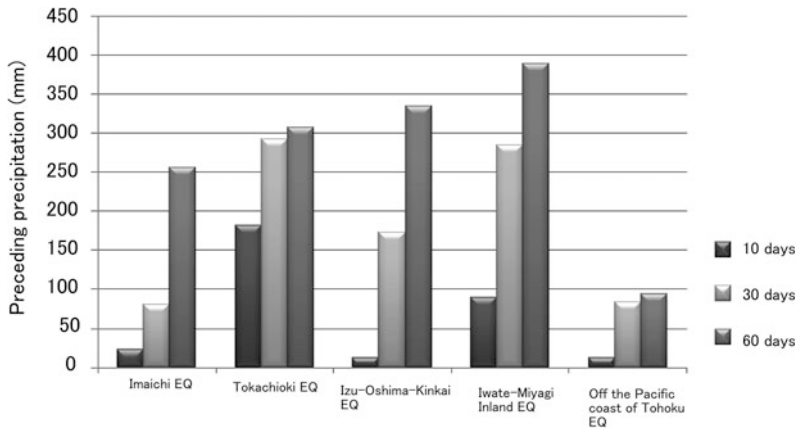
Fig. 15.4 Rainfalls preceding earthquakes that induced landslides of pyroclastic fall deposits (Japan Meteorological Agency). Observatories are located as follows: Imaichi earthquake: Utsunomiya. Off Tokachi earthquake: Hachinohe. Izu-Oshima-Kinkai earthquake: Inatori. Iwate-Miyagi Inland earthquake: Kumanoyu. Tohoku earthquake: Shirakawa

strength for roughly 30 days at least. The Tohoku Earthquake was characterized by a comparative paucity of landslides, and the dryness preceding the quake is presumably a major underlying factor. Assuming for the moment that the occurrence of such landslides is influenced by the amount of preceding rainfall, then, at least with regard to pyroclastic fall deposits, it would seem necessary to include some consideration of rainfall when assessing the stability of a slope under seismic loading. However, as it is currently impossible to forecast earthquakes with any confidence, this approach would be difficult to implement in practice. A more realistic approach would be to assess slope stability on an assumption that a certain amount of rain will fall over some period ahead of the earthquake, in which case we believe from the above that a period of approximately 30 days would be appropriate. Nevertheless, there remains a need to quantitatively assess relations among preceding rainfall, paleosol moisture content, and strength degradation.

5 Conclusions

The 2011 Tohoku Earthquake set off four soil-slide avalanches of pyroclastic fall deposits at Shirakawa, Fukushima Prefecture, and

Nakagawa, Tochigi Prefecture. At Shirakawa, a seismic intensity of 6+ on the JMA scale was recorded; at Nakagawa, 6−. Predominant factors behind these landslides were (1) bedding of pyroclastic fall deposits parallel to the original slopes and (2) a slide surface of weak paleosol at depths of 3 m to 9 m below the slope surface. The paleosol consisted of weathered ash mixed with pumice, was moist and weak, contained macropores, and liquefied when crushed between one's fingers. The transported material was dry and comprised weathered ash, pumice, and scoria; the large majority of the material flowed downhill from the source at a high speed, leading to, in the case of the Shirakawa slide, fatalities. Many of the trees growing on the slopes, supported by root systems, remained standing within their root-soil plate; that is, they were transported and deposited upon the underlying debris in an upright position. The material was highly mobile, as suggested by apparent friction angles of 10° to 16°. A bedded slope structure was determined to have been undercut near the bottom of their slopes before the occurrence of a slide. Pyroclastic fall avalanches very similar to those of the 2011 Tohoku Earthquake occurred with considerable frequency in the 1949 Imaichi Earthquake, the 1968 Tokachi Earthquake, and the 1978 Izu-Oshima-Kinkai Earthquake, thus demonstrating

that some pyroclastic fall deposits are extremely unstable under seismic loading. The relative paucity of pyroclastic fall landslides within the 2011 Tohoku Earthquake is thought to be attributable to a comparatively small amount of rainfall over the days preceding the quake.

References

Aomine S, Wada K (1962) Differential weathering of volcanic ash and pumice resulting in formation of hydrated halloysite. Am Mineral 47:1024–1048

Chigira M (1982) Dry debris flow of pyroclastic fall deposits triggered by the 1978 Izu-Oshima-Kinkai Earthquake: the "collapsing" landslide at Nanama-wari, Mitaka-Iriya, southern Izu Peninsula. J Nat Disaster Sci 4:1–32 (in Japanese with English abstract)

Chigira, M. (1995) Weathering and slope movement. Kinmiraisha, Naboya, 204p. (in Japanese)

Chigira M, Yagi H (2005) Geological and geomorpho-logical characteristics of landslides triggered by the 2004 Mid Niigata prefecture earthquake in Japan. Eng Geol 82:202–221

Chigira M, Yokoyama O (2005) Weathering profile of non-welded ignimbrite and the water infiltration behavior within it in relation to the generation of shallow landslides. Eng Geol 78:187–207

Chigira M, Nakamoto M, Nakata E (2002) Weathering mechanisms and their effects on the landsliding of ignimbrite subject to vapor-phase crystallization in the Shirakawa pyroclastic flow, northern Japan. Eng Geol 66:111–125

Hashimoto S, Chigira M, Nakasuji A et al (2009) The report of the Iwate-Miyagi Nairiku earthquake in 2008 disaster. J Jpn Soc Eng Geol 50:98–108 (in Japanese)

Hsu KJ (1975) Catastrophic debris streams (sturzstroms) generated by rockfalls. Geol Soc Am Bull 86:129–140

Inoue Y, Honsho S, Matsushima M, Esashi Y (1972) Geological and soil mechanical studies on the slides occurred during the 1968 Tokachioki earthquake in southeastern area of Aomori prefecture. Techl Rep Central Res Inst Electr Power Ind 886:1–27

Japan Meteorological Agency (2011a) Distribution of seismic intensity induced by the 2011 off the Pacific coast of Tohoku Earthquake. 25 March 2011. (in Japanese)

Japan Meteorological Agency (2011b) Monthly report on earthquakes and volcanoes in Japan March 2011 (in Japanese)

Kamai T (1990) Failure mechanism of deep-seated landslides caused by the 1923 Kanto earthquake, Japan. In: Proceedings of the sixth international conference and field workshop on landslides, pp 187–198

Kawakami H, Konishi J, Saito Y (1985) Mechanism of slope failures by the Naganoken-seibu earthquake 1984 and the characteristics of pumice. Tsuchi-to-Kiso 33:53–59 (in Japanese)

Kleber et al (2007) Halloysite versus gibbsite: silicon cycling as a pedogenetic process in two lowland neotropical rain forest soils of La Selva, Costa Rica. Geoderma 138:1–11

Morimoto R (1951) Geology of Imaichi district with special reference to the earthquakes of Dec. 26th., 1949. (II). Bull Earthq Res Inst 29:349–358

Oyagi N (1987) The 1984 Ontake-san landslide and its movement. Trans Jap Geomorph Union 8:127–144 (in Japanese)

Sassa K, Fukuoka H, Scarascia-Mugnozza G, Evans S (1996) Earthquake-induced-landslides: distribution, motion and mechanisms. Special Issue of Soils and Foundations, pp 53–64

Suzuki T (1993) Stratigraphy of middle Pleistocene tephra layers around Nasuno Plain, in north Kanto, central Japan. J Geogr 102:73–90 (in Japanese)

Yokota S, Iwamatsu A (1999) Weathering distribution in a steel slope of soft pyroclastic rocks as an indicator of slope instability. Eng Geol 55:57–68

Yoshida M, Chigira M (2011) The relation between weathering of pyroclastic fall deposits and the collapses caused by the 1968 Tokachi-oki earthquake. J Jpn Soc Eng Geol 52:213–221 (in Japanese)

Earthquake-Induced Landslides in the Roadside Slopes of East Nepal After Recent September 18, 2011 Earthquake

16

Ranjan Kumar Dahal, Netra Prakash Bhandary,
Manita Timilsina, Ruichi Yatabe and Shuichi Hasegawa

Abstract

Being located in central part of the Himalayan ranges, Nepal is regarded as one of the earthquake-prone countries in the region. Earthquake is a major concern of Nepal because of rapid population growth, poor land use planning, precarious settlement patterns, and poorly implemented building code. Earthquakes in Nepal have been reported since 1255 while major earthquakes were recorded in 1408, 1681, 1810, 1833, and 1866, 1934, 1980 and 1988. Recent earthquake of September 18, 2011 measuring 6.9 in Richter scale killed 6 people and injured 30 people in Nepal. There were many roadside slope damages near the epicenter area. To assess the roadside slope damages after this earthquake, a field visit was conducted and a landslide inventory map along the roadside slope was prepared for the most problematic area. For this study, Koshi and Mechi highways of eastern Nepal were selected as study area and earthquake-induced landslides on the roadside slopes were evaluated in terms of characteristics and mode of occurrences.

1   Introduction

In the Nepal Himalaya, both rainfall-induced and earthquake-induced landslides are serious threats to settlement and structures that support transportation, natural resources management and tourism. They cause considerable damage to highways, dams, waterways and human settlements. Depending on morphology, size, depth, movement, and mechanism, landslides in the Nepal Himalaya are differentiated into two categories, namely deep-seated and shallow-seated landslides. Generally, the large-scale landslides involve huge mass failure in the form of massive rock creep or gravitational spreading and bounded by clear slip surface (Hasegawa et al. 2009). On the other hand, shallow-seated or shallow landslides have shallow depth of failure and in most of the cases, depth of slip surface is not more than 5 m from the original surface (Dahal and Hasegawa 2008; Hasegawa et al. 2009).

R. K. Dahal (✉)
Department of Geology, Tri-Chandra Campus,
Tribhvuan University, Kathmandu, Nepal
e-mail: ranjan@ranjan.net.np

N. P. Bhandary · M. Timilsina · R. Yatabe
Faculty of Engineering, Ehime University,
Matsuyama, Ehime, Japan

S. Hasegawa
Kagawa University, Takamatsu, Kagawa, Japan

In many cases, both soil and rock are involved in the shallow landslides of the Nepal Himalaya and they extend extensive damage to roads and settlements.

Earthquake-induced landslides are one of the most damaging natural disasters. Generally, damage from earthquake-induced landslides is worse than damage related to the shaking and rupture of the earthquake itself. In recent years, Geographic Information Systems (GIS) and remote sensing have significantly improved our ability to map earthquake-induced landslides. Through the application of aerial photographs and field verifications, landslides induced by earthquakes have been mapped and analyzed in California, El Salvador, Taiwan, Japan, Italy and Pakistan (e.g., Wilson and Keefer 1985; Harp and Keefer 1990; Harp and Jibson 1996; Jibson et al. 2000; Parise and Jibson 2000; Capolongo et al. 2002; Chigira et al. 2003; Chigira and Yagi 2006; Wang et al. 2007; Owen et al. 2008). Several methods have been developed for the assessment of earthquake-induced landslide hazard, including statistical analysis (Keefer 1984, 2000) and deterministic approach (Mankelow and Murpy 1998; Jibson et al. 2000; Luzi and Pergalani 2000; Carro et al. 2003), both of which aim to quantify earthquake-induced landslide susceptibility and hazard zonation. These studies have provided valuable information about the characteristics of earthquake-induced landslides.

There have been many earthquake-induced landslides in Nepal but records of incidents are not well documented. Nepal lies in a seismically active region and its history is full of devastating earthquakes. The major source of earthquake in Nepal and the Himalayan Region is subduction of the Indian plate underneath the Eurasian plate, resulting in contraction effect and stress concentration. Based on the frequency and strength of the past earthquakes, seismicity is considered to be high in this region. Seismicity of the Himalayan region has been studied in terms of its relationship with known geological faults and tectonic activities. During the past 100 years, three great earthquakes (Table 16.1a) occurred along the Himalayan front. From east to west, the sequence includes the 1905 Kangra

Earthquake (Mw ∼ 7.8), the 1934 Bihar-Nepal Earthquake (Mw = 8.1), and the 1950 Assam Earthquake (Mw ∼ 8.6). After 1934 Bihar-Nepal Earthquake in Nepal, seven major earthquakes hit Nepal and the latest is Sikkim/Nepal Border Earthquake of September 18, 2011. Although USGS has named this earthquake as Sikkim/Nepal Border Earthquake, the earthquake epicenter lies in Nepalese territory and is situated at north-east part of Taplejung district, near the Kanchanjunga Base Camp (Fig. 16.1). In this earthquake, 14,544 houses were damaged (6,435 completely destroyed), 6 people were killed and 30 people were injured in Nepal. The shake map produced by USGS immediately after the earthquake (Fig. 16.1) suggests that the earthquake shaking was moderate to strong in east Nepal, Sikkim (India) and a few part of south Tibet (China). During this earthquake, USGS and Department of Mines and Geology of Nepal measured the peak ground accelerations between 38 gal and 90 gal in the Koshi Highway region and 90 gal to 177 gal in the Mechi Highway region. As a result, there were many roadside slope failures along the Mechi Highway in comparison with the Koshi Highway. Many longitudinal as well as transverse cracks were also observed in the ridge part of the roadside slopes during the field visit. Likewise, there were many earthquake-induced landslides in the area near the epicenter. Since, the epicenter lies in a highly elevated glaciated Himalayan region, the landslides in the epicenter area did not cause any socio-economic loss. However, the small-scale failures occurred along the major highways which are situated some 70 to 100 km away in aerial distance from the epicenter drew a commanding attention of the Nepalese planners about the consequences of earthquake-induced landslides in Nepal.

2 The Study Area and Geological Setting

The Koshi and Mechi highways are two major highways of east Nepal and they connect mountains of the north with the southern plain,

Table 16.1 Earthquakes in Nepal

a. Magnitude-frequency data on earthquakes in Nepal and the surrounding region in the period of 1911-1991 (modified after BCDP 1994*)*					
Earthquakes of magnitudes in richter scale	5–6	6–7	7–7.5	7.5–8	>8
No. of events	41	17	10	2	1
Approximate recurrence interval, yr.	2	5	8	40	81

b. Past earthquakes and damage records				
Year	Epicenter	Magnitude	Deaths	Houses destroyed
1934	East Nepal	8.1 (M_W)	8,519 people died out of which 4,296 died in Kathmandu Valley alone	Over 200,000 buildings and temples etc. damaged, about 55,000 buildings affected in Kathmandu Valley (12,397 completely destroyed).
1936	Annapurna	7.0 (M_L)	Record not available	Record not available
1954	Kaski	6.4 (M_L)	Record not available	Record not available
1965	Taplejung	6.1 (M_L)	Record not available	Record not available
1966	Bajhang	6.0 (M_L)	24	6,544 houses damaged (1,300 collapsed)
1980	Chainpur	6.5 (M_L)	103	25,086 buildings damaged (12,817 completely destroyed)
1988	Udayapur	6.5 (M_L)	721	66,382 buildings damaged
2011	Sikkim/ Nepal border	6.9 (M_L)	6 died and 30 injury (2 died in Kathmandu valley alone)	14, 544 house damaged (6, 435 completely destroyed)
M_L—Richter magnitude, M_W—Moment magnitude				
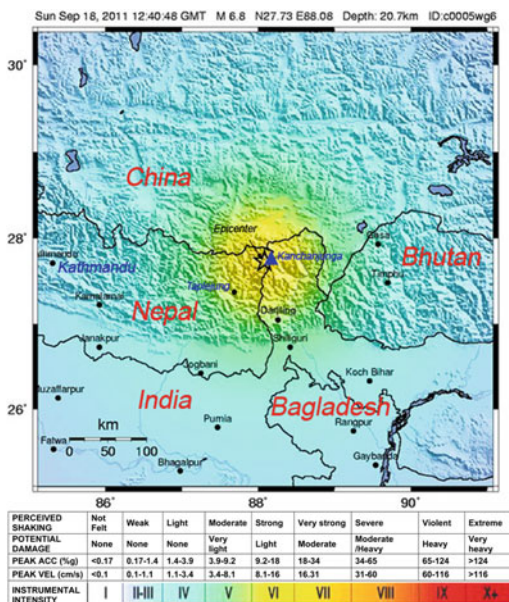
Fig. 16.1 Shake map of the Sikkim-Nepal border earthquake of September 18, 2011 (modified after USGS 2011)

Terai (Fig. 16.2). Especially, the northern part of Mechi Highway and a few parts of the Koshi Highway have been badly affected by the earthquake-induced small-scale debris falls, debris slides and rock falls. Therefore, in this study, the stretches of Koshi and Mechi highways are taken as main study areas which were visited in October 2011. A highly affected stretch of Mechi Highway (Fig. 16.3) is selected for a detailed landslide mapping.

Geologically and tectonically, Nepal is divided into five major tectonic zones, namely, Terai Zone, Siwalik Zone, Lesser Himalayan Zone, Higher Himalayan Zone and Tibetan-Tethys Himalayan Zone (Gansser 1964). These tectonic zones are separated by major thrusts and faults of the Himalaya and those faults and thrusts are named in north to south order (Fig. 16.2) as South Tibetan Detachment System (STDS), Main Central Thrust (MCT), Main Boundary
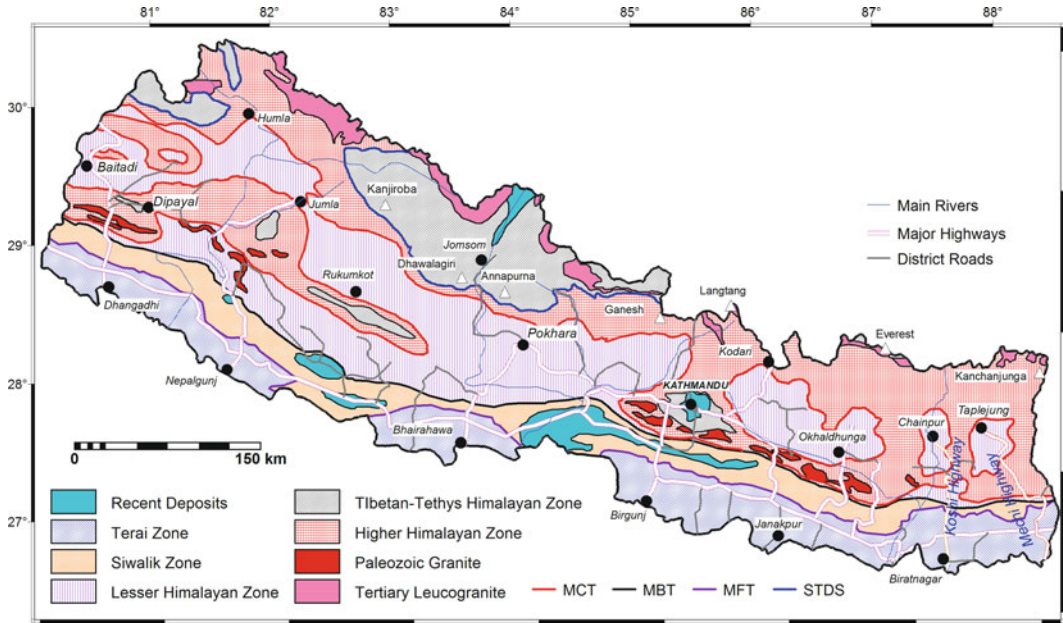
Fig. 16.2 Geological map of Nepal and location of Mechi and Koshi highways in east Nepal

Thrust (MBT) and Main Frontal Thrust (MFT). Likewise, geomorphologically, Nepal is divided into eight units running east–west, namely, Terai, Churia Range, Dun Valley, Mahabharat Range, Midland, Fore Himalaya, Higher Himalaya, Inner and Trans Himalaya (Dahal and Hasegawa 2008).

East Nepal comprises of two tectonic units: a Lesser Himalayan Zone exposed in the window (young rocks, i.e. rocks of the Lesser Himalayan Zone is surrounded by old rocks, i.e. rocks of the Higher Himalayan Zone) and a thrust sheet propagated to the south, near to the MBT as Higher Himalayan Zone. The Lesser Himalayan Zone consists mainly of phyllite, schist, quartzite and augen gneiss of granitic origin with minor association of amphibolites, marbles. The Higher Himalayan Zone consists of mainly garnet, kyanite, sillimanite bearing banded high grade gneiss, interbedded with quartzite. As Koshi and Mechi highways have north–south extension, they run through all geological zones of the Nepal Himalaya. Most sections of the Koshi and Mechi highways pass through Higher Himalayan Zone, especially in the terrain of banded gneiss. Likewise, the

northern parts of both highways situated in tectonic window and run in quartzitic and phyllitic terrains belonging to the Lesser Himalayan Zone (Fig. 16.2 and 16.3). In many sections of northern part, both highways are passing through steep slopes and ridges of elevation greater than 2500 m.

3   Field Visit and Features of the Earthquake-Induced Landslides

Field visit was carried out in both highways in 2nd week of October (after 3 weeks from the earthquake events). It was not possible immediately after the earthquake because of the damaged highways and relief support activities for earthquake victims. First, the Koshi Highway was visited. Total of three days were spent to inspect the roadside slopes of the Koshi Highway and four days were spent to inspect the damages in the roadside slope of Mechi Highway (Fig. 16.3). The status of landslide damages are described in the following subheadings.
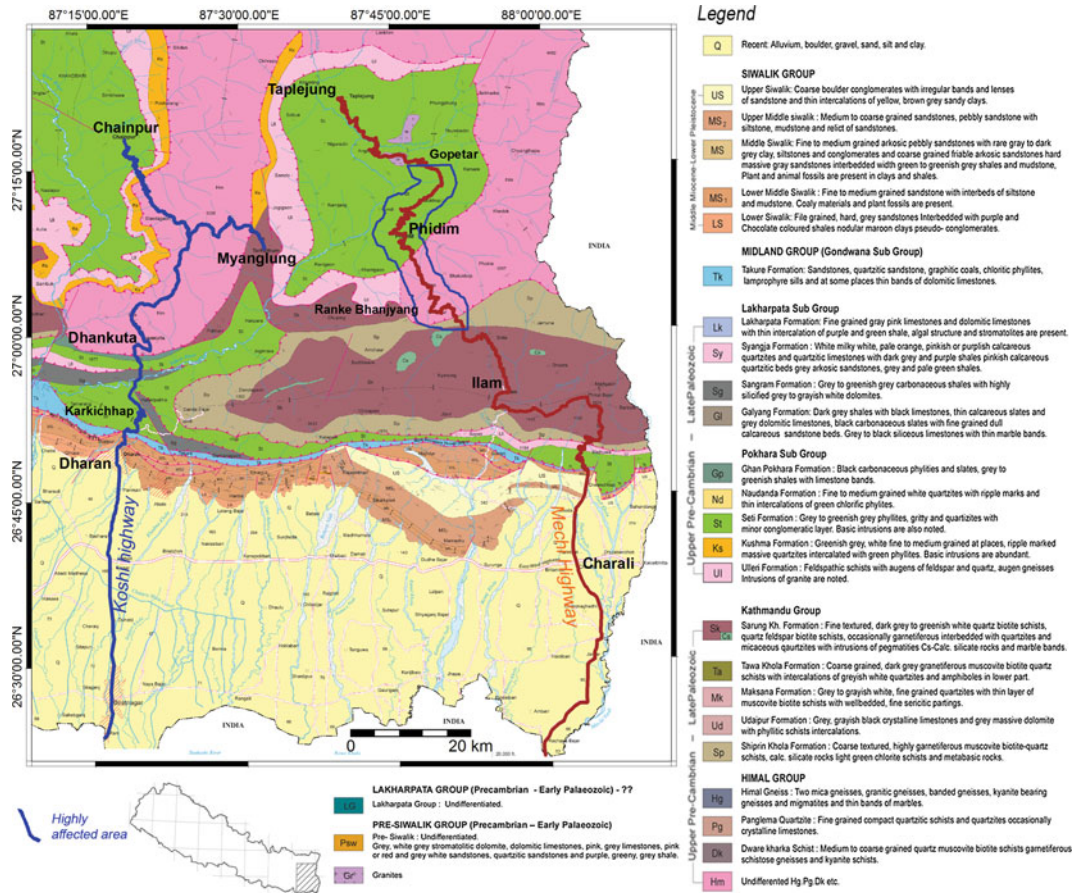
Fig. 16.3 Detail Geological map of the study area (modified after DMG 2011). The highly affected stretch of the Mechi highway is also shown in figure

3.1 Status of Landslides in the Koshi Highway

In more than 100 km stretch of the Koshi Highway, only two sites were identified as major damaged areas. Karkichhap village, near Bhedetar Town along the Koshi Highway had rock fall damage on the roadside slope. A huge rock boulder had toppled down to the road and it damaged two parts of the looped highway section. The quartzitic rock blocks disintegrated into huge boulders and laid down on lower part of the slope (Fig. 16.4). The road was block for more than 12 hours following this rock fall and only single lane was opened by then. During the field visit, it was also noticed that the vehicle movement was difficult through the damaged sections. Few rock fall areas, as seen in Fig. 16.4d were also observed around the Karkichhap village along the Koshi Highway.

The earthquake of September 18 occurred in post monsoon period. So, it was difficult to recognize exactly earthquake-induced landslide in the field. Many interviews with local people were also taken to recognize such landslides. While travelling from Dharan to Myaglung town of Tehrathum district via Dhankuta city (see Fig. 16.3), many rainfall-induced landslides were also found to have reactivated after the earthquake. It was also confirmed through discussions with local people who witnessed the events; however those landslides have not been included in this study.
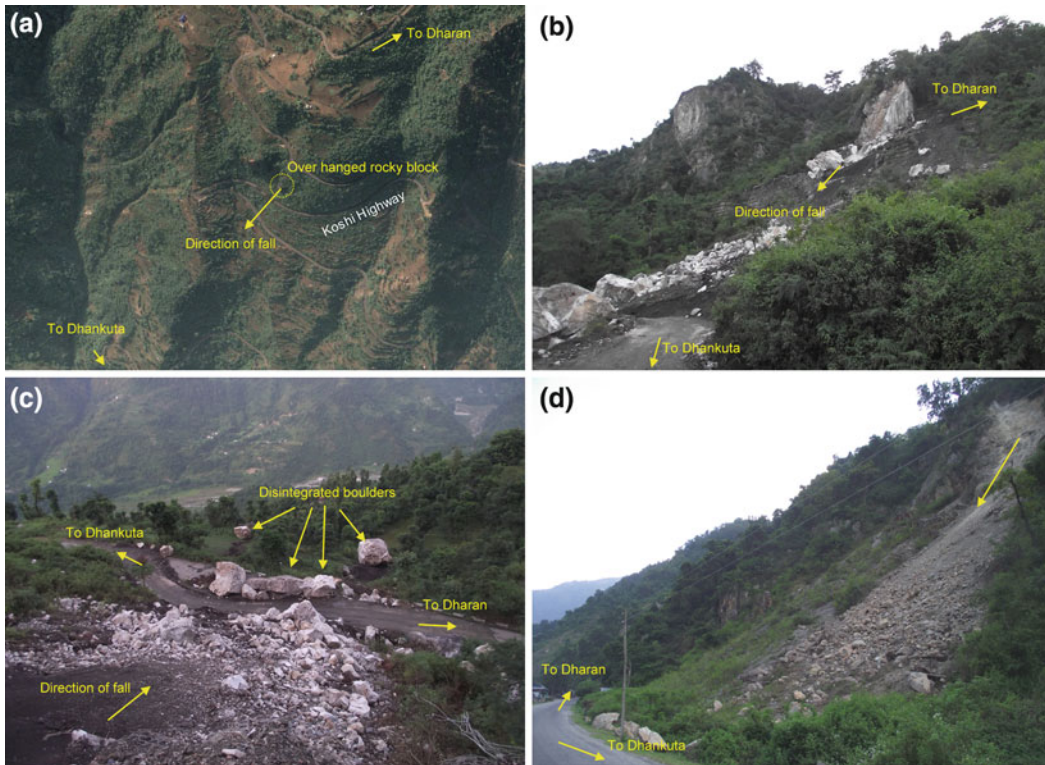
Fig. 16.4 Rock fall in Karkichhap village, near to the Bhedetar town along the Koshi Highway and the road is damaged in two sections, **a** is GoogleEarth image of the site before earthquake, over hanging rock blocks are seen on the image. **b** is the photograph of rock fall, viewing toward south-east. **c** is north (down slope) view of rock fall and damage of road. **d** is small rock fall observed along the Koshi Highway about 3 km north from Karkichhap village towards Dhankuta

3.2 Status of Landslides in the Mechi Highway

Nearly 200 km stretch of Mechi Highway was visited from Charali to Taplejung. Out of the whole section of highway, the stretch between Ranke Bhanjyang-Phidim-Gopetar was found to be the most affected section (Fig. 16.4). For this section, a landslide inventory map was prepared in topographical base map. Most of the landslides had failure depths of less than 2 m, and mostly translational to semi-rotational movement was evident on the failure plane. The area of the landslides ranged from 93 m^2 to 10, 987 m^2. In total 35 failures were identified. Landslide inventory map and photographs of a few representative landslides are shown in Fig. 16.5. In this section of road, many transverse cracks

were also observed on ridges and houses in the vicinity were also damaged (Fig. 16.5). According to the villagers, the highway was blocked for 1 day after the earthquake. During the field visit, at the failure site, only a single lane of the highway was open for traffic movement and some debris was seen on the shoulders. Although there were no human casualties in these earthquake induced-landslides, the road-side slope damages were intense in the section between Ranke Bhanjyang to Phidim.

4 Topographic Effects

Various investigations have shown that topographic features are basically responsible for dissipation of seismic energy (e.g. Gilbert and

Fig. 16.5 Highly damaged road sections of the Mechi highway and representative landslides on roadside slope
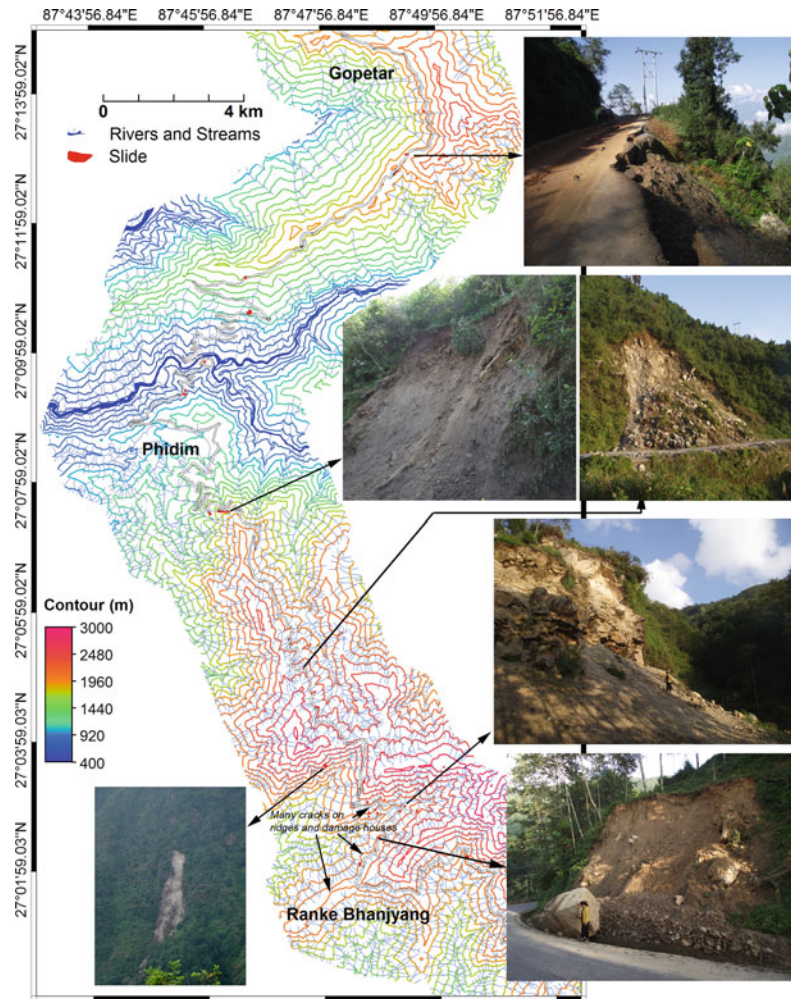
Knopoff 1960) and extremely high accelerations are usually observed at sites located on topographic ridges (e.g. Davis and West 1973; Bannister et al. 1990; Geli et al. 1988; Ambraseys and Srbulov 1995; Miles and Keefer 2000; Lin et al. 2003; Uchida et al. 2004). Observations of the damage patterns of earthquakes, such as the 1987 Whittier Narrows, California Earthquake, the 1989 Loma Prieta (California) Earthquake, the 1994 Northridge, California Earthquake, the 1999 Chi–Chi Earthquake of Taiwan, the 2004 Chuetsu Earthquake of Niigata Prefecture, Japan, and the 2005 Kashmir Earthquake of Pakistan also indicate the occurrence of intense shaking in elevated ridges of rugged topography. Geli et al. (1988) have reported that buildings on crests

suffer more damage than those located at the base, and they conclude that there is always significant amplification of frequencies corresponding to wavelengths nearly equal to mountain width at hilltops with respect to the base. In the case of September 18 Earthquake, the observations of Geli et al. (1988) are quite well evidenced in Ranke Bhanjyang village, where houses on the ridges were damaged and many cracks were also observed on the ridge itself (Fig. 16.5). Similarly, an amplification-deamplification pattern on slopes leads to a strong energy differential on the upper part of the slope. For the case of the Chi–Chi Earthquake, Lin et al. (2003) mentioned that landslide frequency is much higher on or near the crests of hills. To evaluate topographic effect in

the study area, the topographic curvature of stretch between Ranke Bhanjyang to Gopetar (see Fig. 16.4) is calculated in GIS and cross checked with the landslide inventory. Digital Elevation Model (DEM) of 20 m pixel size was used for this purpose. In total 75 % of earthquake-induced landslides were found on ridge slope pixel and 25 % were found on valley slope pixel. This simple evaluation clearly supports that in the Himalayan slopes also, frequency of earthquake-induced landslides is higher on or near the crests of hills.

5   Concluding Remarks

This study evaluates the features of the earthquake-induced landslides in the Nepal Himalaya, which occurred after September 18, 2011 Sikkim/Nepal Boarder Earthquake. Primarily, the study concludes that the Nepal Himalaya has great risk of earthquake-induced landslides and the mountainous roads passing through the highly elevated Himalayan ridges are always subjected to damages in the events of medium to great earthquakes.

References

Ambraseys N, Srbulov M (1995) Earthquake induced displacement of slopes. Soil Dyn Earthq Eng 14:59–71

Bannister SC, Husebye ES, Ruud BO (1990) Teleseismic P coda analyzed by three-component and array techniques: deterministic location of topographic P-to-Rg scattering near the NORESS array. Bull Seism Soc Am 80:1969–1986

BCDP (1994) Building code development project: seismic hazard mapping and risk assessment for Nepal, UNDP/UNCHS (habitat) subproject: NEP/88/054/21.03. Min Housing Phy Planning, Kathmandu

Capolongo D, Refice A, Mankelow J (2002) Evaluating earthquake-triggered landslide hazard at the basin scale through GIS in the upper Sele river valley. Surv Geophys 23:595–625

Carro M, De Amicis M, Luzi L, Marzorati S (2003) The application of predictive modeling techniques to landslides induced by earthquakes: the case study of the 26 September 1997 Umbria-Marche earthquake (Italy). Eng Geol 69(1–2):139–159

Chigira M, Yagi H (2006) Geological and geomorphological characteristics of landslides triggered by the 2004 Mid Niigta prefecture earthquake in Japan. Eng Geol 82:202–221

Chigira M, Wang WN, Furuya T, Kamai T (2003) Geological causes and geomorphological precursors of the Tsaoling landslide triggered by the 1999 Chi–Chi Earthquake Taiwan. Eng Geol 68:259–273

Dahal RK, Hasegawa S (2008) Representative rainfall thresholds for landslides in the Nepal Himalaya. Geomorphology 100(3–4):429–443

Davis LL, West LR (1973) Observed effects of topography on ground motion. Bull Selsm Soc Amer 63:283–298

DMG (2011) Geological map of eastern Nepal. Department of Mines and Geology, Kathmandu

Gansser A (1964) Geology of the Himalayas, Wiley Interscience, London, pp 289

Geli L, Bard PY, Jullien B (1988) The effect of topography on earthquake ground motion: a review and new results. Bull Seismol Soc Am 78(1):42–63

Gilbert F, Knopoff L (1960) Seismic scattering from topographic irregularities. J Geophys Res 65:3437–3444

Harp EL, Jibson RW (1996) Landslides triggered by the 1994 Northridge, California earthquake. Seismol Soc Am Bull 86(1B):S319–S332

Harp EL, Keefer DK (1990) Landslides triggered by the earthquake. In: Rymer MJ, Ellsworth, WL (eds) The Coalinga, California, earthquake of May 2, 1983, US Geological Survey Professional Paper 1487:335–347

Hasegawa S, Dahal RK, Yamanaka M, Bhandary NP, Yatabe R, Inagaki H (2009) Causes of large-scale landslides in the Lesser Himalaya of central Nepal. Environ Geol 57(6):1423–1434

Jibson RW, Harp EL, Michael JA (2000) A method for producing digital probabilistic seismic landslide hazard maps. Eng Geol 58:271–290

Keefer DK (1984) Landslides caused by earthquakes. Geol Soc Am Bull 95:406–421

Keefer DK (2000) Statistical analysis of an earthquake-induced landslide distribution—the 1989 Loma Prieta. Eng Geol 58(3–4):231–249

Lin C-W, Shieh C-L, Yuan B-D, Shieh Y-C, Liu S-H, Lee S-Y (2003) Impact of Chi–Chi earthquake on the occurrence of landslides and debris flows: example from the Chenyulan River watershed Nantou, Taiwan. Eng Geol 71:49–61

Luzi L, Pergalani F (2000) A correlation between slope failures and accelerometric parameters: the 26 September 1997 earthquake (Umbria–Marche, Italy). Soil Dyn Earthq Eng 20:301–313

Mankelow JM, Murpy W (1998) Using GIS in the probabilistic assessment of earthquake triggered landslide hazards. J Earthq Eng 2(4):593–623

Miles SB, Keefer DK (2000) Evaluation of seismic slope-performance models using a regional case study. Environ Eng Geosci 6(1):25–39

Owen LA, Kamp U, Khattak GA, Harp EL, Keefer DK, Bauer MA (2008) Landslides triggered by the 8 October 2005 Kashmir earthquake. Geomorphology 94:1–9

Parise M, Jibson RW (2000) A seismic landslide susceptibility rating of geologic units based on analysis of characteristics of landslides triggered by the 17 January, 1994 Northridge, California earthquake. Eng Geol 58:251–270

Uchida T, Kataoka S, Iwao T, Matsuo O, Terada H, Nakano Y, Sugiura N, Osanai N (2004) A study on methodology for assessing the potential of slope failures during earthquakes. Technical note of National Institute for Land and Infrastructure Management, p 91 (in Japanese with english summary)

USGS (2011) Summary of Sikkim/Nepal Boarder earthquake. Available at http://earthquake.usgs.gov/earthquakes/pager/events/us/c0005wg6/index.html#summary. Accessed 18 Sep 2011

Wang HB, Sassa K, Xu WY (2007) Analysis of a spatial distribution of landslides triggered by the 2004 Chuetsu earthquakes of Niigata Prefecture Japan. Nat Hazards 41:43–60

Wilson RC, Keefer DK (1985) Predicting areal limits of earthquake-induced landsliding. In: Ziony JI (ed) Evaluating earthquake hazards in the Los Angeles region—an earth-science perspective, US Geol Surv Prof Paper 1360, pp 316–345

Characteristics of Earthquake-Induced Landslides in Heavy Snowy Area: The Case of the Northern Nagano Prefecture Earthquake, March 12, 2011, Japan

17

Baator Has, Kiichiro Ogawa, Satoshi Onoda, Tomoyuki Noro, Kiyoteru Maruyama and Akira Nakamura

Abstract

On March 12, 2011, a strong earthquake (Mjma6.7) struck northern Nagano Prefecture and southern Niigata Prefecture, Japan. This earthquake occurred in a heavy snowfall area in Japan, caused serious damage to the focal area. In this paper, for clarify the distribution characteristics of landslides induced by this earthquake, we interpreted the landslide using aerial photographs and also conducted field investigations, analyzed distribution with active fault which considered to caused the earthquake. A remarkable characteristic of the large-scale landslides induced by this earthquake is the long run-out distance. It may because of exist of thick snowpack while the earthquake occurring. We also analyzed the landslide distribution with distance from considered active fault, epicenter of the earthquake and with PGA and seismic intensity. The results showed that most of the landslides occurred on the hanging wall of the active fault, and the size is larger than that on foot wall; the landslides occurred within a distance of 12 km from the active fault, in area where PGA is larger than 500 gal and seismic intensity is larger than 6-lower. The results of this paper clarified the distributing characteristics of landslides, and also provided important date of landslides induced by strong earthquake in heavy snow area in winter season.

1 Introduction

On March 12, 2011, a strong earthquake, $M_{JMA}6.7$, marked seismic intensity of 6-upper in JMA scale (JMA: Japan Meteorological Agency), struck northern Nagano Prefecture and southern Niigata Prefecture, Japan. The epicenter of the mainshock was located about 56 km northeast of

B. Has (✉) · K. Ogawa · S. Onoda
Asia Air Survey, Co., Ltd, Tokyo, Japan
e-mail: has.baator@ajiko.co.jp

T. Noro · K. Maruyama · A. Nakamura
Snow Avalanche and Landslide Research Center,
PWRI, Myoko, Japan

Nagano city. The earthquake occurred in one of the most famous heavy snowfall regions in Japan, caused damage to the focal area, injured 66 people, 73 houses were totally destroyed (as of July 15, 2011, Hokushin Construction Office of Nagano Prefecture 2011; Niigata Prefecture 2011). Railway and other infrastructures were also suffered damage.

This earthquake was considered to be triggered by the huge Tohoku earthquake, Mw9.0, occurred on March 11, 2011 (e.g. Furumura et al. 2011). About the great Tohoku earthquake and its main aftershock (the 4.11 Fukushima Hamadori earthquake), some reconnaissance reports have been published (e.g. Miyagi et al. 2011). Because the Nagano Prefecture and the Niigata Prefecture are famous landslide susceptibility regions in Japan, the northern Nagano Prefecture earthquake was expected may induce a large number of landslides. For clarify the characteristics of landslides induced by this earthquake, we conducted aerial photographs (taken by Asia Air Survey immediately after the earthquake on March 12, 13, 2011, scale of 1:10,000) interpretation. We also conducted field surveys on the main landslides sites after the earthquake. In this paper, we report the results of landslides interpretation of aerial photographs and field surveys.

2 Regional Settings

The northern Nagano earthquake occurred near the boundary of the Nagano Prefecture and the Niigata Prefecture, central northern Japan. The epicenter was located at N37.0, E138.6 with focal depth of 8 km, on a NW–SE pressured reverse fault (JMA).

Study area included the northern Nagano Prefecture and the southern Niigata Prefecture, about 200 km^2 mountainous areas along the Chikuma River and part of Tokamachi city, Niigata Prefecture (Fig. 17.1). The study area is just same as the area that covered by aerial photographs taken after the earthquake. The study area and its surroundings are mostly occupied by mountainous area, ranged about 200–1,000 m of elevation. The

Chikuma River is flowing from southwest to northeast in the area.

Geology of the area is mostly composed of Neogene to Quaternary sedimentary rocks, volcanic rocks and Quaternary volcanic detritus (Fig. 17.2, after AIST 2007). Along the Chikuma River, lower to higher terraces were also developed. A series of active fault distributed in the study area and its surroundings. These active faults belong to Tokamachi fault (TMF in Fig. 17.3) and Western marginal fault of Nagano basin (WMF_NB in Fig. 17.3). The TMF is composed of several segments of reverse faults that are mainly striking NE, dipping to NW, but also includes a part that striking NW and dipping SW (AIST 2009). The WMF_NB is striking NE and dipping to NW. The source fault model of this earthquake has not been determined yet, but the epicenter was just located nearby the Miyanohara fault (MHF in Fig. 17.3). The MHF is one segment of the TMF, consists three reverse faults, striking ENE, and dipping to north.

The study area and its surroundings is one of the most famous heavy snowfall regions in Japan. According to JMA, average snowfall at Tsunan meteorological observation station (see Fig. 17.1) of recent 22 years (1989–2010) was 445 in January, 320 in February and 228 cm in March, respectively. In snowfall season of 2011, it recorded heavy snowfall in this area, 669 in January, 144 in February and 325 cm in March, respectively. Even around the middle of March, we confirmed about 2–3 m snowpack in the study area during our field surveys.

3 Characteristics of Landslide Distribution

A total of 111 landslides were collected in the study area by aerial photographs interpretation (Fig. 17.3). Most of the landslides distributed on the slopes of left bank of the Chikuma River. Based on geological map of the study area (Fig. 17.2), the landslides could bee classified as 6 types in geologically. Shown as Fig. 17.4, almost half number of the landslides occurred in Neogene sedimentary rocks, and about 28 % of the

Fig. 17.1 Location of
study area. Red triangle is
the location of Tsunami
meteorological observation
station of Japan
meteorological agency
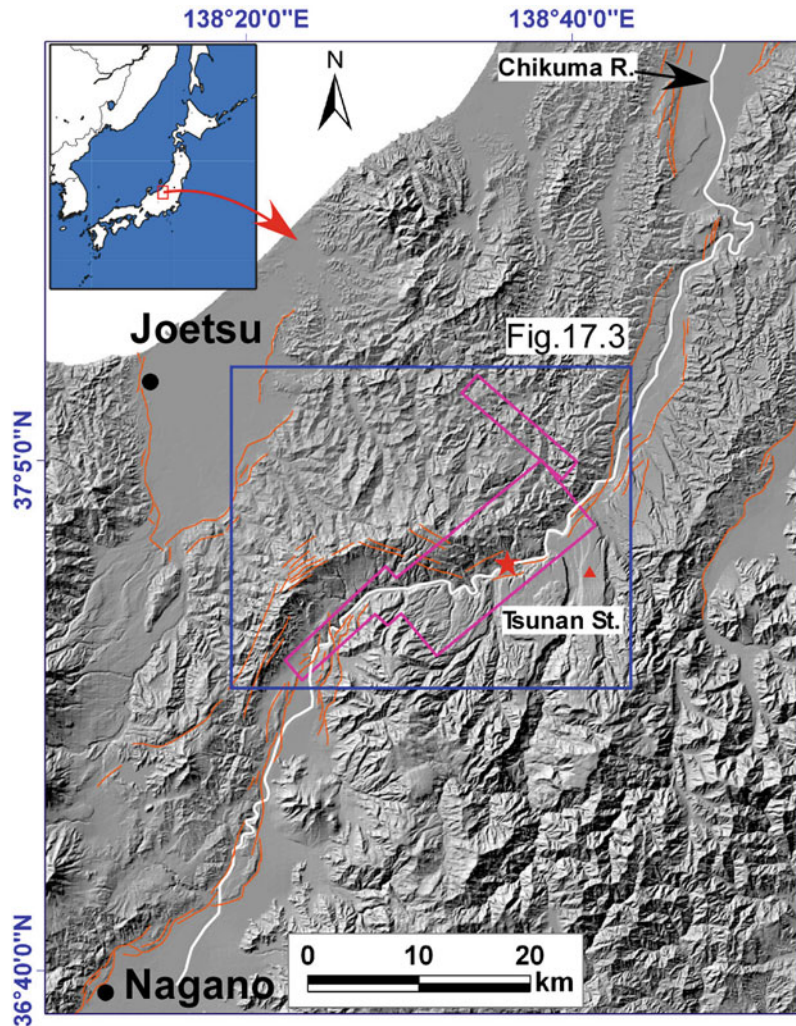
total landslides occurred in Quaternary volcanic
rocks. The result is coincided with the distribution
range of geology. The earthquake focal area is
dominated by Neogene sedimentary rocks and
Quaternary volcanic rocks.

Figure 17.5 showed the frequency of landslide
area. About 63 of the landslides, those area is
smaller than 4,000, and 82 % of landslides
smaller than 6,000 m^2. The result indicated that
most of the landslides induced by this earthquake
are small scaled. However, some large-scale
landslides also occurred, about 11 % of landslides
those area is larger than 10,000 m^2.

The left bank of the Chikuma River is being the
hanging wall of possible source fault corre-
sponding to the MHF. Thus, most of the landslides

occurred on the hanging wall of the active fault.
This result is coinciding with the characteristics of
other recent reverse-fault earthquakes in inland
Japan, such as Chuetsu earthquake in 2004 and
Iwate-Mitagi inland earthquake in 2008 (Hasi
et al. 2010). To clarify the distribution charac-
teristics of landslides related to the active fault, we
calculated the distance from landslides to the
MHF. The distance is calculated as the shortest
distance from center of landslide polygon to
active fault lines. Figure 17.6 showed the fre-
quency of landslide area with distance from the
active fault. The results showed that most of the
landslides (91.9 %) occurred on the hanging wall
of the MHF, and their size tends to larger than that
occurred on the footwall. This characteristic is
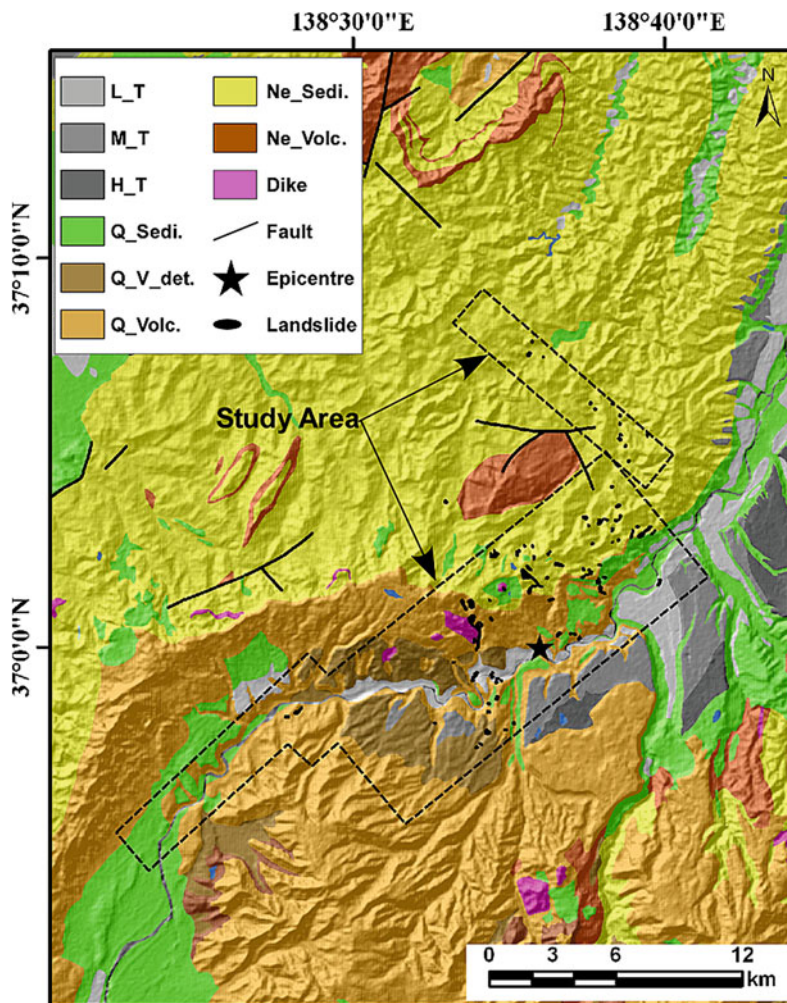
Fig. 17.2 Geological setting of study area. In legend inside, L_T: lower terrace, M_T: middle terrace, H_T: higher terrace, Q: Quaternary, Ne: Neogene, Sedi: sedimentary rocks, Volc: volcanic rocks, V_det: volcanic detritus. Rectangles shown by dashed lines indicate the study area, same as aerial photographs taken area

also coincided with the results of recent inland reverse-fault earthquakes in Japan (Hasi et al. 2010). Figure 17.7 showed the frequency of landslides distance from active fault. Landslides occurred within 12 km from the active fault of MHF. About 83 % of the landslides occurred within 4 km from the MHF. It also showed that the number of landslides tend to decrease with increasing of distance from active fault from 4 km. However, the distance from landslides to epicenter does not show tendency of decreasing number with the distance increasing.

According to intensity map of JMA, the study area is mostly occupied by area of intensity larger than 6-lower. In the study area, all of the landslides located within the area where seismic intensity larger than 6-lower. Based on JMA record, the largest value of PGA (combined of three components) in this earthquake is 1250.9 gal in Hokushin, Nagano prefecture. In the study area, 107 landslides occurred in area where PGA is larger than 500 gal. These results coincided with the result from recent reverse-fault earthquakes (Hasi et al. 2010), indicated that in
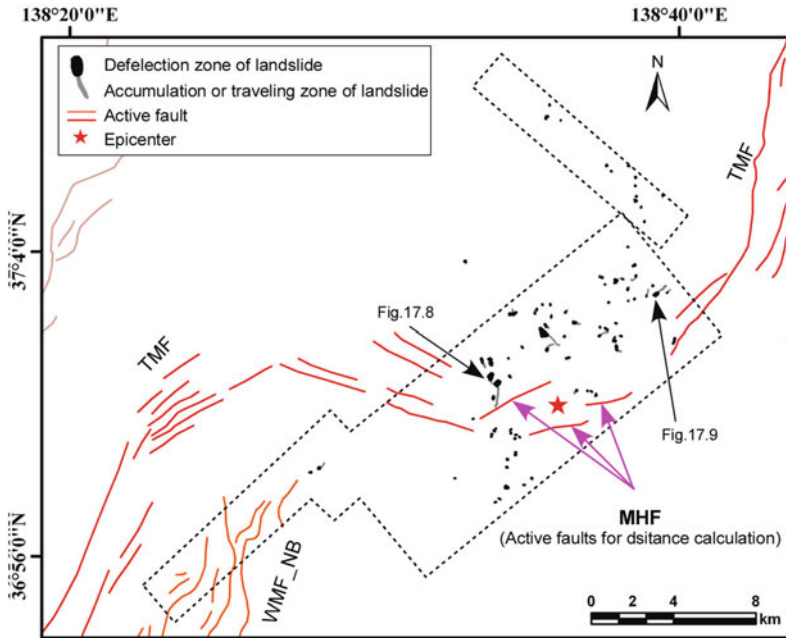
Fig. 17.3 Landslides distribution. TMF: Tokamachi fault, MHF: Miyanohara fault, WMF_NB: Western marginal fault of Nagano basin
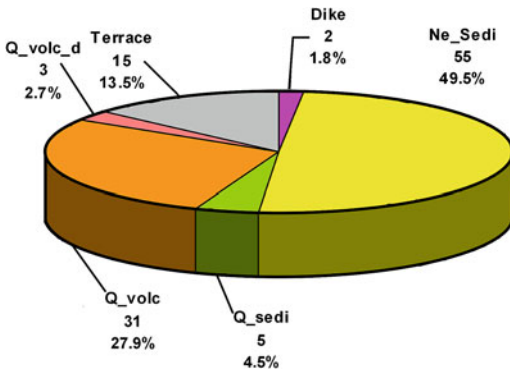
Fig. 17.4 Landslides with geological component Legend is same as Fig. 17.2

Fig. 17.5 Frequency of landslide area

reverse fault earthquakes in mountain areas, larger landslides tend to occur in seismic intensity 5-upper and PGA is larger than 500 gal.

4 Large-Scale Landslide with Long Distance Run-Out

One of the most remarkable characteristics of the landslides induced by this earthquake is they occurred on the slopes that covered by thick snowpack. Due to this, the larger scale landslides showed a characteristic of long distance run-out. Figure 17.8 showed the large-scale landslides occurred in Sakae village, Nagano Prefecture. Two large-scale landslides, one is 280 long and 190 m wide ("a" in Fig. 17.8), another is about 330 long and 220 m wide ("b" in Fig. 17.8) occurred on southwestern faced slopes in a tributary of the Chikuma River. The landslides occurred on slopes composed of Quaternary volcanic rocks, mainly of andesite lava and tuff. Part of the displaced landslide mass deposited
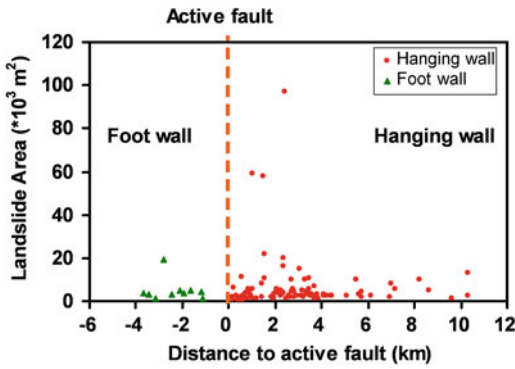
Fig. 17.6 Relationship of landslide area with the distance from active fault
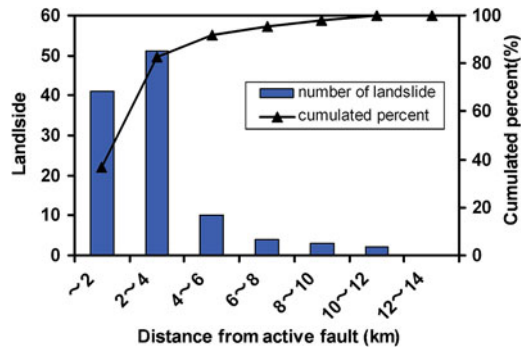
Fig. 17.7 Frequency of landslides distance from active fault

Fig. 17.8 Two large-scale long distance run-out landslides in Sakae Village, Nagano prefecture
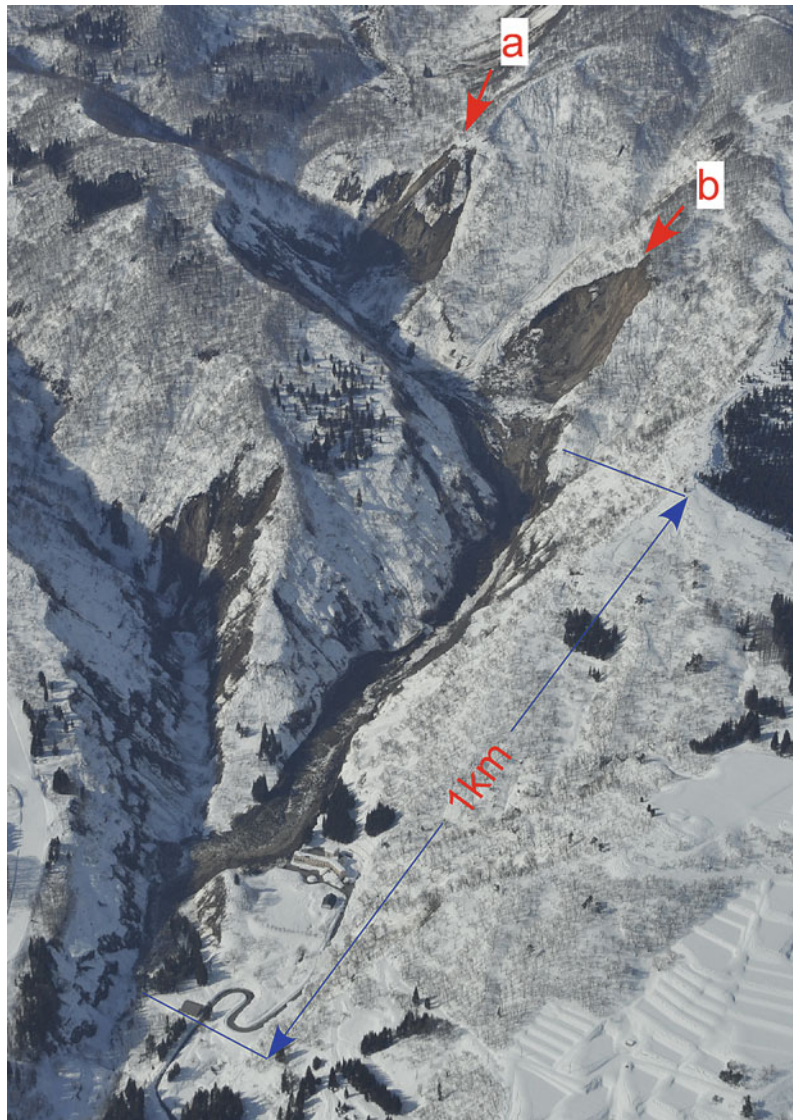
Fig. 17.9 A full view of Tatsukuchi landside in Tsunan town, Niigata prefecture

Fig. 17.10 Slickenlines on slickensided snow surface

under the slopes, but most of the mass flowed along the channel, traveled as long as about 1 to the downstream. Along the channel, coarse sediments, 1 m in diameter of andesite lava were observed in the upper to middle stream within the landslides mass deposited area. However, in the downstream of the landsides mass deposited area, the sediments are snow-mixed.

Another large-scale landslide that traveled long distance is Tatsukuchi landslide, in Tsunan town, Niigata Prefecture (Fig. 17.9). This landslide is about 180 long and 130 m wide, occurred on north faced slope which composed of Neogene to Quaternary sedimentary rocks, consists of sandstones, mudstones and conglomerate. The landslide mass traveled about

500 m from the source, blocked national road and destroyed a house. In this landslide, we observed different deposits in its run-off course, coarse deposits in upper and middle stream, and snow-mixed deposits in lower stream to the end. Even in June, snow blocks were observed in the deposits. A very clear slickenlines (Fig. 17.10) were observed on the snow surface along the right side of the landslide mass traveling course. The characteristics of deposits and the presence of slickenlines may indicate that the landslide mass traveled on the snow surface, mixing and rolling snow, so that traveled a long distance.

Deep-seated landslides and shallow landslides were also observed in the study area. Some of them are moderate scaled, but caused damage. A deep-seated rotational slump occurred in Nakao, Tokamachi city, Niigata Prefecture, destroyed a house on the slope (Maruyama et al. 2011). The landside is 180 long, 70 m wide, occurred on southeast faced slope, mainly composed of siltstone. Most of the landslides occurred in this earthquake are shallow landslides. Some showed shallow landslides observed along the road, it occurred on cut-off slope along the local railway. These landslides are shallow, about 2 m thick, but the landslides mass covered the local railway. Most of the landslides induced by this earthquake occurred on natural slopes. However, along terraces of the Chikuma River, some landslides occurred on artificial slopes along the local railway, had very sharp slip surface and moved translational, and destroyed the railway of 50–80 m wide.

5 Discussion and Conclusion

There are few examples of landslides occurred by strong earthquake in heavy snowfall area, especially in Japan, no such events has been recorded. For this reason, this study may provide a valuable data set for analyzing landslides occurrence and mechanism in that occur in heavy snowfall regions.

We calculated the distribution of landslides with the active fault. But, according to aftershock distribution, the source fault may be a southeast dipping reverse fault, different from the MHF. However, no surface fault has been found (Matsuta et al. 2011). The deformation of the focal area maybe complicated because it is inferred to be triggered by a far distance huge 3.11 Tohoku earthquake. Further studies should be done about the mechanism of landslides, detailed relationship between landslides and source fault.

Based on aerial photograph interpretation and filed survey, we conclude as below.

1) Most of landslides occurred on hanging wall of the Miyanohara fault within a distance of 12 km.
2) Most of landslides are shallow, but included large-scale landslides and deep-seated moderate scale landslides.
3) One unique behavior of large-scale landslides is that traveled long distance due to that occurred in heavy snowfall region.

References

AIST (National Institute of Advanced Industrial Science and Technology) (2007) Seamless digital geological map of Japan 1:200,000, Research Information Database DB084, Geological Survey of Japan

AIST(National Institute of Advanced Industrial Science and Technology) (2009) Active Fault Database of Japan, June 23, 2009 version. Research Information Database DB095, National Institute of Advanced Industrial Science and Technology http://riodb02.ibase.aist.go.jp/activefault/index_e.html

Furumura T, Takemura S, Noguchi S et al (2011) Strong ground motions from the 2011 off-the Pacific-Coast of Tohoku, Japan (Mw = 9.0) earthquake obtained from a dense nationwide seismic network. Landslides 8:333–338

Hasi B, Ishii Y, Maruyama K et al. (2010) Distribution and scale of landslides induced by recent reverse-fault earthquakes in Japan. J Japan Landslide Soc 48(1):23–38 (in Japanese with English abstract)

Hokushin Construction Office of Nagano Prefecture (2011) Disaster of northern Nagano earthquake (as of 15 July 2011). http://www.pref.nagano.jp/xdoboku/hokuken/15saigai/hisaijyoukyou%20H23.7.15.pdf (in Japanese)

Matsuta N, Hirouchi D, Sugito N, Takeshita Y (2011) Surface deformation and damages caused by the Niigata-Nagano boundary earthquake, symposium on behavior of inland active faults and seismicity/crustal movements associated with the 2011 off the Pacific

Coast of Tohoku Earthquake, Japanese society of active fault studies, 11–14 (in Japanese)

Maruyama K, Nakamura A, Noro T, Hasi B (2011) Slope disasters induced by the Northern Nagano prefecture earthquake on March 12. J Japan Soc Erosion Control Eng 64(2):39–44

Miyagi T, Higaki D, Yagi H et al (2011) Reconnaissance report on landslide disasters in northeast Japan following M9 Tohoku earthquake. Landslides 8:339–342

Niigata Prefecture (2011) About the damage of Northern Nagano earthquake occurred on 12 Mar 2011, Report 25. http://www.pref.niigata.lg.jp/kikitaisaku/1306702833686.html (in Japanese)

Types and Characteristics of Typical Landslides Triggered by the M8.0 Wenchuan Earthquake

18

Xiuzhen Li and Jiming Kong

Abstract.

The M8.0 Wenchuan earthquake, which occurred on May 12, 2008 in Sichuan Province, China, induced thousands of geo-hazards. The most important and hazardous one was landslides, and caused serious casualties in worst-hit areas. The landslides show different characteristics compared with the gravity-driven landslides, because of the different responses of different geological and geomorphologic characteristics to earthquake-producing dynamic. On the basis of extensive field investigation, the induced landslides were classified into 3 kinds of basic types: slide-type landslides, slide-flow type landslides and fall-slide type landslides according to the movement characteristics and modes of the landslides. Moreover, according to the characteristics of the sliding and material composition of the slide-type landslides and macro disrupted degree of the sliding mass, sliding landslides were classified into three kinds of secondary types: coherent landslides, disrupted landslides and debris landslides. On the basis, basic characteristics, especially movement characteristics and processes for all types of landslides were thoroughly analyzed by different types of typical landslides cases. This is not only helpful to comprehensively understanding the types and characteristics of earthquake-induced landslides, but also can provide a mitigation and prevention basis for future earthquake-induced landslides.

X. Li (✉) · J. Kong
Key Laboratory of Mountain Hazards and Surface
Process, Chinese Academy of Sciences,
Chengdu 610041, China
e-mail: lxzljt@sina.com

X. Li · J. Kong
Institute of Mountain Hazards and Environment,
Chinese Academy of Sciences,
Chengdu 610041, China

1 Introduction

The M8.0 Wenchuan earthquake, which occurred on May 12, 2008 in Sichuan Province, China, induced thousands of geo-hazards. The most important and hazardous one was landslides, and

caused serious casualties in worst-hit areas. In this earthquake, more than 87,000 people were killed and about 374,640 people injured. About 20 % fatalities were killed by geo-hazards such as landslides. For example, Wangjiayan landslide in Beichuan city buried over 1,600 residents. Daguangbao landslide in Gaochuan Village of An county was the largest landslide triggered by the earthquake. It had a volume of over 742 Million m^3. The earthquake-induced landslides show different characteristics compared with the gravity-driven landslides, because of the different responses of different geological and geomorphologic characteristics to earthquake-producing dynamic. To understand exactly the types and characteristics of the landslides is essential to mitigating and preventing seismic landslides hazard in the future.

At present, some researchers have made some studies on the types and characteristics of earthquake-induced landslides. For example, Zhou and Zhang (1994), based on the data of landslides caused by several historical strong shocks since 1970 in southwestern China, classified the landslides into four types: pushing-landslide, hauling-landslide, bedding-landslide and avalanching-landslide. Keefer (2002), according to a large number of historical earthquake-induced landslides, classified them into fourteen individual types and three main categories on the basis of type of material, type of landslide movement, degree of internal disruption of the landslide mass, and geologic environment. For the landslides induced by Wenchuan earthquake, Xu and Huang (2008) classified the landslides into hard rock type, soft rock or hard rock surface stripping type and loose deposit type, and deeply analyzed the characteristics of each landslide type by using some typical landslide examples. Yin (2009) classified the landslides into five patterns, such as staircase-shaped, convex-shaped, bowel-shaped, slump-shaped and huge rock-stone in a broad sense, and pointed out that most of the landslides experienced the processes of broken—thrown—crushed—high speed debris flow. Kong et al. (2009) classified the landslides into two main categories and five individual types, the two main types are shake-sliding type and collapse-sliding

type. The research results provide some good basis for accurate comprehension and prevention of earthquake-induced landslides.

In this paper, we investigated a large number of landslides in the worst hit regions (Fig. 18.1), and classified the earthquake-induced landslides into three kinds of basic types: slide-type landslides, slide-flow type landslides and fall-slide type landslides according to the movement characteristics and modes of the landslides. Moreover, according to the characteristics of sliding and material composition of the landslides and macro disrupted degree of sliding mass, sliding-type landslides were classified into three kinds of secondary types: coherent landslides, disrupted landslides and debris landslides. On the basis, basic characteristics, especially movement characteristics and processes for all types of landslides were thoroughly analyzed by different types of typical landslides cases. This is not only helpful to comprehensively understanding the types and characteristics of earthquake-induced landslides, but also can provide a mitigation and prevention basis for future earthquake-induced landslides.

2 Types and Characteristics of Landslides Induced by Wenchuan Earthquake

The landslides triggered by the earthquake show different movement characteristics and failure modes with the common landslides under gravity, because of the influence of the different topography, lithology and slope structure etc. On the basis of deeply and thoroughly investigating the typical landslides, we classified the landslides into three basic types: slide-type landslides, slide-flow type landslides and fall-slide type landslides according to the main movement characteristics and modes of the landslides, and the slide type landslides also were classified into three secondary types: coherent landslides, disrupted landslides and debris landslides according to the characteristics of sliding and material composition of the landslides and macro disrupted degree of sliding mass.
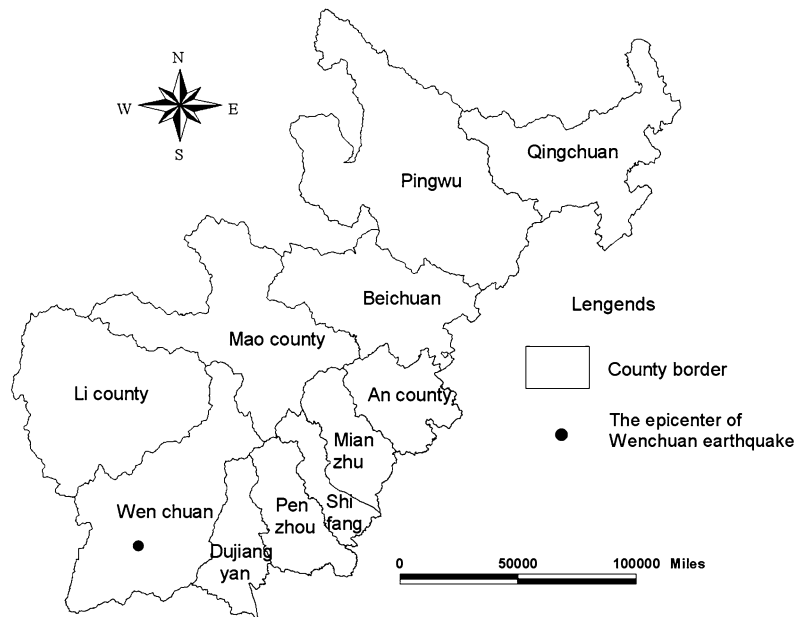
Now, we introduce some typical landslides examples to illuminate the types and characteristics of the landslides in the earthquake.

2.1 Slide Type Landslides

Rock and soil mass on the slopes occurs to slide in the form of whole, fragmentation or debris under earthquake force. Sliding movement is the main movement way of this type of landslides. The landslides include both rock landslides and earth landslides, both superficial landslides and deep-seated landslides. According to the characteristics of sliding and material composition of the landslides and macro disrupted degree of sliding mass, the slide type landslides can be classified into coherent landslides, disrupted landslides and debris landslides.

Coherent Landslides

The landslides start to slide in whole form, and basically keep a whole in the process of movement. They generally have large size and rapid velocity, and slide very quickly under the strong earthquake force. There possibly exist some partition phenomena because of different sliding speed and direction of each part of landslides in the movement, but the integrity of the movement is better from macroscopic view. The front parts of the landslides are easily disintegrated when they are blocked. The type of landslides are very common in Wenchuan earthquake area, such as Wenjiaba landslide, Tangjiashan landslide.

Now, we take Wenjiaba landslide as an example.

The landslide is located on the left bank of Shikan river in Pingwu county of Sichuan province. It belongs to a rock coherent landslide with loose overlay (Fig. 18.2). The geographical coordinate of the leading edge of the landslide is N32° 13′35 .9 ″, E104° 51′53″.

The longitudinal length of the landslide is 800 m, the horizontal width is 600 m, and its volume is about 19 million m^3. The relative height error between the front and back edge is 400 m, and the initial slope degree is about 30°. The landslide body is composed of loose overlay and sandstone of Cambrian system. There are two gullies on the initial slope, which have become the lateral borders of Wenjiaba landslide. The landslide traveled about 150 m, blocked Shikan river and caused the second largest dammed lake in the disaster area. After

Fig. 18.2 Aerial
photograph of Wenjiaba
landslide

Fig. 18.3 Section sketch
map of Wenjiaba landslide
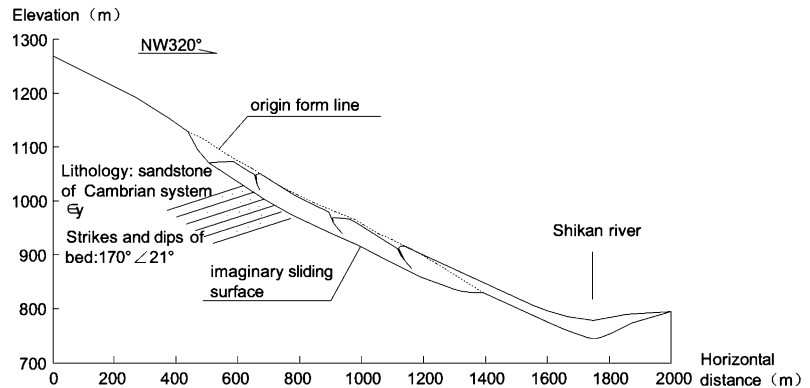
sliding, the landslide surface is split by a series of nearly parallel arc cracks, showing multi-level echelon shape or scarp shape. The scarp of the main posterior on the landslide body has a smaller height, only 1–3 m, while the height of the scarp of the middle landslide body is relatively bigger. This shows some movement features of the landslides, such as starting to move in whole, and sliding successively by traction.

The formation and movement process of the landslide can be summarized as three stages: starting to move in whole, sliding successively by traction and blocked to stop and accumulate. The detailed process is: firstly, the rock and soil mass started to move in whole form along the interface between strong and weak weathering

zone in the slope body under the strong earthquake force; then, the front part moved quickly and dragged the middle and back slope body to slide forward successively because the front part had better free face condition; finally, the landslide body was obstructed by the slope of the right bank of Shikan river and stopped and blocked the river (Fig. 18.3).

Disrupted Landslides

Under persistent seismic waves, the slope rock and soil mass occurs relaxation and fragmentation in the sliding process. Disrupted rock and soil mass slides towards along slope face or structure face. The type of landslides show high or higher disrupted degree, and poor wholeness.

Fig. 18.4 Photos of disrupted landslides

Fig. 18.5 Photos of debris landslides

The fragments generally slide to the foot of steep slopes or partially scatter on the slope face, and can slide dozens and 100 m away on a relatively gentle slope (Fig. 18.4).

Debris Landslides

Loose soil or highly weathered rock mass slides in the form of debris material along slope face under strong earthquake force. This type of landslides are generally shallow landslides, with the thickness of less than 3 m, very high disrupted degree and wide range (Fig. 18.5). The landslides may generally slide to the foot of steep slopes, and can slide several to dozens meters away on a relatively gentle slope.

Fig. 18.6 Source area of Niujuangou landslide

2.2   Slide-Flow Type Landslides

Rock and soil mass on the top of slopes firstly start to slide under earthquake force, then collide with front valley slope and disrupt and disintegrate, finally disrupted rock mass flow at high speed and long distance along the front valley. This type of landslides generally occur in steep slopes of narrow valley and its sliding bed is generally above 30°. They have large sliding range, rapid speed and long distance. If it can obtain more initial kinetic energy in the earthquake, the sliding mass will probably refract several times in the valley, then flow along the valley, such as Niujuangou landslide and Donghekou landslide in Wenchuan earthquake.

Here, we take Niujuangou landslide as an example of this type of landslides.

Niujuangou landslide is located in Yinxiu town of Wenchuan county in Sichuan province. The geographical coordinate of the landslide leading edge is N31° 01′31.4″, E103° 33′21.6″. It is a typical sliding-flow type landslide.

The landslide started to slide at Hejia slope of Yinxiu town. The volume of the initial sliding mass is about 2.6 million m^3. The South of Hejia mountain is Niujuan ditch, a branch of Min river, and its East-North is Lianhuaxin ditch, a branch of Niujuan ditch. The relative height error between the front and back edge is 700 m, and the initial slope degree is about 40°. The lithology in the landslide area is mainly intense weathering plagioclase granite. The landslide travelled to Min river along the Niujuan ditch and Lianhuaxin ditch, and caused a dammed lake, with horizontal movement distance of 2.3 km. In the movement process of the landslide, more and more material was accumulated for the collision, refraction and scraping of many times between the sliding mass and the valley. According to preliminary estimation, the volume of the accumulation is over 5 million m^3. After the earthquake, several debris flows have occurred in Niujuan ditch (Figs. 18.6, 18.7, 18.8, 18.9).

The formation and movement process of the landslide can be summarized as follows (Fig. 18.10):

(1) Sliding start stage

Under the intense earthquake force, the granite mass with the volume of 2.6 million m^3 on Hejia mountain slope started to quickly slide from the elevation of 1450 m in the direction of NE60°along the interface of intense and weak weathering zone. The distance of the source area of the landslide and the earthquake epicenter is only 9 km, and sliding mass has higher energy

Fig. 18.7 Knocking and refracting area of Niujuangou landslide

Fig. 18.8 Flowing area of Niujuangou landslide

of position, so the sliding mass have obtained extremely high speed and momentum from the beginning.

(2) Colliding, refracting and flowing stage

The granite mass with higher speed collided, refracted and scraped several times with the both bank slopes of Lianhuaxin ditch, then flowed at extremely high speed in the direction of SE150°along the Lianhuaxin ditch, and changed

the movement direction at the confluence of Lianhuaxin ditch and Niujuan ditch, then continuously flowed in the direction of NE84°along Niujuan ditch.

(3) Stopping and accumulating stage

With gradual increase of sliding material in the movement process of high speed and gradual decrease of slope gradient of Niujuan ditch, the energy of the flowing rock and soil mass also

Fig. 18.9 Deposit area of
Niujuangou landslide

Fig. 18.10 Section sketch
map of Niujuangou
landslide
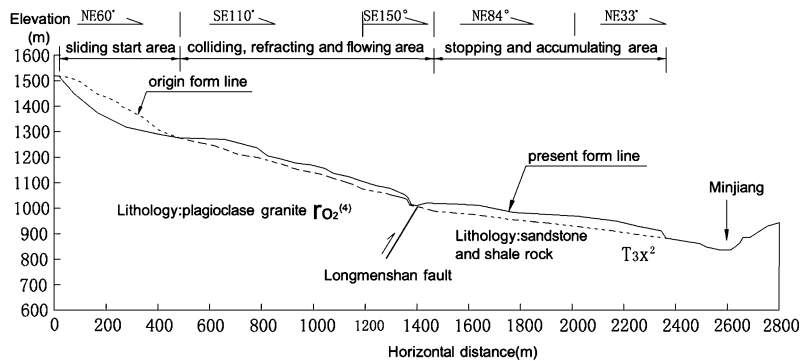
gradually disappeared, finally stopped and accumulated in Niujuan ditch.

2.3   Fall-slide Type Landslides

Rock mass on the top of the high and steep slopes first fall under earthquake force, then the fallen rock blocks push the rock and soil mass of front slopes to quickly move forward, resulting in occurrence of fall-slide type of landslides. This type of landslides generally occur on the slopes with step or step-like shape of steep upper part and gentle lower part, and usually there are a broad valley in front of the slopes. After sliding, collapse tensional surface is nearly vertical or there are residual danger stones on the trailing edge of landslides, and there are obvious sliding traces on the middle and lower part of slopes. Jiufengcun landslide in Wenchuan earthquake belongs to fall-slide type landslide. In the following, we only take Jiufengcun landslide as an example.

Jiufengcun landslide is located in Xiejiadian of Longmenshan county of Pengzhou city in Sichuan province. The geographical coordinate of the landslide leading edge is N31° 17′36″, E103° 50′53″.

The longitudinal length of the landslide is 600 m, the horizontal width is 270 m, and its volume is about 5 million m^3. The relative height error between the front and back edge is 300 m. The origin slope has step shape (the slope degree of upper steep part is over 40° and the slope degree of lower gentle part is about 21°). In the front of the origin slope, there is a broad and smooth valley, i.e., the location of Jiufeng villagers of Xiejiadian. The landslide body is composed of loose overlay and sand rock and lime rock of Triassic system. The landslide blocked Shajin river and caused barrier lake in the earthquake, with the horizontal travel distance of 400 m (Figs. 18.11, 18.12).

According to the movement and deposit characteristics of the landslide, the landslide can be divided into three areas: slumping area of trailing edge, whole sliding area and accumulating area after sliding (Fig. 18.13). The elevation of slumping area is between 1350 and 1540 m, and the relative height error is about 190 m. The initial slope gradient of the area is much deeper, more than 50°. The bedrock experiences intense weathering, and the cracks are well developed. The rock and soil mass in this area mainly occurs partial collapse and small-scale slump disaster. The elevation of whole sliding area is between 1260 and 1350 m. The area in topography shows a protruding shape, and show obvious step shape in section. The slope body in the area slides forward together as a whole. The elevation of the accumulating area after sliding is roughly between 1260 and 1180 m, mainly located in the sites of Jiufengcun village, where there is a broad valley and Shajin river course.

According, the movement and formation of the landslide under the earthquake can be divided into three stages: starting to slump stage of

Fig. 18.13 Section sketch map of Jiufengcun landslide
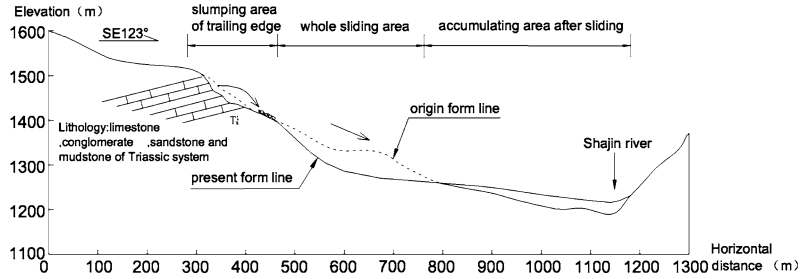
trailing edge, whole sliding stage and stopping and accumulating stage.

but also can provide a mitigation and prevention basis for future earthquake-induced landslides.

3 Conclusions

On the basis of extensive field investigation, we classified the typical landslides induced by Wenchuan earthquake into three kinds of basic types: slide-type landslides, slide-flow type landslides, fall-slide type landslides according to the movement characteristics and modes of the landslides. Moreover, according to the characteristics of sliding and material composition of the landslides and macro disrupted degree of sliding mass, sliding-type landslides were classified into three kinds of secondary types: coherent landslides, disrupted landslides and debris landslides. On the basis, we take typical landslides as examples to thoroughly analysis and study on the basic characteristics, especially movement characteristics and processes of all types of landslides. This is not only helpful to comprehensively understanding the types and characteristics of earthquake-induced landslides,

References

Huang R, Pai X, LI T (2008) Basic characteristics and formation mechanism of the largest scale landslide at Daguangbao occurred during the Wenchuan earthquake. J Eng Geol 16(6):730–741

Keefer DK (2002) Investigation landslides caused by earthquake—a historical review. Surv Geophys 23: 473–510

Kong J, Fayou A, Wenping W (2009) Typical examples analysis the types of Wenchuan earthquake landslide. J Soil Water Conserv 23(6): 66–70

Xu Q (2009) Main types and characteristics of the geo-hazards triggered by the Wenchuan earthquake. J Geologic Hazards Environ Preserve 20(2):86–93

Xu Q, Huang R (2008) Kinetics characters of large landslides triggered by May 12th Wenchuan earquake. J Eng Geol 16(6):721–729

Yin Y (2009) Features of landslides triggered by the Wenchuan earthquake. J Eng Geol 17(1):29–38

Zhou B, Zhang Y (1994) Some characteristics of earthquake-induced landslides in southwestern China. Northwest Seismol J 16(1):96–103

Study on the Development Characteristics of a Typical Case of Sliding-Flow Type Landslide Induced by Wenchuan Earthquake

19

Jiming Kong, Peifeng Han and Yun Cui

Abstract

A large number of seismic landslides have been induced by Wenchuan earthquake, and one of a universal seismic landslide type is fragmentation-sliding seismic landslide. This kind of landslides with the unique sliding characteristics and complexity of power mechanism, and has a large scale in the long distance movement. We bring Niujuan Ditch seismic landslide in Yingxiu of Wenchuan County as a typical example, the author through the fragmentation sliding landslide investigation, and study on the critical control factors of the formation for the fragmentation-sliding such as landforms, litho logy, slope structure, the role of seismic and so on, investigate of earthquake fragmentation sliding type landslide mechanism accord to the dynamic characteristics and movement of landslide, We bring Niujuan Ditch seismic landslide as a typical example for the fragmentation-sliding landslide mechanism under the earthquake then we give a detailed interpretation of the process of fragmentation-sliding with four stages and seven turning points of the direction—"slide to start—collision fragments—debris slide—the accumulation of stagnant". Finally, the application of mechanism—"seismic start—fragmentation—accelerating" has an efficient explanation for why there are features of ultra-high-speed, slip away-way, large-scale for seismic landslide, it is very important to enhance the level of

J. Kong (✉) · P. Han · Y. Cui
Key Laboratory of Mountain Hazards and Surface
Process, Chinese Academy of Sciences,
Chengdu 610041, China
e-mail: jimingk@imde.ac.cn

J. Kong · P. Han · Y. Cui
Institute of Mountain Hazards and Environment,
Chinese Academy of Sciences,
Chengdu 610041, China

P. Han
Graduated School of Chinese Academy of Sciences,
Beijing 100039, China

understanding of the seismic landslide types, reveal the earthquake cracked sliding mechanism of landslide, improve mountain disasters discipline development and guidance for restoration and reconstruction of disaster prevention and reduction.

1   Introduction

At PM 2:28, May.12, 2008, the M8.0 Wenchuan earthquake occurred in Yingxiu (31.0°N, 103.4°E) of Wenchuan county of Sichuan Province, China. The earthquake induced a large number of geo-hazards in a very short time, such as collapses, landslides and ground fissures, because of the shallow source, long duration and enormous energy of the earthquake. The large-scale collapses and landslides in worst-hit areas greatly increase the damage degree caused by the earthquake, and become a kind of main disaster way which have been paid more and more attention by the researchers (Romeo 2000; Papadopoulos and Plessa 2000).

The landslides induced by Wenchuan earthquake show some unique and various characteristics compared with the gravity-driven landslides. The movement ways of the landslides include falling, dumping and ejection, and the movement states include whole sliding and fragmentation sliding types. The disrupted sliding type landslide is one of the most typical earthquake-induced landslides in the landslides (Kong 2001) and has been widely studied by the researchers inside and outside China. A typical example is Niujuan ditch seismic fragmentation-sliding landslide in Yingxiu Town of Wenchuan County, Sichuan Province. Because of sudden occurrence and complex movement process of the landslide, it is not easy to accurately understand the landslide disaster. Some local villagers and researchers think the landslide including the explosion and ejection movement. The landslide has become a hot and difficult problem for some

time in the study of the geo-hazards induced by Wenchuan earthquake.

Based on the field survey and analysis on Niujuan Ditch landslide, we think that the landslide experienced a movement process of rapid slide, collision and disruption, fragment slide and slide stopping under the continuing earthquake force. The process can be divided into four stages: start to slide stage, colliding and disrupting stage, and fragmental sliding stage, accumulating and stopping stage. In the stage of starting to slide, nearly 2.6 million m^3 of granite mass induced by the earthquake rapidly slipped downwards from an altitude of 1800 m, collided with the rock mass on the slope foot at an altitude of 1350 m, and the rock mass was collided into fragment. In the colliding and disrupting stage, the disrupted granite mass flowed towards along Niujuan ditch (a branch ditch of Minjiang River) and collided seven times with the both bank sloped of the ditch, more and more material was accumulated for the collision. According to primary estimation, over 330 million m^3 fragmentation material slipped in Niujuan ditch. After the earthquake, the fragmentation material stopped and accumulated about 200 m long in the branch ditch.

It is difficult to use previous landslide theory to explain the huge energies and complex process of the large-scale and long-distance landslide. On the basis of thoroughly investigating this type of landslides, we chose Niujuan landslide to discuss the formation mechanism of the landslide from the dynamic characteristics and movement ways of the landslide, and analyzed the fragmental sliding mechanism of the landslide under the earthquake force. It is very important to improve

the cognitive level of the seismic landslide types and to reveal the fragmental sliding mechanism of earthquake-induced landslides. This study has important significance and guidance to the prevention and reduction of earthquake-induced disasters in practice.

2 Sliding: Flow Type Landslide Induced by Earthquake and Its Characteristics

2.1 Connotation of Earthquake Fragmentation-Sliding Landslide

Generally speaking, the landslide is a geomorphologic processes and phenomena of the rock and soil mass wholly sliding downward along the weak surface or band within slope mass under the action of gravity. According to different inducing factors, landslides can be classified into seismic landslide, rainstorm landslide, artificial blasting landslide, mechanical vibration landslide and so on (Deng 1996; Huang et al. 1997). Therefore, seismic landslide is a kind of special type landslide.

Seismic landslide, corresponding to a destructive earthquake or earthquake swarm, is a kind of geological events induced by earthquakes. Seismic landslide is an important landslide type and a kind of fast geomorphologic evolution processes and phenomena. Their occurrence has certain inevitability, also has certain abruptness. Their development does not entirely follow the development process of natural landslides. According to the different movement characteristics, seismic landslides can be classified into whole sliding type and fragmentation sliding type. The latter is a special type of earthquake landslide.

Fragmentation sliding type landslide is a kind of seismic landslide of disrupted rock and soil mass sliding along slope surface or valley, after rock and soil mass on the slope starts to slide and disrupts under earthquake force. The type of landslides has some common characteristics. Firstly, generally being composed of rock;

secondly, usually occurring in high steep slope and possessing high energy and high speed; thirdly, fast sliding slope often collides into fragmental stones and the friction is smaller between the stones; finally, the landslide body has sufficient power to make fragmental stones to rapidly slide. The Wenchuan earthquake, with strong vibration time of about 110 s, provides sufficient energy for the slip of disrupted rock mass (Fig. 19.1).

2.2 Slip Characteristics of Earthquake Fragmentation-Sliding Landslide

This type of landslides generally has some apparent characteristics in the occurrence and movement process. The detail is as follows:

(1) Large size, big height difference and obvious partition phenomena

Fragmentation sliding landslides generally have large size and belong to large or huge landslides. This is main characteristics of earthquake inducing landslides in a very short time. Compared with whole sliding type landslides, the type of landslides have poor integrity and apparent partition phenomena because of different sliding speed and direction of each part of landslide body in the movement process.

(2) Slope mass disrupting in the process of sliding and sliding along the slope surface or valley

After landslide body is disintegrated in the movement process of high speed in a short time, the disintegrated rock mass is completely disrupted under the action of collision, extrusion, friction and acceleration. Disrupted block and debris slide along the slope surface or valley.

(3) High sliding speed and long distance

The source area of the type of landslides is generally located in the middle or upper part of slopes. The landslide body itself has high potential energy and its sliding force gradually increases under the constant action of seismic force. Therefore, landslide body can instantly obtain very high velocity, rock mass quickly disintegrated in the fast movement process.
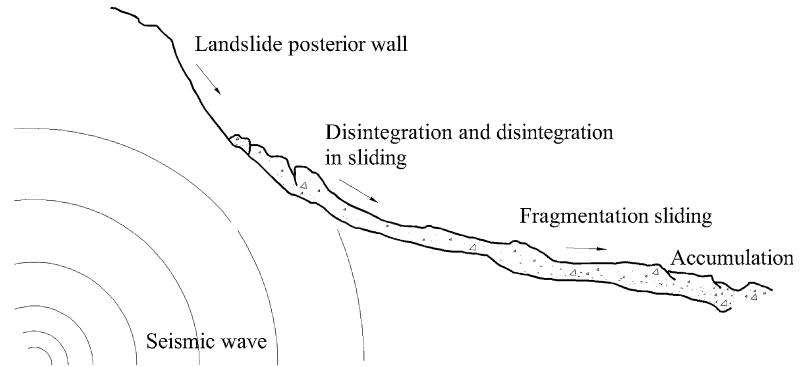
There lies obvious jumping phenomenon in the development stage. Low friction effects among disrupted rock block and debris and continuous seismic action make the type of landslides to travel much farther.

(4) Fragmentation material has no mixing phenomenon in the sliding process

The disrupted material differs from the fluid and its compression performance is very small. In the sliding process, the disrupted material subject to shear stress and normal stress at the same time with concentrated tangential velocity, and the material between upper and lower keeps relatively isolated without turbulent flow mixing effect.

3   Dynamic Interaction Analysis of Earthquake Fragmentation-Sliding Landslide

Based on field investigation and analysis, we find that there are several key dynamic conditions controlling the type of landslides as follows:

(1) High energy dynamic conditions

The types of landslides generally have high energy dynamic conditions. The landslide body is usually located in high or higher position, so there is higher potential energy in the sliding process. Rock and soil mass on the upper part of slopes quickly slides away from the sliding bed with higher potential energy under earthquake force, and landslide body processes higher velocity and kinetic energy in the movement process in a very short time. This provides sufficient energy for disintegration and fragmentation of the sliding body. At the same time, the potential energy from topographic height difference on the sliding path will also provide continuous kinetic energy for the sliding body. So the type of landslides can keep in motion for some time.

(2) Continuous seismic action

Continuous seismic force is the most important dynamic source in the starting and sliding process of the type of landslides. After earthquakes, P wave firstly arrives at the slope body of earth surface and acts on it, which leads to the gradual increase of cracks width and length and slope displacement, and finally results in the instability of slope body. Under gravity and seismic force, slope body starts to slide, collides with rock mass on the slope foot and disintegrates After seismic S wave reaches the surface, strong plane vibration makes the disrupted stones slide the acting force of seismic S wave on the disrupted stones has the following characteristics:

If the vibration of surface stone (its mass denoting as m) has the characteristics of damp harmonic vibration under earthquake wave, then the stone in the vibration is mainly affected by the earthquake force (F_z) and friction (f_m). So, we can get:

$$F = F_z + f_m, \tag{19.1}$$

$$F_z = -kx, \tag{19.2}$$

$$f_m = -bv. \tag{19.3}$$

Where, k is oscillating coefficients, x is the displacement for equilibrium position and b is proportional factor and v is vibration instantaneous velocity.

The above formula (19.1) can be written as:

$$F = -kx + -bv. \qquad (19.4)$$

We can get a motion equation of the stone in the vibration after secondary differentiate of formula (19.4):

$$am = -kx - bv \qquad (19.5)$$

By solving the Eq. (19.5), x displacement of the stone in the vibration can be obtained:

$$x = Ae^{-(r/2)t} \cos(\omega_1 t + \phi) \qquad (19.6)$$

Where, A and φ are arbitrary constants, $r=b/m$, ω_1 is vibration frequency. The formula (19.6) stands for the displacement of the stone in surface vibration.

In order to illustrate the motion characteristics of stones under the seismic S wave, we assume that the direction of positive phase movement is the direction of slope sliding downwards (gravity direction) in a vibration cycle, the direction of positive phase movement is just opposite (Fig. 19.1).

The vibration is in the state of positive phase, the stone displacement direction generated by earthquakes parallels to the gravity direction. So, the two kinds of displacements can be added together to obtain a bigger displacement value.

When the vibration is in the state of negative phase, the displacement direction is opposed to the gravity direction. Because the two displacements offset each other, the stone does not generate the movement of inverse slope direction and maybe keep motionless. The sum of positive phase displacement many vibration period makes the stone continuously slide upwards during the continue vibration process of earthquakes. Therefore, in Wenchuan earthquake, large-scale and long-distance landslides can be induced under the action of the 100 s' duration vibration.

(3) The effect of landslide body with high fragmentation and low friction
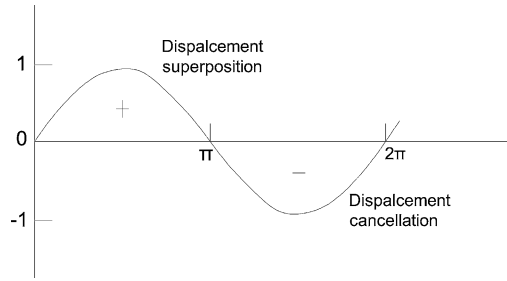
Fig. 19.2 The vibration period

The fragmentation sliding slope is mainly composed of hard rock. Fast earthquake force makes the rock mass to produce brittle deformation and failure, and results in the structure of low strength and high fragmentation of the sliding rock mass. This will greatly decrease the friction force of between loose rock and soil mass (Fig. 19.2).

4 The analysis of the Typical Examples: Niujuan Ditch Landslide

The coordinate of the leading edge of Niujuan ditch landslide is 31°01′31.4″N, 103°33′21.6″E, and its elevation is 1294 m. The Landslide, a typical fragmentation sliding type landslide, changed the movement direction for seven times in the Niujuan ditch, with the volume of more than 3.3 million disrupted material and long movement distance of 2.3 km.

4.1 The Formation Conditions of the Niujuan Ditch Landslide

(1) Geomorphologic conditions

Niujuan Ditch is a branch of right bank of Min river. The geomorphic type in the valley is mainly high mountain, with the terrain of high in the west and low in the east and big terrain elevation difference. The altitudes of the landslide trailing and leading edges are 1800 and 840 m respectively and the relative error between them is nearly 1000 m. The initial slope

Fig. 19.3 Section sketch map of Niujuan ditch landslide
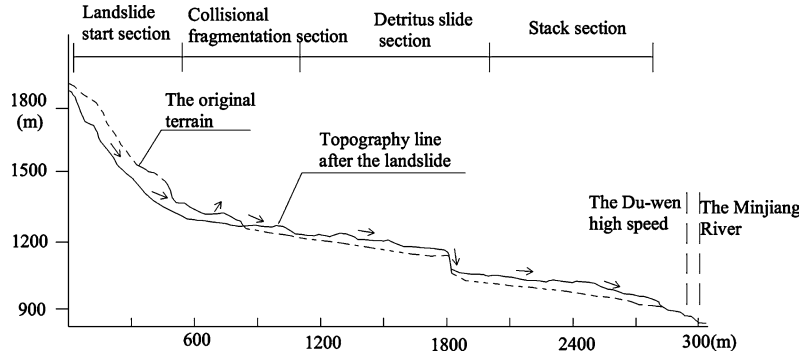
Fig. 19.4 Cross-section profile of development of Niujuan ditch landslide
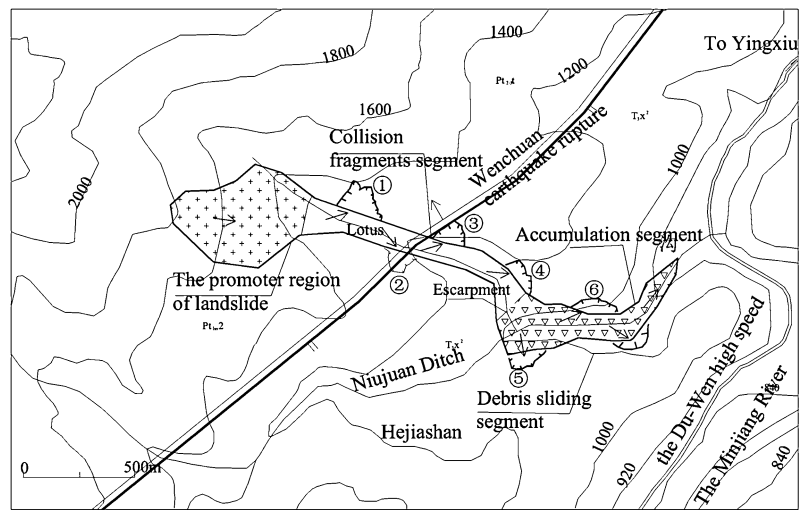
degree of the landslide area is about 35°
(Fig. 19.3). These characteristics provide
enough potential energy and movement space
for the landslide.

(2) Lithology conditions

The stratum and lithology of Niujuan ditch
landslide area can be classified into two main
types with Wenchuan seismic fault as boundary.
The lithology of the start sliding area is mainly
composed of the granite of middle Huangshuihe
group of the Proterozoic (Pt_{hn}^2). The lithology of
the accumulating area is mainly composed of
quartz sandstone and shale which belongs to
Xujiahe group of Triassic system of Mesozoic
(T_3x^2) (Hu 1998).

(3) Slope structure

There are many isolated mountains in
Niujuan ditch landslide area. The mountain
slopes has big free surface, and their slope

angles increase with the increase of elevation.
Moreover, the trend of stratum in this area is
accordant to that of the slopes and dip angle is
less than slope angle. This provides internal
conditions for the occurrence of large-scale
landslide.

(4) Earthquake-induced effect

The seismogenie fault of the great Wenchuan
earthquake, Yinxiu-beichuan fault, passes
through the middle part of the landslide
(Fig. 19.4). Intense earthquake is a primary
condition inducing the landslide. According to
preliminary estimation, the earthquake at least
has a scalar seismic moment of 4.4×1021 N·m
and a moment magnitude of Mw = 7. 9. Both of
the earthquake are much bigger than those of
Tangshan earthquake (the surface wave magni-
tude and the moment magnitude are 7.8 and 7.6)
(Wang et al. 2008; Chen 2008). In this

Fig. 19.5 The promoter region of the fragmentation-sliding landslide in Niujuan ditch

Fig. 19.6 The fragmentation channel at the sliding

earthquake, a lot of main shock records were obtained in the fixed seismic network of Sichuan province. In the collected records, the maximum peak accelerated velocity is 976 gal (Chen 2008; Xu et al. 2008; Zhou 2008).

4.2   Movement Process and Characteristics of Niujuan Ditch Landslide

The most obvious characteristics of Niujuan ditch fragmentation-sliding type landslide are high speed, long distance and large size. Its movement process includes four stages: sliding start stage—Colliding and disrupting stage—debris sliding stage—Stopping and accumulating stage.

(1) Sliding start stage

In lianhuaxin valley, granite mass with the volume of 260 million m^3 on Hejia mountain slope (with the slope gradient of 40°–45°) started from the elevation of over 1450 m under the intense earthquake force, and quickly slipped along the deep bedding plane and weak structural plane. Under the thrashing action of seismic P wave up and down and the swaying action of S wave left and right, the landslide body quickly disrupted into blocks, and continuously slide under the inertia force, and obtained extremely high speed in a very short time (Figs. 19.5, 19.6).

(2) Colliding and disrupting stage

In lianhuaxin valley, the landslide body started to collide with the both bank slope (slope angle about is 20°) and disrupt between the elevation of 1450–1200 m (Fig. 19.3). After the first stage, the sliding body had obtained higher momentum. The sliding body strongly collided with the left bank slope of the valley and induced secondary landslides(number ① in Fig. 19.4). A large number of granite particles occurred sputtering and fragmentation in the collision process, then continuously refracted and more and more material was added into the sliding body, and collided with the right bank slope of the valley, and also induced secondary landslides (number ② in Fig. 19.4). After that, the sliding body collided and refracted with the slopes into landslides and further disrupted in the location of the left bank fault zone (number ③ in Fig. 19.4) and in the location of 1200 m altitude (number ④ in Fig. 19.4) respectively in the same way. In the movement process, more and more material was added into the sliding body, while the sliding body became more and more disrupted. After the sliding body experienced four time's high strength collision and refraction, it had thoroughly become disrupted material.

(3) Debris sliding stage

The stage occurred from the scarp spot of 1200 m elevation to 1000 m elevation (Fig. 19.3). The disrupted sliding body again changed the movement direction from the scarp, poured down from the scarp with 400 m height

Fig. 19.7 The fragment- sliding discount to a cliff

Fig. 19.8 The landslide lake created by fragmentation-sliding collision to the ditch slope

difference and supplied energy to further improve its movement speed. Moreover, the sliding body collided with the right bank slope of Niujuan ditch and also induced secondary landslides similarly (number ⑤ in Fig. 19.4). Then, the sliding body collided with the left bank slope of Niujuan ditch and produced landslides (number ⑥ in Fig. 19.4). After that, the most energy of the sliding body lost by collision. After the sliding body folded towards the right bank slope and completed the 7th struck and caused a small landslide, the speed of the disrupted body decreased greatly (Figs. 19.7 and 19.8).

(4) Stopping and accumulating stage

The stage occurred at the elevation of 1000 m in the Niujuan Ditch and turned to the Minjiang River, with the slope gradient of 5°–10°.

After the seven times collision, slope gradient gradually decreases, the energy of disrupted material sliding and residual energy and seismic force also obviously decreased. Therefore, the sliding body started to accumulate in the ditch, at last the movement of the sliding body completely stopped.

The most obvious characteristic of the landslide is the characteristics inducing by the earthquake. The periodic vibration process of seismic waves controlled the starting and disrupting and sliding movement of the landslide. Just due to the acceleration effect of the great earthquake lasting 110 s, Niujuan ditch landslide traveled 2.3 km long and process the size of 3.3 million m^3.

5 Conclusions

The fragmentation sliding type landslide is a typical seismic landslide type. We choose Niujuan ditch landslide as a typical example of this type of landslides, deeply analyze and discuss the characteristics and movement process of the landslide based on detailed field survey, and divided the movement into stages: sliding start stage—Colliding and disrupting stage—debris sliding stage—Stopping and accumulating stage. This study not only has important academicals value, but also has important practical significance to study the characteristics and development process of fragmentation sliding type landslide.

References

Chen Y (2008) On the magnitude and the fault length of the great Wenchuan earthquake. Sci Technol Rev 26(10):26–27 (in Chinese)

Deng Q (1996) Active tectonics in China. Geol Rev 42(4):295–299 (in Chinese)

Hu Z (1998) Regional geology of Sichuan province. Sichuan Publication House of Science and Technology, Chengdu, pp 210–211(in Chinese)

Huang J, Wang W, Xue H (1997) Dynamic analysis of seismic stability of slopes. Earthq Eng Eng Vib 17(4):113–122 (in Chinese)

Huang R, Weile LI (2008) Research on development and distribution rules of geohazards induced by Wenchuan earthquake on 12th May, 2008. Chin J Rock Mech Eng 27(12):2585–2592 (in Chinese)

Kong J (2001) The non-computation method to differentiate the stability of slope. J Mt Sci 19(5):446–451 (in Chinese)

Papadopoulos GA, Plessa A (2000) Magnitude-distance relations for earthquake-induced landslide in Greece. Eng Geol 58(3–4):377–386

Romeo R (2000) Seismically induced landslide displacements: a predictive model. Eng Geol 58(3–4):337–351

Wang Y, Luo Y, Fen JI (2008) Analysis of the controlling factors on geohazards in mountainous epicenter zones of the Wenchuan earthquake. J Eng Geol 16(6):759–763 (in Chinese)

Xu X, Wen X, Ye J (2008) The Ms8.0 Wenchuan earthquake surface ruptures and its seismogenic structure. Seismol Geol 30(3):597–629 (in Chinese)

Zhou Z (2008) The strong ground motion recordings of the Ms8.0 Wenchuan Earthquake in Sichuan Province. Earthquake research in Sichuan 4(4):25–29 (in Chinese)

Geomorphologic and Geologic Features of Landslides Induced by the 2011 Off the Pacific Coast of Tohoku Earthquake, in Shirakawa Hills, Fukushima Prefecture

20

Hiroyuki Sugimoto, Toshiya Takeshi, Tadakazu Uto and Hiroki Honma

Abstract

The earthquake that occurred on March 11, 2011, off the Pacific coast of Tōhoku triggered many landslides on the natural slopes of Shirakawa Hills, Fukushima Prefecture, Japan. The landslide that occurred in Hanokidaira area caused the most damage and claimed the lives of 13 people; the failure occurred in the thick brown volcanic ash sediment layer on the hill slope and caused rapid soil flow across extensive areas, thereby increasing the resulting damage. There are a number of rapid landslides with similar characteristics even outside the Hanokidaira District; a volcanic soil layer collapsed and flowed a relatively long distance. The locations of many of these landslides are, like that in the Hanokidaira District, running from the crest slope to the upper sideslope located above a valley head and straddling knick lines. The slip surface is weathering tephra, and as in the Hanokidaira District case, presumably occurred with the part which was clay weakened by weathering.

H. Sugimoto (✉)
T. Takeshi (✉)
Public Works Research Institute, Minami-hara, Tsukuba, Ibaraki 305-8516, Japan
e-mail: sugimoto@pwri.go.jp

T. Takeshi
e-mail: takeshi@pwri.go.jp

T. Uto
Eight-Japan Engineering Consultants Inc, Osaka, Japan

H. Honma
OYO Corporation, Saitama, Japan

1   Introduction

The earthquake that occurred on March 11, 2011, off the Pacific coast of Tōhoku triggered many landslides on the natural slopes of Shirakawa Hills in northern Shirakawa City, Fukushima Prefecture, Japan. The landslide that occurred in Hanokidaira area caused the most damage and claimed the lives of 13 people; the failure occurred in the thick brown volcanic ash sediment layer on the hill slope and caused rapid soil flow across extensive areas, thereby increasing
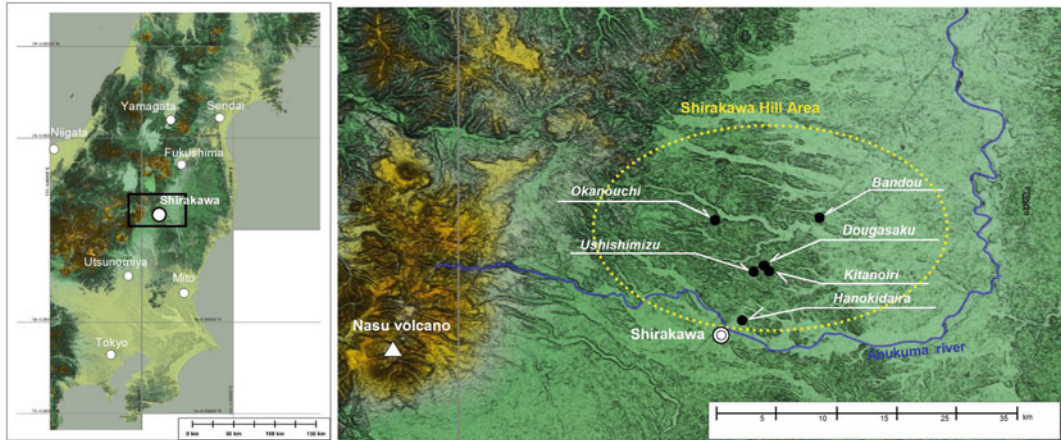
Fig. 20.1 Landslide sites near Shirakawa

the resulting damage. The scale of damage was the second-worst caused by a single landslide in recent years, after the landslide caused by the 1995 Great Hanshin Awaji Earthquake.

On the hills around Shirakawa, concentrated failures occurred on the thick brown volcanic ash slopes, not only in Hanokidaira, but also in other locations with similar characteristics, causing the soil mass to flow over quite a great run-out distance. This study investigates the geomorphological and geological features of six landslide sites, and the causal mechanism of the landslides.

2   Overview of the Area and Occurrence of Landslides on Shirakawa Hills

A large proportion of the area around Shirakawa comprises the Shirakawa Hills, formed by the Shirakawa pyroclastic flow deposit (Yoshida and Takahashi 1991) of the Early Pleistocene. The Shirakawa Hills, dissected by the Abukuma River, are covered by the tephra layer of the Middle-to-Late Pleistocene Nasu Volcano (Suzuki 1992) with a thickness of several meters to several tens of meters.

A seismic intensity of *6 upper* on the Japan Meteorological Agency's scale was recorded for the Tohoku Earthquake of March 11, 2011, in Shirakawa City. As shown in Fig. 20.1, landslides occurred in a concentrated manner on the

Shirakawa Hills in the area north of Shirakawa City. This study assesses the landslides that occurred in the six areas indicated in Fig. 20.1.

3   Survey Method

A microtopographic classification map of the slope was created from stereographic interpretation of aerial photographs, interpretation of topographic maps, and elevation difference map derived from laser-profiling both prior to (December 2006 to January 2007) and after the earthquake (November 2011). The laser profiler data were taken by the Ministry of Land, Infrastructure, Transport and Tourism. The elevation difference map included a correction for the effect of crustal deformation caused by the earthquake. From the interpretation of the aerial photographs and topographic maps, two knick lines were observed (the upper knick line, near the top of the ridge; and the lower knick line, near the valley), which were used for the slope classification. The microtopographic classification method used the nomenclature proposed by Tamura (1987), which is often applied to hilly terrain in Japan.

The geology on the main scarp and side cliff and the surface of rupture of the landslide sites was observed, the areas near the rupture surface was focused on. To determine the physical relationship between the surface of rupture, main scarp, and side cliff, and to observe the

Fig. 20.2 Hanokidaira area: **a** An oblique aerial photograph. **b** Elevation difference map. **c** Topographic map before the earthquake with microtopographic slope-classification. **d** Topographic map after the earthquake

geology of the strata underlying the surface of the rupture, pits and trenches were excavated to a maximum depth of 1 m.

Soil hardness was measured on the surface of the cross section, which was used for geological observation, using a Yamanaka-type soil hardness tester. Samples collected from some of the sections were subjected to physical soil testing.

4   Overview of Studied Landslides

4.1   Hanokidaira Area

This landslide had a maximum length and width of 115 (L1) and 65 m (W1), respectively. The displaced soil mass as a result of the landslide moved a maximum distance of 140 (L2), and was deposited across a large area with a maximum width (W2) of 115, causing significant damage (13 deaths and 10 completely destroyed houses.) Part of the soil mass moved along the slope of a golf practice range located alongside the landslide site and covered a maximum distance of 70 m. The ratios are L2/L1 = 1.2 and W2/W1 = 1.8, suggesting that soil mass flowed over a quite a long distance, spreading widely, which is considered to be the reason for the severe damage. The maximum height difference on the main scarp is 5, while the maximum height difference in the left-side cliff, which is the highest of all the side cliffs, is 13 m.

Comparison of airborne laser profiler (LP) maps before and after the landslide shows that the landslide initiation area (zone of depletion) is located on the top of the ridge and on the shallow northeast-facing slope below, which has slope angles of 10–20° (Fig. 20.2). The slope on which the landslide occurred does not present clear features of landslide topography. Below the shallow slope is an east-facing valley, where the direction of the landslide movement turns from northeast to east. In areas of the landslide mass deposits, earthwork operations were carried out using heavy equipment after the landslide, as can be identified as artificial topography on the LP map (Table 20.1).

4.2 Ushishimizu Area

This landslide had a maximum length and width of 55 (L1) and 50 m (W1), respectively. The displaced soil mass as a result of the landslide moved a maximum distance of 105 (L2) and maximum width of 40 (W2), which give the ratios L2/L1 = 1.9 and W2/W1 = 0.8. The maximum height difference on the main scarp is 10 m. The soil mass flowed a great distance along the valley, which prevented the mass from extensive lateral spread.

The landslide initiation area (zone of depletion) is located on the top of the ridge and on the shallow northeast-facing slope below, which has slope angles of 10–20° (Fig. 20.3). The slope on which the landslide occurred does not present clear features of landslide topography. Below the shallow slope is a northeast-facing valley. The majority of the soil mass flowed down the valley, and a part of the soil mass moved over the ridge to the north.

4.3 Dougasaku (Yabeya) Area

This landslide had a maximum length and width of 145 (L1) and 95 m (W1), respectively. The displaced soil mass as a result of the landslide moved a maximum distance of 265 (L2) and maximum width of 55 (W2), which give the ratios L2/L1 = 1.8 and W2/W1 = 0.6. The maximum height difference on the main scarps is 10 m. The landslides occurred in two adjacent valley-head areas and then merged, flowing along the valley. The soil mass flowed a great distance along the valley, which prevented the mass from extensive lateral spread.

The landslide initiation area (zone of depletion) is located on the top of the ridge and on the shallow south-facing slope below, which has slope angles of 10–20° (main landslide), and on the east-facing slope (auxiliary landslide) (Fig. 20.4). The slope on which the landslide occurred does not present clear features of landslide topography. Below the shallow slope is a west-southwest-facing valley, along which the soil mass flowed.

Table 20.1 Landslide occurrences and movements

	Hanokidaira	Ushishimizu	Dougasaku (Yabeya)	Bandou	Kitanoiri	Okanouchi
Length of landslide slope (L1)	115 m	55 m	145 m	55 m	75 m	70 m
Moving distance of toe (L2)	140 m	105 m	265 m	60 m	205 m	105 m
L2/L1	1.2	1.9	1.8	1.1	2.7	1.5
Width of landslide slope (W1)	65 m	50 m	95 m	70 m	45 m	50 m
Width of landslide mass (W2)	115 m	40 m	55 m	90 m	70 m	80 m
W2/W1	1.8	0.8	0.6	1.3	1.6	1.6
Maximum depth	10 m	10 m	10 m	5 m	10 m	10 m
Area where landslide occurred	Crest slope to Upper sideslope	Crest slope to Upper sideslope	Crest slope to Upper sideslope	Crest slope to Upper sideslope	Crest slope to Upper sideslope	Upper sideslope
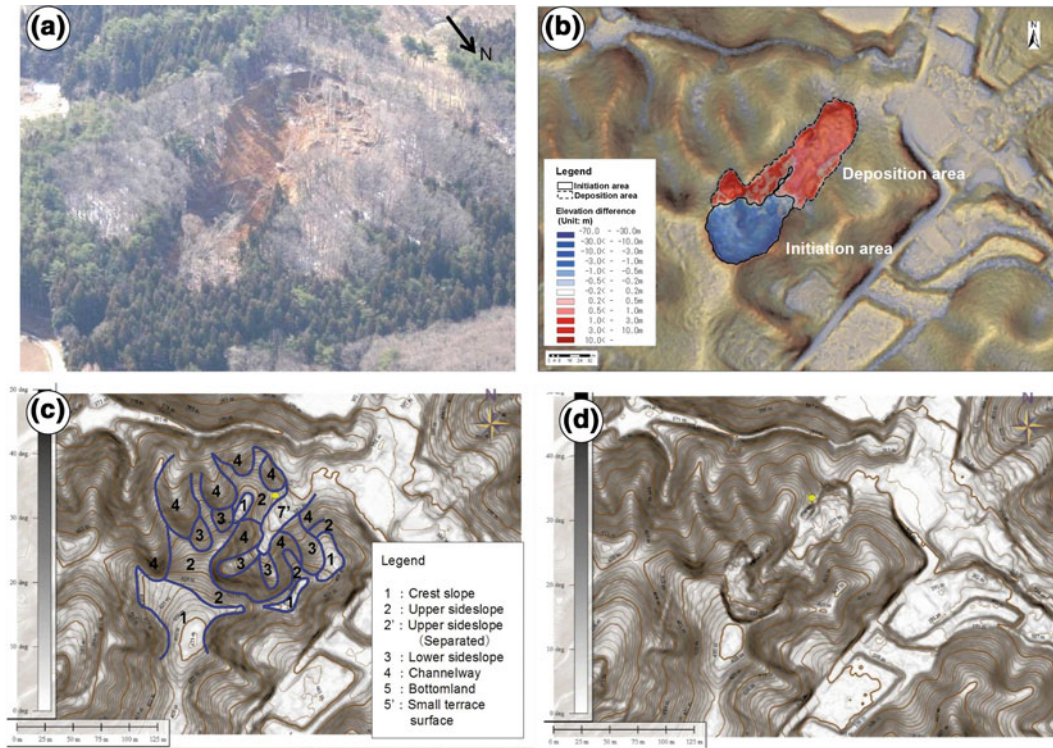
Fig. 20.3 Ushishimizu area: **a** An oblique aerial photograph. **b** Elevation difference map. **c** Topographic map before the earthquake with microtopographic slope-classification. **d** Topographic map after the earthquake

4.4 Bandou Area

This landslide had a maximum length and width of 55 (L1) and 70 m (W1), respectively. The displaced soil mass as a result of the landslide moved a maximum distance of 60 (L2) and maximum width of 90 m (W2), which give the ratios L2/L1 = 1.1 and W2/W1 = 1.3. The maximum height difference on the main scarp is 5 m. The soil mass buried part of the city road. A small landslide also occurred on a south-facing slope, across the city road from the major landslide.

The landslide initiation area (zone of depletion) is located on a shallow north-facing slope with slope angles of 10–20° (Fig. 20.5). The slope on which the landslide occurred does not present clear features of landslide topography. Below the shallow slope is a steep slope, down which the soil mass flowed.

4.5 Kitanoiri Area

This landslide had a maximum length and width of 75 (L1) and 45 m (W1), respectively. The displaced soil mass as a result of the landslide moved a maximum distance of 205 (L2) and maximum width of 70 (W2), which give the ratios: L2/L1 = 2.7 and W2/W1 = 1.6. The maximum height difference on the main scarps is 10 m.

The landslide initiation area (zone of depletion) is located on the top of the ridge and on the shallow southwest-facing slope below, which has slope angles of 10–20° (Fig. 20.6). The slope on which the landslide occurred does not present clear features of landslide topography. Below the shallow slope is a south- to southwest-facing valley; the soil mass followed the valley until it reached the rice paddy fields around the outlet of the valley.
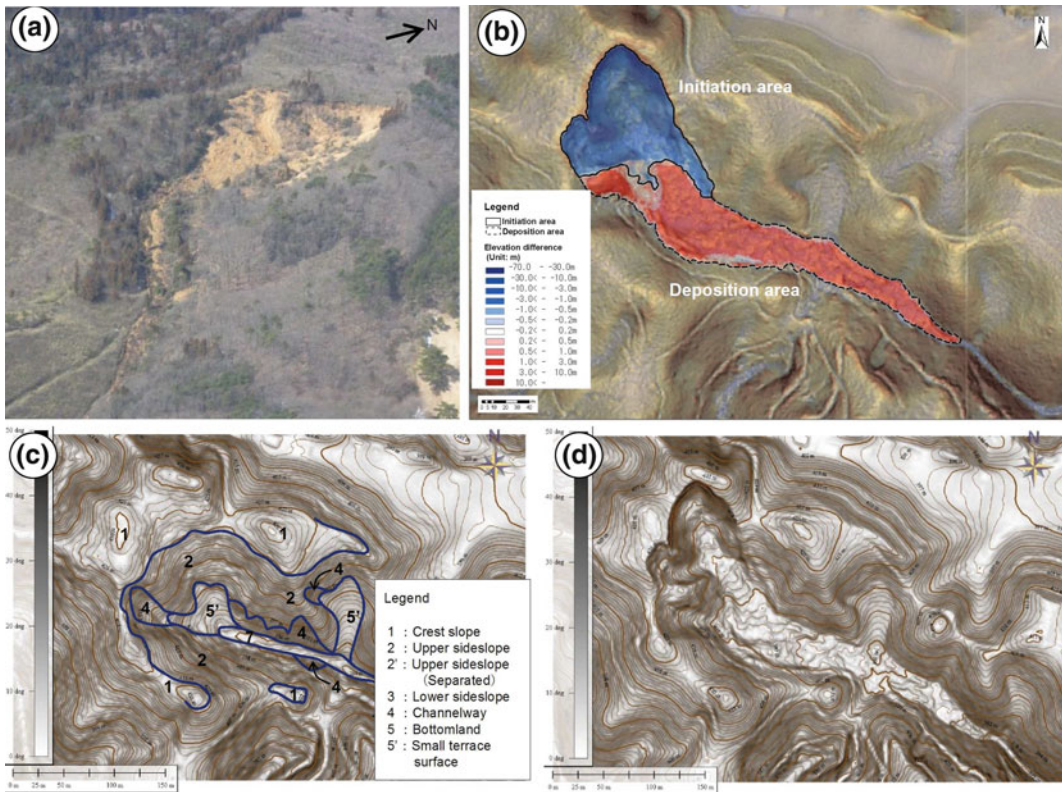
Fig. 20.4 Dougasaku (Yabeya) area: **a** An oblique aerial photograph. **b** Elevation difference map. **c** Topographic map before the earthquake with microtopographic slope-classification. **d** Topographic map after the earthquake

4.6   Okanouchi Area

This landslide had a maximum length and width of 70 (L1) and 50 m (W1), respectively. The displaced soil mass as a result of the landslide moved a maximum distance of 105 (L2), and the deposits stacked and covered a wide area with a maximum width of 80 (W2); one person was killed, and serious damage and destruction of one house occurred. The length and width ratios are L2/L1 = 1.5 and W2/W1 = 1.6. The main scarp has a horseshoe shape with a maximum height difference of 10 m.

The landslide initiation area (zone of depletion) is located on a south-facing ridge slope with an inclination of 20–30°. The slope on which the landslide occurred did not present clear features of landslide topography (Fig. 20.7). Linear depressions (valley-shaped) can be identified on the lateral slopes, running parallel to the axis of the slope of the landslide. The depressions were observed in the field survey; based on their location and morphological features, they are thought to be remnants of previous slope-failure scarps. The accumulation condition of the soil mass at the toe was indistinct because it was previously removed at the time of the survey. The LP map also shows the resulting artificial topography.

5   Survey Results

5.1   Relationship Between Landslide Initiation Areas and Microtopographic Slope Classification

At four of the study sites (other than those of Bandou area and Okanouchi area), the landslide has occurred in the area extending from the crest of the valley side slope to the upper knick line.
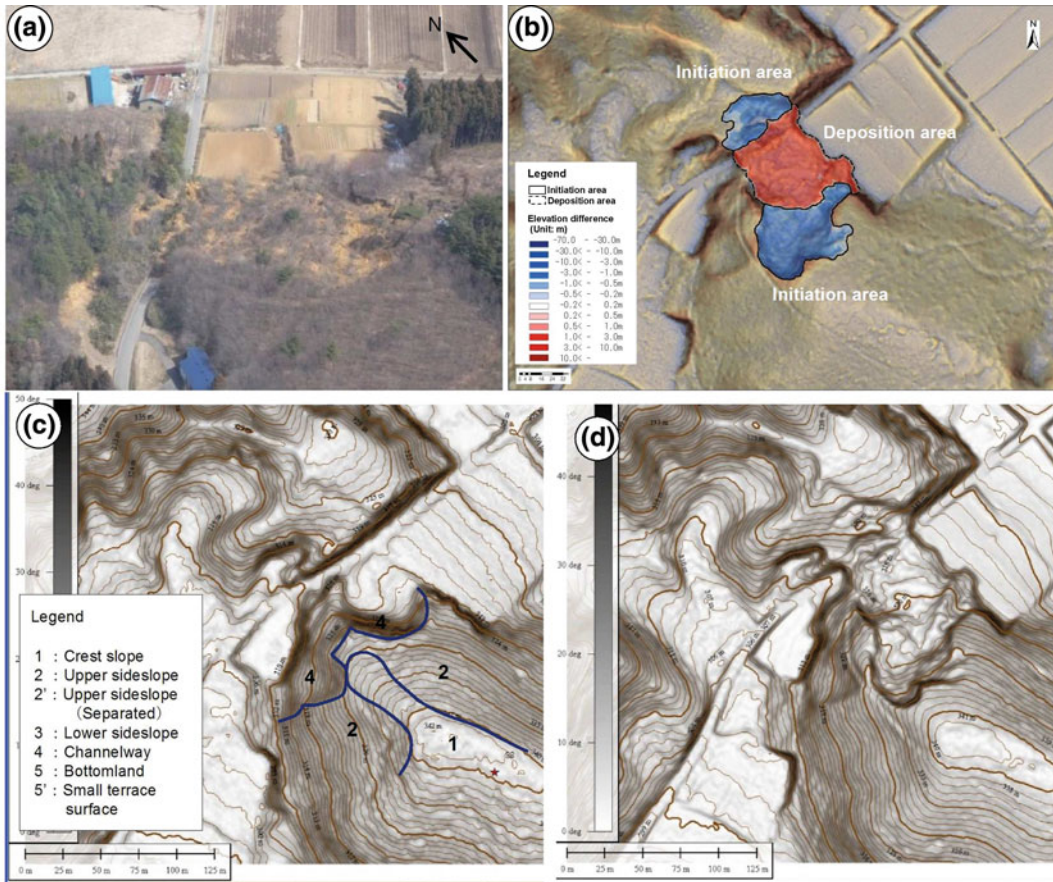
Fig. 20.5 Bandou area: **a** An oblique aerial photograph. **b** Elevation difference map. **c** Topographic map before the earthquake with microtopographic slope-classification. **d** Topographic map after the earthquake

In Bandou and Okanouchi areas, the landslides occurred in the middle of the slope; however, the landslides in these two areas also were initiated in the areas that comprise knick lines, from the shallow slopes to steep slopes, as in the case of the other landslides. Therefore, at all the landslide sites, the landslides were initiated in the convex slopes (longitudinal shape) that comprise the knick lines.

In upper sideslope of the landslide initiation areas, as can be identified from the contour lines, both the longitudinal and transverse shapes of the upper sideslope are characteristically almost linear.

All of the landslides had a long run-out distances. The Kitanoiri landslide had the greatest L2/L1 ratio of 2.7 and that in Bando had the smallest ratio of 1.1. The Dougasaku landslide had the greatest run-out distance of 265 m. Unlike the Dougasaku and Ushishimizu landslides, which flowed only through the valley, the other landslides all have W2/W1 values greater than 1, and their soil mass spread outward as the mass flowed downslope.

5.2   Stratigraphic Horizon for Surface of Rupture

At the crest slopes and upper sideslopes where the landslides occurred, a thick deposit of the brown volcanic ash soil was observed (the thickness of the deposit was approximately
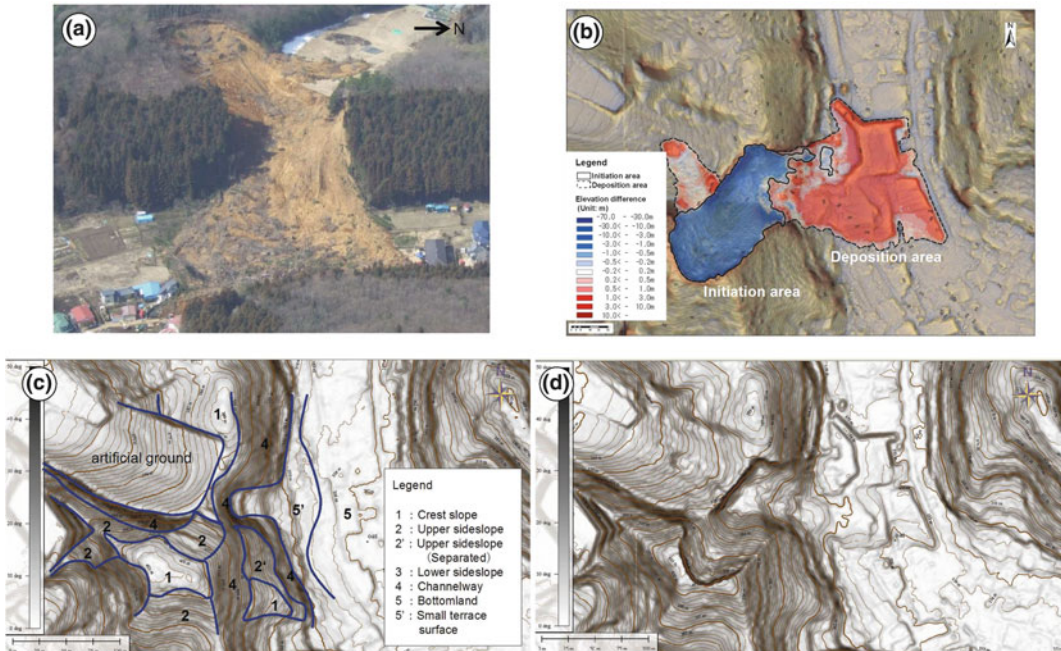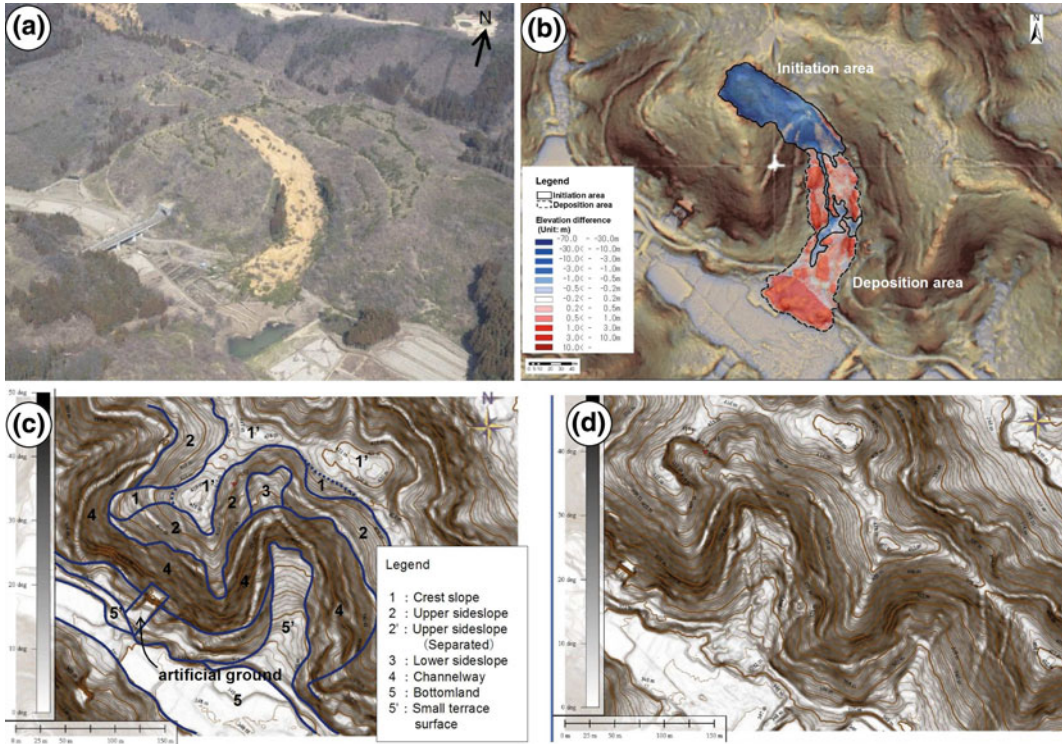
Fig. 20.6 Kitanoiri area: **a** An oblique aerial photograph. **b** Elevation difference map. **c** Topographic map before the earthquake with microtopographic slope-classification. **d** Topographic map after the earthquake

3.5–6.0 m near the main scarps). The brown volcanic ash soil layers comprised several tephra layers, which consisted of scoria, pumice, and similar materials. Based on the constituents, sedimentary facies, and stratigraphy, it is considered that these correspond to Sr8–Sr11 (tephras of the Nasu Volcano) and TkP (Takaku Pamice) of Suzuki (1992). However, in Okanouchi area, it was not possible to identify tephra layers that had a clear physical relationship with the surface of the rupture; accordingly, the Okanouchi area is excluded from the following paragraphs that describe the survey results from the remaining five sites.

The comparison between the isopach map of tephra for the landslide initiation areas covered by this survey and that of areas around the surface of rupture was carried out (Fig. 20.8). The isopach map of tephra that had been identified in previous studies (Suzuki 1992; Yamamoto 1999) was used.

The eruption ages of TkP and Sr10 are estimated to be 330 and around 300 ka, respectively, and the time intervals between Sr8 and Sr11 are estimated to be less than 10 ka by Suzuki (1992). Volcanic ash between the tephra layers partly contain considerable amount of organic matter, suggesting active vegetation. No clear unconformity was observed between TkP and Sr8.

In Hanokidaira, the stratigraphic horizon (Fig. 20.9), which acted as the surface of rupture, was close to Sr10 in the main scarp, left-side cliff, and many other locations. Locally, however, horizons near TkP acted as the surface of rupture at some locations. Therefore, the rupture surface was not necessarily formed by a single, constant horizon. In Dougasaku area (main scarp) and Bandou area (main scarp), the rupture surface was closer to TkP, and in Ushishimizu area (main scarp), the brown volcanic ash layer lower than TkP formed the surface of rupture. In Kitanoiri area (main
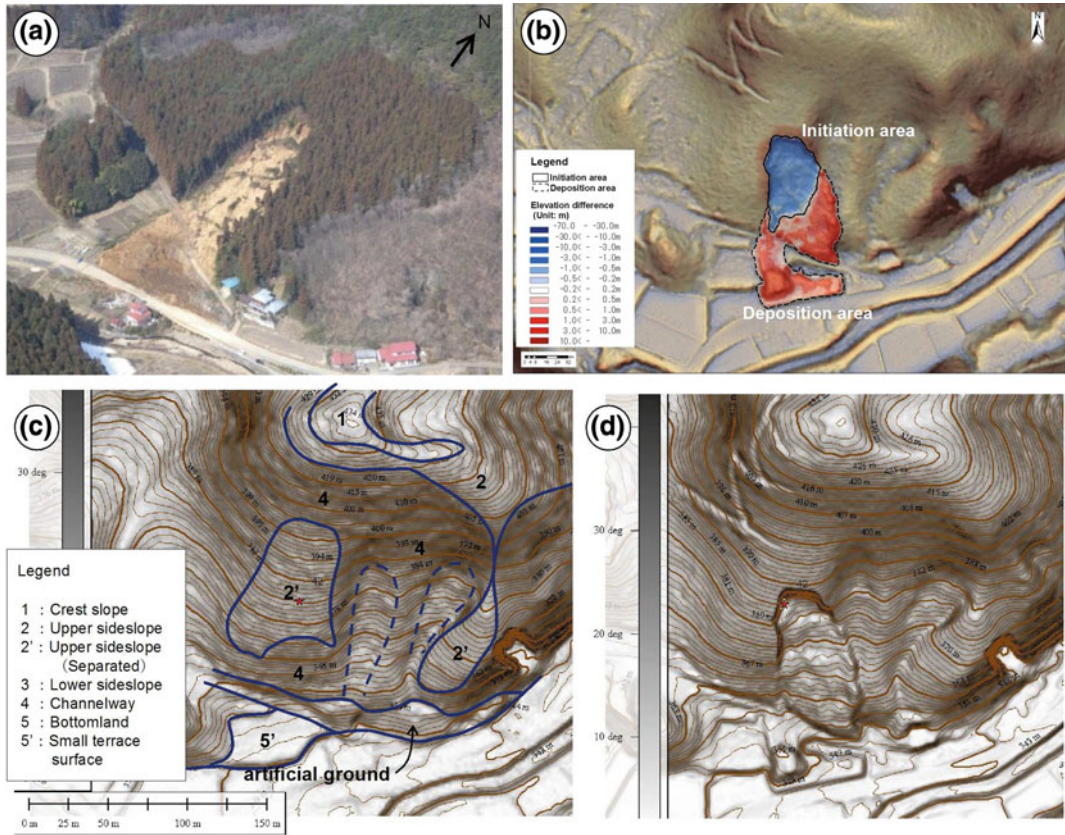
Fig. 20.7 Okanouchi area: **a** An oblique aerial photograph. **b** Elevation difference map. **c** Topographic map before the earthquake with microtopographic slope-classification. **d** Topographic map after the earthquake

scarp), the surface of rupture appeared to be situated between Sr8 and Sr9. In this way, whereas the stratigraphic horizons that acted as the surface of rupture are not always the same, the horizons, from Sr10 to TkP, typically act as the surface of rupture.

Tephra layers Sr9 or higher exhibit lesser degrees of weathering, and thus, they facilitate the observation of accumulation conditions and sedimentary facies. Kitanoiri is an exceptional case, in which Sr8 and Sr9 are partly weathered and the degrees of weathering highly fluctuate laterally. On the other hand, pumice and scoria at Sr10 or lower exhibit advanced weathering to the extent that they can be crushed manually, and thus, they exhibit argillation. The brown volcanic ash-layer soil is sandy in horizons

above Sr9 but clayey in horizons below Sr9, typically showing distinction between those horizons above and below Sr9.

5.3   Soil Properties Around the Surface of Rupture

Figure 20.10 shows examples of hardness profiles around the surface of rupture, measured by the Yamanaka type soil hardness tester. These commonly show that hardness values are high around Sr8 and Sr9, and then suddenly decrease below these horizons. It is suspected that there must have been a boundary near the surface of the rupture, around which hardness changes rapidly.
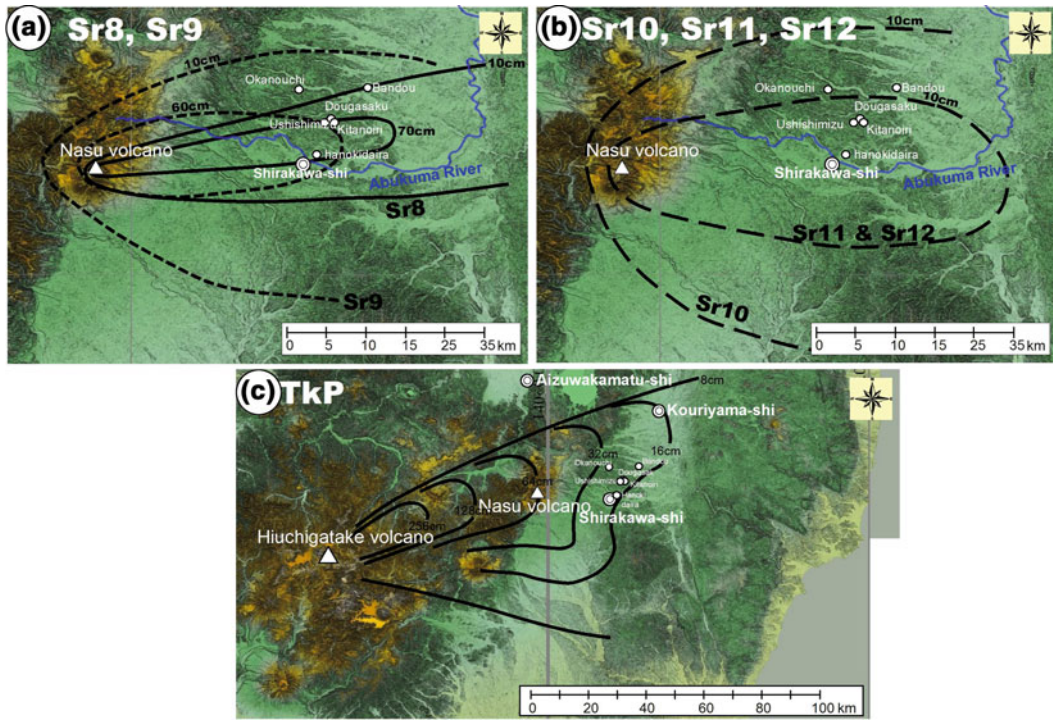
Fig. 20.8 Isopach map of tephra for landslide initiation areas and areas around the rupture surface
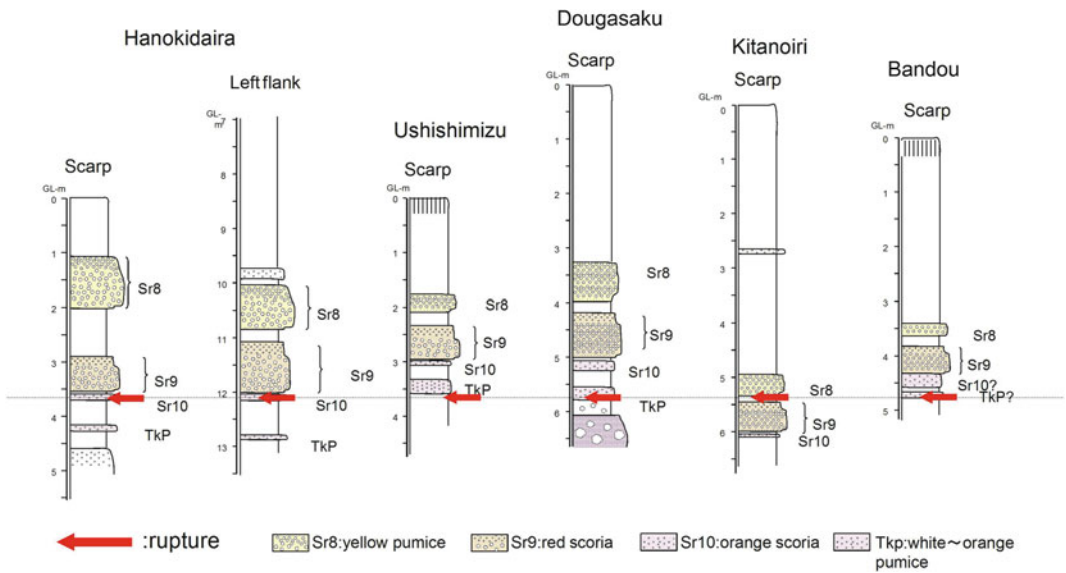
Fig. 20.9 Geological profile at the landslide sites
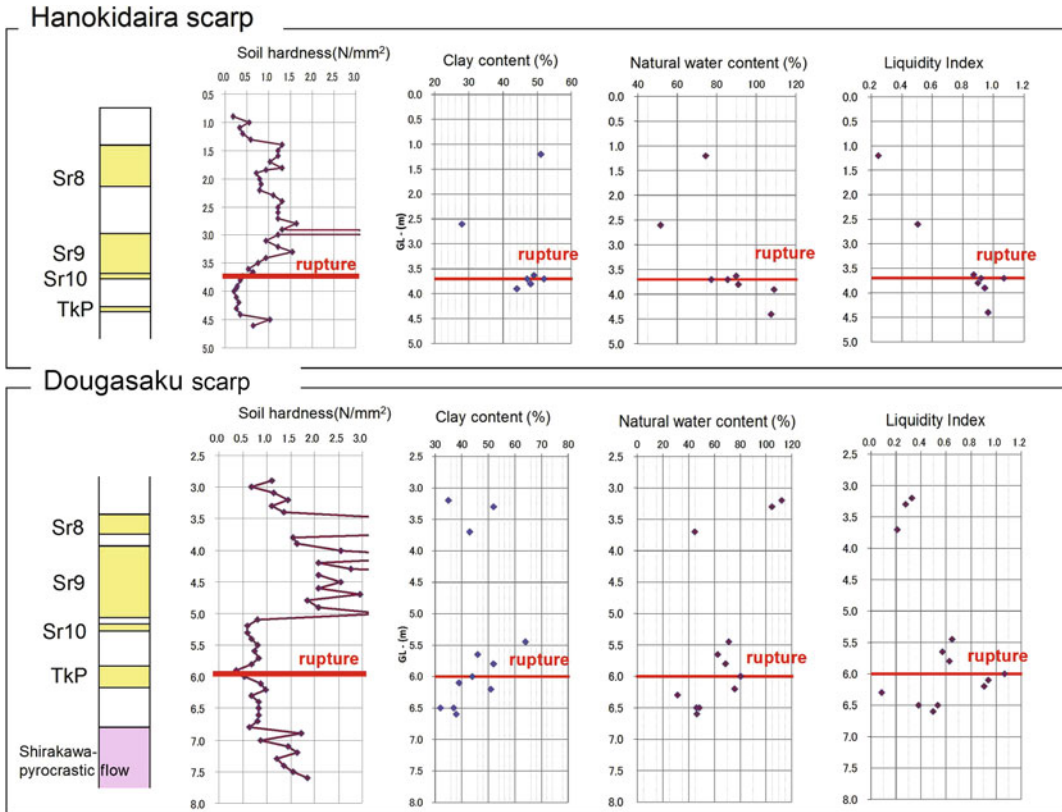
Fig. 20.10 Soil hardness profile on main scarps and side cliff

The test results for Hanokidaira area show that the physical properties of weathered tephra and brown volcanic ash soil, which acted as the surface of rupture, are characterized by higher clay content, natural water content, and liquidity index compared to the brown volcanic ash soil in the upper layer, forming soft and sensitive clay (Fig. 20.10). In the field survey, water was frequently observed seeping from the horizon near Sr10, which became the surface of rupture.

5.4   Tephra that Filled the Valley

At Hanokidaira area, the depths to Sr10 vary significantly; the maximum depths at the main scarp and the left side cliff are 5 and 13 m, respectively, and on the left-side cliff, tephra and other layers are accumulated with an inclination of 30°. Examination of Sr10 and TkP in the transverse direction confirmed that materials were accumulated along the rupture surface of the valley shape. Based on this observation, at the time of tephra deposition such as Sr10, the topography was similar to the surface of rupture that is presently exposed. It is considered that the tephra and the brown volcanic ash soil layer gradually deposited and formed shallow slopes. A similar accumulation structure was seen at Ushishimizu, Dougasaku, and Kitanoiri.

6   Conclusions

At all sites examined in this study, landslides were initiated at areas comprising the knick line. At four sites, landslides were initiated in areas

from the crest slope to the upper sideslope, according to the slope microtopographic classification. It is considered that this behavior was affected by the increase in seismic motion, because the longitudinal shape on the slope becomes convex at the knick line.

In the crest slope and upper sideslope, a thick deposit of volcanic ash was observed (the deposit thickness was approximately 3.5–6 m near the main scarps). The stratigraphic horizons for the rupture surface were typically from Sr10 to TkP. The horizon that became the surface of rupture exhibited argillation due to weathering.

The hardness profile around the rupture surfaces commonly show high hardness values around Sr8 and Sr9, and then, the values suddenly decrease below these horizons. The weathered tephra and brown volcanic ash soil at the surface of rupture were soft clay. Based on these observations, in addition to the weak strength from Sr10 to TkP, which became the surface of rupture, it is concluded that the earthquake caused the concentration of stress in the soft/hard boundary in Sr9 and Sr10, resulting in slope failure at the surface of rupture. It is also considered that as the failure surfaces were the tephra layers that had continuously accumulated on the slope, the nature of the slope-formations in the study areas contributed to triggering the landslides.

Comparison of the tephra isopach map of the landslide initiation sites with areas around the surface of rupture shows that the landslide initiation areas tend to be concentrated around the main axis of the tephra deposits for Nasu Volcano and the like. In particular, landslide sites were distributed where Sr8 and Sr9 near Shirakawa accumulate at greater thickness. The relationship with Sr10 or TkP is not clear. The soil bearing capacity is greater around Sr8 and Sr9; therefore, there is a possibility that, when Sr8 and Sr9 are accumulated thickly, a distinct soft/hard boundary can form, leading to concentration of stress.

The landslides examined in this study are characterized by displacement distances greater than the length of the slope on which the landslide was initiated, and by outward spread of soil mass. It is considered that the displacement distance increased because the landslides were initiated on the upper parts of the slopes (crest slope, upper sideslope) and because the materials moved down the steep slopes of the lower valley walls.

At Hanokidaira area, Sr10 and TkP were accumulated along the valley-shaped surface of the rupture. At the time of deposition of tephra layers, the topography was that of a valley, similar to that of the surface of rupture, on which the tephra and the brown volcanic ash soil layer gradually deposited and formed shallow slopes. It is also considered that the valley topography created a moist environment, which could have accelerated weathering of horizons below Sr10.

Tephra layers may accumulate thickly on some slopes near volcanoes. In such conditions, earthquakes may trigger landslides with deep-seated failure surfaces. It is important to predict possible sites of landslides, similar to that at Hanokidaira, which was triggered by earthquakes. Topographic interpretation can determine the locations of knick lines and slopes thickly covered by volcanic ash, which will enable the monitoring of continuous planes of soft clay layers, and the presence of boundaries between soft and hard soil. It is also considered that steep topography downslope of the landslide initiation area is important factor in long-distance displacement of soil mass.

References

Suzuki T (1992) Tephrochronological study on Nasu volcano. Bull Volcanol Soc Japan 37(5):251–263 (in Japanese)

Tamura T (1987) Landform-soil features of the humid temperate hills. Pedologist 31(2):135–146 (in Japanese)

Yamamoto T (1999) Plinian fall deposits in the Fukushima—Tochigi area during 0.3— 0.1 Ma: stratigraphy of marker tephra layers erupting from Numazawa, Hiuchigatake, Kinunuma, and Sunagohara volcanoes. Bull Geol Surv Japan 50(12):743–767 (in Japanese)

Yoshida H, Takahashi M (1991) Geology of the eastern part of the Shirakawa pyroclastic flow field. J Geol Soc Japan 97(3):231–249 (in Japanese)

A Long-Traveling Landslide in Deep Snow Conditions: A Case Study of the Tatsunokuchi Landslide Induced by the 2011 North Nagano Prefecture Earthquake

21

Shintaro Yamasaki and Hidehisa Nagata

Abstract

The 2011 north Nagano Prefecture earthquake (M_{JMA} 6.7) occurred in a deep snow area of Japan that typically has an annual snow cover of more than 2 m. The earthquake induced landslides involving abundant snow. We examined remnant topographies to deduce the landsliding process of one of these landslides, the Tatsunokuchi landslide, which occurred in deep snow conditions. The studied landslide had a displaced mass that included much snow, traveled a long distance, and damaged a wider area than conventional isometric landslides. Our results indicated the following landsliding process: the landslide occurred by the collapse of a rock mass of $5 \times 10^4 \text{ m}^3$, rock debris plunged into the abundant snow, a mixture of snow and rock debris formed, and the mixture then traveled on top of snow. Eventually, the displaced mass pushed out nearby snow and thus extended the damage area. The displaced mass having a relatively low proportion of debris probably had a low enough density to be buoyant and therefore easily traveled on top of snow. We estimated the velocity of the landslide using Lenau's method and obtained a maximum velocity of 14 m/s. Our observations and the clarified landsliding process suggest that landslides will damage a wider area than expected if they occur in deep snow conditions.

1 Introduction

Inland earthquakes in mountainous regions frequently induce high-velocity landslides. Several recent inland earthquakes, including the 2004 mid-Niigata Prefecture earthquake in Japan (Chigira and Yagi 2006; Wang et al. 2007) and

S. Yamasaki (✉)
Kitami Institute of Technology, Japan
e-mail: yamasaki@mail.kitami-it.ac.jp

H. Nagata
Fu-sui-do co., ltd, Japan

Fig. 21.1 Index map of the Tatsunokuchi landslide site
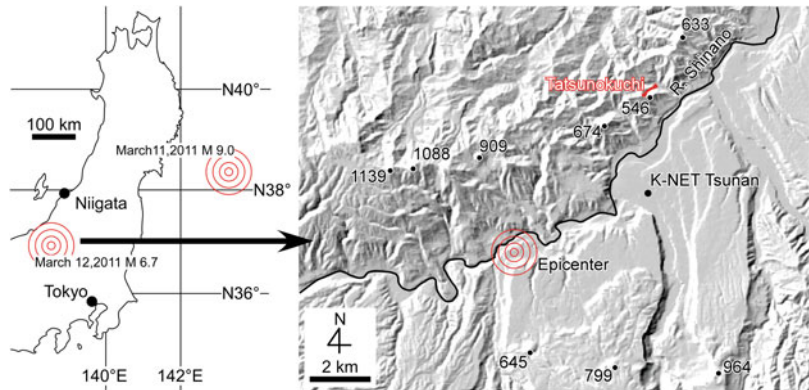
the 2008 Wenchuan earthquake in China (Chigira et al. 2010; Cui et al. 2011), produced many landslides. Snow avalanches may also be triggered by earthquakes, as occurred in the 1964 Alaska earthquake (LaChapelle 1968). Hence, landslides and snow avalanches may occur concurrently if earthquakes occur in deep snow regions. The region along the Sea of Japan is covered with deep snow for about 4 months each year and has experienced many earthquakes. This deep snow region has high potential for landslides and snow avalanches.

A thick snow layer made in one winter season is loose and unstable, is different from a glaciers. In such deep snow conditions, snow can cover mountain slopes and bases. If a landslide occurs, abundant snow on both the slope and base will move, potentially leading to widespread damage. However, there have been few opportunities to observe such complex hazards.

The 2011 north Nagano Prefecture earthquake occurred in central Japan during the snow season. The area was covered with more than 2 m of snow when the magnitude 6.6 (by the Japan Meteorological Agency [JMA] scale) earthquake struck, inducing several landslides and snow avalanches. These cases included landslides that involved snow, traveled long distances, and damaged wide areas. Because snow melts rapidly and topographies made of snow are lost to melting, we investigated these hazards promptly.

In this paper, we report details of topographies formed by the Tatsunokuchi landslide in Tsunami, Niigata, and also discuss the landsliding

process. Several terms used in the paper are defined as follows: A *displaced mass* is a mass of material of any composition that has been displaced by a landslide. *Rock debris* is rock that has been pulverized by landsliding. A *snowball* is a mass of snow that has been displaced by landsliding and has a spherical shape.

2 The 2011 North Nagano Prefecture Earthquake

The epicenter of this earthquake was located in Sakae, Nagano Prefecture (36°59′6″N, 138°35′49.2″E, Fig. 21.1), and the depth of the hypocenter was 8 km (JMA). Strong tremors occurred in Nagano and Niigata prefectures. The earthquake occurred 13 h after an earthquake located off the Pacific coast of Tohoku (M_w 9.0), and the events were likely related. According to data from the National Research Institute for Earth Science and Disaster Prevention (NIED), the maximum acceleration was 804 gal (three-component synthesis). The area around the epicenter is located at the north end of an active tectonic zone known as the Western Marginal Fault Zone of the Nagano Basin. The earthquake induced many landslides and snow avalanches, causing severe damage to infrastructure and isolating villages in mountainous areas. No deaths occurred as a result of the landslides or snow avalanches; however, three people died later as a result of earthquake-related disease.

Fig. 21.2 Results of the field survey of the Tatsunokuchi landslide. Figure after Yamasaki (2011)
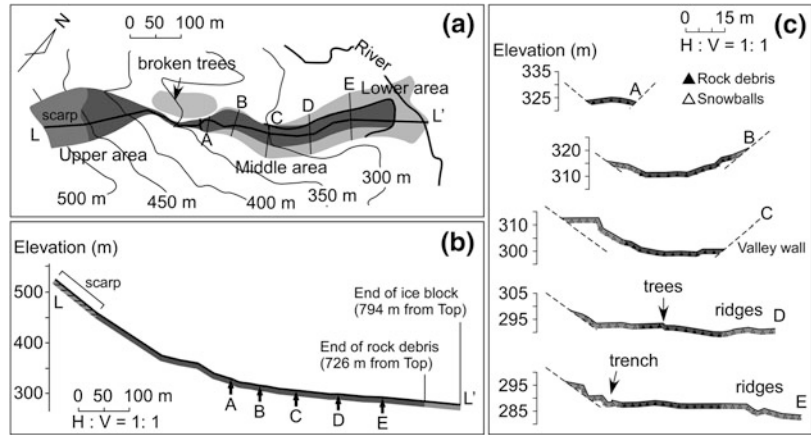
3   Geological and Meteorological Conditions

Most of the large landslides induced by the earthquake occurred in a mountainous area. The Tatsunokuchi landslide was also located within this area (Fig. 21.1). According to Takeuchi et al. (2000), the area consists of volcanic rocks and Pleistocene marine rocks that belong to the Uonuma Formation. A large number of landslides have occurred in the Uonuma Formation area (NIED 2004).

This area is a typical deep snow area of the Sea of Japan region. The annual maximum snow depth is 3–4 m. On March 12, when the earthquake and landslides occurred, 227 cm of snow was measured at the Tunan meteorological station (36°59.8′N, 138°41.0′E). We measured 2.3 m of snow at the road near the Tatsunokuchi landslide on March 17. Because approximately 30 cm of snowfall occurred from March 12 to 17, about 2 m of snow likely covered the Tatsunokuchi site just before the landslide occurred. There had been no significant temperature increases or rainfall during the 10 days before the landslide.

4   Survey Methods

On the day after the earthquake, Asia Air Survey Co., Ltd. and Niigata Prefectural Government took pictures of the Tatsunokuchi landslide from the air. We used these aerial photos and topographic maps to analyze the topography. We then visited the site on March 17 and began investigating. The site of the landslide was accessible in spite of deep snow and traffic disruptions.

5   General Description of the Tatsunokuchi Landslide

The collapsed rock mass was 150 wide and 70 high, with an average thickness of 5 m and a volume of 5×10^4 m^3. Sandstone, mudstone, conglomerate, and pyroclastic rocks were exposed on the scarp, and these rocks were either fresh or weakly weathered. The rock mass separated along some noncontiguous joint planes. These joint planes had attitudes that were roughly vertical and cut across bedding planes. We obtained a longitudinal cross-section and lateral cross-sections by a field survey. The vertical distance from top to toe of the landslide was 245, and the horizontal distance was 795 m (Fig. 21.2).

The displaced mass buried rice plants, a channel, and a road. It also destroyed a shed that was about 700 from the top and carried shed material approximately 50 m from its original position (Fig. 21.3a). The displaced mass totally covered the bottom of a valley and the underlying deep snow. Many depressions formed on the covered area during summer as a result of melting snow.

Fig. 21.3 Photographs of topographies suggesting the landsliding processes: **a** A panoramic view from the air (taken by the Niigata prefectural government, March 12, 2011). **b** Broken trees leaning downstream in the upper area (March 29, 2011). **c** Super elevation at the right side of the valley in the upper area (March 17, 2011). **d** A trench at the right side of the middle area (March 17, 2011). **e** Standing trees on rock debris in the middle area (March 17, 2011), and (**f**) columnar ridges in the lower area (March 12, 2011)
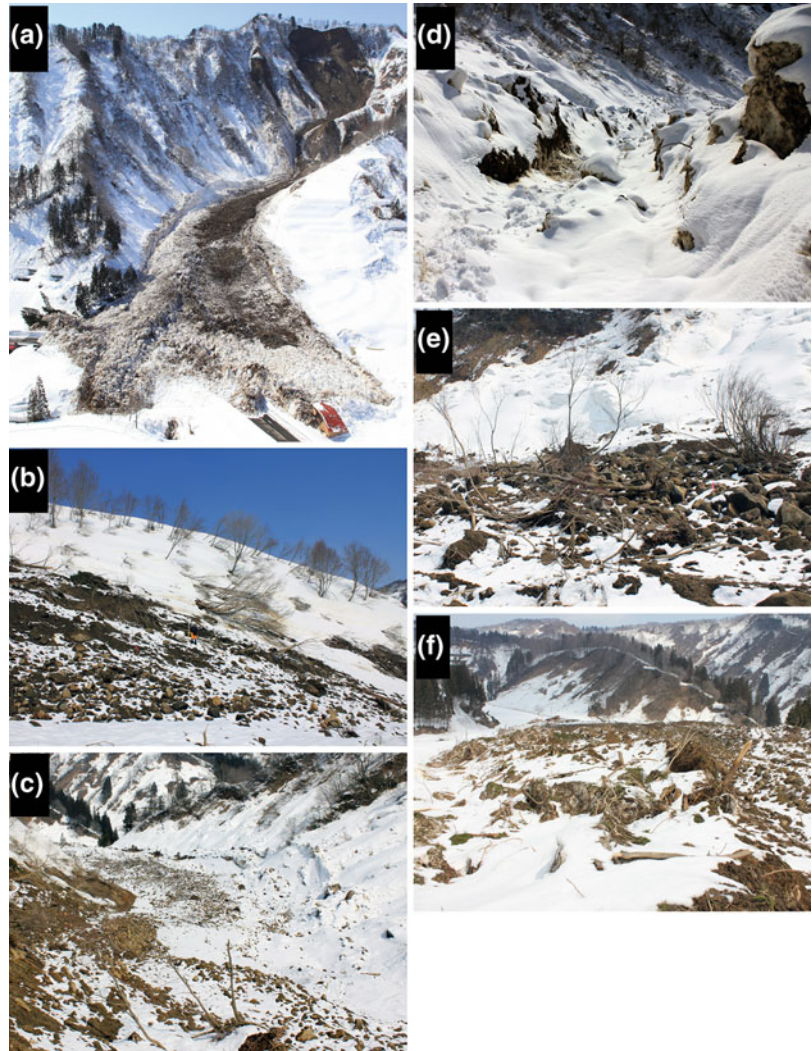
6 Landforms and Structures

To deduce the landsliding process, we observed topographies formed by the landslide. We divided the landslide site into three areas: the upper area, middle area, and lower area (Fig. 21.2). The upper area had scarps and traces marking surface denudation related to the displaced mass, the middle area was partly buried by displaced mass having a smooth surface, and the lower area included a region of displaced mass with swells (e.g., ridges). For ease of understanding, we will describe the landslide topographies within these three divisions.

6.1 Upper Area

The area beneath the scarp consisted of steep slopes of about 30° (Fig. 21.2b). As shown in Fig. 21.3a, the path of the displaced mass was marked by a trace of surface denudation. The trace had a winding pattern because an approximately 5-m ridge interrupted the slide.

6.2 Middle Area

The middle area had a moderate downstream slope of about 10° (Fig. 21.2b). Cross-sections through the displaced mass varied depending on

the width of the valley. The uppermost cross-section (A) was a convex layer of rock debris. The lower cross-sections (B and C) were concave (Fig. 21.2c). The outer part of the displaced mass consisted of a number of semi-solidified snowballs that were generally less than 3 m in diameter. The area containing the snowballs became wider with decreasing elevation. The area also included small amounts of rock debris and plants. Each snowball was stained by fine sediment (smaller than sand) on its outer surface but was clean on the inside.

In the upper part of the middle area, some broken and leaning trees were on the left side of the valley wall (Figs. 21.2a and 21.3b). Most of the trees near the displaced mass were broken. Small trees were broken irrespective of distance from the displaced mass. The broken trees leaned in the downstream direction of the landslide. However, in situ snow that covered the slope with trees was not disturbed and was covered thinly by fine sediment.

The displaced mass had a winding shape along the valley. Thick aggregations of snowballs occurred along the outer sides of the curves, and the displaced mass was higher at the outer sides of meanders than at the inner sides. Cross-section C in Fig. 21.2c shows a corner where the displaced mass curved left. The aggregation at the right side of cross-section C was 12.7 m thick (Fig. 21.3c).

A 450-m-long bank with snowballs was observed on the right valley wall. This bank had a nearly vertical cliff that faced into the valley. An 80-m-long trench having a maximum width of 3 m and a maximum height of 2.5 m ran along the bank (Fig. 21.2c cross-section E; Fig. 21.3d). The interior of the bank was exposed in this trench. We removed 10 cm of the stained surface by hand excavating and exposed the fresh interior structure of the displaced mass. This stripped outcrop contained two facies. The top facies consisted of clasts and matrix. The matrix contained ice with fine sediment, and the clasts consisted of snowballs, rock debris, and plant material. The bottom facies was in situ layered snow (Fig. 21.4a). Snowball clasts in the top facies consisted of

iced snow and soft snow. Some of the soft-snow clasts had ice margins (Fig. 21.4b). The bottom facies was mostly soft layered snow, but some parts consisted of pale brown, iced snow that included clay. The pale brown parts connected with the matrix of the upper facies (Fig. 21.4a).

The surface of the displaced mass was smooth except for some extremely large debris. Some trees stood undamaged at the position of the displaced mass, which was 650 m in horizontal distance from the top of the scarp (Fig. 21.3e).

6.3 Lower Area

The displaced mass had a number of ridges at its front and sides (Figs. 21.3a, f). These ridges had cylindrical tops (Fig. 21.2c, cross-sections d and e), and their shapes were different from the shape of the bank described above.

7 Landsliding and Formation of Topographies

In this section, we describe the important processes of the landsliding on the basis of observed topographies.

7.1 Upper Area

This area was characterized by source material and denudation. Rock debris produced by the collapse of the slope descended and denuded the surface along its path. The slope down which the rock debris descended was steep (about 30°; Fig. 21.2a), which probably allowed the rock debris to accelerate.

7.2 Middle Area

This area was characterized by transportation and deposition. Rock debris first plunged at high velocity into anterior deep snow on a moderate slope. The presence of broken trees and the thin deposition of fine fragments on the in situ snow

Fig. 21.4 An outcrop exposed on the wall of the trench and its structure: **a** A photograph of the outcrop and a detailed sketch of the photograph (March 19, 2011) and (**b**) a close-up view of square B in photograph A. *S* indicates soft snow and *H* indicates hardened iced snow
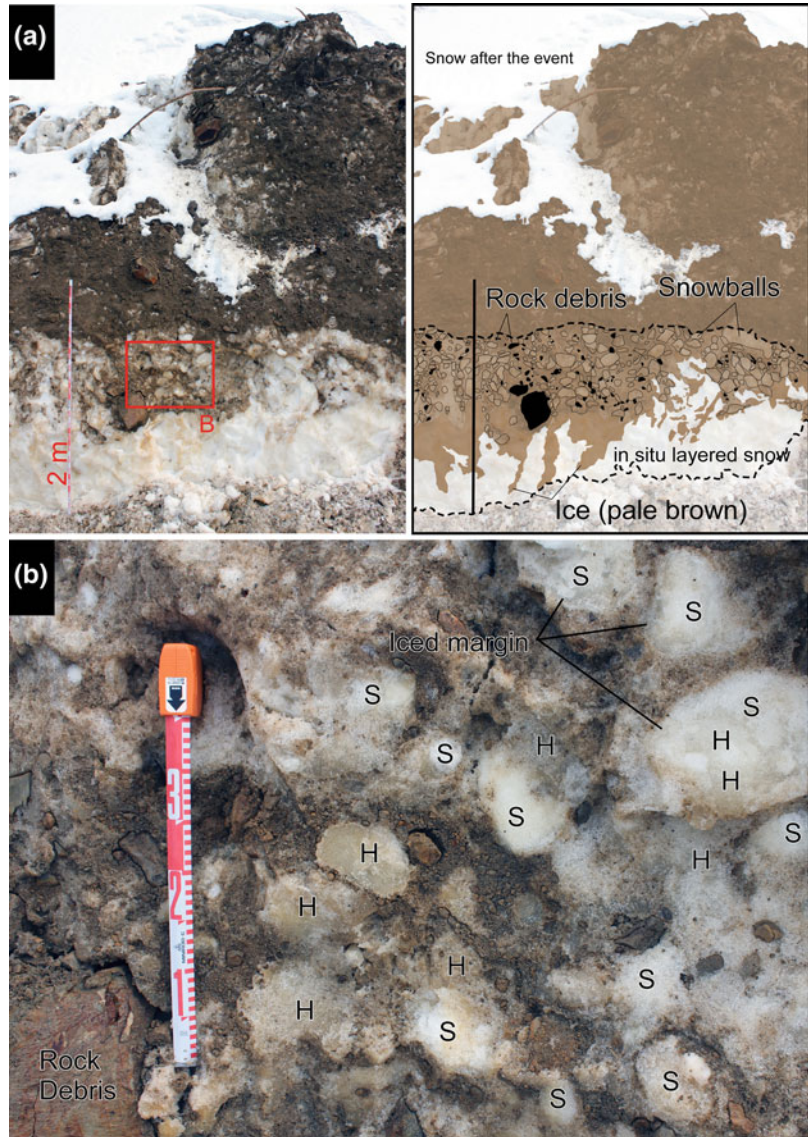
suggest that extremely strong wind blew here (Fig. 21.3b). The wind was probably formed by the intense impact of the landslide. Snowballs were probably formed during this process.

The displaced mass wound its way along the valley, and thick aggregations of snowballs formed at the high positions on the outer sides of meanders (Fig. 21.3c). The displaced mass was higher at the outer sides than at the inner sides (Fig. 21.2, cross-sections b and c). This phenomenon, known as *super elevation* (Takahashi 2007), is common in debris flows and suggests a

fast current of displaced mass. Following slide material then eroded the valley side of the bank and formed a nearly vertical cliff face.

In the lower region, a bank with snowballs was on the right valley wall and there was a trench along that bank (Fig. 21.3d). The displaced mass probably collided with the right valley wall and then turned toward open space to the left (Fig. 21.2a). This process then caused tension, and a trench with a vertical inside cliff formed.

The displaced mass gained in situ snow at its front end.

7.3 Lower Area

This area was characterized by deposition and bulldozing. The displaced mass pushed in situ snow, forming ridges with cylindrical tops by horizontal compression (Figs. 21.3a, f).

8 Mobility of the Landslide

The Tatsunokuchi landslide traveled a long distance. The angle of elevation (or angle of apparent friction, $\tan^{-1}$H/L) of the landslide, which can be used to estimate its mobility, was 17.1°, which is much lower than that for landslides that occur under dry conditions, such as many earthquake-induced landslides. Except for extremely large events, the angles of elevation of dry landslides are expected to approximately equal the angles of repose, which range from 30 to 40°. For example, landslides induced by the 2008 Wenchuan earthquake formed talus with high angles (e.g., Yin et al. 2009). If much water exists around a landslide, the landslide can travel long distances as a debris flow. However, the topographies of the Tatsunokuchi landslide did not wash out and the slide did not become a debris flow. Therefore, we must consider how the Tatsunokuchi landslide traveled such a long distance.

First, we propose that the displaced mass traveled on snow. Figure 21.4 shows that the run-up of the displaced mass occurred on in situ snow. Some standing trees were observed in rock debris 650 m away from the top of the slide (Fig. 21.3e). These findings suggest that the rock debris and snowballs did not rotate or separate from each other but descended as one rigid body. In addition, the displaced mass slid along the ground surface. Because the displaced mass moved as one rigid body, it formed a long trench and bulldozed long ridges. Such slide movement suggests that a low-friction substance existed at the bottom of the displaced mass.

There were many snowballs (e.g., Fig. 21.3a) at the front end and lateral sides of the displaced mass. Such snowballs also form in wet snow

avalanches (Jomelli and Bertran 2001). The angles of elevation of snow avalanches are smaller than those of landslides. For example, cases of snow avalanches reported by Buser and Frutiger (1980) ranged from 9 to 19°. We found that the clast and matrix facies (Fig. 21.4) can be explained as a mixture of snowballs and rock debris. Because the clasts do not have fine sediment inside, each clast resembles a snowball. The bulk density of the mixture was probably lower than that of rock debris, and thus the mixture could have become buoyant on the snow.

The structure of the bottom of the displaced mass (Fig. 21.4) suggests that another phenomenon also may have allowed the slide to travel a long distance. The bottom of the displaced mass was temporarily liquefied. The top facies, as shown in Fig. 21.4a, was the matrix and clast facies. The matrix consisted of ice with fine sediment, which suggests that it was once liquefied and then refroze later. If no liquid water were present, it would be difficult to explain why both hardened snow clasts and soft snow clasts retained spherical forms in the same facies and why some soft snow clasts had ice margins. Shear forces do not exist in liquid. In addition, the fact that regions of pale brown iced snow formed within the in situ snow layer means that liquid water penetrated the in situ layer. The liquid water could have reduced the friction between the displaced mass and the in situ snow and thereby caused high mobility. Groundwater, ground temperature, frictional heating, and/or pressure melting might contribute to the existence of water. However, we cannot discuss these factors from our present study. Further research is needed to clarify this problem.

9 Velocity of Landslides

The velocity of a landslide is important for estimating its destructiveness. The Tatsunokuchi landslide must have made strong winds. Some trees were broken by strong wind (Fig. 21.3b) in the middle of the area. One of these broken trees had a trunk diameter of 15 cm. Applying the
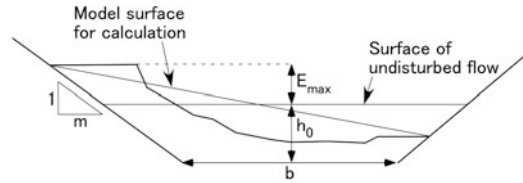
Fig. 21.5 A cross-section showing parameters for the velocity calculation

Beaufort scale for estimating wind velocity, a wind that brakes branches indicates a number 8 (17.2–20.7 m/s) or higher on the scale. However, for a 15-cm trunk to have broken, stronger winds must have blown.

To deduce the velocity of the landslide, two topographic features should be taken into account. The first is the ridge that was beneath the scarp. This ridge was approximately 5 m high. It blocked rock debris from the scarp and bent the slide so it did not overflow it. Hence, taking the coefficient of dynamic friction to be equal to 0 and the acceleration of gravity (g) to be 9.8 m/s^2, we can apply the following relationship:

$$v = (2gh)^{1/2} \qquad (21.1)$$

Thus, we deduced a velocity (v) of up to 10 m/s (36 km/h) at the bottom of the passage beneath the scarp.

The second topographic feature is the super elevation that occurred where the valley and displaced mass curved. Lenau (1979) proposed a method for estimating the height of crests along an outer edge where a bending flow passes through a trapezoidal cross-section. The method was then verified experimentally (Ashida et al. 1981; Takahashi 2007). Lenau's formula is

$$E_{max} = (2mh_0 + b)U^2/2r_0g, \qquad (21.2)$$

where E_{max} is the maximum elevation of the outer edge from the surface of the undisturbed flow, m is the reciprocal of the side slope of the channel cross-section, h_0 is the center line depth of the undisturbed upstream flow, b is the base width of the trapezoidal cross-section, U is the velocity of the undisturbed flow, and r_0 is the center line radius of curvature of the bend

(Fig. 21.5). Here, we rearrange Eq. 21.2 by solving for U and then obtain

$$U = [2r_0gE_{max}/(2mh_0 + b)]^{1/2} \qquad (21.3)$$

Because we could not know the thickness of the displaced mass when it passed through the cross-sections, we took h_0 as the distance from the bottom of the displaced mass to the intermediate height between both of its sides. Our field survey results for cross-section C (Figs. 21.2a, c) provided the following parameters: $E_{max} = 6$ m, m = 1.3, $h_0 = 10$ m, b = 30 m, and $r_0 = 100$ m. We thus calculated that the velocity of the displaced mass (U) at cross-section C was approximately 14 m/s. Therefore, we deduced that the velocities of flow of the Tatsunokuchi landslide were 10 m/s in the upper area and 14 m/s in the middle area.

Although the two estimated velocities were derived by different approaches, their values are close and the value at the lower position was higher, so our estimates seem reasonable. According to the classification of Cruden and Varnes (1996), these velocities are in the highest class (7), indicating that this landslide was highly dangerous.

10 Summary and Implications for Future Landslide Hazards

The Tatsunokuchi landslide involved abundant snow, and the snow contributed to its high mobility. The mixing of snow and rock debris formed a low-density displaced mass that could travel a long distance on snow. The maximum velocity of the landslide was 14 m/s, which suggests the high level of danger posed by this

landslide. In addition, this landslide created a hazardous area that was more spread out than that of an isometric landslide without snow. Inland earthquakes generally induce many landslides. If these landslides occur in deep snow conditions, the landslides may be more destructive than expected.

References

Ashida K, Takahashi T, Arai M (1981) Study on debris flow control (2); debris flow in bends of rectangular section: annual report of the Disaster Prevention Research Institute, Kyoto University, pp 251–263 in Japanese with English abstract

Buser O, Frutiger H (1980) Observed maximum run-out distance of snow avalanches and the determination of the friction coefficients μ and ξ. J Glaciol 26:121–130

Chigira M, Wu X, Inokuchi T, Wang G (2010) Landslides induced by the 2008 Wenchuan earthquake, Sichuan, China: Geomorphology, vol. 118, nos. 3–4, pp 225–238

Chigira M, Yagi H (2006) Geological and geomorphological characteristics of landslides triggered by the 2004 Mid Niigta prefecture earthquake in Japan. Eng Geol 82(4):202–221

Cruden DM, Varnes DJ (1996) Landslide types and processes. In: Turner AK, Schuster RL (eds) Landslides—investigation and mitigation. Transportation Research Board Special Report, vol. 247. National Academy Press, Washington, pp 36–75

Cui P, Chen X-Q, Zhu Y–Y, Su F-H, Wei F-Q, Han Y-S, Liu H-J, Zhuang J-Q (2011) The Wenchuan earthquake (May 12, 2008), Sichuan Province, China, and resulting geohazards. Nat Hazards 56(1):19–36

Jomelli V, Bertran P (2001) Wet snow avalanche deposits in the French Alps: structure and sedimentology: Geografiska Annaler: series A, physical geography, vol. 83, nos. 1–2, pp 15–28

LaChapelle ER (1968) The character of snow avalanching induced by the Alaska earthquake: The Great Alaska Earthquake of 1964. Hydrology, vol. 3, part A, pp 355–361

Lenau CW (1979) Supercritical flow in bends of trapezoidal section. J Eng Mech Div 105(1):43–54

NIED (National Research Institute for Earth Science and Disaster Prevention) (2004) Landslide distribution map of Matunoyamaonsen Sheet Map at 1:50000 in Japanese

Takahashi T (2007) Debris flow: mechanics, prediction and countermeasures, Routledge

Takeuchi K, Yoshikawa T, Kamai T (2000) Geology of the Matsunoyama Onsen district. With geological sheet map at 1:50000, geological survey of Japan, p 190 in Japanese with English abstract

Yamasaki S (2011) A long traveled mass movement induced by the North Nagano earthquake. Japan Soc Eng Geol Annu meet 26:51–52

Wang H, Sassa K, Xu W (2007) Analysis of a spatial distribution of landslides triggered by the 2004 Chuetsu earthquakes of Niigata prefecture Japan. Nat Hazards 41(1):43–60

Yin Y, Wang F, Sun P (2009) Landslide hazards triggered by the 2008 Wenchuan earthquake, Sichuan, China: Landslides, vol 6, no. 2, pp 139–152

Re-Evaluation of Factors Controlling Landslides Triggered by the 1999 Chi–Chi Earthquake

22

Chyi-Tyi Lee

Abstract

Landslides triggered by the 1999 Chi–Chi earthquake were re-mapped from high-resolution SPOT images taken before and after the quake. Their distribution was studied and landslide controlling factors statistically analyzed. Slope gradient, relative slope height, total slope height, closest distance to fault-rupture plane, and Arias Intensity were the most significant factors affecting landsliding. Earthquake-induced landslides were most common on longer and steeper slopes, and occurred at a high position on the slope. Most landslides were concentrated in the regions with peak ground accelerations exceeding 250 gals.

1 Introduction

At 1:47 a.m. local time on September 21, 1999, a shallow M_W7.6 earthquake struck central Taiwan rupturing the Chelungpu fault. The hypocenter was 8 km below the village of Chi–Chi. The main shock severely shook the entire island of Taiwan (Ma et al. 1999; Kao and Chen 2000) causing considerable structural damage and triggering thousands of landslides.

Rapid mapping of landslides from SPOT images for the whole of Taiwan was carried out by Liao and Lee (2000). They documented 9,272 larger landslides of various types (with areas >625 m^2) with a total area of 127.8 km^2. Wang et al. (2002), based on interpretation from aerial photos of the meizoseismal area in central Taiwan, recognized more than twenty-thousand landslides. Factors controlling the earthquake-induced landslides were evaluated by Khazai and Sitar (2003) based on a preliminary landslide inventory. The satellite images used in my work in 2,000 were not at a high resolution and were analyzed in a hurry, so we re-mapped the earthquake-induced landslides from high-resolution SPOT images, and checked using aerial photo-pairs from 2003 to 2008. Landslide types were

C.-T. Lee (✉)
Graduate Institute of Applied Geology, National Central University, Taiwan, No. 300, Jhongda Rd, Jhongli City, Taoyuan County 32001, Taiwan
e-mail: ct@ncu.edu.tw

recognized, deposit areas were separated, and a GIS database was built.

This paper describes the landslide mapping, presents an overview of landslide distribution, basic statistics of factors associated with the landslides, and interpretation of effective factors controlling the landslides. We also discuss the characteristics of the earthquake-induced landslides, which provide insight into where and why earthquake landslides occur.

2   Regional Setting

The island of Taiwan has an area of 36,000 km^2. The highest peak is Yushan, which is 3,952 m above sea level, and numerous other peaks rise to over 3,000 m. Taiwan is tectonically active, as it is in the collision zone between the Asiatic continent and the Luzon Arc (Teng 1990). Active crustal deformation (Bonilla 1975; Yu et al. 1997), frequent earthquakes (Tsai et al. 1977; Wu 1978), numerous typhoons and a high erosion rate (Dadson et al. 2003) presently affect the region.

The island has a north–south running backbone range, surrounded by foothills and coastal plains. Geologically, the range has a metamorphic core, surrounded by slate formations, and fold-and-thrust Neogene sedimentary strata. The Chelungpu fault, which ruptured during the Chi–Chi earthquake, is a thrust fault in the fold-and-thrust belt. A coastal plain and gentle slopes lie to the west of the fault, and hills and high mountains to the east. The majority of the earthquake-induced landslides were located east of the fault.

The climate in Taiwan area is subtropical, with an average annual precipitation of about 2,500 mm. No significant precipitation was observed within 1 month before and for a half month after the Chi–Chi earthquake, simplifying the study of earthquake-induced landslides.

3   Methodology

In this study, we used SPOT satellite images and aerial photographs to identify the landslides, and MapInfo GIS software to digitize their location

and extent. Spatial distribution, as well as numbers and areas of landslides triggered by the Chi–Chi earthquake, were then mapped. Spatial functions in GIS were used to analyze the relationships between the landslide distribution and factors associated with the landslides. Erdas Imagine system was used to process DEM and derive topographic factors for statistics. Strong-motion data were processed using a standardized method by FORTRAN code, and the ground-motion values were interpolated on each grid point in the study area using ordinary Kriging.

3.1   Methods for Evaluating the Effectiveness of a Factor

If a factor can be used to interpret the landslide spatial distribution to some extent, this factor is an effective factor. We propose three different methods to evaluate the effectiveness of a factor. For any given factor, the data set is divided into a *landslide* group and a *non-landslide* group for analysis. Theoretically, if the two groups have almost no intersection and can be easily separated, then this factor should be a perfectly effective factor. If the percentage of landslides increases or decreases with the factor score, then this factor is considered an effective factor.

Flat areas and gentle slopes where the slope gradient is <10 % with an area >1 ha are regarded as stable and were not included in either the *non-landslide* or *landslide* groups. Stable areas were not included in the analysis.

Difference Between *landslide* and *Non-landslide* Groups

The difference between two groups can be visually inspected by plotting the frequency distribution of the two groups and quantified by computing a standardized difference *D* (Davis 2002) from which the effectiveness of a factor as discriminator can be determined:

$$D_j = \frac{\bar{A}_j - \bar{B}_j}{S_{Pj}}, \qquad (22.1)$$

where $\bar{A}_j$ is the mean of factor j for group A (landslide); $\bar{B}_j$ is the mean of factor j for group B (non-landslide); S_{Pj} is the pooled standard deviation of factor j; and D_j is standardized difference of factor j. The larger the standardized difference, the more effective the factor.

Before calculating the standardized difference of a factor, a test of normality is required. A standardized difference value for evaluation is valid only for a normal distributed data set.

Correlation Between Landslide Ratio and the Factor Scores

An effective factor should be correlated with the proportion of landslide cells (Jibson et al. 2000) or the landslide ratio (landslide pixels to total pixels ratio in a factor interval) (Lee et al. 2005). The correlation can be visually inspected by plotting the landslide ratio against the factor score. A correlation coefficient may also be calculated; either a positive or a negative correlation is good for an effective factor.

A threshold may exist for landslides. When the factor score is less than the threshold, the landslide ratio may be zero. Only factor scores greater than the threshold are needed in the calculation of a correlation coefficient. Either probability of failure or landslide probability is used in the following description with the term—landslide ratio.

Success Rate Curve

The success rate curve was firstly proposed by Chung and Fabbri in 1999. It is a cumulative landslide ratio calculated starting from the highest susceptibility of a model. The success rate of a factor is calculated starting from the lowest factor score if there is positive correlation between landslide ratio and factor score; or starting from the highest factor score if there is a negative correlation.

The curve indicates how well a model (or a factor) interprets the data (landslides). The success rate curve has an area under the curve (AUC). This area is between 0 and 1; a higher value indicates a higher success rate, whereas a value near or <0.5 means the factor is not effective at all. In the model

evaluation, we used to classify $AUC \geq 0.9$ as excellent, $0.9 > AUC \geq 0.8$ as good, $0.8 > AUC \geq 0.7$ as fair, $0.7 > AUC \geq 0.6$ as poor, $AUC < 0.6$ as very poor (Lee et al. 2008a, b). In the present evaluation of factors, we classify $AUC \geq 0.8$ as excellent, $0.8 > AUC \geq 0.7$ as good, $0.7 > AUC \geq 0.6$ as fair, $0.6 > AUC \geq 0.55$ as poor, and $AUC < 0.55$ as very poor.

4   Data Acquisition and Processing

The basic data used in this study included SPOT images, a 5-m grid digital elevation model (DEM), 1/5,000 photo-based contour maps, 1:50,000 geologic maps, and earthquake strong-motion records. SPOT images taken before and just after the Chi–Chi earthquake were selected for use and are listed in Table 22.1. The SPOT images were received, processed and rectified by the Center for Space and Remote Sensing Research, National Central University, Taiwan. Both multi-spectral (XS) and panchromatic (PAN) images were used. A fusing technique (Liu 2000) was used to produce a higher resolution false-color composite image to facilitate landslide recognition. The pixel resolution after fusing was 10 m.

The DEMs were acquired from the Department of Interior, Taiwan and were visually checked using a color-shaded image of the DEM. When a defect of more than a few pixels in size was found, this portion was re-digitized from a 1:5,000 scale photo-based contour map. Other abnormal random points were corrected using a median filter. Finally the DEM was smoothed a little and reduced to a 10 m grid for subsequent analyses.

Geological maps (1:50,000) were obtained from the Central Geological Survey, Taiwan. Each map was overlaid with a shaded DEM and visually inspected in GIS. Some abnormal boundaries, mostly associated with alluvial and terrace deposits, were corrected. The Erdas Imagine system was used to transform the geologic vector map to a raster image of 10 m pixels.

Digital strong-motion seismograms were collected by the Central Weather Bureau, Taiwan. They were acquired and processed for ground-

Table 22.1 List of satellite images used in establishing the landslide inventory

Location	Event date	Image	Date	Type
Tahan	1999/09/21	Before	1999/02/18, 1999/04/01, 1999/08/17	XS & PAN
		After	2000/01/02, 2000/01/29	
Fongshan etc.		Before	1999/04/01	
		After	1999/09/27, 1999/10/31, 2000/01/29	
Taan		Before	1999/04/01, 1999/04/02	
		After	1999/10/04, 1999/10/31	
Dajia		Before	1998/07/16, 1999/04/01	
		After	1999/10/31, 2000/01/08	
Wu		Before	1999/04/01, 1999/04/08	
		After	1999/10/31	
Jhuoshuei		Before	1999/04/01, 1999/09/11	
		After	1999/10/31, 1999/11/17, 2000/01/08	
Other area		Before	1999/04/01, 1999/07/01, 1999/07/24	
		After	1999/09/26, 1999/09/27, 1999/10/12	

motion parameters (landslide triggering factors) in this study.

All the vector layers were converted into raster cells of 10 × 10 m in size and these were used for all subsequent processing and analysis for each landslide factor.

4.1 Landslide Mapping

False-color images were used for landslide recognition. Image interpretation was based on image tone, shape, association, and also personal experience. The landslides were digitized in GIS and attributes assigned to establish a landslide map table. Each landslide table was then checked against recent rectified aerial photographs via the GIS. Most misinterpretations due to man-made features or cultivated land could be recognized during this comparison. The landslide tables were further modified using ground data obtained from field checks, and a landslide inventory was formed. Landslide types were noted after examining the characteristics of the landslide's shape, scarring, and deposition on SPOT images, photo-based maps, and by field checking. These data were also recorded as attributes for each landslide object in the GIS.

Rock falls were further analyzed by using slope gradients. They were found largely to be located on slopes >55°, with almost none on slopes of <50°. Rock-fall zones were then defined to be the region where slopes are >50° and where the area is larger than 0.5 ha. Finally the attributes in the database were updated using these rock fall zones to refine the landslide types and differentiate between shallow slides and rock falls.

Landslide deposits were identified by comparing the GIS landslide layer with the 1:5,000 scale photo-based contour maps. The slope angle or concentration of contour lines was used to differentiate deposit from source areas. The final GIS landslide inventory included a detailed description of the date/event, source/deposit, size and type of each landslide object. Finally, a pre-event, a post-event, and an event-triggered landslide inventories were made.

4.2 Event-Based Landslide Inventory

An event-triggered landslide was identified by comparing the pre-event and post-event landslide inventories, and an event-based landslide

Fig. 22.1 Landslides
triggered by the 1999 Chi–
Chi earthquake:
a Landslide distribution,
red star indicates epicenter
of the Chi–Chi earthquake.
b Index map with geology
of Taiwan. **c** Size
distribution of landslides
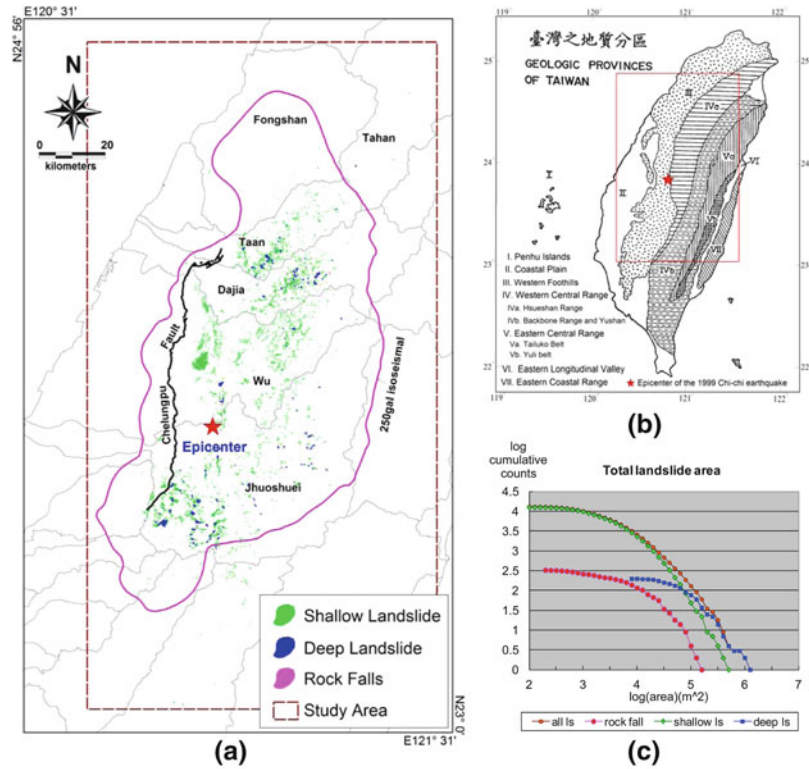
Table 22.2 List of Chi–Chi earthquake-induced
landslides

Type	Number	Area (km^2)	Number[a]	Area (km^2)[a]
Rock falls	326	4.493	310/16	4.291/0.202
Shallow slides	12,651	90.177	12,198/453	86.778/3.399
Deep slides	198	24.834	195/3	24.567/0.267
All	13,175	119.504	12,703/472	115.636/3.868

[a] *Note* Landslides within/outside 250 gal isoseismal

inventory was produced. An event-triggered
landslide could be absent from the pre-event
landslide inventory, or present in both invento-
ries. Landslides found in both inventories were
carefully examined for changes in tone and/or
enlargement in extent. The Chi–Chi earthquake
event-based landslide inventory is shown in
Fig. 22.1, and the number and area of landslides
is listed in Table 22.2.

Landslides triggered by the Chi–Chi earthquake
include rock falls, shallow slides, and deep-seated
landslides. Most landslides occurred within the
250-gal isoseismal line of earthquake shaking. The
deep-seated landslides include two structurally
controlled landslides: the Tsaoling landslide and
the Chiufengerhshan landslide. Landslides due to
lateral spreading were not found in this event.

4.3 Processing of Landslide Causative Factors

We selected several frequently used landslide
factors for analysis: lithology, slope gradient,
slope aspect, roughness, curvature, slope height,
distance to a road, distance to the earthquake
source, and earthquake intensity. The data set for
each factor was first divided into a *landslide*
group and a *non-landslide* group. Data for each
group were then classed into intervals and the
number of pixels in each interval recorded for
plotting the frequency distribution of a group.

The distribution of these two groups was visually inspected and a standard difference between the two groups was calculated.

The landslide ratio for each interval of factor score was calculated first, then plotted to form a landslide probability curve. It was then ready for visual inspection and calculation of a correlation coefficient.

The cumulative landslide probability was then plotted to form a success-rate curve and the AUC was calculated. The superiority of a factor was mostly quantified by the area under the success rate curve.

4.4 Processing of Landslide Triggering Factors

Landslide triggering factors associated with earthquake shaking are related to intensity. These may include peak ground acceleration (PGA), peak ground velocity (PGV), and Arias Intensity (AI), all of which are obtained from the earthquake strong-motion records.

The strong-motion data required initial baseline correction and filtering. These were carried out using standard procedures suggested by the Pacific Earthquake Engineering Research Center (PEER) (Darragh et al. 2004). PGA, PGV and AI were then calculated from each corrected seismogram. The arithmetical mean of the Arias Intensities of the N–S and E–W components was used to represent the earthquake intensity for the strong-motion station site. The geometrical mean of the PGA of the N–S and E–W components were used to represent the horizontal PGA for the strong-motion station site. The geometrical mean of the PGV was also calculated in this way. These values were interpolated on each grid point in the study area using ordinary kriging. Stations located on the tops of ridges were not included in the interpolation.

5 Landslide Controlling Factors and Evaluation

Eight factors were evaluated as more effective for interpreting the landslide spatial distribution.

5.1 Lithology

Geological conditions as well as lithology have a great influence on landslides. The Pleistocene Toukoshan Formation, the Pliocene Series, the Upper Miocene Groups, and the Eocene quartzitic sandstone and slate are more easily influenced by earthquake shaking. The Huoyenshan Conglomerate in the Toukoshan Formation is especially sensitive to an earthquake.

5.2 Slope Gradient

Slope gradient is an important factor controlling landslide occurrence. The present study confirms previous results that more landslides occur on steeper slopes (Fig. 22.2). It reveals a threshold at a gradient of about 40 % and shows a very good positive correlation with the slope gradient. The area under the success rate curve suggests that it is a good factor for all types of landslides. The area under the curve is as high as 0.916 for rock falls, 0.765 for shallow slides, and 0.727 for deep-seated slides.

5.3 Slope Aspect

Earthquake shaking may have a preferred orientation, so landslides may occur more frequently on slopes with a certain aspect. The present study (Fig. 22.3) confirms previous results that more S- and SE-facing slopes collapsed during the Chi–Chi earthquake. This may be explained by the movement of the thrust block, which was moving to the NW and N direction and confirms the results of Ji et al. (2003).

5.4 Slope Curvature

Convex slope surfaces are more stable than concave slope surfaces. The present results generally show a positive correlation between landslide occurrence and curvature. However, Fig. 22.4 shows that among the four curvature measures,

Fig. 22.2 Differences in slope-gradient factor between landslide and non-landslide groups, landslide probability, and success rate counted within 250 gal isoseismal
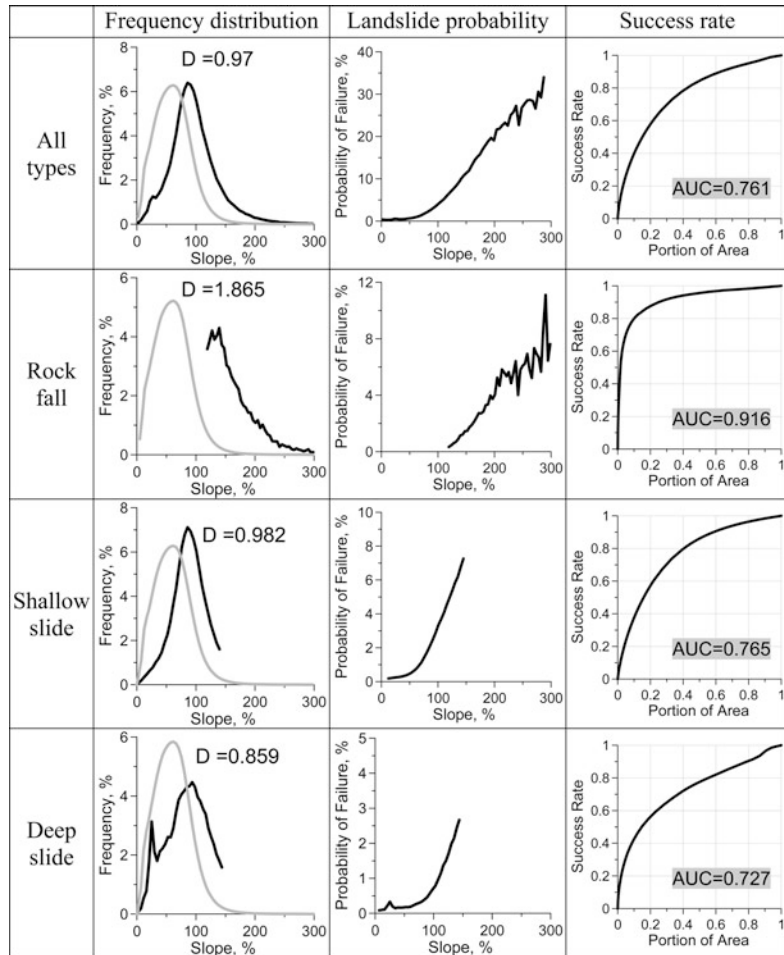
only total curvature showed a fairly good success rate (AUC = 0.634), others are very poor.

5.5   Slope Height

Storm-induced landslides are more common on lower slopes and show a negative correlation with slope height, whereas earthquake-induced landslides are located closer to ridge tops and show a positive correlation with slope height in general. The results of present study show that earthquake-induced landslides have only a poor correlation to the total-slope-height factor (AUC = 0.577), and have a very poor correlation to the local-slope-height factor and the relative-slope-height factor (Fig. 22.5). Relative-

slope-height is defined as the ratio of local-slope-height to total-slope-height and ranges from 0 (toe of slope) to 1 (top of slope).

5.6   Distance to Earthquake Source

We have compared the correlation of landslide occurrence using four different definitions of distance: (1) distance to epicenter, (2) distance to hypocenter, (3) distance to fault-rupture line, and (4) distance to fault-rupture plane. The distance-to-fault-rupture-plane and distance-to-fault-rupture-line are both the factors most affecting landslide occurrence (AUC = 0.661 ∼ 0.663), and distance-to-epicenter and distance-to-hypocenter are also both effective factors (AUC = 0.632 ∼
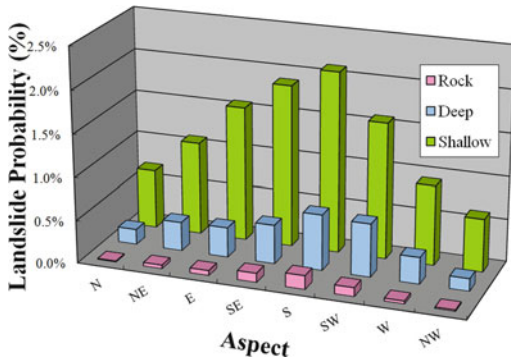
Fig. 22.3 Landslide probability for different slope aspects in three types of landslide, counted within 250 gal isoseismal
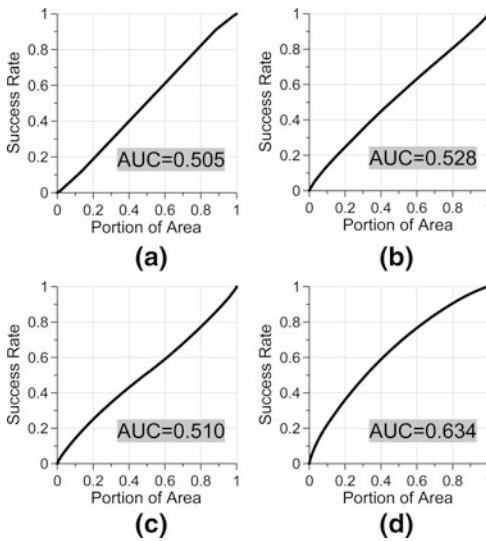
Fig. 22.4 Success rate curves for curvature factors to interpret shallow landslides within 250 gal isoseismal: **a** Plane curvature. **b** Profile curvature. **c** Tangential curvature, and (**d**) total curvature

0.633) (Fig. 22.6). Data on the fault rupture plane was calculated from Cheng et al. (2000).

5.7 Intensity of Ground Shaking

We compared landslide occurrence to three different definitions of intensity: (1) peak ground acceleration (PGA), (2) peak ground velocity (PGV), and (3) Arias Intensity. We found that the three intensity measures are all effective, but the Arias Intensity was the most effective factor for interpreting landslide occurrence. Arias Intensity was a good factor to explain all types of landslides (Fig. 22.7). The area under the success rate curve is as high as 0.714.

6 Characteristics of Earthquake-induced Landslides

Most landslides are either triggered by a storm rainfall or an earthquake. There are some differences in location and other characteristics between the former and the latter. Earthquake-induced landslides are located on steeper and longer slopes than the storm-induced ones, and preferably occur at a higher position on the slope and are closer to the ridge, whereas storm-induced landslides preferably occur at a lower slope position, closer to the river bank. This is clearly shown in Fig. 22.8, that most of the landslides triggered by the Typhoon Aere locate at lower relative slope height and are closer to the river bank (Fig. 22.8c), most landslides

Fig. 22.5 Success rate curve for slope height factor for shallow landslides within 250 gal isoseismal: **a** Local slope height. **b** Total slope height, and (**c**) relative slope height
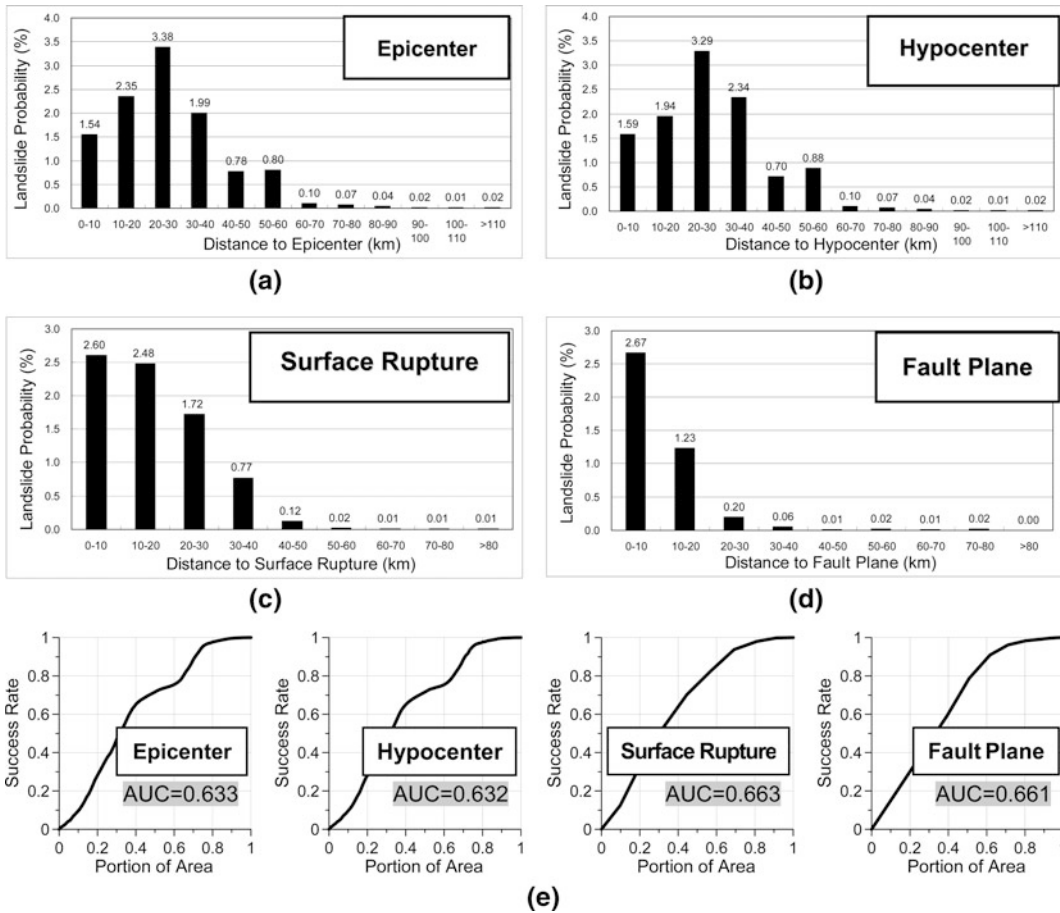
Fig. 22.6 Landslide probability (all types) for (**a**) epicenter distance. **b** Hypocenter distance. **c** Rupture-line distance, and (**d**) fault plane distance, and (**e**) success rate and area under the curve (AUC) computed within the 250-gal isoseismal

triggered by the Chi–Chi Earthquake locate at higher relative slope height closer to the ridge (Fig. 22.8a), whereas storm-induced landslides after the Chi–Chi Earthquake behave in between (Fig. 22.8b). Meunier et al. (2008) found similar results to our studies.

The storm-induced landslides may have a fairly good correlation with the relative-slope-height factor as shown in Fig. 22.8c. The earthquake-induced landslides are only poorly correlated with relative-slope-height factor, although their visual performance still is satisfactory (Fig. 22.8a). The total-slope-height factor is more effective than the relative-slope height factor, and indicates that it occur more

landslides at a longer slope. The slope gradient factor is a good to excellent causative factor for earthquake-induced landslides. Summarizing these, earthquake-induced landslides are most common on longer and steeper slopes, and occurred at a high position on the slope. Topographic amplification may have played a very important role in the occurrence of the earthquake-induced landslides.

Since there are fewer steep and long slopes in the meizoseismal area in northeastern Japan as compared to mountain slopes in Taiwan, the relatively less occurrence of coseismic landslides during the 2011 magnitude 9.0 Tohoku Earthquake may be explained by this topographic
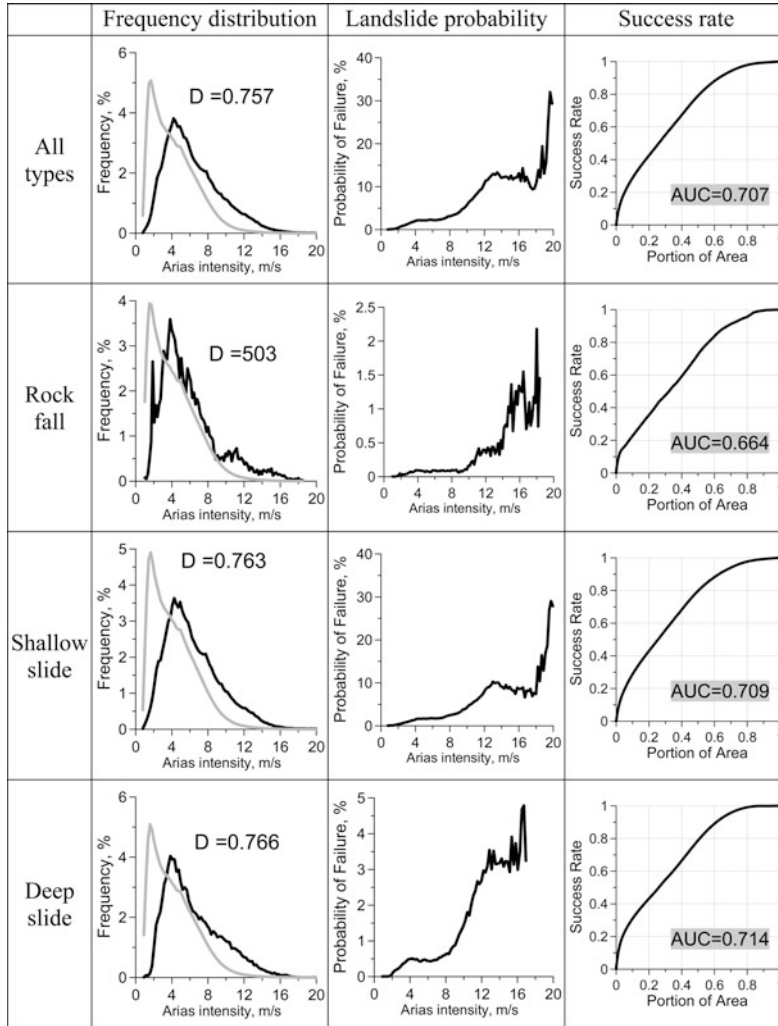
Fig. 22.7 Differences between landslide and non-landslide groups, probability of failure, and success rate counted within the 250-gal isoseismal for Arias Intensity factor
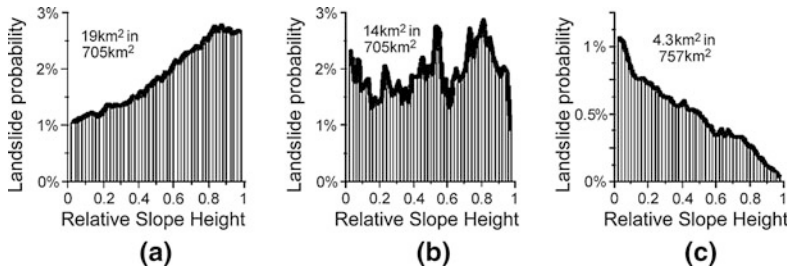
Fig. 22.8 Differences of landslide probability for: **a** Landslides triggered by the 1999 Chi–Chi Earthquake in Kuohsing quadrangle. **b** Landslides triggered by the 2001 Typhoon Toraji in Kuohsing quadrangle, and (**c**) landslides triggered by the 2004 Typhoon Aere in the catchment of Shihmen Reservoir

characteristics besides a possible interpretation by lithological characteristics which may be more resistant to earthquake shaking.

7   Conclusions and Recommendations

Landslides triggered by the 1999 Chi–Chi Earthquake were re-mapped from high-resolution SPOT images and checked by using aerial photo-pairs. Landslide types were recognized and deposit areas were separated, and all were associated with attributes in a GIS database. For earthquake-triggered landslides: (1) slope gradient was the most effective causative factor controlling the occurrence of landslides with an area under the success rate curve as high as 0.916 for rock falls, 0.765 for shallow slides, and 0.727 for deep-seated slides; (2) slope aspect showed some correlations to occurrence of landslides and reflected the fault movement direction; (3) total-slope-height factor roughly explained the occurrence of earthquake-induced landslides, but relative-slope-height could effectively explain the occurrence of storm-induced landslides which were commonly located closer to a river side; (4) closest distance to fault was the most significant source-distance factor associated with the landslides; and (5) Arias Intensity was the most significant intensity measure for interpreting landslide failures.

Most landslides were concentrated in the region exceeding 250 gals. Earthquake-induced landslides tended to occur on longer and steeper slopes and at a higher position on the slope, closer to the ridge. Topographic amplification may have played a very important role in the occurrence of the earthquake-induced landslides.

References

Bonilla MG (1975) A review of recently active fault in Taiwan. U.S. Geological survey open-file report 75–41, 58 p

Cheng CT, Lee CT, Tsai YB (2000) Fault rupture plane and attenuation model associated with the 1999 Chi–Chi earthquake. Proceedings of the 2000 annual meeting of the geological society of China, pp 21–23 in Chinese

Chung CF, Fabbri AG (1999) Probabilistic prediction models for landslide hazard mapping. Photogramm Eng Remote Sens 65:1389–1399

Dadson SJ, Hovious N, Chen H, Dade BW, Willett SD, Hu JC, Horng MJ, Chen MC, Stark CP, Lague D, Lin JC (2003) Links between erosion, runoff variability, and seismicity in the Taiwan orogen. Nature 426:648–651

Darragh B, Silva W, Gregor N (2004) Strong motion record processing for the PEER center. Proceedings of COSMOS invited workshop on strong-motion record processing, Richmond, California, USA, pp 26–27

Davis JC (2002) Statistics and data analysis in geology, 3rd ed. Wiley, Hoboken, 638 p

Ji C, Helmerger DV, Wald DJ, Ma KF (2003) Slip history and dynamic implications of the 1999 Chi–Chi, Taiwan, earthquake. J Geophys Res 108(B9):p. 2412

Jibson RW, Harp EL, Michael JA (2000) A method for producing digital probabilistic seismic landslide hazard maps. Eng Geol 58:271–289

Kao H, Chen WP (2000) The Chi–Chi earthquake sequence: active out-of-sequence thrust faulting in Taiwan. Science 288:2346–2349

Khazai B, Sitar N (2003) Evaluation of factors controlling earthquake-induced landslides caused by Chi–Chi earthquake and comparison with the Northridge and Loma Prieta events. Eng Geol 71:79–95

Lee CT, Huang CC, Lee JF, Pan KL, Lin ML, Dong JJ (2008a) Statistical approach to earthquake-induced landslide susceptibility. Eng Geol 100:43–58

Lee CT, Huang CC, Lee JF, Pan KL, Lin ML, Dong JJ (2008b) Statistical approach to storm event-induced landslide susceptibility. Nat Hazard Earth Syst Sci 8:941–960

Lee CT, Pan KL, Lin ML (2005) Research of landslide susceptibility analyses. Taiwan Central Geol Surv Open-File Rep 94–18, 474 p

Liao HW, Lee CT (2000) Landsides triggered by the Chi–Chi Earthquake. Proceedings of the 21st Asian conference on remote sensing. Volume 1&2:383–388

Liu JG (2000) Smoothing filter-based intensity modulation: a spectral preserve image fusion technique for improving spatial details. Int J Remote Sens 21(18):3461–3472

Ma KF, Lee CT, Tsai YB (1999) The Chi–Chi, Taiwan earthquake: large surface displacements on an inland fault. EOS Trans Am Geophys Union 80(50):605–611

Meunier P, Hovius N, Haines JA (2008) Topographic site effects and the location of earthquake induced landslides. Earth Planet Sci Lett 275:221–232

Teng LS (1990) Geotectonic evolution of late Cenozoic arc-continent collision in Taiwan. Tectonophysics 183:57–76

Tsai YB, Teng TL, Chiu JM, Liu HL (1977) Tectonic implications of the seismicity in the Taiwan region. Mem Geolog Soc China 2:13–41

Yu SB, Chen HY, Kou LC (1997) Velocity field of GPS stations in the Taiwan area. Tectonophysics 274:41–59

Wang WN, Nakamura H, Tsuchiya S (2002) Distributions of landslides triggered by the Chi-Chi Earthquake in central Taiwan on September 21, 1999. Landslides 38:18–26

Wu FT (1978) Recent tectonics of Taiwan. J Phys Earth 26(Suppl):265–299

Earthquake-Induced Landslides in Slovenia: Historical Evidence and Present Analyses

23

Matjaž Mikoš, Mateja Jemec, Mihael Ribičič, Magda Čarman and Marko Komac

Abstract

The paper gives a short overview of the historical earthquakes on the territory of Slovenia since AD 792, with the 1511 Idrija Earthquake ($M_M = 6.8 \pm 0.3$) as the strongest earthquake in this record. Firstly, seismotectonic characteristics of Slovenia are presented together with the seismological map of Slovenia. Secondly, a national landslide database and landslide occurrence map (cadastre) is discussed. Furthermore, different (statistical) models are presented that have been used to prepare landslide (also debris flows and rock falls) susceptibility maps of Slovenia at scale 1:250,000. The role of earthquakes as triggering factors in these models is discussed. Moreover, a field case study is discussed; the conclusions reached by the analysis of the numerous rock falls initiated during the 1998 Posočje earthquake ($M_L = 5.6$; the strongest earthquake in the 20th century with the epicenter in the territory of Slovenia) and the 2004 Posočje earthquake ($M_{LV} = 4.9$) is presented. A short final section on legislative framework in Slovenia with regard to hazard and risk mapping of slope instabilities respectively mass movements (including earthquake-induced landslides) is given.

M. Mikoš (✉)
Faculty of Civil and Geodetic Engineering,
University of Ljubljana, UL FGG, Jamova c. 2,
SI-1000 Ljubljana, Slovenia
e-mail: matjaz.mikos@fgg.uni-lj.si

M. Ribičič
Faculty of Natural Sciences and Technology,
University of Ljubljana, Ljubljana, Slovenia

M. Jemec · M. Čarman · M. Komac
Geological Survey of Slovenia, Ljubljana, Slovenia

1   Introduction

Slovenia is a small Central European country that lies between the Alps and the Mediterranean Sea, where the Adriatic/Apulian sub-plate hits the Eurasian tectonic plate, forming the Periadriatic Seam; to south of it there are the Southern Alps, reaching to Slovenia. Slovenia has a historical

Fig. 23.1 A Geological map of Slovenia at scale 1:500,000 (after Buser and Draksler 1990). *Red line* represents Periadriatic lineament, the diamond represents the 1998 earthquake epicenter and the star represents the 2004 earthquake epicenter
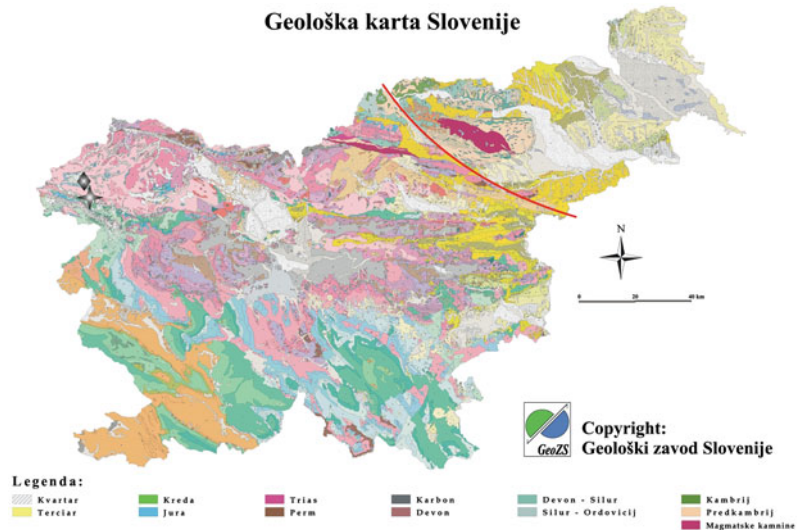
record of frequent but not very strong earthquakes that are less violent as elsewhere in Europe (the 1693 Sicily Earthquake M = 7.5, the Lisbon 1755 Earthquake M = 8.7, the 1783 Calabria Earthquake M = 7.0, the 1908 Messina Earthquake M = 7.2). Fortunately, many earthquakes in Slovenia are not strong enough to trigger landslides (M < 4 after Keefer (1984) or M < 4.3 ± 0.4 after Malamud et al. (2004)). Strong earthquakes are therefore not the most frequent natural hazard in Slovenia, where floods and rainfall-induced landslides are much more frequent (Mikoš et al. 2004).

In Slovenia, landslides are mainly occurring in the lower mountainous, in the Alpine foothills and hilly central part of Slovenia, in the flysch areas in northern Slovenia, and the hills of eastern and northeastern Slovenia. Rock falls and rock slides are common in the northern and northwestern Slovenia, in steep gorges or canyons and thrusts area where carbonate rocks overthrust the softer rocks (usually flysch). Debris flows are rare events and occur in the Alps, Karavanke Mountain, on Pohorje and the Alpine foothills. Before going to the analyses of earthquakes as triggering factors for the before mentioned mass movements, let us present a short description of seismotectonic characteristics of Slovenia together with a short overview of past earthquakes in Slovenia.

2 Seismotectonic Characteristics of Slovenia

The Slovenian territory is tectonically divided by the Periadriatic Seam (line); to its north there is the European plate (Eastern Alps), and to the south of it there is the Adriatic microplate, whose northern margin (Southern Alps, Dinarides) is highly deformed and backthrusted onto the central, less deformed part of the Adriatic microplate (Adriatic Basin) (Poljak et al. 2000). Numerous thrusts and faults are responsible for a rather complex geological setting, shown on a Geological map of Slovenia at scale 1:500,000 (Fig. 23.1).

Using data on historical earthquakes (estimated locations and magnitudes since 792 A.D.) led to a special catalogue prepared for seismic hazard assessment in Slovenia (Živčić et al. 2000). According to this assessment, the territory of Slovenia can be considered to be one of moderate seismicity (Poljak et al. 2000) (see Fig. 23.2).

3 Short Overview of Historical Earthquakes in Slovenia

In Europe, twelve-degree earthquake intensity scales are used. Still in use in Southern Europe is the Mercalli-Cancani-Sieberg Scale or MCS
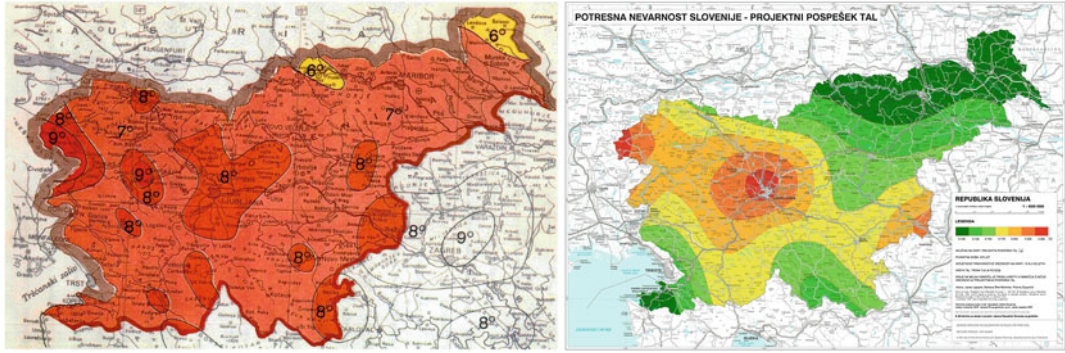
Fig. 23.2 A Seismological map of Slovenia—EMS map (Ribarič [1987]) (*left*) and a Design Ground Acceleration map (more correct name for the map is a Peak Ground Acceleration map—PGA) (Lapajne et al. [2001]) (*right*).

The color legend defines Peak ground accelerations as follows: *dark green*—0.1 g; *green*—0.125 g; *light green*—0.15 g; *yellow*—0.175 g; *light orange*—0.2 g; *orange*—0.225 g; *red*—0.25 g

Scale. In 1964, the first version of the MSK Scale was published by Medveded, Sponhauer and Karnik (Medvedev et al. [1965]). In 1998, the European Macroseismic Scale or EMS-98 Scale was introduced by the European Seismological Commission, now de-facto standard in Europe. In Japan, the seven-degree Japanese Meteorological Agency Scale or the JMA Scale was used; recently modified to a ten-degree scale or JMA 1996 Scale.

As already said, strong earthquakes are rather rare in Slovenia, but they nevertheless have proved in our history to be very dangerous, even though only now and again. The oldest event in the catalogue of earthquakes in Slovenia (Ribarič [1982]) dates back to 792 A.D. Since this event, there has been 1 event of maximum intensity X MSK, two of intensity IX MSK and 11 events that reached the maximum intensity VIII MSK; only three earthquakes of intensity VIII MSK have occurred in the last 200 years (Poljak et al. [2000]). The strongest ever earthquake that has happened on the territory of Slovenia (Slovenia was as independent state established in 1991) is the 1511 Idrija Earthquake ($M_w = 6.8 \pm 0.3$) and the second strongest was 1895 Ljubljana Earthquake ($M_w = 6.1 \pm 0.2$).

In the 20th Century was very strong earthquake the 1976 Friaul Earthquake ($M_w = 6.1 \pm 0.1$) with the epicenter in Italy but close to NW Slovenia. This region in NW Slovenia is a seismically very active area. On April 12, 1998, the strongest earthquake of the last 100 years occurred in the Upper Soča valley ($M_M = 5.8$, maximum intensity VII-VIII EMS). Another strong earthquake shook this area on July 12, 2004 ($M_w = 4.9$, maximum intensity VI-VII EMS-98). These two earthquakes triggered numerous rock falls reported at the end of this paper. Also the 1974 Kozjansko Earthquake in SE Slovenia ($M_w = 4.8$, maximum intensity VII EMS) triggered numerous new landslides and some old ones reactivated (Vidrih [2008]).

4 Analysis of Rock Falls Initiated by Two Recent Earthquakes in Slovenia

In the last two decades, W Slovenia was struck by two strong earthquakes (epicenters are shown in Fig. 23.1). The first event occurred on 12 April 1998 at 10:55UTC with a moment magnitude of 5.6 (diamond in Fig. 23.1). The area that was affected was the Upper Soča valley and the Bovec basin in NW Slovenia (Bajc et al. [2001]; Zupančič et al. [2001]). The total seismic moment was 4.5×10^{17} Nm (10^{24} dyn-cm) implying an average, co-seismic slip of 0.18 m (Bajc et al. [2001]). There was no surface rupture.
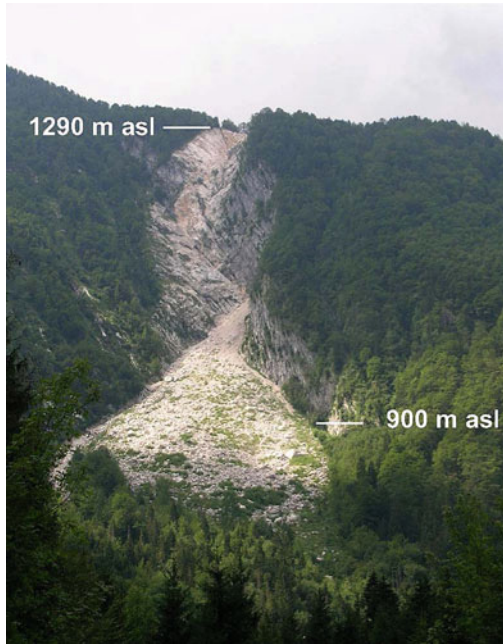
Fig. 23.3 Large rock wedge failure triggered by the Easter 1998 earthquake in the Lepena valley (W Slovenia)

The Easter 1998 Earthquake caused more than 100 failures, among them 50 rockfalls (Vidrih et al. 2001; Mikoš et al. 2006). About 260,000 m³ of rock fall material will remain on hill slopes with no potential of reaching the river network (see example in Fig. 23.3), while ∼ 480,000 m³ may be released to watercourses in a longer period during extreme events. About 200,000 m³ of rock fall debris was deposited in areas from where the material was released to watercourses during rainfall events. As a consequence of the 1998 earthquake, hyperconcentrated flows were observed during floods in some torrential tributary channels of the Upper Soča River (Mikoš and Fazarinc 2000).

A second earthquake ($M_w = 5.2$; $M_S = 4.9$) occurred on 12 July 2004 at 13:04UTC close to the epicentre of the 1998 event (star in Fig. 23.1). Both events show right-lateral, strike-slip kinematics (Bajc et al. 2001; Kastelic et al. 2006). After the earthquake of July 12, 2004, 50 rather superficial slope failures including 38 rockfalls were registered.

5 Slovenian National Landslide Cadastre and Database

In early 2000, several Slovenian Ministries were prepared for financing the construction of the National Landslide Database. The existing landslides data were collected from the different sources. Data were organized in cadastres and internal databases (see Fig. 23.4). The main sources were Geological Survey of Slovenia, Administration of the Republic of Slovenia for Civil Protection (URSZR), The Directorate of the Republic of Slovenia for Roads (DRSC), Ministry for the Environment, Spatial Planning and Energy (ARSO) and other sources (geotechnical companies, municipalities…). The gathered data were acquired in different formats. They were first analyzed and the duplicates removed. Then the data were merged into the centralized database. Komac et al. (2005) stated that the quality is/was questionable to a certain degree because the different databases were rarely updated. The different database attributes and missing or multiplied data were the dominating problem (Komac et al. 2005). At the end of the project there were 6602 slope mass movements in the database, 49.3 % of them (3257) with known location (Komac et al. 2007). The database is unfortunately not operational since 2005.

6 Landslide Susceptibility Map

Based on the extensive national landslide database the Landslide susceptibility map of Slovenia at scale 1:250,000 were completed (Fig. 23.5). The map was derived using statistical analyses of landslide preparatory factors (lithology, slope inclination, slope curvature, slope aspect, distance to geological boundaries, distance to structural elements, distance to surface waters, flowlength, and landcover type) on a landslide learning set (random but geologically representative 65 %) and tested on the remaining test set (35 %). The univariate statistical

Fig. 23.4 A Landslide occurrence map of Slovenia
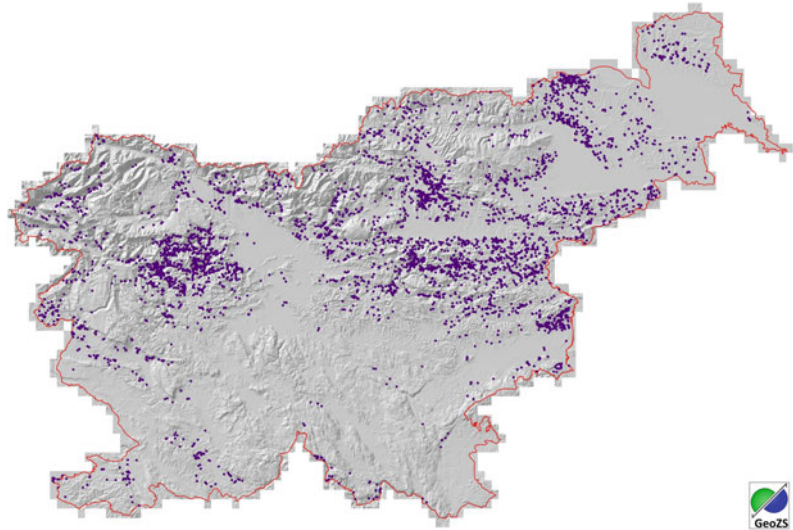
Fig. 23.5 A Landslide susceptibility map of Slovenia (from Komac and Ribičič 2006)
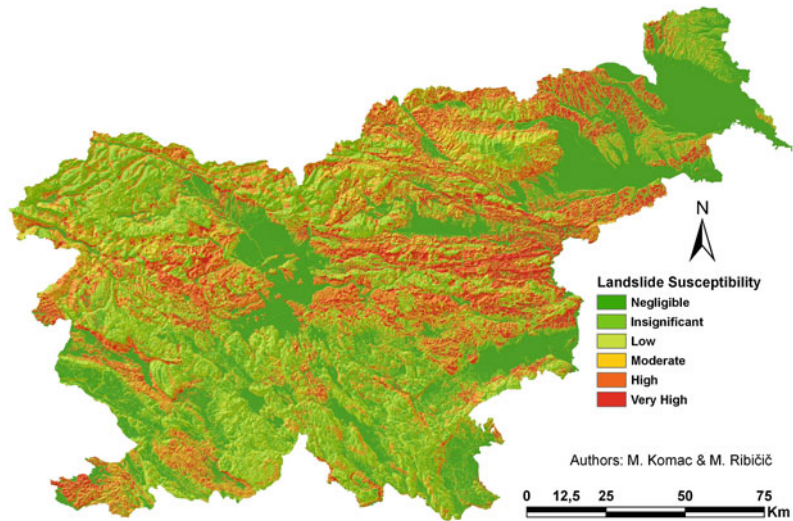
analyses (*Chi Square*) were conducted using GIS in raster format with the 25 × 25 m pixel size. These results were later used as a basis for the development of the weighted linear susceptibility model where several models with various factor weights variations based on previous research were developed. The relation of landslide occurrence to the triggering factors (maximum 24-h rainfall intensity with the return period of 100 years and average annual rainfall) was assessed. The analyses showed that the annual rainfall above 1000 mm proved to be the critical triggering factor for landslide occurrence in more loose soils and above 1600 mm in less resistant rocks. Furthermore, the daily rainfall intensity above 100 mm proved to be critical for landslide occurrence, especially in more loose soils and in less resistant rocks.
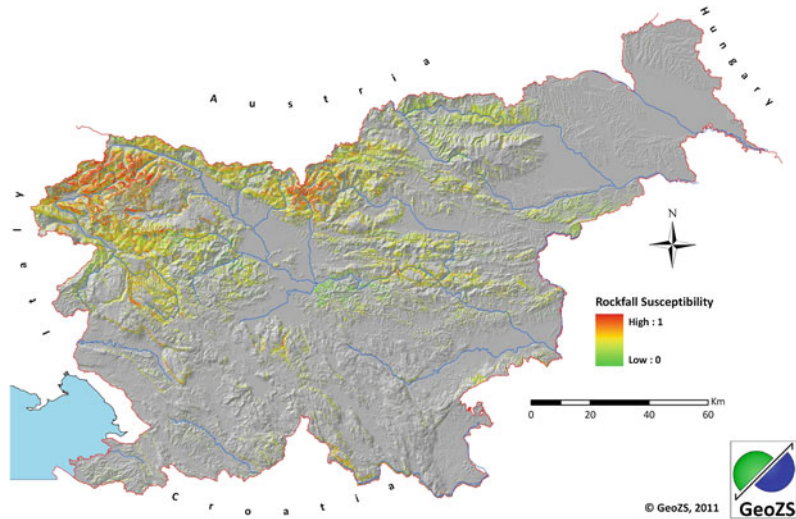
7   Rockfall Susceptibiliy Map

In Slovenia, rockfall susceptibility was relatively poorly investigated. Therefore, a new Map of rockfall susceptibility in Slovenia in scale 1:250,000 was produced (Fig. 23.6) using GIS with the latest spatial data, such as the latest lithological map of Slovenia in scale 1:250,000. The most important factors in the production of the map were: lithology, slope angle and distance to tectonic-structural elements. The existing rockfall susceptibility map, produced in 1997, was also used for the comparison.

To identify areas with high probability of rockfall occurrence, Chi-square analyses with a linear weighted sum model approach was selected on the basis of selected spatio-temporal factors to simplify the approach and to make it transferable to other regions. Unfortunately, there are not enough adequately representative data about rockfalls in Slovenia (consistent rockfall cadastre does not exist and not many historical studies have been done so far) for the quantitative statistical analysis available. This is why expert estimation was used as a complementary approach to Chi-square analysis, with the emphasis on location rather than on time of a rockfall occurrence. Expert estimation approach was based on the experience and historical events gathered from chronicles and eyewitnesses. Cross-validation was performed on 125 such known historical events. This approach is limited mainly by subjectivity and has difficulties with sound argumentation, but at the given state it was a reasonable way to evaluate a Chi-square analysis and to define areas with high(er) probability of rockfall occurrence.

Based on the calculations of several linear models with different weight combinations of spatio-temporal factors and the results of their rockfall susceptible areas prediction success, the best factors' weight combination was selected.

The presented rockfall susceptibility map forms a basis for spatial prediction of rockfall triggering areas. It also gives a general overview of areas susceptible to rockfall in Slovenia and offers guidance for areas of further and more detailed research and the rockfall run-out zones.

This new rockfall susceptibility map complements the set of maps of susceptibility to different mass slope movements (landslides and debris flows susceptibility maps), which have been produced at the Geological Survey in Slovenia in the last five years.
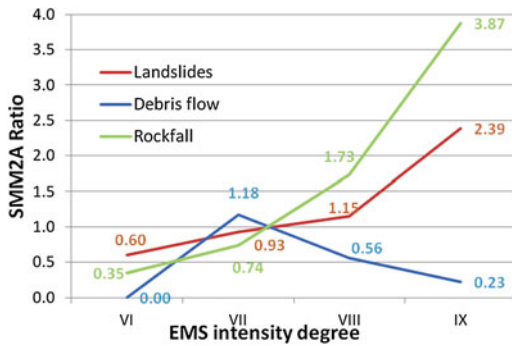
Fig. 23.7 Values of slope mass movements (landslides, debris flows and rockfalls) to area ratio (SMM2A) in relation to EMS intensity degree values
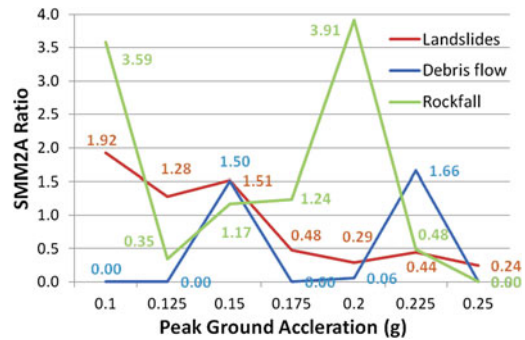
Fig. 23.8 Values of slope mass movements (landslides, debris flows and rockfalls) to area ratio (SMM2A) in relation to peak ground acceleration values (g)

8 Analysis of Slope Mass Movements in Relation to Seismic Intensity in Slovenia

To assess the potential occurrence of three different types of slope mass movements as a result of seismic activity landslide (3693), debris flow (16) and rockfall (110) populations were analyzed according to their spatial occurrence. The analysis based on a simple overlay assessment between point occurrences and areas of different seismic intensity. For the information on the latter we took two sets of seismic data, an EMS intensity degree map (Fig. 23.2—left; Ribarič 1987) and the Design Ground Acceleration (that is actually a Peak Ground Acceleration—PGA) map (Fig. 23.2—right; Lapajne et al. 2001). Slope mass movements were compared to both of the datasets. The results of overlay assessment were normalized to neutralise the impact of the seismicity class area proportion. The slope mass movement to area ratio (SMM2A) that gives realistic occurrence perspective was calculated as following:

$$SMM2A = (NSMM_{class}/NSMM_{total})/(A_{class}/A_{total}),$$
(23.1)

where $NSMM_{class}$ represents the number of slope mass movement occurrences within a specific class of seismic activity, $NSMM_{total}$ represents the total number of slope mass

movement occurrences, A_{class} represents the area of a specific class of seismic activity and A_{total} represents the total area of the analysis (t.i. area of Slovenia).

The occurrence ratio of landslides and rockfalls (Fig. 23.7) show expected correlation with higher EMS intensity degree values. These results clearly show the influence of earthquake intensity as being one of more important triggering factors for landslide and rockfall occurrence. If we, very simplified, assume that the SMM2A ratio value of 1 shows the threshold above which the earthquakes have an influence on the landslides and rockfall occurrence, we can conclude that the EMS intensity degree value of VIII (and higher) influences the triggering of these two slope mass movements. In the case of debris flow similar statement is impossible as the only EMS intensity degree value at which the threshold is reached is VII, but with increasing intensity values the ratio drops substantially. The most probable reason for this is that the major triggering factor for debris flows is rainfall and rarely earthquakes.

In the case of slope mass movements' occurrences in relation to PGA values (Fig. 23.8) the distribution of landslides has a negative related trend, t.i. as PGA values increase the SMM2A ratio decreases. Such a relation is most probably the result of the fact that the areas with the highest GPA values lay in the plains where landslides seldom occur. Occurrences of debris flow and rockfalls show

poor results of correlation with the PGA values. For the debris flows this could be explained with by two facts, first being too small population of debris flow occurrences analyzed and/or second being that most probably rainfall dominates the triggering of these types of slope mass movements.

9   Slovenian Legislation in the Field of Eartquake-Triggered Landslides

Upon its accession to the European Union, Slovenia was forced to adopt its legal and economic system to the common European values. In this respect, new Waters Act was adopted in 2002 that established a special Water Fund. This fresh approach should help to keep the relatively high level of safety against natural hazards in Slovenia, especially against floods. This new Waters Act also prescribes the preparation and acceptance of hazard and risk maps for different natural hazards as a prevention tool. These maps will then be used in spatial planning as a legal basis in the process issuing building permits. At this moment, the preparation of methodologies how to prepare such hazard and risk maps under Slovenian conditions are under way and these methodologies will be given legal status. By doing that we are trying to catch up with the other alpine countries in Europe (Đurović and Mikoš 2004).

10   Conclusions

Slovenia is a small Central European country that lies between the Alps and the Mediterranean Sea, where the Adriatic/Apulian sub-plate hits the Eurasian tectonic plate, forming the Periadriatic Seam. The northern margin of the Adriatic microplate (Southern Alps, Dinarides) is highly deformed and backthrusted onto the central, less deformed part of the Adriatic microplate. Numerous thrusts and faults are responsible for a rather complex geological setting in Slovenia.

Using a database on historical earthquakes since AD 792, the territory of Slovenia can be considered to be one of moderate seismicity. Since AD 792, there has been 1 event of maximum intensity X MSK, 2 of intensity IX MSK and 11 events that reached the maximum intensity VIII MSK; only 3 earthquakes of intensity VIII MSK have occurred in the last 200 years. The strongest ever earthquake that has happened on the territory of Slovenia (Slovenia was as independent state established in 1991) is the 1511 Idrija Earthquake ($M_M = 6.8 \pm 0.3$) and the second strongest was 1895 Ljubljana Earthquake ($M_M = 6.1 \pm 0.2$).

In the last two decades, W Slovenia was struck by two strong earthquakes. The Easter 1998 Earthquake caused more than 100 failures, among them 50 rockfalls. After the earthquake of July 12, 2004, 50 rather superficial slope failures including 38 rockfalls were registered.

Until 2005, a Slovenian National Landslide Cadastre and Database was established, followed by Landslide Susceptibility Map and Rockfall Susceptibility Map of Slovenia in scale 1:250,000.

In the last years, an analysis of slope mass movements in relation to seismic intensity in Slovenia has been performed. To assess the potential occurrence of three different types of slope mass movements as a result of seismic activity landslide (3693), debris flow (16) and rockfall (110) populations were analyzed according to their spatial occurrence. From legislative point of view, the preparation of methodologies how to prepare hazard and risk maps for landslides, rock falls and debris flows in Slovenia are under way.

References

Bajc J, Aoudia A, Sarao A, Suhadolc P (2001) The 1998 Bovec-Krn mountain (Slovenia) earthquake sequence. Geophys Res Lett 28:1839–1842

Buser S, Draksler V (1990) Geološka karta Slovenije 1:500.000. Mladinska knjiga (in Slovenian)

Đurović B, Mikoš M (2004) Preventive management of risk due to natural hazards: procedures in the Alpine

countries and in Slovenia. Acta hydrotechnica 22(36):17–35

Kastelic V, Živčić M, Pahor J, Gosar A (2006) Seismotectonic characteristics of the 2004 earthquake in Krn mountains. Potresi v letu 2004, Slovenian Environment Agency, Seismology and Geology Office, 78–87 (in Slovenian)

Keefer DK (1984) Landslides caused by earthquakes. Geol Soc Amer Bull 95:406–421

Komac M, Šinigoj J, Krivic M, Kumelj Š, Hribernik K (2005) Novelacija in nadgradnja informacijskega sistema o zemeljskih plazovih in vključitev v bazo GIS_UJM. Geološki zavod Slovenije. (in Slovenian)

Komac M, Ribičič M (2006) Landslide susceptibility map of Slovenia at scale 1:250,000. Geologija 49(2):295–309 (in Slovenian)

Komac M, Fajfar D, Ravnik D, Ribičič M (2007) Slovenian national landslide database—a promising approach to slope movement prevention plan. Geologija 50(2):393–402 (in Slovenian)

Lapajne J, Šket Motnikar B, Zupančič P (2001) Potresna nevarnost Slovenije—Projektni pospešek tal. Ministrstvo za okolje in prostor, Uprava Republike Slovenije za geofiziko. (in Slovenian)

Malamud BD, Turcotte DL, Guzzetti F, Reichenbach P (2004) Landslides, earthquakes, and erosion. Earth Planet Sci Lett 229:45–59

Medvedev SV, Sponheuer W, Karnik V (1965) Skala sejsmičeskoj intensivnosti MSK 1964. Sesimic intensity scale: version 1964. Academy of Sciences of the U.S.S.R, Soviet geophysical committee, Moscow

Mikoš M, Fazarinc R (2000) Earthquake-induced erosion processes in two alpine valleys in Slovenia. In: Proceedings of the INTERPRAEVENT congress, pp 143–154

Mikoš M, Brilly M, Ribičič M (2004) Floods and landslides in Slovenia. Acta hydrotechnica 22(37):113–133 ftp://ksh.fgg.uni-lj.si/acta/a37mm.pdf

Mikoš M, Fazarinc R, Ribičič M (2006) Sediment production and delivery from recent large landslides and earthquake-induced rock falls in the Upper Soča River Valley, Slovenia. Eng Geol 86:198–210

Poljak M, Živčić M, Zupančič P (2000) The seismotectonic characteristics of Slovenia. Pure Appl Geophysics 157:37–55

Ribarič V (1982) Seismicity of Slovenia—catalogue of earthquakes (792 A.D.-1981). Seizmološki zavod SR Slovenije. (in Slovenian)

Ribarič V (1987) Seizmološka karta SFRJ—območje Slovenije. Seizmološki zavod SR Slovenije. (in Slovenian)

Vidrih R, Ribičič M, Suhadolc P (2001) Seismogeological effects on rocks during the 12 April 1998 upper Soča territory earthquake (NW Slovenia). Tectonophysics 330(3/4):153–170

Vidrih R (2008) Seismic activity of the upper Posočje area. Agencija Republike Slovenije za okolje. (in Slovenian)

Zupančič P, Cecić I, Gosar A, Placer L, Poljak M, Živčić M (2001) The earthquake of 12 April 1998 in the Krn Mountains (Upper Soča valley, Slovenia) and its seismotectonic characteristics. Geologija 44(1):169–192 (in Slovenian). doi:10.5474/geologija.2001.012

Živčić M, Suhadolc P, Vaccari F (2000) Seismic zoning of Slovenia based on deterministic hazard computations. Pure Appl Geophysics 157:171–184

Karstification as a Predisposing Factor of Seismically Triggered Landslides: Case Study from the Crimean Mountains (Ukraine): Introduction to the Problem

24

Jan Hradecký, Tomáš Pánek, Karel Šilhán
and Veronika Smolková

Abstract

Deep-seated gravitational deformations are significant denudational agents of rock slopes at the margins of karstified plateaus of the Crimean Mountains (CM). The CM evolved during Mesozoic–Cenozoic times as a response to the deformation between the Black Sea domain and East-European platform. The southwestern part of the area is characterized by steep, up to 1000-m-high coastal escarpments consisting of Late Jurassic limestones overlying tuff layers and weak Late Triassic flysch with sporadic small intrusions of Middle Jurassic diorites, gabbros and granites. Steep rock slopes contrast with elevated, highly karstified plateaus situated approximately 500–1300 m a.s.l. The aim of this article is to show long-term evolution of a giant rock slope failure close to the Black Sea coast in the southwestern tip of the CM near Foros Town. The failure evolved in highly anisotropic limestones overlying plastic flysch layers where the main head scarp follows a strike-slip fault. The Foros slope failure is an excellent demonstration of the significance of a preparatory stage in the evolution of large deep-seated slope deformations. Inherited and undisturbed horizontal slickensides on the sub-vertical, inactive fault surface serve as good evidence of significant extensional movement of the surface blocks away from the main headscarp. The studied deformation shows that in a relatively small area tensional (cutting) surfaces can be formed by a great variety of rock discontinuities such as the strike-slip fault, joints and steeply inclined bedding planes. The presence of well-developed, nowadays weathered, speleothems furthermore points to significant karstification that provided additional widening of spaces within rock mass. Gravitational movement

J. Hradecký (✉) · T. Pánek · K. Šilhán ·
V. Smolková
Department of Physical Geography
and Geoecology, Faculty of Science,
University of Ostrava,
Chittussiho 10, Ostrava 710 00, Czech Republic
e-mail: jan.hradecky@osu.cz

destroyed and unroofed several cave systems originally presented at the former edge of a karst plateau. Our findings reveal that large rock slope failures can be added to the factors contributing to the evolution of unroofed caves. Although triggering factors of the activation of individual parts of slope deformations can be determined only hypothetically, lessons learned from widespread landslide activity during and after the 1927 Yalta earthquake and rainfall-driven landslides in the vicinity of Feodosia Town make us consider both seismic loading of slopes and high pore-pressures during heavy winter rainfalls or rapid spring snowmelt to be significant factors. Beside seismic activity, intensive Late Holocene slope processes can be attributed to intensive human activity.

1 Introduction

Karstification can be understood not only as an important complex of denudational processes in areas built by limestones and other rocks sensitive to karstic denudation, but also as an important preparatory factor for the presence of processes leading to geomorphic evolution of mountain belts around the world. This phenomenon can play an important role in the preparation of rock massif weakening and it can lead to more effective imprint of gravitational slope deformations. Presented study deals with large chronic rock-slope failure situated in the mountainous topography of southwestern part of the Crimean Mountains (CM)—Fig. 24.1. One of the main characteristics of CM is great abundance of deep-seated landslides, often connected with dangerous debris flows, rock avalanches or rockfalls (Ena 1987; Nikonov and Sergejev 1996). High density of endokarst and exokarst landforms is an important feature of the studied area.

2 Local Settings

CM evolved during Mesozoic-Cenozoic times as a response to the deformation between the Black Sea domain and East-European platform (Kazantsev 1982; Yudin and Gerasimov 1997; Saintot and Angelier 2002). Middle Jurassic-Early Cretaceous folding and thrusting created main structural features of mountains whereas Late Berriasian to Late Eocene evolution was characterized by subsidence followed by platform sedimentation and burial of alpine structures. Apatite fission-track dating revealed that uplift, exhumation and evolution of contemporary mountain topography commenced in Eocene—Oligocene periods (Pánek et al. 2009a, b).

Southwestern part of the area is characterized by steep, up to 1000 m high coastal escarpments consisting of Late Jurassic limestones overlying tuff layers and weak Late Triassic flysch with sporadic small Middle Jurassic intrusions of diorites (Derenyuk et al. 1984). Steep rock slopes contrasts with elevated, highly karstified plateaus situated ∼ 500-1300 m a.s.l. Karst phenomena in the CM was object of numerous studies (e.g. Dublyanskii and Kiknadze 1977; Amelichev 2004). Coastal escarpments and slopes bounding karst plateaus are almost continuously affected by deep-seated landslides whilst foot slopes are covered by thick diamictons accumulated by shallow landslides, debris flows and rock avalanches. Large reactivation of rockslides and new rockfalls took place in this area during 1927 ∼ 6 M Yalta earthquake (Nikonov and Sergejev 1996).

Our study focuses the Foros slope collapse (44°24′N, 33°46′E) and adjacent deformations that are among the most illustrative examples of compound failures in the CM (Figs. 24.2, 24.3). Slope deformation occupies ∼3 km² on south-

Fig. 24.1 Study site—regional map showing the position of the Crimean Mountains
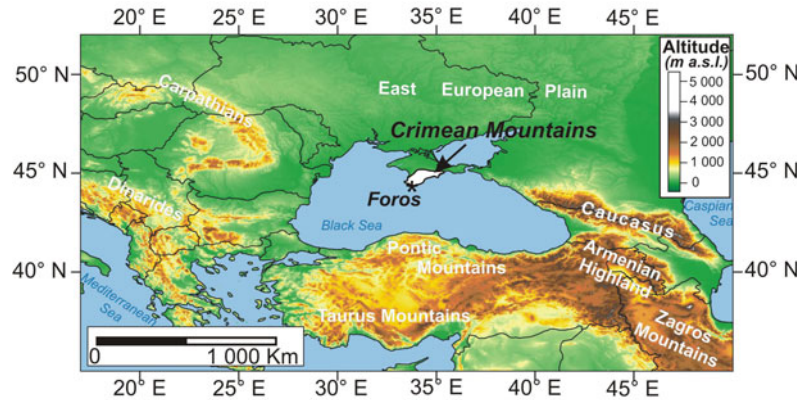
oriented, ∼600 m high steep coastal slopes above Foros town in the southwestern tip of the CM. Instability is hardly to delimitate because it is a part of continuous landslide complex occupying whole coastal strip between towns Balaklava and Alushta. Upper half of deformation evolved on fractured Late Jurassic limestones and landslide body is detached from the rock mass along important strike-slip fault of N45E-N90E direction (Figs. 24.3 and 24.4). Lower part of slope failure affects underlying flysch layers and its surface is covered by thick accumulations of mixed colluvium (Pánek et al. 2009a, b). Limestone complexes are highly karstificated and the presence of endokarst plays an important role in the propagation of slope instability in the edge zone of the main scarp.

3 Methods

The main objective of the study is to specify the time of the evolution and individual stages of the Foros slope failure. The approach is based on radiometric dating of exposed ("dead") speleothems in the headscarp area and wide tensional cracks affecting the landslide body. Results obtained from absolute dating were verified by detailed geomorphic mapping which enabled the determination of relative chronology of individual landform assemblages. Unroofed speleothems, abundant in the source area of the slope collapse, were dated both by conventional radiocarbon (14C) and U-/Th-series dating

methods, which are frequently used in order to determine carbonate age (Walker 2005).

4 Local Preparatory Factors: Role of Karstification

Rock weakening associated with various types of rock-mass transformations represents crucial preparatory stage in the evolution of landslides (Korup 2004; Margielewski 2006). Margielewski (2006) proposed two stages of landslide development: relatively long first stage associated with stress relaxation and abrupt second stage characteristic for the gravitational transport. Gradual stress relaxation within anisotropic materials favors evolution of tension (cutting) surfaces which can be predisposed in sedimentary rocks by tectonic discontinuities (faults, joints etc.) or bedding planes. One of the evidence of such mechanism is evolution of crevice-type caves that are commonly associated with preparatory stages of the evolution of large landslides in anisotropic rocks (Margielewski and Urban 2003, 2004; Pánek et al. 2009a, b).

Foros slope failure is an excellent demonstration of significance of preparatory stage in the evolution of large deep-seated slope deformation. Inherited and undisturbed horizontal slickensides (related to the previous tectonic deformation) on the main headscarp serve as a good evidence of significant extension along
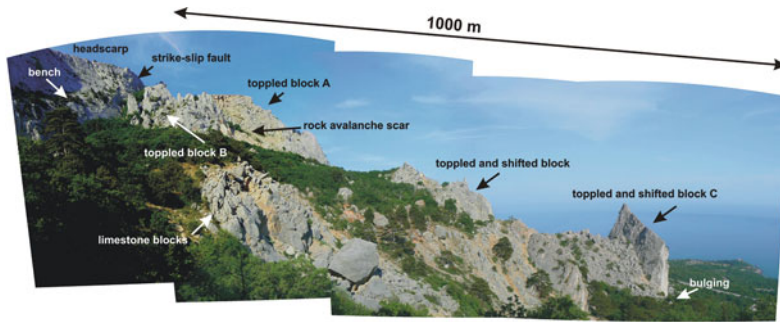
Fig. 24.2 Lateral view of the studied slope deformation with marked morphological elements (eastward camera view). Reprinted from Geomorphology, 108/3-4, Pánek T et al., Time constraints for the evolution of a large slope collapse in karstified mountainous terrain of the southwestern Crimean Mountains, Ukraine, p. 172, Copyright (2009), with permission from Elsevier
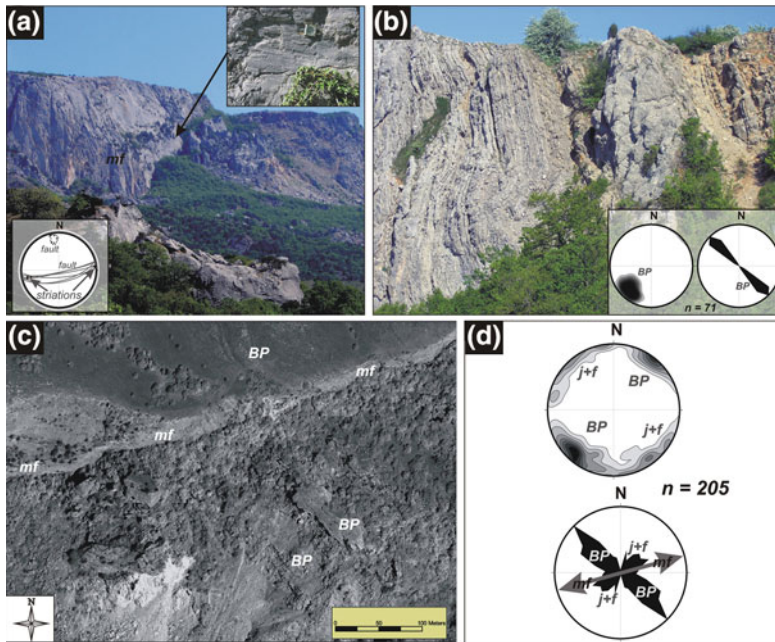
Fig. 24.3 Main discontinuities affecting the evolution of the studied slope failure. **a** strike-slip fault (mf) having formed a detached zone for the evolution of the main headscarp. **b** a strip of thinly bedded limestones (BP) crossing the main headscarp. **c** crossing of the main discontinuity sets (mf + BP) displayed on a QuickBird image. **d** a stereonet and a corresponding rose diagram of the main discontinuities within the landslide body (j + f are minor fractures sub-parallel to the main strike-slip fault). All inserted stereonets are constructed as equal area projections on the lower hemisphere. Reprinted from Geomorphology, 108/3-4, Pánek T et al., Time constraints for the evolution of a large slope collapse in karstified mountainous terrain of the southwestern Crimean Mountains, Ukraine, p. 173, Copyright (2009), with permission from Elsevier

strike-slip fault zone (Fig. 24.3). Studied deformation shows that tensional (cutting) surfaces can be on relatively small area predisposed by intersection of great variety of rock discontinuities such as strike-slip fault, joints and steeply inclined bedding planes (Pánek et al. 2009a, b). Extension and propagation of these surfaces have been related to plastic
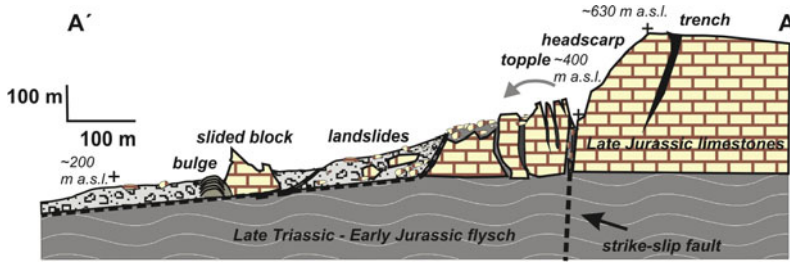
Fig. 24.4 Selected cross-section along the Foros slope deformation (for localization see Fig. 24.5). Reprinted from Geomorphology, 108/3-4, Pánek T et al., Time constraints for the evolution of a large slope collapse in karstified mountainous terrain of the southwestern Crimean Mountains, Ukraine, p. 174, Copyright (2009), with permission from Elsevier
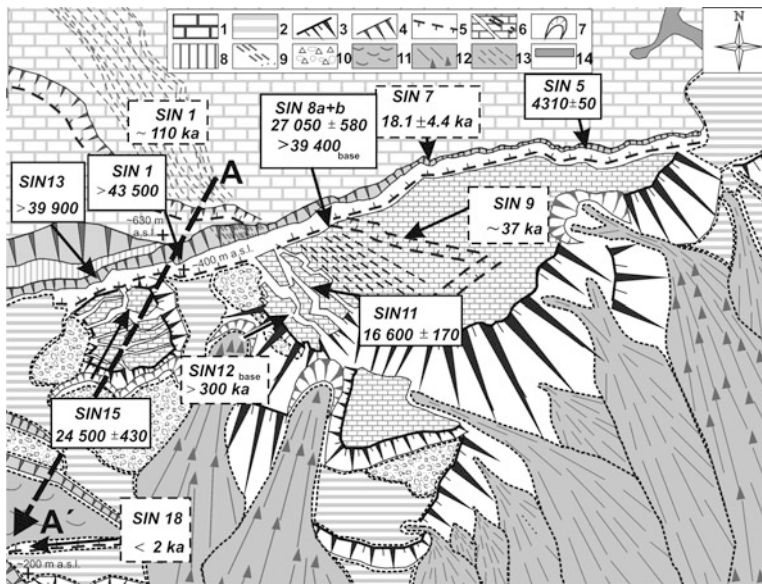
Fig. 24.5 Results of the dating of speleothems. **a** Distribution of ages of the upper layers of unroofed speleothems (except SIN 8b and SIN 12 which reveal basal layers) in the Foros slope failure. Boxes outlined by solid lines display samples dated by conventional radiocarbon dating, dashed boxes show U-/Th-series dating results. Legend of geomorphological map: 1—gently inclined karst plateau on the Upper Jurassic limestones; 2—terrain affected by multigenerational landslides; 3—steep slope of landslide blocks; 4—main headscarp predisposed by strike-slip fault; 5—counter-slope scarp; 6—landslide block with fractures; 7—rock avalanche or rockfall headscarp; 8—bench on the main headscarp; 9—strip of thinly bedded limestone; 10— rockfall accumulation, 11—accumulation of morphologically well delimited minor landslides and earthflows; 12—rock avalanche or rockfall accumulation; 13—talus cone; 14—road. Reprinted from Geomorphology, 108/3-4, Pánek T et al., Time constraints for the evolution of a large slope collapse in karstified mountainous terrain of the southwestern Crimean Mountains, Ukraine, p. 177, Copyright (2009), with permission from Elsevier

deformations of underlying flysch formation. Presence of well-developed, nowadays weathered, speleothemes furthermore points to the significant karstification that provided additional widening of spaces within rock mass (see e.g. Calcaterra and Santo 2004; Pedrozzi 2004). Gravitational movements destroyed and unroofed several cave systems originally presented at the former edge of karst plateau (Figs. 24.5 and 24.6). Our experience thus
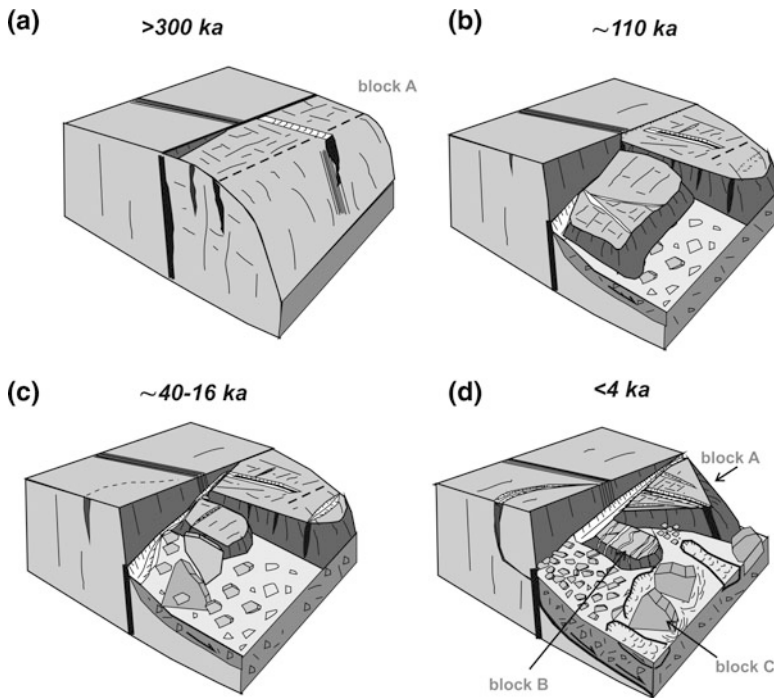
Fig. 24.6 Proposed model of a long-term evolution of the Foros slope failure. **a** Karstification affecting aniso-tropic limestones at the margin of karst plateau. **b** incip-ient stage of the development of the giant slope deformation. **c** eastward propagation of the slope defor-mation along strike slip-fault accompanied by the fragmentation of detached blocks. **d** Final fragmentation of the landslide body connected with onward propagation of deep-seated failure, evolution of shallow landslides and rockfalls. Reprinted from Geomorphology, 108/3-4, Pánek T et al., Time constraints for the evolution of a large slope collapse in karstified mountainous terrain of the southwestern Crimean Mountains, Ukraine, p. 179, Copyright (2009), with permission from Elsevier

pinpoints that large rock slope failures can be added to the factors contributing to the evolution of unroofed caves (sensu Mihevc et al. 1998). These features were defined in the 1990 s as important karst elements in classical karst ter-rains (e.g. Knez and Slabe 1999, 2002; Geršl et al. 1999; Šebela 1999). On the other hand, karstification should be taken into account when analyzing factors leading to the development of large landslides. Some of the largest world landslides evolved in carbonate bedrock (e.g. Prager et al. (2008); Ivy- Ochs et al. (2009)) and their relation to karst features is unclear. Various karstification processes and mechanisms prepar-ing rocks for slope deformations should thus become the objective of future studies dealing with the preparatory factors of large rockslides. In combination with the earthquake as a trig-gering factor, karstification can make crucial

environment for the evolution of huge slope deformations and it can represent a set of trans-formational processes in mountain belts.

5 Long-Term Ridge Disequilibrium

Our data indicate that extension and karstifica-tion affected in the first stage (>300–110 ka BP) mainly first-order structures, which are in the Foros failure presented by localized dense sys-tem of bedding planes with NW strike and zone along main strike slip fault. Well-developed speleothemes dated >300 ka BP are evidence of crack propagation and karstification at those times (Fig. 24.6a). Rock slope collapse itself started to form certainly between ∼40–110 ka BP, when western part of headscarp was
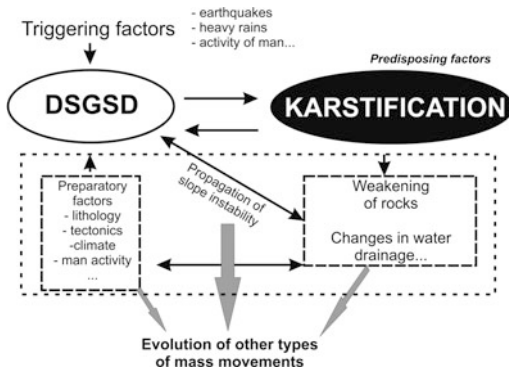
Fig. 24.7 Problem scheme of the interrelation between karstification and deep-seated gravitational slope deformations (DSGSD) and their propagation

exposed (Fig. 24.6b). Large limestone blocks (blocks B + C) were detached off the main wall which increased stress relaxation within their rock mass and gradual fragmentation to several smaller blocks. Collapse of the western part of failure caused unloading that was crucial for the eastward propagation of headscarp and generally for further development of slope failures in the eastern zone. During the terminal phase of Late Glacial ($\sim$40–16 ka BP), majority of headscarp along strike-slip fault was exposed and block A experienced both subsidence and fragmentation connected with propagation of crevices and their collapse (Fig. 24.6c). Minor eastward propagation of headscarp, evolution of easternmost spread ridge and active development of crevices within block A characterize Late Holocene—Recent evolution (<4 ka BP) (Fig. 24.6d). Active toppling and rockfalls at the margin of block A are recorded by large boulder accumulations and fresh talus cones (Pánek et al. 2009a, b). Recent collapses can be connected with the Yalta earthquake of 1927.

6 Conclusion

The Foros rock slope collapse is an example of a contemporary catastrophic geomorphic system that is a result of a long-lasting preparatory stage, minimally of the Middle–Late Quaternary age. The weakening of a rockmass due to gradual

propagation of cracks (cutting surfaces) and karstification of faulted limestone can be traced back to 300 ka BP, while the landslide itself probably started to evolve $\sim$110 ka BP and major slope instabilities continued until the Late Holocene. Contemporary morphology of the failure is a result of the eastward propagation of a deep-seated slope deformation along fault-predisposed headscarp for several tens of thousands of years. Morphology and dating of exposed speleothems along the main headscarp point to more than four recurrent stages of landslide evolution. The presented study suggests the importance of a long-lasting preparatory stage of the evolution of landslides. In settings formed by carbonate bedrock this "relaxation" stage may have a character of sole speleogenesis or a connected effect of extension and solution-based karstification of rocks along gravitational cracks. The latter mechanism could be expected especially where carbonate rocks overlie layers prone to plastic deformation. Karstification as a preparatory factor of the development of catastrophic slope failures in mountainous settings should thus be the objective of our future studies. There is an evident set of feedbacks between the presence of slope disequilibrium and the evolution of karst in the CM. Gravitational fragmentation of mountain ridges plays a role in the karst evolution too. On the other hand, the existence of karsts has caused a weakening of rock massif with a higher potential to the propagation of mass movements (Fig. 24.7).

References

Amelichev GN (2004) Karstovye polya Kryma. Kultura narodov prichernomorya 52:14–21(in Russian)

Derenyuk NE, Vanina MV, Gerasimov MY, Pirovarov SV (1984) Geological map of the Crimea. Geological Ministry of Ukraine 1(200):000 Kiev, scale (in Russian)

Dublyanskii VN, Kiknadze TZ (1977) Karstovye peshchery i shakhty Gornogo Kryma. Leningrad, Nauka. (in Russian)

Ena AV (1987) Vozrastnaja indikacija gravitacionnych obrazovanij Gornovo Kryma (na primere gory Juznaja Demerdzhi). Geomorfologia 2:57–62 (in Russian)

Calcaterra D, Santo A (2004) The January 10, 1997 Pozzano landslide, Sorrento Peninsula, Italy. Eng Geol 75:181–200

Geršl M, Stepišnik U, Šušterčič S (1999) The "unroofed cave" near the Bunker (Laški Ravnik). Acta Carsologica 28:77–90

Ivy-Ochs S, Poschinger AV, Synal HA, Maisch M (2009) Surface exposure dating of the Films landslide, Graubünden, Switzerland. Geomorphology 103:104–112

Kazantsev YV (1982) Tektonika Kryma. Nauka, Moscow (in Russian)

Knez M, Slabe T (2002) Unroofed caves are an important feature of karst surfaces: examples from the classical karst. Zeitschrift für Geomorphologie 46:181–191

Korup O (2004) Geomorphic implications of fault zone weakening: slope instability along the Alpine fault, South Westland to Fiordland. NZ J Geol Geophys 47:257–267

Margielewski W (2006) Structural control and types of movements of rock mass in anisotropic rocks: case studies in the Polish Flysch Carpathians. Geomorphology 77:47–68

Margielewski W, Urban J (2003) Crevice-type caves as initial forms of rock landslide development in the Flysch Carpathians. Geomorphology 54:325–338

Margielewski W, Urban J (2004) Crevice-type cave Dziabla Dziura in Bukowiec (Roznów Foothill, Outer Carpathians) as an initial stage of deep seated landslides development in the Flysch Carpathians. Przegląd Geologiczny 52:1171–1178

Mihevc A, Slabe T, Šebela S (1998) Denuded caves—an inherited element in the karst morphology. Acta Carsologica 27:165–174

Nikonov AA, Sergejev AP (1996) Seismogravitacionnyje narusenia reliefa v Krymu pri zemletrjasenijach 1927 goda. Geoekologia 3:124–133 (in Russian)

Pánek T, Danišík M, Hradecký J, Frisch W (2009a) Morpho-tectonic evolution of the Crimean mountains (Ukraine) as constrained by AFT data. Terra Nova 21:271–278

Pánek T, Hradecký J, Šilán K, Smolková V, Altová V (2009b) Time constraints for the evolution of a large slope collapse in karstified mountainous terrain of the southwestern Crimean Mountains, Ukraine. Geomorphology 108:171–181

Pedrozzi G (2004) Triggering of landslides in Canton Ticino (Switzerland) and prediction by the rainfall intensity and duration method. Bull Eng Geol Environ 63:281–291

Prager C, Zangerl C, Patzelt G, Brandner R (2008) Age distribution of fossil landslides in the Tyrol (Austria) and its surrounding areas. Nat Hazards Earth Syst Sci 8:377–407

Saintot A, Angelier J (2002) Tectonic paleostress fields and structural evolution of the NW-Caucasus fold-and-thrust belt from Late Cretaceous to Quaternary. Tectonophysics 357:1–31

Šebela S (1999) Morphological and geological characteristics of two denuded caves in SW Slovenia. Acta Carsologica 28:175–185

Walker M (2005) Quaternary dating methods. Wiley, Chichester

Yudin VV, Gerasimov ME (1997) Geodynamitcheskaya model Krymsko-Tchernomorskovo i prilegayishtchich regionov. Geodynamika Krymsko-Tchernomorskovo regiona. Simferopol, the Ukraine 16–23 (in Russian)

Low-Gradient Megalandslides at the Northern Boundary of the Caucasus-Crimean Orogene: Seismically Induced?

25

Tomáš Pánek, Jan Hradecký, Karel Šilhán, Alexander Strom, Veronika Smolková and Oleg Zerkal

Abstract

We have detected at least 16 extremely large landslides (0.2–2.8 km^3) in an ∼800 km long stretch of the hilly northern foothills of the Caucasus-Crimean orogene (Russia, Ukraine). All landslides originated within tectonically inverted foredeep basins formed predominantly by the Neogene clay-rich substratum (claystones, marls and occasionally limestones). The landslides, which evolved as blockslides combined in their distal parts with earthflows, are characterized by an extremely low height to length ratio (0.05–0.08). OSL and radiocarbon dating of deposits of the selected landslides pointed to various stages of the last glacial and Holocene. The largest landslide observed in the Kuban river valley/Russia (32 km^2; 2.8 km^3) originated between ca 13 and 35 ka BP during the last glacial. The activity of the Crimean landslides/Ukraine was determined to two main stages: the interval between the end of the last glacial and ca 6 ka BP, and ca 1–1.5 ka BP. Although the determination of triggering factors of ancient megalandslides is difficult, we exemine the palaeoseismic hypothesis considering surface rupturing of some Late Quaternary faults in the vicinity of the landslides. Potential seismic origin of the megalandslide in the Kuban river valley is in line

T. Pánek (✉) · J. Hradecký · K. Šilhán ·
V. Smolková
Department of Physical Geography and
Geoecology, Faculty of Science, University of
Ostrava, Chittussiho 10, 71000 Ostrava, Czech
Republic
e-mail: tomas.panek@osu.cz

A. Strom
Geodynamic Research Center, Hydroproject
Institute, Volokolamskoe Shosse 2,
125993 Moscow, Russia

O. Zerkal
Geological Department, Moscow State University,
GSP-1, Leninskie Gory, Moscow, 119991, Russia

with the presence of nearby situated tectonically deformed late Pleistocene river terraces. Crimean and Kuban landslides are situated along the regional tectonic zones bordering the Alpine orogenic belt and the ancient Scythian platform. Taking into account semiarid continental climatic conditions in the time of the landslide formation, palaeoseismic scenario seems to be quite reliable.

Keywords

Megalandslide · Dating · Clay-rich substratum · Caucasus-Crimean thrust and fold belt

1   Introduction

Despite the fact that the world's largest landslides usually occur within the highest mountain belts (Korup et al. 2007), recent observations have revealed that some of the megalandslides ($V > 1$ km^3) have originated in low-relief landscapes characterized by a low degree of topographically induced stress (Philip and Ritz 1999; Pánek et al. 2008a, b, 2012). Such extremely large slope instabilities with gently inclined slip surfaces usually result from the combination of unfavourable geological structures, weak rocks and high-magnitude triggering factors including heavy rainfalls and strong earthquakes (Philip and Ritz 1999; Aylsworth et al. 2000). The main objective of our paper is to point out a cluster of giant palaeolandslides situated in the foredeep of the Caucasus-Crimean mountain belt (Russia, Ukraine) and discuss a possibility of their seismic origin (Fig. 25.1). Some of these landslides are among the largest within Europe (Pánek et al. 2008a, b, 2012).

structures running between the Crimean peninsula and the Caspian Sea (Fig. 25.1). Northern flanks of the orogene are filled with thick molasse sediments including sandstones, limestones, claystones and marls of the tertiary age (Derenyuk et al. 1984). The most pronounced landslides are situated in the low-gradient terrain (local relief up to 100–200 m) of cuesta-type landscapes armoured by Neogene limestones and claystones in the Kuban case (foredeep of Caucasus/Russia) and by Neogene (Sarmatian) limestones underlain by Palaeogene/Neogene claystones, mudstones, marls and sands in the Crimea case and. The uplift of foredeep deposits took place during the latest orogenic stage of the area connected with Neogene-Quaternary tectonic inversion of foredeep basins (Pánek et al. 2009; Vincent et al. 2011). The foredeep of both Crimean and Caucasus Mountains is characterized by continental climate (annual precipitation total of up to 400 mm) which differs only slightly from the last interglacial (Simakova 2006; Gerasimenko 2007).

2   Regional Settings

Several groups of anomalously large (0.2–2.8 km^3) landslides have been detected in an ∼800 km long stretch of the hilly northern foothills of the Caucasus-Crimean orogene. The Caucasus-Crimean orogenic belt comprises a system of mesozoic-tertiary thrust and fold

3   Methods

Giant landslides in the northern periphery of the Crimean Mountains and Caucasus were detected using the analyses of SRTM 3″ digital elevation model (resolution ca 90 m) and LANDSAT TM images (resolution of ca 30 m). A detailed outline of landslide's internal morphology was
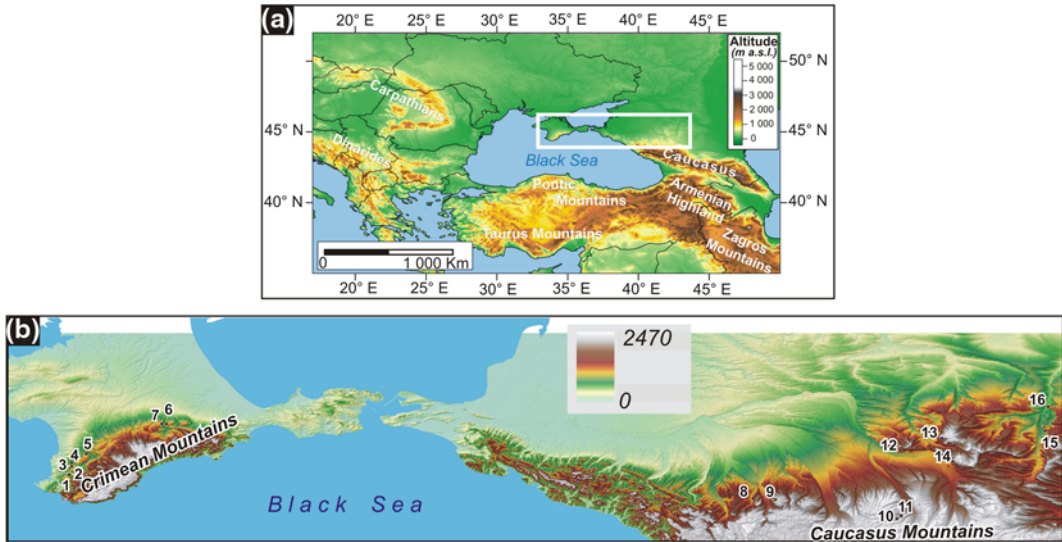
Fig. 25.1 A regional map showing the position of megalandslides in the northern periphery of the Caucasus-Crimean mountain belt. Identification numbers of the landslides are displayed (see Table 25.1)

subsequently performed by Google Earth (SPOT images of ca 10-m resolution) and aerial photographs. Field works connected with field mapping, analysis of outcrops, material sampling for dating, and sedimentological and mineralogical analyses were conducted in May 2006 (area of the Crimean Mountains/Ukraine) and October 2009 (area of the foredeep of the Caucasus in the Kuban river valley/Russia). Estimation of the age of selected landslides was based on the OSL and radiocarbon dating (AMS and conventional) of both deformed soils and loess-like deposits overlying landslide bodies (Pánek et al. 2008a, b, 2012). Besides the analysis of large landslides, we performed a geomorphic study of nearby neotectonic landforms in order to detect possible relationships between palaeoseismicity and slope deformations.

4   Characteristics of Landslides

Large-scale low-gradient ancient landslides estimated at 5.4–18.9 km^2 in area and ∼0.2–1.2 km^3 in volume have been detected in the northern hilly periphery of the Crimean

Mountains (Ukraine) (Fig. 25.1; Table 25.1). They originated on slopes along wide valleys of the Belbek, Kacha, Alma and Biyuk-Karasu Rivers crossing the cuestas of the northern foothills. The slopes generally consist of slightly northward tilted Miocene (mainly Sarmatian) limestones overlying weak, clay-rich lower Neogene–Palaeogene substratum with a significant content of smectite (Pánek et al. 2008a, b). Slip surfaces of the landslides have an inclination of up to 5° on average. The sliding mechanics was probably complex and it involved rotation, translational block displacement and earthflows (Fig. 25.2). All the studied landslides are located in the vicinity of regional faults (e.g. a suture between the Crimean orogene and the Scythian platform), whereas three of them have headscarps aligned along the faults.

Most of the detected megalandslides (∼0.2–2.8 km^3) in the northern foothills of the Caucasus mountains are situated within the drainage basin of the Kuban river (Fig. 25.1; Table 25.1). They also affected slopes along wide river valleys (e.g. Kuban, Belaya) incising uplifted Neogene deposits of the northern foothills of the

Table 25.1 Characteristics of the studied landslides partly based on data published by Pánek et al. ([2008a](#))

Landslide name/ID[a]	V (km³)	A (km²)	H (m)	L (km)	H/L	W (km)	Hs (m)	Ls (km)	Main slope aspect	Mean slope (°)[b]
Belbek (1)	~1.2	18.9	195	4.1	0.047	5.9	90	6.8	NNE	6.8 ± 4.4
Frontovoe (2)	~0.6	12.7	170	2.6	0.065	6.5	120	6.2	S	6.6 ± 4.4
Kacha 1(3)	~0.8	12.9	150	2.4	0.063	8.1	100	9.8	N	7.2 ± 5.3
Kacha 2(4)	~0.2	5.4	100	1.3	0.077	4.7	50	5.7	S	5.8 ± 3.4
Alma (5)	~0.4	10.6	120	2.0	0.06	5.9	50	6.9	NNE	5.8 ± 3.0
Vishennoye 1(6)	~0.4	8.6	150	2.6	0.058	4.2	30	6.1	W	5.6 ± 2.9
Vishennoye 2(7)	~0.05	2.0	100	0.9	0.111	1.5	20	1.5	E	4.8 ± 2.5
Maykop 1(8)	~1.9	31	170	3.9	0.044	11	75	10.6	W	5.4 ± 3.0
Maykop 2 (9)	~0.3	9.5	110	2.1	0.052	6.8	25	8.1	SW	6.0 ± 2.6
Spokoynaya 1(10)	~0.1	2.8	145	2.0	0.073	1.62	25	2.6	NNW	5.2 ± 1.4
Spokoynaya 2 (11)	~0.1	3.0	140	2.1	0.066	1.5	30	2.2	NNW	5.0 ± 2.1
Uspenskoye (12)	~2.8	32	330	6.7	0.049	5.1	100	8.1	S	5.5 ± 3.6
Stavropol (13)	~1.1	13.3	100	4.7	0.043	3.7	80	5.1	S	4.6 ± 3.9
Nevinnomyssk (14)	~0.6	21	500	5.9	0.085	5.1	120	8.1	WSW	6.3 ± 3.4
Svetlograd 1(15)	~0.3	8.9	185	2.9	0.064	3.8	100	5.1	SW	4.5 ± 2.7
Svetlograd 2(16)	~0.2	5.3	150	2.2	0.068	2.8	50	4.4	SW	5.2 ± 3.1

Key: V total displaced volume, A total affected area including scar and deposits, H landslide height, L runout, W maximum width of landslide, Hs maximum height of headscarp, Ls length of headscarp along ridgeline

[a] see localization of landslides according to ID in the Fig. 25.1

[b] including both deposits and headscarp
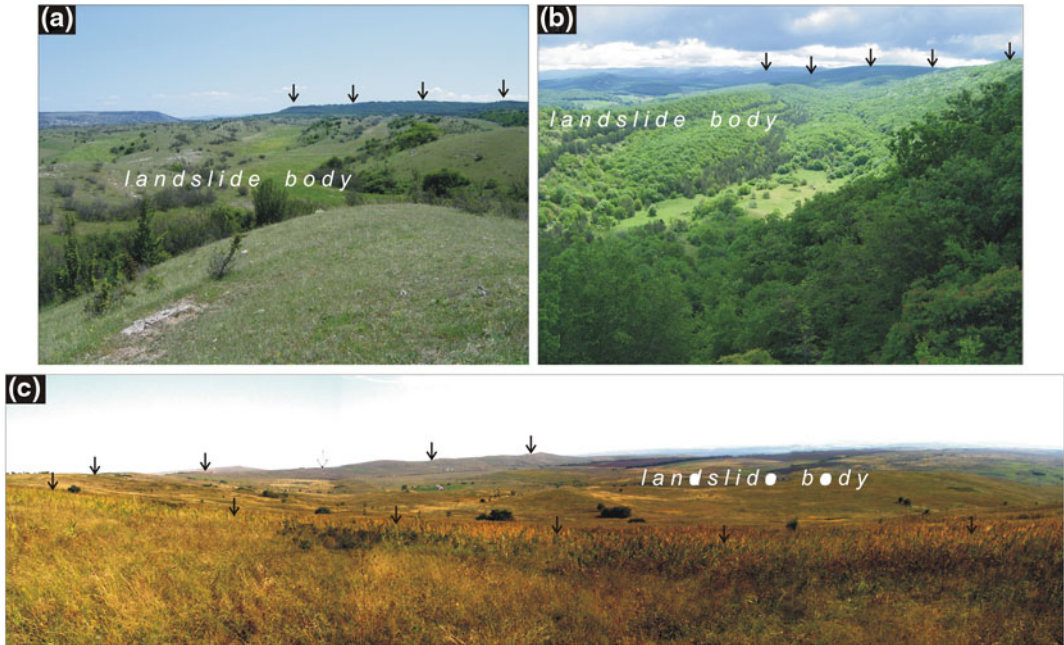
Fig. 25.2 Geomorphic features of selected landslides. **a** Undulating topography of the Kacha1 landslide (Crimean peninsula/Ukraine). **b** Up to 50-m-high landslide blocks within the area of the Belbek landslide (Crimean peninsula/Ukraine). **c** Panoramic view of the proximal part of the Uspenskoye landslide (Northern Caucasus foredeep/Russia). *Black arrows* show the upper edge of headscarps

Fig. 25.3 Completely fragmented and mixed claystones, sandstones and limestones forming the material of the landslide body of the Uspenskoye landslide

Greater Caucasus. Landslides have similar characteristics as Crimean ones; they belong to the group of roto-translational landslides and spreads with signs of flow-type emplacement of distal toes.

One of the largest landslide in the Europe (Uspenskoye megalandslide with volume of about 2.8 km^3 and area 32 km^2) is situated on the right bank of the Kuban river, in the vicinity of

the Armavir town (Fig. 25.1). It has very gently (<5°) inclined slip surface. Proximal domain of the landslide, just below amphitheatre-shaped ∼100-m-high headscarp, is formed by a flat near-scarp depression and a system of large rotated blocks situated mainly at the flanks of the landslide body. The whole depletion zone of the landslide with diameter ca 3 km is covered by loess and its reworked derivates of varied thickness that reaches more than 4.5 m in the central part of the near-scarp depression and up to 1 m on the adjacent slopes. Contrary to the proximal and central zones, the distal part of the megalandslide is characterized by undulated topography with the presence of distinct scarps (up to ∼20 m high) and longitudinal depressions filled by loess. Landslide material exposed in numerous outcrops within gullies suggests a high degree of transformation of the original bedrock structure. There is no evidence of original bedding; the main lithotypes (i.e. claystones, marls and limestones) are completely mixed (Fig. 25.3). Some of these outcrops reveal internally less fragmented 'flowing' blocks embedded in fully fragmented bedrock material. The megalandslide internal structure together with distinct characteristics of its proximal and distal parts points to two stages of gravitational movement. The primary stage was connected to rather catastrophic rotational blockslide which turned into earthflow in its distal part. It is evidenced by strongly fragmented landslide material with flow-type structures. Secondary deformations resulted from numerous younger rotational slides accompanying the collapse of the landslide toe which affects older (original) flow-type landslide structures (Pánek et al. 2012). Clays and claystones sampled from several sites of the landslide body (involving slip surfaces) contain relatively high (>10 %) content of smectite. It indicates high water absorption capacity of material with possible swelling

and shrinking behaviour during wetting and drying, thus leading to the decreasing shear strength of the landslide substratum.

5   Time Constraints of Landslides

The age of megalandslides was determined on the basis of the dating of (i) deposits that had been deformed and incorporated into the material of landslides and (ii) post-landslide deposits directly overlying the deformed landslide body. It was possible to get reliable estimates of the slope failures age (Lang et al. 1999). We dated one giant landslide in the Crimean area (Alma landslide; Pánek et al. 2008a, b) and the Uspenskoye megalandslide in the foothills of the Caucasus mountains (Pánek et al. 2012). Other landslides situated in the Crimean region were dated relatively, i.e. in relation to other dated landforms and deposits (Pánek et al. 2008a, b).

The activity of the Crimean landslides/ Ukraine was determined to two main stages: the interval between the end of the Last Glacial and ca 6 ka BP, and ca 1–1.5 ka BP (Pánek et al. 2008a, b). The largest landslide observed in the Kuban river valley/Russia (Uspenskoye megalandslide) originated between ca 13 and 35 ka BP during the Last Glacial (Fig. 25.4). This time interval was determined on the basis of AMS dating of deformed organic soil within the landslide body and OSL dating of loess overlying landslide body (Pánek et al. 2012). Although the dating of basal sequences of loess and its derivates covering the megalandslide body did not bring fully consistent ages, we can determine a minimum age of the deposition of loess and its derivates covering the proximal part of the megalandslide to ca 18 ka BP, which corresponds to the Last Glacial maximum. Taking into account the age of the deformed palaeosol (ca 35 ka BP), major emplacement of the
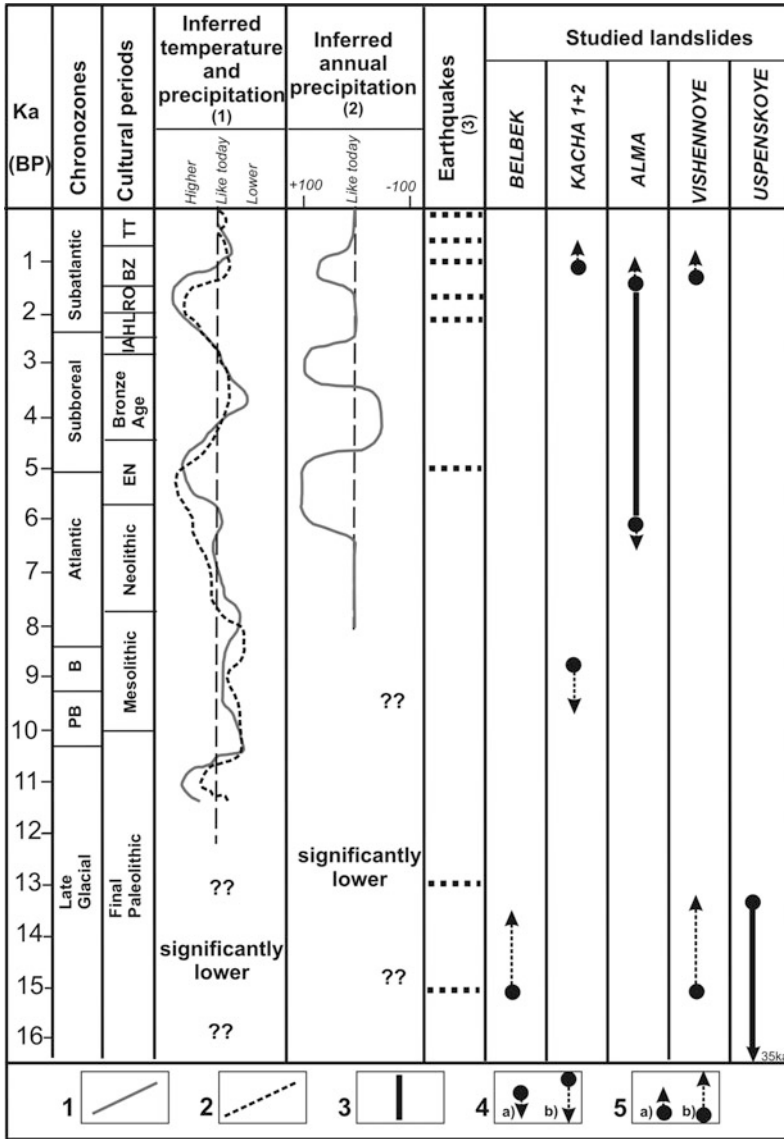
Fig. 25.4 Palaeoenvironmental correlation between climate, palaeoearthquakes and results of dating of individual landslides (A, Cordova and Lehman 2005 (southwestern Crimea); B, Kremenetski1995 (southern Ukraine); C, Nikonov 1995), *EN* Eneolithic, *IA* Iron Age, *HL* Hellenistic, *RO* Roman, *BZ* Byzantine, *TT* Tatar/Ottoman. Legend symbols: (1) palaeoprecipitations; (2) palaeotemperature; (3) stable period in the landslide development; (4) minimal age of a landslide (*a* landslide emerged probably just before dated deposits, *b* significant time lag suggested between dated deposits and the landslide development); (5) maximum age of a landslide (*a* landslide emerged probably just after dated deposits, *b* significant time lag suggested between dated deposits and the landslide development) (modified and completed scheme of Pánek et al. 2008a)

megalandslide can be included into the Late Pleistocene interval between 18 and 35 ka BP. Loess base in the distal part of the landslide, which was affected by subsequent rotational collapse, reveals somewhat younger age falling into ca 13 ka BP. It roughly ranges the activation of the landslide toe within the interval of 13–18 ka BP.

6 Discussion and Conclusion

Megalandslides situated in the low-gradient terrains of the foothills of the Caucasus-Crimean mountain belt form a distinct cluster of extremely large slope deformations situated outside high mountainous areas. Some of these landslides belong to the largest detected slope failures in Europe (Strom 2004; Ivy-Ochs et al. 2009) despite being much smaller than the outstanding Flims landslide (Heim 1883; Poschinger and Haas 1997; Pollet et al. 2005). Although they have recently been affected by secondary shallow slope instabilities, the main landslide bodies are fossil features that predominantly originated in the late Pleistocene and early Holocene phases. All landslides originated within mechanically weak clay-rich sediments containing mineral smectite characterized by swelling and shrinking behavior.

In spite of the fact that the determination of the triggering factors of ancient megalandslides is difficult, we consider the palaeoseismic origin as quite reliable because the landslides are located close to some Late Quaternary faults. This is because hydroclimatic origin of the landsliding was rather unlikely in the period involving the Last Glacial and the Holocene. According to the latest palynologic studies (Gerasimenko 2007), the Last Glacial conditions were characterized by prevailing aridity in this area. Slightly wetter conditions (ca 100 mm higher annual precipitation totals, in comparison with nowadays) occurred during the warmer Middle Valdai Briansk Interstadial (33–24 ka BP; Markova et al. 2002; Simakova 2006), in the
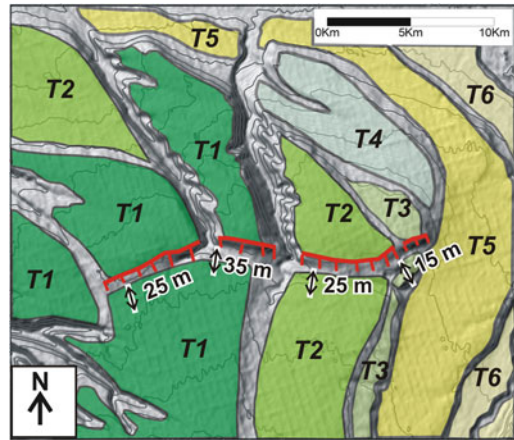
Fig. 25.5 Neotectonic sketch of likely seismogenic fault in the vicinity of the Uspenskoye megalandslide (Caucasus foredeep, Russia). The fault dislocates a sequence of middle-late Pleistocene river terraces. Cumulative vertical offset of terrace levels varies between 35 and 15 m for the oldest (T1) and the youngest (T3) levels respectively. The latest late glacial terraces (T5) and Holocene terraces (T6) were most likely unaffected by the fault activity (according to Pánek et al. 2012)

middle Holocene (5.4–4.5 ka BP; Cordova and Lehman 2005) and during late Holocene subatlantic chronozone (2–1.5 ka BP; Cordova and Lehman 2005) (Fig. 25.4).

Specific stratigraphic evidence of repeated seismic activity in the northern part of the Crimean Penninsula was discussed by Nikonov (1995) who inferred several strong earthquakes during the Late Glacial and Holocene epochs (e.g. 15 , 13 , 5 ka BP; during the first century BC, third century AD, tenth century AD; and the fourteenth and eighteenth centuries AD) (Fig. 25.4). It is therefore probable that paleoseismic events could cause the formation of the studied landslides. Potential earthquake origin of the megalandslide in the Kuban river valley (Uspenskoye megalandslide, Caucasus foredeep) coincides with the presence of nearby situated tectonically deformed Middle to Late Pleistocene river terraces (Fig. 25.5). If the assumption of the seismic origin of the landslides in question is correct and if the earthquakes occurred at a given distance from the landslide sites than, using Keefer's relationship (Keefer 1984),
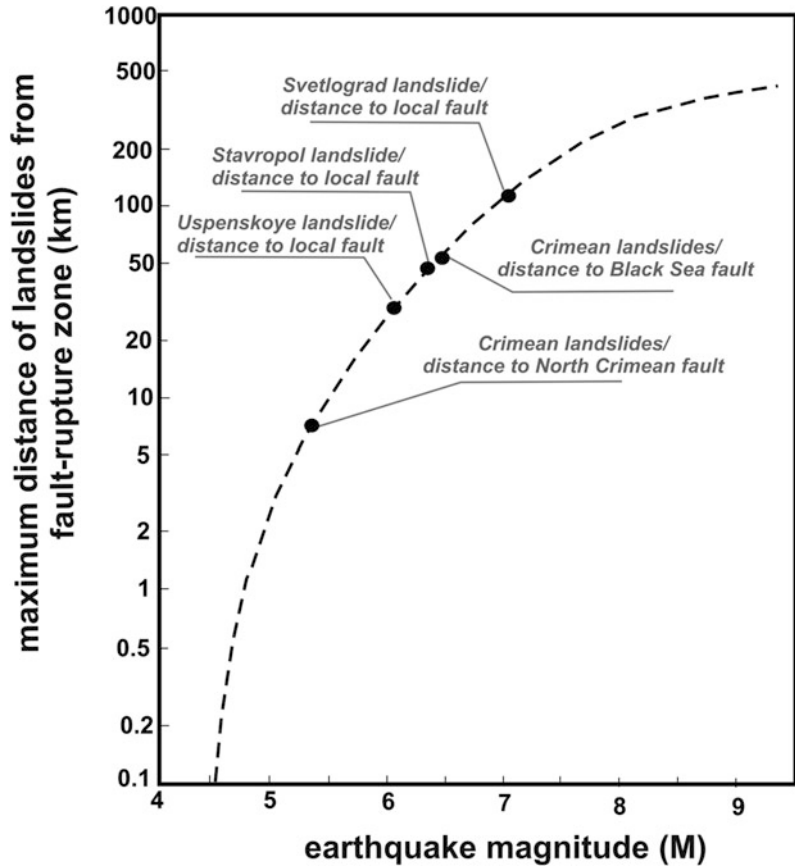
minimal magnitude value of such an earthquake can be estimated (Fig. 25.6). Further work dealing with the relationships between low-gradient megalandslides situated in the foredeep of Caucasus-Crimean orogenic belt should be addressed to the dating of the offset morpho-stratigraphic markers and detailed palaeoseismic investigations.

References

Aylsworth JM, Lawrence DE, Guertin J (2000) Did two massive earthquakes in the Holocene induce widespread landsliding and near-surface deformation in part of the Ottawa Valley, Canada. Geology 28:903–906

Azañón JM, Azor A, Přez-Peña JV, Variolo JM (2005) Late quaternary large-scale rotational slides induces by river incision: the Arroyo de Gor area (Guadix basin, SE Spain). Geomorphology 69:152–168

Cordova CE, Lehman PH (2005) Holocene environmental change in southwestern Crimea (Ukraine) in pollen and soil records. The Holocene 15:263–277

Derenyuk NE, Vanina MV, Gerasimov MY, Pirovarov SV (1984) Geological map of the Crimea. Geological Ministry of Ukraine, Kiev, scale 1:200,000 (in Russian)

Gerasimenko N (2007) Environmental changes in the Crimean Mountains during the last interglacial-

middle pleniglacial as recorded by pollen and lithopedology. Quat Int 164(165):207–220

Heim A (1883) Der alte Bergsturz von Flims. Jb. d. Schweizer Alpenclub, 18 Jg, pp 295–309

Ivy-Ochs S, Poschinger AV, Syna HA, Maisch M (2009) Surface exposure dating of the Flims landslide, Graubünden, Switzerland. Geomorphology 103:104–112

Keefer DK (1984) Landslides caused by earthquakes. Geol Soc Am Bull 95:406–421

Korup O, Clague JJ, Hermanns RL, Hewitt K, Strom AL, Weidinger JT (2007) Giant landslides, topography, and erosion. Earth Planet Sci Lett 261:578–589

Kremenetski CV (1995) Holocene vegetation and climate history of southwestern Ukraine. Rev Palaeobot Palynol 85:289–301

Lang A, Moya J, Corominas J, Schrott L, Dikau R (1999) Classic and new dating methods for assessing the temporal occurrence of mass movements. Geomorphology 30:33–52

Markova AK, Simanova AN, Puzachenko AY, Kitaev LM (2002) Environments of the Russian plain during the Middle Valdai Briansk Interstade (33,000–24,000 yr B.P.) indicated by fossil mammals and plants. Quat Res 57:391–400

Nikonov AA (1995) The stratigraphic method in the study of large past earthquakes. Quat Int 25:47–55

Pánek T, Hradecký J, Smolková V, Šilhán K (2008a) Gigantic low-gradient landslides in the northern periphery ofthe Crimean Mountains (Ukraine). Geomorphology 95:449–473

Pánek T, Hradecký J, Smolková V, Šilhán K (2008b) Giant ancient landslide in the alma water gap (Crimean Mountains, Ukraine): notes to the predisposition, structure and chronology. Landslides 5:367–378

Pánek T, Danišík M, Hradecký J, Frisch W (2009) Morpho-tectonic evolution of the Crimean Mountains (Ukraine) as constrained by apatite fission track data. Terra Nova 21:271–278

Pánek T et al (2012) A megalandslide in the northern caucasus foredeep (Uspenskoye, Russia): geomorphology, possible mechanism and age constraints. Geomorphology (in press)

Philip H, Ritz JF (1999) Gigantic paleolandslide associated with active faulting along the Bogd fault (Gobi–Altay, Mongolia). Geology 27:211–214

Pollet N, Cojean R, Couture R, Schneider J-L, Strom AL, Voirin C, Wassmer P (2005) A slab-on-slab model for the Flims rockslide (Swiss Alps). Can Geotech J 42:587–600

Poschinger AV, Haas U (1997) Der Flimser Bergsturz, doch ein warmzeitliches Ereignis? Bulletin für Angewandte Geologie 2(1):35–46

Simakova AN (2006) The vegetation of the Russian plain during the second part of the Late Pleistocene (33–18 ka). Quat Int 149:110–114

Strom AL (2004) Rock avalanches of the Ardon river valley at the southern foot of the Rocky range, Northern Caucasus, North Osetia. Landslides 1(3):237–241

Vincent SJ, Carter A, Lavrishchev VA, Rice SP, Barabadze TG, Hovius N (2011) The exhumation of the western Greater Caucasus: a thermochronometric study. Geol Mag 148:1–21

On the Tasikmalaya Earthquake Induced Landslide in Indonesia: Field Investigation

26

Aly Ahmed, Budi Brahmantyo and Keizo Ugai

Abstract

On Wednesday September 2nd, 2009 at 14:55 pm the 7-magnitude earthquake struck the southern coast of the main island of Java near Tasikmalaya city in Indonesia. The earthquake and subsequent landslides resulted in at least 75 deaths, more than 900 injuries, and the displacement of more than 88,000 people from nine districts in Central and West Java which are near the epicenter as of September 7. Tremors damaged or destroyed more than 55,000 houses in 13 districts, including the most-affected areas of Tasikmalaya, Cianjur, Garut, and Bandung. The magnitude of this earthquake was strong enough to cause office blocks to sway and windows to shatter in Jakarta. Many houses and commercial buildings had collapsed in the worst-hit areas around the towns of Tasikmalaya and Sukabumi. The US Geological Survey reported that the quake occurred less than 200 km south of Jakarta at a depth of 49 km. The location of this earthquake was found in latitude 7.809° south and longitude 107.259° east. Site investigations were done to explore the hazards induced by the Cikangkareng landslide. Based on site investigations, it was found that there were various disasters and rock avalanches observed in the affected area. The run-out distance of rock avalanches was found approximately 600 m measured from the toe of mount. The profile of the rock avalanche, which was induced by landslide, consists of three segments with different inclination angles.

A. Ahmed (✉)
Civil Engineering Department,
Beni-Suef University, Beni-Suef, Egypt
e-mail: aly_76@hotmail.com

B. Brahmantyo
Department of Geology, Bandung Institute
of Technology, Bandung, Indonesia

K. Ugai
Civil and Environmental Engineering Department,
Gunma University, Kiryu, Japan

1   Introduction

The earthquake that shook most of the West Java province on Wednesday, September 2nd, 2009 at 14:55 pm has caused much damage in various areas, especially in the southern part of West Java. An earthquake with a magnitude-7 caused

USGS ShakeMap : JAVA, INDONESIA
Wed Sep 2, 2009 07:55:01 GMT M 7.0 S7.81 E107.26 Depth: 46.2km ID:2009lbat

Map Version 4 Processed Tue Sep 8, 2009 06:07:10 AM MDT -- NOT REVIEWED BY HUMAN

PERCEIVED SHAKING	Not felt	Weak	Light	Moderate	Strong	Very strong	Severe	Violent	Extreme
POTENTIAL DAMAGE	none	none	none	Very light	Light	Moderate	Moderate/Heavy	Heavy	Very Heavy
PEAK ACC.(%g)	<.17	.17-1.4	1.4-3.9	3.9-9.2	9.2-18	18-34	34-65	65-124	>124
PEAK VEL.(cm/s)	<0.1	0.1-1.1	1.1-3.4	3.4-8.1	8.1-16	16-31	31-60	60-116	>116
INSTRUMENTAL INTENSITY	I	II-III	IV	V	VI	VII	VIII	IX	X+

very pronounced shaking of up to Bandung and Jakarta. The location of this earthquake was found in between latitude 7.809° south and longitude 107.259° east (USGS, 2009). Figure 26.1 shows the intensities of that earthquake based on USGS map. This figure shows that at a distance of 50–75 km from the epicenter of the earthquake reached intensity VI–VII (strong–very strong), Bandung (within 100 miles) intensity V–VI (medium–strong), and Jakarta (195 km) the intensity of III–IV (weak-light). Due to that earthquake, there were numerous large and long run-out landslides occurred in different areas near Tasikmalaya and Sukabumi cities. One of the most hazardous landslides which accompanied rock avalanche occurred after the shock of

earthquake. The site of this rock slide avalanche is close to the epicenter of Java earthquake as presented in satellite map in Fig. 26.2.

Based on field investigations and interview to local people in the most-affected area, it was found that there are many disasters occurred especially due to landslides, which is presented in Fig. 26.3, such as collapse of roads and houses and people loss. The affected areas were valleys in mountains. The fall height of debris was approximately 200 m which is measured from the original ground surface of the valley to the top surface of mountain and the slope of mountains in the site of landslide is steep with the angle approximately of 64°. While after landslide occurred, the angle of the slope in this part was

Fig. 26.2 Satellite map for the induced landslide location at Cianjur, Java Province, Indonesia [Scale 1:12,000] (http://earth observatory.nasa.gov/ NaturalHazards/diunduh 4 May 2010)

Fig. 26.3 Overview for the induced landslide (major affected parts)

found about 50°. The run-out distance of the rock avalanches which is generated by the landslide ranged between 500 and 600 m and the average thickness of the deposit around 30 m with a volume of about approximately 4.8 million cubic meters. Based on the field investigations, the

Fig. 26.4 Examples for the shapes of natural slopes in the Clicangkareng landslide area

profile of the rock avalanche consists of three segments which correspond to the following three angles of 32.4°, 15° and 11° from up slope to down slope, approximately.

2 Gelogical Background of Cikangkareng Landslide Area

Geologically, Cikangkareng landslide area is located in a giant collapse in dissected plateau of South Cianjur, West Java Province, Indonesia.

The dimension of the collapsed valley is approximately 5×6 km^2 in ellipsoidal shape. Cisadea, the main river, flows from north to south, exactly in the center of the ellipsoidal collapse valley. The escarpments of the collapse valley, especially in the west part, have very steep slopes, and some segments are vertical as presented in Fig. 26.4.

The slopes are very prone to landslide, fall or topple movement types. In geological map scale 1:100,000 (Koesmono 1976), the collapsed valley is dominated by a Quaternary sediments of talus and landslide deposits. It is not explained how the

Fig. 26.5 Lineaments
interpretation from
IKONOS imagery
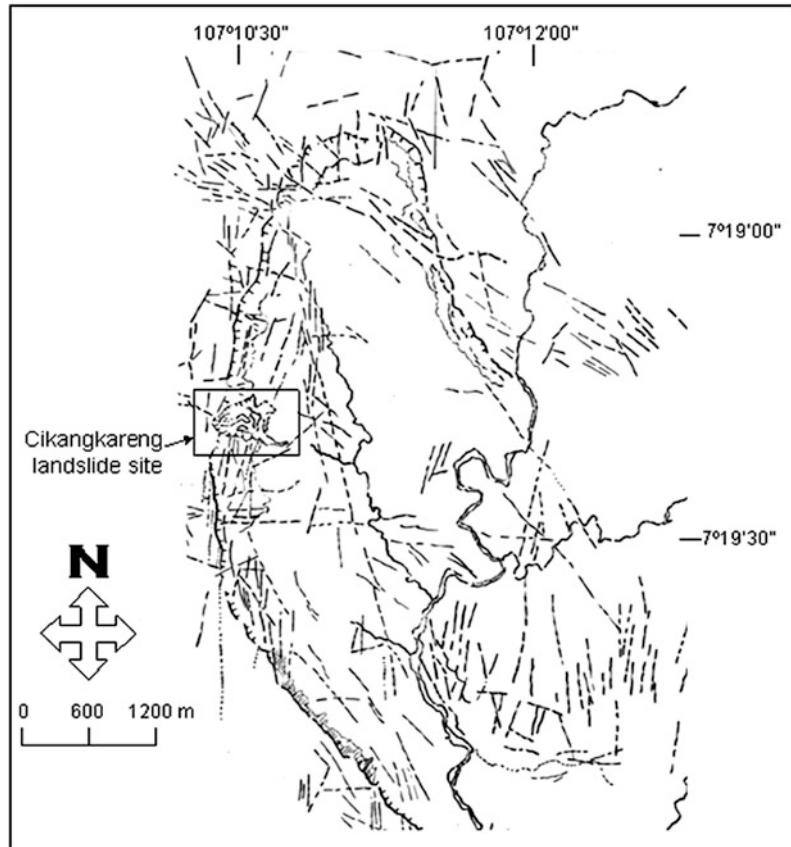
collapsed valley is formed. However, with such giant shape, it is believed that the forming of the collapse is related to tectonic origin. The plateau which formed by almost horizontal bed of the Bentang Formation was collapsed in the phase of uplifting processes of the entire area. (Fig. 26.5)

Lineaments interpreted from IKONOS imagery shows that the collapse is controlled by several orientations, which probably control the forming of the collapse valley as presented in Fig. 26.6. Geomorphological analysis of avalanches in the investigated site, which is presented in Fig. 26.6, shows that the avalanche is mainly controlled by large blocks of rocks consisting generally of sandy tuff. These facts clearly indicate an essential part for the rock formation, which originally originated from the upper collapse part. Blocks of sandstone have the largest diameter up to 5 m,

generally 1 m, and smaller pieces. Upper body is covered by landslide material of pebbly red soil.

3   Interpretation of Landslide Mechanism Based on Field Survey

The Cikangkareng landslide (its name based on the name of the village where it occurred) was induced by the earthquake on September 2nd 2009. The epicenter of the earthquake was about 35 km just south of the landslide site. Report from eyewitness, the landslide was first a lower block collapse and became rock avalanche down-slope. The landslide toe reached 600 m from the escarpment foot. It was then followed by rock avalanche and soil fall from the top of

Fig. 26.6 Interpretation of Cikangkareng landslide body from IKONOS imagery, completed by field observations
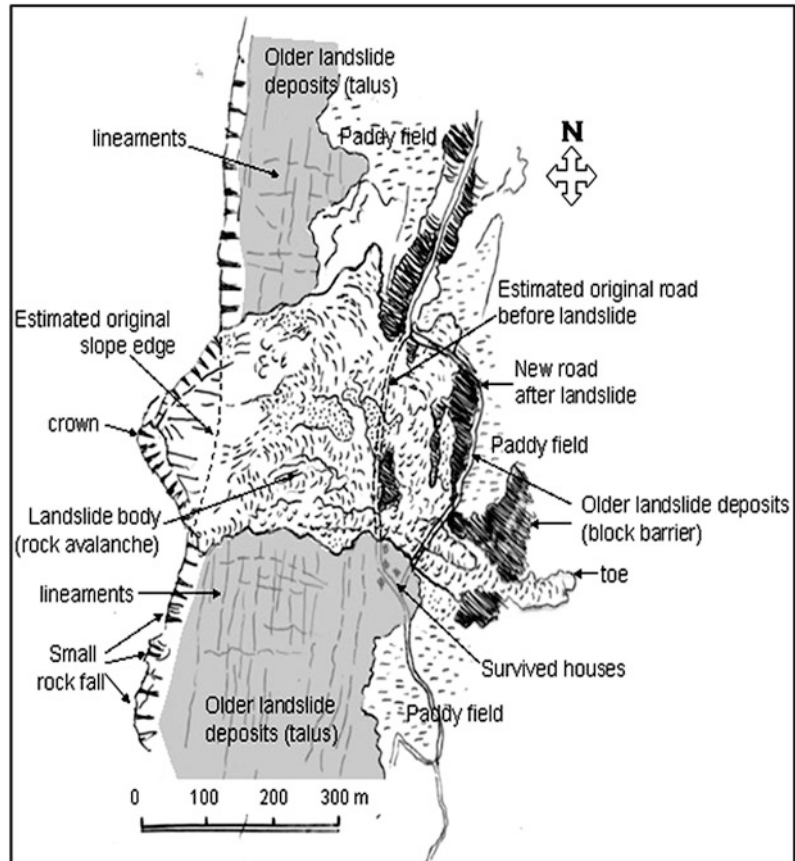
the escarpment. However the remaining huge block is now still on the escarpment, a hazard threat in the future. The interpretation of landslide area drawn from IKONOS imagery and completed with field observation is shown in Fig. 26.6. From the interpretation, it is observed that the lower slopes of the escarpment are the blocks or talus deposits of older (ancient) landslide. During September 2nd, 2009 earthquake, some of these older landslide deposits became block barriers of rock avalanche. That was how the rock avalanche ran in narrower shape following a narrow southern valley to the east of main body which was stopped by the barriers.

Before the earthquake avalanche events on 2nd September 2009, the lower slope area is generally occupied by agricultural farmland, and on gentle slopes near a settlement. It is still seen in other area along the vertical cliff. The situations such as this, which led to the high risk of

such disasters that long time ago hit the area called Urughanapi, coincides with the shock of an earthquake of 2nd September 2009. From field observations and interviews with eyewitnesses, the occurrence of the 2nd September 2009 Cikangkareng avalanches can be resumed into a process that can be seen in Fig. 26.7.

Figure 26.7(1) shows Cikangkareng conditions before landslide. Just as was seen in the morphology of some segments of the cliffs of depression valley, not whole cliff is an intact cliff. There is a block that seems to rely on the cliff area. This is also told by eyewitnesses who stated that before the avalanche he could climb the slope and found several terraces. The foot of high cliffs reaches a height of between 203 and 212 m (the height difference measurements with GPS). The shaded part in the lower slope presents the original cultivated soil which is covered with some rock avalanche previously

Fig. 26.7 The process of the Cikagkareng avalanche
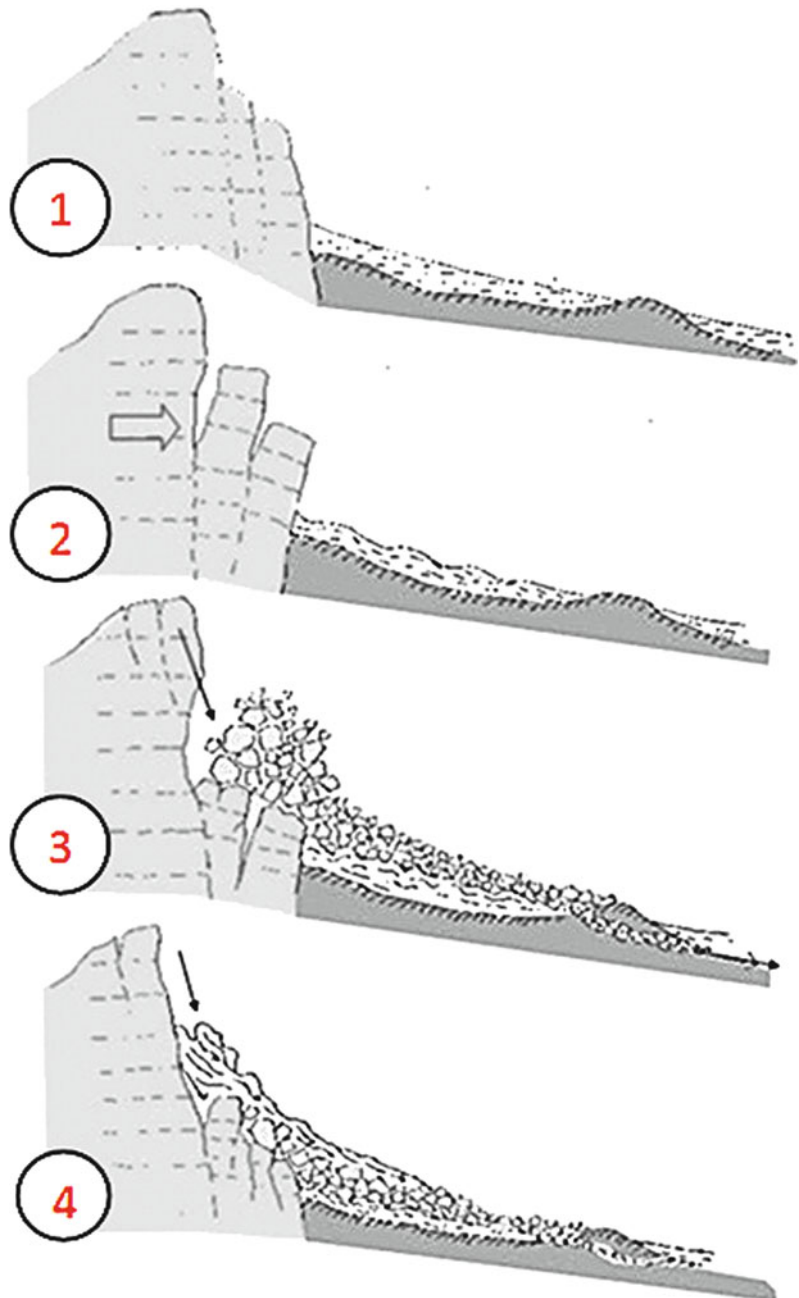
because this site was subjected to landslide prior to September 2nd, 2009.

Figure 26.7(2) shows the estimated initial avalanche occurrence when M-7 earthquake on the 2nd September 2009 shocked the area. The shock of the earthquake is estimated to push the block that rests on a cliff areas resulting in the collapse of blocks such as rapid toppling. Columns presented in this figure are the separated rock blocks from the body mountain, which occurred after the earthquake directly. This is in contrast to the process of slow flexural toppling (Dikau et al. 1996). This process produces lumps of rock debris fraction into a

narrow valley in the downstream direction as presented in Fig. 26.7(3).

Rock debris avalanche was fanned into a small creek stemming the northward and retained by the mounds and ridges which are the ancient landslide deposits. To the south, the avalanches pass through a small valley between the ridges of ancient landslides and then the sediment flowing downstream towards the valley. Witnesses stated that before the top of the slope collapsed, just lower parts of the slope first collapsed and struck the nearest settlement below.

The next process when the collapse of the upper slope lost its support from the bottom parts is presented in Fig. 26.7(4). Cikangkareng avalanche mechanism is expected to last a falling rock (rock block) which was then shattered into smaller blocks of stone covering the first avalanches. This process is documented by eyewitness who saw the fall of the last process in the form of lumps of soil (rock) is generally red soils (weathered sandstone tuff). After the avalanche stops, the remaining blocks of rock seemed to back leaned against the cliff of the depression valley. This condition seemed to return to its original condition and a threat of avalanches in future.

4   Conclusions

IKONOS imagery interpretation that is confirmed by field observations and interviews with eyewitnesses concludes that Cikangkareng avalanche is a landslide triggered by the 2nd September 2009 earthquake. The process is not a simple mechanism. The process was preceded by the pushing of block of rocks on the slope below a tuff formations then broken into pieces and erode downstream into such debris flows as far as 600 m into a small valley. This process is then followed by collapsing of rocks on a cliff with dominant of red soils. This process produced a crown of 250 m width. In the field observations that were carried after the landslide with 8 months approximately, the large blocks still rested on the main cliff. Observations of the crown found that the block against the cliffs have several cracks, as cracks that also occurred in the crown. This situation is considered a hazard of serious avalanche in future if the same area subjected to earthquake.

References

http://earthobservatory.nasa.gov/NaturalHazards/view.php?id=40386. Accessed Feb 2012

http://earthquake.usgs.gov. Accessed Sept 2011

http://earthquake.usgs.gov/earthquakes/eqinthenews/2009/us2009lbat/#details. Accessed Sept 2011

http://www.theage.com.au. Accessed Sept 2011

http://www.theage.com.au/world/40-dead-as-powerful-earthquake-rocks-java-20090902-f8ka.html. Accessed Feb 2012

Dikau R, Brunsden D, Schrott L, Ibsen ML (1996) Landslide recognition, identification, movement and causes. Wiley, Chichester

Koesmono M (1976) Geological Map of Sindangbarang and Bandarwaru Quadrangles, Jave, Scale 1:100,000. Geological Survey of Indonesia, Bandung

Damages of Hillside Embankments in Sendai City During the 2011 Great East Japan Earthquake

27

Tomohiro Mori, Yoshio Tobita and Takashi Okimura

Abstract

The 2011 Great East Japan Earthquake resulted in severe damages to housing and housing lots. In particular the hillside embankments for residential use surrounding the downtown of Sendai city suffered from serious damages. Many hillside lands which had been damaged during the 1978 off Miyagi-Prefecture earthquake were subjected to damages again. Typical damaged hillside embankments in Sendai city were investigated and discussed in this paper. The main cause of the damages of housings is not the seismic motion but the failure of fill embankment. Comparing the damages during the 2011 earthquake with those during the 1978 earthquake, the countermeasures constructed after the 1978 earthquake performed well for preventing the large landslide type failure; however, they were not successful in the reduction with the damages of housing and housing lots, which were attributed to the ground displacements such as cracks, differential settlement, and shallow slips.

T. Mori (✉)
Department of Civil Engineering,
Graduate School of Engineering, Tohoku
University, Sendai, Japan
e-mail: mori@soil1.civil.tohoku.ac.jp

T. Mori
Geotechnical Engineering Laboratory, Aoba 6-6-06
Aramaki, Aoba-ku, 980-8579, Sendai Miyagi, Japan

Y. Tobita
Department of Civil and Environmental
Engineering, Faculty of Engineering,
Tohoku-Gakuin University, Tagajo, Japan
e-mail: tobita@tjcc.tohoku-gakuin.ac.jp

T. Okimura
Construction Engineering, Research Institute
Foundation, Kobe, Japan
e-mail: okimura@kensetsuk.or.jp

T. Okimura
Kobe University, Kobe, Japan

1   Introduction

At 2:46 P.M., March 11th, 2011, a giant earthquake named as "The 2011 off the Pacific Coast of Tohoku Earthquake with the moment magnitude 9.0 attacked east Japan resulting in an enormous loss of human and social facilities. The earthquake and the resulting damages is also called "the 2011 Great East Japan Earthquake". Hereinafter we will use the 2011 earthquake for brevity. A lot of the housing lots in Sendai city suffered damage from the 2011 earthquake, and particularly the damages of valley-filled embankment were remarkable. And, most of the hillside embankments for residential use had suffered damages from the 1978 off Miyagi-Prefecture earthquake were again seriously damaged during the 2011 earthquake despite that the countermeasures such as groundwater drainage wells and restraining piles had placed for the prevention of further hazards.

In this paper, the typical severe damaged housing lots on the hillside embankment in Sendai city are introduced in order to grasp the feature of damage and the damage factor. The effects of countermeasures built after the 1978 off Miyagi-Prefecture earthquake are also introduced.

2   Overview on Damages of Hillside Embankments in Sendai City

The hillside embankments for residential use surrounding the downtown of Sendai city were severely damaged during the 2011 earthquake. More than 4,000 housing lots (corresponding to more than 7,000 houses) were severely damaged and the damaged sites with more than 10 housing lots were counted to be 63 (97 if counted in terms of house unit). The investigation results just after

the earthquake were reported by Koseki et al. (2011), Okimura et al. (2011) and Wakai et al. (2012) among others.

Table 27.1 shows the main results taken from the fundamental data on the 18 damaged sites to which Sendai city carried out the detailed survey and investigation after the 2011 earthquake. Locations of these 18 damaged sites are indicated in Fig. 27.1, and "No." in Table 27.1 corresponds to the number with white circle in Fig. 27.1. One site (Midorigaoka 3 choume) was examined by Miyagi prefecture. The features of items in damaged sites are summarized as follows.

1. The type of hillside embankment: The damages of valley filled embankment were eminent.
2. The soil type: the soils composing the damaged hills containing the high ratio of fine particles (less than 75 μm in diameters) were used for filling, which made it difficult to drain appropriately from the fill embankment. The soils with considerable fine contents also led to the rise-up of the water table in the hillside embankment.
3. The loose state of soils: The state of soils may be identified by the N value from the standard penetration test (SPT for brevity in what follows). The SPT N values from the surface to the 5 m depth range from 0 to 5 in most sites, which clearly show the loose state of hillside embankments in Sendai city.
4. The thickness of fill: the maximum depth of fill ranges from 6.0 m (Jingahara) to 26 m (Matsugaoka) depending on the original topography. The averaged depth of the fill varies from shallow (3.0 m at Aoyama 2 choume) to deep (18.0 m at Matsugaoka).
5. The level of water table: The water level of fill embankments are shallow in most cases, which may be attributed to the soil type with

Table 27.1 Fundamental data on 18 damaged sites to which Sendai city carried out detailed survey and investigation after the 2011 earthquake

No.	Name	Number of damaged housing lot (point)	Developed year (year)	Fill type (–)	Fill material (–)	The character based on the method of classification of geomaterials for engineering purposes	Fine fraction content (%)	Classification of failure types* (–)	Ave.N-value (Dep.=0–5m) (–)	Fill thickness (max./ave.) (m)	Ave.inclination of present ground surface (degree)	Ave.inclination of old ground surface (degree)	Ground water table (G.L.(m))	Representative counter measure work (–)
1	Midorigaoka-2-choume	30	1955–1964	Valley filled	Clay contained sand and gravel	C-SG	76.3	(2)	0–4	8.0/5.0	9	11	−3 to −4	Prevention work Groundwater drainage work
2	Midorigaoka-3-choume	94	1961–1962	Valley filled	Sandy sih contained gravel	SM-G	47.7	(3)	0–8	21.0/10.0	8	7	−13 to −18	Prevention pile Ground water drainage work
3	Midorigaoka-4-choume	107	1960–1965	Valley filled Partially filled	Silty sand	SM	34	(2)	0–3	7.0/5.0	12	8	−0.5 to −6	Retaining wall Prevention pile
4	Ootoya-machi	47	1955–1960	Valley filled	Gravelly clay contained sand	CG-S	61.2	(2) and (3)	0–2	7.0 13.0	11	8	−2 to −6	Prevention work Groundwater drainage work
5	Keiwa-machi	53	1955–1960	Valley filled	Fine sandy gravel	GFS	30.2	(2) and (3)	0–4	15.0/8.0	12~14	4	−1	Sliding control work Groundwater drainage work
6	Aoyama-1-choume	110	1963	Valley filled	Clayey sand contained gravel	SC-G	37	(2)	0–4	21.0/16.0	8	3	−1 to −15	Prevention work Recovery of retainig wall
7	Aoyama-2-choume	25	1963	Partially filled	Silty sand contained gravel	SM-G	33.4	(2)	0–5	8.0/3.0	9	9	−0.5 to −7.3	Anchorwork Lateral bore hole
8	Matsugaoka Area	45	1960–1967	Valley filled	Clayey sand contained gravel	SC-G	36.7	(3) and (4)	3–4	26.0/18.0	7	8	−3	Reinforced soil wall
9	Oritate-5-choume	57	1965–1972	Valley filled	Sandy clay contained gravel	CS-G	59.7	(2) and (3)	1–2	12.0/7.0	8	8	−3.0 to −5.7	Steel pipe pile Culvert
10	SeikaenArea	20	1975–1978	Valley filled	Sandy silt contained gravel Sand	SM-G	49.1	(2)	1~5	10.0/6.0	15	17	−1 to −10	Soil removal work Reinforced soil wort

Table 27.1 (continued)

No.	Name	Number of damaged housing lot (point)	Developed year (year)	Fill type (−)	Fill material (−)	The character based on the method of classification of geomaterials for engineering purposes	Fine fraction content (%)	Classification of failure types* (−)	Ave.N-value (Dep.=0–5m) (−)	Fill thickness (max./ave.) (m)	Ave.inclination of present ground surface (degree)	Ave.inclination of old ground surface (degree)	Ground water table (G.L.(m))	Representative counter measure work (−)
11	Takanohara-1-choume (North Area)	10	1989–1995	Valley filled	Finely sand contained gravel	SF-G	38.3	(2)	5	5.7/4.0	8	10	−1 to −3	Groundwater drainage work
12	Takanohara-1-choume (South Area)	4	1989–1995	Valley filled	Sandy clay contained gravel	CS-G	52.3	(2)	2–4	8.7/6.0	11	13	−9	Soil removal work Counterweight rill work
13	Takanohara-2-choume Takanohara-3-choume	41	1989–1995	Northan slope: partially filled Eastern and Western slope: Valley filled	Sandy clay contained gravel Sand	SC-G S	41.4	(3)	1–3	16.0/12.5	11	6	−6 to −9	Refilling
14	Nakayama-1-choume (TakimichiArea)	22	1965–1975	Valley filled	Silty sand	SM	49.4	(3)	1–3	12.5/6.8	22	25	0 to −3.6	Recovery of retaining wall
15	Nakayama-5-choume	31	1965–1970	Valley filled	Silty sand	SM	36.2	(2) and (3)	0–4	15.0/12.0	8	5	−1 to −3	Prevention work Groundwater drainage work
16	Futabagaoka Area	54	1961–1965	Valley filled	Clayey sand contained gravel	SC-G	Unknown	(3) and (4)	3	16.0/15.0	11	12	−2.5	Steel pipe pile Culvert
17	Nankodai-6-choume	14	1962–1985	Valley filled	Silt sand contained gravel	SM-G	27.9	(3) and (4)	1 ~21 (ave.=6.6)	14.0/10.0	8	5	−2 to −4	Sliding control work Groundwater drainage work
18	JingaharaArea	11	1975–1976	Valley filled	Silty sand contained gravel	SM-G	21.2	(3) and (4)	2 ~3	6.0/5.0	2	4	−2	Hardning work Open ditch and culvert

* Refer to Fig. 27.2
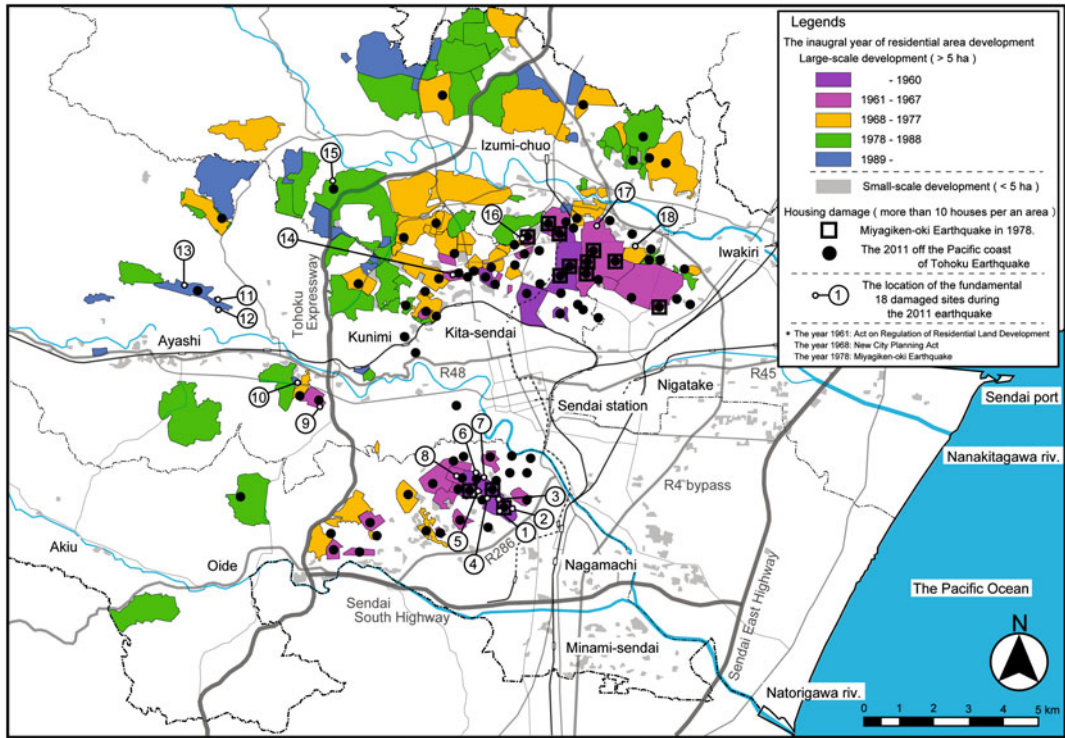
Fig. 27.1 Developed age of residential area, and damaged area in the 1978 earthquake and the 2011 earthquake

fine contents and to the bad performance of groundwater drainage works being constructed in fills.

The predominant features from 18 detailed investigations after the 2011 earthquake may be summarized as follows: (1) the soils used for the construction of hillside embankments contained high ratio of fine particles in most cases, which made it difficult to compact properly and drain from the embankment; (2) The water tables of most hillside embankments are shallow, which may be attributed to the poor permeability of soils and to the original valley topography collecting water from adjacent areas. In damaged residential lands, the ground water level changes rapidly by rainfalls, which may indicate the existence of water passage-away in the embankment. The ground water is also influenced by the performance of ground drainage works during construction. It is also necessary to distinguish a ground water from parched water. Further studies are necessary make clear the reason of the shallow water table in the embankments. The

inappropriate state of filled soils is considered to play an important role on the failure pattern of the damaged hillside embankments. The failure patterns observed in each damaged site are listed in Table 27.1 and illustrated in Fig. 27.2.

The landslide type failure is supposed to occur along the boundaries between the embankment and the original ground, which may be one of the causes of the damage of the embankment. Most of the damages may be classified into the ground displacements, which appears as shallow slips, open cracks, differential settlements due to the densification of loose soils, the lack in bearing capacity of the basement of retaining walls, and the liquefaction of sandy soils. It seems appropriate to note that the loose state of filled soils prevents large scale failure from occurring in many damaged sites, since the large size failure associated with localized deformation such as slip surface needs the sufficient strength of soils in embankments. There was no landslide failure type in the strict sense that this landslide should occur within the original soft ground.
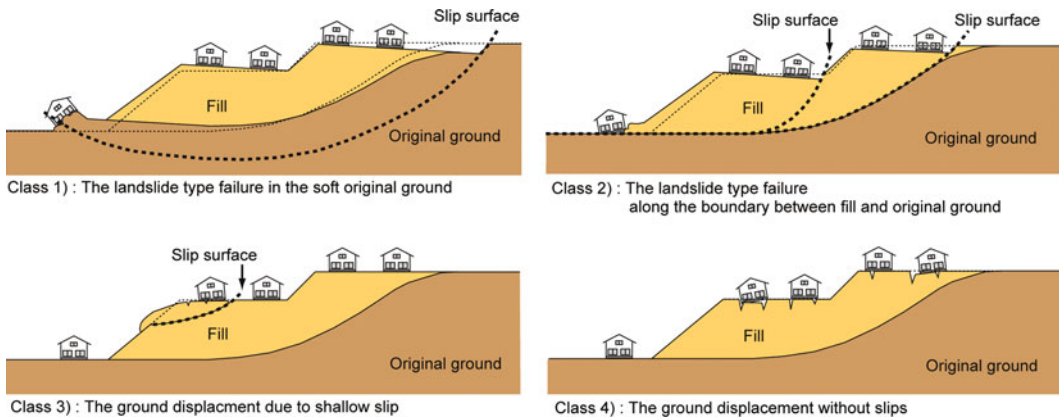
Fig. 27.2 Schematic figures for the tentative classification of failure type

3 Case Studies on Hillside Embankments

We here pick up 3 damaged hillside embankments with different damage mechanisms, which are taken from 18 damaged sites listed in Table 27.1. We discuss the failure type and the mechanisms yielding severe damages for each site.

3.1 Midorigaoka 3 Choume (Failure Type: Landslide Type Failure and Ground Displacements)

Midorigaoka 3 choume being a hillside embankment for residential use suffered severe damages during the 2011 earthquake, which locates 3 km south-west to the JR Sendai station (numbered as 2 in Fig. 27.1; "choume" means a numbered subdivision of an area). The residential land had previously suffered enormous damages due to the landslide type failure during the 1978 earthquake which was supposed to have occurred along the boundary between fill embankment and the original ground (Kawakami et al. (1978)).

After the 1978 earthquake the 427 restraining piles with the 32 cm in diameter were placed into the original ground in 5 rows in a zigzag fashion

almost vertical to the slope movement and two groundwater drainage wells were constructed. The arrangements of them are shown in Fig. 27.3. The housing lots in Midorigaoka 3 choume suffered serious damages again during the 2011 earthquake despite of the countermeasures constructed after the 1978 earthquake. Figures 27.4 and 27.5 show the plan and cross section views of damaged areas, the outline of damages, and the arrangements of piles and wells. There are two relatively narrow valley filled embankments in the land. The fill materials are composed of sandy soils with gravels and cohesive soils with gravels. The latter soils thus used for the creation of hillside embankment are rather poor, since they contain large amounts of fine particles. The clear transition between them was not observed but filled in a mixed way. The range of severe ground displacements (shallow slips and subsidence) and the distribution of surface cracks are shown in Fig. 27.4. The movement and the angles of inclination at the top of restraining piles are also shown in Fig. 27.4. The sand boils were also observed by the resident.

The drainage from the embankment using the two groundwater drainage wells can be supposed to work well, which leads to the lower level of water table observed from −13 m to −15 m from the ground surface. The restraining piles which were fractured during the 2011
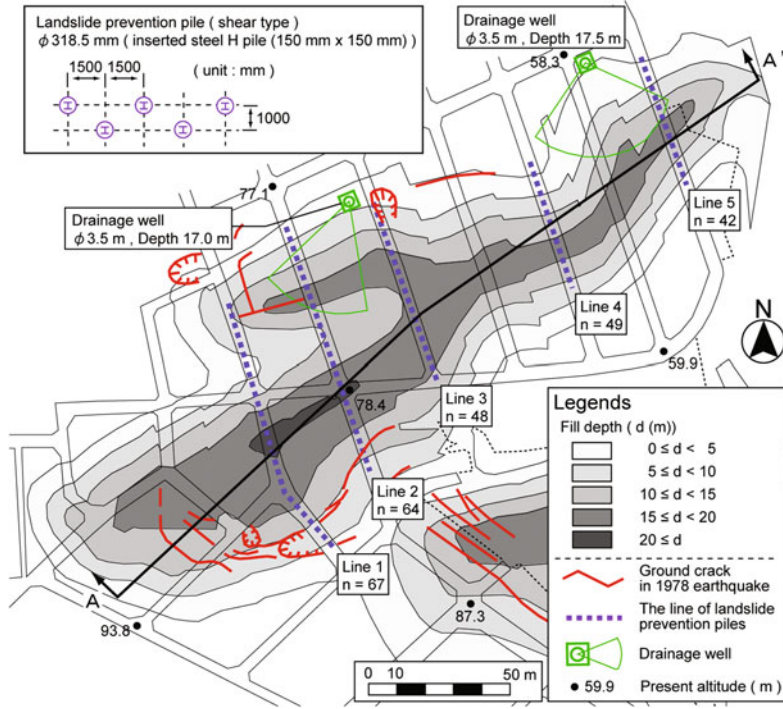
Fig. 27.3 Plan view on ground damage and counter measure of Midorigaoka-3-choume in 1978
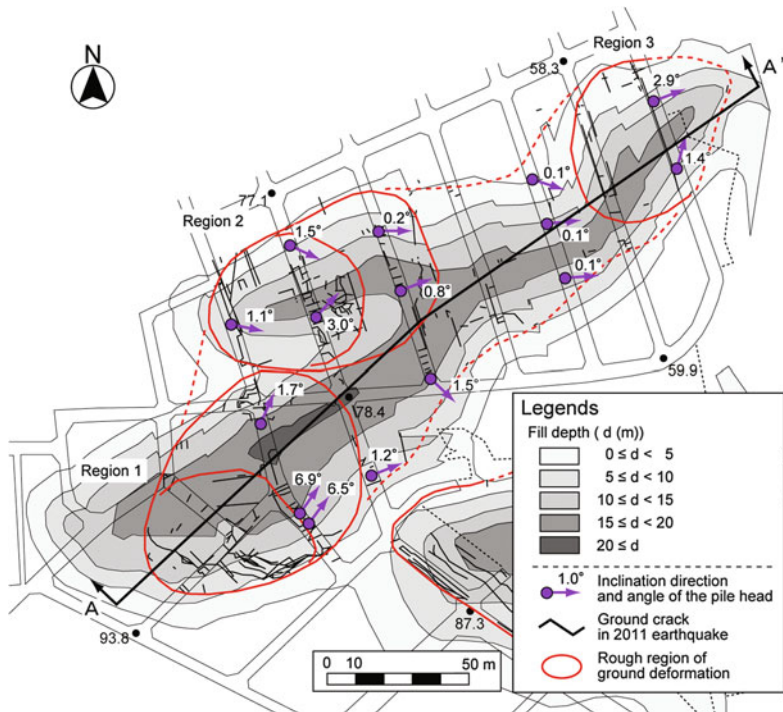
Fig. 27.4 Plan view on ground damage of Midorigaoka-3-choume in 2011
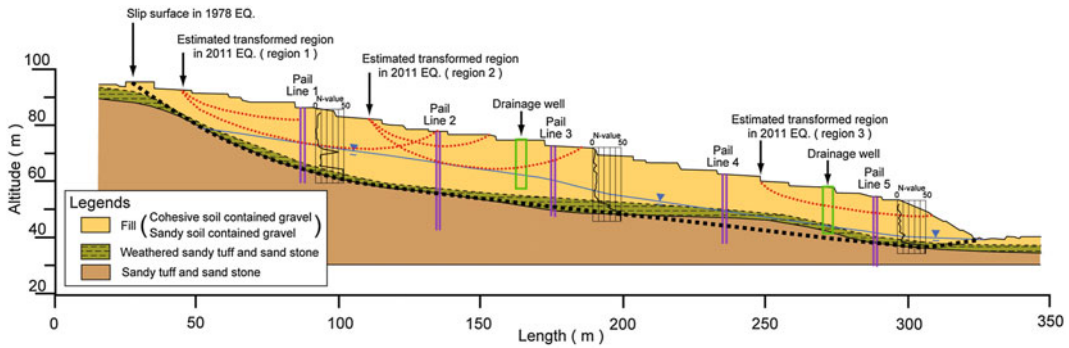
Fig. 27.5 Cross section view of Midorigaoka-3-choume along A–A' in Fig. 27.7

earthquake are also effective to resist the land slide type movement. Both countermeasures appears to have performed well during the 2011 earthquake, nevertheless, the housing lots on the valley filled embankment suffered severe damages, almost equivalent to the damages during the 1978 earthquake. Many modes of displacement occurred in the ground with shallow depths (amounting to 4 m or less). The severe damages during the 2011 earthquake of Midorigaoka 3 choume reinforced with wells and piles may indicate that due attention should be paid to the state of fill materials. The displacements may be attributed to the nature of soft ground which was subjected to seismically cyclic loadings. Ground displacements such as open cracks and differential settlement were observed between the parallel rows of piles. The shear deformation of the fill materials adjacent to the piles were constrained, the accumulation of sear deformation led to the compressive bulging of the ground near the row of piles. Ground displacements occurred in the housing lots resulted in the severe damages of houses.

The main causes leading to severe damages in Midorigaoka 3 choume may be summarized as follows: (1) a valley filled embankment; (2) the higher saturation of fill materials partly due to the considerable amount of fine contents as well as the character of valley filled land as the topography; (3) the relatively steep slope angle of the ground surface (8 degrees on the average) facilitating the down-movement of slopes in the case of liquefied soil.

3.2 Oritate 5 Choume (Failure Type: Landslide Type Failure in Fill and Ground Displacements, no Countermeasure After the 1978 Earthquake)

Oritate residential land locates (numbered as 9 in Fig. 27.1) 8 km west to the downtown of Sendai city and started to create the ground for housing in 1965 and completed in 1972. No damage occurred at this site during the 1978 earthquake. A lot of housing lots and houses suffered serious damages during the 2011 earthquake in this site on a valley filled embankment. Figures 27.6 and 27.7 show the plan and cross section views of this site. The angle of inclination of hillside embankment was from 6 to 8 degrees. The fill material was composed of cohesive soils with gravels; the original ground was composed of silt rock and gravel rock.

The survey after the 2011 earthquake showed that the water table was shallow being −3 m below the surface and the SPT N values were from 0 to 3 indicating the looseness of filled materials. Comparison of two satellite photographs before and after the 2011 earthquake showed remarkable displacements: 0.6 m at the crest, 2.5 m at the center, and 2.0 m at the tip of damaged area. The displacement measured by an in situ strain measures which installed after the earthquake have been less than 10 mm, which indicates that succeeding displacement after the earthquake were not eminent. Eminent and no damage areas were clearly distinguished
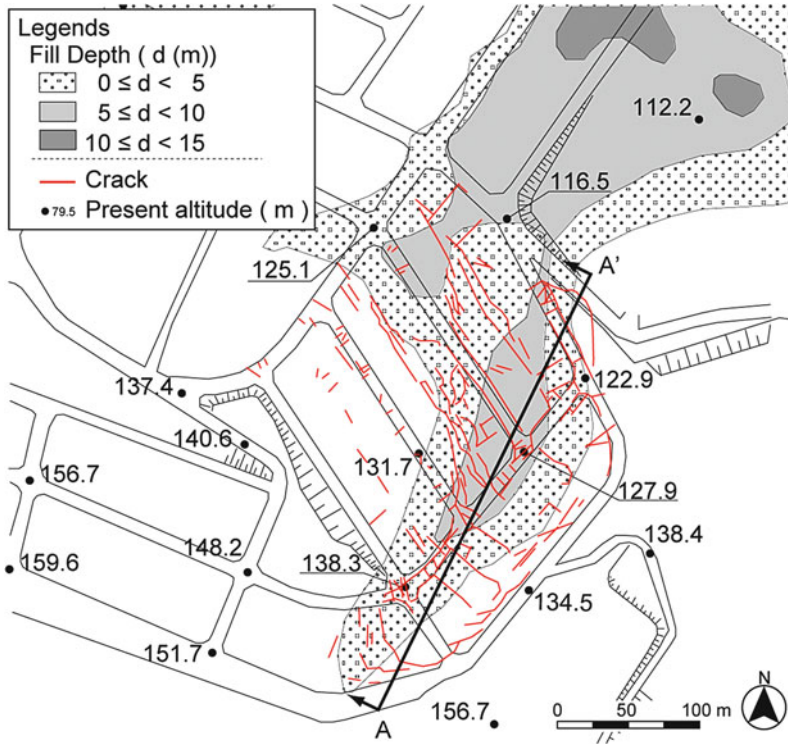
Fig. 27.6 Plane figure of Oritate-5-choume
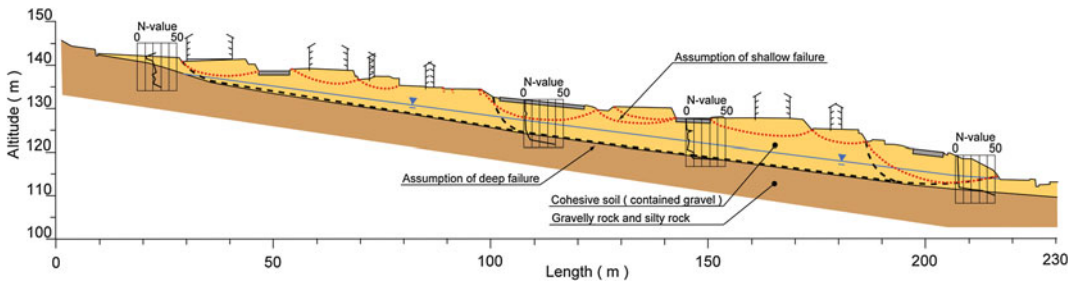
Fig. 27.7 Cross section A–A' of Oritate-5-choume

by the major cracks crossing the road, the near side (supposed to be 'cut' part of the original ground) from the cracks appeared to show no damage, while the far side from the crack was severely damaged.

Fill embankment was severely damaged, the bulging of pavements showing the occurrence of compressive buckling, the walls set up on the top of poorly created retaining walls slid and tilted toward to the road amounting to 1.0 m. Many cracks broke the road into small pieces,

and these cracks may indicate that valley filled cohesive soils were displaced severely due to the complex seismic motions, in particular at the shallow part of the embankment. The depth of displacements in the embankment was estimated to be shallow; the elastic wave exploration indicated that the depth of displacement was about -5.0 m at the center and −7.0 m at the tip of the damaged area. It is worthwhile to note from these observations that severe damages of housing and housing lots at this site can be

primarily attributed to severe displacements of weak fill materials near the surface; the damages were consequences of shallow slip movements, many cracks, and differential settlements. Attention should also be paid to the selection of countermeasures which could prevent the large landslide type failure from occurring.

The causes of severe damages at this site may be summarized as follows: (1) the valley filled embankment with shallow water tables; (2) the filled material composed of cohesive soils; (3) the loose state of soils with the lower SPT N value.

3.3 Nankodai Residential Land (Failure Type: Various Type Failure, no Countermeasure After the 1978 Earthquake)

We here pick up Nankodai residential land damaged twice severely during two earthquakes, where no countermeasure had been constructed, since no large landslide type movement had occurred. The Nankodai residential land is 4 km northeast of the downtown of Sendai city. The creation of fill embankment for residential use started from 1962 to the 1960 s. This area extends 2 km in the north–south axis and 1.5 km in west-east axis, and has 6,450 houses. Site investigation was performed from April 8 to April 26, 2011. The ground surface of this site appears to be a gentle hill. However, the distribution of valley fill embankment is very complicated reflecting the original topography. The houses on this site had suffered damages during the 1978 earthquake. This site was again subjected to severe damages of houses and housing lots again during the 2011 earthquake. The maximum acceleration (in NS direction) measured at Nankodai Higashi elementary school during the 2011 earthquake 699 cm/s^2. The velocity spectrum shows the predominant period to be around 1.0 s (Kamiyama et al. (2012)).

Figure 27.8 shows the distribution of damaged houses and ground cracks. Table 27.2 shows the number of damaged houses, dividing into three categories: completely destroyed, half destroyed, and partially destroyed to indicate the level of damages. The completely and half destroyed house are not suitable for residence. However, partially destroyed house is suitable with some difficulties. The residential area was divided into 3 categories: fill, boundary (between cut and fill), and cut. The detail investigation result is provided from the other paper (see Mori and Kazama (2012)). The numbers of completely destroyed, half destroyed houses are 48, 133 in this site. Most of these destroyed houses were belonging to fill and boundary categories. It seems worthwhile to note that the severely damaged houses were not eminent at the center part of the fill embankment with maximum fill depth. Partially destroyed houses show no predominance, which distribute almost equally among three categories. The partially destroyed houses on the cut area are mostly the failure of roof with tiles and cracks on the plaster, which may be attributed to the seismic motion. The number of major ground cracks were 140, most of which occurred at the boundary part near to the fill area. In order to discuss quantitatively which is most susceptible to house damages, the ratio of the number of damaged house per unit area on fill and boundary parts divided by the number of damages house per unit area on cut part was calculated. Compared with the damaged houses on cut part, the normalized numbers of damaged houses on fill and boundary parts are 26, 25 with respect to the completely destroyed houses, and are 10, 24 for half destroyed house respectively. The calculated results clearly show that completely and half destroyed houses occurred in fill and boundary parts predominantly. The calculated result for partially destroyed houses shows less predominance with three in both parts.

Table 27.3 shows the main mechanisms (mode of ground displacements) of completely and half destroyed houses. Since the duplicate count on the mechanisms is permitted for each damage house, the summation of ratio exceeds 100 %. In Table 27.3, main mechanisms are classified into ground crack, differential settlement, retaining wall failure, slope failure, and seismic motion. In this terminology, slope failure refers to the slope failure at the end of the valley filled embankment, which is peculiar to this site; seismic motion refers to the damage of
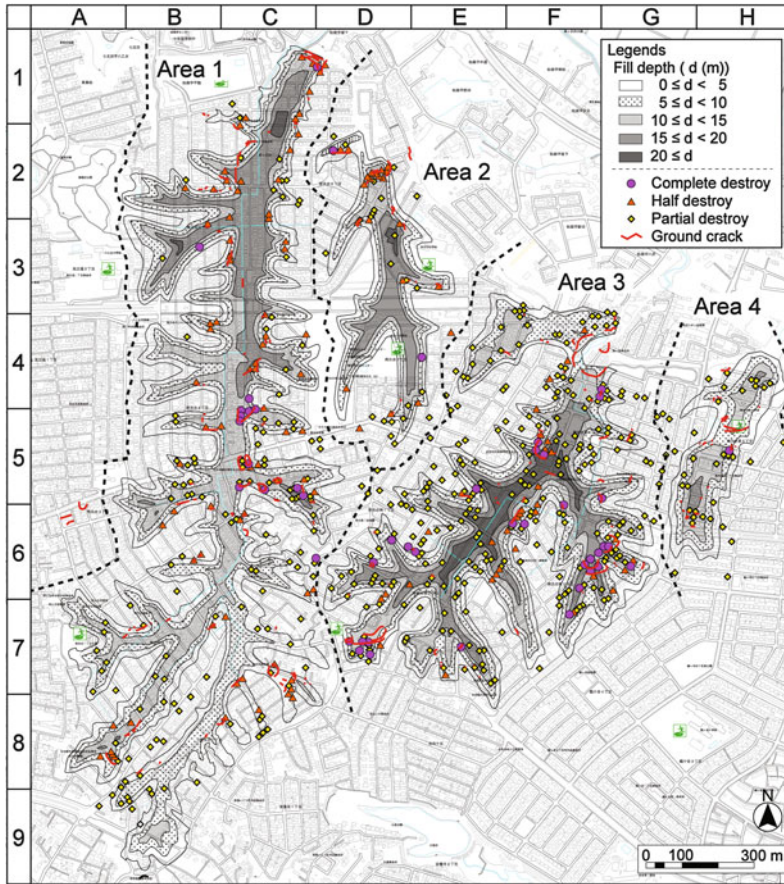
Fig. 27.8 Seismic damage distribution of Nankodai area during the 2011 earthquake

Table 27.2 Number of damage in Nankodai area

Division	Area (km²)	Area ratio (%)	Total houses (houses)	Compo destroy (houses)	Half destroy (houses)	Partial destroy (houses)	Road hair crack (point)	Ground crack (point)	fence (point)
Filled part	1.112	46	3,206	34	67	264	1,189	104	144
Boundary part	0.438	18.1	1,110	13	63	96	373	30	62
Cut part	0.865	35.8	2,224	1	5	73	169	6	33
Total	2.415	100	6,540	48	133	433	1,731	140	239

house in which no remarkable ground displacement was observed. Ground cracks occupies 60 % of failure mechanism of severely (completely and half) destroyed houses. When the cracks passed through the ground beneath the foundation of a house, the house was severely damaged without exception. The differential settlement occupies the second position with the ratio of 31 %. The degree of house damages due to the differential settlement is not so severe compared with the case of ground cracks. Most of damages are belonging to the half destroyed categories at most. The damages due to the failure of retaining walls mainly for private

Table 27.3 Main mechanism of completely and half destroyed houses

Disaster factor	Filled part		Boundary of filled and cut part		Cut part		Sub total	Ratio (%)
	Compo	Half	Compo	Half	Compo	Half		(Total houses: 181)
Ground crack	25	34	10	38	0	1	108	59.7
Differential settlement	3	29	2	22	0	0	56	30.9
Retaining wall failure	14	8	2	3	0	1	28	15.5
Fill slope failure	0	7	1	2	0	0	10	5.5
Seismic motion	1	3	1	3	0	3	11	6.1

*Compo Complete destroy, *Half* Half destroy
*Selection of plural disaster factors is possible on one disaster housing site

residence occupies 16 %, the damage due to this mechanism has a specific feature that most of damages occurred in the fill area. The damages due to slope failure amount to 6 %. The damages induced by seismic motion are 6 %, this type of failure can occur everywhere, showing less dependency on the area categories. Summing up above findings, on the Nankodai housing land with the branch-like valley filled embankment, the damages of houses mainly occurred on the fill and boundary categories, 80 % of the severely damaged houses are associated with the ground displacements such as cracks, differential settlement. The damages due to seismic motion with no noticeable ground displacement are found to be very small.

This result may be influenced by the local features of geotechnical conditions of Nankodai residential land. In order to get common features of the main mechanisms leading to the damages of houses on the hillside embankments in Sendai city, further studies are necessary. It is however suggested that more attention should be paid to the fact that ground displacements can be the main mechanisms leading to the severe damages of houses.

4   Conclusions

The 2011 Great East Japan Earthquake brought about the severe damages of hillside embankments for residential use in Iwate, Miyagi and Fukushima prefectures. Particularly the damages

in Sendai city was widespread and more than 7,000 houses were damaged. The causes of the damages of hillside embankments and the relationship between the patterns of the ground displacements and the degree of the damages of housings were discussed in this paper. The main conclusions from this study may be summarized as follows:

1. Most of the damaged housings may be attributed to the ground displacements of the soft filled materials of the hillside embankment. The houses damaged due to the seismic motion without ground displacements were few and the degree of the damage was not severe.

2. The fill materials of hillside embankments severely damaged were composed of soils containing high ratio of fine particles, which may result in the poor compaction during construction works, the rise up of water tables, and the degradation of hillside embankments with the elapsed time.

3. The landslide type failure along the boundary between fill and original ground was limited and the ground displacements due to shallow slips and due to strong earthquake motions were devastating to the housing damages.

4. The residential land which had been seriously damaged during the 1978 off Miyagi Prefecture Earthquake and the countermeasures had been set up were again damaged during the 2011 earthquake. Comparing the damages in two earthquakes, we may conclude that the countermeasures set up after the 1978

earthquake was effective to prevent the landslide type failure from occurring; however, they were not effective to reduce the housing damages.

References

Kamiyama M, Matusukawa, Anazawa M (2012) Strong ground motions observed by Small-Titan during the 2011 Great East Japan Earthquake. 9th International Conference on Urban Earthquake Engineering and 4th Asia Conference on Earthquake Engineering, Tokyo

Kawakami F, Asada A, Yanagisawa E (1978) Failures of embankment in the Off Miyagi Prefecture Earthquake. Tsuchi to Kiso (JSSMFE) 26(12):25–31 (in Japanese)

Koseki J, Wakai A, Mitsuji K (2011) The damage investigation report about the 2011 off the Pacific Coast of Tohoku Earthquake -Damages in the inland of Miyagi prefecture. Geotech Eng Mag (JGS) 59(6):40–43 (in Japanese)

Mori T, Kazama M (2012) The damage investigation of filled valley residential area in Sendai city Izumi ward about the 2011 off the Pacific coast of Tohoku Earthquake. J Geotech Eng (JGS) 7(1):163–173 (in Japanese)

Okimura T, Nabeshima Y, Okada H, Nonami K (2011) Report on the damages of residential land in and near Sendai city due to the Tohoku Earthquake, submitted to JGS (in Japanese)

Wakai A, Sato S, Mitsuji K, Mori T, Kazama M, Koseki J (2012) Investigation of damage caused by the 2011 off the Pacific coast of Tohoku Earthquake—Brief report on the residential lands in Sendai City—off the Pacific coast of Tohoku Earthquake—Brief report on the residential lands in Sendai City. J Geotech Eng (JGS) 7(1):79–90 (in Japanese)

Common Geographic and Geological Features of Earthquake-Induced Landslides in Northern Ibaraki Prefecture

28

Yuichi Ueno

Abstract

As a result of the 2011 Great Earthquake off the Pacific coast of Tohoku, four large landslides occurred in northern Ibaraki Prefecture and caused damage that closed roads. These landslides were characterized by the following geological and geographic features: 1, each slide occurred near the tip of a ridge; 2, each ridgeline was almost perpendicular to a line drawn from the landslide to the epicenter; and 3, geologically, each slope was a dip slope of soft Neogene sandstones and/or siltstones. In an earthquake, the ground motion of the upper part of the slope is bigger than that of the lower part of the slope. We can infer that if the tip of the ridge is equivalent to the upper part of the slope, then a large amount of ground motion likely occurred there in the 2011 Great Earthquake; this might have placed fracture stress along the bedding planes of the dip slope, thus triggering a landslide. In future disaster management, we need to be aware of slopes that have the geographic and geological features mentioned above.

1 Introduction

In the 2011 Great Earthquake off the Pacific coast of Tohoku, which occurred at 2:46 p.m. on 11 March 2011, northern Ibaraki (about 300 km from the epicenter) was subjected to an intensity of 6-lower on the Japanese intensity scale (over 1,000 gal) (Fig. 28.1). Four large-scale landslides occurred (Fig. 28.2).

Although these landslides resulted in neither human damage nor large-scale river channel blockages, events such as road closures occurred.

We examined the geographic and geological features common to these four landslides, and we present them here as characteristics of the slope disasters that occurred in Ibaraki Prefecture as a result of the 2011 Great Earthquake.

Y. Ueno (✉)
Disaster Prevention Division, Nippon Koei Co., Ltd,
4-2 Kojimachi Chiyoda-ku, Tokyo 102-0083, Japan
e-mail: ueno-yc@n-koei.jp
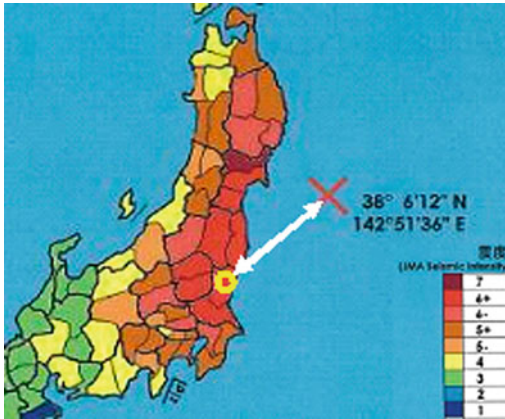
Fig. 28.1 Direction of the line between northern Ibaragi and the epicenter

Fig. 28.2 Locations of four landslides

2 Outline of Each Landslide

2.1 Tanaya Landslide (Hitachi-Ohta City)

This landslide occurred in the Tanaya district of the city of Hitachi-ohta, along a prefectural road known as the Hitachiohta-Nasu-Karasuyama Route. The landslide is 50 m long and 40 m wide. The maximum depth of moving soil was about 10 m, with a volume of approximately 20,000 m^3 (Nakajima et al. 2011) (Fig. 28.3).

The slope above the road collapsed over about 70 m of extension. The moving soil flowed out and buried the road, breaching retaining walls and a guardrail fence. The disaster caused the road to be closed.

The moving block left behind it a clear main scarp 5 m high and a graben 15 m wide. A small-scale graben 5 m wide was also formed in the middle of the landslide.

Geologically, the landslide slope consisted of Neogene sandstone forming a dip slope; the angle of descent of the tilted bed was 20°. The direction of the landslide paralleled the direction of dip of the stratum.

The landslide is located near the tip of the ridge, and the ridgeline is almost perpendicular to a line between the landslide and the epicenter (Figs. 28.4, 28.5).

Asano et al. (2006) pointed out that seismic acceleration is strongly amplified by topographic effects, such that the top of a convex slope would be expected to shake much more strongly than the bottom. During the 2011 Great Earthquake, the slope on which the Tanaya landslide occurred likely had greater ground motion than the surrounding ground. This strong ground motion might have caused fracture stress along the bedding planes of the dip slope, thus triggering the landslide.

2.2 Morosawa Landslide (Hitachi-Omiya City)

This landslide occurred in the Morosawa district of Hitachi-omiya City, along a prefectural road known as the Yamagata Suifu Route. Many sediment-related disasters, such as landslides, have occurred around the Morosawa district.

The landslide is 80 m long and 50 m wide. The maximum depth of moving soil was about 10 m, with a volume of approximately 45,000 m^3 (Inoue et al. 2011) (Fig. 28.6).

It slipped down the road for about 45 m and formed a main scarp 3 m high. Because of the disasters, the road was closed. In addition, the landslide clod dammed a downslope channel, but only a small volume of water was ponded.

Fig. 28.3 Bird's eye view of the Tanaya landslide
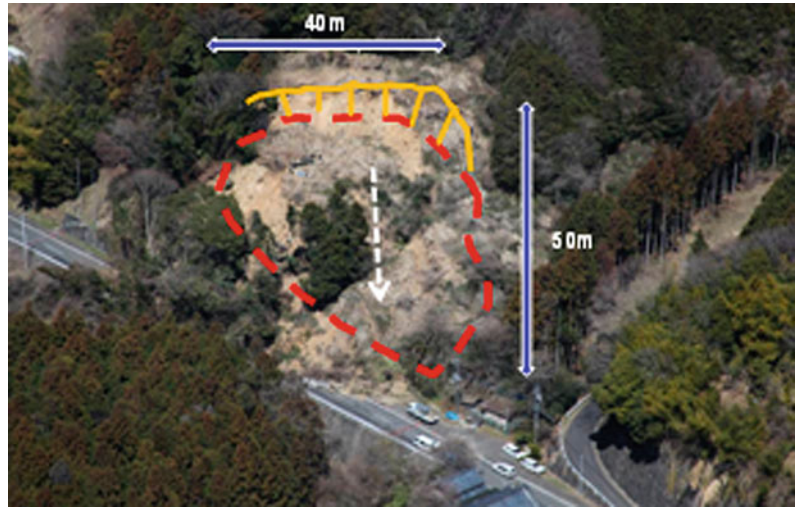
Fig. 28.4 Bird's eye view of the Tanaya landslide and ridgeline

A graben 3 m high and 5 m wide was formed in the middle of the landslide.

The landslide occurred on a steep, convex slope on the south-west tip of a slender ridge. Geologically, the landslide slope consisted of Neogene sandstone and conglomerate forming a dip slope; the angle of descent of the tilted bed was 25°. The direction of the landslide paralleled the direction of dip of the stratum.

The landslide is located near the tip of the ridge, and the ridgeline is almost perpendicular to a line between the landslide and the epicenter (Figs. 28.7, 28.8).

During the 2011 Great Earthquake, the slope on which the Morosawa landslide occurred likely had greater ground motion than the surrounding ground, as occurred in the Tanana landslide. This strong ground motion might have led to fracture stress along the bedding planes of the dip slope, triggering the landslide.

2.3   Ono Landslide (Hitachi-Omiya City)

This landslide occurred in the Ono district of Hitachi-omiya City, along City Road No. 4389.

Directions of the Tanaya landslide, the ridgeline, and the dip-strike of the stratum
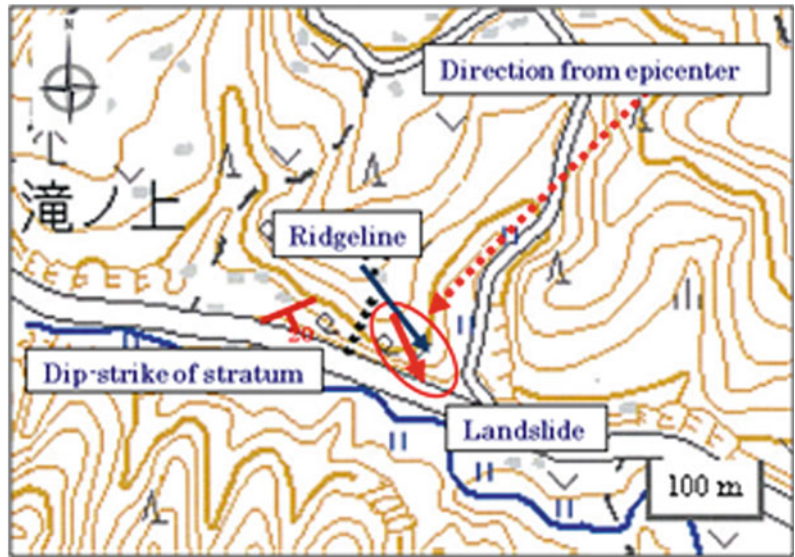
Bird's eye view of the Morosawa landslide

The landslide is 50 m long and 100 m wide. The maximum depth of moving soil was about 10 m, with a volume of approximately 30,000 m^3 (Yamashita et al. 2011) (Fig. 28.9).

Because the moving soil covered about 140 m of sidewalk along the city road, and the landslide formed a clear main scarp 5 m high, the head of which was considered to be dangerous, the city road was closed

The landslide occurred in a cutting slope constructed in the late 1980s. The slope had been protected by framework and vegetation mats, but these were destroyed by a small-scale graben 3 m wide that formed in the middle of the landslide.

Geologically, the landslide slope consisted of Neogene sandstone and siltstone forming a dip slope; the angle of descent of the tilted bed was

Fig. 28.7 Bird's eye view of the Morosawa landslide and ridgeline
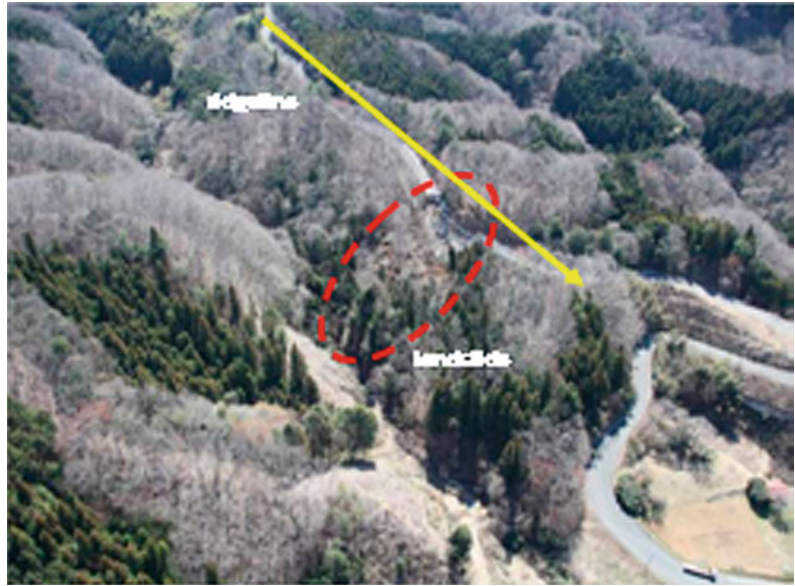
Fig. 28.8 Directions of the Morosawa landslide, the ridgeline, and the dip-strike of the stratum
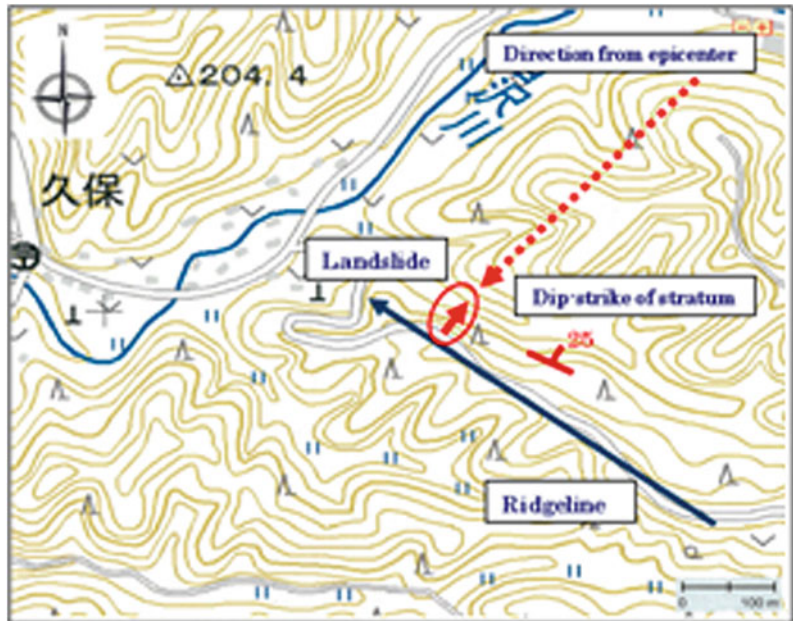
35°. The direction of the landslide paralleled the direction of dip of the stratum.

Before the construction works, the slope was located near the tip of a slender ridge. The ridgeline is almost perpendicular to a line between the landslide and the epicenter (Figs. 28.10, 28.11).

During the 2011 Great Earthquake, the slope on which the Ono landslide occurred likely had greater ground motion than the surrounding ground, as was the case in the Tanaya landslide. The strong ground motion might have caused fracture stress along the bedding planes of the dip slope, thus triggering the landslide.

Fig. 28.9 Bird's eye view of the Ono landslide
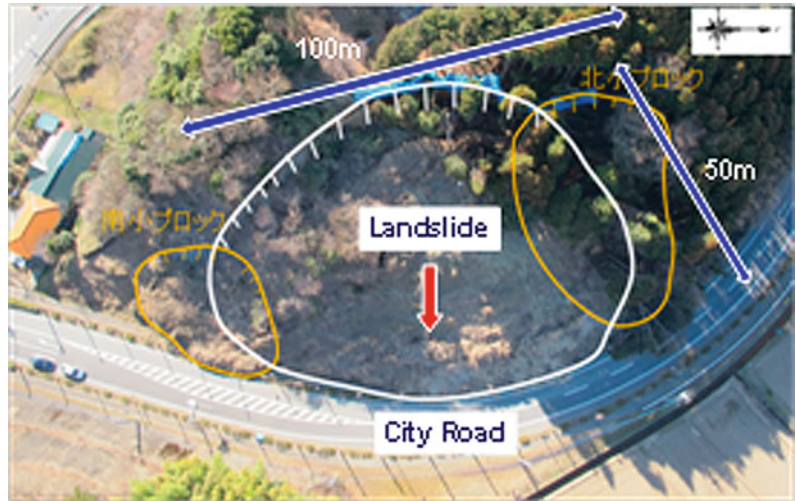
Fig. 28.10 Bird's eye view of the Ono landslide and ridgeline
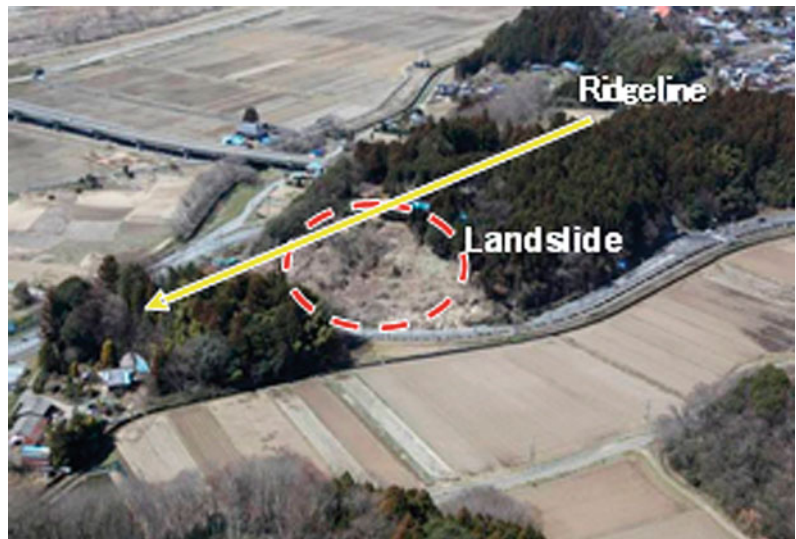
2.4 Hanabusa Landslide (Hitachi-Ota City)

This landslide occurred in the Hanabusa district of Hitachi-ota City, along the national highway Route 293. It is 100 m long and 60 m wide. The maximum depth of moving soil was about 10 m, with a volume of approximately 40,000 m^3 (Fig. 28.12).

This landslide formed a clear main scarp 5 m high and 10 m wide at its head and blocked a waterway along the national highway. However, the highway was not closed, because the sediment discharge to the highway was slight. With monitoring, it is currently possible to pass along the highway below a temporary protection fence.

There was also a small-scale scarp 1 m high in the middle of the landslide.

Geologically, the landslide slope consisted of Neogene sandy siltstone forming a dip slope; the angle of descent of the tilted bed was 10°. The direction of the landslide paralleled the direction of dip of the stratum.

Fig. 28.11 Directions of the Ono landslide, the ridgeline, and the dip-strike of the stratum
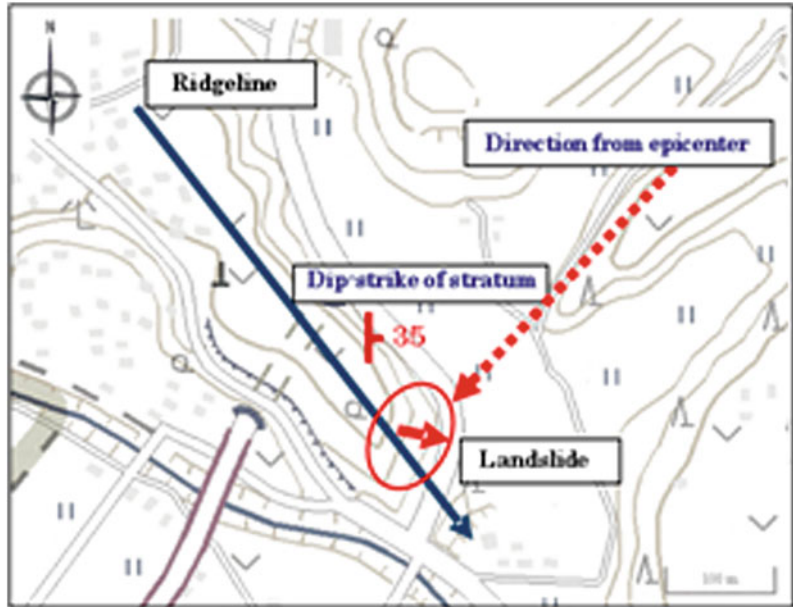
Fig. 28.12 Bird's eye view of the Hanabusa landslide

The landslide occurred on a convex slope on the western part of a slender ridge. The ridgeline is almost perpendicular to a line drawn from the landslide to the epicenter (Figs. 28.13, 28.14).

During the 2011 Great Earthquake, the slope on which the Hanabusa landslide occurred was likely subject to greater ground motion than the surrounding ground, as was the case in the Tanaya landslide. This strong ground motion might have led to fracture stress along the bedding planes of the dip slope, thus triggering the landslide.

3 Discussion and Conclusions

The characteristics of the four landslides are compared in Table 28.1.

Fig. 28.13 Bird's eye
view of the Hanabusa
landslide and ridgeline

Fig. 28.14 Directions of
the Hanabusa landslide, the
ridgeline, and the dip-strike
of the stratum
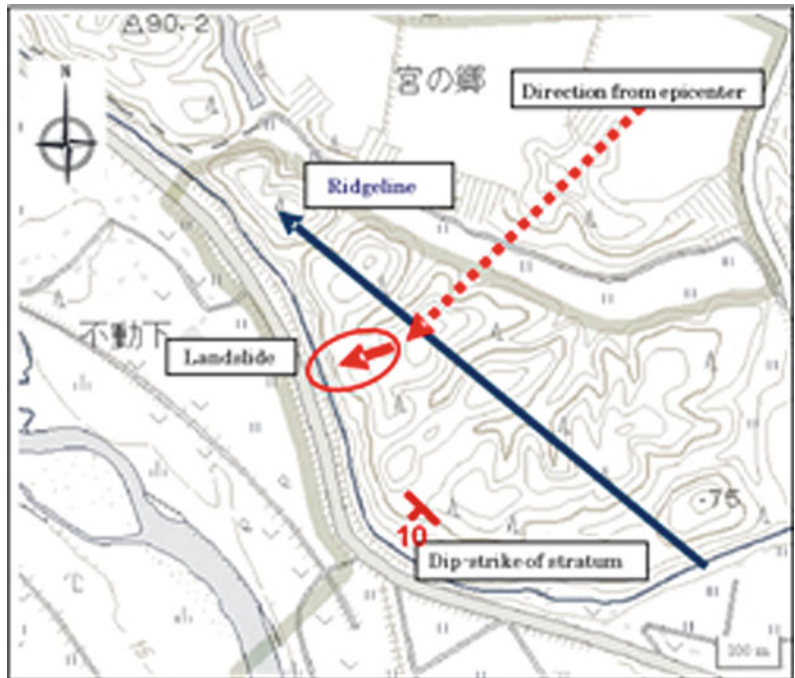
The following common features can be seen
from Table 28.1:

1. Geologically, each slope consisted of soft
   Neogene sandstones, conglomerate, and/or
   siltstones.
2. Each slope was a dip slope, and the direction
   of the landslide paralleled the direction of dip
   of the stratum.

3. Each slide occurred near the tip of a
   slender ridge or on the convex slope of
   the ridge. Asano et al. (2006) pointed out
   that seismic acceleration was strongly
   amplified by topographic effect, such that
   the top of convex slope would be expec-
   ted to shake much more strongly than the
   bottom.

Table. 28.1 Comparison of the four landslides

Landslide	Tanaya	Morosawa	Ono	Hanabusa
Intensity scale	6-lower	6-lower	6-lower	6-lower
Width (m)	40	50	100	60
Length (m)	50	80	50	100
Maximum depth (m)	10	10	10	10
Volume of moving soil (m^3)	20,000	45,000	30,000	40,000
Direction of movement	SSE	NE	E	WSW
Angle of surface( )	20–40	20–30	35–40	20–40
Type of slope	Cut	Convex	Cut	Convex
Geological area	Neogene	Neogene	Neogene	Neogene
Rock	Sandstone	Sandstone conglomerate	Sandstone and siltstone	Sandy siltstone
Structure	Dip slope	Dip slope	Dip slope	Dip slope
Direction of dip	SSE (20)	NE (25)	E (35)	SW (10)
Location of landslide	Tip of slender ridge	Tip of slender ridge	Tip of slender ridge	Slender ridge
Direction of ridgeline	NW to SE	NW to SE	NW to SE	NW to SE
Direction of epicenter	NE	NE	NE	NE
Main scarp height (m)	5	3	5	5
Relative scarp height above riverbed (m)	40	45	45	50
Graben in middle	Yes	Yes	Yes	Yes
Relative graben height above riverbed (m)	20	25	20	30
Groundwater level	Low	Low	Low	Low
Snow cover	None	None	None	None

4. The ridgeline was perpendicular to a line drawn from the landslide to the epicenter. This meant that the direction of the minor axis of the ridge paralleled the direction in which the seismic motion came. In accordance with this and point 3, each landslide during the 2011 Great Earthquake would be expected to have been located where the ground motion was greater than in the surrounding ground. This strong ground motion likely led to fracture stress along the bedding planes of the dip slope, thus triggering the landslide.

5. The main scarp at the landslide head formed at a relative height of about 40 m above the riverbed.

6. In the middle of the landslide a small-scale graben formed at a relative height of about 20 m above the riverbed. This point and point 5 indicate that the whole landslide did not occur at once, but that during the earthquake a small-scale slide occurred first on the lower part of the slope, then the upper part of the slide followed.

7. There was no snow cover, and the groundwater level in the sliding soil was not high at the time of the landslide. Groundwater was therefore not likely to have been a factor in these earthquake-induced landslides.

In our future disaster management, we should be aware of slopes that have the geographic and geological features described above.

References

Asano S, Ochiai H, Kurokawa U, Okada Y (2006) Topographic effects on earthquake motion that trigger landslides. J Jpn Landslide Soc 42(2005–2006)(6):1–10

Inoue T, Shibasaki N, Kobayashi M (2011) Investigation report of the earthquake-induced landslide. In: Proceedings of the 50th annual conference, Japan landslide society, Shizuoka, Japan, 2011, pp 9–10

Nakajima T, Fukazawa T, Terakado T, Yamada T, Ueno Y, Ura M (2011) Investigation report of the earthquake-induced landslide crossing the road obliquely. In: Proceedings of the 50th annual conference, Japan landslide society, Shizuoka, Japan, 2011, pp 7–8

Yamashita T, Fujiwara T, Inagaki Y, Nakamura F (2011) Investigation report of the earthquake-induced landslide occurring in the cutting slope. In: Proceedings of the 50th annual conference, Japan landslide society, Shizuoka, Japan, 2011, pp 61–62

A Review of Recent Case Studies of Landslides Investigated in the Tien Shan Using Microseismic and Other Geophysical Methods

29

Almaz Torgoev, Laura Lamair, Isakbek Torgoev
and Hans-Balder Havenith

Abstract

This paper reviews recent case studies completed on mass movements (and landslide dams) with probable (post-) seismic origin or susceptible to seismic failure in the Tien Shan, Central Asia. Geophysical investigations and seismological and microseismic surveys presented here were carried out on the Kainama earthflow in the Southern Kyrgyz Tien Shan, on loess landslides in Tajikistan as well as on unstable slopes and a landslide dam in the Central Kyrgyz Tien Shan. The latter investigations were completed in summer 2011 using electrical tomography combined with seismic refraction and microseismic measurements as well as earthquake recordings. For all sites complex 3D models were built (with the GOCAD software). For some sites 2D numerical modelling of seismic slope stability allowed us to make accurate assessment of their susceptibility to seismic failure. Modelling of the seismic amplification potential of various slopes confirmed the results obtained from the seismological surveys: strongest amplifications generally affect the upper parts of the slope close to the crest of the mountains—not only due to topographic effects but also due to the presence of weaker rocks or thicker soft deposits in these areas. The results of the dynamic modelling further show that a combination of seismic and hydrologic factors (pore pressure build-up during the seismic shaking and post-seismic rise of groundwater level) was necessary to trigger the failure.

A. Torgoev (✉) · L. Lamair · H.-B. Havenith
Georisks and Environment, Department of Geology,
University of Liege, 4000 Liege, Belgium

A. Torgoev · I. Torgoev
GEOPRIBOR, Institute of Geomechanics and
Development of Subsoil, 720035
Bishkek, Kyrgyz Republic

1 Introduction

During the last 10 years, after a series of disastrous earthquake events in mountain regions in Taiwan (1999), El Salvador (2001), Pakistan (2005) and China (2008), increasing attention has been addressed to landslides triggered by earthquakes.

Most efforts are spent on understanding the co-seismic trigger mechanisms, but also post-seismic failure should be taken into consideration as our first example will show. For all case histories we studied in Central Asia we could note that an effective seismic landslide risk management is only possible with a clear understanding through modelling of the geometry, behaviour and dynamics of the landslides and triggering seismic ground motions. To this end, extensive geophysical–seismological surveys were carried out on a series of co- or (assumed) post-seismically triggered landslides (see, e.g., Havenith et al. 2000; Havenith et al. 2002; Danneels et al. 2008).

The first investigation presented here was carried out in 2005 on the Kainama earthflow, mainly composed of loess, which occurred in April 2004 and killed 33 people. Geophysical and seismological data were used to build a reliable 3D model of the geometry and properties of the subsurface layers. Then, we present results from microseismic measurements on loess landslides in Tajikistan that may have a seismic origin. They are located close to the area that was affected in 1949 by the M = 7.4 Khait earthquake and the numerous landslides triggered during the event, including the Khait rock avalanche.

In 2011, an extensive geophysical-seismological survey was carried on an unstable slope and a landslide dam in the Central Tien Shan, Kyrgyzstan. Here, electrical tomography data combined with seismic refraction and microseismic measurements as well as earthquake recordings allowed us to build complex 3D models (with the GOCAD software) of the sites and to assess their susceptibility to seismic failure.

The main goal of the seismological and microseismic surveys and dynamic numerical modelling was to find a correlation between the thickness and type of the soft sediment cover, the surface morphology and the measured resonance frequencies and associated amplification potential.

2 Regional Context

The Tien Shan is a high intracontinental mountain belt in Central Asia, with an East–West extension of about 2500 km and a maximum width of more than 500 km (Fig. 29.1). Its structure is characterised by alternating, roughly East–West trending mountain ranges and intra-montane basins. The relatively young age of the Tien Shan Range (10 Myr) makes that it is still tectonically and also seismically very active. Most prone to neotectonic and seismic movements are the thrust faults bounding the ridges and depressions as well as the major strike-slip faults. During the last century, several strong earthquakes occurred along some of these faults (location in Fig. 29.1), the Kemin (Ms = 8.2, 1911), the Chatkal (Ms = 7.5, 1946), the Khait (Ms = 7.4, 1949) and the Suusamyr (Ms = 7.3, 1992) earthquakes. Most M > 7 events were accompanied by large surface ruptures and numerous mass movements. According to Nadim et al. (2006) the global landslide hazard in Central Asian Mountains (partly connected with the seismic activity) can be rated as medium to very high. They further noted that some areas in Tajikistan are marked by highest mortality risk due to landslides.

Over the last 12 years, a series of rockslides and soft-sediment landslides (mostly triggered by earthquakes) have been investigated in the Kyrgyz Tien Shan (see review in Havenith and Bourdeau 2010) and Tajikistan. Those include: the Bielogorka 'twin' rock avalanches in northern Kyrgyzstan assumed to have been triggered by the M = 6.9 Belovodsk earthquake in 1885; the Ananevo rockslide triggered by the M = 8 Kemin earthquake in 1911; landslides triggered by the M = 7.3 Suusamyr earthquake in 1992; co- and post-seismic landslide activity around the Fergana Valley (including the Kainama case study presented here); seismically triggered landslides in loess deposits in northern Tajikistan.

3 Case Studies

3.1 Kainama

The first study presented here was carried out on a loess landslide in Kainama (location in South
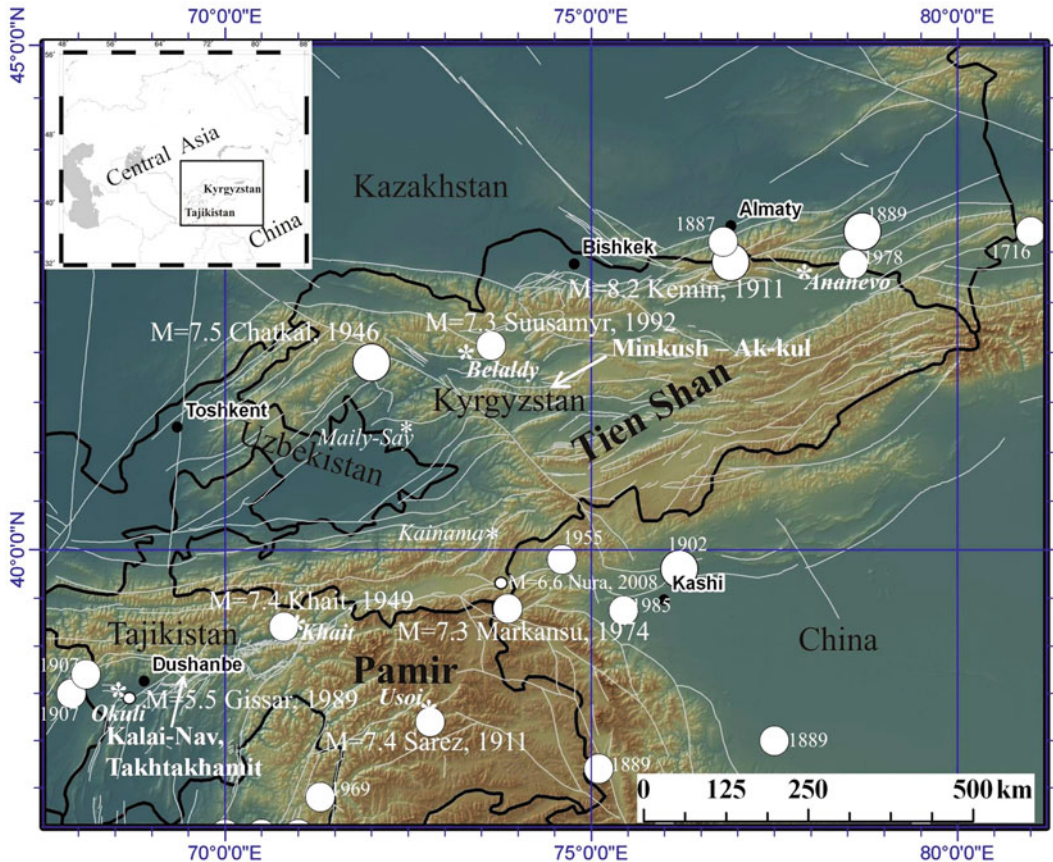
Fig. 29.1 Map of Tien Shan and Pamir Mountains in Central Asia (general map in *upper left corner*) with location of major faults and earthquakes; cited earthquake-triggered mass movements and landslides are marked by stars with names in italic (modified from Havenith and Bourdeau 2010)

Kyrgyzstan marked by star in Fig. 29.1), which had killed 33 people on April 26, 2004 (Fig. 29.2). It occurred 4 weeks after two local Ms = 4–4.5 earthquakes, and, thus, is clearly post-seismic—just as a series of other known landslides in the region. The landslide has been investigated in 2005 through a geophysical and seismological survey as well as numerical modelling (Danneels et al. 2008).

The analysis has shown that the strong site effects (see modelling results in Fig. 29.3) must have contributed to the generation of possible liquefaction effects and/or fracturing of the slope inducing local co-seismic deformation. The massive post-seismic failure was probably related to increased water infiltration in the co-seismically deformed parts of the slope.

3.2   Tajik Landslides

Two landslides, Takhtakhamit and Kalai Nav (location in Northern Tajikistan marked by arrow in Fig. 29.1, latter landslide shown in Figs. 29.4, 29.5), were studied in the Faizabad valley, located in the Southern Tien Shan. These landslides (as many others in this region) occurred in loess deposits.

We used the microseismic H/V method to map the thickness of the landslide mass. Existing resistivity data complemented the information for one site. Generally the H/V data allowed us to identify the depth of the sliding surface, with the exception of the areas where loess is mixed with other soft sediments and where the terrain is influenced by minor slides. 3D
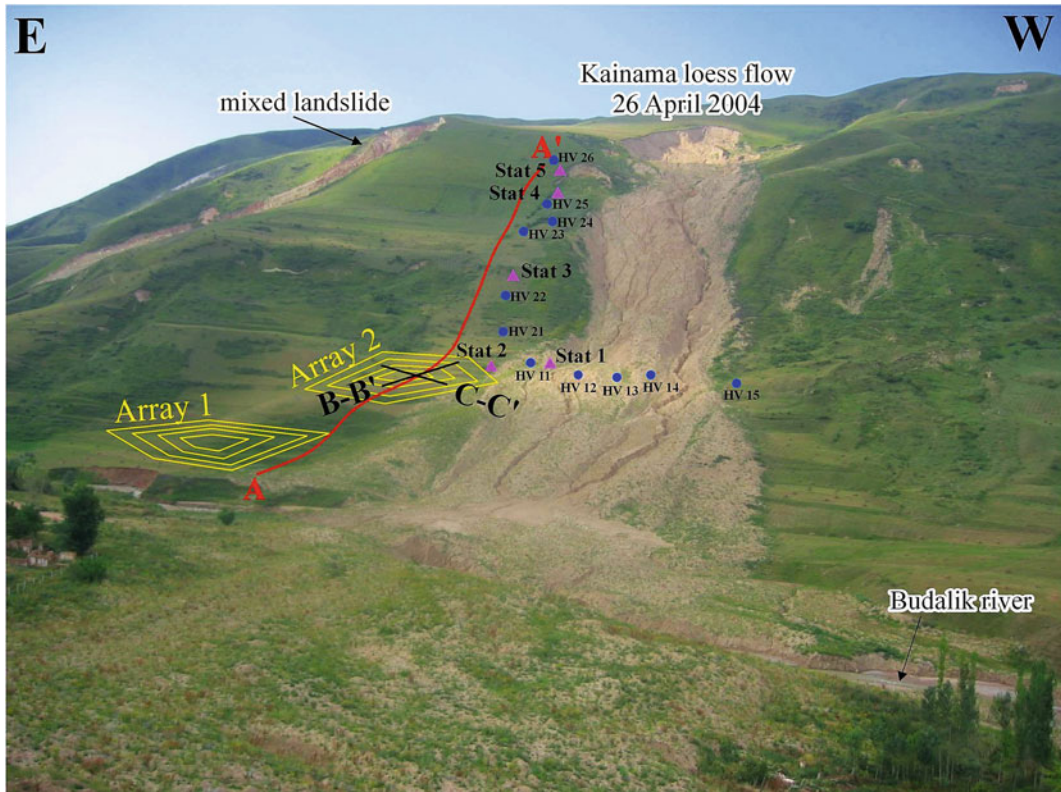
Fig. 29.2 Investigated slope in Kainama—840 m long geoelectric profile (*red line*), seismic arrays (*yellow polygons*), seismic tomography profiles (*black*), earthquake recordings and H/V measurements (*violet ant blue dots*). (Danneels et al. 2008)

geomodelling was performed for these two landslides. The representation of the sliding surfaces based on the microseismic data (see low resonance frequencies of 1–2 Hz in the central part of the slide in Fig. 29.4 corresponding to its largest thickness up to 45 m) provided a better visualisation of the geometry of the slides. It also helped to better understand and interpret the sliding mechanisms that are mainly controlled by collapsing and slumping. Actually, the sliding surface has a very low dip (<10°) towards the river in the South and bounding fractures with main vertical displacement indicate that the first movements were probably controlled by settling (subsidence) of the ground. This is a typical behaviour of loess before sliding: it starts with the compaction of the material and water expulsion.

3.3   Minkush–Ak-kul

A field survey had been carried out in the Central Tien Shan from July 19-August 3, 2011, by researchers from Kyrgyzstan, the Slovak Republic and Belgium. Two sites have been investigated in the Minkush region (location indicated by arrow in Fig. 29.1) by 10 geoelectric profiles, 140 microseismic H/V measurements and recordings of about 30 earthquakes by 5 seismic stations: the Tuyuk Suu landslide (Fig. 29.6) close to Minkush and the Ak-kul landslide dam located 15 km W of Minkush.

The combination of all processed data shows that the Tuyuk-Suu landslide is composed of three blocks separated by deep fractures, with a total volume of up to 700000 m^3. The landslide material (colluvium and disintegrated rocks) can
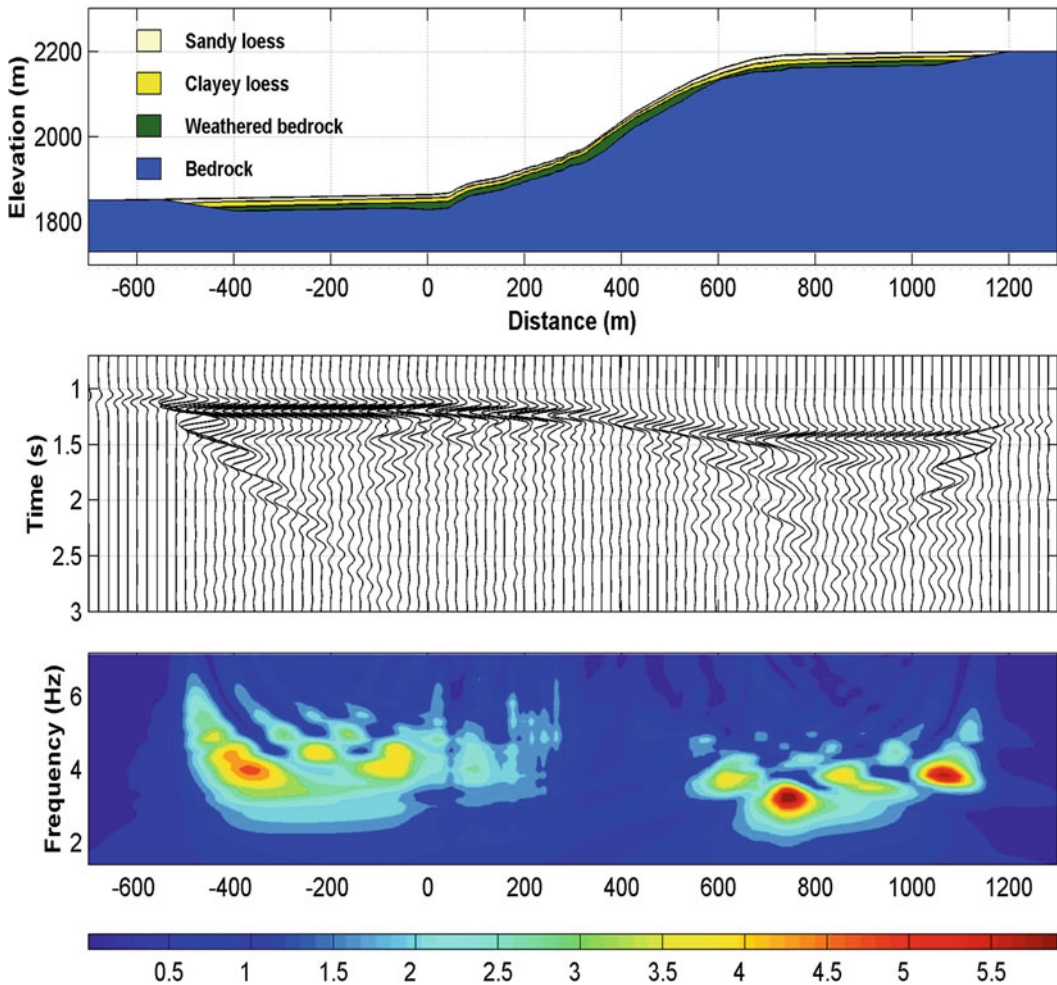
Fig. 29.3 **a** Schematic representation of the topography and the geology of Kainama slope (bedrock is made of soft Cretaceous sandstones). **b** Horizontal accelerations computed every 20 m along the ground surface. **c** Spectral horizontal amplifications (see colour scale) computed along the ground surface. (Danneels et al. 2008)

be well identified along the main geoelectric profile (Fig. 29.6 below) by the lower resistivities (<150 Ohm m, blue-green colours) on top of the high resistivity zone representing the stable bedrock (red carboniferous sandstone with layers dipping by 30° towards the northwest, obliquely to the topographic slope dipping towards the west).

Permanent markers had been installed on the Tuyuk Suu landslide to monitor slope displacements. Measurements of positions of markers, of fractures and of all measurement sites have been

completed with differential GPS. These measurements are now continued to identify landslide movements. First results show, e.g., that the M = 6.1 earthquake of July 19, 2011 in Southern Fergana (about 300 km SW of Minkush) produced an acceleration of the movement of the two upper blocks of the landslide (the largest displacement of 33 cm during the month following the earthquake was measured on the fracture, a 1 m high scarp, marking vertical landslide movements along the crest: between markers R22 and R23 in Fig. 29.6). Also, the
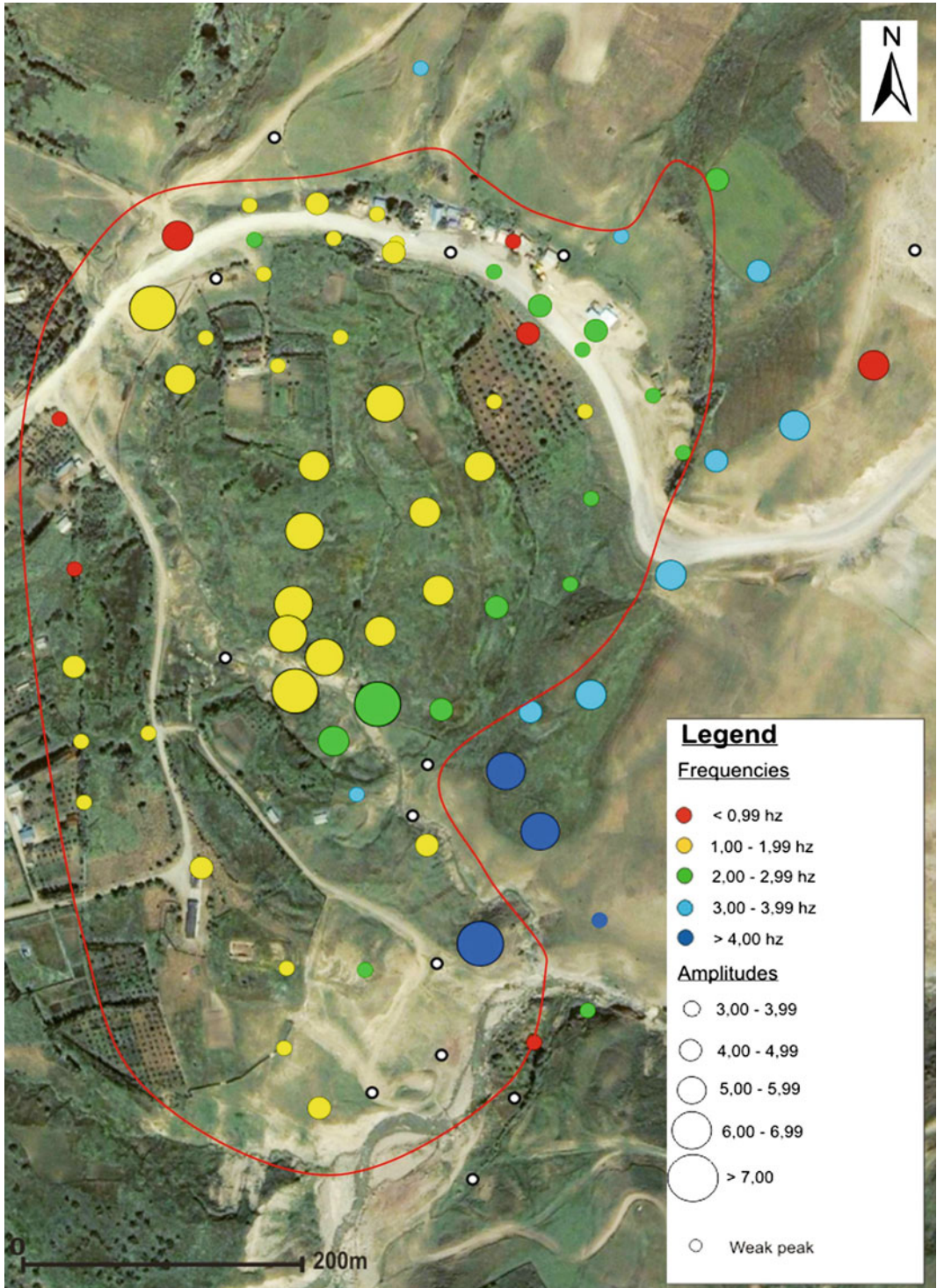
Fig. 29.4 Landslide of Kalai Nav (see *red outline*): representation of amplitudes (*size of circles*) and resonance frequencies (*colours of circles*) measured by H/V method

The Kalai-Nav landslide : 3D reconstruction of the sliding surface
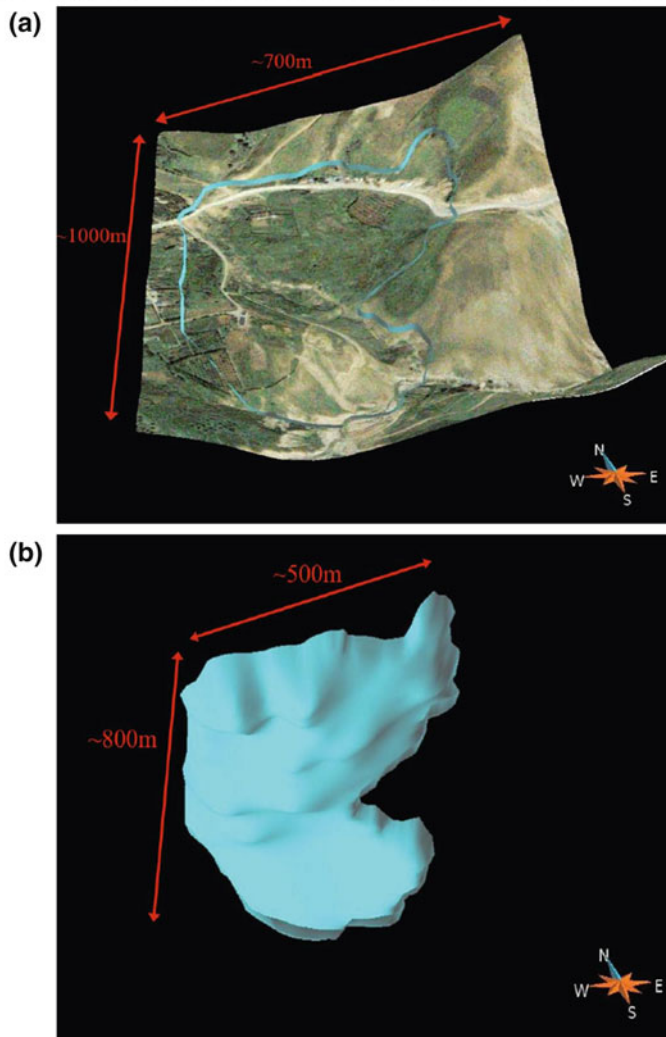
Fig. 29.5 **a** Perspective view of the landslide with intersecting sliding surface (*blue line*). **b** The entire sliding surface (depth obtained from microseismic measurements) constructed with GOCAD

last M = 5.2 earthquake on February 5, 2012 in the Naryn Valley (at 50 km SE of Minkush) has triggered a movement of a few centimetres in the same parts.

Microseismic H/V data and earthquake recordings show that the main part of the landslide mass has a resonance frequency between 3 and 6 Hz, corresponding to a thickness ranging from 15 m (6 Hz) to 30 m (3 Hz). However, most resonance peaks are not very clear

indicating that the impedance contrast between the sliding mass and the bedrock is not high—and does not induce strong amplification. Therefore, most parts of the unstable slope (especially the lower at present most acitve block) are considered as not particularly prone to seismically triggered failure. Movements of these parts are controlled by climatic conditions while the upper block obviously also moves after light shaking (<0.01 g on rock for the
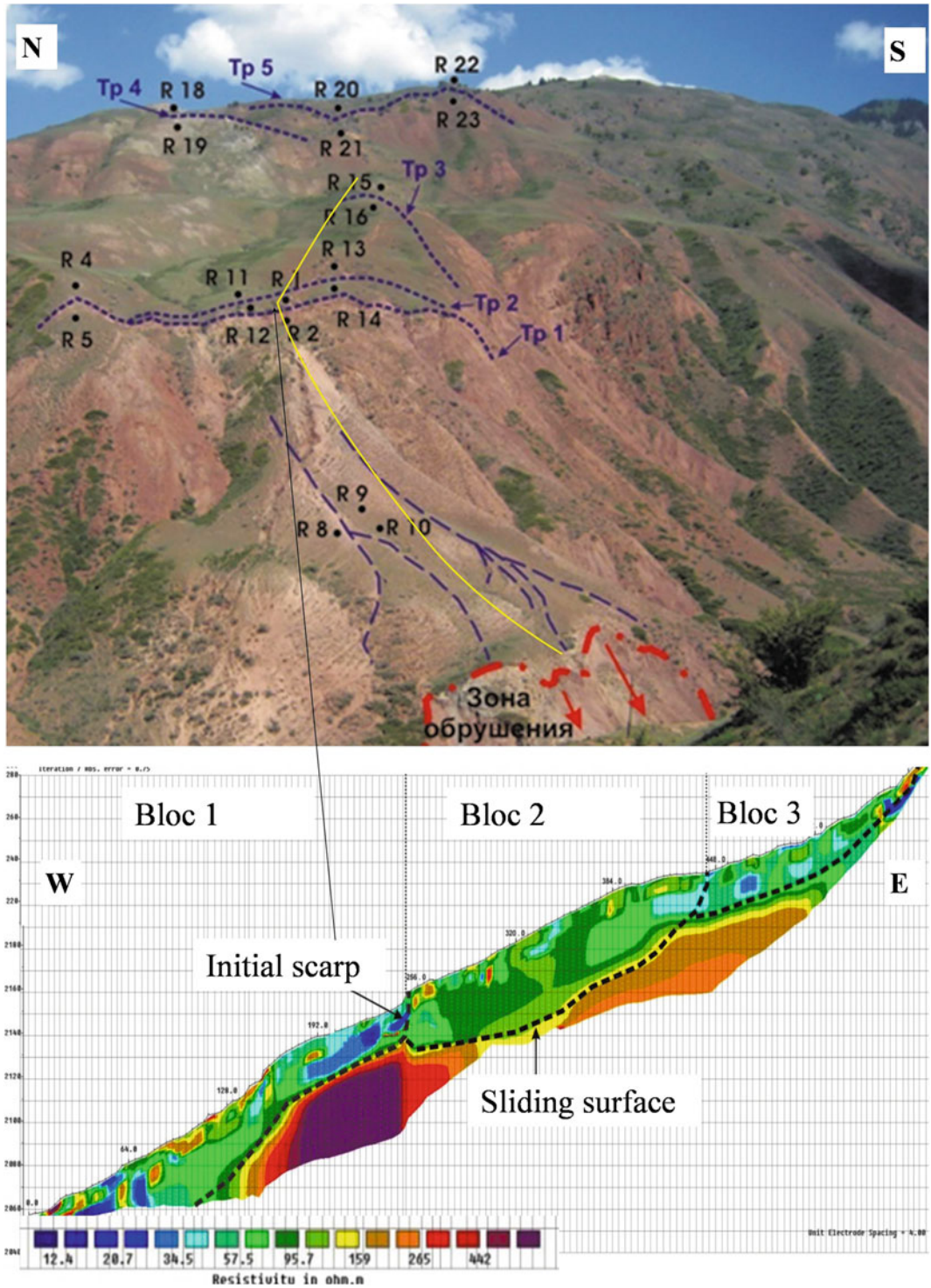
Fig. 29.6 View (to ESE) of Tuyuk Suu landslide and location fractures (*blue dotted lines*), markers (R1-23) and the main 700 m long geoelectric profile (in *yellow*, above). Main 700 m long geoelectric profile with blocks marked by *dashed lines*
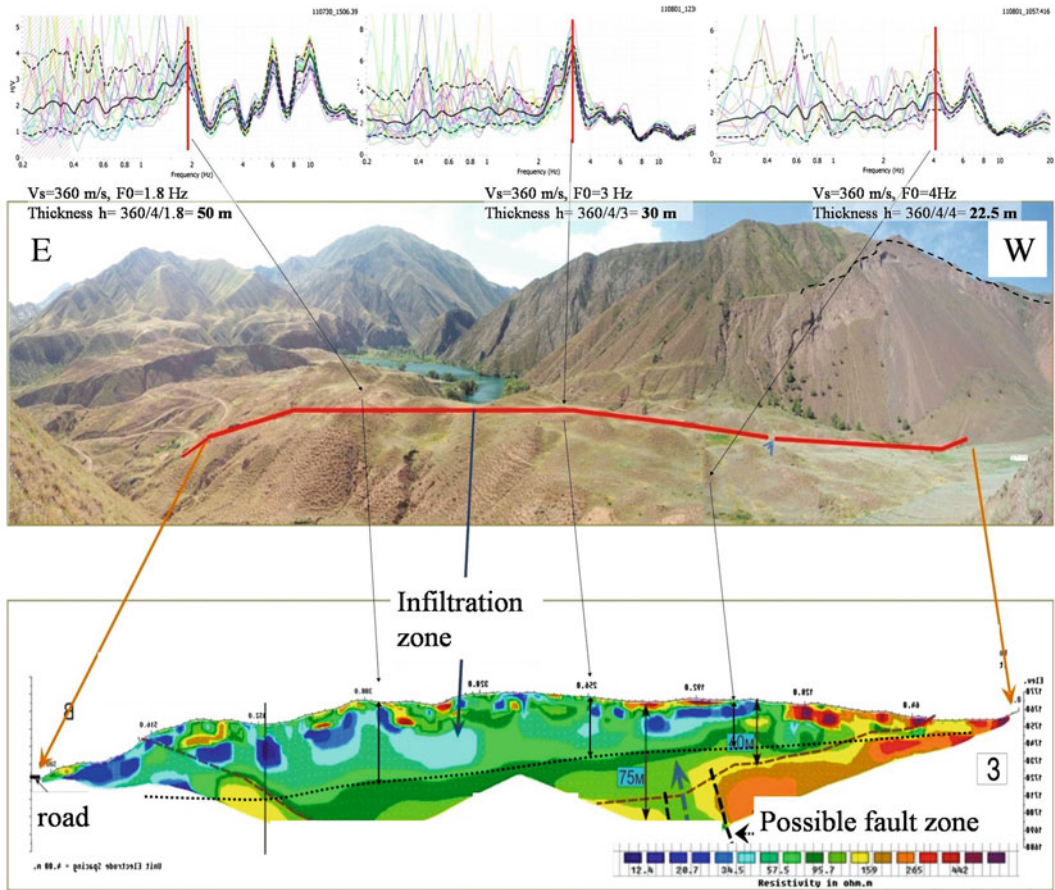
Fig. 29.7 Above: Selected H/V ratios for three sites on the landslide dam. Middle: View (to S) of the Ak-kul landslide dam and location of the main 700 m long geoelectric profile (in *red*). Scarp is on the right (see *black dashed line*), the dammed lake can be seen in the middle part. Below: Main 700 m long geoelectric profile with basis of the landslide mass outlined by a black dashed line, the local thickness inferred from H/V data is indicated for three sites (see H/V spectra above)

distant Ferghana earthquake, about 0.03 g for the Naryn earhtquake)—but probably marked by very low ground motion frequencies.

The Ak-kul landslide dam formed as the result of an ancient rock avalanche; it has a volume of about 10 million m^3 and dams a lake with a volume of about 2.7 million m^3. A bathymetry survey of the lake showed that the lake is composed of two basins, both with a maximum depth of 20–25 m, a small northern one and the larger southern basin, separated by a high of the lake ground of 5 m depth. The northern basin is dammed by a narrow (probably artificial) and highly saturated fill that can be easily destabilized. The southern basin is drained by two pipes crossing the dam in its narrowest place (about 5 m width). The maximum thickness of the dam is 70 m as identified along the main 700 m long E-W oriented geoelectric profile in Fig. 29.7.

The fundamental resonance frequency of the dam measured in most places is about 3 Hz indicating an average thickness of 30–35 m. Locally, this frequency could be lower (down to 1.3 Hz) where the thickness is close to 70 m. The fundamental resonance peaks in the central part are well outlined by large amplitudes.

Therefore, it can be expected that there is a clear impedance contrast between the dam material and the bedrock which can induce larger amplification of seismic shaking, making the dam susceptible to seismic failure. It can be added that the azimuth of strongest shaking is generally oriented parallel to the local elongation of the landslide body.

Since the earthquake recordings were partly made with seismometers and partly with accelerometers, they cannot be directly compared. However, H/V ratios computed from earthquake windows clearly show that the amplitudes are at least two times higher in the middle part of landslide dam than along the borders.

4   Conclusions

A series of case studies completed in the Kyrgyz and Tajik Tien Shan were presented in this paper. They show that landslides can be well characterized by geophysical and seismological methods. The latter also allow us to assess the seismic response of the landslide body and/or of the in situ rocks. The very simple microseismic H/V method can help identify the fundamental frequency of the landslide body. This frequency changes with the local thickness of the mass. Since the equipment is very light (station and seismometer: <12 kg) and the ambient noise measurements short (20 min are generally enough), a large number of microseismic data (70 on Tuyuk Suu landslide, 50 on Ak-Kul dam) can be acquired within a few days. Combined with information on the average S-wave velocity of the ground from seismic refraction profiles, the H/V results provide an almost continuous picture of the thickness of the soft material.

Electrical tomography is now commonly used for investigations of landslides since they provide a clear image of the resistivity distribution and thus of the surficial geological layers and their water-saturation. Often this can help identify the sliding surface between the landslide mass and the in situ rock. Our case studies show that the combination of electric and seismic methods is well adapted to determine both the geomechanic (elastic) and hydrogeological characteristics of the landslide material and underlying rocks. The microseismic methods— best coupled with earthquake recordings and modelling—further allow us to define possible site amplification effects. This information can be used to assess the seismic failure potential of the landslide slope.

References

Danneels G, Bourdeau C, Torgoev I, Havenith HB (2008) Geophysical investigation and numerical modelling of unstable slopes: case-study of Kainama (Kyrgyzstan). Geophys J Int 175:17–34

Havenith HB, Jongmans D, Abdrakhmatov K, Trefois P, Delvaux D, Torgoev I (2000) Geophysical investigation of seismically induced surface effects: case study of a landslide in the Suusamyr valley, Kyrgyzstan. Surv Geophys 21:349–369

Havenith HB, Jongmans D, Faccioli E, Abdrakhmatov K, Bard PY (2002) Site effects analysis around the seismically induced Ananevo rockslide, Kyrgyzstan. Bull Seismol Soc Am 92:3190–3209

Havenith HB, Bourdeau C (2010) Earthquake-induced hazards in mountain regions: a review of case-histories from Central Asia. Geologica Belgica 13:135–150

Nadim F, Kjekstad O, Peduzzi P, Herold C, Jaedicke C (2006) Global landslide and avalanche hotspots. Landslides 3:159–173

Topographical and Geological Features of Landslides Occurred in Kamikashiwazaki District in Tochigi Prefecture Causing by Great East Japan Earthquake

Yoshimi Usui, Hiroshi Shimada, Hiroyuki Innami, Kiyoshi Amao, Takami Kanno and Tomoyuki Hiramatsu

Abstract

Many landslides occurred in Kamikashiwazaki district in the northern part of Tochigi prefecture causing by the Great East Japan earthquake which is magnitude 9.0 that produced approximately 24 km in depth of southeast approximately 130 km of Ojika Peninsula as seismic center on March 11, 2011. The landslide phenomena produce main scarps of landslide head occurring on 3-5 m length of behind location from the top of slope of relative height approximately 30 m and slope incline 30° facing west direction. Most of sliding soil mass is not seen in the generating landslide source area. Landslides are observed pumice layer showing in the high liquidity in the foot of these slopes. The landslide phenomena are high-speed and formed long-distance movement. These landslides have the sliding topography on the neighborhood slopes to show the trace that the landslide generated in the past.

Keywords

Earthquake-induced landslide · Tohoku–Pacific ocean earthquake · High-speed landslide · Volcanic cohesive soil

Y. Usui · H. Shimada
Yaita public Works Office Tochigi Prefectural Government, Tochigi, Japan

Ootawara Public Works Office Tochigi Prefectural Government, Ootawara City, Japan

Engineering Management Division Tochigi Prefectural Government, Tochigi, Japan

H. Innami · K. Amao
Sabo and Water Resources Division Tochigi Prefectural Government, Tochigi, Japan

T. Kanno (✉) · Tomoyuki. Hiramatsu
Kawasaki Geological Engineering Co. Ltd, 2-11-15 Mita, Minato Ward, Tokyo, Japan
e-mail: hiramatsut@kge.co.jp

1 Overview of the Landslide Disaster

Landslides occurred from the slope shoulder of the western end of a flat upland at a relative elevation of 25 m. Scarps developed 3–5 m behind the original shoulder, and a parallel fracture developed 15 m behind the scarps (Photo 30.1).

Landslides were clearly identified at two locations. Their respective scales are given in Table 30.1.

The scarps formed steep slopes at 30°–45° gradients. Few displaced soil masses remained in the landslide source area but instead

Table 30.1 Scales of the landslides

Block	Width (m)	Length (m)	Depth (m)	Volume (m^3)
A3	50	195	6.5	7600
C6	40	125	8.0	10000

Table 30.2 Scales of the fractures

Distance from the slope shoulder	~3 m	~5 m (Photo 30.2)	~15 m
Width of opening	0.3–0.5 m	0.3 m	0.15 m
Vertical offset	0.5–0.6 m	0.2 m	0.05 m
Continuous length	20 m	10 m	5–6 m

Fig. 30.1 Results of aerial laser survey

accumulated flatly on a lower slope, suggesting that further displacement of the soil mass in the future is unlikely. However, open fractures exist on the flat surface behind the scarps, raising concerns about additional landslides.

Fractures developed intermittently on the flat surface behind the shoulder and even at locations away from the sites of the landslides. These fractures are located approximately 3, 5, and 15 m from the slope shoulder and are perpendicular to the direction of tilt of the slope. The scale of each fracture is listed in Table 30.2, Photo 30.2.

Within this group of fractures, large ground deformations of more than 30 cm horizontally and more than 50–60 cm vertically developed, causing some buildings to tilt and collapse. The fracture that developed 3 m from the slope shoulder corresponds to the location of the scarps from two distinct landslides.

A depression formed at the footslope beneath the scarp, where the height difference relative to side ground was as high as 7 m. A pool of water formed in the depression; this water originated from a spring, suggesting that the footslope had abundant groundwater.

On both sides of the depression, colluvial soil containing pumice was deposited up to a level 2.5 m higher than the original ground surface (Photo 30.3). A fallen cedar was observed beneath the colluvial deposit (Photo 30.4, Fig. 30.2).

2 Emergency Response

Prompted by the landslide and concerns that heavy rain infiltrating fractures or future earthquake aftershocks could cause further landsliding, emergency measures were taken for the flat surface within 15 m of the shoulder slope. These measures included sheet curing over the open fracture group, developing an extensometer auto-monitoring system, and developing an alert and evacuation system.

Additionally, the following emergency surveys were conducted to obtain the landscape and geological information necessary for designing countermeasure constructions:

- A detailed block division of the area was done by studying and interpreting the landscape and exploring land surface via aerial laser survey.
- A boring survey was done for geological analysis.
- Pipe strain indicators were installed for dynamic observation of future sliding.

The aerial laser survey enabled gaining an accurate of the disaster area by providing details of topographical features of the depression along the footslope, the amount of colluvial material deposited at the side cliff, and the deposited soil mass slipped from source area (Fig. 30.1).

Additionally, it was presumed that similar landslides topographical features have occurred in the past, as indicated by the characteristics of adjacent slopes.

3 Processes of Landslide Occurrence

The landslide phenomena in this district can be categorized into two patterns:

1. Landslides in which soil mass slipped over an arc-shaped surface and came to slide farther down the slope.
2. Phenomena without traces of slippage, despite the breakout of precursor vertical offsets and fracture openings.

The pattern 1 landsliding process can be explained from landscape and geological characteristics. Given that the amount of residual deposited soil in the landslide area is very small and that the soil deposits slipped from source area are nearly horizontal, it is presumed that a high-speed landslide occurred, and the soil masses slipped all the way down and then stabilized. Figure 30.2 shows a representative cross section of the landslide.

The surface of slippage has an arc shape, implying that the slope is made of homogenous material. Cohesive homogenous volcanic soil and locally bank (clay with pebbles) were confirmed by the boring survey

Along the slide cliff side of the depression (Fig. 30.2), slickenside of 30° slopes formed as a result of the landslide. This gradient is consistent with the existing slope of the cliff side

Colluvial soil accumulated to 2.5 m along the depression suggesting that the footslope rose temporarily, causing soil to spread sideways. The presence of the springs and pumice layer observed at the depression indicates that the footslope may consist of fragile ground with abundant groundwater. (Wakai 2012)

This landslide is believed to have progressed in the following manner: Slopes consisting of cohesive volcanic soil (relative height: 20 m or more, slope gradient: 30° or more) slipped as a result of the earthquake and accumulated and
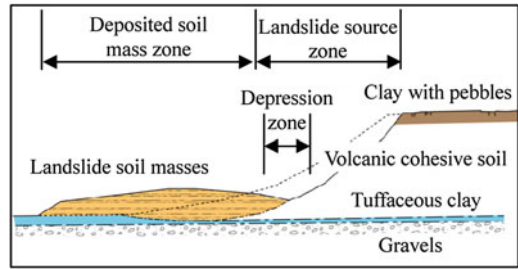
Fig. 30.2 A representative cross section of the landslide
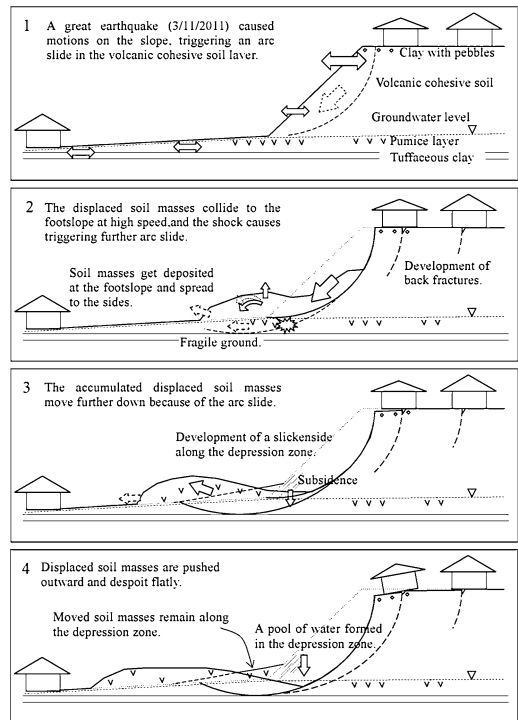
Fig. 30.3 Progression of the landslide

spread at the footslope. The momentum of the mass of soil caused the material at the footslope to slip further, forming an arc-shaped surface. The displaced soil masses were then pushed forward along the slope, forming a depression with relative elevations of up to 7 m (Fig. 30.3).

Houses were damaged by the opening fractures and ensuing vertical movements of the flat surfaces behind the scarp. Unstable soil masses developed and remained at the back of the scarp.

Table 30.3 Classification of landslide locations

Landslide pattern	Relative elevation	Gradient	Sharpness of slope shoulder	Gully	Number of location
1. Ditinct landslide movement	≥20 m	≥30°	sharp	Exists	2
2. Only fractures and offsets at the shoulder	<20 m	<30°	sharp-round	None- exists	9
No deformation	<20 m	<30°	round	None	–

Photo 30.1 An aerial photograph of the landslide (block A3)

Photo 30.2 Fractures are located 5 m from slope shoulder opening width: 0.3 m, vertical offset: 0.2 m

A similar landslide triggered by the same earthquake occurred in Hanokidaira, Shirakawa City, Fukushima (The Japan Landslide Society 2012). Both landslides had similar features:

Photo 30.3 Colluvial soil deposited on one side cliff of the depression

Photo 30.4 The pumice layer and a fallen cedar in the colluvial soil

- A cohesive volcanic soil layer was present.
- Soil masses moved completely from the landslide source area.
- Two-block slippage, i.e., upper and lower, occurred.
- Highly aqueous ground was involved in the lower-block slippage.

- The lower-block slippage cuts colluvial soil from the upper-layer slippage.

4   Classification of Landslide Locations

As noted in the previous section, landslides in this district can be categorized into two patterns. These landslides are classified from the geological features of their slopes, as shown in Table 30.3.

Pattern 1 landslides have 20 m higher relative elevations and 30° higher gradients. Gullies have formed around their footslope, and groundwater is abundant. On the other hand, pattern 2 landslides have 20 m lower relative elevations and 30° gradients. Slides do not occur, even within gullies. Locations with no deformation have a low relative elevation and a slope gradient of about 15°.

5   Conclusions

Landscape and geological characteristics of the earthquake-triggered landslides in Kamikashiwazaki District are summarized below

1. Two patterns of landslides were identified: slipped landslide blocks and landslides with only fractures and vertical offsets at the crown. The different characteristics are due to differences in relative elevation, gradient, and amount of groundwater.
2. The slippage surface of landslides in which the soil mass had slipped was arc-shaped, indicating that it occurred within a homogenous layer (cohesive volcanic soil).
3. More than 2.5 m of colluvial soil was deposited along the footslope sides. This may have been due to an accumulation of displaced soil masses at the footslope from a series of landslides.
4. Landslides accumulated and spread at the footslope and then cut across the displaced soil masses farther downward. This indicates that the soil mass slipped at high speed, causing fragile ground at the footslope to move further down the slope with an arc-like slippage motion.
5. Although moved soil masses usually form a thick deposit at the footslope, a depression was formed in this case in spite of landslide toe area.
6. The described landscape characteristics were also observed by an aerial laser survey. The characteristics of adjacent slopes indicate that similar landslides occurred in the past.
7. A landslide that occurred in Hanokiidaira, Fukushima Prefecture, also triggered by the same earthquake, is an example of a landslide similar to those described in this paper.
8. A group of open fractures with vertical offsets developed on the flat surface behind the landslide scarp, and emergency countermeasures were taken to mitigate the possible danger of more landslides caused by heavy rain or aftershocks.

References

Abe S, Hayashi K (2011) Morphologic features of landslide induced by recent large-scale earthquakes and their geomorphologic and geologic features. J Jpn Landslide Soc 48(1):52–61

The Japan Landslide Society (2012) Earthquake- induced landslides. The Japan Landslide Society, p 302

Wakai A (2012) Landslides in northern Kanto area induced by The 2011 Off the Pacific Coast of Tohoku Earthquake. http://geotech.ce.gunma-u.ac.jp/∼wakai/info/JLS20120420Wakai.pdf. Accessed 21 May 2012

Predicting Volume and Runout of Single Gully Debris-Flow Using Hypsometric Integral Value in the Wenchuan Earthquake Area

31

Huaizhen Zhang, Jianrong Fan and Qing Liu

Abstract

Debris-flow volume and runout zone are estimated from empirical equations which are based on the most important morphometric characteristics of a catchment and have the limitation of requiring uncertain input parameters. In addition, due to extraordinary abundant loose solid materials and local short-time heavy rainfall by extreme climate in the Wenchuan earthquake area, large errors will occur if the existing empirical equations are directly used. In order to enhance the applicability of those empirical equations in this area, we use Strahler's Hypsometric (area-altitude) analysis method to quantitatively describe the geomorphological conditions, develop models that quantitatively depict spatial distribution of mainly available loose sediment in debris-flow catchment and with integral values T, G_1 and G_2 as quantitative parameters of loose sediment's spatial conditions. Grouping-occurring debris-flows triggered by the September 24, 2008 rainstorm in Beichuan County and the August 13, 2010 regional rainstorm in Qingping Town, Mianzhu County are selected. Applying multivariate regression analysis, Hypsometric integral value S is used in

H. Zhang · J. Fan · Q. Liu
Key Laboratory of Mountain Hazards and Surface
Process, Chinese Academy of Sciences,
Chengdu, Sichuan, China

H. Zhang · J. Fan (✉) · Q. Liu
Institute of Mountain Hazards and Environment,
Chinese Academy of Sciences and Ministry
of Water Conservancy,
Chengdu 610041, Sichuan, China
e-mail: fjrong@imde.ac.cn

H. Zhang
Institute of Remote Sensing Applications, Chinese
Academy of Sciences, Beijing 100101, China

H. Zhang · Q. Liu
Graduate University of the Chinese Academy of
Sciences, Beijing, 100049, China

estimating debris-flow volume and runout distance models; and T, G_1 and G_2 are used as the coefficients of correction. The results showed that the hypsometric integral value S was suitable for the prediction of the debris-flow volume and runout zones in the Wenchuan earthquake area; the predicted results were more accurate when T, G_1 and G_2 are used. The introduction of S, T, G_1 and G_2 will enhance the applicability of existing empirical equations in Wenchuan earthquake area.

1   Introduction

Debris-flows volume and runout predictions are important and useful for a hazard assessment. From the point of view of the evaluation of a potential hazard, debris-flow volume, M, is one of the most important parameters. As a rough approximation, the debris-flow volume can then be used to estimate of the associated peak discharge, Q_p, the total travel distance, L, and also the runout distance on the fan, L_f (Rickenmann 1999). Now, there are many empirical equations to estimate debris-flow volume or runout distance. In general, a spectrum of possible debris-flow volumes can be expected to occur with different probabilities (Rickenmann 1999; Bovis and Jakob 1999).

Existing empirically-based models predict potential volumes or runout zones of debris flows in different regions and geologic settings. The virtue of empirically-based models is that it does not address the material rheology or mechanics of movement (Benda and Cundy 1990; Fannin and Rollerson 1993; Fannin and Wise 2001). Fannin and Wise (2001) developed an empirical-statistical model called UBCDFLOW based on forensic field observations and inspection of 449 debris flow events in Queen Charlotte Islands (OCI), British Columbia. It offers a practical means of predicting the mode of debris flow behavior, and has been used in estimating the size and travel distance of Klapperhorn Mountain debris flows for risk analysis along railway, Canada (Hengxing et al. 2008). Gartner et al. (2008) developed empirical models to predict the volume of debris-flows generated by burned basin using data from

53 recently burned basins in Colorado, Utah and California. Refer to the above model, Jianqi et al. (2009) developed an improved model that is suitable to predict the volume of debris-flow which affected by earthquake and main loose sediment was collapse and landslide, based on the observation data of debris-flow in Jiangjia gully, Yunnan, China. The above cases indicated that some of empirically-based models are suitable to other regions if modifying model by local data, the reason is that most empirically-based models are based on the most important morphometric characteristics of a debris-flow catchment.

Now many attempts have been made to spatially analyse the debris-flow with the aid of GIS, like GIS-assisted modeling for debris-flow hazard assessment (Toyos et al. 2007; Kneisel et al. 2007), Morphometric analysis of debris flows and their source areas using GIS (Chien-Yuan and Fan-Chieh 2011), and quantifying the spatial distribution of soil mass wasting processes after the 2008 earthquake in Wenchuan, China (Baofeng et al. 2010). However, little of those studies have given the spatial parameter of environmental conditions in debris-flow gullies. Therefore, one of the purposes of this paper is to introduce spatial parameters.

Chuan T, Jing Z, Ming et al. had built an empirical statistical model for predicting debris-flow runout zones in the Wenchuan earthquake area (Chuan et al. 2012). This model was just based on the rain storm-induced debris-flows of September 24, 2008 in Beichuan County. The scope of the paper iss to use Strahler's Hypsometric (area-altitude) analysis method to
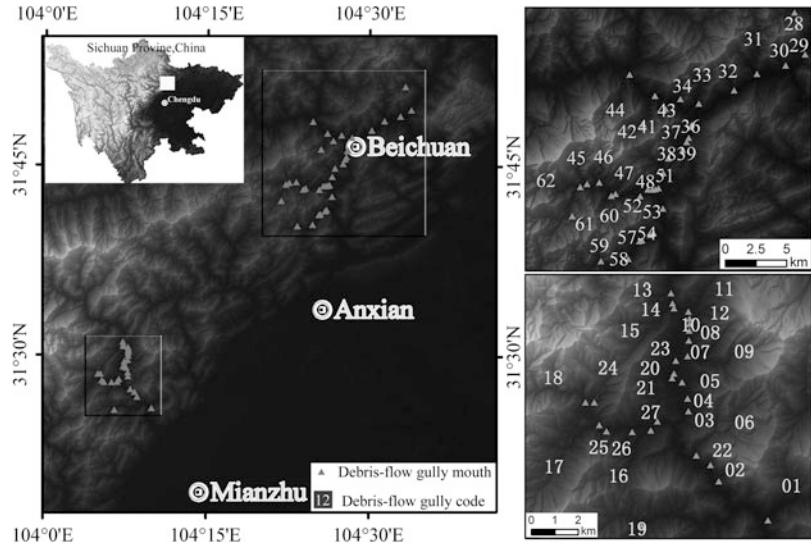
quantitatively describe geomorphological conditions and then develop models that quantitatively depict spatial distribution of mainly available loose sediment in debris-flow catchment, using integral values T, G_1 and G_2 as quantitative parameters of loose sediment's spatial conditions. Using the data of grouping-occurring debris-flows triggered by the September 24, 2008 rainstorm in Beichuan County and the August 13, 2010 regional rainstorm in Qingping Town, Mianzhu County, and applying multivariate regression analysis, the existing empirically-based models were modified by introduction of S, T, G_1 and G_2. In the multivariate regression analysis course, the Hypsometric integral value S was used in estimating debris-flow volume and runout distance models; and T, G_1 and G_2 were used as the coefficients of correction. We hope this way will enhance the applicability of existing empirical equations in Wenchuan earthquake area.

2   The Study Area

The study area situated in the central Wenchuan earthquake-affected area, mainly including Qingping town of Mianzhu city and Beichuan county, Sichuan Province (Fig. 31.1). The structural orientation of the study area is NE/SW. The Yinxiu-Beichuan Fault, which triggered the

Wenchuan earthquake, is located immediately southeast of the study area. This fault is a NW dipping thrust fault with an angle of 60–70°. The Cambrian sandstones form its hanging wall, while its footwall consists of Silurian and Devonian limestones (Chuan et al. 2009). Extraordinary abundant loose solid materials and local short-time heavy rainfall by extreme climate in the Wenchuan earthquake region were the basic reasons of the debris-flow occurrence (Qiang 2010). Debris-flow in the earthquake affected area has become more frequent. On 14 August 2010, debris-flows occurred in more than 20 gullies in the upstream of Mianyuan River, Mianzhu, Sichuan, at stimulus of regional rainstorms (see Table 31.1) (Pengcheng et al. 2011). During the early morning of 24 September 2008, a heavy rainstorm in Beichuan County, triggered numerous debris flows (see Table 31.2) (Chuan 2012).

3   Methodology

3.1   Quantitative Geomorphological Conditions

Strahler (1952) firstly used the integral of the percentage hypsometric curve (area-altitude curve), which relates horizontal cross-sectional area of a drainage basin to relative elevation

Table 31.1 Data set of debris-flows in upstream of Mianyuan River, 2010.08.13

Gully name	Gully code	Volume of sediment V_L (10^4 m³)	Catchment internal relief H (km)	Catchment area A (km²)	Debris-flow volume M (10^4 m³)	S
Nanmu	D01	40.0	1.23	9.55	10.00	0.451
Changtan	D02	120.0	1.14	1.14	30.00	0.500
Chajia	D03	5.6	0.47	0.45	1.20	0.447
Tianyang	D04	8.6	0.65	0.62	2.00	0.382
Lianjia	D05	7.8	0.77	1.40	1.48	0.466
Shihui	D06	184.8	1.31	8.34	4.80	0.536
Didong	D07	1.6	0.30	0.18	0.68	0.458
Wawa	D08	59.0	0.75	0.64	9.00	0.402
Wenjia	D09	8000.0	1.46	7.81	450.00	0.490
Dongzi	D10	2.6	0.11	0.10	1.24	0.346
Zhoumaling	D11	466.5	1.14	5.70	30.00	0.452
Luojia	D12	130.8	1.40	2.50	16.02	0.381
Dianzhan	D13	2.3	1.16	1.38	0.30	0.604
Liubaizi	D14	0.3	1.04	0.64	0.10	0.512
Yongjia	D15	195.0	1.60	5.07	45.00	0.427
Lanni	D16	130.0	1.20	5.31	70.00	0.435
Qishu	D17	330.0	1.80	18.11	30.00	0.473
Zhongshu	D18	1400.0	2.56	16.20	200.00	0.455
Huashi	D19	60.0	1.29	10.27	10.00	0.439
Caodun	D20	10.3	0.70	0.53	2.40	0.542
Maliuwan	D21	13.0	0.83	0.91	3.00	0.543
Chengqiang	D22	2.4	0.84	0.65	0.40	0.719
Bojiyan	D23	5.0	0.64	0.84	0.70	0.419
Gangou	D24	240.0	1.58	5.12	60.00	0.411
Liangjiashan	D25	1.1	0.84	0.59	0.25	0.512
Changzi	D26	0.5	0.72	0.60	0.13	0.388
Zhangjiacao	D27	41.5	0.42	0.71	1.50	0.413

Note the debris-flow data is mainly from paper of Pengcheng. This debris-flow event occurred in upstream of Mianyuan River, near to Qingping Town, Mianzhu Country, Sichuan Pronvice, China

above basin mouth, to analyse the morphometric of basins quantitatively.

$$y = f(x) \tag{31.1}$$

$$S = \int_0^1 f(x)dx \tag{31.2}$$

$$x = \frac{a}{A} \quad y = \frac{h}{H}$$

Where:

x ratio of area between the contour and the upper perimeter (Area a) to total drainage basin area (area A).

a area of the contour and the upper perimeter

A total drainage basin area

y ratio of height of contour above base (h) to total height of basin (H)

h height of contour above base

H total height of basin

S integral of the percentage hypsometric curve (area-altitude curve)

Table 31.2 Data set of debris-flows in Beichuan country, 2008.09.24

Gully name	Gully code	Max.runout distance, L_f (km)	Lateral width, B_f (km)	Volume of sediment, V_L ($10^6 m^3$)	Catchment internal relief, H (km)	Catchment area, A (km^2)	S
Tongbao	D28	0.19	0.22	1.24	0.88	1.06	0.563
Yunlicun	D29	0.24	0.23	4.46	1.1	1.94	0.462
Huangjiaba	D30	0.38	0.31	6.47	1.14	2.41	0.475
Xiaonan	D31	0.11	0.11	0.65	0.66	0.69	0.570
Hualin	D32	0.25	0.46	4.85	1.18	3.52	0.511
Dongxi	D33	0.24	0.38	12.05	1.16	7.49	0.491
Loufangping	D34	0.23	0.22	5.14	1.02	2.49	0.548
Xinjiecun	D35	0.18	0.12	0.3	0.69	0.29	0.472
Shenjia	D36	0.35	0.26	3.17	0.85	0.83	0.520
Sujia	D37	0.19	0.13	3.32	1	1.52	0.453
Weijia	D38	0.32	0.15	5.1	1.12	1.36	0.504
Shiyicun	D39	0.21	0.16	0.13	0.7	0.27	0.369
Caoshan	D40	0.49	0.46	17.6	1.47	10.15	0.453
Caoshanzigou	D41	0.13	0.24	3.16	1.06	1.81	0.466
Dashuicun	D42	0.14	0.35	2.99	0.93	1.12	0.538
Shilong	D43	0.35	0.31	8.72	1.54	9.91	0.493
Qingjiecun	D44	0.25	0.27	2.11	0.82	0.57	0.514
Pashancun	D45	0.43	0.38	10.21	1.24	7.6	0.542
Guanmenzi	D46	0.44	0.33	10.01	1.5	5.5	0.513
Daancun	D47	0.21	0.23	7.21	1.3	3.67	0.381
Xujiacun	D48	0.21	0.19	0.09	0.58	0.6	0.427
Liulincun	D49	0.16	0.20	0.62	0.56	0.45	0.502
W.Liulincun	D50	0.27	0.26	0.15	0.6	0.46	0.416
Yingding	D51	0.20	0.18	0.96	0.54	0.32	0.449
Guoniucun	D52	0.18	0.30	2.88	0.84	0.81	0.529
Shiyan	D53	0.24	0.22	1.87	0.88	1.07	0.480
Chafangcun1	D54	0.11	0.15	1.44	0.9	0.64	0.507
Chafangcun2	D55	0.13	0.15	0.9	0.94	0.59	0.447
Datiancun1	D56	0.11	0.12	1.39	0.92	0.55	0.454
Datiancun2	D57	0.25	0.21	6.35	1.02	2.56	0.505
Wuxingcun	D58	0.21	0.29	3.96	0.98	1.47	0.446
Fanzaocun	D59	0.37	0.34	6.69	0.92	4.69	0.599
Tianbacun	D60	0.31	0.25	3.03	0.82	6.29	0.542
Nanxingcun	D61	0.32	0.37	2.09	0.56	3.11	0.543
Qiaoluocun	D62	0.11	0.13	1.42	0.7	0.73	0.506

Note the debris-flows data is mainly from paper of Chuan T. This debris-flow event occurred in Beichuan Country, Sichuan Pronvice, China

Strahler (1956, 1957) used other parameters to analyse the slope and watershed geomorphology quantitatively. Nanshan (1987, 1988) reviewed the traditional geomorphy theory—Davis's Theory of Geomorphological Cycle from a systematical view, building concept of comentropy in erosional drainage-system and computing method, based on the Strahler's curve and integral. Debris-flow basin is erosional drainage-system, the geomorphical information entropy was explored and discussed in debris-flow study. The entropy value was used to analysis the activity and process of debris-flow quantitatively (Zhongxin 1989, 1992).

3.2 Quantitative Spatial Distribution Parameter

Debris flow is defined as a poorly sorted mixture of soil, rock, vegetation and water that rapidly flows down a slope in response to gravity (Iverson 1997). Available loose sediment, torrential rainfall, and topographic conditions are important factors for the initiation of debris flows. In the past, we paid much attention to the physical measured characteristics of a catchment, such as volume of sediment V_L, catchment internal relief H, and catchment area A. The study of spatial distribution of loose sediment is little, especially quantitative spatial distribution parameter.

Refer to Strahler's area-altitude analysis method; we build the spatial analysis model to depict spatial distribution of mainly available loose sediment.

$$y_1 = f(x_1) \qquad (31.3)$$

$$T = \int_0^1 f(x_1)dx_1 \qquad (31.4)$$

$$x_1 = \frac{s}{A_s} \quad y_1 = \frac{h_s}{H}$$

Where:

x_1 ratio of area between the contour and the upper perimeter loose sediment region area (s) to total loose sediment distribute area (A_s)

s area of the contour and the upper perimeter loose sediment region

A_s total loose sediment region area

y_1 ratio of height of loose sediment region above base (h_s) to total height of basin (H)

h_s height of loose sediment region above base

T integral of the loose sediment region area-altitude curve

$$y_2 = f(x_2) \qquad (31.5)$$

$$G_1 = \int_0^1 f(x_2)dx_2 \qquad (31.6)$$

$$x_2 = \frac{s_1}{A_s} \quad y_2 = \frac{d_1}{D_1}$$

Where:

x_2 ratio of area between loose sediment region area (s_1) in the range of d_1 distance from gully to total loose sediment distribute area (A_s)

s_1 area of loose sediment region in the range of d_1 distance from gully

y_2 ratio of distance of loose sediment region from gully to total distance from gully

d_1 distance of loose sediment region from gully

D_1 max distance of loose sediment region from gully

G_1 integral of the loose sediment region area-gully distance curve

$$y_3 = f(x_3) \qquad (31.7)$$

$$G_2 = \int_0^1 f(x_3)dx_3 \qquad (31.8)$$

$$x_2 = \frac{s_1}{A_s} \quad y_2 = \frac{d_1}{D_1}$$

Where:

x_2 ratio of area between loose sediment region area (s_1) in the range of d_1 distance from gully-mouth to total loose sediment distribute area (A_s)

s_2 area of loose sediment region in the range of d_2 distance from gully-mouth

y_2 ratio of distance of loose sediment region from gully-mouth to total distance of basin from gully-mouth

Table 31.3 Descriptive statistics and significance values for the prediction equations

Equations	Min (km)	Max (km)	Mean (km)	Variance	Standard deviation	Multiple correlation	Residual standard error
10	0.144	0.396	0.243	0.0071	0.0736	0.732	0.0685
11	0.150	0.377	0.248	0.0069	0.0682	0.715	0.0667

d_2 distance of loose sediment region from gully-mouth

D_2 max distance of loose sediment region from gully-mouth

G_2 integral of the loose sediment region area-gully-mouth distance curve

3.3   Development of Debris-Flow Volume Model

Empirical equations of debris-flow volume are usually based on the most important morphometric characteristics of a catchment, especially the most important morphometric catchment characteristics. Some of the empirical relationships also include information on expected rainfall conditions or on the lithologic characteristics of the catchment (Rickenmann 1999). In this paper, we try to introduce S (integral of the area-altitude curve) to build the prediction model of debris-flow volume. The model was evaluated by logistic regression analyses from the debris-flow data set of Table 31.1.

$$M = 0.257 V_L^{2.011S} \quad (31.9)$$

Where M is the predicted debris-flow volume; V_L is the volume of sediment. In the course of logistic regression analyses, some of data were eliminated, like D06, D09 and D18. The multiple correlation (R Square) was 0.987.

3.4   Development of Debris-Flow Runout Zones Model

Large amounts of loose material were deposited in the debris-flow catchments from the earthquake-induced landslides, in the Wenchuan earthquake area. Existing debris-flow runout models have the limitation in assessing the hazardous zones in this area (Chuan et al. 2012). For this reason, Chuan et al. (2011) used the data of debris-flow during the rainstorm-induced debris-flows of September 24, 2008 in Beichuan County and established an appropriate model for predicting the possible debris-flow runout zones on the alluvial fans after the Wenchuan earthquake. Now we use most of the data again, and introduce S (integral of the area-altitude curve), build the prediction model. Table 31.3 shows the descriptive statistics and significance values for the prediction model equations.

$$L_f = 0.557 A^{\frac{s}{10}} + 0.041(V_L H)^s - 0.406 \quad (31.10)$$

$$B_f = 0.901 A^{\frac{s}{10}} + 0.020(V_L H)^s - 0.708 \quad (31.11)$$

Where:

L_f the predicted maximum runout distance (km);

B_f the maximum width (km);

V_L the volume of removable sediment in the catchment (10^6 m^3);

A the debris-flow catchment area (km^2);

H the catchment internal relief (km);

S the integral of the area-altitude curve.

4   Results and Discussion

4.1   Test of Model Equations

In order to test the regression equations, we choose some debris-flow gullies situated in the Wenchuan earthquake-affected area that were not used in multivariate regression analysis. As shown in Table 31.4, three of the four debris-flow gullies located in Beichuan country occurred debris-flows on 24 September 2008; and one

Table 31.4 Data set of debris-flows for testing debris-flow volume model

Gully name	Volume of sediment, V_L ($10^6 m^3$)	Catchment internal relief, H (km)	Catchment area, A (km^2)	Event date
Weijia	5.31	0.31	1.23	24/09/2008
Xijia	2.14	0.71	1.73	24/09/2008
Huashiban	5.75	0.67	1.31	24/09/2008
Hongchun	3.84	5.50	1.26	14/08/2010

Table 31.5 Comparison between the predicted debris-flow volume values and field-measured values

Gully name	S	Debris-flow volume M ($10^4 m^3$)		
		Field measured	Predicted value	Error (%)
Weijia	0.369	10.5	27.05	157.59
Xijia	0.453	16.6	34.11	105.49
Huashiban	0.504	23.5	161.06	585.35
Hongchun	0.486	71.1	86.24	21.29

Table 31.6 Data set of debris-flows for testing debris-flow runout zones model

Gully name	Max. runout distance, L_f (km)	Lateral width, B_f (km)	Volume of sediment, V_L ($10^6 m^3$)	Catchment internal relief, H (km)	Catchment area, A (km^2)
Hongchun	0.39	0.35	3.84	1.26	5.50
Shaofang	0.17	0.18	3.08	1.04	0.71
Xiaojia	0.17	0.26	0.49	1.07	0.49
Wangyimiao	0.22	0.21	0.73	1.00	0.47
Mozi	0.23	0.27	6.22	1.60	5.33

locates in the upstream of Minjiang rive, Yingxiu, Wenchuan occurred debris-flows on 14 August 2010.

From Table 31.5, we find that the predicted value error is much high in the Beichuan debris-flow gullies, especially Huashiban gully, while the predicted value of Hongchun gully is close to field measured value. By comparing the volume of sediment V_L with debris-flow volume M, we find that the M is too little, relative to V_L in the Weijia, Xijia, Huashiban gully. In other words, those gullies have the possibility of occurring bigger debris-flows. The estimated results are useful to predict the bigger debris-flow volume than this time.

As shown in Table 31.6, on 14 August 2010, debris-flows occurred in these five gullies in the upstream of Minjiang river, Yingxiu town, Wenchuan county. The predicted values of runout

distance and width are close to the empirical-statistical model of Chuan (Table 31.7). The error range was considered to be still acceptable for comparison with other empirical models (Rickenmann 1999; Prochaska et al. 2008).

4.2 Improving Debris-Flow Runout Predict Model

Based on SPOT remote sensing images, the falls and landslides induced by '5.12′ earthquake were identified (Fig. 31.2). Combining with GIS software, spatial distribution parameters were computed with the Eq. (3–8). T, G_1 and G_2 are used as quantitative parameters to describe the spatial distribution of debris flow gully's sediment supply. Taking five debris flows as examples (Table 31.6), quantitative parameters were

Table 31.7 Comparison between the predicted debris-flow runout zone values and field-measured values

Gully name	S	Maximum runout distance, L_f (km)			Lateral width, B_f (km)		
		Field measured	Predicted value	Error (%)	Field measured	Predicted value	Error (%)
Hongchun	0.486	0.39	0.292	−25.04	0.35	0.314	−10.32
Shaofang	0.481	0.17	0.218	28.63	0.18	0.213	18.49
Xiaojia	0.432	0.17	0.170	0.00	0.26	0.181	−30.46
Wangyimiao	0.392	0.22	0.176	−0.20	0.21	0.184	−12.19
Mozi	0.519	0.23	0.341	48.54	0.27	0.341	26.17
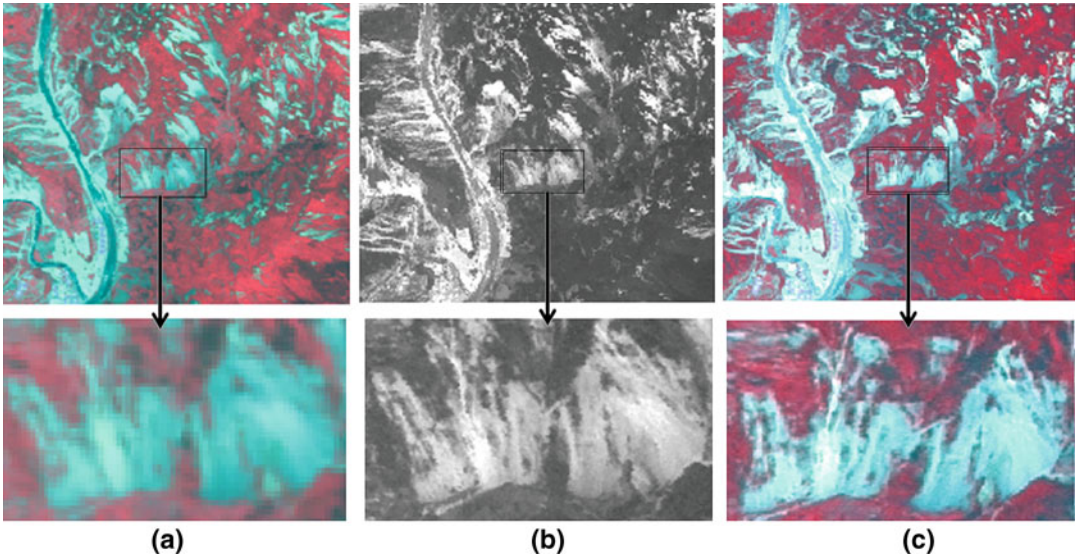
Fig. 31.2 Different remote sensing image resolution of falls and landslides in the study area

used in estimation of these debris flow depositional zones.

$$L_f = 0.557A^{\frac{s}{10}} + 0.041(V_L H)^s - 0.406 + \varepsilon(T, G_1, G_2) \tag{31.12}$$

$$B_f = 0.901A^{\frac{s}{10}} + 0.020(V_L H)^s - 0.708 + \delta(T, G_1, G_2) \tag{31.13}$$

where ε and δ are the coefficients of correction. The value of ε and δ is decided by quantitative parameters T, G_1 and G_2. In these five debris-flow gullies, the value of ε and δ are calculated from the following equations:

$$\varepsilon = 1.473G_2 - 0.717T - 0.386G_1 + 0.053 \tag{31.14}$$

$$\delta = 2.767T - 1.267G_1 + 2.720G_2 + 1.455 \tag{31.15}$$

From Table 31.8, we find that the results of predicted debris-flow runout distance are more close to actual value when quantitative parameters of spatial distribution of fall and landslide debris accumulation regions were used. But it is just a preliminary model, and need more data to test it.

5   Conclusions

The debris-flow process is very complex, and the simple empirical relationships can provide a

Table 31.8 Results of improve debris-flow runout predict model

Gully name	T	G_1	G_2	Maximum runout distance, L_f (km)		Lateral width, B_f (km)	
				Predicted value	Error (%)	Predicted value	Error (%)
Hongchun	0.480	0.529	0.289	0.361	−7.35	0.325	−7.18
Shaofang	0.413	0.389	0.316	0.147	−13.72	0.159	−11.51
Xiaojia	0.413	0.432	0.295	0.146	−14.05	0.238	−8.54
Wangyimiao	0.467	0.486	0.266	0.253	−15.00	0.239	−14.00
Mozi	0.415	0.430	0.325	0.273	18.98	0.309	14.32

rough approximation and acceptable prediction value of debris-flow parameter, like debris-flow volume, runout distance on the fan and so on. But the empirical relationships are changeable in different regions and geologic settings. It cannot be denied that empirically-based models should be based on the most important morphometric characteristics of a debris-flow catchment. In most cases, just the coefficients of morphometric characteristics were selected as variable in the empirical relationships. If the coefficients were confirmed by the particular conditions of debris-flows, the applicability of existing empirical equations will be enhanced.

In the Wenchuan earthquake area, the debris-flows have their own specialty, like extraordinary abundant loose solid materials and local short-time heavy rainfall by extreme climate. But the empirical relationships must be also based on the most important morphometric characteristics of a debris-flow catchment.

The empirical-statistical model for predicting debris-flow runout zones is based on the rain-storm-induced debris-flows of September 24, 2008 in Beichuan County (Chuan et al. 2012). Using the most important morphometric characteristics (V_L, A, H) in this paper, we try to introduce the spatial parameter (S, T, G_1 and G_2) preliminarily. We need more detailed data and spatial analysis to get more accurate estimates.

The last point remained to be cleared up, the empirical-statistical models were established in this paper without using the rainfall parameters, but the debris-flow data was based on the debris-flows events at the stimulus of short-time heavy rainfall by extreme climate.

References

Baofeng D, Hongjuan Z, Minghua Z et al. (2010) Quantifying the spatial distribution of soil mass wasting processes after the 2008 earthquake in Wenchuan, China : a case study of the Longmenshan area. Remote Sens Environ 114:761–771

Benda LE, Cundy TW (1990) Predicting deposition of debris flows in mountain channels. Can Geotech J 27:409–417

Bovis J, Jakob M (1999) The role of debris supply conditions in predicting debris flow activity. Earth Surf Proc Land 24:1039–1054

Cannon SH, Gartner JE, Rupert MG et al (2010) Predicting the probability and volume of post wildfire debris flows in the intermountain western United States. Geol Soc Am Bull 122:127–144

Chien-Yuan Ch, Fan-Chieh Y (2011) Morphometric analysis of debris flows and their source areas using GIS. Geomorphology 129:387–397

Chuan T, Jing Z, Li WL, Liang JT (2009) Rainfall-triggered debris flows following the Wenchuan Earthquake. Bull Eng Geol Environ 68:187–194

Chuan T, Jing Z, Ming C, Jun D, Xin Q (2012) An empirical statistical model for predicting debris-flow runout zones in the Wenchuan earthquake area. Quat Int 250:63–73

Fannin RJ, Rollerson TP (1993) Debris flows: some physical characteristics and behavior. Can Geotech J 30:71–81

Fannin RJ, Wise MP (2001) An empirical-statistical model for debris flow travel distance. Can Geotech J 38:982–994

Gartner JE, Cannon SH, Santi PM et al (2008) Empirical models to predict the volumes of debris flows generated by recently burned basins in the western U.S. Geomorphol 96:339–354

Hengxing L, Derek Martin C, Zhou CH (2008) Estimating the size and travel distance of Klapperhorn Mountain debris flows for risk analysis along railway, Canada. Int J Sedim Res 23:275–282

Iverson RM (1997) The physics of debris flows. Rev Geophys 35(3):245–296

Jianqi Z, Peng C, Yonggang G et al. (2009) Hazard assessment of debris-flow valleys along Dujiangyan-Wenchuan highway after Wenchuan devastating. Earthquake 41(3):131–139 (in Chinese)

Kneisel C, Rothenbuhler C, Keller F et al (2007) Hazard assessment of potential periglacial debris flows based on GIS-based spatial modelling and geophysical field surveys: a case study in the Swiss Alps. Permafrost Periglac Process 18:259–268

Nanshan A (1987) Comentropy in erosional drainage-system. J Soil Water Conserv 1(2):1–8 (in Chinese)

Nanshan A, Tianxiang Y (1988) Second discussion of the commentropy of erosional drainage-system. J Soil Water Conserv 2(4):1–9 (in Chinese)

Pengcheng S, Fangqing W, Hangzhong F et al (2011) Causes and effects of group-occurring debris flow disasters in Qingping Town, Mianyuan river upstream Sichuan. J Mt Sci 29(3):337–347 (in Chinese)

Prochaska B, Santi M, Higgins D, Cannon H (2008) Debris-flow runout predictions based on the average channel slope (ACS). Eng Geol 98:29–40

Qiang X (2010) The 13 August 2010 catastrophic debris-flows in Sichuan province: characteristics, genetic mechanism and suggestions. J Eng Geol 18(5):596–609 (in Chinese)

Rickenmann D (1999) Empirical relationships for debris flows. Nat Hazard 19:47–77

Strahler N (1952) Hypsometric (area-altitude) analysis of erosional topography. Bull Geol Soc Am 63:1117–1142

Strahler N (1956) Quantitative slope analysis. Bull Geol Soc Am 63:1117–1142

Strahler N (1957) Quantitative analysis of watershed geomorphology. Trans Am Geophys Union 38:913–920

Toyos G, Oramas Dorta D, Oppenheimer C et al (2007) GIS-assisted modeling for debris flow hazard assessment based on the events of May 1998 in the area of Sarno, Southern Italy: part I. Maximum run-out. Earth Surf Proc Land 32:1491–1502

Zhongxin J (1989) Exploring and discussing of the geomorphical information entropy in rectangle basin. Bull Soil Water Conserv 9(6):83–87 (in Chiese)

Zhongxin J (1992) Superentropy in drainage-system of debris flow. Chin J Geol Hazard Control 3:33–40

Features of Two Adjacent Landslides in Western Gunma Prefecture, Japan

32

Hiroshi Hasegawa, Yasuhito Sato, Yoshiyuki Kotei
and Yukio Hatakeyama

Abstract

The geological features and structures in Gunma Prefecture are uniquely diverse and very complex. As geology is one of many trigger factors inducing landslides, approximately 430 landslide hazardous sites within Gunma exhibits varying characteristic structures and failure mechanism for each geological setting. Two adjacent large-scale landslides: the Sugo landslide and Wamisawa landslide (which are part of 430 landslides in Gunma), occurred in the western part of Gunma Prefecture. These landslides were affected by igneous intrusions which penetrated the side walls of the host rock, affecting the stratigraphic and structural form of the rock. Field monitoring showed a relative differences in hydrogeology and motion mechanisms between the two landslides. Failure mechanisms of both landslides are different and independent of each other. Geotechnical remediation work was selected in consideration of the landslide failure mechanism. Result from remediation work shows that the landslides have been stabilized.

1 Introduction

Stratigraphy of Gunma Prefecture shows wide distribution of rocks dating from Paleozoic era to Quaternary period. Intermittent within these rocks are volcanic rock deposits. Moreover, many volcanoes exist in Gunma. They include Asama, Haruna, Akagi and Shirane volcanoes. Characteristic geological settings have contributed to numerous landslide cases in Gunma Prefecture.

This paper concentrates on the Sugo landslide and the Wamisawa landslide, which located in the Western part of Gunma Prefecture, also on the opposite side of Karuizawa, a famous summer resort for holiday-makers and tourists (Fig. 32.1).

H. Hasegawa (✉) · Y. Sato
Gunma Prefecture, Maebashi, Japan
e-mail: shinrinho@pref.gunma.lg.jp

Y. Kotei · Y. Hatakeyama
Japan Conservation Engineers and Co. Ltd,
Maebashi, Japan

Fig. 32.1 Geologic map
of Gunma Prefecture,
(Gunma Prefecture
Committee for Geological
Mapping 1999) and
position of targets
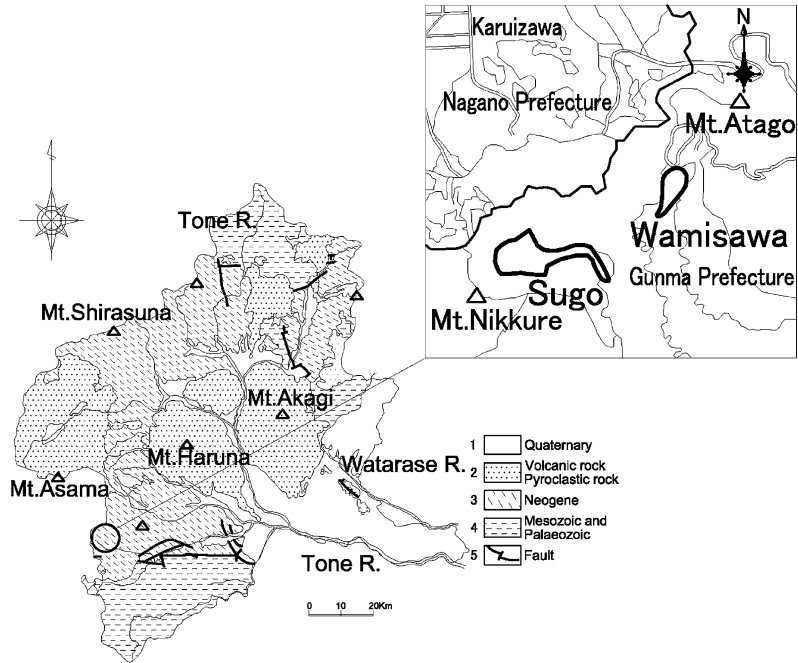
The composite rocks of these two landslides
are Neogene (marine) sedimentary deposits with
minor Neo-quaternary igneous intrusions. The
sedimentary layers are deposits of Lower-middle
Miocene epoch and are made up of sandstones,
siltstones and tuffaceous aggregates. Separating
the marine Miocene deposits from underlying
Mesozoic and Paleozoic strata are coeval
andesitic lava and pyroclastics conglomerates.
We believe debris avalanche deposits distributed
in this area originate from a sector collapse of a
nearby mountain induced by a volcanic earth-
quake at Mt. Asama.

Neogene sediments are relatively unconsoli-
dated as to their accumulated fairly recently in
the geological time scale. This makes them
vulnerable to landslides and slope failures when
they form a dip-slope or are fractured as some
kind of geological deformation such as faults
develop in the vicinity affecting their geome-
chanical properties. Landslide occurrences often
coincide with those areas where intruding igne-
ous rocks develop or debris avalanche deposits
accumulate, which naturally work as a water
catchment.

2   Geological Features of the Two Landslides

The Sugo and Wamisawa landslides are char-
acterized by Miocene sands, silts, and tuffs with
plutonic igneous rocks intruding into the sedi-
mentary layer. The structural style of landslides
in the area is bottleneck-shaped slopes which
were initiated by intrusive igneous rock on the
sides of the landslides.

Results obtained from geological observation
of outcrops and aerial photographs show linea-
ment features, disjointed and folded zones which
is believed to have made the slope vulnerable to
landslide.

Furthermore, debris avalanche deposit (to a
relative thickness) formed the uppermost sedi-
ment. The deposits are generally loose, poorly
sorted with clastic angular grains, covering the
Neogene sediments in both landslides and filling
void spaces between the intrusive bodies. Mate-
rials of the debris avalanche were provided from a
sector failure of an intrusive rock occurred ups-
lope of the landslide. Field investigations have

Fig. 32.2 Geological map around Sugo landslide and Wamisawa landslide
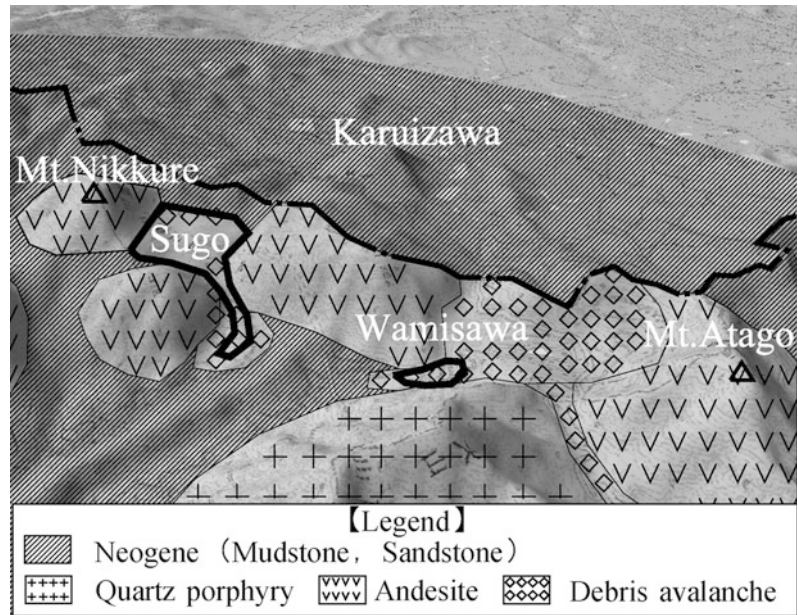
revealed that the Sugo landslide is debris avalanche from Mt.Nikkure while the Wamisawa landslide is from Mt. Atago (Kanto Branch of Japanese Geotechnical Society 2007) (Fig. 32.2).

3 Difference of Two Landslide Mechanisms

The two landslides share the same geological characteristics but differ in terms of hydrogeological, topographic and geomorphological features. These unique factors were used to explain the motion mechanism of the two landslides.

3.1 Mechanism of the Sugo Landslide

Materials of the Sugo landslide consist of tuffaceous aggregates which overlay Miocene sandstone and mudstone sediments creating discontinuous surface. Cutting discordantly into the sedimentary layers are Andesite dykes narrowing the path of the landslide. Filling up spaces around the intrusive rock bodies are deposits of the debris avalanche.

The length of the landslide is 900 m and the width is 300 m. A narrow area divided the landslide into an upper block and a lower block. The effect of the division made the blocks to show different hydrogeological characteristics (Figs 32.3, 32.4).

The upper block is comprised of thick layers of very permeable tuffaceous aggregates and debris avalanche deposits underlain by sandstone and mudstone layers; artesian water infiltrated through the highly disjointed and fractured intrusive rocks is accumulated within the tuff aggregates and deposits layers. In the region of the narrow area separating the two blocks, the sandstone and mudstone layers assume a convex structure which works to prevent the water flow causing groundwater level to easily increase (Figs. 32.3, 32.4).

Initially, the slip surface of the upper block was formed at the bottom of the tuffaceous aggregates layer, thus a drainage tunnel was installed in the narrowed section formed by the sandstone-mudstone layers for stabilizing the slope. However, continuous sliding activities led slip surface to form deeper down and eventually cut through the convex-shaped sandstone-mudstone layers near the narrowed section. During this process, the already-

Fig. 32.3 The geology bird's-eye view of Sugo landslide
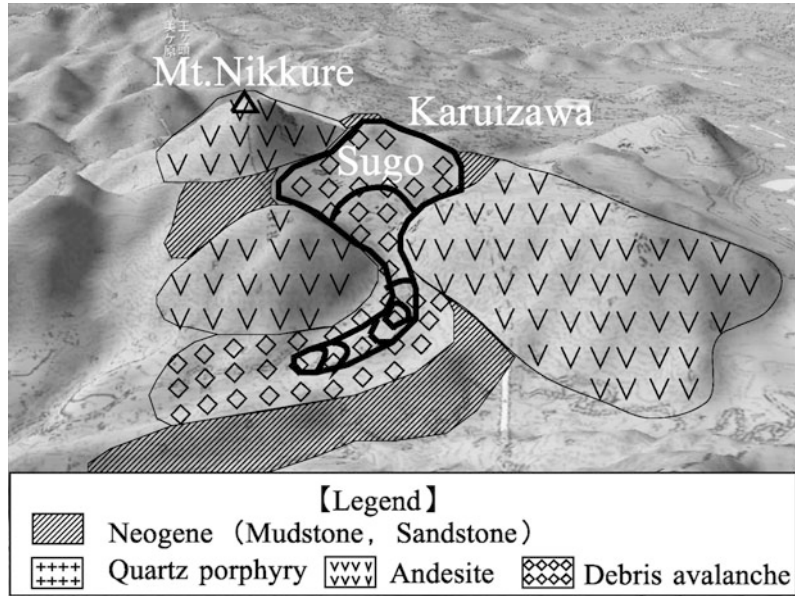
Fig. 32.4 The geologic cross section of Sugo landslide
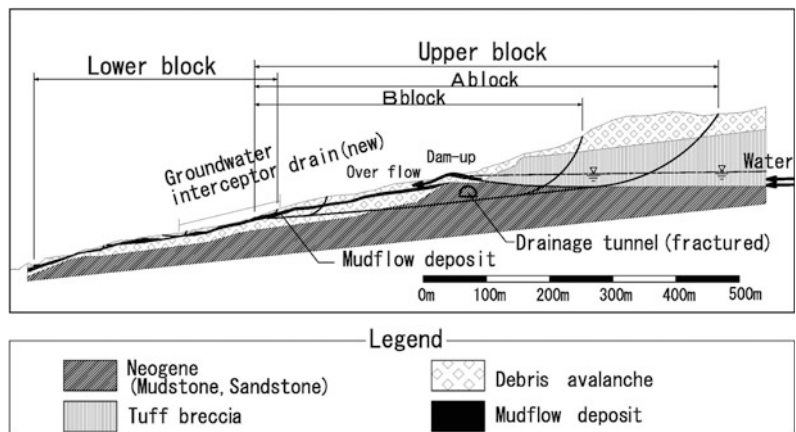
installed drainage tunnel was fractured as it was placed in a way that crossed the newly formed slip surface (Photo 32.1).

At the section of the lower block, debris avalanche deposits are distributed over the mudstone and sandstone layers (covering old subterranean layer). Maximum depth of shallow section of debris avalanche deposits is about 10 m, with mudflow deposits layer (of thickness between 10 cm and 2 m) intermittently sandwiched between layers. Although the mudflow deposits are moderately consolidated, massive and weak. In terms of permeability, debris avalanche deposits have higher permeability values than that of mudflow deposits (permeability value is negligible). As the subsurface water supplied from the upper block and overflew the convex shaped layers was unable to permeate through the deposits layer, the slip surface of the lower block was formed in the mudflow deposits.

The motion mechanism of the Sugo landslide is characterized by sequential movement in which the displacement of the upper block follows that of the lower block. Furthermore, field investigations revealed that the lower block was still active with recordable speed of several meters in a year.

Photo 32.1 The cut drainage tunnel
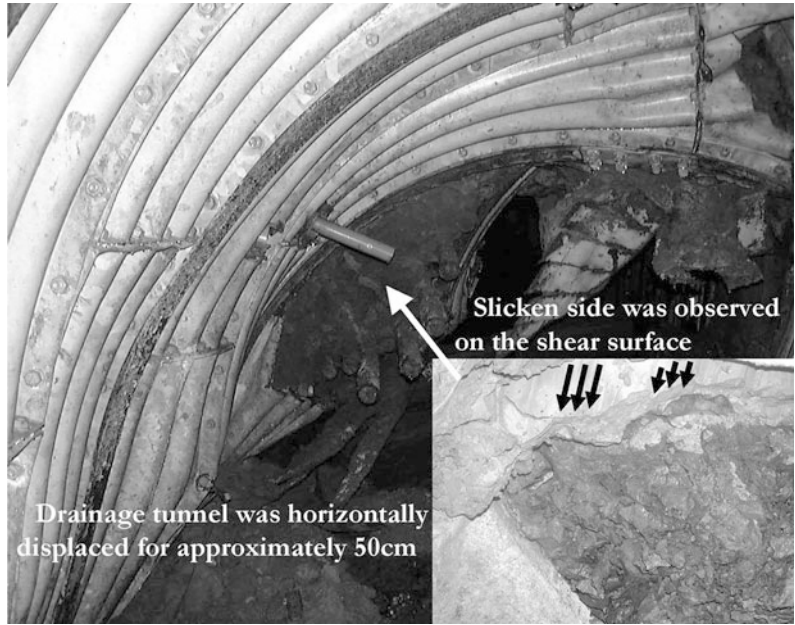
Fig. 32.5 The geology bird's-eye view of Wamisawa landslide
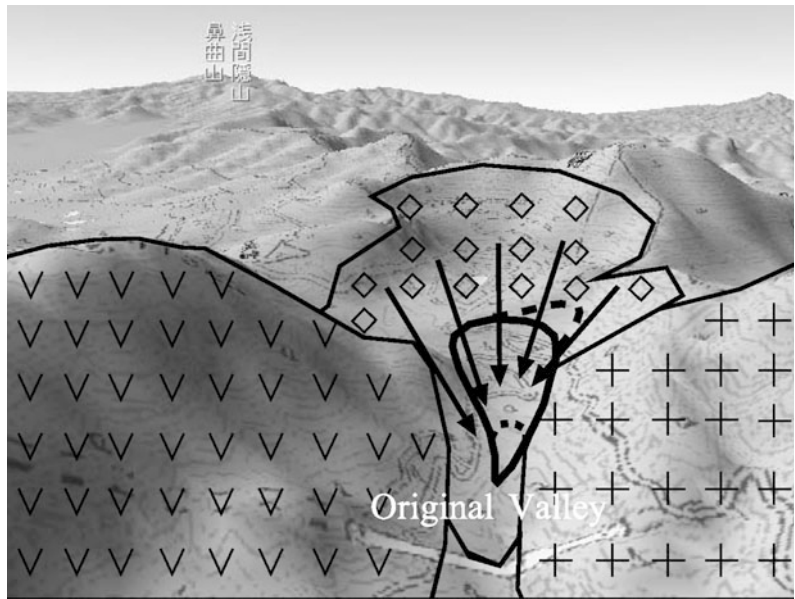
Fig. 32.6 The geologic
cross section of Wamisawa
landslide
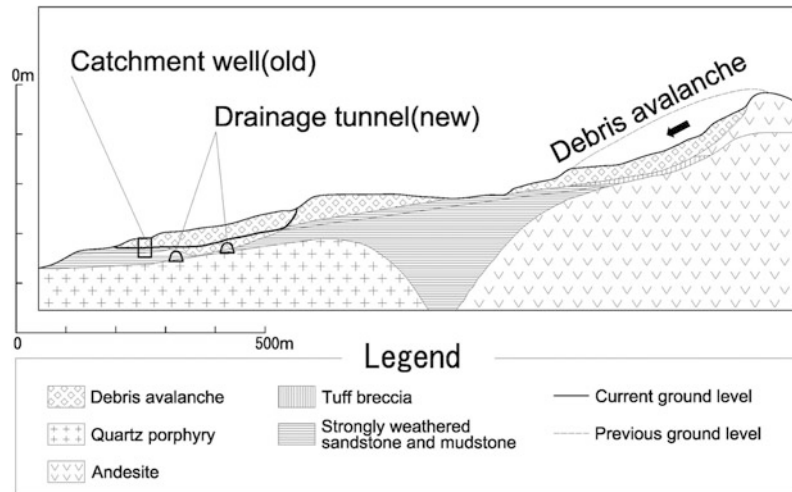
3.2 Failure Mechanism of Wamisawa Landslide

The Wamisawa landslide material is largely composed of Miocene sandstone and mudstone with discordant dykes of Andesite and quartz-porphyry. Filling spaces between the intrusive rock bodies are debris avalanche deposits from Mt. Atago. The deposited debris moved downward through the confinement formed by igneous rock intrusion, and, as a result, flat terrain was formed at the upper part of the landslide. This permeable debris avalanche deposits forming a flat terrain allows rainfall to easily infiltrate underground contributing to the rise of the groundwater level.

This landslide is located in the slope of the flat terrain outer edge with slope length of 350 m and width of 150 m. A narrow valley was formed due to intrusive rocks in the area. High permeability and unconsolidated nature of debris avalanche deposits enhanced easy infiltration of surface water which inadvertently caused groundwater level to rise in the deposits layer. The rise in groundwater level reduced the shear resistance of the sediments. Consequently, a slip surface was formed at the base of the debris avalanche deposit which caused the slope to fail (Figs. 32.5, 32.6).

Strain gauges installed in the slopes recorded displacement values of 10,000 $\mu\varepsilon$. In contrast, result from surface measurements recorded only 10 cm for the Wamisawa landslide. This result is relatively smaller than values obtained from the Sugo landslide.

3.3 Hydrogeological Disparity Between Sugo Landslide and Wamisawa Landslide

As mentioned above, the Sugo landslide and the Wamisawa landslide share some geological similarities. Nonetheless, significant difference between the two landslides is due to the existence of an intrusive rock within the underlying sediment; the source and nature of groundwater influx; and the motion mechanism of the landslides (Table 32.1).

4 Geotechnical Remediation

Several hazard mitigation and prevention works have been carried out on the landslides, depending on the nature of the landslides. Initially, landslide stabilization was carried out by installing drainage tunnel and channels to control groundwater increase. Other necessary remediation works have been added depending on subsequent stability or degree of movement. Designs and specifications of the drainage works

Table 32.1 Difference between Sugo landslide and Wamisawa landslide

Landslide Name		Slide surface	Source of the groundwater	Groundwater	The amount level of movements
Sugo landslide	Upper block	The deep-seated slide in mudstone and tuff breccia	Intrusive rock	Deep-seated groundwater in tuff breccia	Small–Middle Drainage tunnel was cut
	Lower block	The shallow-seated slide of the mudflow deposit in debris avalanche	Upper block	Shallow-seated groundwater in a mudflow deposit	Large–Middle Several meters movement per year
Wamisawa landslide		The deep-seated slide at the bottom of the debris avalanche deposits	Debris avalanche deposits of the upper part	Deep-seated groundwater in the debris avalanche deposits	Small A total of 10 cm or less

were selected according to the differences in hydrogeological nature of the materials.

4.1 Groundwater Drainage Works of Sugo Landslide

In the Sugo landslide, geotechnical stabilization was preferentially carried out on the lower block because the stability of the upper block was relatively dependent on the activities of the lower part.

On the lower block, large groundwater interceptor drain was installed to control groundwater influx since groundwater from the upper block caused the slope to fail. This countermeasure helped divide the two active blocks by cutting the supply of subsurface groundwater from the upper block to the lower block by draining excess groundwater.

Within the upper block, as mentioned above, drainage tunnel installed in the narrow gully was damaged by the slip surface. To prevent the slip surface from expanding, another drainage tunnel was installed at the upper part of the block which helped stabilize the slope.

4.2 Groundwater Drainage Works of Wamisawa Landslide

The Wamisawa landslide was triggered by steady rise in groundwater level within the debris avalanche deposits; increase in groundwater level was affected by steady influx from the narrow valley. Continuous influx into the permeable debris avalanche deposits caused excess water within the deposits layer.

At first, remedial work was carried out by constructing a catchment well within the narrow valley. However, it was observed that water influx into the catchment well was greater than its discharge capacity. This was controlled by adding two more drainage wells which stabilized the slope (Photo 32.2).

Photo 32.2 The catchment state in the drainage tunnel
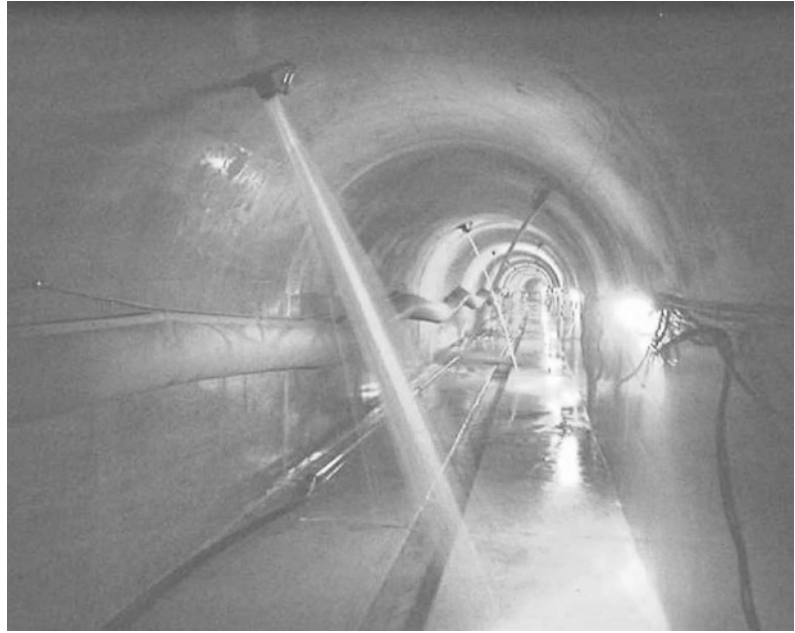
5   Summary

In this paper, failure mechanisms of two adjoining landslides in the western part of Gunma Prefecture were studied and preventive measures applied to stabilize the slopes were analyzed.

The geomorphology of the two landslides show a bottleneck-shaped structure affected by an intrusive rock that cuts discordantly into overlying Neogene sedimentary strata forming walls on both sides. Field investigations, monitoring data and topographic maps analyses show that the landslides were triggered by excess groundwater trapped in the bottleneck-shaped structural feature.

Moreover, structural patterns of the two landslides are similar. Field investigations revealed that the contact between debris avalanche deposits (spaces between the intrusive outcrops were filled by debris avalanche sediment), and intrusive igneous rock bodies is the slip surface.

In contrast to their similar structural features, they share different hydrogeological network and failure mechanism.

Geotechnical remediation works (drainage pipe installation) carried out on the two landslide sites were done considering these differences.

Geotechnical stabilization works on the Sugo and Wamisawa landslides were completed in 2009 and 2010 respectively.

6   Conclusion

Landslides, slope failures and associated disasters in Gunma Prefecture are affected by highly complicated geological nature of the area. The nature of the terrain has initiated various slope failure mechanisms and structural styles for different landslide site.

Furthermore, triggering factors of the slope failures and landslides in Gunma Prefecture are not limited to rainfall or snow-melting. It should be noted that the recent earthquake-triggered landslide which has attracted wide attention. Gunma Prefecture has many active volcanoes. The interplay between volcanic activity and earthquake has contributed to the complex structure of Gunma Prefecture, thus increasing risk of slope failure, landslides and associated natural hazards. Because the public spending has been reduced, we need counter measures that are both efficient as well as effective.

To effectively implement geotechnical remediation and stabilization works on landslides, it is necessary to understand the hydrogeological network and motion mechanisms of the landslide for every site. This can be achieved by conducting field investigations, topographic and geotechnical analyses in order to properly evaluate and assess the landslides. Furthermore, the result obtained from the evaluation should be used in hazard prevention and mitigation.

References

Gunma Prefecture Committee for Geological Mapping (1999) Gumma Prefecture Geological Map, 1:100,000

Kanto Branch of Japanese Geotechnical Society (2007) Ground of Gunma: from the investigation to design and construction

Case Study on Heavy Rainfall-Induced Reactivation of Seismically Disturbed Slope Caused by the 2011 off the Pacific Coast of Tohoku Earthquake

33

Yoshimi Usui, Hiroshi Shimada, Hiroyuki Innami, Kiyoshi Amao, Koji Higashi and Hideki Kawabata

Abstract

The stability of slopes that have developed cracks because of strong seismic activity is thought to be vulnerable to rainfall as their soil strength is reduced. Nonetheless, it is difficult and technically challenging to estimate such risk. This paper attempts to offer insights into this problem by presenting a case in which a seismically struck slope failed after intense rainfall. The Kuragasaki district of Sakura City, Tochigi Prefecture (Fig. 33.1), is situated on a 70-m-high terrace cliff, where Pliocene sediments are overlain by unconsolidated pyroclastic flow deposits and volcanic ash soil. On March 11, 2011, the date of the off the Pacific coast of Tohoku Earthquake, significant cracks and vertical drops appeared, which extended to approximately 600 m along the edge of the terrace cliff. Six months after the earthquake, the cracks extended further because of intense rainfall, which led to extensive slope failure, discharging 10,000 m^3 of debris downslope. The cause of the failure is

Y. Usui (✉) · H. Shimada
Yaita Public Works Office Tochigi Prefectural
Government, Yaita, Japan
e-mail: usuiy02@pref.tochigi.lg.jp

H. Shimada
e-mail: shimadah01@pref.tochigi.lg.jp

H. Innami · K. Amao
Sabo and Water Resources Division Tochigi
Prefectural Government, Tochigi, Japan
e-mail: innamih01@pref.tochigi.lg.jp

K. Amao
e-mail: amaok01@pref.tochigi.lg.jp

K. Higashi · H. Kawabata
Japan Conservation Engineers and Co.,Ltd, Saitama,
Japan
e-mail: higashi@jce.co.jp

H. Kawabata
e-mail: kawabata@jce.co.jp

thought to be a combination of factors and events. First, the impermeable pyroclastic flow deposits were fractured by the shaking. Second, the intense rainfall, which had infiltrated the ground, accumulated above the pyroclastic layer. Finally, the pore water pressure increased within the fracture zone, which eventually led the slope to fail.

Keywords

Earthquake · Slope stability · Pyroclastic flow deposits · Volcanic ash soil

1 Introduction

The study area is located in Tochigi Prefecture in a rift valley between mountains on the east and west sides. The bedrock of the rift valley consists of Pliocene sediments with overlying Quaternary volcanic deposits as well as gravels. Located on a large terrace cliff, the slope is 70 m high and has a 45° gradient. In contrast, the Pleistocene gravel layer overlain by unconsolidated pyroclastic flow and volcanic ash deposits is horizontal. The pyroclastic deposits are 200,000–300,000 years old, whereas the volcanic ash deposits are approximately 10,000 years old (Suzuki 2000) (Fig. 33.1).

2 Seismic Activity and Slope Displacement

2.1 Earthquake and Weather Conditions

The 2011 off the Pacific coast of Tohoku Earthquake with a recorded magnitude of 9.0, occurred at 14:46:18 on March 11, 2011 off the coast of the Ojika Penninsula and 25 km below sea level. The focal region of the seismic activity included the coastline from Iwate to Ibaraki, which extended to 500 km in the north–south direction and 200 km in the east–west direction. Within the Tochigi area, the rift valley experienced seismic intensity of 5 upper to 6 upper in JMA scale, where the volcanic deposits and gravel layers were selectively well shook (Fig. 33.2). The maximum acceleration of the seismic ground motions was 436 Gal, whereas the maximum horizontal acceleration value was 378 Gal and the maximum vertical acceleration value was 376 Gal (K-NET: TCG006 Ogawa Fig. 33.3).

In terms of weather at the time of the earthquake, the registered precipitation was 42 mm on February 18, 20 days prior to March 11, and 11 mm on March 7. Nonetheless, these two rainfall events are believed to have contributed little to the condition of the slope.

2.2 Slope Displacement

The seismic activity caused the development of cracks and vertical drops up to 1.6 m along the edge of the terrace cliff extending to 600 m. Nonetheless, no slope failure or extrusion occurred (Photo 33.1).

3 Slope Displacement and Intense Rainfall

3.1 Weather Conditions

Six months after the earthquake in March, a heavy rain fall associated with the typhoon No. 15 hit the Tochigi area on September 21, 2011. In the Kuragasaki district, the cumulative rainfall was 226 mm, whereas the hourly maximum rainfall was 48 mm by 21:00 on the same day (Fig. 33.4). The recorded rainfall was the second highest in the last 27 years. In addition, a level 2 earthquake struck the region two hours prior to the slope failure at 10:00 PM.
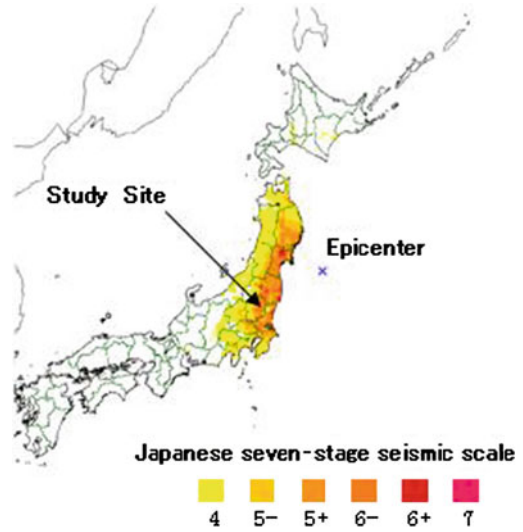
Fig. 33.2 Isoseismal map on the Japanese seismic scale (Japan Meteorological Agency)

3.2 Slope Displacement

Three hours after the rain stopped, the slope failed on the AA' line (indicated in Photo 33.2 and 33.3) at 0:45 on September 22 and the volume of the displaced debris reached 10,000 m^3. Where the debris accumulated, a residence was fully destroyed; nonetheless, no lives were lost.

We believe that the shear surface of the slope failure was created within the pyroclastic flow deposit layer (Fig. 33.5), because groundwater discharge was recognized at several locations in the layers, above the pyroclastic layer, that continued for a few days after the failure. The overlaying volcanic ash soil was dry as they had developed horizontal cracks and thus were permeable. Some of horizontal cracks were penetrated by roots. This suggests the past seismic motion triggered the formation of cracks.

Cracks had developed for 250 m near the shoulder of the terrace on the BB' cross section line since the end of August, and the intense rain brought by the typhoon induced further displacement, which resulted in a 10 cm vertical drop (Photo 33.4).
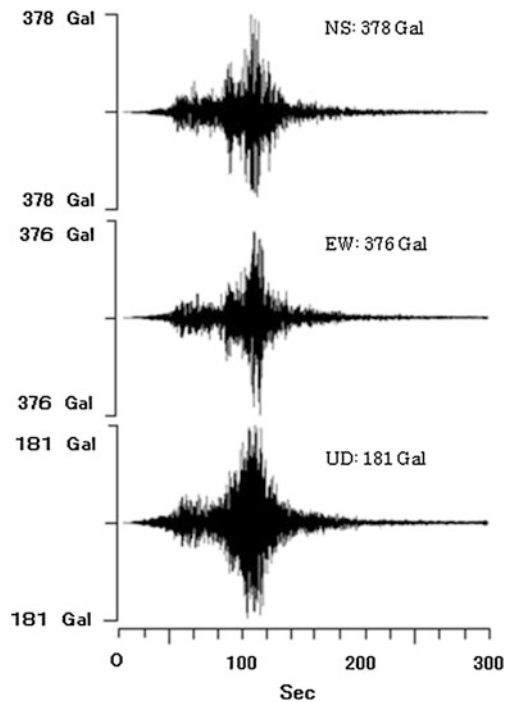
Fig. 33.3 Maximum acceleration of the seismic ground motion recorded at the time of the earthquake (K-NET:TCG006)

Photo 33.1 Slope displacement induced by the 2011 off the Pacific coast of Tohoku Earthquake (BB' cross section)

Fig. 33.4 Rainfall prior to slope failure
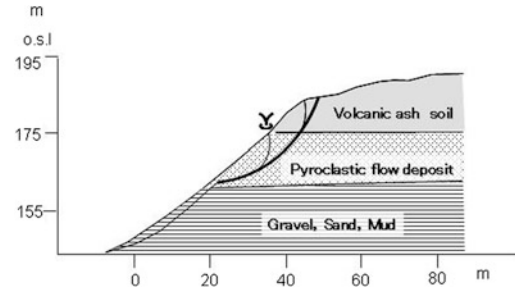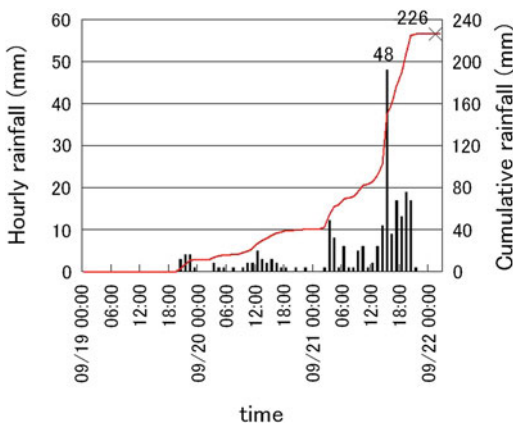
Fig. 33.5 Schematic cross section along the AA' line

Photo 33.2 Aerial photos prior to the slope failure **a** Photo taken in March, 2011 **b** Photo taken in October, 2011
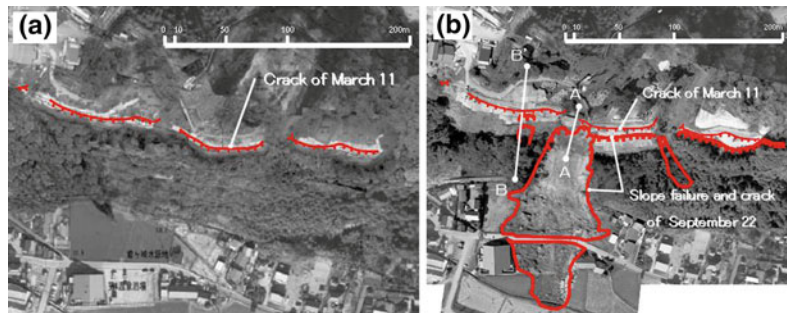
Photo 33.3 Displaced slope (AA' cross section) **a** Volcanic ash deposits, **b** Pyroclastic debris deposits, **c** unconsolidated gravels arrows: outlets of groundwater discharge (springs)

Photo 33.4 Vertical drops appeared on the BB' cross section

3.3 Field Data Analysis

(1) Groundwater analysis

Figure 33.6 shows the groundwater electrical resistivity values recorded at BV-3 on the BB' cross-section line.

According to Fig. 33.6, the groundwater table is shown approximately above the pyroclastic flow deposits on the basis of significant recovery of the resistivity values. Furthermore, additional recovery of the resistivity was recorded a few meters below. As groundwater permeated through the volcanic ash soil with the well-developed horizontal cracks, it reached the top surface of the highly impermeable pyroclastic flow deposit on which groundwater accumulated.
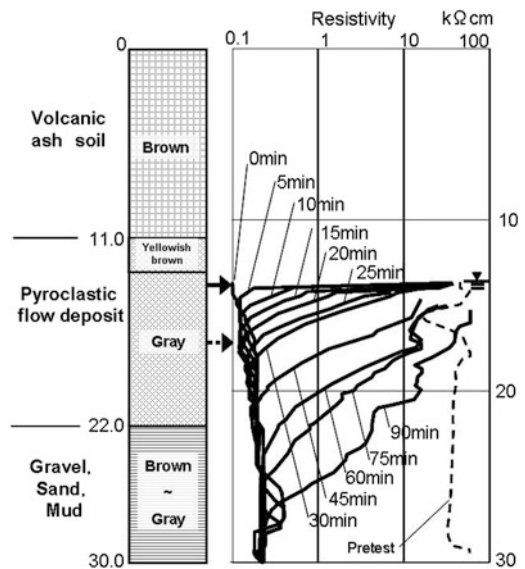
Fig. 33.6 Groundwater analysis diagram (BV-3) Pretest: Electrical resistivity of groundwater before adding sodium chloride/0 min: Resistivity of groundwater after adding sodium chloride

Furthermore, groundwater was estimated to exist in the horizontally developed cracks within the pyroclastic layer.

(2) Strain-Gauge-Type Inclinometer Measurement

Strain-gauge-type inclinometers installed in the BV-3 and BV-4 indicated strain increase upslope and decrease downslope (Fig. 33.7). In addition, the amount of strain was less than 500 μ which was relatively small. Hence, we
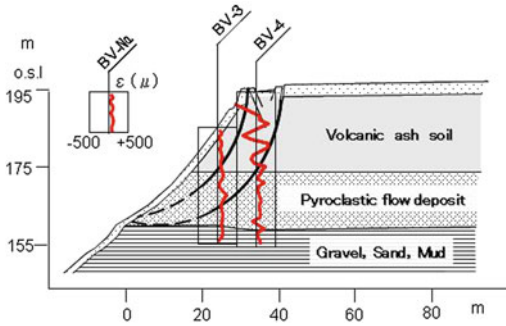
Fig. 33.7 Strain gauge analysis (BB' cross section) The cumulative distribution of strain was recorded from April to December 2011
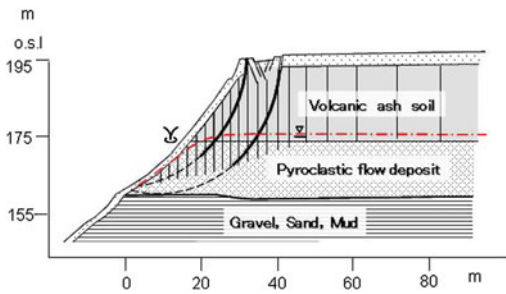
Fig. 33.8 Schematic of the slope failure mechanism (BB' cross section)

Table 33.1 Results of the soil property tests

Material	Volcanic ash soil	Pyroclastic flow deposit
Specific gravity of soil particle (Gs)	2.694	2.646
Natural water content Wn (%)	91.4	67.7
Particle size distribution		
Gravel (%)	0	1
Sand (%)	20	19
Silt (%)	35	51
Clay (%)	45	29
Liquid limit WL	112.6	61.0
Plastic limit Wp	50.1	36.9
Wet density Pt (gcm^3)	1.30–1.38	1.59–1.60
Saturation Sr (%)	83–94	97–100

Table 33.2 Results of the direct shear tests (consolidated drained)

Material	Y(kN/m^3)	c'(kPa)	ϕ'(°)
Volcanic ash soil	14	50	30
Pyroclastic flow deposit	16	50	20

Table 33.3 Results of the slope stability analysis

Cross section	Fs	Pyroclastic Flow deposit	
		c'(kPa)	ϕ'(°)
AA'	0.95	12	20
BB'	1.00	33	20

believe that the upper layers loosened as the fracture zone developed, whereas the lower layers are yet to develop a fracture zone and thus registered minimal strains (Table 33.1).

(3) Stability Analysis

We used the modified Fellenius' method to conduct stability analysis on the failed AA' and BB' cross sections. Since the fracture zone developed within the pyroclastic layer, we used inverse calculations to obtain a cohesion value by assuming the safety factor at the time of the rainfall event. The average cohesion value of the pyroclastic layer was between 12.0 and 32.9 kPa (Table 33.3), which was below the cohesion value of 50 kPa of the nonfracture zone obtained from direct shear tests (Table 33.2). This suggests that the average cohesion of the pyroclastic layer decreased as the fracture zone developed because of the 2011 off the Pacific coast of Tohoku Earthquake (Table 33.3).

4　Slope Failure Mechanism

On the basis of field investigations and the analysis results, the slope failure mechanism is described below (Fig. 33.8).

4.1   Contributing Factors

(1) Terrain is easy to amplify ground motion

A large terrace cliff had developed in the area, which is 70 m high with a 45° gradient.

(2) Geology is easily fractured

The geology of the area is characterized by a Pleistocene gravel layer overlain by unconsolidated pyroclastic flow and volcanic ash soil with horizontal layering.

(3) Geological structure is prone to develop groundwater aquifers

The volcanic ash soil is highly permeable because of well-developed horizontal cracks, whereas the pyroclastic flow deposits are little permeable, and groundwater accumulates above the pyroclastic layer when it rains.

(4) Fracture zone developed by the earthquake

The slope partially lost stability when the 2011 off the Pacific coast of Tohoku Earthquake occurred and a fracture zone developed on the terrace cliff, which appeared as cracks on the terrace surface. Although the displacement amounted to 1.6 m at the head, it did not result in extrusion at the foot. As a result, the slope did not fail even though the slope was steep.

4.2   Trigger factors

(1) Groundwater accumulated by the intense rainfall.

Groundwater accumulated above the pyroclastic flow deposits as the intense rainfall brought by the typhoon infiltrated the ground.

(2) Groundwater influx to the fracture zone.

Groundwater influx to the fracture zone within the pyroclastic layer led to increase in pore water pressure, which subsequently weakened the foundation strength. As a result, the destabilized slope failed.

5   Issues

In this case, a strong earthquake fractured the impermeable pyroclastic flow deposits, while groundwater from the heavy rainfall accumulated above the layer. These two processes coincided and this eventually led to slope failure as the pore pressure increased. This case raises some important issues, which are discussed below.

(1) Slope stability evaluation after earthquake

If a fracture zone developed by the earthquake experiences rain infiltration for the first time, the risk of slope failure increases. Hence, groundwater conditions and average soil strength at the time of the rainfall need to be estimated in order to properly evaluate slope stability. Since estimating groundwater conditions is difficult without field data obtained at the time of intense rainfall, reliable methods to needs to be established to obtain field data and analyze.

Meanwhile, the saturation of the slope materials and groundwater influx, as well as the soil strength of the fracture zone, may be unknown before an earthquake strikes. In that case, the slope movement and groundwater influx should be monitored to detect potential sliding trends to facilitate decision making, while interested personnel should continue to be on alert.

(2) Expansion of the fracture zone after earthquake

Although the fracture zone is estimated not to have developed at the foot of the slope, it was extensively developed at the head because of the earthquake. In such cases, groundwater may continue to work on the fracture zone and aftershocks may expand the fracture zone downslope toward the foot. Furthermore, as the average soil strength gradually decreases, the risk of slope failure increases. Hence, slopes require special attention after seismic activity and the decrease in soil strength should be considered in the design of countermeasures.

Reference

Suzuki T (ed) (2000) Nihon no chikei 4 (Topography of Japan 4) Kanto-Izu-Ogasawara, Tokyo University Press, p 172–183 (in Japanese)

The Characteristics of Landslides Induced by the Wenchuan Earthquake Based on High Spatial Resolution Remote Sensing Images

34

Jianqiang Zhang and Fenghuan Su

Abstract

The Ms = 8.0 Wenchuan Earthquake (May 12, 2008) induced many landslides in wide area; however, it is difficult to investigate by field work thoroughly. The remote sensing technology could extract information for large scale area very quickly, so the remote sensing images were widely used in the investigation of earthquake-induced landslides. Generally the earthquake influenced areas are very large, so the remote sensing images are mainly medium resolution images. The landslide data extracted by medium resolution images couldn't distinguish the different parts of each landslide. These data will induce big errors for the landslides topographic characteristics analysis and susceptibility assessment. The Subao river basin, Beichuan County, was taken as study area. There were many landslides induced by Wenchuan earthquake in the basin. The high resolution remote sensing images were used such as aerial images (ADS40) and WorldView images (both have a resolution of 0.5 m) to covering the whole basin. The interpretation signs for different part of landslides were built, and the generating areas of landslide were extracted. Then the topographic characteristics of landslides were analyzed.

Keywords

Wenchuan earthquake · Landslide · High resolution remote sensing

1 Introduction

Landslide is one of common maintain hazards induced by the earthquake. They always have characteristics of large numbers or scale, wide distribution. Research on distribution and characteristics of landslides triggered by earthquakes is a basic work for landslide hazard analyses, such as landslide susceptibility assessment and

J. Zhang (✉) · F. Su
Key Laboratory of Mountain Hazards and Earth Surface Process/Institute of Mountain Hazards and Environment, Chinese Academy of Sciences, Chengdu, China
e-mail: zhangjianqiang83@163.com

landslide risk assessment. The precision of landslides inventories will affect the result of landslide hazard analyses.

Because of these characteristics of earthquake-induced landslides, most of landslides inventories following moderate to large earthquakes are either incomplete or only record landslide location (Mahadavirfar et al. 2006; Qi et al. 2010). A great deal of information for landslides is not been recorded. With the development of Remote Sensing (RS) technology and Geographical Information System (GIS) technology, the inventories of landslides become more comprehensive in terms of (1) covering the entire area affected by landslides (2) including all landslides down to a size of 1–5 m in length, and (3) depicting landslides as polygons rather than dots (Cheng et al. 2004; Duman et al. 2005; Marcelino et al. 2009; Guzzetti et al. 2012; Harp et al. 2011). This type of landslide data takes more convenience for the landslide hazard analyses; some error also is brought simultaneously. The morphology of landslides is complicated. Generally, a landslide is constituted by different parts, such as main scarp, landslide body, surface of rupture and so on. Different analyses will need corresponding data. For example, the landslide susceptibility assessment does not need the data of landslide transport and deposit regions, but rather the occurrence region of landslides. So if a landslide was taken as a unity, it will take errors in the analyses. Hereinafter, the word "landslide covering area" includes not only occurrence area but also debris transported and deposited area.

The magnitude $M_w = 8.0$ earthquake in Wenchuan, China of 12 May, 2008 occurred at the east edge of Tibetan Plateau. The focal mechanism of the earthquake was successive massive rock fracturing 15 km in depth at Yingxiu (Cui et al. 2009a). It is found that the Wenchuan earthquake triggered over 56,000 landslides, with a total area of 811 km^2, over an area of about 41,750 km^2 (Dai et al. 2011). After the earthquake, lots of studies on landslide distribution and characteristics were carried out (Cui et al. 2009b; Yin et al. 2009; Huang and Li 2009; Sato and Harp 2009; Ouimet 2009; Chigira et al. 2010). Most of these studies utilized the polygons to describe landslide covering area as basic data.

Subao river basin in Beichuan county, Sichuan province, where was seriously damaged by the Wenchuan earthquake. The high spatial resolution images were utilized in the research to get the boundaries of landslides and then distinguish different parts of landslides. Base on these data, the characteristics of landslide covering areas and landslide occurrence areas were analyzed separately.

2 Study Area

The Subao River basin (Fig. 34.1), with an area of 72.76 km^2, is in the northeastern part of Beichuan County, Sichuan Province. The basin was well covered by forest and shrub before the earthquake (Fig. 34.2), and the geo-hazards were rare in this basin. The Beichuan-Yingxiu Fault (F2) passes through the eastern part of the basin, heavily damaged by the earthquake. The study area is under a humid subtropical monsoon climate, which is warm and wet. The mean annual temperature is 15.6 °C. The mean annual precipitation is 1399.1 mm, and the maximum annual precipitation was 2340 mm (1967). The maximum daily precipitation was 101 mm, and the Maximum hourly precipitation was 42 mm. The rainfall concentrates between June and September, which account for 70–90 % of the annual precipitation (the maximum percentage appeared in 1981).

The geologic age of the bedrock in the study area ranges from Cambrian to Carboniferous, including Early Cambrian ($\in$1), Middle Ordovician (O2), Middle Silurian (S2), Early Devonian (D1), Middle Devonian (D2), Late Devonian
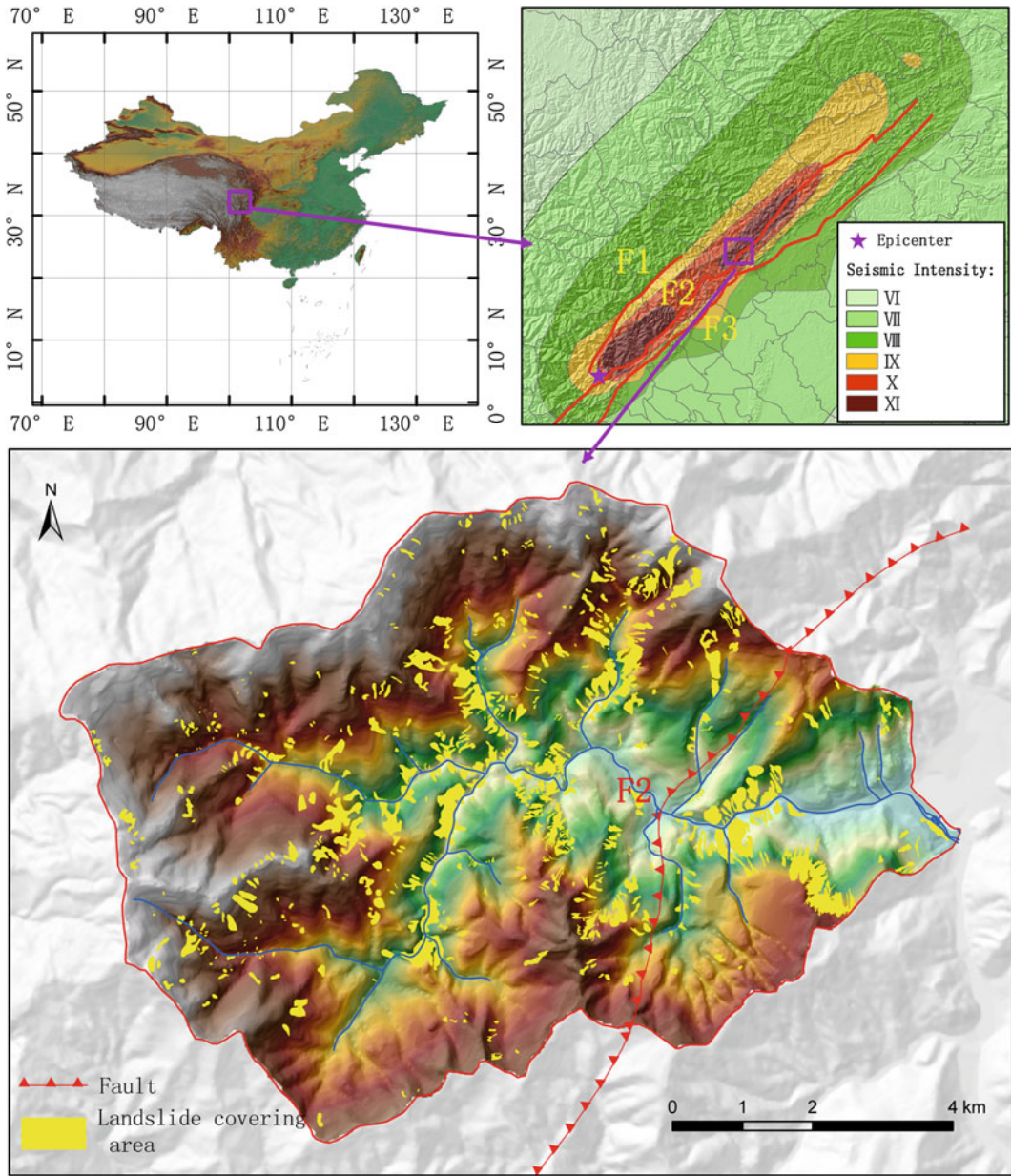
Fig. 34.1 Location map of the Subao River basin

(D3), Early Carboniferous (C1), and some Quaternary (Q) deposits near the outlet of the basin.

Dolomite, siltstone, sandstone, phyllite, dolomitic limestone and shale all outcrop along the Longmenshan fault in the study area, with different rock assemblages classified into 8 types:

Dolomite and dolomitic limestone (P), siltite and quartz sandstone (S), limestone intercalated with phyllite, sandstone (LS), marlite and limestone (ML), phyllite intercalated with limestone (PL), limestone, shale and sandtone (LSS), shale and sandstone (SS), gravel sand and siltite (GS).
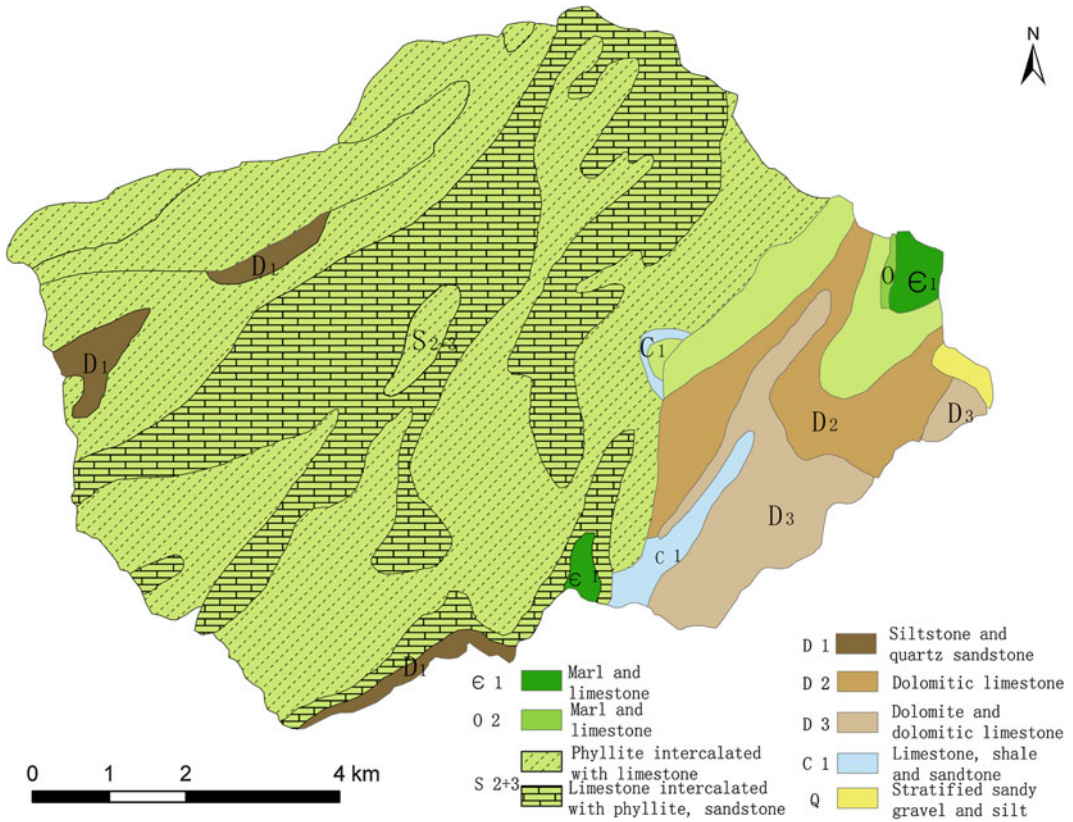
Fig. 34.2 Geological map of Subao River basin

Table 34.1 Remote sensing images used in Subao River basin

	Spatial Resolution (m)	Date	Type
ADS40 aerial images	0.5	2008-6	True color
WorldView images	0.5	2008-12-12	Black-and-white

3 Remote Sensing Images Processing and Information Extraction

3.1 Remote Sensing Images

Two types of remote sensing images were utilized in this study, ADS40 aerial images and WorldView images (Table 34.1). Both of them have a 0.5 m in spatial resolution. The ADS 40 arial images are true color images and the WorldView images are black and white image. All of these images covered the whole basin.

3.2 Landslide Interpretation Keys

Hue and Brightness

The ADS40 images have colors corresponding with the surface of the earth. The landslides show yellow or white colors. The vegetations grew well before the Wenchuan earthquake, so the landslides easy to be recognized. In the images of WorldView, landslides were interpreted mainly through brightness. Landslides covering areas were much brighter than vegetation areas. And inside the landsides, the areas of landslide occurence areas were brighter than the deposit areas.

Fig. 34.3 Different type of landslides in the ADS40 image: **a** rock slide; **b** rock valanche; **c** rock slump
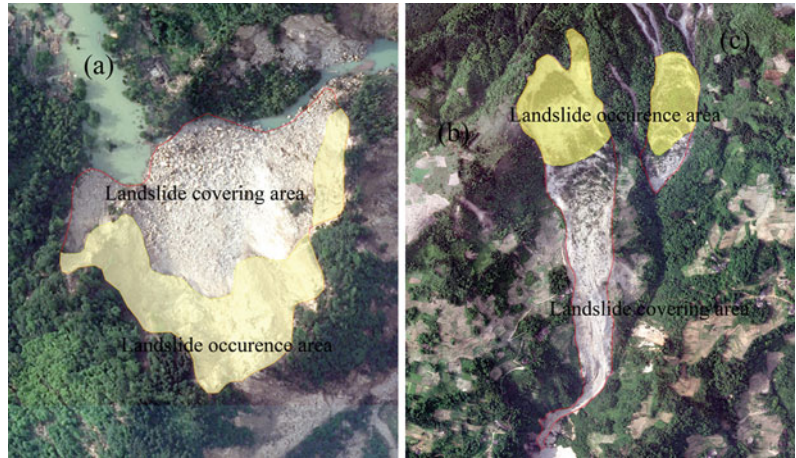
Texture

The grain compositions were different in each part of landslides. Generally speaking, in landslides occurrence areas are bed rock without big stones,so the regions had single color without textures in the remote sensing images. But in the deposit areas of landslides, especially for the rock slide, the landslide bodies cracked into many blocks of stones. In the remote sensing images, the deposit areas of landslides showed some regular textures.

Topography

Characteristics of topography could be take the as reference to distinguish the landslide covering areas and landslide occurrence areas. The areas of landslide occurrence located in the upside of slopes where were steep, and the areas of landslide deposit located at the foot of slopes, in the gullies or rivers, or gentle regions. These characteristics could check the result of interpretation.

3.3   Landslide Types

Rock fall (Fig. 34.3a) was the main type of landslide in Subao river basin. The landslide bodies were highly disrupted and deposit at the foot of hill. The quantity of rock slumps (Fig. 34.3c) was less. Landslide bodies of these landslides moved down along the surface of rupture and not disrupted. Vegetations in part of landslide bodies kept well. The boundaries of occurrence area were corresponding with the landslide bodies. A rock avalanche (Fig. 34.3b) was occurred in study area. Form the ADS40 image, the long transport region and deposit region could be extracted.

About 530 landslides comprise an area of about 696 ha, accounting for 9.57 % of the entire basin (Fig. 34.4). Landslides occurrence area was 294.53 ha. The area of the smallest landslides in the basin was 187 m^2, and the area of the largest landslides was more than 45 ha.

4   Characteristics Analyses of Landslides

4.1   Landslides Covering Area and Landslides Occurrence Area with Topography

Elevation was a basic factor for analyzing the spatial distribution of landslides. The DEM data with 25×25 m grid was utilized in this study. Figure 34.5a shows the landslides covering area and landslides occurrence area at different elevations. It was observed that, landslides covering areas concentrated in the zones with elevation of 1000–1250 m and 1250–1500 m, and in these regions, the landslide covering area density were very high. Both of the percentages were greater than 2 %. The landslides
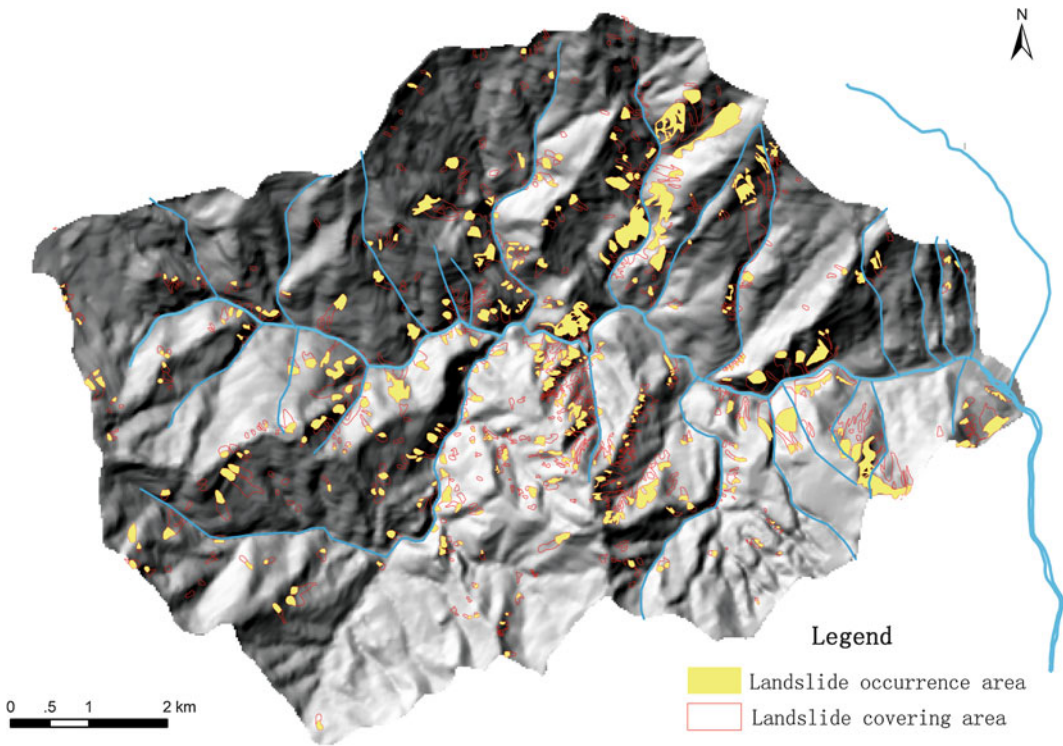
Fig. 34.4 Landslide inventory map for Subao river basin

occurrence areas in these regions were very big. In regions with elevation of 750–1000 m, 1000–1250 m, and 1250–1500 m, the areas of landslide covering area were much greater than landslide occurrence areas. It could be get that landslide deposit areas were located in these areas, especially in the regions with elevation of 750–1000 m, 1000–1250 m.

The units for slope aspect were much bigger than landslides, the differences between landslide covering areas and landslide occurrence areas were not significant (Fig. 34.5b). In the aspect of Northeast, east, southeast and south, the areas of landslide covering and landslide occurrence were major large. Landslide area densities in north aspect slopes with the 4 type of aspect slopes aforementioned were much larger. But characteristics of landslide occurrence area density with aspect were not significant, may because the study area was too small and too close to the active faults.

Slope angle was a very important factor for affecting the landslides induced by earthquake. Slope angle was calculated form the DEM, and the slope map was constructed intervals of 10°, then mean slopes of landslide area were calculated (Fig. 34.5c). It was observed that, landslide covering areas concentrated in the regions with slope of 20–30°, 30–40° and 40–50°, so did the landslide occurrence areas. But the landslide area density was rather different from the landslide area. The plot showed that the percentages of landslide covering areas and occurrence areas were increased with the slope degree. So it could be got that, the susceptibility of landslide increasing with slope degree.

Earth's surface curvature, a factor describing the degree of distortion of any point on the Earth's surface, has two vectors–the profile curvature and the plan curvature respectively, in the vertical direction and the horizontal direction. The profile curvature is in the down-slope direction along a

Fig. 34.5 Area and area density of landslide covering area (C) and landslide occurrence area (O): **a** Elevation **b** Slope aspect **c** Slope degree **d** Curvature **e** Lithology. Lithology is classified as: Dolomite and dolomitic limestone (P), siltite and quartz sandstone (S), limestone intercalated with phyllite, sandstone (LS), marlite and limestone (ML), phyllite intercalated with limestone (PL), limestone, shale and sandstone (LSS), shale and sandstone (SS), gravel sand and siltite (GS)
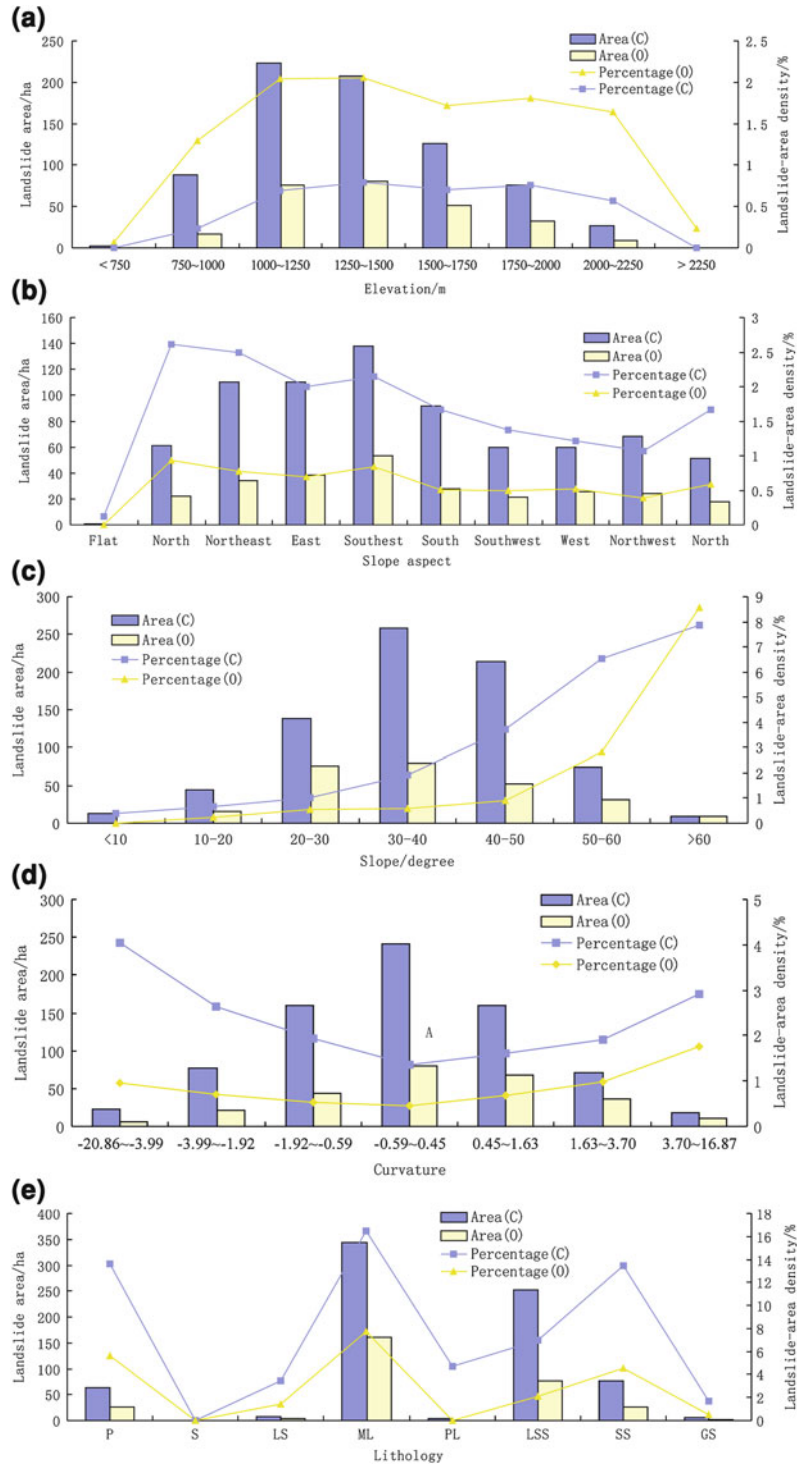
line formed by the intersection of an imaginary vertical plane with the ground surface. The plan curvature is the curvature of the topographic contours or the curvature of a line formed by the intersection of an imaginary horizontal plane with the ground surface (Ohlmacher 2007).The equations of curvature are:

$$K = \frac{f_{xx} \cos^2 \beta + 2f_{xy} \cos \beta \sin \beta + f_{yy} \sin^2 \beta}{\cos \varphi \sqrt{q}}$$

where: $q = f_x^2 + f_y^2 + 1$, $f_x = \partial f / \partial x$, $f_y = \partial f / \partial y$, $f_{xx} = \partial^2 f / \partial^2 x$, $f_{yy} = \partial^2 f / \partial y^2$, $f_{xy} = \partial^2 f / \partial x \partial y$.

where β is the angle between the tangent of the curve and the x-axis in the horizontal plane and φ is the Earth's surface curvature. When it is a positive value, the slope plane is convex in shape, i.e., the larger the curvature, the more concave it will be; when the curvature is equal to zero, the slope plane is flat; when the curvature is a negative value, the slope plane is concave in shape, i.e., the smaller the curvature, the more concave the slope. The values of curvature were calculated from the DEM data.

Form Fig. 34.5d which could be got that, landslides induce by Wenchuan earthquake in Subao river basin, mostly located in the concave slopes with curvature value great than −1.92, and in the convex slopes with curvatures value small than 1.63. Different with the landslide area, the plots of landslide area density showed that the convex slopes with higher curvature value and the concave slopes with lower curvature value were more prone to earthquake triggered landslide. For landslides covering area density, the percentage was larger in concave than in convex regions, but for landslides occurrence area density, the percentage in concave regions was much smaller than in convex regions. Landslides occurred in the convex slopes, and the landslide bodies transported along the slope and accumulated in the concave regions like foot of hill and gully. So if the landslide covering area density with curvature was taken as a factor for landslide susceptibility assessment, errors will be brought in.

4.2 Landslides Covering Area and Landslides Occurrence Area with Lithology

There are eight major geologic units in the geologic map (Fig. 34.2). Figure 34.5e shows the landslides area and landslide area density in different geological units. Because of the geologic units much bigger than the topographic units, the differences between landslides covering areas with landslide occurrence areas were relatively small. Most of landslides located in the units of marlite and limestone, limestone, shale and sandstone. From the landslide area density plots, it could be got those three geologic units: the Dolomite and dolomitic limestone, marlite and limestone, shale and sandstone had higher percentage of landslides. These rock were generally hard, but the surface and near-surface rock mass was fragmented. Slopes that were composed of these rocks were typically steep and prone to landslides (Chigira et al. 2010; Dai et al. 2011).

5 Conclusions

Inventories to landslides induced by earthquakes become more detailed and comprehensive. They allow us to advance landslide hazard analysis in the area where the earthquake occurred. To meet different requirement of landslide hazard analysis, different levels of landslide inventories should be acquired by using new technologies and methodologies. In this paper, the Subao river basin, where the active fault of Longmenshan faults pass through, was taken as study area. The high spatial resolution images, which contain ADS40 aerial images and WorldView images with 0.5 m spatial resolution, were utilized to distinguish the occurrence areas and accumulated areas, besides the boundary of landslides covering areas. About 530 landslides comprise an area of about 696 ha, accounting for 9.57 % of the entire basin. The landslides occurrence area was 294.53 ha.

The characteristics of two parts of landslides: landslide covering areas and landslides occurrence areas were analyzed and contrasted by utilizing area and area density. Factors of elevation, slope aspect, slope degree, curvature and lithology were analyzed. Generally speaking, the landslide area density was more appropriate than landslide covering area to explain the susceptibility. Some of the factors, like elevation, slope aspect and lithology, the plots of landslide area densities were corresponding with landslide areas. But the factors of slope degree and curvature, the characteristics of landslides area density and landslide area were much different.

To some landslide hazards analysis, like susceptibility assessment, landslide inventory should be used landslide occurrence areas rather than landslide covering areas. The characteristics of topographic factors in landslide occurrence areas were different from the landslide covering areas, especially for the curvature factor. For landslides covering area density, the percentage was larger in concave than in convex regions, but for landslides occurrence area density, the percentage in concave regions was much smaller than in convex regions.

Generally speaking, the earthquake induced landslides were distributed widely, so it was too expensive to use high spatial resolution images to do the landslides inventory. Some typical regions could be chosen to deduce characteristics of landslides in the whole area.

References

Cheng KS, Wei C, Chang SC (2004) Locating landslides using multi-temporal satellite images. Adv Space Res 33:296–301

Chigira M, Wu X, Inokuchi T, Wang G (2010) Landslides induced by the 2008 Wenchuan earthquake, Sichuan, China. Geomorphology 118:225–238

Cui P, Chen XQ, Zhu YY et al (2009a) The Wenchuan Earthquake (May 12, 2008), Sichuan Province, China, and resulting geohazards. Nat Hazards (Online First). doi:10.1007/s11069-009-9392-1

Cui P, Zhu YY, Han YS et al (2009b) The 12 May Wenchuan earthquake-induced landslide lakes: distribution and preliminary risk evaluation. Landslides 6:209–223

Dai FC, Xu C, Yao X et al (2011) Spatial distribution of landslides triggered by the 2008 Ms 8.0 Wenchuan earthquake China. J Asian Earth Sci 40:883–895

Duman TY, Can T, Emre O et al (2005) Landslide inventory of northwestern Anatolia, Turkey. Eng Geol 77:99–114

Guzzetti F, Mondini AC, Cardinali M et al (2012) Landslide inventory maps: new tools for an old problem. Earth Sci Rev 112:42–66

Harp EL, Keefer DK, Sato HP et al (2011) Landslide inventories: the essential part of seismic landslide hazard analyses. Eng Geol 122:9–21

Huang R, Li W (2009) Analysis of the geo-hazards triggered by the 12 May 2008 Wenchuan Earthquake, China. Bull Eng Geol Environ 68:363–371

Mahadavirfar MR, Solaymani S, Jafari MK (2006) Landslides triggered by the Avaj, Iran earthquake of June 22, 2002. Eng Geol 86:166–182

Marcelino EV, Formarggio AR, Maeda EE (2009) Landslide inventory using image fusion techniques in Brazil. Int J Appl Earth Obs Geoinf 11:181–191

Ohlmacher GC (2007) Plan curvature and landslide probability in regions dominated by earth flows and earth slides. Eng Geol 91(2–4):117–134

Ouimet WB (2009) Landslides associated with the May 12, 2008 Wenchuan earthquake: implications for the erosion and tectonic evolution of the Longmen Shan. Tectonophysics doi:10.1016/j.tecto.2009.09.012

Qi SW, Xu Q, Lan HX et al (2010) Spatial distribution analysis of landslides triggered by 2008.5.12 Wenchuan earthquake China. Eng Geol 116:95–108

Sato PH, Harp EL (2009) Interpretation of earthquake-induced landslides triggered by the 12 May 2008, M7.9 Wenchuan earthquake in the Beichuan area, Sichuan Province, China using satellite imagery and Google Earth. Landslides 6:153–159

Yin YP, Wang FW, Sun P (2009) Landslide hazards triggered by the 2008 Wenchuan earthquake, Sichuan, China. Landslides 6:139–152

A Case Study of Behavior Observation of Landslide Induced by Snowmelt After an Earthquake

35

Hiroomi Nakazato, Daisuke Shoda, Keisuke Inoue
and Hisato Suzuki

Abstract

The landslide movement was recognized on April 19th, 2011 in Shimizu, Tokamachi city after the earthquake of M6.7 with the epicenter in Sakae village, Nagano Prefecture, occurred on March 12th, 2011. This landslide was probably induced by the snowmelt after the earthquake. This landslide is a reactive landslide, and the bedrock of this landslide is the Pliocene mudstone. The size of this landslide block is 100 m in width, 500 m in length, and 20 m in depth. Only this landslide greatly acted though a lot of landslide blocks were distributed around this landslide. To estimate the risk for the construction work of disaster recovery, the displacement monitoring using GPS and the groundwater level observation were executed in advance. The displacements were only detected when it rained heavily. The advanced landslide monitoring system performed in this case was effective to investigate for the disaster recovery safely because participants can share remotely landslide displacement data on semi-real time.

Keywords

GPS · Displacement monitoring · Snowmelt · Earthquake · Information sharing

1 Introduction

The earthquake of M6.7 with the epicenter in Sakae village, Nagano Prefecture, occurred on March 12th, 2011, the next day when the 2011 off the Pacific coast of Tohoku Earthquake occurred. The maximum seismic intensity was 6-plus of the JMA seismic scale measured around the northern part of Nagano Prefecture, and strong tremor also raided the Chuetsu district of Niigata Prefecture. The landslide movement was recognized on April 19th, 2011 after the earthquake in Shimizu, Tokamachi city, Niigata Prefecture, Japan located 20 km away from the epicenter of this earthquake (Fig. 35.1), and the landslide moved 100 m to downward (Fig. 35.2). It is thought that snowmelt induced

H. Nakazato (✉) · D. Shoda · K. Inoue · H. Suzuki
National Agriculture and Food Research
Organization, 2-1-6 Kannondai,
Tsukuba 305-8609, Japan
e-mail: h_nakazato@affrc.go.jp

Fig. 35.1 Index map and distribution of the estimated seismic intensity of the earthquake of M6.7 occurred on March 12, 2011 (after JMA)
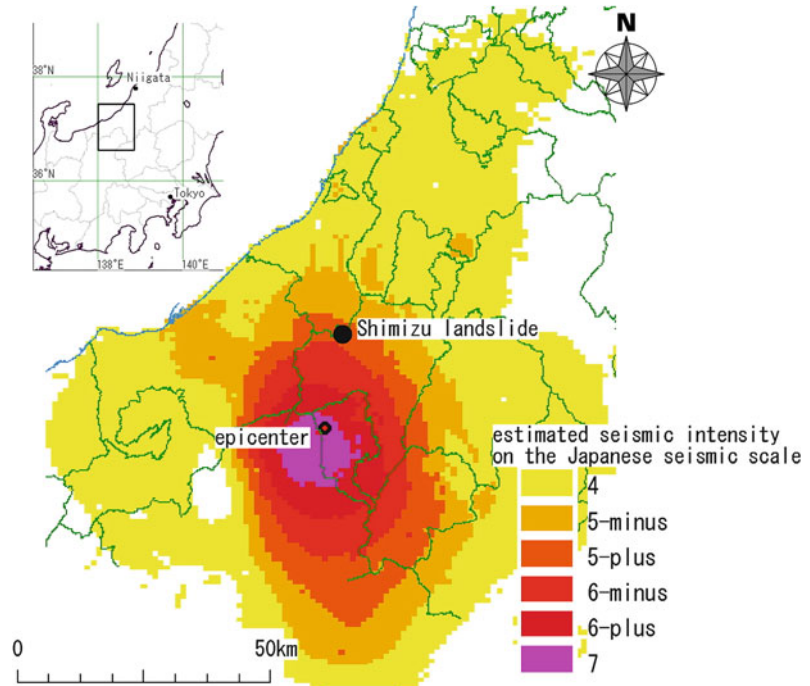
this landslide after the earthquake. In this study the authors report on a behavior of the landslide movement after snowmelt.

2 Shimizu Landslide

This landslide is formed by reactivation of an old landslide. The bedrock of landslide is the Pliocene mudstone that corresponds to the Tamugigawa Formation. The size of the landslide block is 100 m in width, 500 m in length, and 20 m in depth (Fig. 2). The landslide site is located in a heavy snow district. Due to thick snow, the state of landslide just after the earthquake was not observed. However, the significant landslide movement was detected on the 19th of April and later. Since a lot of snowmelt was produced in this term, the authors supposed that the snowmelt infiltrated the landslide block where the crack had developed by the earthquake, and then the landslide block moved. Only this landslide greatly moved though a lot of landslide blocks were distributed around this landslide. The features of this landslide activity are the following three points.

(1) The main scarp was 30 m high; and fresh bed rock was exposed on the scarp.
(2) The landslide mass traveled 100 m to downward, and the mounds, which consisted of sediment, were formed along lateral edges. These mounds resembled a form of natural levee, were probably lateral ridges of landslide.
(3) The toe of the landslide reached the opposite river side, and formed a small-sized landslide dam.

3 Landslide Behavior Observation

The landslide slope was used as a terraced paddy field and the landscape played an important role as a tourist attraction. Neither the landslide activity nor the safety of the site were confirmed though it was necessary to hurry up the disaster recovery. To estimate the risk for the investigation work of the disaster recovery, the displacement monitoring using GPS was executed from May 19th to November 5th, 2011. The groundwater level in the bore holes near the GPS observation stations
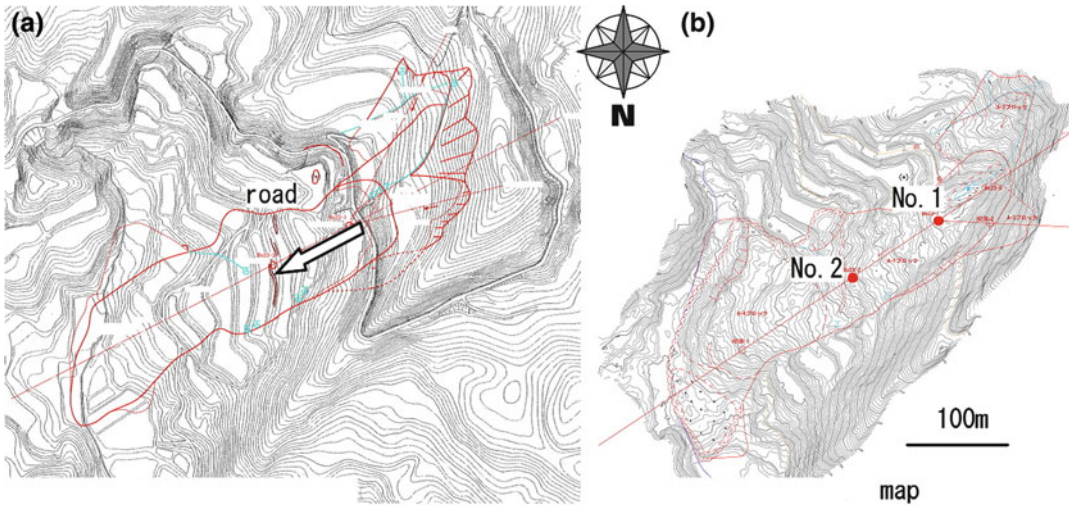
Fig. 35.2 Topographic change before and after the landslide and the location of observing station (GPS and bore-hole)

Fig. 35.3 GPS observing station

was monitored from July 11th, 2011. And, authors paid attention to the relation among the landslide displacement, the rainfall, the groundwater level fluctuation, and the aftershock.

Two GPS observation stations were set up in the landslide block (Figs. 35.2, 35.3) and one GPS fixed station was set up at immovable ground. The baselines were 519–520 m, and the horizontal error margin was ±5.5 mm. The automated

observation system was used, and it conducted by the mobile phone. The displacement data were distributed to administrative participants through the internet every 6 h (Fig. 35.4).

The GPS observation results showed rapid movement from July 30th to 31st and gradual movements from June 20th to July 10th and September 21st to 28th (Fig. 35.5). The data of displacements suggest rainfall events induced

Fig. 35.4 Block diagram
of GPS monitoring system
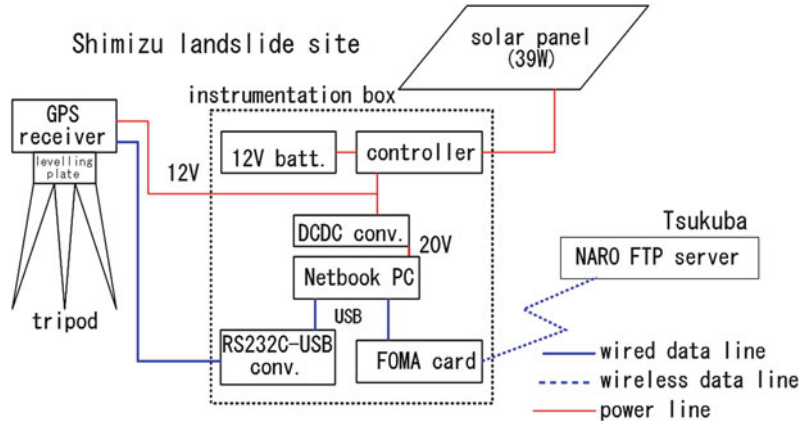
Fig. 35.5 Displacement
monitoring result
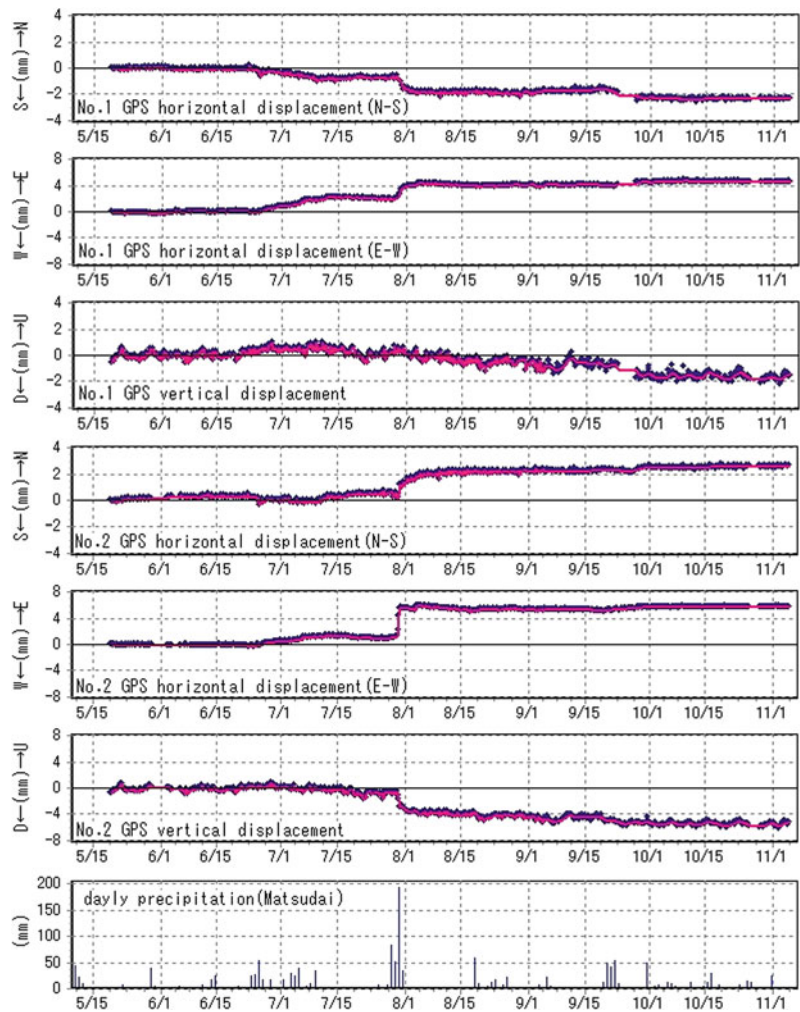
Fig. 35.6 Comparison between the horizontal displacement and the groundwater level change
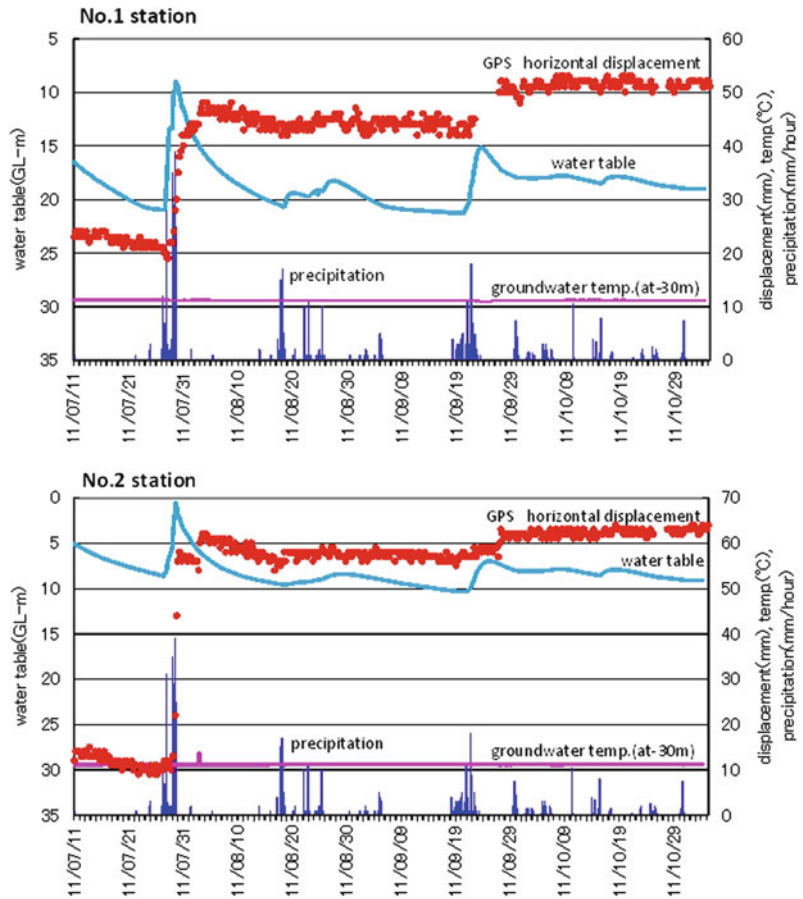
significant displacement of the landslide. In addition, the data suggest the landslide did not have plastic movement and progressive movement. Moreover, the displacement was not detected when the aftershocks of seismic intensity 3 were observed by the nearest observatory on June 2nd and October 2nd. The significant landslide movement at the end of July was due to the Niigata and Fukushima heavy rainfall disaster in July 2011. On July 29th and 30th, 244 mm of total amount of rainfall was observed at Matsudai, Tokamachi city, and the horizontal displacement increased 27 mm and the groundwater level rose of 12 m at No. 1 station, and the horizontal displacement increased 50 mm and the groundwater level rose 8 m at No. 2 station (Fig. 35.6). The measurement method to obtain such landslide movement was effective to execute the investigation for countermeasure construction safely.

4   Conclusion

The Shimizu landslide was probably induced by infiltrations of snowmelt after the big earthquake. This landslide moved significantly when it rained heavily. The displacement at one of observing station on landslide mass increased 50 mm when the heavy rainfall event of total rainfall of 244 mm occurred on July 29th and 30th, 2011. The advanced landslide monitoring system performed in this case was effective to investigate for the disaster recovery safely because participants can share remotely landslide displacement data on semi-real time.

Landslides Induced by a 7.6 Magnitude Earthquake in the Northern Part of Pakistan on October 8, 2005 and Landslide Risk Reduction Through Implementation of Non-Structural Measures

36

Yasushi Momose and Pucai Yang

Abstract

A 7.6 magnitude earthquake struck the northern part of Pakistan on October 8, 2005. Muzaffarabad city, the capital of Azad Jammu and Kashmir, located close to the epicenter, was worst affected by the earthquake. The death toll in the city and its surrounding area rose to more than 70,000. Also, many landslides were induced by the earthquake and the road network was cut, which was detrimental to the rapid recovery of the city from the earthquake damages.In addition to these landslides directly induced by the earthquake, many open cracks were observed on the slopes of the hilly areas surrounding the city and landslide risks had increased in the coming rainy season. Under these circumstances, it was necessary to take drastic measures such as execution of landslide countermeasures and realignment of existing road in the landslide-affected sections. However, these drastic measures required a lot of time and cost and it was unrealistic to treat all landslide-prone slopes in the earthquake-affected areas.The author stayed in Pakistan for more than one year in total after the earthquake as a member of the JICA Study Team, and studied the landslides that occurred during the rainy season in Muzaffarabad city. In the study, the landslide hazard was assessed based on the results of ground mapping and field data obtained from automatic rain gauges and extensometers that were installed before the rainy season. For risk reduction of landslide hazards, the JICA Study Team assisted Muzaffarabad city in establishing early warning systems by organizing the framework for landslide disaster management and installing early warning devices. Furthermore, the team conducted evacuation drills to enhance the early warning system, as well as community-based landslide hazard mitigation activities such as crack filling works of landslides. As a result of the above efforts, there were no serious accidents in the project area despite the occurrence of many small landslides and debris flows near the area. Establishment of early warning and evacuation systems was useful

Y. Momose (✉) · P. Yang
Nippon Koei Co., Ltd, Tokyo, Japan
e-mail: a4073@n-koei.co.jp

to deduce landslide hazard risks in the situation where drastic measures were difficult to be undertaken due to time and cost restrictions.

1   Introduction

The October 8, 2005 earthquake (M = 7.6) in Pakistan (USGS (2005) Home Page), in addition to the loss of more than 70,000 lives in Muzaffarabad city and its surrounding area (ERRA (2005) Home Page), triggered numerous landslides in the city and its surroundings (Fig. 36.1). These landslides, which had mostly became active after the earthquake, posed considerable hazards to the local population during rainy seasons. Landslides and associated debris flows had great potential hazards to people and property, because most of the local people are living in the earthquake-affected areas or impacted areas.

Due to this dangerous condition, it is necessary to take drastic measures such as execution of landslide countermeasures and relocation of residential houses in the impacted areas. However, these drastic measures require great time and cost. Therefore, it is indispensable to develop and implement a warning and evacuation system before the coming of the rainy season to prevent and mitigate damage to the inhabitants from landslide and debris flow hazards.

Under the above situation, landslide hazard mitigation project was carried out in "The Urgent Development Study on Rehabilitation and Reconstruction in Muzaffarabad city in the Islamic Republic of Pakistan" by JICA[1] (2006–2007). The purpose of the project was to establish a timely warning and speedy evacuation system to reduce the risk of death, injury, property loss, and damage.

---

[1] "JICA" means the Japan International Cooperation Agency, the official agency responsible for the implementation of the technical cooperation of the Government of Japan.

2   Development of Warning and Evacuation System

2.1   Establishing Disaster Management Section

For the administration authority to carry out timely warning and speedy evacuation, a Disaster Management Section (DMS) was set up in the Municipal Corporation Muzaffarabad (MCM). The DMS has full responsibility for the operation of warning and evacuation system, and its main roles are listed as follows:

- Informing about threats, hazards, and protective actions to community-based organization (CBO);
- Notifying, warning, and communicating procedures;
- Officially announcing evacuation/de-evacuation to affected family members in an emergency;
- Conducting emergency response;
- Providing shelter management and relief services; and
- Managing the warning system.

Under the DMS, four groups, namely: monitoring group, warning information group, evacuation and rescue group, and technical analysis group, were constituted as shown in Fig. 36.2.

2.2   Early Warning and Evacuation System

Based on a hazard map prepared immediately after the earthquake, the pilot project area was selected in the eastern hilly area of Muzaffarabad City. Four active landslides had been identified in the project area and people afflicted by the landslides and their associated debris flows were estimated at approximately 30,000.

Fig. 36.1 Location map

Fig. 36.2 Organizational chart of disaster management section in Muzaffarabad city (PACET and NK 2007)
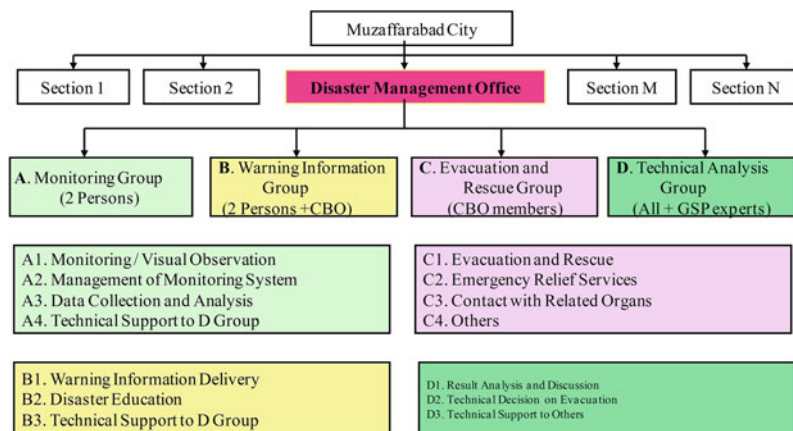
Fig. 36.3 Schematic illustration of warning system (PACET and NK 2007)
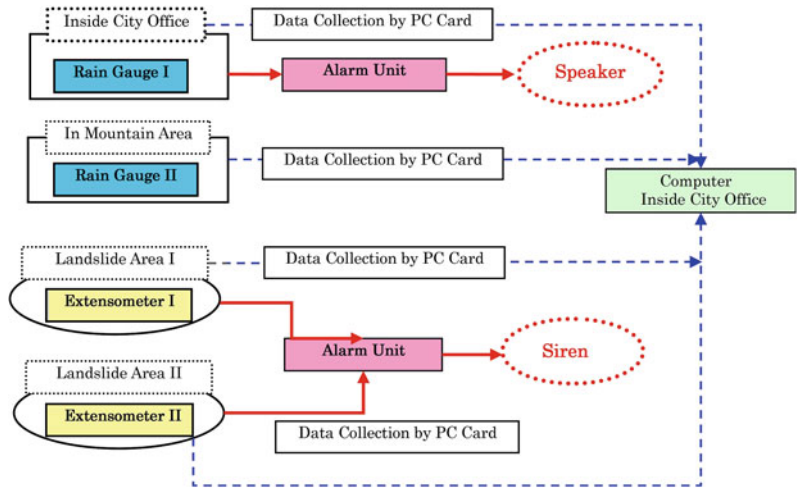
Table 36.1 Tentative standard values (PACET and NK 2007)

Warning level	Standard values	Monitoring method	Monitoring frequency
Normal	Rainfall: below 10 mm/h Extensometer: below 1 mm/h	Regular, 9:00–16:00	One time per week
Attention	Rainfall: below 10–20 mm/h Extensometer: 1–2 mm/h	Regular, 9:00–16:00	One time every three days
Warning	Rainfall: below 20–30 mm/h Accumulative: above 80 mm Extensometer: 2–4 mm/h	Strengthening monitoring	24 h
Evacuation	Rainfall: above 30 mm/h Accumulative: above 120 mm Extensometer: above 4 mm/h	Evacuation	

As shown in Fig. 36.3, one of the two rain gauges was installed near the City Office. The rainfall data were transmitted directly to the DMS set in the City Office. Also, the rain gauge was connected to a siren and speaker for delivering a warning. Moreover, two extensometers installed respectively in the head of two landslides were connected to an alarm unit including a siren and speaker.

2.3 Standard Values and Warning Level

In the pilot project area, information regarding standard values of rainfall and extensometer for early warning were not available; some standard values were tentatively installed as shown in Table 36.1 based on the experiences in Japan, and were modified based on the collected data during operation.

The warning was catalogued into four levels, and the main activities in each level are as follows:

- **Normal Level**—Normal monitoring and observation on a regular basis shall be conducted.
- **Attention Level**—Normal monitoring and observation on a regular basis shall be conducted, but the frequency of monitoring and observation shall be increased, e.g., once a day to once every three days, depending on the present status of ground deformation and meteorological change.
- **Warning Level**—This means that the hazards of landslides and debris flows are becoming higher and higher. The local people in these hazardous areas may evacuate on their own judgment when they receive warning information.
- **Evacuation Level**—An official announcement of evacuation shall be made, and the concerned communities and peoples in these hazardous areas shall swiftly move to the designated evacuation areas.

The cancellation of warning is technically decided by DMS and then issued by the mayor/administrator of MCM.

The criteria for the cancellation of warning are as follows:

- No precipitation for over 24 h is confirmed; and
- The decreased movement of landslide is checked from the results of monitoring and observation for over 24 h.

The flowchart of warning and evacuation system is shown in Fig. 36.4.

2.4 Evacuation Drill

Evacuation drill was conducted twice before and during rainy season to:

- Afford an opportunity for DMS staff, focal persons, and local communities to learn practically in case of the real event;
- Find out the availability and performance of the equipment and resources deployed to run the warning and evacuation system; and

- Ensure greater clarity of roles of the key players, i.e., DMS, focal persons, and local communities.

Key lessons learned from the training are:

- The participants showed keen interest in evacuation drill;
- The participants actively participated in the group activity especially role play and presentations. Almost all participants were given a chance to participate in group discussions, role plays, and presentations;
- The focal persons were clear about their role in case of landslide hazard; they have already started raising awareness on warning and evacuation system amongst the community members in their respective wards; and
- The community members appreciated the effort of JICA Study Team[2] on disaster prevention education and setting up of early alarm system.

2.5 Community Participation in Mitigation Measures

Crack filling activity had been suggested as an effective and economically feasible measure which can be undertaken through community participation to prevent water infiltration in surface drain ditches and avoid hydraulic thrusts in open cracks within landslide area which may trigger landslide.

The focal persons in CBOs and 33 community members including seven women gathered on the identified sites and started crack filling work. They gathered clay in the surrounding areas and plugged the cracks under the supervision of the landslide expert of the JICA Study Team. The community members showed keen

---

[2] The "JICA Study Team" means the JICA Study Team for the Urgent Development Study on Rehabilitation and Reconstruction in Muzaffarabad City in the Islamic Republic of Pakistan, formed under the contract between JICA and a joint venture of PACET Corp. and Nippon Koei Co., Ltd., consisting of the members from the said companies.

Fig. 36.4 Flowchart of
the warning and evacuation
system (PACET and NK
2007)
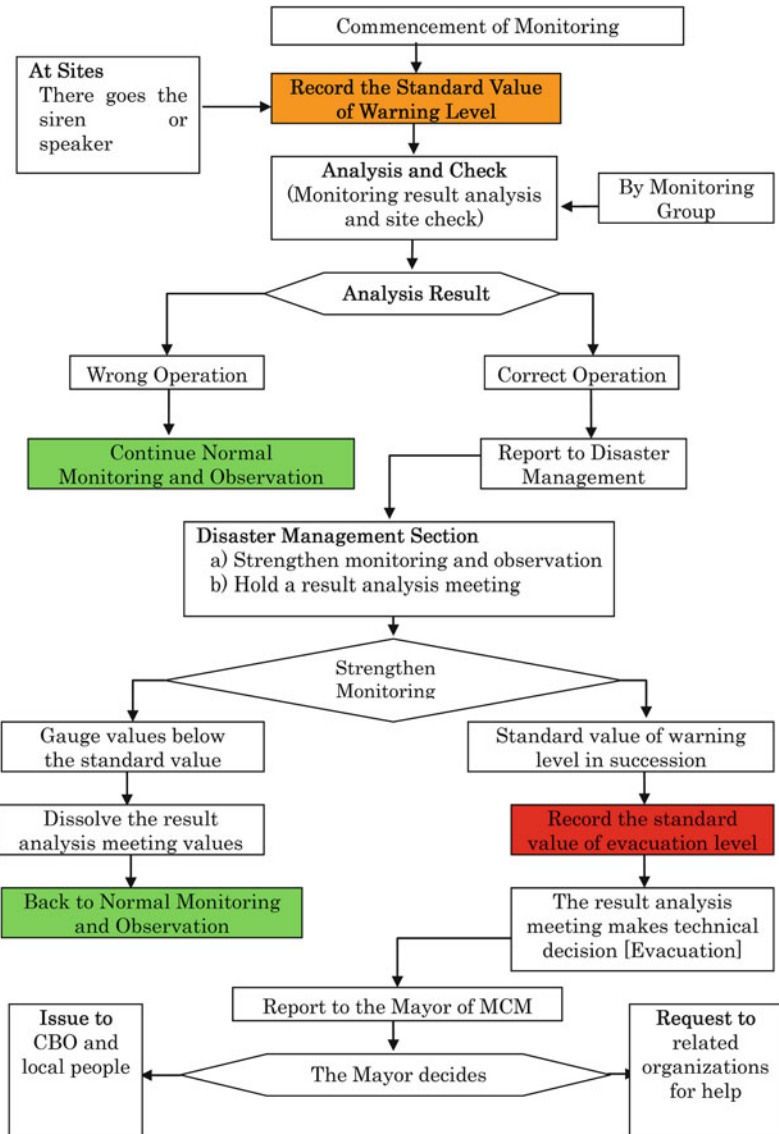
interest and actively participated in the crack
filling work.

3   Landslides that Occurred
       During the Rainy Season
       in 2006 After the Earthquake

Characteristics of landslides and associated
debris flows that occurred during the rainy sea-
son in 2006 are as follows:

- Many debris flows occurred;
- Main sources of debris flows were colluvial
  deposits during the 2005 earthquake;
- Limestone mountains behind Muzaffarbad
  city were damaged and were likely to slide
  during the rainy season;
- There was a clear correlation between rainfall and
  occurrence of landslides (especially more than
  20 mm/h or about 100 mm/24 h before); and
- Early warning system based on rainfall data
  was effective to predict natural hazards.

Warning sirens and lights installed at the project area alerted three times in the rainy season according to the rain gauge of MCM Office. However, DMS of MCM did not work effectively. Concerning the issues of timely early warning system, a follow up meeting was held between the JICA Study Team and DMS staffs. The key concerns of DMC staffs regarding the institutionalization of the warning and evacuation system are as follows:

- There are difficulties in the operation of early warning at midnight;
- Heavy rainfall is concentrated in 1 or 2 h;
- Lack of resources to make DMS sustainable;
- Staff deputed to DMS has dual roles, i.e., also working for MCM. Landslide experts are needed in DMS;
- Capacity of staff to run the system is questionable and they need more training;
- DMS staff should be provided incentive for their hard work; and
- Policy and legal backing are essential to operate DMS effectively.

4 Results of the Project and Lessons Through the Activities

Early warning and evacuation system was established in Muzaffarabad city and landslides were monitored by rainfall gauges and extensometers during the rainy season immediately after the 2005 earthquake.

The capabilities of both DMS staffs and CBOs against landslide hazard were enhanced through the pilot project, although some remediation is still necessary.

Evacuation drill and activities against landslide hazards encouraged self-help efforts in CBOs.

As a result of the above efforts, there were no serious accidents in the project area despite occurrence of many small landslides and debris flows near the area.

It can be judged that the establishment of early warning and evacuation systems was useful to deduce landslide hazard risks in the situation where drastic measures were difficult to be undertaken due to time and cost constraints.

References

Earthquake Reconstruction & Rehabilitation Authority, Government of the Islamic Republic of Pakistan (ERRA), Pakistan Earthquake—Oct 2005 in ERRA home page. http://www.erra.pk/eq2005.asp

PACET & NK (2007) The urgent development study on rehabilitation and reconstruction in Muzaffarabad city in the Islamic Republic of Pakistan. Final report II: urgent rehabilitation project. Report prepared for Japan International Corporation Agency, Tokyo. PACET Corp and Nippon Koei Co., Ltd., May 2007. http://libopac.jica.go.jp/search/detail.do?rowIndex=14&method=detail&bibId=0000171955

United States Geological Survey (USGS), Earthquake data in earthquake hazards program home page. http://earthquake.usgs.gov/earthquakes/eqinthenews/2005/usdyae/

Research on the Triggering Factors Analysis and Relevant Countermeasures of FaTing Mountain Landslide Induced by Wenchuan Earthquake

37

Linrong Xu, Zheng Han, Shuyang Chen and Hongwei Chen

Abstract

FaTing mountain landslide, which locates in Xue town, Li county of Sichuan Province, is a seismic secondary geological hazard triggered by Wenchuan earthquake of May.12.2008. The tremendous earthquake caused the trailing edge of the FaTing mountain slide cracking and the soil of slide surface a large deformation. This earthquake-induced landslide was also triggered by the heavy rainfall, and it had been recognized as a serious threat to the houses and roads below the slope before it was prevented and mitigated. In this paper, based on the field investigation, an exhaustively comparison of the basic characteristics of landslide before and after earthquake is proposed, thus the coupling progress between endogenetic and exogenetic geological processes is analyzed, and the landslide triggering factors by earthquake are analyzed, too. According to studies above, stability calculation before and after the earthquake is conducted and the landslide countermeasures is proposed, including crack sealing, interception drain, loose mass removal and retaining wall. This study is also supposed to serve as a consult for related landslide mitigation and monitoring work.

1 Introduction

The Wenchuan Ms8.0 earthquake of May.12.2008 was a disastrous one occurred in the densely populated mountain areas, with the highest magnitude and most tremendous destructiveness within the last 100 years in Chinese mainland (Huang 2009). This unprecedented earthquake also have induced more than 15000 landslides and rock falls, which

L. Xu (✉) · Z. Han · S. Chen · H. Chen
School of Civil Engineering, Central South University, Changsha 410004, Hunan, China
e-mail: lrx@mail.csu.edu.cn

Z. Han
e-mail: kerohank@csu.edu.cn

S. Chen
e-mail: 178149618@qq.com

caused about 20,000 deaths and huge economic loss (Yin 2008). Due to the particularity of the earthquake progress and its special dynamical characteristics Wenchuan earthquake presented (Burchfiel et al. 2008; Zhou et al. 2008; Cui et al. 2008), the characteristics of geo-hazards earthquake induced, including landslides, rock falls and debris flows are quite different from ones under the general gravity force, and this phenomenon is hard to describe and explain with the limit of knowledge in this field (Huang et al. 2008; Xu 2009; Cui et al. 2010).

Many hypotheses have been put forward to explain this phenomenon since it has been witnessed. Some of these have invoked to the coupling progresses between endogenetic and exogenetic geological processces (Zhang et al. 2009, 2011). Exogenetic geological progress was long time regarded to be the main triggering factor for geo-hazard and was widely emphasized by the researchers before Wenchuan earthquake, and a series of achievements have been put forwards based on this theory (Maurizio and Sdao 1999; Coe et al. 2004; Zhang 1996). Exogenetic geological progress, although its effect on the geo-hazard development and evolution was identified (Martel 2004), was only presented in formations of experiential judges and qualitative studies due to its rarely direct observation before Wenchuan earthquake (Zhang et al. 2009).

Recent years, exogenetic geological progress and its coupling with endogenetic geological progress get more and more attentions by the researchers. Xu (2009) have observed that the development characteristics of landslide triggered by strong shaking of the earthquake have a close relationship with the rock structures and the topography condition, and the critical, initiate and slide phases of landslide were different where it occurred in hard rock region, soft rock region and the loose accumulation. And Huang (2009) have conducted the analysis between distribution feature of geo-hazard and the faulting effect in the region, which indicated that the transition and staggering styles are closely related to the development and evolution of landslide, giant landslide are commonly intensely

developed along the region ranged from 0 to 7 km in the hanging wall of fault. And Zhang et al. (2009, 2011) have further summarized the general manifestations of coupling processes between endogenetic and exogenetic geological progress in mountainous area based on the field investigation at earthquake-stricken area.

The aim of this study was to compare the development characteristics and stability change of landslide before and after Wenchuan earthquake, and to conduct a preliminary study on the landslide formation and evolution mechanism based on the coupling between endogenetic and exogenetic geological progress. For this purpose, the field investigation and tracking research was carried out on the FaTing mountain landslide, Xue town, Sichuan province, supported by the "*Geo-hazard Emergency Mitigation Project at Earthquake-stricken Area*", Sichuan province. Based on the studies above, proper countermeasures were proposed. The study was also supposed to serve as a consult for related landslide mitigation and monitoring work.

2 Basic Characteristics of Landslide

2.1 General Description of the Landslide

The FaTing Mountain Landslide is located at the left part of the slope of the FaTing mountain, facing directly to the Xue town's court, in southwest Xue Town of Li County, Sichuan Province, with the center geographic coordinates of 31°33′05″N, 103°18′39″E. The slope shapes like long strip-type, with 320 m in length and 260 m in width. The slope terrain is higher in the southeast and lower in the northwest, with the relative height by 210 m, from 1610 to 1820 m, with 30°–45° in overall gradient and 320° in direction. There are altogether six landslides and collapses in this area as shown in Fig. 37.1, except for the landslide 1#, the rest of which are all in stable or basically stable state, and cause no loss to the civilians and their houses at the toe of the slope ever since the 5.12 Earthquake. By sealing the

Fig. 37.1 General view of the FaTing mountain landslide

external cracks and clearing the soil mass which had already slid as well as the solitary stones over 0.5 m in diameter, the hazard of the slope is not severe any more.

However, through investigating the Landslide 1#, it is found that there were obvious Backseat Phenomenon in the trailing edge and two sides, with a general sliding trend and instability. This hidden danger would severely threaten the safety of those at the toe of the slope in Xue Town, including 22 civilian buildings, a 200 m country road, some farmland, several fruit trees and 200 civilians nearby. Once the slope lost integrated stability and began to slide, the potential economic losses would be estimated as much as 5 million RMB.

2.2 Shaping Characteristics

The plan shape of this landslide mass was like a long tongue as shown in Fig. 37.2, whose leading edge was 1598–1604 m in elevation and 67 m in width, straight to the Xue Town's court and the country road, while its trailing edge was 1712 m in elevation and 74 m in width. This landslide mass was approximately 135 m in projected length, 108 m in relative elevation, and 35°–42° in gradient. Meanwhile, the area of

the landslide mass was about 9941 m^2, which was around 320° in sliding direction, 2–11 m in slip surface depth, and 59640 m^3 in total volume.

Analyzing from the deformation state of the partial slope movement and the distribution characteristics of crack band, the sliding surface of the FaTing mountain slope was covered basically between the loose Quaternary diluvial layer as well as the gravelly soil with slightly dense rate. It needs to be noticed that there are already some surfacely slide along the phyllite-bedrock and the slope mass

The landslide trailing edge, where there was a tensile crack in growth (showed in Fig. 37.3), with 0.1–0.5 m in width, 0.2–0.8 m in visible depth and 0.2–0.5 m in diastrophism distance. It was found that there were obvious diastrophism traces of both sides edge (showed in Fig. 37.4), whose diastrophism distance is 0.1–0.5 m.

2.3 Deformation Characteristics Before and After the Earthquake

Before the earthquake, the shallow landslide mass of the FaTing mountain of Xue town had already begun creeping deformation slowly under the long-term function of gravity.
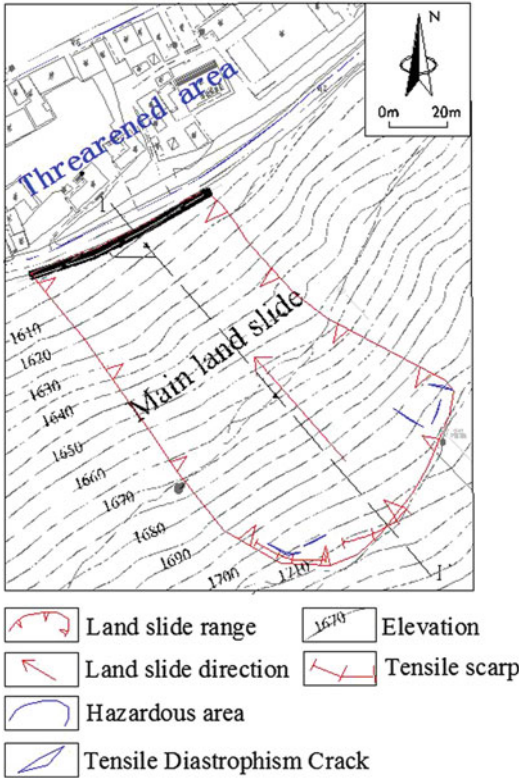
Fig. 37.2 The plan of FaTing mountain landslide

Therefore, as early as May 2007, the Xue Town government had just organized experts to monitor the sliding deformation trace of this landslide. The monitoring data showed that the deformation extent of the landslide mass was tiny before the earthquake occurred.

Since the Wenchuan Ms8.0 Earthquake on May 12, 2008, this slope shear zone gradually cut through, and the soil mass began to shear-creep toward the impending direction. With the slope emerging tensile cracks from earth surface to depths, the shearing plane cut through even further, which made the cracks on slope surface increase constantly. Therefore, the trailing edge came up a deformation failure in varying degrees, which basically focused on the surface slope soil mass nearby the two sides' gully. The major deformation patterns were partial sliding, cracking, and seat-site deforming. According to the investigation, the landslide mass trailing edge emerged the tensile crack and obvious

diastrophism traces after the earthquake (shown in Figs. 37.3 and 37.4) mentioned above.

From May 12, 2008 to June 2009, the monitoring data showed that the landslide mass had already slid for 8 cm. In the middle part of the slide mass, there is a toepath, whose surface was covered with completely-weathered phyllite rock, and a small amount of loose mass had slid to the bottom of the toe path. There are also some other locals who discovered that a water pipe on a scarp of 3–4 m height at the toe of the mountain was pushed (shown in Fig. 37.5). Therefore, it is supposed that the landslide mass may cut through at this position mentioned above.

Due to the loose soil, neither of the exploratory trench nor well showed any obvious sliding plane. According to the drilling results, the 1# landslide mass held thicker soil mass and abrupt slope, of which the sliding surface was supposed to be the soil-rock interface. Once the landslide mass began to slide entirely, it would directly threaten the safety of those at the toe of the slope, including the country road, the Xue Town's court, the nearby civilian buildings, and civilian's life and property.

3 Triggering and Forming Factors Analysis of the Landslide

Endogenetic and exogenetic geological progress are indispensible to the geological hazard's developing process, wherein, the major influencing factors of endogenetic geological progress include the earthquake effect, geological structure and stratigraphic lithology, while that of exogenetic geological progress include the topography, geomorphology, and rainfall conditions. Before the Wenchuan Ms8.0 Earthquake, the researches on landslide were mainly focused on the exogenetic geological progress. However, since the earthquake occurred, the issues that landslide evolution and deformation failure would be impacted by endogenetic geological progress, had received extensive attention recently. This paper aims at the coupling

Fig. 37.3 Tensile diastrophism crack of the landslide mass trailing edge emerged after the earthquake

Fig. 37.4 Diastrophism surface of the landslide mass left edge emerged after the earthquake

progresses between endogenetic and exogenetic geological progress of the Fa Ting Mountain landslide in Xue Town, elaborating the developing and evolution mechanism for this small landslide.

3.1   Endogenetic Geological Progress

(1) Earthquake Effect

Wenchuan Ms8.0 Earthquake on May 12, 2008 was the major triggering factor of this landslide. The slope destabilization under the earthquake effect basically performed as accumulating and triggering impacts (Gou et al. 2012). The earthquake not only triggered the small-scale slide in some partial sections, which caused the water pipe on the slope toe scarp pushed to deformation, but also facilitated the developing of the cracks at different levels. For the landslide's accumulation effects by frequent aftershock, the cracks at different levels were expanded even further, the slope's rock and soil structure got worse, and the structural plane strength was also reduced, which provided favorable spatial conditions for the later surface water's infiltration and runoff.

(2) Stratigraphic Lithology and Rock-soil Mass Structure

The stratigraphic conditions of this landslide basically include the Paleozoic Devonian, and the loose accumulation layer of the Quaternary system, in which the main deposits are loam, breccias and gravelly soil. Due to the loose structure and the well water permeable characteristics, since the earthquake occurred, the water permeability of soil mass became even larger, while its strength got further reduced. The underlying bedrock is mainly the Devonian phyllite, which is basically of the completely

Fig. 37.5 Pushing trace of the water pipe

and severely weathered within the exploration depth. Because of the crushing degree and connectivity differences restricted by lithology, the bedrock became the major water storage to converge underground water, which directly reduced the shearing strength of the rock-soil interface. Therefore, the weak structural plane (zone) emerged, which became the potential sliding plane (zone) of the landslide.

3.2 Exogenetic Geological Progress

(1) Topography and Geomorphology

The FaTing Mountain Landslide of Xue Town locates in the high-mountain and valley area of West Sichuan, where the primary slope is straight and cliffy, with 174 m in relative elevation, 320° in slope direction, and 30–45° in topographic gradient. The geomorphology type is mountain under denudation and erosion, with sparse slope vegetation, which mainly exist as weeds and a small amount of mixed shrub. Such conditions of topography and geomorphology of this slope would facilitate the emerging of the shallow and surface landslide.

(2) Rainfall Conditions

Rainfall is one of the major inducing factors of the landslide emerging and developing. The average annual rainfall of the landslide area is 609.6 mm, while the maximum is 790.1 mm (in 1992) annually, 55.9 mm daily, and 22.3 mm hourly. From May to September every year, the rainfall is relatively concentrated, that 420.6 mm amount of precipitation occupies 69 % of that in 1 year. The shallow and surface water flow generated by rainfall is the major inducing factor of the slope sliding. The rainfall could increase the self-weight of the loose soil mass and the sliding force. At the same time, it would also soften the soil mass, whose shearing strength would be reduced. Additionally, due to the effect of the cliffy slope, the potential water head drop and hydrodynamic pressure are both relatively high. Therefore, the rainstorm or sustained rainfall would cause the cracks induced by earthquake to widen and deepen even further. Eventually, the potential sliding plane would connect with the cracks, which could lead to the integrated sliding failure of the entire slope ultimately.

3.3 Coupling Between Endogenetic and Exogenetic Geological Progress

The lithology of the FaTing Mountain slope in Xue Town is basically the loose accumulation

layer of quaternary system, while the soil structure is loose, and the underlying rock stratum is highly weathered and crushed. But since the Wenchuan Ms8.0 Earthquake on May 12, 2008, the slope cracks developed and accumulated further, which caused the slope to crack and deform, and reduced the slope stability, inducing the secondary landslide hazard. In the later period, infiltration of relatively concentrated rainfall and biggish aftershock would become the major inducing factor of the instability failure for landslide. Therefore, under the coupling effect between endogenetic and exogenetic geological progress, landslide could easily occur in the Fa Ting Mountain slope of Xue Town, which would be quite devastating.

4   Stability Comparison Before and After the Earthquake

4.1   Safety Factor Analysis of Different Condition

Limit equilibrium method, which is recommended by the current codes and standards in China, was introduced in the stability comparison. And the mechanical model of polygonal-shape was built to conduct the calculation on landslide stability. What need to be noticed is that Morgenstern-Price method was used in the landslide stability calculation, because it was an advanced solution for Limit equilibrium method as recommended by current codes and standards.

The calculation section I-I' was selected, because of this section, the soil mass above the slope was thickest, and the construction threatened was more important than others. The interface between loosen mass and phyllite bedrock was chosen as the sliding surface, the slope above this surface then was separated to seven or nine sticks according to the shape of landslide and sliding surface. Two shear-outlets were selected as shown in Figs. 37.6 and 37.7, one was at the top of the country road with the elevation 1622 m, for where a water pipe was witness to be pushed and deformed, and one was at the toe of the slope with the elevation 1601 m. Four
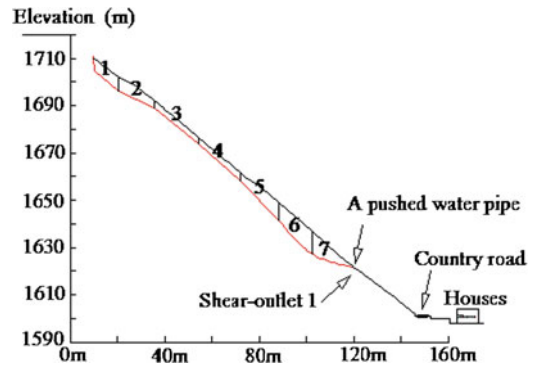
Fig. 37.6 Stability calculation at shear-outlet 1
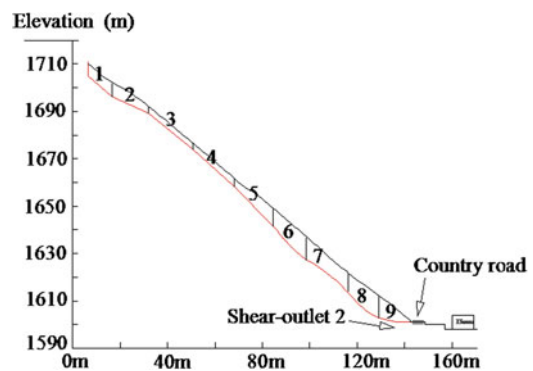
Fig. 37.7 Stability calculation at shear-outlet 2

different calculation conditions were considered, custom condition, rainfall condition, earthquake condition with peak acceleration of 0.10 g and 0.15 g. The landslide stability at both shear-outlets were calculated and analyzed under these four conditions. As shown in Table 37.1, all the parameters used for stability analysis were obtained by the soil mechanical experiments.

As shown in Table 37.2, under the natural condition, the safety factor K_f of the FaTing mountain landslide, Xue town, are both greater than 1.15, which means the integrated landslide was stable. And under the rainfall condition and earthquake condition with the horizontal peak seismic acceleration value of 0.10 g, the safety factor K_f was greater than 1.05 at shear-outlets 1 and 1.00 at shear-outlets 2, it shows that the landslide was relatively stable before Wenchuan earthquake of May.12.2008, with little possibility to slide. And under the rainfall and earthquake

Table 37.1 Soil parameters value used in stability calculation

Soil horizon	Natural density (kN/m³)	Saturation density (kN/m³)	Natural shearing strength		Saturation shearing strength	
			Internal friction angle φ (°)	Cohesive strength C (kPa)	Internal friction angle φ (°)	Cohesive strength C (kPa)
Shingle	19.5	20.1	32.0	11.0	30.0	9.0
Gravel	20.5	21.1	33.0	12.0	31.0	10.0
Completely-weathered phyllite	19.5	20.5	34.0	13.0	32.0	10.0
Severely-weathered phyllite	23.2	23.5	38.0	18.0	35.0	15.0
Moderately-weathered phyllite	24.7	25.0	/	/	/	/

Table 37.2 Stability calculation result of the selected section I-I'

Combination of load	Calculation condition	Solution method	Safety factor of shear-outlet 1 (K_f)	Safety factor of Shear-outlet 2 (K_f)
Basic combination	Natural condition	Morgenstern-price method	1.290	1.277
	Rainfall condition		1.232	1.219
Special combination	Rainfall and earthquake condition (0.10 g)		1.063	1.034
	Rainfall and earthquake condition (0.15 g)		0.972	0.945

Note based on the <Restoration construction rule after earthquake for Wenchuan area>, the horizontal peak seismic acceleration is 0.10 g before earthquake, and 0.15 g after

condition with the horizontal peak seismic acceleration value of 0.15 g, the safety factor K_f at both shear-outlets are less than 1.00, which shows this landslide was at the understable condition after earthquake, and facing a great danger to slide down at both shear-outlets. By comparing the safety factors at both shear-outlets under these calculation conditions, it can be found that safety factor of shear-outlet 2 are generally less than that of shear-outlet 1, it illustrates that the FaTing landslide is likely to shear out prior at this place and requires engineering mitigation.

4.2 The Analysis of Relationship Between Safety Factor and Horizontal Peak Seismic Acceleration

More safety factor calculations with different levels of horizontal peak acceleration were conducted. Based on these calculation data, a relationship between the horizontal peak seismic acceleration was proposed as shown in Figs. 37.8 and 37.9.

With the increment of the horizontal peak seismic acceleration, the safety factors generally decreased linearly at both shear-outlets of this landslide, and relevant fitting formulas were obtained based on the curves as shown above. And then from the field investigation, the landslide had no yet wholly failed, that meant the safety factor K_f would be greater than 1.00, meanwhile an estimation could be put forward that the maximum horizontal peak seismic acceleration of this area was between 0.13–0.11 g.

5 Relevant Countermeasures of Landslide

Based on the preliminary discussion on the formation and evolution mechanism of earthquake-triggered landslide, the endogenetic and
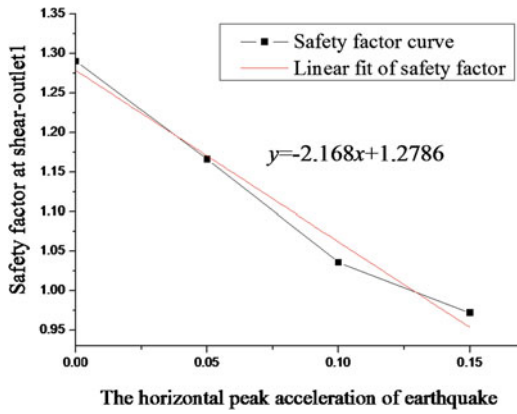
Fig. 37.8 The relationship between horizontal peak seismic acceleration and safety factor at shear-outlet 1
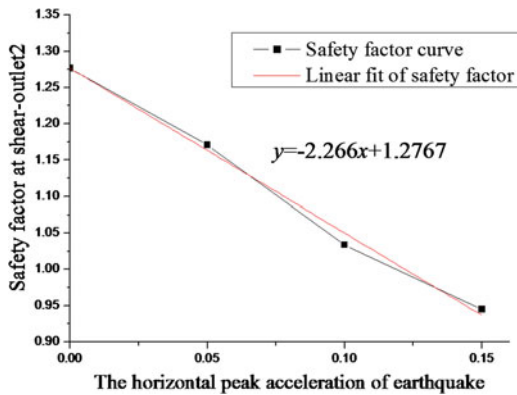
Fig. 37.9 The relationship between horizontal peak seismic acceleration and safety factor at shear-outlet 2

exogenetic geological progress factors of Xue town landslide was figured out, and thus the proper hazard countermeasures are proposed as shown in Fig. 37.10, including packing sealing, constructing retaining wall and setting intercepting drain.

5.1 Tensile Cracks Sealing

The cracks at the trail edge of this landslide with the elevation between 1700 and 1710 m were suggested to be sealed, packed and tamped by the clay material, which could prevent the further development of cracks, and about 50.7 m³ volume of clay material was used, cost about only
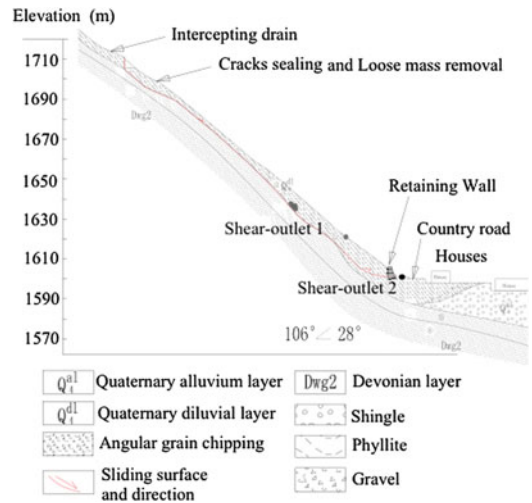
Fig. 37.10 The countermeasure against fating mountain landslide

7,100 RMB totally; The intercepting drain was suggested to be set along the outer ring of landslide, which could reduce the water permeation.

5.2 Mass Removal and Load Decrease

The shallow landslide mass of the FaTing mountain of Xue town had already begun creeping deformation slowly under the long-term function of gravity, due to the influence of Wenchuan earthquake, the soil mass began to shear-creep toward the impending direction. So a mass removal work was suggested to be conducted. The shallow loose mass and moveable rocks at the crown of landslide should be removed, especially the parts where serious deformation presented, and load distributed on the landslide surface is greatly decreased. Thus, the moveable rocks at the trail of landslide and the loose mass of landslide surface with the elevation between 1710 to 1685 m at the shear-outlet 1 were removed from the top down for safety. About 1,500 m³ volume of landslide mass were removed, cost about 26,300 RMB totally.

With this mass removal work, the safety factor K_f at shear-outlet 1 would increase to 1.062, which indicated that the upper part of landslide

above shear-outlet 1 would be generally stable under the rainfall and earthquake condition with the peak acceleration value of 0.15 g. Although the safety factor K_f at shear-outlet 2 would increase to 0.985, which was yet below 1.00, and whole landslide still remained unstable, more mitigation work was required at this shear-outlet.

5.3   Retaining Wall

And based on the calculation of pushing force and investigation of landslide characteristics, a retaining wall was also suggested to be constructed at the toe of the slope with the elevation from 1600 to 1610 m, where the landslide could shear out. The grouted rubble made retaining wall was 5.0 m high, 1.0 m deep, 1.9 m wide of the longitudinal section, and 68.5 m long of the transverse section, with the gravel level MU30 and mortar level M10. The connection of retaining wall surface and landslide was called as gravel water filtration layer, with the thickness of 0.40 m, and PVC drain was arranged quincuncially in the wall, with the interval of 2.0 m. The suggested countermeasure above was supposed to improve the stability of FaTing mountain landslide.

6   Conclusions

(1) The FaTing mountain landslide in Xue Town shape like long tongue pattern, which was $5.964 \times 10^4 \mathrm{m}^3$ in total volume. This landslide mass mainly contained the loose accumulation layer of Quaternary system, as well as the phyllite completely and severely weathered, with quite crushed rock mass. Influenced by the Wenchuan Ms8.0 Earthquake on May 12, 2008, the cracks in the slope developed and accumulated even further, which caused the slope to crack and deformation, and reduced the slope stability. In the later period, infiltration of relatively concentrated rainfall and biggish aftershocks would cause the landslide instability failure, which would be quite devastating.

(2) Limit equilibrium method and its Morgenstern-Price method-based solution was used in the stability calculation of the FaTing mountain landslide. The calculation results indicated that the landslide was stable under the natural condition, and relatively stable under the rainfall condition and earthquake condition with horizontal peak seismic acceleration value of 0.10 g, but understable under the earthquake condition with peak acceleration value of 0.15 g after earthquake. By comparing the safety factor at both shear-outlets, FaTing mountain landslide may slide down prior at the shear-outlet 2.

(3) Based on the field investigation of landslide characteristics and the discussion about the coupling between endogenetic and exogenetic geological progress, a preliminary analysis on the triggering and formation factors of the FaTing mountain landslide was conducted. Thus countermeasures including crack sealing, intercepting drain loose mass removal and retaining wall were suggested on the purpose to reduce the water permeation and improve the stability of this landslide. This study is also supposed to serve as a consult for relevant earthquake-induced landslide mitigation work.

References

Burchfiel BC, Royden LH, Vander RD (2008) A Geological And Geophysical Context For The Wenchuan Earthquake Of 12 May 2008, Sichuan, People's Republic Of China[J]. GSA Today 18(7):4–11

Coe JA, Godt JW, Baum RL et al (2004) Landslide susceptibility from topography in Guatemala[C]. Landslides: Evaluation Stabilization. Taylor & Francis Group, London, pp 69–78

Cui P, Wei F, Chen X (2008) Geo-hazards in Wenchuan earthquake area and countermeasures for disaster

reduction[J]. Bull Chin Acad Sci 23(4):317–323 (in Chinese with English abstract)

Fang H, Cui P (2010) Study on mechanical mechanism and controlling factors of high speed distant landslides induced by the Wenchuan Earthquake[J]. J Catastr 25:120–130 (in Chinese with English abstract)

Gou F, Wang YS, Wu JF (2012) Characteristics and formation mechanism of high slope landslide induced by Wenchuan earthquake in Miaoba county Of Dujiangyan city[J]. J Eng Geol 20(1):21–29 (in Chinese with English abstract)

Huang R (2009) Mechanism and geo-mechanical modes of landslide hazards triggered by Wenchuan 8.0 earthquake[J]. Chin J Rock Mech Eng 25(6):1239–1249 (in Chinese with English abstract)

Huang R, Li WL (2009a) Fault effect analysis of geo-hazards triggered by Wechuan earthquake[J]. Chin J Eng Geol 17(1):19–28 (in Chinese with English abstract)

Huang RQ, Li WL (2009b) Fault effect analysis of geo-hazards triggered by Wechuan earthquake[J]. Chin J Eng Geol 17(1):19–28 (in Chinese with English abstract)

Martel SJ (2004) Mechanics of landslide initiation as a shear fracture phenomenon[J]. Mar Geol 203(3/4): 319–339

Maurizio P, Sdao F (1999) The role of rainfall in the landslide hazard: the case of the Avigliano urban area (Southern Apennines, Italy)[J]. Eng Geol 53(3): 297–309

Xu Q (2009) Main types and characteristics of the geo-hazards triggered by The Wenchuan earthquake [J]. J Geol Hazards Environ Preserv 20(2):86–93 (in Chinese with English abstract)

Xu Q, Huang R (2008) Dynamic characters of large-scale landslides triggered by "5.12" Wenchuan earthquake[J]. J Eng Geol 16(6):721–729 (in Chinese with English abstract)

Yin Y (2008) Researches on the geo-hazards triggered by Wenchuan Earthquake, Sichuan[J]. J Eng Geol 16(4):433–444 (in Chinese with English abstract)

Zhang Z (1996) Mechanism of groundwater effect landslide stability and control construction[J]. J Eng Geol 4(4):80–85 (in Chinese with English abstract)

Zhang Y, Shi JS, Sun P (2009) Coupling between endogenic and exogenic geological processes in the Wenchuan earthquake and example analysis of geo-hazards[J]. J Geomech 15(2):131–141 (in Chinese with English abstract)

Zhang Y, Su SR,Wu SR (2011) Research on relationship between fault movement and large-scale landslide in intensive earthquake region[J]. Chin J Rock Mech Eng .30:3503–3513 (in Chinese with English abstract)

Zhou R, Huang R, Lei JC (2008) Surface rupture and hazard characteristics of Wenchuan earthquake with magnitude 8.0 in Sichuan Province[J]. Chin J Rock Mech Eng 27(11):2173–2183 (in Chinese with English abstract)

Part IV

Mechanism

On the Initiation and Movement of Hanokidaira Landslide from the 2011 Tohoku Earthquake, Japan

38

Gonghui Wang, Akira Suemine, Yoshiya Hata and Toshitaka Kamai

Abstract

A flow type landslide was triggered in Hanokidaira area by The 2011 off the Pacific coast of Tohoku Earthquake, killing more than ten people. The slope consists of pyroclastic flow deposits that were formed at different times, with a layer of paleosol that was outcropped. Above the paleosol there is a layer of pumice and scoria, which is very rich in natural moisture content (~ 145 %). From field observation, we inferred that the sliding surface originated on the boundary between the paleosol layer and the layer of pumice and scoria. To examine the possible trigger and movement mechanism of these landslides, we monitored the aftershocks on landslide area, and inferred the possible seismic response of the landslide area during the main shock. We took samples from both layers, and performed undrained static and cyclic shear tests on them in fully saturated or in natural water content states. The results showed that high pore-water pressure could be generated after failure with increase of shear displacement, resulting in great loss in the shear strength. We also performed seismic simulation tests on these samples by using the inferred seismic waveform, and the test results showed that the amplified vertical motion may have played a key role in the initiation of this landslide.

Keywords

Hanokidaira landslide · The 2011 off the Pacific coast of Tohoku earthquake · Shear behavior · Seismic loadings · Pore-water pressure generation

1 Introduction

A massive and extremely catastrophic earthquake of magnitude of 9.0 (M_w) occurred at 14:46 JST on 11 March 2011, Tohoku Region, Japan (Fig. 38.1). This earthquake, which was named "The 2011 off the Pacific coast of Tohoku Earthquake", was the most powerful one known ever to have hit Japan.

G. Wang (✉) · A. Suemine · T. Kamai
Disaster Prevention Research Institute, Kyoto University, Gokasho Uji, Kyoto, 6110011, Japan
e-mail: wanggh@landslide.dpri.kyoto-u.ac.jp

Y. Hata
Research and Development Center, Nippon Koei Co., Ltd, Tsukuba-shi, Japan

Fig. 38.1 Locations of the epicenter of the 2011 off the Pacific coast of Tohoku earthquake and the Hanokidaira landslide (after Google earth)

The earthquake triggered extremely powerful tsunami, causing a great number of casualties (15854 reported death, 3089 missing, and 6025 injured as of 28 March 2011, according to the Japanese National Police Agency) and severe destruction of the infrastructure on Tohoku Region, Japan.

Many landslides had been triggered by this quake in the wide area of Tohoku Region, and some of them were highly concentrated in the southern part of Fukushima Prefecture, hilly residential areas of Miyagi and Fukushima Prefecture, and island areas of Matsushima coast. Although the scales of the landslides were small irrespective of the great magnitude of the earthquake, many landslides showed high mobility with features of flowslides. Because these landslides were sparsely located on different areas, and there was no precedent precipitation, better understanding their initiation and movement mechanism are of great importance to the mitigation of coseismic geohazards in the future. After the quake, we performed reconnaissance field surveys of landslides, and conducted detailed investigation of some catastrophic ones. Here we describe one landslide occurring on Hanokidaira area in Shirakawa City, Fukushima Prefecture, and discuss their possible initiation and movement mechanisms.

2   Hanokidaira Landslide

Hanokidaira landslide (Fig. 38.2a) originated on a southeast facing slope of a hill, which is approximately 1 km north of JR Shirakawa Station in Shirakawa City. The displaced material was estimated to be approximately 1×10^5 m^3 with a horizontal travel distance of about 290 m and a difference in elevation of about 50 m. 13 people were killed and ten houses were completely destroyed by the landslide debris. A small portion of the displaced materials "flowed" into the golf course and deposited thinly. Using a handy laser measurement, we surveyed the plan of the landslide area, and also the longitudinal section (Fig. 38.2b). The main part of the displaced materials spread on the residential area on the foot of the hill, showed "flow" characteristics. The mobilized friction angle of the slide was about 9.6 degrees. This landslide occurred in relation to Pleistocene volcanic ash and welded tuff layer in hilly area in the eastern areas of Ōu Mountains. Detailed information of the geological setting can be obtained from Chigira (1982).

The slope consists of different geological layers. From the bottom to the top, these layers are welded tuff, paleosol, pumice, scoria, weathered volcanic ash, and forest soil. Paleosol outcropped in the source area with stria on its surface. We dug the deposits on the golf course, and found that the grass on the golf course was brought down and buried by the displaced materials, but was not cut or moved from its original places. Above the grass there was an ∼10 cm thick paleosol layer, which was overlain by loose pumice. Many trees stood vertically while being transported.

No standing ground water was found on the landslide source area. However, water contents of the outcropped soil layers were very high

Fig. 38.2 Hanokidaira landslide. **a** Oblique view (after Takeshi 2011); **b** longitudinal section along line I-I'; **c** buried grass on the golf course and paleosol layer above the grass
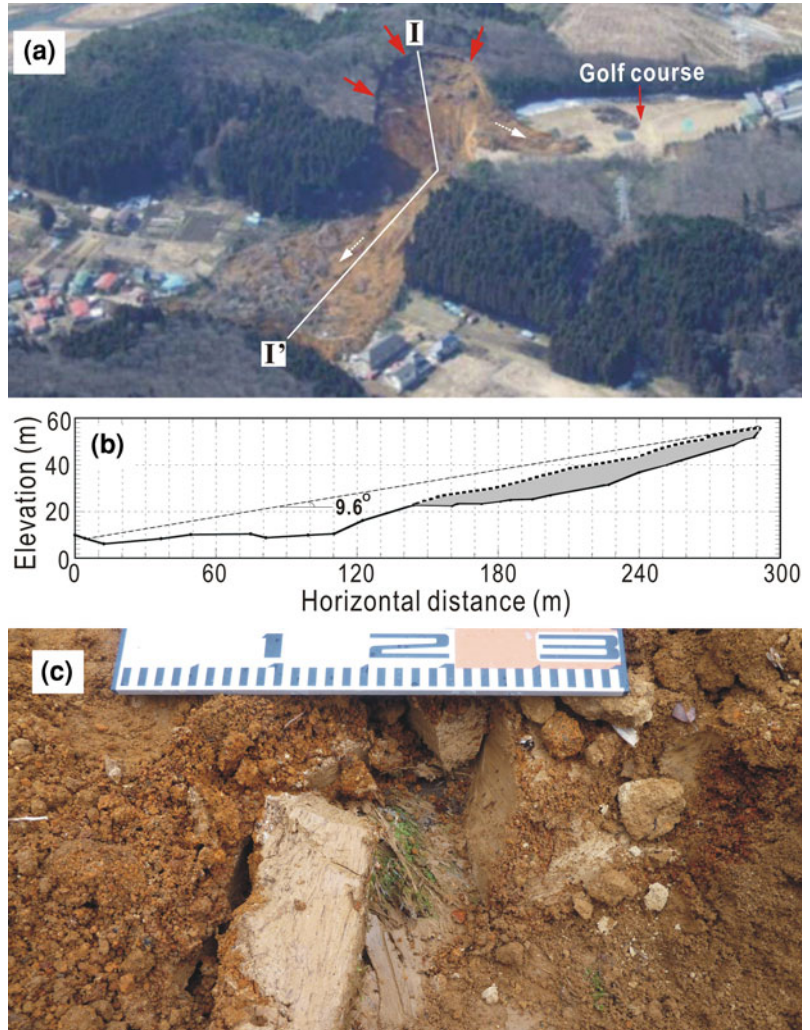
($\sim$ 160 % for paleosol layer and $\sim$ 145 % for the pumice layer). We were told that the rice paddy on the toe of the slope was always in a state of quagmire although no irrigation was performed. Therefore, we inferred that the water at the rice paddy came from the slope, which indicated that the slope could be rich in ground water.

3   Initiation and Movement Mechanisms

In the following chapters, the possible reasons for the initiation and long distance of movement were examined from the point of view of

geomorphic, seismic motion and geotechnical aspects of the landslide areas.

3.1   Geomorphic Feature

Figure 38.3 shows the topographic map of the landslide area. It is noticed that the toe part of the landslide was a steep slope, below which landscape of valley was well developed. As indicated by Chigira (2011), this kind of topography suggests that the toe part of the slope might have been cut such that the stability of slope had been already lowered before the earthquake. On the other hand, formation of this kind of topography

Fig. 38.3 Topographic map of Hanokidaira landslide area (after the planning map of Shirakawa city)
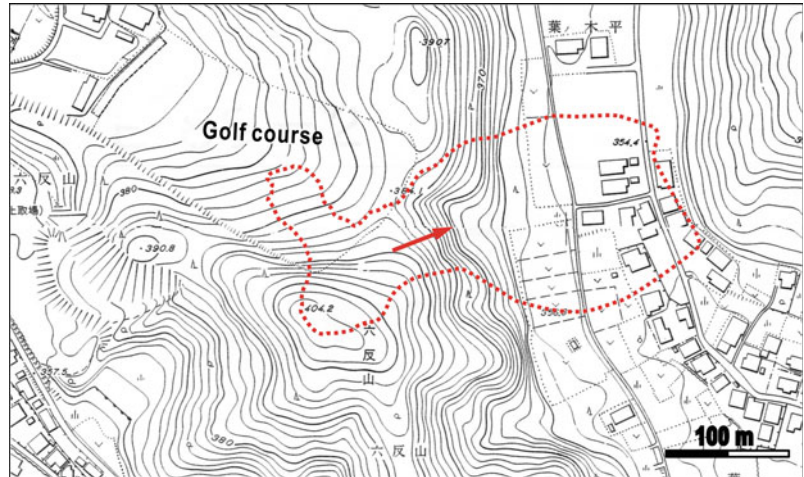
might be due to the existence of rich groundwater, because rich groundwater may enable the appearance of piping and reduce the resistance of soil layer to runoff erosion. Namely, the landslide source area might be rich in ground water.

3.2 Seismic Motion

It is well known that seismic station had been densely installed in Japan. In Shirakawa city, there are two permanent strong motion observation stations. One is the Kyoshin Net (K-Net) station of National Research Institute for Earth Science and Disaster Prevention (NIED), Japan. Another one is the Japan Meteorology Agency (JMA). Both stations had their UD motion being the smallest, and NS being the greatest. Nevertheless, the maximum values for each station are different. The K-Net had a maximum acceleration of 1295.2 gal, while the JMA recorded a maximum acceleration of 371.5 gal, approximately 3.5 times smaller. Because the JMA Shirakawa station is approximately 0.8 km south of Hanokidaira landslide area, it is reasonable to believe that Hanokidaira area had the same level of seismic response during the main shock. Nevertheless, it is well known that the seismic response of a given site depends greatly on the underground structure. To better understand the seismic motion of Hanokidaira area during the main shock, we installed a seismometer on the top of the landslide area and

recorded a large number of aftershocks since April 11, 2011. Using the monitored aftershocks, the possible seismic response of the landslide area during the main shock had been estimated (Fig. 38.4) (Hata et al. 2011). The estimated seismic wave had a maximum acceleration of about 907 gal in NS. Next, we will use this referred seismic motion to examine the possible seismic response of the slope during the main shock.

3.3 Geotechnical Aspects

The field survey revealed that all these landslides had paleosol as their bed layer, and all the materials above this layer had been displaced. This suggests that the boundary between this paleosol layer and overlain pumice layer might have played key role in the initiation and movement of these landslides. Liquefaction was the most possible reason for the high mobility of these landslides. However, our field survey failed to find standing ground water, i.e., the soil layers might not be in fully saturated state. Nevertheless, we found that the field moisture content of the soil layers on the slope were very high (~ 145 %); also this landslide was triggered on a slope above small valley, which may be the result of paleo-valley that had been identified by late engineering constructions. This paleo-valley may enable the converge of ground water. Therefore, we inferred

Fig. 38.4 Estimated seismic movement for Hanokidaira landslide area
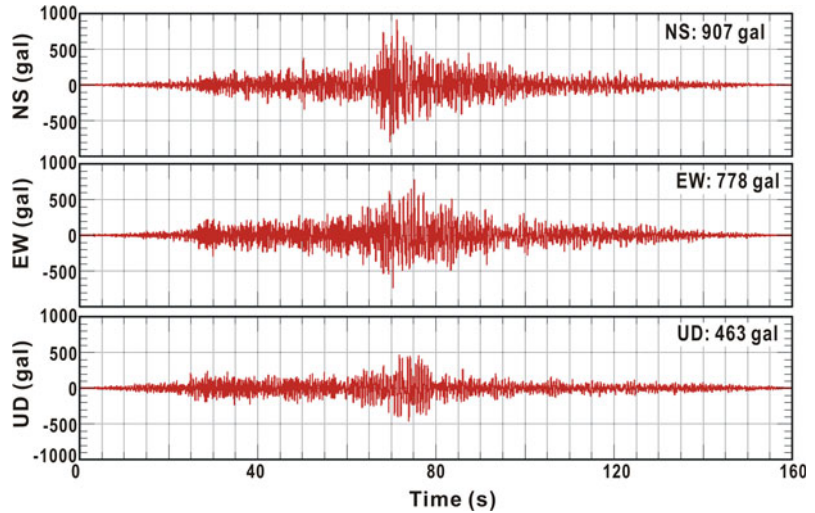
that the soil layers near the sliding surface were at very high moisture content or nearly fully saturated condition, and liquefaction occurring within them might be the reason for the high mobility of these landslides. To examine this, we took samples from the source area, and sheared them undrained at fully saturated sate or at natural moisture content by using ring shear apparatus.

Two kinds of samples, paleosol (S1) and pumice with scoria (S2), were taken from the source area and used in the tests. Because the tests aimed to examine the shear behavior of the soil in the source area, test conditions were designed to represent a soil element on the sliding surface overlain by a soil layer about 8 m thick. The normal and shear stresses on the sliding surface were therefore calculated using a slope angle of 16 degrees that was measured along the sliding surface on the source area (Fig. 38.2b), and a unit weight of 11.4 kN/m^3, which was calculated from the measured in situ density of the sample. Thus, the estimated normal stress (σ_i) was 84 kPa and shear stress (τ_i) was 24 kPa. All the shear tests utilized this initial stress state.

We performed undrained ring shear tests on saturated samples following the steps as: (1) putting oven-dried samples into the shear box; (2) saturating the samples by means of CO_2 and de-aired water; (3) normally consolidating the sample; (4) undrained shearing the sample by applying cyclic loadings or increasing shear stress only (static shearing). For tests on samples in natural moisture contents, we put the natural samples (taken from the field and kept in plastic bags to keep the in situ moisture) into the shear box and then went to above-mentioned step (3) and step (4).

4   Results of Cyclic Shearing

Undrained cyclic shear tests were conducted on both samples at saturated state at first. After being saturated and normally consolidated, the samples were applied to a cyclic shear stress with its amplitude being 24 kPa and frequency being 0.5 Hz under undrained condition. In the test, normal stress was kept the same. Figure 38.5 presents the results in time series data for both samples. In both tests, pore-water pressure was generated with cycles and shear resistance decreased correspondingly. With the continuing of cyclic shearing, the accumulated pore-water pressure reached a value great enough such that the shear resistance decreased to a value smaller than the initial shear stress. This enabled the continuing of shear failure such that shear resistance lowered further and finally reached to zero approximately. From Fig. 38.5, we can conclude that the soil layers near the sliding surface are highly liquefiable.

Fig. 38.5 Undrained cyclic shear test on saturated samples S1 (**a**) and S2 (**b**)
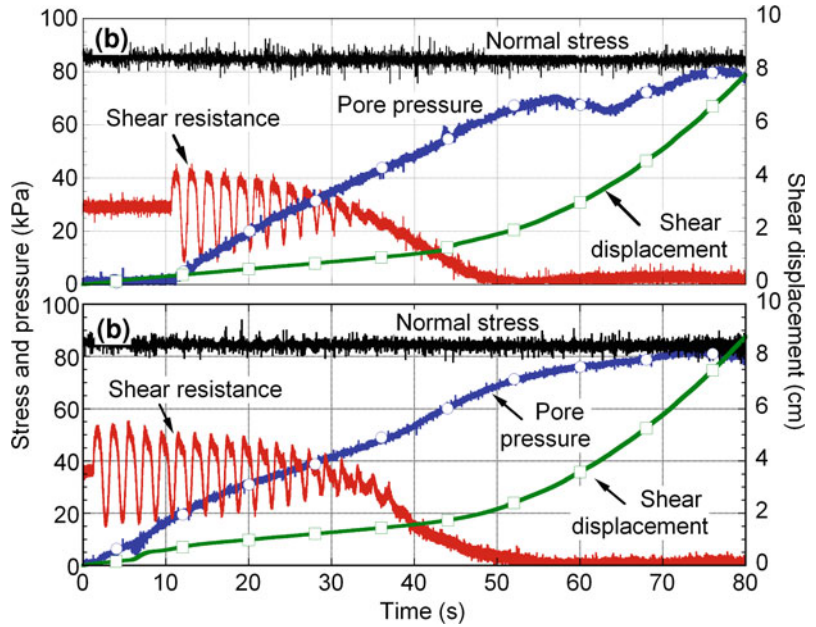
Fig. 38.6 Time series data of stresses, pressure and shear displacement (**a**), as well as vertical displacement (**b**), for the undrained shear test on sample S2 (water content: 126 %)
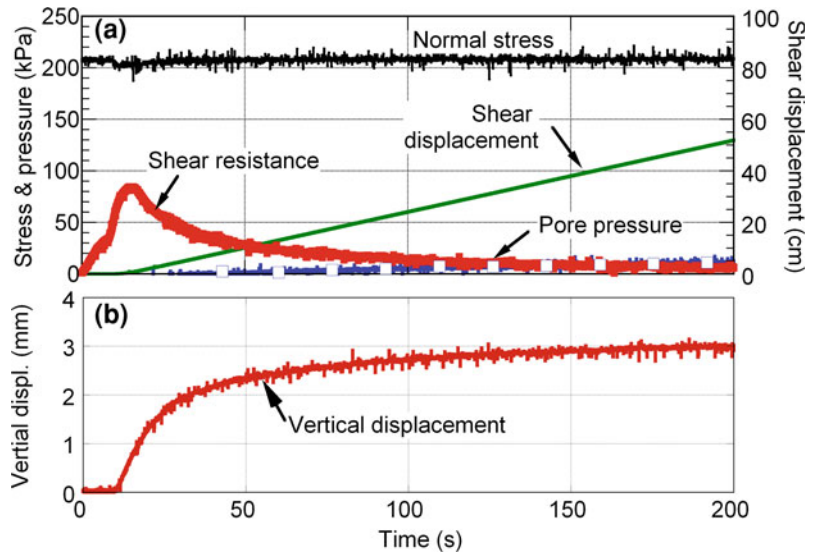
5   Undrained Shear Test on Sample in Natural Water Content

It is noted that in the field survey, we did not find standing ground water, but found that the soil layers near the sliding surface were at high water content. Therefore, it is of great importance to examine the possible shear behavior of these soils at high water content but not at fully saturated state. Therefore, undrained shear tests were conducted on samples in natural water content. We sheared the sample by increasing the shear stress monotonically. Figure 38.6 shows one example of this kind of tests on S2 in natural water content (126 %). After shear failure occurred, shear resistance lowered to a very small value near zero with progress of shearing. Vertical displacement also increased with progress of shearing.

Fig. 38.7 Residual shear resistance of saturated S1 at different shear rates
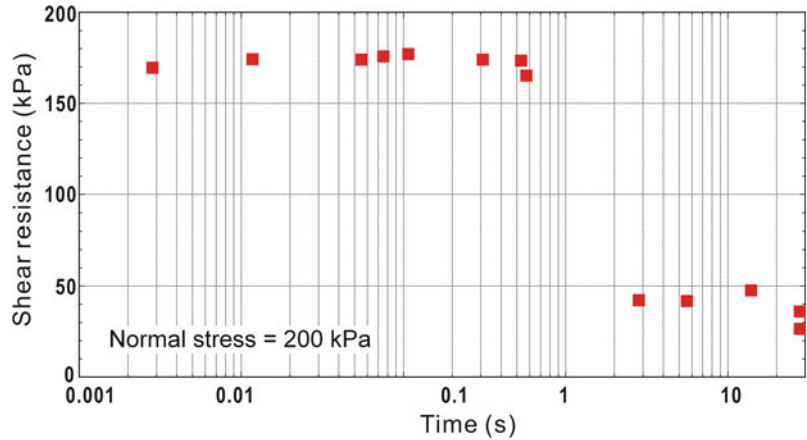
Although the monitored pore-water pressure was very small, probably due to the existence of pore air that could result in wrong measurement in the pore-water pressure, we inferred that the lowered shear resistance resulted from the generation of high pore-water pressure within the shear zone. It is noted that after the shearing was finished, we opened the drainage system, and there was water expelling from the shear box. Therefore, we concluded that even though the sample was not in fully saturated state, the abundant water in the sample enabled the generation of high pore-water pressure after shear failure was triggered.

6 Shear Rate Dependency of Paleosol

Once shear failure occurred, it could be expected that the displaced landslide material would experience movement at different velocity. To check the possible shear rate effect, we sheared paleosol at different shear rates. The sample was first saturated, and consolidated under a normal stress of 200 kPa. After consolidation, the sample was sheared to residual state using a shear-speed-controlled method. We performed multi-stage testing, which has been found to produce results similar to testing of individual samples (Bromhead 1992; Tika et al. 1996; Tiwari and Marui 2004; Suzuki et al. 2004; Wang et al. 2010). Following the measurement of residual shear strength at a given shear rate, we changed

the shear rate and then measured the residual shear strength at this differing shear rate. Through this method, the residual shear strengths at different shear rates were measured. The results are presented in Fig. 38.7, from which it is noticed that the effect of shear rate on the residual shear strength is significant. The residual shear strength was greater than 150 kPa when the shear rate was smaller than 0.6 mm/s, but was smaller than 50 kPa when the shear rate was greater than 1 mm/s. Although the reason for this kind of sharp decrease in shear resistance with shear rate is not clear at present, it can be concluded that the shear resistance became very small when the displaced material moved faster. This decreasing tendency of shear resistance with increasing shear rate may give an explanation to why the grass on the golf course was less damaged.

7 Seismic Simulation Tests

Using the estimated seismic waveforms shown in Fig. 38.4, a series of seismic simulation tests were performed on both samples by means of ring shear apparatus. Because the estimated seismic waveforms present that of the seismic bedrock in earthquake engineering, and the real seismic response of the slope could be amplified by the topography and also by the saturation degree of the soil layers (Yang and Sato 2000), we amplified the seismic movement shown in

Fig. 38.8 Synthesized seismic loadings on the sliding surface
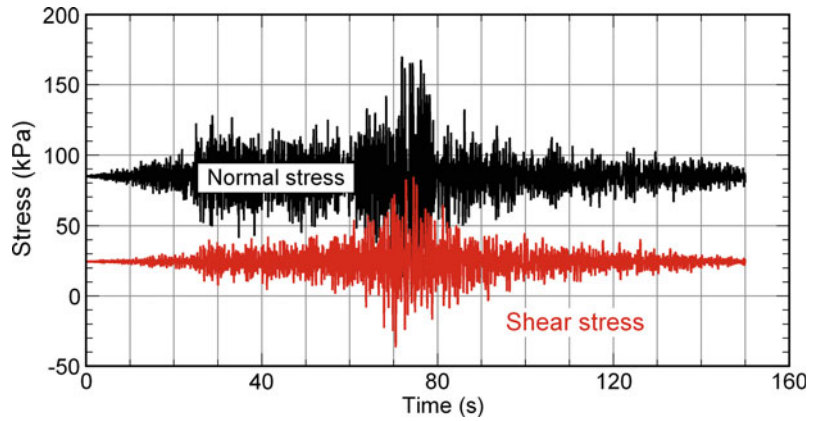
Fig. 38.9 Results of seismic simulation tests on **a** S1 and **b** S2, respectively
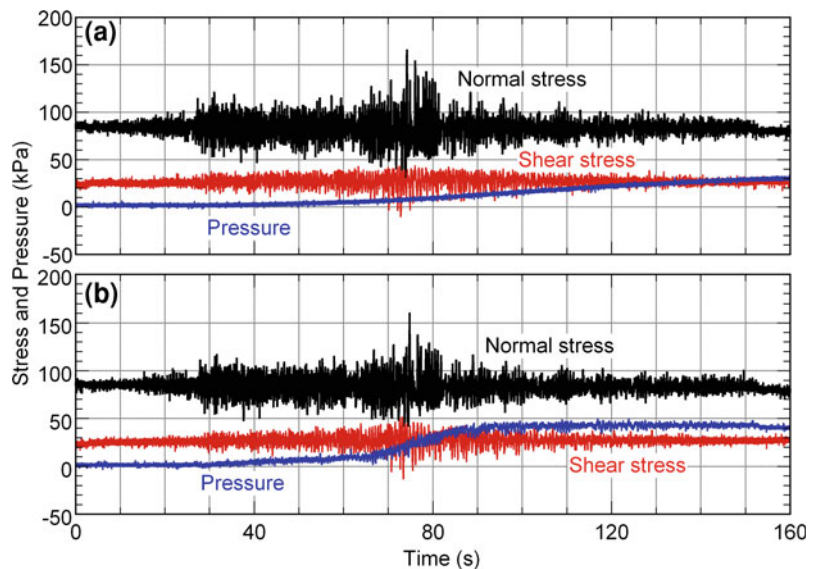
Fig. 38.4 by three times in each components. We estimated the possible seismic normal stress and shear stress by calculating the possible seismic accelerations parallel and perpendicular to the potential sliding surface. Detailed procedures for obtaining this kind of seismic loadings can be obtained from Wang and Sassa (2009). Figure 38.8 shows the calculated seismic normal stress and shear stress on the sliding surface during the earthquake loadings.

Using the DRPI-5 ring-shear apparatus, seismic simulation tests were performed on both samples. After the samples were fully saturated and normally consolidated by the initial stress state, the shear box was switched to undrained state, and then the seismic loadings shown in

Fig. 38.8 were applied. Fig. 38.9 presents the results, where it is found that although certain of excess pore water pressure had been built up in each test, no shear failure was triggered by the introduction of seismic loadings in either test. Because the landslide occurred during the main shock of the earthquake, the test results shown in Fig. 38.9 may imply that we may need to examine the possible amplification of UD motion. Normally, the trampoline effect and effect of unsaturated soil layer may result in great amplification in UD (Yang and Sato 2000; Tobita et al. 2010), but the effects of UD on the triggering of coseismic landslide had normally been ignored. Further scrutiny on the role of UD in the initiation of Hanokidaira is needed and is on the progress.

8 Conclusions

During the 2011 off the Pacific coast of Tohoku Earthquake, many landslides were triggered in urban residential region and also on natural slopes, directly killing many people and destroying many houses. Hanokidaira landslide was in small scale but it was characterized by high mobility and long travel distance. Through the field survey, analysis of seismic motion, and experimental geotechnical examination, the possible initiation and movement mechanisms were examined. Some conclusions can be made as follows.

(1) Hanokidaira landslide occurring on pyroclastic fall deposits showed very high mobility with occurrence of liquefaction phenomenon. Landform of valley was well developed on the toe part of the landslide. This indicates that the upper slope of the landslide source area might have been in less stable state before the quake.

(2) Although the epicenter was far from these landslides (about 280 km), the seismic motion on the landslide area was very strong.

(3) Sliding surface was along the boundary between the paleosol and overlain pyroclastic fall deposits (pumice and scoria). Both soil layers are highly liquefiable in saturated condition when subjected to cyclic shear loading. High pore-water pressure can also be generated in both soil layers even though they are not at fully unsaturated states.

(4) Seismic simulation tests showed that the seismic movement on the slope should have been greatly enlarged due to the effect of topography and also the effect of unsaturated soil layer. The asymmetric vertical motion may have played a key role in the initiation of the landslide.

References

Bromhead EN (1992) Stability of Slopes, 2nd edn. Surrey University Press, London

Chigira M (1982) Dry debris flow of pyroclastic fall deposits triggered by the 1978 Izu-Oshima-Kinkai earthquake: the "collapsing" landslide at Nanamawari, Mitake-Iriya, Southern Izu Peninsula. J Nat Disaster Sci 4(2):1–32

Chigira M (2011) Survey results of the landslides (in Fukushima and Tochigi prefectures) and earthquake faults (in Fukushima) occurring during the 2011 off the Pacific coast of Tohoku Earthquake. http://www.dpri.kyoto-u.ac.jp/web_j/saigai/tohoku2011/jiban_20110426.pdf

Hata Y, Wang G, Kamai T, Suemine A, Nozu A (2011) Seismic waveform estimation at the Hanokidaira landslide induced by the 2011 off the Pacific coast of Tohoku Earthquake based on site effects substitution method. J Jpn Landslide Soc (in press)

Suzuki M, Kobayashi K, Yamamoto T, Matsubara T, Hukuda J (2004) Influence of shear rate on residual strength of clay in ring shear test. Research Report, School of Engineering, Yamaguchi University, vol 55(2), pp 49–62

Takeshi T (2011) Landslide hazards immediately after the 2011 off the Pacific coast of Tohoku Earthquake and landslides in Shirakawa city, Fukushima. Report on the debriefing session of landslide hazards triggered by the 2011 off the Pacific coast of Tohoku Earthquake, Japan Landslide Society

Tika TE, Vaughan PR, Lemos L (1996) Fast shearing of pre-existing shear zone in soil. Géotechnique 46(2):197–233

Tiwari B, Marui H (2004) Objective oriented multistage ring shear test for shear strength of landslide soil. J Geotech Geoenviron Eng 130(2):217–222

Tobita T, Iai S, Iwata T (2010) Numerical analysis of near-field asymmetric vertical motion. Bull Seismol Soc Am 100(4):1456–1469

Wang G, Sassa K (2009) Seismic loading impacts on excess pore water pressure maintain landslide triggered flowslides. Earth Surf Processes Landf 34(2):232–241

Wang G, Suemine A, Schulz WH (2010) Shear-rate-dependent control on the dynamics of rainfall-triggered landslides, Tokushima Prefecture, Japan. Earth Surf Processes Landf 35(4):407–416

Yang J, Sato T (2000) Interpretation of seismic vertical amplification observed at an array site. Bull Seismol Soc Am 90(2):275–285

Numerical Insights into Mechanisms of Earthquake-Induced Catastrophic Landslides on Gentle Slopes in Liquefiable Soils

39

Aurelian C. Trandafir, Ko-Min Tjok and Xiaoyan Long

Abstract

Catastrophic landslides characterized by large and extremely rapid movements are among the most destructive phenomena associated with failure of slopes during earthquakes. An understanding of the mechanism involved in the occurrence of catastrophic slope failures is of major importance in the process of developing effective mitigation strategies against such geohazards. This paper employs numerical analysis to illustrate two major concepts addressing the geomechanics of catastrophic landslides on gentle slopes in liquefiable soils due to earthquakes. For slope angles less than 20° but greater than about 10°, results from laboratory geotechnical research indicate that the mechanism controlling the high mobility of the slide mass after failure appears to be the gradual loss in shear strength with progressive shear displacement, culminating in ultimate steady state strengths smaller than the static (gravitational) driving shear stress. Numerical results from a dynamic sliding block analysis addressing the seismic performance of a well-documented earthquake-induced catastrophic landslide in Japan are used to illustrate this failure mechanism. Slopes characterized by very mild gradients approaching horizontal ground conditions may experience large landslide movements due to earthquake-induced ground liquefaction as a result of void redistribution and formation of water films in liquefied deposits with continuous low permeability interlayers. A numerical example employing a finite-element scheme for transient seepage coupled with changes in volumetric strains due to excess pore pressure dissipation is used to illustrate the evolution of the water film developed beneath a low permeability interlayer in a liquefied sand deposit.

A. C. Trandafir (✉) · K.-M. Tjok · X. Long
Fugro GeoConsulting, Inc, 6100 Hillcroft Ave,
Houston, TX 77081, USA
e-mail: atrandafir@yahoo.com,
        atrandafir@fugro.com

1   Introduction

Catastrophic landslides characterized by large and extremely rapid movements are among the most destructive phenomena related to failure of slopes during earthquakes. Several catastrophic landslides triggered on gentle slopes (i.e., $\leq 20°$) in liquefiable materials by past earthquakes in Japan have been reported in the literature (e.g., Hamada 1992; Konagai et al. 2003; Matsuo et al. 2002; Sassa 1996; Tohno and Shamoto 1985). An understanding of the catastrophic failure mechanism is of major importance in the process of developing effective mitigation strategies against such geohazards. In the light of published experimental outcomes from laboratory geotechnical research, this paper illustrates using numerical analysis two major concepts addressing the geomechanics of catastrophic landslides on gentle slopes in liquefiable soils due to earthquakes, i.e., the concept of an ultimate shear strength smaller than static driving shear stress and the concept of water film development in liquefied deposits with low permeability interlayers.

2   Ultimate Steady-State Strength Smaller than Static Driving Shear Stress

Experimental results from laboratory monotonic and cyclic undrained shear tests conducted on soil specimens collected from various earthquake-induced catastrophic landslide sites in Japan have been reported in the literature (e.g., Sassa 1996; Trandafir and Sassa 2006). In general, the investigated soils subjected to undrained monotonic shearing demonstrated phase transformation while approaching failure, transitioning from a contractive behavior during the initial stages of deformation to a dilative

behavior prior to failure. Significant excess pore pressure generation and associated shear strength loss was observed during the post-failure shearing stage with progressive shear displacement (e.g., Trandafir and Sassa 2006). Figure 39.1c shows typical features of the shear resistance (τ_r) versus shear displacement (s) relationship measured from such undrained monotonic shear tests. For gentle slopes described by slope angles between $10°$ and $20°$, the gradual loss in shear strength with progressive shear displacement after failure culminated in ultimate steady state (USS) strengths smaller than the static (gravitational) driving shear stress (Trandafir and Sassa 2005), as illustrated in Fig. 39.1c. These experimental results demonstrated the susceptibility of the slide mass to an accelerated motion (i.e., catastrophic failure) if the shear strength loss due to some transient disturbance (e.g., earthquake) was sufficient to definitively bring the shear resistance (τ_r) along the sliding surface below the static driving shear stress (τ_0) acting at the potential sliding surface.

A dynamic displacement analysis of a high mobility translational landslide, i.e., Tsukidate landslide (Fig. 39.1a), triggered by the 26-May-2003 Sanriku-Minami earthquake in Tsukidate town, Miyagi Prefecture, Japan, was undertaken to illustrate the catastrophic landslide mechanism associated with the geotechnical concept described in this section. The landslide with a volume of about $10,000$ m^3 traveled over a horizontal distance of approximately 180 m measured from the main scarp to the toe tip of the displaced material, and the estimated landslide velocity was about 6–7 m/sec (Konagai et al. 2003). Post–earthquake reconnaissance surveys revealed that failure took place in a fully saturated cohesionless soil categorized as silty-sand based on results from laboratory index properties tests (Trandafir and Sassa 2006). Figure 39.1b depicts the features of the

Fig. 39.1 **a** Original slide mass geometry, **b** representative infinite slope model and **c** experimental shear resistance-displacement curve used in the seismic sliding block analysis of May 2003 Tsukidate landslide

$$\ddot{s} = (a - k_y\, g)\ \cos \beta \qquad (39.1)$$

where $\ddot{s}$ represents the relative acceleration in the direction parallel to the sliding surface, β is the infinite slope angle, a is the horizontal earthquake acceleration, g is gravitational acceleration, and k_y is the yield coefficient.

The horizontal yield coefficient for undrained conditions on the sliding surface is given by the following equation:

$$k_y = (\tau_r/\tau_0 - 1) \tan \beta \qquad (39.2)$$

where τ_r is the undrained shear resistance of the soil on the sliding surface.

Equation (39.2) makes use of the shear resistance-displacement relationship from undrained monotonic shear tests (Fig. 39.1c) in order to update the value of the undrained yield coefficient of the sliding mass for a specific value of shear displacement during the earthquake. A step–by–step numerical integration procedure is required to calculate the dynamic displacements, as described by Trandafir and Sassa (2005) and Trandafir et al. (2006).

Figure 39.1c shows the shear resistance-displacement relationship characterizing the undrained shear behavior of the material on the sliding surface of May 2003 Tsukidate landslide, which was used in the dynamic displacement analysis. This relationship was obtained from an undrained monotonic ring shear test conducted on the silty-sand collected from the landslide site, for initial stress conditions at the sliding surface estimated based on the infinite slope characteristics depicted in Fig. 39.1b (Trandafir and Sassa 2004, 2006). Apparently, the data in Fig. 39.1c indicate an ultimate steady state (USS) strength after failure smaller than static driving shear stress, τ_0. In these circumstances, a shear displacement at the end of seismic excitation exceeding the critical level s_0 (Fig. 39.1c) translates into a "catastrophic failure" (Trandafir and Sassa 2005) since the sliding mass is expected to develop an accelerated motion even after the earthquake loading has ceased, due to the static driving shear stress exceeding the undrained shear resistance on the sliding surface (Fig. 39.1c).

equivalent infinite slope model considered in the dynamic displacement analysis of Tsukidate landslide, developed based on the slide mass geometry before failure shown in Fig. 39.1a.

The dynamic analysis employed a modified sliding block formulation developed by Trandafir and Sassa (2004, 2005) that accounts for the sensitivity of the yield acceleration of the slide mass to the amount of earthquake-induced shear displacement along the sliding surface. Assuming the slide mass in Fig. 39.1b as a rigid body in translation, driven downslope by a horizontal seismic force, the equation of motion may be written as

Fig. 39.2 Horizontal earthquake record used in the seismic sliding block analysis of May 2003 Tsukidate landslide

Fig. 39.3 Computed time histories of **a** dynamic displacement and **b** driving shear stress, τ_d, and undrained yield resistance, τ_r, on the sliding surface of May 2003 Tsukidate landslide during earthquake

The seismic performance of the slide mass shown in Fig. 39.1b was investigated for the input horizontal accelerogram depicted in Fig. 39.2. The acceleration data were recorded during the 26 May 2003 Sanriku-Minami earthquake at Mizusawa K-net station (station code IWT011) which has the same epicentral distance as the site of Tsukidate landslide triggered by this seismic event. The particularity of this seismic record compared to other earthquake acceleration data available at almost the same epicentral distance, is related to the site altitude of Mizusawa station (i.e., 44.8 m), which is about the same as the average altitude of Tsukidate landslide site. Therefore, the likely topographic effects affecting the seismic wave at this altitude were captured in the earthquake acceleration data obtained at Mizusawa station.

Figure 39.3a depicts the simulated evolution of the earthquake–induced shear displacement of Tsukidate landslide, whereas Fig. 39.3b illustrates the computed time history of driving shear stress (τ_d) and shear resistance (τ_r) at the sliding surface during the earthquake. As seen in Fig. 39.3a, the deformation experienced by the slide mass attained the critical stage (i.e., $s = s_0$) during the strong ground motion. The damage potential associated with the high landslide mobility after the onset of a catastrophic failure can be inferred by examining the analysis results in Fig. 39.3b indicating that the slide mass has reached a shear displacement of 10 m in about 3.5 s after the critical value, s_0, has been reached, assuming no changes in the topography of the traveling path.

3 Water Film Development in Liquefied Deposits with Low Permeability Interlayers

Liquefiable soil deposits featuring very mild slopes of gradients approaching horizontal ground conditions are typically characterized by undrained ultimate shear strengths greater than the static driving shear stress along the potential sliding surface (e.g., Amini and Trandafir 2008). Therefore, the geotechnical concept discussed in the previous section cannot explain the mechanism of large landslide displacements of the order of meters observed on such slopes. A mechanism which appears to provide a reasonable explanation for the large lateral landslide movements observed on very gentle slopes in liquefied soils is void redistribution due to upward seepage associated with earthquake-induced ground liquefaction.

The hydraulic gradient generated by the excess pore pressure developed in a liquefied soil deposit causes the pore water to migrate

Fig. 39.4 Finite-element computed excess pore pressure dissipation pattern due to transient seepage in a fully liquefied sand deposit with low permeability silt interlayer
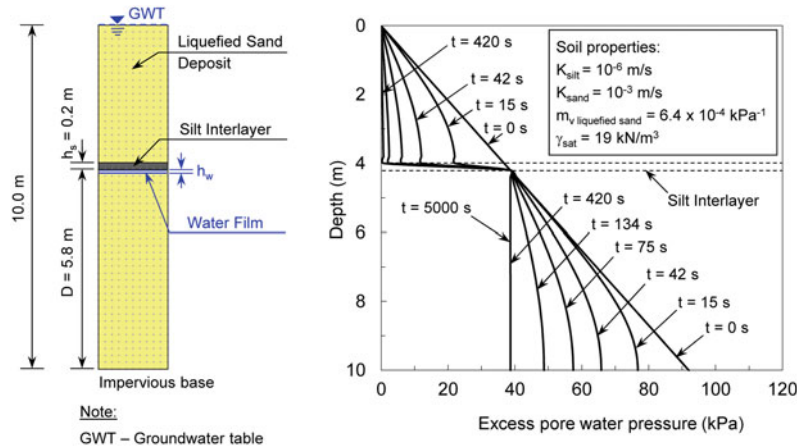
from the lower portion of the deposit upward towards the ground surface. The presence of a low permeability interlayer within the liquefied deposit (e.g., a silt or clay seam) may act as a barrier thus impeding or slowing down the flow of water. This process may result in the accumulation of water and formation of a water film at the upper boundary of the liquefied zone overlain by the lower permeability interlayer, as illustrated in Fig. 39.4. The water film may be regarded as a localized zone of nearly zero shear strength, thereby accommodating large lateral displacements even for very small static (i.e., gravitational) driving shear stresses as encountered on nearly-horizontal slopes. The comprehensive research undertaken by Kokusho (2003) on the void redistribution mechanism provides field evidence of a continuous, low permeability thin interlayer within the liquefied deposit documented at the site of a catastrophic landslide triggered on a nearly-horizontal slope due to the 1964 Niigata earthquake. Additionally, laboratory shaking table test results confirmed the development of water films in layered soil models (Kokusho 2003).

An example of numerical analysis employing a one-dimensional finite-element scheme for transient seepage coupled with changes in volumetric strains due to excess pore pressure dissipation is used in this paper to provide insight into the evolution of the water film developed beneath a low permeability silt interlayer within

a fully liquefied sand deposit. The assumption of one-dimensional vertical seepage is reasonable for the case of a nearly-horizontal ground surface characterizing the very gentle slopes addressed in this section. Figure 39.4 shows the finite-element model of a 10 m- thick liquefied sand deposit with impervious base that comprises a low permeability silt interlayer of thickness $h_s = 0.2$ m, located at a height $D = 5.8$ m from the base of the liquefied sand deposit. The soil properties utilized in the coupled numerical analysis are also provided in Fig. 39.4, and include the saturated unit weight of the soil deposit (γ_{sat}), the coefficient of volume compressibility of liquefied sand ($m_{v \ liquefied \ sand}$), and the saturated hydraulic conductivities of the sand (K_{sand}) and silt (K_{silt}) materials comprising the soil deposit. The earthquake-induced excess pore pressure ratio within the soil deposit at the beginning of the numerical simulation process is assumed to be 100 %, situation corresponding to a fully liquefied soil.

Figure 39.4 illustrates the finite-element computed excess pore pressure profiles throughout the liquefied soil deposit at various times during the transient seepage and associated void redistribution. The portion of the sand deposit located below the silt interlayer attains a steady-state flow condition at a time $t = 420$ s from the beginning of the void redistribution process, as indicated by the constant excess pore

pressure profile corresponding to that time in Fig. 39.4. In the absence of cracks or other natural drainage paths within the soil deposit, the thickness of the generated water film (h_w) can be estimated based on the settlement of the liquefied zone located beneath the low permeability interlayer and the volume of excess pore water dissipated through the low permeability interlayer. As seen in Fig. 39.5, the water film builds up in a first stage to a maximum thickness attained at the same time when the steady-state flow condition is achieved throughout the lower portion of the liquefied sand deposit (Fig. 39.4). Subsequent to that moment, the water film thickness continues to diminish with time until a zero thickness is reached indicating complete dissipation of the water film through the silt interlayer (Fig. 39.5).

The results of a sensitivity study addressing the influence of thickness (h_s), relative position (D) and saturated hydraulic conductivity (K_{silt}) of the low permeability interlayer on the water film evolution are illustrated in Fig. 39.5. Apparently, the relative position of the low permeability interlayer (D) has a major impact on the computed maximum water film thickness. An increase in D from 5.8 to 6.8 m translates into a significant increase in the maximum water film thickness by about 44 %, i.e., from 9 to 13 cm (Fig. 39.5b). A somewhat smaller impact of parameters h_s and K_{silt} can be noted with regard to the computed maximum water film thickness (Fig. 39.5a, c). An increase in h_s from 20 to 60 cm is associated with an increase in the maximum water film thickness by only about 4 %. Likewise, a reduction in the saturated hydraulic conductivity of the silt interlayer by one order of magnitude (i.e., from 10^{-6} to 10^{-7} m/s) resulted in an increase in the maximum water film thickness by only about 8 %. Figure 39.5 also shows the time required to achieve complete dissipation of the water film through the low permeability interlayer after reaching maximum thickness. The computational results indicate that larger h_s and D values as well as lower K_{silt} values translate into lower water film dissipation rates (Fig. 39.5).
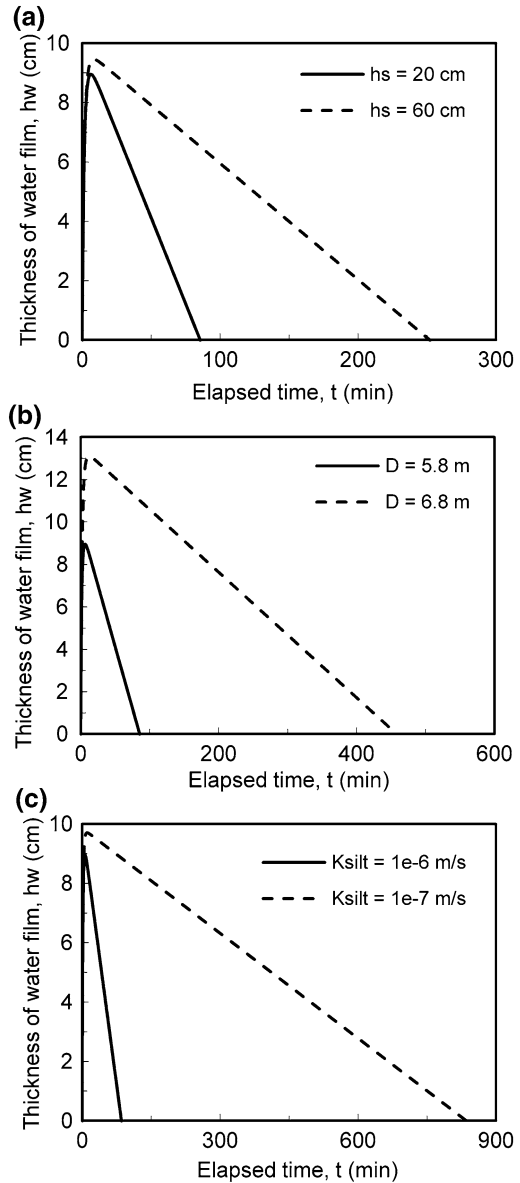
Fig. 39.5 Influence of **a** thickness, h_s, **b** relative position, D, and **c** saturated hydraulic conductivity, K_{silt}, of the low permeability silt interlayer on the water film evolution in a liquefied sand deposit

4 Concluding Remarks

Assessments of the catastrophic failure hazard due to earthquake on gentle slopes in liquefiable soils, characterized by ultimate steady state strengths smaller than the static (gravitational)

driving shear stress, may be performed using dynamic displacement analysis methods that are able to account for the sensitivity of the yield acceleration of the slide mass to the amount of earthquake-induced shear displacement. Nearly-horizontal slopes susceptible to void redistribution phenomena due to earthquake-induced ground liquefaction may be analyzed using numerical schemes for transient seepage coupled with changes in volumetric strains due to excess pore pressure dissipation in order to evaluate the evolution of water films developed beneath low permeability interlayers within the liquefied deposit. This information is useful in the design of mitigation measures such as vertical prefabricated or sand drains used to prevent the development of water films and associated landslide hazard.

References

Amini ZA, Trandafir AC (2008) Postliquefaction shear behavior of Bonneville silty-sand. In: Proceedings of the 4th decennial geotechnical earthquake engineering and soil dynamics conference, Sacramento, California, 18–22 May 2008 (on CD-ROM)

Hamada M (1992) Large ground deformations and their effects on lifelines: 1964 Niigata earthquake. Technical Report NCEER-92-0001, vol 3, pp 1–123

Kokusho T (2003) Current state of research on flow failure considering void redistribution in liquefied deposits. Soil Dyn Earthq Eng 23:585–603

Konagai K, Ito H, Johansson J (2003) Features of Tsukidate landslide mass in the May 26, 2003, South–Sanriku earthquake. In: Proceedings of the 42nd annual conference, Japan Landslide Society, Toyama, Japan, 20–21 August 2003, vol 1, pp 233–236

Matsuo O, Saito Y, Sasaki T, Kondoh K, Sato T (2002) Earthquake-induced flow slides of fills and infinite slopes. Soils Found 42(1):89–104

Sassa K (1996) Prediction of earthquake induced landslides. In: Balkema AA (ed) Proceedings of the 7th international symposium on landslides, Trondheim, Norway, 16–21 June 1996, vol 1, pp 115–132

Tohno I, Shamoto Y (1985) Liquefaction damage to the ground during the 1983 Nihonkai-Chubu earthquake in Akita Prefecture. Nat Disaster Sci 7(2):67–93

Trandafir AC, Sassa, K (2004) Newmark deformation analysis of earthquake-induced catastrophic landslides in liquefiable soils. In: Balkema AA (ed) Proceedings of the 9th international symposium on landslides, Rio de Janeiro, 28 June–2 July 2004, vol 1, pp 723–728

Trandafir AC, Sassa K (2005) Seismic triggering of catastrophic failures on shear surfaces in saturated cohesionless soils. Can Geotech J 42(1):229–251

Trandafir AC, Sassa K (2006) Performance-based assessment of earthquake-induced catastrophic landslide hazard in liquefiable soils. Geotech Geol Eng 24:1627–1639

Trandafir AC, Sidle RC, Kamai T (2006) Mitigation of earthquake-induced catastrophic landslide hazard on gentle slopes by surface loading. In: Proceedings of the INTERPRAEVENT international symposium on "disaster mitigation of debris flows, slope failures and landslides", 25–29 September 2006, Niigata, Japan. Universal Academy Press, Inc., Tokyo, pp 515–521

Effects of Excess Pore Water Pressure on the Displacement of Failed Dip Slopes in 2004 Niigata-Ken Chuetsu Earthquake

40

J. L. Deng, H. Kameya, Y. Miyashita, J. Kuwano, R. Kuwano, J. Koseki and L. Z. Chen

Abstract

The effects of excess pore water pressure on the behavior of earthquake-induced dip slope failure were evaluated by field investigation, laboratory tests and numerical calculation. Two dip slopes which failed in the 2004 Niigata-ken Chuetsu Earthquake were investigated intensively. One is at Yokowatashi, Ojiya, and the other is at Yamakoshi Village (currently Nagaoka City). In both cases, the sliding plane was mainly along a weak thin layer. Laboratory test results showed that excess pore water pressure possibly increased during earthquake and/or during sliding. The displacement calculation was executed by using extended Newmark and Janbu method which considers the effects of irregular geometry of the sliding plane and the excess pore water pressure increase or the strain softening property of the weak layer. The calculation results showed very significant effects of excess pore pressure or strain softening.

J. L. Deng (✉) · L. Z. Chen
Shanghai Jiao Tong University, 800 Dongchuan
Road, Shanghai, 200240, China
e-mail: dengjianliang@gmail.com

H. Kameya
Energy Business Division, OYO Corporation 43
Miyukigaoka, Tsukuba, 305-0841, Japan

Y. Miyashita · J. Koseki
Institute of Industrial Science, the University of
Tokyo 4-6-1 Komaba, Meguro-ku, Tokyo, 153-
8505, Japan

J. Kuwano
Geosphere Research Institute of Saitama University,
255 Shimo-Okubo, Sakura-ku, Saitama 338-8570,
Japan

R. Kuwano
Institute of Industrial Science, the University of
Tokyo 4-6-1 Komaba, Meguro-ku, Tokyo, 153-
8505, Japan

1   Introduction

The Niigata-ken Chuetsu Earthquake on October 23 in 2004, with a main shock of Mj = 6.8, triggered extensive slope failures in Mid Niigata Prefecture, Japan. After the mainshock, many large aftershocks repeatedly struck this area within about two months. According to aerial photo interpretation (MLIT 2005), 3,791 slopes failed with total breakdown volume of about 100×10^6 m^3 over an area of about 1,310 km^2.

Besides the main shock and large aftershocks, the rainfall before the earthquake is likely to have affected the extensive slope failure as well. This area had been subjected to a continuous heavy rainfall, more than 100 mm/day, leading up to 20th October, so the soil was well saturated and the ground water level was raised from the normal level. With saturated soil and higher ground water level, long run-out earthquake-induced slope failures are more likely to occur than under normal conditions (e.g., Kieffer et al. 2006).

Excess pore water pressure generation within a saturated weak layer during the earthquake was studied extensively in many researches (e.g. Sassa et al. 1996). The significant effects of excess pore water pressure on the behavior of earthquake-induced slope failure can be shown by large sliding displacement (e.g. Kazama et al. 2011).

In the present research, case histories on two dip slope failures in the 2004 Niigata-ken Chuetsu Earthquake was performed. One slope failure (Slope 1, for short) located at Yokowatashi, Ojiya City near Shinano River and the other one (Slope 2, for short) at Higashi-Takezawa in Yamakoshi Village (currently Nagaoka City) were investigated. A feature of both failures is that, at the sliding plane, there existed a weak layer. This paper focuses on the generation of excess pore pressure within the weak layer and its effects on the slope displacements.

2   Geometries of Failed Slopes

In Slope 1, the failed slope is 40 m wide and 70 m long with a dip angle of about 22° (Fig. 40.1). The residual displacement estimated at the site is about 53 m at the top part and over 90 m at the toe part (Fig. 40.2)

The field investigation revealed the following features (JSCE 2005):

(a) The sliding plane was within a weak tuff sandy rock layer (Fig. 40.3). Cavities were found in the sandy rock layer in the vicinity of the failed slope.

(b) This weak sandy layer on the sliding plane had been possibly saturated before the earthquake.

In Slope 2, The failed dip slope is about 295 m wide and 350 m long with a dip angle of 18°at the toe region and 24°at the top region of the slope (Figs. 40.4 and 40.5). The residual displacement estimated at the site is about 115 m at the top part and about 80 m at the toe part.

The field investigations revealed the following features (JSCE 2006):

(a) The pre-existing sliding plane was smooth and continuous. The new sliding plan was mainly along the pre-existing one. Neither slickenside nor slickenline was found.

(b) On the exposed pre-existing sliding plane, there was strongly weathered silt rock (Fig. 40.6). At the bottom of this silt rock, a fairly saturated soft sandy silt layer with a thickness of several millimeters was observed. Water was flowing through the observed section. As the ground water level in the sliding mass was higher than the sliding plane at the time of the investigation (Fig. 40.5), it is expected that at least most of the soft sandy silt layer on the sliding plane had been saturated before the earthquake.
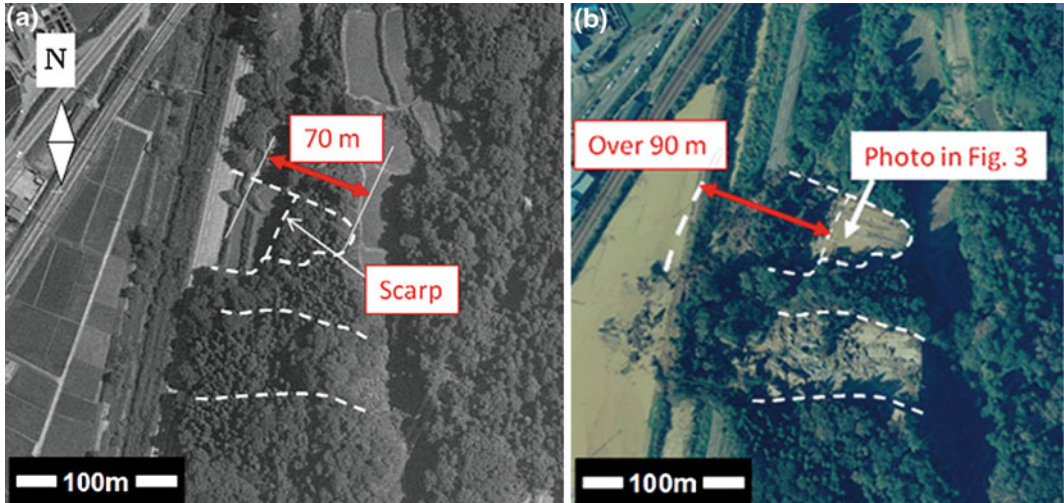
Fig. 40.1 Investigated slope at Yokowatashi site (Slope 1) before and after the earthquake. a) in 1999 b) on 24th October, 2004

Fig. 40.2 Sliding plane obtained by field investigation (Slope 1; after JSCE 2005)
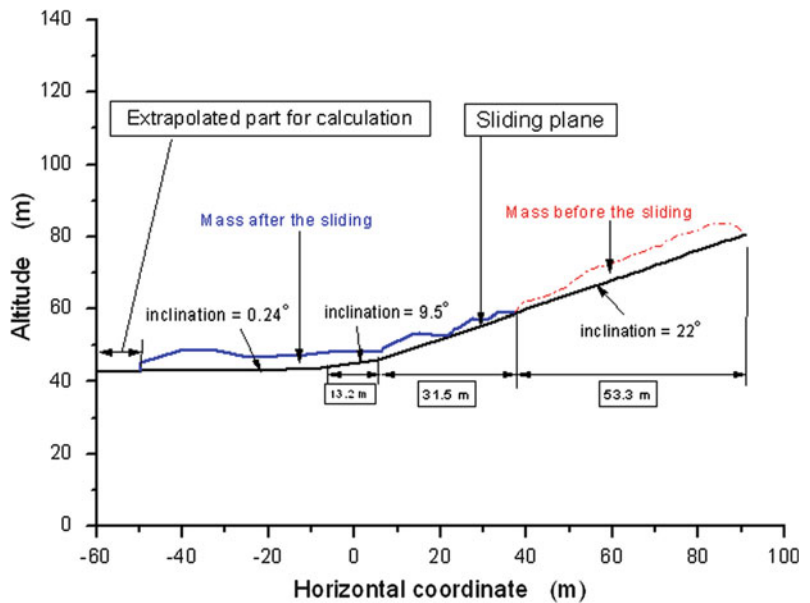
3   Test Results on Excess Pore Water Pressure

For Slope 1, plane strain compression (PSC) tests and triaxial compression (TC) tests were performed on three groups of undisturbed specimens to evaluate the strength of the soils before and during sliding.

Although direct shear tests and ring shear tests are usually conducted in studies on slope failure, triaxial compression tests were performed in this research due to the existence of a sandy layer within which a shear band would be formed. It should be noted that the exact location of the shear band could not be predicted accurately before shear. Direct shear tests and ring shear tests have limitations in investigating the

Fig. 40.3 Sliding plane on the thin sandy layer (Slope 1)
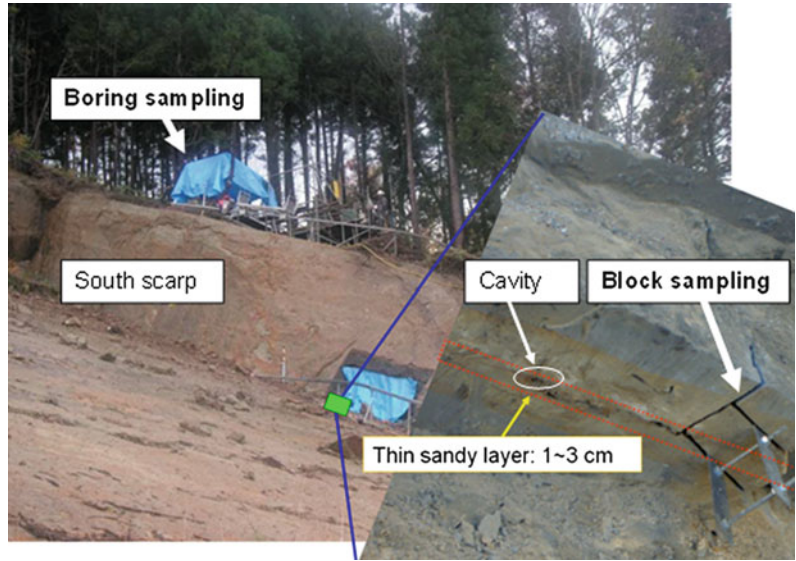
Fig. 40.4 Failed slope at Higashi-Takezawa site (Slope 2; modified from Kokusai Kogyo 2004)
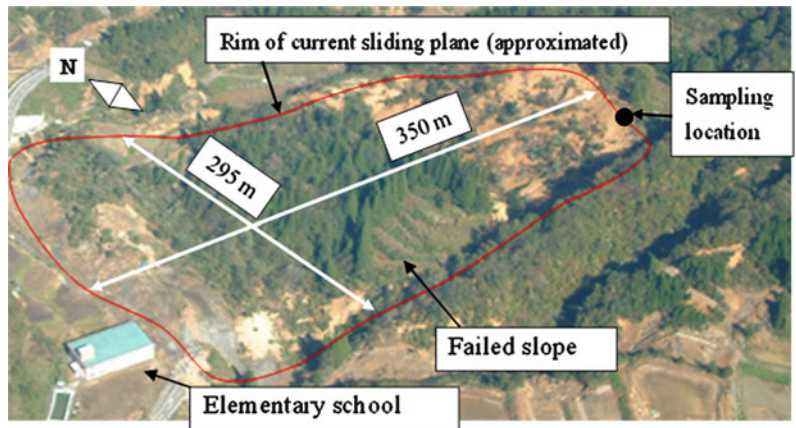
Fig. 40.5 Sliding plane by field investigation. (Slope 2; modified after JSCE 2006and SABO Technical Center 2005)
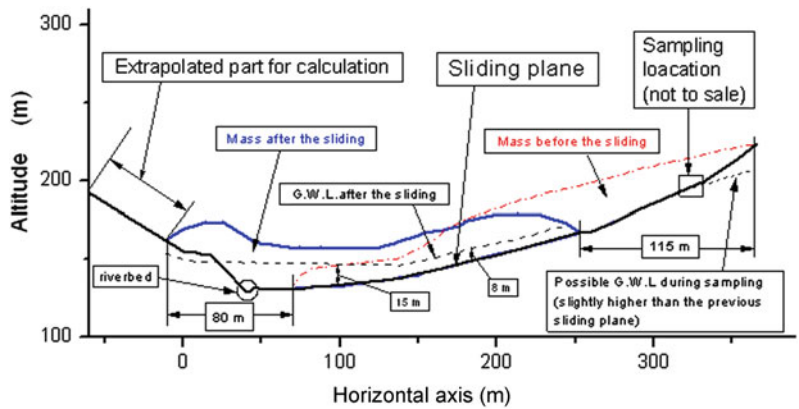
Fig. 40.6 Sketch showing details of the sandy silt layer and its vicinity (Slope 2; by JSCE 2006)
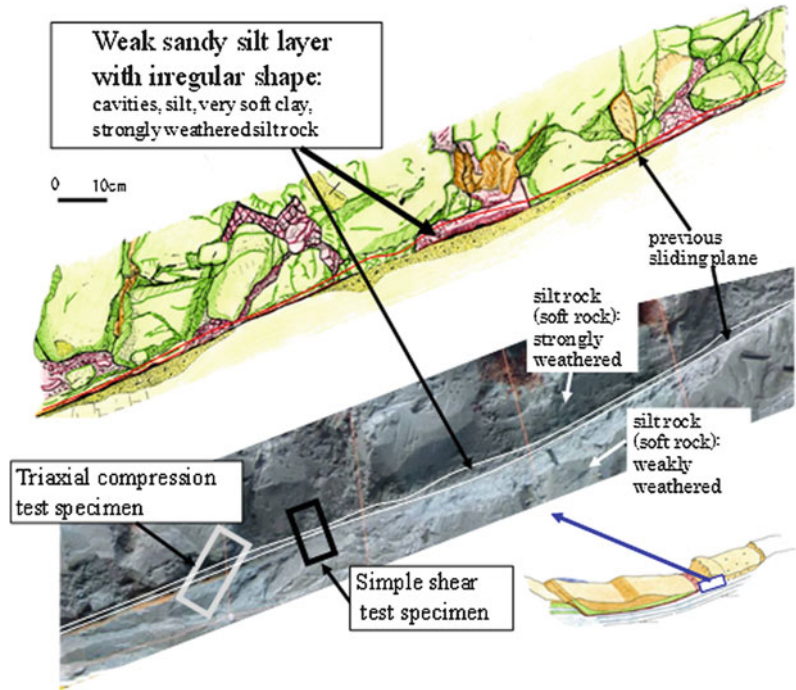
strength of such specimens, because a clear sliding surface should be determined before shear in these tests. On the contrary, in triaxial compression tests, shear band can form without any artificial interference.

The test results revealed the following aspects (refer to Deng et al. 2011a for the details).

The peak strength property mobilized along the saturated sandy ($D_{50} = 0.16$ mm) layer in terms of effective stress was $c' = 0$, $\phi' = 39°$ in plane strain compression tests and triaxial compression tests under saturated conditions.

Full liquefaction did not occur under undrained cyclic loading condition. This may be affected by the system compliance (Deng et al. 2011b) and the exclusion of large cavities in the sandy layer of specimens.

An excess pore pressure ratio, defined as $R_u = \Delta u / \sigma'_{\alpha i}$ (where $\sigma'_{\alpha i}$ is the effective normal stress acting on the sandy layer), was calculated for tests Y-1 and Y-2 respectively (Fig. 40.7). The excess pore water pressure ratio increased to a high level: the R_u value exceeded 0.5 when the shear band can be observed and the failure occurred.

For Slope 2, triaxial compression tests and simple shear tests were performed on undisturbed saturated specimens with the sandy silt layer to evaluate the strength of the weak layer before and during sliding. In order to obtain the strength parameters mobilized on the sliding plane after a long sliding displacement, four simple shear tests (tests S1–S4) were performed on undisturbed specimens.

The test results revealed the following aspects (refer to Deng et al. 2011c for the details).

The specimens had a weak sandy silt ($D_{50}=0.053$ mm) layer, which was 3–32 mm thick, according to the measurements taken after failure. A shear band with an irregular interface formed within this sandy silt layer in all of the triaxial compression tests and simple shear tests. Near the sampling spot, this sandy silt was found predominantly on the current sliding plane.

The peak strength properties that were mobilized along the weak layer, in terms of the effective stress, were $c'=0$ and $\phi' = 36.2°$ in the triaxial compression tests under saturated conditions. The increment in strain induced by undrained cyclic loading under constant deviator

Fig. 40.7 Relationships between effective normal stress and shear stress mobilized on weak layer (Slope 1)
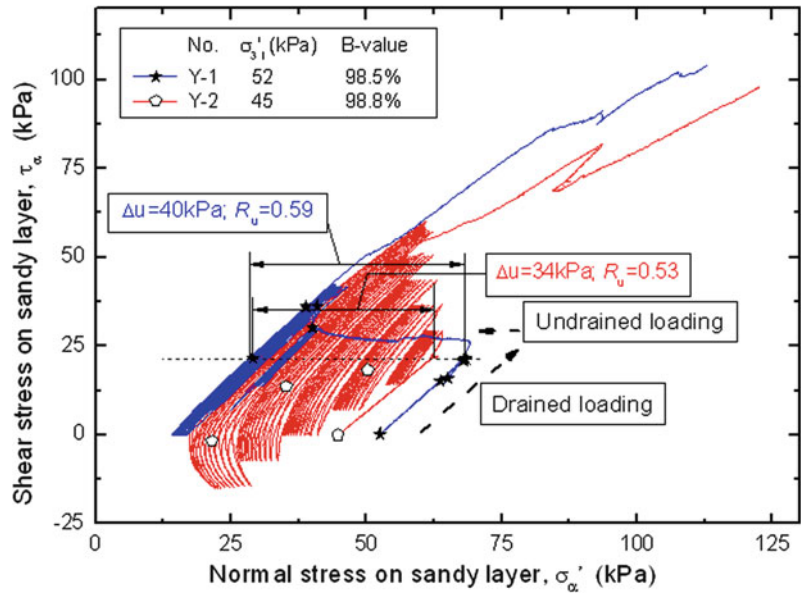
Fig. 40.8 Relationships between effective normal stress and shear stress mobilized on weak layer (Slope 2)
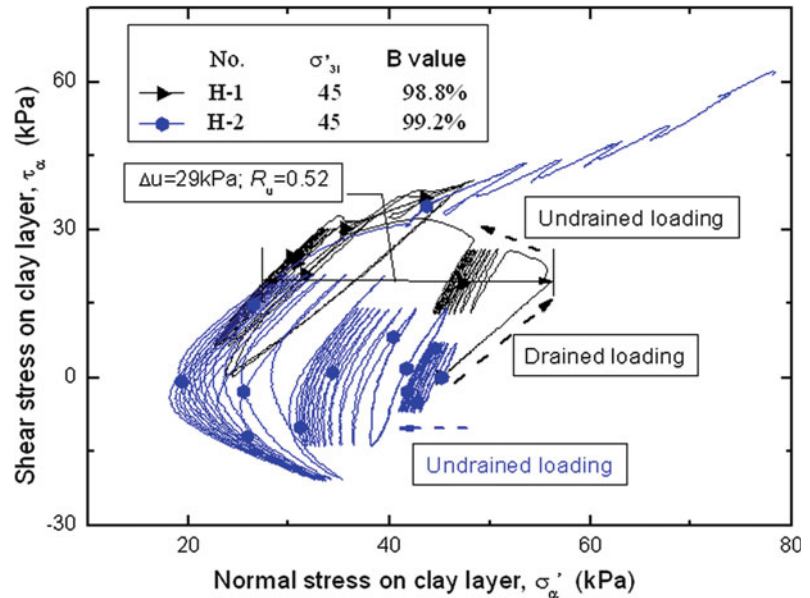
stress amplitude was very limited, and full liquefaction did not occur. However, at the final cyclic loading stage in Test H-1, the excess pore water pressure ratio R_u increased to 0.52 (Fig. 40.8).

Significant strain softening at the large deformation of the weak layer was observed in cyclic simple shear tests under saturated conditions, while keeping the specimen height and the

shear displacement amplitude constant (Fig. 40.9). After the accumulation of the absolute shear displacement increment in each cyclic loading exceeded 60 cm, the value of shear stress ratio τ/σ'_{v0} in terms of the initial effective vertical stress, became nearly constant at 0.296, which corresponded to an apparent friction angle of $\phi = 16.5°$. Such a reduction in the apparent friction angle corresponds to an equivalent R_u

Fig. 40.9 Envelopes for relationships between stress ratio and accumulation of horizontal displacement (Slope 2)
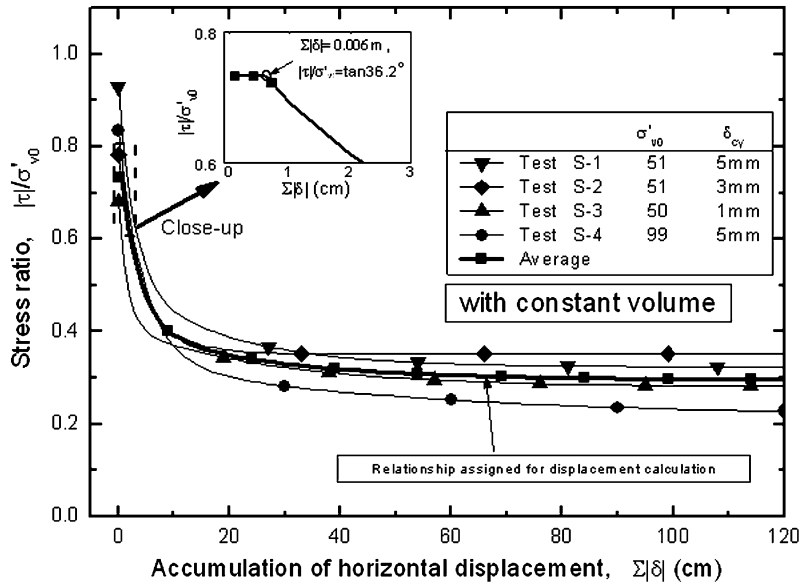
value of 0.60 (=$1-\tan 16.5°/\tan 36.2°$). The difference between the equivalent R_u value in cyclic simple shear tests and the R_u value in undrained triaxial compression tests with cyclic loading is found to be small.

In the above two cases with the two types of tests, the maximum R_u value was over 0.5. The large excess pore pressure is possibly related to the loose state of weak layers as observed in the field investigation.

4   Displacement Calculation by Considering Excess Pore Water Pressure

Extended Newmark and Janbu method was used to evaluate the displacement of the two slopes. In this method, the sliding mass is divided into multiple blocks. In the present study, it was made by employing several vertical slices, while assuming that all the slices share a common horizontal velocity. In the calculation, first, the value of yield seismic coefficient K_y is calculated. Fundamentally, the procedure to calculate K_y is based on the original Janbu method, while a modification is made by considering the effects of earthquake inertia force and excess pore water pressure. Second, after the K_y value has been

obtained, horizontal displacement is obtained by following the procedure of Newmark's sliding block method (Newmark 1965). Therefore, the above procedure is an extended version of the combination of Newmark and Janbu methods (named as extended NJ method). Refer to Deng et al. (2010) for the details of the calculation procedure.

It should be noted that the angle of sliding plane for each slice may change with the slope displacement. Generally, it induces an increase in the values of the yield seismic coefficient K_y because the sliding plane becomes flatter after undergoing a certain displacement (e.g., Stamatopoulos et al. 2011).

As the input ground acceleration, a strong motion record at Ojiya Station (EW component), which is located 4 km away from the failed slope (NIED 2004), is employed as shown in Fig. 40.10. The effects of possible amplification of the seismic response of the slope are not considered in this study. The time interval of ground acceleration history is 0.01 s.

Two different values of R_u are employed: $R_u = 0.55$ (Case 1-1) as mentioned before, and $R_u = 0$ (Case 1-2) for comparison.

The cross-section obtained by field investigation (JSCE 2005) was used in the analysis. The strength parameters of the sandy layer

Fig. 40.10 Yield seismic coefficient history (Slope 1; Earthquake motion recorded by NIED 2004)
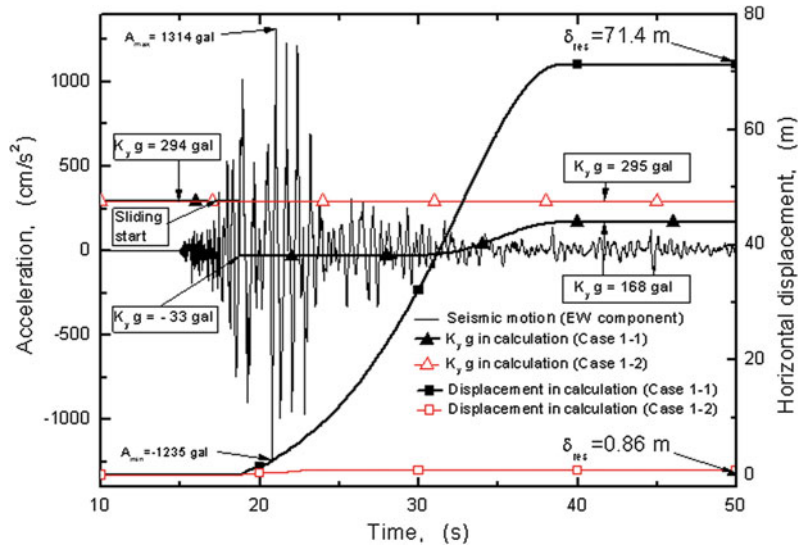
Fig. 40.11 Ground acceleration (JMA 2004) and typical calculation result on time history of yield seismic coefficient (Slope 2)
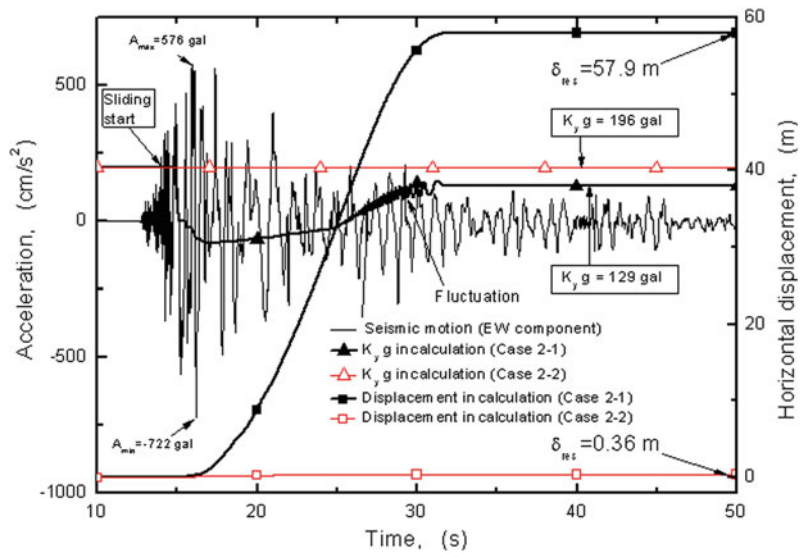
obtained from the laboratory test results: $c' = 0$, $\phi' = 39°$ were used. The material densities are set as: $\rho = 1.73$ g/cm^3 (for soil), $\rho_w = 1.0$ g/cm^3 (for water). Vertical slices were used in the analysis. The width of each slice (b_i) was about 1 m. The ground water level was set on the sliding plane.

Figure 40.10 shows the calculated K_y and displacement. With $R_u = 0.55$, the calculated K_y value becomes negative, which induces an accelerated sliding. On the contrary, if the effect

of excess water is not considered (Case 1-2), K_y remains positive during the whole sliding process and the residual displacement is quite limited ($\delta_{res} = 0.86$ m). The calculated residual displacement with $R_u = 0.55$ ($\delta_{res} = 71.4$ m) are similar to the actual displacement which is about 53 m at the top part and over 90 m at the toe part, as mentioned previously.

Similarly, for Slope 2, the input ground acceleration was an EW component of strong motion record (Fig. 40.11, after JMA 2004) at

Takezawa Station, which is located 3 km away from the failed slope. The effects of possible amplification of the seismic response of the slope are not considered in this study. The time interval of the acceleration is 0.01 s.

The cross-section obtained by field investigation (Fig. 40.5) was used in the analysis. The strength parameters of the sandy silt layer obtained from the TC test results: $c = 0$, $\varphi' = 36.2°$ were used. The material densities are set as: $\rho = 1.89$ g/cm^3 (for soil), $\rho_w = 1.0$ g/cm^3 (for water). Vertical slices were used in the analysis. The width of each slice (b_i) was about 1 m. The ground water level is set to be 12 m above the sliding plane.

For the apparent friction angle mobilized on the sliding plane, according to the results from TC tests and simple shear tests, the following conditions are assigned (Case 2-1):

$$\varphi = 36.2° \quad \text{(if } \delta < 0.006 \text{ m)}$$

and

$$\varphi = \arctan$$

$$\times \left(\begin{array}{c} 0.29623 + 0.12455 \times \exp\left(-\dfrac{\delta \times 100}{23.19425}\right) \\ +0.38174 \times \exp\left(-\dfrac{\delta \times 100}{3.14084}\right) \end{array} \right) \times \dfrac{180°}{\pi}$$

(if $\delta \geq 0.006$ m) where δ is a computed horizontal displacement of the slope with a unit of meter. When the δ value becomes extremely large, the φ value approaches to 16.5°. The above relationship is shown in Fig. 40.9, after converting the apparent friction angle into the shear stress ratio.

For comparison, another calculation (Case 2-2) was conducted, where the effect of excess water is not considered (i.e., $\varphi \equiv 36.2°$) under otherwise the same conditions as in Case 2-1.

The reduction in the apparent friction angle induces a decrease in the yield seismic coefficient K_y, while the value of K_y is affected by the shape of sliding plane. As shown in Fig. 40.11, due to the gradual decrease in the apparent friction angle, the value of K_y decreased when sliding started in Case 2-1. However, it increased in the subsequent stage of sliding due to the change of

the geometry of the sliding plane, including the inverse slope that appears on the left hand side of Fig. 40.5. On the other hand, in Case 2-2, such decrease in K_y did not occur since the apparent friction angle is set to be constant; the significant increase in K_y did not occur, either, since sliding mass did not reach the inverse slope.

The δ_{res} value evaluated in Case 2-1 is 0.36 m, which is significantly smaller than the residual displacement estimated at the site (Fig. 40.5). This is caused by the assumption employed in Case 2-1 that the material exhibited a much higher strength than the actual one.

It should be noted that the calculation method which can consider the change of geometry of sliding plane in sliding is necessary in obtaining rational displacement calculation results. Otherwise, the calculated displacement may become infinitely large due to the effect of large reduction of the apparent friction angle or large R_u value.

5 Conclusions

In order to evaluate the effect of excess pore water pressure on the displacement of dip slopes which failed in earthquake, the field investigation, laboratory tests and numerical calculation were performed on two dip slopes. The results can be summarized as follows:

(1) In Slope 1, the sliding plane is on a weak sandy layer which was several millimeter to 50 mm thick with a good continuity according to the measurement after failure. The sandy layer is deeply weathered tuff rock with many cavities. In Slope 2, on the exposed pre-existing sliding plane, there was strongly weathered silt rock. At the bottom of this silt rock, a fairly saturated soft sandy silt layer with a thickness of several millimeters was observed. Cavities were observed in the soft sandy silt layer.

(2) Both in cyclic triaxial tests and cyclic simple shear tests on undisturbed specimens retrieved from the two slopes, the maximum value of the measured excess pore water pressure ratio R_u or its equivalent value based on the measured reduction in the mobilized internal friction angle exceeded 0.5. These properties are

possibly related to the loose state of the weak layers as observed in the field investigation.

(3) A new method was applied to evaluate the effect of excess pore water pressure on the earthquake-induced displacement. In this method, the Janbu method for slope stability analysis and Newmark's sliding block method for displacement computation are combined. By using the parameters that were assigned based on the results from the laboratory tests and field investigations, the calculated displacements became similar to the actual measurements. However, if the effect of excess pore water pressure was not considered, the calculation underestimated largely the displacements.

References

Deng JL, Tsutsumi Y, Kameya H, Koseki J (2010) A modified procedure to evaluate earthquake-induced displacement of slopes containing a weak layer. Soils Found 50(3):413–420

Deng JL, Kameya H, Tsutsumi Y, Sato T, Kuwano J, Kuwano R, Koseki J (2011a) Study on a failed dip slope in 2004 Niigata-ken Chuetsu Earthquake. Eng Geol 123(4):302–314

Deng JL, Miyashita Y, Kameya H, Sato T, Kuwano R, Koseki J (2011b) Effects of system compliance on liquefaction behavior of thin sandy layer in undrained cyclic triaxial test. Soils Found 51(3):549–558

Deng JL, Kameya H, Tsutsumi Y, Kuwano J, Kuwano R, Koseki J (2011c) Study on slope failure at Higashi-takezawa induced by 2004 Niigata-ken Chuetsu earthquake. Soils Found 51(5):929–943

Japan Meteorological Agency (JMA) (2004) http://www.seisvol.kishou.go.jp/eq/kyoshin/jishin/041023_niigata/1756/dat/EA231755_65041.ac

Japan Society of Civil Engineering (JSCE) (2005) Report on boring and sampling investigation at Chuetsu on creation of a comprehensive data archive, Project earthquake damage in active-folding areas: creation of a comprehensive data archive for remedial measures for civil-infrastructure systems, pp 2_1–2_72 (in Japanese)

Japan Society of Civil Engineering (2006) Report on boring and sampling investigation at Chuetsu on creation of a comprehensive data archive, Project earthquake damage in active-folding areas: creation of a comprehensive data archive for remedial measures for civil-infrastructure systems, pp 2_1–2_47 (in Japanese)

Kazama M, Mori T, Kabuki H, Matsui T (2011) Sliding analysis of the Aratosawa Landslide generated in the Iwate-Miyagi Nairiku Earthquake in 2008. J Japan Assoc Earthquake Eng 11(5):68–79

Kieffer DS, Jibson R, Rathje EM, Kelson K (2006) Landslides triggered by the 2004 Niigata Ken Chuetsu, Japan, earthquake. Earthquake Spectra 22(S1):s47–s73

Kokusai Kogyo (2004) http://www.kk-grp.jp/csr/disaster/200410_niigata_eq/n/09.html

Ministry of Land, Infrastructure and Transport (2005) Information on the Chuetsu Earthquake. http://www.mlit.go.jp/kisha/kisha05/05/050113.html (in Japanese)

National Research Institute for Earth Science and Disaster Prevension of Japan (NIED) (2004) http://www.k-net.bosai.go.jp/k-net/quake/

Newmark NM (1965) Effects of earthquakes on dams and embankments. Geotechnique 15(2):139–160

Sassa K, Fukuoka H, Scarascia-Mugnozza G, Evans S (1996) Earthquake-induced landslides: distribution, motion and mechanisms, Soil Found, Special Issue on the 1995 Hyogo-ken Nambu Earthquake, pp 53–64

SABO Technical Center (2005), A business report on the examination of countermeasure for landslides at Terano and Higashi-Takezawa in 2004. (in Japanese)

Stamatopoulos CA, Mavromihalis C, Sarma S (2011) Correction for geometry changes during motion of sliding-block seismic displacement. J Geotech Geoenviron Eng 137(10):926–938

Velocity-Displacement Dependent Friction Coefficient and the Kinematics of Giant Landslide

41

Jia-Jyun Dong, Che-Ming Yang, Wei-Lun Yu, Chyi-Tyi Lee, Yuki Miyamoto and Toshihiko Shimamoto

Abstract

Friction characteristics on the sliding surface of giant landslide is important for investigating the triggering, moving, and deposition. In this research, we incorporating a velocity-displacement dependent friction law into the Newmark method to predict the kinematics of a giant landslide. The parameters of the friction law are determined from the high velocity rotary shear experiments of shale and the fault gouge collected from the Tsaoling landslide site triggered by Chi–Chi earthquake in 1999. Based on the strong ground motion data and the account of a survivor, the proposed approach is validated. It is concluded that the Newmark method incorporating into a velocity-displacement dependent friction law can be used to precisely reproduce the detachment, rapid moving, and long run-out of a giant landslide.

Keywords

High velocity rotary-shear test · Giant landslide · Kinematic · Frictional coefficient

J.-J. Dong (✉) · C.-M. Yang · W.-L. Yu · C.-T. Lee
Graduate Institute of Applied Geology,
National Central University, 300, Jhongda Rd,
Jhongli, Taoyuan 32001, Taiwan
e-mail: jjdong@geo.ncu.edu.tw

Y. Miyamoto
Department of Earth and Planetary Systems
Science, Graduate School of Science, Hiroshima
University, Japan

T. Shimamoto
State Key Laboratory of Earthquake, Dynamics,
Institute of Geology, China, Earthquake
Administration, Beijing, China

1 Introduction

Giant landslides frequently induced catastrophic hazard. Key issues to mitigate the related hazard are to predict the process of triggering, moving, and deposition of the unstable mass. Among others, the strength (e.g., equivalent friction angles and cohesive strengths) on the sliding plane play the crucial role on the kinematics of landsliding.

The 1999 Chi–Chi earthquake triggered several giant landslides in central Taiwan. Many researchers attempted to explore the kinematics of these landslides (Chen et al. 2003; Chang et al. 2005; Dong et al. 2009; Tang et al. 2009; Kuo et al. 2009; Miyamoto et al. 2009; Yano et al. 2009). The results indicating the fast moving and long run-out of the giant landslides is dominated by the strength weakening on the slip surface after large displacement of the moving mass with high velocity. These results also highlighted the importance for determining the displacement/velocity dependent frictional coefficient of sliding surface experimentally.

Early attempts for determining the frictional coefficient of rock or gouge materials experimentally in laboratory were mainly focused on discovering the puzzle related to the fault dynamics (e.g., Shimamoto and Tsutsumi 1994; Tsutsumi and Shimamoto 1996, 1997; Hirose and Shimamoto 2005; Di Toro et al. 2006; Mizoguchi et al. 2007; Han et al. 2007). Recently, the high-velocity rotary-shear frictional testing apparatus were utilized to study the fast moving and/or long run-out behaviors of the giant landslides (Ferri et al. 2010; Yano et al. 2009; Miyamoto et al. 2009). The kinematics of these studied landslides could be qualitatively depicted. However, quantitatively calculating the time history of a large, fast moving mass is still a challenge.

In this study, Newmark displacement analysis is utilized to calculate the time history of the displacement, velocity, and acceleration of a sliding mass triggered by earthquake. The required velocity/displacement dependent friction law on sliding surface is derived from the high-velocity rotary-shear frictional testing apparatus. Accordingly, the frictional coefficient on the sliding surface will evolve with the displacement and velocity of the moving mass. The information reported (from survivor and records of the strong motion station nearby) of the largest landslide triggered by the 1999 Chi–Chi earthquake—Tsaoling landslide—was used to validate the model. The detached time of the rock mass and the time required to hit the Mt. Daogiaoshan on the opposite valley are calculated and compared with the reported data.

2   Methods

2.1   High Velocity Rotary-Shear Frictional Test

Bedding parallel fault gouge and grinded shale, which is probable candidates of sliding materials, were sampled and tested utilizing the high-velocity rotary-shear testing apparatus. The frictional coefficients of these materials were measured under a normal stress (σ_n) of 3 MPa with different slip velocities. The normal stress applied roughly equals to the overburden of a mass with 150 m in thickness. An equivalent slip velocity (V) (Shimamoto and Tsutsumi 1994) is used to analogize the shear velocity on the sliding surface. The tested materials were sandwiched by a pair of solid-cylindrical Belfast gabbro with 25 mm in diameter. The end of the cylinders was ground with the #80 silicon carbide abrasive. Hollow-cylindrical Teflon sleeve was used to hold the testing materials between two cylinders. The weight of the testing materials is about 1 g. Water is added into the samples to keep the water content (w) equals to the nature water content of the gouge in situ. The testing conditions are listed in Table 41.1. The details for preparing the samples can be found in Miyamoto et al. (2009).

2.2   Velocity-Displacement Dependent Friction Law

Figure 41.1 shows the evolution of frictional coefficient with shear displacement (d) under high-velocity rotary-shear condition. The frictional coefficient attains peak (μ_p) only within small shear displacement. The frictional coefficient drops subsequently after the peak and

Table 41.1 Rotary-shear test conditions and tested materials

	Fault gouge	Shale powder
V	$0.22 \sim 1.3$ m/s	$0.22 \sim 1.3$ m/s
σ_n	3 MPa	3 MPa
w	~ 25 %	~ 25 %

Fig. 41.1 Schematic diagram of shear displacement-dependent friction law

approaches a steady-state value (μ_{ss}) with increasing shear displacement. D_c is a shear-weakening distance defined as the shear displacement with a 95 % reduction from peak value to steady-state value. This shear displacement weakening phenomenon can be described by a velocity-displacement dependent friction law (Mizoguchi et al. 2007; Togo et al. 2009) as follows:

$$\mu(d, V) = \mu_{ss}(V) + \left(\mu_p - \mu_{ss}(V)\right) \exp\left(\ln(0.05)^{d}/_{D_c}\right) \tag{41.1}$$

The velocity dependent steady-state frictional coefficient $\mu_{ss}(V)$ can be expressed by:

$$\mu_{ss}(V) = \mu_{ss}|_{v=\infty} + \left(\mu_p - \mu_{ss}|_{v=\infty}\right) \exp\left(-^{V}/_{V_c}\right) \tag{41.2}$$

where the frictional coefficient $\mu_{ss}|_{v=\infty}$ is defined as the steady-state frictional coefficient when the shear velocity approaches to infinite and V_c is a material constant. The shear-weakening distance D_c is function of normal stress and velocity (Mizoguchi et al. 2007). In this research, the normal stress remains constant and D_c can be calculated by

$$D_c(V)\,(m) = a \cdot \left(V^b\right)(m/s), \tag{41.3}$$

where a and b are material constants.

2.3 Newmark Displacement Analysis

Newmark (1965) proposed a procedure for evaluating potential deformations of an embankment

dam due to earthquake shaking. When the earthquake produces an acceleration greater than the critical acceleration of the sliding mass, the mass will start to move. The velocity of the mass can be derived from integrating the acceleration larger than the critical one. The permanent displacement of the sliding mass can be obtained by integrating the velocity of the mass. Traditionally, the critical acceleration is a constant which can be express as the function of the friction angle on the sliding surface. Dong et al. (2009) suggested that the critical acceleration could be function of the sliding mass velocity. We here incorporate the velocity-displacement dependent friction law (Eqs. (41.1, 41.2, 41.3) into the Newmark sliding block analysis. The time history of the moving block can therefore be calculated.

3 Results

3.1 Shear Velocity/Displacement Dependent Frictional Coefficient

The results of the rotary-shear test are shown in Fig. 41.2a, b. Solid lines in Fig. 41.2a, b are the frictional coefficients of gouge and shale powder, respectively, under different shear velocity. Eq. (41.1) is then used to fit the experimental results, which are indicated by the dashed lines.
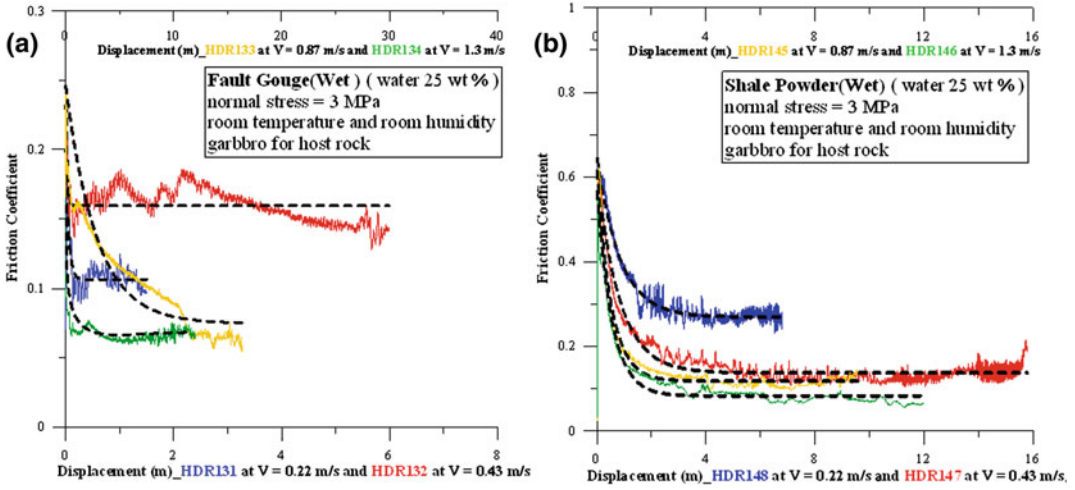
Fig. 41.2 Experimental results of (**a**) fault gouge, and (**b**) shale powder under different shear velocity (*solid lines*). The curve fitting results from Eq. (41.1) are indicated by *dashed lines*
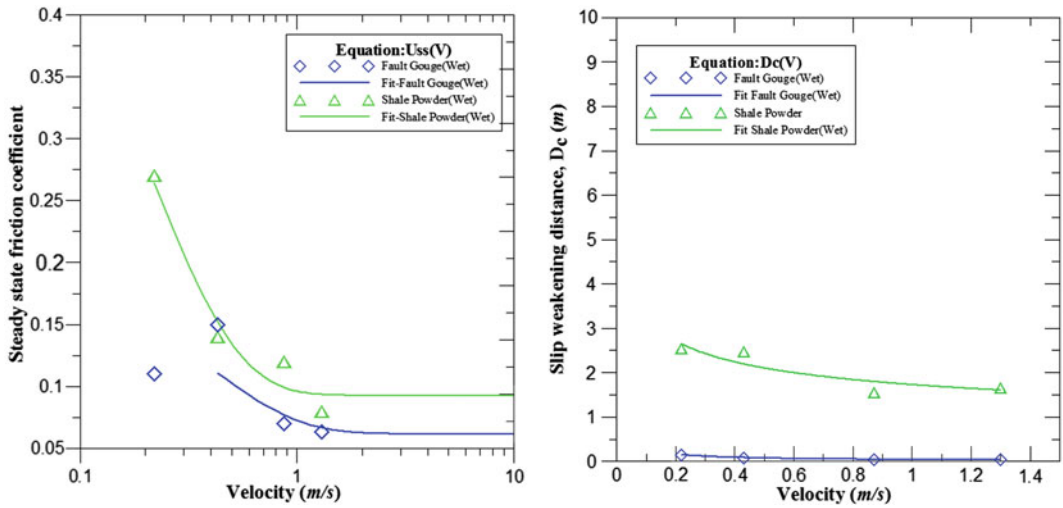
Fig. 41.3 Parameters calibration of Eq. (41.2) and (41.3). (**a**) Curve fitting to derive the and and (**b**) Curve fitting to derive the constants a and b

Table 41.2 Calibrated parameters of the shear velocity/displacement dependent frictional coefficient

	μ_p	$\mu_{ss}|_{v=\infty}$	$V_c (m/s)$	a, b
Fault gouge	0.22	0	0.994	a = 5.65, b = −2.91
Shale powder	0.61	0.093	0.198	a = 1.73, b = −0.28

The peak frictional coefficients of different velocity are averaged.

Next, we calibrated the parameters $\mu_{ss}|_{v=\infty}$ and V_c in Eq. (41.2), respectively (Fig. 41.3a). The peak frictional coefficient μ_p is assumed as a velocity independent constant and an averaged value is used. Finally, the parameters of the velocity dependent shear-weakening distance $D_c(V)$ in Eq. (41.3) are calibrated (Fig. 41.3b). The calibrated parameters of the tested materials are listed in Table 41.2.
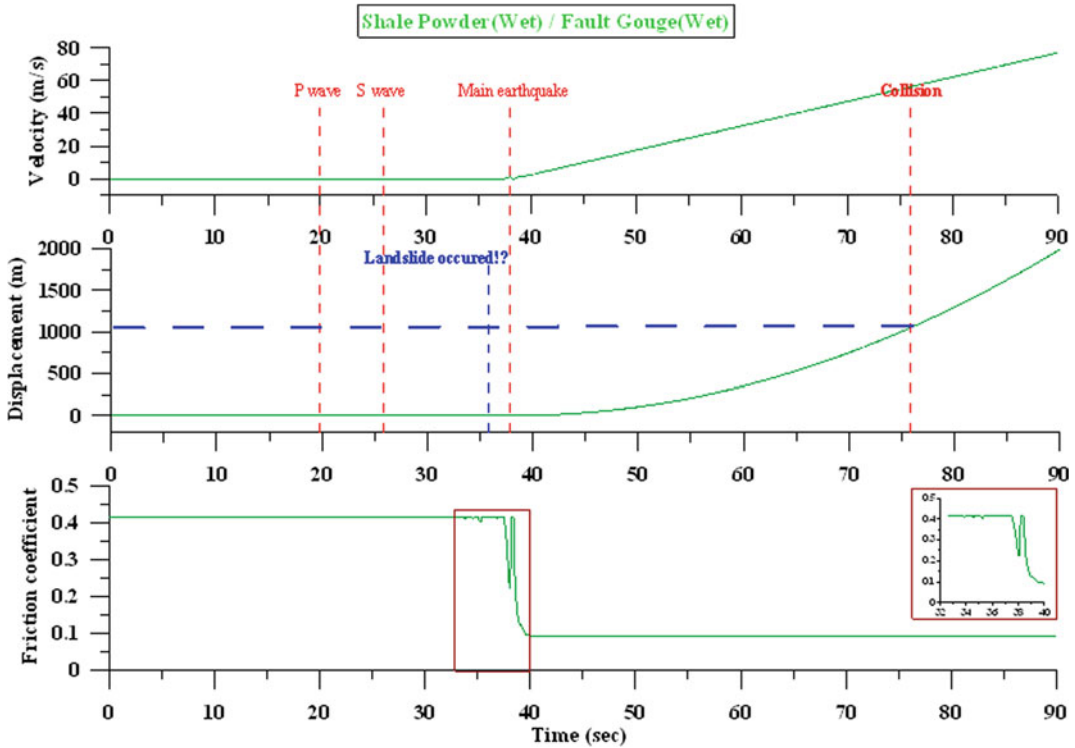
Fig. 41.4 The calculated velocity and permanent displacement of the sliding mass triggered by the Chi–Chi earthquake, as well as the frictional coefficient on the sliding surface predicted by the shear velocity/displacement dependent friction law

3.2   Kinematics of the Moving Mass (Newmark Method Incorporating the Friction Law)

Based on the field works, the sliding surface is probably constituted with discontinue bedding parallel faults and bedding plane of shales. The averaged peak frictional coefficient of fault gouge and shale powder ($\sim$0.415) is utilized to derive the initial critical acceleration. Since the experimental results of the shale powder and the bedding-parallel fault gouge are quite similar after the peak value, the parameters of shale powder are used to calculate the kinematics of sliding mass.

Figure 41.4 shows the calculated velocity and permanent displacement of the moving mass, as well as the evolving frictional coefficient on the sliding surface predicted by the shear velocity/displacement dependent friction law. The initial frictional coefficient on the sliding surface is 0.415. The frictional coefficient decreased with increasing velocity and displacement. The lowest frictional coefficient is about 0.093 which equals to $\mu_{ss}|_{v=\infty}$ of the shale powder.

There is a strong motion station near the Tsaoling landslide site (with a distance less than 500 m) and a complete seismic record was available. Meanwhile, a survivor is still alive after the landslide "fly" across the valley. The survivor reported that the sliding happened at about 10 s after "strong shaking" (10 s after the S wave is indicated by a blue dotted line in Fig. 41.4). This time (36 s) is close to the modeled detached time where the frictional coefficient began decreasing (about 38 s). Kuo et al. (2009) observed unusual high frequency signals at t = 75.8 s and lasting for about one second (the red line in Fig. 41.5) on CHY080 during the Chi–Chi earthquake. The travel distance predicted by the proposed model is 1,048 m at t = 75.8 s, which is very close to the distance between the source area of Tsaoling

Fig. 41.5 Vertical acceleration recorded by the station CHY080 during Chi–Chi earthquake (modified from Kuo et al. 2009)
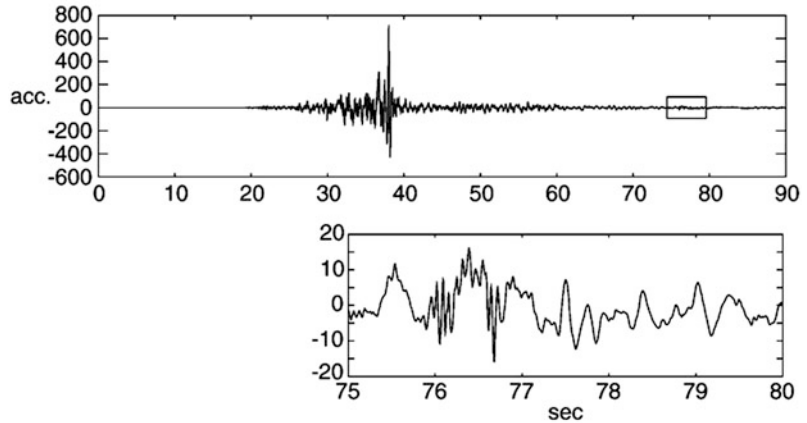
landslide and the Mt. Daogiaoshan (about 1,100 m). The result shows that a simple rigid block model incorporating a velocity/displacement friction law derived from rotary- shear tests depicts the kinematics of Tsaoling landslide successfully.

4   Discussion and Conclusions

This research tries to predict the kinematics of Tsaoling landslide phenomenologically. Hung (2000) speculated that there might exist an air cushion under the sliding mass of Tsaoling landslide triggered by the 1999 Chi–Chi earthquake. Other possible explanations for dynamic weakening of giant landslides are discussed. Lin et al. (2001) found pseudotachylite on the sliding surface of Jiufengershan area triggered by Chi–Chi earthquake. He conjectures that the frictional heat plays an important role during sliding. Ferri et al. (2010) suggested thermal pressurization of pore fluid in the clay-rich gouge is one of the possible mechanisms responsible for dynamic weakening of landsliding. Thermal decomposition may induce dynamic weakening (Han et al. 2007). However, direct evidence indicating the mechanism involved is difficult to be discovered during rapid sliding of a giant landslide.

Although the mechanisms dominating the rapid and long run-out of a giant landslide are vague, this study suggests that the velocity-displacement dependent friction law could be used to precisely determine the kinematics of the giant landslides. For the Tsaoling case, the peak strengths of the bedding plane of shales and that of the bedding-parallel fault contribute to the triggering of sliding during earthquake. To estimate representative peak strength of the sliding surface is still a challenging issue. Relatively, the experimentally determined low steady-state frictional coefficient (~ 0.1) is similar for bedding parallel fault gouge or shale powder. That is, the kinematics of the sliding mass is not sensitive to the material on the sliding plane for Tsaoling case. Notably, the high-velocity rotary-shear tests are kind of total stress approach for the generation of the excess pore pressure can not be evaluated. Three bullet point of this research are summarized as follows:

(1) The Newmark method incorporating into a velocity- displacement dependent friction law can be used to precisely reproduce the detachment, rapid moving, and long run-out for the Tsaoling landslide.

(2) The extremely low steady-state frictional coefficient on the sliding surface (~ 0.1) contributes to the rapid moving and long run-out of the Tsaoling landslide.

(3) The mechanisms involved in the friction behavior of the rapid sliding materials are

still vague and need to be studied in more
detail in the future.

References

Chang KJ, Taboada A, Lin ML, Chen RF (2005)
  Analysis of landsliding by earthquake shaking using
  a block-on-slope thermo-mechanical model: example
  of Jiufengershan landslide, central Taiwan. Eng Geol
  80:151–163
Chen TC, Lin ML, Hung JJ (2003) Pseudostatic analysis
  of Tsao-Ling rockslide caused by Chi–Chi earth-
  quake. Eng Geol 71:31–47
Di Toro G, Hirose T, Nielsen S, Pennacchioni G,
  Shimamoto T (2006) Natural and experimental
  evidence of melt lubrication of faults during earth-
  quakes. Science 311:647–649
Dong JJ, Lee WR, Lin ML, Huang AB, Lee YL (2009)
  Effects of seismic anisotropy and geological charac-
  teristics on the kinematics of the neighboring Jiuf-
  engershan and Hungtsaiping landslides during Chi–
  Chi earthquake. Tectonophysics 466:438–457
Ferri F, Di Toro G, Hirose T, Shimamoto T (2010)
  Evidence of thermal pressurization in high-velocity
  friction experiments on smectite-rich gouges. Terra
  Nova 22:347–353
Han R, Shimamoto T, Hirose T, Ree JH, Ando J (2007)
  Ultra-low friction of carbonate faults caused by
  thermal decomposition. Science 316:878–881
Hirose T, Shimamoto T (2005) Growth of molten zone as
  a mechanism of slip weakening of simulated faults in
  gabbro during frictional melting. J Geophys Res
  110:B05202. doi:10.1029/2004JB003207
Hung JJ (2000) Chi–Chi earthquake induced landslides in
  Taiwan. Earthquake Eng Eng Seismol 2:25–33
Kuo CY, Tai YC, Bouchut F, Mangeney A, Pelanti M,
  Chen RF, Chang KJ (2009) Simulation of Tsaoling
  landslide, Taiwan, based on Saint Venant equations
  over general topography. Eng Geol 104:181–189
Lin A, Chen A, Liau CF, Lee CT, Lin CC, Lin PS, Wen
  SC, Ouchi T (2001) Frictional fusion due to co-
  seismic landsliding during the 1999 Chi–Chi

(Taiwan) ML 7.3 earthquake. Geophys Res Let t
  28:4011–4014
Miyamoto Y, Shimamoto T, Togo T, Dong JJ, Lee CT
  (2009) Dynamic weakening of bedding-parallel fault
  gouge as a possible mechanism for catastrophic
  Tsaoling landslide induced by 1999 Chi–Chi earth-
  quake, The next generation of research on earth-
  quake-induced landslides: an international conference
  in commemoration of 10th anniversary of the Chi–
  Chi Earthquake, pp 398–401
Mizoguchi K, Hirose T, Shimamoto T, Fukuyama E
  (2007) Reconstruction of seismic faulting by high-
  velocity friction experiments: an example of the 1995
  Kobe earthquake. Geophys Res Lett 34:L01308 doi:
  10.1029/2006GL027931
Newmark NM (1965) Effects of earthquakes on dams and
  embankments. Geotechnique 15:139–159
Shimamoto T, Tsutsumi A (1994) A new rotary-shear
  high-speed frictional testing machine: its basic design
  and scope of research. J Struct Geol 39:65–78
Tang CL, Hu JC, Lin ML, Angelier J, Lu CY, Chan YC,
  Chu HT (2009) The Tsaoling landslide triggered by
  the Chi–Chi earthquake, Taiwan: insights from a
  discrete element simulation. Eng Geol 106:1–19
Togo T, Ma SL, Hirose T (2009) High-velocity friction
  of faults: a review and implication for landslide
  studies, The next generation of research on earth-
  quake-induced landslides: an international conference
  in commemoration of 10th anniversary of the Chi–
  Chi Earthquake, pp 205–216
Tsutsumi A, Shimamoto T (1996) Frictional properties of
  monzodiorite and gabbro during seismogenic fault
  motion. Geol Soc Japan 102:240–248
Tsutsumi A, Shimamoto T (1997) High-velocity fric-
  tional properties of gabbro. Geophys Res Lett
  24:699–702
Yano K, Shimamoto T, Oohashi K, Dong JJ, Lee CT
  (2009) Ultra-low friction of shale and clayey fault
  gouge at high velocities: implication for Jiufenger-
  shan landslide induced by 1999 Chi–Chi earthquake.
  The next generation of research on earthquake-
  induced landslides: an international conference in
  commemoration of 10th anniversary of the Chi–Chi
  Earthquake, pp 402–406

The Interpretation for Landslide Mechanism and The Proposal of Landslide Countermeasures in Abay Gorge in Ethiopia

42

Masao Yamada, Kensuke Ichikawa, Takeshi Kuwano, Tomonari Takeuchi and Atsushi Nakagawa

Abstract

Main road 3, a major arterial road in Ethiopia, that passes through the Abay Gorge steeply climbs nearly 1,500 m over 40 km. It is plagued by landslides in the rainy season from June to September. Especially, the road receives big damages in L/S00, L/S05, L/S22, L/S27, and L/S28 points. The various investigation and movement observation of drilling survey, electric soundings, seismic exploration, borehole extensometer, borehole inclinometer, groundwater level meter and so on were executed in these districts. Though a lot of landslides are colluvial deposit slides, weak tuff layers are related to landslide movement. For the relationship between rainfall, groundwater level and landslide deformation, a continuous rainfall for at least four days is necessary to cause the groundwater level rising and landslide deformation. Also the time lag for water level rising after the practical effective rainfall is one day, and the time lag between water level rising and landslide deformation is two days. This paper introduces results of a full-scale investigation analysis project that executes various investigational observations and the integrated analyses lead by JICA concerning overseas landslides. Because the hydrogeological structure of landslides in Abay Gorge has been clarified from these results of investigation and landslide movement observations, the interpretation for landslide mechanism and the proposal of landslide countermeasures in Abay Gorge is shown in this paper.

M. Yamada (✉)
Information Conservation Engineers Co.,Ltd, Japan

K. Ichikawa · T. Kuwano
KokusaikogyouCo.,Ltd, Japan

T. Takeuchi · A. Nakagawa
JICA, Japan

1 Introduction

The area is characterized by the central Ethiopian highlands. Geologically, the gorge is made by thick stratified Mesozoic sedimentary rocks
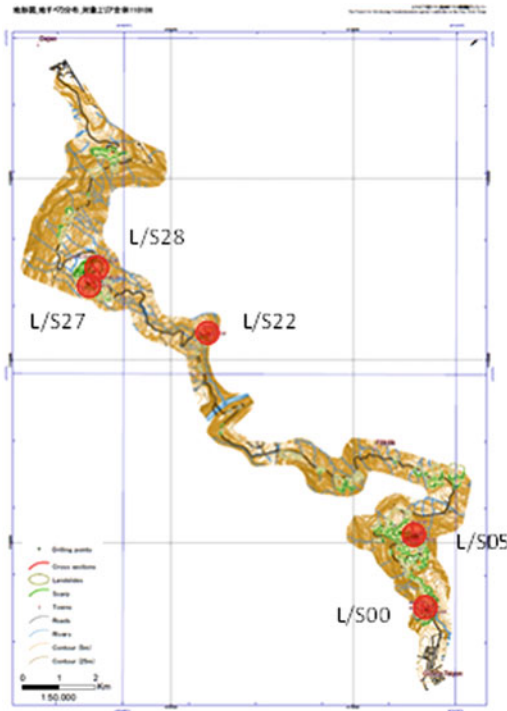
Fig. 42.1 Local map in Abay area

and overlain by a series of basaltic lava flows. Adigrat Formation is covered conformably by Abay Formation and Antalo Formation, which were deposited Middle to Late Jurassic. Ashangi Formation which was deposited during Tertiary covers them partially.

There are many mechanisms that cause landslides, such as geomorphological features, geology, and other man-made and natural conditions. In the Abay Gorge, water is the direct and primary cause of a landslide. Since groundwater is fundamentally recharged by rain, the relation between a landslide and rain is close. When groundwater increases the pore water pressure also increased, and effective stress will decrease. As a result, shear resistance decreases and triggered a landslide.

According to topographic analysis due to satellite photograph and site reconnaissance, we judged five landslide areas shown in Fig. 42.1 as the next most dangerous areas which we have to investigate and make countermeasure.

2 Outline of Landslide Investigation in Abay Area

Figure 42.2 shows the flow chart of the landslide investigation and the landslide analysis. Steps of the landslide investigation and countermeasures planning are shown as follows,

(1) "①" in Fig. 42.2 is the flow of acquisition of the satellite image, and "②" is the field investigation, respectively. Identification of landslide area and delineation of landslide blocks are executed along this flow.

(2) "③" is the flow of drilling survey, and "④" is the flow of geophysical exploration, respectively. The point geological data are obtained by drilling survey, and the line data are obtained by geophysical exploration.

(3) Investigation of the displacement "⑤" of the landslide blocks and water level observation "⑥" are executed by using the borehole.

(4) Landslide block and the slip surface are identified by detailed field investigation, drilling survey, geophysical exploration, monitoring of the displacement of the landslide, water level observation and so on.

(5) The stability analysis is executed by comprehensive investigations and the soil strength obtained from the soil test.

(6) The landslide countermeasure works are planned based on these results of the comprehensive study, and the planned countermeasure works are executed step by step.

(7) After countermeasure works are set up, reevaluation of the stability of the landslide is planned to evaluate the mechanism and effectiveness of countermeasure works by continuous monitoring using extensometers, water level gauges and inclinometers and so on.

3 Features of Each Landslide District

Moving characteristics of landslide blocks are described as follows.

Fig. 42.2 Flow chart of landslide investigation and landslide analysis
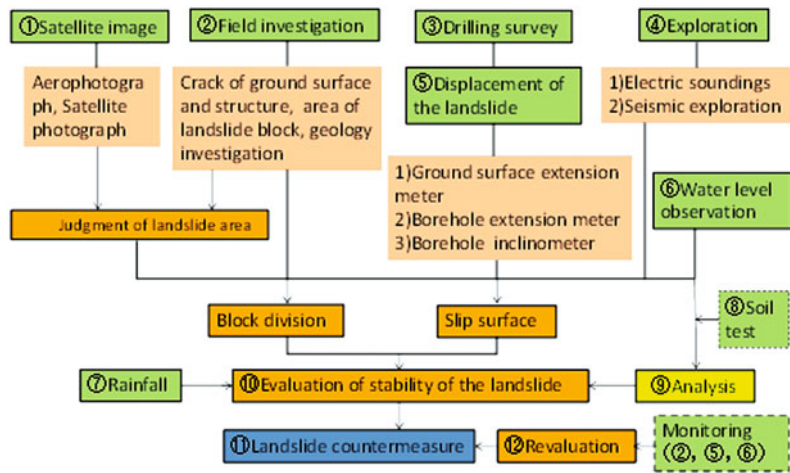
Photo 42.1 Landslide situation in L/S00 site

3.1   L/S00 site

In view of the landslide situation, block 00-08 is assumed to be a "complex slide". The scarp zone is at the eastern end of the road, and the end zone is in the terrace located east-southeast of the road. Depression zone is formed as a result of the horizontal movement of the soil mass in the middle slope. The block is assumed to have moved from the embankment of the road, due to the rising of the ground water level in the rainy

season from 2009 to 2011. The extrusion is observed at the end zone. New cracks occurred in this extrusion, and landslide blocks 00-07, 00-10, and 00-11 are assumed to have been triggered by this extrusion (Fig. 42.3, Photo 42.1).

Spring water was observed at several points through all season of 2010 and 2011 (see Fig. 42.3).

Multi-tuff layers existed at 27.8–28.4 m depth and 31.5 m depth in B00-12, and a multi-tuff layer or a clay layer existed in another
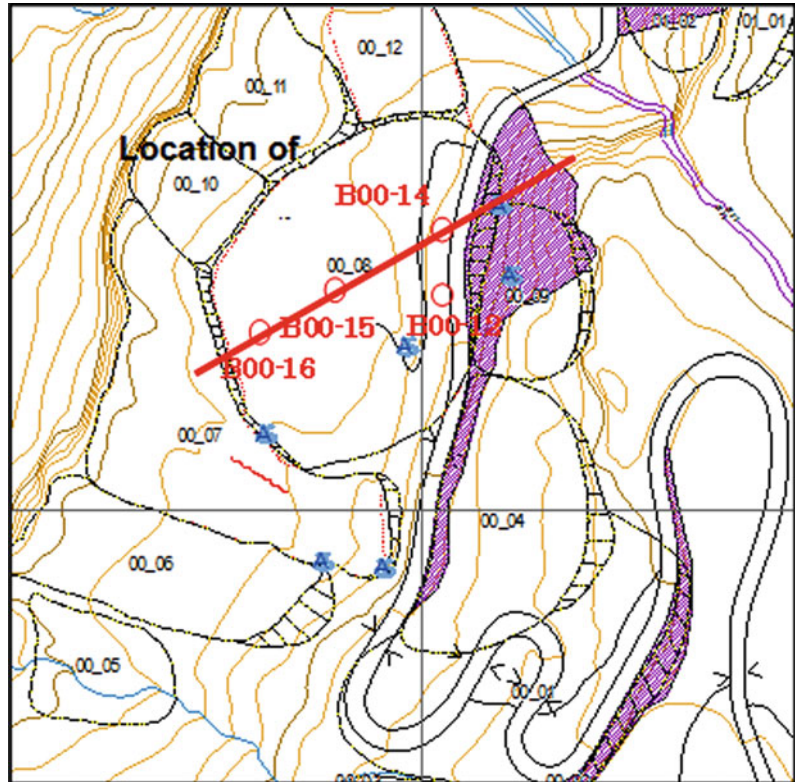
borehole. A tuff layer existed on the line connected at 25 m depth in the embankment and 15 m depth in the middle to lower slope. It is assumed that the tuff layer forms the slip surface because the layer has low shear strength. It is possible that the tuff layer expands to the upper slope and develops into a potentially large landslide. Further investigation is needed.

Displacement of block 00-08 was detected at a depth of 17.0 m depth by a borehole inclinometer in 2010. This displacement is assumed to have occurred at the inner embankment of the road. However, it could also extend to the entire block 00-08. From the additional borehole investigation result, it is found that strongly weathered basalt at the depth from 19.0 to 22.6 m in borehole B00-15 and weathered tuff layer at the depth from 21.0 to 24.0 m in borehole B00-16 existed.

In consideration of the above mentioned results of the investigation and the monitoring, slip surfaces are discussed and determined. The thick red line in Fig. 42.4 denotes the possibility of the slip surfaces. Slip surface (1) is related to a landslide of the embankment which is the smallest volume in the area; slip surface (2) is related to a landslide continuing from the road to the end of the field plane; and slip surface (3), which might exist at 31.5 and 33.7 m depth, has the old clear slickenside in borehole B00-12. The landslide is constituted from the upper part of the basalt slope to the end of the field plane.

From the groundwater logging result in B00-16, a pressured groundwater flowing layer was recognized at the depth from 19.5 to 20.5 m. Based on these results, it is reasonable to consider that, after passing the basalt and pyroclastic rock, the groundwater formed a flow in the clay layer and weathered tuff layer which is located along the boundary between colluvial deposit and basalt layer, and then became pressured groundwater and infiltrated into the colluvial deposit, finally, formed a inter-stratum water and flow in the colluvial deposits.
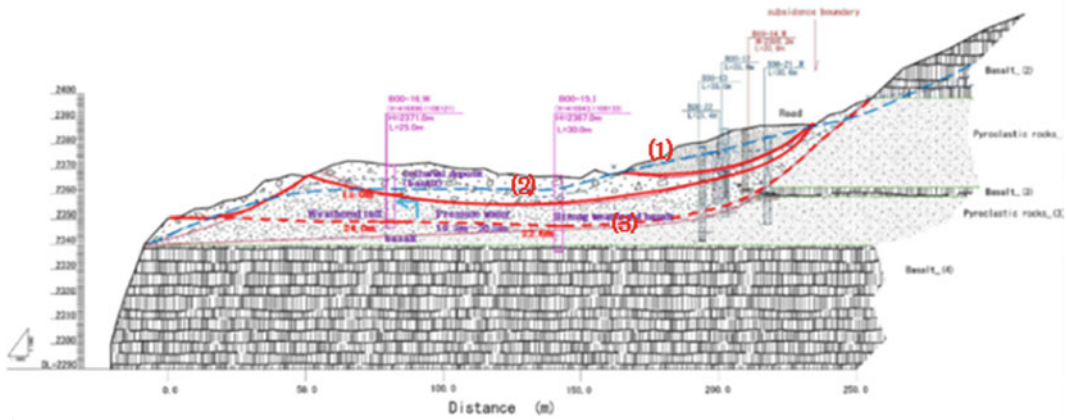
Fig. 42.4 Landslide cross section in L/S00 site

Photo 42.2 Landslide
situation in L/S05 site
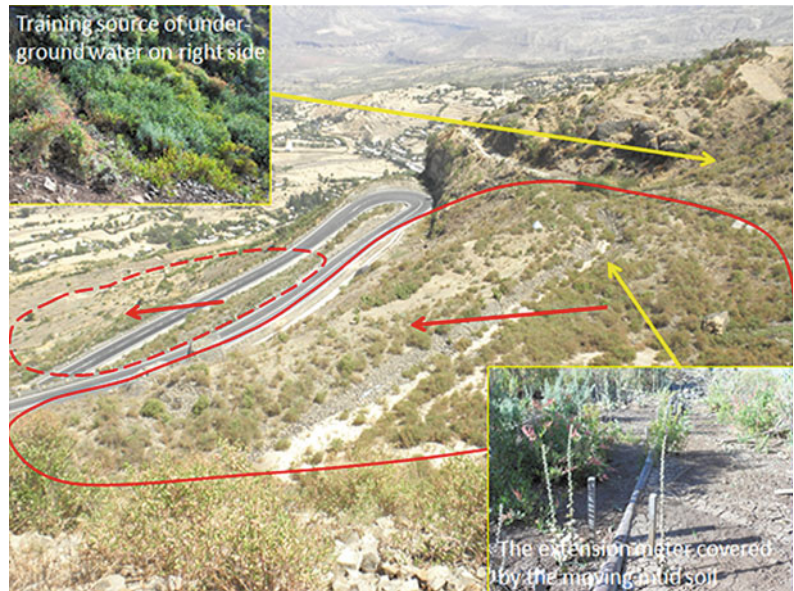
3.2   L/S05 site

Two roads exist in the landslide area. The
cracks on the ground surface and retaining
walls of the road due to the landslide suggest
that the block is divided into an upper block
(block 05-01) and a lower block (block 05-02).
In the upper block, the scarp zone is just below
the terrace of the upper slope, and the end zone
is the slope shoulder of the upper road. In the
lower block, the scarp zone is located on the
lower road, and a new crack is observed on the
road. The block 05-07 is treated as an

independent block that is subdivided block
05-02 (Fig. 42.5, Photo 42.2).

Spring water is observed at several points
during the rainy season of 2010(see Fig. 42.5).
Also, spring water is observed at the mountain-
ous side of the slope in the dry season. The
spring water level analyzed to draw the landslide
cross section in Fig. 42.6.

The upper block (i.e., block 05-01) is a slide
of colluvial deposit and pyroclastic material,
located in the upper level of the limestone.
However, no slip surface has been detected.
Further investigation is needed.

Fig. 42.5 Landslide plane in L/S05 site
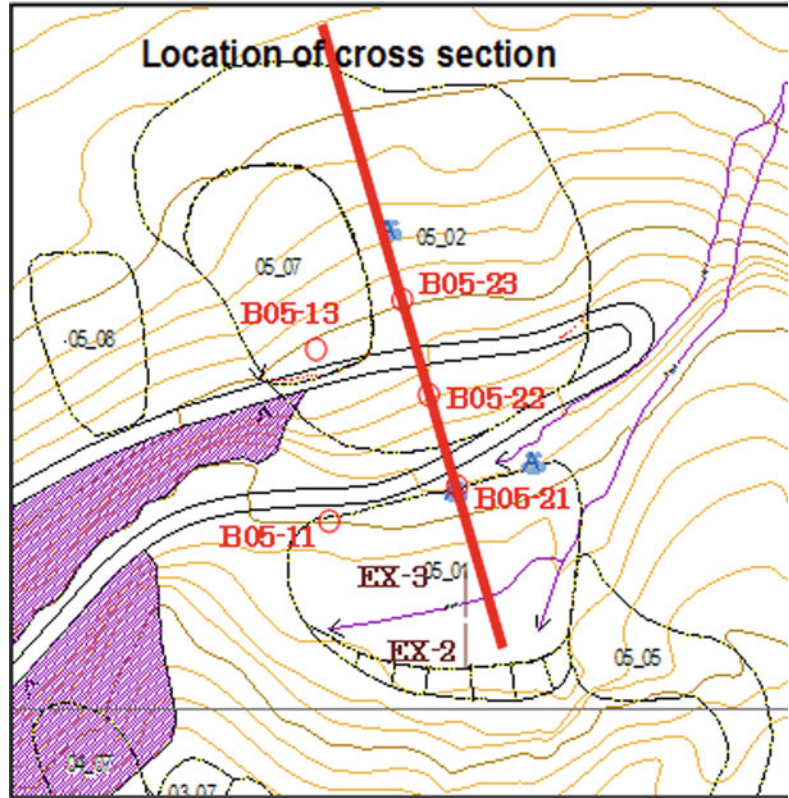
Photo 42.3 Landslide situation in L/S27 site
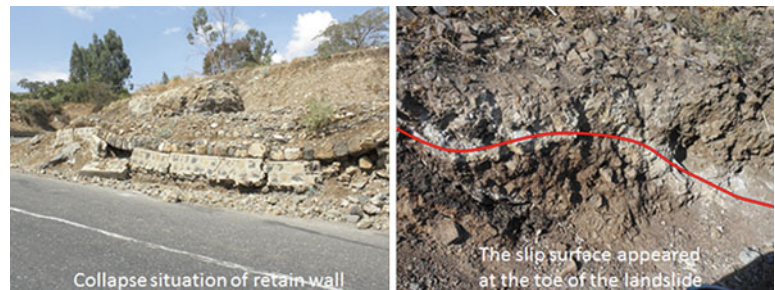
Displacement is observed at depths of 6.6 m depth in B05-21 and 11.6 m depth in B05-22 using a borehole inclinometer; this result indicates that the lower block is an active landslide. Multi-tuffaceous siltstone layers are confirmed in the limestone layer. Currently actualized landslides may develop into a large landslide, including an upper block and a lower block. Further investigation is needed.

In July 2011, borehole investigation was conducted in borehole B05-13 and B05-23. Borehole B05-13 was also used for groundwater monitoring and inclinometer monitoring, while borehole B05-23 was used for inclinometer monitoring. The groundwater level in borehole B05-13 is 35–40 m depth, which is below the slip surface. The inclinometer monitoring result indicates that the accumulated displacement at 12.5 m depth in borehole B05-13, while similar displacement was indicated by the result at 3.5 and 17.5 m in borehole B05-23. In the lower block, the slip surface is located at the bottom of the colluvial deposit, or in the strongly weathered limestone. In the upper block, there is no obvious deformation in the extensometers No.2 and No.3 which were set up at the gentle place, and there is

Fig. 42.6 Landslide cross section in L/S05 site
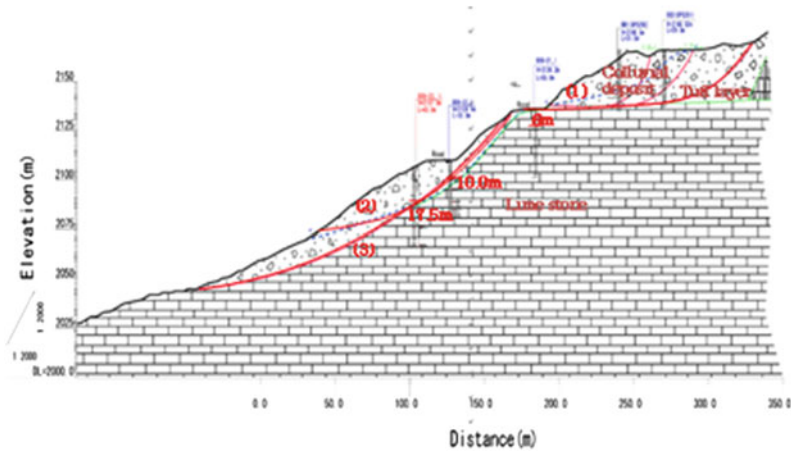
Fig. 42.7 Landslide plane in L/S27 and L/S28 site
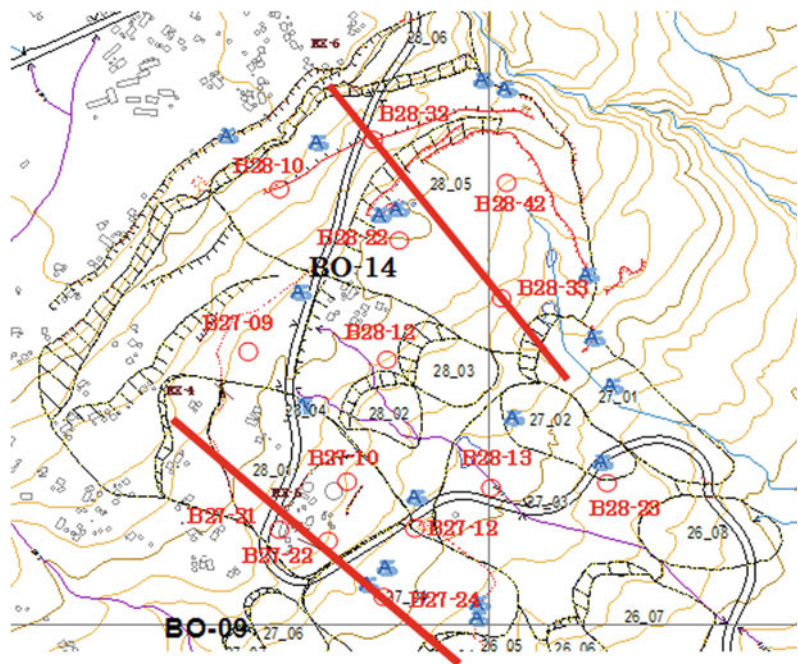
no obvious deformation in the underground extensometer installed in borehole B05-11. However, the displaced debris reached the height of the extensometer pipe set at the slope surface.

In consideration of the above mentioned results of the investigation and the monitoring, slip surfaces were discussed. The thick red line in Fig. 42.6 denotes the possibility of the slip surface. Slip surface (1) is a landslide of colluvial deposit and pyroclastic material on the upper slope; slip surface (2) is a small landslide

on the lower slope; slip surface (3) is a landslide continuing from the lower slope to the field area.

3.3 L/S27 site

In L/S27 area, the landslide block continues from the upper slope to the lower slope. The landslide movement is remarkable along the cross section line. Landslide anomalies such as new cracks extending to extensometer EX-4, cracks in the

Fig. 42.8 Landslidecross section in L/S27 site
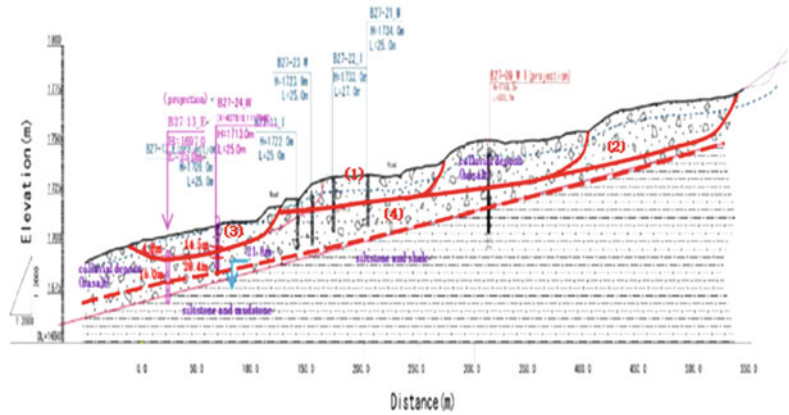
Photo 42.4 Landslide situation in L/S28 site

right side wall of the road, continues cracks nearby the church, and cracks in the scarp zone in lower block containing the road shoulder can be found along the cross section line (Fig. 42.7, Photo 42.3).

Two blocks damaged the road along the cross section line. In the upper block 28-01, the scarp zone of the landslide has cracks that continue to extensometer EX-4, and the end of the landslide is the lower road. In blocks 27-04, the scarp zone of the landslide is the lower road shoulder, which crosses over to the end zone of the upper block.

Block 28-01 is assumed to be a slide of colluvial deposit containing mainly basalt, and the matrix is siltstone and shale. The thin tuff layer is assumed to be the slip surface of the valley side wall of block 28-01 in the outcrop.

Spring water is observed at several points in the rainy season of 2010(see Fig. 42.7). This spring water is assumed to continue to the depression zone on the left side. The spring water in the valley side slope is observed in the dry season. The spring water level is analyzed by the landslide cross section in Fig. 42.8.

Borehole bending is at 7.5 m depth for B27-21 and accumulated extension displacement using a borehole inclinometer at 15.0 m depth for B27-22. Additional borehole surveys and further variation investigation are needed.

In 2011, borehole investigation was conducted at B27-09 and B27-10 along the BO-08 measure line. In B27-09, groundwater level monitoring and inclinometer monitoring is conducted; while in B27-10, inclinometer monitoring is conducted. The groundwater level in B27-09 kept almost constant around 15–16.5 m and did not show any increase (because of a trouble, the monitoring could not be conducted after 26 July). While in borehole B27-10, the groundwater level varied between 20.0 and 25.5 m which is lower than the slip surface. In borehole B27-09, it becomes impossible to conduct the inclinometer monitoring from the depth of 19.2 m. Within five days of 16 August, the accumulated rainfall in this area exceeded 600 mm. As a result, rapid increasing was observed in the surface ground extensometer

Fig. 42.9 Landslide cross
section in L/S28 site

Fig. 42.9 Landslide cross section in L/S28 site
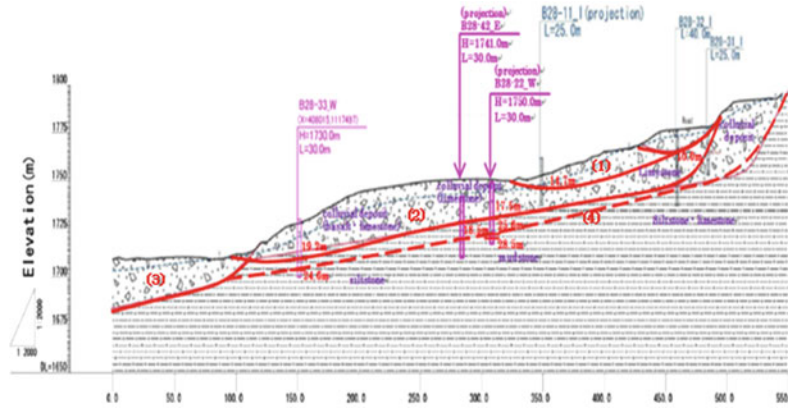
No.4 and No.5 and ground extensometer in B27-12, and block 28-01 became active again.

From the situation of the landslide blocks, it is considered that two types of landslide may exist in this area; one is a shallow slide in the shallow colluvial layer, the other is a deep slide along the bottom of the deep colluvial deposit.

In consideration of above mentioned results of the investigation and the monitoring, slip surfaces were discussed. The thick red line in Fig. 42.8 denotes the possibility of the slip surface. Slip surface (1) is a landslide of colluvial deposit near the road and the settlement; slip surface (2) is a large landslide from the upper slope to the lower road; and slip surface (3) is a landslide of the lower field area and slip surface (4) is a deep landslide continuing from the colluvial deposit on the upper slope to the end of the field plane.

The groundwater level in borehole B27-24 in dry season was 21.75 m, this makes the deep slip surface can always be kept under the groundwater. Additionally, the groundwater logging result shows a downward flowing existed below the depth of 21.75 m. It is estimated that an upward flowing should occur in rainy season. However, the groundwater monitoring result up to now did not show the upward flowing.

3.4   L/S28 site

In the L/S28 area, the landslide block continues from the upper slope to the lower slope. The large cracks of the scarp zone extend over the L/S27 area and the L/S28 area at an altitude of 1,810 m. The depression zone, which is just below the scarp zone, is a source of water supply (Fig. 42.7, Photo 42.4).

While the colluvial deposit in the L/S27 area is composed of siltstone and shale, the one in the L/S28 area is different for each borehole. The colluvial deposit in B28-11 is composed of siltstone and shale, which in B28-21 is gravel of basalt and tuff, and that in B28-31 is limestone.

In the past, a large landslide occurred in the L/S27 and L/S28 areas. That the colluvial deposit of L/S27 is silt stone and shale shows the possibility of a deep landslide exists. Because the colluvial deposit of B28-21, B28-31 and B28-32 are different from each other, geological differences between B28-31 and B28-32 may exist, and the landslide blocks in them may differ. Another borehole survey and further variance investigation are needed.

Blocks 28-03 and 27-02 exist under the landslide which length is 400 m from middle to upper part of the slope. Block 27-02, which has a scarp located at altitude of 1,715 m, damages the road in the end zone.

Spring water is observed at several points in the rainy season of 2010 (see Fig. 42.7). There are ponds in the slope toe on the valley side of the road and in the end zone of the dry season. Ponds form in the depression zone, and rain infiltrates from the zone. Therefore, infiltration water becomes spring water and oozes. The spring water level analyzed by the landslide cross section in Fig. 42.9. From the landslide

block situation, it is also considered that two types of landslide may exist in this area: one is a shallow slide in the shallow colluvial layer, and the other is a deep slide along the bottom of the deep colluvial deposit.

In consideration of above mentioned results of the seismic exploration, the investigation and the monitoring, slip surfaces were discussed. The thick red line in Fig. 42.9 denotes the possibility of the slip surface. Slip surface (1), which was identified by drilling survey, is a landslide from the upper slope to the end of the field; slip surface (2), which is needed to be identified on additional surveys, is a large landslide deeper than (1); slip surface (3) is a landslide on the lower slope; and slip surface(4) is a deep landslide continuing from the colluvial deposit on the upper slope to the end of the field plane.

The groundwater level in borehole B28-10 in dry season was 31.5 m. This makes the deep slip surface can always be kept under the groundwater. Additionally, the groundwater logging result of borehole B28-10 shows a weakly pressured groundwater flowing existed in the siltstone and shale layer at the depth between 33.5 and 33.75 m. It may be possible that after passing the weathered siltstone, the groundwater infiltrated into the colluvial deposits mixed with basalt gravels.

Along the measure line BO-13, borehole investigation was conducted at B28-13 and BO-10 after July 2011 in this landslide. Both boreholes are located at the toe of the lower block of the landslide. In Borehole B28-13, an inclinometer was installed for monitoring, while, B28-23 was used to monitor the groundwater level. As with the monitoring results in B28-23, the water level increased by 4 m from 6 July to 13 July, and increased by 6 m from 20 July to 22 July. Two times water level increasing were recognized. The measurement of inclinometer became impossible when the depth reached 9.6 m. The monitoring results of surface extensometer No.6 show that a gradual displacement was generated from February. The displacement is not caused by rainfall, but results from slope creeping. From July, the displacement at No.6 extensometer ceased.

4 Landslide Countermeasures in Abay Gorge

4.1 Expected Countermeasures in Each Landslide Block

Table 42.1 lists expected landslide countermeasures in the Abay Gorge area. Table 42.1 is separated into two stages. The first stage includes relatively cheap landslide control works including horizontal drainage borings and buttress fill work. In the second stage, drainage wells in order to further reduce the ground water level should be installed; otherwise piles should be constructed to ensure a proper safety factor.

4.2 Remarks in Practice

Landslides can be triggered in the rainy season by rising ground water levels. Therefore, it is rational that groundwater control work such as horizontal drainage borings would be constructed to reduce the landslide activity. However horizontal drainage borings might not be effective in some cases. Therefore the effect of the groundwater control work should be examined by monitoring movement and water level. Buttress fill work is also relatively cheap but could trigger another landslide block depending on the construction site. The influence of buttress fill work for other blocks should also be examined in advance.

Many types of erosion of the ground surface and collapses are confirmed due to rain intensity. Surface drainage work on the slope is effective to prevent rainfall water from infiltrating into moving mass of landslide and controlling rising water levels. Additionally, although drainage well effectively reduces the ground water level, residents may consume the ground water for domestic use.

Table 42.1 Design of countermeasures

Area	Plan #	Stage 1		Stage 2	
		Counter measures	Remarks	Counter measures	Remarks
L/SOO	(1)	Horizontal drainage borings (embankment and upper part of the road)	Examination of effects horizontal drainage borings bymonitoring of movement and water.level.	Improvement of safety factor landslide by piles or drainage wells (depression zone and toe zone)	(a)Examination in the construction techno1ogy cost and so on (b) Monitoring of movement and water level for drainage wells
	(2)	Buttress fill works (depression zone)	Examination about the influence for lower Hocks in advance	Buttress fill works (light embankment + anchors)	(a) Examination of constru:tion techno1ogy cost and so on.
L/S05	(1)	Horizontal drainage a) borings + surface drainage works (flat landing ∼ per zone of the slope, block 05-02, 05-03, 05-04) + retaining wooden structures (block 05-02, 05-03)	Examination of effects horizontal drainage borings by monitoring of movement and water level retaining b) Retaining structures in block 05-02, 05-03 for unstable sediment	Piles or drainage wells (depression zone and toe zone)	(a) Examination of co:nstruction techno1ogy cost and so on (b) Monitoring of movement and water level for drainage wells
L/S27	(1)	Horizontal drainage borings (upper part and lower part of the road)		Piles (upper block of the road) or drainage wells (depression zone)	(a)Examination of the construction techno1ogy cost and so on considerations of water supply for residents
L/S28	(1)	Horizontal drainage borings (upper part and lower part of the road) + channels	Examination r£ effects horizontal drainage borings by monitoring of movement and water.level. b)bigger channels	Improvement of safety factor in the land slide by piles(depression zone) or drainage wellls(middle slope)	(a)Examination of in the construction technology cost and so on (b) Monitoring of movement and water level for drainage 'wells

4.3 Requirements for Setting Appropriate Countermeasures

a. Investigation and monitoring

A drilling survey of the necessary volume is planned for deciding the configuration of the slip surface after selecting an appropriate site where the landslide block will need landslide countermeasures.

The drilling survey should be done while recording the water level a day before and after completing drilling. Borehole inclinometer and water level meter should be installed in the boreholes for monitoring purpose. Water level monitoring is especially important for obtaining a reliable ϕ' in stability analysis.

The rain duration is short in the Abay area, so the sampling time should not exceed about 10 min. If it is difficult to install a borehole inclinometer due to cost, it is possible to replace it with borehole extensometer.

b. Examination of practical effects of countermeasures

If groundwater control works such as horizontal drainage borings and drainage wells are to be conducted, the effect of the groundwater control work should be examined by monitoring the ground movement and water level. The accuracy of the safety factor could be improved by reviewing soil constants c′ and ϕ' in the stability analysis. Selecting an appropriate ϕ' makes a big difference for the effectiveness of the groundwater control works.

c. Establishment of objective safety factors

Even in Japan, it is difficult to establish an objective safety factor for landslides. For landslide countermeasures, it has been progressing from just setting existing safety factor and the construction works to comprehensive countermeasures including both landslide preventing works like constructions and management works after occurrence of landslides such as making hazard maps.

Considering Ethiopia's economic situation, this program involves feasibility in construction technology and economic efficiency. In the near future, the landslide administration in Ethiopia should develop a policy for achieving a certain safety factor at any level and start practicing hard countermeasure works. Nevertheless, a certain level of safety factor should be established to prevent landslides for specified levels of rainfall because landslides usually occur in the rainy season every year. The Project is hence important for establishing the guidelines. If a certain level of safety factor has not been set against landslides, precautionary evacuation measures including installation of a slope monitoring system should be in place.

d. Feasibility of construction technology and economic efficiency

It is necessary to investigate the feasibility of construction technology, the construction period, the economic efficiency, and the environment and social consideration in Ethiopia. Generally speaking, are more preferable rather than low feasibility countermeasures.

Those countermeasures which are relatively cheap and cost effective are proposed in the first stage of Table 42.1. However, it is necessary to re-examine the effectiveness and determine the safety factor that should be establish at certain level. In case a safety factor is proposed at the 1.05–1.10 level, countermeasure plans in the second stage in Table 2 are required. Because the safety factor changes with the landslide size and elements at risk, the study team must pay attention to these points as well.

References

JICA (2012) Final report. The project for developing counter measures against landslides in the Abay River Gorge in the federal democratic Republic of Ethiopia

JICA (2011): Manual for survey and analysis on landslide. The project for developing countermeasures against landslides in the Abay River Gorge in the federal democratic Republic of Ethiopia

Development of a Cyclic Box Shear Apparatus to Elucidate Mechanisms of Earthquake-Triggered Landslides

Yoichi Hasegawa, Tatsuya Shibasaki and Takanari Yamasaki

Abstract

In this study, we have developed a cyclic box shear apparatus for elucidating the mechanisms of earthquake-triggered landslides. We conducted a cyclic box shear test, on undisturbed slip-surface clay samples and obtained excess pore water pressure behavior which can provide dynamic strength under seismic condition.

Keywords

Cyclic box shear test · Cyclic loading test · Undisturbed sample · Dynamic strength

1 Introduction

Recently, inland-type earthquakes have frequently occurred in Japan. In the 2004 Niigata Chuetsu Earthquake and the 2008 Iwate-Miyagi Inland Earthquake, many landslides occurred in mountainous areas. In order to take appropriate measures, it is necessary to understand the triggering mechanisms of earthquake-induced landslides and a number of studies have been conducted. A seismic response analysis helps understand the behavior of earthquake-induced landslides, and thus, many studies have been performed using various analysis methods (for example, Hata 2007; Wakai 2008). The soil parameters are the key parameter in determining the mechanisms and what parameters are used in these analyses literally determine the outcome of the analyses. Methods of asking for the dynamic strength of a soil and rock sample include the method by the triaxial test (Okada 2009), the method of the simple shear test (Ohneda 1984), and the method of the ring shear test (Sassa 1993). But, box shear test is mechanistically simple and clear, in the case of asking for the shear strength of discontinuity in rock mass like a slip surface (Oshima 1998; Kamitani 2007). We have developed a cyclic box shear apparatus in order to elucidate the mechanisms of earthquake-triggered landslides. This paper describes the structure and performance of this apparatus, and

Y. Hasegawa (✉) · T. Shibasaki
Japan Conservation Engineers & Co.,Ltd, 34-12,
Shimizumae, Minamiyanome, Fukushima-shi,
Fukushima 960-0112, Japan
e-mail: hasegawa@jce.co.jp

T. Shibasaki
e-mail: shibasaki@jce.co.jp

T. Yamasaki
Japan Conservation Engineers & Co.,Ltd, 2-12-
11,Kitaurawa, Urawa-ku,
Saitama-shi, Saitama 330-0074, Japan
e-mail: yamasaki@jce.co.jp

①shear force loading equipment
  (servomotor)
②normal force loading equipment
  (servomotor)
③normal load cell
④upper shear box(movable)
⑤lower shear box(fixation)
⑥shear load call
⑦shear displacement gauge
⑧specimen(φ60×H20mm)
⑨lower loading plate
⑩loading shaft
⑪horizontal displacement gauge
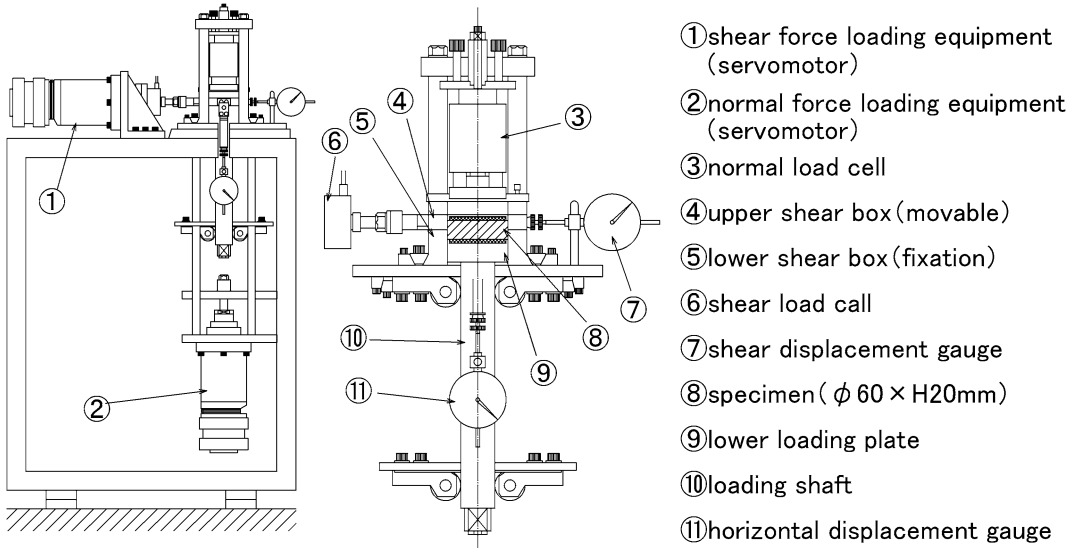
Fig. 43.1 The outline of a testing apparatus

discusses the results of a cyclic box shear test conducted using undisturbed slip-surface clay samples.

2   Outline of the Apparatus

The overall features of the apparatus are shown in Fig. 43.1. Characteristically, servomotor is mounted on the apparatus allowing precise displacement-controlled or stress-controlled tests with feedback system of normal force or shear force/displacement. For cyclic loading tests, either sine waves or random waves such as real seismic waves can be applied.

For constant volume shear tests, the apparatus uses feedback control using measured relative displacement between the lower loading plate and the upper shear box, rather than simply fixing the box mechanically with bolts. Since constant-volume tests give the change in effective stress, this method can provide the shear behavior of fully-saturated and undrained samples without measuring pore water pressure. This apparatus can apply normal stresses up to 1.0 MPa, it recreates the maximum effective overburden pressure to the slip-surface sample with an overburden of about 50–100 m.
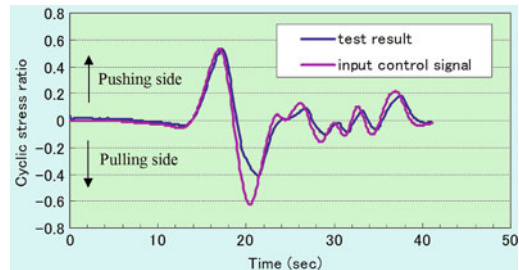
Fig. 43.2 The wave form (input control signal) and the cyclic stress ratio (test result)

3   Cyclic Box Shear Test by Random Wave

We used undisturbed specimens of Quaternary pumice tuff that was sampled from a landslide triggered by the 2008 Iwate-Miyagi Inland Earthquake. After consolidating the sample at $\sigma_c = 170$ kPa, we tested it using the wave form shown in Fig. 43.2. The seismic response analysis subsequently reproduced the shear wave pattern of the location where the samples were taken at the time of the 2008 Iwate and Miyagi inland earthquake.

As indicated by the cyclic stress ratio shown in Fig. 43.2, the temporal measured shear stress (blue line) showed very small difference with the
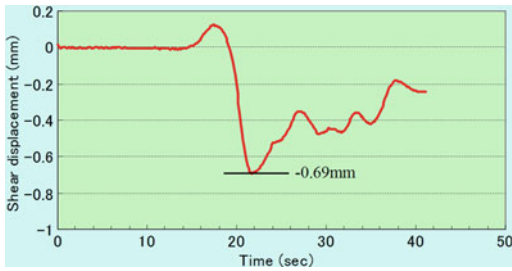
Fig. 43.3 The shear displacement
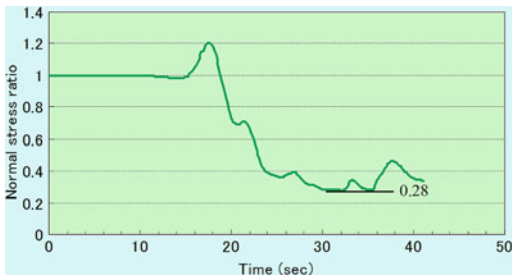
Fig. 43.4 The normal stress ratio

Fig. 43.5 The sinusoidal waveform with amplitudes of stepping-up

Fig. 43.6 The test result

input control signal (red), except the pulling side of around 20 s. This difference at around 20 s could be interpreted as the one between shear load and shear resistance. The maximum shear displacement was-0.69 mm (Fig. 43.3). The normal stress ratio (see Fig. 43.4) decreased to 0.28 at the lowest, which suggests that significant excess pore water pressure generation is expected (This is equivalent to an excess pore water pressure ratio of 0.72). These results suggest that the generation of excess pore water pressure in the weathered rock layer during cyclic loading, can trigger catastrophic landslides.

4   Cyclic Box Shear Test by Sinusoidal Waveform of Stepping Up Amplitude

The clay sample used in the above test was undisturbed Neogene tuff obtained from a landslide sliding surface of that was triggered by the 2008 Iwate and Miyagi Inland Earthquake. We prepared specimens of sliding surface sample and consolidated by four different normal

stresses σ_c (25, 50, 75, and 100 kPa). After consolidation, we followed the following steps:
(a) Apply predetermined normal stress and maintained it all through the test.
(b) Shear at a constant rate of 0.1 mm/min until 28 cm of shear displacement.
(c) Apply cyclic shear stress of sinusoidal waveform with amplitudes of stepping-up with constant increment as shown as the red line in Fig. 43.5. Each step consists of 20 cycles.

The obtained cumulative shear displacement is shown as red curve in Fig. 43.6. In this figure, shear displacement started to increase from zero around 2,100 s. Since then, the peak of each cyclic shear stress got smaller than control signal as shown in Fig. 43.5. This means instantaneous shear took place when shear stress exceeded shear resistance. The envelope of those shear stress peaks apparently decreased gradually until the end of the test, possibly due to any collapse of internal structure of the specimen, which may appears as generation of excess pore pressure under fully saturated and undrained condition. We measured the dynamic peak and residual strength for each consolidation stress, and calculated the strength parameters (Fig. 43.7). In comparison with static residual strength, the dynamic peak strength increased by 26 % and dynamic residual strength increased by 23 %.
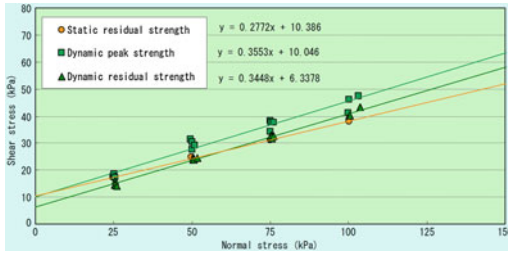
Fig. 43.7 The strength parameter

5 Conclusions

We developed a cyclic box shear apparatus that can apply either sinusoidal waveform or arbitrary waveforms including actual seismic waveforms. This apparatus can provide shear behavior of the samples under fully-saturated and undrained condition, by maintaining constant-volume of the shear box. In the series of the tests, we used undisturbed samples of slip-surface clay that was obtained from sliding surface of an earthquake-induced landslide. We confirmed high excess pore water pressure generating behavior during dynamic loading. We succeeded to measure the dynamic peak and dynamic residual strength by applying sinusoidal shear stress and compared with static strength. Both of the dynamic strength showed more value.

References

Hata Y, Sugiyama H, Shinya H, Kuraoka S, Sato S, Shiraishi Y (2007) A seismic response calculation of the landslide considering the effect of the excess pore water pressure. J Jpn Landslide Soc 44(1);39–45 (In Japanese)

Kamitani K, Hasegawa M, Hongo T (2007) An estimate of liquefaction strength by cyclic constant volume direct box shear tests, In:42 th Japan national conference on geotechnical engineering, pp 425–426 (In Japanese)

Ohneda H, Umehara Y, Higuchi Y (1984) Cyclic strength properties of normally consolidated clays under simple shear conditions. Report of the Port and Harbor Research Institute 23(4):71–94 (In Japanese)

Okada T, Ito H (2009) Development of a method for evaluating the dynamic shear strength of soft rock, Civil Eng Res Lab Rep (08061): 1–12 (in Japanese)

Oshima A, Takada N, Sumi T, Hongo T (1998) Comparison of cyclic shear tests on sand by direct box shear and triaxial tests. In: 33th Japan national conference on geotechnical engineering pp 721–722 (In Japanese)

Sassa K, Fukuoka H (1993) Measurement of the internal friction angle of soils during motion by the high-speed ring shear apparatus. J Jpn Landslide Soc 29(4):1–8 (In Japanese)

Wakai A (2008) 3.4 Simulation for large-scale landslide in Higashi-Takezawa former Yamakoshi, Earthquake-induced landslide disasters in middle mountains-study report on the 2004 Mid-Niigata Earthquake part II—geotechnical engineering. Jpn Landslide Soc, 119-126 (in Japanese)

Empirical Modal Decomposition of Near Field Seismic Signals of Tsaoling Landslide

Kuo-Jen Chang, Shao-Kuan Wei, Rou-Fei Chen, Yu-Chang Chan, Pi-Wen Tsai and Chih-Yu Kuo

Abstract

Giant landslides can achieve high-speed sliding and long run out distances and estimating the kinematic is crucial for the next generation of the hazard mitigation system. Direct measurement data when landslides are in motion are valuable for the purpose. However, because of their scarce occurrences and short flow durations, such measurements are rarely recorded with instruments. In 1999, the Chi–Chi earthquake triggered a major landslide in this area, with a source volume 125×10^6 m^3. Near the scar area, there is a strong ground motion station, CHY080, recorded the seismic signals during the earthquake and the recorded data exhibit some distinctive signatures. We analyze the polarizations of the seismic waves and use Ensemble Empirical Mode Decomposition (EEMD) with an additional clustering analysis to decompose the seismic signals. Series of peculiar wave packets associated with the landslide are identified. Based on these results, a complementary rigid sliding model is deployed to verify the sliding process. The results reveal that with the sliding distance 1,990 m, the

K.-J. Chang
Department of Civil Engineering, National Taipei
University of Technology, Taipei, Taiwan

S.-K. Wei · P.-W. Tsai
Department of Mathematics, National Taiwan
Normal University, Taipei, Taiwan

R.-F. Chen
Department of Geology, Chinese Cultural
University, Taipei, Taiwan

Y.-C. Chan
Institute of Earth Sciences, Academia Sinica,
Taipei, Taiwan

C.-Y. Kuo (✉)
Research Center for Applied Sciences, Academia
Sinica, Taipei, Taiwan
e-mail: cykuo06@gate.sinica.edu.tw

maximum velocity reaches 78 m/s, and the mass generates a large collision impact against the riverbed and the steep slope on the other side of the river. The friction angle of the sliding surface could be as low as 6.9°. These results are agreeable with the numerical simulation of the landslide. These findings provide the evidence that the earthquake and the landslide induced ground motion coexist in the seismogram records.

1   Introduction

Landslides pose long-lasting threats to human lives and properties because of their devastating destructive capabilities. Among the reported incidences, landslides triggered by earthquakes are usually the most devastating ones in terms of the numbers of the fatalities (Turner and Jayaprakash 1996), and about one-half of the disasters are classified as rock avalanches (large, extremely rapid landslides).

These rock avalanches, particularly the ones with large volumes, are usually capable to travel long distances at high speeds and, with their kinetic energy, they are expected to induce significant ground motions through the interactions with the bedding topography. In recent years, we have witnessed the increase of data inventory, for example, the seismic signatures of Mount St. Helen's landslide (Brodsky et al. 2003; Kanamori et al. 1984) Stromboli Volcano (La Rocca et al. 2004) and rock-fall avalanche events in the Alps (Deparis et al. 2008), etc. However, to the authors' limited knowledge, there have yet no records showing the simultaneous coupling between the earthquake and the landslide induced ground motion. Due to their relatively scarce occurrences and surface damping/dispersive effects, such events have rarely been instrumentally recorded, despite advances in seismic instrumentation technologies. This arises our interests whether the landslide motion can be identified by such records along with the earthquake. This is a challenging issue, and, in what follows, we will show that the strong motion records of the Tsaoling landslide in Taiwan could provide valuable data for this purpose.

2   Tsaoling Landslide

Taiwan is situated on an active orogenic belt possesses, therefore, high seismicities and geological hazards (Malavieille et al 2002). On September 21st, 1999, in the center of the island, which is associated with the Chelungpu thrust faulting (Kao and Chen 2000; Lallemand 2000; Angelier et al. 2003), the Chi–Chi earthquake, at $M_L = 7.3$, occurred (Ma et al. 2006). The earthquake triggered more than 10,000 landslides (Chang et al. 2005). Among the enormous number of landslides, the Tsaoling rock-and-soil avalanche was the largest event (Chang and Taboada 2009).

The Tsaoling region is about 33 km southwest away from the epicentre. The slid volume was about 125×10^6 m³, by 150 m thick. It slides about 1990 m away from its initial position and deposits into 150×10^6 m³ debris. The gigantic deposit blocks the gorge of the Chinshui River for over 5 km, with a height of 50 m at the upstream and 150 m at the downstream, and forms a dammed lake. It is worth noting that in Tsaoling, at least five historical catastrophic events, caused either by earthquakes or heavy precipitation, have occurred since 1862 (Chen et al. 2006; Hung et al. 2002).

The landslide initiated from the northern slope of the Chinshui River and the dip angle is about 14°, oriented NNE–SSE. This is in the same direction as the topographic profile, whose slope
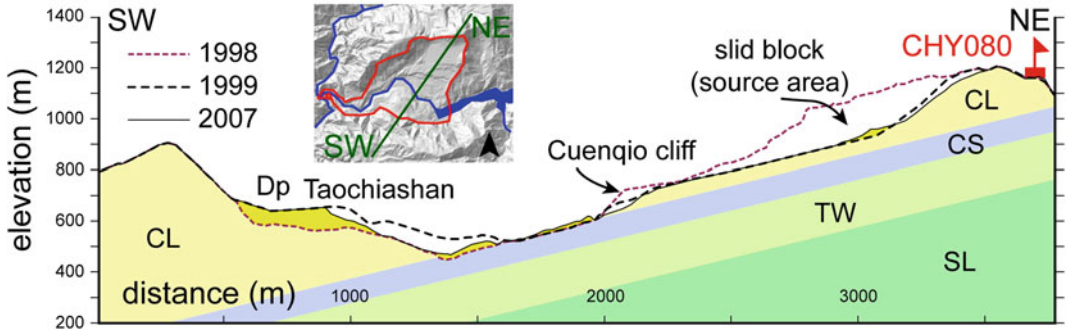
Fig. 44.1 Geological profile of the Tsaoling area, see Fig. 44.6 for its location in Taiwan. The NE-SW profile is defined through the gravity center of the slid mass and is in parallel to the slid direction. Geological formation: *SL* Shihliufeng shale; *TW* Tawo sandstone; *CS* Chinshui shale; *CL* Cholan formation; *Dp* debris deposit

angle is about 15.8° measured from the foothill of the detached scarp to the northern riverbank. A cliff with an average height of 30 m, called Cuenqio cliff, lays within 500 m from the foothill. On the southern side of the river, there is a scarp slope and the topology is much steeper than the north. The sliding surface, composed of fine layered shale and silty mudstone, is in parallel to the stratigraphic bedding plane. After the landslide, thin layers of pseudotachylytes are found scattered on the sliding surface, indicating frictional heating and melting of the sliding plane during the sliding process (Lin et al. 2001).

About four fifths of the slid mass are transported across the river and deposit around the Taochiashan hill. The hill, composed of rock debris generated by the previous events, is about 140 m higher than the Chinshui riverbed before the earthquake. This existing topology implies that the slid material reaches a substantially high speed, and with such kinetic energy, the mass is able to fly over the river valley and to overflow the Taochiashan hill. The characteristics of flow morphology, e.g. the up-hill moving and reflected debris flow surges, are observed in the field. Figure 44.1 illustrates the morphological profile of the depletion and the accumulation area.

3 Seismic Ground Motion

Because of the high seismicity of the island, Taiwan built one of the densest earthquake monitoring networks (Tsai and Lee 2005). In the Tsaoling area, a strong motion seismological station, code-named CHY080 (120.67770 E, 23.59720 N, El. 840 m, indicated on Fig. 44.1), was installed on the top of the slope in the 90s. It is located less than 1 km north-west of the depleted mass center and was safe from the violent seismic shaking and the landslide and remained fully functional.

The total duration of the earthquake signals recorded by CHY080 is 159 s at a sampling rate 200 Hz. The peak ground acceleration (PGA) values are 792.4, 841.5 and 715.9 gal for the E–W, N–S, and the vertical components, respectively (Lee et al. 2001). The arrival of the S-wave is at 25.2 s identified from seismic wave form analysis and also been calculated from seismic source wave propagation of 1D velocity profile. The horizontal trajectories of the acceleration and displacement are shown in Fig. 44.2. The trajectories reveal that an instance of motion, *F*, highlighted by the red/green line segments, has a principal orientation in the NE-SW direction, actually 37° to the east according to the principal component analysis. This is nearly in parallel to the direction of the sliding and the strata dip. Its sudden appearance and the agreement between the dominant acceleration/displacement direction and the sliding course of the landslide indicate that it is caused by the block-breaking initiation and separation of the landslide mass from the bedrock. This feature also agrees with the displacement direction of the surface Rayleigh wave
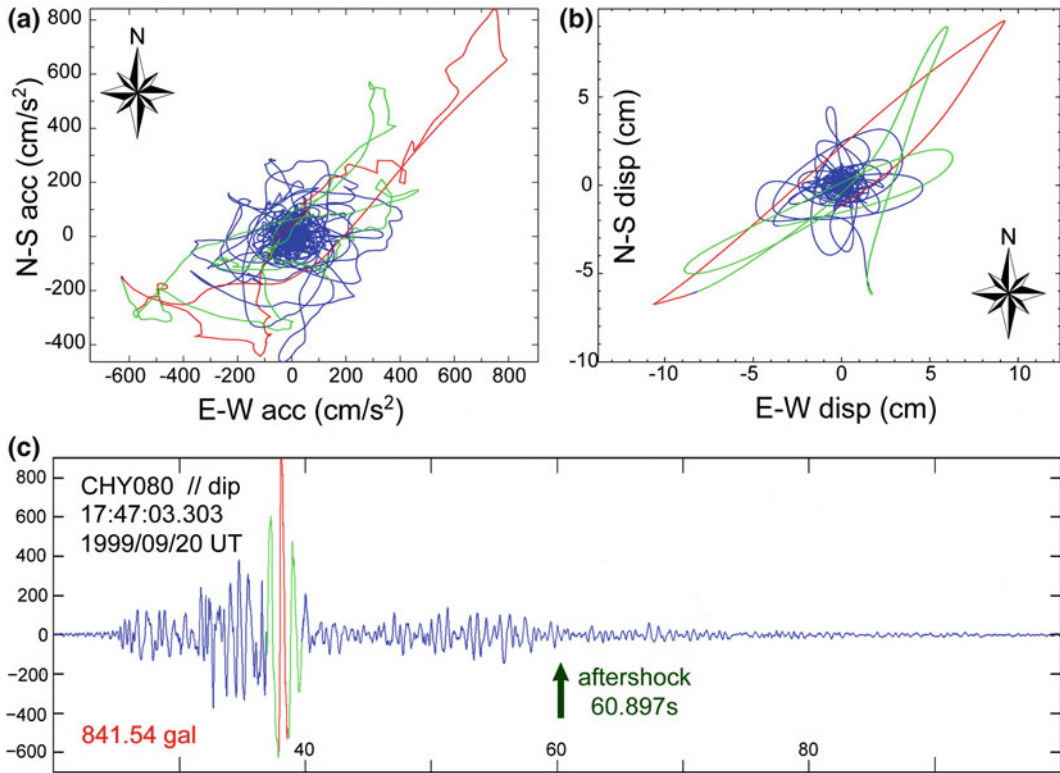
Fig. 44.2 Seismic record of the CHY080 strong motion station. The horizontal trajectories of (**a**) acceleration, (**b**) displacement, and (**c**) the transient acceleration component in the dip direction. *The colored line segments* (*red/green/magenta*) are for highlighting the wave polarizations among the subfigures

predicted by the shallow single-force theory applied in the same direction (Dahlen 1993).

4 Empirical Model Decomposition

There are other details in the signal waveforms after the main shock, say from 70 to 85 s. To analyse these details, we use the method of Ensemble Empirical Mode Decomposition (EEMD). (Huang et al. 2001; Wu and Huang 2009; Zhang et al. 2003; Huang et al. 2008) Through the EEMD procedure, the raw signals are decomposed in a deterministic way into a sequence of modes, called the intrinsic mode functions (IMFs). The procedure itself is an iterative scheme where the IMF is extracted by removing the transient mean, defined by the bounding envelopes of the signals. A small portion of assisting white noise is injected to enhance the modal decomposition for intermittent signals through the ensemble averaging procedures. (Wu and Huang 2009; Huang et al. 2008) The decomposed IMFs are sorted according to their characteristic time scales, from the shortest (with the highest frequency contents) to the longest. The detail scheme and verification are relegated to the cited references.

Applying the method to the CHY080 data (20 Hz low-pass filtered and re-sampled to 100 Hz), with a white noise level at 10 % of the standard deviation of the signals, we find that the raw signals are decomposed into 9–11 IMFs depending on the type of the signals (displacement or acceleration), see Fig. 44.3 for the vertical component. The main earthquake contents are likely to be classified into the third to the
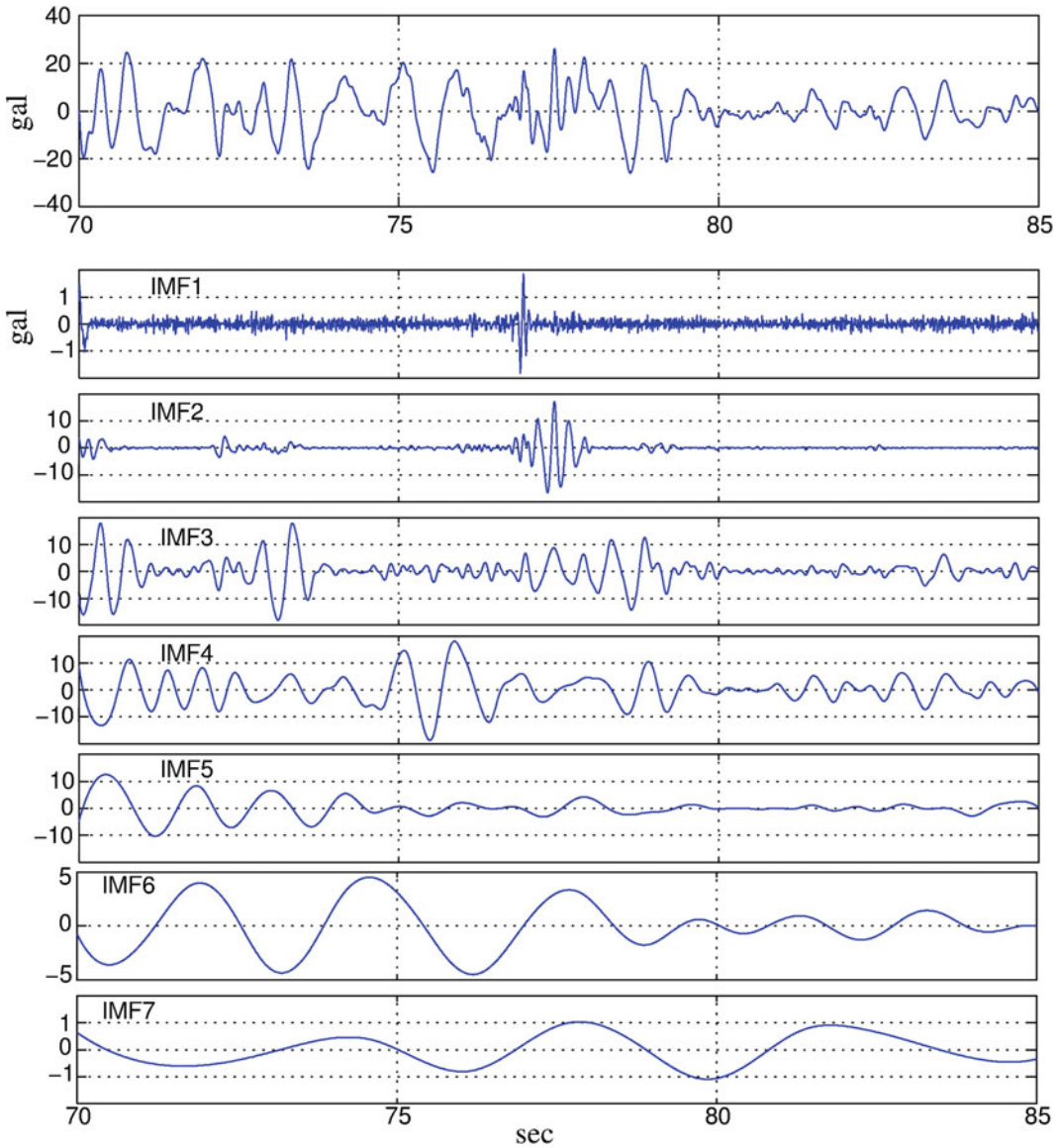
Fig. 44.3 N–S component (70–85 s) of ground acceleration (*topmost panel*) and the intrinsic mode functions (IMFs). Note the vertical scales vary among panels. Due to the space limit, the E–W and vertical components are not shown and the same applies to Fig. 44.4

fifth IMFs because they in total contain more than 83 % of the spectral energy of the acceleration. Another distinctive characteristic is that outstanding wave packets are found between 76 and 78 s in the first two IMFs (with shorter time scales) for all of the three acceleration components. The significance of IMF white noise is tested, according to the method proposed in [22]. As shown in Fig. 44.4a, IMF_1 is close to the margin of white noise and hence is omitted in the following analysis.

In addition to the visual identification and the energy content check, statistical properties of the IMFs are further to be investigated. This is because the decomposed IMFs may suffer from an over-complete problem, i.e. the signals may be decomposed into a number of IMFs that is more than necessary. For example, the main earthquake
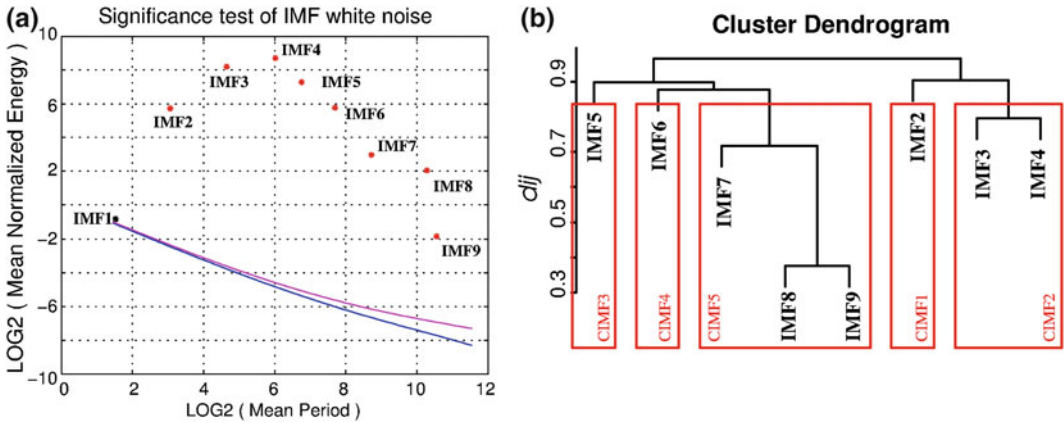
Fig. 44.4 **a** Significance test of IMF white noise. The *upper pink* (*blue*) *solid line* represents the upper bound of Gaussian noise at 99 % (95 %) confidence level. **b** The hierarchical cluster dendrogram and the clustered IMF (CIMFs)
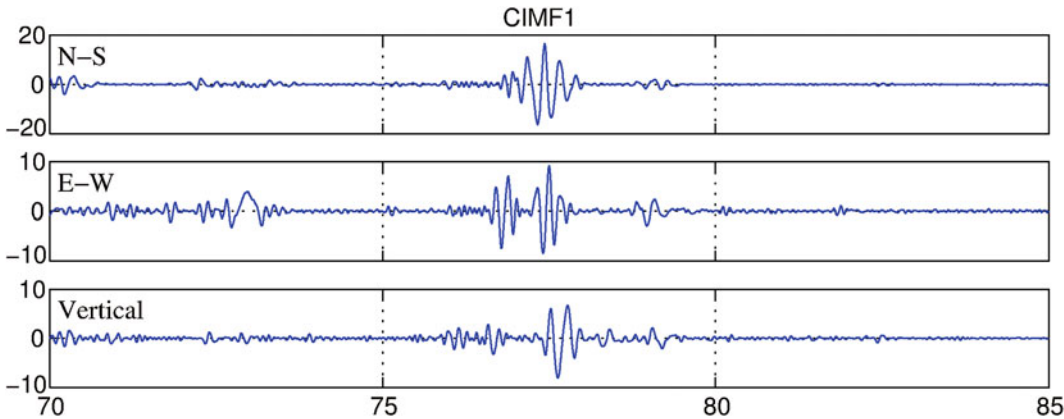
Fig. 44.5 CIMF1 of N–S, E–W, and vertical components of ground acceleration. Wave packets between 76 and 78 s are defined Instance *I*

signals are expanded into at least three IMFs as described above. Based on the assumption that signals share the same sources of the signals present similar statistical characteristics, the statistical clustering analysis, the hierarchical cluster method (Lattin et al. 2003), with the single linkage is employed. In the cluster method, we define the distance between two IMFs (*i*th and *j*th) to be $d_{ij} = 1 - \text{corr}(\text{IMF}_i, \text{IMF}_j)$, where $\text{corr}(\text{IMF}_i, \text{IMF}_j)$ is the correlation coefficient. Figure 44.4b presents the dendrogram, the hierarchy of distances among the IMFs. Determining the cluster level from the dendrogram is a somewhat exploratory approach. Nevertheless, the

second IMFs (IMF_2) of the three acceleration components are identified to have in general large distances to other clusters. After clustering the IMFs, we define a set of clustered IMFs (CIMFs), as in Fig. 44.4b. The intriguing first CIMFs (CIMF_1, containing IMF_2) of the three ground motion components are sketched in Fig. 44.5.

Notably, the peculiar wave packets between 76 and 78 s, Fig. 44.5, are almost at the end of a series of intermittent signals and further intermittent signals become much less frequent and much smaller in amplitudes. This indicates that, for these 2 s, an event which is able to generate a broadband impulse response occurs. Their peak

accelerations are about 8–5 gal, implying that if there were no background main earthquake, the ground motions would be equivalent to a small earthquake at $M_L \approx 4$. Hence, we refer these peculiar wave packets as Instance I.

We now examine whether Instance I is associated with aftershocks. There are in total 296 aftershocks analysed and documented after the Chi–Chi main-shock, as reported by Chang et al. (2007) Based on the catalogue, Fig. 44.6 depicts the spatial distribution of the aftershocks within 3 min immediately after the main-shock. They are labelled with timestamps. If CHY080 recorded one of the aftershocks, the signals should appear at the moment of the aftershock, shifted by the travel time of the seismic wave to the station. Correlating the spatial distribution and the timing of all 15 events, only one aftershock (M_L = 5.6, 120.940 E, 23.051 N, depth 8.9 km) generated at GMT 17:48:04 (48.3 s after the mainshock, calibrated to 60.9 s in Fig. 44.2), is a candidate. This aftershock is identified by ten arrival signals among TCU 137, TCU072, TCU074, TCU089, TCU084 stations, and its epicentre is situated about 57 km NNE of the CHY080 station. The arrivals exhibit bursts of high frequency signatures superposed on the background main shocks. Because this aftershock occurred simultaneously with the main shocks, extra caution is taken to cross-examine its propagation among the stations, especially those on the pathway to and nearby CHY080. We use the same EEMD method to track the propagation of high frequency bursts, and the stations investigated are marked in Fig. 44.6. We find that most of the high frequency contents are lost when arriving at TCU084. While this may be due to the site effect of this particular station, the bursts are not distinguishable in the pathway stations, e.g. TCU129, CHY024, CHY028 and CHY029 to the Tsaoling area. This indicates that this candidate aftershock and its associated high frequency contents are localized in the region nearby its epicentre. In addition, from the short time scale and duration of Instance I, we conclude that the source of this event cannot be far from the CHY080 station, and its influences are limited in the Tsaoling region.

According to these observations, it is highly likely that Instance I is generated by the impact of the slid block with the Chinshui riverbed or the southern steep slope on the other side of the river. The disturbances generated by the surface impingement are inherited with high damping and dispersive in propagation. This explains why the signals were localized and screened by the surrounding topography of the Tsaoling region.

5 Rigid Block Sliding

The sliding mechanism is hence proposed as key for the landslide assessment. Let us perform a simple kinematic estimation with a simple rigid sliding model. The same model has been applied widely for landslide assessments. (Kanamori et al. 1984; Jibson 1993; Chang et al. 2005) From the seismic records, the gap between the arrival of the S-wave to instance I is about 51 s. The travelling time of the impact generated seismic wave to the CHY080 station is neglected because the travelling distance is short and the surface wave speed is much faster than the flow speed.

Assuming that the sliding mass is rigid and the slope is planary at an average inclination angle $\theta = 15.8°$, we estimate that the constant acceleration is 1.53 m/s^2 with the total travelling distance 1990 m (L) and the travelling time 51 s. This acceleration is the gravity acceleration along the slope deducted by a Coulomb friction with a constant friction coefficient (μ):

$$a_s = g \sin \theta - \mu g \cos \theta$$

where g is the gravity acceleration of 9.81 m/s^2. This acceleration produces a maximum flow speed about 78 m/s (V) and the friction coefficient is calculated as low as 0.12; i.e., the friction angle is 6.9°. The friction angle and the flow speed are in excellent agreement with numerical simulation using a continuum flow model (Kuo et al. 2009) parameters. Further based on the idealized approach, we have the impact energy, the total energy subtracted by the friction dissipation

$$E_{impact} = \rho g V L(\sin \theta - \mu \cos \theta),$$
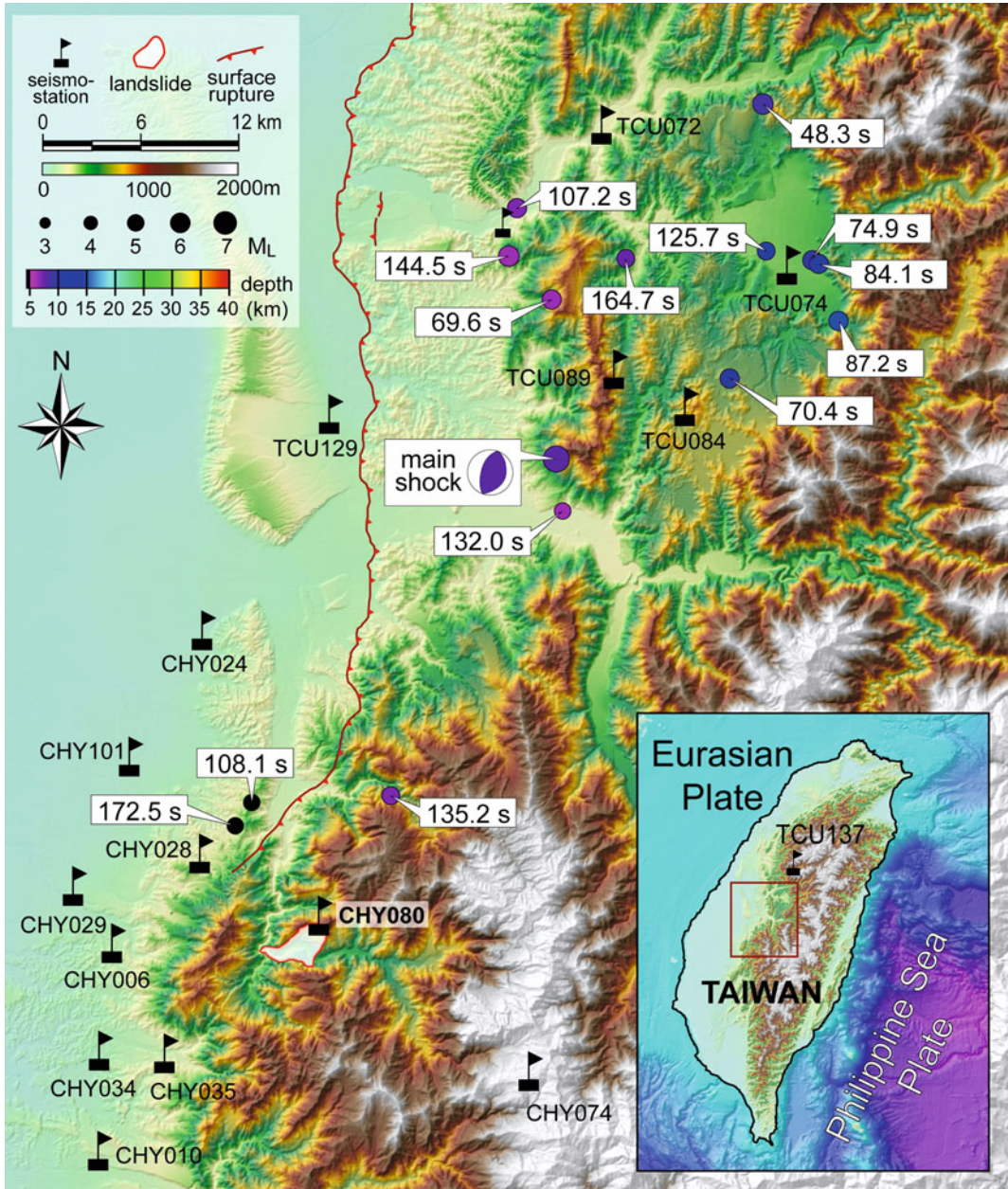
Fig. 44.6 The seismostations, the epicentre of the Chi–Chi earthquake and the epicentres of the aftershocks. The seismostations used in this study are labelled by its station name. The epicentres of the aftershocks are labelled together with the timestamps

which is about 8.7×10^{14} Joule with the debris material density ρ at 2,500 kg/m. Assuming that this energy is equal to the seismic energy of an equivalent earthquake, it generates an estimated seismic motion at an energy magnitude (Boatwright and Choy 1986) $M_e = 3.9$. This magnitude agrees reasonably with the previous EEMD analysis for Instance *I*.

6 Conclusion

The rapid motion of the Tsaoling landslide is previously identified by the field observation and the numerical back-analysis. However, these methods cannot precisely deduce the time of the event. The seismogram data can complement this analysis. Complications arise for this particular event because the earthquake is still in motion during the landslide. To cope with the difficulty, we analyze the seismic wave polarization and use the EEMD method to resolve the landslide signatures. The seismic motion produced by the block-breaking initiation and the impact of the slid mass is confirmed, which is similar to the mechanism proposed in Ref. 6. Based on the results, we verify the basal friction and flow speed by the simple rigid body analysis and also find excellent agreements with those obtained by the simulation of the continuum model. These findings provide the evidence that the earthquake and the landslide induced ground motion coexist in the seismogram records. Further research has been initiated to address into the mechanical interactions between the two sources of the ground motion.

References

Angelier J, Lee JC, Hu JC, Chu HT (2003) Three-dimensional deformation along the rupture trace of the September 21st, 1999, Taiwan earthquake: a case study in the Kuangfu school. J Struct Geol 25:351–370

Boatwright J, Choy G (1986) Teleseismic estimates of the energy radiated by shallow earthquakes. J Geophys Res 91:2095–2112

Brodsky EE, Gordeev E, Kanamori H (2003) Landslide basal friction as measured by seismic waves. Geo Res Lett 30:2236–2240

Chang KJ, Taboada A (2009) Discrete element simulation of the Jiufengershan rock-and-soil avalanche triggered by the 1999 Chi–Chi earthquake Taiwan. J Geophys Res 114:F03003 1–17

Chang KJ, Taboada A, Chan YC (2005a) Geological and morphological study of the Jiufengershan landslide triggered by the Chi–Chi Taiwan earthquake. Geomorphology 71:293–309

Chang KJ, Taboada A, Lin ML, Chen RF (2005b) Landsliding by earthquake shaking using a block-on-slope thermo-mechanical model: example of Jiufengershan landslide, central Taiwan. Eng Geol 80:151–163

Chang CH, Wu YM, Zhao L, Wu FT (2007) Aftershocks of the 1999 Chi–Chi, Taiwan, earthquake: the first hour. Bull Seismol Soc Am 97:1245–1258

Chen RF, Chang KJ, Angelier J, Deffontaines B, Lee CT, Lin ML, Yan IH (2006) Topographical changes revealed by high-resolution airborne LiDAR images: the 1999 Tsaoling landslide induced by chichi earthquake. Eng Geol 88:160–172

Dahlen FA (1993) Single-force representation of shallow landslide sources. Bull Seismol Soc Am 83:130–143

Deparis J, Jongmans D, Cotton F, Baillet L, Thouvenot F, Hantz D (2008) Analysis of rock-fall and rock-fall avalanche seismograms in the french alps. Bull Seismol Soc Am 98:1781–1796

Huang NE, Chern CC, Huang K, Salvino LW, Long SR, Fan KL (2001) A new spectral representation of earthquake data: Hilbert spectral analysis of station TCU129, Chi–Chi, Taiwan, 21 September 1999. Bull Seismol Soc Am 91:1310–1338

Hung JJ, Lee CT, Lin ML (2002) Tsao-Ling rockslides, Taiwan, catastrophic landslides: effects, occurrence, and mechanisms:Reviews in engineering geology. Geol Soc Am XV:91–115

Huang NE, Wu Z (2008) A review on Hilbert–Huang transform: method and its applications to geophysical studies. Rev Geophys 46:RG2006. doi:10.1029/2007RG000228

Jibson RW (1993) Preficting earthquake-induced landslide displacements using Newmark's sliding block analysis. Transp Res Rec 1411:9–17

Kanamori H, Given JW, Lay T (1984) Analysis of seismic body waves excited by the Mt. St. Helens eruption of May 18, 1980. J Geophys Res 89:1856–1866

Kao H, Chen WP (2000) The Chi–Chi earthquake sequence:active out-of-sequence thrust faulting in Taiwan. Science 288:2346–2349

Kuo CY, Tai YC, Bouchut F, Mangeney A, Pelanti M, Chen RF, Chang KJ (2009) Simulation of Tsaoling landslide, Taiwan, based on Saint Venant equations over general topography. Eng Geol 104:181–189

La La Rocca M, Galluzzo D, Saccorotti G, Tinti S, Cimini GB, Del Pezzo E (2004) Seismic signals associated with landslides and with a tsunami at Stromboli volcano Italy. Bull Seismol Soc Am 94:1850–1867

Lallemand S (2000) Was the Chi–Chi earthquake a "subduction earthquake"? Terrest Atmosph Ocean Sci 11:709–720

Lattin JM, Carrol D, Green PE (2003) Analysing multivariate data, Duxbury, Belmont

Lee WHK, Shin TC, Kuo KW, Chen KC, Wu CF (2001) Data files from "CWB free—field strong—motion data from the 921 Chi–Chi (Taiwan) earthquake". Bull Seismol Soc Am 91:1370–1376

Lin A, Chen A, Liau CF, Lee CT, Lin CC, Lin PS, Wen SC, Ouchi T (2001) Frictional fusion due to co-seismic land sliding during the 1999 Chi–Chi (Taiwan) ML 7.3 earthquake. Geophy Res Lett 28:4011–4014

Ma KF, Wang CY, Hung JH, Song SR, Tsai YB, Mori J, Tanaka H, Yeh EC, Sone H, Kuo LW, Wu HY (2006) Slip zone and energetics of a large earthquake from the Taiwan Chelungpu-fault Drilling Project. Nature 444:473–476

Malavieille J, Lallemand SE, Dominguez S, Deschamps A, Lu CY, Liu CS, Schnurle P, the ACT Scientific Crew (2002) Arc-continent collision in Taiwan. New marine observations and tectonic evolution. In: Byrne TB, Liu CS (eds) geology and geophysics of an arc-continent collision, Taiwan, Republic of China. Boulder, Geological Society of America Special Paper 358, 187–211

Tsai YB, Lee CP (2005) Strong motion instrumentation programs in Taiwan: NATO Science Series 58. Springer, Dordrecht, pp 255–278

Turner AK, Jayaprakash GP (1996) Introduction. In: Turner AK, Schuster RL (eds) Landslides; investigation and mitigation, Special report, vol 247. Transportation Research Board, National Academy of Sciences, Washington, pp 3–11

Wu Z, Huang NE (2009) Ensemble empirical mode decomposition: noise assisted data analysis method. Adv Adaptive Data Anal 1:1–41

Zhang RR, Ma S, Hartzell S (2003) Signatures of the Seismic source in EMD-based characterization of the 1994 Northridge, California, earthquake recordings. Bull Seismol Soc Am 93:501–518

Examining Fluidisation Mechanisms of Hikagemori Landslide Triggered by Iwate-Miyagi Nairiku Earthquake in 2008 by Laboratory Soil Tests

45

Yasuhiko Okada, Ushio Kurokawa and Shiho Asano

Abstract

The Iwate-Miyagi Nairiku Earthquake in 2008 triggered a complex debris slide—earth flow on the east slope of Mt Hikagemori, Kurihara city, Miyagi prefecture. In situ surveys 6 days after the occurrence revealed that the earth flow body was mostly unsaturated, but near the slip surface pore fluid pressure was built up with suspension of fine soil particles. From undrained cyclic loading triaxial compression tests on undisturbed samples taken from the head scarp of the landslide, a measured cohesion was at least 50 kPa, and a structural collapse could take place in a case. In mass flow experiments by means of a large-scale model flume, an unsaturated mass moved and slid smoothly over the muddy water travelling a long distance for a specimen with sufficient water inside. This may not reproduce the exact fluidisation behaviour of the complex Hikagemori landslide, though it may also explain a part of the long travelling mechanisms of the Hikagemori landslide.

Keywords

Complex Hikagemori landslide · Pore-fluid pressure · Soil test · Long travel distance

1 Introduction

The Iwate-Miyagi Nairiku earthquake in 2008 occurred in the south of the inland of Iwate Prefecture at 8:43 JST, 14 June 2008 ($M_j = 7.2$), triggering many landslides (debris slides, debris flows, rock falls, etc.) largely in Miyagi and Iwate Prefectures. The authors visited the landslide sites 6 days after the occurrence, finding long-travelling flow-type of landslides could be grouped into two: usual debris flows in which debris was saturated with water; and, earth flows and debris

Y. Okada (✉)
Department of Soil and Water Conservation, Forestry and Forest Products Research Institute, Matsunosato 1, Ibaraki, Tsukuba, Japan
e-mail: okada10@ffpri.affrc.go.jp

U. Kurokawa · S. Asano
Kansai Research Center, Forestry and Forest Products Research Institute, Kyoto, Japan

flows in which earth and debris were not saturated. Mechanisms of long travelling motion and fluidisation found in an unsaturated earth flow on the east slope of Mt Hikagemori, Kurihara city, Miyagi Prefecture is reported in this paper with results of triaxial compression tests and mass flow experiments by means of a large-scale model-flume.

2 The Complex Hikagemori Landslide (Debris Slide-Earth Flow)

The Hikagemori landslide is a complex type (debris slide-earth flow) generated on the east slope of Mt Hikagemori in Miyagi Prefecture (Photo 45.1). The Hikagemori debris slide occurred on a slope having a cap-rock structure: welded tufa underlain by unwelded pumiceous tufa. The width of the head-scarp was about 75 m, the height was about 20 m (Photo 45.2), the debris-slide-mass moved in a rotating mode and little disturbance was found in the main body. The width of deposition of debris slide was about 120 m and a slip surface was formed within the unwelded pumiceous tufa. Most of the soil stopped after moving about 20 m, however, a left-part of them moved down the concave slope, fluidised on the course travelling more than 150 m. Photo 45.1 is the result of compass surveying, showing the longitudinal section of deposition area, runout area of the earth flow and left-part of debris slide (about 10 m inside from the left-flank). It was a very gentle slope (smaller than 10°) on the earth flow deposition area. However, at the final edge of the earth flow deposition area, a relatively steep slope was formed at about 25° (Photo 45.3). Also a sediment of fine soil particles was found, where muddy water exuded around from the slip surface and fine particles settled. The sediment was about 10 mm high (Photo 45.4), it expanded about six metres ahead. In the earth flow deposition and run-out areas, it was not found that the soil mass was saturated, indicative that the soil mass probably moved down under the unsaturated conditions. While, based on the formation
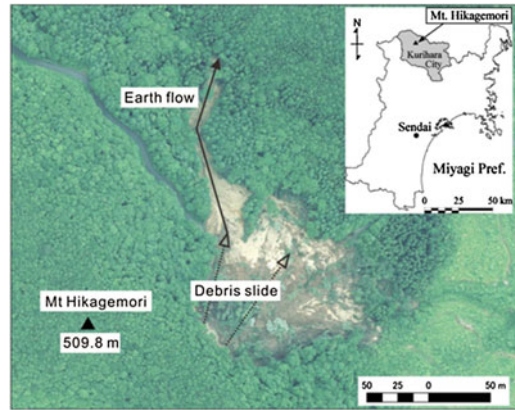
Photo 45.1 An ortho image of a complex Hikagemori landslide (Revised from an orthonised aerophtograph by Geographical Information Authority of Japan)

of the thin layer of the fine soil particles' sediment, it was assumed that fine soil particles suspended within the pore-fluid near the slip surface, building-up an excess pore-fluid pressure. When the earth flow mass stopped, pore-fluid pressure reduced and fine soil particles exuded forming a thin layer of sediment. In addition, it should be mentioned that a part containing much water was found in the run-out area. At that part, the soil easily liquefied when vibrated by foot (Photo 45.5).

3 Triaxial Compression Tests

In order to examine fluidisation mechanisms, undrained triaxial compression tests were conducted. Undisturbed specimens were sampled with 100-ml tubes (0.05 m high) from the head-scarp. The cylindrical-shape specimen was trimmed to be 0.1 m high and 0.05 m in diameter in the laboratory. A mean soil particle size $(D_{50}) = 0.32$ mm, a uniformity coefficient $(U_c) = 18.9$ $(D_{10} = 0.028$ mm, $D_{60} = 0.53$ mm), soil particle density $(\rho_s) = 2,662$ kg/m^3. Under 15 kPa confining stress, the specimens were saturated under the 0.3 m water-head-difference for three to 12 h. After consolidation, axial load was applied in sinusoidal wave form 30 times at 1 Hz under undrained conditions. When the specimen did not fail, further 30 waves were applied, in which the

Photo 45.2 Views of the Hikagemori landslide. **a** debris slide, **b** head-scarp

Photo 45.3 A sediment formed ahead of earth flow deposition area of the Hikagemori landslide

Photo 45.4 A close view of the vertical section of the sediment

amplitude of the waves were enlarged (Table 45.1). The loading was stopped when the axial strain reached 15 %.

An effective stress path of test-TTA is shown in Photo 45.2. Since the specimen had low pore pressure coefficient *B* (Skempton 1954), neither pore-water pressure build-up nor abrupt reduction of shearing resistance was observed. A failure envelope was observed, an internal friction angle was about 18° and a cohesion was as much as 60 kPa. Also in test-TTB, pore-water pressure build-up and abrupt reduction of shearing resistance were not found. An effective stress path of test-TTC which had the largest void ratio of the three is shown in Photo 45.3. When the amplitude of the axial load was small, it was not observed the pore-water pressure build-up and abrupt reduction of shearing resistance. However, given the larger axial load, abrupt reduction of shearing resistance was observed, in which large pore-water pressure build-up was not found. This would be probably

attributable to a collapse of soil skeletal structure taking place during stain softening behaviour. This fact proved that abrupt reduction of shearing resistance due to the collapse could take place under certain conditions of void ratio, the degree of saturation, and stresses.

4 Mass Flow Experiment by Means of Large-Scale Model-Flume

In order to investigate the long travelling behaviour of the Hikagemori earth flow, mass flow experiments using a large-scale model-flume were conducted on a disturbed sample taken from the head-scarp of the Hikagemori landslide. Details of the large-scale model-flume (Photo 45.4) are found in Okada and Ochiai (2008). It is totally 13 m long, 1 m deep, and 0.6 m wide, and consists of two parts: the inclination of the upper part can be varied from 10 to

Photo 45.5 Easily-liquefied soils exposed at the run-out area of the Hikagemori landslide

45°, while the lower part is horizontal. Specimens (0.6 m^3) were set in the upper end portion of the inclined segment (1 m long) and retained by a water-proof casement gate. The water proof casement gate was controlled electronically to release the specimen at the start of each experiment run. Roughness was provided on the bottom surface of the flume by placing a sheet on which 0.4–2.0 mm sand grains were sprayed. Pressure transducers were set in the base of the flume to measure basal fluid pressure, and laser displacement transducers were positioned above them to measure normal flow depth. These data were logged by a PC at 500 Hz. In addition, the movement of the material was monitored by digital video cameras (60 fps). Four time-code indicators were set around the flume to show the elapsed time with a resolution of one hundredth of a second. The digital video cameras were situated so that they could film the time-code indicators. Using this system, the basal fluid pressure, the normal flow depth data, and the filmed images could be synchronised.

Although high pore-fluid pressure was probably built-up near the slip surface, most of the earth flow body assumed to be unsaturated conditions. Then, a specimen was saturated only in the bottom half in the first experiment (Ex-FEA). When releasing the material on a slope of 30°, the material decelerated even on the inclined portion and the main body deposited only 2.5 m downslope from the water-proof

gate. Pressure heads measured on the base of the flume did not exceed the normal flow depth. A cohesion of the specimen should be reduced based on the scaling of the model flume (Kagawa 1978), however, it was difficult. Because the cohesion was not reduced in the experiment, it likely worked too much and prevented the material from travelling downslope further. An equivalent coefficient of friction was 0.545.

In the second experiment (Ex-FEB), water was percolated for 3.5 h through whole specimen to be saturated. In this case, pressure head measured at position 1 (Photo 45.4) exceeded normal flow depth between 27 and 27.5 s (Photo 45.5). During this period, higher basal pore-fluid pressure was likely built-up. Whereas, pressure head remained negative between 30 and 36 s. This was probably due to an insufficient saturation of the specimen even though water was slowly percolated for 3.5 h.

Some parts of the material deposited on the inclined portion, but some parts travelled long distance up to 6.6 m ahead from the connection of the inclined portion and horizontal portion. Filmed images revealed that the unsaturated mass moved and slid on the muddy water, and finally deposited (Photo 45.6). This mass positioned at near the head when moving down the inclined portion, then, after reaching the connection of the inclined and horizontal portions, it travelled further splitting off during the movement. Muddy water insisted that the fine soil particles were suspended in the water, and a higher apparent density of the fluid resulted in generation of higher basal fluid pressure. An equivalent coefficient of friction of Ex-FEB was only 0.256, a high mobility was reproduced in the experiment of the specimen with sufficient water inside.

Although the experiments were conducted by means of the large-scale model flume, it was revealed that the long travelling behaviour was difficult for the sample with the high cohesion to be reproduced especially in Ex-FEA. While, a long travelling behaviour was observed in Ex-FEB, in which the unsaturated mass moved and slid on the muddy water. This may not explain the exact mobility of the Hikagemori earth flow, it may also insist that the mass will travel long distance when

the slip zone is saturated and high pore-fluid pressure reduces the shearing resistance.

5   Concluding Remarks

The Hikagemori landslide triggered by the Iwate-Miyagi Nairiku Earthquake in 2008 was a complex type: debris slide-earth flow. The slope of earth flow toe was at least 25°, fine soil particles exuded around from the surface of separation. These suggested that most of the mass was unsaturated but near the slip surface high pore-fluid pressure was built-up with suspension, resulting in the long travel distance. Undrained triaxial compression tests revealed that cohesion was at least 50 kPa, reduction of shearing resistance due to collapse of soil skeleton

structure would take place in a case. Mass flow experiments showed that unsaturated mass moved and slid on the muddy water travelling the long distance in the experiment of the specimen with sufficient water inside. This may explain a part of the long travelling mechanisms of the Hikagemori landslide.

References

Kagawa T (1978) On the similitude in model vibration tests of earth-structures. Proc Jpn Soc Civil Eng 275:69–77

Okada Y, Ochiai H (2008) Flow characteristics of 2-phase granular mass flows from model flume tests. Eng Geol 97:1–14

Skempton AW (1954) The pore pressure coefficients A and B. Géotechnique 4:143–147

Shaking Table Test of Embankment on Inclined Ground Affected by Rainfall

46

Takaki Matsumaru, Motoaki Suga and Ryosuke Uzuoka

Abstract

During the Nigata-ken Chuetsu Earthquake having occurred in 2004, a number of railway and road embankments collapsed in mountainous regions. It appears that the main reasons of these damages were inclined ground conditions and the rainfall caused by the typhoon just prior to the earthquake. In this paper, the authors performed shaking table tests of embankments on inclined ground affected by rainfall intended for evaluating the adverse effect of rainfall seepage on seismic resistance. We conducted two cases using permeable ground and impermeable one. Rainfall was poured into the embankment until confirming rise of degree of saturation and partial formation of water level. The shaking was conducted until the embankment collapsed with increasing the maximum acceleration. From two cases of shaking table tests; it was revealed that the seepage boundary conditions of the ground affected behaviors of the embankment. In the case without shaping of water level, the response of acceleration at the top of the embankment increased excessively and the embankment deformed to a shape of circular. On the other hand, in the case with shaping of water level, the embankment collapsed with flow, so the response of acceleration decreased during the shaking. Furthermore, the mechanism of stopping of increasing of pore water pressures during shaking was revealed.

T. Matsumaru (✉) · M. Suga
Structures Technology Division, Railway Technical
Research Institute, 2-8-38 Hikari-cho, Kokubunji-
shi, Tokyo 185-8540, Japan
e-mail: matumaru@rtri.or.jp

M. Suga
e-mail: suga@rtri.or.jp

R. Uzuoka
Faculty of Engineering, University of Tokushima,
2-1, Minamijyousanjima-cho, Tokushima,
770-8506, Japan
e-mail: uzuoka@ce.tokushima-u.ac.jp

1 Introduction

During the Nigata-ken Chuetsu Earthquake which occurred in 2004, a lot of railway and road embankments collapsed in mountainous regions. It appears that these damages were caused mainly due to inclined ground conditions, the increased degree of water saturation and the increased water level in the embankments caused by the typhoon just prior to the earthquake. Therefore, the evaluation of the seismic resistance for embankment subjected to rainfall is important.

There are few researches about shaking table tests of embankment affected by rainfall. Ichii (2005) revealed by shaking table tests that the seismic resistance of embankment subjected to rainfall was decreased. Isono et al. (2008) conducted rainfall-sprinkling test and shaking table test of embankment with precise measurement of degree of saturation and pore water pressure. Furthermore, there are several researches about shaking table tests affected by seepage water from backfill. Matsuo et al. (2002) conducted a series of dynamic centrifuge tests on the embankment affected by seepage water. They showed the relationship between the residual displacement and the density of the embankment or the water level, and the effects of counter-measure methods. Nakamura et al. (2010) conducted series of centrifuge shaking table tests in which moisture condition in the embankment and liquefaction of the foundation ground were chosen as test parameters. Moreover, there are several researches focusing on seismic behavior of sandy slopes considering the existence of seepage water (Robertson and Fear 1997; Dobry et al. 1997; Pilgrim 1998). However, only a few researches previously conducted focused on evaluating the mechanism of collapse.

In this paper, we conducted shaking table tests of embankment located on inclined ground affected by rainfall with intention of evaluating
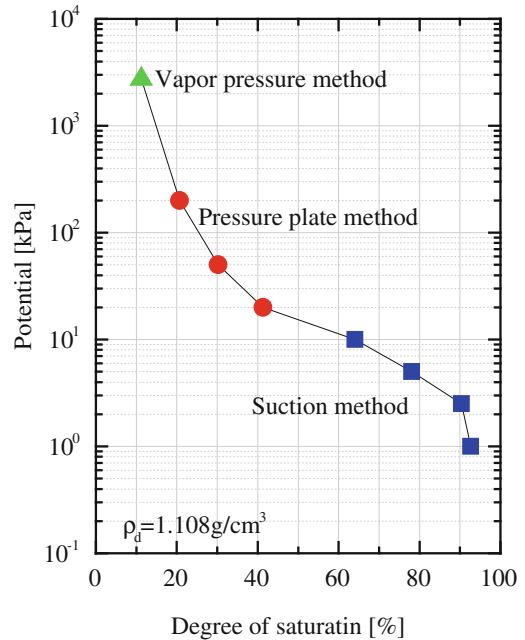
Fig. 46.1 Soil water characteristic curve

the adverse effect of the rainfall on seismic resistance. It was focused on this paper how the permeability conditions on inclined ground affected the seismic resistance of embankment.

2 Conditions of Shaking Table Tests

2.1 Materials of Embankment

The material of the embankment was Inagi sand, whose particle density G_s was 2.723; 50 % diameter on the grain size diagram D_{50}, 0.134 mm; the uniformity coefficient U_c, 9.29; the fine fraction content F_c, 23.6 %; and the maximum dry density, 1.517 g/cm^3. The embankment was prepared so that the dry density and the water content would be 1.108 g/cm^3 and about 13 % respectively. The saturated permeability with dry density

Fig. 46.2 Experimental model of embankment and arrangement of measurement
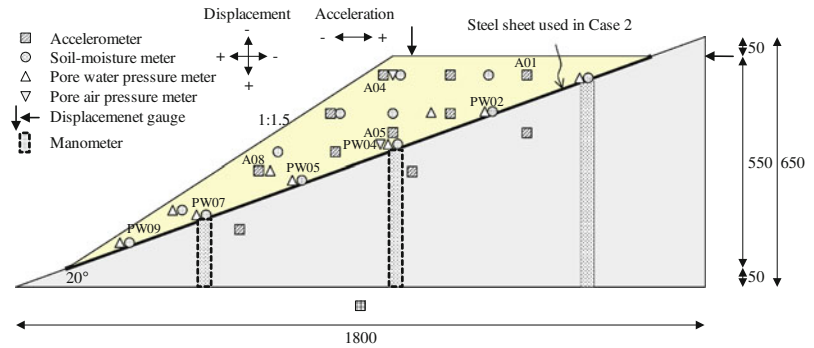
1.108 g/cm^3 was 1.86×10^{-4} m/s, obtained from the constant head permeability test in the laboratory. The dry density of the embankment was set much smaller than the maximum dry density, in order to make the seepage easy and to avoid setting the cohesion excessive taking similarity law into consideration. Figure 46.1 shows the soil water characteristic curve obtained from the pressure plate method, suction method and vapor plate method. Furthermore, the cyclic undrained triaxial test was conducted in order to obtain the liquefaction strength of the material of embankment. From the test, the cyclic shear strength ratio to 20 cycles (R_{l20}), in which the double amplitude of linear strain (DA) was 5 %, was 0.119. On the other hand, the ground was constructed using crushed stone for mechanical stabilization, with efficient compaction for avoiding the occurrence of settlement and liquefaction.

2.2   Experimental Model and Measurement

Figure 46.2 shows the experimental model of the embankment. The dimension of the embankment was 55 cm in height and 1:1.5 in gradient of slope. The gradient of the inclined ground was 20°. We conducted two cases of shaking table test under two different seepage conditions between the embankment and the ground: Case 1 of permeable condition and Case 2 of impermeable condition. In Case 2, the steel sheet with efficient

friction was set along the boundary of ground and embankment in order to avoid seepage from the embankment to ground.

The measurements included the degree of saturation and water level for evaluating water content just before the shaking, and acceleration, pore water pressure and displacement for making dynamic behavior of the embankment clear. The pore water pressure meters were connected with ceramic filters, in order to measure negative pore water pressure in unsaturated regions. Furthermore, we photographed reference points in the embankment with a high-speed camera and analyzed the obtained data in order to estimate a deformation mode. We set three manometers in the embankment for measuring the water level. The direction of measured acceleration and displacement was shown in Fig. 46.2.

2.3   Conditions of Rainfall and Shaking

The rainfall was given from the water-sprinkler located above the shaking table, with about 20 mm/h in intensity of rainfall. The shaking was conducted after confirming the rise of degree of saturation and water level at the toe of embankment. We used sinusoidal wave of 5 Hz as the inputted motion. For both the cases, the shaking table test was continued with gradual increase of the amplitude of acceleration until the embankment collapsed.

Fig. 46.3 Distributions of degree of saturation and water level

(a) Case 1

Degree of saturatin (%)

(b) Case 2

Degree of saturatin (%)

Pore water pressure
2.67 kPa

8.43 kPa

Supposed water level
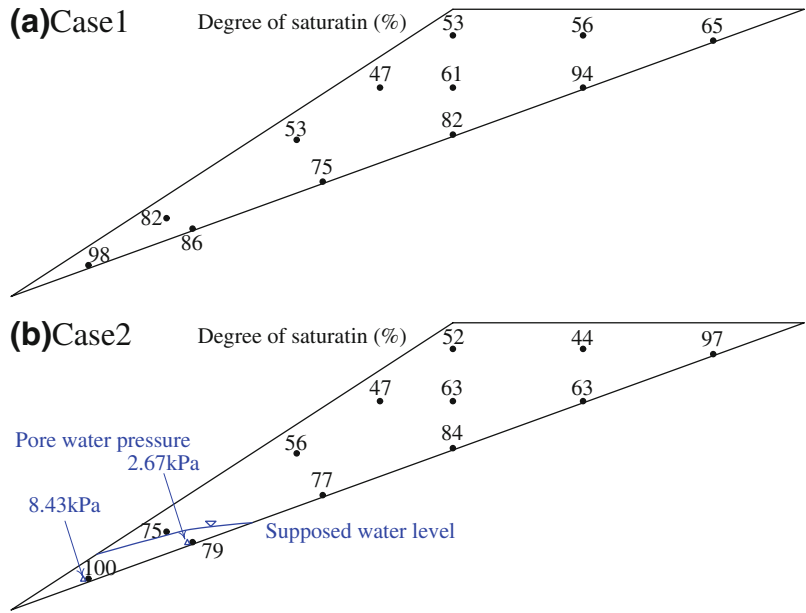
3 Results and Discussions

3.1 Degree of Saturation and Water Level Just Before Shaking

Sprinkling of rainfall was continued for about 240 min in Case 1 and 150 min in Case 2. During sprinkling, small deformation of the embankment was observed partially at the top and the toe, but its initial shape was maintained.

Figure 46.3 shows the distributions of the degree of saturation and the water level estimated from the pore water pressure meters just before starting the shaking table tests. The degree of saturation was calculated by using the moisture content measured by the soil-moisture meters. The water content $w = 13\%$, which was the value at the time of the construction of the embankment, corresponds to the degree of saturation $S_r = 24\%$. It was revealed that the degree of saturation increased at all positions of installed soil-moisture meters. However, the distributions of degree of saturation for two cases were quite similar to each other. On the other hand, in Case 2, power water pressures (P.W.P.) at PW07 and PW09 shown in Fig. 46.2, which showed
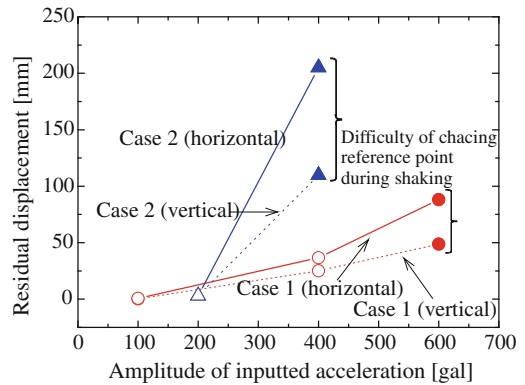
Fig. 46.4 Relationship between inputted motion and residual displacement **a** case 1 **b** case 2

negative values before starting rainfall, increased during sprinkling of rainfall and became positive values just before shaking. From this phenomenon, water level was supposed to be formed just before shaking in Case 2, as shown in Fig. 46.3. Furthermore, P.W.P. would be larger than hydrostatic pressure, judged from the value at P07 and P09. In Case 1, P.W.P. was increased during sprinkling rainfall, but all pore water pressure gages showed negative values. So, the water level would not be formed.

Fig. 46.5 Photographs after shaking **a** case 1 (600 gal) **b** case 2 (400 gal)
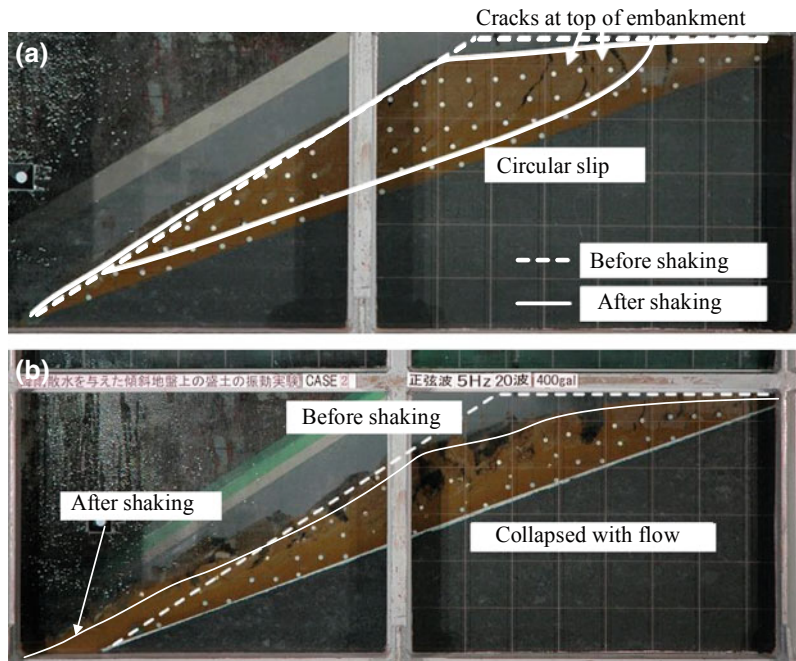
3.2 Differences of Failure of Embankment

Figure 46.4 shows the relationship between the amplitude of the inputted motion and the horizontal and vertical residual displacement at the top of embankment. In Case 1, the deformation of embankment did not occur by 100 gal shaking. However, the embankment started to be deformed by 400 gal shaking and was deformed largely by 600 gal shaking, so we finished the series of the shaking table test. In Case 2, the deformation little occurred by 200 gal shaking, but the embankment started to be deformed more largely than in Case2, by 400 gal shaking. Figure 46.5 shows the photographs of the embankment after 400 gal shaking in both the cases. In Case 1, the top of embankment settled and moved toward the direction of the slope, and a lot of cracks appeared at the top. The embankment was deformed with the shape of circular slip, judged from the movement of reference points. On the other hand, in Case 2, the embankment collapsed with flow failure without maintaining the initial shape.

3.3 Response of Acceleration

Figure 46.6 shows the time histories of the responses of accelerations at A01, A05 and A08. In Case 1, the response did not change during shaking by 100 gal shaking. Therefore, the embankment would behave integrally with the ground. In Case 1, by 400 gal shaking, the response at A01 was increased dramatically though the responses at A05 and A08 did not change during shaking. It seems that the inclination of ground affected the response of embankment around its top. On the other hand, in Case 2 with 400 gal shaking, all accelerometers showed the reduction of response with increase of the response at the beginning of shaking at some places. Furthermore, the time of start of the reduction of the response differed depending on position of the accelerometers. In this case, the embankment collapsed with flow failure at the toe of embankment, so the reduction of the response would have started from the toe to the top.
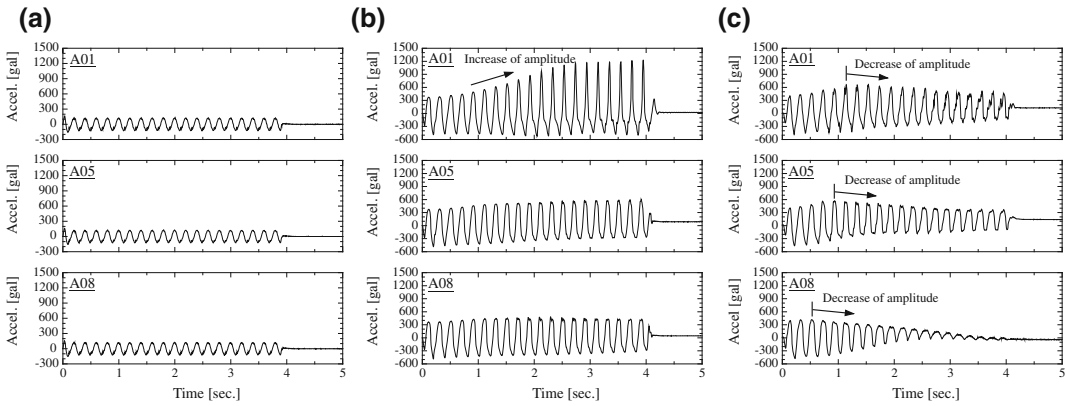
Fig. 46.6 Time histories of acceleration for each case **a** case 1 (100 gal) **b** case 1 (400 gal) **c** case 2 (400 gal)
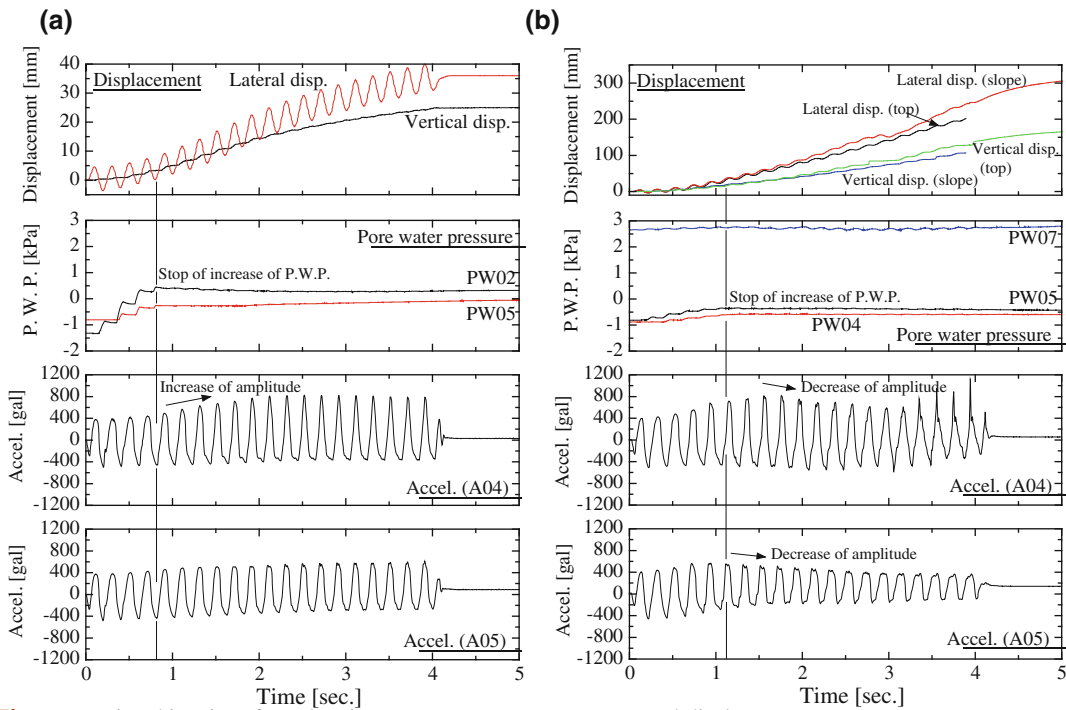
Fig. 46.7 Time histories of acceleration, excess pore water pressure and displacement

3.4 Mechanism of Collapse of Embankment

In order to study the behavior of the embankment during earthquake, we focused on the shakings by 400 gal-sinusoidal waves in both the cases. Figure 46.7 shows the time histories of the responses of acceleration (A04 and A05 in Fig. 46.2), P.W.P. and the displacement at the top

of embankment. In the time history of the displacement, we showed it obtained from the analysis of the reference points located at the top of the embankment. In Case 2, chasing of the reference points at the toe became impossible during shaking, so the time history of the reference point located in the slope was also plotted. The direction of displacement was shown in Fig. 46.1 by sings of plus (+) and minus (−). The P.W.P.s plotted in

these figures were located in the unsaturated region and increased during shaking, so the selected pore water pressure gauges were different between both the cases.

As an overall trend, the response of acceleration and displacement were different between two cases. As shown in the time history of displacement, though the increase of the displacement stopped just after stopping the shaking at about 4 s in Case 1, the displacement continued to be increasing in Case 2. This difference would have been caused due to the presence or absence of water level.

On the other hand, the responses of P.W.P. were similar between two cases. For both cases, the P.W.P. in unsaturated area was increased during shaking, so the effective stress would have been decreased. But, large positive pressure did not appear. In order to clarify the reason of the increase of the P.W.P., we compared the time histories of the displacement and P.W.P. The P.W.P. was increased not immediately after starting of shaking but after a brief interval. We evaluated the distributions of strain in the embankment at each time, based on the analysis of coordinates of the reference points. For both the cases, large shear strain appeared in the embankment at 0.2–0.3 s. This indicated that the P.W.P. increased by the occurrence of the negative dilatancy accompanying the deformation of the embankment.

The increase of P.W.P. stopped at about 0.8 s in Case 1 and at about 1.2 s in Case 2, though the shaking was continued after these time points. In the shaking table tests in which embankment constructed on flat ground was affected by seepage water or rainfall, P.W.P. continued to increase during shaking (Matsumaru et al. 2009 and Isono et al. 2008); so this phenomenon would be typical of the embankment constructed on inclined ground.

In order to clarify the mechanism of the stop of the increase of P.W.P., we compared the time history of P.W.P. with response of acceleration. In Case 1, the response of acceleration continued to increase after the stop of the increase of P.W.P. It is difficult to recognize that the liquefaction occurred in embankment during

shaking because of the stop of the increase of P.W.P. It seems to be that the element in the embankment reached shear failure.

On the other hand, in Case 2, the response of acceleration at A04 and A05 changed from increase to decrease when the increase of P.W.P. stopped. Though the P.W.P. in unsaturated zone of embankment increased during shaking, the amount of increase was small. Moreover, the maximum value of P.W.P. was still negative. It seems to be difficult to recognize that the liquefaction occurred in the unsaturated region of embankment. In Fig. 46.7, P.W.P. at P07, under the supposed water level, were also plotted. The value of P.W.P at P07 showed positive one and was supposed to be larger than hydrostatic pressure. Therefore, the region around the toe of embankment would be in almost liquefied state just before shaking. It seems to be that the toe of embankment was completely liquefied during shaking and the confining stress became loose in lateral direction due to the occurrence of the liquefaction. For this reason, the stop of the increase of P.W.P. in the unsaturated region would have occurred.

For clarifying the failure mechanism of embankment, more precise research including analytical approach is necessary.

4 Conclusions

For clarifying the behavior of embankment located on inclined ground and affected by rainfall, the shaking table tests of embankment were performed. In experiments, two cases of shaking with different permeable conditions of inclined ground were conducted, in order to study the effect of the water content on seismic resistance of the embankment. As the results, we arrived at the following conclusions:

1. According to the results of two cases of experiments, though the distributions of degree of saturation were quite similar to each other, the shaping of water level was different depending on permeable conditions. By shaking, the embankment was deformed

with the circular slip in the case without the shape of water level, but flow phenomenon occurred from the toe of embankment in the case with shaping of water level.

2. The responses of accelerations in the embankment were largely different between two cases. In the case without shaping of water level, the response of the acceleration was affected by the inclined ground. On the other hand, the response was changed from increase to decrease due to the occurrence of the flow failure at the top of the embankment.

3. For both cases, the P.W.P. was increased in unsaturated region of embankment, but the increase was stopped during shaking. The reason was supposed that the shear failure occurred in the embankment in the case without the water level. In the case with the water level, the confining stress in horizontal direction was loosed due to the occurrence of the flow failure.

References

Dobry R, Taboada V, Liu L (1997) Centrifuge modeling of liquefaction effects during earthquakes. In: Balkema AA (ed) Proceedings IS-TOKYO'95/The 1st International Conference on E.q Geotech Engrg, Tokyo, pp 1291–1324

Ichii K (2005) Experimental study on seismic resistance reduction of embankment due to rainfall. J Earthq Eng 1–8 (in Japanese)

Isono J, Matsumaru T, Tateyama M, Isono J, Koseki J, Watanabe H (2008) Seismic design method for embankment affected by seepage water using Newmark method. Proceedings of the 40th Japan National Conference of Geotechnical Engineering. pp 1149–1150 (in Japanese)

Matsumaru T, Kojima K, Tateyama M, Watanabe K Watanabe H (2009) Calculation method for residual displacement during earthquake for embankment affected by seepage water. Proceedings of the International Symposium of Geotechnical Engineering

Matsuo O, Saito Y, Sasaki T, Kondoh K, Sato T (2002) Earthquake-induced flow slides of fills and infinite slopes. Soils Found 42(1):89–104

Nakamura S, Higuchi S, Sawada S, Yoshida N (2010) Effect of moisture condition on failure characteristics of embankment based on centrifuge shaking table test. J Civil Eng 66(2):446–456 (in Japanese)

Pilgrim NK (1998) Earthquake-related deformation beneath gently inclined ground. Geotechnique 48(2):187–199

Robertson PK, Fear CE (1997) Liquefaction of sands and its evaluation. In: Balkema AA (ed) Proceedings IS-TOKYO'95/The 1st National Conference on Earthquake Geotech Engrg, Tokyo, pp 1253–1289

Dynamic Ring Shear Characteristics of Artificially Cemented Sand

47

Motoyuki Suzuki, Hiroshi Takahara and Takeo Umezaki

Abstract

In recent earthquakes, lots of landslides occurred in natural slopes composed of weakly cemented and during or immediately after earthquake. The slope failure may be resultant from any loss of cementation formed between sand particles. Therefore, it is important to clarify strength property of natural cemented sand on a slip surface subjected to dynamic shearing. In this study fast and cyclic shear characteristics of cemented sands were considered based on results of ring shear test. In laboratory, artificial cementation property was reproduced by adding a cement agent to sand. A series of dynamic ring shear tests was carried out on both of non-cemented and cemented sands. Consequently, it was shown that the importance of shear strength of cemented sand was recognized when we correctly assess the stability of the slope during or after an earthquake.

1 Introduction

Landslides occur in natural slopes during or immediately after earthquake. The 2004 Niigata Prefecture Chuetsu earthquake triggered numerous landslides in natural slopes composed of sedimentary rocks such as sandstone; mudstone and other weakly cemented soils (see Fig. 47.1). According to many case histories, it was shown that an earthquake-induced landslide occurred either on a slip surface in sandstone or on a bedding plane between sandstone and mudstone. Such soils possess natural cementation property due to diagenesis for a long period.

Such collapse may be due to any loss of cementation formed between sand particles. Therefore, it is important to analyse seismic slope stability based on the shear strength of natural cemented sand on the slip surface subjected to rapid and dynamic loading. However, the

M. Suzuki (✉)
Yamaguchi University, Ube, Japan

H. Takahara
Penta-Ocean Construction Co., Ltd, Tokyo, Japan

T. Umezaki
Shinshu University, Nagano, Japan

Fig. 47.1 Tufaceous sandstone on slip surface at Yokowatashi in Nagaoka

dynamic behavior and strength characteristics of cemented sand have not yet been clarified.

The aim of this study was to clarify cyclic shear behavior of cemented sand, and to develop a method for evaluating its seismic slope stability. We developed a cyclic loading ring shear test apparatus under a constant volume condition. Monotonic fast and cyclic shearing tests were carried out on both non-cemented and cemented sands using this apparatus. Laboratory-simulated cementation was artificially reproduced by adding a cementing agent to Toyoura sand. This paper describes the behavior and shear strength of cemented sand subjected to dynamic loading and the rate effect on the shear strength.

2 Fast Shearing of Sands in Ring Shear Test

2.1 Outline of Test

The purpose of our test was to investigate the rate effect on the steady-state strength of cemented and non-cemented sands. A series of ring shear tests was carried out using different shear displacement rates on multiple specimens. The soil samples used were two kinds of sands collected at landslides from the Niigata Prefecture Chuetsu earthquake, namely, Terano and Higashi-Takezawa A. In addition, Toyoura standard sand was used for testing cemented sand. The shear displacement rate was changed within the range of 0.1 and 20 mm/min.

Fig. 47.2 Grading curves of soil samples used

2.2 Physical Properties of Soil Samples Used

Sands were collected at croplines at the bottom of landslide slopes and labeled "*Terano*" or "*Higashi-Takezawa A*" accordingly. The samples to be used for the shear test were passed through a 0.85-mm sieve. The grading curves of samples are shown in Fig. 47.2.

As above mentioned, Toyoura standard sand was also used in this study, mixed with a small amount of bentonite. The physical property of the bentonite used was $\rho_s = 2.716$ g/cm^3, $w_L = 479$ % and $w_P = 37$ %. The cemented sand was mixed at a weight ratio of Toyoura sand: bentonite: cement: distilled water of 73.7 %: 5.6 %: 2.0 %: 18.7 %. The cement content with respect to the soils was 2.5 %.

Table 47.1 Physical properties of sands used in this study

Soil sample	D_{max} (mm)	$\rho_s (g/cm^3)$	U_c	U'_c
Terano	0.85	2.616	2.1	0.9
Higashi-Takezawa A	0.85	2.588	2.1	1.5
Toyoura sand	0.85	2.639	2.1	1.0

The cemented sample was cured in a mold for 3 days. After that, a specimen was cut from the sample. The non-cemented sample was mixed at a weight ratio of Toyoura sand: bentonite: distilled water = 75.6 %: 5.7 %: 18.7 %. The sample was pre-consolidated until the end of the primary consolidation elapsed. After the consolidation, a specimen was cut from this sample. Reproduced samples were labeled "*Cemented sand*" and "*Non-cemented sand*", respectively. The ring shear test was conducted on both samples. The physical properties of the samples are listed in Table 47.1.

2.3 Test Apparatus and Procedure

Figure 47.3 shows a view of the test apparatus. The ring-shaped specimens had inner diameters of 6 cm, outer diameters of 10 cm, and a wall thickness of 2 cm. The specimens were sheared at a level of 1 cm from the base plate. During testing, shear stress, normal stress, frictional force and normal displacement were all measured and automatically recorded. The frictional force along the perimeter of the rings, which is generated by vertical displacement of the specimen, was measured by a load cell. In this test, the net normal stress acting on the shear surface was calculated based on the measurement of the frictional force.

The specimen was carefully compacted with three layers using a tamper in order to ensure that the initial dry density of the specimen could be established uniformly. The upper surface of the specimen was finished flat. After that, the specimen was normally consolidated by consolidation stress, σ_C, for 1 h. The value of σ_C was varied within the range of 294–490 kPa, since the depth of the slip surface in both

Fig. 47.3 Ring shear test apparatus used

landslides was equivalent to about 30 m. After consolidation, the specimen was sheared under a constant total normal stress, σ_N, until shear displacement, δ, became a value sufficiently large to reach a steady state. Here δ is defined as an intermediate circular arc between the inner and outer rings. Before the shearing, the minimum gap between the rings was opened in order to remove the friction between the rings, and to avoid the outflow of the sample from the shear surface.

3 Results and Discussions

Determination of the strength parameter for dense dried sand and its rate effect are discussed in this section. Figure 47.4a and b show test results of Terano and Higash-Takezawa A. The relationships between the peak and steady-state strengths, τ_p, τ_{ss}, and the normal stress with different shear displacement rates are shown in these figures. The steady state of sand was defined as an ultimate state in which the stress ratio, τ/σ_N, of sand did not change as the shearing proceeded. The strength parameters at the peak and steady states as shown in these figures were determined by fitting to the measurement of the relationship among the peak strength, the steady-state strength, and the
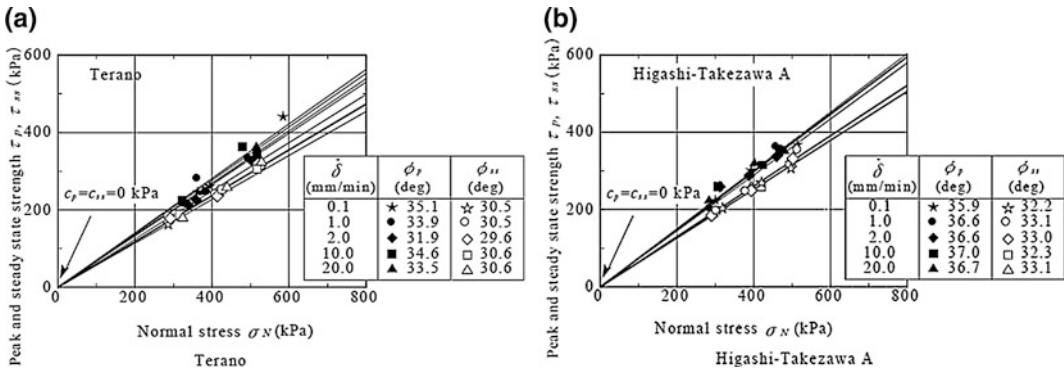
Fig. 47.4 Peak and steady-state strength lines of **a** Terano and **b** Higashi-Takezawa A
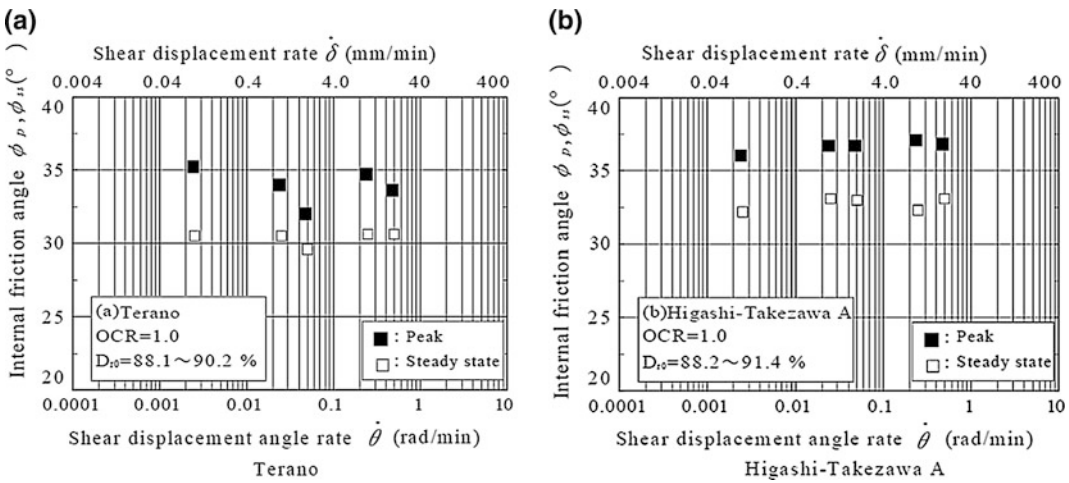
Fig. 47.5 Relationship between internal frictional angle in peak and steady states and shear displacement rate

normal stress using the least square method. It can be seen from this figure that the apparent cohesion in all cases was almost zero, because of dried sand. On the other hand, there can be seen a slight change in the gradient of the peak and steady-state strength lines.

Next, the rate effect observed in dense sands was considered. Figure 47.5a and b show the relationships between the internal friction angle at peak and steady states, and the shear displacement angle rate for Terano and Higashi-Takezawa A. The peak value for Terano slightly increased or decreased within the range of 0.1–20 mm/min, whereas the steady-state value remained almost constant in the same

range. On the other hand, the internal frictional angles at both states for Higashi-Takezawa A remained almost constant in the same range. At least, the internal friction angle at the steady state was not changed by any change in the shearing speed. This finding is consistent with that of dense Toyoura sand. However, these sands were well graded as compared that of Toyoura sand. It was shown that the internal frictional angles at the peak and steady states were not affected by any change in the shearing speed.

Figure 47.6 shows the relationship between shear stress and normal stress on the shear surface for cemented and non-cemented sands. In this

Fig. 47.6 Stress paths and strength lines of cemented and non-cemented sands
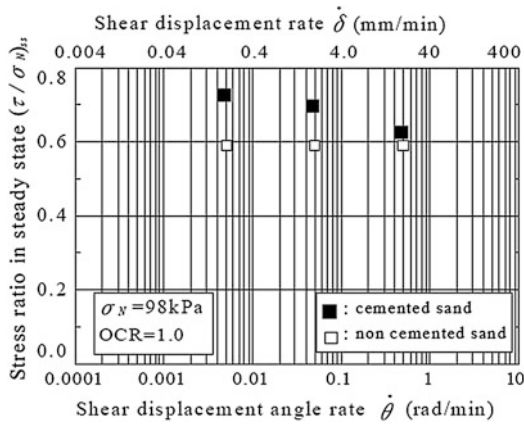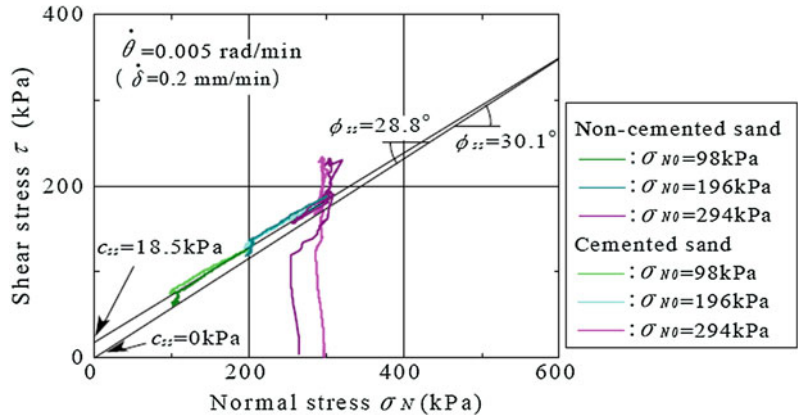
Fig. 47.7 Relationship between steady-state stress ratio and shear displacement rate of cemented and non-cemented sands

test, the normal stress was gradually decreased in the steady state. The internal friction angles in the steady state of both sands were at the same level as that of Toyoura sand. The apparent cohesion of the cemented sand was c_{ss} = 18.5 kPa, the large value of which may be due to development of the cementation.

Figure 47.7 shows the relationship between the stress ratio in steady state and the shear displacement rate in a logarithmic scale for non-cemented and cemented sands. These data were obtained by shear testing using a single specimen as shown in Fig. 47.6. The stress ratio for non-cemented sand was almost constant despite the change of the shear displacement rate. On the other hand, the stress ratio

for cemented sand decreased with increases of the shear displacement rate and then became close to that for non-cemented sand. It was suggested that the cementation property of the shearing zone in the cemented sand was gradually damaged by shearing and eventually disappeared.

Figure 47.8 shows the relationship between the residual or steady-state strength of various soils and shear displacement rate from previous study. Sandy soils generally exhibit higher shear strength than clayey soils. However, the residual strengths of some clay are higher than those of sands. In the case of clay, the residual stress ratio increased, decreased, or remained constant according to the change of the shear displacement rate. This tendency appeared with the change of effective normal stress on the shear surface owing to the generation of excess pore water pressure. In the case of dried sands, there did not exist excess pore water pressure as in clay. In the range of high normal stress, the amount of dilation was small, so that the rate effect was negligible.

Figure 47.9 shows grading curves of Terano before and after the shearing. This figure shows that the fine content of the sample increased after shearing. According to Lupini et al. (1981), the transitional shearing zone contained sliding, and turbulent shearing modes occurred within the range of F_{clay} = 23–43 %. Crushable soil seems to move toward the steady state while its fine content increases during shearing.
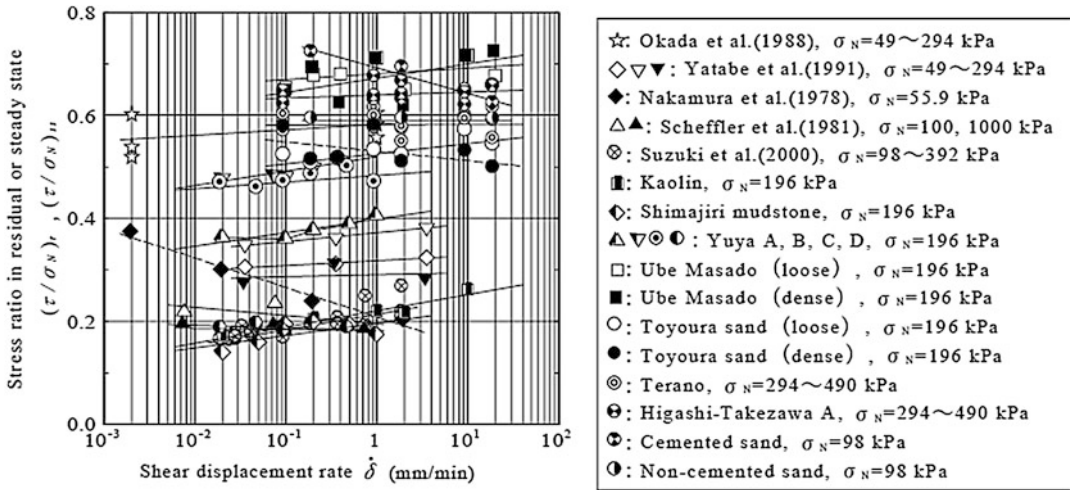
Fig. 47.8 Effect of shear displacement rate on residual or steady-state shear strength of various soils
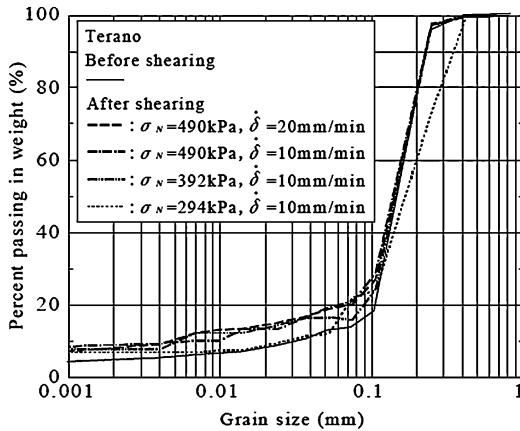
Fig. 47.9 Change of grading curves of Terano before and after shearing

4   Cyclic Shearing of Sands in Ring Shear Test

4.1   Outline of Test

In the Niigata Prefecture Chuetsu earthquake of 2004, a number of landslides occurred. In particular, it was found that natural slope consisting of sandstone was vulnerable to seismic motion. It is considered that undisturbed sand loses its cementation property by cyclic shearing, and reduces its intrinsic strength, which then led to large-scale collapse. Many researchers are researching the dynamic shear strength of clay and silt. However, the cyclic shear strength and shear behavior of sandy soil having low cementation has not been clarified. Therefore, the purpose of this test was to elucidate the cyclic shear strength of minimally cemented soil. By adding the cementing agent to the soil sample, cemented sand was constituted as a model of natural cementation. The shear behavior of weakly cemented sand was examined using the constant volume cyclic loading ring shear test.

4.2   Specimen Preparation and Physical Properties of Sample

As above mentioned, the samples used in this study were artificially reproduced by mixing Toyoura standard sand with a small amount of bentonite and cement. Cemented sand was cured for 3 days under constant temperature. The soil hardness value of the specimen reached the field value equivalent of 26.3 mm during 2 or 3 days of curing. After the curing, the specimen was cut 6 cm in inner diameter, 10 cm in outer diameter, and 2 cm in height. Cyclic ring shear tests were carried out on cemented and non-cemented sands.

Fig. 47.10 Cyclic ring shear test system

4.3   Test Apparatus and Procedure

Figure 47.10 shows the constant volume cyclic loading ring shear test apparatus. This apparatus consisted of a cyclic ring shear test apparatus and pneumatic servo controller, two bellofram cylinders, constant volume-control device, dynamic strain data logger, and personal computer for data recording.

A specimen was placed in the ring shear box, and consolidated by applying consolidated pressure $\sigma_N = 98$–294 kPa. After the consolidation, the specimen underwent cyclic shearing. During the testing, shear stress, τ, normal stress, σ_N, horizontal displacement, δ, frictional force and vertical displacement, v, were all measured and automatically recorded.

4.4   Results and Discussions

Figure 47.11 shows the time histories of σ_N, τ, v and δ for non-cemented and cemented sands. With the progress of the shear, σ_N was reduced so as to maintain a constant volume condition, which eventually became constant. The amplitude of τ was gradually increased, and finally became almost constant. On the other hand, δ

increased gradually. In addition, v was controlled to be a small and constant volume. In this study, the waveform of the applied shear stress during cyclic shearing is like a sine wave. However, the measured waveform was more or less different from the applied one.

Therefore, the measured curve was replaced by a τ–t curve with a constant amplitude equivalent to that with irregular amplitude. The determination of the cyclic shear stress ratio and the number of cycles at failure was carried out based on the equivalent τ–t curve. The cyclic shear failure was defined as the point at which δ had reached -2 mm.

Figure 47.12 shows the relationship between σ_N and τ of Toyoura sand, non-cemented and cemented sands, respectively. In addition, this figure shows the steady-state strength line (SSSL) obtained from another ring shear test under constant pressure. The stress paths of Toyoura sand and non-cemented sand reached their steady-state strength line. The stress path of cemented sand reached its steady-state strength line. Each stress paths obtained by the cyclic shearing reached the SSSL of the material. This suggested that cemented sand can collapse before loss of cementation. After the cementation property of cemented sand layer was lost by
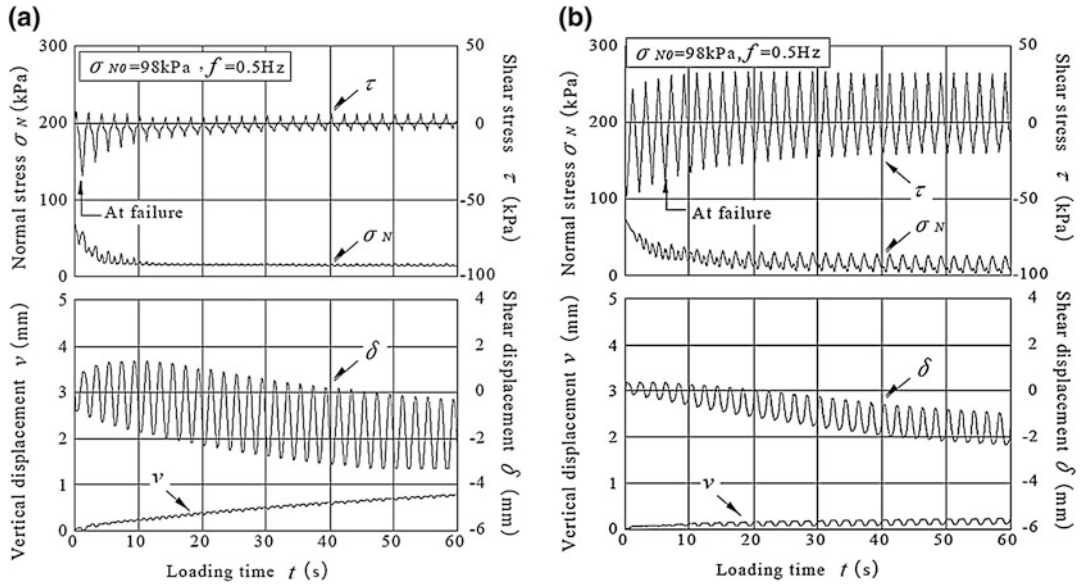
Fig. 47.11 Time history of cyclic behavior of **a** non-cemented and **b** cemented sands, respectively
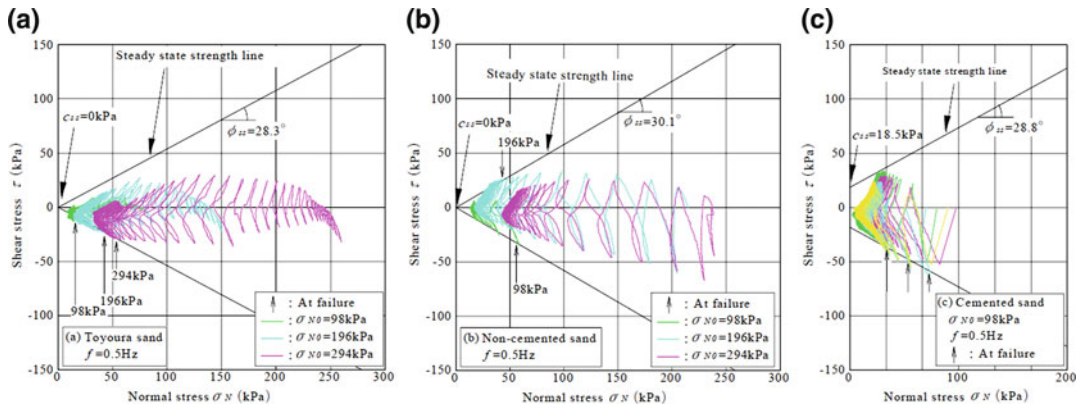
Fig. 47.12 Stress paths and steady state strength lines of **a** Toyoura sand, **b** non-cemented sand and **c** cemented sands during cyclic shearing, respectively

earthquake, general shear failure might occur in the slope.

Figure 47.13 shows the relationship between the shear stress ratio, τ/σ_{N0}, and the number of cycles at failure point, N_f. Here, σ_{N0} is the initial normal stress in the process of cyclic shearing. This figure shows the results of non-cemented and cemented sands. In both sands, τ/σ_{N0} becomes larger when N_f becomes smaller. There seems to be a correlation between τ/σ_{N0} and N_f. The τ/σ_{N0} and N_f curve of

cemented sand may move upward when the amount of cementing agent was increased. In the τ/σ_{N0}–N_f curve, the effect by cementation was confirmed.

Figure 47.14 shows the results of non-cemented sand before and after the submergence. It can be seen from this figure that the τ/σ_{N0} and N_f curve in submerged condition was lower than that in non-submerged condition. The cyclic stress ratio can be reduced by the submergence.
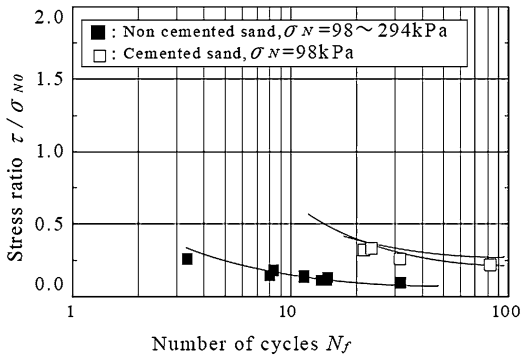
Fig. 47.13 Relationship between stress ratio and number of cycles for non-cemented and cemented sands
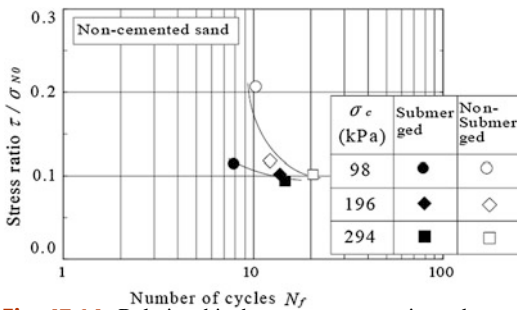
Fig. 47.14 Relationship between stress ratio and number of cycles for non-cemented sand before and after submergence

5 Conclusions

The following conclusions can be derived from the results and the discussion. (1) The steady-state strength of non-cemented sand was hardly affected by changes in the shear displacement rate within the range of 0.1–20 mm/min. (2) The fine content of sand specimens with high dry density increased owing to particle crushing during fast shearing. (3) As the shear displacement rate increased at the steady state, the shear stress of cemented sand gradually decreased. Finally, the shear stress mobilized on the slip surface reached the steady-state strength of non-cemented sand. (4) At the end of cyclic loading, the stress path of cemented sand reached its steady-state strength line, which could be determined by a consolidated drained ring shear test. Simultaneously, the cumulative displacement rapidly increased. (5) The seismic stability of a slope consisting of naturally cemented soil can be evaluated based on its steady-state strength line and the effective stress state on the slip surface at cyclic failure.

References

Lupini JF, Skinner AE, Vaughan PR (1981) The drained residual strength of cohesive soils. Géotechnique 31(2):181–213

Nakamura H, Shimizu K (1978) Soil tests for the determination of shear strength along the sliding surface. Landslide 15(2):25–32 (in Japanese)

Okada F, So E (1988) Relation between residual strength and microstructure. Proceedings of the 23th Japan National Conference on Geotechnical Engineering. pp 227–228 (in Japanese)

Scheffler H, Ullrich W (1981) Determination of drained shear strength of cohesive soils. Proceedings of 10th I.C.S.M.F.E. vol 10. pp 775–778

Suzuki M, Umezaki T, Kawakami H, Yamamoto T (2000) Residual strength of soil by direct shear test. J Geotech Eng 645(III-50):37–50 (in Japanese)

Yatabe R, Yagi N, Enoki M (1991). Ring shear characteristics of clays in fractured-zone-landslide. J Geotech Eng 436(III-16):93–101 (in Japanese)

Re-Estimation Method of Landslide-Triggering Rainfall Thresholds After an Earthquake with the Two Conceptual Models

48

Yasuhiro Shuin, Norifumi Hotta, Masakazu Suzuki, Keigo Matsue, Kazuhiro Aruga and Toshiaki Tasaka

Abstract

This study used two conceptual models to examine the effects of rainstorms on post-earthquake landslides: a tank model to calculate the soil water index and a process-based model employing a digital terrain model with 10-m resolution to calculate the regional potential for shallow landslides, based on the distribution of shallow infiltration water, Darcy's law, and a safety factor estimated by infinite-slope stability analysis. The two models were applied to the Funyu Experimental Forest of Utsunomiya University, Tochigi Prefecture, Japan. In August 1998, a heavy rainfall event caused many shallow landslides in the study area, whereas other heavy rainfall events in 1994–2003 did not cause severe landslides. The two indices were closely correlated, confirming the validity of both approaches for the estimation of rainfall properties. Response analysis of the effect of earthquakes on soil strength parameters indicated that landslide-triggering rainfall thresholds varied with decreasing effective soil cohesion, implying that the relationships between effective soil cohesion and the soil water index derived from the two conceptual models were valid for the re-estimation of the influence of rainfall properties on post-earthquake landslide occurrence.

Y. Shuin (✉) · K. Matsue · K. Aruga · T. Tasaka
Utsunomiya University, 350 Mine-cho,
321-8505 Utsunomiya, Japan
e-mail: shuin@cc.utsunomiya-u.ac.jp

N. Hotta
Graduate School of Life and Environmental
Sciences, University of Tsukuba, Tsukuba, Japan

M. Suzuki
Graduate School of Agricultural and Life Sciences,
University of Tokyo, Tokyo, Japan

1 Introduction

In highly populated mountainous countries, such as Japan, the quantification of landslide hazards and other risks induced by heavy rainfall is important. Establishing effective risk management requires information about the characteristics of the heavy rainfall events that trigger

landslides and about inherent spatial factors, such as geologic, geomorphic, and vegetation factors. Many researchers have proposed a variety of methods and indices for estimating the heavy rainfall conditions associated with landslides (e.g., Suzuki and Kobashi 1981; Okada et al. 2001). Okada et al. (2001) proposed a soil water index (SWI) derived from a three-layer tank model. This index has been used for the early warning system operated by the Ministry of Land, Infrastructure, Transport, and Tourism (MILT) and the Japan Meteorological Agency (JMA) since 2007 (Osanai et al. 2010). Inherent spatial factors, such as soil engineering properties and geomorphology, can be temporally varied by anthropogenic activities such as logging, or by natural influences such as an earthquake. Temporal changes in such inherent factors are known to have a large effect on the rainfall thresholds required to trigger landslides (i.e., Keefer 1994; Chang and Slaymaker 2002; Dhakal and Sidle 2003). After an earthquake, sediment yields increase (Dadson et al. 2004; Lin et al. 2006) and landslide-triggering rainfall thresholds decrease compared with their pre-earthquake values (Tomita et al. 1996; Lin et al. 2003; Hotta et al. 2005; Tang and Liang 2008; Ou et al. 2010). Recently in Japan, the SWI mentioned above was re-estimated for the time period following the 2011 earthquake that occurred off the Pacific coast of Tohoku; the index was reduced in the area where the earthquake had a profound effect (JMA 2011). In general, the re-estimation and practical application of rainfall thresholds are based on basic data, such as past rainfall and landslide occurrences, and often fail to consider temporal changes in inherent spatial factors.

A few studies have examined the effects of earthquake-influenced temporal changes in inherent factors on rainfall thresholds (Chang et al. 2007; Torii et al. 2007; Wang et al. 2010). Using logistic regression analysis, Chang et al. (2007) examined temporal changes in rainfall that were and were not associated with landslides for a time period that spanned the Chi-Chi earthquake. Additionally, temporal changes in soil properties caused by an earthquake have been examined using soil mechanical tests (Torii

et al. 2007; Wang et al. 2010). Torii et al. (2007) reported that the seismic waves from the southern Hyogo Prefecture earthquake in 1995 decreased soil cohesion and resulted in the reduction of rainfall thresholds. Although logistic regression analysis can be used for the re-estimation of rainfall thresholds related to earthquake-influenced temporal changes in inherent factors over a wide area, this method is not based on temporal changes in soil properties. However, the use of soil testing to re-estimate rainfall thresholds related to temporal changes in mechanical soil properties is difficult to apply to a wide area due to the difficulty of obtaining detailed spatial information.

This paper proposes a methodology for the re-estimation of landslide-triggering rainfall thresholds related to temporal changes in soil strength after an earthquake over a wide area (a few square kilometers). The methodology of this study was based on response analysis with two kinds of conceptual model: a three-layer tank model for calculating SWI, and a model that takes into account the effects of soil strength and subsurface flow on landslide occurrence (Shuin et al. 2011).

2 Materials and Methods

2.1 Study Area

The study area (5.3 km^2) was the Utsunomiya University experimental forest in Funyu, central Tochigi Prefecture, Japan at 36°45′–48′N, 139°47′–50′E (Fig. 48.1). This artificial forest is predominantly Hinoki cypress (3.2 km^2). Soil thickness ranges from tens of centimeters to more than a meter, and most soils are andosols. Elevations in the study area range from 260 to 600 m and four-fifths of the area has slopes exceeding 25° (mean: 24.6 ± 9.9°). The main basement geology is Tertiary quartz trachyte. The mean annual air temperature is 12 °C and the mean annual precipitation is about 1,700 mm. Although this area is not where the JMA and MILT decreased rainfall thresholds based on the SWI after the 2011 earthquake off the Pacific coast of Tohoku, heavy rainfall in

Fig. 48.1 Location and map of the study area
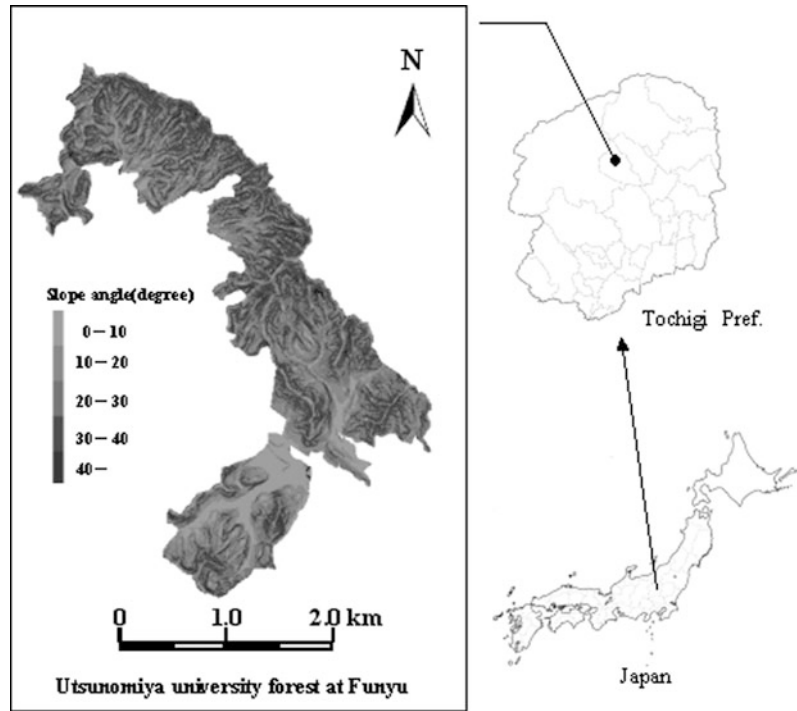
late August 1998 caused 36 shallow landslides
(total area: 3.1×10^{-2} km^2; Utsunomiya Uni-
versity, Research section of University forest
1999) in this area, whereas other rainfall events
in 1994–2003 did not cause landslides to a
similar extent.

2.2   Data Collection

Topographic information for this study consisted
of a digital terrain model with 10 m cell resolu-
tion that was constructed from the forest base map
(scale: 1:5000). Hourly rainfall data for 1994–
2003 were obtained from the closest automated
meteorological data acquisition system (AMe-
DAS) station, at Sioya (34°45′N, 139°50′E).

2.3   Rainfall Indices for Analysis

Two kinds of rainfall index were used: the SWI
used by the JMA and MILT, which has been
used widely for the warning and evacuation
system in Japan; and the potential landslide area

index (PLAI) proposed by Shuin et al. (2011).
Both indices are calculated at hourly intervals
every year.

The model framework of the PLAI, proposed
by Okimura and Ichikawa (1985), uses a digital
terrain model with 10 m resolution to calculate
the regional potential for shallow landslides.
Although the original model was entirely pro-
cess based, we used a conceptual model that was
not linked to any physical parameter, similar to
the three-layer tank model used for calculating
SWI. The model consisted of a groundwater
table calculation and an infinite-slope analysis,
as described below.

The entire study area was delineated by a grid
of 10×10 m cells. Hourly fluctuation in
groundwater level in each cell was calculated
using Eq. 48.1 and Darcy's law, expressed as
Eqs. 48.2 and 48.3:

$$\lambda \frac{\partial h}{\partial t} + \frac{\partial q_x}{\partial x} + \frac{\partial q_y}{\partial y} = r \qquad (48.1)$$

where h (m) is the apparent groundwater table
above bedrock, q (m^2/h) is the flow volume per
cell width and unit of time, r (m/h) is the effective
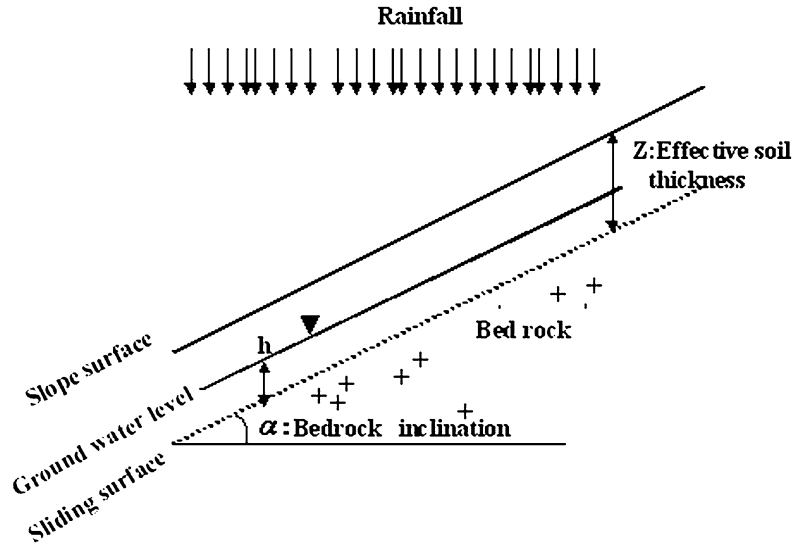
Table 48.1 Model parameters for calculation

Symbol	Value	Unit	Description	Note
v_w	9.81	kN/m^3	Unit weight of water	Fixed
γ	17.66	kN/m^3	Unit weight of the moist soil	Fixed
λ	0.35	–	Effective porosity of the soil layer	Fixed
k	1.8	m/hr	Effective hydraulic conductivity	Fixed
z	1.0	m	Effective soil thickness	Fixed
φ	30.0	Degree	Effective soil internal angle	Fixed
C	0.1-6.0	kPa	Effective soil cohesion	Varied

hourly rainfall measured by a rain gauge (i.e., hourly rainfall observed at the AMeDAS Sioya station), and λ is the effective porosity of the soil layer. Darcy's law is given as below:

$$q_x = hkI_x \qquad (48.2)$$

$$q_y = hkI_y \qquad (48.3)$$

where k (m/h) is the effective hydraulic conductivity and I is the hydraulic gradient.

Subscript x indicates east–west groundwater flow and subscript y indicates north–south flow.

An infinite-slope stability model was used to calculate the potential for landslide occurrence in each cell (Fig. 48.2). The safety factor for each cell was determined using Eq. 48.4:

$$F = \frac{(yz - y_w h)\cos^2\alpha \tan\phi + C}{yz \cos\alpha \sin\alpha} \qquad (48.4)$$

where F is the safety factor, C is the effective soil cohesion (kPa), ϕ is the effective soil internal friction angle (°), α is bedrock inclination (°), γ is the unit weight of the moist soil (kN/m^3), γ_w is the unit weight of water (kN/m^3), h is the groundwater table above the bedrock surface (m), and Z is the effective soil thickness above the bedrock surface (m).

When calculating the safety factor for each cell unit, this study assumed that the inclination of the bedrock surface was the same as the inclination of each cell and that the slip surface appeared at the boundary between regolith and bedrock. Table 48.1 shows the model parameter values used in this study. These values were not linked to any physical parameter because the model was conceptual, but the parameter values of Okimura and Ichikawa (1985) were used. In the model runs, effective soil cohesion was varied at 0.1 kPa increments ranging from 0.1 to 6.0 kPa, but other parameters were kept

constant. Unstable cells were defined as those having a safety factor <1.0, and the PLAI was defined as unstable cell area exempt from unstable cells under the condition of no rainfall.

2.4   Analytical Procedure

Although both rainfall indices were continuously calculated at hourly intervals every year, the rainfall duration period was divided into rainfall events for the comparison of rainfall characteristics. Consecutive rainfall data from 1994 to 2003 were divided into individual rainfall events bounded by periods (>24 h) of no rainfall. Maximum values of the two indices were used for the consideration of both rainfall indices (i.e., SWI and PLAI) during the rainfall event time period. An outline of the analytical procedure follows.

1. Consecutive rainfall was divided into individual rainfall duration events.
2. Heavy rainfall events were chosen according to the criterion that the rainstorm, 24-hour rainfall, or hourly rainfall intensity ranked in the top 30 events for the study period.
3. Maximum SWI values were identified for heavy rainfall events.
4. Response analysis of the PLAI was conducted by comparing heavy rainfall events associated and not associated with landslides.
5. The two indices were compared.
6. Criteria for landslide-triggering rainfall thresholds were determined using the PLAI.
7. Criteria for landslide-triggering rainfall thresholds that accounted for earthquake-related temporal changes in soil engineering properties were proposed.

3   Results and Discussion

3.1   Characteristics of Heavy Rainfall Events Between 1994 and 2003

Consecutive rainfall was divided into 698 rainstorms occurring between 1994 and 2003, of which 50 heavy rainfall events were selected for model simulation. The characteristics of these events are shown in Table 48.2.

In Table 48.2, the rainfall events are numbered chronologically and the maximum SWI value for the event's duration is shown. Event 318 (rainfall with landslides) corresponds to heavy rainfall in late August 1998 that caused 36 shallow landslides in the study area, and its SWI is highest (206 mm) among the 50 events. The other heavy rainfall events did not cause landslides in this area. The SWI of event 591 (rainfall without landslides) ranked second, at 191 mm.

3.2   Response Analysis of the PLAI with a Comparison Between Two Heavy Rainfall Events

The PLAI for an individual event was used as an index for the effect of rainfall properties on landslides. Although the PLAI naturally decreases with increasing effective soil cohesion, the recognition of differences in PLAI among heavy rainfall events is essential for the estimation or discrimination of rainfall properties associated or not associated with landslides. In the response analysis, the PLAI was calculated using effective soil cohesion values ranging from 0.1 to 6.0 kPa at 0.1 kPa increments. The SWIs for events 318 and 591 ranked first and second, respectively, and the PLAIs for events 318 and 591 always ranked first and second, respectively, throughout this range. The relative difference ratio of the PLAI (RD_PLAI) between event 318, which caused 36 shallow landslides, and event 591, which caused no landslide, was examined using Eq. 48.5:

$$RD\_PLAI = 1 - \frac{PLAI_{591}}{PLAI_{318}} \qquad (48.5)$$

where $PLAI_{591}$ and $PLAI_{318}$ are unstable cell areas for events 591 and 318, respectively. Figure 48.3 shows the relationships between effective soil cohesion and RD_PLAI. The trend of increasing RD_PLAI with increasing effective soil cohesion occurred between 0.1 and 5.0 kPa,

Table 48.2 Characteristics of 50 detected rainstorms

Event_No	TR (mm)	MaxI (mm/hr)	Max 24 h (mm/24 h)	SW (mm)
22	173	28	167	110
42	132	35	91	80
46	71	25	69	68
47	141	14	38	78
93	96	9	74	80
103	112	10	61	89
105	87	25	58	75
110	90	23	53	75
125	113	8	73	84
171	34	30	34	41
176	54	22	54	55
186	91	12	84	81
223	145	13	80	98
231	133	24	133	118
236	87	33	87	79
240	118	39	86	96
250	94	9	41	67
316	110	15	42	66
318	567	62	265	206
322	189	31	187	127
332	115	19	63	97
364	93	16	92	85
377	210	19	107	117
380	268	23	109	136
389	160	27	111	107
393	135	52	135	129
400	68	30	35	65
402	85	26	70	69
447	76	14	76	75
452	36	22	36	50
454	115	22	115	89
462	41	33	41	55
470	82	25	82	88
471	143	18	113	116
473	95	13	87	80
524	95	24	48	69
530	168	26	163	119
531	146	35	90	119
534	190	19	128	120

(continued)

Table 48.2 (continued)

Event_No	TR (mm)	MaxI (mm/hr)	Max 24 h (mm/24 h)	SW (mm)
541	126	12	126	97
566	84	9	84	89
591	320	37	215	191
593	71	27	69	84
595	76	22	52	66
601	88	33	60	64
604	97	13	57	81
610	129	29	124	129
662	73	39	51	78
673	97	9	46	61
695	80	9	78	80

TR, total rainfall; Max_I, maximum hourly intensity
Max_24 h, 24-h maximum rainfall; SWI, soil water index
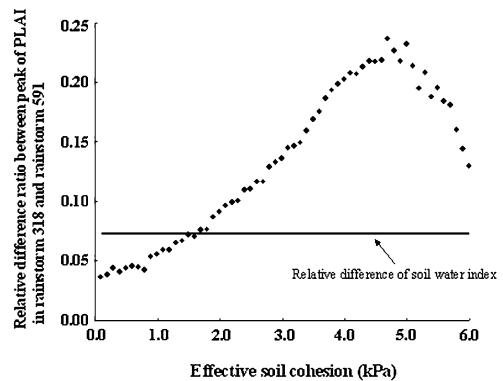
Fig. 48.3 Relationships between effective soil cohesion and RD_PLAI in rainstorm events 318 and 591

the peak value (~ 25 %) was reached at 5.0 kPa, and RD_PLAI decreased from 5.0–6.0 kPa. Figure 48.3 also shows the relative difference ratio of the SWI (~ 7 %) between events 318 and 591. Although the effective soil cohesion value was a conceptual model parameter and not based on results of a soil test, such as a shear test, the PLAI at 5.0 kPa showed obvious discrimination between rainfall properties associated with the presence and absence of landslides compared with the SWI. Considering the effectiveness of the index for the discrimination of

rainfall properties that trigger landslides, the PLAI at 5.0 kPa was used in the model run.

3.3 Comparison of Rainfall Indices Obtained with the PLAI and SWI

In this section, the relationship between the PLAI and SWI is examined (Fig. 48.4). Figure 48.4 shows that the two indices are closely correlated. Figure 48.4 also shows the regression curve of the power function, the exponent of which is 1.9 (>1.0). This result suggests that both indices are valid for the estimation of landslide-triggering rainfall properties, and the PLAI shows obvious discrimination of rainfall properties with increasing extent of heavy rainfall, as compared with the SWI.

Shuin et al. (2011) proposed 13×10^{-2} km^2 as the cutoff PLAI value for discriminating rainfall properties associated with landslides from those not associated with landslides, based on a probability analysis of the PLAI in the study area. In this study, we used the value of 13×10^{-2} km^2 as the threshold value for triggering landslides.

3.4 Analysis of Rainfall Indices Considering the Influence of Earthquakes on Soil Engineering Properties

Previous investigations of the effects of earthquakes on landslides have indicated that landslide-triggering rainfall thresholds decrease after an earthquake compared with their pre-earthquake values, and that earthquake-induced temporal changes in soil properties reduce soil strength. Torii et al. (2007) reported that seismic waves reduced soil cohesion, as indicated by the results of soil mechanical tests. The results of this study follow.

1. The PLAI and SWI show cross-correlation.
2. The cutoff PLAI value for discriminating rainfall properties associated with landslides from those not associated with landslides in the study area is 13×10^{-2} km^2.
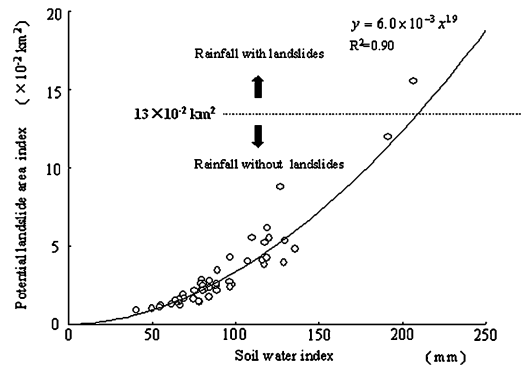
Fig. 48.4 Relationships between soil water index and potential landslide area index for 50 rainfall events

On the basis of these results, post-earthquake temporal change in the rainfall threshold index was examined with the assumption that soil engineering properties in the study area were influenced by earthquakes and that landslide-triggering rainfall thresholds would decrease compared with the pre-earthquake condition.

The specific analytical procedure is as follows.

1. Effective soil cohesion was varied at 0.1 kPa decrements from 5.0 kPa.
2. Effective soil cohesion values indicating the critical PLAI value (i.e., 13×10^{-2} km^2) were detected for 50 heavy rainfall events.
3. The relationship between the SWI and detected values of effective soil cohesion was examined.

Figure 48.5 shows landslide threshold areas derived from the relationships between effective soil cohesion and the SWI. The figure shows that the landslide-triggering SWI value decreased with effective soil cohesion. Tomita et al. (1996) reported that the decrement of the landslide-triggering rainfall amount after the southern Hyogo Prefecture earthquake of 1995 was 50–70 % compared with the pre-earthquake amount. Figure 48.5 also shows 50 % and 70 % lines of the SWI for triggering landslides and the corresponding lines of effective soil cohesion, with the assumption that the earthquake in the study area had the same effect as the 1995 southern Hyogo Prefecture earthquake. Based on soil testing, Torii et al. (2007) reported that the 1995 earthquake affected soil engineering properties by decreasing soil cohesion and that the
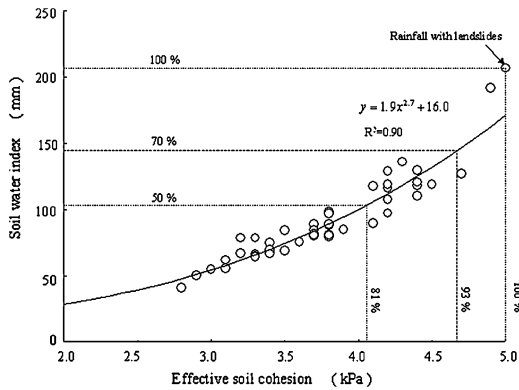
Fig. 48.5 Diagram of landslide threshold areas derived from relationships between effective soil cohesion and the soil water index

decrement percentage of soil cohesion was about 20 %. In comparison, our results show that a 50 % decrement of the SWI for triggering landslides corresponds to a 19 % decrement of effective soil cohesion (Fig. 48.5). Although the effective soil cohesion value was not a physical parameter based on soil tests and geotopographic features in the study area differ from those of southern Hyogo Prefecture, this result implies the possibility of re-estimating landslide-triggering rainfall thresholds in a wide area by considering post-earthquake temporal changes in soil strength. Especially in regions with a high potential for huge earthquakes, such as Japan, the methodology presented in this study could be useful for decreasing the risk of sediment-related disasters induced by heavy rainfall after an earthquake.

4 Conclusion

This study presents a methodology for the re-estimation of landslide-triggering rainfall thresholds over a wide area after an earthquake. This method enables the re-estimation of rainfall thresholds by accounting for earthquake-induced temporal variations in soil mechanical properties. Two kinds of rainfall index were used for this study: an SWI derived from a three-layer tank model that has been applied widely in the practical warning evacuation system existing in Japan since 2007, and a PLAI derived from model calculations and based on a

process-based model. The results of this study follow.

1. The SWI and PLAI show cross-correlation and both indices are useful for the discrimination of rainfall properties associated with landslides from those not associated with landslides.
2. The PLAI shows obvious discrimination of landslide-triggering rainfall properties with increasing extent of heavy rainfall, compared with the SWI.
3. Because it considers the effect of temporal change in effective soil cohesion, the use of the PLAI enables the re-estimation of rainfall thresholds affected by earthquake-induced changes in soil engineering properties over a wide area.

References

Chang KT, Chiang SH, Hsu ML (2007) Modeling typhoon and earthquake-induced landslides in a mountainous watershed using logistic regression. Geomorphology 89:335–347

Chang JC, Slaymaker O (2002) Frequency and spatial distribution of landslides in a mountainous drainage basin : Western Foothills, Taiwan. Catena 46:285–307

Dadson SJ, Hovius N, Chen H, Dade WB, Lin J, Hsu M, Lin C, Horng M, Chen T, Milliman J, Stark CP (2004) Earthquake-triggered increase in sediment delivery from an active mountain belt. Geology 32:733–736

Dhakal AS, Sidle RC (2003) Long-term modeling of landslides for different forest management practice. Earth Surf Process Landf 28:853–868

Hotta N, Kan Y, Shuin Y, Wei T, Zhang Z, Chen H, Suzuki M (2005) Relationship between slope failures and precipitation before and after the Chi-Chi earthquake investigated using long-term repair records of forestry roads in the National Taiwan University Forest. J Jpn Soc Eros Control Eng 58(1):3–13

Keefer DK (1994) The importance of earthquake-induced landslides to long-term slope erosion and slope-failure hazards in seismically active region. Geomorphology 10:265–284

JMA (2011) Temporal operation for weather warnings and advisories of heavy rainfall associated with the 2011 off the Pacific coast of Tohoku earthquake and the earthquake occurrence on March 12th in northern area of Nagano prefecture. JMA press release statement on March 12th 2011 (in Japanese)

Lin CW, Shieh CL, Yuan BD, Shieh YC, Liu SH, Lee SY (2003) Impact of Chi-Chi earthquake on the occurrence of landslides and debris flows: example from

the Chenyuan river watershed, Nantou, Taiwan. Eng Geol 71:49–61

Lin CW, Liu SH, Lee SY, Liu CC (2006) Impacts of the Chi-Chi earthquake on subsequent rainfall-induced landslides in central Taiwan. Eng Geol 86:87–104

Okada K, Makihara Y, Shimpo A, Nagata K, Kunitsugu M, Saito K (2001) Soil water index. Tenki 47:36–41

Okimura T, Ichikawa R (1985) A prediction method for surface failures by movements of infiltrated water in a surface soil layer. Nat Disaster Sci 11:41–51

Osanai N, Shimizu T, Kuramoto K, Kojima S, Noro T (2010) Japanese early-warning for debris flows and slope failures using rainfall indices with radius basis function network. Landslides 7:325–338

Ou GQ, Pan HL, Liu JF, Fan JR, You Y (2010) Characteristics of sediment-related disasters triggered by the Wenchuan earthquake. Int J Eros Control Eng 3(1):59–68

Shuin Y, Hotta N, Matsue K, Aruga K, Tasaka T (2011) Estimating landslide-triggering rainfall thresholds using two conceptual model for soil water and potential landslide area indices with 30 years of hourly rainfall data, J Jpn Soc Eros Control Eng 63(5):37–42

Suzuki M, Kobashi, S (1981) The critical rainfall for the disasters caused by slope failures. J Jpn Soc Eros Control Eng 34(2):16–26

Tang C, Liang JT (2008) Characteristics of debris flows in Beichuan epicenter of the Wenchuan earthquake triggered by rainstorm on September 24, 2008. J Eng Geol 16:49–61

Tomita Y, Sakurai W, Naka N (1996) Study on the extension of collapse caused by rainfall after the earthquake in Rokko mountain range. J Jpn Soc Eros Control Eng 48(6):15–21

Torii N, Okimura T, Kato S (2007) Experimental study on slope failure mechanism induced by rainfall after earthquake. J Jpn Soc Civ Eng Ser C 63(1):140–149

Utsunomiya University, Research section of University forest (1999) Preliminary research of the damage in Utsunomiya University forest at Funyu caused by the heavy rainfall at the late of August 1998. Bull Utsunomiya Univ For 35:119–123

Wang J, Yao L, Arshad H (2010) Analysis of earthquake-triggered failure mechanisms of slopes and sliding surfaces. J Mt Sci 7:282–290

Niaozhisuo Landslide Dynamic Process

49

Yunsheng Wang, Qiang Li, Yun Chen, Junfeng Wu, Junsheng Yue and Qinlong Hu

Abstract

There are a series of large scale old seismic landslides in the Middle reach of Daduhe River, they played a major role in the evolution of landforms in the area, in which Niaozhisuo landslide is a typical one. Based on detailed site investigation and ATM geophysical exploration, combined with engineering geological condition analysis and research on basic characteristics and genetic mechanism, the landslide characteristics can be concluded as follows: Niaozhisuo landslide, formed in 2.0×10^4 years ago, is a huge seismic landslide on the left bank of the Daduhe river with a volume of 3.64×10^8 m^3; The landslide is composed of huge blocks with cataclastic texture in the front part, middle cemented sandy granules in the main parts and well cemented sandy granules in the toe. The strong E-W compress in Paleozoic made the Proterozoic granite form the "bedding" rock, the flow direction of Daduhe River is parallel to the main strike of the texture planes, the quick cutting of Daduhe River and its branches created a projecting spur relief and strong unloading in high slope, frequent seismic activities speeded up the upper slope deformation, a strong seismic waves (Ms $\geq$ 7.5) were enlarged in the landslide source region of the high slope, at last, the slope failed under the huge seismic inertia force; After long time damming, it broke and Daduhe River was forced to change its river channel westward. Since the end of Late Pleistocene, the debris flow from Miaozi gully on the right bank has pushed the River channel eastward again, the front part of the landslide has been laterally eroded by Daduhe River, the part failure was frequent and the steep front has been left up to now.

Y. Wang (✉) · Q. Li · Y. Chen · J. Wu · J. Yue ·
Q. Hu
State Key Laboratory of Geological Hazards
Prevention, Chengdu University of Technology,
Chengdu 610059, China
e-mail: wangys60@163.com

1 Introduction

Wenchuan earthquake on May 12, 2008 triggered a series of huge landslides in the Longmen mountainous area, in which 34 seismic landslides dammed the Rivers such as Tangjiashan landslide (Hu et al. 2009). Upstream flooding as the impounded lake water level rises and downstream flooding due to dam breach and rapid release of the impounded water can seriously threats people life and property (Dai et al. 2005). These harmful phenomena draw a lot of attentions of many researchers (Perrin and Hancox 1990; Korup 2002; Yin 2008; Cui et al. 2009; Yu et al. 2010). There is a river segment with VIII–IX intensity in the middle reach of Daduhe River, strong historic earthquakes happened in the area and triggered a series of large scaled landslides. Some of the seismic landslides ever dammed the Daduhe River and forced the Daduhe River changed its course. A typical one is Niaozhisuo landslide. As the landslide accumulation has been cemented and later topography alteration, the former researchers have not mentioned the landslide in the literature up to now.

Based on image interpretation, detailed site survey and ATM geophysical exploration, the authors considered Niaozhisuo landslide to be an old high slope seismic landslide on the left bank of the Daduhe River. On one hand, the seismic landslide not only choked the Daduhe River for a long time but also forced the River to change its course at least 500 meters westward; On the other hand, the landslide accumulation was alternated by a thrusting fault, showing Daduhe fracture is active in Holocene.

2 Geological Setting

The landslide area is located in the convergence of the NE–SW trending Longmenshan fracture (e, f, g in Fig. 49.1), NW–SE trending Xianshuihe fracture (b, c in Fig. 49.1) and N–S trending Daduhe fracture (h, i in Fig. 49.1). It was the north part of Chuan (Sichuan)–Dian (Yunnan) S–N trenching tectonic belt during the Paleozoic and Mesozoic. This area is one of the most seismically active areas in China. Six faults are involved in the zone. They are Moxi fault(c), Changchang fault (h), Guadagou fault(h), Gengda-Longdong fault (e); Yanjing-Wulong fault (f); Dachuan Shuangshi fault (g). The regional tectonic stability is controlled primarily by the active Xianshuihe fracture.

The Moxi fault strikes generally in N30–40°W, dips to SW with the dip angle of 60–80°. There are valleys and hot springs developed along the fault. The earthquakes were frequent in the history (Fig. 49.1). Changchang fault and Guadagou fault belong to Daduhe fracture, they strike in S–N, dip to the east, with dip angle of 50–77°. Their formation in Mesozoic made the intrusive rock slope to be bedding one which parallels to the flow direction of Daduhe River, but they seem less active in Holocene. Erlangshan fault and Ganyanggou fault belong to Longmenshan fracture, they strike in N40–50°E, dip to SE with the dip angle 42–51°, the ESR (electron spin resonance) dating shows its strong activity age happened in $9.9 \pm 0.52 \times 10^4$ years ago. A series of earthquakes happened along the Xianshuihe fracture, the seismic intensity is high, recorded highest historic intensity is VIII–X. The regional geostress reach to 20–25 MPa.

3 The Geological Environments in the Landslide Area

Daduhe River flows by the landslide toe from north to south. It is a wide bottom valley and the slopes on the two banks are with 30–50°angle. There are two EW-trending deep cutting branches in the left bank, Dazhai valley in the

Fig. 49.1 The regional seismic-structure diagramt **a** Yuke fault; **b** Xianshuihe fault; **c** Moxi fault; **d** Jinping fault; **e** Gengda-Longdong fault; **f** Yanjing-Wulong fault; **g** Dachuan-Shuangshi fault; **h** Guadagou fault, **i** Changchang fault; The *rectangle* with shadow: the landslide region
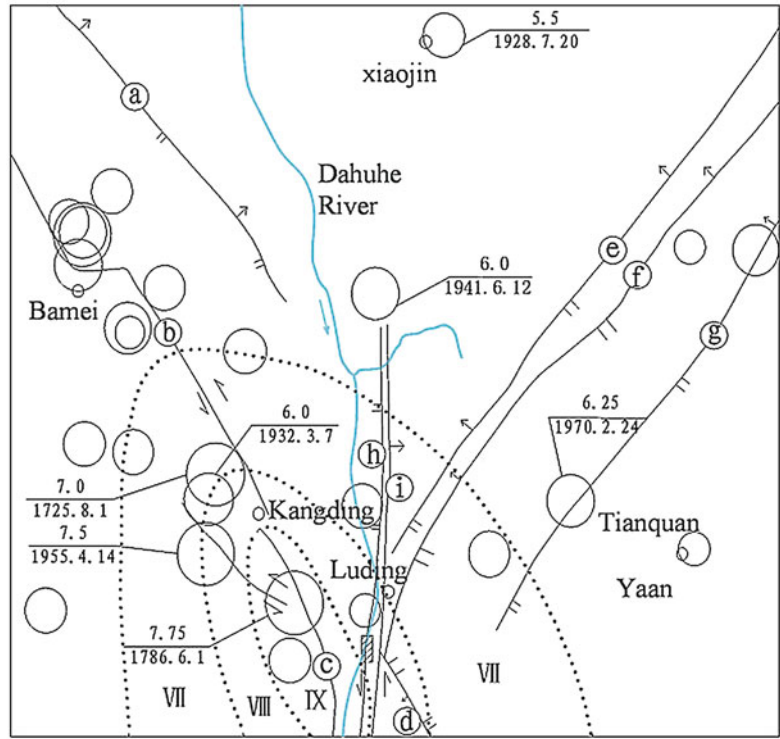
Fig. 49.2 The geological diagram in the landslide area
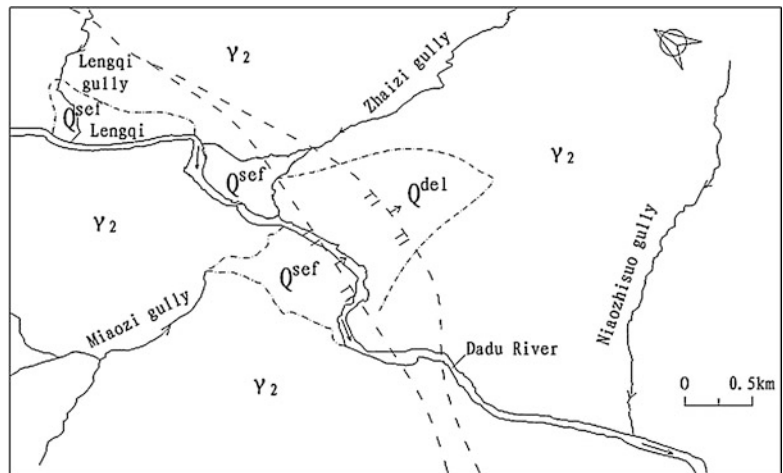
upsteam and Niaozhisuo valley in the downstream, they cut the Niaozhisuo slope a triangle shape. The bedrock of landslide is composed of Proterozoic diorite and granite (Fig. 49.2). Due to tectonic compression of EW and the activities of the faults, the structural texture planes of the bedrock are well developed. There is a large fluvial fan in the opposite bank (right bank) (Fig. 49.3), it pushes the Daduhe River channel bending towards the east.

Fig. 49.3 Geological setting of landslide
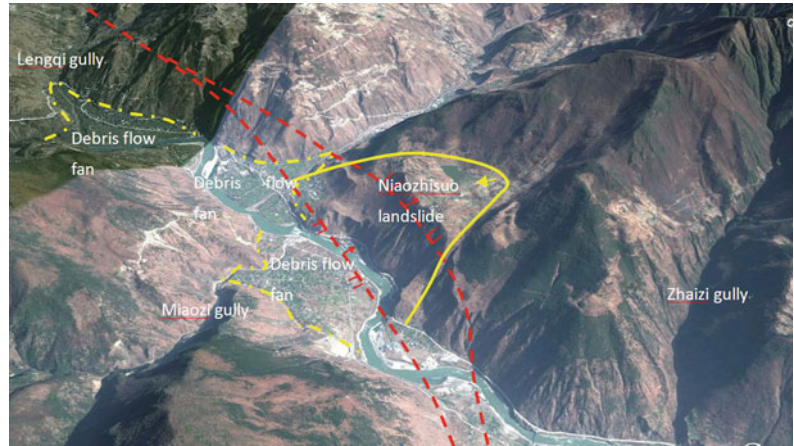
Fig. 49.4 The geophysical prospecting interpretation (the *white line* represents the slip surface)

Fig. 49.4 The geophysical prospecting interpretation (the *white line* represents the slip surface)
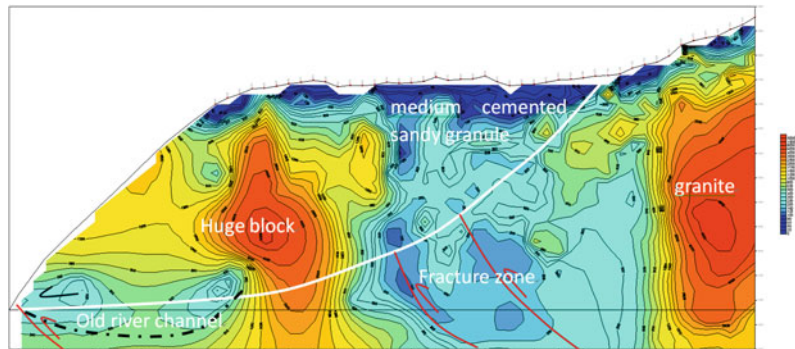
4 Characteristics of Landslide

Niaozhisuo landslide is an old high slope seismic landslide. The elevation of front toe is 1220 m and its back edge elevation is 1810 m, the elevation difference of landslide is 610 m. The back cliff is 810 m high, with a mean width of 1000 m. The landslide platform is clear, with a pond on the back position of the platform, the shape of the landslide area likes an armchair. The front is cut by Daduhe River and steep (60–70) slope is left.

The landslide is 1400 m in length, 1300 m in mean width along the Daduhe River, 1.12 km^2 in area. The average thickness of landslide is 200 m and its volume is 3.64×10^8 m^3. It belongs to super large-scale landslide. Main sliding direction is 290°. The landslide was formed in 2.0×10^4 years ago by TL (Thermoluminescence) dating.

In order to reveal the landslide thickness and the inner texture, we deployed a survey line of geophysical prospecting. The total length of the survey line is 1125 m and the distance between two measuring points is 25 m, 45 measuring points in total actually (Fig. 49.4). From the Fig. 49.4, we can learn that the result of AMT prospecting: the result profile reflects the formation clearly, and there are big resistivity differences in rear edge and front-end where landslide platform begins to go down. In the profile, low resistivity region (line distance: 650–950 m) are composed of granule and silty clay, there is a small lake on the surface. The bedrock of landslide is composed of Proterozoic diorite and granite with characteristic of high resistivity, from 1500 to 10000 Ω•m. Because properties of rock and soil mass are poor, slip surface is shown as relatively low resistivity. One section of 625 ∼ 1000 measuring points is

Fig. 49.5 The huge blocks in the landslide accumulation
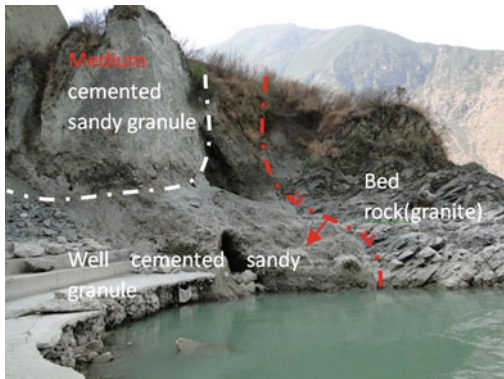
Fig. 49.6 Medium cemented and well cemented sandy granule in the accumulation

a low-resistivity abnormal zone, we can speculate a relatively large-scale fault structure developed in the section.

The landslide can be divided into three parts according to the composition difference: huge blocks with cataclastic texture in the front part (Fig. 49.5), middle cemented sandy granules in the main parts and well cemented sandy granules in the toe (Fig. 49.6).

5   The Formation and Evolution of the Landslide

Learnt from the conditions of the secondary geological disasters, the high slope failures are controlled by topography, hanging wall, the distance

from the seismic fault and so on. The Niaozhisuo landslide formation results in following factors. (1)topography: projecting spur relief in source region easily fails during strong earth quake for strongest unloading and amplifier effect of seismic waves; (2) the tectonic texture planes: a: $210° < 43°$, b: $56° < 70°$, 3, c: $278° < 35°$, d: $244° < 69°$, e: $127 < 32°$, in which the combination of c and d is advantageous to the slope deformation, (3) hanging wall: it is located on the hanging wall of the Daduhe fracture, the rock mass is para-bedding for the cutting by the tectonic texture planesc and d. These favorable conditions made the high slope easily fail induced by the strong earthquake.

The landslide evolution and dynamic process can be concluded as follows (Fig. 49.7): the Niaozhisuo high slope with strong unloading was triggered by a strong historical earthquake, forming a large scale landslide and damming the Daduhe River. The dam was about 200 m high and large reservoir was formed. The reservoir was filled with the thick sediments, it still remains along the two banks. The dam broke along the right bank and cut the rock slope, forming a new River channel; the Daduhe fracture thrusted and altered the landslide accumulation; the tributary debris flow happened and pushed the River channel bending earthward, the front was eroded and the landslide remains with steep front slope present.

Although the remains are stable on the whole, the front part is potentially unstable, if they are reactive triggered by the future earthquake or storm, they can partly dam the Daduhe River again and cause huge geo-hazards. At the same time people's activities speed up the unstableness of landslide, because the road construction has sharpened the slope of the landslide.

6   Conclusion

According to the detailed site investigation and ATM geophysical exploration, several ideas can be concluded as follows:

Niaozhisuo landslide is formed in 2.0×10^4 years ago on the left bank of the Daduhe River, and its volume is 3.64×10^8 m^3. The landslide accumulation can be divided into three parts:
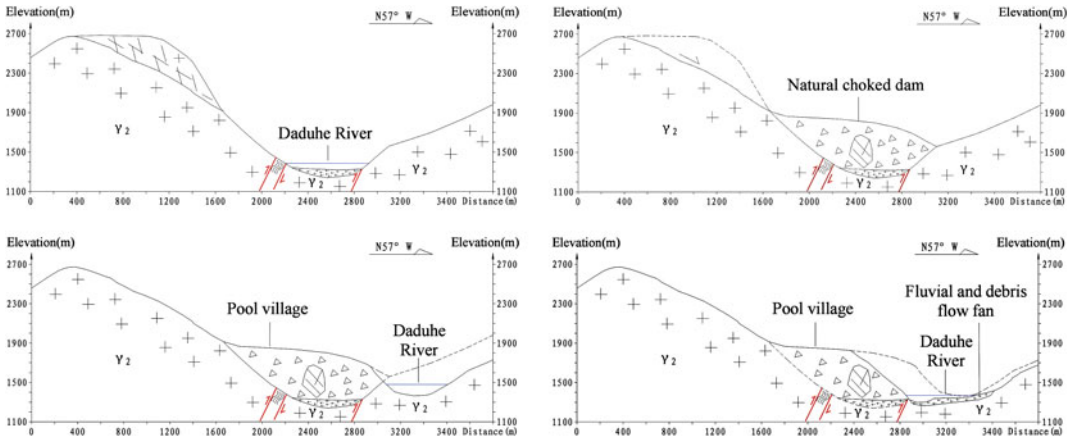
Fig. 49.7 The evolution of the landslide

huge block with cataclastic texture, medium cemented sandy granule, strong cemented sand with granule and detritus. The bedrock of landslide is composed of Proterozoic diorite and granite. Favorable seismic environment, topography, combination of the tectonic texture planes and hanging wall effect made the landslide formation and dammed the Daduhe River.

According to the result of AMT prospecting, low resistivity regions are composed of completely disintegrated clastics. High resistivity zone is granite and slip surface is shown as relatively low resistivity;

Niaozhisuo high slope with strong unloading was triggered by a strong historical earthquake, forming a large scale landslide and damming the Daduhe River. The reservoir was filled with thick sediments. The dam broke along the right bank and cut the rock slope, forming a new River channel; the Daduhe fracture thrusted and altered the landslide accumulation; the tributary debris flow on the opposite bank happened and pushed the River channel bending earthward, the front was eroded and the landslide remains with steep front slope present for the lateral cutting.

Although the remains are stable on the whole, the front part is potentially unstable, if they are reactive triggered by the future earthquake or storm, they can dam the Daduhe River again and cause huge geo-hazards.

References

Costa JE, Schuster RL (1988) The formation and failure of natural dams [J]. Geol Soc Am Bull 100:1054–1068

Cui P, Han Y, Chen X (2009) Distribution and risk analysis of dammed lakes induced by Wenchuan earthquake [J]. J Sichuan Univ (Eng Sci Ed) 41(3):35–42

Dai FC, Lee CF, Deng JH, Tham LG (2005) The 1786 earthquake-triggered landslide dam and subsequent dam-break flood on the Dadu River, southwestern China. Geo-morphology 65:205–221

Ding J, Yan Y (2007) Analysis of the geological hazards distribution and development trend in Dadu River Catchments of Sichuan Province. Chin J Geol Hazard Control 18:22–25

Erisman TH, Abele G (2001) Dynamics of rockslides and rockfalls. Springer-Verlag, Berlin

Hu X, Huang R, Shi Y, Lu X, Zhu H, Wang X (2009) Analysis of blocking river mechanism of Tangjiashan landslide and dam-breaking mode of its barrier dam[J]. Chin J Rock Mech Eng (11):2349–2359

Huang RQ (2005) Main characteristics of high rock slopes in southwestern China and their dynamic evolution. Adv Earth Sci 20(03):292–297

Korup O (2002) Recent research on landslide dams a literature review with special attention to New Zealand [J]. Prog Phys Geogr 26(2):206–235

Perrin ND, Hancox GT (1990) Landslide dammed lakes in New Zealand—Preliminary studies on their distribution, causes and effects [J]. Landslide 22:1457–1465

Read SA, Beetham RD (1991) Lake Waikar-emoana barn a large landslide dam in New Zealand [J]. Landslide News 54(1):1481–1487

Schuster RL, Costa JE (l986) Effects of landslide damming on hydroelectric projects [A]. In Anon Proceeding fifth international association engineering geology [C], [s. J], [s. n] pp 1295–l307

Sun GZ (1984) On the mechanical model of rock mass. Chin J Geol 4:423–428

Sun YK, Yao BK (1983) Principal geological models of deformation and failure of rock slopes in China. Chin J Rock Mech Eng 1:19–22

Yan TZ (1981) Analysis of some characteristics in the structural mechanics of landslides. Earth Sci J China Univ Geosci 2:223–239

Terzaghi K (1950) Mechanism of landslide. Geol Soc Am Berkey Volume:83–123

Varnes DJ (1978) Slope movement types and processes. Special Report-Transportation Research Board, National Research Council, vol 176, pp 11–33

Wang YS et al (2009) An intensive erosion event in last glaciation in the west of China. In: Proceeding of the 2nd international conference on earth observation for global changes, vol 5, pp 25–29

Wang LS, Zhang ZY (1985) Basic Geo-mechanics models of slope deformation and failure. Geological Publishing House, Beijing

Wu JH, Lin JS, Chen CS (2009) Dynamic discrete analysis of an earthquake-induced large-scale landslide Int J Rock Mech Min Sci 46(02):397–407

Yin Y (2008) Researches on the geo-hazards triggered by Wenchuan earthquake Sichuan [J]. J Eng Geol 16(4): 433–444

Yu G, Wang Z, Huang H, Liu H (2010) Geomorphology and environment effects of landslide dams (dammed lakes). Adv Earth Sci 25(9):934–940

Initiation and Motion Mechanism of the Donghekou Rapid and Long Runout Landslide Triggered by the 2008 Wenchuan Earthquake, China

50

Fawu Wang, Ping Sun, Lynn Highland and Qiangong Cheng

Abstract

The 2008 Wenchuan earthquake triggered many rapid and long runout landslides, which directly caused great loss of property and human lives and were responsible for a large percentage of total damages. For landslide disaster mitigation, it is very important to understand the initiation and motion mechanism of the rapid and long runout landslides, which can potentially be the deadliest of ground failures. In this paper, results of field investigation and ring shear tests simulating the initiation and motion of the Donghekou landslide is presented. It is found that groundwater caused great drop-down of the shear resistance during the initiation and rapid motion of this landslide when it was triggered by the great earthquake.

Keywords

Wenchuan earthquake · Rapid and long runout landslides · Initiation · Motion · Hydrogeological condition

F. Wang (✉)
Department of Geoscience, Interdisciplinary Faculty of Science and Engineering, Shimane University, Matsue, Japan
e-mail: wangfw@riko.shimane-u.ac.jp

P. Sun
Institute of Geomechanics,
Chinese Academy of Geological Sciences,
Beijing, China

L. Highland
National Landslide Information Center, U. S. Geological Survey, Denver, USA

Q. Cheng
School of Civil Engineering, Southwest Jiaotong University, Chengdu, China

1 Introduction

The Wenchuan earthquake occurred at 14:28 local time (Beijing time) on 12 May 2008 in Sichuan Province of China (Cui et al. 2009; Huang and Li 2009). The earthquake's epicenter was located at Yingxiu Town, Wenchuan County (30.40° N, 103.47° E, and its depth was 14 km). The earthquake magnitude was Mw7.9 according to U.S. Geological Survey and Ms8.0 according to the China Earthquake Administration. The most affected area was along the central and frontal faults of the Longmen Shan fault system in the western part of Sichuan, in a 300-km-long belt-shaped zone (Fig. 50.1). Numerous
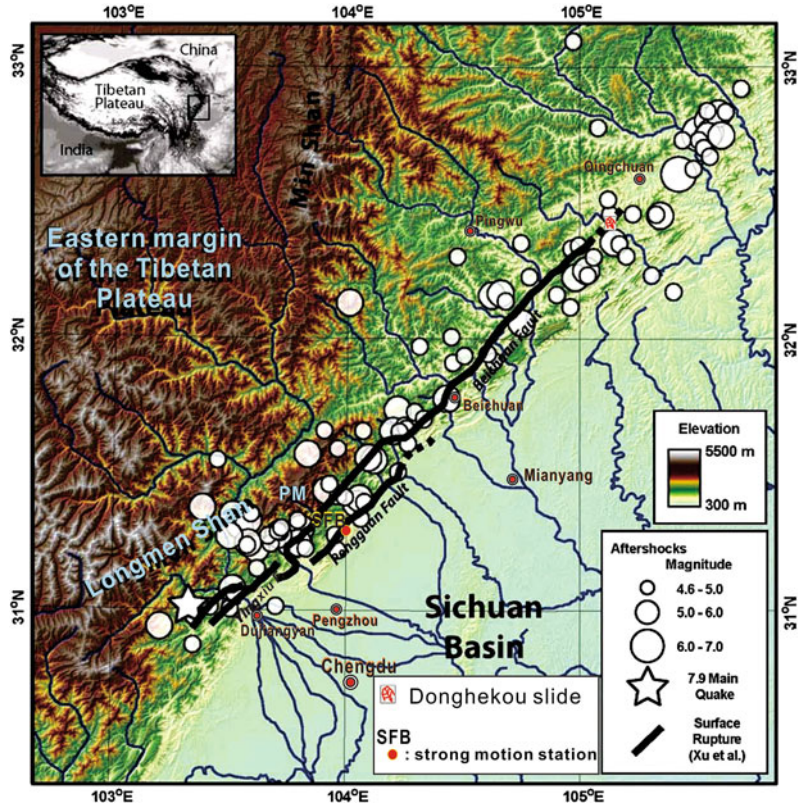
landslides were triggered in this zone (Yin et al. 2009; Tang et al. 2009). According to Chinese State Officials, the earthquake resulted in 69,200 known deaths, 18,195 missing, 374,216 injured, 5,362,500 houses collapsed, 21,426,600 houses badly damaged, and more than five million people were left homeless (Cui et al. 2009).

Among the losses and damages, about one third was caused by earthquake-induced landslides (Yin et al. 2009). Why was there so much damage caused by landslides during this earthquake? We consider that an answer is a combination of large-magnitude earthquake, topographical aspects, and population distribution in this area. Tectonically, the Longmen Shan fault system, which includes the main active fault that caused the Wenchuan earthquake, formed the lower boundary between Sichuan basin and Tibetan Plateau. Because of the rapid uplift and an eastward extrusion of the Tibetan Plateau due to the motion of the Indian Plate colliding with the Eurasian Plate, steep

mountains and river systems are formed at the boundary between the Tibetan Plateau and the Sichuan Basin, making this area susceptible to landsliding and erosion (Yi et al. 2006; Burchfiel et al. 2008; Ouimet 2010). On the other hand, the relative gentle topography that also exists in areas of the Longmen Shan fault system attracted people to live there, as the area also provided a good groundwater supply and mild climate.

The meteorological conditions just prior to the earthquake are vital for framing the explanation as to why the landslides were so large and numerous. In the earthquake-affected area, there are three meteorological monitoring stations, located in Dujiangyan City, Pingwu County, and Mianyang City. The one located in Pingwu County is almost at the center of the earthquake-affected area, and is 50 km west of the Donghekou slide. The daily rainfall data in 2008 are shown in Fig. 50.2, indicating that the total precipitation in 2008 was 718.5 mm. Considering the rainfall intensity and frequency, the

Fig. 50.2 Daily rainfall data monitored at Pingwu Meteorological Station in 2008
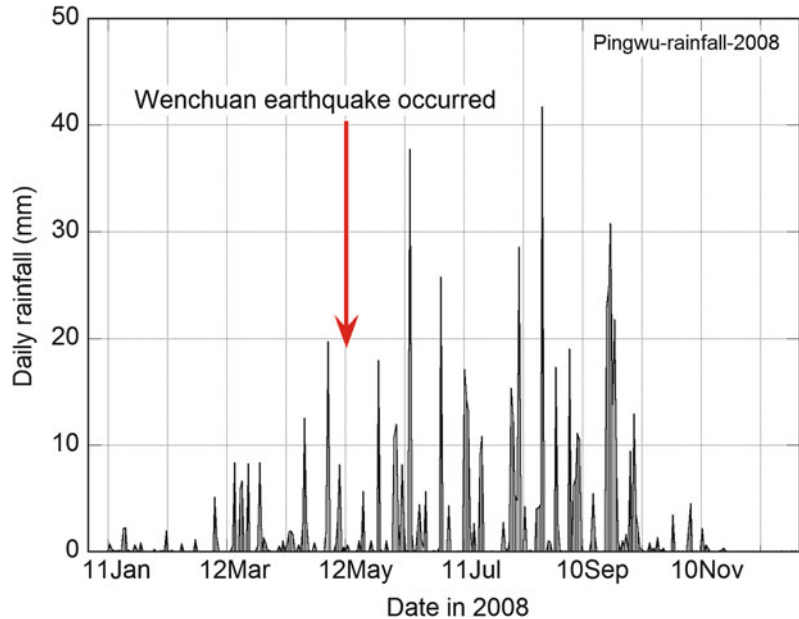
period from March to May can be classified as medium rainfall, while June to September can be classified as heavy rainfall. The Wenchuan earthquake occurred during a medium rainfall season. The antecedent rainfall before the earthquake was 58.8 mm for one month (from 12 April to 12 May), and 33.3 mm for 10 days (from 2 May to 12 May).

Donghekou slide is located in Qingchuan County. The study includes field investigation, soil sampling, and geo-simulation test on the soil samples from the Donghekou slide, with application of seismic wave analysis, for the Wenchuan earthquake. According to Wang et al. (2010) and Lu et al. (2010), there are three strong-motion stations, i.e., Wolong, SFB, and MZQ, located around the Longmen Shan fault system, and the site of SFB station experienced a similar seismic intensity effect as that of the Donghekou slide. According to Li et al. (2008), the Donghekou slide and the SFB station located in the same seismic intensity zone of level-VIII in China Seismic Intensity Scale.

The SFB strong-motion station was located about 1.2 km from the secondary fault rupture and it recorded a large vertical fault slip in Bajiao town, Shifang County (Lu et al. 2010). The site is primarily alluvium, and the observation point is

ground type of free-field station. The seismometer was set 20 m below the ground surface. During the Wenchuan earthquake, the SFB station successfully recorded the three components (E-W, S-N, and Up-Down) of the seismic wave (Fig. 50.3). The PGAs (peak ground acceleration) at E-W, S-N, and U-D directions are 557.2 gal, 633.7 gal, and 581.9 gal, respectively. The three components of the wave are used to form the seismic input for the geo-simulation test to clarify the initiation mechanism of the Donghekou slide during the earthquake.

2 Field Investigation Results on Donghekou Complex Slide

In July 2008, the first investigation was conducted in the Donghekou complex slide. Two landslide dams caused by this slide were not yet excavated or modified. In February 2009 (a dry season in this area), the second investigation was conducted and it was found that groundwater was flowing out of the slide surface and source area.

Donghekou slide is a large-scale rockslide occurred on the mountain behind Donghekou Village. Movement was triggered by the earthquake,

Fig. 50.3 Three
components (E-W, N-S,
and U-D) of the Wenchuan
earthquake recorded at
SFB strong-motion station
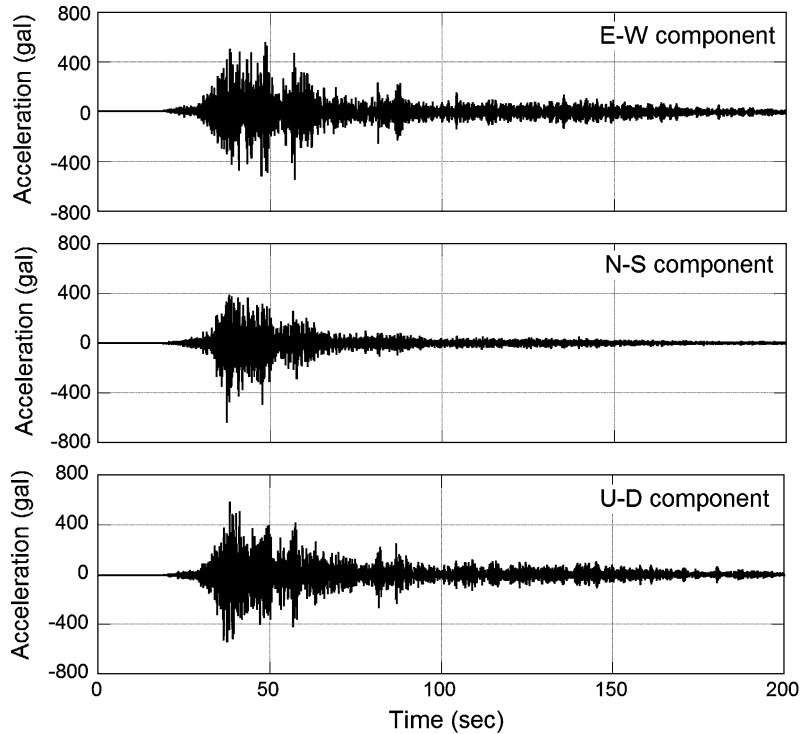
and the initial rockslide became a debris flow as it moved down from the mountain to the valley.

Figure 50.4a, b are an air photo and topographic map of the Donghekou complex slide. Donghekou village was located at the convergence of the Hongshi River and the Xiasi River. The debris flow dammed the Xiasi River and its tributary Hongshi River, and formed two landslide lakes. Part of the displaced slide mass entered the Xiasi River and flowed down the stream as a debris flow. In the source area, the average length is about 1 km, the average width is about 920 m, and the total length of the rockslide and debris flow reached about 3 km.

Before the earthquake, many houses were built along the Hongshi River. There were about 1500 people living in this village. At this location, the Hongshi River formed a fan with alluvial and flood deposits. At the two sides of the Hongshi River near the converging point, the ground level is less than 1 m over the water level. Connecting to the water level in the Hongshi River, the groundwater table in the alluvial and flood deposit is estimated to be very

shallow. Obviously the valley deposits were in a fully saturated condition.

The landslide destroyed all of the houses in this village, and dammed the rivers. Four villages and an elementary school were destroyed, and about 700 people were killed. It occurred as a rockslide when it was triggered by the earthquake, then became to a debris flow when it travelled at the base of the mountain on the alluvial deposit, and finally flowed along the Xiasi River. The landslide dam in the main stream of the Xiasi River is not very thick. Because of the long travel distance, the debris-flow deposits became wide and thin.

The slickenside faces at the mountain where the slide occurred and the adjacent mountain which also experienced the rockslide motion, indicate strong energy and a high velocity of movement of the sliding mass. Local eyewitness said three buses full of local travelers were buried by the rapid debris because the buses had no time to escape. The flat deposits of the complex slide indicate the characteristic of a flow-slide. There are almost no large blocks in the travel path,
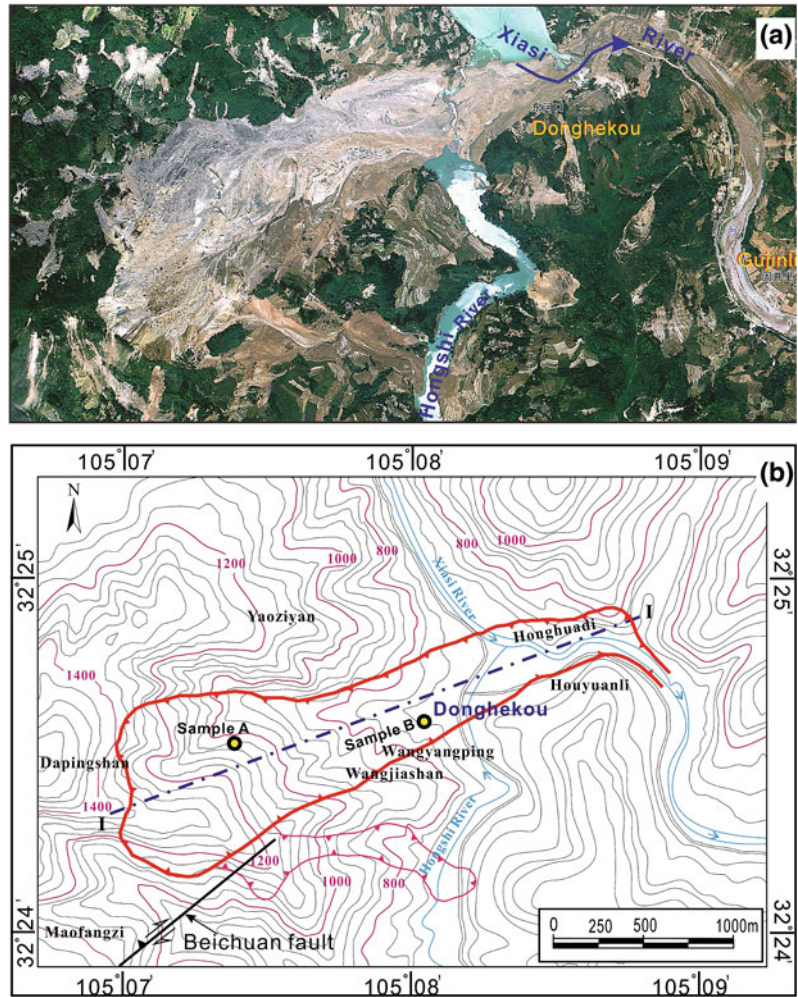
showing a highly fractured property of the sliding mass before it formed the landslide.

Figure 50.5 shows the central longitudinal section of the Donghekou complex slide. The average thickness of the slide mass in the source area is about 75 m, with the maximum thickness of 110 m, and the total volume of the Donghekou rockslide is about 69 million m^3. In Fig. 50.5, by means of connecting the top point of the rockslide and the toe of the debris flow, the apparent friction angle of the rockslide/debris flow was determined to be 11 degrees. This value indicates a high mobility for the rockslide/debris flow. In the source area, there was lots of slide debris left covering the sliding surface of the landslide, making it difficult to determine the material in the slide zone.

Combined with the observation on the slide mass distributed in the lower part (traveling path and deposit area), it is indicated that the sliding zone existed in the carbon-siliceous slate of the Qiujiahe formation of the Cambrian period. The structure of the slide mass during the earthquake consisted of two layers, i.e., fragmented limestone of the Sinian period overlaying weathered Carbon-rich siliceous slate of the Cambrian period. In the first investigation conducted in July 2008, it was observed that the weathered slate was in a soft-plastic state and fully saturated in a natural slope near the Donghekou slide.

In the second field investigation in February 2009, sampling from the source area (sample A) and valley deposit (sample B) was carried out. At the
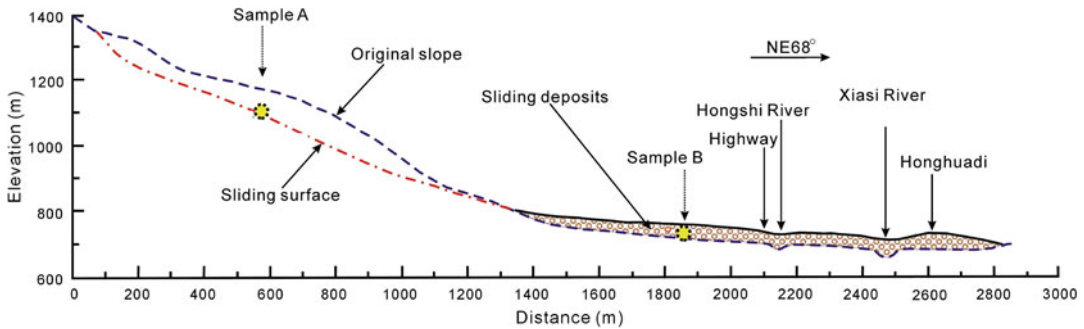
Fig. 50.5 Longitudinal section of the Donghekou complex slide showing landslide topographical characteristics, and locations from which samples A and B were taken

source area, weathered Carbon-siliceous slate was labeled as Sample A. Although the debris around the mountain was dry, a small amount of water was flowing down the valley. Lineaments representing shearing, indicated by the layered structure of slate with an intrusion of soft yellow clay were observed at the sampling point. Considering the size limitation of the ring shear apparatus which will be employed for soil testing, boulders and gravels were sieved out during sampling, and only the grains smaller than 4.75 mm were collected, as a disturbed sample A. This kind of treatment in sampling may affect the peak value of shear resistance, while have no effect on the residual shear strength or that in steady state (Sassa et al. 2004). An old valley deposit was found beneath the displaced debris that moved in this event, and it became sample B which was taken, by the same method as sample A.

3   Simulation Tests for the Initiation and Motion Mechanism of the Donghekou Slide

3.1   The Geotechnical Simulation Test for Landslide Triggered by Actual Seismic Wave

In a geotechnical simulation test, the initial stress level, i.e., the initial normal stress, shear stress, and pore-water pressure existing in the slope before earthquake should be reproduced at first to simulate the initial stress condition in the slope, and then the cyclic loading caused by a seismic wave can be applied to observe the effect on slope caused by earthquake. Because the Donghekou complex slide is so large and the earthquake was so strong, it is impossible to simulate both the initial stress of the initial slope and cyclic loading from the earthquake at the same time. In this test, in considering the stress capacity of the ring shear apparatus, the initial slope angle of the Donghekou slide was kept, while the thickness of the sliding mass was decreased to a much lower level. The real seismic wave components of the Wenchuan earthquake monitored at SFB strong-motion station were used (Wang 2008). Through transforming the three components of the seismic wave to two components occurring along the sliding surface (increment of shear stress) and perpendicular to the sliding surface (increment of normal stress), the input signals were formed (Wang et al. 2000), and applied to sample A (source area).

Considering the average slope angle of 25 degrees at the source area of the Donghekou rockslide, when the thickness of the sliding mass was assumed to be 20 m, the unit weight of 18 kN/m^3, the initial normal stress is 295.7 kPa, and the initial shear stress is 137.9 kPa. Figure 50.6 shows the synthesized input wave of normal stress and shear stress for the Donghekou slide. The initial stress condition of the initial slope before the earthquake, and the stress increment caused by the earthquake are included. Because the earthquake occurred during a

medium rainy season, the static pore-water pressure acting on the potential sliding surface was ignored, but the sliding surface itself was estimated in a fully saturated condition.

The test was conducted with disturbed sample A from the source area. The sample was dried in an oven at 105 degrees centigrade at first, and then separated into grains by gently applying a wooden hammer. By means of free fall deposition method (Ishihara 1993), the dry sample grains were set in the shear box, and saturated by carbon dioxide gas and de-aired water. The saturation degree was confirmed by the B_D value supposed by Sassa (1988). When the B_D value is higher than 0.95, the sample is recognized as fully saturated. In this test, the B_D value was 0.97, showing a fully saturated condition. After normal consolidation at 295.7 kPa, the initial shear stress 137.9 kPa was loaded gradually while keeping the sample in a drained condition to avoid excess pore-water pressure generation. At this moment, the void ratio of the soil sample reached 0.650. Then, the sample was changed to

an undrained condition, and the input signals were loaded to simulate the condition of the original slope when the earthquake motion was applied as the initiation factor.

Figure 50.7 shows the entire data series for the geo-simulation test on the Donghekou slide. A large decrease of the shear resistance and a rapid generation of the excess pore-water pressure to the value of normal stress can be observed. It can be seen that the sample failed at about 10 s from the beginning of the earthquake, and the shear displacement accelerated at about 25 s. At the same time (from 20 s), the pore-water pressure shows a rapid increase, and reached the same value as the normal stress at about 45 s, reaching the point of full liquefaction. Corresponding to the rapid increase of the pore-water pressure, the shear resistance decreased rapidly, and reached a very low value of about 15 kPa. At the end of the seismic loading, the shear displacement reached about 35 m with a high speed of 0.38 m/s (the maximum speed of the apparatus at the selected gear).

Fig. 50.7 Geo-simulation test results for the Donghekou rockslide using the real seismic wave components as the triggering process. Graph "**a**" shows stress (kPa) and graph "**b**" shows stress and pore-water pressure (kPa)
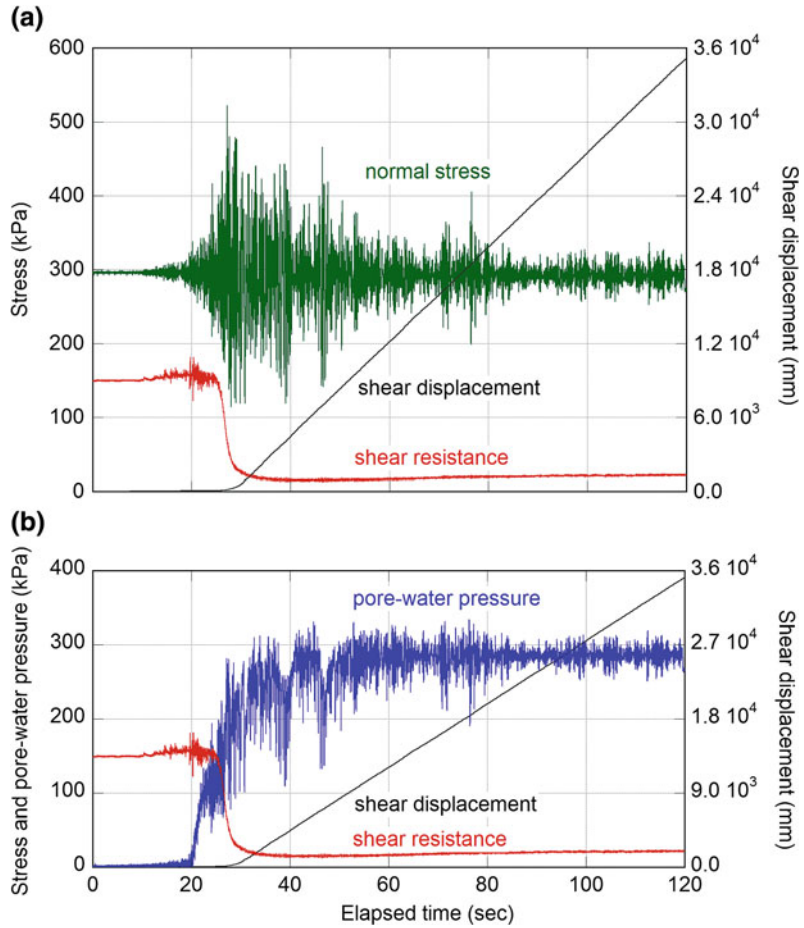
3.2 Results of the Simulation Test Showing the Impact of Failed Slide Mass Loading onto the Valley Deposit

To simulate the process of a debris flow triggered by a rockslide, the model (Fig. 50.8) proposed by Sassa et al. (1997) was applied. The slide mass moved down the slope (I), and applied load onto the valley deposits at the foot of the slope (II). When a surface-water stream or subsurface flow existed and some of the deposits were saturated, the valley deposit was sheared by undrained loading and transported downstream together with the sliding mass (III) (Sassa et al. 2004). In this study, we change the saturated condition of valley deposits to three patterns: dry, partially saturated, and fully saturated, to observe the
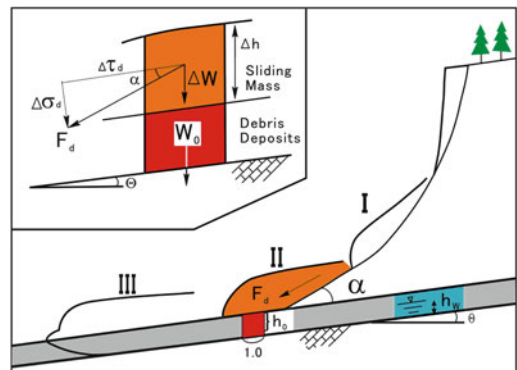
Fig. 50.8 Model of the landslide triggered by debris flow (Sassa et al. 1997)

significance of the hydrogeological conditions. A column of unit width, which is a part of the valley deposit, was considered. In the position (I)
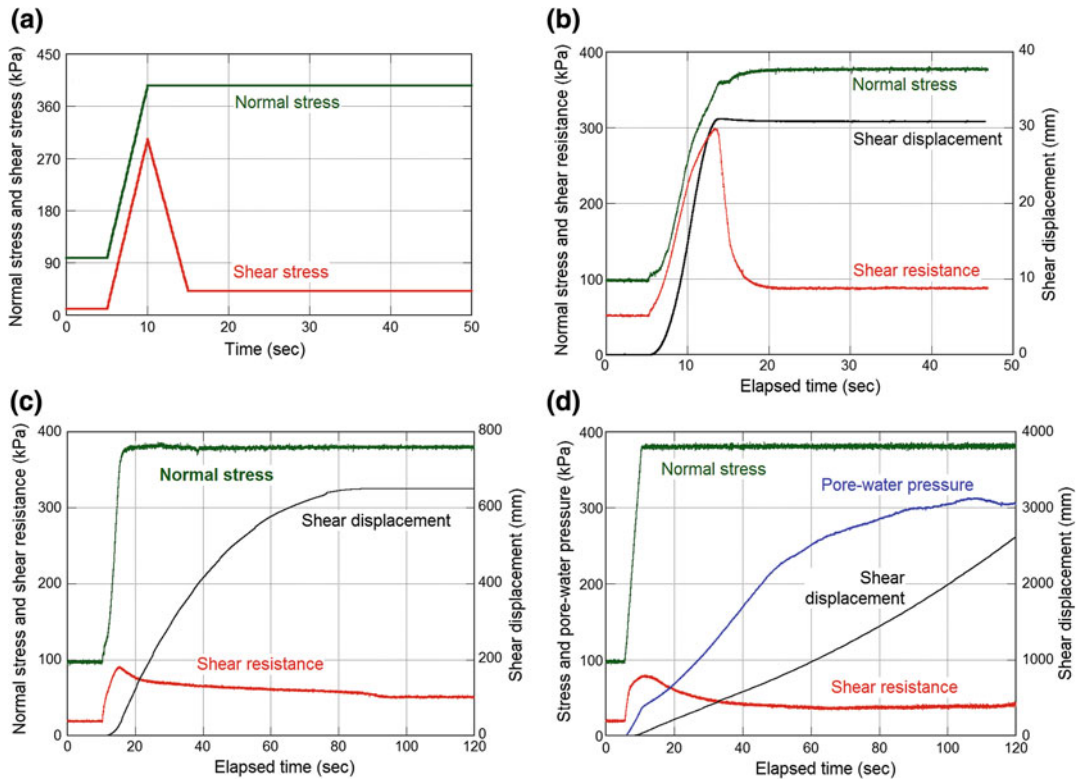
Fig. 50.9 Loaded stress signals (shown in graph **a**) and results of the Donghekou complex slide motion simulation test using Sample B. Graph (**b**) shows results of dry condition, Graph (**c**) shows results of unsaturated condition, graph (**d**) shows results of fully- saturated condition

of the sliding mass, the weight of the column (W_0) was in effect. When the sliding mass moved onto the valley deposit (II) with a certain velocity, it provided dynamic loading of the column. Here, it is assumed that the applied stress on the valley deposits was the sum of the static stress, W (load due to the weight of the sliding mass) and the dynamic (impact) stress, F_d, working in the direction of motion of the sliding mass.

The input parameters were determined by considering the actual slope condition at sampling point B and capacity of the apparatus as explained in the previous test. By using $\alpha = 17°$, $\theta = 6°$, h = 5 m, $h_w = 0$, $\Delta h = 15$ m, $\gamma_t = 18$ kN/m^3, $F_d = 1$, the impact stresses (normal stress and shear stress) for sample B were formed as shown in Fig. 50.9a. The impact forces increased to peak at 5 s, and disappeared in 5 s. After the impaction, the valley deposits

flowed down the gentle slope with the sliding mass from the source area of the rock slide.

Graphs b–d shown in Fig. 50.9 illustrate the results for the three conditions (dry, partially saturated, fully saturated). The measured shear displacement is not necessarily representing the actual sliding displacement of landslide in the actual situation. The values shown in the figures can only be used for the comparison for the different degrees in the saturation. When the failed sliding mass traveled down to the valley deposits, in a dry condition, only very limited shear displacement occurred, and when the valley deposits were fully saturated, a large travel distance together with high speed motion occurred. The high pore-water pressure was measured, and the shear resistance was very small (about 45 kPa). This should be a possible reason for the long runout motion for a more

than 2 km-length of the Donghekou complex
slide. Figure 50.10 shows the total stress path
and effective stress path of the test with the
fully-saturated soil sample. Started from the
same point, the total stress path (TSP) moved to
the right side and then dropped down to a lower
level of shear resistance, which means a
increasing in normal stress at first and decreas-
ing in shear resistance, while the effective stress
path (ESP) moved to the right at once, then
returned to the left. This path shows the process
of excess pore pressure generation. The apparent
friction angle (the inclination of the line con-
necting the end of TSP and the original point) is
only 6.0 degrees. It means a high mobility of the
sliding mass when it loaded on the saturated
valley deposits. The small apparent friction
angle will result in high velocity and long trav-
elling distance of the sliding mass.

As mentioned previously, the angle from the
toe of the Donghekou slide and the source area is
about 11 degrees. It should be careful to compare
the actual apparent friction value with that
obtained in ring shear tests. The most important
difference is that the total normal stress in ring
shear test is constant, while in the actual case, the
normal stress generally decreases to lower level
because the sliding mass always becomes thinner
and thinner. Other reasons causing this difference
may include energy dissipation caused by the
impact of the collision of the debris among the
sliding mass, some parts may not be in a fully-
saturated condition and mobilized to a higher
shear resistance. While, the test in laboratory was

conducted in a simple and ideal situation of fully
saturated and undrained condition. These factors
may cause the difference between the actual
apparent friction angle and test value. Moreover,
it is clear that the test shows that the existence of
the water is a very important factor for the rapid
movement and long travel distance.

4 Conclusions

Through field investigation of the long runout
landslides triggered by the Wenchuan earth-
quake and experimental study of the Donghekou
slide, it is found that the groundwater played key
roles in the long runout and rapid landslide
motion process during the great earthquake. It is
suggested that in the source area, the landslide
can gain velocity when the "sliding surface
liquefaction" phenomenon occurred as a result
of undrained shearing in a saturated sliding
zone. In turn, the displaced sliding mass can
exert impact on the valley deposit. When the
valley deposit is also saturated, it can be lique-
fied again, and works as a sliding zone with low
shear resistance to transport the sliding mass
from the source area for long distance.

References

Burchfiel BC, Royden LH, Van der Hilst RD, Hager BH, Chen Z, King RW, Li C, Lü J, Yao H, Kirby E (2008) A geological and geophysical context for the Wenchuan earthquake of 12 May 2008, Sichuan, People's Republic of China. GSA Today 18(7):4–11

Cui P, Zhu YY, Han YS, Chen XQ, Zhuang JQ (2009) The 12 May Wenchuan earthquake-induced landslide lakes: distribution and preliminary risk evaluation. Landslides 6(3):209–223

Huang RQ, Li WL (2009) Development and distribution of geohazards triggered by the 5.12 Wenchuan Earthquake in China. Sci China Ser E Tech Sci 52(4):810–819

Ishihara K (1993) Liquefaction and flow failure during earthquakes. Géotechnique 43(3):351–451

Li XJ, Zhou ZH, Yu HY, Wen RZ, Lu DW, Huang M, Zhou YN, Cu JW, (2008) Strong motion observations and recordings from the great Wenchuan Earthquake. Earthq Eng Eng Vib 7:235–246

Lu M, Li XJ, An XW, Zhao JX (2010) A preliminary study on the near-source strong-motion characteristics of the great 2008 Wenchuan earthquake in China. Bull Seismol Soc Am 100(5B):2491–2507

Ouimet WB (2010) Landslides associated with the May 12, 2008 Wenchuan earthquake: implications for the erosion and tectonic evolution of the Longmen Shan. Tectonophysics 491:244–252

Sassa K (1988) Geotechnical model for the motion of landslides. Special lecture of 5th international symposium on landslides. Landslides 1:37–55

Sassa K, Fukuoka H, Wang FW (1997) Mechanism and risk assessment of landslide- triggered-debris flows:
lesson from the 1996.12.6 Otari debris flow disaster, Nagano, Japan. In: Cruden DM, Fell R (eds) Landslide risk assessment, Proceedings of the international workshop on landslide risk assessment, Honolulu, pp 347–356, 19–21 February

Sassa K, Fukuoka H, Wang G, Ishikawa N (2004) Undrained dynamic-loading ring-shear apparatus and its application to landslide dynamics. Landslides 1(1):7–19

Tang C, Zhu J, Liang J (2009) Emergency Assessment of Seismic Landslide Susceptibility: A Case Study in the 2008 Wenchuan Earthquake Area. Earthq Eng Eng Vib 8:207–217

Wang D, Xie LL, Abrahamson NA, Li SY (2010) Comparison of strong ground motion from the Wenchuan, earthquake of 12 May 2008 with the next generation attenuation (NGA) ground-motion models. Bull Seismol Soc Am 100(5B):2381–2395

Wang FW, Sassa K, Fukuoka H (2000) Geotechnical simulation test for the Nikawa landslide induced by 1995.1.17 Hyogoken-Nambu earthquake. Soils Found 40(1):35–46

Wang ZF (2008) A preliminary report on the Great Wenchuan earthquake. Earthq Eng Eng Vib 7(2):225–234

Yi GX, Wen XZ, Wang SW (2006) Study on fault sliding behaviors and strong-earthquake risk of the Longmenshan–Minshan fault zones from current seismicity parameters. Earthq Res China 22(2):117–125 (in Chinese)

Yin YP, Wang FW, Sun P (2009) Landslide hazards triggered by the 2008 Wenchuan earthquake, Sichuan, China. Landslides 6(2):139–152

Natural Gas Eruption Mechanism for Earthquake Landslides: Illustrated with Comparison between Donghekou and Papandayan Rockslide-Debris Flows

51

Quentin Z. Q. Yue

Abstract.

This paper presents a new genesis and associated mechanism responsible for causing landslides and particular rapid and long runout landslides during earthquakes. This new genesis is the huge expansion power of highly compressed natural gas as the main force causing landslides during earthquake. The associated mechanism involves a rapid migration and transportation of highly compressed natural gas from deep crust through geological faults or discontinuities (weak zones) to slope grounds during earthquake. The gas expansion power suddenly breaks the ground rocks and soils. Instantly, it accelerates, erupts and ejects the broken rock fragments and soil particles (the debris) out of their original places and into the sky. Subsequently, the debris with high initial velocity or momentum rapidly fly, run and flow down the slope for long travel distance. During the flying, impacting and flowing, the debris can be further disintegrated. This paper uses the Donghekou and the Papandayan rockslide-debris flows as examples to illustrate the genesis and mechanism.

1 Introduction

Earthquake can produce, induce and/or trigger widespread landslides and rockfalls in mountainous areas. The conventional mechanism may be described as follows. A sudden rupture of active geological fault in deep ground causes an earthquake and creates seismic waves to propagate in the crust and to ground surface. The seismic waves can add a dynamic loading to shake the slope. This strong seismic shaking can be amplified by hilly topographic effect. The amplified shaking loading triggers the slope to be instable and to occur landslide or rockfall. Furthermore, the occurrences of landslides and rockfalls during an earthquake can be widespread because the ground shaking loading is widespread and the mountainous areas have numerous

Q. Z. Q. Yue (✉)

Department of Civil Engineering, The University of Hong Kong, Pokfulam Road, Hong Kong, China
e-mail: yueqzq@hku.hk

slopes vulnerable to landslides or rockfalls. This conventional mechanism has been widely accepted and effectively used in landslide hazard prevention and mitigation around world.

However, this conventional mechanism has also encountered challenges. For example, the El Salvador earthquake (Mw 7.6) of January 13, 2001 triggered a high destructive flowslide of pyroclastic materials, i.e., the Las Colinas Landslide at Santa Tecla (Crostaa et al. 2005). Evans and Bent (2004) indicated in the conclusion that "The mechanism of long runout at Las Colinas remains undetermined." In fact, many events of rapid and long runout large landslide-debris flows or rockslide-debris flows have occurred during earthquakes around the world. Each such event caused tremendous loss of life and properties. The Great Wenchuan Earthquake of May 12, 2008 caused 35,000 to 110,000 landslides including about 100 rapid and long runout large rockslide-debris flows that caused huge disasters. The conventional mechanism cannot consistently and logically explain the mechanism of the many huge destructive and devastating landslides (or rock avalanches).

2 The New Mechanism of Ground Gas Eruption

This paper aims to propose and demonstrate a new genesis and mechanism responsible for causing large, rapid and long runout landslide-debris flows (rockslide-debris flows, or rock avalanche and rock debris flows) during earthquakes. The author has studied and investigated many aspects of earthquakes, landslides, soil and rock mechanics, geotechnical engineering and geology over past 30 years (Yue 1983, 1986, 1988, 1992, 1995; Yue et al. 1994, 1995, 2004; Yue and Lee 2002; Yue and Xiao 2002; Yue and Yin 1999). In particular, he has investigated the genesis and mechanism of the devastating Wenchuan Earthquake since May 12, 2012. Yue (2008, 2009, 2010a, b, 2011a, b, c, d, e) discovered and demonstrated a new genesis and mechanism of ground gas eruption causing the catastrophic landslide-debris (or rock-slide debris flows, or

rock-avalanche and debris flows). The genesis and mechanism of gas causing landslides can be described in the following six stages.

During earth quaking, a huge amount of natural gas with high pressure quickly escapes the deep crust traps and migrates and flows through tectonic faults, geological faults, weak zones and/or porous channels into the rock masses forming mountains or hillside slopes. Since the rock materials can have relatively high strengths and rigidity, the rock mass can resist the initial loading of the quickly migrated gas. Quickly, more and more gas would migrate and seep into the rock masses and fully saturate their voids and fissures and apertures. Eventually, the expanding powers of the gas in the rock masses would instantly break, erupt and/or explode the rock masses with limited confining in situ pressures and force them to flow out of their original positions and form the landslides with broken rock masses and long distance ejections and flows.

In the ensuing, the author uses the Donghekou and the Papandayan rockslide-debris flows as examples to illustrate the genesis and mechanism.

3 The Donghekou Rockslide-Debris Flow

Donghekou rockslide-debris flow disaster happened during the Wenchuan Earthquake that lasted 110 s according to seismograph records. The rapid and long distance and powerful movement of a huge amount of broken rock particle debris instantly destroyed and buried villages and a school and killed 780 people down the flow path. The disaster can be briefly described as follows.

As shown in Figs. 51.1, 51.2, 51.3, 51.4, 51.5, the flow and deposition path of up to 600 m wide and 2500 m long was on hilly terrain slopes with three intersected stream courses. The broken rock particle debris was originally a part of the rock mass forming the top portion of a mountain ridge slope (the first slope) from the elevations of 1350–1100 m above the sea level. The rock mass was estimated to have a volume
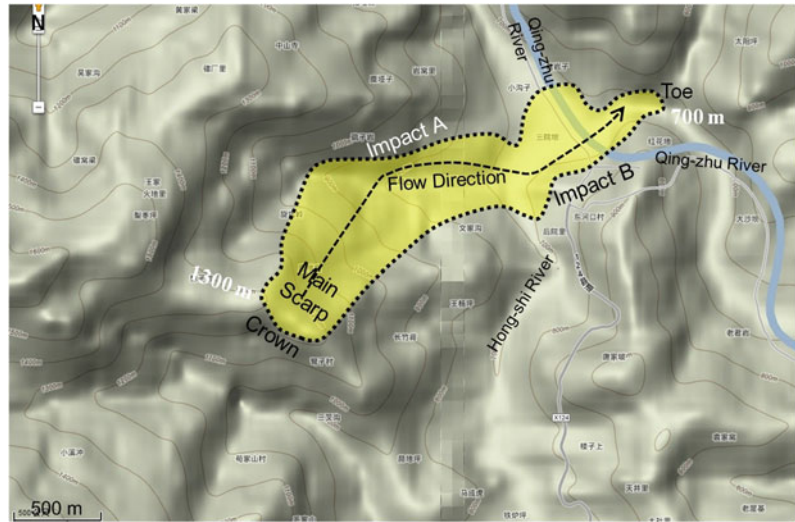
of 30–100 (or 140) million m^3 of about 400 m wide, 200 m long and 300 m high (Sun et al. 2011; Yuan et al. 2010; Zhang et al. 2011). It was ejected upwardly out of its original position (the main scarp or Zone 1 in Figs. 51.1, 51.2, 51.3) toward the slope dip direction (i.e., N34°E) and flew over the remaining upper-middle portion of the first slope. The upper-middle ground surface of the first slope was not stripped by its upper broken rock debris and kept the original vegetations and trees (Zone 2 in Fig. 51.3).

Subsequently, the broken rock mass debris flew over the first V-shaped stream course for about 700 m horizontal distance. It strongly impacted on a lower portion surface of the elevations between 900 m to 700 m of a second mountain ridge slope opposite the first slope over the first stream course (the Impact A in Figs. 51.1, 51.2, 51.3, 51.4, 51.5). The debris stripped the surface materials of both the middle to lower portion of the first slope (Zone 3) and the lower portion of the second slope (Zone 4). The impacting and stripping altered the main flow direction of the debris by 61° following the strike direction of the stripped surface of the second slope (i.e., N95°E).

A part of rock debris deposited in the first stream between the first and second slopes (Zone 5). Another part then continued to flow and deposit along the new direction for about

1000 m horizontal distance over the second V-shaped stream course (i.e., the Hongshi river). It strongly impacted the lower portion surface of the elevations between 800 m and 700 m of the third mountain slope opposite the second slope over the second stream course (the Impact B in Figs. 51.1 and 51.5). Again, the debris stripped the surface material of the lower portion of the third slope. The impacting and stripping altered back the main flow direction of the rock mass debris by 43° following the strike direction of the stripped surface of the third slope (i.e., N52°E).

A part of the rock debris also deposited in the second stream course between the second and third slopes. Another part of the rock debris continued to flow and deposit along the new direction for about 900 m horizontal distance over the third stream course (i.e., Qingzhu river). The debris reached and stopped by the fourth slope forming the other bank the third stream at the elevation about 700 m (the toe in Figs. 51.1 and 51.5). The debris filled up the first stream course and blocked the second and third stream courses and formed two independent and adjacent landslide dammed lakes.

The author carried out field investigations at this site many times. The first time was conducted on June 18, 2008. It was discovered that this powerful rapid and long runout

Fig. 51.2 Estimated vertical topographical profiles of Donghekou rockslide-debris flow (based on Google Maps with modifications)

Fig. 51.3 The upper to middle portion of Donghekou rockslide-debris flow (Zones 1–6: Main scarp and ejected rock mass source; flying; debris stripping; debris impacting and stripping; flowing and deposition; Air stripping slope)
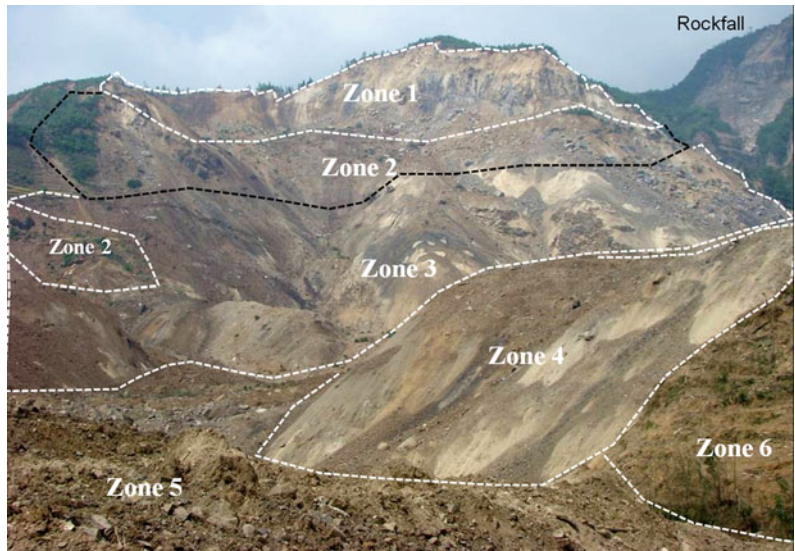
Fig. 51.4 Impact A and stripped surface of second slope opposite first slope over a V-shaped stream course of Donghekou rockslide-debris flow

Fig. 51.5 Impacts A and B and stripped surfaces, downstream debris flow and deposition and toe of Donghekou rockslide-debris flow

rockslide-debris flow (or rock avalanche) was caused by expansion power of highly compressed natural gas (Yue 2008, 2009). The gas rapidly migrated from deep ground to the upper portion of the first slope via rock discontinuity channels such as the faults and weak bedding planes.

4   The Papandayan Rockslide-Debris Flow

It is well recognized that eruptions of volcano gases can destruct rock mountain slopes and cause large and devastating landslides. For example, the eruption of the Mount St. Helens volcano on May 18, 1980 in Washington caused a massive rapid and long runout landslide of huge amount rock mass forming the north flank slope of the mountain. It was observed that the gas eruption power forced the rock debris to travel at about 48.6–69.4 m/s for several tens kilometers.

The Mount Papandayan was considered as a complex stratovolcano controlled by faults, situated in Garut Regency, West Java, Indonesia. Stratovolcanoes usually erupt in an explosive way. The gas channels in the volcano mountain can be clogged and locked up by formerly broken and/or chemically altered rocks. The gas

migrated from deep crust can be trapped and accumulated in the voids and fissures of the mountainous rock mass. So, the gas volume and pressure can increase with time. Once the equilibrium between the rock mass strength and the gas expansion power is reached, the gas expansion power can result in a sudden and explosive eruption of its upper rock mass. The gas power can break the rock mass forming the mountain slopes, eject the broken rock mass debris out of their original positions, and produce a rapid and long runout rockslide-debris flow. The rockslide-debris flow can cause catastrophic rock-debris avalanche disasters to local people because the sleeping time period can be tens to hundreds years.

The Mount Papandayan erupted explosively on 1772 for the first time. The eruption caused the northeast flank to collapse and produced a catastrophic rock-slide debris avalanche that destroyed 40 villages and killed nearly 3,000 people. The second major explosive eruptions occurred from November 11 to December 8, 2002 (Abidin et al. 2005). On November 15, 2002, at 06:30 local time, the largest eruption occurred with big rumble. The ash plume went up to 4,000 m above the crater. 6,000 villagers were evacuated. The eruptions have significantly

Fig. 51.6 Estimated topographical map of Papandyan rockslide-debris flow in Garut Regency, Bandung, West Java, Indonesia at (107°43′40″ E, 7°19′23″ S) (based on Google map)
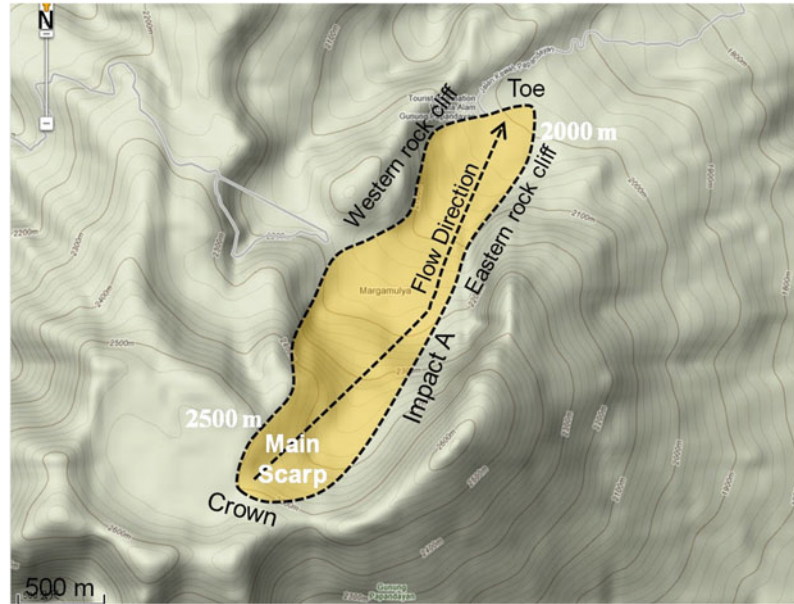
changed the morphology of the mountainous slopes. They triggered three main landslides on the rock cliff crest area (rim). One was a rapid and long runout rock-avalanche-debris flow of large amount of rock fragments/debris. The debris entered three landslide-dammed lakes in series and surged a large volume of lake water to a down-stream river destroying 245 houses (Lavigne et al. 2005).

The author investigated the site on July 7, 2011. As shown in Figs. 51.6, 51.7, 51.8, 51.9, he observed the main scarp (Zone 1 in Fig. 51.8), long and wide debris deposition belts and dead trees. The main scarp had bare, fresh, irregular and stepped ground surface, showing tensile and brittle fracture failure of the upper mountain rocks. The debris were mainly broken or altered sedimentary rocks of tensile and brittle fracture failure in nature. The long trace of debris deposition clearly showed the features of a rapid and long runout flow of the rock fragments. The dead or live trees rooted in the debris ground were broken in tension or bent. Their trunks and branches lain down the debris ground showed the sign that they were swept by rapid and forceful debris movement. These features and other related phenomena clearly show that a rapid and long runout rock avalanche-debris flow happened during the

explosive eruption in November 2002. Furthermore, it is noted that as shown in Fig. 51.6, the rainfall catchment area of the cliff valley is limited for occurring any heavy flooding to induce a large amount of rock fragments to flow downstream.

It can be evident that the rock avalanche-debris flow was caused by the explosive eruption of the highly compressed natural gas (steam) coming from the deep Papandayan mountainous rock mass. The steam expansion power broke the upper rock mass in the main scarp area and then ejected the fragments out of their place upwardly and horizontally toward the slope dip direction. After having gained the initial velocity and momentum, the rock fragments/debris flew into the sky possibly toward the slope dip direction along N46°E. Subsequently, due to downward gravity, they undertook a parabolic flight and possibly with a gas/air cushion. So, they flew a long distance. Subsequently, they impacted, shoveled and stripped the downstream ground of the two cliff bounded valley with an angle of incidence. Then, the debris together with some stripped debris continued to rapidly flow down the valley course possibly with a changed main flow direction along N23°E. The flow direction angle was changed by 23°. As they rapidly flowed down, the debris made

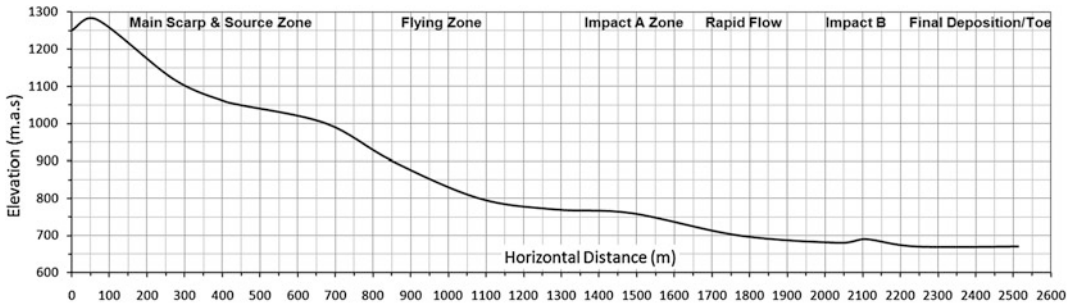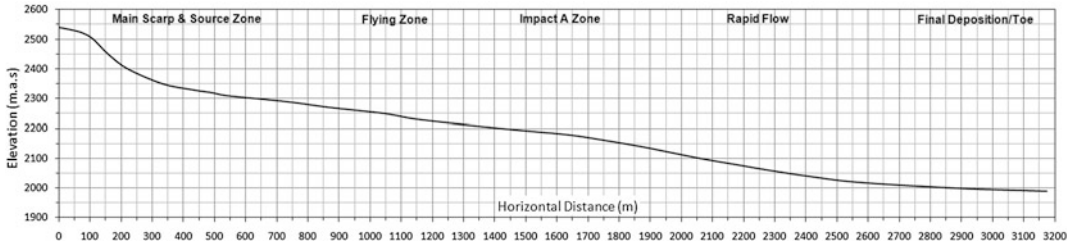**Fig. 51.7** Estimated vertical topographical profiles of Papandyan rockslide-debris flow (based on Google Maps with modifications)

Fig. 51.8 Main scarp and upper portion of Papandyan rockslide-debris flow with Zones 1, 2, 3 and 5: Main scarp and ejected rock mass source; flying; debris stripping; flowing and deposition (photo taken on July 7, 2011)
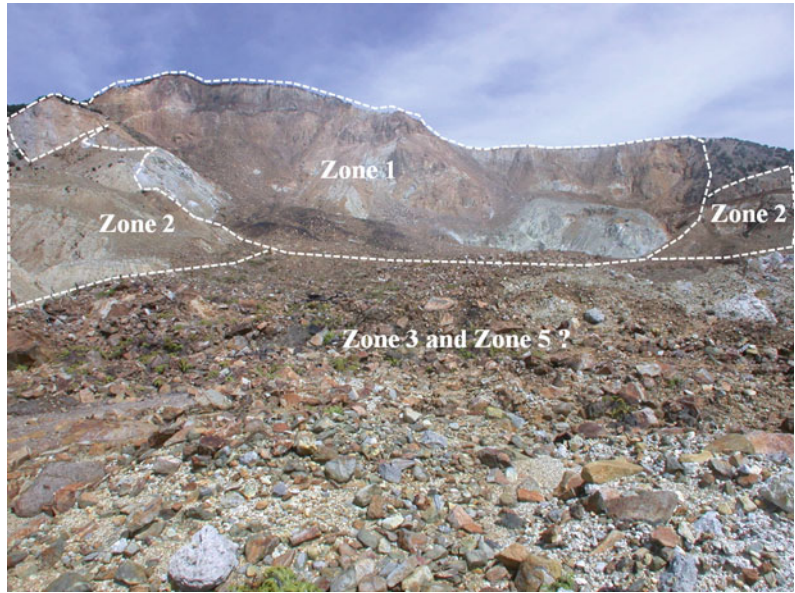
Fig. 51.9 Impact A, downstream debris flow and deposition and toe of Papandyan rockslide-debris flow (Photo taken on July 7, 2011) (the near vertical rock cliffs on east and west sides were formed suddenly by the explosive eruption in 1772)
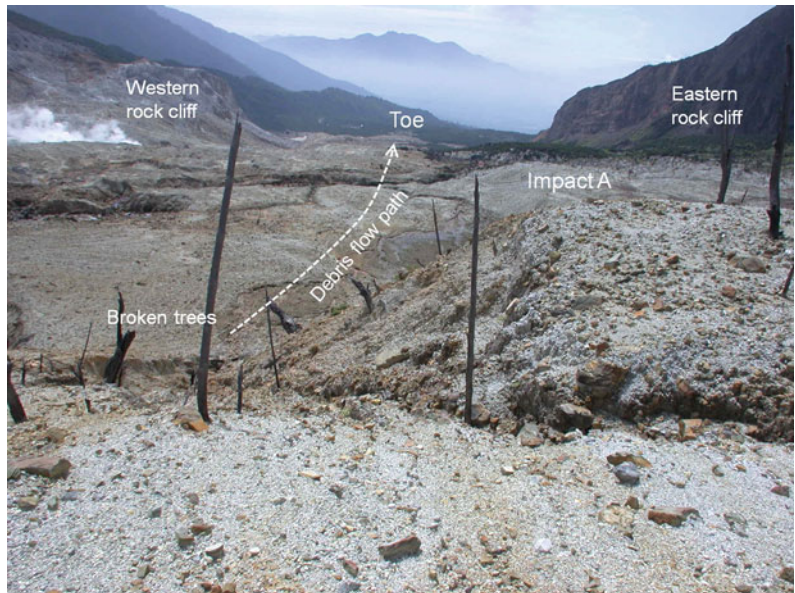
depositions on the path. Some debris reached and stopped at the toe area eventually.

5 Comparisons of Two Rockslide-Debris Flows

The Donghekou and Papandyan rock-slide debris flows have about 2500 and 3100 runout distances, respectively. Their main scarp areas are about 230×10^3 m^2 and 210×10^3 m^2, respectively. Their total affected areas are about 1.3×10^6 m^2 and 1.4×10^6 m^2, respectively. Their travel angles are about 14° and 11°, respectively. Their debris volume could also be similar. It is noted that the angle of repose for the broken rock debris of the two sites should be greater than 33°.

The main scarps of the Donghekou and Papandyan rock-slide debris flows are similar in nature. They are all irregular and stepped rock surfaces, which shows the same tensile and brittle rupture nature. Their scarps are clean of rock debris, which shows the same ejection nature.

The rocks composing the Donghekou rock-slide debris are mainly dolomite limestone, carbonaceous slate and siliceous phyllite with coal seams. Their bedding orientations are 330°/25° and 070°/40°. The slate and phyllite have thin beddings and tensile strengths of 11.7 and 2.15 MPa in dry condition and 6.7 and 1.2 MPa in water saturated condition (Sun et al. 2011). The rocks composing the Papandyan rock-slide debris are mainly sandstone and other altered rocks. The sandstone is hard and brittle. The rock fragments are angular while the chemically altered rocks in Papandyan are sub-angular to sub-rounded. The rock fragment sizes at the two sites are similar. Furthermore, there are deep geological faults at the two sites.

The rapid fly and flow of rock debris at Donghekou encountered two nearly face to face impacts with shoveling and stripping, which significantly changed the main flow directions two times. The rapid fly and flow of rock debris at Papandyan possibly encountered one side by side impact with shoveling and stripping, which slightly changed the main flow direction one time. In addition, the debris at Donghekou tried to flow upward at the toe where they encountered a upward slope. The debris at Papandyan might encountered three existing landslide-dammed lakes, surged the lake water and infilled the lakes.

At Papadyan, strong fumaroles has been active. The gases collected in the fumaroles consist mostly of H_2O with minor amount of CO_2 and H_2S and very low SO_2, HCl, H_2, N_2 and CH_4 (Mazot et al. 2008). Since Oct. 2008, at Donghekou debris site, gas fumaroles had happened for many months. There were 40–50 fumarolic spots over a 700 m to 800 m long area. The white steams were about 2–3 m high. The gas was flammable and natural gas with 60 % CH_4 (Wang et al. 2009).

It was witnessed that during the explosive eruptions of Papandyan, big ground rumbles were heard, gray or white color ash plumes were observed, and ground tremors were felt by local people. Similarly, according to witness, big ground explosive sounds were heard. Many rock fragments were falling down. Nobody could stand on the ground and everyone had to, facing downward, lie on the ground surface. The sky was fully filled with fine particles and suddenly became dark. Nothing could be seen. After the sky was clear, it was observed that part of the upper mountains was taken off and the village houses were swept away and/or buried by the debris.

6 Discussions and Conclusions

The above descriptions and comparisons can demonstrate that the two rapid rockslide (or rock avalanche) debris flows at Donghekou and Papandyan have many similarities in long travel distance, low travel angle, large irregular and tensile scarp, long and wide flow area, tensile rock fragment debris, ejection, impact, shoveling and stripping, fumaroles, ash plumes, big explosive sound, ground tremor, and sky change. Therefore, the powers and energies breaking the huge amount of rock masses, ejecting them into

sky and accelerating them with high initial velocities and moments at the two sites must be similar or equivalent. It can be argued that the power and energy at Papandyan were the volumetric expansion power and energy of a huge amount of volcano gases (mainly steam gas). Such gas driven explosion is powerful and its suddenly released energy is huge.

Therefore, we must ask and answer the following question: What was the power and energy suddenly released at Donghekou?

Based on the above descriptions and analyses, this question can be easily answered. The answer is that the power and energy at Donghekou were the volumetric expansion power and energy of a huge amount of highly compressed natural gas (methane gas). The gas was migrated from deep crust via the faults and weak zones and could have much higher (or more than ten times) pressure than that of the steam at Papandyan. So, the massive rock-avalanche debris flow at Donghekou was unexpected and devastating. The mechanism follows the description in Sect. 51.2 above.

This answer is consistent with the author's hypothesis of earthquake genesis and energy that earthquakes themselves are caused by the volumetric expansion power of highly compressed methane gas in deep crust traps (Yue 2008, 2009, 2010a, 2010b, 2011a, b, c, d, e, f). An earthquake is an adiabatic process associated with the instantaneous interaction between the upward flying and expanding of huge natural gas of abnormally high pressure escaped from its traps in deep fault zone of the crest and the surrounding upper and lateral rocks under the confinement of down-ward gravity, in situ tectonic stresses & rock strengths. The 2008 Wenchuan Earthquake was caused by the volumetric expansion energy of a huge amount of highly compressed natural gas escaped from the deep crust traps via Longmen Shan faults (Yue 2008, 2009, 2010a, b, 2011a, b, c, f). The volumetric gas expansion with a velocity of 2–3 km/s penetrated, fractured, expanded, uplifted, moved, waved, deformed and damaged rock masses along the fault zones, which generated the elastic seismic waves.

References

Abidin HZ, Andreas H, Gamal M, Suganda OK, Meilano I, Hendrasto M, Kusuma MA, Dartnawan D, Purbawinata MA, Wirakusumah AD, Kimata F (2005) Ground deformation of Papandayan volcano before, during, and after the 2002 eruption as detected by GPS surveys. GPS Solut 10(2):75–84

Crostaa GB, Imposimatob TS, Roddemanb D, Chiesac S, Moiad F (2005) Small fast-moving f low-like landslides in volcanic deposits: the 2001 Las Colinas Landslide (El Salvador). Eng Geol 79:185–214

Evans SG, Bent AL (2004) The Las Colinas landslide, Santa Tecla: a high destructive flowslide triggered by the January 13, 2001, El Salvador earthquake. Natural Hazards in El Salvador. The Geological Society of America, Inc., USA, pp 25–38

Lavigne F, Hadisantono R, Surmayadi M, Flohic F, Geyer F (2005) The November 2002 eruption of the Papandayan volcano (Indonesia): direct and induced hazards, with emphasis on lahars. Zeitschrift Fur Ggeomorphologie Supplement Series 140:151–165

Mazot A, Bernard A, Fischer T, Inguaggiato S, Sutawidjaja IS (2008) Chemical evolution of thermal waters and changes in the hydrothermal system of Papandayan volcano (West Java, Indonesia) after the November 2002 eruption. J Volcanol Geotherm Res 178(2):276–286

Sun P, Zhang YS, Shi JS, Chen LW (2011) Analysis on the dynamical process of Donghekou rockslide-debris flow triggered by 5.12 Wenchuan earthquake. J Mountain Sci 8(2):140–148

Wang CS, Deng B, Zhu LD, Li Y, Wang XN (2009) Discovery of hot spring and natural gas exposure spots in Donghekou, Qingchuan County, Sichuan Province, China. Geol Bull China 28(7):991–994 (in Chinese)

Yuan RM, Xu XW, Chen GH, Tan XB, Klinger Y, Xing HL (2010) Ejection landslide at northern terminus of Beichuan rupture triggered by the 2008 M(w) 7.9 Wenchuan earthquake. Bull Seismol Soc Am 100(5B):2689–2699

Yue ZQ (1983) On seismogeological stability of yuncheng basin and Zhongtio Mountain's North faults. Thesis for BSc Degree, Department of Geology, Peking University, Beijing (in Chinese)

Yue ZQ (1986) Analytical solution of transversely isotropic elastic layered system and its application to coal mining. Thesis for M.Sc. Degree, Department of Geology, Peking University, Beijing (in Chinese)

Yue ZQ (1988) Solutions for the thermoelastic problems in vertically inhomogeneous media. Acta Mechnica Sinica (English Edition) 4:182–189

Yue ZQ (1992) Mechanics of rigid disc inclusion embedded in saturated poroelastic medium. Thesis for Ph D Degree, Department of Civil Engineering, Carleton University, Ottawa

Yue ZQ, Selvadurai APS, Law KT (1994) Excess pore pressure in a poroelastic seabed saturated with a compressible fluid. Can Geotech J 31:989–1003

Yue ZQ (1995) On generalized Kelvin solutions in multilayered elastic media. J Elast 40(1):1–44

Yue ZQ, Bekking W, Morin I (1995) Application of digital image processing to quantitative study of asphalt concrete microstructure. Transportation Research Record No. 1492, Transportation Research Board, Washington DC, pp 53–60

Yue ZQ, Yin JH (1999) Layered elastic model for analysis of cone penetration testing. Int J Numer Anal Method Geomech 23:829–843

Yue ZQ, Lee CF (2002) A plane slide that occurred during construction of a national expressway in Chongqing, SW China. Q J Eng Geol Hydrogeol 35:309–316

Yue ZQ, Xiao HT (2002) Generalized Kelvin solution based boundary element method for crack problems in multilayered solids. Eng Anal Boundary Elem 26(8):691–705

Yue ZQ, Lee CF, Law KT, Tham LG (2004) Automatic monitoring of rotary-percussive drilling for ground characterization—illustrated by a case example in Hong Kong. Int J Rock Mech Min Sci 41:573–612

Yue ZQ (2008) What caused the catastrophic landslides during the May 12 Wenchuan earthquake in Sichuan, China. In: Abstract and oral presentation at the 12th international conference of international association for computer methods and advances in geomechanics (IACMAG), Goa, India, pp 135, 1–6 October 2008

Yue ZQ (2009) The source of energy power directly causing the May 12 Wenchuan Earthquake: Huge extremely pressurized natural gases trapped in deep Longmen Shan faults. News J China Soc Rock Mech Eng 86(2):45–50

Yue ZQ (2010a) Features and mechanism of coseismic surface ruptures by Wenchuan Earthquake. In: Xie F (ed) Rock stress and earthquake. Taylor & Francis Group, London, ISBN 978-0-415-60165-8, pp 761–768

Yue ZQ (2010b) On an unknown mode of earthquake energy propagation and damage. In: Proceedings of abstracts of symposium of earthquake genesis and prediction in continents, Wuhan, China, p 47, Nov 5–6 2010 (In Chinese)

Yue ZQ (2011a) On the common energy and gas source for causing earthquakes and natural gas. Bull Earth Sci Philos No.1 in 2011 and Total No.50:21–64 (in Chinese)

Yue ZQ (2011b) Five experiences from Wenchuan earthquake relevant to seismicity of Hong Kong. South China J Seismol 31(2):14–20 (in Chinese)

Yue ZQ (2011c) On nature of earthquakes with one hypothesis (abstract). In: Proceedings of international symposium on earthquake induced landslides and disaster mitigation at the 3rd anniversary of the Wenchuan earthquake, Chengdu, China, p 20, May 12–15 2011

Yue ZQ (2011d) On an unknown and unused deterministic precursor possibly one to one corresponding to the occurrence of damaging earthquakes (Abstract). In: Proceedings of the second IAA workshop on coordination and cooperation for global environmental impact, Beijing, China, September 2–3 2011, p 39 (in English), 17 (in Chinese)

Yue ZQ (2011e) Investigation and Significance of Natural Hazards in Indonesia. In: Proceedings of papers and/or abstracts of the 2011 annual conference of geological society of China. Beijing, Editor-in-Chief: Meng Xian-lai, November 3–5 2011, pp 573–574 (in Chinese)

Yue ZQ (2011f) The expansion energy of high compressed natural gas causing the Great East Japan Earthquake and Tsunami of March 11, 2011. Newspaper: Metro Daily, April 21, 2011 (in Chinese) http://www.metrohk.com.hk/index.php?cmd=detail&id=159815

Zhang LM, Xu Y, Huang RQ, Chang DS (2011) Particle flow and segregation in a giant landslide event triggered by the 2008 Wenchuan earthquake, Sichuan, China. Nat Hazards Earth Syst Sci 11(4):1153–1162

Three-Dimensional Stability Analysis for Evaluation of Drainage Effect for Earthquake-Triggered Large Landslides

52

Atsushi Nakamura, Masashi Koizumi, Fei Cai and Keizo Ugai

Abstract

The mechanism by which a landslide would occur was investigated by Nakamura et al. (2008). By taking into consideration the geographical features of a large-scale landslide induced by an earthquake. An investigation was performed by paying special attention to the generation of an excess of pore water pressure caused by the earthquake. In this paper, the groundwater level at the time of the earthquake was assumed following the field investigation and the safety factor of the large slope failure was calculated by the limit equilibrium method. The groundwater level was calculated by three-dimensional seepage analysis (finite element method) after the drains were installed and their effect on the stability evaluated by the three-dimensional limit equilibrium method (in case of liquefaction). The drainage effect to groundwater level and the negative effect of excess pore water pressure can be correctly taken into consideration by conducting a slope stability analysis using a three-dimensional limit equilibrium method.

A. Nakamura (✉) · M. Koizumi
Structural Engineering, FORUM8 Co. Ltd, 2-1-1, Nakameguro GT Tower 15F Kamimeguro, Meguro-ku, Tokyo, Japan
e-mail: atsushi@forum8.co.jp

M. Koizumi
e-mail: koizumi@forum8.co.jp

F. Cai · K. Ugai
Department of Structural Engineering, Gunma University, Kiryu, Gunma 376-8515, Japan
e-mail: cai@ce.gunma-u.ac.jp

K. Ugai
e-mail: ugai@ce.gunma-u.ac.jp

1 Introduction

The mechanism by which a landslide would occur was investigated by Nakamura et al. (2008). By taking into consideration the geographical features of a large-scale landslide induced by an earthquake. An investigation was performed by paying special attention to the generation of an excess of pore water pressure caused by the earthquake. The work was carried out by studying the geographical features present before the landslide occurred. The fall of the

groundwater level by installing drainage wells and the rise of the excess pore water pressure due to the earthquake were taken into consideration. Analysis was conducted using the two-dimensional limit equilibrium method. The excess pore water pressure which occurs due to an earthquake is proportional to the effective overburden pressure. Therefore, the drainage effect under an earthquake condition was lowered. However, two-dimensional stability analysis uses the deepest cross section of landslides. Actual landslides are three dimensional. It is thought that two-dimensional stability analysis is not sufficient to accurately estimate the drainage effect.

In this paper, the groundwater level at the time of the earthquake was assumed following the field investigation and the safety factor of the large slope failure was calculated by the limit equilibrium method. The groundwater level was calculated by three-dimensional seepage analysis (finite element method) after the drains were installed and their effect on the stability evaluated by the three-dimensional limit equilibrium method (in case of liquefaction). Regarding the case of liquefaction, inertia was ignored and the ΔU method was used, which considered only the influence of the excess pore water pressure.

2 The Influence of Excess Pore Water Pressure

2.1 Undrained Cycle Triaxial Tests on the Undisturbed Soil Samples

In order to investigate the effect of the strong earthquake motion on the landslide, undrained cyclic triaxial tests were performed on the undisturbed samples. The initial consolidation pressures were 200 and 375 kN/m^2. As a result, excess pore water pressure was suddenly generated and remained high even after unloading. The residual pore water pressure in the sample after the cyclic triaxial tests can be seen in Table 52.1. Regardless of how much greater the effective overburden pressure was it can be found that the

Table 52.1 The residual pore water pressure of the soils after cyclic loading Ugai K et al. (2007)

Initial confined pressure 200 kN/m^2 (A)		Initial confined pressure 375 kN/m^2 (A)	
Principal stress difference	(B)	Principal stress difference	(B)
155	109	299	215
140	155	277	166
127	118	254	241
115	151	231	264
B/A(Av)	0.67	B/A(Av)	0.59

Note (B) Residual excess pore water pressure after the cyclic loading
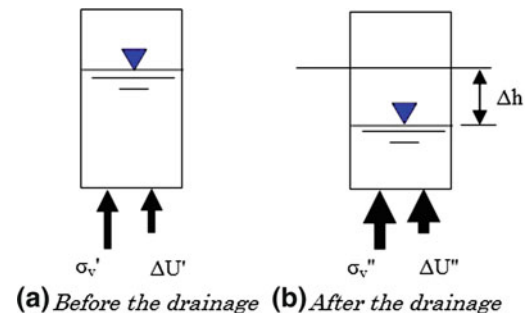
Fig. 52.1 Effective overburden and excess pore water pressure in cross-sectional view

residual excess pore water pressure was about 60 % of the initial confined pressure.

2.2 Drainage Effect and Its Relationship with Excess Pore Water Pressure

It can be understood from the results of the cyclic tri-axial tests that the large excess pore water pressure occurs as a result of the vibrations of the earthquake. Moreover, the shear strength of the soil was lowered. This is the reason that the landslides occurred with a long run out distance.

Therefore, in this report, the influence of excess pore water pressure (ΔU) at the time of the earthquake has been examined by using the ΔU method. The ΔU method is illustrated in the diagram below. Figure 52.1a shows a slice division

piece before the drainage, and Fig. 52.1b shows after the drainage.

(1) Effective overburden pressure before the drainage $\Sigma\sigma_v'$

If the effective overburden pressure is σ_v' and the excess pore water pressure ratio is α, the excess pore water pressure is $\Delta U' = \alpha/\sigma_v'$ at the time of the earthquake before drainage. Therefore, effective overburden pressure $\Sigma\,\sigma_v'$ before the drainage becomes Eq. 52.1

$$\Sigma\sigma_v' = \sigma_v' - \Delta U' = (1-\alpha)\sigma_v' \qquad (52.1)$$

(2) Effective overburden pressure after the drainage $\Sigma\sigma_v''$

Stress increases (Δv) as water level falls (Δh) as shown in Eq. 52.2.

$$\Delta v = \Delta h(\gamma_t - \gamma') = \Delta h\gamma_w \qquad (52.2)$$

The increase in excess pore water pressure as a result of the earthquake can be calculated by Eq. 52.3.

$$\Delta u'' = \alpha\Delta v = \alpha\Delta h\gamma_w \qquad (52.3)$$

Therefore, incremental effective overburden pressure becomes Eq. 52.4.

$$\Delta v - \Delta u'' = \Delta h\gamma_w - \alpha\Delta h\gamma_w = (1-\alpha)\Delta h\gamma_w$$
$$= (1-\alpha)\Delta v$$
$$(52.4)$$

Thus, effective overburden pressure $\Sigma\sigma_v''$ after the drainage can be obtained by Eq. (52.5).

$$\Sigma\sigma_v'' = \Sigma\sigma_v' + (1-\alpha)\Delta v = (1-\alpha)(\sigma_v' + \Delta v) \qquad (52.5)$$

(3) Drainage effect decrease due to the excess pore water pressure

It is found that the substantial effective stress increment at the time of earthquake was equal to $(1-\alpha)\ \Delta v$, in which the excessive pore water pressure was considered. Therefore, it is possible that the maximum effect of drainage decreases by $(1-\alpha)$ times.

Nakamura et al. (2008) reported that the drainage effect in the case of liquefaction was lower than that in the case of normal conditions
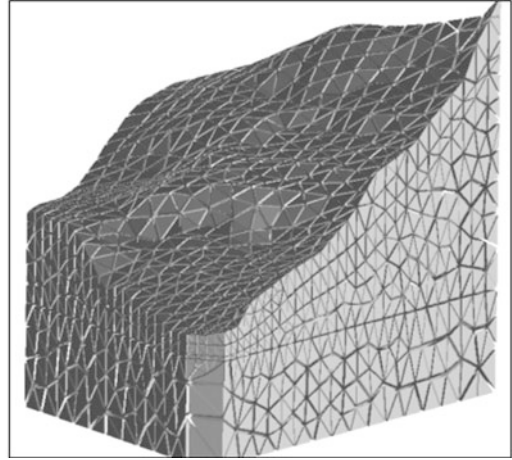
Fig. 52.2   Three-dimensional seepage analysis mesh

when the effect was evaluated using the two-dimensional cross section. However the three-dimensional landslide-prone topography was considered to be a closer representation of the real phenomenon.

3   Stability Analysis

3.1   The Estimate of the Groundwater Level

The groundwater level before and after the drainage was calculated using three-dimensional FEM seepage analysis. Figure 52.2 shows the analysis mesh. Figure 52.3a and b show the results of the analysis before drainage. Figure 52.4a and b show the results after drainage. Section B was taken where it is thought that the landslide was the deepest. As can be seen, water levels fell by around 3.0 m after drainage.

3.2   Slope Stability by Limit Equilibrium Method

(1) Soil properties

In section B, the first layer is a cohesive silt layer of alluvial soil, and the second layer is strongly weathered mudstone. These two layers become moving stratum. The friction angle for the strongly
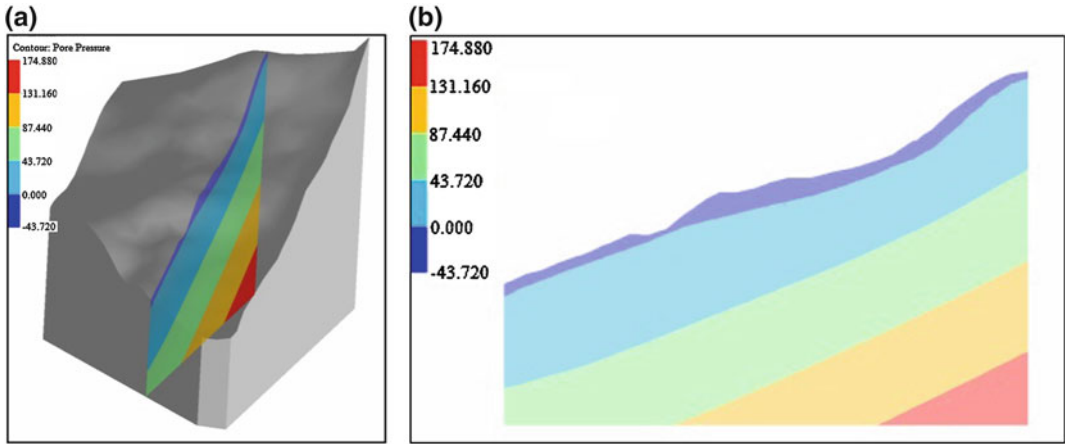
Fig. 52.3 **a** Seepage analysis result before drainage (3D). **b** Seepage analysis result before drainage (Section B)
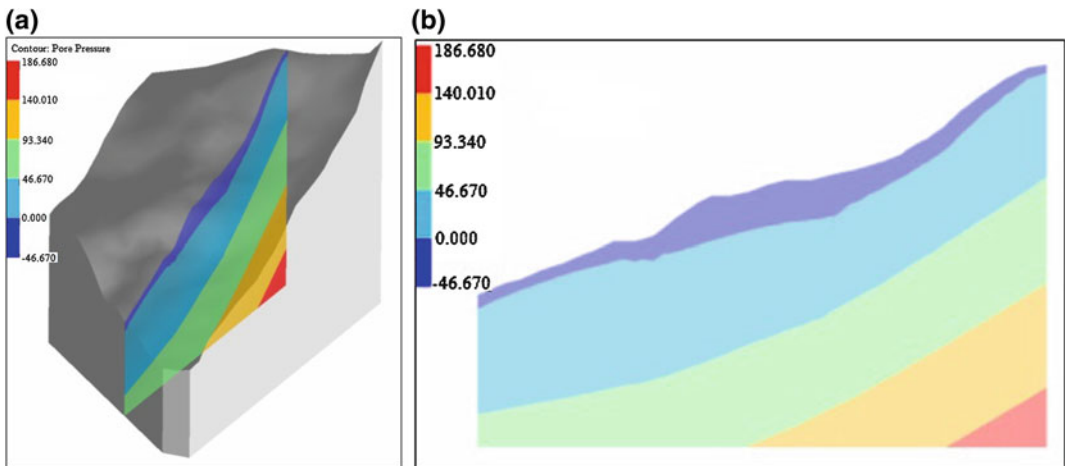
Fig. 52.4 **a** Seepage analysis result after drainage (3D). **b** Seepage analysis result after drainage (Section B)
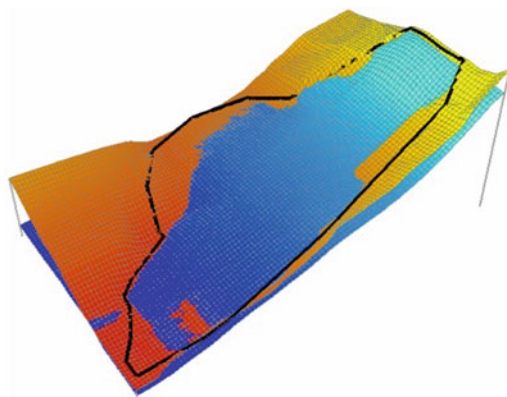
Fig. 52.5 Landslide slope stability analytical model

weathered mudstone is 39°. The maximum depth of the landslide is about 25 m and average depth is thought to be about 20 m. Therefore the adhesive strength of the moving stratum was adjusted to 20 kN/m². The wet unit weight of the soil was assumed to be 18 kN/m³. An analytical model was created by three-dimensional limit equilibrium method and is shown in Fig. 52.5.

(2) 3-D slope stability analysis

A safety factor is calculated by the 3-D simplified Janbu's method (FORUM 8 Co., Ltd. 2005).

Table 52.2 Safety factor before drainage (3D)

Case	$\Sigma\tau$	ΣS	Fs = $\Sigma\tau$/ΣS
Normal	3569405.7	2233106.9	1.598
Liquefaction	1739181.6	2233106.9	0.779

Table 52.3 Safety factor after drainage (3D)

Case	$\Sigma\tau$	ΣS	Fs = $\Sigma\tau$/ΣS
Normal	3956077.8	2185328.5	1.810
Liquefaction	2190474.6	2185328.5	1.002

Table 52.4 The improvement rate of the safety factor (3D)

Case	Before	After	Fs
Normal	1.598	1.810	1.132(0.212)
Liquefaction	0.779	1.002	1.286(0.223)

Table 52.5 The improvement rate of the safety factor (2D)

Case	Before	After	Fs
Normal	1.435	1.656	1.154(0.221)
Liquefaction	0.593	0.680	1.147(0.087)

$$F_s = \frac{\sum\sum \left[\frac{c\Delta A + (\Delta W - u - \Delta u)\tan\phi}{\cos\alpha_{yz}\cdot m_\alpha}\right]}{\sum\sum \Delta W \tan\alpha_{yz}}$$

4   Slope Stability Analysis Result

(1) Before drainage (Table 52.2)
(2) After drainage (Table 52.3)
(3) The improvement rate of the safety factor (3D) (Table 52.4)
(4) The improvement rate of the safety factor (2D)

The improvement rate of the two-dimensional safety ratio in one row (B section) of columns is shown in Table 52.5.
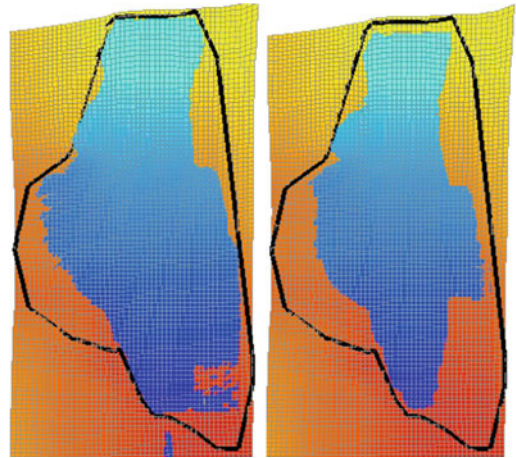
Fig. 52.6 Domain below the groundwater before after

Table 52.6 Columns of which the base was below the groundwater level (WL)

Case	Columns of which the base was below the WL	Total columns	Rate
Before drainage	2415	3076	0.785
After drainage	1907		0.620

5   Conclusions

In a two-dimensional stability analysis of the deepest cross section, the drainage effect on the safety factor in case of liquefaction induced by earthquake is lowered compared with that in case of the normal condition. This means that the influence of excess pore water pressure appears to be significant in a two-dimensional stability analysis.

In this paper, the drainage effect was investigated using the three-dimensional limit equilibrium method. As a result, it turned out that the safety factor in the case of liquefaction was

improved greatly compared with that calculated using two-dimensional stability analysis.

Since the excess pore water pressure was only generated on the columns of which the base was below the groundwater level, the number of columns of which the base was below the groundwater level decreased with the drainage. Therefore, the resistance to sliding increased. If there are many such columns, it can be thought that reduction of the drainage effect by excess pore water pressure became small.

The number of columns of which the base was below the groundwater level is shown in Fig. 52.6 before and after drainage. The rate is shown in Table 52.6. The number of such columns of which the base was below the groundwater level decreased largely in number by 17 % by drainage.

The drainage effect to groundwater level e and the negative effect of excess pore water pressure can be correctly taken into consideration by conducting a slope stability analysis using a three-dimensional limit equilibrium method.

References

Ugai K, Wakai A (2007) Mechanism of a large landslide composed of mudstone debris induced by the 2004 mid Niigata prefecture earthquake. In Proceedings of the 46th annual conference of Japan landslide society, Mie, Japan, pp 87–90

FORUM 8 Co., Ltd (2005) UC-1 3-D Slope stability analysis (LEM3D) (http://www.forum8.co.jp/)

Nakamura A, Cai F (2008). An investigation into the effect of drainage on large slope failure during earthquakes. In Proceedings of the 47th annual conference of Japan landslide society, Kanagawa, Japan, pp 5–8

Centrifuge Model Tests on Seismic Slope Failure

Chiharu Mikuni, Satoshi Tamate, Tomohito Hori
and Naoaki Suemasa

Abstract

In this study, experimental analyses were carried out to investigate characteristics of slope failure by earthquakes and potential risks of secondary failure. A 1/50 scale model slopes were made of Kanto loam to simulate the shallow unsaturated soil in slopes. Seismic acceleration was applied on a shaking table in centrifuge, so that shear strain in the shallow unsaturated soil increased as the number of seismic cycles. It was found that the slopes failed as a result of accumulation of the plastic shear strain. In addition, changes in height and angle of slopes were measured in the upper remaining section after seismic failures. The potential risks of secondary failure (R_v) were analyzed using Taylor's stability chart. It was ensured that the value of R_v on the upper section decreased as the collapsed soil increased.

Keywords

Centrifuge model test · Slope failure · Secondary failure · Earthquakes

1 Introduction

Earthquakes cause a lot of slopes failure, and after recovering operations such as removal of collapsed soil are required to access the roads (Hakuno 1992). However potential risks of secondary failure also exist in the failed slopes because of loosened soil and development of cracks. Accordingly, safety measures must be taken to save workers' lives during the recovering operations.

Several sets of centrifuge model tests were carried out to investigate the risks of secondary failure in damaged slopes by earthquakes. Sinusoidal cycle acceleration was applied in the model slopes to simulate the seismic failure. This paper describes potential risks of secondary failure in damaged slopes through analyses on stability and distribution of shear strength in soil.

C. Mikuni (✉) · N. Suemasa
Tokyo City University, 1-28-1, Tamazutsumi,
Setagaya, Tokyo, Japan
e-mail: g1181714@tcu.ac.jp

S. Tamate · T. Hori
National Institute of Occupational Safety and
Health, 1-4-6, Umezono, Kiyose, Tokyo, Japan
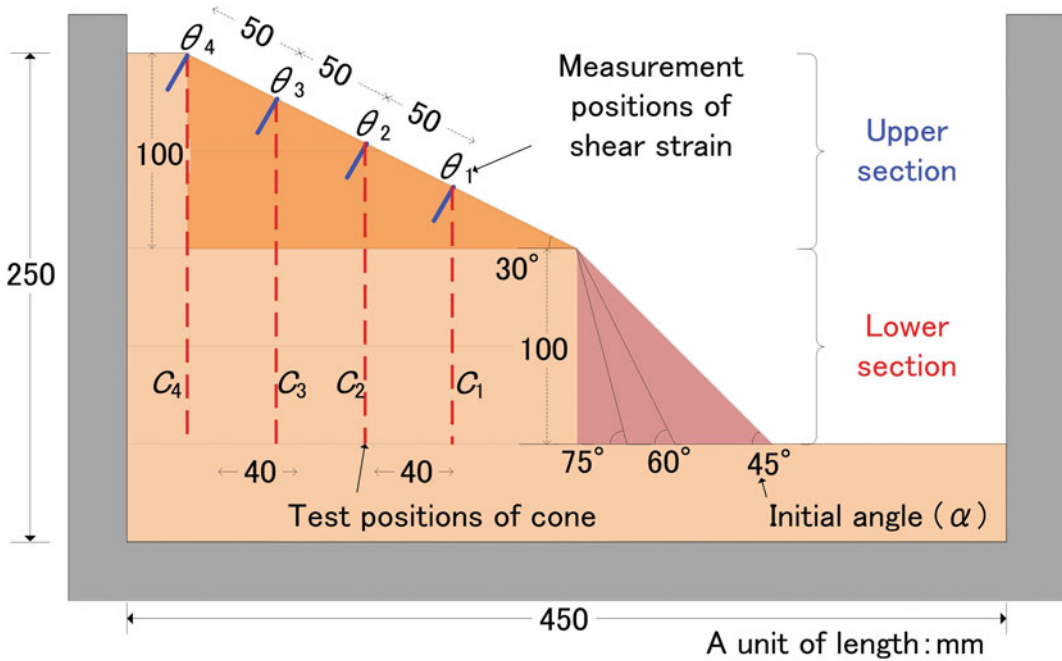
Fig. 53.1 Profile of the model slopes

2 Experimental Outline

2.1 Material and Method

Centrifuge model tests were carried out to simulate slope failure. A 1/50 model slope was composed of Kanto loam with the optimum moisture content. Table 53.1 shows the physical properties of Kanto loam. Kanto loam was uniformly deposited into an experimental container that measures 450 mm in width, 150 mm in length and 250 mm in height. A static compression at 50 kPa was carried out to reproduce the shear strength in the shallow section of the slopes. A uniform pressure was provided on each layer through a loading plate.

A constant value of the pressure was kept for 12 h on each layer. Figure 53.1 shows a profile of the model slopes. Different values of the slope angle were provided in the upper and the lower sections. Values of the initial angle (α) were selected as 45, 60 and 75 degrees for the lower section whereas 30 degree was commonly set for the upper. Plastic transparent films with 10 μm in

Table 53.1 Physical property of Kanto loam

Density of soil particles	2.739
Sand (0.075–2 mm) (%)	6.2
Fine fraction (0.075 mm less than) (%)	93.8
Silt (0.005–0.075 mm) (%)	45.3
Clay (0.005 mm less than) (%)	48.5
Maximum grain diameter (mm)	2
Liquid limit (%)	158.3
Plastic limit (%)	97.7
Plasticity index	60.6
Optimum moisture content (%)	102

thickness were placed on walls of the container lubricated by soft silicon grease to reduce the friction between the walls and the soil. In addition, the films were separated vertically with stripe shapes to move the soil without any constraints.

2.2 Shaking Condition

A geotechnical centrifuge, which was composed of 2.5 m of effective radius, was used for the model

(a) α=45 degree, A_i=300 gal   (b) α=60 degree, A_i=300 gal
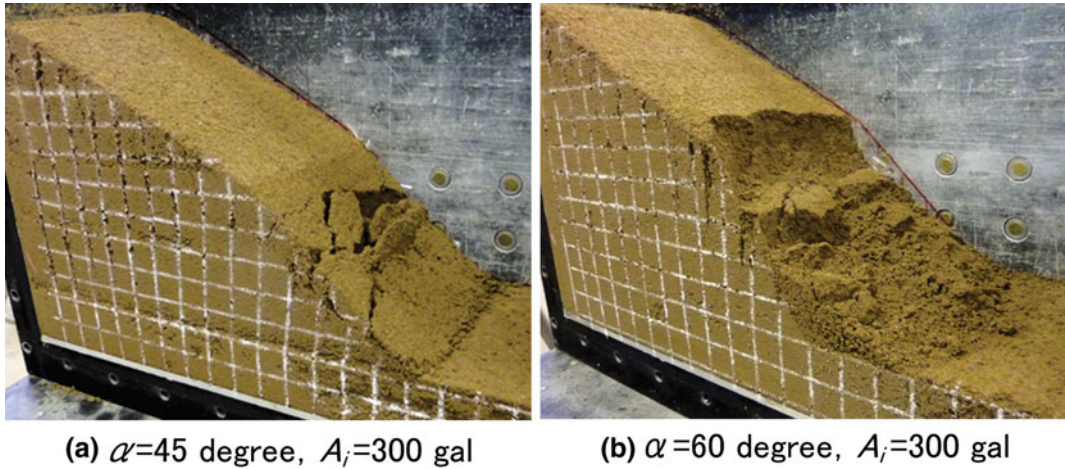
Fig. 53.2 Comparison failure type of slope composing same angle of 45 degree

tests. Horizontal shaking acceleration was applied to simulate seismic failure in the model slopes at 50 g of enhanced gravity. Applied sinusoidal waves were composed of 20 cycles including both six cycles of gradual increase at the beginning and six cycles of gradual decrease at the end. Standard conditions of the horizontal shaking acceleration in the model wave were 15 g and 50 Hz corresponding to 300 gal and 1 Hz in prototype, respectively. Configurations of model slopes were measured before and after the shaking tests.

3 Stability in the Lower Section of Slopes

3.1 Shapes of Slopes After Seismic Failure

Table 53.2 shows conditions of the tests. Figure 53.2 shows comparison of the types of slope failure that was simulated in three sets of the shaking model tests. 300 gal in amplitude and 50 Hz in frequency of the cycle acceleration were commonly applied to the models which were composed of angles of 45 and 60 degrees in the lower section (α).

A model slope in Cs1 had 45 degree in α. Although the shallow section of the lower slope collapsed, separated soil blocks remained in the slope. Grid lines in the section profile showed

Table 53.2 Conditions of the tests

Codes	Initial angle (α)	Input acceleration (A_i)
Cs1	45	300 gal
Cs2	60	
Cs3	75	
Cs4		400 gal
Cs5		200 gal

soil blocks to tilt by lateral movements. The lower section of the slope failed entirely from the upper in Cs2. Collapsed soil slid down and deposited in front of the slope. Another steep slope appeared in the upper after the prior failure.

Different levels of shaking acceleration (A_i) were exerted on three models in the same condition to compare the damage of failure as shown in Fig. 53.3. Soil block slid down from the upper by application of 200 gal in A_i, and a part of the slope in Cs5 became steeper by the slope failure as well as Cs2. Catastrophic failure occurred in both the lower and the upper sections. Collapsed soil overlaid in the lower of the slope.

3.2 Experimental Analyses of Stability of Failed Slopes

Experimental analyses were carried out to evaluate instability of slopes after seismic

(a) Prior to failure (b) α=75 degree, A_i=200 gal (c) α=75 degree, A_i=300 gal
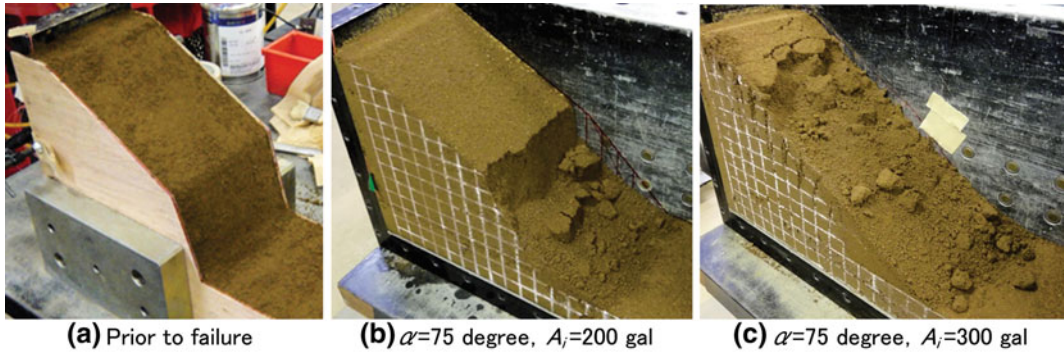
Fig. 53.3 Comparison failure type of slope applied different acceleration

$$V_f = (V_1 + V_2)/2$$
$$V_R = V_f / V_0$$

V_1

Collapsed soil (V_2)

Amount volume of slope (V_0)
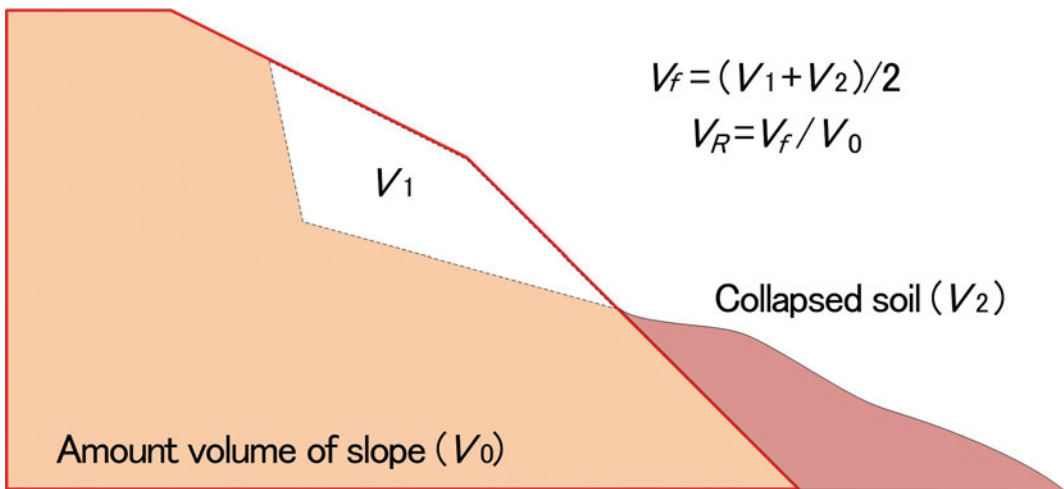
Fig. 53.4 Concept of failure magnitude (R_v)

failure. The ratio of failure magnitude (R_v) was defined as the ratio of V_0 to V_f as shown in Eq. (53.1).

$$R_v = V_f / V_0 \qquad (53.1)$$

where V_0 is the initial volume of soil in slopes and V_f is the volume of failed soil. Figure 53.4 shows an outline of R_v. V_f is calculated using Eq. (53.2).

$$V_f = (V_1 + V_2)/2 \qquad (53.2)$$

where V_1 is the volume of the upper failed slope and V_2 is the volume of the lower deposit soil. Accordingly, V_f is a mean value of V_1 and V_2.

This study discusses instability on two sections in the slopes after seismic failure. As shown in Fig. 53.5, H_1 in a height of the cut that appeared in the upper slope after the failure and the danger ratio of the upper slope (D_1) is defined by Eq. (53.3) (Mikuni et al. 2011).

$$D_1 = H_1 / H_{c1} \qquad (53.3)$$

H_2 is a height of lower slope made of soil deposit and the danger ratio of the lower slope (D_2) is defined by Eq. (53.4).

$$D_2 = H_2 / H_{c2} \qquad (53.4)$$
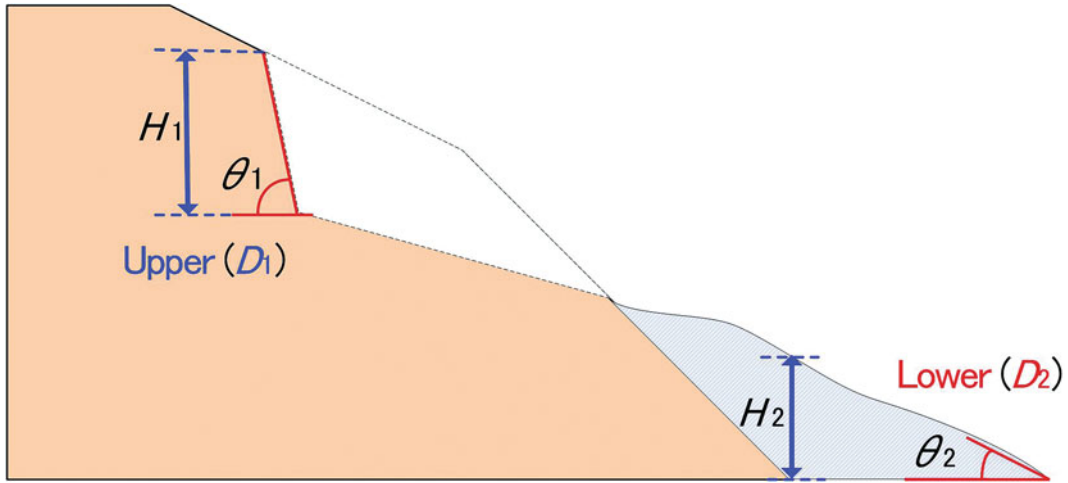
Fig. 53.5 Concept of potential risk of secondary failure

Fig. 53.6 Relationship between D_1 and A_i, α

(a) D_1 and A_i

(b) D_1 and α
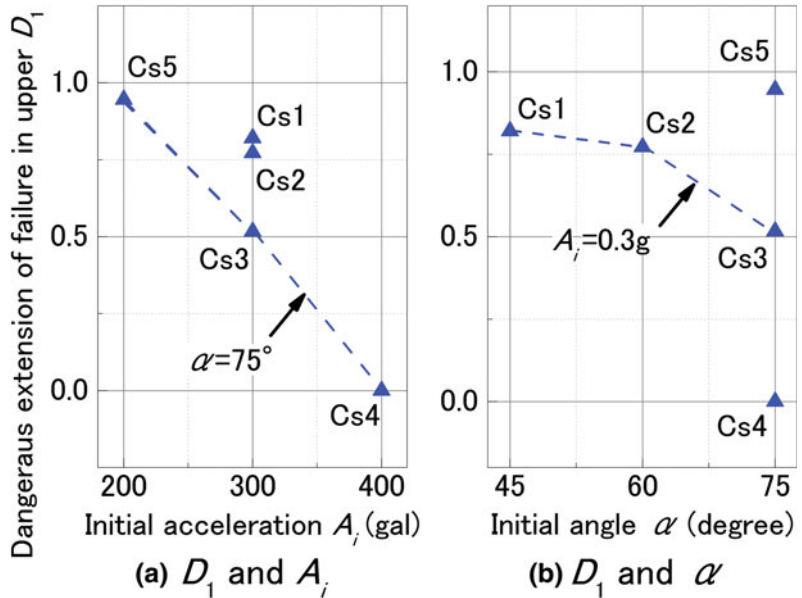
where H_1 and H_2 are measured values from the shaking model test, H_{c1} and H_{c2} are obtained from Taylor's stability chart (Taylor 1948) for simplicity.

Figure 53.6a shows relationship between D_1 and input acceleration (A_i). Values of D_1 tend to decrease where angle of slope is 75 degrees. Figure 53.6b shows that D_1 decreases with an increase of the angle of slope where A_i is kept at a constant value of 300 gal. Figure 53.7 shows relationship between D_2 and A_i. The value of D_2 shows an increase to A_i.

Figure 53.8 shows relationship between R_v and D_n. A significant decrease in D_1 with R_v can be observed whereas D_2 is scattered.

Fig. 53.7 Relationship between D_2 and A_i, α
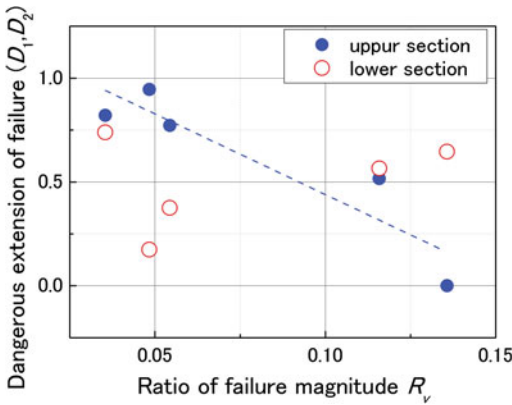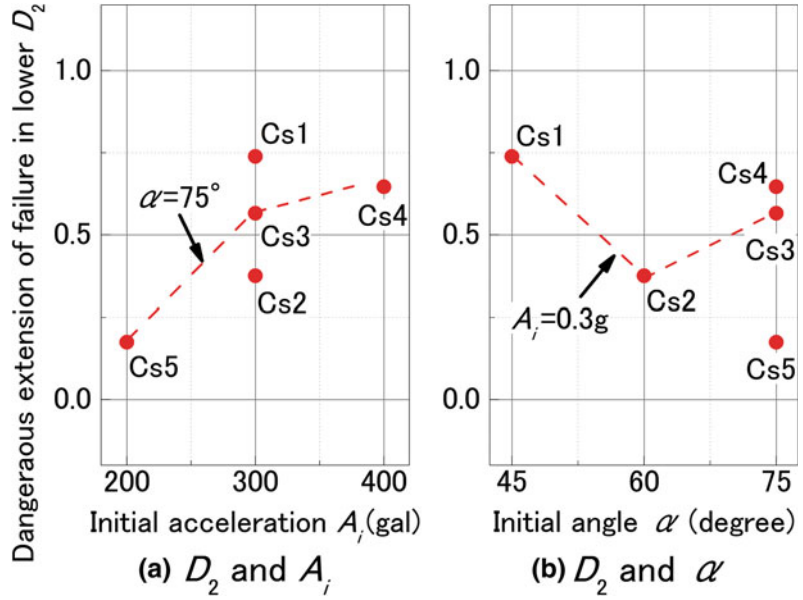
Fig. 53.8 Relationship between D_1 and R_v, D_2 and R_v

4 Damages in the Upper Section of Slopes

4.1 Observations of Damages

Table 53.3 summarizes condition of the tests and the results. Figure 53.9 shows comparison of the types of slope failure that simulated in the same models with angle of 45 degrees.

In Cs6, a failure with cracks on surface can be seen. However, collapsed soil remained on the slope. Damage in the Cs6 seems to be small. In Cs7, failure occurred in the mid height of the lower section of the slope. Collapsed soil slid down. Therefore, obvious damage appeared in Cs7. In Cs8, catastrophic failure occurred, and a large amount of soil was deposited in the lower section of the slope. Accordingly serious damage was caused in Cs8.

4.2 Increment of Shear Strain in Shallow Section of Slopes

Figure 53.10 shows Short Pipe Strain transducer (SPS) Tamate and Endo 2007) that is consisted of thin steel plate and two strain gages. The size is 15 mm in length, 5 mm in width and 0.1 mm in thickness. The SPSs were penetrated in the normal direction on the surface in the upper section

(a) Cs6, small failure **(b)** Cs7, middle failure **(c)** Cs8, large failure
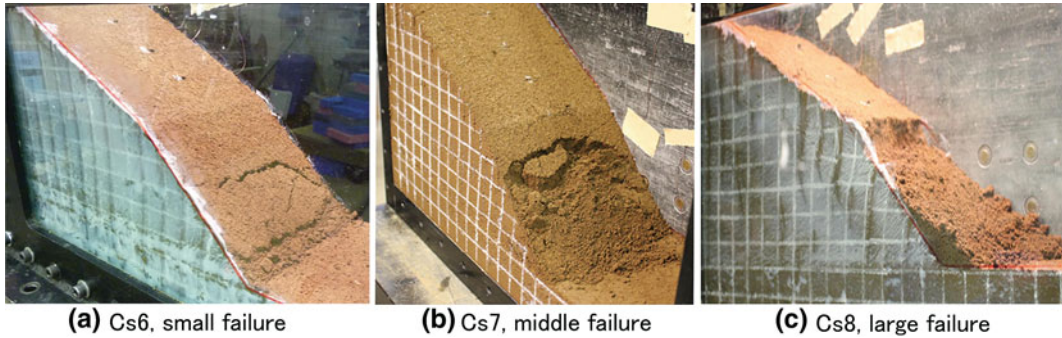
Fig. 53.9 Simulations of different shape of failure

Fig. 53.10 Short pipe strain transducer (SPS)
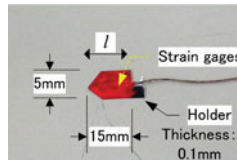
Table 53.3 Experimental case

Codes	Magnitude of failure
Cs6	Small
Cs7	Middle
Cs8	Large

of slopes. The SPSs might be bended in reaction to the shear deformation that occurred in the upper shallow section induced by seismic failure in the lower slope (Tamate and Itoh 2009).

Interpreted shear strain (θ_i) is defined as the ratio of a deflection (s) to an effective length (L) as shown in Eq. (53.5).

$$\theta_i = s/L \times 100 \qquad (53.5)$$

Relationship between electronic output of strain gages (r_s) and θ_i was obtained as shown in Eq. (53.6).

$$\theta_i = 0.002 r_s \qquad (53.6)$$

Figure 53.11 shows three sets of time histories on both input shaking acceleration (A_H) and the reactions of shear strain in θ_1 and θ_3. A_H gradually

increases at the beginning of shaking and decreases at the end. θ_1 and θ_3 commonly increase as a result of the shaking, and then the amplitudes show the maximum at 25 (sec) in θ_1 whereas 29 (sec) in θ_3. Required time to reach the maximum in θ_1 is faster than that in θ_3 while a value of the amplitude in θ_3 is longer than that in θ_1.

4.3 Cone Penetration Tests

Cone penetration test was carried out to investigate the damage in upper section of slopes after seismic failure as shown in Fig. 53.12. q_{u1} indicates the cone penetration resistance that was measured at the positions from C1 to C4 prior to the shaking table tests. q_{u2} also expresses the measured values at the same positions after the test.

Figure 53.12 shows comparison of distributions of q_{u1} and q_{u2} at C3 in three sets of the tests Cs6, Cs7 and Cs8. q_{u1} increased gradually to the depth followed by the rapid increase in the shallow section. Thus, almost uniform strength was reproduced in the slopes prior to the shakes. Values of q_{u2} normally become smaller than those of q_{u1}. Accordingly, it was observed that damage increased by shakes as the values decrease.

Different values of decrease from q_{u1} to q_{u2} can be seen in the tests. The most decreased value was measured in Cs8 that failed largely in

Fig. 53.11 Relationship between A_i and T, θ_i and T
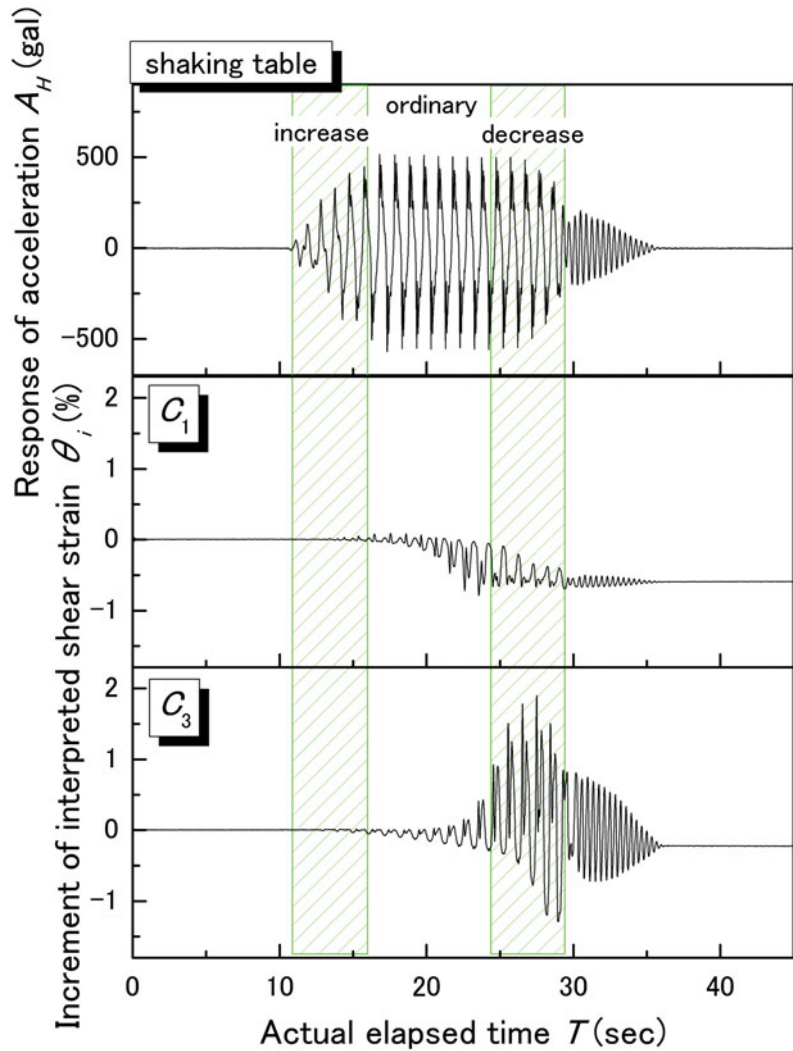
the lower slope. By contrast, small decrease appeared in Cs6 with smaller failure. Accordingly, it is ensured that the upper damage depends on the magnitude of failure in the lower slopes.

Ratio of slope strength (S) was defined from the relationship between q_{u1} and q_{u2} as shown in Eq. (53.7).

$$S = q_{u1}/q_{u2} \qquad (53.7)$$

Fig. 53.12 Distribution of q_u
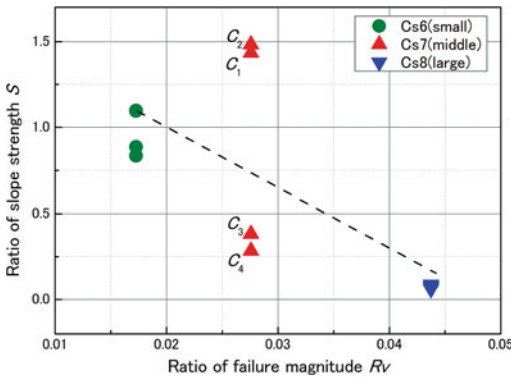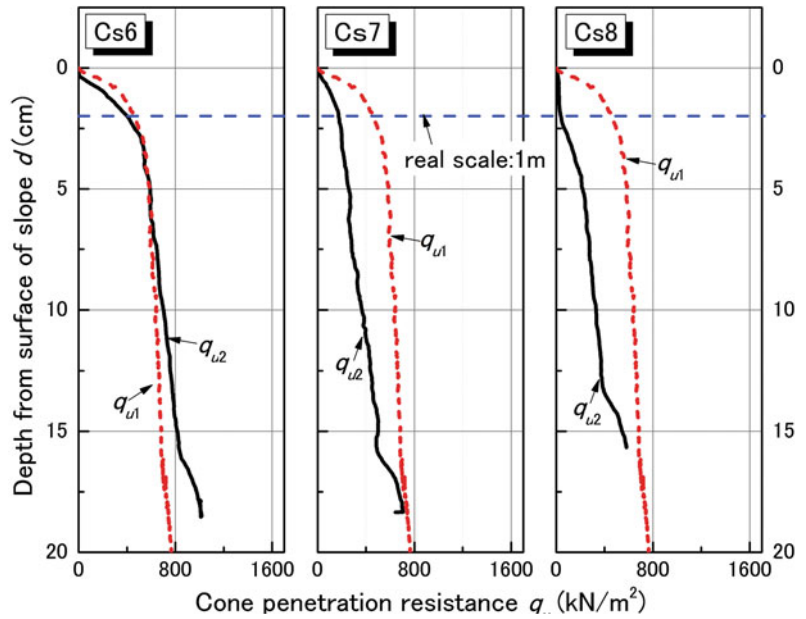
Fig. 53.13 Relationship between S and R_v

where, $S \geqq 1.0$ means the slope is healthy and $S < 1.0$ means slopes have damages. In this analysis, the measured results use $d = 2.0$.

Figure 53.13 shows the relationship between S and R_v. Values of S ranged around 0.9 and value of R_v was 0.017 in Cs6. Whereas value of S was around 0.1 and R_v was 0.044 in Cs8. Therefore, value of S tends to decrease to R_v.

5   Conclusions

Several sets of shaking table tests in centrifuge were carried out to investigate the damage in slope after earthquakes. Shear deformation was measured in the shallow section in the model slopes during the test and cone penetration tests were performed to compare the values of resistance before and after the shakes. This paper concludes the potential risks of

secondary failure in slopes after earthquakes as follows.

The angle of slope decreased in catastrophic failure, so that soil deposit became stable. In the upper section of the slope, however, shear strength of soil was also reduced by the failure. Therefore, potential risks in the upper section increased where the lower soil deposit was removed with the recovering operations.

When small failure occurred, the angle of the slope was kept steep and the soil became softer due to seismic disturbance. Then, potential risks of secondary failure increase in the lower during the removal operations.

As a result, safety countermeasures are required for the recovering operations against potential risks of secondary failure caused by following earthquakes. Further studies are also needed to clarify the potential risks caused by the layer condition in slopes and the seismic condition on duration time and amplitude.

References

Hakuno M (1992) Earthquake damage: the mother of earthquake engineering learning from the observation of earthquake damage. Kajima Institute Publishing, Tokyo, pp 42–71

Mikuni C, Suemasa N, Katada T, Tamate S, Hori T, Itoh K, Kikkawa N (2011) Experimental analyses on instability of slope after failure. In: 46th Japan national conference on geotechnical engineering, pp 1613–1614 (in Japanese)

Taylor DW (1948) Fundamentals of soil mechanics. Wiley, New York

TamateS, Endo A (2007) Development of the short pipe strain transducer (SPS) comprising a screw end and experimental analysis on it's applicability for safety monitoring in slope works. Specific Research Report of the National Institute of Occupational Safety and Health, JONOSH-SRR-NO.35, pp 107–128 (in Japanese)

Tamate S, Itoh K (2009) Monitoring of shear strain in shallow section of slopes to detect increased risk of slope failure. In: Proceeding of the 17th international conference on soil mechanics and geotechnical engineering, pp 2143–2146

Genetic Types of Large-Scale Landslides Induced by the Wenchuan Earthquake

54

Q. Xu, S. Zhang and X. J. Dong

Abstract

The 5.12 Wenchuan earthquake had induced thousands of large-scale landslides. Through the field investigations and surveys on deformation and destroy characteristics of 20 landslides induced by the Wenchuan earthquake, and combined with the shaking table test and numerical simulation, we found that the deformation and mechanical mechanism of these large-scale landslides are different from those landsides induced by routine gravity. On the condition of strong shock, the most essential deformation and destroy element of the slope rock mass are tension-cracks and shearing slide, and mainly based on tension-cracks. According to the geological and topographical change, the large-scale landslides induced by the Wenchuan earthquake can be classified into five genetic types, i.e. tension-strike slip, crack-bedding slip, tension-horizontal slip, tension-scattering slip, and tension-shearing slip.

1 Introduction

For the type and genetic model of geological disasters induced by earthquake, a number of relevant researches have been conducted. In which, the representative is the Seismic Landslide Classification System established by Keefer (1984). Taking into account of the material composition, the motion characteristics, the internal damage and the ground water content, the earthquake-induced rock landslides are classified into the five categories (Keefer (1984)) rock falls, rock slides, rock avalanches, rock slumps and the

Q. Xu (✉) · X. J. Dong
State Key Laboratory of Geohazard Prevention and Geoenvironment Protection, Chengdu University of Technology, Chengdu 610059, China
e-mail: xuqiang_68@126.com

S. Zhang
Department of Civil and Environment Engineering, The Hong Kong University of Science and Technology, Hong Kong, China
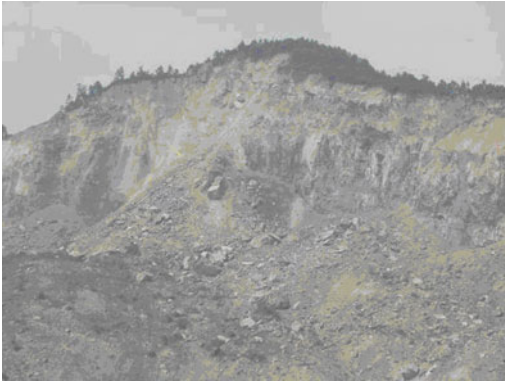
Fig. 54.1 Steep scarp with coarse cracks from Donghekou landslide, Qingchuan

rock block slides. The earthquake-induced soil landslides are classified as soil falls, disrupted soil slides, soil avalanches, soil slumps, soil block slides, slow earth flows, soil lateral spreads, rapid soil flows and subaqueous landslides. Huang (2009) classified the Wenchuan earthquake-induced geological disasters as five major categories and 14 subclasses according to the slope instability process and slope geological structure, respectively. The five major types are sliding, falling, projecting, stripping, and shattering.

After Wenchuan earthquake, by investigating more than 20 earthquake-induced large-scale landslides, Xu et al. (2009a, b) found that there have significant differences between the earthquake-induced landslides and the regular landslides, mainly reflect the differences of deformation failure mode and sliding mechanisms. The earthquake-induced landslides have steep scarp with tension coarse cracks at the trailing edge (Fig. 54.1). In order to identify the slope instability mechanisms, shaking table test was conducted for simulating earthquake-induced landslides under varieties of working conditions (Xu et al. 2009a, b), which revealed the typical deformation and failure mode of the slope rock mass under strong shock are mainly of the tensile failure. Five genetic models of earthquake-induced landslides were established after investigating the deformation characteristics of more than 20 large-scale landslides in Wenchuan earthquake zone.

2 Dynamic Instability Mechanism of Earthquake Induced Landslide

Zheng et al. (2009) adopted the numerical simulation to explore the failure mechanism of seismic slopes and the mechanical properties of failure surface. The results show that the slope failure can be contributed to the tensile failure in the upper part combined with the shear failure in the lower part of slope. Both the tensile cracking surface and shear sliding surface composed of the landslide failure surface.

Under normal gravity conditions, the stress state in the superficial part can be described as followed: the maximum principal stress is parallel to the slope surface; the minimum principal stress is vertical to the slope surface; the intermediate principal stress is parallel to the strike direction of slope. Therefore, the shear stress concentration occurred at weak surface and slope toe part, which resulted in shear deformation and failure following Morh-Coulomb criterion along the weak plane, i.e. weak structural plane or the ancient sliding surface. With shear deformation developed, an apparent tensile stress concentrated at the trailing edge of the slope, and resulted in many tensile cracks (Fig. 54.2). During the earthquake, the minimum principal stress of the slopes is performed as a repeated pull-compressive stress state on the influence of seismic waves. Due to the elevation amplification effect, the horizontal acceleration in the upper part of the slopes is always larger than 1 g. Thus, the seismic horizontal inertia force is far more than the tensile strength of rock mass itself. Griffith proposed a criterion of crack propagation, i.e. $\sigma_3 > \sigma_\tau$, which illustrated that the rock mass of slope are prone to generate the crack surface parallel to the free surface under seismic conditions. Sustained shaking will contribute to widen and deepen the crack surface during the earthquake, then a deep tension crack parallel to the strike direction formed at the top of the slope. Subsequently, crack-shear slip surface will develop at the bottom of the slope and landslide happened eventually (Fig. 54.3).
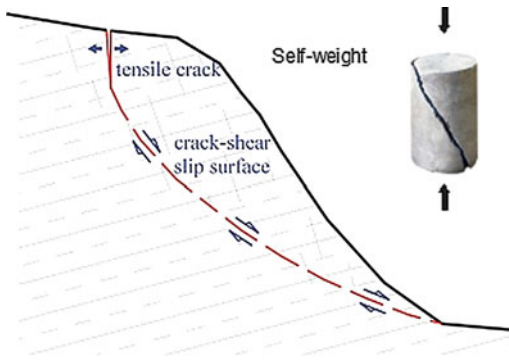
Fig. 54.2 Typical deformation and failure mode of the slope rock under self-weight operative force
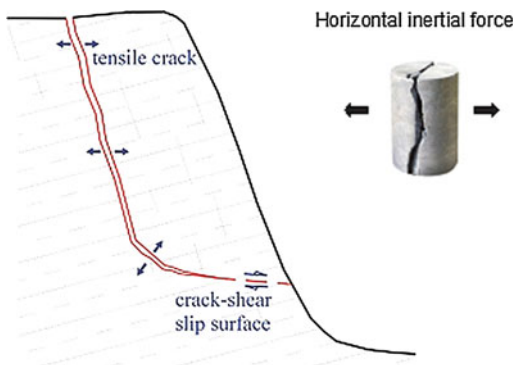
Fig. 54.3 Typical deformation and failure mode of the slope rock mass under strong shock

The above results of shaking table test are consistent with the results of numerical simulation conducted by Zheng (2009). By making a comparison between Figs. 54.2 and 54.3, a large difference either exists in the slopes as described above, or has a significant difference in other ways. For example, under normal gravity, a typical sliding is always occurred along the weak plane followed by tensile cracks in the trailing edge, while under earthquake conditions, a deep tension crack is developed in the trailing edge firstly, and then shear slip appeared along the bottom of the slope. Regarding to the landslides during the earthquake, the tension crack is deep, steep, roughly in the part of trailing edge. The shear slip surface at the bottom surface is relatively short, which is dominant by cracking in trailing edge. However, the sliding surface of landslide happened under normal conditions is

longer with shear characteristics. The cracking surface is generally shallow and small, which is dominant by shear sliding at the bottom of slope.

3   Failure Modes of the Earthquake-Induced Landslides

By the knowable, tension and shearing slip are the basic failure mode of earthquake-induced landslide. The bottom shearing slip would occur along the different structure surface which is decided by the rock structure.

3.1   Tension-Strike Slip

Three conditions can contribute to the tension-strike slip. (1) The slope is mainly composed of gently, dipping (range from 20° to 40°) and stratified rock, such as limestone; (2) the structural surface is normally parallel to the bedding plate, meanwhile, in addition to the frontal surface, a free face should exist on one side of the slope; (3) On the influence of dynamic loading caused by earthquake, a cracking surface will be developed by tracking the structural surface along the dip direction, a tension-strike landslide will occur along the weak surface.

In the Wenchuan earthquake zone, Daguang-bao landslide is a typical tension-strike slip. As long as the topography and slope structure are eligible, the tension-strike landslide can also occur under normal gravity condition. The Daguangbao landslide is the largest one happened during the Wenchuan earthquake, which is located in Ga-ochuan, with a volume of approximately 750 million m^3 (Huang et al. 2008, 2009). The source area is mainly composed of a higher weathering argillaceous limestone in Sinian (Z_d), with partially phosphate and its associated minerals formed in Devonian (D_s). The SE side of landslide is steep which caused by the cutting of Menkanshi Gulley (Fig. 54.4). Two groups of large structure surfaces which parallel to the strike and dip direction are developed in the slope, with the attitude of N40° W/NE ∠80–85° and N 55–60° E/SE ∠ 60°.
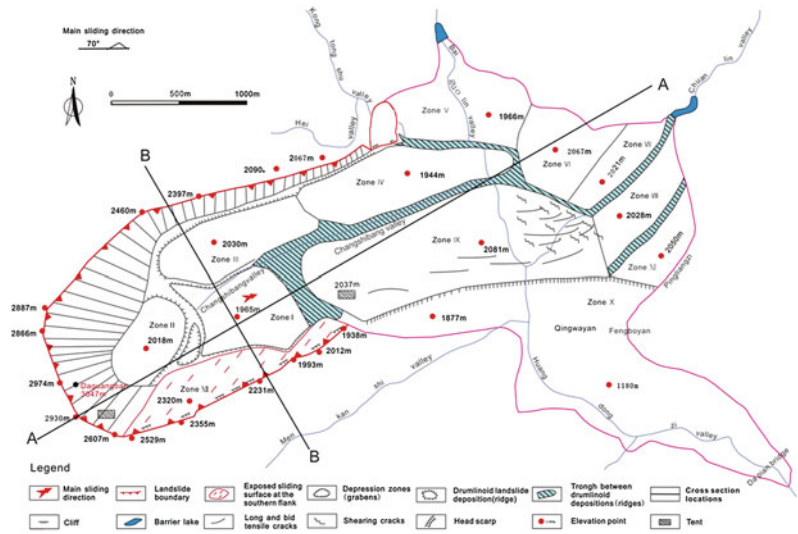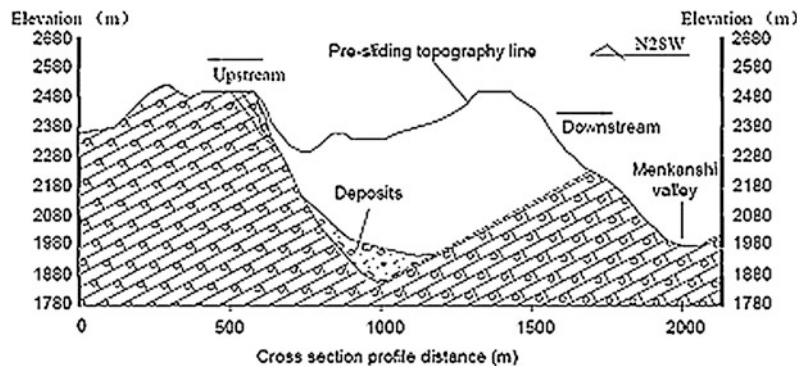
The two structural surfaces combined with the free surface at E and S side can cut the rock mass into blocks (Huang et al. 2009). Under the dynamic role of the earthquake, the sliding mass is firstly depart from structure surface in the trailing edge of landslide in NW direction, then the landslide happened by taking the NE steep dip structure as the lateral crack surface and the sand soft layers as the slip surface (Figs. 54.5 and 54.6).

Based on the slickenside in bottom slip surface, it can be speculated that the slip mass cannot completely slide along the strike direction. As shown in the Fig. 54.4, a cross angle can be observed between the sliding and strike direction in the initial stage of the slope sliding. However, the sliding deformation along this direction can be blocked by the mountain nearby, the slip mass had to gradually shift to the other direction in order to slide out smoothly (Fig. 54.4).

Fig. 54.6 Aerial view of Daguangbao landslide with main sliding direction of NE

3.2 Crack-Bedding Slip

In the bedrock area with steep dip angle, the slope failure will occur along the bedding weak plane, i.e.

Fig. 54.7 Overview of the Tangjiashan landslide, Beichuan

the interface between soft and hard rock, intra-formational weak plane. Such tension failure accompanied by loss of cohesion is caused by the dynamic loading during earthquake. Subsequently, a high-speed sliding happened along the failure surface under the constant dynamics role of earthquake, which named as crack-bedding slip. The Tangjiashan landslide in Beichuan County is a crack-bedding and high speed slip triggered by Wenchuan earthquake. The run-out distance of the landslide is approximately 0.9 km with a velocity of 30 m/s. A 20 million m^3 landslide dam formed in the Jian River with length of 803.4 m, width of 611.8 m, thickness of 124 m. As shown in Fig. 54.7, the capacity of the barrier lake is 300 million m^3 (Hu et al. 2009a, b). About 100 people were killed during this disaster. Immediately sluice dug in the landslide dam make the flood discharged and the potential danger relief timely.

Before the Wenchuan earthquake, the average slope gradient of Tangjiashan landslide is 40°, the elevation of Tangjiashan catchment is ranged from 665 to 1500 m, with a relative relief of 835 m. The landslide area is mainly underlain by mudstones and siliceous consisting the Qingping group, Cambrian. The outward bedding rock layer has the dip angle range from 50° to 85°. Weak layers of mudstone exist in the slope consist of the potential sliding surface. If the potential sliding surface was invisible, a cutting-bed surface will appear under the dynamic role of earthquake. Such phenomenon is more prone to happen in the soft rock slopes

(Fig. 54.8), like Tangjiashan landslide and Zhengjiashan landslide in Pingwu County. If the potential sliding surface is visible at the front of the slope, landslide will happen along the direct linear sliding surface. Such phenomenon is prone to happen in hard rock slope. The occurrence of bedding slip is very common in the earthquake zone.

3.3   Tension-Horizontal Slip

When the outward rock slope stratum is nearly horizontal, with influence of strong horizontal seismic inertia force, there will appear steep pull-apart plane at the trailing edge. Affected by seismic force continuously, the rock mass outside the pull-apart plane will slide along stratum and form a tension-horizontal sliding landslide. With the elevation amplification effect of seismic wave and the terrain amplification effect of cuesta, tension-horizontal sliding landslide is concentrated in some special terrain, such as long ridge and mountain projection. Steep scarp is always locating at the downstream of slippery source area, so that the slip mass could fly over the scarp with a larger initial velocity than normal landslide, which also lead to the slip mass throw out from mountain and move longer distance. A typical representative of tension-horizontal sliding landslide is Donghekou landslide, which locates in the Donghekou Village, Hongguang County, Qingchuan. The landslide stratum consists of Upper Sinian Yuanji Group (Z$_y$), Lower Cambrian Qiujiahe Group ($\in_q$,) and Youfang Group ($\in_y$), which is nearly horizontal with dip angle of 12°. The slope has a sandwich (i.e. hard-soft-hard) structure (see Fig. 54.9). Controlled by a fault at right boundary and a fracture zone at left boundary, a steep pull-apart plane appeared at the trailing edge of slope under strong horizontal seismic load. Afterwards, the rock mass outside the pull-apart plane slide along soft stratum and left a large groove in the source area (Fig. 54.10). After being thrown out, the rock mass flied over a steep scarp with high speed and then crashed to the ground. The rock mass fragment moved forward about
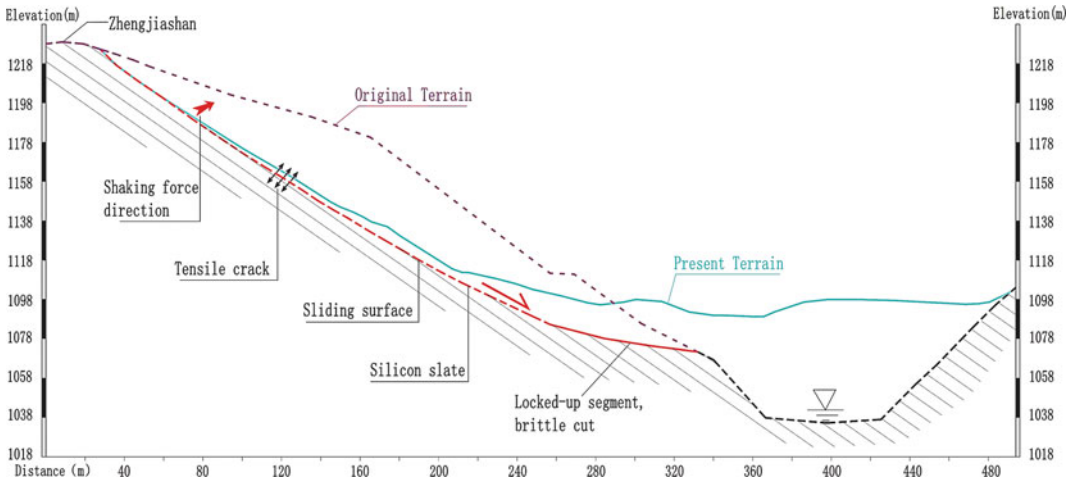
Fig. 54.8 Typical longitudinal section and genetic mode of No.1 landslide, Zhengjiashan
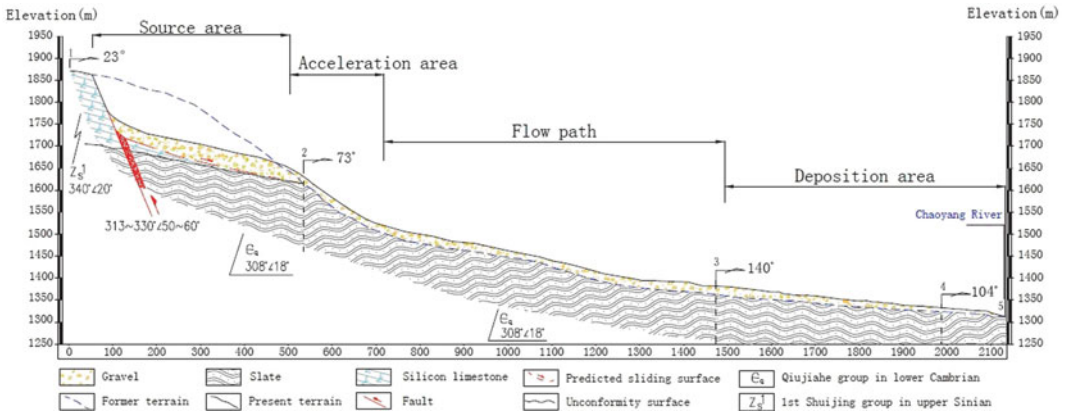
Fig. 54.9 Geological section of Donghekou landslide, Qingchuan
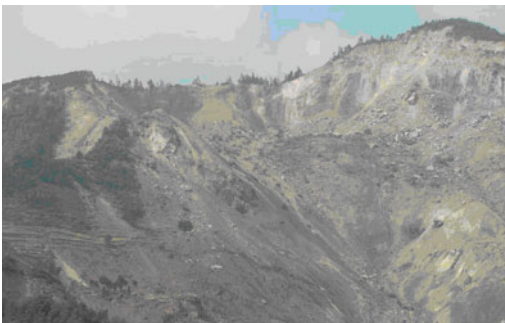
Fig. 54.10 Large scar left in the source area after Donghekou landslide

2 km along the valley as a debris flow (Sun et al. 2009).

3.4 Tension-Scattering Slip

The slope rock mass composed of limestone, dolomite, granite and other hard rock will develop a multi-group structural plane under geological structure force, which is always tension due to weathering and unloading (especially the steep vertical structure plane). Strong

Fig. 54.12 Shattering-cracking

Fig. 54.11 Large blocks in the deposition zone of Beichuan new middle school landslide

Fig. 54.13 Scattering-sliding

earthquake force loosen the superficial rock mass and then a number of vertical tension crack was formed. Afterwards, the loose rock mass disintegrated and formatted so called tension-scattering sliding with the help of reciprocate earthquake load.

A typical representative of tension-scattering sliding is Beichuan new middle school landslide (Fig. 54.11). This landslide located in the back of mountain of new district, Beichuan. Limestone of Carboniferous Yanguan group (C_{1y}) consists of the slope rock mass in the source area. Multi-group structural plane cut the slope rock into

blocks. Therefore, numerous landslides or rock falls occurred in this area before. During the Wenchuan earthquake, the superficial rock mass of slope disintegrated and slip along one group of structural plane finally (Fig. 54.12). The accumulation zone of this type of landslide is mainly composed of granular boulder (Fig. 54.13).

3.5 Tension-Shearing Slip

In the counter-inclined bedding slopes, a deep crack surface developed outward formed at the

posterior edge on the influence of the horizontal inertial force caused by earthquake. Subsequently, the separated slope slide along the bottom of the deep crack surface with the sustained earthquake dynamics forces. Ultimately a tension-shearing slip is developed. The failure process can be summarized into four stages as shown in Fig. 54.14.

In the earthquake area, the counter-inclined bedding slopes as well as the massive rock slope are widely distributed, especially concentrated along the hanging wall of Yingxiu-Beichuan fault. Therefore, the tension-shearing slip is very common, e.g. Wangjiayan landslide in Beichuan Town, Guershan landslide in Beichuan Town, Zhengjiashan landslide in Pingwu County, Guantan landslide in Anxian County, Dongjia landslide in Qingchuan County. From the longitudinal section and deformation and failure mode of Zhengjiashan landslide (see Fig. 54.15), the large-scale landslides have the failure conditions of tension-shear slip. Most importantly, the bottom slip surface of tension-
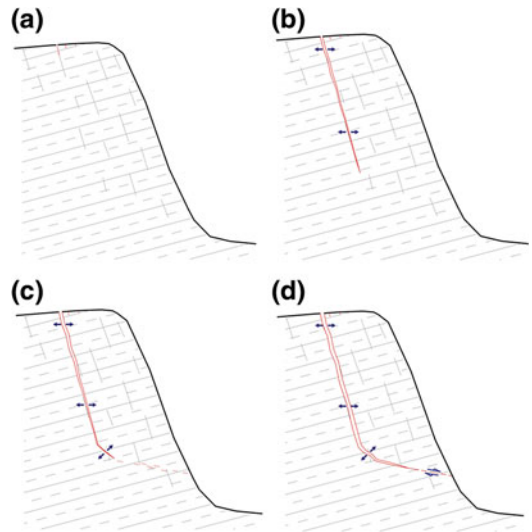
Fig. 54.14 Failure process of typical landslide with tension-cracking and shearing. **a** The shallow of the top of the slope was shattered and cracked in a large scale; **b** a deep and large pull-apart plane, along the sub-vertical discontinuities, was induced from the top; **c** tension-shearing and shear failure was appeared on the pull-apart plane; **d** in sequent sliding plane was formed on the bottom and the whole slope commerce to slide
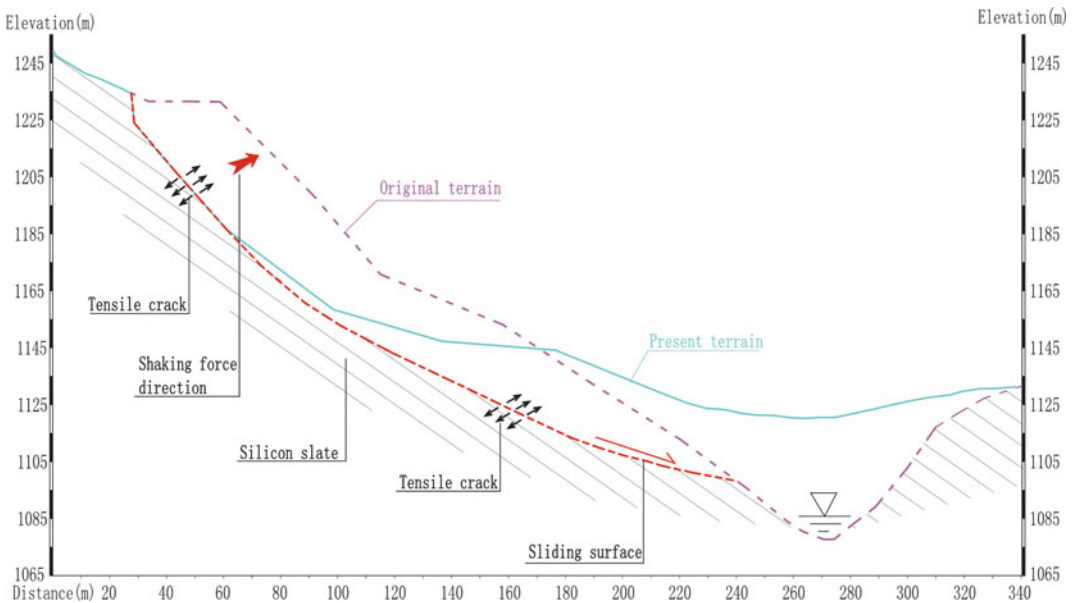
Fig. 54.15 Longitudinal section and deformation and failure mode of No. 2 landslide, Zhengjiashan

shear landslide is developed by cutting the rock mass, while the bottom slip surfaces of the other types of landslides are basically developed by tracking the existing structure surface. Therefore, the tension-shearing slip is relatively difficult to develop a slip surface at the bottom. The landslides happened shortly after the earthquake is mostly belong to the tension-shearing slip, among which the most typical one is Wangjiayan landslide, in Beichuan County.

According to the eyewitness descriptions, the Wangjiayan landslides happened 10 min later after the Wenchuan earthquake. The main reason of this laggard phenomenon can be concluded as a partial crack surface in trailing edge had developed during the earthquake, the locked segment was remained stable until the shake stopped. After the earthquake, the separated slip mass was only supported by the rock beneath. Finally, under the effect of stress caused by weight, the left locked section was completely cutted and shear slip surface formed then the tension-shear slip occurred.

4   Conclusions

From the study on earthquake-induced landslides in this paper, the following conclusions can be drawn,

1. The deformation and failure mode of earthquake-induced landslides is significantly different from the landslides under normal conditions. On the condition of strong earthquake, the horizontal acceleration on the middle-top of the declivity can exceed 1 g, and its earthquake horizontal inertia enormously exceeds the tension strength of the rock mass. A vertical crack surface will easy to develop at the trailing edge of the slope. With the continuous influence of earthquake, a tension-shear slip surface developed at the bottom and the earthquake triggered landslides happened at the same time. Therefore, a deep, vertical and rough crack surface is developed in the earthquake-induced landslides.

2. On the condition of strong shock, the most essential deformation and destroy element of the slope rock mass are tension-cracks and shearing slide, and mainly based on tension-cracks. As far as different slope structures, the bottom shearing slide will occur with different discontinuities. According to the geological environment of the landslide source region as well as the characteristics of the slope form and lithological association, the large-scale landslides induced by earthquake can be divided into five genetic types, i.e. tension-strike slip, crack-bedding slip, tension-horizontal slip, tension-scattering slip, and tension-shearing slip.

References

Hu XW, Huang RQ, Shi YB, Lv XP, Zhu HY, Wang XR (2009a) Analysis of blocking river mechanism of Tangjiashan landslides and dam-breaking mode of its barrier dam. Chin J Rock Mech Eng 28(1):181–189 (in Chinese with English abstract)

Hu XW, Luo G, Huang RQ, Zheng Y, Lv XP (2009b) Study of stability of remnant mountain body in back scarp of Tangjiashan lasndslide after "5.12" Wenchuan earthquake. Chin J Rock Mech Eng 28(11):2349–2359 (in Chinese with English abstract)

Huang RQ (2009) Mechanism and geomechanical modes of landslide hazards triggered by Wenchuan 8.0 earthquake. Chin J Rock Mech Eng 28(6):1239–1249 (in Chinese with English abstract)

Huang RQ, Pei XJ, Li TB (2008) Basic characteristics and formation mechanism of the largest scale landslide at Daguangbao occurred during the Wenchuan earthquake. J Eng Geol 16(6):730–741 (in Chinese with English abstract)

Huang RQ, Pei XJ, Zhang WF, Li SG, Li BL (2009) Futher examination on characteristics and formation mechanism of Daguangbao landslide. J Eng Geol 17(6):725–736 (in Chinese with English abstract)

Keefer DV (1984) Landslides caused by earthquakes. Geol Soc Am Bull 95(4):406–421

Sun P, Zhang YS, Yin YP (2009) Discussion on long run-out sliding mechanism of Donghekou landslide debris flow. J Eng Geol 17(6):737–744 (in Chinese with English abstract)

Xu Q, Chen JJ, Feng WK, Xiao RH, Zuo YY (2009a) Study of the Seismic Response of Slopes by Physical

Modeling. J Sichuan Univ (Eng Sci Ed) 41(3):266–272 (in Chinese with English abstract)

Xu Q, Pei XJ, Huang RQ (2009b) Large-scale landslides induced by the Wenchuan Earthquake. Science Press, Beijing (in Chinese)

Zheng YR, Ye HL, Huang RQ (2009) Analysis and discussion of failure mechanism and fracture surface of slope under earthquake. Chin J Rock Mech Eng 28(8):1714–1723 (in Chinese with English abstract)

Kinetic Friction Coefficient and Mass Movement Process of Large Rock Avalanches Triggered by the Wenchuan Earthquake

Jiawen Zhou, Zhiman Su and Xingguo Yang

Abstract

Kinetic friction coefficient and mass movement process of large rock avalanches are very important to understand the dynamic mechanical characteristics during the sliding process. This paper presents a simple slab model based on energy conservation to determining the kinetic friction coefficient and sliding velocity during the mass movement process. The rock avalanche is assumed as a rigid, non-deformable object moving down slope and subject to the sole Coulomb friction for the presented slab model, and the kinetic friction coefficient is assumed as a certain value during the mass movement process. Five large rock avalanches triggered by the Wenchuan earthquake are selected as the case study examples, and simplified to two stages for these rock avalanches: acceleration stage and accumulation stage, the kinetic friction coefficient and sliding velocity are back analysed by the presented simple slab model. Computed results show that, the kinetic friction coefficient for Donghekou, Woqian, Wenjiagou, Niumiangou and Xiejiadianzi rock avalanches are 0.235, 0.229, 0,306, 0,243 and 0.279, respectively; and the maximum sliding velocity are about 63 m/s, 59 m/s, 64 m/s, 67 m/s and 60 m/s, respectively.

Keywords

Rock avalanches · Wenchuan earthquake · Mass movement · Energy conservation · Kinetic friction coefficient · Landslide velocity

J. Zhou (✉) · Z. Su
Key Laboratory of Mountain Hazards and Earth Surface Processes, Chinese Academy of Science, 610044, Chengdu, China
e-mail: jwzhou@scu.edu.cn

J. Zhou · X. Yang
State Key Laboratory of Hydraulics and Mountain River Engineering, Sichuan University, 610065, Chengdu, China

1 Introduction

Mass movements occur in a variety of geological materials (soils, rocks, sediments, ice), on different scales, and are found in almost any environment where slopes are present (Hungr et al. 2005). Rock avalanches are defined as an extremely rapid, massive, flow-like motion of fragmented rock, which exhibits much greater

mobility, the impact of the avalanche's flow can cause extensive damage to human lives and engineering structures in its path (Dufresne and Davies 2009). Rock avalanches make a serious threat throughout the mountain regions, which are among the most threatening flow-like landslides because of their large volumes and spreading (Sosio et al. 2008; Pirulli 2009). Fast-moving, flow-like landslides are the most destructive among all slope instability phenomena and can be quite dangerous both for human lives and built areas (Xu et al. 2009).

In the past few years, some case studies for rock avalanche have focused on the triggering mechanisms, the movement dynamics and the properties of the material, induced the slope failure and mass movement process under seismic loading (Davies and McSaveney 2009; Yin et al. 2009; Dai et al. 2011). From a practical point of view, rock avalanches are among the most threatening flow-like landslides because of their large volumes and spreading, which make them potentially very costly in terms of human lives and engineering structures. Rock avalanches have been rarely observed directly (Dykes and Warburton 2007; Qi et al. 2011). Because of fragmentation occurs during the rock avalanching, the dynamic process will be much more complicated to simulate. There are two approaches to evaluate rock avalanches dynamics: experimental methods and numerical analyses (Ayotte and Hungr 2000; Manzella and Labiouse 2009). Experimental methods include field tests and empirical studies. Field test is impossible to test the initial conditions (velocity, mass, location) and natural topography. Therefore, field tests are typically used to calibrate numerical models. Modelling calibration usually relies on the field test results of debris extension and elevation, erosion depth, deposit thickness and branching (Manzella and Labiouse 2008).

Modelling rock avalanche can provide a guidance to estimate the extent of the potential impact area, and to get an insight into the propagation mechanism (Fu et al. 2011; Yoshida et al. 2012). The mass movement of rock avalanches is often predicted by the Coulomb slide block model, where the flow thickness is small with respect to the total length and the resistance is concentrated at the flow base (Hungr et al. 2005). Although a continuing discussion in the literature on emplacement mechanisms and dynamics of rock and debris avalanche offers a wide range of models to explain dynamical characteristics of rock avalanche, but the mechanisms governing the high mobility of debris avalanches are not yet well understood to date.

2 Rock Avalanches Triggered by the Wenchuan Earthquake

On 12 May 2008, a strong (Ms 8.0) earthquake occurred in the Longmenshan region at the eastern margin of the Tibetan Plateau, Sichuan Province, southwest of China (Yin et al. 2009). Numerous geo-hazards were triggered, including slope collapses, debris flows and landslides. Earthquake-triggered geo-hazards have aroused the large amount deaths of people and huge economic losses because of the Wenchuan earthquake (Qi et al. 2011). Particularly in mountainous areas, the damage caused by earthquake triggered landslides is more severe than the direct damage caused by the earthquake itself. Hundreds of thousands of landslides were triggered by the Wenchuan earthquake, such as rock falls, slides and rock avalanches, and many of which formed landslide dammed lakes.

Hundreds large landslides were triggered by the Wenchuan earthquake, and 112 large landslides' volume were larger than 50×10^4 m^3, including the Tangjiashan landslide in Beichuan County, the Donghekou and Woqianshe landslides in Qinchuan County, the Wenjiagou landslide in Mianzhu City and the Daguangbao landslide in Anxian County (Xu et al. 2009). Most the large landslides distance to the central fault are less than 3.0 km, the ratio is about 70 %. Because the earthquake happened at the mountain region of Southwest China, and the earthquake is strong, so that rock avalanches is a typical landslide type of the large landslides triggered by the Wenchuan earthquake, the mechanism of dynamic process of rock avalanche is very complicated, including the mass movement and accumulation process. Here, five large rock avalanches are selected for the study of
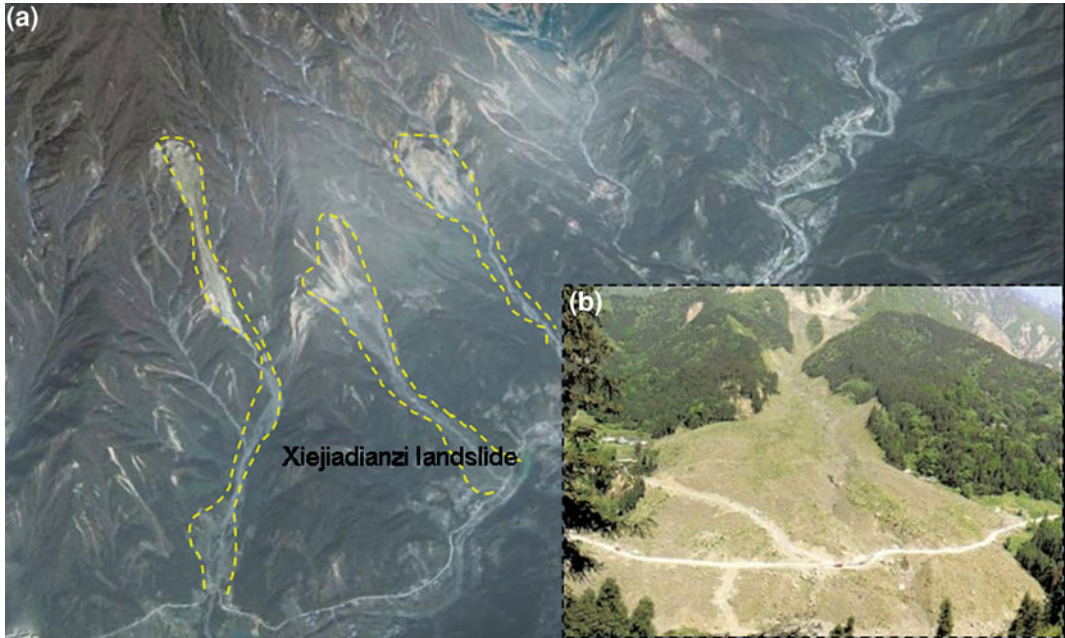
Fig. 55.1 Overview of the rock avalanches triggered by the Wenchuan earthquake in Pengzhou City: **a** remote sensing image and **b** site photo of Xiejiadianzi rock avalanche

kinetic friction coefficient and mass movement process of large rock avalanches, including the Donghekou and Woqian rock avalanche in Qingchuan County, the Niumiangou rock avalanche in Wenchuan City, the Wenjiagou rock avalanche in Mianzhu City and the Xiejiadianzi rock avalanche in Pengzhou City.

Figure 55.1 shows the overview of the rock avalanches triggered by the Wenchuan earthquake in Pengzhou City.

As shown in Fig. 55.1a, several large rock avalanches are triggered by the Wenchuan earthquake in Pengzhou City, the largest one is Xiejiadianzi rock avalanche (as shown in Fig. 55.1b). Main characteristics for large rock avalanche triggered by the Wenchuan earthquake are large volume, long travel distance with a large height, travel in a narrow valley.

Table 55.1 shows the main landslide parameters of five large rock avalanches triggered by the Wenchuan earthquake.

As shown in Table 55.1, the travel distance of these large rock avalanches is larger than 2000 m, with a height more than 500 m, the landslide volume is very large, especially for the Wenjiagou

Table 55.1 Main landslide parameters of 5 large rock avalanches triggered by the Wenchuan earthquake

Rock avalanche	Travel distance (m)	Height (m)	Volume (m³)
Donghekou	2280	535	1500×10^4
Woqian	2230	510	1200×10^4
Wenjiagou	3430	1050	2750×10^4
Niumiangou	2610	658	750×10^4
Xiejiadianzi	2060	575	300×10^4

rock avalanche, the volume is about 2750×10^4 m³. Figure 55.2 shows the overview of the Wenjiagou rock avalanche in the Mianzhu City.

As shown in Fig. 55.2, the travel distance of Wenjiagou rock avalanche is about 3430 m, the landslide initiation volume is about 2750×10^4 m³. There are three landslide zones for the Wenjiagou rock avalanche, initiation zone, acceleration zone and accumulation zone. Because of the Qingping town is located at the foot of the mountain and the Mianyuan River run though this region, so that during the earthquake, several buildings were buried or damaged and hungered people are dead, and also
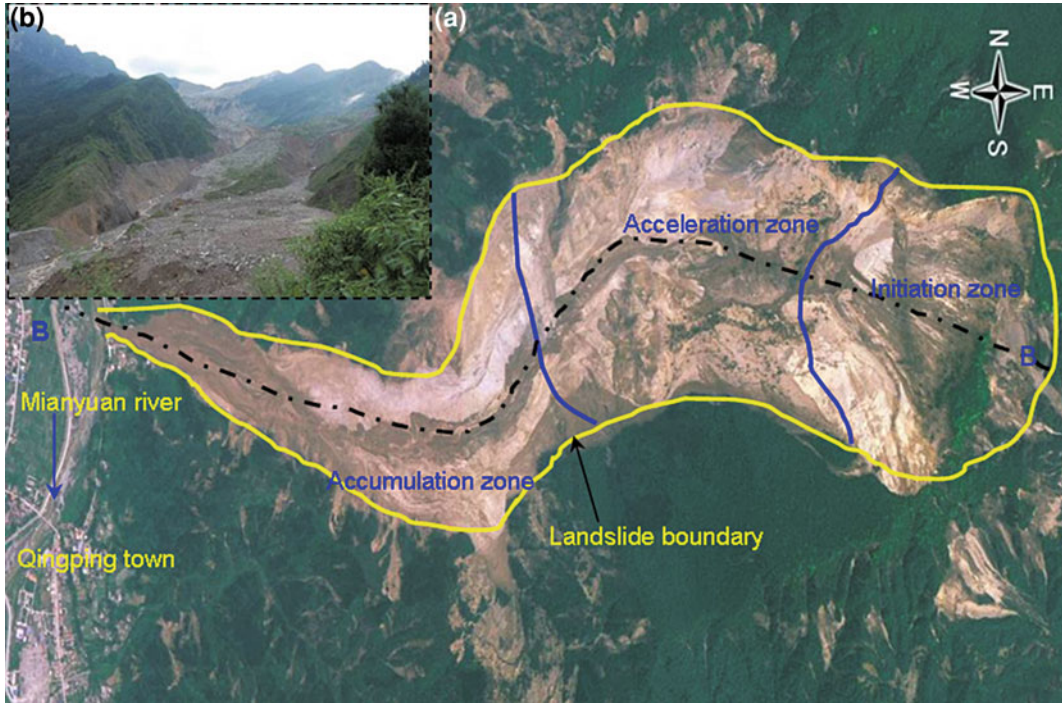
Fig. 55.2 Overview of the Wenjiagou rock avalanche (B–B section is main landslide profile): **a** remote sensing image and **b** site photo

the a dammed lake is formed by the blocking of Mianyuan River. Furthermore, a large volume of loose landslide deposits are located at the mountain valley, during the heavy rainfall season, several times debris flows occurred in the Wenjiagou gully, resulted in huge economical loss and death of lives.

3　A Simple Mass Movement Model Based on Energy Conservation

3.1　Basically Assumptions

For the mass movement problem of rock avalanche, the rock avalanche is assumed as a rigid, non-deformable object moving down slope and subject to the sole Coulomb friction. This avoids the difficult calculations of the internal deformations within the granular medium. The landslide process is influenced by the terrain with different slope inclination, and rock avalanche can be partially accounted for modelling the landslide as a slab and taking the average properties of the terrain. The slab model allows introduce a parameter representing the resistance of the medium, called the kinetic friction coefficient. The rock avalanche usually changes its geometrical lengths during the flowing process, normally starts as a single slab unit with high cohesion. As it slides and strongly disintegrates because of collision or free fall, huge energy dissipation makes it transform into a deformable granular flow, the lateral friction and pressure makes it widen and flatten.

Based on those assumptions, a simple slab model is introduced to simulate the mass movement process of the rock avalanche problem, and the mass movement velocity is computed under the principle of energy conservation. Figure 55.3 shows the slab model for mass movement problem of rock avalanche based on energy conservation.

As shown in Fig. 55.3, **A** is the centre point of rock slab; **B** is the centre point of deposits; g is the gravity acceleration and equal to 9.81 m/s^2; m is mass of the rock slab, keep a constant

Fig. 55.3 Slab model for mass movement problem of rock avalanche based on energy conservation
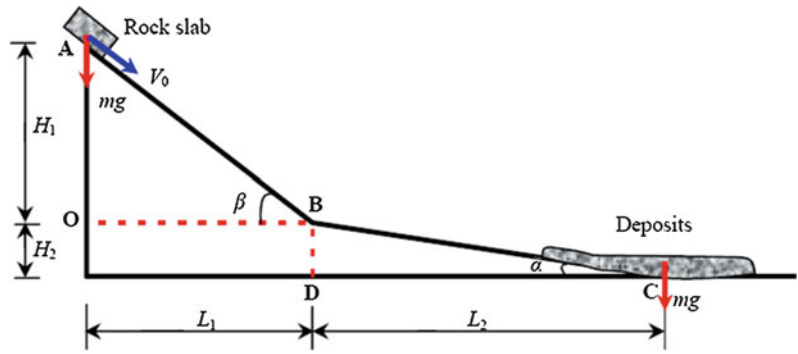
during the landslide process; v_0 is the initiation velocity of the mass; the inclination of slope **AB** and **BC** are β and α, respectively; the height of slope **AB** and **BC** are H_1 and H_2, respectively; the length of slope **AB** and **BC** are L_1 and L_2, respectively; the total height and length of the rock avalanche can be computed as follow,

$$H = H_1 + H_2 \qquad (55.1)$$

$$L = L_1 + L_2 \qquad (55.2)$$

Along the sliding path, the general equation of motion of a rigid mass m sliding down slope can be written as,

$$m\frac{dv}{dt} = mg\sin\phi - \text{F}_{\text{RES}} \qquad (55.3)$$

where v is the velocity of the sliding mass; ϕ is the slope inclination; F_{RES} is the resistance force.

If the generic force of resistance $\text{F}_{\text{RES}}(t)$ is given, the velocity can be calculated integrating the Eq. (55.3) to yield,

$$v_t = v_0 + \int_0^t \frac{dv}{dt}dt = v_0 + \int_0^t a_t dt \qquad (55.4)$$

where v_0 is the initiation velocity of the sliding mass; v_t is the mass velocity at any time; t is the time; and a_t is the acceleration of sliding mass.

The resistance force for sliding mass can be computed as follow,

$$\text{F}_{\text{RES}} = f \cdot mg\cos\phi \qquad (55.5)$$

where f is the kinetic friction coefficient, here it's assumed as a constant during the flowing process.

The acceleration parallel to the slope is computed as follow,

$$a_t = \frac{dv}{dt} = g(\sin\phi - f\cos\phi) \qquad (55.6)$$

If the acceleration a_t is larger than 0, the velocity of sliding mass is increased with the time, and if the acceleration a_t is less than 0, the velocity of sliding mass is decreased with the time, until the movement of sliding mass is stopped, and the velocity of sliding mass is 0.

3.2   Calculation of the Velocity with Slope Path

As shown in Fig. 55.3, the mass movement velocity is increased during the flowing path **AB** and decreased during the flowing path **BC**. When the mass flowing at the point **B**, it got the maximum velocity v_{max}, and stopped at point **C**, the velocity is 0. Combined with the principle of energy conservation, two energy conservation equations can be obtained during the landslide processes of **AB** and **BC**,

$$\frac{1}{2}mv_0^2 + mgH_1 - mgH_1 f\cot\beta = \frac{1}{2}mv_{\text{max}}^2 \tag{55.7}$$

$$\frac{1}{2}mv_{\text{max}}^2 + mgH_2 - mgH_2 f\cot\alpha = 0 \quad (55.8)$$

Fig. 55.4 Main sliding section of the Niumiangou rock avalanche (Xu et al. 2009; modified)
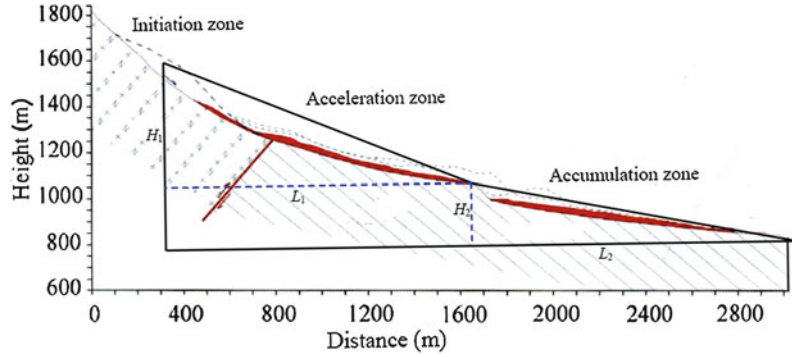
where v_0 is assumed as a certain value, the initiation velocity of sliding mass is equal to 0.

Combined Eq. (55.7) with Eq. (55.8), then the kinetic friction coefficient during the landslide process can be determined,

$$f = \frac{1/2 \cdot v_0^2 + g(H_1 + H_2)}{gH_2 \cot\alpha + gH_1 \cot\beta} \quad (55.9)$$

where

$$\cot\alpha = L_2/H_2, \text{ and } \cot\beta = L_1/H_1 \quad (55.10)$$

The mass movement process of the large rock avalanches triggered by Wenchuan earthquake is simulated by the upper slab model.

4 Simulated Results for Mass Movement of Rock Avalanches

In this section, the simple slab model is applied to simulate the mass movement process of the large rock avalanches triggered by the Wenchuan earthquake, the kinetic friction coefficient and sliding velocity are computed.

4.1 Landslide Parameters

For the five large rock avalanches triggered by Wenchuan earthquake, the mass movement path is simplified to two parts: acceleration zone and accumulation zone, according to the simple slab model based on energy conservation. Figure 55.4

Table 55.2 Geometry parameters for the large rock avalanches triggered by the Wenchuan earthquake according to the simple slab model

Rock avalanche	H_1 (m)	L_1 (m)	H_2 (m)	L_2 (m)
Donghekou	410	890	125	1390
Woqian	290	500	220	1730
Wenjiagou	510	1160	148	1550
Niumiangou	570	1180	480	2250
Xiejiadianzi	350	600	225	1460

shows the main sliding section of the Niumiangou rock avalanche.

As shown in Fig. 55.4, the geometry parameters for Niumiangou rock avalanche can be obtained for the mass movement process simulation. Table 55.2 shows the geometry parameters for the large rock avalanches based on the simple slab model. The kinetic friction coefficient during the mass movement process is assumed as a certain value.

As shown in Table 55.2, the travel distance of Wenjiagou rock avalanche is the largest one, about 3430 m, and the travel distance of Xiejiadianzi rock avalanche is the lowest one, about 2060 m.

4.2 Kinetic Friction Coefficient

The kinetic friction coefficient is computed by Eq. (55.9), Table 55.3 shows the simulated results of kinetic friction coefficient for the large rock avalanches.

Table 55.3 Simulated results of kinetic friction coefficient for the large rock avalanches

Rock avalanche	Donghekou	Woqian	Wenjiagou	Niumiangou	Xiejiadianzi
Kinetic friction coefficient	0.235	0.229	0.306	0.243	0.279

Fig. 55.5 Compute results of the sliding velocity during the mass movement process
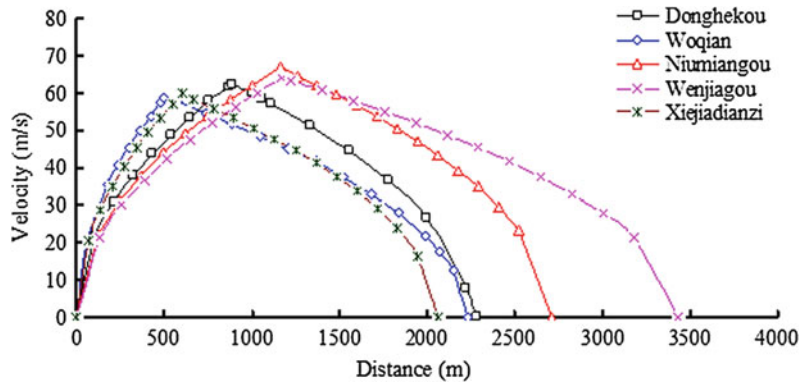
As shown in Table 55.3, the kinetic friction coefficient for Donghekou, Woqian, Wenjiagou, Niumiangou and Xiejiadianzi rock avalanches are 0.235, 0.229, 0,306, 0,243 and 0.279, respectively. The back analysis results of kinetic friction coefficient are computed base on the simple slab model, and assumed as a certain value. In fact, the kinetic friction coefficient is hard to obtained, because it is influenced by the topography, geomorphology, lithology, vegetation and rock fragmentation situation.

4.3   Sliding Velocity During the Mass Movement Process

Combining Eq. (55.7) with Eq. (55.8), the sliding velocity during the mass movement process can be computed. Figure 55.5 shows the compute results of the sliding velocity during the mass movement process.

As shown in Fig. 55.5, the maximum sliding velocity of these large avalanches is larger than 50 m/s, the maximum sliding velocity of Niumiangou rock avalanche is about 67 m/s, Donghekou rock avalanche is about 63 m/s, Woqian rock avalanche is about 59 m/s, Wenjiagou rock avalanche is about 64 m/s, Xiejiadianzi rock avalanche is about 60 m/s.

5   Conclusions

For the mass movement problem of rock avalanche, the rock avalanche is assumed as a rigid, non-deformable object moving down slope and subject to the sole Coulomb friction. Based on those assumptions, a simple slab model is introduced to simulate the mass movement process of the rock avalanche problem, and the mass movement velocity is computed under the principle of energy conservation. In this paper, five large rock avalanches triggered by the Wenchuan earthquake are selected for the study of kinetic friction coefficient and mass movement process. The kinetic friction coefficient and sliding velocity are back analysed by the presented simple slab model. Compute results show that, the kinetic friction coefficient for Donghekou, Woqian, Wenjiagou, Niumiangou and Xiejiadianzi rock avalanches are 0.235, 0.229, 0,306, 0,243 and 0.279, respectively. The maximum sliding velocity for Niumiangou, Donghekou, Woqian, Wenjiagou and

Xiejiadianzi rock avalanche are about 67 m/s, 63 m/s, 59 m/s, 64 m/s and 60 m/s, respectively.

References

Ayotte D, Hungr O (2000) Calibration of a runout prediction model for debris flows and avalanches. In: Wieczorek, GF, Naeser, ND (Eds.), Proceedings 2nd international conference on Debris flows, Taipei, pp 505–514

Dai FC, Tu XB, Xu C, Gong QM, Yao X (2011) Rock avalanches triggered by oblique-thrusting during the 12 May 2008 Ms 8.0 Wenchuan earthquake, China. Geomorphology 132(3–4):300–318

Davies TR, McSaveney MJ (2009) The role of rock fragmentation in the motion of large landslides. Eng Geol 109(1–2):67–79

Dufresne A, Davies TR (2009) Longitudinal ridges in mass movement deposits. Geomorphology 105(3–4):171–181

Dykes AP, Warburton J (2007) Mass movements in peat: a formal classification scheme. Geomorphology 86(1–2):73–93

Fu BH, Shi PL, Guo HD, Okuyama S, Ninomiya Y, Wright S (2011) Surface deformation related to the 2008 Wenchuan earthquake, and mountain building of the Longmen Shan, eastern Tibetan Plateau. J Asian Earth Sci 40(4):805–824

Hungr O, Corominas, J, Eberhardt E (2005) Estimating landslide motion mechanism, travel distance and velocity. In: Proceedings of the international conference on landslide risk management, pp 99–128

Manzella I, Labiouse V (2008) Qualitative analysis of rock avalanches propagation by means of physical modelling of not constrained gravel flows. Rock Mech Rock Eng 41(1):133–151

Manzella I, Labiouse V (2009) Flow experiments with gravel and blocks at small scale to investigate parameters and mechanisms involved in rock avalanches. Eng Geol 109(1–2):146–158

Pirulli M (2009) The Thurwieser rock avalanche (Italian Alps): description and dynamic analysis. Eng Geol 109(1–2):80–92

Qi SW, Xu Q, Zhang B, Zhou YD, Lan HX, Li LH (2011) Source characteristics of long runout rock avalanches triggered by the 2008 Wenchuan earthquake China. J Asian Earth Sci 40(4):896–906

Sosio R, Crosta GB, Hungr O (2008) Complete dynamic modeling calibration for the Thurwieser rock avalanche (Italian Central Alps). Eng Geol 100(1–2):11–26

Xu Q, Pei XJ, Huang RQ (2009) Large-scale landslides induced by the Wenchuan earthquake (in Chinese). Science Press, Beijing

Yin YP, Wang FW, Sun P (2009) Landslide hazards triggered by the 2008 Wenchuan earthquake, Sichuan, China. Landslides 6:139–151

Yoshida H, Sugai T, Ohmori H (2012) Size-distance relationships for hummocks on volcanic rockslide-debris avalanche deposits in Japan. Geomorphology 136(1):76–87

Topographic Effect on Seismic Slope Behavior in a Shaking Table Test

56

Qiang Xu and Hanxiang Liu

Abstract

Statistical analysis of the spatial occurrence of slope instability features due to the 2008 great Wenchuan earthquake has shown the remarkable lithological and topographic effects, and seismic parameters play an important role in spatial distribution of geo-hazards. As the slope response to seismic waves is only poorly understood, the present research was undertaken to clarify the slope response effect with help of model tests. A model slope was designed to possess a lithologic combination of low strength material overlying high strength material, and the size of the model is 2.14 m wide, 1.5 m high and has a slope angle of 60. A number of accelerometers were embedded in the model to collect quantitative data. The model slope was excited at the bottom by a broad range of shaking levels of horizontal and vertical motions scaled from the actual great Wenchuan earthquake waves in 2008, and to synthetic sine waves. Analysis was conducted based on the peak accelerations and their corresponding amplification factors. Results show that apparent topographic amplification effect occurs in both horizontal and vertical component motions, however, develops in a different way. Strong vertical response is observed by comparative analysis between these two components. In addition, topographic effects are influenced much by motion intensity and frequency of input waves, and they decay when subjected to high level of real waves. Results can help improve the seismic slope stability analysis and geo-hazards prevention and mitigation.

Keywords

Slope · Shaking table test · Seismic behavior · Topographic effect

Q. Xu (✉) · H. Liu
State Key Laboratory of Geohazards Prevention and Environment Protection, Chengdu University of Technology, Chengdu 610059, China
e-mail: xuqiang_68@126.com

1 Introduction

After the 12 May Wenchuan earthquake of 2008 in Sichuan Province, China, quantitative results have been obtained from co-seismic recordings

Table 56.1 Physical and mechanics parameters of prototypes and its scaled models

Lithology		Density ρkN/m^3	Cohesion cMPa	Frictional angleφ°	Elastic modulus EMPa	Poisson's ratio μ
Stiff rock	Prototype	22	10–50	35–50	5000–10000	0.2–0.35
	Model	22	0.12	40	56.3	0.23
Soft rock	Prototype	20	0.5–20	15–30	800–3500	0.2–0.4
	Model	20	0.05	23.8	15.2	0.31

by digital strong earthquake networks arranged in and out of Sichuan, and aftershock recordings by post-earthquake monitoring in earthquake region (Zhou et al. 2010; Wang et al. 2011). Statistical analysis of the spatial occurrence of slope instability features due to the 2008 great Wenchuan earthquake has shown the remarkable lithological and topographic effects, and seismic parameters play an important role in spatial distribution of geo-hazards (Huang and Li 2009; Yin et al. 2009; Qi et al. 2010; Dai et al. 2011; Gorum et al. 2011). However, most of the results are needed to be verified before they are generalized, and physical model test is taken for granted to be the preferred way. Model tests contribute to reveal some phenomena visually which can not be realized through the numerical modeling or the analytical solution.

The present study attempts to explore the seismic response of slopes to some extent with the typical lithology and geological structures in the Wenchuan earthquake region. A shaking table test, one of the most commonly used model tests in vibration engineering, was conducted on two rock slope models with composite lithologies: low strength materials overlying high strength materials and the opposite combination. A total of 32 accelerometers were arranged inside and on the surface of models to investigate the topographic effects. In order to explore the response laws of seismic response to shaking intensities, a broad range of shaking levels of horizontal and vertical motions scaled from actual Wenchuan earthquake waves and synthetic sine waves were used to excite models. Limited to the space, only the slope model with low strength materials overlying high strength materials will be discussed.

2   Set up of Test

Before performing a shaking table test, there will be much work for preparation in materials, model box, test device. Prior to all of them, similitude between the prototype slope and the model slope should be designed. In this paper, based on the dimensional analysis and Buckingham's π theorem, a set of similitude relations was built in Xu and Liu (Xu et al. 2010), of which the similitude constants for length l, densityρ and elastic module E are 100, 1.0 and 100 respectively.

2.1   Materials and Construction

In this test, two models with horizontally layered contact surfaces and different composite lithologies were designed: stiff materials overlying soft materials (Model 1) and soft materials overlying stiff materials (Model 2). Barite powder, quartz sand, gypsum, glycerol and water were mixed in a proportion of 32:53:5:1:9 to make stiff materials in two models simulating the property of limestone, while the same mixture in a proportion of 33.5:55.5:2.5:2:6.5 were used to make soft materials simulating the mudstone. Table 56.1 lists the material properties of the prototype slope and the model slope determined by direct shear tests and uniaxial compression strength tests.

After the similitude materials were determined, they would be installed into a rigid steel model box with an outline length of 3.1 m, width of 2.78 m, and height of 2.45 m (seen in Fig. 56.2). Two single-free-surface model slopes were constructed face to face in a model box
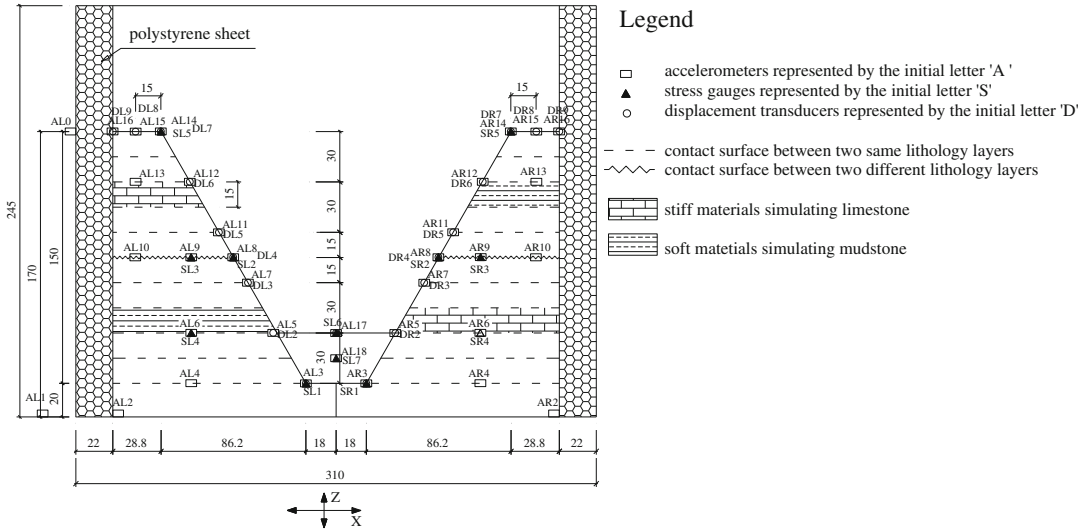
Fig. 56.1 Cross section of model slopes (unit: cm). (In each index, 'L' indicates the model with high strength materials overlying low strength materials, 'R' indicates the model with low strength materials overlying high strength materials, and the following number distinguishes the sampling positions.)

forming a 'U' shape valley, and gravelly soils of 30 cm height were filled at the bottom of the valley. Two models had an identical shape shown in Fig. 56.1. To reduce the reflecting phenomenon when waves encountered the rigid boundary during propagation, a 22 cm thick polystyrene sheet with outside wrapped polyethylene film was placed in four sides of the box.

2.2 Test Device and Sensors

Test was completed in the seismic simulation test system of 6 degree of freedom (3 translational motions and 3 rotational motions) in China Merchants Chongqing Communications Research & Design Institute (Fig. 56.2). The test system includes a high speed multi-channel data acquisition system, a numerical control system and a shaking table apparatus. A total of 60 sensors were installed at different elevations within two models, among which were 32 accelerometers with measuring range of $\sim$ 2.0 g, 16 displacement transducers with measuring range of $\sim$ 200 mm, and 12 stress gauges with measuring range of $\sim$ 200 kPa. The arrangement of sensors in two

Fig. 56.2 Seismic simulation test system

models was symmetric. Accelerations were the most important collection objects in this study, so they were embedded both inside the model and on the free face to measure the horizontal and vertical motion components. A few stress gauges were also embedded inside and on the free face to measure the vertical stress. Guyed-strain displacement transducers were only embedded on the free face to measure the horizontal motions. Besides, one accelerometer was fixed on the table surface to check the input waves, and another one was fixed on the top of model box to calibrate its rigidity during
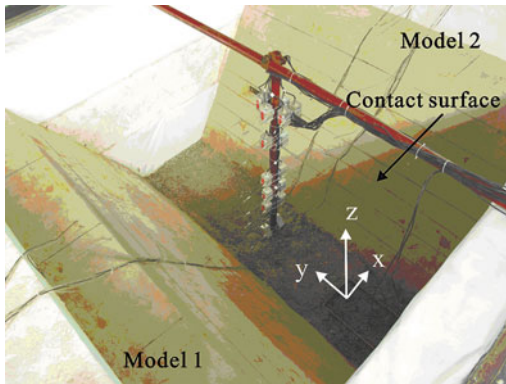
Fig. 56.3 Instrumented physical models

shaking. The layout of all sensors is shown in Fig. 56.1, and the already instrumented models are shown in Fig. 56.3.

2.3 Input Waves and Loading Sequence

In the test, the influencing factors incorporated loading wave kind, excitation direction and amplitude. The horizontal and vertical components of accelerations recorded by Wolong seismic station during 2008 great Wenchuan earthquake, where the maximum co-seismic ground motions were recorded, were scaled at different levels for the main loading waves. Sine waves were another kind of loading waves used in the test, and had the model vibration frequencies of 10 Hz and 15 Hz. The excitation directions for real waves included horizontal input only (x-excitation in Fig. 56.3), vertical input only (z-excitation in Fig. 56.3) and horizontal and vertical input at an composite angle of 45 (zx45 -excitation), while the sine waves considered horizontal input only and vertical input only. The seismic slope response to different ground motion intensities was also the main research work in our study, so the input amplitudes of real waves and sine waves were loaded on models increasingly.

At the first stage, white noise was used to check the initial dynamic characteristics of models. Before inputting real waves in large

amounts, sine waves were loaded from an amplitude of 0.05–0.25 g step by step. Each step lasted for about 10.8 s which was downscaled by a ratio of 1:10 from the main shock duration of Wenchuan earthquake in Wolong station. Between two steps, there was a break to examine if models had any deformation or failure. In order to obtain the seismic slope response to increasing intensity as clearly as possible, both sine waves and real waves were loaded until models appeared large deformation. In this way, when the test finished, the peak input acceleration amplitudes for sine waves and real waves arrived at 0.6 g and 1.1 g respectively.

3 Test Result

Peak ground acceleration (*PGA*) was extracted through maximizing each recording. Dimensionless amplification factor of responsive acceleration (*r*) is introduced here to reflect the response intensity of model slopes, which is defined by the ratio of *PGA* at any monitoring point in a model to that on the table surface in one direction which was same with the vibration condition. No amplification factor will be calculated for two recordings in orthotropic directions, avoiding an infinite ratio when the denominator tends to zero. Due to the space limitation, only the slope model with low strength materials overlying high strength materials will be discussed, as seen in the model 2 of Fig. 56.1.

As Fig. 56.1 shows, a column of three-component accelerometers indexed by AR3, AR5, AR7, AR8, AR11, AR12, AR14 was embedded on the surface of model 2 to explore the topographic effect, and relative elevations to model bottom were 20 cm, 50 cm, 80 cm, 95 cm, 110 cm, 140 cm and 170 cm. Another column indexed by AR4, AR6, AR9, AR13, AR15 was embedded inside the model 2 to do the similar analysis, and relative elevations were 20 cm, 50 cm, 95 cm, 140 cm and 170 cm. By comparing the responses at the same level (e.g. AR8 and AR9), the response laws horizontally toward the outside also can be obtained.

Fig. 56.4 Topographic effects for different kinds of input waves in horizontal direction when shaking intensity is increased (the *solid line* represents the response on the surface of the model; the *dashed line* represents the response inside the model)
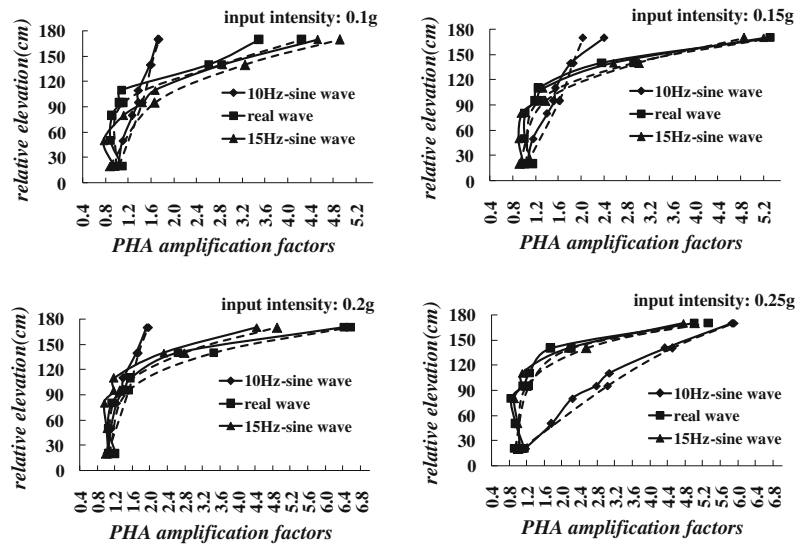
During test, the model was excited wave by wave with increasing intensity until it failed, so many sensors were destroyed or removed from their original position making the recordings invalid, especially the sensors at the crest of the model slope. Nonetheless, in order to keep the curve integrate, invalid data were still plot in Figs. 56.5 and 56.7.

3.1   Horizontal Acceleration Response

Figure 56.4 shows that topographic effect represented by the accelerations occurs when subjected to three kinds of input waves characterizing different frequency. For 10 Hz-sine wave shaking, the amplification factor increases from bottom to top linearly, while the factor increases fast only in the middle to top of model for both the 15 Hz-sine wave and real wave shaking, nonetheless, the factor value for the latter two kinds is much larger than that of the former when the input amplitude is smaller than 0.2 g (including 0.2 g). In the lower part, the factor shows a decreasing tend for the latter two kinds of waves. When the input amplitude exceeds 0.2 g, the 10 Hz-sine wave shaking demonstrates the largest response in the model. Apart from the difference in value, the shaking intensity makes a weak effect on the

topographic response law for each kind of wave. What is important to note is that the topographic effects for 15 Hz- sine wave and real wave assemble each other, which is attributed to the same predominant frequency.

Then Fig. 56.5 further depicts that the peak horizontal acceleration (*PHA*) at each monitoring point on the surface of the model increases as the input intensity is strengthened, while its corresponding amplification factor decreases in the upper part of model and keeps stable in the lower part, which indicates a decay in topographic effect. The phenomenon occurs much more obviously in real wave excitation than in the other two sine wave excitations. Fig. 56.5(c-2) shows that the topographic amplification effect decreases fast when the real wave excites the model with an increasing intensity.

In Fig. 56.5, the model began to generate great deformation on the top of model and the sensor became to lose effect (AR14 in Fig. 56.1) when the input amplitude reached 0.3 g for 10-Hz sine wave shaking and 0.25 g for 15-Hz sine wave shaking, the successive sine wave excitation sped up the failure of model and sensors in other positions lost effect. By contrast, the model kept a slow deformation progress for real wave shaking. It seems that higher level excitation will be demanded for the real wave than for the sine wave so that the topographic effect decays

Fig. 56.5 Response laws of *PHA* (the *left column*) and their amplification factors (the *right column*) with the increasing input intensity for each monitoring point on the surficial model slope (the *red line* in each figure was drawn from the invalid data)
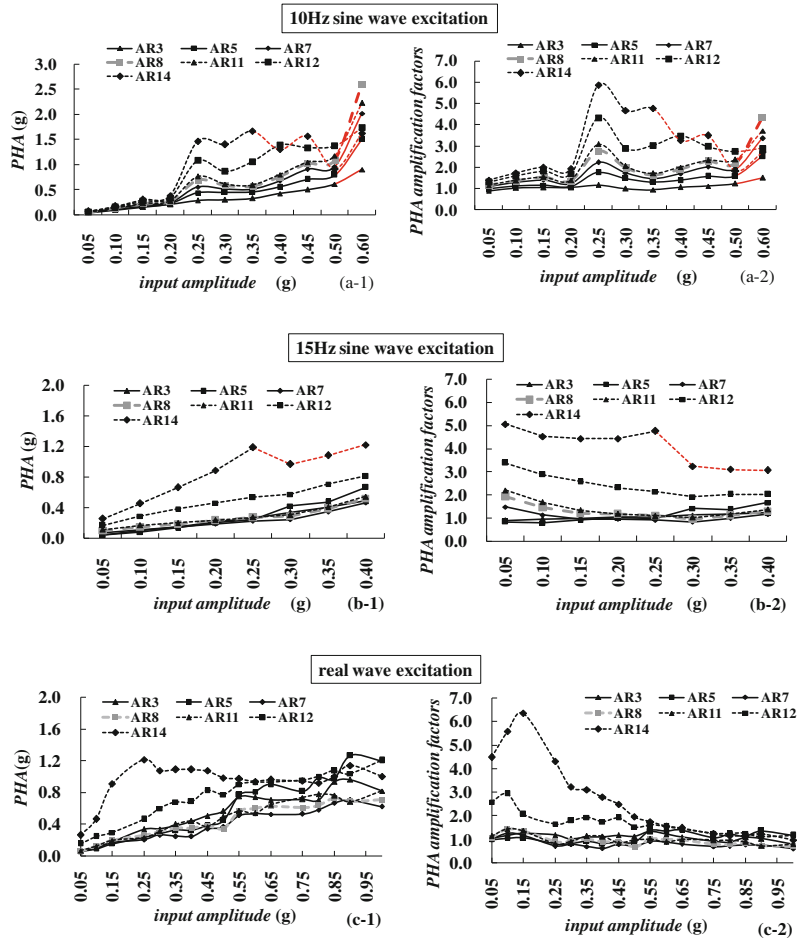
Fig. 56.6 Topographic effects for different kinds of input waves in vertical direction when shaking intensity is increased (the *solid line* represents the response on the surface of the model; the *dashed line* represents the response inside the model)
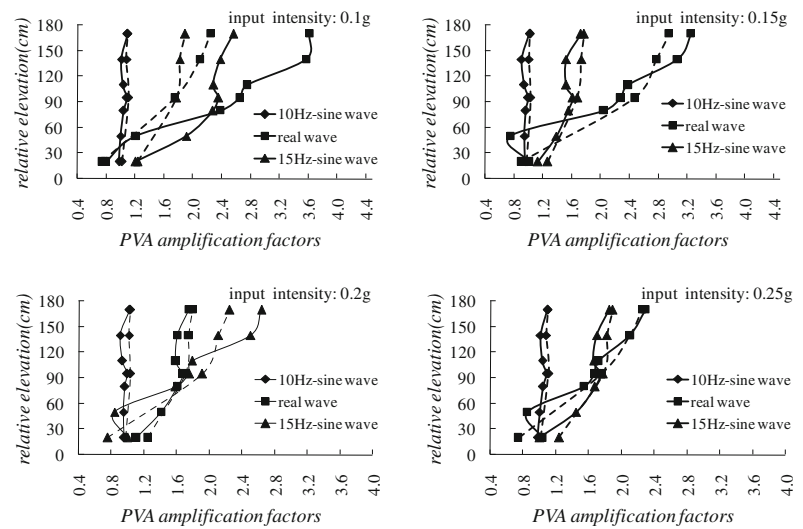
Fig. 56.7 Response laws of *PVA* (the *left column*) and their amplification factors (the *right column*) with the increasing input intensity for each monitoring point on the surficial model slope (the *red line* in each figure was drawn from the invalid data)
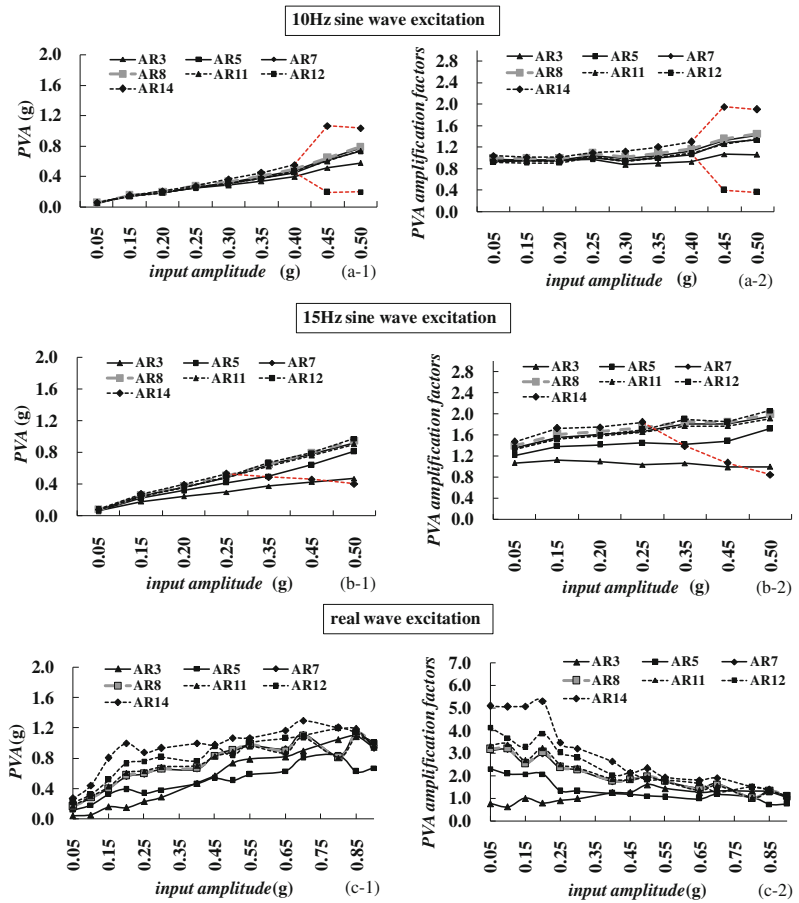
to the same level. Hence, the wave with the more concentrative frequency may produce more destruction in an earthquake event.

3.2   Vertical Acceleration Response

The same analysis procedure as above will be used herein. Different results between the horizontal- and vertical-component responses will be stressed bellow.

Figure 56.6 shows that the peak vertical acceleration (*PVA*) has little topographic amplification on surface of the model when subjected to 10 Hz-sine wave shaking, which is much different from what is observed in the *PHA* response. Topographic amplification effect occurs when subjected to the other two kinds of waves, and the effect is more apparent for the real wave shaking.

It's obvious that the topographic response laws are the same for the two sine wave shakings. It shows that the *PVA* increases faster in the lower part of the model than in the upper part, which is another distinctive response compared to the horizontal component. Moreover, the maximum *PVA* is significantly smaller than the maximum *PHA*, but in the lower part, the *PVA* exceeds the *PHA* when subjected to 15 Hz-sine wave and real wave excitations.

In Fig. 56.7, deformation and failure progress of the model make the curves dramatically rise or drop for the sine-wave shakings with the reason discussed above. However, Fig. 56.7 shows clearly that the *PVA* at each monitoring point increases with intensifying excitation. The corresponding amplification factor still decreases as what occurs in the *PHA* response for the real wave shaking, however, the factor demonstrates a

rising trend for the sine-wave excitation, which indicates the topographic amplification effect is strengthened. The latter phenomenon can be in part explained by the weaker nonlinear effect caused by the model materials in compression condition of vertical component relative to in the shear condition of horizontal component.

4 Conclusion

A model slope with low strength materials overlying high strength materials is designed to explore the seismic slope behavior with the aid of shaking table test. The following main conclusions could be drawn:

Topographic amplification effect exists in both horizontal components and vertical components. Peak horizontal acceleration (PHA) is amplified fast in the upper parts of the model, while peak vertical acceleration (PVA) is amplified relatively slow.

The maximum PHA amplification factors are larger than the maximum PVA amplification factors, which occurs on the top of model. However, the PVA exceeds the PHA in the other parts when subjected to the real wave.

Topographic effect is influenced much by the frequency distribution of the shaking wave. Waves having the approximate predominant frequency have the similar topographic effect. Moreover, waves with the more concentrative frequency may produce more destruction in an earthquake event.

Topographic effect decays when the intensity of the shaking wave is increased, but the anomaly sometimes exits in the vertical component due to the weaker nonlinearity.

References

Dai FC, Xu C, Yao X et al (2011) Spaitial distribution of landslides triggered by the 2008 Ms 8.0 Wenchuan earthquake, China. J Asian Earth Sci 40(4):883–895

Gorum T, Fan XM, Westen CJ et al (2011) Distribution pattern of earthquake-induced landslides triggered by the 12 May 2008 Wenchuan earthquake. Geomorphology 133(3–4):152–167

Huang RQ, Li WL (2009) Analysis of the geo-hazards triggered by the 12 May 2008 Wenchuan Earthquake, China. Bull Eng Geol Environ 68:363–371

Luo YH, Wang YS, Wang FH et al (2010) Monitoring of slope seismic response during aftershocks of Wenchuan earthquake in Qingchuan county. J Eng Geol 18(1):27–34 (in Chinese)

Qi SW, Xu Q, Lan HX, Zhang B et al (2010) Spatial distribution analysis of landslides triggered by 2008.5.12 Wenchuan Earthquake China. Eng Geol 116:95–108

Wang XY, Nie GZ, Wang DW (2011) Relationships between ground motion parameters and landslides induced by Wenchuan earthquake. Earthq Sci 23(3):233–242

Xu Q, Liu H X, Zou W et al. (2010) Study on slope dynamic responses of accelerations by large-scale shaking table test. Chin J Rock Mech Eng 29(12):2420–2428 (in Chinese)

Yin YP, Wang FW, Sun P (2009) Landslide hazards triggered by the 2008 Wenchuan earthquake, Sichuan, China. Landslides 6:139–151

Zhou RJ, Lai M, Yu H et al (2010) Strong motion records of Wenchuan Ms8.0 earthquake from digital strong earthquake networks in Sichuan and its neighbouring regions. Chin J Rock Mech Eng 29(9):1850–1858 (in Chinese)

Evaluation of Effective Stress of an Unsaturated Soil Under Cyclic Loading

57

T. Nishimura

Abstract

Earthquakes rapidly impose cyclic loading and soils respond in undrained conditions during seismic performance. Geotechnical earthquake engineering historically has focused extensively on evaluation of liquefaction resistance in sandy soils since deformations tend to be large when sandy soils experienced liquefaction. Recently, the role of unsaturated soil mechanics in geotechnical earthquake engineering is required for unsaturated soil structures subjected to cyclic loading or earthquake motion. The shear strength theory of unsaturated soils has been formulated in terms of two independent stress state variables (i.e., net normal stress and matric suction). This study conducted out undrained cyclic triaxial tests for compacted unsaturated soil. Both excess pore-water pressure and excess pore-air pressure were measured in unsaturated soil and described changing of matric suction during cyclic loading. The cyclic triaxial test was performed for saturated soil in order to compare with excess pore water pressure behaviour of unsaturated soil. This study focuses excess pore-water pressure as one component of effective stresses in unsaturated soil and saturated soil. The influence of matric suction on occurrence of excess pore-water pressure was appeared.

Keywords

Unsaturated soil · Matric suction · Cyclic triaxial test · SWCC

1 Introduction

Critical state framework is successful to analysis of soil liquefaction both under static and cyclic loads. There is also ambiguity about the definition of liquefaction, although fundamentally, it should be defined when the soil has reached a liquefied state with zero effective stress and strength in classic saturated soil mechanics (i.e., Terzaghi effective stress theory) (Yamamuro and Covert 2001). It may seem that the phenomenon of static liquefaction is conventionally explained using mean normal effective stress versus void ratio space.

T. Nishimura (✉)
Ashikaga Institute of Technology, Tochigi, Japan

Other hand, the seismic performance of geotechnical structure or earth structure namely; embankment, natural slope and retaining wall often require an estimate of potential and post-earthquake displacement. Earthquakes rapidly impose cyclic loading and soils respond in undrained conditions during seismic performance. Geotechnical earthquake engineering historically has focused extensively on evaluation of liquefaction resistance in sandy soils since deformations tend to be large when the sandy soils experienced liquefaction. However, Japan suffered from several large earthquakes which caused extensive damages to earth structures (Koseki et al. 2009). Liquefaction mechanism focuses on the influence of fine content on liquefaction potential (Monkul et al. 2011).

Recently, the role of unsaturated soil mechanics in geotechnical earthquake engineering is required for unsaturated soil structures subjected to cyclic loading or earthquake motion. The shear strength theory of unsaturated soils has been formulated in terms of two independent stress state variables (i.e., net normal stress and matric suction). At least controlling of matric suction is required to investigate the seismic performance of unsaturated soil subjected to cyclic loading. Nishimura et al. (2011) was successful to measure both pore-air pressure and pore-water pressure of compacted silty soil under monotonic loading using pressure membrane technique. The static liquefaction was observed on undrained triaxial compression testing.

This study conducted out undrained cyclic triaxial tests for compacted unsaturated soil. The relatively low matric suction was applied using pressure membrane technique. The matric suction was defined as the difference between pore-air pressure and pore-water pressure in this study. Both excess pore-water pressure and excess pore-air pressure were measured in unsaturated soil and described changing of matric suction during cyclic loading. The cyclic triaxial test was performed for saturated soil in order to compare with excess pore water pressure behaviour of unsaturated soil. In addition, cyclic loading was applied to re-saturated soil

Table 57.1 Summary of physical properties of silt used in this study

	Silt
Specific gravity	2.65
Percentage of sand fraction %	1.0
Percentage of silt fraction %	87.0
Percentage of clay fraction %	12.0
Liquid limit	24.7
Plastic limit	22.8
Plasticity index	1.9
United Soil Classification System	ML
Maximum dry density g/cm^3	1.53
Optimum water content %	17.0

Note ML = Low plastic silt
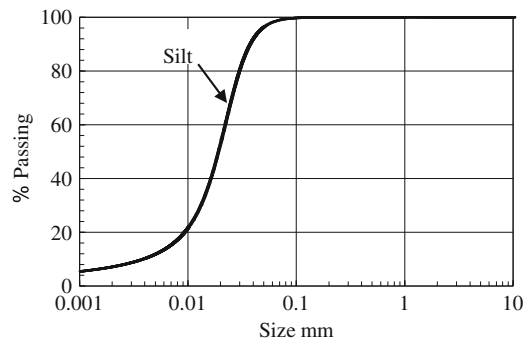
Fig. 57.1 Grain size distribution of silt

and increment of excess pore-water pressure was discussed. This study focuses excess pore-water pressure as one component of effective stresses in unsaturated soil and saturated soil. The influence of matric suction on excess pore-water pressure was appeared.

2 Test Procedure

2.1 Soil Materials

Silt was used in this test program. The properties of the soil are summarized in Table 57.1 and the grain size distribution curves are shown in Fig. 57.1.

Compaction test using standard mold employed in Japanese Industrial Standards (Test method for soil compaction using a rammer, JIS
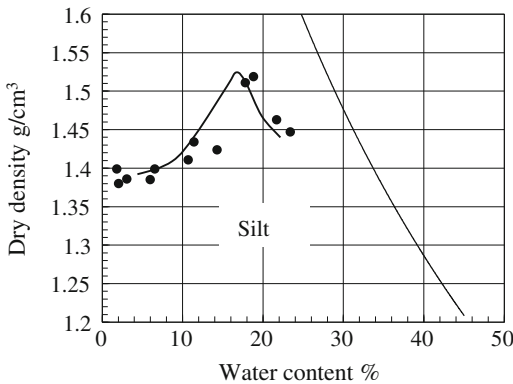
Fig. 57.2 Compaction curve of silt

Table 57.2 Micro-porous membrane used in the test program

Thickness μm	Air-entry value kPa	Pore diameter μm	Material
140	250	0.45	Polyether sulfone

A 1210: 2009) was performed for determination of a dry density of unsaturated cyclic triaxial tests. The mold for compaction test had a diameter of 100 mm and a height of 127.3 mm. The soil material was compacted in 3 equal layers with applying 25 numbers of blows and rammer drop height of 300 mm to each layer by 2.5 kg rammer in order to achieve compaction energy of 1Ec (where 1.0Ec = 551.25 kJ/m^3). Figure 57.2 describe the compaction curve (i.e., relationship between dry density and water content). The compaction curve described the maximum dry density of 1.53 g/cm^3 and the optimum water content of 17 %, respectively.

For cyclic triaxial tests, the soil specimens were statically compacted in the steel mold at the compacted water content of 10 %. The compacted soil sample had a dry density of 1.39 g/cm^3 (13.6 kN/m^3), a degree of saturation of 29.2 %. The compacted specimen had a diameter of 50 mm and a height of 100 mm, respectively.

2.2 Micro-Porous Membrane

The micro-porous membrane used in this study is cellulose consisting mainly of glucose and as a result, the membrane is essentially cellulosic biomass. The treatment of the micro-porous membranes for bacteria has been described in ASTM F838-83, 2002. The micro-porous membranes can be classified into either hydrophilic or hydrophobic membranes depending on their method of treatment. The properties of the micro-porous membrane used in this test program are summarized in Table 57.2.

Richards 1941 presented an experimental procedure for studying physical as well as chemical properties of soil solutions using the pressure membrane extraction apparatus. The apparatus composed a cellophane membrane, instead of a high air-entry disk. Recently, Nishimura et al. (2012) measured the soil–water characteristic curve (SWCC) of several soils using the micro-porous membrane described in Table 57.2. In addition, Nishimura et al. (2012) indicated that the equilibrium time required for the SWCC measurements using the micro-porous membrane was much shorter than the equilibrium time required when using the high air-entry ceramic disk. Nishimura et al. (2012) also measured SWCCs using different micro-porous membranes with varying air-entry values. The pressure difference across the micro porous membrane induced air diffusion (Tuwiner et al. 1962; Fick 1855). Fredlund 1975 mentioned that occurrence of air diffusion influenced the quality of unsaturated soil test results. Padilla et al. (2006) actually measured the mount of air diffusion for ceramic filter with different air entry values. As in previous test, the air diffusion was measured under a constant air pressure of 20 kPa. The amount of air diffusion was negligible.

2.3 Soil–Water Characteristic Curve Apparatus

The soil–water characteristic curve was measured using the modified SWCC apparatus in pressure membrane technique. The micro-porous membrane summarized in Table 57.2 was used in this
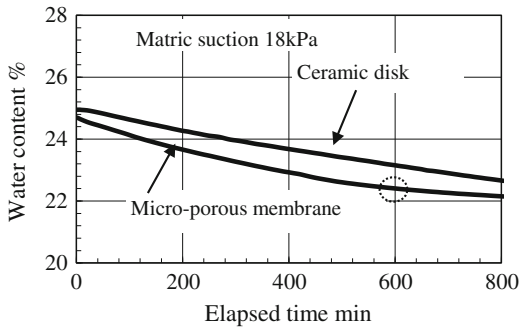
Fig. 57.3 Changing of water content in the pressure technique

Fig. 57.4 Cyclic triaxial apparatus for unsaturated soil

apparatus. The modified SWCC apparatus consisted mainly of a modified pedestal, a steel mold, a triaxial chamber and a double glass burette connected to a differential pressure transducer. A water compartment was located below the modified pedestal and was connected to the double glass burette. Soil water is allowed to flow into the double glass burette. A differential pressure transducer was attached to the lower portion of the double glass burette. The differential pressure transducer was calibrated to give a direct relationship between voltage and the volume of water in the double glass burette.

Comparisons regard to equilibrium time were made between micro-porous membrane and high air-entry disk (i.e., ceramic disk) having air entry value of 500 kPa. The SWCC tests were performed for statically compacted Inagi sand with the dry density of 1.55 g/cm^3. Figure 57.3 shows the changes in water content using both the micro-porous membrane and the ceramic disk when the applied matric suction was 18 kPa. At end of the test, the elapsed time was around 800 min. In the case of micro-porous membrane, the water content decreased significantly till the elapsed time of 600 min. Also, the specimen approached equilibrium with the applied matric suction.

In the case of ceramic disk, the decrement was lower than that of the micro-porous membrane. The specimen did not approach equilibrium at the end of test. The equilibrium time for the measurement was longer than that using the micro-porous membrane.

2.4 Cyclic Triaxial Apparatus

Figure 57.4 show a cyclic triaxial apparatus. The apparatus consist of vibrator, control equipment, tri-axial cell, supply system for cell pressure, pore-water pressure and pore-air pressure. The cell pressure, pore-water-pressure and pore-air pressure can be controlled independently. Inner cell was used for measuring volume change of the soil specimen. Volume change of soil specimen was measured using gap sensor installed into the inner cell. The gap sensor measured voltage changes which can be translated to volume changes. In addition, a solenoid controlled valve is installed near specimen cap which connected pressure sensor. The sensor with capacity of 200 kPa measured pore-air pressure in the specimen. The open or close of solenoid controlled valve was controlled outside of cell chamber. Figure 57.5 shows both the pressure sensor and solenoid controlled valve in the cell.

A double glass burette installed with a difference pressure sensor was connected to the triaxial cell. The difference pressure sensor measured the change of water in the soil specimen due to external isotropic loading or applied matric suction.

Unsaturated soil tests have been performed mainly using the axis translation technique (Richards 1938; Hilf 1948, 1956). The axis
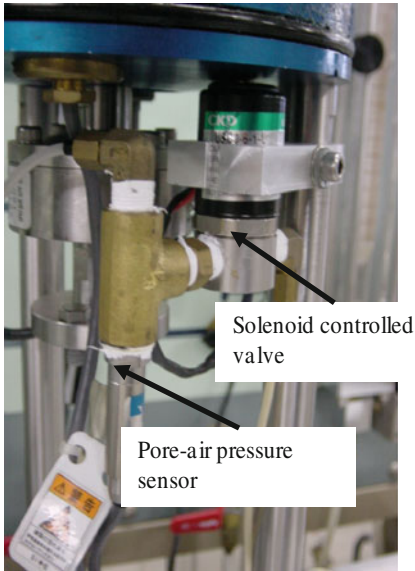
Fig. 57.5 Solenoid controlled valve and pore-air pressure sensor in the triaxial cell

Fig. 57.6 Modified pedestal for pressure membrane technique triaxial cell

translation technique consists of increasing the ambient air pressure to values greater than atmospheric pressure, so as to translate the pore-water pressure into the positive range. Olson and Langfelder 1965 measured the relationship between matric suction and soil moisture using a ceramic disk, and they called "pressure plate technique" similar to axis translation technique.

The micro porous membrane which had an air en-try value of 250 kPa was installed into the pedestal as shown in Fig. 57.6. The surface of the micro porous membrane is following the axis translation technique by Hilf (1956). A saturated micro-porous membrane with a diameter of 45 mm was placed on top of the saturated porous stone. Four bolts were used to fasten the modified pedestal to the steel mold.

2.5 SWCC Testing Program

The specimens were statically compacted in the mold. Two different dry densities were prepared for SWCC tests that were 1.41 g/cm^3 and 1.36 g/cm^3. Two compacted, unsaturated specimens were soaked in the triaxial chamber for a period of 24 h. It was reasonable to assume that

after soaking the matric suction of the specimen would decrease to values close to zero. Subsequently, the ambient air pressure was applied in the triaxial chamber. The specimens received air pressure from the top surface. The soil water began to drain in response to the applied air pressure. The soil water was drained to the double burette through a tube. The water in the double burette remained at atmospheric pressure. As a result, the applied matric suction was defined as the ambient air pressure because the matric suction was the difference between the pore-air and the pore-water pressures. After the specimen came to equilibrium with the matric suction, the air pressure was progressively increased to 20 kPa following the drying path.

At the end of the test, the gravimetric water content (i.e., water content) of the specimen corresponding to each applied matric suctions was computed using a back-calculation procedure. Then the soil–water characteristic curve was determined.

2.6 Cyclic Undrained Triaxial Testing Program

Cyclic undrained triaxial testing consists three cases in this study. Figure 57.7 shows flow of cyclic triaxial testing program. All compacted,

Fig. 57.7 Flow of cyclic
triaxial testing program

```
┌─────────────────────────────────────────────┐
│      Compacted unsaturated specimen           │
└─────────────────────────────────────────────┘
                      │
                      ▼
┌─────────────────────────────────────────────┐
│    Apply net normal pressure of 100 kPa       │
└─────────────────────────────────────────────┘
                      │
                      ▼
┌─────────────────────────────────────────────┐
│    Saturation duet to apply back pressure     │
└─────────────────────────────────────────────┘
                      │
                      ▼
┌─────────────────────────────────────────────┐
│  Consolidation under effective stress of 100 kPa │
└─────────────────────────────────────────────┘
          │                            │
          ▼                            ▼
┌──────────────────────┐    ┌──────────────────────┐
│ Apply matric suction  │    │ CASE 1: Cyclic        │
│ of 20 kPa and net     │    │ triaxial test under   │
│ normal stress of      │    │ undrained condition   │
│ 100 kPa               │    │                       │
└──────────────────────┘    └──────────────────────┘
          │
          ▼
┌──────────────────────┐    ┌──────────────────────────────┐
│ CASE 2: Cyclic triaxial│   │ Re-saturation duet to apply  │
│ test under undrained-  │   │ hydraulic head of 50 cm      │
│ exhaust condition      │   │ under effective stress       │
│                        │   │ of 100 kPa                   │
└──────────────────────┘    └──────────────────────────────┘
                                          │
                                          ▼
                            ┌──────────────────────┐
                            │ CASE 3: Cyclic        │
                            │ triaxial test under   │
                            │ undrained condition   │
                            └──────────────────────┘
```

unsaturated specimens were applied a net normal stress of 100 kPa under undrained-exhaust condition. After consolidation equilibrium, back pressure was applied from bottom portion through pedestal. It was assumed the specimen reached to saturation even if degree of saturation is not equal to 100 %. Subsequently, back pressure reduce to zero and effective stress of 100 kPa was remained in the specimen. The cyclic triaxial test was performed to the saturated specimen under undrained condition in CASE 1. The excess pore-water pressure was measured.

In CASE 2, a matric suction of 20 kPa was applied to saturated specimen under net normal stress of 100 kPa. The pressure membrane technique was used to the specimen. After the specimen equilibrium matric suction of 20 kPa, the cyclic triaxial test was performed to unsaturated specimen under undrained-exhausted condition. Both the excess pore-water and pore-air pressure was measured. The pore-water pressure was measured at outside of triaxial cell and the pore-air pressure was measured by pressure sensor installed at the solenoid controlled valve.

Head of water 50cm
Hydraulic conductivity 4.18×10^{-6} m/sec
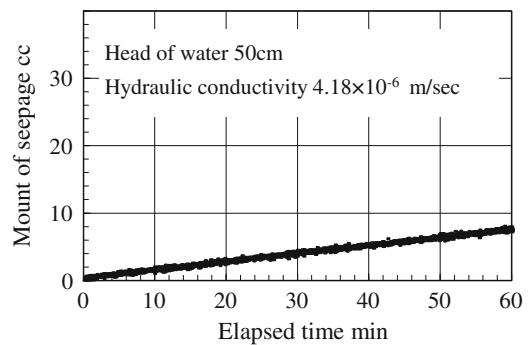
Fig. 57.8 Result of hydraulic conductivity test

In CASE 3, the unsaturated specimen with matric suction of 20 kPa was soaked through the micro-porous membrane under a head of water of 50 cm. The unsaturated sample reached to re-saturation. Figure 57.8 shows relationship between mount of seepage flow and elapsed time under a head of water of 50 cm in sample. Hydraulic conductivity was determined as 4.18×10^{-6} m/sec. Subsequently the re-saturated sample was supplied cyclic loading under undrained condition.
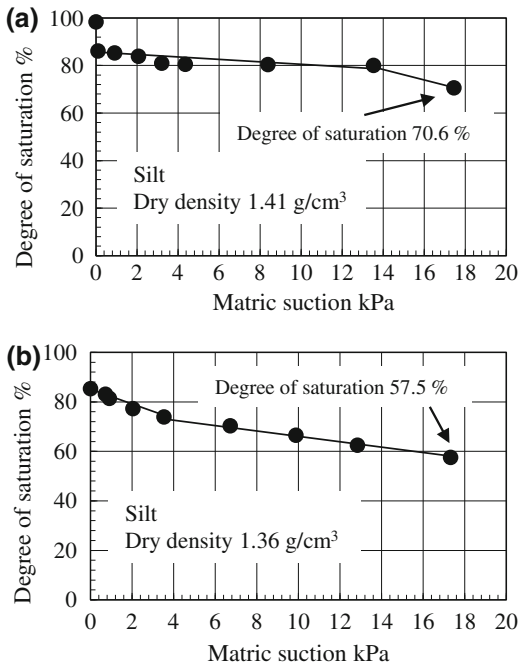
Fig. 57.9 **a** SWCC of silt (dry density is 1.41 g/cm^3). **b** SWCC of Silt (dry density is 1.36 g/cm^3)

In all test cases, initial cyclic stress ratio was 0.24 and applied loading frequency was 1.0 Hz. Sampling frequency was 50 Hz. Sensor interface used in testing was PCD 30A (KYOWA Co. Ltd.).

3 Test Results

3.1 Soil–Water Characteristic Curve

Figure 57.9a, b show the changes in degree of saturation for Silt with two dry densities. For the dry density of 1.41 g/cm^3 (13.8 kN/m^3), degree of saturation decreased to 86 % at beginning of applying of pore-air pressure. Degree of saturation decreased smoothly till matric suction was 13.5 kPa. It was 70.6 % when matric suction was 17.4 %.

For the dry density of 1.36 g/cm^3 (13.3 kN/m^3), degree of saturation described 81.3 % when matric suction was 0.9 kPa. Degree of

Fig. 57.10 **a** Change of excess pore-water pressure for saturated sample. **b** Change of effective confining pressure for saturated sample

saturation decreased linearly with increasing of matric suction and described 57.5 % at matric suction of 17.3 kPa. The influence of dry density on soil–water characteristic curve was described at range from 0 kPa to 20 kPa in matric suction.

3.2 Change in Effective Stress Under Undrained Condition Due to Cyclic Loading

Figure 57.10a shows increasing of excess pore-water pressure of saturated specimen in CASE 1. The saturated sample had an effective confining

pressure of 100 kPa before cyclic loading. The excess pore-water pressure increased rapidly at beginning of cyclic loading. Increment of excess pore-water pressure was constant when cyclic number was from ten to forty. After number was forty, increment of excess pore-water pressure became large and approach to 100 kPa at number of forty-four. Figure 57.10b shows decreasing of effective confining pressure under cyclic loading. The confining pressure was zero when cyclic number was forty-four. Double amplitude of linear strain (DA) was 6.3 % at end of test.

Figure 57.11a shows change in excess pore water pressure of unsaturated sample. The specimen was supplied both matric suction of 20 kPa and net normal stress of 100 kPa. The excess pore-water pressure was measured in unsaturated condition. At beginning of cyclic loading excess pore-water pressure occurred. The excess pore-water pressure approached to 20 kPa when cyclic number was around ten. Beyond number was twenty, the excess pore water pressure of 20 kPa remained till end of test. Maximum excess pore-water pressure of unsaturated sample is less than that of saturated sample as shown in Fig. 57.10a. Measured pore-air pressures were absolutely small and possible to neglect. The matric suction was calculated which was defined as deference between pore-air pressure and pore-water pressure. The matric suction decreased to zero due to cyclic loading as shown in Fig. 57.11b. The cyclic loading under undrained condition caused the decreasing of effective stress for unsaturated sample. Also double amplitude of linear strain (DA) was 0.2 % at end of test. It was smaller than that of saturated sample.

Re-saturation was performed for unsaturated sample with matric suction of 20 kPa in testing program CASE 3. It was described that re-saturated sample indicated increment of excess pore-water pressure due to cyclic loading. Figure 57.12a shows change in excess pore-water pressure. The excess pore-water pressure
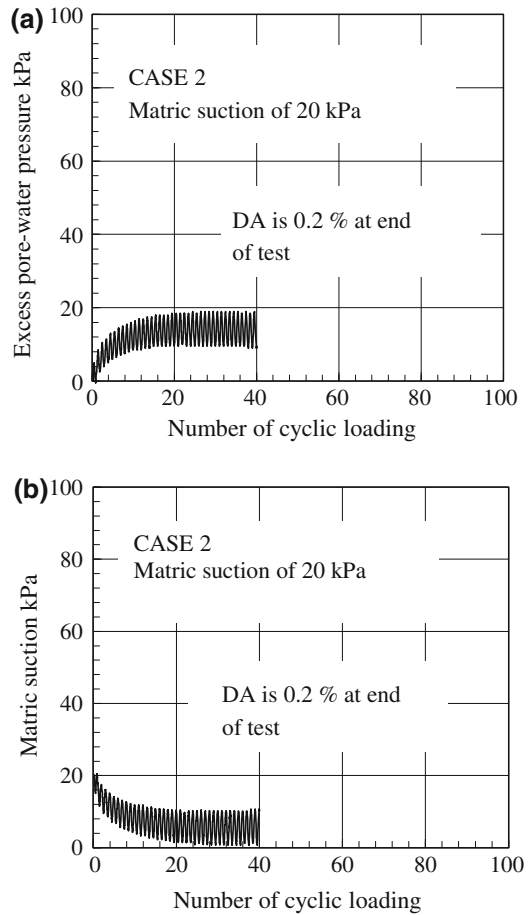
Fig. 57.11 **a** Change of excess pore-water pressure for unsaturated sample. **b** Change of matric suction for unsaturated sample

increased rapidly similar to saturation sample in testing program CASE 1. Increment of excess pore-water pressure was smooth until cyclic number was seventy. Beyond seventy, excess pore-water pressure indicated large increment and approach to 100 kPa. The effective confining pressure approach to zero at around eighty cycles. Double amplitude of linear strain (DA) was 7.8 % at end of test. DA increased due to decrease of matric suction.
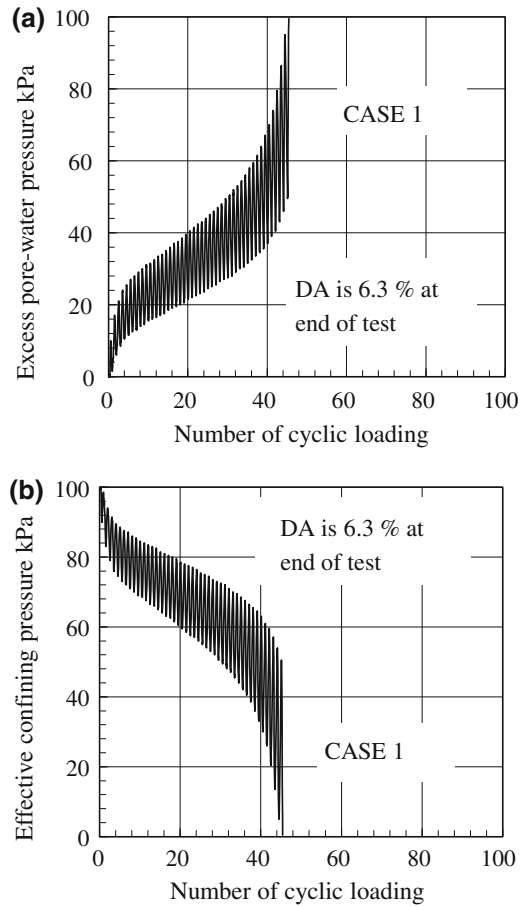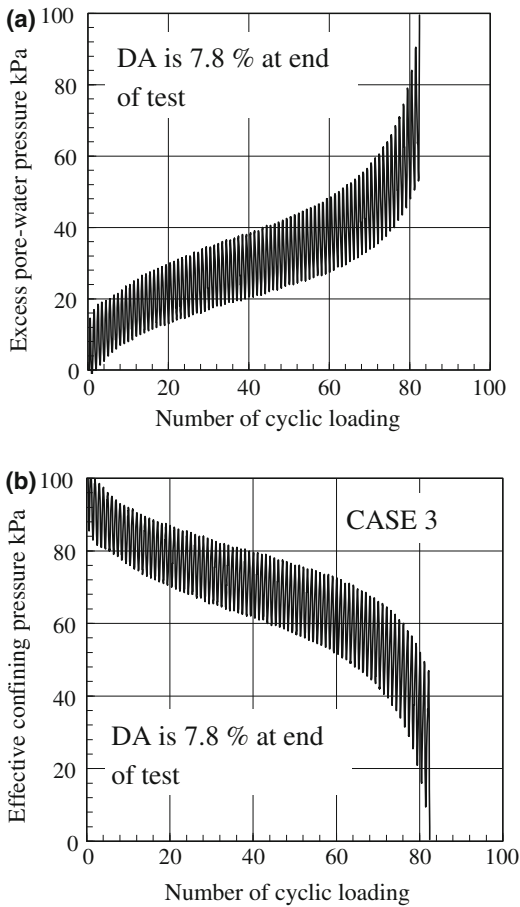
Fig. 57.12 **a** Change of excess pore-water pressure for re-saturated sample. **b** Change of effective confining pressure for resaturated sample

compacted unsaturated soil with two different dry densities.

(1) Soil–water characteristic curve using pressure membrane technique described that magnitude of dry density influenced the relationship between matric suction and degree of saturation.

(2) Increment of pore-air pressure was absolutely small in unsaturated soil subjected to cyclic loading and would be negligible. Matric suction in unsaturated soil decreased due to occurrence of excess pore-water pressure.

(3) In saturated sample or re-saturated sample, large excess pore water pressure was generated. Effective confining pressure approached to zero by cyclic loading.

(4) Double amplitude of linear strain (DA) for unsaturated soil at end of cyclic triaxial test increased due to saturation (i.e., delete matric suction).

References

Fick A (1855) Ueber diffusion. Ann der Phys (Leipzing), 94:59–86

Fredlund DG (1975) A diffused air volume indicator for un-saturated soils. Can Geotech J 12:533–539

Koseki J, Nakajima S, Tateyama M, Watanabe K, Shinoda M (2009) Sesmic performance of geosynthetic-reinforced soil retaining walls and their performance-based design in Japan. In: Proceedings of the international conference on performance-based design in earthquake geotechnical engineering, IS-Tokyo pp 149–162

Hilf, J. W (1948) Estimating construction pore pressures in rolled earth dams. In: Proceedings of 2nd international conference on soil mechanics and foundation engineering, Rotterdam, Vol.III: 234–240

Hilf JW (1956) An investigation of pore-water pressure in compacted cohesive soils, Ph.D. Dissertation, Tech. Memo. No. 654, U.S. Department of the

4   Conclusions

This study conducted using cyclic triaxial tests for unsaturated soil. The relatively low matric suction was applied to compacted unsaturated sample using pressure membrane technique. Excess pore-water pressures were focused in order to evaluate effective stress of unsaturated soil and saturated soil. Also, soil–water characteristic curve tests were performed for

interior, bureau of reclamation, design and construction division. Denver, CO., 654

Monjkul MM, Yamamuro JA (2011) Influence of silt size and content on liquefaction behavior of sands. Can Geotech J 48:931–942

Nishimura T, Koseki J, Rahardjo H (2011) Effect of density for sand on hysteresis in soil-water characteristic curve. 5th Asia-Pacific conference on unsaturated soils, UNSAT-Asia pp 391–396

Nishimura T, Koseki J, Fredlund DG, Rahardjo H (2012) Micro-porous membrane technology for measurement of soil-water characteristic curve. Geotech Test J, the American Society for Testing and Materials, American Society for Testing and Materials, 35:201–208, GTJ103670

Olson RE, Langfelder LJ (1965) Pore water pressure in unsaturated soils. J Soil Mech Found Div, Proc Am Soc Civil Eng, SM4: 127–150

Padilla JM, Perera YY, Houston WN, Perez N, Fred-lund DG (2006) Quantification of air diffusion through high air-entry ceramic disk. In: Proceedings of the fourth international conference on unsaturated soils, UNSAT 2006, Arizona, 2:1852–1863

Richards SJ (1938) Soil moisture content calculations from capillary tension records. Soil Science Society of America, Proceedings 3:57–64

Richards LA (1941) A pressure membrane extraction apparatus for soil suction. Soil Sci 51:377–386

Tuwiner SB, Miller LP, Brown WE (1962) Diffusion and membrane technology. Reinhold Publishing Corporation. pp 38–61

Yamamuro JA, Covert KM (2001) Monotonic and cyclic liquefaction of very loose sands with high silt content. J Geotech Geoenvirom Eng 127(4):314–324

Analysis of the Factors Affecting Slope Failures Distribution Within Northern Kanto Area due to The East Japan Great Earthquake

58

Takanori Kimura, Akihiko Wakai and Kunihiro Higuchi

Abstract

In this study, the factors affecting various types of slope failures in the Northern Kanto area, i.e., the input motion, the geological and geomorphological conditions, are analyzed by the observed distribution of the slope failures due to the East Japan Great Earthquake. The data for the location of each slope failure have been collected from the prefectural government offices as well as our site investigation for the study area. The observed data for the strong ground motion were referred to the K-net website managed by The National Research Institute for Earth Science and Disaster Prevention, Japan. The distribution of the acceleration response spectrum in the range of longer periods calculated from the above data was found to have a correlation to the deep-seated landslides distributions. It was also found that, the thicker the loam depth in the ground, the higher the landslide risks.

1 Introduction

On March 11, 2011 at 14:46 pm, The 2011 off the Pacific coast of Tohoku Earthquake, which generated on the offing of Pacific Ocean as the seismic center, caused serious disaster at the whole East Japan, Kanto from Tohoku. Moreover, this earthquake caused many large-scale slope disasters. As a result, collapse of roads and buildings were caused as well.

In order to reduce the damages caused by the slope disaster at the time of such an earthquake disaster, it is very important to understand the tendency of the distributions of these slope disasters.

2 Purpose of Study

The type of the slope disaster caused by the earthquake is changed by geomorphological

T. Kimura (✉) · A. Wakai
Gunma University, Gunma, Japan

K. Higuchi
Kuroiwa Survey and Design Office Co., Ltd,
Gunma, Japan
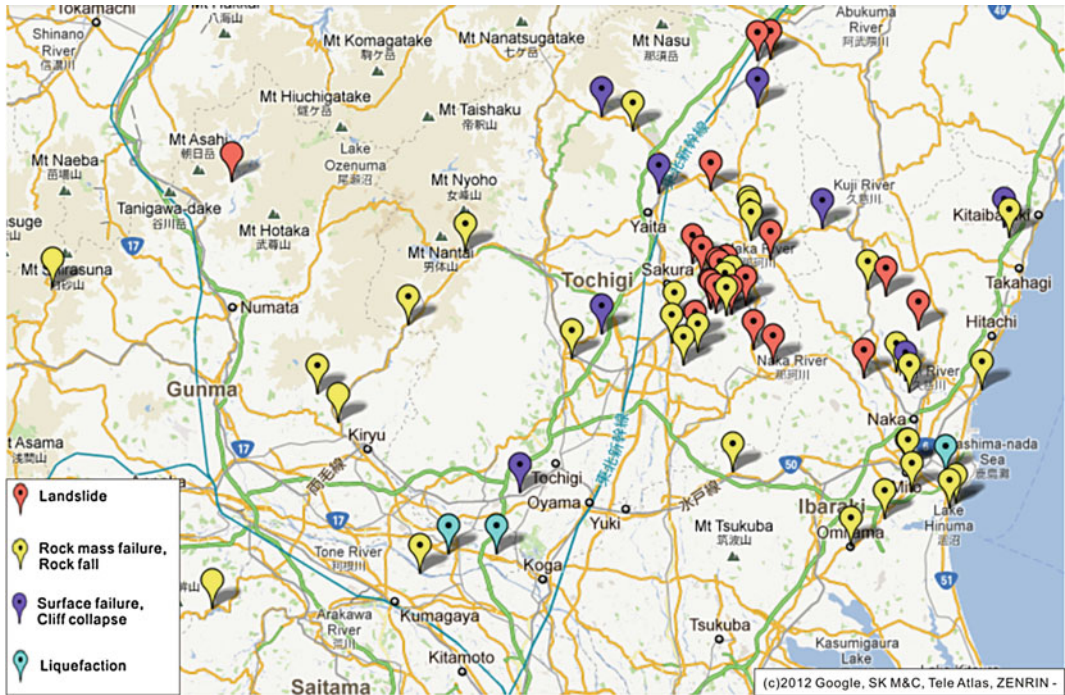
Fig. 58.1 Distribution of the slope disasters in the north Kanto area.tif

conditions, geological conditions and earthquake motion characteristics. This research analyzes how these conditions influence generating of the slope disasters.

3 Types and Distributions Map of Slope Disasters

The North Kanto area is the investigation scope in this study. The northern end of this area borders on south part of Fukushima prefecture where the slope disasters were serious. On the other hand, the southern end of this area borders on the metropolitan area where the soil disasters hardly occurred, except for liquefactions near the reclaimed land and the entrance of rivers. This area is the southern limit of the area where the inland slope disasters were conspicuous. The south part of this area is in contact with the north edge of the Kanto Plain. The other area is occupied by the alluvial fan, the latest volcanic products, the hills and mountains formed by the upheaval since the Tertiary Period.

Distribution of the slope disasters which occurred in this earthquake in the North Kanto area is shown in Fig. 58.1 In this figure, the slope disasters are classified with the characteristics and generation mechanisms.

Type1: Landslide (especially for deep-seated landslides).

Type2: Rock mass failure, Rock fall.

Type3: Surface failure, Cliff collapse.

Locally, the landslides of the volcanic clayey slopes which occurred intensively in the middle east of Tochigi prefecture are very characteristic. In the other area, on the whole, many slope failures in steep slopes and the rock mass failures in rock slopes, e.g. tuff, occurred.

Figure 58.2 shows that these slope disasters correlate with topographic classification. There are many failures as Type1 in terraces and edges of plain, On the other hand, Type2 are in mountains in Ashio and Nikko, and Type3 are in areas with local steep cliffs.

Discussing the above from a viewpoint of geology, occurrence of landslides in the east and north of Tochigi prefecture are characteristic.
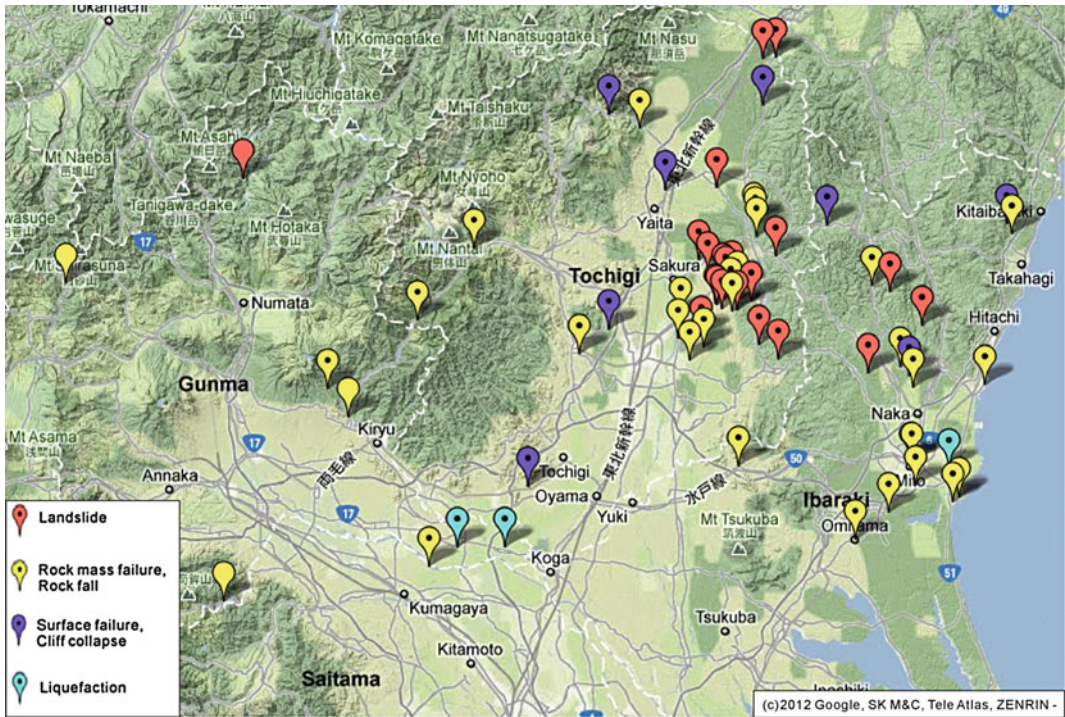
Fig. 58.2 Distribution of the slope disasters in the north Kanto area (with topographic map).tif

These landslides were directly affected by geographical features which tend to amplify the earthquake motion (cf. ridges and head of terraces). And they were also affected by cyclic softening of thick clayey layer. Furthermore, these areas have catchment topography, and the debris with high liquidity caused long-distance movement and brought serious damages to the lower part of the slopes.

Figure 58.3 shows the landslide which occurred on a gentle slope in Kanaga, Nasukarasuyama city, Tochigi prefecture. It seems that material of the upper part of the slope became weak, enough to be fluidized by the earthquake motion.

In addition to the above, comparing Fig. 58.4 of the loam-layers thickness distributions in Tochigi prefecture with Fig. 58.1 of the damaged slopes, it is found that the loam layers and the generation of landslides have correlations.

Other than these landslides, various slope disasters occurred. Figure 58.5 shows various rock mass failures. Firstly, Fig. 58.5a shows a

Fig. 58.3 Landslide in Kanaga, Nasukarasuyama city.tif

rock mass failure in Mt. Iwafune, Tochigi prefecture. Many joints are observed in the rock mass which consists of tuff breccia. The thin ridge collapsed as V-shape. Secondly, Fig. 58.5b shows a rock mass failure in Daigo town, Ibaraki. The slope consisting of white tuff of Tertiary Period was collapsed.

Fig. 58.4 Distribution of thickness for loam layer in Tochigi (m).tif
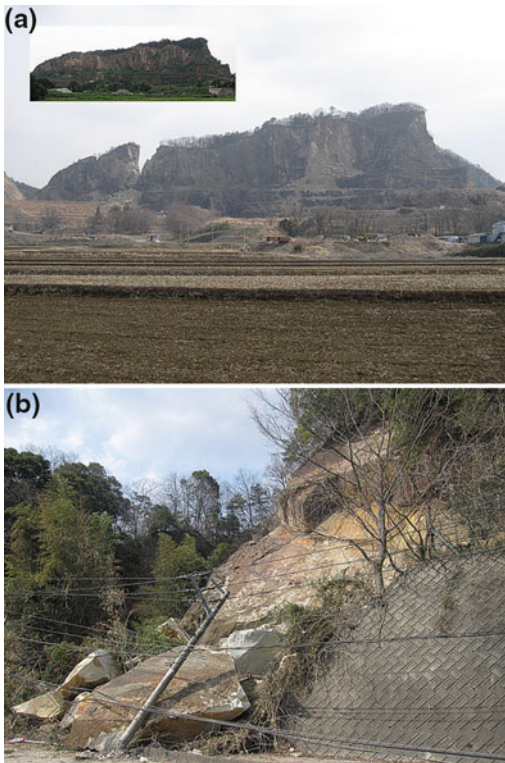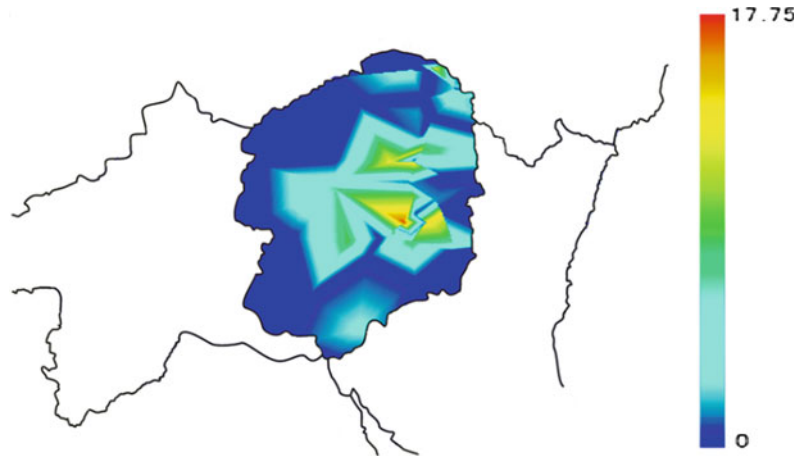
Fig. 58.5 **a** Rock mass failure at Mt. Iwafune, Tochigi prefecture.tif **b** Rock mass failure in Daigo town, Ibaraki prefecture.tif

Figure 58.6 shows many surface failures. The examples which occurred in the river terrace are shown in the Fig. 58.6a, b. And the example which occurred at the eroded seashore cliff is shown in the Fig. 58.6c. As for these examples,

collapsed soil remained in the lower part of the slope. These damages were limited.

4 Analytical Method

Generally, earthquake waves which are observed at the ground surface are influenced by their seismic response characteristics. Therefore, it can not be always suitable for strict analyses. However, because of its convenience, in this study, the earthquake motion data observed by K-net (NIED) in north Kanto area were used, in order to analyze the correlativity of distributions of various slope disasters and the ground surface motions.

5 Comparison with the Earthquake Motion

The contour map for PGA (Peak Ground Acceleration) is shown in Fig. 58.7. There are clear concentrations in the both of the littoral and inland regions in the northern Ibaraki. Comparing this map with Fig. 58.1, cliff collapses and slope failures occurred intensively within these concentrations. Accordingly, there is a correlativity in these slope disasters and PGA distribution. The contour map for PGV (Peak Ground Velocity) is shown in Fig. 58.8. There is a concentration in Nasukarasuyama

Fig. 58.6 **a** Surface failure in Utsunomiya city, in Tochigi prefecture.tif. **b** Surface failure in Nakagawa town, Tochigi prefecture.tif. **c** Surface failure in Hitachi city, Ibaraki prefecture.tif

city, Tochigi prefecture where many landslides occurred. Accordingly, there seems to be a correlativity in landslides and PGV distribution.

In addition, acceleration response spectrums calculated based on the earthquake wave observed at the ground surface are investigated in detail.

About the NS and EW seismic motions, the contour maps of the averaged value of the acceleration response spectrums (about the periodic band for 0.1–0.4 s) are shown in Fig. 58.9 and 58.10, respectively. Similarly, the contour maps about the periodic band for 1.0–2.0 s are shown in Figs. 58.11 and 58.12.

As seen in Figs. 58.9 and 58.10, there are clear concentrations both in the littoral and inland regions in the northern Ibaraki, which is similar to PGA. According to this, it seems that the cliff collapses and slope failures were influenced by the shorter period of the acceleration response spectrums.

As seen in Figs. 58.11 and 58.12, there is a clear concentration in Nasukarasuyama city, Tochigi prefecture. The natural vibration period of the slopes where the loam is accumulated thickly is supposed to be around the periodic band. This is in agreement with the fact that there are many deep-seated landslides around Nasukarasuyama city.

6   Conclusions

The obtained results are summarized as follows:
(1) In this earthquake, there occurred many surface failures and rock mass failures in North Kanto area. Locally, the occurrence of landslides in Tochigi prefecture was characteristic.
(2) Many landslides in Tochigi prefecture affected by the cyclic softening of the aeolian loam. These landslides were directly affected by the geographical features which tend to amplify the earthquake motion. It turned out that there was a correlativity between the distribution of these landslides and the loam layer thickness in Tochigi prefecture.
(3) About the earthquake motion, the shorter period of acceleration waves tend to affect surface failures. On the other hand, the longer period of acceleration waves (i.e., the

Fig. 58.7 Distribution of
PGA (Gal).tif
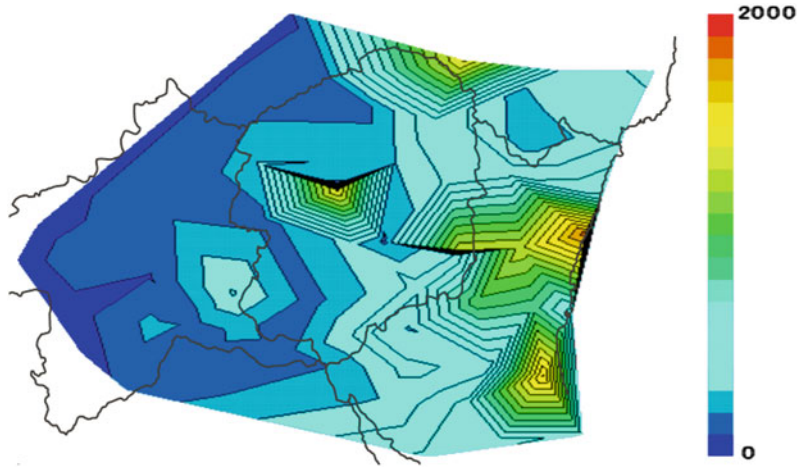
Fig. 58.8 Distribution of
PGV (Kine).tif
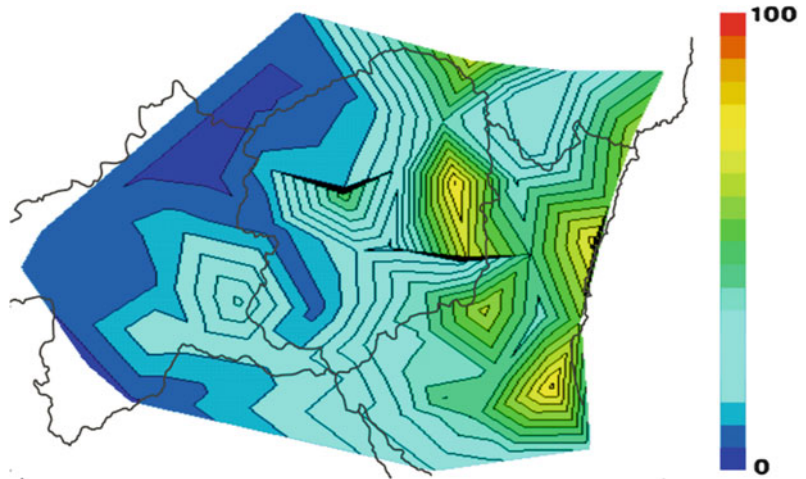
Fig. 58.9 Distribution of
averaged values of the
acceleration response
spectrum (NS), at the
period bands for 0.1–0.4 s
(Gal).tif
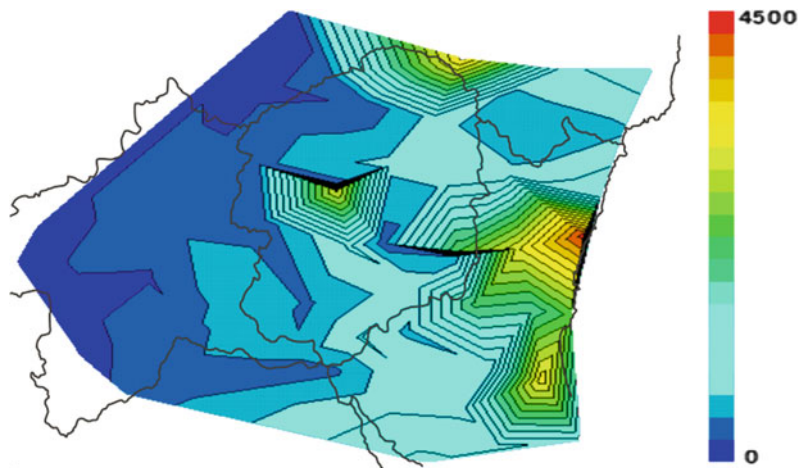
Fig. 58.10 Distribution of averaged values of the acceleration response spectrum (EW), at the period bands for 0.1–0.4 s (Gal).tif
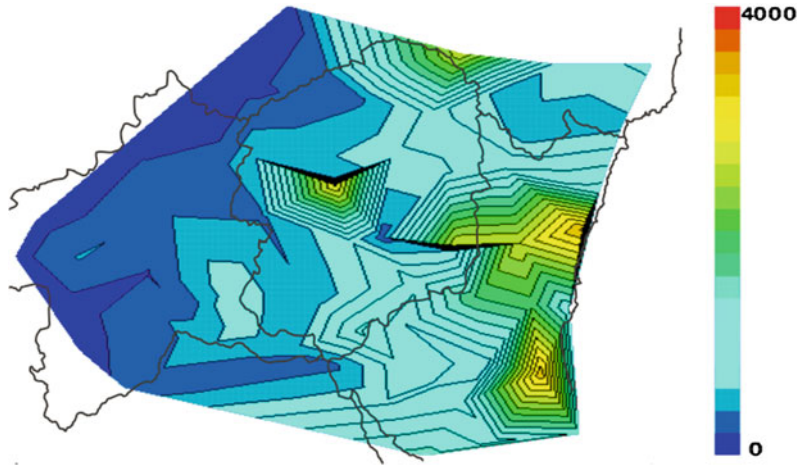
Fig. 58.11 Distribution of averaged values of the acceleration response spectrum (NS), at the period bands for 1.0–2.0 s (Gal).tif
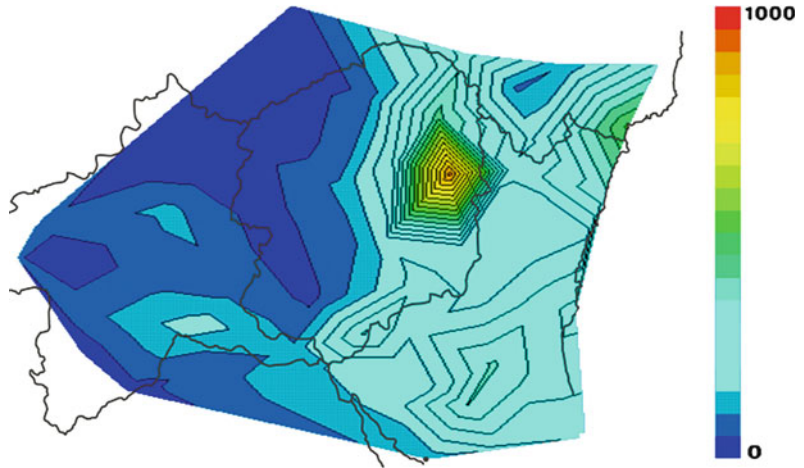
Fig. 58.12 Distribution of averaged values of the acceleration response spectrum (EW), at the period bands for 1.0–2.0 s (Gal).tif
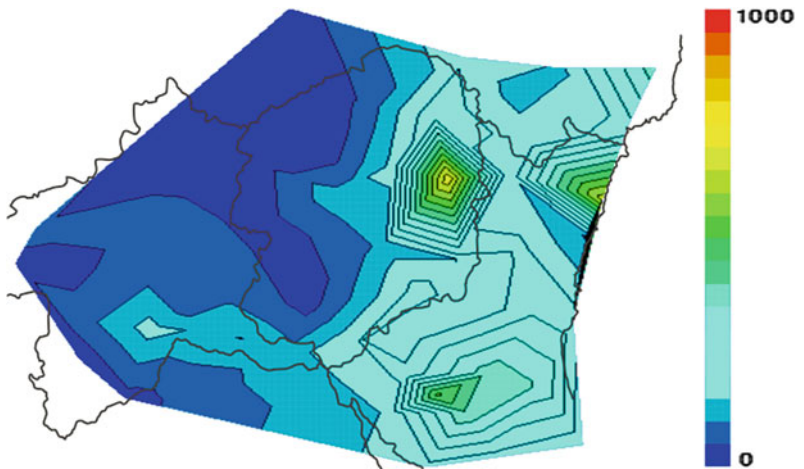
velocity) tend to affect deep-seated landslides.

Reference

Wakai A, Higuchi K (2011) Slope disasters in northern Kanto area induced by The 2011 off the Pacific Coast of Tohoku earthquake (Part 1). In: Proceeding 50th annual meeting of the japan landslide society, pp 5–6 (in Japanese)

Landslide Risk Evaluation in a Suffered Inland Area in Tochigi Prefecture Due to the Great East Japan Earthquake

59

Asumi Tabata, Akihiko Wakai, Kazunori Hayashi,
Norihiro Tanaka and Shinro Abe

Abstract

In this study, an effective numerical system is used to evaluate the landslide risk in a suffered inland area in Tochigi Prefecture due to the Great East Japan Earthquake on March 11th, 2011. Around the investigated area, a large number of landslides, with long-distance for soil movement, is occurred especially near the sharp slopes and terraces. It is mainly composed of sensitive volcanic and loamy clay under the conditions where the level of groundwater was high. In our numerical analysis, the soils are modeled as elasto-plastic materials with considering appropriate hysteretic characteristics under cyclic loading conditions during earthquake. The obtained results are compared with the actual landslide distributions to verify the proposed system.

1 Introduction

Many slope disasters were induced in a wide area from Tohoku to North Kanto by the Great East Japan Earthquake (Fig. 59.1). Particularly, characteristic slope disasters concentrated in the Middle Eastern district of Tochigi Prefecture (Kimura et al. 2012). In this study, the characteristics of the slope disaster in the area are analyzed. Moreover, an effective numerical system is used to evaluate the landslide risk in the investigated area.

2 Target Area and Slope Disasters

2.1 Description for the Investigated Area

The investigated area is a range over Takaneza-wa-town and Nasukarasuyama-city (approximately 6 km × 6 km) located in the Middle

A. Tabata (✉) · A. Wakai
Gunma University, Gunma, Japan
e-mail: tabata@geotech.ce.gunma-u.ac.jp

K. Hayashi · N. Tanaka · S. Abe
Okuyama Boring Co., Ltd, Yokote, Japan
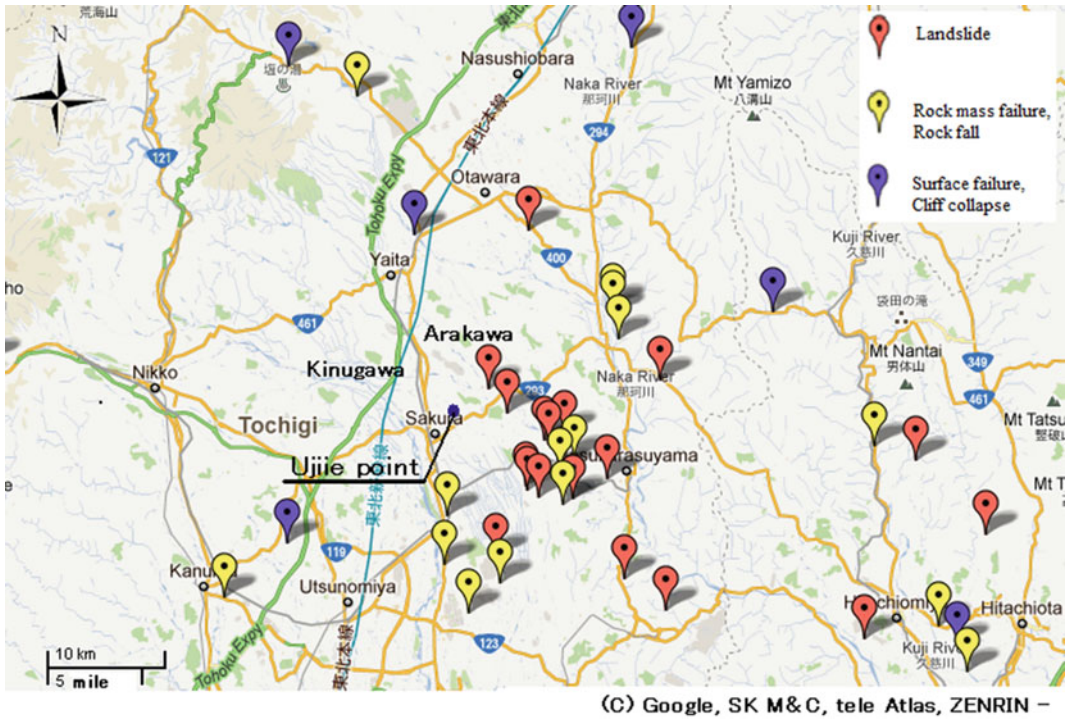
Fig. 59.1 Distribution of damaged slopes

Fig. 59.2 Closed view of the center part of Figure 1

Fig. 59.3 Landslide in Sanga district

Eastern district of Tochigi Prefecture (Fig. 59.2). This area is formed as the low lands and the terraces. The low lands are formed by Kinugawa lying in the western part and Arakawa lying in the eastern part. The terraces are formed by the relatively thick sedimented loam. As typically the loam was disturbed by the earthquake motion, it suddenly lost the strength and caused the catastrophic landslide.

Fig. 59.4 Landslide in Kami-Kashiwazaki district (a)

Fig. 59.6 Landslide in Fujita district

Fig. 59.5 Landslide in Kami-Kashiwazaki district(b)

2.2 Slope Disasters in the Area

Figure 59.3 is at the right bank of Arakawa in Sanga district, Nasukarasuyama-city. The slope mainly consists of volcanic cohesive soil. The landslide caused a long-distance movement due to the fluidization of soil. Thereby, natural dam was caused temporally in Arakawa adjacent to the slope.

Figures 59.4, 59.5 show the damaged slopes in the Kami-Kashiwazaki district, Takanezawa-town (Usami et al. 2011). In this area, two places of landslides occurred at the top along the terrace row. In similar to Sanga district, the material in the slope is supposed to be mainly composed of volcanic cohesive soil. In addition, the cracks running intermittently 600 meters occurred at the top of the cliff. The inclination and the relative height of both slopes are approximately 35° and 25 meters, respectively. The sliding block involving the foot of the cliff was strongly disturbed and moved 40 m horizontally in both slopes. A portion of the debris behaved like fluid and was finally moved approximately 100 meters downward along the valley. Abundant groundwater supplied from the rear area may promote the movement, which was suggested by the fact that a little flooding was observed in a concave topography adjacent to the cliff foot after the earthquake.

Figure 59.6 show the damaged slope in Fujita district, Nasukarasuyama-city. In this area, the landslides of two places, one is big and the other is small, occurred. Similarly, the material in the slope is supposed to be mainly composed of volcanic cohesive soil. In this spot, the fluidity is in particular remarkable; a portion of the debris behaved like fluid and was finally moved approximately 200 meters downward.

3 Method of Analysis

3.1 System of Analysis

The earthquake-induced landslide risk is studied in the area mentioned above, using "The wide-area seismic intensity prediction system with FEM" summarized in Wakai et al. (2008), Hayashi et al. (2011). To carry out a prediction of the seismic intensity systematically, the whole

Fig. 59.7 Substructure
and core domain in the
analysis

Fig. 59.8 Altitude of ground surface
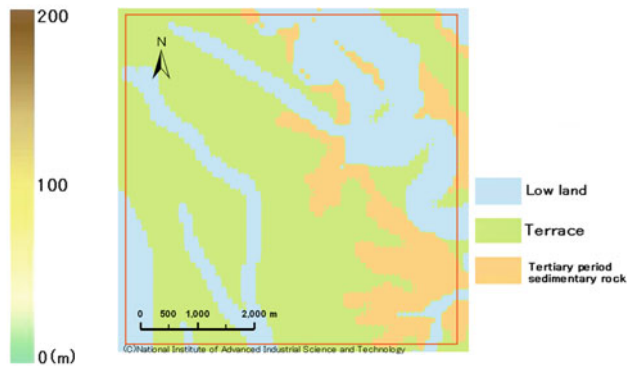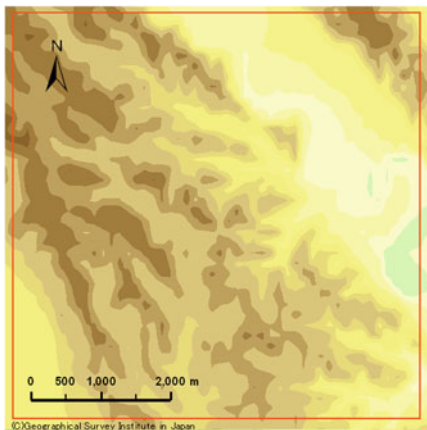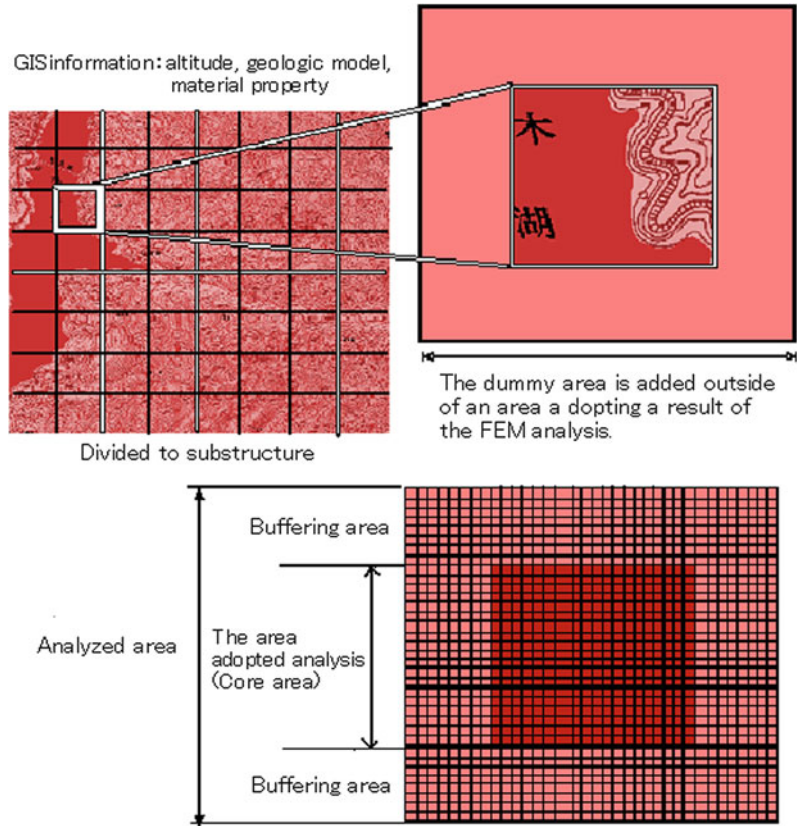
Fig. 59.9 Geological features distribution

objective area is divided into substructures
through GIS. To reduce the influence of reflection
waves at the end of each substructure, the dummy
area is added outside of the area where the results

of the FEM analysis are adopted (Fig. 59.7). The
model considering both of the shear strength and
the dynamic deformation characteristics (Wakai
and Ugai 2004) was applied to the constitutive
model of soils in the analysis.

Table 59.1 Input material properties

Layers	Physical property	Depth	Thickness (m)	Geological features	Unit weight (kN/m^3)	Young's modulus (kN/m^2)	Poisson's ratio	Internal frictional angle (°)	Cohesion (kN/m^2)	B·γ·G$_0$	N	Rayleigh damping α	β
1	Low land	1	10	Sand and gravel	19	124,000	0.45	15	30	1.25	2.27	0.171	0.00174
		2	20	Sand and gravel	21	959,000	0.40	40	50	1.48	2.35	0.171	0.00174
		3	30	Sand and gravel	22	1,514,000	0.35	40	100	1.48	2.35	0.171	0.00174
		4	100	Base rock	24	5,989,000	0.25	40	1,000	1.33	2.4	0.171	0.00174
2	Terrace	1	10	Loam	16	46,000	0.45	20	30	1.35	1.9	0.171	0.00174
		2	20	Sand and gravel	21	959,000	0.40	40	50	1.48	2.35	0.171	0.00174
		3	30	Sand and gravel	22	1,514,000	0.35	40	100	1.48	2.35	0.171	0.00174
		4	100	Base rock	24	5,989,000	0.25	40	1,000	1.33	2.4	0.171	0.00174
3	Tertiary period sedimentary rock	1	10	Surface soil	19	868,000	0.40	25	50	2.35	2.15	0.171	0.00174
		2	20	Weathered soil	21	2,081,000	0.35	40	200	1.92	2.21	0.171	0.00174
		3	30	Base rock	22	3,732,000	0.30	40	500	1.30	2.53	0.171	0.00174
		4	100	Base rock	24	5,989,000	0.25	40	1,000	1.33	2.4	0.171	0.00174

Fig. 59.10 N−S
component of input motion
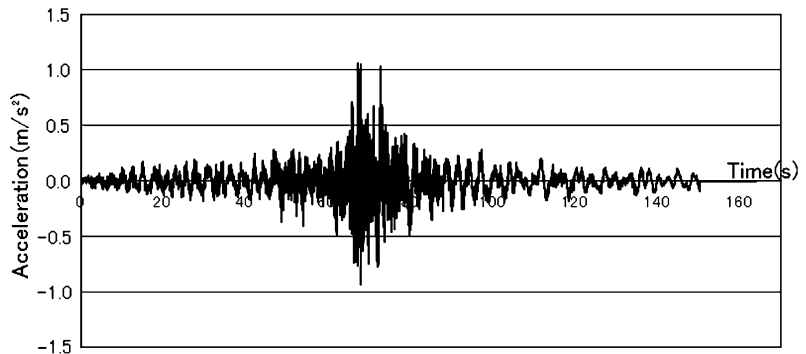
Fig. 59.11 E−W
component of input motion
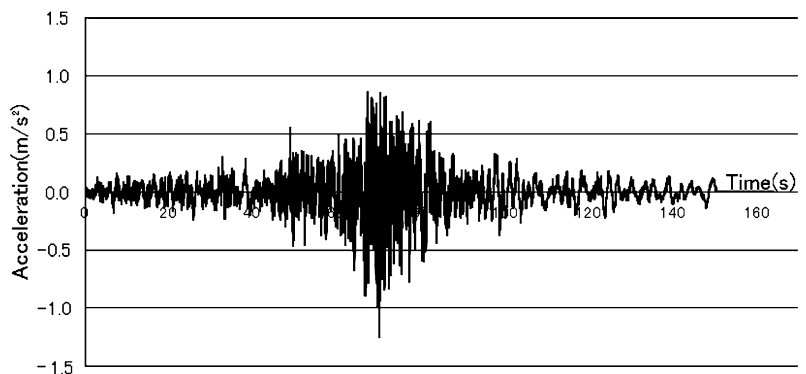
3.2   The Input Data

As for the altitude data, "The digital map in 50 meters meshes" published by Geographical Survey Institute in Japan was used (Fig. 59.8). The analytical data was arranged into 100 meters meshes. Also, the GIS software "ArcView9" of ESRI for a handling of geological conditions data was used. The geological model was referred to Geological Survey Synthesis Center in National Institute of Advanced Industrial Science and Technology "Seamless Digital Geological Map of Japan (1:200000)". The input geological map (Fig. 59.9) was determined in reference to that geologic model and the data of the KiK-net (NIED) observation point near the targeted area. The input seismic wave processed from an observed seismic wave record at an Ujiie point is used in the analysis. As a method of the processing, the observation seismic wave was back-analyzed to the bottom of the analysis ground (−50 m above sea level). Micro SHAKE (Jishin Kogaku Kenkyusyo, Inc.)

was used to pull it back. It was trimmed as 15000 steps (Figs. 59.10, 59.11). Because it would take a long time if all the duration of the input wave is used for the analysis, therefore only a part of the time history with larger acceleration amplitude is used alternatively. Such a simplification above may provide us the difference of the calculated displacement from the actual one, and our discussion should be focused only in the point of relative comparison. The input material properties were estimated based on the existing data which have been measured at the time of the construction works in this area, as presented in Table 59.1, Figs. 59.10, 59.11.

4   Analytical Results

4.1   Overall Examination

Figure 59.12 shows the calculated maximum horizontal acceleration at the ground surface
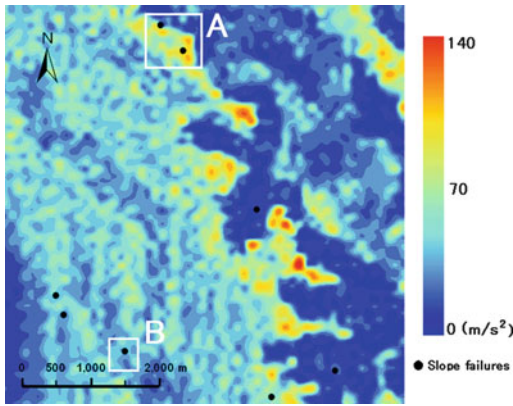
Fig. 59.12 Maximum horizontal acceleration distribution
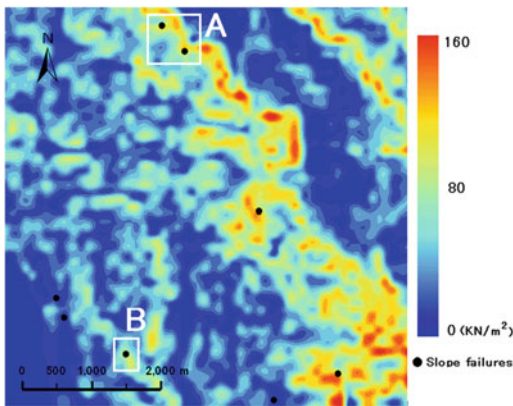
Fig. 59.13 Maximum shear stress distribution

Fig. 59.14 Maximum horizontal acceleration distribution in the area A
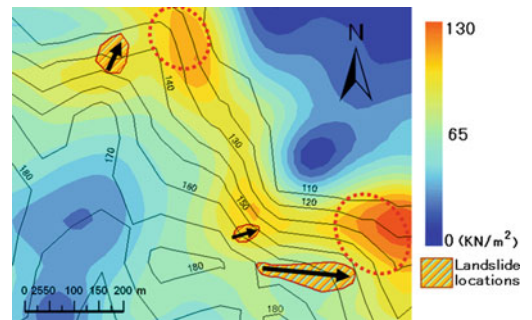
Fig. 59.15 Maximum shear stress distribution in the area A
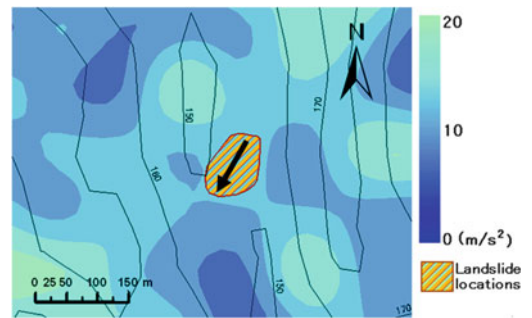
Fig. 59.16 Maximum horizontal acceleration distribution in the area B

(PGA). The locations where the slope failures really occurred were plotted as black circles in the figure. It can be seen that the acceleration is especially amplified around the ridges and the terraces in this area. In addition, the amplification of acceleration is also observed around the border between the loam and the Tertiary deposit areas. Such a spatial discontinuity in the material properties or the natural vibration periods may cause the amplification of acceleration as well.

Figure 59.13 shows the calculated maximum shear stress in the surficial layer in the ground. The locations where the slope failures really

occurred were plotted as black circles, which is similar to the previous figure. The maximum shear stress tends to be larger at the points with larger elevation gaps such as high cliffs.
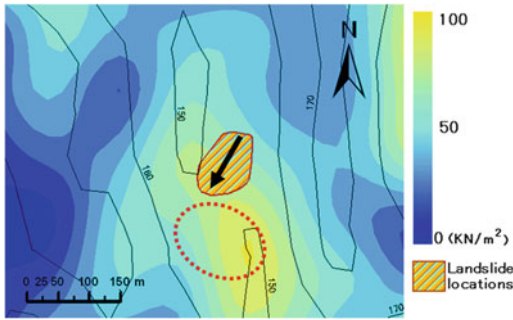
Fig. 59.17 Maximum shear stress distribution in the area B
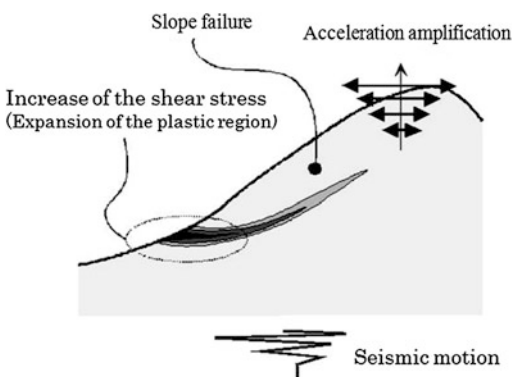
Fig. 59.18 Mechanism

4.2 Examination of the Details

The enlarged figures of the area A in Figs. 59.12, 59.13 are shown in Figs. 59.14 and 59.15, respectively. The landslide locations are plotted as the slant-lined zones in Figs. 59.14 and 59.15. It can be seen that the acceleration is amplified at the upper part of the landslide zones, while the shear stress is large at the lower part of the landslide zones.

In similar to the above, the enlarged figures of the area B in Figs. 59.12 and 59.13 are shown in Figs. 59.16 and 59.17, respectively. The landslide locations are plotted as the slant-lined zones in Figs. 59.16 and 59.17. The general tendencies that can be seen in these figures for the acceleration and the shear stress are almost the same as the one in the previous figures, although the contrasts of each value are a little smaller than the previous one.

According to the above, the obtained facts in the analysis are summarized as in Fig. 59.18, indicating that the risks for earthquake-induced landslide can be explained by a simple rule for the mechanical conditions in the acceleration and the shear stress in the slope. In the slopes where the acceleration is amplified, the inertia force acting in the slope body becomes large particularly. On the other hand, the strength degradation in the volcanic cohesive soil layers is caused by the cyclic loading of the inertia force. The degree of the stress concentration can be easily seen as the shear stress values acting at the ground surface in the lower part of the slope. The above mechanism may promote the formation of the landslide mechanism in the slope.

5 Conclusions

In the suffered inland area in Tochigi Prefecture due to the Great East Japan Earthquake, the characteristics of the slope disaster were analyzed and an effective numerical system was used to evaluate the landslide risk.

The main conclusions obtained in this study are as follows:

1) The geological feature is mainly consists of volcanic cohesive soil in a suffered inland area. When a loam catches the stimulation such as the seismic motion, it suddenly loses strength, and a softening phenomenon happens.
2) The acceleration amplification can be seen around ridges and terraces. The maximum shear stress is large at places of the large difference of elevation and the Tertiary deposit area.
3) The amplification of acceleration is large at the upper part of the collapsed area. On the other hand, at the lower part of the collapsed area, the shear stress is large.

References

Akihiko W, Keizo U (2004) A simple constitutive model for the seismic analysis of slopes and applications, soils and foundations 44(4):83–97

Akihiko Wakai, Norihiro Tanaka, Shinro ABE, Hiroyuki Yoshimatsu, Kousei Yamabe, Taisuke Watanabe (2008) Large-area damage prediction system based on finite element method for risk assessment of seismic slope failure in mountains area. J Jpn Landslide Soc 45(3):21–32 (in Japanese)

Kazunori H, Akihiko W, Norihiro T, Shinro A (2011) Risk evaluation method for earthquake-triggered landslide enhanced by cooperation of topographical-geological analysis and finite element analysis. J Jpn Landslide Soc 48(1)1–11 (in Japanese)

Hirotatsu U, Takami K, Tomoyuki H, Akihiko W (2011) A case of landslide occurred in Kamikashiwazaki, Takanezawa at the time of 2011 Tohoku Earthquake. In: Proceeding 8th Annual Meeting of Kanto Branch of Japanese Geotechial Society pp 102–104 (in Japanese)

Takanori K, Akihiko W, Kunihiro H (2012): Analysis of the factors affecting slope failures distribution within Northern Kanto Area due to the East Japan Great earthquake. In: Proceeding International Symposium on Earthquake-induced Landslides (inprint)

Part V

Simulation

Dynamic Simulation and Analysis of High-Speed and Long Run-Out Landslide Triggered by the Wenchuan Earthquake, China

Yuan Jiao Zhang, Long Zhu Chen, Ai Guo Xing and Chao Qi

Abstract

Many landslides with characteristics of high-speed and long run-out triggered by the Wenchuan Earthquake pose significant damages to lives and infrastructure. To be familiar with this type of landslide, acquire empirical value to forecast it and reduce damages to lives, event of Niujuangou rockslide-debris avalanche in Yingxiu Town was researched as an example in this paper. A dynamic model DAN, a program used to model the post-failure motion of rapid landslides including cases induced by earthquake, was adopted to analysis this case studies. In the process of modeling, two different rheology rules of basal material were back-analysis and three patterns of single friction flow rheology, single Voellmy fluid assumption and combination of them were individually simulated.The analysis emphasized on landslide travel distance, velocity characteristics at different times, length and thickness of the deposits, while the volume and travel time were estimated. The results reveal that combination of friction and Voellmy flow rheology relations can provide reasonable results to the event, and the best fitting rheological parameters have been found through back analysis. Additionally, effects of earthquake and terrain are main factors which affect velocity and travel time of the landslide.

1 Introduction

Rapidly moving landslides exact a steady toll of injury and damage on the populations of hilly and mountainous regions around the world (Hungr 2009), and earthquakes are one of the most triggers of these landslides. Coupled with

Y. J. Zhang (✉) · L. Z. Chen · A. G. Xing · C. Qi
Department of Civil Engineering, Shanghai Jiao
Tong University, 800 Dongchuan RD. Minhang
District, Shanghai, China
e-mail: sjzhangyjcumt0113@sjtu.edu.cn

characteristics of high altitude, high speed and long run-out, the landslides triggered by the Wenchuan Earthquake have led to significant topographic changes and costly damages for human beings.

Through field investigation of landslides triggered by the Wenchuan Earthquake, Xu and Huang (2008) recognized that geologic disasters which triggered by earthquake had quite different dynamic characteristics. Limited to lower economic development, monitoring technique and other factors, motion of the landslides are rarely record, and sampling is also difficult in environment of aftershock and rainfall. All these confined conditions make dynamic simulation important to these events. With that, Huang et al. (2009) applied finite element numerical simulation of rock avalanche mechanism of slope under condition of earthquake, and adopted smoothed particle hydrodynamics (SPH) to model travel process of landslides induced by earthquake; Zheng et al. (2009) used FLAC3D to numerically analyze slope failure mechanism in condition of earthquake; the identical method was employed to research recurrence mechanism of landslide under earthquake loading (Xia et al. 2010); Bi et al. (2009) studied slope dynamic response laws under seismic action utilized ABAQUS; Cui et al. (2009) made use of UDEC numerical simulation method to model movement of landslide under the seismic action, and key controlling factor inducing slope collapsing and sliding on the conditions of known seismic tectonics, structure and tectonics of slope mass was obtained. Other approaches (e.g., 2D-BLOCK) also utilized by researchers to discuss the motion mechanism of landslides (cf. Su et al. 2010).

This paper adopts DAN (dynamic analysis) which is a versatile dynamic simulation model for mass movement, to simulate the whole movement of Niujuangou rockslide-debris avalanche, and aims at revealing the dynamic characteristics of the event.

2 The Dynamic Model

2.1 Description of DAN

The pseudo-three-dimensional model DAN, which is based on an explicit Lagrangian solution of the equations of unsteady non-uniform flow in an open channel, was developed by Hungr (1995) and scope of application was widened after several upgrade. The models have been verified against a number of controlled laboratory landslide experiments, and numerous studies have been analyzed and a valuable database of calibrated parameters has been created (e.g., Hungr1995; Mancarella and Hungr 2010).

The basic hypothesis of DAN is "equivalent fluid" which assumed rock mass as uniform flow. In curvilinear coordinate, displaced materials of a landslide are represented by a number of boundary elements and mass elements. Formulation of the governing equations is based on the law of conservation of momentum for the boundary elements, and mass conservation is applied to the mass elements. Internal stress conditions are assumed to "Modified Savage-Hutter" assumption which was described in detail by Hungr (2008). Relationships of resistant force are determined by material rheology. Within a moving Lagrangian reference frame, solutions are explicit and occur in time steps. When the model is stopped, most concerned factors, such as travel distance, velocity, thickness of deposition, are presented to researchers.

2.2 Rheological Relationships

Various geological conditions produce different rheological responses from the moving material. The models are capable of several rheological relationships for the moving mass. Friction flow and Voellmy fluid are most frequently used since the model was developed. Friction flow can be supplied to rock avalanche and give the similar run-out with field observation. Veollmy fluid

typically produces better simulations for debris flow A switch from friction to Vollemy is often required to produce satisfactory simulation when events initate on open slopes and then become channelized (McKinnon et al. 2008). To test these formulas whether suitable in Chinese, this paper adopts friction model, Voellmy model and the combination model which is made up of friction flow and Voellmy fluid to simulate the event.

Friction flow is a single variable rheology function, and the resistance force relation is presented by Eq. (60.1):

$$\tau = \sigma(1 - r_u)\tan\phi \qquad (60.1)$$

where τ is the basal shear stress, σ is the total bed-normal stress, r_u is the ratio of pore pressure and always assumed constant, ϕ is bulk dynamic basal friction angle of dry, broken rock, considering effect of earthquake value of ϕ is less than normal value (Hungr 2008).

Voellmy fluid has two parameters, and the resistance force relation is presented by Eq. (60.2):

$$\tau = \sigma f + \rho g \frac{v^2}{\xi} \qquad (60.2)$$

where f is the friction coefficient, ρ is the material density, g is the acceleration due to gravity, v is the flow velocity, and ξ is turbulence parameter which has same form as the Chezy formula for turbulent flow in open channels.

Variables of these rheological functions must be constrained by trial and error back-analysis of know real landslides (Hungr 2009).

3 Niujuangou Rockslide-Debris Flow

3.1 Description of Niujuangou Rockslide-Debris Avalanche

Niujuangou rockslide-debris avalanche is located at Niujuangou creek where 2 km away from YingXiu town. Transport path of the landslide which went across the Main Longmenshan Fault, was divided into source area, Lianhuaxin segment and Niujuangou creek segment (Fig. 60.1). Additionally, Lianhuaxin creek is a tributary of Niujuangou creek which is a small tributary of the Minjiang River-one of the main rivers in Sichuan province. The landslide happened in rainy season when two creeks had flowing.

Originally, detached mass in source area whose top and toe elevations were 1,780 m and 1,350 m, was thrown out owing to the huge earthquake effect of horizontal and vertical, and then rapidly moved in LianHuaxin creek, struck to side by Lianhuaxin creek and smashed into Niujuangou creek. Sliding mass ran about 1,200 m in Niujuangou creek and impacted mountains along the path three times, it finally stopped at place where 250 m away from Minjiang River. The totally horizontal travel distance was about 3.0 km. Remote sensing image before and after the landslide manifests that the extension of initial sliding mass has a 150–200 m elevation difference, 300–400 m width and 100 m thickness (Yin2009a). More detailed information of motion was described by Yin (2009b); Kong et al. (2009); Zhang et al. (2011).

Material of detached mass mainly is fragmentized granodiorite, and entrained colluvial soil in motion. Stratum of the landslide area is divided into two types by the earthquake fault. Source area of the landslide is the archean granite, and part of Lianhuaxin creek which was located in the hanging wall covers several kinds of schist. In the footwall, sandstone, shale and thin coal seam can be recognized (Kong et al. 2009).

3.2 Model Setup and Parameters

Three models were built as pre-scribed. Friction model was made up of friction flow and Voellmy model consist of Voellmy fluid. In combined model, friction flow was used to express
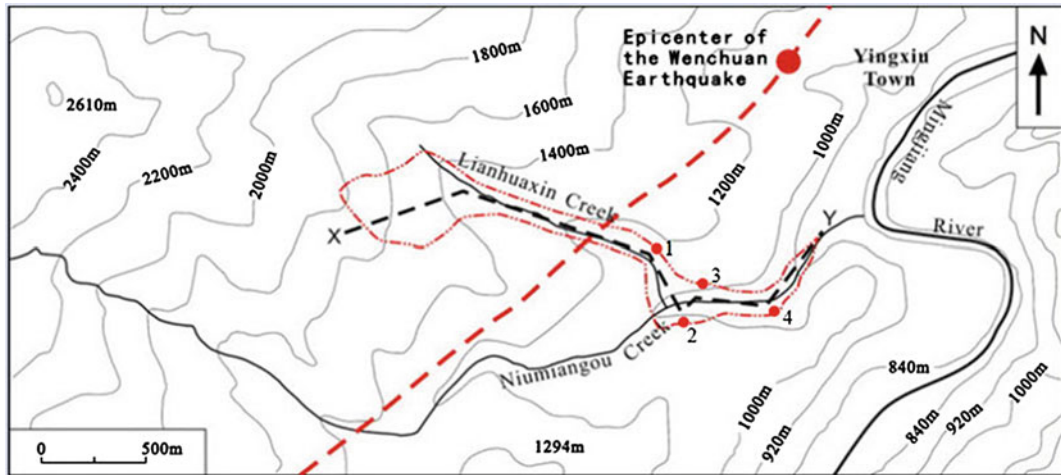
Fig. 60.1 Topography of Niujuangou rockslide-debris avalanche (modified by (Zhang et al. 2011), red dashed line is Main Longmenshan Fault; red line is the boundary of Niujuangou rockslide-debris avalanche; black dashed line is longitudinal cross-section; black numbers indicate location of impact)

resistance relation of source area and Lianhuaxin creek segment and Voellmy fluid presented resistance relation of Niujuangou creek segment where sliding mass moved like flow after taking account of different movement characteristics in different path and varied material. To be convenient, the combined model was called F–V model in the following part. Control parameters and material parameter of unit weight were set as default. Internal frictional angle set value of 30° (cf. Mancarella and Hungr 2010). Notably, shape factor get value of 0.5 due to the terrain, and a function of trajectory was turned on. Considering the run-up of impact point, two observations were set in location of impact three and four to record the velocity and deposit thickness. And comparison of with field observation was made in following part.

Trial-and-error back-analysis showed longitudinal profile of deposition was reasonably simulated when F–V model was used. If kept parameters same, run-out was overestimate by friction model and conservative in Voellmy model, so we chose the most suitable model (i.e., F–V model) to present simulated results. Optimum parameters of F–V model were: dynamic friction angle of friction flow $\varphi = 11°$, two parameters of Voellmy fluid $f = 0.2$ and $\xi = 200$ m/s^2.

3.3 Results Analysis

Run-out and Deposition

Longitudinal profiles of sliding mass at different moments with F–V model were noted and shown by Fig. 60.2. The final profile showed that travel distance was 2,919 m, which mostly in accordance with field investigation. The model was manually stopped when run about 200 s, sliding mass was steady at this time, and had little effect on results.

Longitudinal length of deposition was about 2,700 m which can recognize from Fig. 60.3. It explained that the maximum thickness of deposition reached 60 m and estimated average thickness was about 30 m. Accumulation on Lianhuaxin creek appeared as a mountain which had a peak, but it became uniform distribution in Niujuangou creek. In the movement of the landslide, sliding mass entrained surface weathered rock instructed by Zhang et al. (2011), enlarge the volume of deposition. Results showed that final volume was about 7,400,000 m^3 and the average erosion depth along the path was 3 m.

Velocity

Variations of velocity and thickness of impact points 3 and 4 were plotted on Figs. 60.4 and 60.5. These graphs indicated the maximum value

Fig. 60.2 Longitudinal profiles of Niujuangou rock avalanche-debris flow at different moments with F–V model
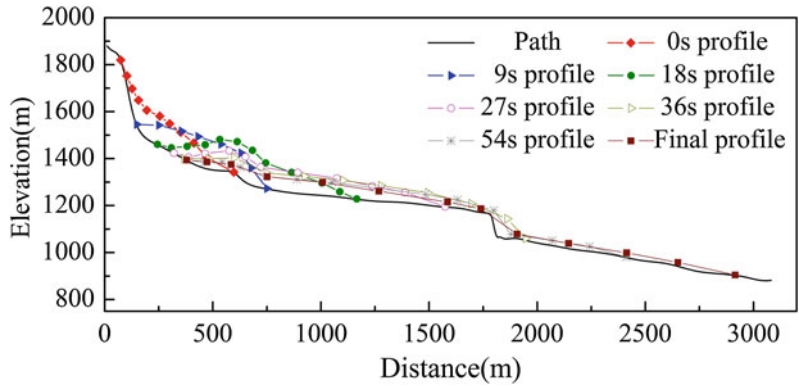
Fig. 60.3 Simulation result of deposit distribution of Niujuangou rock avalanche-debris flow with F–V model
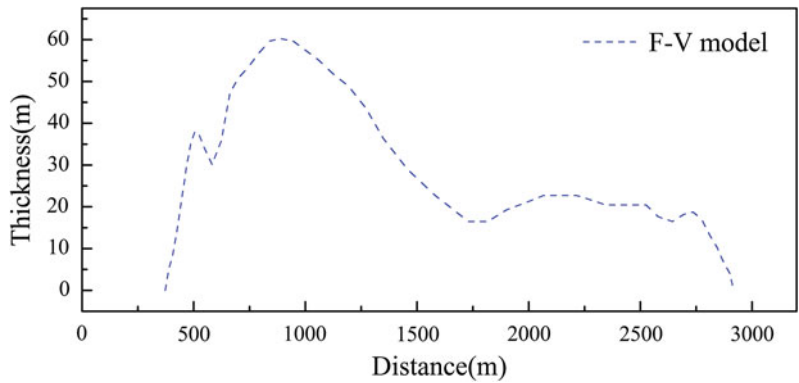
Fig. 60.4 Velocity and thickness of impact point 3
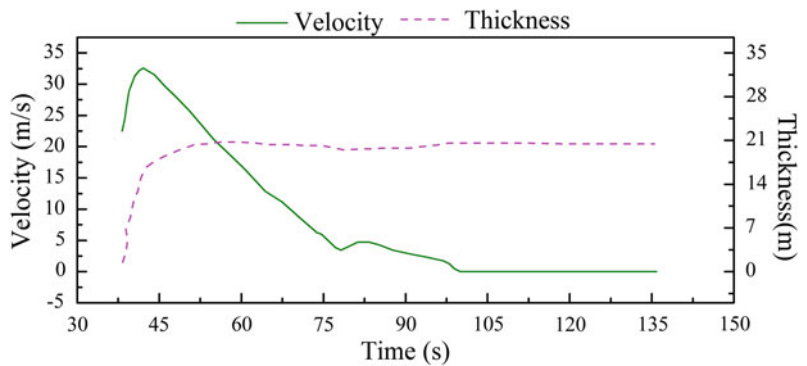
Fig. 60.5 Velocity and thickness of impact point 4
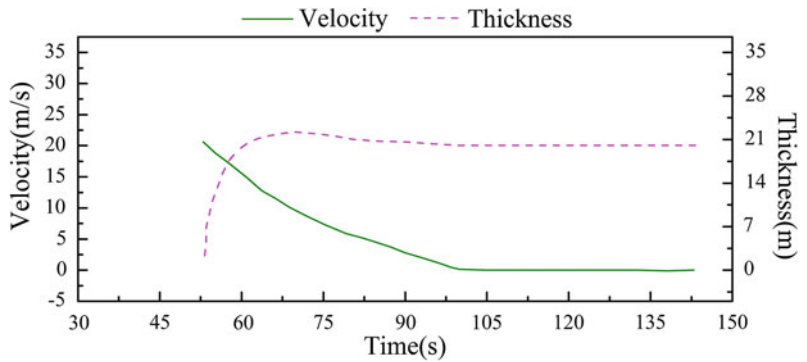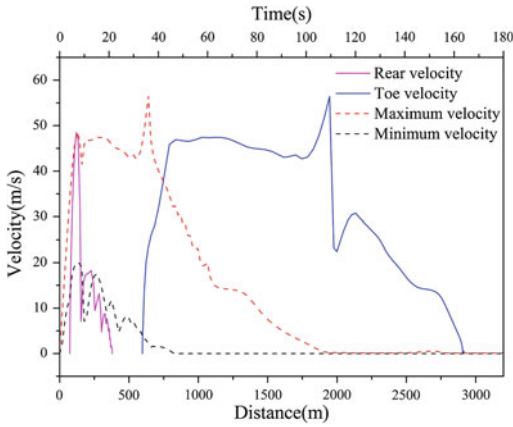
Fig. 60.6 Variations of velocity (*Blue* is the toe velocity *vs*. distance; *pink* is the rear velocity *vs*. distance; *red* is the maximum velocity *vs*. time; *black* is the minimum velocity *vs*. time)

of impact point three and four were 32.6 m/s and 21 m/s. Field observations told us that run-up in impact point three and four were 65.3 m and 25.8 m. Therefrom, calculated velocities with empirical method separately were 36 m/s and 21 m/s (Zhang et al. 2011). Little distinction between them, thus velocity variations can be reasonable simulated by F–V model.

Velocity variations (ex. toe velocity *vs*. distance) were plotted by Fig. 60.6 which also recorded maximum and minimum velocity changes with time. Variation of toe velocity told that high speed was kept in Lianhuaxin creek, and peak velocity took place at about 1950 m. Maximum velocity happened at 38 s, and sliding mass totally stopped after 110 s.

Figure 60.7 showed velocity distributions of sliding mass as a series of time lapse images. Combined with Fig. 60.6, maximum velocity of the landslide was recognized as 57.42 m/s, and average velocity can be estimated as 24.3 m/s. The two graphs intuitively expressed that velocity was large enough in early age, distributions at different time and the maximum velocity of rear and toe can be apparently visualized.

4 Discussion

Simulation of the event illustrates that run-out, velocity, distribution and volume of deposition can be modeled by DAN. Confined of model with pseudo-three-dimension, features of impacting are lose in the course of simulation.

Fig. 60.7 Velocity distributions of Niujuangou rock avalanche-debris flow at different times with F–V model
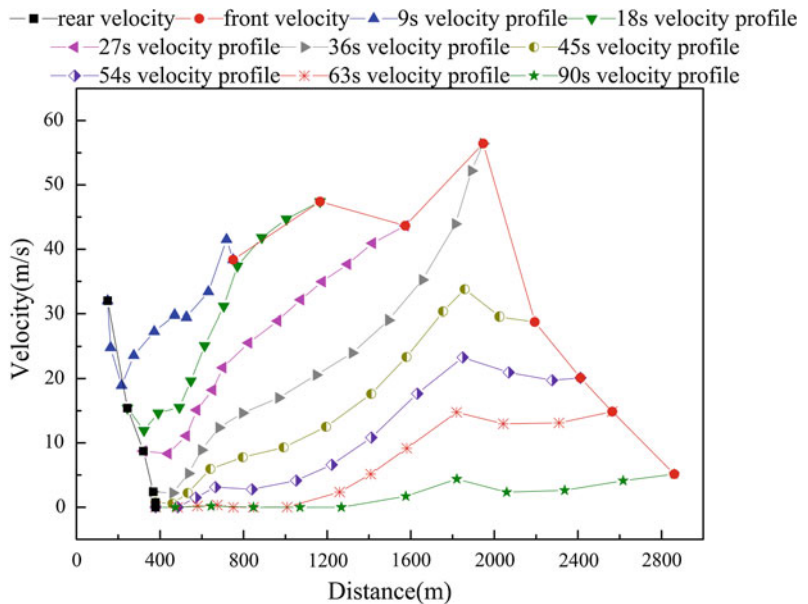
However, it cannot hamper the key features obtained. When simulated with complex landslides, combined model is superior to single rheology model (e.g., friction flow, Veollmy fluid), and F–V model can perfectly model Niujuangou rockslide-debris avalanche. For complex type of landslides, in order to well simulate the process of landslide, two or more reasonable rheology should be selected according to different stages especially entrainment happened.

High speed in early age of the landslide can be deemed as the huge effect of earthquake. In later stage, velocity was apparently decreased but a long travel distance still made. It follows that travel distance is concerned with movement type, and debris avalanche or debris flow is easier to a longer distance. In conclusion, maximum velocity of the landslide happened at intersection of Lianhuaxin creek and Niujuangou creek, where elevation difference was about 40 m and sliding mass was thrown down. The primary cause was that potential energy of sliding mass transformed into kinetic energy, making the maximum speed happen here.

Frequent aftershocks, abundant substance with the addition of rainstorm, Niujuangou debris flow happened in September 2008, made sampling of sliding mass impossible, but DAN provides a new approach to study landslides like Niujuangou case that key features are captured.

5   Conclusion

Dynamic program DAN was used to simulate the process of Niujuangou rockslide-debris avalanche, results certified that combined model of friction flow and Voellmy fluid can implement modeling this event. Suitable parameters of Niujuangou landslide were dynamic angle $\varphi = 11°$, friction coefficient $f = 0.2$ and turbulent coefficient $\xi = 200$ m/s^2.

The maximum velocity of Niujuangou rockslide-debris avalanche was 57.42 m/s, run-out time approximately was 110 s which was similar with duration of earthquake. Total volume of deposition was 7,400,000 m^3, and average erosion depth along the path was 3 m.

Lianhuanxin creek segment had a huge speed and shorter travel time with a comparison with Niujuangou creek segment. The maximum velocity of the event happened in intersection of Lianhuaxin creek and Niujuangou creek where large elevation difference existed. And effects of earthquake and terrain are main factors which affect velocity and travel time of the landslide.

References

Bi ZW, Zhang M, Jin F, Ding DX (2009) Dynamic response of slopes under earthquake. Rock Soil Mech 30(supp 1):180–183

Cui FP, Hu RL, Yin YP, Xu Q, Zhang M (2009) Numerical simulation of slope collapsing and sliding due to single or combined actions of seismic and waves with time difference. J Eng Geol 17(4):455–462

Huang RQ et al (2009) Geohazard assessment of the Wenchuan earthquake. Science Press, Beijing, pp 422–485

Hungr O (1995) A model for the runout analysis of rapid flow sildes, debris flows, and avalanches. Can Geotech J 32:610–623

Hungr O (2008) Simplified models of spreading flow of dry granular. Can Geotech J 32(4):1156–1168

Hungr O (2009) Numerical modeling of the motion of rapid, flow-like landslides for hazard assessment. KSCE J Civ Eng 13(4):281–287

Kong JM, Cui Y, Tian SJ, AF Y (2009) Typical case study on the development characteristics of fragmentation-sliding seismic landslide. J Sichuan University (Engineering Science Edition) 41(3):119–124

Mancarella D, Hungr O (2010) Analysis of run-up of granular avalanches against steep, adverse slopes and protective barriers. Can Geotech J 47:827–841

McKinnon M, Hungr O, McDougall S (2008) Dynamic analyses of Canadian landslides. In: Locat J, Perret D, Turmel D, Demers D, Leroueil S. Proceedings of the 4th Canadian conference on Geohazards, from caused to management

Su SR, Zhang YS, Li S, Hao LL, Wang K, Mei H (2010) Numerical analysis on motion mechanism of high-speed and long runout landslide by Wenchuan earthquake. J Earth Sci Environ 3:277–287

Xia M, Ren GM, Guo YS, Lv SD, Liu RQ (2010) FLAC3D numerical simulation of recurrence mechanism of landslide under earthquake loading. J Eng Geol 18(3):305–311

Xu Q, Huang RQ (2008) Kinetics characteristics of large landslides triggered by May 12th Wenchuan earthquake. J Eng Geol 16(6):721–729

Yin YP (2009a) Features of landslides triggered by the Wenchuan earthquake. J Eng Geol 17(1):29–38

Yin YP (2009b) Rapid and long run-out features of landslides triggered by the Wenchuan earthquake. J Eng Geol 17(2):153–166

Zhang M, Yin YP, Wu SR, Zhang YS, Han JL (2011) Dynamics of Niumiangou rock avalanche triggered by 2008 Ms 8.0 Wenchuan earthquake, Sichuan China. Landslides 8:363–371

Zheng YR, Ye HL, Huang RQ (2009) Analysis and discussion of failure mechanism and fracture surface of slope under earthquake. Chin J Rock Mech Eng 28(8):1714–1723

Simulation of the Largest Landslide Caused by the 2008 Wenchuan Earthquake by Rapid-Landslide-Movement Simulation

61

T. Satoshi, S. Kyoji and N. Osamu

Abstract

One of the world's largest landslides occurred on May 12, triggered by the 2008 Wenchuan earthquake, in China. The landslide (Daguangbao landslide) covered 7.8 km² with a maximum width of 2.2 km and had a collapsed volume of about 700 million m³. The landslide mechanism considered is that the strong and long-period ground shaking may have reduced the frictional strength of the substrate by shattering the rock mass, and seismic acceleration may have resulted in generated a large shear stress by the landslide gravity.In this study, a simulation to reproduce the movement from landslide initiation up to deposition was conducted by using the LS-RAPID (Sassa et al. 2010). The basic equations of the model are established on the assumption in which all potential energy is consumed as the frictional energy on the sliding surface. The simulation results showed that the head of the landslide began to move downwards including the summit of Mt. Daguangbao about 30 s afterwards, and that the toe of the main mass reached the valley located in the lower western region. About 120 s subsequently the landslide movement gradually slowed and then the toe of the mass buried the valley by about 300 m. This simulation result mostly shows the geographical deposition after the actual landslide. We would like to introduce the method and parameters used for calculation in this paper.

Keywords

Wenchuan earthquake · ALOS satellite · DEM extraction · Numerical simulation of landslide mass

1 Introduction

Large inland earthquakes with magnitudes greater than 6 usually cause rockslides, avalanches and debris flow on mountain slopes. Such landslide movements induced by earthquakes often hit areas of generally low relief and generate serious

T. Satoshi (✉)
Shizuoka University, 836 Ohya Suruga-ku, Shizuoka-shi, Japan
e-mail: afstuti@ipc.shizuoka.ac.jp

S. Kyoji · N. Osamu
International Consortium on Landslides, Kyoto, Japan

Fig. 61.1 View of Daguangbao landslide from ALOS-AVNIR image (June 4, 2008, provided by JAXA)

damage to the residential area including loss of human life. The Wenchuan earthquake, which occurred on the Longmenshan fault on May 12, 2008, measured magnitude 8 on the Richter scale and caused broad catastrophic landslide disasters centering in the western region of Sichuan Basin. The number of people killed and missing as a result of the earthquake reached about 87,000. Also, huge landslides of incomparable scale and many rock avalanches and debris flow occurred. In particular, the Daguangbao landslide in Anxian County was the largest, with an area of about 4 km long and about 2 km wide. This bedrock collapse occurred on the west-northwest slope of Mt. Daguangbao (3047 m) including the mountain's peak with a layer thickness of about 600 m. The resulting landslide mass broadly and thickly buried the downstream valley, and a tip of the mass extended over the ridge of Mt. Daguangbao (Fig. 61.1).

In this study, to understand the mechanism of how a mass of about 600 m thickness flowed and stopped we attempt to reproduce the flow process by numerical simulation. As the duration of the main shaking of the Wentuan earthquake was long, about 120 s, a strong vibration must have markedly affected the landslide mass in the flow. Therefore, seismic ground motion was applied in the simulation, giving suitable soil strength and coefficient of soil pressure among other factors for highest reproducibility by trial and error. It is expected by this simulation that soil strength or flow-down velocity during the event will be successfully estimated, bringing useful information for research and development about the flow simulation of rapid landslide mass movement. A digital elevation model (DEM) was used to simulate a large-scale rapid landslide movement like the Daguangbao landslide, with a desirable mesh size of about 50 m. The DEM of the terrain collapsed was extracted from the image taken using an ALOS-PRISM sensor, and the DEM before the collapse was obtained from Google Earth.

2 Acquisition of Digital Elevation Model

2.1 Acquisition Method

High precision and stable orientation are required when generating a DEM from satellite imagery. However, in the orientation of a high-resolution satellite imagery, an algebraic model using the generalized parameter is used rather than a geometric relation like a center projection model, because detailed information on the trajectory and the sensor is not exposed. Yamakawa et al. (2010) performed an orientation experiment using four algebraic orientation models in an IKONOS satellite image. As a result, they clarified that three models without orbit information give the same orientation precision as the RPC model (Fraser and Hanley 2005). In addition, a two-dimensional affine model showed stable analysis characteristics with fewer standards.

Two images of nadir and rear taken using ALOS-PRISM (June 4, 2008) were used. A stereo matching of the analysis region was performed on the image with orientation using a two-dimensional affine model (Yamakawa et al. 2010). The DEM was generated in 20 m mesh size. The two-dimensional affine model based on the affine geometry is close to parallel projection because of the sensor having a narrow field angle of a satellite image. By applying an affine model exaggerated parameterization, which often arises as a problem in the use of center projection formulas, can be avoided (Hattori et al. 2003).

The relation between the pixel coordinate of rear and nadir in images (x_l, y_l), (x_r, y_r) and the ground coordinate (X, Y, Z) are expressed in Eq. (61.1) with unknown coefficients $a_1 \cdots a_4, b_1 \cdots b_4, c_1 \cdots c_4$, and $d_1 \cdots d_4$.

$$
\begin{bmatrix} x_l \\ y_l \\ x_r \\ y_r \end{bmatrix} = \begin{bmatrix} a_1 & a_2 & a_3 \\ b_1 & b_2 & b_3 \\ c_1 & c_2 & c_3 \\ d_1 & d_2 & d_3 \end{bmatrix} \begin{bmatrix} X \\ Y \\ Z \end{bmatrix} + \begin{bmatrix} a_4 \\ b_4 \\ c_4 \\ d_4 \end{bmatrix}
$$

(61.1)

Here, transposing unknown coefficients unrelated to (X, Y, Z) in right-hand side of Eq. (61.1) to left-hand side and I, A, R are set as Eq. (61.2) respectively, X, Y, Z are determined by $R = A^{-1}I$.

$$
I = \begin{bmatrix} x_l - - & a_4 \\ y_l - - & b_4 \\ x_r - - & c_4 \\ y_r - - & d_4 \end{bmatrix},
$$
$$
A = \begin{bmatrix} a_1 & a_2 & a_3 \\ b_1 & b_2 & b_3 \\ c_1 & c_2 & c_3 \\ d_1 & d_2 & d_3 \end{bmatrix}, R = \begin{bmatrix} X \\ Y \\ Z \end{bmatrix}
$$

(61.2)

Generally four points or more are needed as reference points, the 16 unknown coefficients were determined using the least-squares method. In this study, the six (X, Y, Z) ground coordinates on Google Earth and the pixel coordinates corresponding to the six ground-based points from the images of rear and nadir are given. The ground surface coordinates before the Daguangbao landslide were chosen using free software (uTrekGE, Eugene Software Inc.) on the Google Earth screen. The altitudes were reproduced by an equivalent for a ground surface of 50 m mesh size, and set to the DEM before the landslide.

3   Comparison of Pre- and Post-landslide Terrains

Figure 61.2 shows the topographical map before the landslide occurred and the extent of the landslide. It is shown based on Google Earth. The shape of the slope of the center part where the
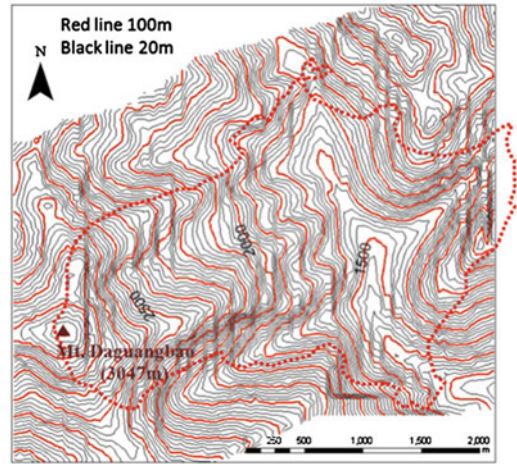
Fig. 61.2 Topographical map before landslide and range of extent of landslide
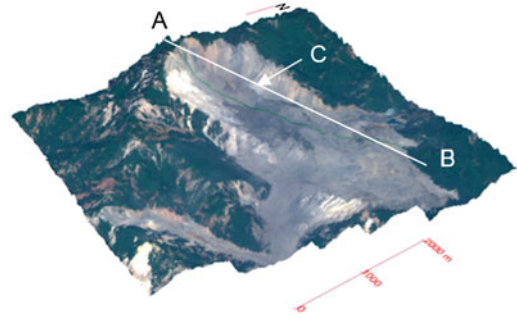
Fig. 61.3 Three-dimensional view of the terrain after landslide with AVNIR image of the DEM extracted

landslide initiated is observed as slightly concave and the ridge extended from Mt. Daguangbao (3047 m altitude). The landslide mass was initiated to collapse nearly the summit of Mt. Daguangbao in the west-northwest direction and overflowed on the south side valley of 2000 m altitude, burying the next valley of 1400–1600 m altitude. Finally, the mass stopped in the opposite slope of about 2000 m altitude.

Figure 61.3 shows the post-landslide terrain overlaying an ALOS-AVNIR color image stereoscopically on the post-landslide DEM extracted from the satellite imagery. The collapsed bedrock was greatly scooped out from the summit of Mt. Daguangbao up to the mid slope and flowed down the slope roughly. The landslide mass filled

Fig. 61.4 Topography changes before and after landslide in main vertical section and cross section
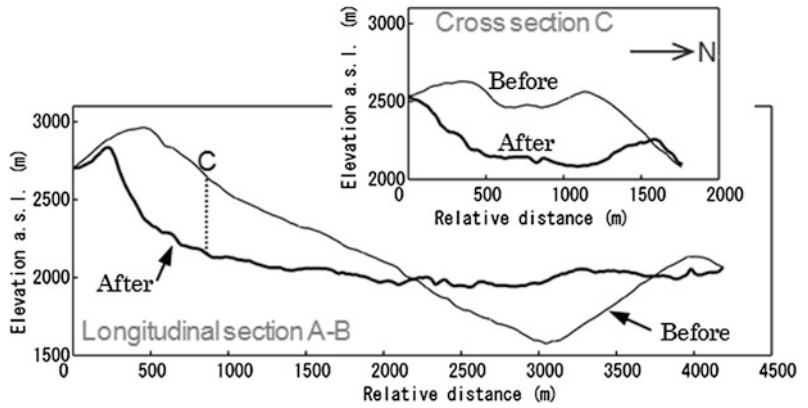
the valley which located on the south side and then flowed downwards along the direction of the valley, as shown in Fig. 61.2.

As shown in Fig. 61.4, the vertical section of the ground surface after the landslide dropped almost perpendicularly, and the landslide mass accumulated horizontally between the central part of the slope and the opposite slope. Therefore, it is suggested that the destructive rocks moved down aggregately at a relatively high speed. Also, the failed surface of the upper landslide was about 600 m lower from the original ground surface with a bowl-shaped form. On the basis of the cross sections obtained about every 300 m from the landslide head in Fig. 61.4, the volume of the collapsed and moved rock mass can be estimated to be about 690 million m³ for in situ volume. Although the estimated amount is slightly small compared with that in previous literature (Chigira et al. 2010; Huang et al. 2012), it is considered to be almost equally.

4 Analysis of Rock Mass Movement by Numerical Simulation

The numerical simulation used for reproducing the movement of the rock mass is called LS-RAPID, which was developed by Sassa et al. (2010). This simulation software employs a physical model that can express landslide
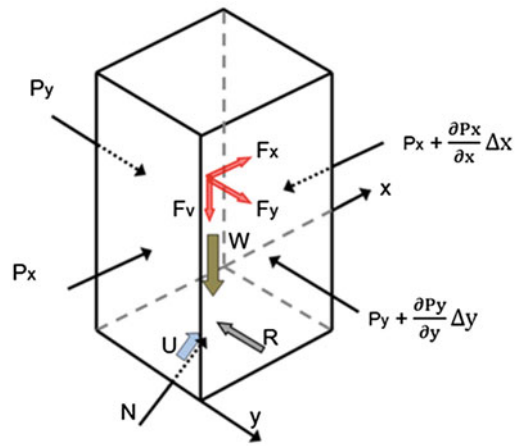
W: Self weight (=mg, g: Gravity); Fx & Fy: Horizontal seismic force; Fv: Vertical seismic force; Px, Py: Lateral pressure acting on the side wall; R: shear resistance acting on the bottom; N: Normal stress acting on the bottom; U: pore pressure acting on the bottom

Fig. 61.5 Forces acting on column

movement from initiation to steady-slide condition in consideration of strength reduction and the following process of soil mass expansion and stoppage. It can also reproduce the rapid landslide movement induced by heavy rainfall or earthquake or both combined (Sassa et al. 2010).

The vertical imaginary column shown in Fig. 61.5 is considered as a moving landslide mass inside, and the forces acting on the column are as follows: self-weight of the column, seismic force, lateral pressure acting on the side walls,

shear resistance acting on the bottom, normal stress acting on the bottom given from the stable ground as a reaction of a normal component of the self-weight, and pore pressure acting on the bottom. The landslide mass is accelerated by the acceleration given by the sum of these forces shown in Eq. (61.3), such as driving force plus lateral pressure plus shear resistance.

$$
\begin{aligned}
am &= W + Fx + Fy + Fv \\
&\quad + \left(\frac{\partial Px}{\partial x}\Delta x + \frac{\partial Py}{\partial y}\Delta y\right) + R + f_d, f_d \\
&= \alpha\left(\frac{1}{2}mv^2\right)
\end{aligned}
\tag{61.3}
$$

The vertical component to the slip surface among the seismic force and self-weight was canceled by the subgrade reaction and the excess pore water pressure generated, only the horizontal component of the slope contributed as the assumed acceleration a. Moreover, the water pressure that exerted in soil by rainfall and the subgrade reaction force are included in the shear resistance. The vertical component of a seismic force also affects the horizontal soil pressure because it changes the vertical soil pressure.

In a large-scale landslide, the mass might divide into many subblocks and collide mutually. Therefore, the assumption of Eq. (61.3) that all the energy is consumed while moving and converted into the frictional energy is invalid, and some places where continuity cannot be maintained may appear in the movement. The value f_d proportional to the kinetic energy in Eq. (61.3) is subtracted as a frictional resistance in places where such extraordinary occurrences appear. In this analysis, f_d is applied with $\alpha = 1.0$ at points where the velocity exceeds 50 m/s.

In the simulation, all force and movement are projected to a horizontal plane to solve a three-dimensional problem in two dimensions on a horizontal plane. The landslide mass movement is analyzed under the assumption that the height of the mass in the column element increases depending on only the amount of the soil that flowed into the element, and the density of the soil mass does not change during movement.

5   Results of Simulation

5.1   Seismic Data and Input Parameters

According to the seismic record of the Wenchuan earthquake (Li et al. 2008), a very strong wave continued in the first duration from 30 to 40 s, and then a relatively large shaking hit from 70 to 80 s. Such a strong ground shaking would have affected the landslide mass movement after the collapse.

Figure 61.6 shows the wave applied to LS-RAPID, which is transformed in the landslide movement direction from the observed record in the NS-EW direction. The seismic record was observed at Qinping station (about 10 km away from the Daguangbao landslide) in Mianzhu (Li et al. 2008). The seismic vibration reached more than 500 gal horizontally in 10 s after the start of the quake and continued for 30 s. After that, the wave magnitude decreased to approximately 100 to 200 gal 70 s after the start of the quake. Then the magnitude kept 300 gal for 20 s. Then the magnitude decreased gradually, and the seismic record terminated 260 s after the start of the quake.

In the LS-RAPID simulation, the DEM before the landslide occurred was applied to the surface elevation as shown in Fig. 61.2. The slip surface was given using the ellipse slip surface, creating a function installed in LS-RAPID. Referring to Fig. 61.3, the lower edge at the intersection of the slip surface and ground surface was equal to the landslide mass of 690 million m^3, which was obtained previously.

The parameters used in the simulation are listed in Table 61.1. Considering that the rock mass after the collapse flowed down in a large block in this case, the unit weight of the soil mass was set to 20 KN/m^3, the internal soil cohesion to 0.3 kPa, and the coefficient of

Fig. 61.6 Acceleration data applied to LS-RAPID (Data are changed into the landslide direction from NS-EW obtained at the Qinping station in Mianzhu (Li et al. 2008)
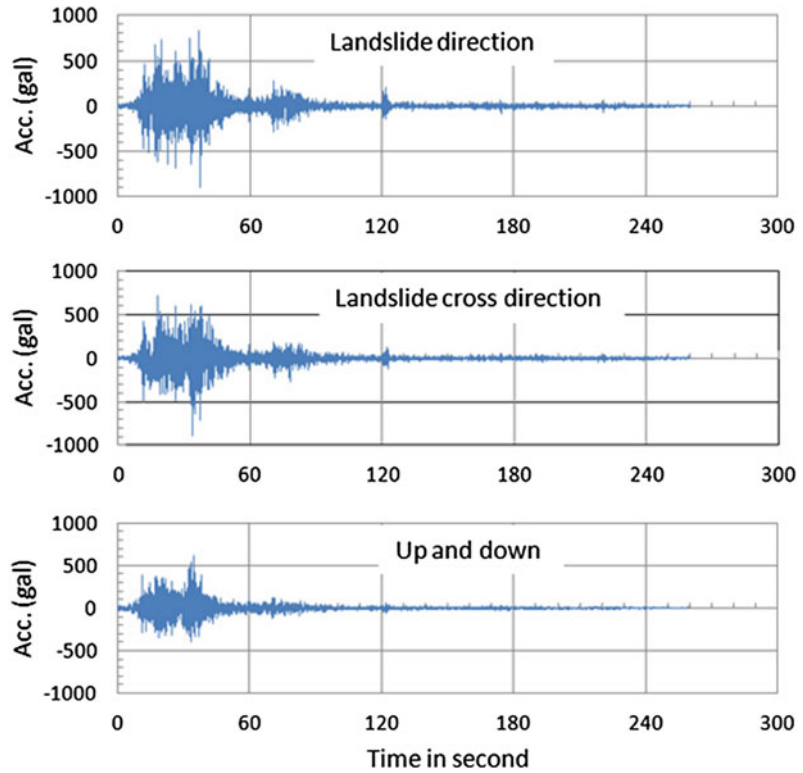
Table 61.1 Input parameters used in simulation with LS-RAPID

Unit weight of soil (kN/m3)	20.0
Cohesion of soil (kPa)	0.3
Cohesion of shear surface (kPa)	0.2
Lateral pressure ratio	0.5
Friction coefficient in soil	0.3
Friction coefficient at shear surface	0.2
Shear strength.at steady state (kPa)	50.0
Excessive pore water pressure generation rate	0.0
Friction coefficient of shear surface at peak	0.3
Cohesion of shear surface at peak (kPa)	10.0

internal soil friction to 0.3. The coefficient of friction of the slip surface during the movement was given as 0.2, as this may be presumed smaller than that inside of the landslide mass.

Moreover, the lateral pressure ration was set to 0.5 and the pore pressure to 0 because ground water was not involved in the mass movement. The shear resistance of the steady state, which is related to the stoppage of the soil mass, was set to 50 kPa.

5.2   Velocity of the Landslide Mass

The velocity of the landslide has not been obtained thus far. However, boulders about 5 to 10 m in diameter can be seen scattered broadly in the sedimentation area. This suggests that the movement of the landslide mass with high speed has resulted in bedrock collapse in the rock mass or soil mass.

Figure 61.7 shows the mean velocity of the moving soil mass obtained from the simulation (direction AB shown in Fig. 61.3). The landslide movement stopped 324 s after the landslide occurred. According to Fig. 61.7, the velocity reached 22.1 m/s at peak velocity 30 s after the start of the landslide movement, and then decreased to about 8 m/s within 30 s and gradually stopped. The relative high velocity of 30 s duration 120 s after the quake in Fig. 61.7 was
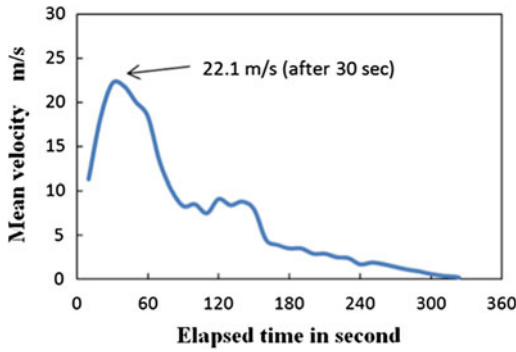
Fig. 61.7 Change of mean velocity of the soil mass in down movement

due to the slightly large but temporal acceleration at this time, as shown in Fig. 61.6.

5.3 Flow Down Process

Figure 61.8 shows the distribution of the landslide mass 5, 30, 120, and 240 s after the start of the simulation. The area inside the red line marked in each figure indicates the range of slide and accumulation. The landslide mass moved down slightly extent within 5 s after the start of simulation and then the front of the landslide mass flow reached the valley located on the lower west side of the landslide. At this time, the landslide mass overflowed to the right banks at 30 s after the start with a maximum velocity at 22.1 m/s, shown in Fig. 61.7. The result at 30 s after the start of simulation in Fig. 61.8 also shows the bulged contour line at the center of the landslide. Then the landslide mass buried the valley, extended to the left and right directions, and reached the opposite slope as shown in the figure, 120 s after the start of simulation, shown in Fig. 61.8. Also, an area where the flow of the landslide mass does not cross over exists on the south downstream side.

After the start of simulation 240 s, the landslide mass started to flow down the valley toward the lower stream. The other area did not differ largely from the accumulation range shown at 120 s. After that, the movement velocity decreased gradually, reaching zero 324 s afterward. The accumulated range after 240 s shown

Fig. 61.8 Downward movement and distribution of simulated soil mass with time

in Fig. 61.8 is approximately equal to the actual distributed range shown in Fig. 61.1, and reproduces the flow into the valley. The obtained simulation results generally satisfy the initial purposes of our study.

6 Conclusions

To evaluate the landslide scale and understand the circumstances of landslide mass movement in the large Daguangbao landslide triggered by the Wenchuan earthquake of 2008, a rapid-landslide-movement simulation using LS-RAPID was applied. From this simulation, the following results were obtained.

The collapsed volume is about 690 million m^3, and the landslide mass buried the lower western valley in almost flat terrain with a depth of 200–300 m.

About 30 s after the earthquake, the velocity of the landslide mass reached a maximum of 22 m/s, then decreased gradually.

The landslide mass, while burying the valley after about 120 s and expanding the valley from side to side, reached the opposite slope.

About 120–240 s after the collapse, the tip of the landslide mass began to move downstream of the valley.

The landslide mass reached the sedimentation area about 120 s after the collapse, and continued to move down to the valley until 324 s after the collapse and stoppage.

References

Chigira M, Wub X, Inokuchic T, Wang G (2010) Landslides induced by the 2008 Wenchuan earthquake Sichuan, China. Geomorphology 118(3–4):225–238

Fraser C, Hanley H (2005) Bias-compensated RPC's for sensor orientation of high resolution satellite imagery. Photogramm Eng Remote Sens 71(8):909–915

Hattori S, Yamakawa T, Ono T, Hasegawa H (2003) Orientation of satellite line scanner images based on affine projection. Proc JSCE 730:1–13 (in Japanese)

Huang R, Pei X, Fan X, Zhang W, Li S, Li B (2012) The characteristics and failure mechanism of the largest landslide triggered by the Wenchuan earthquake, May 12, 2008 China. Landslides 9(1):131–142

Li X, Zhou Z, Yu H, Wen R, Lu D, Huang M, Zhou Y, Cu J (2008) Strong motion observations and recordings from the great Wenchuan earthquake. Earthq Eng Eng Vib 7(3):235–246

Yamakawa T, Fraser CS, Hanley HB (2010) High-precision 3D ground point positioning from IKONOS imagery. J Photogramm Remote Sens 41(2):36–43 (in Japanese)

Sassa K, Nagai O, Solidum R, Yamazaki Y, Ohta H (2010) An integrated model simulating the initiation and motion of earthquake and rain induced rapid landslides and its application to the 2006 Leyte landslide. Landslides 7(3):219–236

Pseudo-Static Stability Analysis of High Fill Slopes by the Shear Strength Reduction FEM

62

Ting-Kai Nian, Dong-Chen Li, Hai-Yang Xu and Guang-Qi Chen

Abstract

Three ground treatment methods such as gravel piles, shallow or deep dynamic replacement, are introduced to stabilize a high fill foundation. A typical engineering geological profile for the formed high fill slope under three ground treatments, is used to calculate the static and pseudo-static stability by shear strength reduction FEM (SSR-FEM). In the study, the pseudo-static seismic loading, together with gravity are exerted to the high fill slope, numerical analysis of slope stability and the corresponding failure criterion is combined to implement the procedure of automatic searching for the factor of safety (FOS) and critical sliding surface (CSS). In particular, without reducing soil strength parameters, comparative studies of displacements and shear strains of the high fill slope subjected to pseudo-static seismic loading are also performed under different ground treatments. The results show that the three ground treatments for the relative soft foundation within slope toe can not only enhance effectively the slope stability, but also reduce the maximum displacements and shear strains. From a practical viewpoint, the treatment method with dynamic replacement to 10 m depth is the optimal one in the three cases discussed in the present project after a reasonable comparative analysis.

T.-K. Nian (✉) · D.-C. Li · H.-Y. Xu
School of Civil Engineering and the State Key
Laboratory of Coastal and Offshore Engineering,
Dalian University of Technology,
116024 Dalian, China
e-mail: tknian@dlut.edu.cn

G.-Q. Chen
Department of Civil and Structural Engineering,
Kyushu University, Fukuoka 812-8581, Japan

1   Introduction

The stability and failure mechanism for the high fill slopes under seismic loading has been an interesting issue. With the rapid development of economy in China, quite a lot of large-scale civil projects such as airports (Chen et al. 2011), have to be built on the high fill foundations located in valleys and oceans because of the intensive lands. In the construction, many artificial slopes with complex material properties and soil layers are formed, some new geotechnical problems occur. For example, the overall deformation and stability of the high fill slopes under impact loading and earthquake inertia forces becomes the vital problem. To ensure the safety of the airport, some analytical and numerical modeling techniques are required to evaluate the static and dynamic stability of the high fill slopes.

2   Finite Element Method with Shear Strength Reduction Technique (SSR-FEM)

Many methods were developed to evaluate the seismic stability of slopes, such as limit equilibrium method (LEM) based on pseudo-static concept, limited sliding displacement method, circular sliding method using FE technique, and so on (Liu et al. 2005). Among these methods, LEM is readily to understand, and can be easily implemented in the current slope analysis, because of its simplicity and practicality. However, it is rather hard to deal with the irregular geometry, complex soils layers and soil structures. In particular, LEM needs to assume the

shape and location of critical slip surface in advance, whereas it is difficult to do this when the slip surface is irregular under some complicated circumstance. On the contrary, the shear strength reduction FEM (SSR-FEM) can provide simultaneously the safety factor, stress state and failure mode. Thus, this approach is being experimentally used to analyze the static and pseudo-static stability of high slopes. In this approach, seismic loading is simplified to a kind of constant equivalent load. Despite the advantages of time domain analysis technique, many practioners are still intended to use pseudo-static analysis based on SSR-FEM to evaluate the seismic stability of slope because of its simplicity and more accumulated experiences (Hu et al. 2011).

The strength reduction method was first proposed by Zienkiewicz et al. (1975), and was later used by many researchers (Ugai 1989; Dawson et al. 1999). The reduced parameters are expressed as below:

$$c'_{\mathrm{m}} = c'/SRF, \quad \phi'_{\mathrm{m}} = \arctan\left(\frac{\tan \phi'}{SRF}\right) \quad (62.1)$$

where SRF is defined as strength reduction factor in Eq. (62.1), c' and ϕ' are the parameters of the available shear strength, c'_{m} and ϕ'_{m} are those of the reduced strength or mobilized shear strength. Herein, an elasto-perfectly plastic constitute model combined with the Mohr–Coulomb failure criterion and the non-associated flow law is adopted to model the soils. When the algorithm cannot converge within a user-specified maximum number of iterations (i.e., 1000), together with a dramatic increase in nodal displacements within the mesh or equivalent plastic strain is connected from the toe to the top of
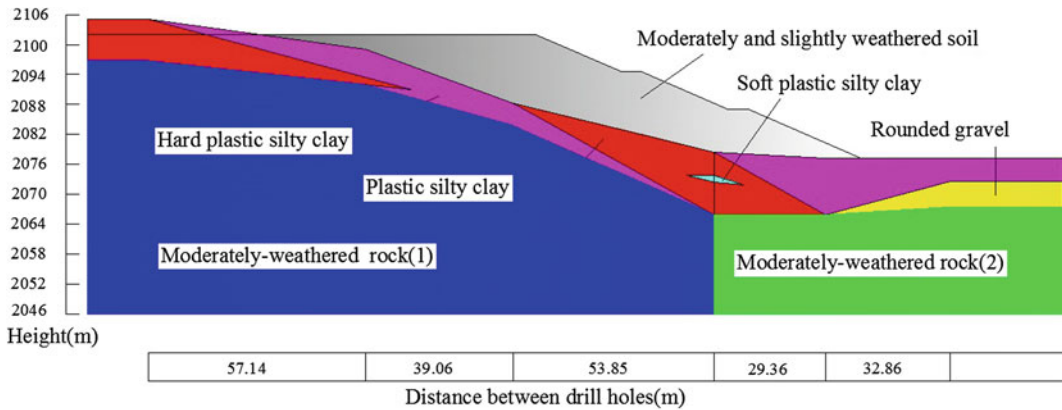
Fig. 62.1 Typical profile of high fill slope

slopes, this implies that no stress distribution can be found that is simultaneously able to satisfy both the failure criterion and global equilibrium. That is to say, failure has occurred.

The calculation progress of elasto-plastic FEM based on strength reduction technique can be described as below: (1) The elasto-plastic analysis to the original slope without fill by using the real strength parameters; (2) The geostress equilibrium progress is implemented by making the computed displacement zero; (3) To reduce gradually the strength parameters (c' and ϕ'), and use the new reduced parameters (c'_m and ϕ'_m) to recalculate until the occurrence of slope failure. At that time, the shear reduction factor SRF is the factor of safety FOS for a slope. That is, $SRF = FOS$.

In this paper, the shear strength reduction FE program based on Abaqus is implemented to analyze the static and pseudo-static stability of a typically high fill slope. The results are compared with those calculated by simplified Bishop's method and those obtained by Plaxis software, and are expected to give some meaningful guidance for practical project.

3   Finite Element Model of a Typical Case

Figure 62.1 shows a typical profile of high fill slope in certain airport of southwest China (Chen et al. 2011). The geometry dimensions, slope ratio and height (33.6 m) are also shown in Fig. 62.1,

the material properties are listed in Table 62.1. Moderately weathered bedrock is overlain by several complex soil layers, which are composed of hard, moderate & soft plastic silty clay and rounded gravel.

In order to improve the bearing capacity of foundation and increase the stability of high fill slope, three ground treatments are considered in the present analysis, including the foundation treated by gravel piles, dynamic replacement with 10 m and dynamic replacement to the top of bedrock (Fig. 62.2).

In the FE models, the left and right boundaries are restrained at the horizontal direction, the bottom boundaries are restrained on the horizontal and vertical directions. The FE mesh for the typical model is shown in Fig. 62.3.

4   Static Analysis

4.1   FOS of Fill Slope Under Static Condition

The static stability of high fill slope under 4 cases is analyzed using the SSR-FEM. The obtained FOS are listed in Table 62.2, and compared with those from Simplified Bishop's method and FEM using Plaxis in Chen et al. (2011).

The results shows that the present solutions from SSR-FEM is rather lower (difference within 2 %) than those from Simplified Bishop's method, whereas somewhat higher than those

Table 62.1 Material properties for the high fill slope (after Chen et al. 2011)

Soil layers	Cohesion, c (kPa)	Friction Angle, ϕ (°)	Unit weight, γ (kN·m^{-3})	Young's Modulus, E (MPa)	Possion's ratio, v
Moderate-slight weathered soils	23.8	24.3	20.1	15.10	0.23
Soft plastic silty clay	13.0	8.0	17.5	1.12	0.42
Plastic silty clay	30.0	12.0	18.5	3.12	0.35
Hard plastic silty clay	36.0	16.0	19.0	6.25	0.25
Rounded gravel	5.0	25.0	19.0	10.00	0.25
Foundation with gravel piles	20.8	19.3	20.3	7.82	0.28
Foundation with dynamic replacement	21.6	22.5	21.4	11.20	0.23
Moderate weathered bedrock (1)	900.0	30.0	22.0	12000.00	0.20
Moderate weathered rock (2)	1200.0	40.0	26.3	16000.00	0.30

Fig. 62.2 Three ground treatment cases. **a** Case 1-foundation with gravel piles **b** Case 2-foundation with dynamic replacement to 10 m depth **c** Case 3-foundation with dynamic replacement to the top of bedrock
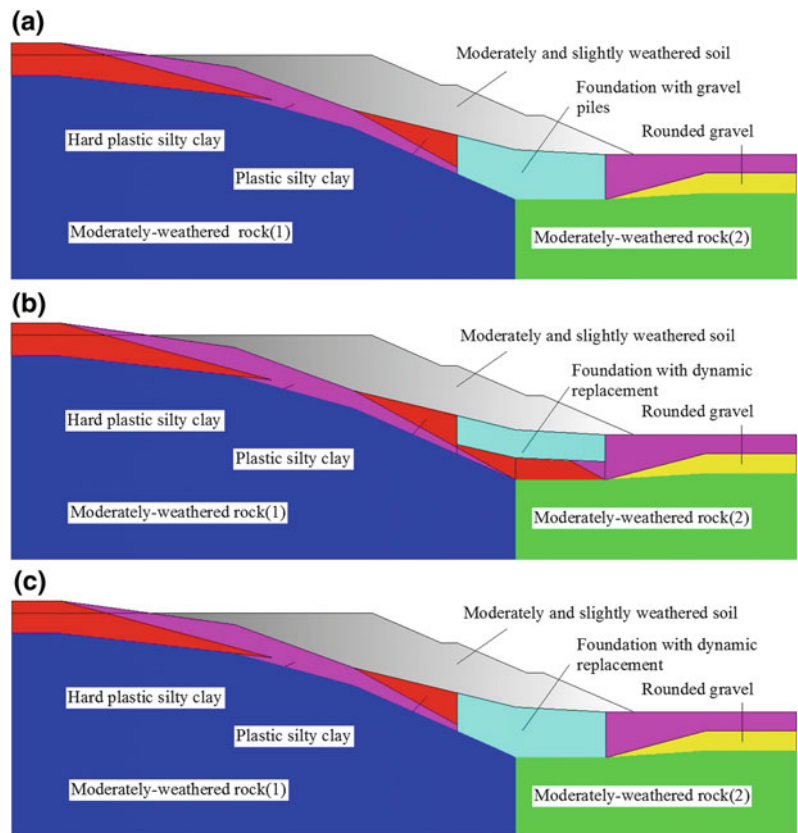
from FEM using Plaxis. It proves that the shear strength reduction FEM is versatile for dealing with the complicated high fill slopes. It also indicates that the three treatment methods effectively increase the slope stability. In particular, the ground treatment depth has a remarkable influence on the overall stability of high fill slope. When the stabilization depth arrives at the top of the bedrock, that is to penetrate the soft soil layers, the FOS of slopes stabilized by gravel piles or dynamic replacement method, are significantly improved from 1.25 to approximate 1.50.
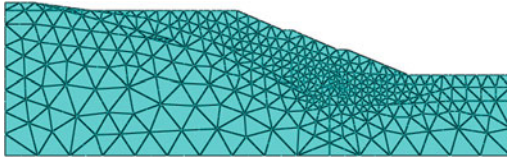
Fig. 62.3 FE mesh for a typical model

4.2   Critical Sliding Surface

Figure 62.4 shows the equivalent plastic strain contours of slope at convergence.

Figure 62.4a shows that the critical sliding surface (CSS) crosses through the soft plastic silty clay and goes well along the interface between hard plastic silty clay and plastic silty clay. The peak value of shear strain is located at soft plastic silty clay zone. Fig. 62.4c shows the peak shear strain moves upwards from the soft plastic silty clay zone because the soft layer are treated by dynamic replacement with a 10 m depth. Without significant change in CSS is observed from the comparison of Fig. 62.4a, c.

Figures 62.4b, d show that the CSS become rather shallower when the treatment depth of gravel piles and dynamic replacements arrives at the top of bedrock (throughout the soft layer). Moreover, the high shear strain zones significantly move upwards. Further, it can be seen from the comparison of Fig. 62.4c, d with Fig. 62.4a that, the peak value zone of shear strain moves upwards and is located at the interface between hard plastic silty clay and plastic silty clay when the treatment depth of dynamic replacement is greater than 10 m. In other words, the critical zone that affects the stability of the high fill slope is moved upwards located at the interface between hard plastic silty clay and plastic silty clay rather than that zone beneath the enhanced area of dynamic replacement. Clearly, the dynamic replacement over 10 m depth improves the slope stability, and also changes the shape and location of CSS as well as the critical high shear strain zone. From a practical viewpoint, a 10 m depth of dynamic replacement is enough to ensure the stability of high fill slope under static conditions.

5   Pseudo-Static Analysis

Horizontal earthquake load is considered in the present model as given below:

$$F_{\mathrm{hi}} = {a_{\mathrm{h}} \xi W_i a_i}/{g} \qquad (62.2)$$

where ξ the reduction factor, valued 0.25; w_j is the gravity of particle i; a_{i} is the dynamic distribution coefficient of the particle, valued 1.75; a_h is the designed horizontal earthquake acceleration, valued 0.2 g (g represents the acceleration of gravity) (Liu et al. 2009).

5.1   FOS Under Pseudo-Static Condition

Table 62.3 lists the FOS calculated using the pseudo-static SSR-FEM. The results show that the FOS remarkably decreases as the pseudo-static horizontal earthquake loads (0.2 g) are considered under the four treatment cases. The greatest FOS decline (19.7 %) is found in case 1, that is to say, the fill slope without treatment is the worst to resist the earthquake loading. On the other hand, FOS in case 3 with a dynamic replacement to 10 m depth decreases least (3.3 %), which indicates that the capability to resist the failure of slope under pseudo-static condition in case 3 is the strongest.

It can be seen from Table 62.4 that the pseudo-static FOS of the fill slopes with three ground treatments are all not less than 1.25, and also have a remarkable increase compared with that without treated slopes under pseudo-static condition. However, from a practical and economic viewpoint, it is the optimal choice to use the dynamic replacement to a 10 m depth.

5.2   Critical Sliding Surface

Figure 62.5 shows the shear strain distribution of fill slope at convergence under pseudo-static condition. The shape and location of CSS as well as the high shear strain zone are rather similar to those under static loading, but the

Table 62.2 FOS for high fill slope under static condition

Case	Treatment method of foundation	Simplified Bishop's method (Chen et al. 2011)	Solutions from Plaxis (Chen et al. 2011)		Present static solutions	
			FOS	Error/ %	FOS	Error/ %
Case 1	Untreated	1.269	1.221	3.9	1.247	1.7
Case 2	Gravel piles to the top of bedrock	1.499	1.475	1.6	1.488	0.7
Case 3	Dynamic replacement to 10 m depth	1.352	1.331	1.6	1.346	0.4
Case 4	Dynamic replacement to the top of bedrock				1.499	
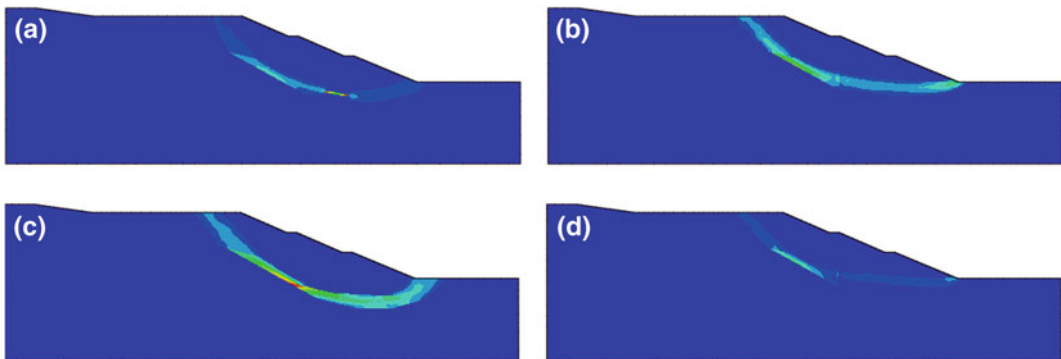
Fig. 62.4 Plastic strain contour of slope at convergence under static conditions **a** Case 1 **b** Case 2 **c** Case 3 **d** Case 4

Table 62.3 FOS for high fill slope under pseudo-static condition

Case	Treatment method of foundation	Present static solutions	Present pseudo-static solutions	Decline ratio of FOS/ %
		FOS	FOS	
Case 1	Untreated	1.247	1.001	19.7
Case 2	Gravel piles to the top of bedrock	1.488	1.249	16.1
Case 3	Dynamic replacement to 10 m depth	1.346	1.301	3.3
Case 4	Dynamic replacement to the top of bedrock	1.499	1.393	7.1

Table 62.4 FOS improvement ratio of different treatment of foundation

Case	Treatment method of foundation	Present static solutions		Present pseudo-static solutions	
		FOS	Improvement ratio/ %	FOS	Improvement ratio/ %
Case 1	Untreated	1.247	—	1.001	—
Case 2	Gravel piles to the top of bedrock	1.488	16.2	1.249	24.8
Case 3	Dynamic replacement to 10 m depth	1.346	7.9	1.301	30.0
Case 4	Dynamic replacement to the top of bedrock	1.499	20.2	1.393	39.2
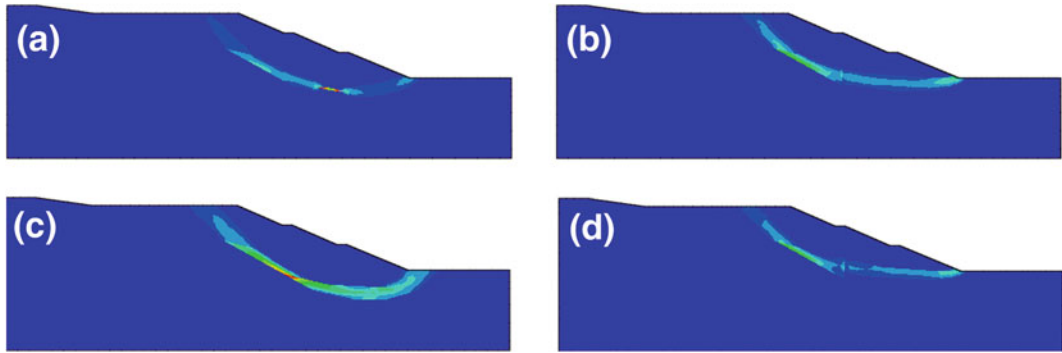
Fig. 62.5 Shear strain contour of slope at convergence under pseudo-static conditions **a** Case 1 **b** Case 2 **c** Case 3 **d** Case 4

Fig. 62.6 Displacement contours in case 3 without reducing soils parameters
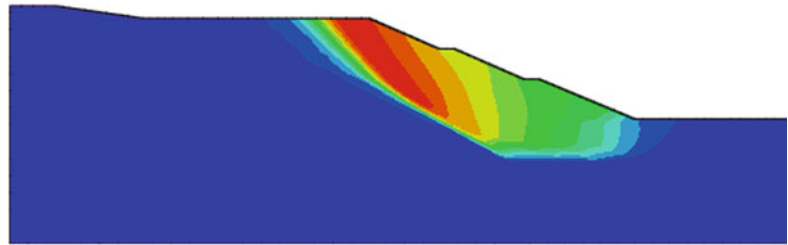
Table 62.5 Horizontal and vertical displacement in case 3

Cases	Static condition		Pseudo-static condition	
	Horizontal displ. (U1)	Vertical displ. (U2)	Horizontal displ. (U1)	Vertical displ. (U2)
Case 1	0.657	1.330	1.363	1.304
Case 2	0.484	0.955	0.985	0.870
Case 3	0.575	1.059	0.813	0.839
Case 4	0.428	0.898	0.487	0.565

depth of CSS under pseudo-static loading is rather shallower than that under static loading.

ground treatment, regardless of static or pseudo-static loading conditions.

5.3 Displacement Under Pseudo-Static Loading

The displacements of high fill slope in case 3 with dynamic replacement to a 10 m depth, subjected to pseudo-static seismic loading are performed without reducing soil parameters. The typical displacement contours are shown in Fig. 62.6, the results are listed in Table 62.5.

It can be seen from Table 62.5 that the horizontal and vertical displacements in case 2, 3 and 4 are both less than that in case 1 without

6 Conclusions

1) The shear strength reduction FEM is feasible to evaluate the stability of high fill slopes with irregular geometry, complex material properties and multi-layers soils.
2) Both gravel piles and dynamic replacement methods are able to improve effectively the static and pseudo-static stability of high fill slopes. From a practical viewpoint, the treatment method with dynamic replacement

to 10 m depth is the optimal one in the three cases discussed in the present project.

3) Pseudo-static method can be effectively used to evaluate the dynamic stability of high fill slope. A time domain response analysis based on real earthquake waves is essential to achieve the more real deformation and stability during an earthquake.

References

Chen J, Song E, Xu M (2011) Application of strength reduction FEM to stability analysis of high fill slope in Kunming new airport. Rock and Soil Mech 32(s1):636–703 (In Chinese)

Dawson EM, Roth WH, Drescher A (1999) Slope stability analysis by strength reduction. Geotechnique 49(6):835–840

Hu C, Lu K, Zhu D, et al (2011) Analysis of pseudo-static seismic stability for three-dimensional slopes. Chin J Rock Mech Eng 30(s1):2904–2912 (In Chinese)

Liu H, Bo J, Liu D (2005) Review on study of seismic stability analysis of rock-soil slopes. Earthq Eng Eng Vib 25(1):164–171 (In Chinese)

Liu J, Li J, Zhang Y et al (2009) Stability analysis of Dagangshan dam abutment slope under earthquake based on pseudo-static method. Chin J Rock Mech Eng 28(8):1562–1570 (In Chinese)

Ugai K (1989) A method of calculation of total factor of safety of slopes by elasto-plastic FEM. Soils Found 29(2):190–195

Zienkiewicz OC, Humpheson C, Lewis RW (1975) Associated and non-associated visco-plasticity and plasticity in soil mechanics. Geotechnique 25(4):671–689

Fully Coupled Dynamic Effective Stress Analysis of the Nigiri Landslide Triggered by 2004 Niigata-Chuetsu Earthquake

Fei Cai, Keizo Ugai, Akihiko Wakai and Seiichiro Kuroda

Abstract

Many landslides were triggered by the 2004 Niigata-Chuetsu Earthquake (Mj = 6.8). The Nigiri landslide, one of the largest landslides, 500 m wide and 200 long, displaced about 40 m. This paper carried out fully coupled dynamic finite element analysis to reenact the ground liquefaction of Nigiri landslide. The ground water level was calculated using unsaturated–saturated finite element analysis, and considering the rainfall before the earthquake. Numerical results show that the increase of the excess pore water pressure was one of the main reasons for the occurrence of the huge landslide. Numerical analyses were also carried out to clarify the effectiveness of landslide stabilizations, such as dewatering system and piles. Numerical results show that the dewatering system was more effective than the stabilizing piles.

Keywords

Landslides · Liquefaction · Stabilization · Numerical analysis

1 Introduction

Annual rainfall of Japan is about two times the average annual rainfall of world (URL1 2012). Moreover, about 20.5 % of the world's earthquakes with a magnitude larger than M6 are occurred in Japan. Consequently, many landslides have been triggered, and unfortunately, will be continually triggered by rainfall and earthquakes in Japan.

Many landslides were triggered by the Niigata-Chuetsu Earthquake (Mj = 6.8) on 23 October, 2004. The Nigiri landslide, as shown in Fig. 63.1, one of the largest landslides, 500 m wide and 200 long, displaced about 40 m. The earthquake was obviously the main triggering factor for the landslide; however, 2 days before the earthquake Typhoon No. 23 with a total about 100 mm of rainfall attacked the same area of the Nigiri landslide on 21 October, 2004. The ground water level (GWL) rose because of the rainfall infiltration; the ground water level has also influence on the occurrence of the Nigiri landslide.

F. Cai (✉) · K. Ugai · A. Wakai · S. Kuroda
Department of Civil and Environmental
Engineering, Gunma University, 1-5-1 Tenjin-cho
Kiryu, Gunma 376-8515, Japan
e-mail: feicai@gunma-u.ac.jp

This paper investigates the influence of the GWL on the stability, and clarifies the mechanism of the Nigiri landslide triggered by the Niigata-Chuetsu earthquake using fully coupled dynamic effective stress analysis. The effectiveness of the stabilizing piles is also numerically investigated.

2 Fully Coupled Dynamic Effective Stress Analysis

A fully coupled dynamic effective stress analysis software UWLC (Forum 8 Co. Ltd. 2005) was used, which consists of three parts: (1) a program used to determine the parameters of constitutive laws by simulating the laboratory tests, (2) a program to calculate the initial stress before the earthquake, and (3) a fully coupled dynamic effective stress analysis program to calculate the seismic response.

The fully coupled dynamic effective stress analysis program uses the u–p formulation. Based on Biot's theory, the dynamic governing equation is given by

$$\mathbf{M}\ddot{\mathbf{u}} + \mathbf{C}\underline{\mathbf{u}} + \mathbf{K}\mathbf{u} - \mathbf{Q}\mathbf{p} = \mathbf{f}^u \qquad (63.1)$$

where $\mathbf{M}$ is mass matrix, $\mathbf{C}$ is damping matrix, $\mathbf{K}$ is stiffness matrix, $\mathbf{Q}$ is coupled matrix, $\mathbf{u}$ is displacement vector, $\mathbf{f}^u$ is external load vector, and $\mathbf{p}$ is excess pore water pressure vector.

The governing equation for the pore water pressure is given by

$$\mathbf{Q}^T\dot{\mathbf{u}} + \mathbf{H}\mathbf{p} + \mathbf{S}\underline{\mathbf{p}} = \mathbf{f}^p \qquad (63.2)$$

where $\mathbf{H}$ is seepage matrix, $\mathbf{S}$ is compression matrix, $\mathbf{f}^p$ is external load vector for the pore water.

Dynamic governing equation is integrated in time domain using Newmark's method of direct integration. Using the acceleration, velocity, and displacement, excess pore water pressure rate, and excess pore water pressure at time step n, those at time step $n + 1$ can be given by

$$\ddot{\mathbf{u}}_{n+1} = \ddot{\mathbf{u}}_n + \Delta\ddot{\mathbf{u}}_n \qquad (63.3)$$

$$\dot{\mathbf{u}}_{n+1} = \dot{\mathbf{u}}_n + \ddot{\mathbf{u}}_n\Delta t + \theta_1\Delta\ddot{\mathbf{u}}_n\Delta t \qquad (63.4)$$

$$\mathbf{u}_{n+1} = \mathbf{u}_n + \dot{\mathbf{u}}_n\Delta t + \frac{1}{2}\ddot{\mathbf{u}}_n\Delta t^2 + \frac{\theta_2}{2}\Delta\ddot{\mathbf{u}}_n\Delta t^2 \qquad (63.5)$$

$$\dot{\mathbf{p}}_{n+1} = \dot{\mathbf{p}}_n + \Delta\dot{\mathbf{p}}_n \qquad (63.6)$$

$$\mathbf{p}_{n+1} = \mathbf{p}_n + \dot{\mathbf{p}}_n\Delta t + \theta\Delta\dot{\mathbf{p}}_n\Delta t \qquad (63.7)$$

where θ_1, θ_2, and θ are integration coefficients. For numerical stability, $\theta_1 = \theta_2 = 0.5$, and

Fig. 63.2 Rainfall intensity
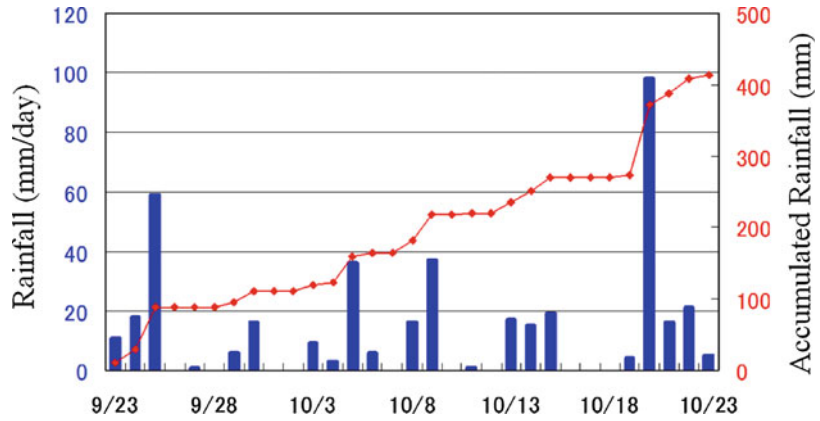
$\theta = 0.5$ was used. Inserting Eqs. (63.3)–(63.7) into Eqs. (63.1) and (63.2), the following equation can be obtained.

$$\begin{bmatrix} \mathbf{M} + \theta_1 \Delta t \mathbf{C} + \frac{\theta_2}{2} \Delta t^2 \mathbf{K} & -\theta \Delta t \mathbf{Q} \\ -\theta \Delta t \mathbf{Q}^{\mathrm{T}} & -\frac{\theta}{\theta_1}(\theta \Delta t \mathbf{H} - \mathbf{S}) \end{bmatrix} \begin{Bmatrix} \Delta \ddot{\mathbf{u}}_n \\ \Delta \dot{\mathbf{p}}_n \end{Bmatrix}$$
$$= \begin{Bmatrix} \boldsymbol{\psi}_{n+1}^u \\ \boldsymbol{\psi}_{n+1}^p \end{Bmatrix}$$

(63.8)

where $\boldsymbol{\psi}_{n+1}^u$ and $\boldsymbol{\psi}_{n+1}^p$ are residual vectors, and given by

$$\boldsymbol{\psi}_{n+1}^u = \mathbf{f}_{n+1}^u - \mathbf{M}_{n+1} \ddot{\mathbf{u}}_{n+1} - \mathbf{C}_{n+1} \dot{\mathbf{u}}_{n+1}$$
$$- \int_\Omega \mathbf{B}^{\mathrm{T}} \sigma' d\Omega + \mathbf{Q}_{n+1} \mathbf{p}_{n+1} \qquad (63.9)$$

$$\boldsymbol{\psi}_{n+1}^p = -\frac{\theta}{\theta_1}(\mathbf{f}_{n+1}^p - \mathbf{Q}_{n+1} \dot{\mathbf{u}}_{n+1} - \mathbf{H}_{n+1} \mathbf{p}_{n+1}$$
$$+ \mathbf{S}_{n+1} \mathbf{p}_{n+1}) \qquad (63.10)$$

Inital stiffness method was used to solve Eq. (63.8). Rayleigh damping with a damping coefficient of 0.02 was also introduced. The time increment of 0.001 s was used.

In this paper, the generalized plasticity for sand developed by Pastor et al. (1990) and modified in some aspects (Cai et al. 2002) was used for the soil layer below the GWL, and UW model was used for other ground materials. After the earthquake, sampling was conducted, and static triaxial drained compression tests and cyclic triaxial compression tests were performed. Such laboratory test results were used to identify the parameters of the generalized plasticity model.

Observed seismic motion at station NIG019 of K-net located at Ojiya city was used to determine the input wave of fully coupled dynamic effective stress analysis.

3   Outlines of Numerical Analysis

First, saturated–unsaturated finite element seepage analysis (Cai and Ugai 2004) was carried out to determine the GWL before the earthquake. In the saturated–unsaturated finite element seepage analysis, the rainfall intensity, as shown in Fig. 63.2, recorded at the Nigiri area was used. The return period of the rainfall was 3–4 years, estimated using the probability of rainfall intensity at the Nigiri area. The cross section and the hydraulic parameters are determined based on the geological investigation report. The ground water level before the earthquake was determined using the calculated water pressure contours.

Two cross sections used in the fully coupled effective stress analysis are shown in Fig. 63.3. The GWL of cross Sect. 63.1 was determined by the saturated–unsaturated finite element seepage analysis; however, the GWL of cross Sect. 63.2 was lowered in the steep slope where drains were assumed to be constructed. A total of 6 cases listed in Table 63.1 were analyzed.
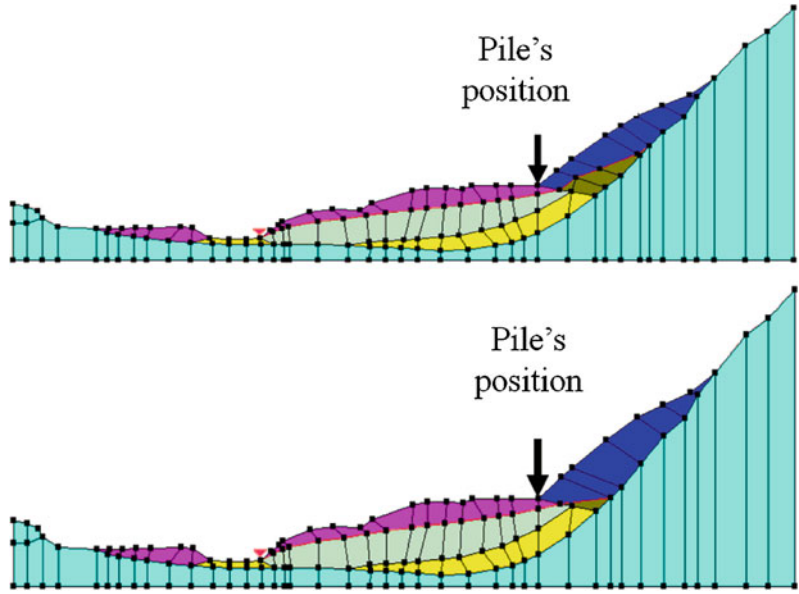
Case	Cross section	Steel-pipe piles
Case 1	Cross Sect. 63.1 (High GWL)	NA
Case 2	Cross Sect. 63.2 (Low GWL)	NA
Case 3	Cross Sect. 63.1	Piles (D = 900 mm, t = 40 mm)
Case 4	Cross Sect. 63.2	Piles (D = 900 mm, t = 40 mm)
Case 5	Cross Sect. 63.1	Piles (D = 1500 mm, t = 40 mm)
Case 6	Cross Sect. 63.1	Piles (D = 350 mm, t = 24 mm)

Fig. 63.4 Deformed mesh for case 1
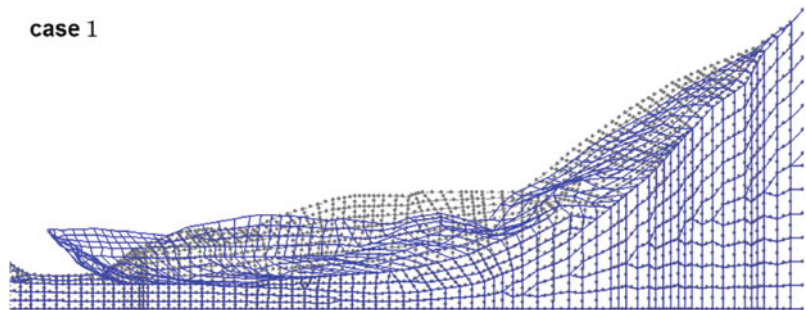
4 Numerical Results

The numerical results of cases 1 and 2 in Figs. 63.4 and 63.5 shows that the displacement of case 2 was totally smaller than that of case1, especially for the steep part of the landslide. This is because the GWL in the steep part of the landslide for case 2 was lower than that for case 1. Fig. 63.6 show that the extensive gentle part of the landslide had liquefied with a high excess pore water pressure for case 1, and it is similar for case 2. Figs. 63.7 and 63.8 show that the displacement and excess pore water pressure ratio increased dramatically 6–12 s after the start of the earthquake.

Figures 63.9 and 63.10 show respectively the displacements of cases 5 and 6. For case 5, the displacement of the gentle part of the landslide
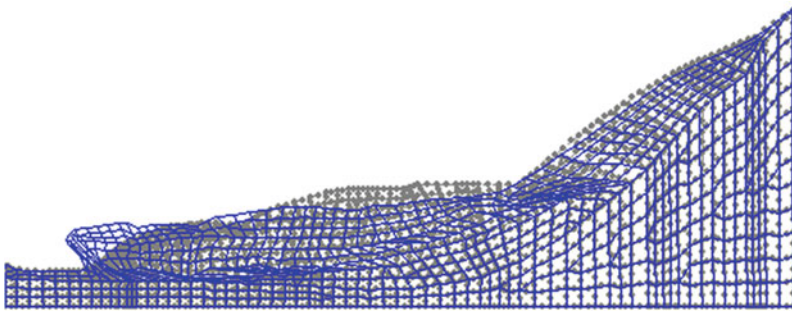
Fig. 63.5 Deformed mesh for case 2
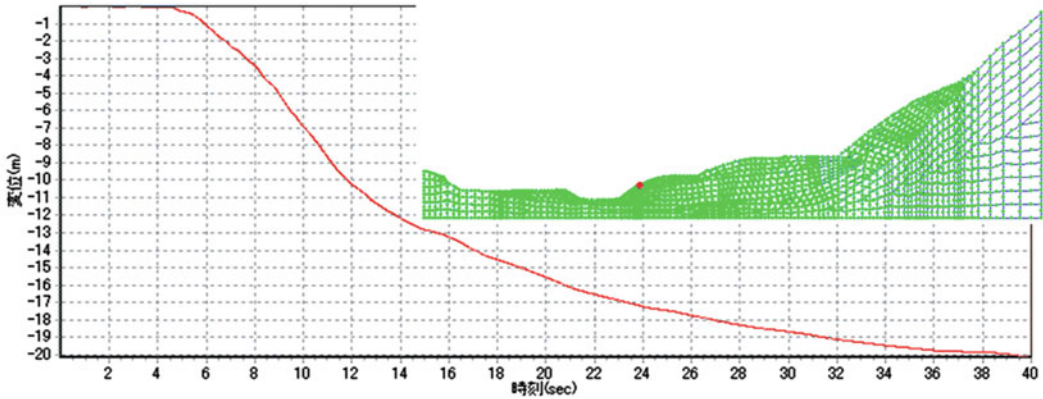
Fig. 63.6 Histogram of displacement of the red point for case 1
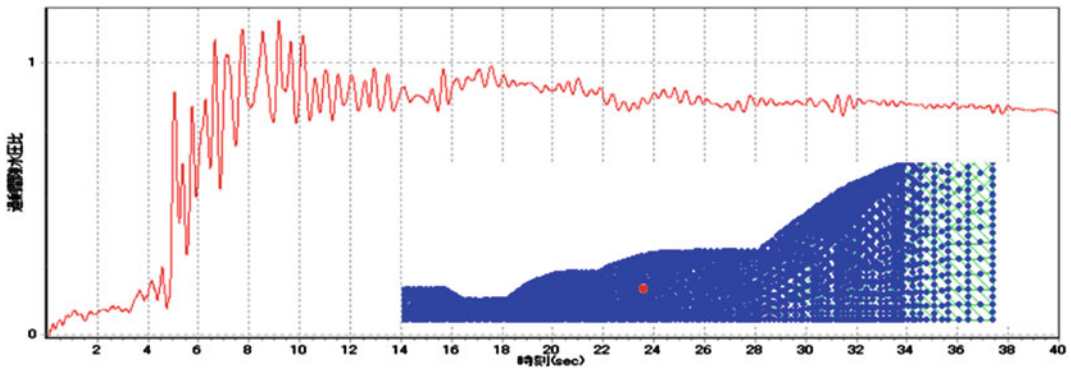
Fig. 63.7 Histogram of excess pore water pressure of the red point for case 1

was similar to that of case 2, and obviously smaller than that of case 1 because the diameter, D, and wall thickness, t, of the steel pipe piles for case 5 are large enough to resist the thrust force from the steep part of the landslide. However, the sliding of the steep part of the landslide over the pile head occurred because the pore water pressure increased and thus the shear strength reduced in the soil layer under GWL of the steep part of the landslide. For case 6, because the piles are more

Fig. 63.8 Contours of excess pore water pressure ratio just after the earthquake for case 1
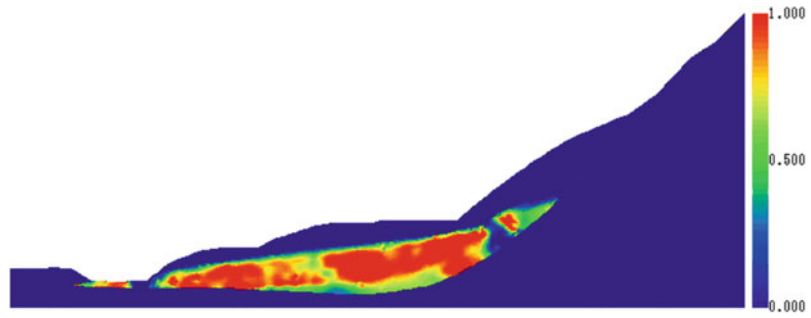
Fig. 63.9 Deformed mesh for case 5
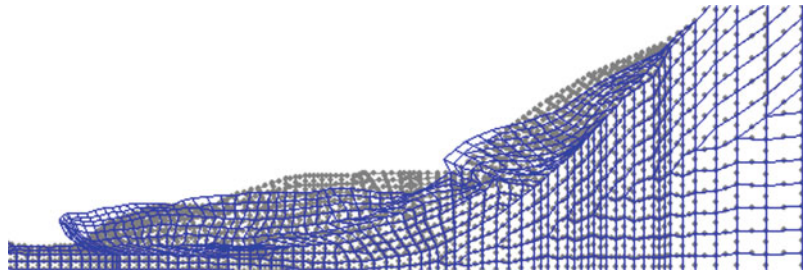
Fig. 63.10 Deformed mesh for case 6
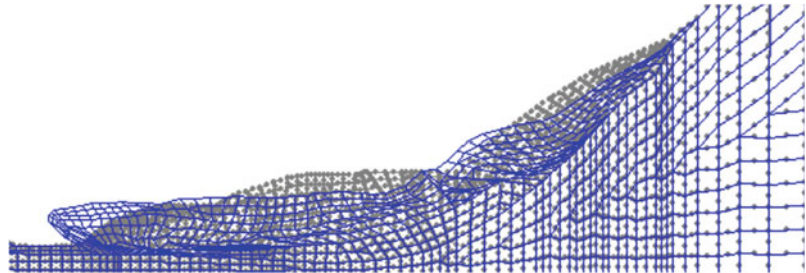
flexible than those for case 6, the piles could not stop the movement of the steep part of the landslide, the displacement of the gentle part of the landslide was larger than that of case 6.

5   Conclusions

The calculated displacement was only half the observed displacement for the Nigiri landslide. However, one of the main reasons for the occurrence of the Nigiri landslide was the increase of the pore water pressure induced by the earthquake. The high GWL induced by the rainfall 2 days before the earthquake resulted in

a larger potential liquefiable soil layer, and thus lager displacement of the landslide during the earthquake. Lowering the GWL was an effective measure to reduce the displacement of the landslide. To fully mobilize the function of piles, the piles have to be stiff enough to resist the lateral movement of the landslide. However, if the shear strength of the part of the landslide higher than the pile head reduced because of the pore water pressure induced by the earthquake, the part possibly slides over the pile head. Consequently, the numerical results show that the drainage is first priority to stabilize the landslides if there is liquefiable soil layer below the GWL.

References

Cai F, Hagiwara T, Imamura S, Ugai K (2002) 2D Fully coupled liquefaction analysis of sand ground under tank. In: Proceeding 11th Japan earthquake engineering symposium. pp 819–824 (in Japanese)

Cai F, Ugai K (2004) Numerical analysis of rainfall effects on slope stability. Int J Geomech ASCE 4(2):69–78

Forum 8 Co. Ltd. (2005) Finite element fully coupled dynamic effective stress analysis program (UWLC). Electrical Manual, http://www.forum8.co.jp

Nagaoka Regional development Bureau of Niigata Prefecture (2005) Investigation report of the Nigiri landslide

Niigata Branch of The Japan Landslide Society (2007): Niigata-Chuetsu earthquake and landslides, Part VI: the Nigiri landslide, The 35th annual field study of Niigata branch of the Japan Landslide society

Pastor M, Zienkiewicz, OC, Chan AHC (1990): Generalized plasticity and the modeling of soil behavior. Inter J Numer Anal Meth Geomech 14:151–190 http://www.mlit.go.jp/river/pamphlet_jirei/bousai/saigai/kiroku/suigai/suigai_3-1-1.html

Numerical Analysis of Two Wooden House Damages Induced by Dune Liquefaction During 2007 Niigata Chuetsu-Offshore Earthquake

Lingyu Xu, Fei Cai, Guoxin Wang, Keizo Ugai, Akihiko Wakai, Qingqing Yang and Atsuo Onoue

Abstract

This paper studies the effectiveness of liquefaction countermeasures for residential houses using fully coupled dynamic effective-stress finite element procedure in conjunction with a generalized plasticity model. Numerical analyses were carried out on two wooden houses damaged in varying degrees due to dune liquefaction during the 2007 Niigata Chuetsu-offshore earthquake, Mw = 6.8: house A only with horizontal drainage pipes was entirely damaged, while house B, improved by soil–cement mixtures, horizontal drainage system and steel-pipe piles, was slightly deformed. Numerical results show that the mechanisms of damages to the two houses were some different. For house B, it was shown that steel-pipe piles were more effective.

Keywords

Fully coupled effective-stress analysis · Generalized plasticity model · Dune liquefaction · Liquefaction countermeasures · Slope effect · Damage mechanism

1   Introduction

Over the years, various mitigation measures have been proposed to reduce earthquake-induced liquefaction hazards, such as concrete piles, cement grouting, sheet piles, and so on. However, limited research efforts were devoted to develop liquefaction countermeasure techniques for residential houses. This was probably because such liquefaction countermeasures are too costly for most owners of houses to afford. Hence, it is necessary to study the cost-effective design of liquefaction countermeasures for residential houses.

L. Xu · G. Wang
School of Hydraulic Engineering, Dalian University of Technology, 116024, Dalian, China

L. Xu · F. Cai (✉) · K. Ugai · A. Wakai · Q. Yang
Department of' Civil and Environment Engineering, Gunma University, Kiryu, 376-8515, Japan
e-mail: feicai@gunma-u.ac.jp

A. Onoue
International Geotechnical Institute, Hunabashi, 274-0081, Japan

During the 2007 Niigata Chuetsu-offshore Earthquake, Mw = 6.8, most wooden houses were damaged due to dune liquefaction. Such houses were rebuilt after they had been damaged also by the dune liquefaction induced by the 2004 Niigata Chuetsu Earthquake, Mw = 6.8, and various techniques were used for various houses to mitigate the potential effects of liquefaction. After 2007 Niigata Chuetsu-offshore earthquake, two wooden houses were inspected in Kariwa village, Kashiwazaki City, Niigata Prefecture. The two houses suffered different level of damages: house A, where the ground was improved simply using horizontal drainage pipes, was completely damaged; however, house B, where the ground was improved using a horizontal drainage system to lower the groundwater level (GWL), soil–cement mixtures and steel-pipe piles, was slightly deformed. In this paper, case studies are carried out on these two houses using a finite element code UWLC in conjunction with a modified generalized plasticity model. The model parameters were quantified by laboratory tests on undisturbed samples and Standard Penetration Test (SPT) data. The seismic input motions in the directions of the cross sections of the two houses were calculated by SHAKE91 using the observed seismic motion at the site of Kashiwazaki-Kariwa Nuclear Power Plant (KK-NPP). The numerical analyses of the two houses were carried out and the mechanisms of damages to the two houses were investigated. Finally, the effectiveness of each countermeasure for house B was studied.

2   Case Histories

The Inaba district locates at the eastern foot of a dune which separates the Japan Sea and the of Kariwa plain. Most wooden houses from house A to house B in Fig. 64.1, built at the eastern foot of the dune were intensively damaged due to dune liquefaction. However, the rebuilt wooden house A, where the ground was improved only using horizontal drainage system, displaced horizontally by 130 cm, and vertically by 120 cm upward, and

inclined forward by about $\overset{\circ}{9}$, was completely damaged. However, the rebuilt wooden house B, where the ground was improved by horizontal drainage system to lower the GWL, soil–cement mixtures, and steel-pipe piles, slightly settled by 12 cm. The details of such house damages have been reported by Isobe et al. (2008), Inotsume et al. (2008), and Yamada et al. (2008).

As liquefaction mitigation measures for house B, horizontal drainage system to lower the GWL, soil–cement mixtures, and steel-pipe piles were constructed. The drainage system had a standard cross section 50 cm wide and 40 cm high, which was constructed by wrapping gravel with mat and had a sand filter. Porous concrete pipe 100 mm in diameter was buried in the gravel, and Netlon pipe 75 mm in diameter was used as a reserve pipe. The drainage system was buried around house B with a bottom depth of 1.7–2.4 m. Ground water from the western dune and the neighboring houses was also shut out, and the drainage system was connected to a side ditch of the road. Soil–cement mixtures of house B used 10 tons cement, and mixed 1 m of the surface ground. The average uniaxial compression strength was 545 kN/m2 of three samples. A total of 92 steel-pipe piles 6 m long, 4.5 mm thick, and 114.3 mm in outer diameter were installed.

3   Fully Coupled Dynamic Effective Stress Analysis

In this chapter, a fully coupled dynamic effective stress analysis software UWLC (Forum 8 Co. Ltd. 2005) was used for liquefaction analysis based on u-p Biot dynamic equations (u is the soil skeleton displacement and p is the pore water pressure), which consists of three parts: (1) a program used to determine the parameters of constitutive laws by simulating the laboratory tests, (2) a program to calculate the initial stress before the earthquake, and (3) a fully coupled dynamic effective stress analysis program to calculate the seismic response.
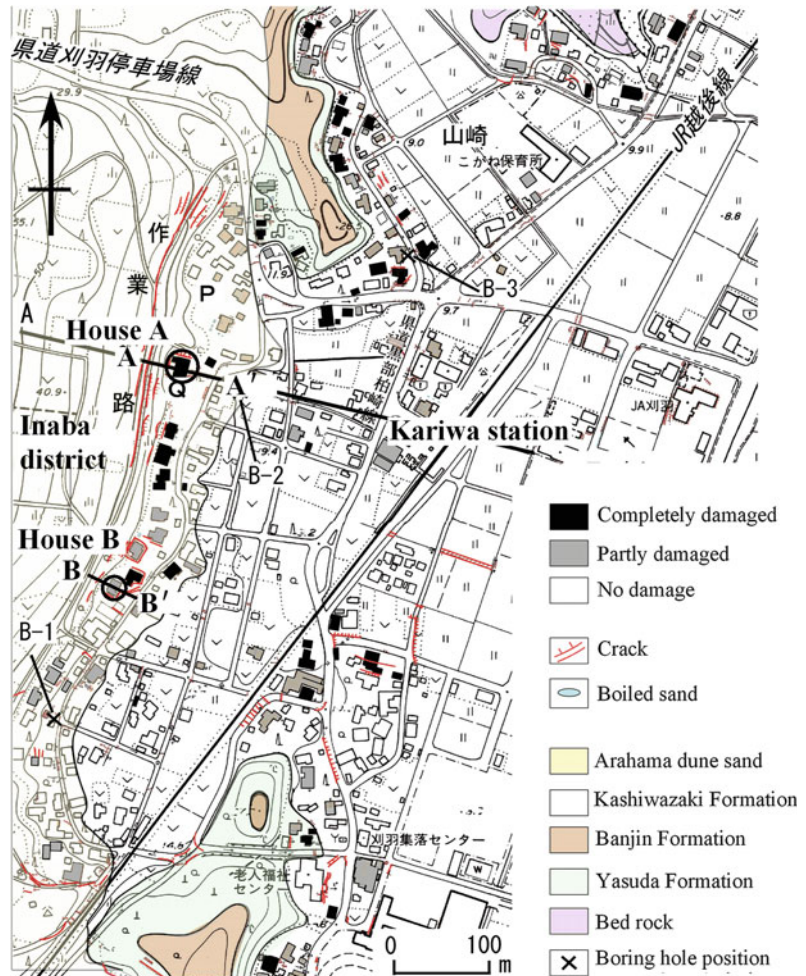
4 Finite Element Model

In this section, finite element models for house A and house B were first built, and then model parameters for each layer in the finite element models were determined. After that, seismic input motions for the two houses were inversed by SHAKE91.

4.1 Analysed Cross Section

Analysed cross sections for the two houses were determined based on the investigated profile as shown in Fig. 64.2 and a geological cross section 2 km from the Inaba district Niigata Prefecture Geotechnical Consultants Association (2002). The soil layers were simplified as three layers: (1) younger sand dune layer (Asd), (2) older sand dune layer (Dsd), and (3) alluvial clayey soil layer (Ac), based on the site investigations after the earthquake by Isobe et al.(2008) and Inotsume et al.(2008).

The cross sections in the finite element analysis for the two houses are shown in Fig. 64.2. Because there was a clayey soil layer at the left side of the analysed extent, an extent of 100 m was selected for this side. The boundary of the right side was set at 200 m away from the right side of the house. The bottom was set at the older sand dune layer at the elevation

Fig. 64.2 Cross section analyzed: **a** house A and **b** house B. Asd_1: younger sand dune layer above the GWL; Asd_2 & Asd_3: younger sand dune layer below the GWL; Dsd_1: older sand dune layer above the GWL; Dsd_2: older sand dune layer below the GWL; Ac_1: upper clayey soil layer; Ac_2: lower clayey soil layer; Su_1 and Su_2: soil just-under the house
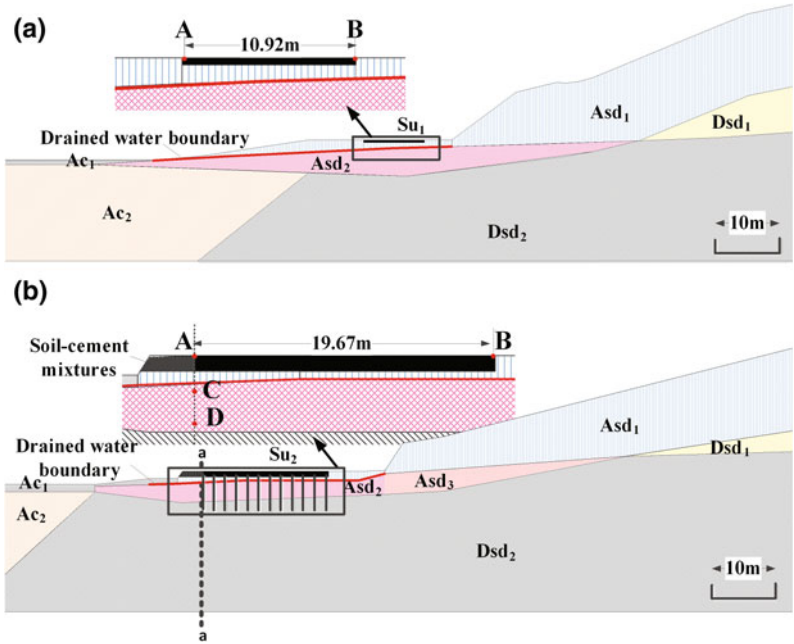
of -7 m. The width and thickness of the potential liquefied the younger sand dune layer were determined by liquefaction resistance based on SPT data near the two houses.

4.2 Model Parameters

In this paper, the generalized plasticity model referred as to Pastor-Zienkiewicz (PZ) III model (Pastor et al. 1999) with some modification by Cai et al. (2002) was adopted to describe the behaviors of dune sands. The parameters of the constitutive model were quantified by laboratory tests on undisturbed samples and SPT data as shown in Table 1.

After the earthquake, sampling of the younger sand dune was conducted near house A, and static triaxial drained compression tests and cyclic triaxial compression tests were carried out. Such laboratory test results were used to identify the parameters of the generalized plasticity model for the younger sand dune. The simulated liquefaction strength of the younger sand dune was also consistent with the results of cyclic triaxial
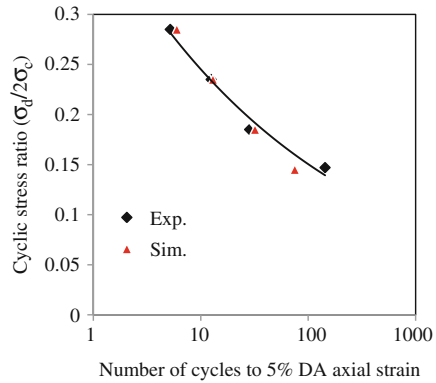
Fig. 64.3 Liquefaction strength of younger dune sand

compression tests using the identified parameters, as shown in Fig. 64.3. The identified parameters were used for Asd_1 and Asd_2.

If, however, the laboratory data are not available, the constitutive model parameters can also be collaborated based on the liquefaction strength determined from SPT blow count values according to the Japanese Design Specifications of Highway Bridges. This method was used to determine model parameters of the younger sand dune layer deposited below the

sand dune slope near house B, which referred to Asd$_3$. From our back-analysis, if the identified parameters from the laboratory tests were assigned to this layer, the large deformation of the sand dune slope would be obtained, which is not consistent with the investigation results. It implies liquefaction strength of this layer was underestimated because of its high SPT values under the sand dune slope according to our investigation. As expected, the calculated liquefaction strength of this layer is as much as 0.38, which is much larger than that from laboratory tests.

An elastic model was used for soil–cement mixtures (Su$_2$) and steel-pipe piles. Elastic modulus of steel-pipe piles was set as 200GPa; cross-sectional area 9.27×10^{-4} m^2 and cross-sectional moment of inertia 1.4×10^{-6} m^4 of steel-pipe piles were calculated based on the number of piles per unit width of house B. The parameters of Su$_1$ were the same as Asd$_1$. The stress–strain characteristics of both the older sand dune layer (Dsd$_1$ and Dsd$_2$) and alluvial clayey soil layer (Ac$_1$ and Ac$_2$) were described by modified Hardin-Drnevich (HD) relationship (Hardin and Drnevich 1972):

$$\tau = \frac{G_{max}\gamma}{1 + G_{max}\gamma/\tau_f} \qquad (64.1)$$

where τ is the shear stress; γ is the shear strain; τ_f is the maximum shear stress (a function of friction angle φ and cohesion c of the clay). In order to capture the influence of confining pressure on stiffness degradation, the maximum shear modulus, G_{max}, is calculated as follows:

$$G_{max} = G_0 P_a \left(\frac{P'}{P_a}\right)^m \qquad (64.2)$$

where G_0 is the coefficient of shear modulus; P' is the mean effective stress, m is a material constant which controls the rate of decay of stiffness with stress; and P_a is the atmospheric pressure. G_{max} at $P'=P'_0$ was determined by $G_{max} = \rho v_s^2$, where P'_0 is the typical mean effective stress of a soil layer; ρ is natural

Table 64.1 Parameters of Pastor–Zienkiewicz III model

Parameter		Asd$_{1,2}$	Asd$_3$
M$_f$	Slope of failure line in p$'$-q plane	1.4	1.38
M$_g$	Slope of the critical state line in p$'$-q plane	1.8	1.45
C	Ratio of Mg in extension side of triaxial test to that in compression side	1	0.8
α_f	Parameter related to yield	0.45	0.45
α_g	Parameter related to plastic flow	0.45	0.45
K$_{evo}$	Coefficient of bulk modulus	304	180
G$_{eso}$	Coefficient of shear modulus	537	235
m$_v$	Exponent of bulk modulus	0.5	0.5
m$_s$	Exponent of shear modulus	0.5	0.5
β_0	Parameter related to soil softening	1.06	8
β_1	Parameter related to soil softening	0.1	0.86.
H$_0$	Coefficient of loading plastic modulus	1700	2000
H$_{U0}$	Unloading plastic modulus (kPa)	6800	6000
γ	Parameter related to reloading plastic deformation	7	12.8
γ_U	Parameter related to unloading plastic modulus	5.095	11

density set as 1700 kg/m^3 and 2000 kg/m^3 for the older sand dune layer (Dsd$_1$ and Dsd$_2$) and alluvial clayey soil layer (Ac$_1$ and Ac$_2$) respectively; and v_s is elastic shear wave velocity. The elastic shear wave velocities used in this paper were measured at the site of Kariwa village and detected at the site of KK-NPP. Other parameters of HD model were selected as typical values as listed in Tab. 2.

4.3 Seismic Input Motion

The seismic input motion was determined using the acceleration recorded at the service hall of KK-NPP. The program SHAKE91 was
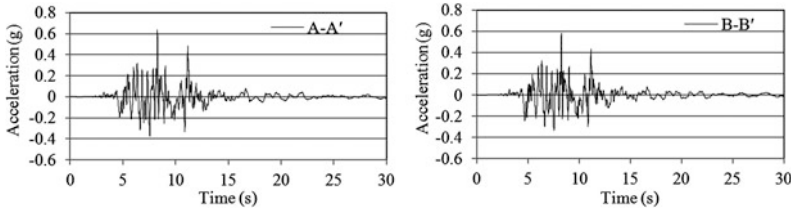
Fig. 64.4 Seismic input motions at the bottom of older sand dune layer for house A (*left*) and house B (*right*)

employed to calculate the seismic motion at the bottom of the older sand dune layer (at elevation of -7 m). The soil properties of this site were identified by Tokimatsu et al. (2008) and adopted in this paper. First, the seismic motion at the bottom of the older sand dune layer in NS and EW was calculated, and then the seismic motion at the bottom of the older sand dune layer in the direction of the analysed cross section was calculated. The difference between the seismic motions for the two houses was induced by the different directions of the cross section for house A and house B, as shown in Fig. 64.4. Because the distance between the service hall of KK-NPP and the two houses was about 400 m, the influence of the distance from the epicenter on the seismic motions was considered to be negligibly small.

5   Numerical Results

In this section, numerical results for the two houses were first presented, and then the damage mechanisms of the two houses were studied.

5.1   Numerical Results for the Two Houses

Based on numerical results, house A spread laterally by about 2.22 m, heaved vertically as much as 0.03 m. House B displaced horizontally by about 0.12 m and settled vertically less than 0.01 m. Fig. 64.5 shows the deformation of

surface ground for the two houses. It can be found that for house A, the calculated and measured deformations were generally consistent with one another. One of the main reasons for this was because the finite element analysis cannot satisfactorily simulate the cracks and sliding deformation occurred. However, for house B, the simulated results of the ground surface deformation after the earthquake corresponded well with the measured results.

5.2   Mechanisms of Damage for the Two Houses

Because the two houses in the case studies are located at the terrace adjacent to the sand dune slope, the damage they sustained may have come from two causes: the liquefaction flow of the younger sand dune layer or the failure of the sand dune slope due to soil liquefaction or softening under the slope. To attempt to clarify the mechanism that produced the damage in the homes, an additional two cases were studied assumed that the sand dune slope was removed, and then compared with the original two cases as discussed in Sect. 5.1 respectively.

Figure 64.6 shows the effects of the sand dune slope on the deformation of the two houses. For house A, after the removal of the slope, the lateral displacement at the left side (see point A in Fig. 64.2a) was largely reduced to 1.00 m at the end of shaking while the vertical displacement changed to 0.22 m downward. The sliding of the sand dune slope in the original case pushed the house forward and the settlement of the slope caused the house to heave upward. Consequently,

Fig. 64.5 Deformation of the surface ground for the two houses: **a** house A and **b** house B
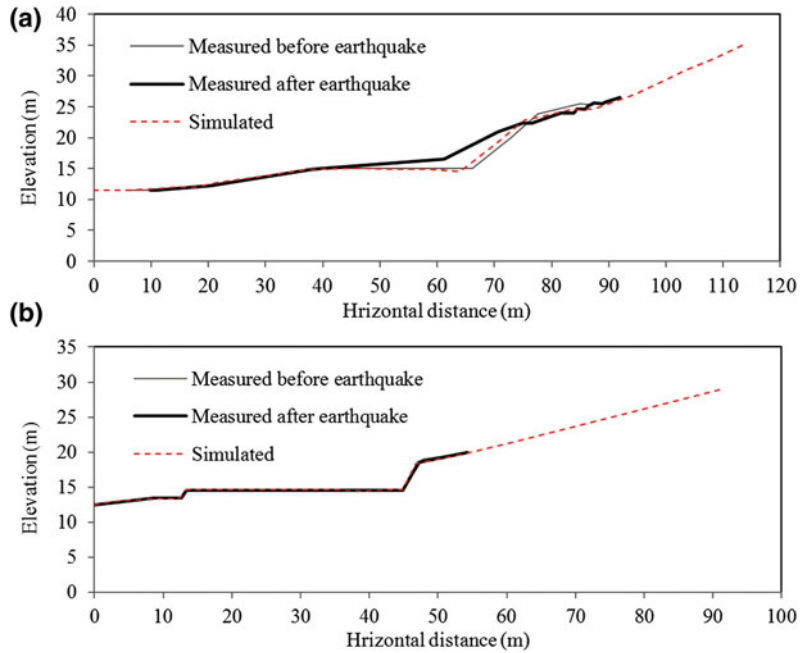
Fig. 64.6 Effects of sand dune slope on the two houses
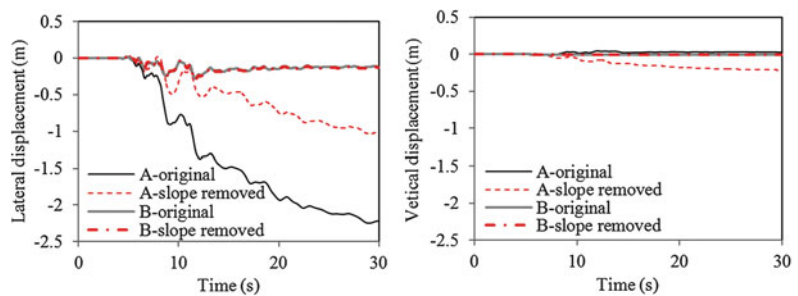
the failure of the sand dune slope was a more significant factor in the damage sustained by house A than liquefaction flow. As a result, special consideration should be given to slope stability when constructing residences under geological conditions similar to those found at the site of house A. However, for house B, the sand dune slope had far less influence on the amount of lateral spreading or settlement. The deformation of the sand dune slope was not a significant factor in producing the damage at house B. This result implies that the cause of the deformation of house B was mainly due to liquefaction-induced deformation associated with the large lateral pressure acting on the piles. Hence, these

mitigation measures constructed for house B can also be extended to the houses in the plain area.

6   Evaluation of the Effectiveness and the Mechanisms of Various Countermeasures

In this section, the effectiveness of each countermeasure hypothetically constructed for house B were studied by analyzing an additional four cases with details in Tab. 64.3.

Figure 64.7 shows a histogram of both lateral and vertical displacements at the left side of house B (see point A in Fig. 64.2b) for case 1 to case 5.

Fig. 64.7 Histogram of deformation of house B for case 1 to case 5
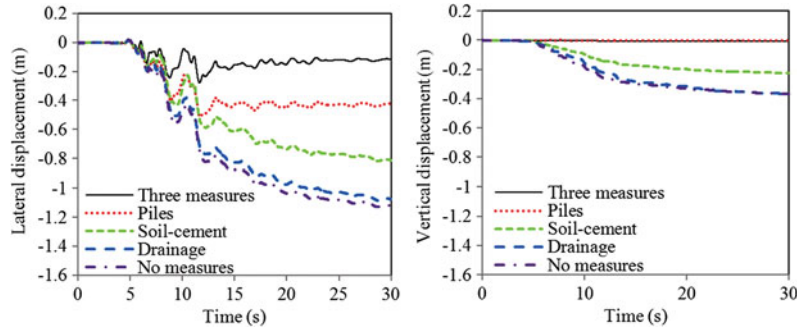
For case 5, the house underwent large spreading of approximately 1.12 m and settlement as much as 0.37 m. When only the horizontal drainage system was installed, the lateral displacement was reduced laterally by 4.0 % and the vertical displacement was almost as large as that in case 5. When the only countermeasure was soil–cement mixtures, the deformation was reduced by 27.5 % and by 38.5 % in terms of lateral spreading and settlement respectively. If the house was only reinforced by steel-pipe piles, the lateral spreading was sharply reduced by 62.1 % and settlement was controlled within 0.01 m. When the house was constructed with three countermeasures, the deformation of the ground was favorably controlled as discussed in Sect. 5.1.

Figure 64.8 depicts the distribution of computed residual horizontal displacements along section a–a marked by the dashed line in Fig. 64.2b for case 1 to case 5 after earthquake. It can be noticed that: (1) the residual horizontal displacements of the older sand dune layer for all cases were very similar and contributed little to lateral spreading of the house. This demonstrates that the mechanism of damage to house B was the liquefaction of the younger sand dune layer below the foundation as discussed in Sect. 5.2; and (2) both the soil–cement mixtures and the horizontal drainage system had the same effect on increase of the thickness of the overlying unliquefied soil and, consequently, reduced the permanent displacement of the house to a certain extent. However, in such cases, the lateral spreading of the unimproved region in the younger sand dune layer was still as large as that in case 5 (no countermeasures). The result is consistent with the previous research conducted by (Cai et al.
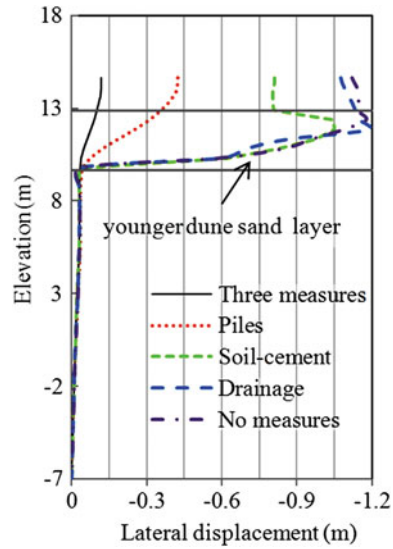
Fig. 64.8 Distribution of computed residual horizontal displacements along section a–a after earthquake

2007) that demonstrated the settlement of an unimproved region was identical at various depths to that found in the case with no improvements for tank ground.

Based on Figs. 64.7 and 64.8, the following conclusions can be drawn: (1) steel-pipe piles were more effective than other countermeasures. The piles bore most of lateral pressure caused by liquefaction and provided vertical support that prevented settlement. As a result, the deformation of the house in cases 1 and 2 was largely mitigated; (2) soil–cement mixtures was less effective. The mixtures lead to better soil strength at surface ground, but these mixtures did not reduce lateral spreading of the unimproved region in the younger sand dune layer, as discussed above. Thus, soil–cement mixtures

Table 64.2 Parameters of Hardin-Drnevich model

Soil	G_{max}(kN/m^2)	P'_0(kN)	m	v(Poisson's ratio)	c(kN/m^2)	φ
Ac$_1$	38250	5	0.6	0.35	30	0
Ac$_2$	24480	74	0.6	0.35	80	0
Dsd$_1$	96800	376	0.5	0.25	20	30
Dsd$_2$	845000	452	0.5	0.25	30	30

Table 64.3 Details of various cases for house B

Case no.	Countermeasures
1	Three countermeasures were built.
2	Only steel-pipe piles were installed.
3	Only soil–cement mixtures was adopted.
4	Only horizontal drainage system was installed.
5	No countermeasures were constructed.

must be applied to a certain depth if they are to be effective; and (3) horizontal drainage system was not of significant value as a countermeasure under conditions like those in this study. The drainage system was ineffective because the elevation of the side ditch of the road that provided the drainage outlet restricted the maximum depth of the horizontal drainage system in case 4. As a consequence, the decrease of the GWL in this case was limited. Perhaps horizontal drainage system installed at greater depths could reduce the permanent deformation of the house. It is possible the deeper the system was installed, the more deformation would be reduced. Based on the results of the case studies, the countermeasures were ranked in order of effectiveness: steel-pipe piles, soil–cement mixtures, and horizontal drainage system.

7 Conclusions

In this paper, a two-dimensional, fully coupled dynamic effective-stress finite element procedure together with the modified PZ III model was used to investigate the mechanisms of damages to the two houses induced by failure of sand dune slope and liquefaction flow, and the effectiveness of various countermeasures. From the numerical results, the following conclusions can be obtained:

1) The mechanisms of damages to the two houses were different: the damage of house A was induced by both the slope failure and liquefaction flow, and the slope failure was more influential; while liquefaction-induced deformation was the main cause of the slight damage to house B. Consequently, special consideration should be given to slope stability when constructing residential housing under similar geological condition to those of house A.

2) Steel-pipe piles were found to be most effective in reducing the permanent deformation of the house. Soil–cement mixtures was less effective because the mixtures at the surface ground did not reduce the lateral spreading in the younger sand dune layer. The effect of horizontal drainage system was insignificant in this study because the maximum depth of the horizontal drainage system was restricted to the elevation of the drainage outlet. Thus, the last two countermeasures should reach a certain depth to achieve their efficiency.

References

Research Group for Hazard of Niigataken Chuetsu-oki Earthquake (2008) The Niigataken Chuetsu-oki earthquake in 2007, the association for the geological collaboration in Japan (in Japanese)

Isobe K, Ohtsuka S, Hirade T, Hayashi K, Sugimura S (2008) Seismic damage of residential area by 2007 Niigataken Chuetsu-oki Earthquake (Part4 Kariwa

village). In: Proceedings of the 20th Japan national conference on geotechnical engineering, pp 1749–1750 (in Japanese)

Inotsume T, Onoue A, Tsuchida K, Ohzawa H, Ugai K, Wakai A, Cai F, Higuchi K, Kuroda S (2008) An example of ground deformation difference induced by the existence or no liquefaction mitigation measures. In: Proceedings of the 25th annual conference of Niigata civil engineering society, pp 152–155 (in Japanese)

Yamada S, Towhata I, Ezoe A, Olivahal B, Tanaka R (2008) Liquefaction of the residential land ground due to the Niigata Chuetsu Oki Earthquake-Inaba, Kariwa. In: Proceedings of the 20th Japan national conference on geotechnical engineering, pp 1775–1776 (in Japanese)

Forum 8 Co. Ltd (2005) Finite element fully coupled dynamic effective stress analysis program (UWLC), Electrical Manual http://www.forum8.co.jp

Niigata Prefecture Geotechnical Consultants Association (2002) Niigata Prefecture ground map editing committee (ed) Niigata Prefecture ground map guide

Pastor M, Zienkiewicz OC, Chan AHC (1999) Generalized plasticity and the modeling of soil behavior. Inter J Numer Anal Meth Geomech 14:151–190

Cai F, Hagiwara T, Imamura S, Ugai K (2002) 2D Fully coupled liquefaction analysis of sand ground under tank. In: Proceedings of the 11th Japan earthquake engineering symposium, pp 819–824 (in Japanese)

Hardin BO, Drnevich VP (1972) Shear modulus and damping in soils: design equations and curves. J Soil Mech Found Div 98:667–692

Tokimatsu K, Arai H, Minowa K (2008) Soil nonlinearity and bedrock strong motions estimated from downhole array records at Kashiwazaki-Kariwa Nuclear Power Plant during the 2007 Niigata-ken Chuetsu-oki Earthquake. J Struct Constr Engng 73:1273–1280 (in Japanese)

Cai F, Takahshi C, Watanabe T, Hagiwara T, Ugai K (2007) 2D fully coupled liquefaction analysis of grouted sandy ground under tank. In: Proceedings of the JSCE earthquake engineering symposium, pp 646–653

Three-Dimensional Virtual Reality Modeling of the Cikangkareng Rock Avalanche in Indonesia

Andhitiawarman Nugraha and Keizo Ugai

Abstract

On September 2nd 2009, the 7.3 Richter scale earthquake hit the Cikangkareng Village, South Cianjur, which is located at the far southern edge of West Java Province in Indonesia. The earthquake has triggered an avalanche of rock cliffs in the hills surrounding the Cikangkareng Village. Debris of the giant rock avalanche had caused dozens of people buried alive. Facts of the scene showed unique phenomena one of which the collapsed rock hill had a height of 200 m but the rock avalanche reached horizontally up to 600 m. Investigation of the rock avalanche has been done to find the mechanism and to know the actual collapse phenomena of the rock avalanche. By using the results of the investigation the Three-Dimensional Virtual Reality Modeling (3DVRM) has been developed to simulate the Cikangkareng rock avalanche. It is suggested that the 3DVRM would be a very useful tool to examine the mechanism of the rock avalanche and to pursue methods of the disaster mitigation. The 3DVRM technology played an important role as a visualization medium which is proven to be effective in connecting perceptions among all related people including local residents and experts. Discussion using the 3DVRM simulation showed to create a common understanding among them about the Cikangkareng rock avalanche. The mechanism of the rock avalanche could be visualized in detail, accurately and comprehensively through the 3DVRM. It will be also useful to simulate real time disaster phenomena by which local residents and experts can propose disaster risk reduction methods for evacuation, preventive countermeasures and determination of safer areas for residential relocation.

A. Nugraha (✉)
PT. Fujicon Priangan Perdana, MTC Kav.J31 Jalan Sukarno-Hatta 590, Bandung, Indonesia
e-mail: andhi@fujicon-japan.com

K. Ugai
Gunma University, Tenjin-1-5-1 Kiryu, Gunma, Japan
e-mail: ugai@ce.gunma-u.ac.jp

1 Introduction

Indonesia, a vast archipelago, straddles continental plates and is prone to seismic activity along what is known as the Pacific Ring of Fire, an arc of fault lines circling The Pacific Basin which is

Fig. 65.1 Cikangkareng
rock avalanche location
(Cikangkareng Village,
South Cianjur, West Java,
Indonesia)
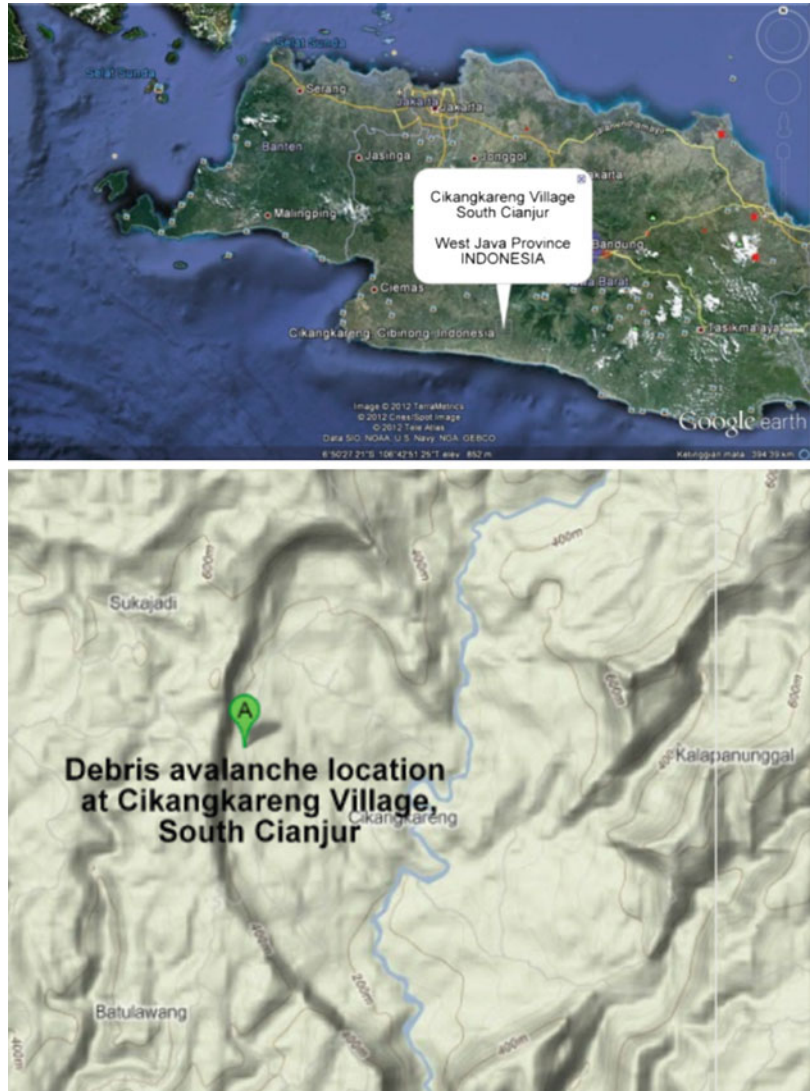
prone to frequent earthquakes and volcanic eruptions.

In Cianjur regency, southern edge of West Java Province, the force of earthquake hit was categorized in the scale of III Modified Mercally Intensity (MMI). Based on geographical condition, there found many medium to high scale of landslide susceptibility in Cianjur regency, so that the earthquake was potentially followed by another disaster such as landslide that occurred in Cikangkareng Village (Fig. 65.1).

This disaster has changed the lives of the residents in a few minutes, and had taken 70 victims, of which 29 people died and 41 others missing.

This disaster will be in vain if passed without a single lesson we can achieve. Therefore, this time, we tried to reconstruct this disaster with the Three-Dimensional Virtual Reality Modeling (3DVRM) method, with the expectation that could be useful in the future.

Fig. 65.2 Giant rocks avalanches

Our Special Thanks to Mr. Budi Brahmantyo (Geologist of ITB Bandung), that have helped us much in in this project.

2   Analysis of Debris Avalanches

The morphology of Cikangkareng and surrounding areas are formed by a steep slope of rock hills with level of moderate to high slope. Debrisavalanche site was located at valley surrounded by high steep slope.

Bellows are data description of Cikangkareng debris avalanches:

Height of slope:200 m
Avalanche length:600 m
Maximum width of landslide material: 300 m
Cliff slope: 70–90°

Debris avalanches from the top of cliff are topsoil or ground reddish with thick about 6 meters. Beneath topsoil there were so many of scattered sedimentary rocks with vary thickness from a few centimeters to several meters (Fig. 65.2).

Cikangkareng landslides was triggered by earthquakes, which occurred on the cliffs with -steep slopes (70–90°) and elevation of slope approximately 200 m. Landslide material dominated by giant rocks with fall–out and rolling motion, so that these types can be classified as rock debris avalanches.

To analyze and investigate the actual condition of debris avalanches, it became necessary to make a reconstruction of landslide mechanism using Three-Dimensional Virtual Reality Modeling.

3   Method

Three-dimensional Virtual Reality modeling process started with data collection information from eyewitnesses and geologist expert. Its initial modeling result is then used as the subject of discussion in a workshop.

Advantages of real time (after-before) and weather simulation shown by Three-dimensional Virtual Reality could be effective visualizing the reconstruction of landslide, and also could be obtained an interactive visual display that is accurate, detailed and complete which is so easily understood by all parties.

Utilization of Three-dimensional Virtual Reality aim as following:

- To describe existing topography condition, before and after the landslides occurred.
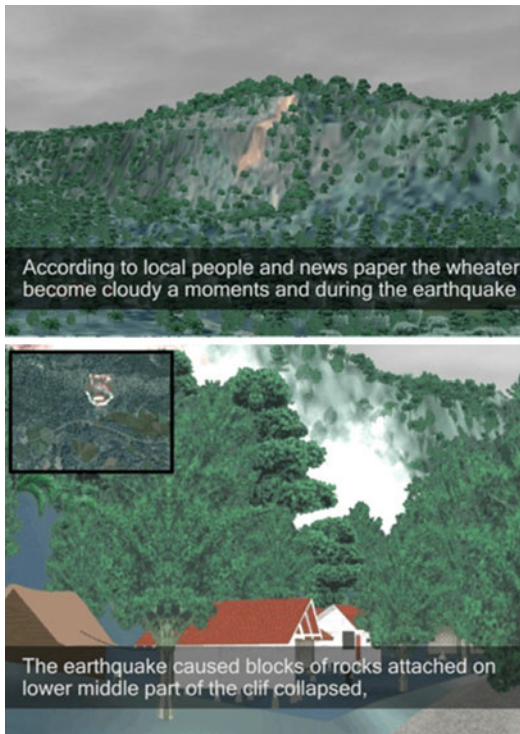
Fig. 65.4 Virtual space that was developed to unify the different point of view and perceptions

- To visualize the surrounding geology condition.
- To reconstruct of landslides mechanism happened just after earthquake occurred.
- To create an effective communication media that can be use in a discussion.

3.1 Three-Dimensional Virtual Reality Process

The results of Three-Dimensional Virtual Reality modeling are then used as subject discussion in a workshop with inhabitants and geologists experts.

During workshop, eyewitnesses told about their testimony. The examples of testimony are as shown below:

- "… Just before the earthquake, the sky suddenly darkened and foggy."
- "… Just before the landslide, the smoke was rising from the bottom of the cliff."
- "… I heard a loud noise. Sounded like a broken stone."
  Etc.

Not a single person who knew all about the chronology as a whole. Therefore, we try to bring testimonials of people and the scientific facts in a chronological order, then visualize into 3DVRM, so that we can better understand what exactly happened at that time.

Three-Dimensional Virtual Reality Modeling Workflow shown in flowchart below (Fig. 65.3):

As illustrated in the figure above, we start by doing data collection and information. We made observations to the field. Based on the facts in the field, we try to arrange a hypothesis about the chronology at the time of the disaster.

Simultaneously, we have a dialogue with local people who are the main eyewitnesses in this incident.

Data and information from the people are not always exactly the same direction. At the time of the disaster, each of the witnesses was being in different places and different conditions. This allows each person has a different perspective.

To unify these differences, we build a virtual space, which can visualize the condition before and after disasters accurately.

As a basis for developing the virtual space, we use the contour, which is obtained from Bakosurtanal (Coordination Agency for Surveys and Mapping) Indonesia. Also, we use satellite imagery to get an overview about the condition before and after the disaster.

In virtual space, we visualize each scene presented witnesses, and to reconstruct the chronology of the disaster in a timeline. Virtual space that is developed is also able to accommodate and display coordinate information, time, weather conditions and even animation avalanche (Fig. 65.4).

We had discussions with the witness again in a workshop, with 3DVRM as a table discussion. By visualizing each perception and compiling them in a timeline, each person can have the same perception about the condition of the

Fig. 65.3 Flowchart of
three-dimensional virtual
reality modeling process
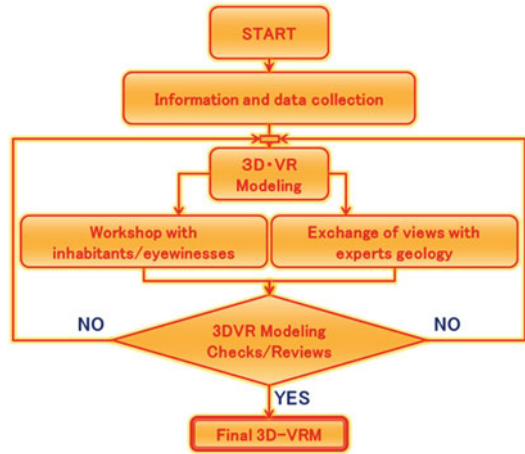
Fig. 65.5 Analysis rock
avalanche by Dr Budi
Brahmantyo
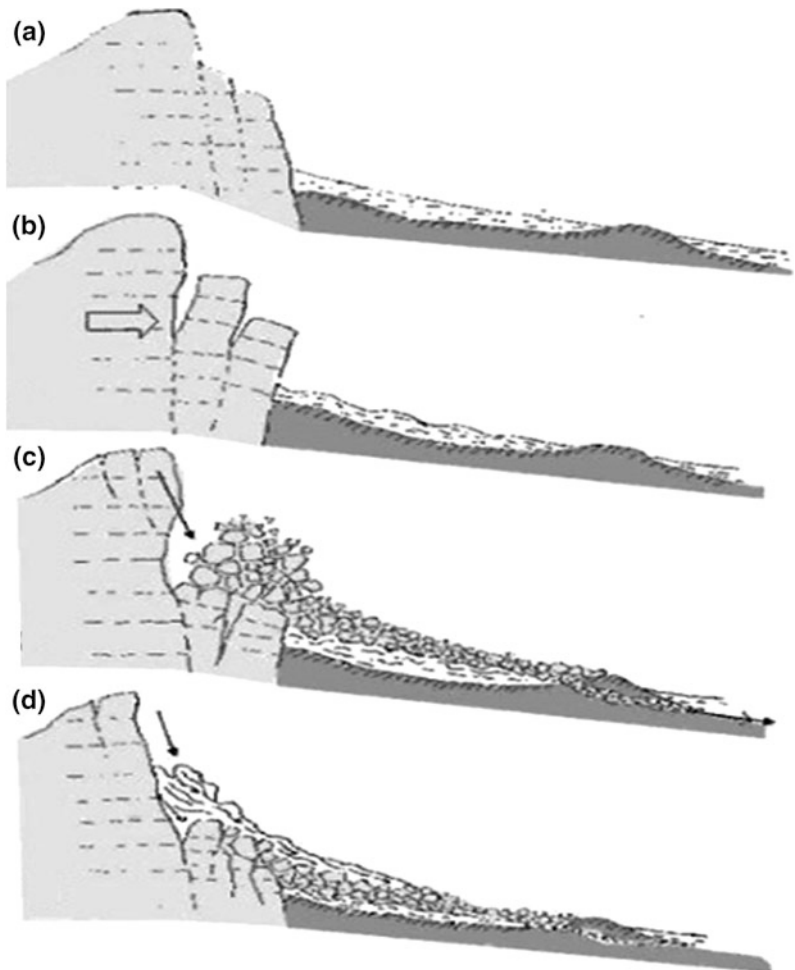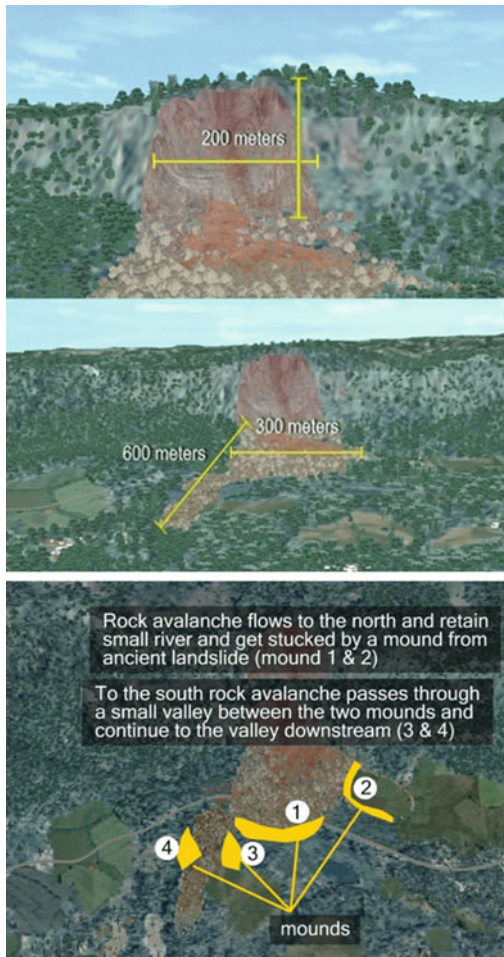
Fig. 65.6 Screenshot of 3DVRM around rock avalanche location

macro. In this way, we can also analyze preventive measures to avoid undesirable conditions in the future.

3.2 Conclusions of Debris Avalanche Mechanism

Simulation using 3DVRM results same perception among geologist and local residents about mechanism of Cikangkareng debris avalanches.

Bellows are scientific analysis presented by Dr. Budi Brahmantyo, geologist expert from Institute Technology of Bandung, regarding Cikangkareng debris avalanche mechanism, that also visualized by 3DVRM (Fig. 65.5).

Pictures above described four main conditions in the reconstruction of this disaster.

A. Condition before the avalanche. There was block of rock attached to the cliff
B. The earthquake force cause the block of rocks collapsed with fast topple movement.
C. Collapsed block of rock smashed forming a rock avalanche. In the middle of the way, the avalanche stopped by a mound from ancient landslide.
D. After the lower part of cliff collapsed, there is nothing else to support the upper part, and finally the upper part that contains soil and rocks also came down (Fig. 65.6).

4 Summary

Three-Dimensional Virtual Reality technology takes part in important role as a visualization medium which is proven to be effective in connecting perceptions among all related parties.

Discussion using three-dimensional Virtual Reality simulation showed that it is possible to have a common understanding about Cikangkareng landslide. Reconstruction of debris avalanche mechanism can be visualized in detail, accurate and comprehensive through three-dimensional Virtual Reality modeling.

Visualization of three-dimensional Virtual Reality can also be useful as case study to determine disaster mitigation. It is also useful to simulate real time disaster condition so that the experts can analyze disaster risk reduction by making preventive stages such as mitigation, evacuation route and determine safer area for residential relocation.

References

Brahmantyo B Dr Faculty of earth science and technology, Institute of Technology Bandung (*Special thanks for him*)

Mitigation Team of The Agency for The Assessment and Application of Technology (2009) Rapid assessment:

field facts and analysis of landslide caused by earthquake on 2nd September, 2009 in Cibinong. Cianjur Regency, West Java Province

Sidik MJ (2009) Antara news: cikangkareng landslide, not just an earthquake (published on 7th September, 2009)

Numerical Analysis of the Largest Landslide Induced by the Wenchuan Earthquake, May 12, 2008 Using DDA

Yingbin Zhang, Guangqi Chen, Lu Zheng and Yange Li

Abstract

The Daguangbao landslide, with an estimated affected area of about 7.3–10 million m^2 and a volume of 750–840 million m^3, is the largest landslide induced by the 2008 Wenchuan earthquake. The sliding mass travelled about 4.5 km and blocked the Huangdongzi valley, forming a landslide dam nearly 600 m high. In order to investigate the landslide progression and reproduce the post-failure configuration, the kinematic behavior of sliding mass was simulated by a dynamic discrete numerical analysis method called DDA that has been widely applied for geotechnical engineering problems due to its superiority in modeling the discontinuous material. In this simulation, based on the shape of failure surface and the character of slope topography, the whole slope was divided into three parts: base block, upper sliding mass, and lower sliding mass. Then two sliding masses were divided into the smaller discrete deformable blocks based on pre-existing discontinuities. Corrected real horizontal and vertical ground motion records were applied as volume forces act to the base block. The simulation results of landslide progression, sliding distance, and shape of post-failure were in good agreement with those obtained from post-earthquake investigation, description from the survivors. Therefore, the methodology applied in this paper is able to capture essential characteristics of the landslide and give a post-failure configuration.

1 Introduction

Landslide is one of the worst natural disasters. Earthquake, as one of the main trigger, can easily induce collapse of slopes and produce landslides and these disasters often caused serious damages to not only human lives but also infrastructures. Over the last decade, large earthquakes, e.g. the Kobe earthquake in Japan (1995), Chi–Chi

Y. Zhang (✉) · G. Chen · L. Zheng · Y. Li
Department of Civil and Structure Engineering, Geo-disaster Prevention Laboratory, Kyushu University, West 2-1110, 744 Motooka, Nishi-ku, Fukuoka 819-0395, Japan
e-mail: yingbinz719@126.com

earthquake in Taiwan (1999), Chuetsu earthquake in Japan (2004), Wenchuan earthquake in China (2008), and Tohoku-oki earthquake in Japan (2011) have severely damaged structures and taken many lives. Among them, the Wenchuan earthquake (Ms = 8.0) occurred in Sichuan Province, China at 14:28 CST on 12 May 2008 induced as many as 60,104 landslides (Gorum et al. 2011) that caused mass wasting greater than orogenic growth (Parker et al. 2011). It is estimated that over one third of the total lost from the 2008 Wenchuan earthquake was caused by the earthquake induced landslides. In addition, according to field investigation and remote sensing image, the Wenchuan earthquake triggered hundreds of rock avalanches, which directly caused more than 20,000 deaths (Yin 2009). Hence, not only stability analysis but also runout analysis of seismic slope is one of the most important aspects of geotechnical earthquake engineering, especially when the slopes are situated close to residential areas.

The Daguangbao landslide is located on the hanging wall of the Yingxiu-Beichuan fault, only 7 km away from the fault (Fig. 66.1). The extent of the damage caused by the Daguangbao landslide is reflected in the following statistics:

(1) The affected area covered 7.8 km^2;
(2) Estimated volume of collapsed rock mass is 750–840 million m^3;
(3) The sliding surface is more than 1 km length in the source area;
(4) The sliding mass travelled about 4.5–4.7 km;
(5) Formed a landslide dam nearly 600 m high.

Many studies on the Daguangbao landslide have been done and that provides the necessary background information for further engineering analysis. Immediately after the sliding, several times inspections were made by Huang group of Chengdu University of Technology, China. Their papers (Huang et al. 2008, 2009, 2012) gave a general introduction of the Daguangbao landslide focused on the characteristics, failure mechanism, and geological property. After that, several post-earthquake field investigations were carried out by Huang group and more deeply
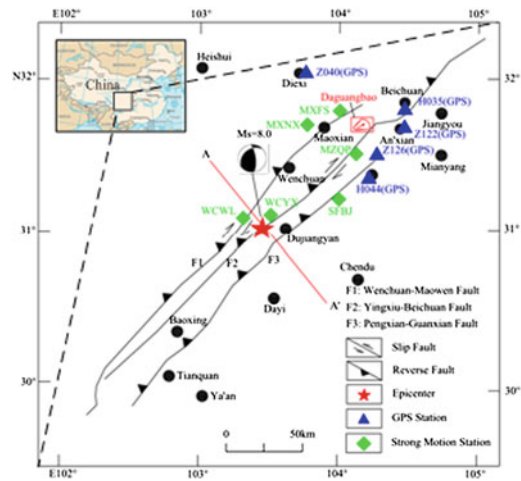
Fig. 66.1 Locations of the Daguangbao landslide, GPS stations and strong motion stations; and surrounding geological setting

studies on characteristics and failure mechanism were presented (Huang et al. 2009, 2012). In addition, remote sensing research on the Daguangbao landslide was carried out by Yin et al. (2011). These researches provide the best information available.

In rock engineering, a rock mass can be divided into small blocks based on pre-existing discontinuities. The mechanical properties and geometric distribution of discontinuities dominate the behavior of a rock mass. In order to predict and estimate the traveling distance and velocities of collapsed rock blocks, two discontinuum-based numerical approaches, Distinct Element Method (DEM) and Discontinuous Deformation Analysis (DDA), which can introduce fractures explicitly in the model, will be effective tools. In comparison to DEM, DDA has a simpler and more straightforward physical meaning (Wu 2003; Wu and Chen 2011).

Based on the original DDA program developed by Shi and Goodman (1989), the latest program version was extended and conducted in this paper, which can more accurately consider the influence of multi-direction earthquake forces on slope stability and runout.

2 Geologic Outline of the Daguangbao Landslide

The Daguangbao landslide has very distinctive scarps and flanks (Huang et al. 2012). The pre-earthquake topography of the landslide area indicates that the elevation descended from the west to the east, with the highest points of 3,047 above sea level at the peak of the Daguangbao point and the lowest point of 1,450 m above sea level at the bottom of the Huangdongzi valley. The altitude difference is about 1,600 m over a horizontal distance of 3 km.

Figure 66.2 shows the post-earthquake aerial photo of the Daguangbao landslide and contour map of the post-earthquake accumulation. Figure 66.3 gives the geological map of the Daguangbao landslide area.

3 Ground Motion

For the present study, there are two problems needed to be addressed regarding the adoption of input ground motions. The first problem is selecting appropriate strong ground motions from the host of records as input. The other one is baselines of the selected near-fault motions records with a large co-seismic displacement that different from general acceleration records.

3.1 Selection of Input Ground Motion

At time of the 2008 Wenchuan Earthquake, China's digital accelerograph network, under the auspices of China Earthquake Administration, collected a rich set of acceleration records. Two criteria for choosing acceleration records are considered in this study. The first criteria is that the accelerograph station should be located as close to the Daguangbao landslide as possible. The second one is the ground co-seismic displacement of accelerograph stations should be similar with that of the site. Several candidate
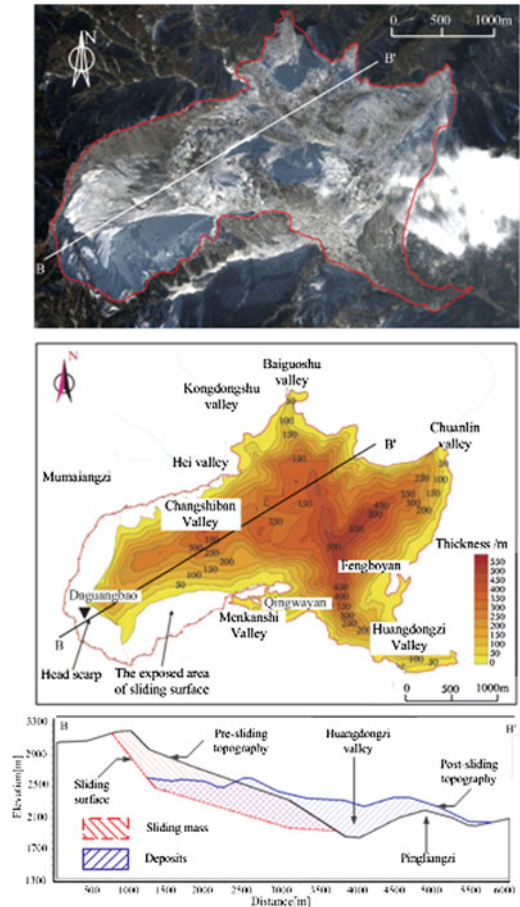
Fig. 66.2 Overview the Daguangbao landslide. **a** Post-earthquake aerial photo (from Google Earth). **b** Contour of the accumulation (Modified from Yin et al. 2011). **c** Post-earthquake B-B' section of the Daguangbao landslide

accelerograph stations are located close to the Daguangbao landslide as shown in Fig. 66.1. Based on the latest studies on the surface co-seismic displacement of the Wenchuan earthquake (de Michele et al. 2010), Pengxian-Guanxian fault (F3 in Fig. 66.1) dominate the surface displacement trend in the study area although the Yingxiu-Beichuan fault is the main shock fault (F2 in Fig. 66.1). Hence, the MZQP station records are adopted as input source for analysis and these acceleration records are depicted in Fig. 66.4. Each set of seismic data is a 100 acceleration record, comprising 20 of

Fig. 66.3 Geology near the Daguangbao landslide (modified from Huang 2012)
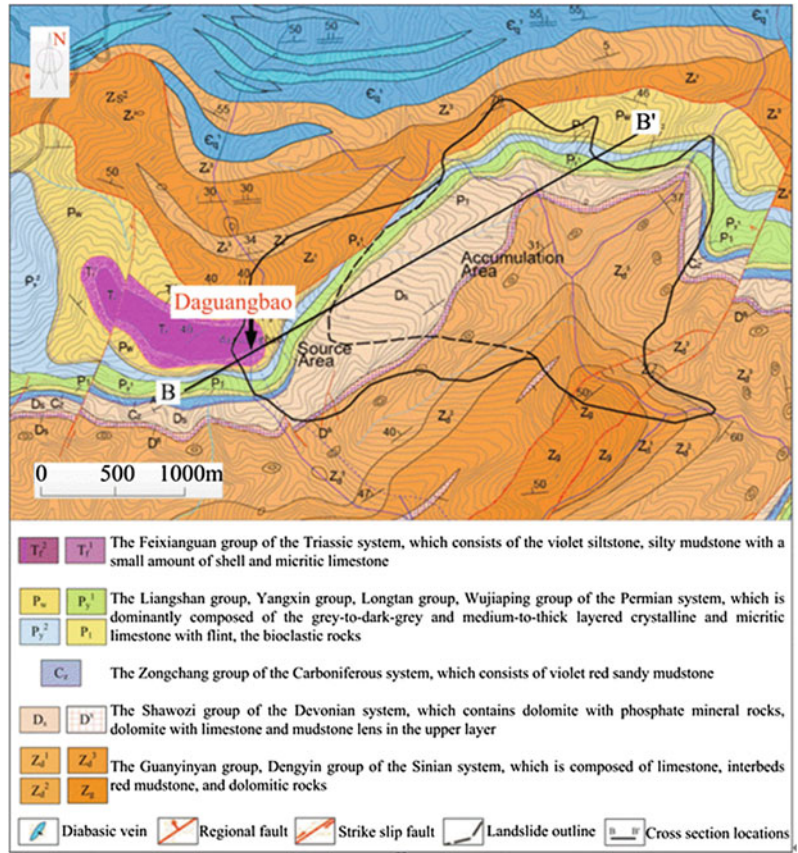
Fig. 66.4 Ground accelerations records of strong motion MZQP
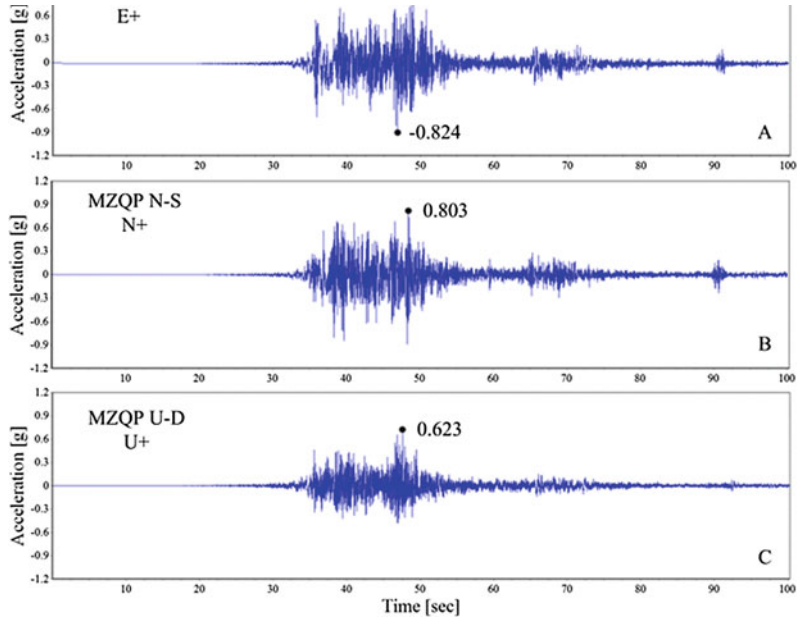
The baseline
correction scheme and
ground velocity history of
MZQP E-W component
after baseline removal
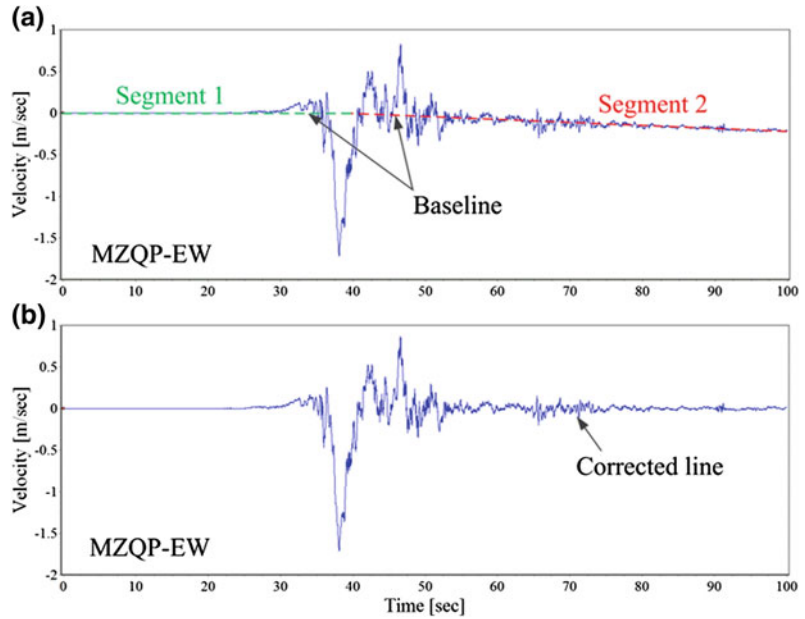
Permanent
displacement from GPS
stations near the
Daguangbao landslide

Station	Longitude (°)	Latitude (°)	E–W displacement (cm)	N–S displacement (cm)	U–D displacement (cm)
Z040	103.68	32.04	31.0	−3.4	–
Z126	104.25	31.51	−122.1	37.9	−20.4
H044	104.19	31.35	−98.3	39.7	−12.3
H035	104.44	31.80	−237.9	48.1	−67.5
Z122	104.45	31.69	−94.5	43.9	−46.6

pre-event data and 80 s of the earthquake data.
The peak ground accelerations from the station
are—0.824 for E–W component, 0.803 for N–S
component and 0.623 g for U-D component,
respectively.

3.2 Baseline Correction

Baseline correction is usually conducted to
eliminate the integration errors for time domain
seismic analysis. Two linear baselines for two
horizontal records and three linear baselines for
vertical records are used for baseline correction
in this paper. The baseline correction progress
for horizontal record is depicted in Fig. 66.5 in
which two linear baselines are first obtained, one
for the first 20 pre-event, and the other for the

last 20 s of the velocity history which is
obtained by once integration from acceleration
record. These lines are extended until they meet
and that gives a composite baseline.

The permanent ground displacements,
obtained by double integrating the seismic
accelerations, must be identical to the ground
movements measured by the GPS at the same
position. However, the locations of the GPS
stations are not entirely consistent with the
strong motion stations in China. Table 66.1
represents the co-seismic displacements that
were measured during the Wenchuan Earth-
quake by the GPS stations that were near the
Daguangbao landslide and located in the same
southeastern foothill geologic zone. The ground
permanent displacements so obtained compare
favorably with the GPS data from Z126, Z122,

H035 and H044. Figure 66.6 shows the comparisons of corrected co-seismic displacement histories with data from GPS stations.

4 Discontinuous Deformation Analysis

4.1 Method Outline

The discontinuous deformation analysis is formulated based on block theory where each block can move and deform independently, and the interaction between blocks is idealized by contact springs. For a two-dimensional problem, each block of arbitrary geometry has six degrees of freedom, among which three components are rigid body motion terms and the other three are constant strain terms. So the deformation variable of block i can be written as

$$D_i = \left(u_0 v_0 r_0 \varepsilon_x \varepsilon_y \gamma_{xy}\right)^{\mathrm{T}} \qquad (66.1)$$

Where u_0, v_0 are the translations of block centroid (x_0, y_0) along the x and y axes, r_0 is the rigid rotation around (x_0, y_0), and $(\varepsilon_x \varepsilon_y \gamma_{xy})$ are the normal and shear strains of block at (x_0, y_0). The displacement $U = (u, v)$ at any point (x, y) of a block can be represented as follow:

$$U = TD_i \qquad (66.2)$$

Where the displacement transformation matrix T is defined as

$$T = \begin{bmatrix} 1 & 0 & -(y-y_0) & x-x_0 & 0 & (y-y_0)/2 \\ 0 & 1 & x-x_0 & 0 & y-y_0 & (x-x_0)/2 \end{bmatrix} \qquad (66.3)$$

DDA computation takes the first order approximation of the displacement function, which represents the constant stress and strain at

any arbitrary point within the block. The rock is assumed to be elastic, and the shear resistance at the boundary is assumed to follow the Mohr–Coulomb yield criterion when the rocks make contact with each other.

A system of blocks is formed from the individual blocks through contacts among blocks and displacement constraints on individual blocks. For the block system, the simultaneous equilibrium equations are similar to the system equations in the FEM, i.e. Hamilton's principle and minimized potential energy.

$$M\ddot{D} + C\dot{D} + KD = F \qquad (66.4)$$

Where D, $\dot{D}$, $\ddot{D}$ are the matrixes of displacement, velocity and acceleration, respectively; M is the mass matrix, in DDA contains only diagonal term, M_{ii}, and each M_{ii} is a fully populated consistent mass matrix, C is the damping matrix, K is the stiffness matrix. F is the forcing matrix. The damping matrix C in Eq. (66.4) can be rewritten as follows in terms of viscosity η and mass matrix M:

$$C = \eta M \qquad (66.5)$$

The physical meaning of viscosity η is the damping of the rock itself, the viscosity of air around the rock surfaces and the vegetation on the surface of a rock slope. In this study, no viscous damping is introduced and the energy loss is Coulomb in nature due to the adoption of Mohr–Coulomb yield criterion that controls the block sliding.

The kinematic Eq. (66.4) is solved by Newmark's β and γ method by using parameters $\beta = 0.5$ and $\gamma = 1.0$ as Eqs. (66.6) and (66.7)

$$D_{n+1} = D_n + \Delta t_n \dot{D}_n + \Delta t_n^2[(1 - 2\beta)\ddot{D}_n + 2\beta\ddot{D}_{n+1}]/2 \qquad (66.6)$$

$$\dot{D}_{n+1} = \dot{D}_n + \Delta t_n[(1 - \gamma)\ddot{D}_n + \gamma\ddot{D}_{n+1}] \quad (66.7)$$

Where subscript n notes calculation step 'n' in the computations. From Eqs. (66.6) and (66.7), assuming the initial displacement D_n at calculation step 'n' is 0 because of the updating Lagrange descriptions are used in the analysis. Then

$$\ddot{D}_{n+1} = \frac{D_{n+1} - D_n - \Delta t_n \dot{D}_n - \Delta t_n^2(1 - 2\beta)\ddot{D}_n/2}{\beta\Delta t_n^2}$$

$$(66.8)$$

Substitution of Eqs. (66.8) into (66.4) forms the global form.

The algebraic equation for the increase in displacement is solved for each time increment by the following equation:

$$\widetilde{K} \cdot D_{n+1} = \widetilde{F}_{n+1} \qquad (66.9)$$

Where $\widetilde{K}$ and $\widetilde{F}$ are effective stiffness matrix and effective force matrix, respectively.

For the dynamic landslide simulation in this paper, the ground excitation applying on base block is employed as acceleration input and forms the force matrix F in Eq. (66.9). In addition, this dynamic numerical method gives unique solutions for problems having large displacement and deformation by evaluating correct contact patterns between rocks during a landslide. The large displacement behavior of each block can be traced by updating the coordinates of each block at the end of each calculation step.

4.2   Simulations

The main sliding direction of the landslide had a trend of N60°E. Figure 66.7 shows the input combined acceleration records. Velocity and displacement time histories are obtained by once and twice integration from acceleration record, respectively. The residual values of displacement time histories indicate that the Daguangbao slope moved in that direction during the earthquake. The horizontal earthquake wave is the projection combination in the main sliding direction (N60°E) using the MZQP acceleration records in E-W and N–S directions. The DDA model is depicted in Fig. 66.8. In this simulation, based on the shape of failure surface and the character of slope topography, the whole slope was divided into three parts: base block, upper sliding mass, and lower sliding mass. Then two sliding masses were divided into the
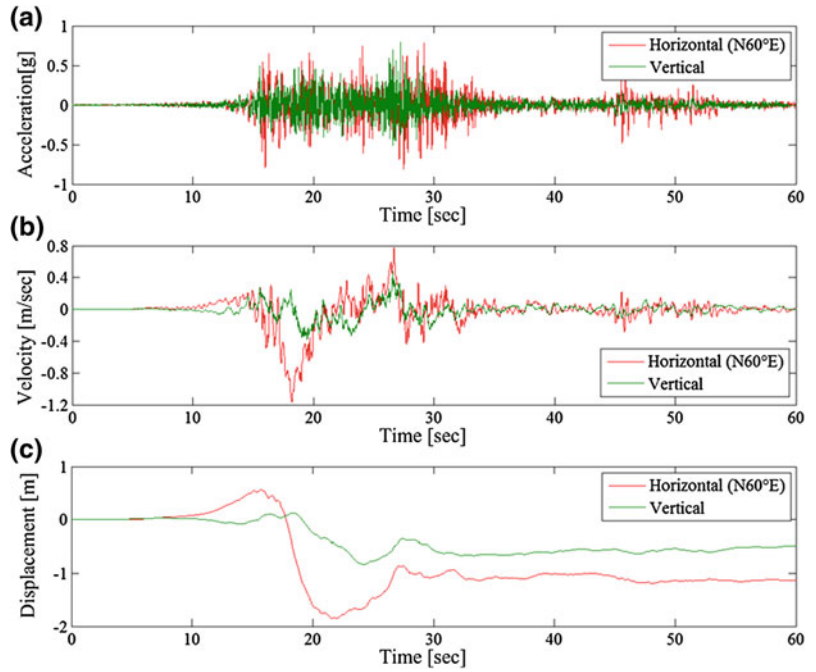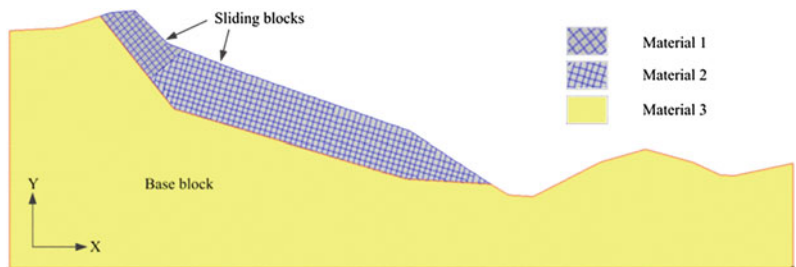
	Material 1	Material 2	Materia 3
Density (ρ): g/cm^3	2.5	2.6	260,000 (virtual)
Unit weight of rock (γ): kN/m^3	25	26	0(virtual)
Elastic modulus (E) : GPa	1.86	2.63	14.76
Poisson's ratio (v)	0.2	0.2	0.1
Friction angle of discontinuities (φ): °	10.8	12.18	23.53
Cohesion of discontinuities (c): MPa	1.276	1.576	4.052
Tensile strength of discontinuities (σ_t): kPa	12	32	556

Fig. 66.9 Horizontal and vertical velocities and displacements of base block
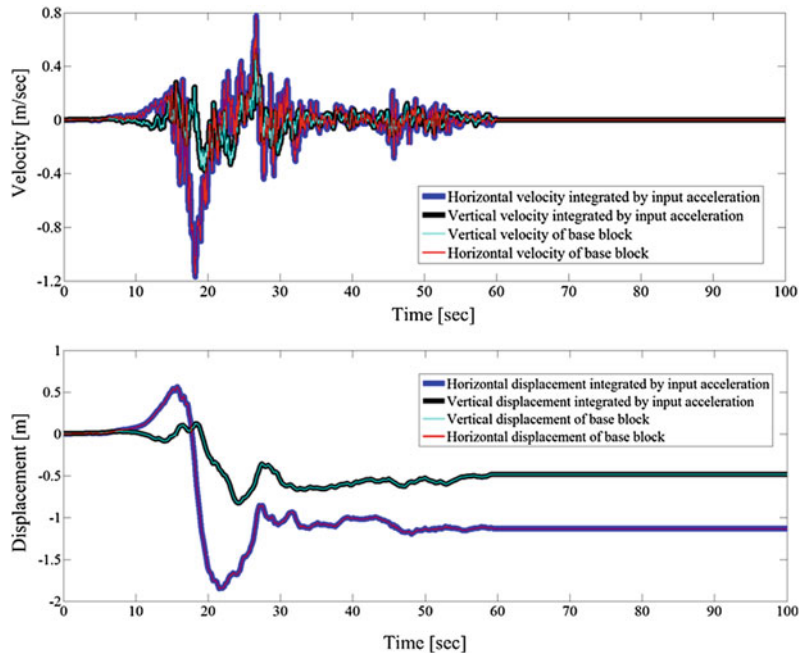
Table 66.3 Control parameters for DDA

Assumed maximum displacement ratio (g_2)	0.001
Total number of time steps	20,000
Time step (g_1)	0.005 s
Contact spring stiffness (g_0)	5.0×10^8 kN/m
Factor of over-relaxation	1.3

smaller discrete deformable blocks based on pre-existing discontinuities.

Table 66.2 shows the analytical conditions and material properties and Table 66.3 shows the control parameters used in DDA simulation. It should be noted that: in order to get the same value between input and output motion response for base block, its mass is defined as 10^5 times to avoid the influences for the response by an additional mass of base block, and the body force caused by gravity acceleration acting downward is set to zero to eliminate up-down free vibrations of the slope block. The slope system is free at both horizontal and vertical directions.

The inputted horizontal earthquake wave is the projection combination in the main sliding direction (N60°E) use the MZQP acceleration

records in E-W and N–S directions. The inputted vertical earthquake wave is the MZQP acceleration records in U-D direction. The duration of earthquake wave is 60 s (20–80 s in Fig. 66.4). The horizontal and vertical waves are acted on the base block at the same time.

4.3   Results

Figure 66.9 shows the seismic velocity and displacement time histories of the base block while applying acceleration records in both horizontal and vertical directions. It can be obviously found that the computational results obtained after the end time of the seismic data coincide well with input seismic data.

Figure 66.10 shows the post-failure behavior of the Daguangbao landslide simulated by seismic DDA. After comparison the final step of the DDA calculation and the topographic cross-section at the Daguangbao landslide (Fig. 66.2), the deposit pattern of the simulated Daguangbao landslide coincides well with local topography.
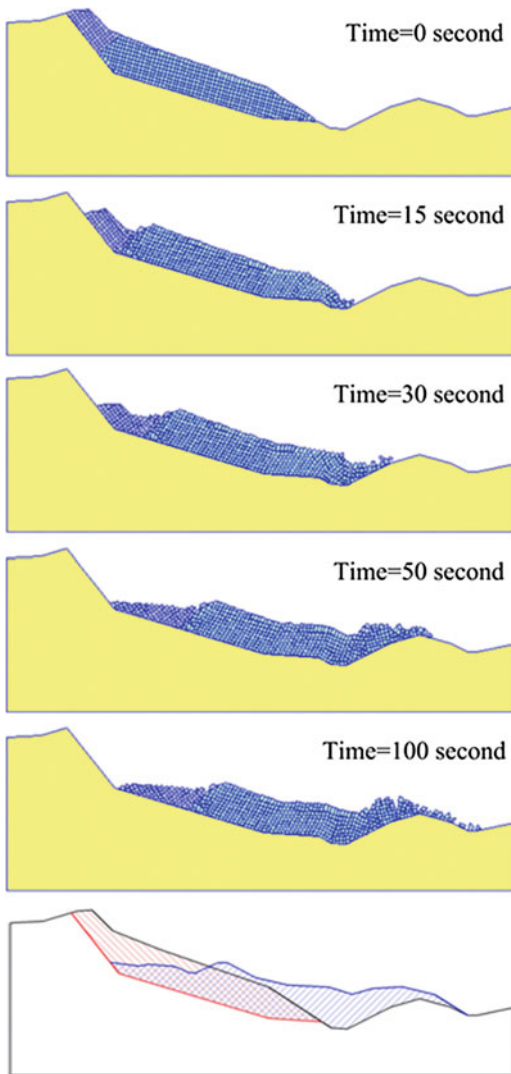
Fig. 66.10 Post-failure behavior of the Daguangbao landslide

5   Conclusions

Post-failure discrete analysis of the Daguangbao landslide induced by Wenchuan earthquake was carried out using modified DDA program. Despite the uncertainties involved, the study is able to reproduce a post failure configuration consist with that observed in the field investigation. Thus, DDA is a useful tool for simulating

the response of a block assembly under considering an earthquake shaking.

References

de Michele M, Raucoules D et al (2010) Three-dimensional surface displacement of the 2008 May 12 Sichuan earthquake (China) derived from synthetic aperture radar: evidence for rupture on a blind thrust. Geophys J Int 183(3):1097–1103

Gorum T, Fan X, van Westen CJ, Huang RQ, Xu Q, Tang C, Wang G (2011) Distribution pattern of earthquake-induced landslides triggered by the 12 May 2008 Wenchuan earthquake. Geomorphology 133(3–4):152–167

Huang R, Pei X et al (2008) Basic characteristics and formation mechanism of the largest scale landslide at Daguangbao occurred during the Wenchuan earthquake. J Eng Geol 16(6):730–741 in Chinese

Huang R, Pei X et al (2009) Further examination on characteristics and formation mechanism of Daguangbao landslide. J Eng Geol 17(6):725–736 in Chinese

Huang R, Pei X et al (2012) The characteristics and failure mechanism of the largest landslide triggered by the Wenchuan earthquake, May 12, 2008, China. Landslides 9(1):131–142

Parker RN, Densmore AL et al (2011) Mass wasting triggered by the 2008 Wenchuan earthquake is greater than orogenic growth. Nat Geosci 4(7):449–452

Shi G, Goodman R (1989) Generalization of two-dimensional discontinuous deformation analysis for forward modelling. Int J Numer Anal Method Geomechanics 13:359–380

Wu JH (2003) Numerical analysis of discontinuous rock masses using discontinuous deformation analysis. PhD dissertation. Kyoto University, Kyoto, Japan

Wu J, Chen C (2011) Application of DDA to simulate characteristics of the Tsaoling landslide. Comput Geotech 38(5):741–750

Yin Y (2009) Features of landslides triggered by the Wenchuan earthquake. J Eng Geol 17(1):29–38 in Chinese

Yin Y, Yu C et al (2011) Remote sensing research on Daguangbao gigantic rockslide triggered by Wenchuan earthquake. J Eng Geol 19(5):674–684 in Chinese

Extension of the Liquefaction Strength Concept Under Cyclic Loading to the Modeling of Volcanic Clayey Soils

Shigeki Tanaka, Hirotatsu Usami, Keisuke Matsushita and Akihiko Wakai

Abstract

The concept of liquefaction strength curve, which is often used for description of the possibility for liquefaction of loose sand in practical design, is tried to be applied for the simulation of the cyclic softening behavior of volcanic clayey soils during earthquake. The method of drawing a liquefaction strength curve based on the UW softening model with the total stress formulations is proposed here. The relationships between the input material parameters in the model and the curvilinear shape acquired is clarified. The obtained results can be useful for future development of numerical applications with the elasto-plastic finite element method to the landslide simulations.

1 Introduction

The dynamic elasto-plastic finite element method (FEM) has been recognized as an effective way to predict the deformation of slopes induced by earthquake.

At the time of the East Japan Great Earthquake occurred in March 2011, numerous landslides with high mobility triggered by the softened volcanic clayey soils in the slope were observed. Thus, the modeling the dynamic characteristics of volcanic clayey soils is an effective way of prediction of future landslides to avoid the occurrence of such problems. It is known that volcanic clayey soils are a kind of special soils behaving as sensitive clays.

In this study, an attempt is done to the simulation of the cyclic softening behavior of volcanic clayey soils, while the liquefaction strength curve is used to describe the phenomena of liquefaction of loose sand.

For this purpose, the method of drawing a liquefaction strength curve based on the UW softening model with the total stress formulations is proposed. The relationships between the input material parameters in the model and the curvilinear shape acquired is clarified. By catching the correlations, it will become possible to determine the parameters of the UW softening model easily from the observed liquefaction strength curve obtained by cyclic triaxial tests.

S. Tanaka (✉) · H. Usami · K. Matsushita ·
A. Wakai

2   Analytical Model

2.1   Strain-Softening Model with Total Stress Formulations

For developing a new constitutive model to simulate the strain-softening behavior at the slip surface, it is necessary to choose one of the two different stress formulation strategies i.e., either the total stress formulation or the effective stress formulation. The effective stress formulations with the stress-dilatancy relationships are applicable for simulating strain-softening phenomenon caused primarily by the increase in excess pore water pressure in loosen sandy soils, such as liquefaction. Conversely, total stress formulation is suitable for strain-softening phenomenon that is primarily affected by the degradation of original cohesion coming from sedimentation, even though the increase in excess pore water pressure may influence the phenomena to some extent.

The basic concept of the UW softening model (Wakai et al. 2010) is the same as the simple cyclic loading model originally proposed by Wakai and Ugai (2004). In these models, the undrained shear strength τ_f with Mohr–Coulomb's c and φ is specified as the upper asymptote of the hyperbolic stress–strain curve.

In addition, in the new softening model, the shear strength value τ_f was modified so as to become a simply decreasing function of the accumulated plastic octahedral shear strain γ^p (Wakai et al. 2005). Thus, the shear strength value τ_f during an earthquake is given as follows:

$$\tau_f = \tau_{f0} + \frac{\tau_{fr} - \tau_{f0}}{A + \tau_{f0}}\gamma^p \qquad (67.1)$$

where τ_{fr} is the residual shear strength after large shear deformation, which is usually much smaller than initial shear strength τ_{f0}. A is a softening parameter determined based on experimental data. In the two-dimensional plane strain analysis, γ^p is defined as follows:

$$\gamma^p = \int d\gamma^p_{\max} \qquad (67.2a)$$

$$d\gamma^p_{\max} = \left| d\varepsilon^p_1 - d\varepsilon^p_3 \right| \qquad (67.2b)$$

The initial shear strength τ_{f0} is denoted as follows:

$$\tau_{fo} = c^\bullet \cos\phi + \left(\frac{\sigma_1 + \sigma_2}{2}\right)_{initial} \times \sin\phi \quad (67.3)$$

The shear elastic modulus G_0 is assumed to decrease in proportion to the decrease in the shear strength value τ_f. Other elasto-plastic formulations are the same as the original model, and were reported in detail previously by Wakai and Ugai (2004).

2.2   The Concept of Liquefaction Strength Curve of Loose Sand

Liquefaction during an earthquake can be explained by the mechanism that accumulation of excess pore water pressure due to negative dilatancy at the time of cyclic loading may reduce the effective confining pressure. One of the methods to simulate this phenomenon in the laboratory is the cyclic undrained triaxial test. As the deviatoric stress is applied repeatedly, the pore water pressure increases, making the effective stress reached to zero gradually. By plotting the observed results of liquefactions as the applied deviatoric stress in the vertical axis and the number of cycles to liquefaction in the horizontal axis, the liquefaction strength curve can be drawn.

2.3   Modeling Cyclic Loading of Volcanic Clayey Soils

Sometimes, volcanic clayey soils have a large rigidity and strength in appearance. However, the strength can be decreased if the skeletal structure has been destroyed by the disturbance due to the earthquake motion.

In this study, the concept of liquefaction strength of loose sand widely used in practical design is applied to simulate the cyclic softening behaviors of the volcanic clayey soils.

Fig. 67. 1 An example of hysteresis curves simulated by the UW softening model
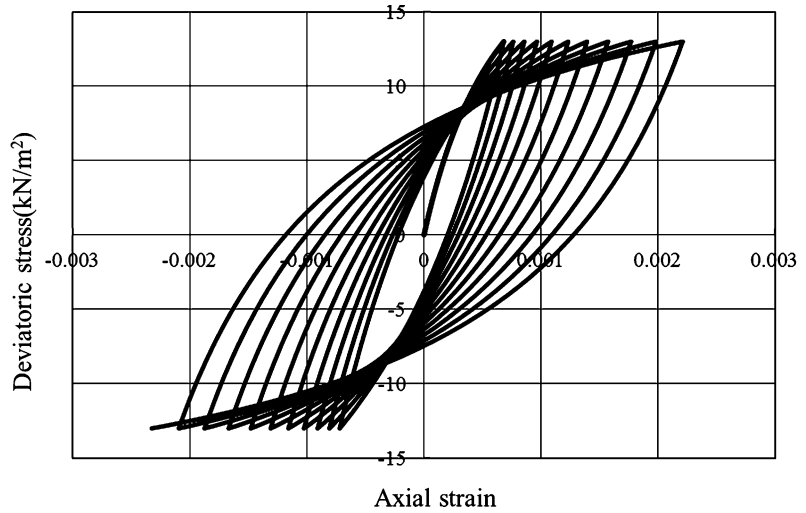
Figure 67.1 shows an example of the stress–strain curves simulated by the UW softening model. The accuracy of the modeling is limited to minimum requirements in practical usages, because of the simplicity of the numerical model. As seen in the figure, the model can simulate the liquefaction including the behaviors where the rigidity of soil is gradually decreased with cyclic loading which is similar to the actual behaviors in the cyclic triaxial tests.

2.4 Analytical Procedure for Obtaining Liquefaction Strength Curves

The procedure for obtaining the liquefaction strength curves based on the UW softening model is the same one in the usual laboratory tests. Assuming a certain value of the deviatoric stress amplitude, the number of cycles to reach the liquefaction can be easily calculated by the obtained hysteresis curves. Usually, reaching to 5 % of axial strain amplitude is considered to be liquefying. The shear stress ratio that is referred as the vertical axis of each plot, is defined as the deviatoric stress amplitude divided by a value of two times initial effective confining pressure. Then, a liquefaction strength curve is drawn.

Table 67.1 Material parameters used in parametric studies for drawing liquefaction strength curves

Young's modulus $E(kN/m^2)$	$1.0 \times 10^4 \sim 1.0 \times 10^6$
Poisson's ratio v	0.4
Cohesion $c(kN/m^2)$	$0 \sim 50$
Internal friction angle $\phi(°)$	$1 \sim 40$
Dilatancy angle $\psi(°)$	0
$b_{\gamma Go}$ (Parameter for damping)	$0.5 \sim 15$
n (Parameter for damping	$1.1 \sim 10$
τ_{fr}/τ_{f0} (Parameter for softening)	$0 \sim 0.9$
A (Parameter for softening)	$0.005 \sim 1$

The material parameters used in the following analyses are summarized in Table 67.1. Undrained conditions with total stress formulations were assumed, and von Mises-type plastic potential was adopted. Therefore, the dilatancy angle was able to be maintained at zero during earthquake. This assumption made it possible to eliminate the need for parameter K_{cv} in the original constitutive model. A case of the numeral simulation for an earthquake-induced landslide will be reported in Fukushima et al. (2012), adopting the UW softening model to simulate the cyclic softening behaviors of a clayey loam (Fig. 67.2) in the slope. Their formulations are the same one as presented in this paper.

Fig. 67.2 Sensitive clayey loam in the slope

3 Parametric Studies

As mentioned above, the test results of liquefaction strength curve can be simulated by using the UW softening model. However, to determine the parameters must be in trial and error, and it takes a significant amount of time. Therefore, in order to develop a more efficient method to determine the parameters, series of parametric studies for evaluating the sensitivity of each parameter in the influences to the liquefaction strength curve is performed. Such knowledge will make the parameters determination process more smartly.

3.1 Sensitivity Analysis on Young's Modulus E

Figure 67.3 shows the results of sensitivity analysis on the Young's modulus E varied in the range of $1.0 \times 10^4 \sim 1.0 \times 10^6$ kN/m^2. The increase of E increases the liquefaction resistance generally.

3.2 Sensitivity Analysis on Cohesion C and Internal Friction Angle φ

Figure 67.4 shows the curves drawn under the initial shear strength of 50, 100, and 150 kN/m^2, i.e. varied in the range of $0 \sim 50$ kN/m^2 and

$1 \sim 40°$, as cohesion c, and internal friction angle φ, respectively. The increase of the initial shear strength clearly increases the liquefaction strength.

3.3 Sensitivity Analysis on Hysteretic Parameters $b_{\gamma G0}$ and n

Figure 67.5 shows the results of the sensitivity analysis. The parameters $b_{\gamma G0}$ and n were varied in the range of $0.5 \sim 15$ and $1.1 \sim 10$, respectively. These parameters affect the stress paths in the stress–strain relationships. However, as far as look at the graph, it is found that the liquefaction strength curve has almost not been affected.

3.4 Sensitivity Analysis on Strain-Softening Parameters τ_{fr}/τ_{f0} and A

Figure 67.6 shows the results of the sensitivity analysis on the strain-softening parameters τ_{fr}/τ_{f0} and A, respectively. They were varied in the range of $0 \sim 0.9$ and $0.005 \sim 1$. A is a parameter that handles the ease of approach to residual strength. It can be seen that τ_{fr}/τ_{f0} correlates with the liquefaction strength if the value is given as larger than a certain value. On the other hand, A is found to affect the liquefaction strength curves strongly.

3.5 Simulation of Actual Volcanic Clay

Figure 67.7 shows the observed liquefaction strength curve of actual volcanic clay with the simulated curve by using the UW softening model as the parameters shown in Table 67.2. The observed results were well simulated by the proposed method in this study.

Fig. 67.3 Sensitivity analysis on Young's modulus E
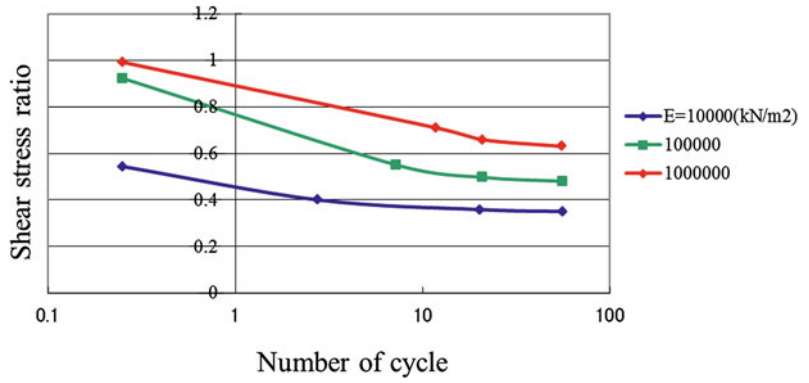
Fig. 67.4 Sensitivity analysis of cohesion c and internal friction angle φ
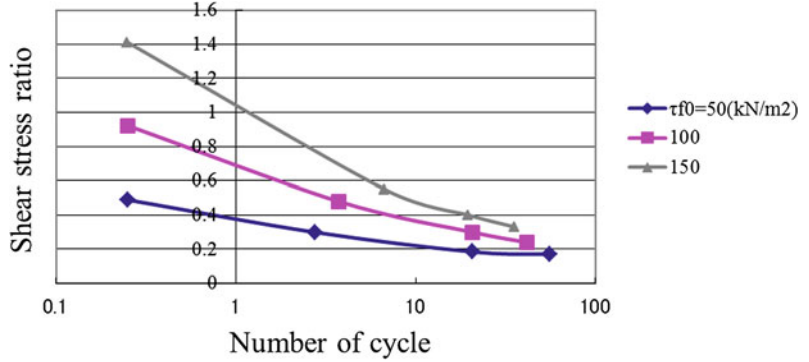
Fig. 67.5 Sensitivity analysis on hysteretic parameters $b\gamma_{G0}$ and n
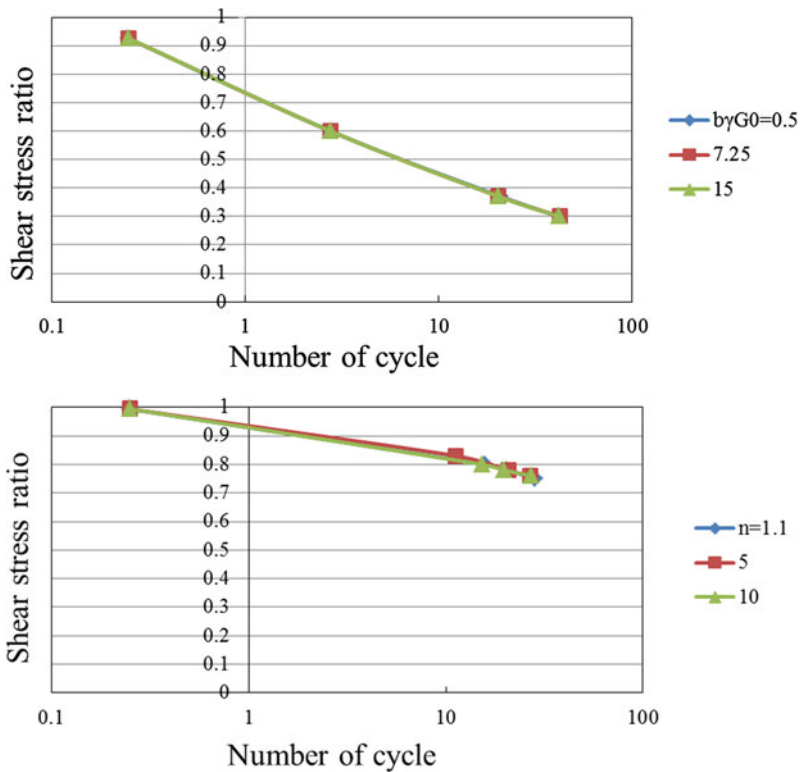
Fig. 67.6 Sensitivity analysis on strain-softening parameters τ_{fr}/τ_{f0} and A
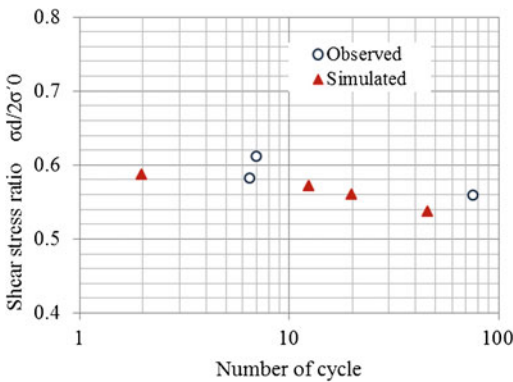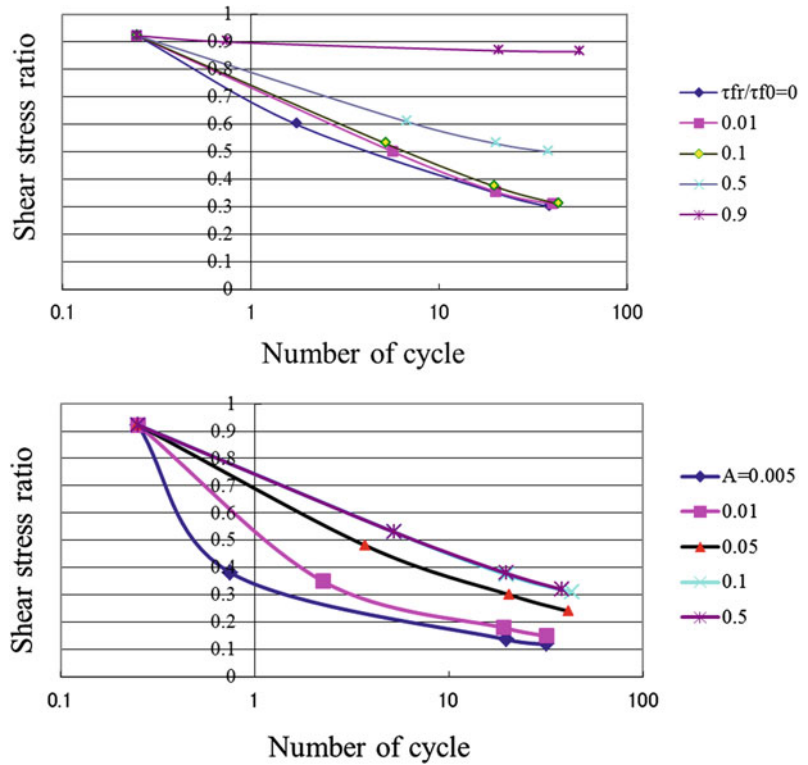
Fig. 67.7 Liquefaction strength curve of volcanic clay samples in Okanouchi

Table 67.2 Material parameters for simulating softening behavior of volcanic clayey soils in Okanouchi

Young's modulus E (kN/m^2)	1,35,400
Poisson's ratio v	0.4
Cohesion c (kN/m^2)	49.3
Internal friction angle ϕ $(°)$	7.1
Dilatancy angle ψ $(°)$	0
$b_{\gamma Go}$ (Parameter for damping)	2.5
n (Parameter for damping	2.2
τ_{fr}/τ_{f0} (Parameter for softening)	0.333
A (Parameter for softening)	11

4 Conclusions

The primary results in the present study are as follows:

(1) The concept of the liquefaction strength curve, which is often used for description of the possibility of liquefaction of loose sands, was applied for simulating the cyclic softening behaviors of volcanic clayey soils during earthquake.

(2) According to the comparisons of results between the observed and simulated liquefaction strength curves, it has been confirmed that the proposed procedures are effective for modeling such sensitive clayey soils.

References

Wakai A, Tamura M, Hayashi K, Kamai T, Shimizu N (2007) Simple evaluation method for seismic performance of slightly-inclined residential ground based on surface-wave investigation and dynamic elasto-plastic finite element method. J Appl Mech JSCE 10:581–591 in Japanese

Wakai A, Ugai K (2004) A simple constitutive model for the seismic analysis of slopes and its applications. Soils Found 44(4):83–97

Akihiko W, Keizo U, Atsuo O, Seiichiro K, Kunihiro H (2010) Numerical modeling of an earthquake-induced landslide considering the strain-softening characteristics at the bedding plane. Soils Found 50(4):515–527

Wakai A, Kamai T, Ugai K (2005) Finite element simulation of landfill collapse in Takamachi Housing complex, Proceedings of symposium on safeness and performance evaluation of ground for housing, JGS, pp 25–30 in Japanese

Parametric Numerical Study of Seismic Slope Stability and Verification of the Newmark Method

68

Almaz Torgoev and Hans-Balder Havenith

Abstract

2D dynamic modelling of seismic slope stability is applied to a landslide-prone area in Central Asia, the Mailuu-Suu Valley, situated in the south of Kyrgyzstan. The calculations are made with models constructed from five long profiles located in the target area, presenting different geological, tectonic and morphological settings. These input data were extracted from a 3D structural geological model built with the GOCAD software. Geophysical and geomechanical parameters were defined on the basis of results obtained by multiple surveys performed in the area over the past 15 years. These include geophysical investigation, seismological experiments and ambient noise measurements. Dynamic modelling of slope stability is performed with the UDEC version 4.01 software that is able to compute deformation on the basis of discrete elements. Inside these elements pure elastic materials (similar to rigid blocks) were used. Various parameter variations were tested to assess their influence on the final outputs. The total parametric study involved more than 50 different models (about 400 computation hours). Preliminary results allow us to evaluate the influence of topography and geology on the amplification of Areas Intensity, which is a very important parameter needed for the computation of Newmark displacements using different GIS approaches [Jibson et al. (US Geol Surv Open file report 98–113,1998); Miles and Ho (Soil Dyn Earth Eng 18:305–323,1999), among others]. The final results of our studies should allow us to define

A. Torgoev (✉)
Georisks and Environment, Department of Geology,
University of Liege, 4000 Liege, Belgium

A. Torgoev · H.-B. Havenith
GEOPRIBOR, Institute of Geomechanics and
Development of Subsoil, 720035 Bishkek,
Kyrgyz Republic

the limitations of the simplified GIS-based Newmark displacement modelling; thus, the verified method would make landslide susceptibility and hazard mapping in seismically active regions more reliable.

1   Introduction

The Mailuu-Suu River Valley is characterized by a combination of geological and tectonic settings favouring intense landslide activity in this area (Alioshin and Torgoev 2000; see landslides as dotted light areas in Fig. 68.1). Together with the hazardous environmental situation due to the presence of radioactive tailings close to some active mass movements, landslide activity itself poses significant risk to society. During the last years significant efforts from responsible agencies, such as the Ministry of Emergency Situation, were spent on environmental risk reduction measures. These efforts also take into account the possibility of a regional environmental catastrophe caused by landslide failure, uranium waste tailing destruction and penetration of radioactive material to Mailuu-Suu River flowing to the densely populated Fergana Valley. But, the effectiveness of risk reduction measures strongly depends on results of landslide hazard and risk studies, because some measures, like the removal of radioactive material and its transportation to another site, demand reliable estimation of landslide hazard in any new place of radioactive material disposal.

Nowadays GIS-based methods of landslide susceptibility mapping are widespread because of the relative low costs and the better effectiveness. But, in a lot of cases such kinds of approaches are suffering from over-simplification and need a deeper review of applied techniques. The goal of the current study is to verify the simplified Newmark displacement method developed on the basis of the original Newmark method (Newmark 1965) and adapted for GIS analyses (Jibson et al. 1998; Miles and Ho 1999, among others).

Numerical simulations are applied to five long profiles passing through different landslides to compute seismically induced displacements. These results are compared with those obtained by GIS spatial analysis based on the simplified Newmark approach. Further perspectives include 3D dynamic modelling of a landslide site situated in another study area, the valley of Min-Kush River. This site was investigated by geophysical and seismological methods, which together with ongoing displacement monitoring allow us to compare displacements caused by real seismic events with those obtained by numerical simulations and by simplified GIS-based approaches. Fig. 68.1 presents the geological map of the target area in Mailuu-Suu river valley together with profiles indicated on this map.

The northern slopes of the Maily-Say Valley are mainly made up of Paleozoic and partly of Jurassic rocks (Formations CALI and JUCLA in Fig. 68.1) while the foothills in the south are formed by Tertiary sedimentary rocks. The central part of the valley hosting the town of Maily-Say shows a series of folds. The cores of the open anticlines are made of soft siltstone and sandstone (Cretaceous rocks: formations RED, LIGH and SALM) overlain by alternating by Paleogene to Neogene claystone and limestone (Formation LIM, PURP and MAIL in Fig. 68.1). On the basis of a new geological map, the slope instability distribution in the Maily-Say Valley was compared with the geologic setting. The comparison indicates that the highest landslide density is observed for the Purp Formation made of Paleogene claystone. The directly underlying LIM Formation made of Paleogene limestone is the second most susceptible formation to landslide processes. Field observations confirmed that landslides are generally located within soft
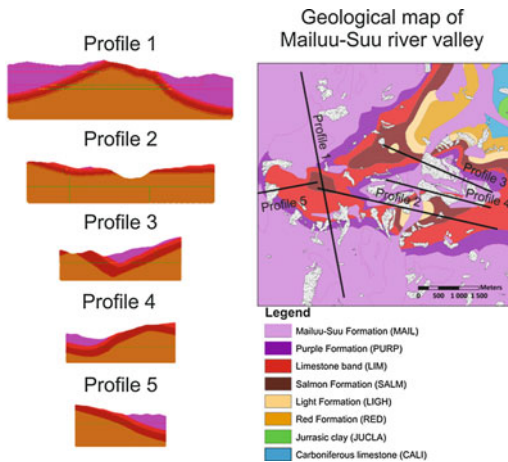
Fig. 68.1 Geological map of Mailuu-Suu river valley with landslides and profiles indicated

sediments composed of clay material or loess overlying the limestone layers. The fieldwork revealed that many slope instabilities have their head-scarps in the limestone layers. This means that they were initiated there, but affected mostly material of the adjacent units. Landslide occurrence also spatially correlates with structural and morphological factors, such as strike-and-dip of the limestone layers, the slope aspect, slope angle, and curvature.

The landscape in the Maily-Say Valley is continuously changing owing to the high landslide activity. The extent of this potentially dangerous evolution was quantified statistically. The total area affected by landslides increased from 1.0 % ($\sim$1.2 km^2) in 1962 to 3.3 % in 1984, 4.5 % in 1996, 4.3 % in 2002 and 5.6 % ($\sim$6.5 km^2) in 2007 compared to the entire investigated area along the Maily-Say Valley. Landslide size is quite variable; it ranges from 335 m^2 for the smallest detected landslide to 348,425 m^2 for the largest one in 2007. Further, the results indicate that the absolute number of large and very large landslides increases over time while the absolute number of small landslides decreases.

In this area, only a few co-seismically triggered landslides are known. However, several post-seismic landslides are likely to be related to partial co-seismic slope failure. Indeed, one of

the largest landslides called 'Tektonik' first failed massively in 1992, seven weeks after a local $Ms = 6.2$ earthquake. Another, small landslide was monitored during several years and fracture opening of several tens of centimetres during a distant $Ms = 5.9$ earthquake could be proved at the end of the 90. In 2005, this slope finally failed to produce a 700 m-long earthflow made of loess.

2   Dynamic Modelling Settings

Modelling was performed with the UDEC software (version 4.01) combining computation with discrete elements (allowing for detachment or sliding of blocks along joints) and finite difference zones (filling the blocks and allowing for elastic or elasto-plastic deformation of the bulk material).

Topographic settings of constructed models were defined using DEM with cell size 20×20 m, obtained from SPOT satellite imagery in target area (Schlogel et al. 2010). Geological and tectonic settings were defined using a geological map of scale 1:10,000 together with 3D geological model of central part of area (Schlogel et al. 2010). In many cases, initial profiles were extended to a distance of 3–5 km to avoid boundary effects during dynamic modelling. The upper parts of all models with a depth down to 300–500 m were filled with FD-zones using an edge length of 7.5 m, while zones in the lower parts of models have an edge length of 15 m. All external boundaries, besides the surface, were designed to have viscous damping in x- and y-directions to avoid refraction effects during dynamic loading. The materials used in the models were those presented by the geological map and the 3D geological model. Some of the geological layers were integrated into one group according to the similarity of the geotechnical properties (Table 68.1). Dynamic properties of internal contacts (joint normal stiffness and joint shear stiffness) were assigned on the basis of the shear modulus of the upper layer in contact. At the beginning, all constructed profiles were cycled to obtain an unbalanced force value of less than 10^{-5} N. The stabilized profiles were subjected to

Table 68.1 Geotechnical settings of different material types used in dynamic modelling

Material code	Geological code	Cohesion, MPa	Friction angle, deg	Density, kg/m^3	Vp, m/sec	Vs, m/sec	Bulk modulus, MPa	Shear modulus, Mpa
Mat1	Purp, Mail (paleogene-neogene loose sediments)	0.04	26	2200	1000	500	1467	550
Mat2	Lim (limestone layer with average thickness of 100 m)	0.1	30	2400	4000	2200	22912	11616
Mat3	Salm (cretaceous loose sediments with average thickness of 155 m)	0.03	30	2200	1500	800	3073	1408
Mat4	Ligh, Red (cretaceous bedrock)	0.08	30	2200	2500	1300	9592	4056

dynamic loading using a Ricker wavelet as vertically (from the model base) propagated input signal. The maximum value of acceleration of the input signal was about 1.44 m/sec^2 (0.15 g) and the spectral range of the input signal was between 0.3 and 9.0 Hz. The duration of dynamic loading was 15 s—within this period of time the recording of different dynamic properties (acceleration, velocity and displacement of ground motion) was recorded by several receivers situated along the surface of model. Obtained recordings were analysed to compute the values of Areas intensity (Ia) recorded in those points. All models were analysed using two different cases—the case of unique material all over the model and the case of varying (real) geological materials. The first case was used to analyse pure topographic effects on the seismic amplification (with respect to a receiver on a flat hard rock site) of Areas intensity (At), while the second case presented the mixed effects of geology and topography on the seismic amplification of this parameter (Atg). Later, obtained values of seismic amplification were analysed to link this value with topographic parameters (curvature, slope angle, elevation) and geological settings. Five long profiles were analysed with a total length of 18.23 km and 101 receivers providing recordings of physical parameters

3 Analyses of Area Intensity Amplification Factor

3.1 Topographic Effect

There were some research attempts used to study effect of topography and geology on amplification of input seismic signal (Geli et.al. 1988; Jibson et.al. 1998; Miles and Ho 1999; Peng et.al 2009)—the results of these activities inspired some attempt of our research. Pure topographic amplification factors (At) for each receiver were obtained by dividing the Ia value in this point by the one obtained for the point situated close to the model basis (from which the ground motion was propagated). Some receiver points were not taken into consideration due to artificial shaking effects

generated along layer contacts and external boundaries. The remaining majority of points were used to relate At with topographic parameters, like curvature, slope angle and elevation.

Figure 68.2 presents correlations between these topographic features and pure topographic amplification factors obtained through numerical modelling. As it can be seen from Fig. 68.2a, concave topography favours to deamplification of Areas Intensity down to 60 % of initial values of Ia, while convex topography amplifies initial Ia values up to 80 %. Flat topography does not bring any effect on Ia amplification, which means At = 1. Figure 68.2b indicates that steeper slope angles favour deamplification of Ia, which generally was also found by former related research (Havenith and Bourdeau 2010; Danneels et. al. 2008; Geli et al. 1988). These three topographic parameters were used to obtain predicted values of pure topographic amplification of Areas Intensity (Atcalc). Formula (1) presents this relationship.

$$
\begin{aligned}
\text{Atcalc} = & \left(0.6037 * C^3 + 0.3225 * C^2 + 0.42 \right. \\
& \left. * C + 1.0468\right) * \left(0.5352 * \exp^{-0.0069*S}\right) \\
& * \left(2 * 10^{-9} * E^3 - 5 * 10^{-6} * E^2 + 6 * 10^{-3}\right. \\
& \left. * E - 1.5571\right)
\end{aligned}
\tag{68.1}
$$

where C curvature, S slope angle (deg), E elevation (m)

The correlation coefficient between At and Atcalc was 0.87, which indicates a good prediction for this relationship. Figure 68.3 presents the comparison between At and Atcalc.

3.2 The Effect of Geology

Pure geological amplification factor (Ag) was obtained by subdividing of amplification values gained for combined effect of geology and topography (Atg) on ones for pure topographic case (At). In the analyses of Ag there were around 50 % of points filtered out owing to different artificial effects caused along contacts and boundaries in the model. Remaining points were used to calculate predicted amplification factors

purely affected by the material type (Agcalc). Table 68.2 presents the results of Agcalc estimation. As it can be seen from this Table, the highest values of Ia amplification are presented by material 3 (mean value—2.86), which is explained by the structural and geomechanic characteristics of this layer. In general, this layer of soft, low-velocity material is "sandwiched" between two hard layers, which normally leads to wave focusing and consequently to high values of Areas Intensity. Material 1 also has comparatively high values of Ag (1.73), which can be explained by the fact that this layer is the softest one. However, along all profiles it is located above the hard limestone that may have some "screen" effect on wave propagation, reflecting waves back into material 3, Salm. Therefore, this layer made of the softest material 1 does not present the highest amplification. Pure geological deamplification in the material 2 is caused by the presence of high-velocity material between two low-velocity ones. Material 4 in our modeling was considered to be the bedrock and there is slight, but not significant amplification in this layer.

3.3 Combined Effect of Topography and Geology

Predicted values of combined amplification factor affected by both topography and geology (Atgcalc) were calculated as multiplication of topographic amplification factor (Atcalc) by geological one (Agcalc). Real values of combined amplification factor (Atg) have a correlation coefficient 0.75 with predicted values of this parameter (Atgcalc). This still indicates a good relationship between constructed relationship and observed values of this parameter. Figure 68.4 presents the plot of Atg versus Atgcalc.

4 Conclusions and Perspectives

The goal of this study is to integrate the results concerning the Arias Intensity and its amplification factors into the calculation of Newmark displacement. At present, the various modified

Fig. 68.2 The plots of real values of amplification factors (At) versus: *a* curvature; *b* slope angle; *c* elevation
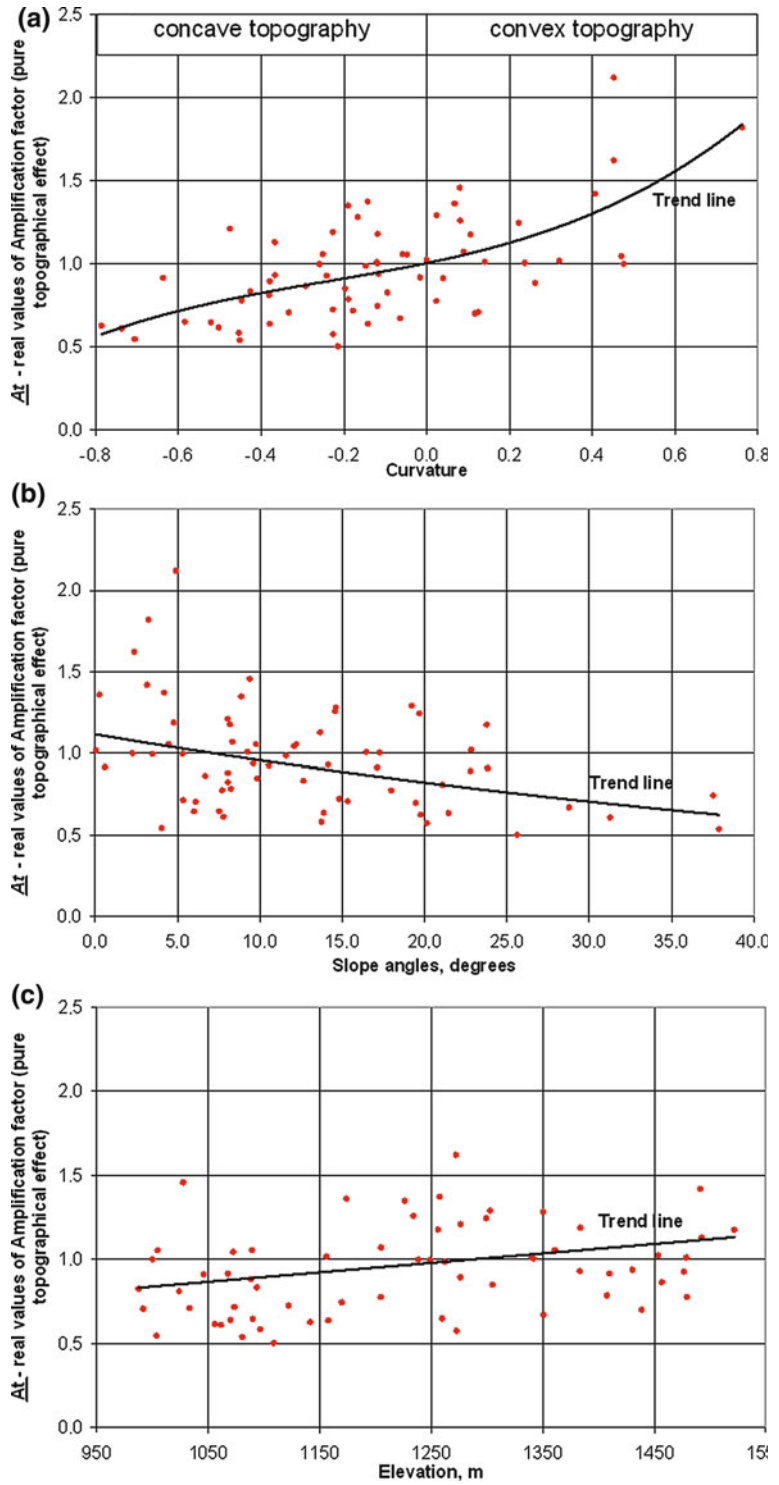
Fig. 68.3 The plot of real values of amplification factors (At) versus predicted values of amplification factor (Atcalc) for pure topographic effect

$Atcalc = f(\underline{curvature}^3, \exp(\underline{slope\ angle}), \underline{elevation}^3)$
Correlation coefficient between $\underline{Atcalc}$ and $\underline{At}$ is $\underline{0,87}$
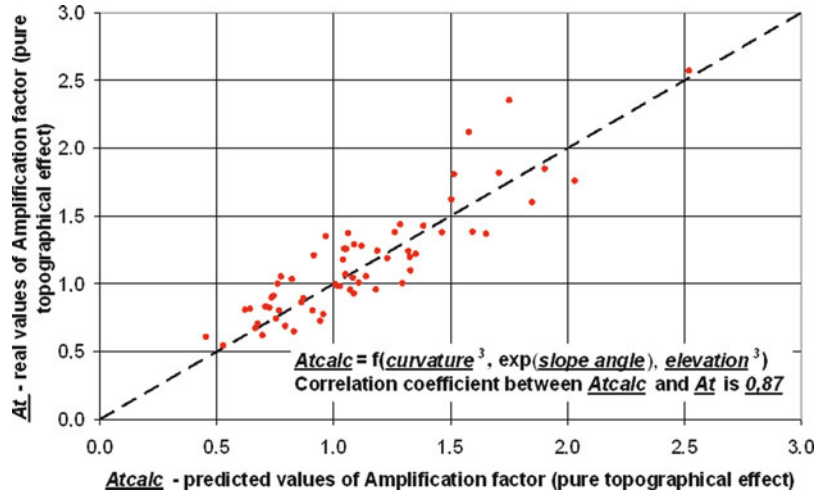
Table 68.2 Predicted values of amplification factors (Agcalc) purely affected by material type

Material code	Mean value of predicted amplification factor	Standard deviation for predicted amplification factor	Number of receivers analysed
Mat1	1.73	0.43	22
Mat2	0.81	0.25	9
Mat3	2.86	0.67	14
Mat4	1.19	0.15	5

Fig. 68.4 The plot of real values of combined amplification factors (Atg) versus predicted values of amplification factor (Atgcalc) for combined effect of topography and geology

$Atgcalc = \underline{Atcalc} * \underline{Agcalc}$
Correlation coefficient between $\underline{Atgcalc}$ and $\underline{Atg}$ is $\underline{0,75}$
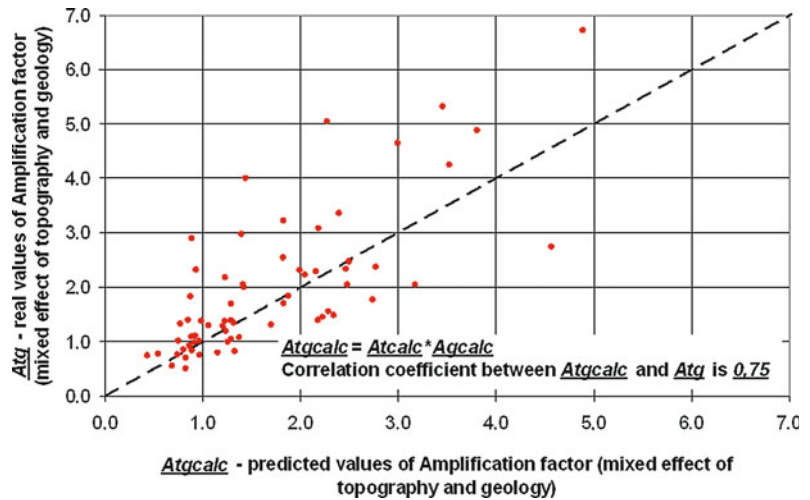
Newmark approaches consider only regionally varying Ia values (due to seismic wave attenuation from the epicenter). Such kind of prediction of amplification factor of Ia (here called 'Atgcalc') can easily be integrated into the widely used GIS-based analyses of seismic landslide susceptibility mapping. To be able to do so, the perspectives of our current activity involve more extended numerical studies in the target area both in the elastic and elasto-plastic domain. Elasto-

plastic dynamic modelling allows us to compare obtained values of displacements with those calculated with the Newmark displacement method (some preliminary tests have been started). Another perspective of the current activity also includes 3D dynamic numerical modelling of a target site situated in another area, where real seismic events caused certain amount of displacement in different parts of the landslide. This site was also studied from seismological and geophysical points of view, which finally give more reliable estimates of input parameters and provide good verification of obtained results. Final results of current study should make the Newmark displacement method more reliable in the mapping of landslide susceptibility in different parts of the world.

References

Alioshin Y, Torgoev I (2000) Radioactive ecology of Mailuu-Suu: Bishkek -Ilim

Danneels G, Bourdeau C, Torgoev I, Havenith HB (2008) Geophysical investigation and numerical modelling of unstable slopes: case-study of kainama (Kyrgyzstan). Geophys J Int 175:17–34

Geli L, Bard PY, Jullien B (1988) The effect of topography on earthquake ground motion: a review and new results. B Seismol Soc Am 78(1):42–62

Havenith HB, Jongmans D, Abdrakhmatov K, Trefois P, Delvaux D, Torgoev I (2000) Geophysical investigation of seismically induced surface effects : case study of a landslide in the Suusamyr valley, Kyrgyzstan. Surv Geophys 21:349–369

Havenith HB, Jongmans D, Faccioli E, Abdrakhmatov K, Bard PY (2002) Site effects analysis around the seismically induced ananevo rockslide, Kyrgyzstan. B Seismol Soc Am 92:3190–3209

Havenith HB, Bourdeau C (2010) Earthquake-induced hazards in mountain regions: a review of case-histories from Central Asia. Geologica Belgica 13:135–150

Jibson RW, Harp EL, Michael JA (1998) A method for producing digital probabilistic seismic landslide hazard maps: an example from Los Angeles, California, Area, US Geol Surv Open-file Report 98–113

Miles SB, Ho CL (1999) Rigorous landslide hazard zonation using newmark's method and stochastic ground motion simulation. Soil Dyn Earth Eng. 18:305–323

Nadim F, Kjekstad O, Peduzzi P, Herold C, Jaedicke C (2006) Global landslide and avalanche hotspots. Landslides 3:159–173

Newmark N (1965) Effects of earthquakes on dams and embankments. Geotechnique 15(2):139–160

Peng W-F, Wang C-L, Chen S-T, Lee S-T (2009) A seismic landslide hazard analyses with topographic effect study in the 99 peak region, Central Taiwan. Environ Geol 57:537–549

Schlogel R, Torgoev I, De Marneffe C, Havenith H-B (2010) Assessment of landslide activity in the Maily-Say Valley, Kyrgyz Tien Shan. Earth Surf Proc Land 36(12):1658–1669

Numerical Simulation of Granular Flows by DDA

69

Qingqing Yang, Fei Cai, Keizo Ugai, Zhiman Su
and Lingyu Xu

Abstract

Despite of extensive efforts made by many researchers, the mechanisms involved in rapid, dry, dense granular flows are thought only understood in broad line. In this paper, Discontinuous Deformation Analysis (DDA) was applied to simulate some experimental flows in a large flume and a large rock avalanche triggered by the Wenchuan earthquake, as a step to make clear some mechanisms in rock avalanches. Simulated results show that DDA was able to capture essential characteristics of granular flows and friction coefficient was a key parameter in the numerical analysis. Furthermore, the apparent friction coefficient, which was determined by field investigation, served as a reasonable parameter to reproduce the field event, rather than the friction coefficient measured in the laboratory.

1 Introduction

DDA has emerged as an attractive model for geomechanical problems because other numerical methods cannot easily replace its advantages. The objective of this paper is to present some numerical simulations by DDA and to investigate propagation mechanisms involved in rock avalanches. DDA was applied to reproduce a series of granular flows released in a large flume to demonstrate the applicability of DDA for realistically describing the dynamic behavior of granular flows. The application of DDA was then extended to a large rock avalanche triggered by the Wenchuan earthquake.

Q. Yang (✉) · F. Cai · K. Ugai · L. Xu
Department of Civil and Environmental
Engineering, Gunma University,
Kiryu 376-8515, Japan
e-mail: yangqq_71@126.com

Z. Su
Institute of Mountain Hazards and Environment,
Chinese Academy of Sciences,
Chengdu 610041, China

F. Cai
State Key Laboratory of Geo-Hazard Prevention and
Geo-Environment Protection, Chengdu University
of Technology, Chengdu 610059, China

L. Xu
Department of Hydraulic Engineering, Dalian
University of Technology, Dalian 116024, China

2   Experimental Set-up

The large flume tests were conducted to investigate some of the propagation mechanisms involved in the rapid, dry, dense granular flows in a large flume and to identify factors influencing the mass-front velocity of the flows. The two-part flume used in the tests was 15.5 m long, 5.7 m high, 1.0 m wide, and 1.0 m deep. An upper slope that was 5.5 m long and at a 45° incline was connected to a lower slope that was 10.0 m long and at a 10° inclined (Fig. 69.1). A gate was arranged near the top of the upper slope to control the release of materials. The gate covered the entire 1.0 m width of the flume and could be manually (but rapidly) opened to free the granular materials behind the gate. One flume sidewall was made of transparent, reinforced PMMA to allow the movement of materials to be viewed from the side of the flume. Each test was filmed by three digital video cameras operating at 30 frames per second. A detailed description of the large flume tests was presented by Yang et al. (2011).

3   Simulation of Large Flume Tests

The geometry and initial configuration of the numerical model were based on a 2D reproduction of the experimental conditions. Cube-shaped blocks with 0.1 and 0.05 m sides were called large cubes and small cubes, respectively. Cobbles were simulated by hexagons that were as close as possible in shape to those employed in the tests. The gravel layer was randomly divided into an assembly of polygons with different shapes and sizes. The mechanic properties of the granular materials were measured in the laboratory. Some of the numerical control parameters are as follows: the time step size = 0.001 s; the maximum allowed displacement ratio = 0.00085; the contact spring stiffness = 1×10^{6} kN/m; and the factor of over-relaxation = 1.3.

3.1   Mono-materials

Several tests were conducted on the mono-materials of cubes (case 2), gravel (case 3), and cobbles (case 10), respectively.

Figure 69.2 shows the simulated and measured mass-front velocities for cases 2, 3, and 10, respectively. The trend of the simulated velocities corresponded well with that of the measured velocities. Both the simulated and measured velocities fluctuated due to the propulsion of subsequent particles to the slowed front by impact. DDA accurately reflected this important phenomenon; this was an advantage of DDA over simple lumped mass models in which a moving mass is simplified as a rigid body without regard to collisions between particles.

In case 10, cobbles were simulated by regular octagons. The simulated velocity of a regular octagon was much higher than that of a hexagon and also much higher than the velocity measured in the tests. A majority of the octagonal blocks moved beyond the flume and stopped on the horizon, while a different situation occurred in the tests. Thus, velocity and run-out were highly sensitive to the shape and angularity of the granular elements in the numerical analysis. This conclusion corresponded with that drawn by Hatzor et al. (2004), who found that the DDA simulation results are extremely sensitive to the geometrical configuration, i.e., the computed mesh. Therefore, the shape and angularity of the blocks had to be determined carefully in the numerical model because the use of unrealistic granular elements may cause the grain behavior to be modeled inaccurately.

3.2   Composites

Two composites were tested, including a composite of gravel and cubes in case 4 and a composite of gravel and cobbles in case 14. The cube and gravel composite was initially arranged
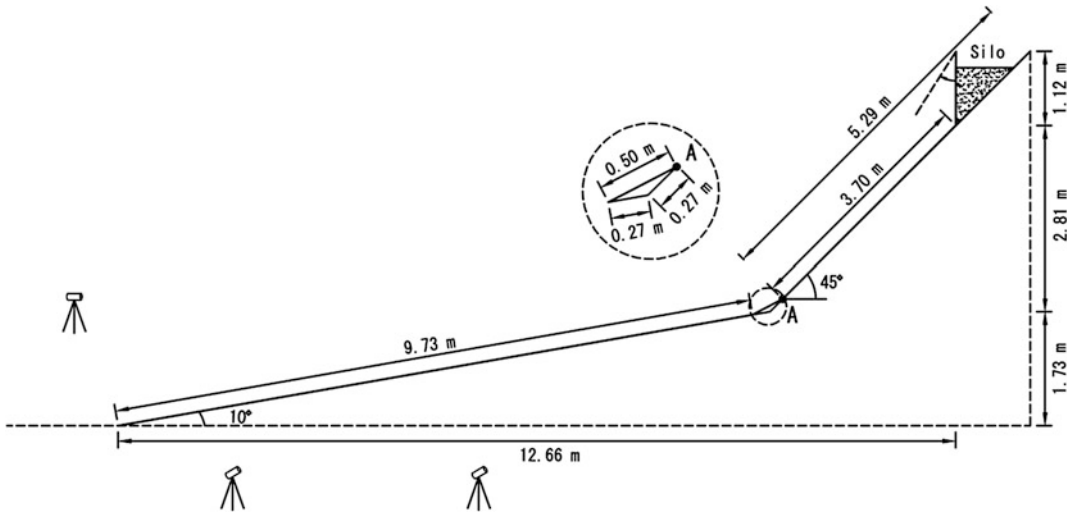
Fig. 69.1 Schematic illustration of the model flume and arrangement of cameras
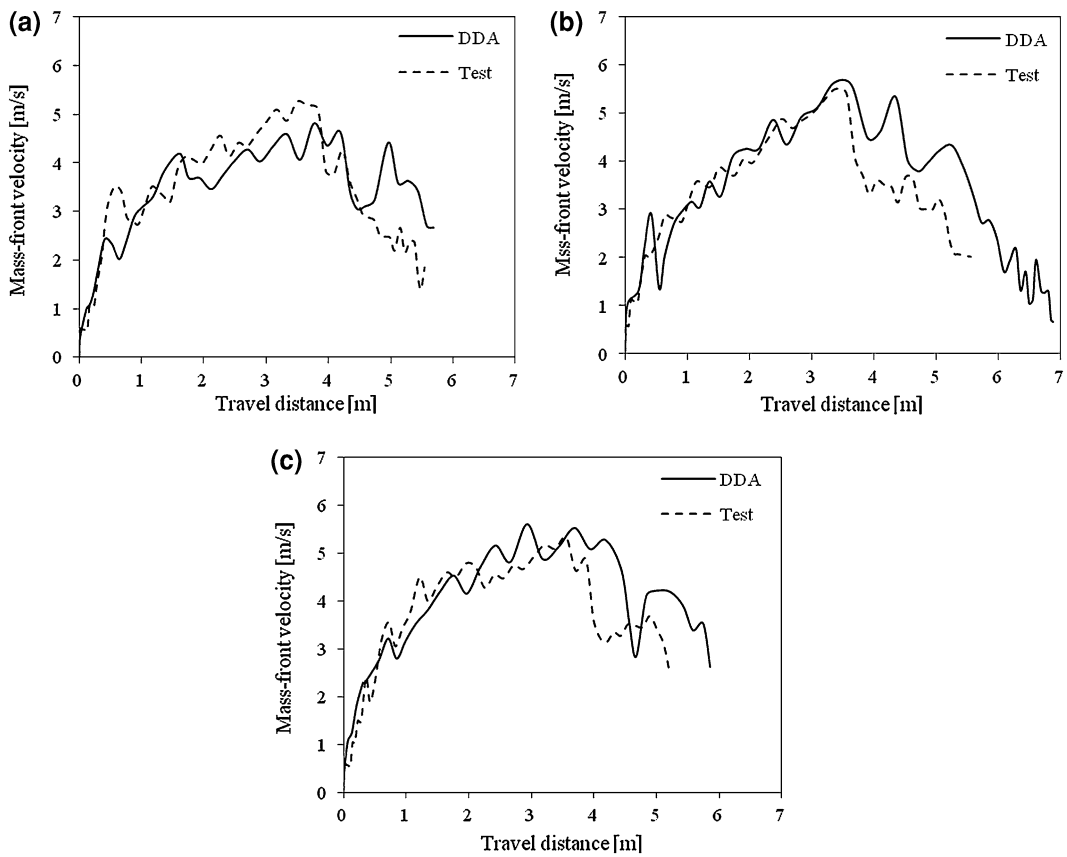
Fig. 69.2 Comparison of the simulated and measured velocities in cases 2, 3 and 10 (**a**) Case 2 (**b**) Case 3 (**c**) Case 10
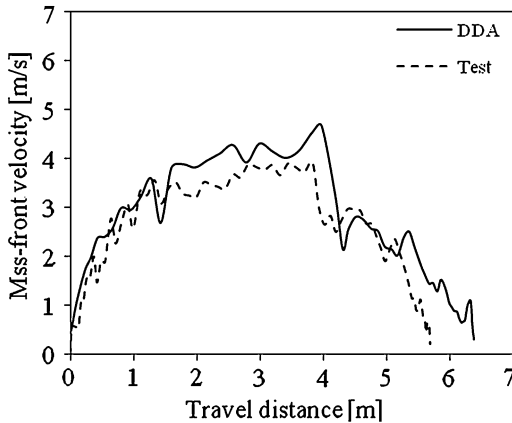
Fig. 69.3 Comparison of the simulated and measured velocities in case 4
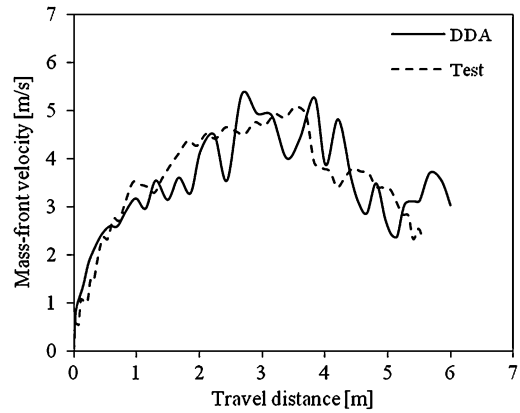
Fig. 69.4 Comparison of the simulated and measured velocities in case 14

as alternating layers of cubes and gravel. A total of 68 cubes were arranged in the position as close as possible to that in the tests. Two layers of gravel were divided into 153 irregular polygons with different shapes and sizes. Though only a few irregular polygons were used in the numerical model and their shape was not exactly the same as that in the tests, the simplification was feasible with the objective of capturing the main features of granular flows.

DDA accurately predicted the lowest velocity of this composite for each of the studied cases Fig. 69.3. The agreement between the simulation and experiment indicates that DDA effectively described the granular flows. The cube and gravel composite with a large volume displayed a lower mobility than the cube and gravel mono-materials with small volumes because more energy was consumed by intergranular friction between the cubes and gravel. DDA accurately modeled the energy dissipation caused by friction between particles; this is another advantage of the DDA over simple lump mass models in which retardation only resulted from the constant basal friction between a moving mass and the underlying surface without regard to intergranular friction.

An unexpectedly high velocity that was almost the same as those for the mono-materials was observed for the cobble and gravel composite in case 14. The velocity of this composite was considerably higher than that of the cube

and gravel composite (case 4) because the cobbles rolled on the surface of the gravel more easily than the cubes. The global tendency of the simulated velocities, which are represented by the solid line, coincided with the experimental data, which are represented by the dashed line (case 14, Fig. 69.4). However, the simulated velocity fluctuated more because the DDA did not take the energy loss due to the collisions between particles and between particles and the flume into account. Thus, the velocity of the frontal particles increased more significantly when subsequent high-velocity particles provided propulsion to allow them to accelerate. Collisions occurred frequently and considerably dissipated the energy. A restitution coefficient had to be introduced to consider the energy loss caused by collisions. Ma et al. (2011) proposed a modified DDA method to address this problem when simulating rockfall. The simulated results were compared with test results, and the authors found that the velocity is most accurately predicted using a restitution coefficient of 0.7.

4   Simulation of a Large Rock Avalanche

In this section, we extended the application of DDA to the reproduction of a large rock avalanche, which was selected due to its relevance

Fig. 69.5 Final deposit
when the measured friction
coefficient was used

and the relatively large amount of data recorded
before and after the failure.

4.1   Description of the Donghekou Rock Avalanche

The Donghekou rock avalanche, triggered by the
Wenchuan earthquake on May 12th, 2008, bur-
ied 7 villages and killed 780 people. It was a
typical rapid, long run-out rock avalanche with
an altitude difference of 540 m between the toe
and main scarp, a sliding distance of 2,270 m,
and a volume of 15 million m^3 (Xu et al. 2010).
The landslide consisted of sandstone, shale, and
schist from the Cambrian age, and was located
approximately 4 km from the active fault-rup-
ture (Yin et al. 2009). After the event, a valley
bottom of 1.08 km^2 was covered with deposit
with a maximum thickness of 60 m, and an
impounded lake with a capacity of 250 million
m^3 was formed (Huang et al. 2011).

4.2   Numerical Simulation

The 170 quadrilaterals composing the failed mass
were randomly generated. The failed mass had an
initial horizontal velocity to briefly consider
earthquake energy. The initial horizontal velocity
was 1 m/s, based on the effects of topographic
amplification, seismic horizontal peak velocity
and distance to faults. The laboratory-measured
mechanical properties were reported by Huang
(2009), and the main numerical control parameters
are as follows: the time step size = 0.01 s; the
maximum allowed displacement ratio = 0.0015;
the contact spring stiffness = 5 × 10^8 kN/m; and
the factor of over-relaxation = 1.3.

The calculated deposit was combined with
the actual final deposit observed in the field, as
illustrated in Fig. 69.5. The sliding mass

remained in approximately the same place at
200 s (20,000 time steps) after the inception of
motion. The calculated run-out was much
shorter than the actual run-out. The trial calcu-
lations show that the friction coefficient signifi-
cantly affected the simulation results, and it was
difficult to reproduce the extremely long run-out
of the rock avalanche by the laboratory mea-
sured friction coefficient. This result implies that
the 'size effect' should be considered when
simulating field events, where 'size effect'
means that the deposits of a natural rock ava-
lanche with a volume larger than approximately
10^6–10^7 m^3 typically extend much farther than
those of smaller avalanches and extend much
farther than the deposits simulated by a friction
model (e.g. Scheidegger 1973; Hsü 1975; Eris-
mann and Abele 2001). The long run-out is thus
not expected to relate to the friction coefficient
measured in the laboratory. To account for this
discrepancy, the apparent friction coefficient,
which is the tangent of the apparent friction
angle and refers to the inclination to the horizon
of the line joining the top of the breakaway scar
and the distal end of the deposit, was used as a
measure of the mobility of the rock avalanche.
The apparent friction coefficient was typically
much smaller than the measured friction coeffi-
cient for large rock avalanches.

The apparent friction coefficient of 0.238
from the study by Xu et al. (2010) was used in
two simulations. When the apparent friction
coefficient was used, the calculated deposit
corresponded well with the actual deposit in
both cases (Fig. 69.6).

It is worth noting that the simulation that used
the friction coefficient measured in the labora-
tory reasonably predicted the velocity of gran-
ular flows in the flume tests because the volume
of granular materials released in the tests was
much smaller than 10^6 m^3, and the size effect
was unavailable. For large events, however, a

volume-dependent apparent friction coefficient
should be used to consider the 'size effect'. This
result was confirmed by the Davies and
McSaveney's conclusion (1999) (Davies and
McSaveney 1999) that granular avalanches with
volumes ranging from 10^{-4} m^3 to approxi-
mately 10^5 m^3 show consistent run-out behavior,
but the run-out behaviors of those with volumes
greater than approximately 10^6–10^7 m^3 differ
significantly from those at smaller scales.

The maximum simulated velocity among the
sliding blocks was 60.2 m/s, and this block was
located near the slope surface. This block trav-
eled 447 m from its initial position, reaching the
maximum velocity at an elapsed time of 19.7 s.
This block accelerated and bounced due to the
propulsion provided by subsequent blocks with
higher velocities. Continuous propulsion was
one of the potential causes for the high velocities
and long run-outs of field rock avalanches.

5 Conclusions

In this study, certain granular flows released in a
large flume and a natural rock avalanche trig-
gered by the Wenchuan earthquake were accu-
rately simulated by DDA. DDA captured the
main features of granular flows in the flume
tests, and the simulated velocity corresponded
well with that measured in the tests. Energy
dissipation caused by intergranular friction was
accurately described in DDA. The simulated
results were highly sensitive to the shape and
angularity of the granular elements; thus, the use
of realistic elements was important for obtaining
reliable results.

The friction coefficient strongly influenced the
simulation results for the large rock avalanche.
The calculated deposit was only similar to the

actual deposit when the apparent friction coeffi-
cient, which was determined by field investiga-
tion, was used instead of the friction coefficient
measured in the laboratory. In contrast, for the
flume tests, the measured friction coefficient
served as an available parameter to predict the
velocity of experimental granular flows.

References

Davies TR, McSaveney MJ (1999) Runout of dry
    granular avalanches. Can Geotech J 36:313–320
Erismann TH, Abele G (2001) Dynamics of rockslides
    and rockfalls. Springer, Heidelberg, pp 253–264
Hatzor YH, Arzi AA, Zaslavsky Y, Shapira A (2004)
    Dynamic stability analysis of jointed rock slopes
    using the DDA method: king Herod's palace, Masada,
    Israel. Int J Rock Mech Min Sci 41:813–832
Hsü KJ (1975) Catastrophic debris steams (sturzstroms)
    generated by rockfalls. Geol Soc Am Bull
    86:129–140
Huang RQ (2009). Geohazard assessment of the
    Wenchuan earthquake. Chinese Science Press, Beij-
    ing, pp 408 (in Chinese)
Huang Y, Zhang WJ, Xu Q, Xie P, Hao L (2011) Run-out
    analysis of flow-like landslides triggered by the Ms
    8.0 2008 Wenchuan earthquake using smoothed
    particle   hydrodynamics.   Landslides.   doi:
    10.1007/s10346-011-0285-5
Ma GC, Matsuyama H, Nishiyama S, Ohnishi Y (2011)
    Practical studies on rockfall simulation by DDA.
    J Rock Mech Geotech Eng 3(1):57–63
Scheidegger AE (1973) On the prediction of the reach
    and velocity of catastrophic landslides. Rock Mech
    5:231–236
Xu Q, Pei XJ, Huang RQ (2010). Large-scale landslides
    induced by the Wenchuan earthquake. Chinese
    Science Press, Beijing, pp 245 (in Chinese)
Yang QQ, Cai F, Ugai K, Yamada M, Su ZM, Ahmed A,
    Huang RQ, Xu Q (2011) Some factors affecting mass-
    front velocity of rapid dry granular flows in a large
    flume. Eng Geol 122:249–260
Yin YP, Wang FW, Sun P (2009) Landslide hazards
    triggered by the 2008 Wenchuan earthquake, Sichuan,
    China. Landslides 6:139–151

Analysis of a Embankment Landslide in Baoji-Chengdu Railway Induced by the 2008 Wenchuan Earthquake

70

Shu-Wei Sun, Wei-Xin Dong, Yu-Zhen Yu and Jing Zheng

Abstract

The Wenchuan earthquake occurred at 2:28 pm local time on May 12, 2008 near the west edge of the Sichuan Basin in China. During the earthquake, local transportation in the area was substantially damaged. An embankment slope at K439 + 450 ∼ + 680 in Baoji-Chengdu railway collapsed due to the intense near field ground motion. This paper presents the local geological and environmental conditions of the embankment landslide. Embankment material properties were determined through field investigations and laboratory tests. Static and pseudo-static analyses were performed to acquire a quantitative assessment of the embankment stability. The failure mode of the embankment was investigated through fully coupled nonlinear dynamic analyses. The results show that the failure surface obtained by limit equilibrium method was deeper than observed. The failure surface obtained by fully coupled dynamic response analysis agreed well with the post-failure observations, but the maximum permanent displacement was almost five times than those observed.

S.-W. Sun (✉)
Faculty of Resources and Safety Engineering,
China University of Mining and Technology
(Beijing), Beijing, 100083, China
e-mail: sunshuwei@cumtb.edu.cn

W.-X. Dong · Y.-Z. Yu
State Key Laboratory of Hydroscience and
Engineering, Tsinghua University, Beijing, 100084,
China

J. Zheng
Northwest Research Institute Co Ltd. of C.R.E.C,
Lanzhou, 730000, China

1 Introduction

The Wenchuan earthquake was the most destructive event in China's recent history, which led to 69,200 fatalities, 18,195 persons missing, 374,216 persons injured, 5,362,500 collapsed homes, 21,426,600 homes that were badly damaged, and more than five million people left homeless (Cui et al. 2009). An outstanding characteristics of this earthquake is that it was accomplished by fault rupture over a
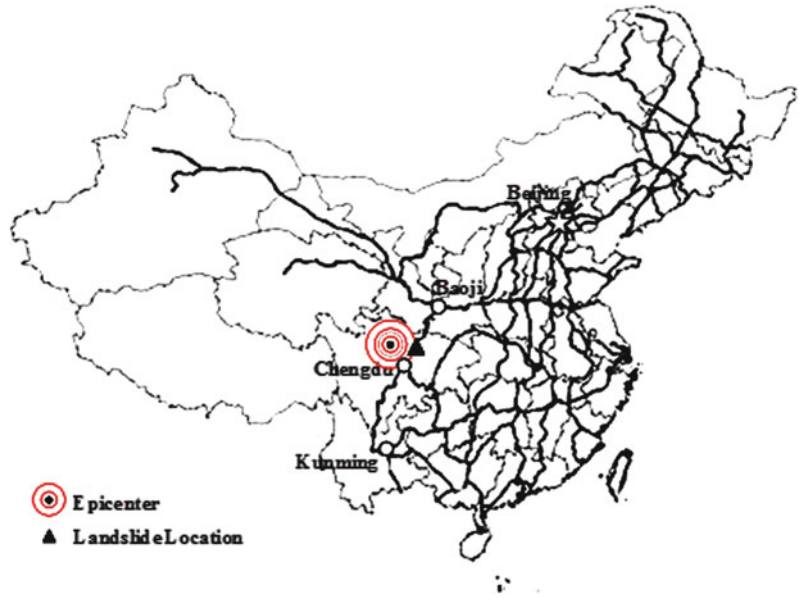
distance of 270 km (Burchfiel et al. 2008), and
thus the affected area was far larger than that of
recent earthquakes in mountainous areas, such as
the 1999 Chi–Chi earthquake in Taiwan (Wang
et al. 2003), the 2004 Mid Niigata Prefecture
earthquake in Japan (Chigira and Yagi 2005),
and the 2005 Northern Pakistan earthquake
(Sato et al. 2007). Engineering aspects of the
earthquake are reported by Yin et al. (2008) and
Chigira et al. (2012).

The landslide, known as the K439 landslide
was situated 209 km northeast of the earthquake's
epicenter, just east of the Baoji-Chengdu railway
which runs from north-east to southwest, as
shown in Fig. 70.1. Baoji-Chengdu railway is an
important component of local transportation sys-
tem, and has played a key role in economic and
social development since the 1950s in China. The
landslide caused the railway to be out of service
for a long time. About 100 m long of the
embankment fill deformed and spread into the
eastern valley of the railway (see Fig. 70.2).

In this study, an investigation of the landslide is
presented. Material properties are determined
through field investigations and laboratory tests.
The parameters are used as a basis for calculation
by limit equilibrium and fully coupled non-linear
dynamic analyses. Finally, a comparison is made

between the observed landslide mechanism and
the results of these two sets of calculations.

2   Geologic Setting

The study area is underlain by sedimentary rocks
of Jurassic Age. The sedimentary rocks are
mainly mudstone and sandstone. The rocks are
striking ENE-WSE and dip to the south, and the
dip angle of the bedding planes is between 15–
25 °. Above the sedimentary rocks are Quater-
nary deposits and soils. The embankment was
constructed nearly 60-years-ago, and had an
approximate height of 30 m with an inclination
of 1:1.5 (see Fig. 70.3).

Figure 70.3 shows the deformation character-
istics of the embankment slope. As we can see
from Fig. 70.3, the major sliding surface is gen-
erated in the upper embankment fill. The outlet of
landslide is just at the head of earth-retaining wall,
which can be determined by the cracks on revet-
ment (see Fig. 70.2). The observed maximum
value of displacement around cracks is about
30 cm. Local groundwater table exists in the fis-
sure of the sandstone and mudstone. Figure 70.3
illustrates the groundwater flow path in sandstone
and mudstone.
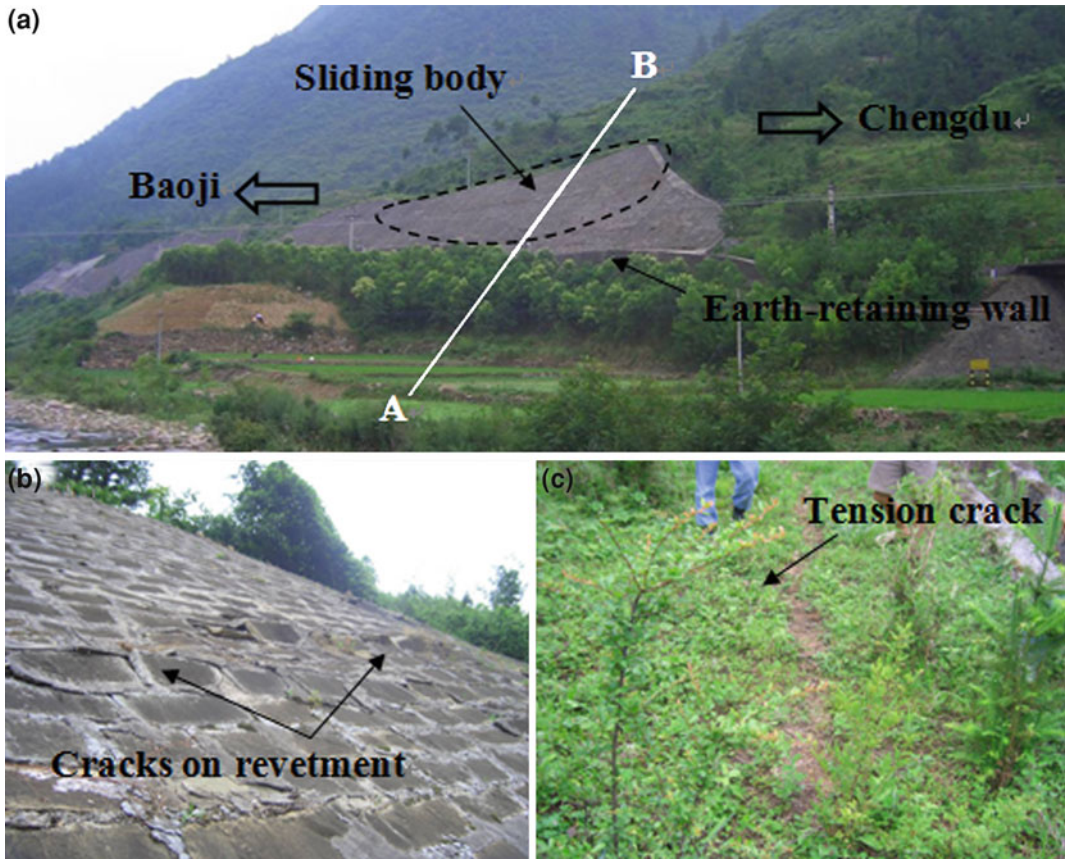
Fig. 70.2 Images of the landslide

Fig. 70.3 Cross-section of the landslide (The cross-section line AB is located in Fig. 70.2)
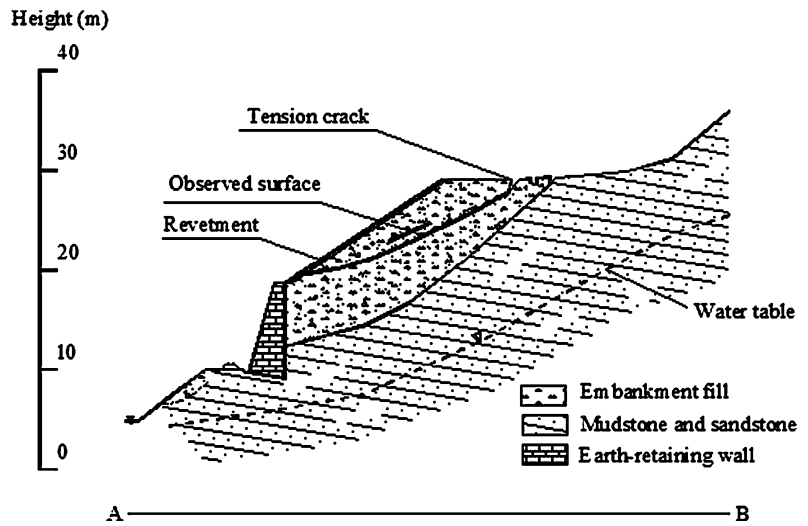
Table 70.1 Material parameters

Parameters	Embankment fill	Bedrock	Earth-retaining wall
Young's modulus, E (MPa)	30	6,000	8,000
Poission's ratio, v	0.25	0.22	0.20
Unit weight, γ (kN/m^3)	16.0	22.0	-
Cohesion, c (kPa)	10.0	150.0	-
Friction angle, ϕ (°)	25.0	40.0	-

Fig. 70.4 Slope stability analyses results (M1 is earth-retaining wall, M2 is embankment fill, M3 is bedrock above the water table, and M4 is bedrock below the water table)
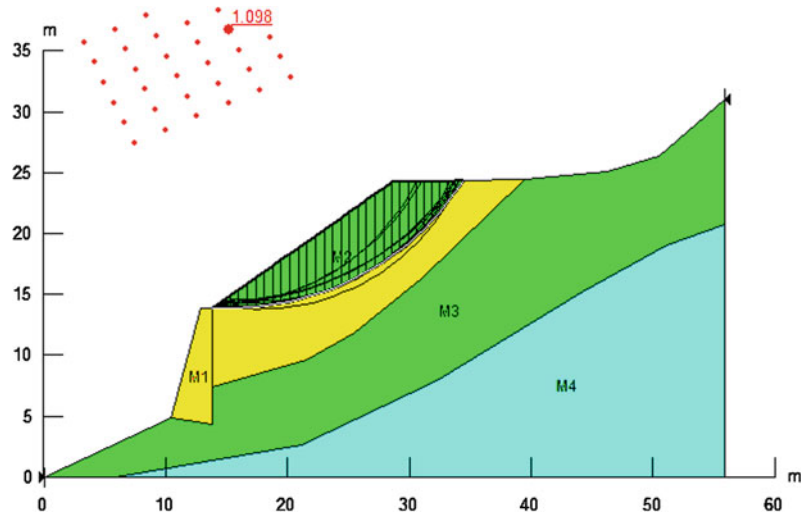
3 Material Properties

There are four mainly materials in the embankment slope, which are embankment fill, mudstone and sandstone, earth-retaining wall and revetment, respectively. The revetment is a thin layer and the actual construction quality is not good at all. Therefore, the revetment was discarded and replaced as embankment fill for simplicity in this study.

The earth-retaining wall is considered to behave linearly elastic. The shear strength of the embankment fill is defined by the Mohr–Coulomb failure obtained through direct shear tests, and the elastic modulus of embankment fill is assessed through consolidated undrained triaxial compression tests. The bedrock was assumed to behave non-linearly following Hoek and Brown failure criterion. For this purpose, the uniaxial compressive strength of the intact rock pieces,

the value of the Hoek–Brown constant m_i for these intact rock pieces, the value of the geological strength (GSI) for the rock mass, and the disturbance factor were required. By employing these parameters, the $\varnothing$ and c of the rock mass were determined for instantaneous normal stress levels via Roscience software. Table 70.1 shows the mechanical properties of materials adopted for the following studies.

4 Stability Analysis

4.1 Static Stability Analyses

Limit equilibrium analyses using SLOPE/W software (1998) were performed on the representative soil cross-section shown in Fig. 70.4. Properties of the embankment fill and bedrock materials used in the analyses are presented in Table 70.1. The static safety factors of the
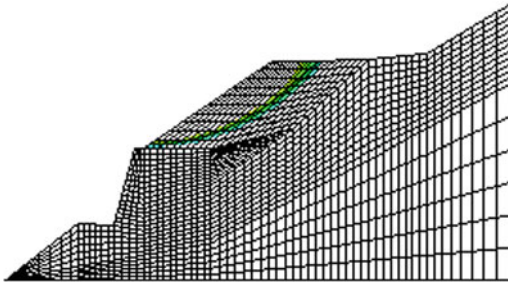
Fig. 70.5 Variations of the SSI

Fig. 70.6 Contours of permanent displacements

embank slope is near 1.10 predicted by the limit equilibrium method. As can be observed in Fig. 70.4, the position of critical failure surfaces identified by the Simplified Bishop's method is rather deeper with respect to that observed following Wenchuan earthquake, for which a static factor of safety of 1.16 is computed by the same method.

4.2   Pseudostatic Stability Analyses

The pseudostatic method is widely used in geotechnical engineering practice for the assessment of seismic slope due to easiness of implementation and familiarity. In this study, the maximum average horizontal acceleration, k_{max}, was adopted based on earthquake resistant level of the site as 0.1 g.

The pseudostatic stability analyses were performed by the non-linear numerical methods. The program FLAC3D (Itasca Consulting Group Inc 2005) was used to develop the numerical model (see Fig. 70.5) and to simulate the response. The Mohr–coulomb model was employed to simulate the nonlinear soil behavior. Within the model, the elastic behavior of the fill is defined by bulk and shear moduli, while the strength is defined by the angle of internal friction and cohesion. The bottom boundary was fixed in vertical and horizontal directions, while the lateral boundaries were fixed in horizontal direction only. The results of pseudostatic analyses revealed that the factor of safety under earthquake conditions was calculated as low as 0.78.

5   Dynamic Response Analyses

To better understand the mechanism of the slope instability, a finite difference dynamic analysis of the landslide was performed by using the software FLAC3D. Viscous lateral boundary was applied to the model (see Fig. 70.5) in order to prevent spurious reflections of outward propagating waves from artificial boundaries. The Mohr–Coulomb elastic-perfectly plastic constitutive model was utilized for the embankment fill and bedrock. The predictive capability of the model for shaking-induced permanent deformations has been demonstrated by comparison with centrifuge tests on model embankments (Roth et al. 1986). Shear strength parameters of the soil layers were selected to be the same as used in the limit equilibrium analyses. Besides, 5 % material damping was used in the model to simulate the mechanical damping of the vibration energy. To simulate the strong ground motion record site, El Centro record (Yu et al. 2007) was decomposed to be bedrock motion by means of two-dimensional site response analysis and scaled to produce peak ground accelerations of 0.30 and 0.17 g, respectively at embankment site.

Figure 70.5 shows the variations of the maximum shear strain increment (SSI) over the slope section during dynamic response analysis. Compare Figs. 70.5 with 70.3, we can see that the most critical failure plane predicted by fully coupled dynamic response analysis agree well with the head of the observed landslide.

Figure 70.6 presents the permanent displacement contours computed by finite difference analyses. The maximum value of displacement (1.36 m) is located at head of wall, which is uniformed to that observed. However, the computed value of the maximum residual displacement is almost five times than those observed.

6   Conclusions

The paper presents the stability and failure mechanisms of the observed seismically induced landslide at k439 + 450 ∼ + 680 along the railway from Baoji to Chengdu during the 2008 Wenchuan earthquake. Special attention is paid to present the observed ground deformations, the results of field investigations and analyses of observed landslide mechanisms by a suite of methods. The results of slope stability analyses revealed that the computed failure surface by limit equilibrium method was deeper than observed, and the failure surface configuration obtained by fully coupled dynamic response analysis agreed well with the post-failure observations, however, the computed displacement was almost five times than those observed.

References

Burchfiel BC, Royden LH, Vander Gilst RD (2008) A geological and geophysical context for the Wenchuan earthquake of May 12, 2008, Sichuan, People's Republic of China. GSA Today 18(7):4–11

Chigira M, Yagi H (2005) Geological and geomorphological characteristics of landslides triggered by the 2004 Mid Niigata prefecture earthquake in Japan. Eng Geol 82:202–221

Chigira M, Wu XY, Inocuchi T (2012) Landslides induced by the 2008 Wenchuan earthquake, Sichuan, China. Geomorphology 118:225–238

Cui P, Zhu YY, Han YS (2009) The 12 May Wenchuan earthquake-induced landslide lakes: distribution and preliminary risk evaluation. Landslides 6:209–223

GEO-SLOPE International Ltd (1998). SLOPE/W for slope stability analysis, Getting Started Guide, Canada

Itasca Consulting Group Inc (2005) FLAC3D-fast lagrangian analysis of continua in 3-dimensions, Version 3.0, User's Manual. Minneapolis, Minnesota: Itasca

Roth WH, Scott RF, Cundall PA (1986) Nonlinear dynamic analysis of a centrifuge model embankment. In: Proceedings of the third US national conference on earthquake engineering, Charleston, vol I

Sato PH, Hasegawa H, Fujiwara S (2007) Interpretation of landslide distribution triggered by the 2005 northern Pakistan earthquake using SPOT 5 imagery. Landslides 4:113–122

Wang WN, Furuya T, Chigira M (2003) Geomorphological precursors of the Chiufenerhshan landslide triggered by the Chi–Chi earthquake in Central Taiwan. Eng Geol 69:1–13

Yin YP (2008) Researches on the geo-hazards triggered by Wenchuan earthquake, Sichuan. J Eng Geol 16:433–444 (in Chinese)

YU YZ, Deng LJ (2007) Centrifuge modeling of seismic behavior of slopes reinforced by stabilizing pile. Chinese J Geotech Eng 26(6):843–845 (in Chinese)

Mechanism and Stability Analysis of the 2010 Yushu Earthquake (Ms7.1)-Induced Landslide Based on Point Safety Factor of Stress State

71

Wu Honggang, Yang Tao, Ma Huimin and Zhang Hongli

Abstract

A group of landslides was induced along the road on the Batang River bank to the Yushu airport in Qinghai province, China, during the 2010 Yushu earthquake (Ms7.1). The main materials of the landslides are diluvial, with their lower boundary being along the second and third terrace of the river. The bed rocks of these landslide areas are limestone and slate. The slopes deformed and many cracks occurred during the Yushu earthquake, showing great potential of further landsliding and threatening to the safe operation of the road to the airport. To understand the initiation mechanism of these landslides and then take proper countermeasure works to stabilize these slopes, using the FLAC3D, we analyzed the three-dimensional stress state of the slopes. During the analysis, we proposed a concept of point safety factor, which is defined as the ratio of the shear strength and shear stress. The formation process of the landslide was analyzed through analyzing the distribution of the safety factor of differing areas. The case study on one landslide showed that this kind of stress-state analysis is a workable method to understanding the initiation mechanisms of coseismic landslides.

Keywords

Earthquake · Landslide · Point safety factor of stress state · Stability analysis

1 Introduction

The road of Yushu to Batang Airport in Qinghai Provence (referred to as "Airport Road" hereinafter) is in K821 + 400 ∼ K840 + 580 segment on National Highway G214, which is totally about 19 km long. This road had been widened from two lanes to four lanes in 2009. Yushu Airport Road is constructed on the left bank of Batang river, locating on the First and

W. Honggang (✉) · M. Huimin · Z. Hongli
Northwest Research Institute Co., Ltd. of CREC,
Lanzhou 730000, China
e-mail: ztxbywhg@yahoo.com.cn

Y. Tao
Department of Geotechnical Engineering,
Southwest Jiaotong University,
Chengdu 610031, China
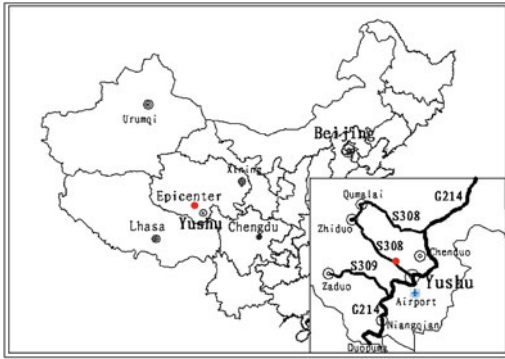
Fig. 71.1 The 2010 Yushu earthquake (Ms7.1) position schemes

Second terrace. The slope mainly consists of pebbles, gravels, and clayey soil. These materials were mainly colluvial and alluvial. The April 14, 2010 Yushu earthquake (Ms7.1) (as shown in Fig. 71.1) triggered a ground of landslides (landslide No.1, No.2 and No.3) on the right side of Batang river in K822 + 888 ∼ K824 + 400 segment along Airport Road (as shown in Fig. 71.2).

The occurrence and development of these landslides not only destructed the Xihang aqueduct, blocked the airport road, but also threat the safe operation of Airport Road. If not govern, it will impact seriously on the earthquake relief and reconstruction. To understand the initiation mechanism of these landslides and then take proper countermeasure works to stabilize these slopes, we made a detailed analysis on the possible initiation process of the landslides during the earthquake, and also analyzed the post-earthquake stability of these landslides. The results will be presented in this paper.

2 Landslides Along the Airport Road

3 landslides (No.1, No.2, and No.3 in Fig. 71.2) were triggered on the Batang river bank slope along the Airport Road. Landslide No.2 was initiated in colluvial deposits with cracks at the left side directing NW79°. These cracks

occurred during the earthquake. Figure 71.3 presents its section along line I–I in Fig. 71.2. The slope gradient is relatively gentle (about 10°) (Fig. 71.3). The head of landslide is bounded nearly the elevation of 3774 m, and the toe of landslide is located on the top surface of the first terrace near the inside highway cutting.

From the topography and deformation characteristics of the landslide, we inferred that the main sliding directed towards NE46°, which was nearly vertical to the road. The longitudinal length (along the road) of the landslide was about 317 m, width was about 482 m, and the thick of sliding body was about 22.8 m in maximum with an average thickness of about 19.8 m. Therefore the landslide volume was estimated as 2.9×10^6 m^3. The slip surface is relatively flat (only 3° in average).

The occurrence of this landslide was identified by cracks that developed on both sides of landslide and discontinuous transverse cracks along the upper slope (head of the landslide). This landslide can be divided into two sub-blocks: the toe part one and main-body one. The sliding zone of the toe part of landslide developed between the second terrace and the younger deposits. And the head of the toe part of landslide is close to Xihang aqueduct. The sliding surface of the main-body is close to the upper boundary of the second terrace.

The cracks of the toe part of landslide developed intensively and deformed seriously. Three main cracks developed parallel to the road, and their widths reached about 10–30 cm, extending length was up to 200 m. These cracks on the sliding body normally had a depth of 10–40 cm. The cracks of the main-body landslide are mainly located on the lateral platform of Xihang aqueduct. The rest cracks of the slope develop only at the right side of landslide, and a micro-crack develops at the trailing edge extending to about 5 m, with width 2–5 cm.

Mechanism and Stability Analysis of Landslide Deformation

Landslide No. 2 is distributed on the Batang river terraces. The main block of upper part is composed of gravelly soil, soil breccias, and other loose debris, so the entire slope possess a

Fig. 71.2 Overview of landslide group along Yushu Airport road
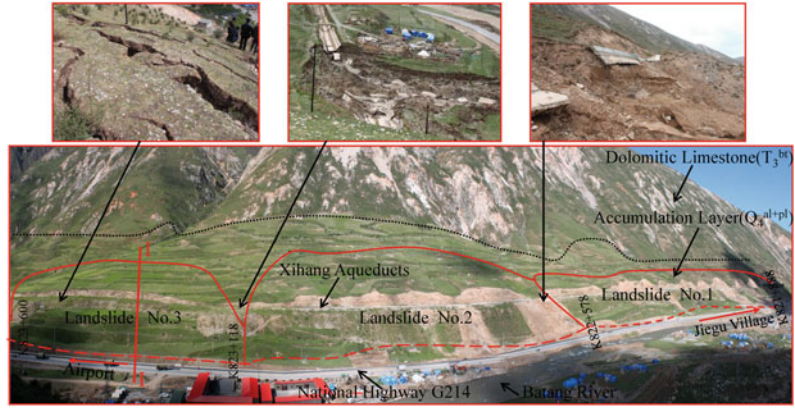
loose slope structure. On the influence of Yushu to Ganzi fracture seismic zone, it was happening here of the Yushu 4.14 earthquake and then resulting in deformation of loose slope along Yushu Airport Road.

If the stress state of one point of slope achieves yield state with security reserved, it would be in destruction state. The yield state with security refers to the ratio of the shear strength to the design stability factor.

2.1 Point Safety Factor of Stress State

According to geotechnical strength of the material yield criterion, failure will occur when one point of geotechnical material of slope reaches the yield state. In other words, the stability of the rock mass is determined by its stress state and yield strength criterion. Based on Mohr–Coulomb yield criterion, Fs is defined as the ratio of the shear strength to the shear stress.

According to Mohr–Coulomb strength yield criterion, the yield function f is

$$f = [(\sigma_1 - \sigma_3)/2] \\ - [c \, \cos\phi - 0.5(\sigma_1 - \sigma_3)\sin\phi] \\ = 0 \tag{71.1}$$

where $[(\sigma_1 - \sigma_3)/2]$ is defined as the shear stress $[c \, \cos\phi - 0.5(\sigma_1 - \sigma_3)\sin\phi]$ is defined as the shear strength.

So, the point safety factor of slope Fs is

$$F_s = [c \, \cos\phi - 0.5(\sigma_1 + \sigma_3)\sin\phi]/[(\sigma_1 - \sigma_3)/2] \tag{71.2}$$

2.2 Mechanism Analysis of Landslide initiation

In order to analyze the initiation process of the landslide due to the introduction of earthquake, and then provide the basis for the design calculating of landslide, the dynamic response of the slope and landslide developing process are analyzed by numerical simulation.

According to the basic information of landslide, we used FLAC3D to simulate the deformation induced by earthquake (Itasca Consulting Group, Inc., 2003). The calculation parameters are selected comprehensively referring to the report (China Highway Engineering Consulting Group Co., Ltd, 2008), the sliding zone testing parameters, spreadsheet results and experiences (Table 71.1). The model is imposed by an acceleration time history, which examines the response of the slope in the vibration process. In order to show the evaluation of the important changes of the slope distinctive position relative to the acceleration process, nine monitoring points (Fig. 71.4) were set up in the main section of the sliding zone (P1, P2 and P3),
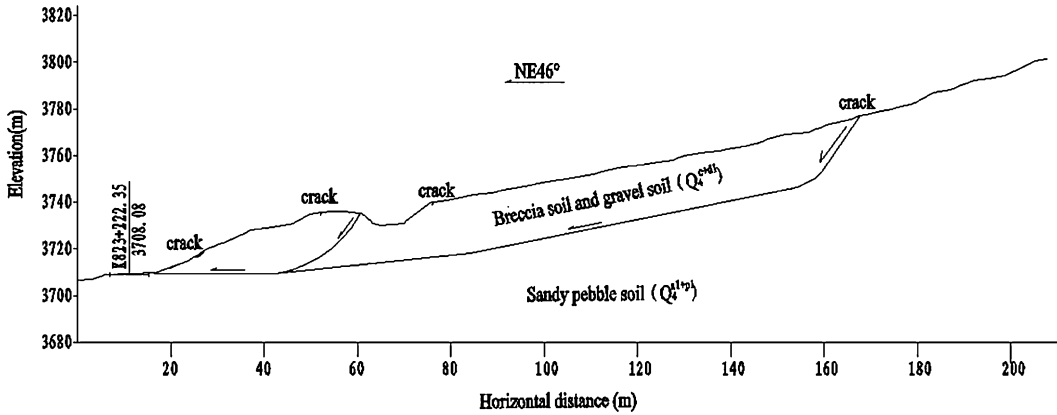
Fig. 71.3 The I–I section diagram of landslide No. 2

Table 71.1 Basic physical parameters of various strata

Stratigraphic and lithologic	Modulus of elasticity E (Gpa)	Poisson's ratio μ	Density γ (kN/m^3)	Cohesion c (MPa)	Angle of internal friction φ (°)
Accumulation	1.50	0.30	20.0	0.15	23
Sliding zone	0.23	0.38	19.0	0.02	10
Dolomitic limestone	1.80	0.28	23.0	0.40	43

Fig. 71.4 Overview of the model cross section and the monitoring sites
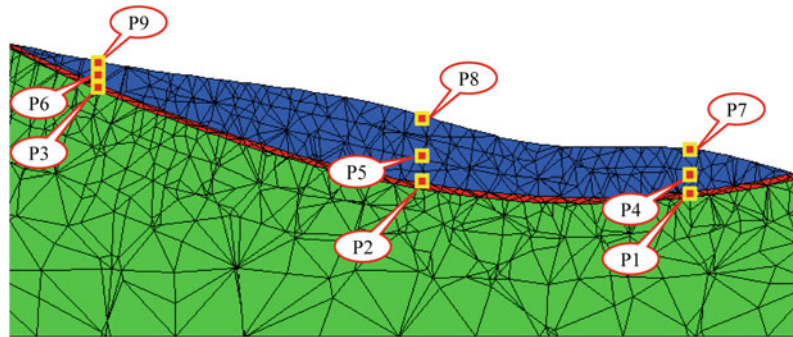
slippery body (P4, P5 and P6) and slope surface (P7, P8 and P9).

When the earthquake comes in, each point safety factor of slope changes all the times, and then failure occurs in some part of the slope with progress of time. The slope does not fail suddenly as a whole. Figs. 71.5 and 71.6 show that when earthquake acceleration approaches the peak, the whole sliding zone in most of the areas where the point safety coefficients is less than or equal to 1. The trailing edge and lateral boundary of slope produce tensile failure. The other part of slope occurs plastic shear deformtion. At the end of calculation, the range of plastic sliding zone reduced heavily, and most of safety factor increase to more than 1.2. The crack length of trailing edge and deformation scope of slope decrease obviously. The plastic shear zone is mainly distributed in the lateral margin and toe part of landslide. From the simulation results, we can find that the stability of slope during the earthquake is much lower than that after earthquake. The geotechnical stress of slope is formed by superposition of dynamic stress and gravity stress. The size of the dynamic stress and direction are changing times during
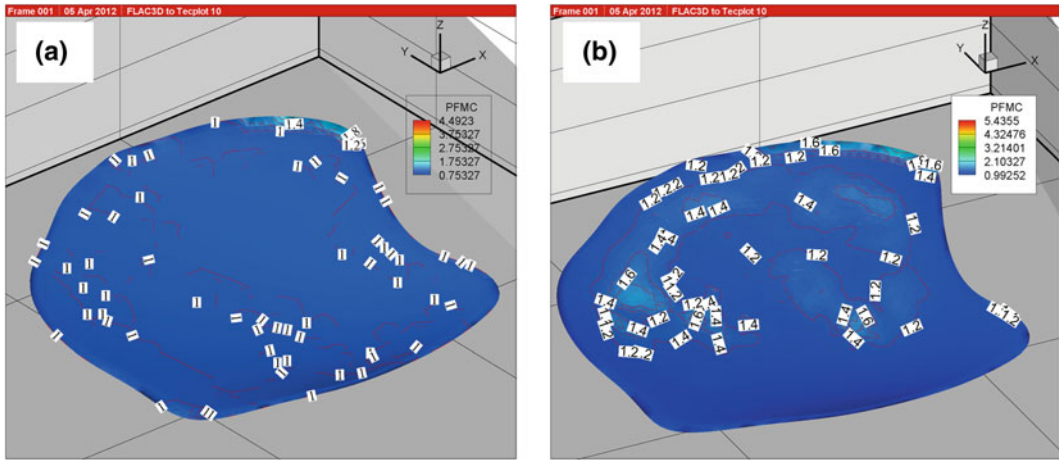
Fig. 71.5 Distribution and variation diagram of the safety factor of sliding zone. **a** When peak acceleration; **b** Calculation end
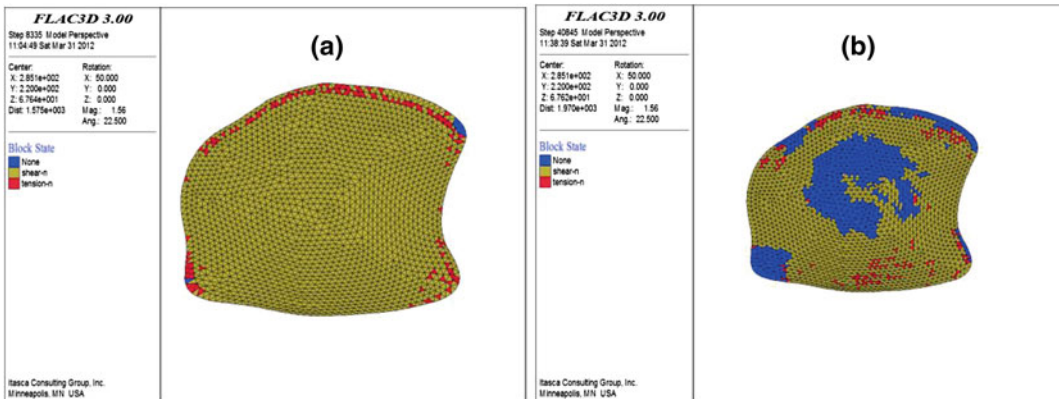
Fig. 71.6 Distribution and variation diagram of plastic sliding zone (**a**) When peak acceleration (**b**) Calculation end

earthquake. With relatively short time earthquake effect, the sliding resistance of slope changes very small, and the sliding force increases remarkable. Therefore, the coefficient of slope stability during earthquake is overall much smaller than that after earthquake.

During the earthquake, the response of landslide has been obvious amplified, and all parts of slope show certain hysteresis and nonuniformity to the earthquake response. As shown in Fig. 71.7, the peak acceleration of the monitoring points all appeared at 1.65 s later, and with the increase of elevation, peak values appeared in late time. The points of the sliding zone (P1,

P2 and P3) reached peak earlier than that of internal and surface points of slope (P4–P9). No matter for the sliding zone, slippery body internal or surface monitoring points (Fig. 71.7), the higher the elevation, the greater the acceleration. Based on the amplification effect, the acceleration causes instantaneous stress and produces arc cracks, and then leads to the slope stability reduced.

The landslide deformation mechanism under the effects of earthquake presents overall as tensile and shear destruction shown by the calculation above. During the earthquake, Tensile-shear effect firstly produces tensile cracks in the
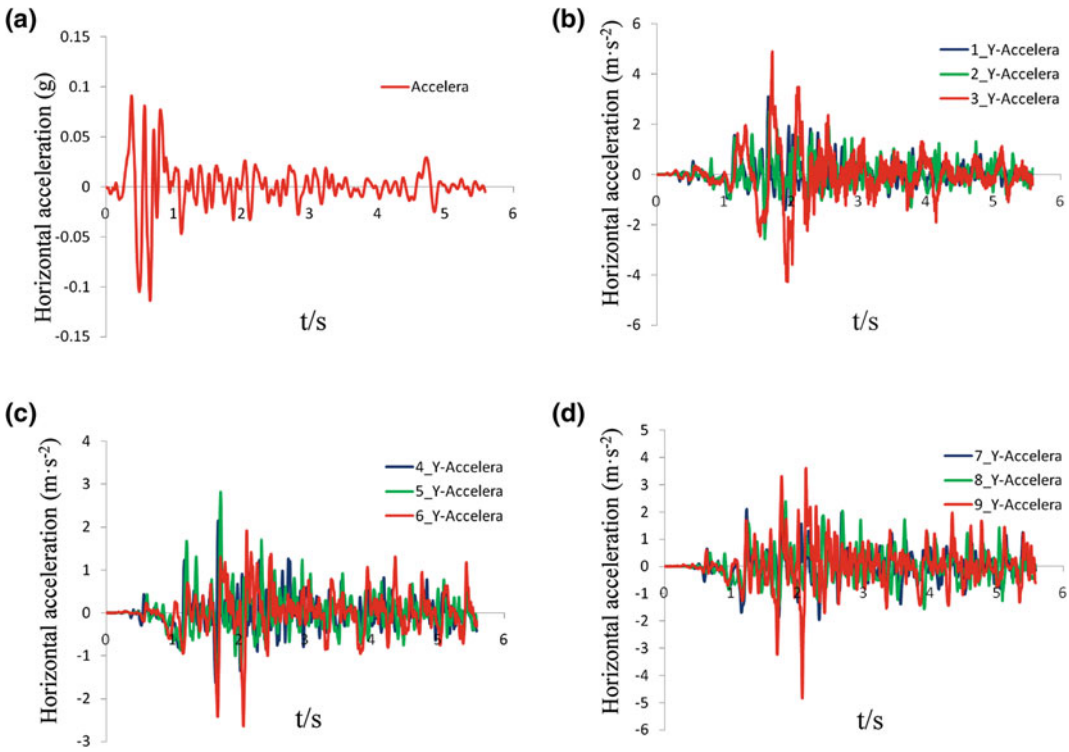
Fig. 71.7 Characteristic curves of acceleration schedule of the monitoring points (**a**) Input earthquake acceleration (**b**) Sliding zone monitoring points (**c**) Slippery body monitoring points (**d**) Slope surface monitoring points

Table 71.2 Stability evaluation of landslide after the earthquake

Case	Bulk density γ(kN/m³)	Internal friction angle φ(°)	Cohesion c(kPa)	Safety factor	Remarks
1	20	9.3	15	1.03	Limit equilibrium
2	20	8.1	15	1.23	Stable state

Remarks Case1 is related to the toe part of landslide, as well as case2 is related to the main-body of landslide

surface of slope, and produces potential dynamic shear deformation in the slippery body. This is the main reason for slope deformation. After that, the tensile plastic zone and shear plastic zone formed, and then slope displacement develops directing to free face.

2.3 Analysis of Landslide Stability

In order to verify the reliability of point safety factor of stress state, according to this method the calculation results have been compared with the results of transfer coefficient method transfer coefficient method. On the basis of landslide basic original form and features, we inspect count of safety factor by selecting the representatives of the cross section. In the light of determining the mechanical parameters of the main sliding section while considering of the spreadsheet results, laboratory geotechnical test results and value of experience, we calculated the safety factor by the transfer coefficient method (Table 71.2). If there is heavy rain or earthquake, the stability factor may be less than 1.0, and then there is the possibility of overall instability.

Results of the traditional coefficient transfer calculation method show that the landslide is overall in natural stable state at present, although it may be instability in period of the heavy rains and earthquakes. Analysis results of the point safety factor are really in agreement with the traditional coefficient transfer calculation method, and then we may conclude that the method of stability analysis is more reliable in both of data and conclusions.

3   Concluding Remarks

Through the analysis, following conclusions are made.

(1) Landslide No.2 along Airport Road with a loose slope structure is distributed in the Batang River terraces, which is mostly composed of pebble, gravel, and clayey soil from the bottom to the third band. The earthquake could produce cracks and deformation for slope, ultimately lead to reducing the stability of slope and then result in landslide and other diseases.

(2) The distribution characteristics of point safety factor of stress state, show that on the peak of seismic acceleration, the landslide overall was in the state of instability, accompanied by such features as tensile cracks at the trailing edge of landslide and a shear failure area in the main-body. At the end of calculation, the bottom of landslide is in a less stable state. The trailing edge of landslide produces cracks due to the stability instantly reducing during the earthquake. The characteristics of numerical analysis and the geological analysis of macroscopic deformation are extremely similar, indicating that

the approach of point safety factor of stress state for the seismic-induced landslide evaluation is more effective, which can be used to explain the deformation mechanism and stability of the calculation and analysis of landslide.

(3) In light of highway cutting of landslide No.2 in the state of poor stability after the earthquake, authors recommend us to strengthen the toe part reinforcement of slope and monitor at least in one or two rainy season and then take appropriate measures.

References

Bo J, Liu D (2005) Review on study of seismic stability analysis of rock-soil slopes [J]. Earthq Eng Eng Vib 25(1):164−171

China Highway Engineering Consulting Group Co., Ltd (2008) The report on highway construction drawings and design engineering geological survey of the Yushu to Batang Airport segment on the National Highway G214 [R]

Crespellani T, Madiai C, Vannuchi G (1998) Earthquake destructiveness potential factor and slope stability [J]. Geotechnique 48(3):411–419

Itasca Consulting Group,Inc (2003) Fast Lagrangian analysis of continua in three dimensions (version 3.0) user's manual [R]. Itasca Consulting Group,Inc

Liu H,Fei K,Gao Y (2003) Time-history analysis method of slope seismic stability [J]. Rock Soil Mech 24(4):553–556

Qi S, Wu F, Liu C et al (2004) Engineering geology analysis of stability of slope under earthquake [J]. Chin J Rock Mech Eng 23(16):2792–2797

Wang FW,Cheng QG,Lynn H et al (2009) Preliminary investigation of some large landslides triggered by Wenchuan earthquake in 2008, Sichuan Province,China [J]. Landslides 6(1):47–54

Xu Q, Huang R (2008) Kinetics characteristics of large landslides triggered by May 12th Wenchuan earthquake [J]. J Eng Geology 16(6):721–729

Strong Motion Estimation at the Kanaga Landslide, Nasukarasuyama City, Induced by the 2011 off the Pacific Coast of Tohoku Earthquake (M_W9.0) Based on Empirical Site Amplification and Phase Effects

Yoshiya Hata, Gonghui Wang, Atsushi Nozu
and Toshitaka Kamai

Abstract

Many landslides were triggered by the 2011 off the Pacific coast of Tohoku Earthquake (M_W9.0). Among them, a large-scale landslide occurring in Kanaga, Nasukarasuyama City, Tochigi Prefecture, destroyed several houses and killed two people. To clarify the triggering mechanism of this landslide, it is great importance to estimate the seismic waveform at Kanaga Landslide site with higher accuracy, taking into account the site effects. In this study, seismic waveform at the Kanaga Landslide was estimated based on site-effect substitution method, while the site effects were evaluated based on aftershock records. Difference of site effects between the Kanaga Landslide and the nearby strong motion observation stations was presented, and discussed.

Keywords

Strong motion · Site effects · Aftershock observation · Landslide · The 2011 off the Pacific coast of Tohoku Earthquake

Y. Hata (✉)
R&D Center Nippon Koei Co., Ltd. 2304,
Inarihara Tsukuba, 3001259, Japan
e-mail: hata-ys@n-koei.jp

G. Wang
Disaster Prevention Research Institute, Kyoto
University, Gokasho Uji 6110011, Japan

A. Nozu
Head of Engineering Seismology Division, Port and
Airport Research Institute, 3-1-1 Nagase
Yokosuka, 2390826, Japan

T. Kamai
Disaster Prevention Research Institute, Kyoto
University, Gokasho Uji 6110011, Japan

1 Introduction

To clarify the causes and mechanisms of seismic damage caused by a large-scale earthquake, it is important to understand the strong motions at different sites. The 2011 off the Pacific coast of Tohoku, Japan, earthquake caused significant damage, not only due to tsunamis but also due to strong motions.

As one of the methods to estimate strong motions from a large-scale earthquake at a site of interest, a practical strong motion estimation method, which was called 'site-effect substitution method', was proposed by Hata et al. (2011). The

method is based on records of aftershocks both at the site of interest and at a nearby permanent strong motion observation station, and on the record during the main shock at the observation station. Because it focuses not only on the difference of site amplification factors, but also on the difference of site phase effects between the site of interest and the observation station, this method can estimate time histories of strong ground motions at the site of interest with high accuracy. Another advantage of this method is its simplicity. Unlike full strong motion calculations such as those based on the Stochastic Green's Function Method (e.g., Nozu et al. 2009), this method does not require a fault model of the large event. It is sometimes difficult to obtain a fault model of a large event at an early stage of response to a large event. The method is expected to satisfy the needs of engineering community by providing a prompt estimation of strong motions.

Many landslides occurred during the 2011 off the Pacific coast of Tohoku Earthquake (M_W9.0). Among them, a catastrophic one occurred in Kanaga area, Nasukarasuyama City (Wakai and Higuchi 2011; Matsushita and Wakai 2011; Fukushima et al. 2011), killing two people, and destroyed several houses completely. This landslide had a length of about 210 m, elevation difference of 40 m, and width of 30 m. The displaced landslide debris was estimated approximately 30,000 m^3. Although the volume is relatively small, the displaced landslide material showed very high mobility. To clarify the landslide mechanism, it is necessary to estimate the seismic waveform at the landslide site with sufficient accuracy, taking into account the site effects.

In this paper, we first applied the site-effect substitution method to estimate the strong ground motions at some permanent observation stations around the Kanaga Landslide in Nasukarasuyama City, Tochigi Prefecture, Japan, during the 2011 off the Pacific coast of Tohoku Earthquake, and then estimated the strong motions at these stations. The validity of the method was confirmed by checking the estimated strong motions, which were very consistent with the observed ones. We then used this method to estimate the strong motion at Kanaga landslide site.
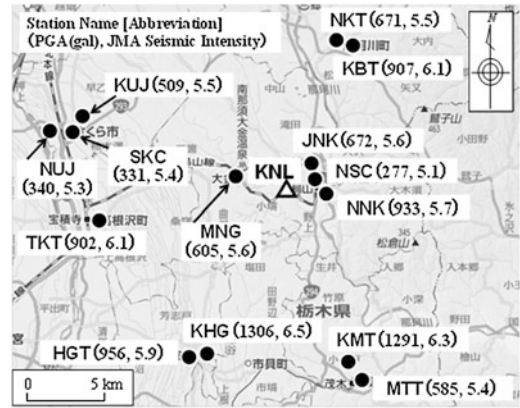
Fig. 72.1 The distribution of strong motion observation records around Kanaga (KNL) site during the 2011 main shock

2 Ground Motion Record and Aftershock Observation

In Tochigi prefecture, besides nationwide networks operated by such organizations as NIED (K-NET and KiK-net; e.g., Aoi et al. 2004), JMA (e.g., Nishimae 2004) and NILIM (e.g., Uehara and Kusakabe 2004), a dense strong motion network is also operated by the local government, which is now a part of SK-net (e.g., Takano et al. 2005). Thus, a large amount of strong motion records was obtained in the 2011 Tohoku Earthquake. The locations of the strong motion stations around Kanaga landslide (KNL) site are shown in Fig. 72.1, with peak ground accelerations (PGAs) and JMA seismic intensities (e.g., Nishimae 2004). The list of the stations with abbreviations can be found in Table 72.1. Here, at NNK, only the indices of the seismic motion (see Fig. 72.1) were recorded (time history data were not recorded) to obtain the seismic intensity data for quick and efficient emergency response decisions.

For instance, although JNK, NSC and NNK are close to each other, the JMA seismic intensities and PGAs at these sites are quite different (see Fig. 72.1), which indicates the significant difference of the site effects at these stations and the importance of the consideration of the site effects in estimating strong ground motions. Figure 72.2 shows detailed locations of JNK, NSC and NNK with KNL.

Table 72.1 The list of strong motion observation stations

Abbreviation	Station name
KNL	Kanage landslide(Temporary aftershock observation site)
JNK	JMA Nasukarasuyama
NNK	NILIM Nakagawa
KBT	K-NET Batou
KUJ	KiK-net Ujie
NUJ	NILM Ujie
KHG	KiK net Haga
KMT	K-NET Motegi
NSC	Nasukarasuyama city hall
MNG	Minaminasu government office
NKT	Nakagawa town hall
KTG	Kitsuregawa government office
SKC	Sakur city hall
TKT	Takanezawa town hall
HGT	Haga town hall
MTT	Motegi town hall

SK-net Shutoken Kyoshin networks

In this study, temporary aftershock observation site was performed at the toe of KNL site. The observation continued 8 days (within the limitation of power supply from battery) to investigate the ground shaking characteristics. The details of the instruments of the aftershock observation system can be obtained from Senna et al. (2006). The observation was conducted for 3 components (NS, EW and UD), and the sampling frequency was 100 Hz.

Table 72.2 is the list of the observed earthquake events at KNL site. The observed earthquake events were moderate ones, and the observed motions were used for the evaluation of the site amplification factor at KNL site.

3   Site Amplification Factor

The site amplification factors for K-NET and KiK-net stations have already been evaluated in the study by Nozu et al. (2007) based on spectral inversion. However, the site amplification factors at JMA, NILIM, SK-net stations and KNL

Fig. 72.2 Location of Kanaga (KNL) and nearby strong motion observation stations

site have not been reported yet. In this study, the spectral ratio method (e.g., The Japan Port and Harbor Assoc. 2007) is applied to evaluate the site amplification factors at JNK and KNL sites.

The method is based on the moderate earthquake records obtained at the reference station and the target sites simultaneously. The target sites are JNK and KNL sites. The reference station is the KBT site.

For each combination of the target and the reference, the spectral ratio of the Fourier amplitude of the records at the reference station and the target site is calculated. Here, the moderate earthquake records before the 2011 main shock were used for JNK site. For KNL site, the records after the 2011 main shock were used (see Table 72.2). The effects of geometrical spreading and anelastic attenuation are considered as the path effect (Boore 1983; Satoh and Tatsumi 2002) to correct the Fourier spectra. The mean of the corrected spectral ratio (the target site/the reference station) is calculated.

Finally, the site amplification factor at the target site can be obtained as the product of the site amplification factor of the reference station and the spectral ratio. Here, the frequency range for the evaluation of the site amplification factor is from 0.2 to 10 Hz, because the site amplification factor at the reference station is reliable in this frequency range (Nozu et al. 2007).

Figure 72.3 shows the site amplification factors for the K-NET and KiK-net stations (KBT, KUJ, KHG, KMT sites) given by the spectral inversion method (Nozu et al. 2007) and those at the JNK and KNL sites given by the above-mentioned method (all the site amplification factors

Table 72.2 The list of observed earthquakes

Year/Month/Day	Hour: Min. (JST)	Source region	JMA Magnitude
2011/09/22	14:46	Off Ibaraki pref.	Mj4.4
2011/09/23	04:59	Off Fukushima pref.	Mj4.7
2011/09/23	17:15	Northern Ibaraki pref.	Mj5.1
2011/09/26	22:46	Northern Ibaraki pref.	Mj4.2
2011/09/29	04:18	Off Fukushima pref.	Mj4.3
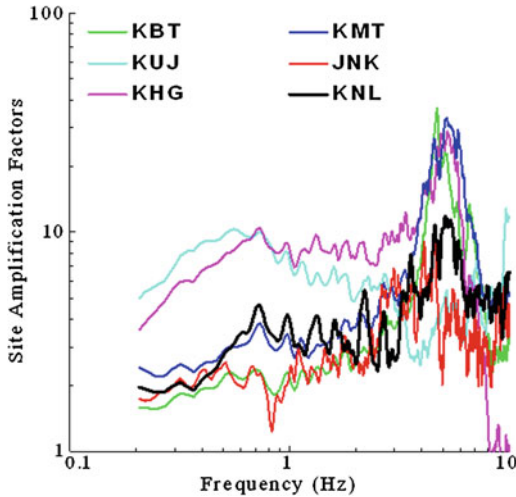
Fig. 72.3 Comparison of the site amplification factors

correspond to the horizontal component). As shown in Fig. 72.3, the characteristics of the site amplification factors are not similar between JNK site and KNL site. It suggests that the main shock record at JNK site cannot be used directly as the estimated ground motion at KNL site for the 2011 main shock.

4   Strong Motion Estimation

4.1   Estimation Method

Figure 72.4 shows the framework of strong motion estimation at target sites (KBT, KUJ, KHG, KMT and KNL sites) using the site-effect

substitution method (Hata et al. 2011). The method is simply composed of three steps. First, the Fourier amplitude at the evaluation sites for the 2011 main shock is evaluated by correcting the observed Fourier amplitude at JNK site for the difference of the path effect (Boore 1983; Satoh and Tatsumi 2002) and the site amplification factors (see Fig. 72.3) at the target sites and JNK site. Here, although NSC site is a permanent observation station which is the closest to KNL site (see Fig. 72.2), the site amplification factor cannot be evaluated. This is because at NSC, only the ground motion due to the 2011 main shock was recorded (the ground motion due to the other moderate earthquakes were not recorded).

Then, the Fourier phase at the target sites during the 2011 main shock is approximated by the Fourier phase for off Ibaraki Prefecture earthquake (2011/09/22 14:46 Mj4.4; see Table 72.2) that occurred close to the main rupture area of the 2011 main shock.

Finally, inverse Fourier transform is conducted to obtain causal time history (Nozu et al. 2009) of strong ground motions at the target sites during the 2011 main shock. In order to confirm the validity of the estimation method, the strong ground motions at KBT, KUJ, KHG and KMT sites for the main shock are evaluated by correcting the observed strong ground motion at JNK sites. The observed velocity waveforms (the black traces) and the synthetic velocity waveforms (the red traces) at KBT, KUJ, KHG and KMT sites are compared in Fig. 72.5 for NS and EW components. Here,

Fig. 72.4 Framework of
the strong motion
estimation method
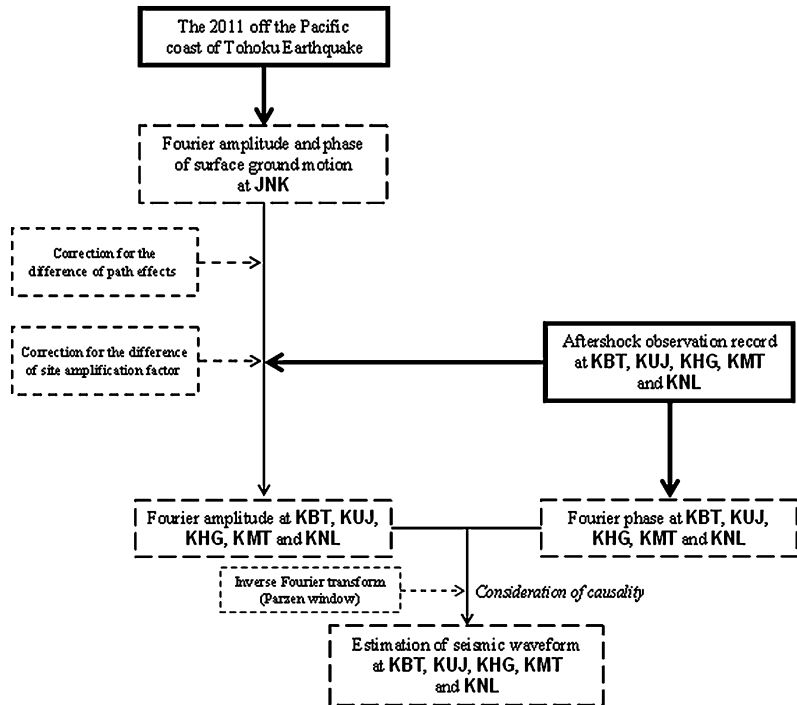
both traces are band pass filtered between 0.2
and 2.0 Hz. In Fig. 72.5, the similarity of all
traces indicates the applicability of the estima-
tion method.

4.2   **Strong Motion Estimation**

Figure 72.6 shows the estimation results of
velocity and acceleration waveforms at KNL
site. Here, the velocity waveforms are band pass
filtered between 0.2 and 2.0 Hz. The PGA for
the composition of NS and EWcomponents at
KNL site is 978 gal. The JMA seismic intensity
at KNL site is 5.6 based on the horizontal two
components.

Figure 72.7 is the comparison of estimated
response spectra (damping: 5 %) at large-scale
landslide sites due to recent damaging earth-
quakes in Japan (Hata et al. 2010, 2012a, b) and
the estimated response spectra (damping: 5 %)
at KNL site. In Fig. 72.7, first, Higashitakezawa
(2004) indicate the estimated ground motion for
N60°W component at Higashitakezawa land-
slide site due to the 2004 Mid Niigata Prefecture
Earthquake (Hata et al. 2012a). Then, Aratoza-
wa (2008) indicate the estimated ground motion
for NS direction at Aratozawa landslide L1 site
due to the 2008 Iwate-Miyagi Nairiku Earth-
quake (Hata et al. 2010). Finally, Hanokidaira
(2011) indicate the estimated ground motion for
NS direction at Hanokidaira landslide site due to
the 2011 off the Pacific coast of Tohoku Earth-
quake (Hata et al. 2012b).

As shown in Fig. 72.7, the evaluated
response spectra for the Higashitakezawa
Landslide site (due to the 2004 Mid Niigata
Prefecture Earthquake) and KNL site (due to
the 2011 off the Pacific coast of Tohoku
Earthquake) are similar.

Fig. 72.5 Confirmation of the validity of the strong motion estimation method
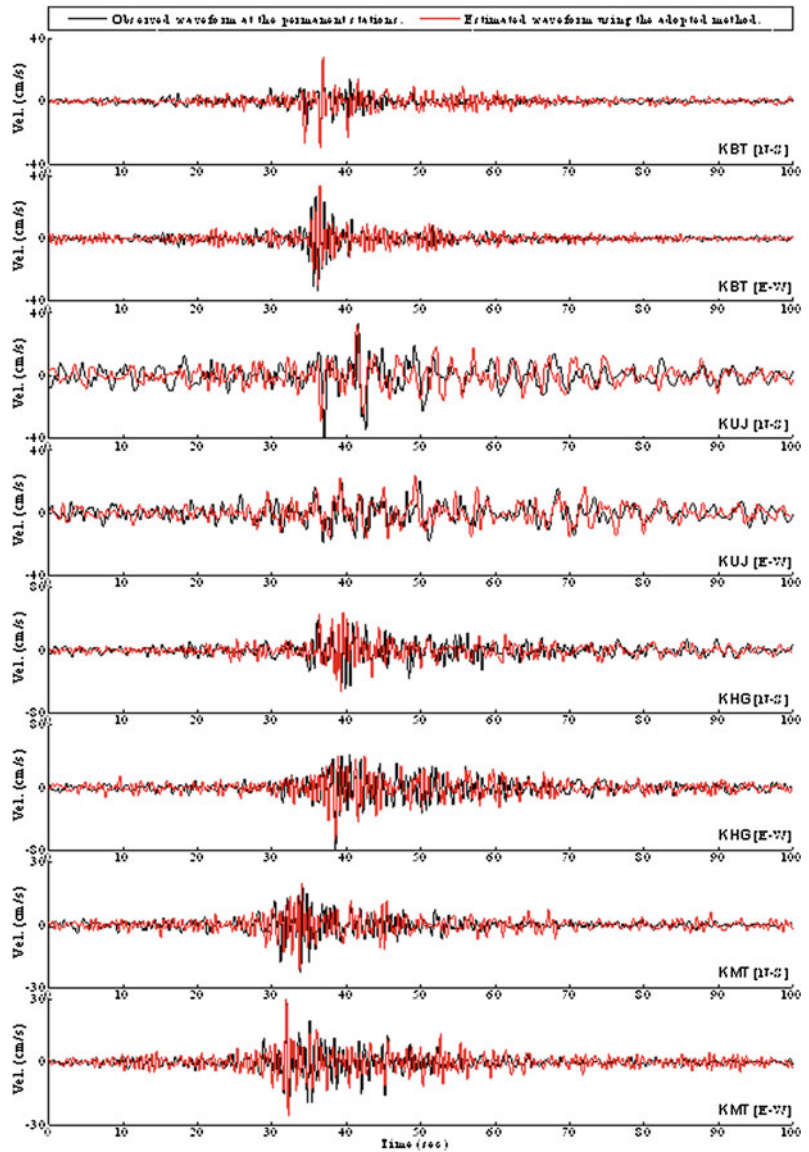
5   Summary and Conclusions

The strong ground motions at Kanaga Landslide site and nearby strong motion observation stations due to the 2011 off the Pacific coast of Tohoku Earthquake (M_W9.0) were evaluated based on the site-effect substitution method. The estimated seismic waveforms at strong motion

stations with the site-effect substitution method are consistent with the observed ones, indicating the validity of the method. Finally, the evaluation method was used to estimate strong ground motions at Kanaga Landslide site.

As a result, it was found that, in the natural period range between 0.1 and 10.0 s, the evaluated response spectra between the Higashi-takezawa Landslide site (due to the 2004 Mid
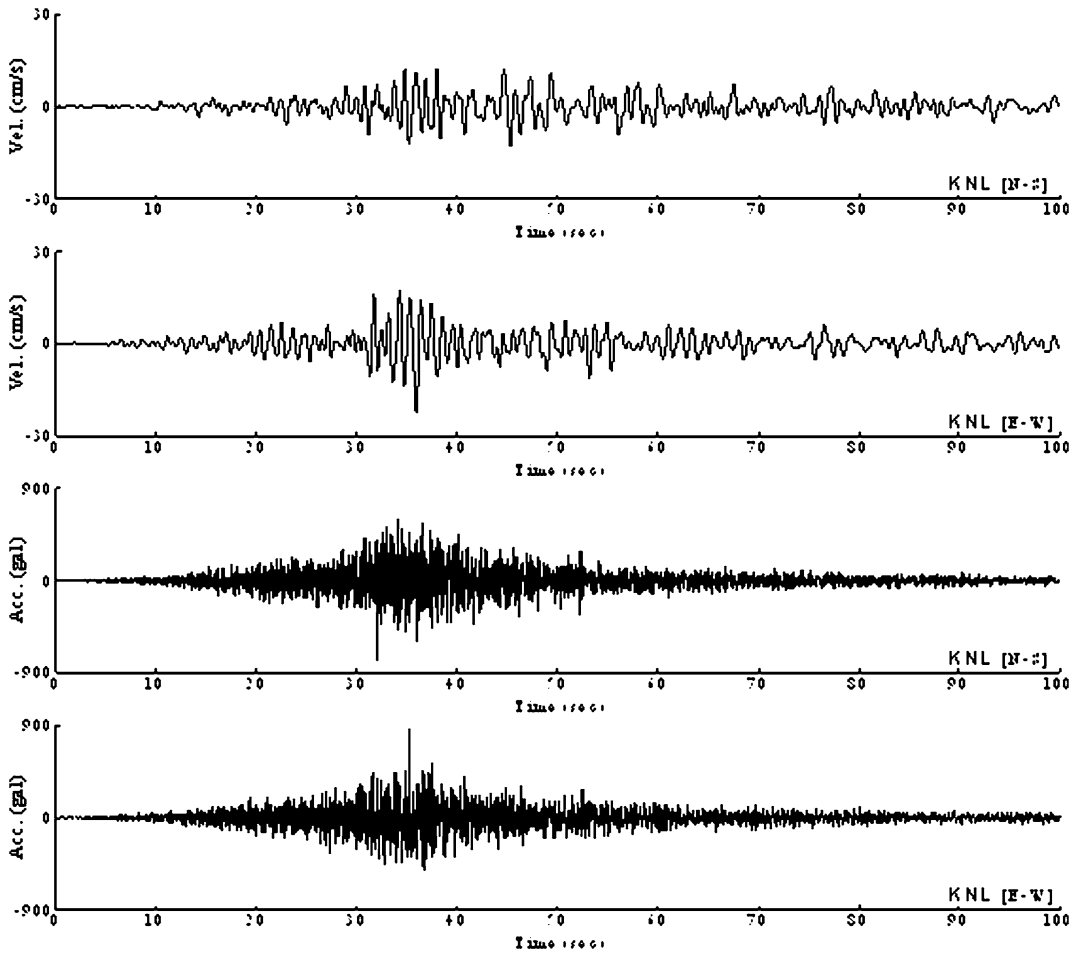
Fig. 72.6 Estimated velocity and acceleration waveforms at KNL during the 2011 main shock
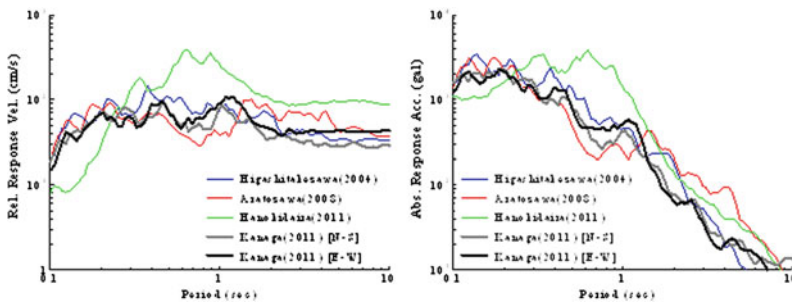
Fig. 72.7 Comparison of estimated response spectra at large-scale landslide sites due to recent damaging earthquakes in Japan and the estimated response spectrum at KNL site (damping: 5 %)

Niigata Prefecture Earthquake) and Kanaga Landslide site (due to the 2011 off the Pacific coast of Tohoku Earthquake) are similar respectively.

In the future study, the seismic response analysis of the Kanaga Landslide will be carried out using the estimated ground motion.

References

Aoi S, Kunugi T, Fujiwara H (2004) Strong-motion seismograph network operated by NIED: K-NET and KiK-net. J Japan Assoc Earthq Eng 4:65–74

Boore D M (1983) Stochastic simulation of high-frequency ground motions based on seismological models of the radiated spectra. B Sesimol Soc Am 73(6A):1865–1894

Fukushima T, Matsushita K, Usami H, Wakai A (2011) A case of landslide occurred in Kanaga, NasuKarasuyama at the time of 2011 Tohoku Earthquake. Proc. Geo-Kanto 2011 8:105–107 Kofu (in Japanese)

Hata Y, Ohsumi T, Nozu A, Kamai T (2010) Evaluation of strong motion at the Aratozawa site induced by the 2008 Iwate-Miyagi Nairiku earthquake based on empirical site simplification and phase effects. J Japan Landslide Soc 45(5):247–254 (in Japanese with English abstract)

Hata Y, Nozu A, Ichii K (2011) A practical method to estimate strong ground motions after an earthquake based on site amplification and phase characteristics. B Seismol Soc Am 101(2):688–700

Hata Y, Nozu A, Kamai T (2012a) Seismic waveform estimation at the Higashi-takezawa landslide induced by the 2004 Mid Niigata prefecture earthquake based on empirical site amplification and phase effects. J Japan Landslide Soc 49(2):51–60 (in Japanese with English abstract)

Hata Y, Wang G, Kamai T, Suemine A, Nozu A (2012b) Seismic waveform estimation at the Hanokidaira landslide induced by the 2011 off the Pacific coast

of Tohoku earthquake based on site effects substitution method. J Japan Landslide Soc 49(3):109–118 (in Japanese with English abstract)

Matsushita K, Wakai A (2011) Slope disasters in northern area induced by the 2011 off the Pacific coast of Tohoku earthquake (Part II). In: Proceedings of JLS annual meeting, 50:179–180, shizuoka (in Japanese)

Nishimae Y (2004) Observation of seismic intensity and strong ground motion by Japan meteorological agency and local governments in Japan. J Japan Assoc Earthq Eng 4:75–78

Nozu A, Nagao T, Yamada M (2007) Site amplification factors for strong-motion sites in Japan based on spectral inversion technique and their use for strong-motion evaluation. J Japan Assoc Earthq Eng 7(2):215–234 (in Japanese with English abstract)

Nozu A, Nagao T, Yamada M (2009) simulation of strong ground motions using empirical site amplification and phase characteristics: modification to incorporate causality. J JSCE, Ser. A (Structural Eng. & Earthquake Eng.) 65(3):808–813 (in Japanese with English abstract)

Satoh T, Tatsumi Y (2002) Source, path, and site effects for crustal and subduction earthquakes inferred from strong motion records in Japan. J Struct Constr Eng AIJ 556:15–24 (in Japanese with English abstract)

Senna S, Adachi S, Ando H, Araki T, Iisawa K, Fujiwara H (2006) Development of microtremor survey observation system. In: Proeedings of Japan geoscience union annual meeting 2006, No.S111-P002 in CD-ROM, Makuhari

Takano K, Koketsu K, Kudo K, Furumura T, Yamanaka Y, Tobe S, Doi K (2005) Shutoken Kyoshin network: SK-net. In: Proceedings of symposium on the 50th anniversary of strong-motion earthquake observation in Japan: NIED, 119–122, Tsukuba (in Japanese with English abstract)

The Japan Port and Harbor Association (2007) Technical standards and commentaries of port and harbor facilities. Ports and Harbours Bureau, Ministry of Land, Infrastructure and Transport. 336–341 (in Japanese)

Uehara H, Kusakabe T (2004) Observation of strong earthquake motion by National Institute for land and infrastructure management. J Japan Assoc Earthq Eng 4:90–96

Wakai A, Higuchi K (2011) Slope disasters in northern area induced by the 2011 off the Pacific coast of Tohoku Earthquake (Part I). In: Proceedings of JLS annual meeting 50:5–6, shizuoka (in Japanese)

Finite Element Simulation for An Earthquake-Induced Landslide Considering Strain-Softening Characteristics of Sensitive Clayey Loam

73

Tomoyuki Fukushima, Keisuke Matsushita, Hirotatsu Usami and Akihiko Wakai

Abstract

Landslide with fluid-like mass movement is one of the typical features within the observed slope damages due to The East Japan Great Earthquake. In many slopes mainly composed of sensitive clayey loam with higher water content in northern Kanto district, the sudden strength degradation of the soil under the strong earthquake motion caused a long-distance travelling failure. In this study, a case of such catastrophic phenomena, at Okanouchi in Shirakawa-city, is simulated by the dynamic elasto-plastic finite element method where the cyclic loading characteristics of the sensitive clayey loam are numerically formulated by the UW softening model. By adopting the appropriate parameters based on the laboratory element tests with the undisturbed specimens, the obtained analytical results agreed with the observed phenomena.

1 Introduction

The East Japan Great Earthquake caused various damages, such as landslide disasters, tsunami and liquefaction, in the Tohoku and Kanto districts. Especially in landslide disasters, landslides with fluid-like mass movement that the clayey loam became soft and moved long distance by large and long-time vibration, were observed in the central and eastern part of Tochigi Prefecture. One of the causes for the generation of landslides is the sudden strength degradation of the soil under cyclic loading. In this study, a case of such landslides with fluid-like mass movement, at Okanouchi in Shirakawa-city, is simulated by the dynamic elasto-plastic finite element method. In order to simulate the softened soil, liquefaction strength curve was evaluated by cyclic triaxial tests.

2 Objective Landslide

The upper part of the slope had slid downward for more than 50 m as shown in Fig. 73.1. Such a long-distance traveling failure is one of the typical cases of landslides occurred in the hill area around the Shirakawa-City in Fukushima Prefecture at the time of the earthquake. A slope in the ridge greatly deformed and the debris covered the adjacent houses and road. The material has been strongly disturbed and it was mainly composed of softened clayey loams

T. Fukushima (✉) · K. Matsushita · H. Usami · A. Wakai
Gunma University, Maebashi City, Gunma, Japan

Fig. 73.1 Landslide at Okanouchi
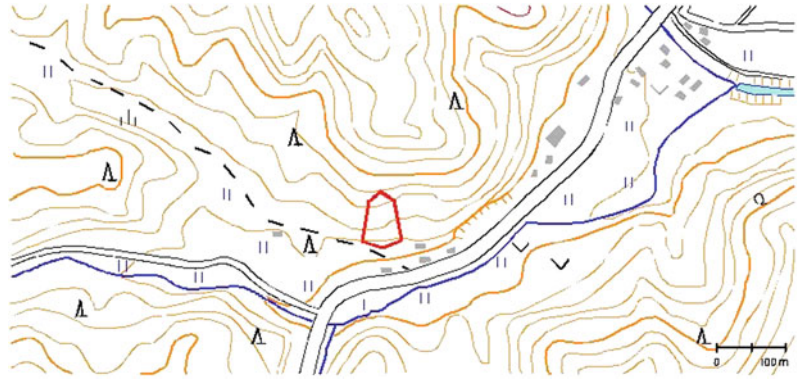
Fig. 73.2 Whole view of the landslide

containing a large number of light-coloured stiffer loamy lumps which have been crushed into around 0.3–1 m in diameter (Fig. 73.2).

A portion of the scratched planar slip surface was exposed at the centre of the collapsed area. The material appears to be a clayey loam including a lot of small stone pieces (Fig. 73.3) about 0.2–0.5 m in diameter, which may have been produced from tuffaceous rocks in the upstream area of this mountain. The inclination of the planar surface is approximately 16°, which is almost the same as the dip angle. The geological formations and the observed slip surface at the centre cross section in the slope are shown in Fig. 73.4. The maximum depth of the sliding

block is about 10 m below the slope surface. Because the suffered-slope topography is asymmetry in the right and left direction, the thickness of the sliding block in the west (right-hand side) part is larger than that shown in this figure.

The volcanic cohesive soil or loam as a dominant material in the slope contains a few types of loamy layers with different stiffness and particle sizes, including a thin pumice layer as well. In the exposed cliff, there also can be found three thin layers with a lot of small tuffaceous stone pieces, suggesting this slope has experienced several times of large-scale landslide events up to now. This is probably related to the tephra of about 0.1 million years ago was found

Fig. 73.3 Stone pieces in the slip surface

Fig. 73.4 Geological formations at the centre cross section in the slope

in the middle of the cliff, the sliding block may contains the sediments older than the tephra.

The observed planer slip surface passed between the following two layers; the lower loam layer reinforced with mixture of small tuffaceous stone pieces and the upper clayey loam layer that may be easily softened by seismic excitation. The stress concentration effect around the stiffness-changing depth might promote such a catastrophic landslide induced by the strength degradation of clayey loam due to cyclic softening.

Figure 73.5 is a close-up of a block soil sample used to investigate the mechanical properties of the material around the slip surface. This block sample was harvested at the foot of the exposed vertical cliff. The material is a brown-coloured clayey loam and rich with fine materials. The natural water content and the liquid limit of the material are 83.9 % and 97.8 %, respectively. Those values are closer to each other and it implies that the material can easily behave like a fluid after sudden strength degradation due to the seismic disturbance. The estimated sensitivity ratio from unconfined compression tests was about 3.0, which was not a particularly low value. The cohesion and the internal friction angle as the peak strength under the natural water content conditions were found to be 7.1 kN/m^2 and 49.3°, respectively.

3 Cyclic Loading Characteristics of the Problematic Clayey Loam

A series of the undrained cyclic triaxial tests of undisturbed specimens were performed as well. The soil specimens were kept to have natural water content, which means all the tests have been carried
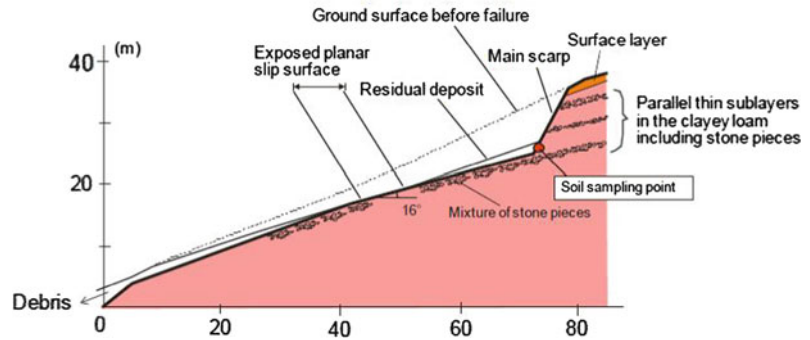
out under unsaturated conditions to represent the field conditions. The initial effective confining pressure in the tests was set as 100 kN/m², that corresponds to the stress level around the bottom of the sliding block. Figure 73.6 shows one of the examples of the observed results in the cyclic triaxial tests. It can be seen that the apparent shear resistance gradually decreased, like liquefaction of loose sands under cyclic loading, while the excess pore water pressure ratio has been kept to be much lower than 1.0. It suggests that the undrained shear strength of the unsaturated clayey loam in the slope can be decreased without the remarkable accumulation of the excess pore water pressure during the earthquake. This fact suggest that simple liquefaction models in effective stress formulations exclusively for saturated soils, may not be applicable in the numerical simulation for this event.

The apparent liquefaction strength curve for DA = 5 % measured by the cyclic triaxial tests, i.e., the relationships between the amplitude of shear stress ratio and the number of cycles to achieve the axial strain amplitude of 5 %, are shown in Fig. 73.7. Also, the strain dependency on the equivalent shear deformation modulus and the damping ratio were observed in the series of undrained cyclic triaxial tests, as shown in Fig. 73.8. In these figures, the simulated curve by the UW softening model in total stress formulations (Wakai et al. 2010) is compared to the observed results. In the model, the effect of the excess pore water pressure under cyclic loading is modelled as the decreasing functions of the undrained shear strength parameters with the accumulated shear strain. The material parameters used for the simulation are summarized as

the material named "Clayey loam with softening" in Table 73.1. The simulated curves agree with the results obtained by the laboratory tests.

4 Simulation of the Landslide

Based on the above numerical modelling, the finite element simulation for the investigated landslide has been performed. The assumed geological structure used in the analysis is shown in Fig. 73.9. The discretized finite element meshes (8-nodes) are also overdrawn in the same figure. The calculated acceleration and displacement histories at Point A in Fig. 73.9 are shown in detail later herein. As for the clayey loam layer with a possibility of cyclic softening, the UW softening model with the above parameters is adopted, while the lower layer with a lot of stone pieces is modelled as the original UW model without cyclic softening (Wakai and Ugai 2004). The parameters for other materials are shown in Table 73.1 as well.

The amplitude of the input waves at the base has been adjusted so that the corresponding horizontal component of the observed records at K-net Shirakawa by NIED should be realized at the ground level in the finite element meshes. The time history of the input horizontal acceleration is shown in Fig. 73.10. While, Fig. 73.11 shows the time histories of horizontal acceleration and displacement at the surface of the slope in the sliding block, namely, Point A in Fig. 73.9. The figure indicates that a catastrophic failure occurred in this case. The horizontal displacement became approximately 11 m at the end of the earthquake.
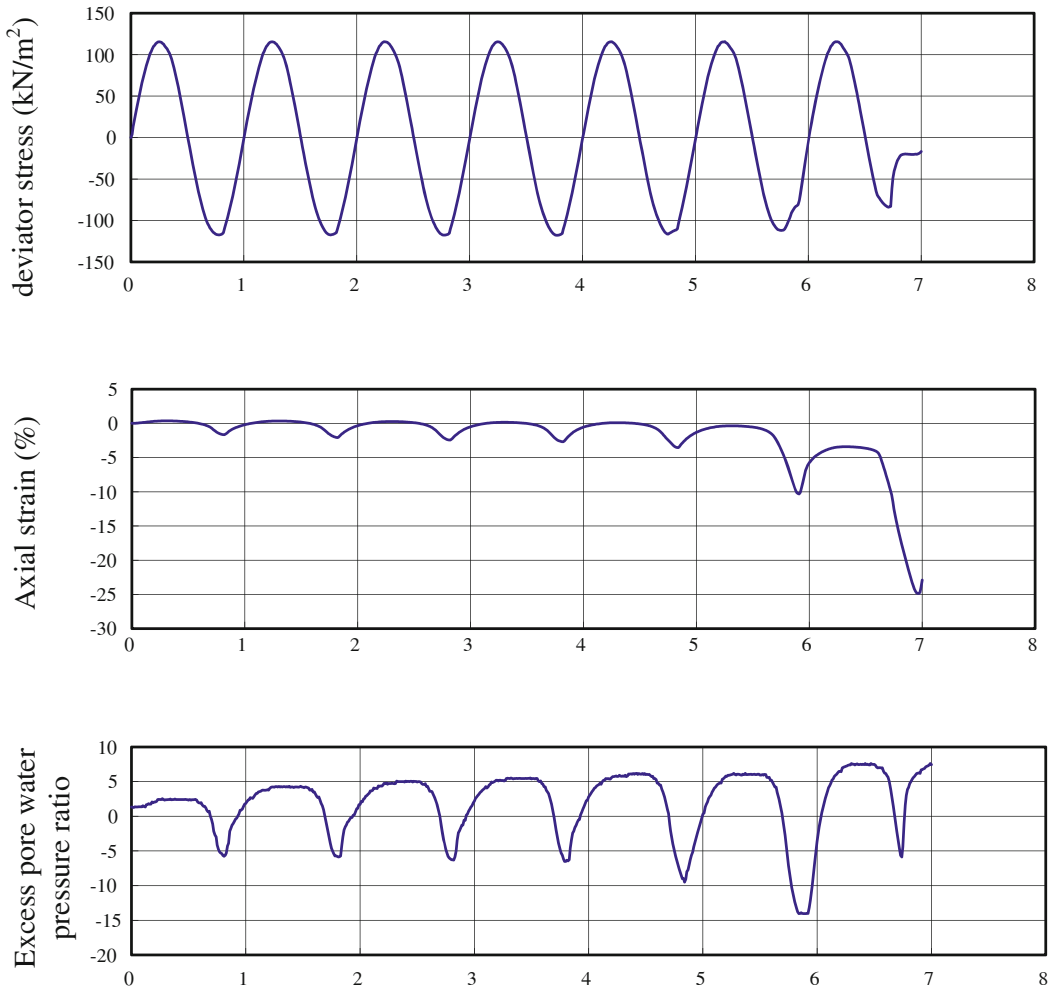
Fig. 73.6 An example of the observed result of the cyclic triaxial tests for the clayey loam with the natural water content
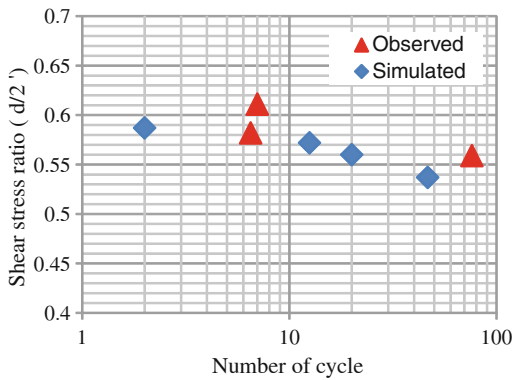
Fig. 73.7 Observed and simulated apparent liquefaction strength curve of the clayey loam
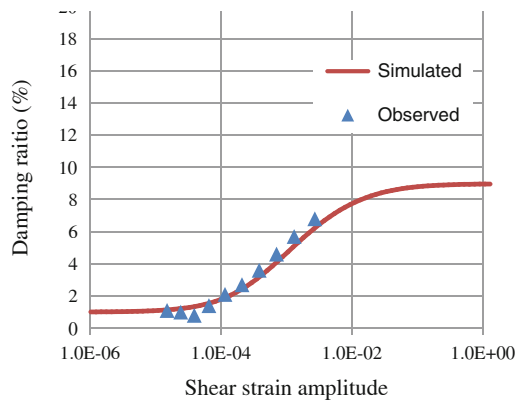
Fig. 73.8 Observed and simulated dynamic deformation characteristics of the clayey loam

Fig. 73.9 Finite element meshes
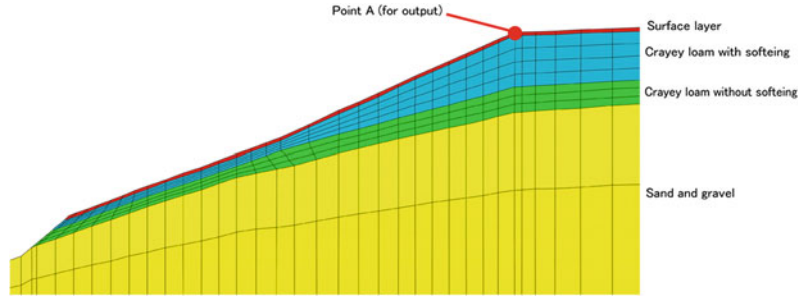
Table 73.1 Analytical parameters used for the simulation of the clayey loam behaviour by the UW softening model

Materials	Surface soil	Clayey loam		Sand and gravel
		With softening	Without softening	
Young's modulus E (kN/m^2)	100000	$13540 \times (p_0)^{0.5}$ p_0: Initial confining pressure		1000000
Poisson's ratio v	0.4	0.4		0.3
Cohesion c (kN/m^2)	50	49.3		100
Internal friction angle φ (°)	0	7.1	45	45
Dilatancy angle ψ (°)	0	0		0
$b \cdot \gamma_{G_0}$ (Parameter for damping)	6.28	2.5		-
n (Parameter for damping)	1.58	2.2		-
Unit weight γ (kN/m^3)	15	15.28		18
Residual strength ratio τ_{fr}/τ_{f0}	-	0.5	-	-
A (Parameter for softening)	-	10	-	-
Rayleigh Damping				
α				β
0.0571				0.000578

Fig. 73.10 The input seismic wave
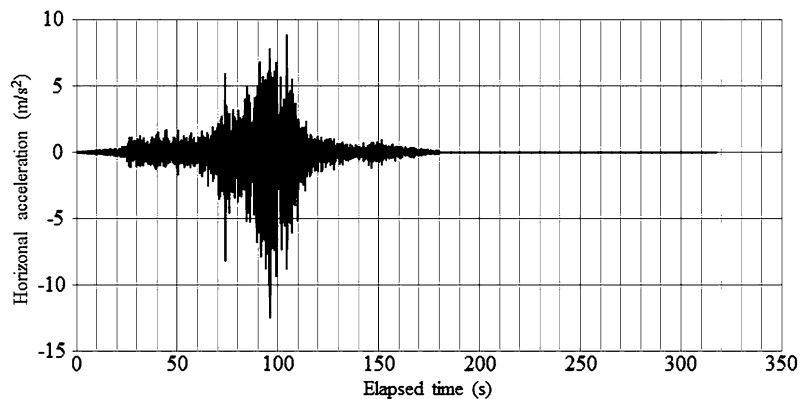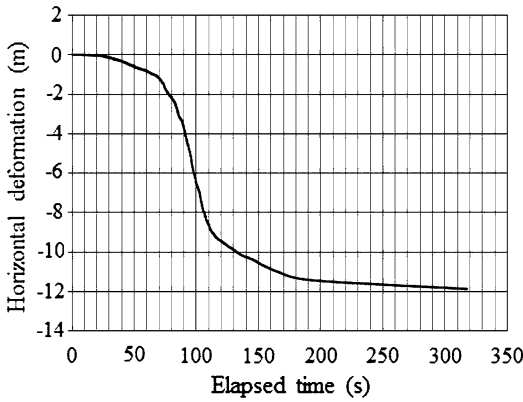
Fig. 73.11 Time history at the point A
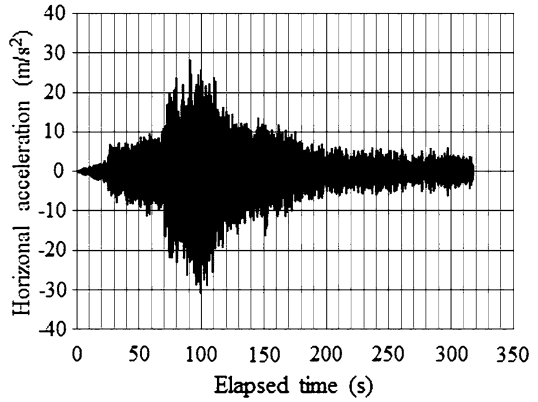
Fig. 73.12 Residual deformation s after the end of the earthquake
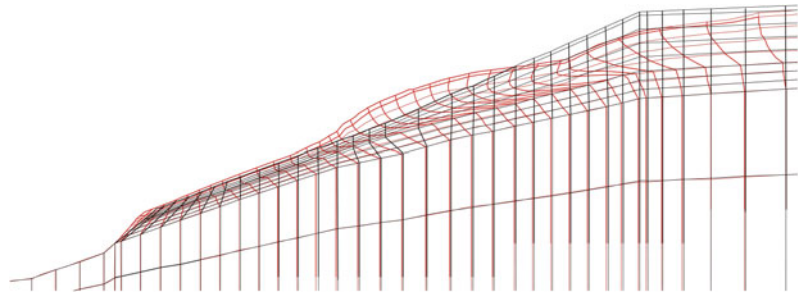
Fig. 73.13 Input seismic waves assuming past smaller earthquakes
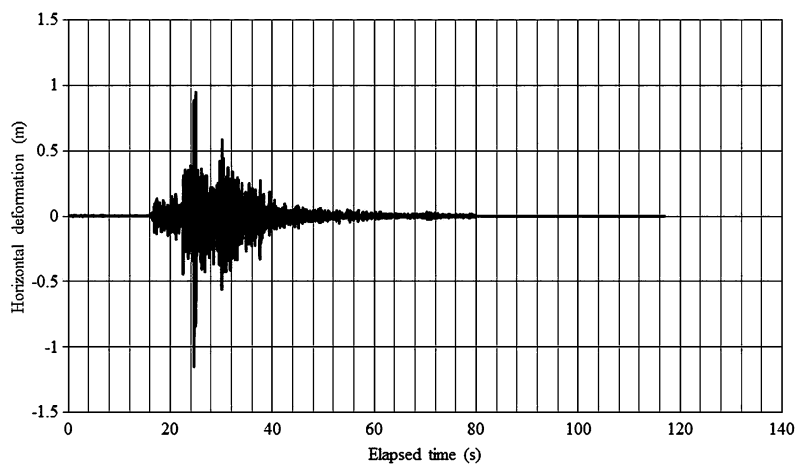
Note that this value continued to increase even after the earthquake motion ended. During continuing the movement, the acceleration response continues to be unstable.

The residual deformations and the shear strain distribution at 130 s after the end of the seismic motion are shown in Fig. 73.12a, b, respectively.

The long-distance movement of the sliding block along the upper end of the stiffer layer is clear as presented in the figures. This result is in agreement with the actual phenomenon.

By using a smaller earthquake motion, simulation which assumed the past earthquake motion that this slope received is performed. Figure 73.13
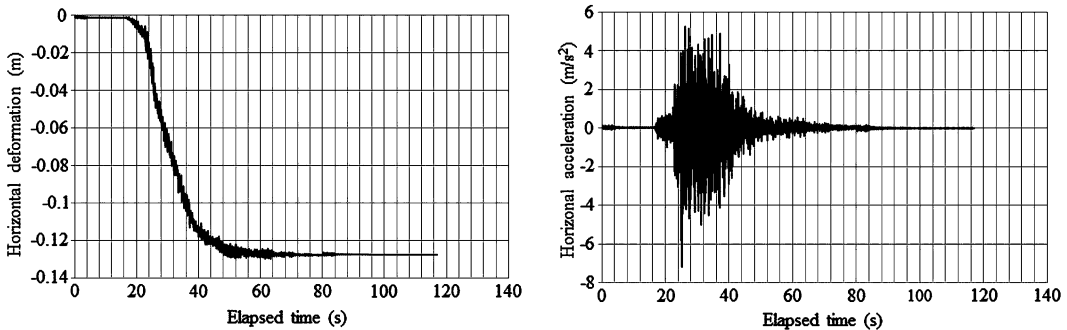
Fig. 73.14 Time history at the point A

shows the used seismic wave observed at Shirak-awa. No conditions other than seismic wave, such as a mesh and a material constant, are changed. Figure 73.14 shows the time histories. In this simulation, horizontal displacement did not increase after the end of the input motion

Note, however, that the predicted velocity of the sliding mass may not have sufficient accuracy. In order to simulate precisely the sliding behaviour after having started such high-speed motion, it would be better to improve the numerical model for the friction and damping at the bedding plane, which will be a subject for future investigation. Although an exact simulation of the high-speed movement cannot be obtained, this analysis provides information and guidelines for judging the occurrence of such a catastrophic failure.

5   Conclusions

In the present study, the observed phenomena in an earthquake-induced catastrophic landslide, occurred at the time of the 2011 disaster of the Great Tohoku and Kanto Earthquake in Japan, are appropriately simulated by the dynamic finite element method where the stress–strain relationships under cyclic loading for the clayey loam are numerically modelled as the proposed elasto-plastic constitutive model.

However, since the trial and errors have to be performed to simulate the liquefaction strength curve, it takes long time to determine the material constants. A quick method of determining material constants is required.

References

Tanaka S, Usami H, Matsushita K, Wakai A (2012) Extension of the liquefaction strength concept under cyclic loading to the modeling of volcanic clayey soils (in print)

Wakai A, Ugai K (2004) A simple constitutive for the seismic analysis of slopes and its applications, soils and foundations 44(4):83–97

Wakai A, Ugai K, Onoue A, Kuroda S, Higuchi K (2010) Numerical modeling of an earthquake-induced landslide considering the strain-softening characteristics at the bedding plane, soils and foundations 50(4):533–545

Case Studies on Seismically Induced Slope Failures in Terms of Energy

74

Takaji Kokusho and Tomohiro Ishizawa

Abstract

An energy approach proposed to make a simple evaluation of travel distance of debris has been applied to seismically induced slope failures during recent two earthquakes. Mobilized friction coefficients have been back-calculated, revealing their strong dependency on initial slope inclinations. The friction coefficients are found to become smaller than the initial slope inclinations in gentler slopes presumably due to seismic shock. The friction coefficients also tend to decrease with increasing volume of failed slopes, which is consistent with previous case studies on huge landslides. Most importantly, the average thickness of failed soil mass seems to serve as a good indicator for specifying the mobilized friction coefficient to predict the travel distance using the energy approach.

1 Outline of Energy Approach

In order to evaluate slope failures including long distance debris flow from their initiation to termination, an energy approach was first proposed by Kokusho and Kabasawa (2003) and further developed by Kokusho and Ishizawa (2007). In that method, four energies; gravitational potential energy change $-\delta E_p$, earthquake energy contributing to slope failure E_{EQ}, dissipated energy in the sliding debris E_{DP}, and its kinetic energy E_k are correlated in the following equation;

$$E_{EQ}/E_{IP} = 4\alpha/(1+\alpha)^2 \qquad (74.1)$$

Based on shake table model test results and their interpretation in terms of the rigid block theory using Eq. (74.1), an energy-based evaluation method for run-out distance of earthquake-induced slope failure was proposed by Kokusho et al. (2009a).

T. Kokusho (✉)
Department of Civil and Environment Engineering, Chuo University, Tokyo, Japan
e-mail: kokusho@civil.chuo-u.ac.jp

T. Ishizawa
National Research Institute for Earth Science and Disaster Prevention, Tsukuba, Japan
e-mail: ishizawa@bosai.go.jp

In the method, site-dependent seismic input energy E_{IP} given by a simple formula assuming the spherical energy radiation of the body waves from a hypocenter was used. Then, a sloping ground was idealized as an equivalent horizontal 2-layers system consisting of an upper layer, which includes the slope, and a base layer. By subtracting the energy E_d, that is reflected downward into the base layer due to the impedance contrast at the layer boundary, from the input energy E_{IP}, the earthquake energy E_{EQ}, which is transmitted into the upper layer, can be computed (i.e., $E_{EQ} = E_{IP} - E_d$). Assuming that all the energy E_{EQ} transmitting into the upper layer is absorbed by the slope failure as observed in the shake table model tests, the energy ratio E_{EQ}/E_{IP} can be formulated as (Kokusho et al. 2007):

$$E_{EQ}/E_{IP} = 4\alpha/(1+\alpha)^2 \tag{74.2}$$

where $\alpha = (\rho Vs)_{upper}/(\rho Vs)_{base}$ is the impedance ratio of the upper layer to the base layer. A small portion out of the energy transmitted into the upper layer (E_{EQ}) may be dissipated by cyclic straining of soil or internal soil damping. If this portion is denoted as E'_{EQ}, the energy causing the slope failure is ($E_{EQ} - E'_{EQ}$). In the following, E'_{EQ} is assumed to be negligibly small compared to E_{EQ}, because soil conditions are normally not so soft or liquefiable in sloping ground.

For slopes that are not straight as illustrated in Fig. 74.1, $\beta = \tan\theta$ is taken as a global inclination of a straight line PQ (directly connecting the centroids of a soil mass before and after failure) which is different from the initial inclination β_0, and $\mu = \tan\phi$ as the average mobilized friction coefficient over the travel distance. The sliding mass M in Fig. 74.1 may be determined by conventional slip surface analyses, where a potential slip surface with the lowest factor of safety is found. However, in quite a few natural slopes, the potential slip surface may be reasonably assumed to coincide with a bedding plane or a weak seam observed in site investigations. The drop height PO ($-\delta E_p/Mg$) divided by the horizontal
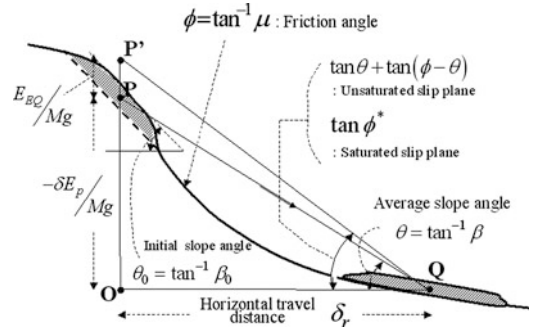
Fig. 74.1 Graphical evaluation method for run-out distance of seismically induced slope failure (Kokusho et al. 2009a)

displacement OQ (δ_r) corresponds to the global inclination $\beta = \tan\theta$ of the slope

$$\frac{-\delta E_p/Mg}{\delta_r} = \tan\theta \tag{74.3}$$

Corresponding to the earthquake energy, the centroid of the sliding soil mass M can be considered to rise from P to P' by E_{EQ}/Mg (the dimension is length). The inclination of the line P'Q, or the ratio of the height P'O expressed as $\left(-\delta E_p/Mg + E_{EQ}/Mg\right)$ to the horizontal displacement (δ_r), OQ, can be expressed as

$$\frac{-\delta E_p/Mg + E_{EQ}/Mg}{\delta_r} = \tan\theta + \tan(\phi - \theta) \tag{74.4}$$

For cases of saturated slip plane, the same inclination can be expressed as:

$$\frac{-\delta E_p/Mg + E_{EQ}/Mg}{\delta_r} = \tan\phi^* \\ = (\sigma'_{n0}/\sigma_{n0})\tan\phi \tag{74.5}$$

where σ_{n0} and σ'_{n0} stand for total stress and effective stress normal to the slip plane, respectively (Kokusho et al. 2011).

Consequently, the procedure for run-out distance evaluation is:
1. Determine the dimension of a potential sliding soil mass and its centroid P.
2. Determine the mobilized friction coefficient μ.

3. Evaluate the earthquake energy E_{EQ} from E_{IP} at a base layer using Eq. (74.2).
4. Locate Point P′, which is higher than P by the length E_{EQ}/Mg as shown in Fig. 74.1.
5. Starting at Point P′, draw a line with an inclination of $\tan \theta + \tan(\phi - \theta)$ or $\tan \phi^*$ for an unsaturated or saturated condition, respectively, until it intercepts the slope surface (Point Q). Then from the geometry of the slope, δ_r can readily be obtained based on Eq. (74.4) or Eq. (74.5).

This very simple procedure may be conveniently used to evaluate the run-out distance for seismically induced slope failures in developing hazard maps if the mobilized friction coefficient $\mu = \tan \phi$ of a particular slope is known.

2 Case Studies on Slope Failures During Two Earthquakes

In the proposed energy approach, it is essential that the mobilized friction coefficient μ be properly determined in advance. It may be possible in some cases to evaluate it directly from soil samples recovered from specific sites. However, due to complexity of actual slope failures in the field, a more robust method may be to collect as many case histories as possible and back-calculate the friction coefficients.

During the 2004 Niigata-ken Chuetsu earthquake ($M_J = 6.8$, thrust fault, focal depth 13 km), more than 4,000 slope failures occurred 200 km north of Tokyo in the main island of Japan. Slopes were composed of weak sedimented rock of Neogene age, consisting of inter-bedded layers of strongly weathered sandstones and mudstones, and bedding planes had a strong effect on the slope failures. The failures due to this earthquake may be classified into 3 types:

Type-A: Deep slips parallel to bedding planes (dip slips), in gentle slopes of around 20° or lower. The displaced soil volumes were very large and the soil blocks sometimes showed little surface disturbance

Type-B:

Shallow slips of 1–2 m deep not parallel to bedding planes in slopes of around 30° or steeper. These failures far outnumbered the Type-A failures, but the individual soil volumes were not very large. Moving masses were highly disrupted internally

Type-C: Slope failures in highly weathered colluvial soils in places where Koi-ponds and terraced paddy fields were located. Though this type may be a variant of Type-A, underlain by dip mudstone, the displaced soil mass was highly weathered because of repetitive slope failures in the past and hence developed into a mud flow

During the 2008 Iwate-Miyagi Inland earthquake ($M_J = 7.2$, thrust fault, focal depth 8 km) about 1800 slope failures occurred 400 km north of Tokyo in the main island of Japan. The geology was mostly of volcanic rocks of Miocene and Pleiocene age, consisting predominantly of welded/non-welded tuff, sandstone, and siltstone. The failures were classified into three types as follows, although the classification may not be so clear as the 2004 earthquake, presumably because the rocks are of volcanic origin without clear bedding plane.

Type-a: Large scale slides moving almost as a rigid body along a deep slip plane.

Type-b: Medium size slides with characteristics in between Type-a and Type-c.

Type-c: Small size shallow slides with disintegrated debris.

Among the slope failures during the earthquake, the largest one occurred at Aratozawa, where a mass 1.2 km long by 0.8 km wide slid almost horizontally more than 350 m along a deep-seated slip plane toward a man-made reservoir. It is classified as Type-a, with total volume about 35 million m^3 and the gradient of the slip plane around 5°.

Cross-sectional changes in failed slopes were developed from the DEM data before and after the earthquake. The slip surface in a failed slope, difficult to detect from DEM, was determined reliably from the exposed scarp or slip plane in
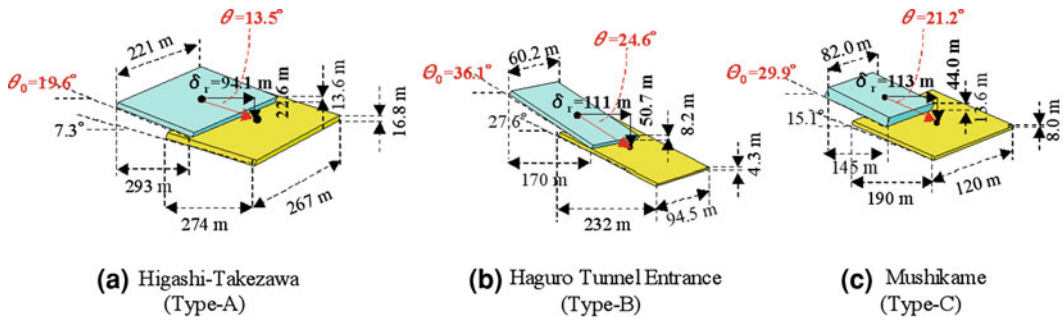
Fig. 74.2 Simplified rigid block models for 3 representative slope failures of Type-A (**a**), Type-B (**b**) and Type-C (**c**) during the 2004 earthquake (Kokusho et al. 2009a)
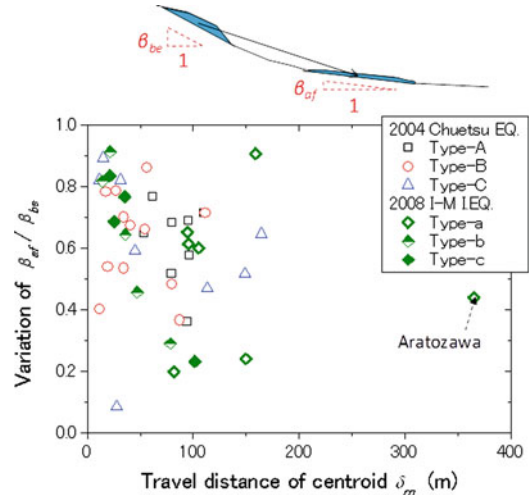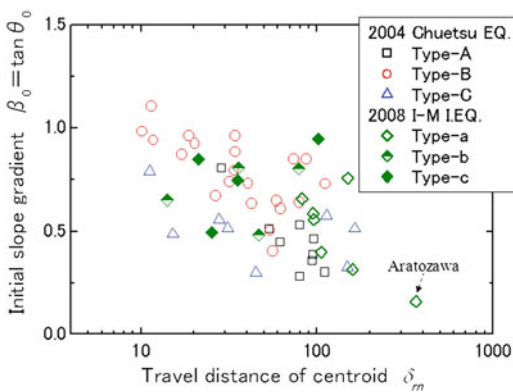
Fig. 74.3 Initial slope gradient of failed soil mass β_0 plotted versus runout distance δ_{rn} for three types of failures during the 2004 and 2008 earthquakes

Fig. 74.4 Volume of failed soil mass V_f plotted versus Initial slope gradient β_0 for various failure types

the upslope side, the original location of the valley in the downslope side, and the global change of slope configuration. Then, failed soil mass was idealized by a rectangular block as exemplified in Fig. 74.2, for Type-A to C in case of the 2004 earthquake. In the soil block, horizontal dimensions, thicknesses and slope inclinations before and after the failure, horizontal displacements of the centroid δ_{rn} and the global inclination β of the line connecting the centroid of the block before and after the failure were specified.

In Fig. 74.3, the initial slope gradient $\beta_0 = \tan \theta_0$ is correlated with the runout distance at the centroid δ_{rn} on the semi-logarithmic chart. Here the value β_0 was approximately evaluated as a gradient of the line connecting the highest and lowest surface elevations of the failed mass in its initial condition. The data points for the 2004

earthquake, despite the significant dispersions, indicate an unexpected trend that the runout distance clearly increases with decreasing β_0 not only for Types-A, B and C individually, but also globally. The plots for the 2008 earthquake including Aratozawa seem to indicate the same unexpected trend, though they are more randomly dispersed. One may wonder if the unexpected results reflect some topographical features in the damaged areas. In Fig. 74.4, β_{af}/β_{be}-values are plotted versus the travel distance δ_{rn}, where $\beta_{be}(=\beta_0)$ and β_{af} are the slope gradient before and after the failure. If δ_{rn} tends to increase with increasing β_{af}/β_{be}-value, it indicates that the travel distance depends strongly on
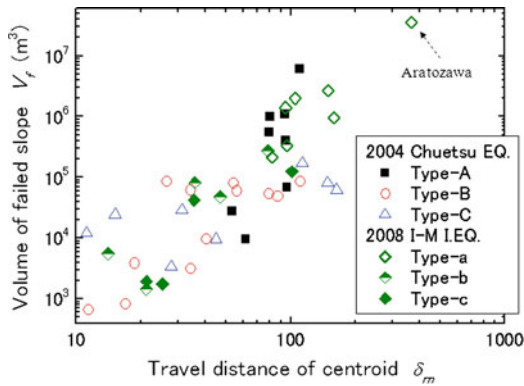
Fig. 74.5 Volume of failed soil mass V_f plotted versus runout distance δ_{rn} for various failure types during the 2004 and 2008 earthquakes

Fig. 74.6 Friction coefficients μ versus runout distance of centroid δ_{rn} for three types of failures during the 2004 and 2008 earthquakes

the slope profile in the down-slope direction. However no such trend can be recognized for the two earthquakes in Fig. 74.4 despite data scatters. This seems to indicate that the increasing trend of travel distance with decreasing slope gradient can be considered to be quite intrinsic, not so much affected by local topography.

In Fig. 74.5, the runout distance δ_{rn} is correlated with the failed debris volume V_f on the log–log diagram. Obviously the distance δ_{rn} increases with V_f as a whole despite large data scatters, and the trend is consistent between the two earthquakes. The Aratozawa plot, though apart from the others, does not seem to be located quite differently in the global trend.

3 Back-Calculation of Friction Coefficients

The energy-based simple evaluation method has then been applied to a number of slopes that failed during the 2004 Niigataken Chuetsu earthquake and the 2008 Iwate-Miyagi Inland earthquake to back-calculate the friction coefficients and to discuss how the values are to be determined in accordance to pertinent parameters. Though ground water conditions in a number of failed slopes studied were not known clearly, the slip plane was assumed to be saturated for all slopes and Eq. (74.5) was used with

the assumption of $\sigma'_{n0} \approx \sigma_{n0}$ to back-calculate the mobilized friction coefficient $\mu = \tan\phi = \tan\phi^*$ from the solid block models such as in Fig. 74.2 (Kokusho et al. 2011).

The input energies, E_{IP}, during the two earthquakes at the base layers of the slopes were evaluated from vertical array records of KiK-net (Strong motion observation network operated by NIED, Japan) around the two areas (Kokusho 2009). Then, the maximum earthquake energy E_{EQ}/A to be used for each slope failure was calculated from Eq. (74.2) as $E_{EQ}/E_{IP} = 0.71$ assuming the impedance ratio between sloping surface layers and base layers as $\alpha = 0.3$ (Kokusho and Ishizawa 2009a). The internally dissipated energy E'_{EQ} by liquefaction or soil damping was assumed to be negligibly small compared to other energies and the total density of the soil, ρ_t, was approximated as 1.8 t/m^3 (Kokusho et al. 2009b).

Figure 74.6 shows the plots of the back-calculated friction coefficients μ versus the runout distance of the centroid δ_{rn} for a number of slopes failed during the earthquakes. The μ-value tends to increase drastically on the semi-log chart with decreasing runout distance for all the failure types of the two earthquakes, although the trend for smaller runout distance looks different in each earthquake and each failure type. Though the Aratozawa plot is located far to the right of the others with the largest runout distance and the
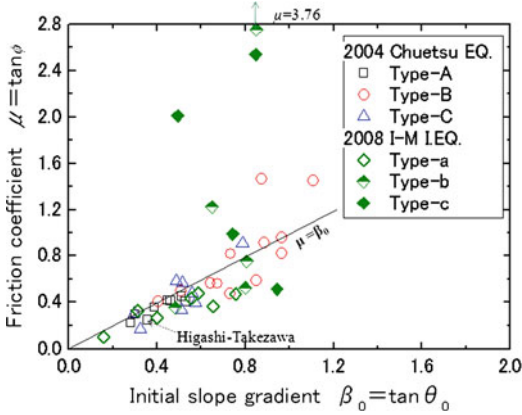
Fig. 74.7 Friction coefficients μ versus initial slope gradient β_0 for 3 types of failures during the 2004 and 2008 earthquakes

Fig. 74.8 Energy ratio $-\delta E_p / E_{EQ}$ versus failed soil volume V_f for 3 types of failures during the 2004 and 2008 earthquakes

lowest friction coefficient, it appears to be consistent with the global trend.

In Fig. 74.7 the back-calculated friction coefficients, μ, are plotted versus initial slope gradients, $\beta_0 = \tan \theta_0$. Note that, for smaller values of β_0 corresponding to Type-A, C of the 2004 earthquake and Type-a of the 2008 earthquake, all of the back-calculated μ-values are below or almost upon the diagonal line of $\mu = \beta_0$, indicating that the back-calculated friction coefficients μ, originally larger than β_0, decreased due to the effect of earthquake shaking and subsequent sliding. The μ-value is smaller than β_0. This implies that the failed debris accelerates first and then decelerates due to gentler or reverse slope angles in down-slope sections. In contrast, the data points with higher values of β_0 (typically belonging to Type-B and Type-c) are plotted on both sides of the diagonal line $\mu = \beta_0$. They tend to be above the line with increasing μ despite large data scatters.

It should also be noted in Fig. 74.7 that the mobilized friction coefficients back-calculated from the case studies are highly dependent on the initial slope gradients. It is quite different from artificial slopes in which strength parameters are normally considered to be independent of a slope gradient. This may indicate that the friction coefficients of natural slopes strongly reflect their long-time exposures to previous natural loads; namely, steeper slopes survived previous seismic

and rainfall events because of their higher mobilized friction coefficients.

In Fig. 74.8, the energy ratios $-\delta E_p / E_{EQ}$ evaluated in the back-calculation are plotted versus the volumes of failed slopes V_f. It is remarkable that, for all the slope failures with their volumes larger than around 10^5 m^3 during the two earthquakes, the value $-\delta E_p / E_{EQ}$ is 10 or larger. For some plots including Aratozawa with the volume exceeding 10^6 m^3, the value is almost around 100. This indicates that the larger the failed volume, the smaller the contribution of the earthquake energy compared to the potential energy. This finding also indicates that accuracy in determining the energy E_{EQ} may not be so critical for the large volume failures. However, the contribution of earthquake energy seems still important not directly by supplying the driving energy but more indirectly by reducing friction coefficient μ to initiate the slide through cyclic loading, although internal dynamics of the sliding/flowing mass may determine μ once failure initiates.

As already explained in Fig. 74.2, the failed slope debris is idealized as a rectangle of average thickness D_{av} (average depth of slip plane) in this study. In Fig. 74.9, the back-calculated friction coefficients are correlated with the average thicknesses (average depths of slip planes D_{av}). Though there exists some difference between the two earthquakes, it clearly shows a very similar D_{av} –
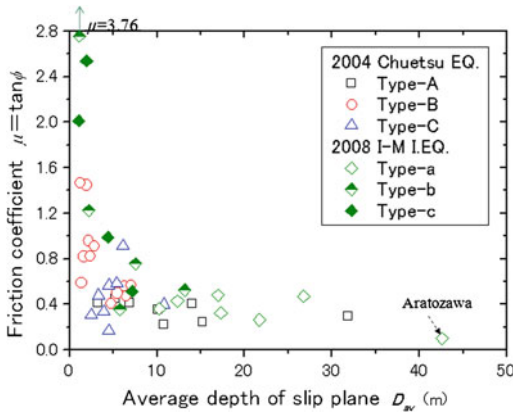
Fig. 74.9 Friction coefficients μ versus depths of slip plane D_{av} for 3 types of failures during the 2004 and 2008 earthquakes
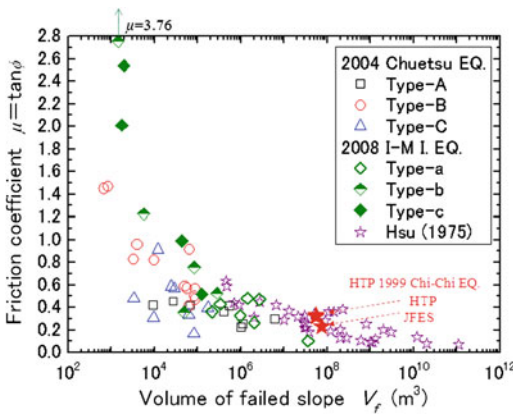
Fig. 74.10 Friction coefficients μ versus failed soil volume V_f obtained in this research, compared with analogous relationship for huge landslides published by Hsu

dependent change of the friction coefficient; μ-value tends to be 0.2–0.6 for the depth larger than $D_{av} = 5$–10 m while it tends to increase drastically with decreasing D_{av}. In many cases, the depths of slope failures seem to be easier to predict than other variables, and D_{av} may serve as a convenient parameter for slope failure evaluations.

The back-calculated μ-values for the two earthquakes are plotted again versus the volumes of failed slopes on the semi-logarithmic diagram in Fig. 74.10. Despite large scatters in the data, a decreasing trend of μ can be clearly observed as the volume V_f increases from 10^3 to 10^7 m^3 irrespective of the failure types. The V_f-dependent

trend of μ-value is particularly obvious for small-volume failures, Type-B for the 2004 earthquake and Type-c for the 2008 earthquake.

A similar relationship based on case histories of huge landslides not necessarily associated with earthquakes (Hsü 1975) is superposed on Fig. 74.10 with star symbols. Unlike the present research, the friction coefficient μ in the previous research was defined in a slightly different manner as the gradient of a line connecting the top of the scarp and the tip of the displaced mass, though it normally gives a similar gradient to that connecting the centroids (the global inclination β). Figure 74.10 shows a remarkable consistency in the upper bound of the data points of the two studies in the wide range of the failed soil volume, 10^3–10^{11} m^3, particularly for the small volume failures of Type-B and Type-c. For the failures of Type-A, C and Type-a, most of the data points are much lower than the upper bound, presumably due to the effect of dip slip planes in Type-A and high water content in Type-C for the 2004 earthquake. In addition, two other μ-values back-calculated from huge landslides during 1999 Chi–Chi earthquake, JFES and HTP (Dong et al. 2007, Ishizawa et al. 2008) are shown on the chart, which seem to be compatible with Hsü's data and also with the global trend including the present research.

Thus, the back-calculated friction coefficients are found to have clear dependency on slope gradient, failed soil volume, its average thickness, dip plane, water content, etc. Among these factors, the average thickness of sliding soil mass seems to serve as a relevant parameter for determining mobilized friction coefficients in predicting travel distance in seismically induced slope failures.

4   Conclusions

From case studies of a number of slope failures during recent two earthquakes, the following has been revealed:

1. Runout distance δ_{rn} tends to increase with decreasing initial slope gradient β_0 despite

data scatters. Though slightly different depending on the earthquakes and the failure types, this unexpected trend is essentially the same for the two earthquakes. The distance δ_{rn} also tends to increase with increasing volume of the displaced debris volume V_f.

2. Friction coefficients μ back-calculated using the energy principle are highly dependent on the initial slope gradient β_0 and mostly tend to increase with increasing β_0.

3. On the $\mu \sim \beta_0$ plane, the back-calculated μ-values are plotted below the line $\mu = \beta_0$ for relatively low values of β_0. This indicates that the back-calculated μ, originally larger than β_0, decreases after earthquake shaking. In contrast, for higher values of β_0, the μ-value tends to be higher than β_0.

4. For slope failures of large volumes, the energy ratio $-\delta E_p / E_{EQ}$ is very large. This indicates only a small contribution from the earthquake energy E_{EQ} compared to the potential energy- δE_p. However, the earthquake energy still plays an important role as a trigger of failure by reducing soil strength rather than by directly driving the soil mass.

5. A clear decreasing trend for μ can be recognized as the failed soil volume increases from 10^3 to 10^7 m^3 irrespective of the failure types. The decreasing trend in this research is consistent with previous research results on huge landslides in the world.

6. Among variables associated with slope failures, slip plane depth (average thickness of sliding mass) seems to be promising to conveniently evaluate the mobilized friction coefficient in predicting travel distance of failed slope debris.

References

Dong J–J, Lee W-R, Lin M-L, Huang A-B, Lee Y-L (2007) Effects of seismic anisotropy and geological characteristics on the kinematics of the neighboring Jiufenger-shan and Hungtsaiping landslides during Chi–Chi earthquake, Tectonophysics 466:438–457, Elsevier

Hsü J (1975) Catastrophic debris streams generated by rockfalls. Geol Soc Am Bull 86(Doc. no. 50117):129–140

Ishizawa T, Kokusho T, Nshida K (2008) Evaluation of seismically induced slope displacement in terms of energy and a case study during Chi–Chi earthquake. In: Proceedings of 3rd Taiwan-Japan joint workshop on geotechnical hazards from large earthquakes and heavy rainfall, Keelung, Taiwan, pp 273–280

Kokusho T, Kabasawa K (2003) Energy approach to flow failure and its application to flow due to water film in liquefied deposits, In: Proceedings of international conference on fast slope movements, prediction and prevention for risk mitigation, Naples, pp 297–302

Kokusho T, Ishizawa T (2007) Energy approach to earthquake-induced slope failures and its implications. J Geotech Geoenviron Eng ASCE 133(7):828–840

Kokusho T, Motoyama R, Motoyama H (2007) Wave energy in surface layers for energy-based damage evaluation. Soil Dyn Earthq Eng 27:354–366, Elsevier

Kokusho T (2009) PBD in earthquake geotechnical engineering and energy-based design. Special discussion session—future directions of performance-based design. Performance-based design in earthquake geotechnical engineering—from case history to practice. In: Proceedings of international conference on performance based design in earthquake Geotechnical Engineering (IS-Tokyo 2009), Balkema, CRC Press, Rotterdam, pp 359–362

Kokusho T, Ishizawa T, Nishida K (2009a) Travel distance of failed slopes during 2004 Chuetsu earthquake and its evaluation in terms of energy. Soil Dyn Earthq Eng 29:1159–1169, Elsevier

Kokusho T, Ishizawa T, Hara T (2009b) Slope failures during the 2004 Niigataken Chetsu earthquake in Japan, Earthquake Geotechnical case histories for performance-based design. Balkema, CRC Press, Rotterdam, pp 47–70

Kokusho T, Ishizawa T, Koizumi K (2011) Energy approach to seismically induced slope failure and its application to case histories. Eng Geol 122(1–2):115–128, Elsevier

Part VI

Hazard Mapping and Risk Management

The Tree-Ring Reconstruction of Slope Instabilities Associated with Earthquakes (The Crimean Mts., Ukraine)

75

Karel Šilhán, Tomáš Pánek and Jan Hradecký

Abstract

The Crimean Mountains in Ukraine constitute a seismically active region that is abundant in various types of mass movement. The limestone escarpments that rise above the Black Sea coast in the vicinity of the town of Yalta are particularly subject to considerable rockfall, landslide and debris flow processes that often endanger infrastructure and human life. The aims of this study were (i) to employ tree-ring analysis to reconstruct a record of slope instabilities (mainly block-type movement, rockfall, landslide and debris flows) within the Taraktash slope deformation over a period of more than two centuries and (ii) to establish the degree of correlation between periods of enhanced slope activity and both historical earthquakes. The temporal frequency of significant slope processes was addressed through a tree-ring analysis that took 738 increment cores from 255 Crimean pine trees *(Pinus nigra* ssp. *pallasiana)*. The tree-ring record reveals periods of increased activity of block-type movements, rockfall and sliding during major earthquakes in 1790, 1875, 1927 and 1986.

1 Introduction

Mass movement processes play a crucial role in determining the morphology of mountain belts (Korup et al. 2010). They are very effective geomorphic agents in seismically active areas (Keefer and Moseley 2004). When unfavourable predisposing factors (e.g. weak rocks and tectonic deformations) are also present, some slopes in these environments support recurrent instabilities for which the frequency of

K. Šilhán (✉) · T. Pánek · J. Hradecký
Faculty of Science, Department of Physical Geography and Geoecology, University of Ostrava, Chittussiho 10, 71000 Ostrava, Czech Republic
e-mail: karel.silhan@osu.cz

Zone	Sampled trees	Increment cores	Minimum age (years)	Maximum age (years)	Mean age (years)
A	39	78	91 (AD 1918)	412 (AD 1597)	204.6 (stdev: 68.1)
B	114	456	18 (AD 1991)	380 (AD 1629)	154.7 (stdev: 92.4)
C	48	96	178 (AD 1831)	367 (AD 1642)	283.7 (stdev: 41.6)
D	54	108	46 (AD 1963)	299 (AD 1710)	166.9 (stdev: 92.8)

activation roughly coincides with the recurrence intervals of strong earthquakes (Chigira et al. 2003). Of the available dating techniques (Lang et al. 1999), dendrogeomorphic methods based on tree-ring analysis are especially capable of providing high-resolution data at decennial and centennial time-scales. Moreover, dendrogeomorphology has also been successfully pioneered in palaeoseismic research (Jacoby et al. 1997). Table 75.1.

The Crimean Mountains are among the regions with the most active slope processes in Europe (Pasynkov et al. 1992). Slopes affected by hazardous processes such as landslides, debris flows and rockfalls are concentrated in the immediate vicinity of the town of Yalta.

The objectives of this study are twofold: (i) to reconstruct the temporal activity of various types of mass movements using tree-ring analysis in the Crimean Mountains (Taraktash slope deformation) in the last 230 years and (ii) to identify any relationship between slope instabilities and historical earthquakes.

2   Study Area

The Crimean Mountains are a part of the Alpine Caucasus–Crimean thrust and fold belt, which evolved during the Mesozoic–Cenozoic in response to deformation of the tectonic boundary between the Black Sea domain and the East-European platform (Muratov et al. 1984; Pánek et al. 2009b) (Fig. 75.1a). The epicentres of historical earthquakes in the Crimean Mountains are distributed mainly offshore and along the narrow southern coastal strip in the vicinity of Yalta

(Fig. 75.1b). To date, the most destructive historical seismic events were two successive earthquakes in the year 1927. The first ($M = \sim 6.0$) occurred on the 26th of June and brought about more than 20 slope failures, while the second ($M = \sim 6.8$) took place on the 11th of September and produced 63 major slope instabilities. In both cases, the epicentres were situated ~ 30 km offshore, on the bottom of the Black Sea (Nikonov and Sergeyev 1996).

The Taraktash slope deformation (centred on 44°29.120′N, 39°5′E) is a rockslide of unknown age reaching ~ 1400 m at runout and affecting almost horizontally-inclined, thin-bedded Jurassic limestones. The depletion zone of the rockslide (zone A) (Fig. 75.1b) is dominated by block-type movement (lateral spreading, toppling, and incipient sliding). Rockfall is the major geomorphic process in the central sector of the slope (zone B). Ancient rockslide accumulation (zone C) form part of a secondary sliding system of minor headscarps and tension cracks. At the same time, the rockslide accumulation makes up the local base level of an adjacent high-gradient valley, which is periodically affected by debris flows forming a fan (zone D) (Fig. 75.1c). The whole Taraktash slope, except for the most active parts of the talus cones, is covered with forest, more than 300 years old, consisting almost exclusively of Crimean pine (*Pinus nigra* ssp. *pallasiana*).

Annual precipitation totals in the uppermost part of the slope reach 1050 mm and the mean temperature is 7.5 °C (Ai Petri meteorological station; 4 km SE from the Taraktash slope deformation), whereas the lowermost part of the slope deformation receives 580 mm of total
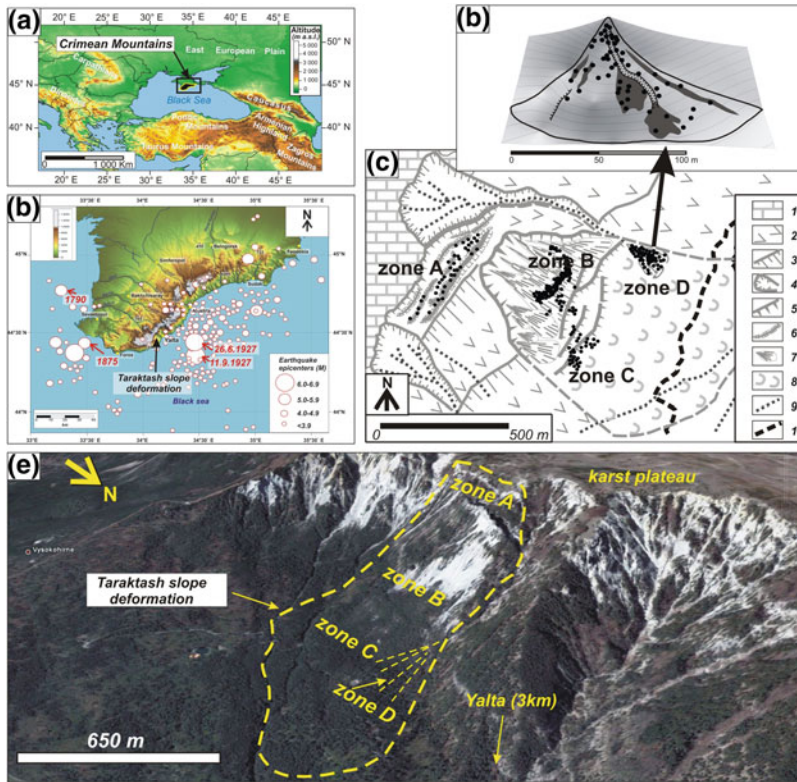
Fig. 75.1 The study area. **a** Localization of the Crimean Mountains, **b** Localization of the Taraktash slope deformation in the vicinity of the town of Yalta including the epicentres of historical earthquakes, **c** Geomorphic map and structural settings of the Taraktash slope deformation with positions of sampled trees (black dots) (*1* karst plateau, *2* steep soil-mantled slope, *3* rock slope, *4* debris flow basin, *5* landslide headscarp, *6* rock towers and pinnacle (*block*), *7* debris flow cone, *8* rockslide accumulation, *9* stream, *10* road), **e** Oblique Google Earth satellite image showing the morphological context of the slope studied and the domains of individual hillslope processes, **d** Detail of a debris flow cone. Reprinted from Geomorphology, in press, Šilhán, K. et al., Tree-ring analysis in the reconstruction of slope instabilities associated with earthquakes and precipitation (the Crimean Mountains, Ukraine), Copyright (2012), with permission from Elsevier

annual precipitation and its mean temperature is 13 °C (Yalta meteorological station).

3   Materials and Methods

All trees (*P. nigra*) with obvious signs of growth disturbances caused by the geomorphic processes under study were mapped (Fig. 75.1c) and sampled for dendrogeomorphic analyses. Tree-ring analysis of a total of 738 increment cores from 255 of *P. nigra* was carried out. In comparison with other coniferous trees, *P. nigra* is characterized by somewhat limited possibilities for dendrogeomorphic analysis, largely

because of its strong heliotropism (an inclination towards the direction of insolation; Berthier and Stokes 2005), its sensitive reactions to climatic changes, although the ducts were not employed as indicators of past geomorphic processes in this study. Further validation of tree-ring analysis is revered to (Šilhán et al. 2012). In spite of these complications, *P. nigra* is very often used in dendrogeomorphic studies, but a very careful application of reference chronology is vital (Pelfini and Santilli 2008; Ruiz-Villanueva et al. 2010). In the course of data processing, abrupt growth suppressions within the tree-rings of reference trees that were not connected with any known geomorphic processes emerged. Since

various types of mass movement were being addressed by the research, the temporal reconstruction of each of them required a different dendrogeomorphic approach.

3.1 Dating of Landslides and Block-Type Movements (Zone A and C)

The sampling for tree-ring analysis related to block-type movement (zone A; 39 trees) and sliding (zone C; 48 trees) comprised two increment cores per tree taken with a Pressler increment borer at the level of maximum stem bending (roughly 1–2 m from the ground). A major reaction of trees affected in such a way is the formation of reaction (compression) wood on the down-facing side of the stem (coniferous trees). Dated growth disturbances in particular years were added up and the block and landslide activity was expressed by the "response index" (I_t; Shroder 1978):

$$I_t = \frac{\left(\sum R_t\right)}{\left(\sum A_t\right)} \cdot 100 \ \% \qquad (1)$$

where R_t is the number of trees containing a growth disturbance as a response to landslide/block activity in the year t and A_t is a number of living trees sampled in the year t.

3.2 Dating of Rockfall (Zone B)

Four increment cores per tree (one upslope, one downslope and two from both sides of the trunk, perpendicular to the slope direction) were taken in the dendrogeomorphic analysis of rockfall (zone B; 114 trees) at the height of maximum density of stem damage (about 0.8 m).

The impact of rocks was identified in increment curves or on sample surfaces in the form of abrupt growth suppression/release, reaction wood formation and/or callus tissue formation (Stoffel et al. 2005). Rockfall activity was expressed in terms of "rockfall rate index" (RR) (Stoffel et al. 2005), which is expressed as:

$$RR = \sum \frac{RE_y}{ED_y} \qquad (2)$$

where RE_y is the number of rockfall events dated on all trees in year y and ED_y (exposed diameter) is the sum of the diameters of all trees in year y. The ED of one tree in year y is defined as the yearly increment rate of the tree multiplied by the age of the tree in years. The yearly increment rate was calculated as tree diameter (calculated from tree circumference at sampling height) divided by tree age.

3.3 Dating of Debris Flows (Zone D)

The sampling for tree-ring analysis related to debris flows (zone D; 54 trees) comprised two increment cores per tree. Temporal analysis of debris flows was based on dating growth disturbances (abrupt growth suppression/release and the formation of reaction wood and/or callus tissues) related to debris flow activity, i.e. reactions to stem burial, tilting of trees by lateral pressure of debris mass or stem surface abrasion by debris material.

3.4 The Processing of Samples and Reference Chronology

In addition to the disturbed trees, 20 trees were sampled from outside the Taraktash slope deformation in order to create a reference chronology to reflect climatic conditions only. The processing of all samples followed standard procedure as described by, for example, Bräker (2002). Individual steps included drying the samples, sticking them to supports, core sanding, counting of tree-rings and measuring the widths of rings (to within 0.01 mm) using Time Table and PAST4 software (V.I.A.S. 2005), and subsequent sample cross-dating with reference chronology to identify false or missing tree-rings. Furthermore, in order to ensure that the changes in tree-ring width resulted from the impacts of debris flows or rockfalls and to neglect the effect of solar radiation, only cases of

Table 75.2 Mean activity of individual processes in years related to earthquakes in years of activity for individual processes (statistical evaluation). *Bold numbers*—significant results ($p < 0.05$)

		Block movement (It)	Rockfall (RR)	Landslide movement (It)	Debris flow (events/year)
	Mean value of intensity	2.02	0.18	1.05	1.60
During earthquake	Mean	6.51	0.37	1.74	1.67
	t test (*p* value	**0.0011**	**0.0009**	**0.0381**	0.1885
One year after earthquake	Mean	0.27	0.08	1.75	1.25
	t test (*p* value	0.1871	**0.0001**	**0.0458**	0.1449
Five years after earthquake	Mean	1.28	0.12	0.90	1.44
	t test (*p* value	0.3073	**0.0053**	0.3580	0.2650
Ten years after earthquake	Mean	1.15	0.14	0.82	1.36
	t test (*p* value	0.0588	**0.0093**	0.2265	0.1183

severe growth suppression and strong growth release that differed from the reference chronology were considered plausible evidence.

4 Results

4.1 Block-Type Movements (Zone A)

The numbers of trees sampled, increment cores, ages of the oldest and youngest trees, and the mean age of the trees sampled are summarized for all zones (A to D) in Table 75.2. A total of 33 event years was identified on the basis of tilted trees. The highest I_t was dated to the year 1927, when 38.5 % of sampled trees were affected. Other years with a relatively high I_t value (all > 20 %) were 1777, 1790, 1839, 1855, 1872, 1875, 1901 and 1939 (Fig. 75.2a).

4.2 Rockfall-Dominated Slope (Zone B)

The mean *RR* value for the entire period is 0.18 hits m^{-1} $year^{-1}$, and the highest value was dated to 1875 (1.5 hits m^{-1} $year^{-1}$). However, the following years also show significantly increased activity of rockfall (six times higher than average): 1790 (1.43 hits m^{-1} $year^{-1}$), 1792 (0.81), 1802 (0.9), 1820 (0.73), 1829 (0.99) and 1927 (1.24) (Fig. 75.2b).

4.3 Landslide Movements in Rockslide Accumulation Area (Zone C)

Forty five event years with reaction wood formation were established, with a mean interval of 6.8 years (Fig. 75.2c). The mean I_t value, which never exceeded 20 %, was 7.2 %. The most active sliding, as represented by the highest I_t value (18.8 %), was recorded in 1906, 1912 and 1939. Other years showing significantly higher I_t values were 1839, 1875 and 1981.

4.4 Debris Flow Cone (Zone D)

The reconstruction of debris flow events was possible for a period of 269 years (1741–2009). Based on the dating of tree growth disturbances and their spatial analysis, 47 debris flow events, generated for 30 individual years (one event per 9 years on average), were detected (Fig. 75.2d).

5 Discussion

5.1 Dendrogeomorphic Implications and Mass Movement Chronology

Tree-ring analysis of a total of 738 increment cores from 255 of *P. nigra* was carried out.
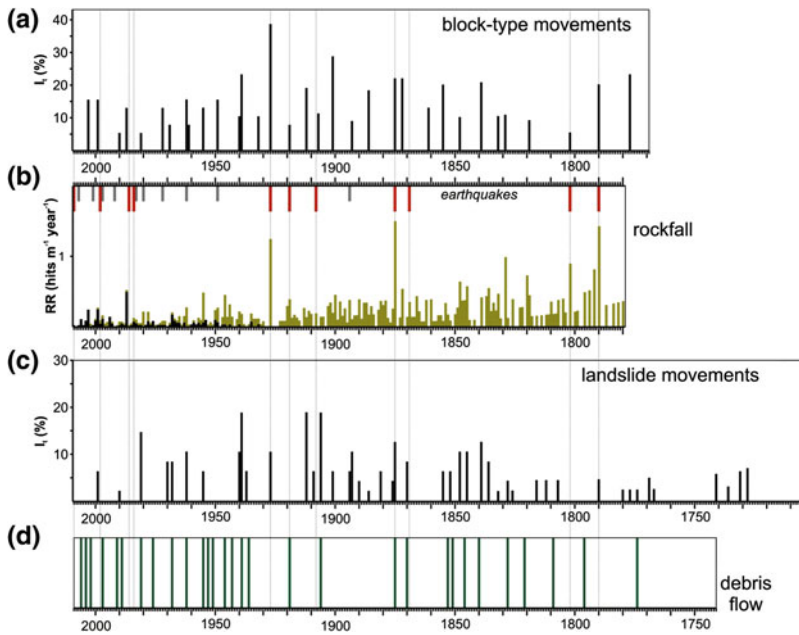
Fig. 75.2 Yearly values of the activity of individual processes compared with significant earthquakes (*short line M* = 3.0–4.0, *long line M* ≥ 4.0); *black RR* values— values related to data for young trees. Reprinted from Geomorphology, in press, Šilhán, K. et al., Tree-ring analysis in the reconstruction of slope instabilities associated with earthquakes and precipitation (the Crimean Mountains, Ukraine), Copyright (2012), with permission from Elsevier

In comparison with other coniferous trees, *P. nigra* is characterized by somewhat limited possibilities for dendrogeomorphic analysis, largely because of its strong heliotropism (an inclination towards the direction of insolation; Berthier and Stokes 2005), its sensitive reactions to climatic changes, although the ducts were not employed as indicators of past geomorphic processes in this study. Further validation of tree-ring analysis is revered to Šilhán et al. (in press). In spite of these complications, *P. nigra* is very often used in dendrogeomorphic studies, but a very careful application of reference chronology is vital (Pelfini and Santilli 2008; Ruiz-Villanueva et al. 2010). In the course of data processing, abrupt growth suppressions within the tree-rings of reference trees that were not connected with any known geomorphic processes emerged.

5.2 Seismic Trigger of Slope Instabilities

Our study is one of the first attempts to use dendrogeomorphic techniques to interpret the behaviour of slope failures that are assumed to be largely driven by seismic activity (Yadav and Kulieshius 1992; Carrara and O′Neill 2003).

Our study shows that dendrogeomorphic techniques are appropriate to highly sensitive detection of earthquake-accelerated slope processes. Figure 75.2b shows significant rockfall activities during the strongest recorded earthquakes (i.e. events in 1790, 1802, 1875 and 1927). However, elevated *RR* values are also reached during the relatively weak Crimean/Black Sea earthquakes of $M \geq 4.0$. We compared the maximum distance between slope failures and the epicentres of world earthquakes of a certain
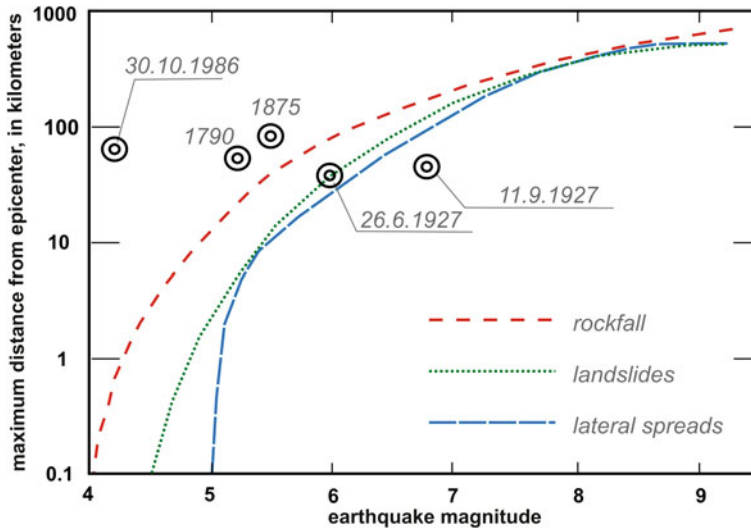
Fig. 75.3 Distance of the Taraktash slope deformation from the epicentres of major historical earthquakes responsible for the activation of mass movement reconstructed from tree-ring analysis. For comparison, we include curves displaying the upper boundaries of various types of slope movements as a function of earthquake magnitude (Keefer 1984). Reprinted from Geomorphology, in press, Šilhán, K. et al., Tree-ring analysis in the reconstruction of slope instabilities associated with earthquakes and precipitation (the Crimean Mountains, Ukraine), Copyright (2012), with permission from Elsevier

magnitude (Keefer 1984) with the magnitude and epicentre distance of the most important earthquakes recorded in the Taraktash tree rings. Except for the two 1927 earthquakes that fall within the boundary of Keefer's model, the epicentres of all other important seismic events that accelerated rockfalls on the Taraktash slope (1790, 1875 and 1986) were situated beyond boundaries, i.e., the real distance is larger than the distance expected in association with a particular slope process (Fig. 75.3). This evidence suggests that rockfall processes affecting the slopes above Yalta reacted to seismic loading in a very sensitive way. Such a high susceptibility of the cliffs to rockfall results from the presence of unstable bedrock formed by mechanically weak, thin-bedded limestones disturbed by pervasive fractures and deep-seated slope deformations. This weakness of the rocks is further exacerbated by the processes of karstification, which create conditions for the development of various types

of slope failures (Pánek et al. 2009a). Rockfall on such cliffs is thus activated by earthquakes that are somewhat weaker than those included in the Keefer scheme (e.g., Keefer 1984). Furthermore, the activity of blocks (e.g., toppling and spreading) and landslide reactivations clearly point to an intensification of movements during the strongest recorded earthquakes.

Table 75.2 provides an insight into the influence of earthquakes on the activity of particular slope processes within individual slope zones. It shows that the rates of block-type movement, rockfall and landsliding are significantly higher (than mean value of intensity) in years with the occurrence of earthquakes ($p = 0.05$). However, the behaviour of individual geomorphic processes in the years following each seismic event is rather complex. For instance, "rockfall rate" value is very low for a period of 10 years after an earthquake (0.14 in comparison with mean RR values—0.18). In our opinion, this phenomenon can

be explained by antecedent removal of available debris from the cliff as part of major rockfalls occurring during seismic shocks. In such circumstances, earthquakes play the role of instantaneous accelerators of rockfall activity that is considerably reduced in years following seismic shocks. In contrast, higher activity in the first year after an earthquake is associated only with landslide movement (in comparison with overall mean intensity). Nevertheless, only the first year after an earthquake is statistically significant (in case of landslide movement). Long-term influence of seismic loading was not demonstrated for block-type movement activity and debris flows. Especially for debris flows, there is no temporal relationship with historical earthquakes.

6 Conclusion

Tree-ring data derived from 738 increment cores from 255 individuals of *P. nigra* growing on the highly instable Taraktash slope provide a high-resolution record of mass movement activity covering more than the last three centuries. These slope instabilities comprise block-type movements (lateral spreading, toppling and incipient sliding), rockfalls, landslides and debris flows. Late Holocene block-type movements, rockfalls and sliding on the Taraktash slope have mainly been driven by seismic activities with epicentres occurring along the Black Sea coast, particularly by the major earthquakes in 1790, 1875, 1927 and 1986. The study demonstrates the great applicability of dendrogeomorphic techniques to the reconstruction of the chronology of slope processes driven by earthquakes.

References

Berthier S, Stokes A (2005) Phototropic response induced by wind loading in Maritime pine seedlings (Pinus pinaster A.). J Exp Bot 56:851–856

Bräker OU (2002) Measuring and data processing in tree-ring research—a methodological introduction. Dendrochronologia 20:203–216

Carrara PE, O'Neill M (2003) Tree-ring dated landslide movements and their relationship to seismic events in southwestern Montana, USA. Quat Res 59:25–35

Chigira M, Wang WN, Furuya T, Kamai T (2003) Geological causes and geomorphological precursors of the Tsaoling landslide triggered by the 1999 Chi–Chi earthquake, Taiwan. Eng Geol 68:259–273

Jacoby GC, Bunker DE, Boyd EB (1997) Tree-ring evidence for an A.D. 1700 Cascadia earthquake in Washington and northern Oregon. Geology 25:999–1002

Keefer DK (1984) Landslides caused by earthquakes. Geol Soc Am Bull 95:406–421

Keefer DK, Moseley ME (2004) Southern Peru desert shattered by the great 2001 earthquake: implications for paleoseismic and paleo-El Niño-Southern oscillation records. Proc Nat Acad Sci 101:10878–10883

Korup O, Densmore AL, Schlunegger F (2010) The role of landslides in mountain range evolution. Geomorphology 120:77–90

Lang A, Moya J, Corominas J, Schrott L, Dikau R (1999) Classic and new dating methods for assessing the temporal occurrence of mass movements. Geomorphology 30:33–52

Muratov MV, Archinov IV, Uspenskaya EA (1984) Structural evolution of the Crimean Mountains and comparison with the western Caucasus and the eastern Balkan ranges. Int Geol Rev 26:1259–1266

Nikonov AA, Sergejev AP (1996) Seismogravitacionnyje narusenia reliefa v Krymu pri zemletrjasenijach 1927 goda. Geoekologia 3:124–133

Pánek T, Hradecký J, Šilhán K, Smolková V, Altová V (2009a) Time constraints for the evolution of a large slope collapse in karstified mountainous terrain of the southwestern Crimean Mountains, Ukraine. Geomorphology 108:171–181

Pánek T, Danišík M, Hradecký J, Frisch W (2009b) Morpho-tectonic evolution of the Crimean mountains (Ukraine) as constrained by apatite fission track data. Terra Nova 21:271–278

Pasynkov AA, Plachotnyi LG, Gobratyuk VM (1992) Morfotektonika Krymskogo poluostrova i ei svyaz s razvitiem exogennych geologicheskich procesov. Geologicheskiy Jurnal 52:79–91

Pelfini M, Santilli M (2008) Frequency of debris flows and their relation with precipitation: a case study in the Central Alps, Italy. Geomorphology 101:721–730

Ruiz-Villanueva V, Diez-Herrero A, Stoffel M, Bollschweiler M, Bodoque JM, Ballesteros JA (2010) Dendrogeomorphic analysis of flash floods in a small ungauged mountain catchment (Central Spain). Geomorphology 118:383–392

Shroder JF (1978) Dendrogeomorphological analysis of mass movement on Table Cliffs Plateau, Utah. Quat Res 9:168–185

Stoffel M, Schneuwly D, Bollschweiler M, Lièvre I, Delaloye R, Myint M, Monbaron M (2005) Analyzing rockfall activity (1600–2002) in a protection forest—a case study using dendrogeomorphology. Geomorphology 68:224–241

Šilhán K, Pánek T, Hradecký J (2012) Tree-ring analysis in the reconstruction of slope in stabilities associated with earthquakes and precipitation (the Crimean Mountains, Ukraine). Geomorphology 173–174:174–184

V.I.A.S. (2005) Vienna Institute of Archaeological Science. Video time table. Installation and instruction manual. Rev. 2.1, Vienna

Yadav RR, Kulieshius P (1992) Dating of earthquakes: tree ring response to the catastrophic earthquake of 1887 in AlmaAta, Kazakhstan. Geogr J 158:295–299

Case Example of GIS Utilization on Abay Gorge's Landslide Survey in Ethiopia

76

Yoshimizu Gonai, Satoru Tsukamoto, Mitsuya Enokida, Kensuke Ichikawa, Atsushi Nakagawa and Tomonari Takeuchi

Abstract

This report introduces Geographic Information System utilization in the landslide survey thought the case example "The Project for Developing Countermeasures against Landslides in the Abay River Gorge in the Federal Democratic Republic of Ethiopia" which is one of the official development assistance project implemented by Japan International Cooperation Agency. The collected data specifically was topographical map, satellite image, geological map, digital elevation model data, movement bodies, scarps, cracks, springs, meteorological stations, drilling/monitoring position, cross section lines and so on. Based on these data, the analysis was conducted such as the following; analysis of the relationship with landslide distribution and elevation/geology, slope analysis and land covers classification for risk evaluation of debris flow/rock fall. The following maps are also made using the above collected data and analysis results; field survey map for investigation of the drilling, landslide, rockfall and debris flow distribution map, risk rank/hazard map and etc.

Keywords

GIS · Spatial analysis · Hazard map · Ethiopia

1 Introduction

This report introduces Geographic Information System (GIS) utilization in the landslide survey such as data collection, organizing, preprocessing, analysis methods, output and mapping thought the case example "The Project for Developing Countermeasures against Landslides in the Abay River Gorge in Ethiopia" (hereafter the Project) which is one of the Japan's Official Development Assistance (ODA) project (Japan International

Y. Gonai (✉) · S. Tsukamoto · M. Enokida ·
K. Ichikawa · A. Nakagawa · T. Takeuchi
Overseas Operations Department, Kokusaikogyo
Co., Ltd, 2 Rokubancho, Chiyoda-ku,
Tokyo 102-0085, Japan
e-mail: yoshimizu.gonai@gmail.com

Table 76.1 General work flow of the landslide study

Step	Contents	Description
(1) Preliminary survey	Literature search, Topographical and geomorphological interpretation	This survey is implemented to grasp the overview of the study area, to predict the landslide of large area using literature, topographical map, aerial photo and etc.
(2) Reconnaissance survey	Field survey, Planning of the detailed survey	This survey is implemented to judge the immediacy of landslides, and to implement the detailed survey efficiently. This survey often contains the topographic survey and brief land surface survey.
(3) Detailed survey	Topographical mapping, Geological survey, Slip-surface survey, Land surface displacement survey, Groundwater survey, Soil survey, Hydrological survey	This survey is implemented to confirm the assumed landslides, to analyze its mechanism in details. This step often is called a mechanism investigation.

Cooperation Agency 2012). The area for the Project is shown in Kuwano et al. (2012).

GIS is a technology for editing and managing geographical coordinate of 2-D plane and elevation, and it is usable for multidimensional analysis/visualization. In the case of landslide survey study, planning and countermeasure works take a long period. Therefore, it is required for landslide movement monitoring to manage not only geographical information of topography and geology but also monitoring devices such as extensometer, borehole inclinometer and water-level gauge. On the other hand, update on the monitoring data is also needed every day. Furthermore, the countermeasure and facility design should be planed using analysis results. GIS is usable to comprehensively support the works based on the database and utilization function. GIS has basic functions such as data archive, conditional/spatial search and thematic mapping visualization. Additionally, GIS is usable to customize the data and to process for geometric analysis, spatial analysis, statistical arithmetic processing and the others with computer program. The data dealt with GIS are also compatible with external data including Computer Aided Design (CAD) data. Furthermore, GIS is effective for e.g., map making, compiling field survey result.

Landslide study is divided roughly (1) preliminary survey, (2) reconnaissance survey and (3) detailed survey (Japan Association for Slope

Disaster Management 2012). Table 76.1 shows that the general work flow of landslide study.

It is difficult to obtain the detailed data in the preliminary survey, because the field survey is not implemented at the step. Therefore, the output such as map and analysis results are made by the processing and compiling based on the available data at the step. The data which has accurate information will be obtained in progress of the detailed survey such as topographical, geomorphological, geological, hydrological and other surveys. And we will be also able to make detailed map and advanced analyses.

2   Data Collecting and Compilation

This section describes collecting and compiling information related to landslide survey using example of the Project. The implementation procedure for data collecting and compiling is given below (Road Maintenance Technology Center 2007); (1) Review and arrangement of the existing data, (2) Investigation and request to acquire the data from counterpart of the Project and related organizations, (3) Checking, preprocessing and compiling the collected data for GIS database. Table 76.2 shows the data collected by the Project.

Table 76.2 Data collected by the project

No.	Name	Type	Scale/Resolution	Source
1	Populated place	SHP(Point)	1:1,000,000	Digital chart of the World website
2	Major road	SHP (Line)	1:1,000,000	
3	Major river	SHP (Line)	1:1,000,000	
4	National boundary	SHP (Polygon)	1:1,000,000	
5	Administrative boundary	SHP (Polygon)	1:1,000,000	Map library website
6	Administrative boundary(Region, Zone, Wereda)	SHP (Polygon)	–	Ministry of Agriculture and Center for Development and Environment in Ethiopia
7	Basin	SHP (Polygon)	–	
8	River	SHP (Polygon)	–	
9	Towns	SHP (Point)	–	
10	Road	SHP (Line)	–	
11	River	SHP (Line)	–	
12	ASTER-GDEM(Digital elevation model)	Satellite (Raster)	30 m	ASTER-GDEM website
13	SRTM(Digital elevation model)	Satellite (Raster)	90 m	United States Geological Survey
14	LANDSAT	Satellite (Raster)	30 m	
15	GLS	Satellite (Raster)		
16	Road shapes and benchmarks of Gohatoshion-Dejen	CAD	1:2,500	The project for rehabilitation of trunk road phase III
17	Landslide Area Topography (contour, road shapes, etc)	CAD	1:2,000	
18	Contour map	CAD	1:500	Ethiopia road authority
19	Cross section	CAD	1:500	
20	Road map	Raster(Hard copy)	1:2,000,000	
21	Topographical map (250 k)	Raster (Hard copy)	1:250,000	Ethiopia map agency
22	Topographical map (50 k)	Raster(Hard copy)	1:50,000	
23	Geological map	Raster (Hard copy)	1:2,000,000	Geological survey of Ethiopia
24	General Geology Reconnaissance map	Raster(Hard copy)	1:50,000	
25	GEO-EYE	Raster (Satellite)	0.5 m	Japan Space Imaging co., ltd.

(continued)

Table 76.2 (continued)

No.	Name	Type	Scale/Resolution	Source
26	Topographical map	CAD/SHP	1:5,000/10,000	The project
27	Cross section	CAD	1:200	
28	Drilling and monitoring point	Coordinate values	On-site survey	
29	Landslide geomorphological analysis result	SHP (Polygon, line)	On-site survey	
30	Spring water	SHP	On-site survey	
31	Geological map	SHP	On-site survey	
32	Hazard map	SHP	On-site survey	
33	Rock fall scarp	SHP	On-site survey	
34	High risk debris flow streams	SHP	On-site survey	
35	Cracks	SHP	On-site survey	
36	Access roads to drilling points	SHP	On-site survey	
37	Streams	SHP	On-site survey	
38	Landslide distribution by elevation	SHP	On-site survey	
39	Landslide distribution by geology	SHP	On-site survey	
40	Catchment area of streams	SHP	On-site survey	
41	Slope	SHP	On-site survey	
42	Rain gauging stations	SHP	On-site survey	
43	Land cover classification result	SHP	1 m	

3 Analysis and Mapping By Compiled Data

Based on the compiled data, the analysis and mapping were conducted. ArcGIS was used for this analysis. Landslides that are shown in the landslide distribution map are classified into blocks, according to the movement direction, scale, activity and mechanism. A landslide distribution map is created after identifying the landslide landform from satellite images and conducting a field survey to grasp and classify the conditions of the main scarps, cracks, steps and moving mass and confirm the detailed landslide boundary. To create this map, the landslide distribution and changes over the last 30 years were identified by interpreting GeoEye-1 satellite images (taken on June 3 and 7, 2010) and the aerial photos taken by Ethiopia Map Agency (EMA) in 1982. The results obtained by interpreting the photos were confirmed at the site to determine if any modifications and/or additions were needed.

The results of aerial and satellite image interpretations were combined with those of the rockfalls and debris flow analysis. They were compiled into the "landslide, rockfall and debris flow distribution map" organized using GIS, which is shown on Fig. 76.1.

3.1 Analysis Example of the Relationship Between Landslide and Elevation

The data on landslide distribution and altitude were combined using GIS to study the relationship between the number of landslides and the altitude. With respect to the number of landslides for every 200 m altitude, on the Goha Tsiyon side, the number is highest between 2,400 and 2,600 m, followed by 2,000, 2,200, 2,200 and 2,400 m. Contrary to Goha Tsiyon side, on the Dejen side, many landslides are observed between 1,800 and 2,000 m, while few are observed at other altitudes. Figs. 76.2 and 76.3 show result of the analysis.
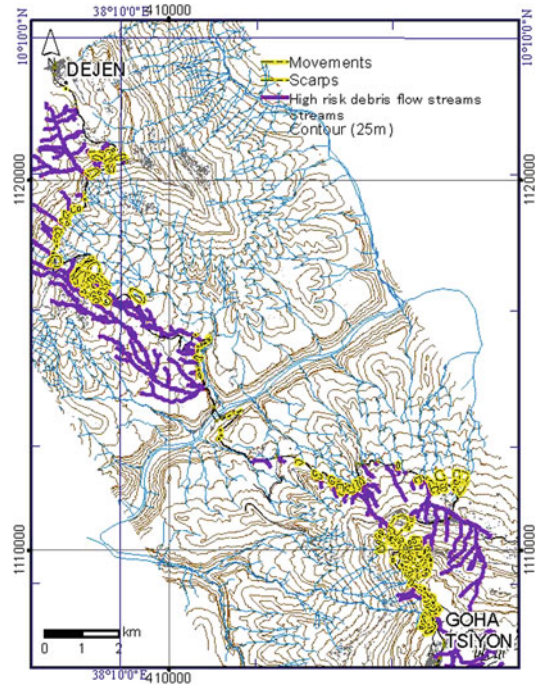
Fig. 76.1 Landslide, rockfall and debris flow distribution map
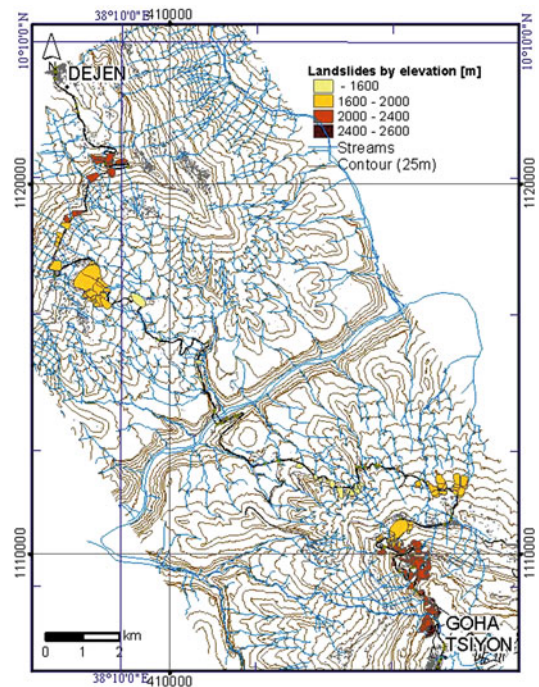
Fig. 76.2 Mapping of landslide distribution by altitude

Fig. 76.3 Landslide distribution by altitude (*Left* Goha Tsiyon side, *Right* Dejen side)
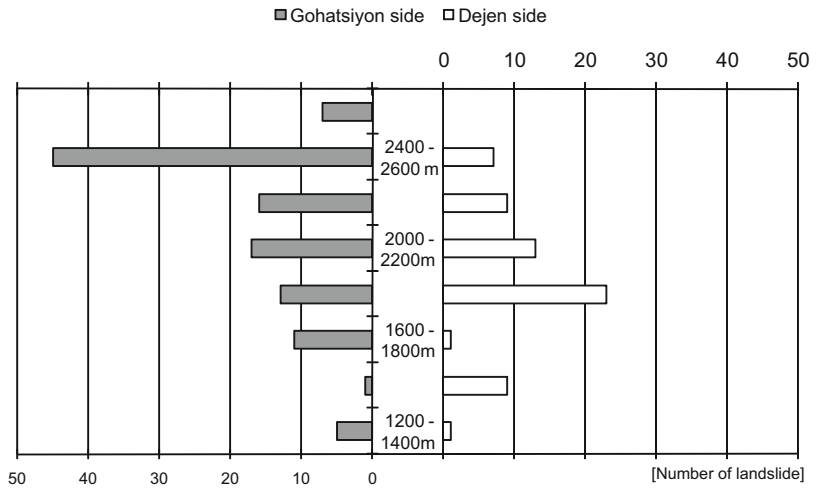
Fig. 76.4 Geological map with landslide overlay
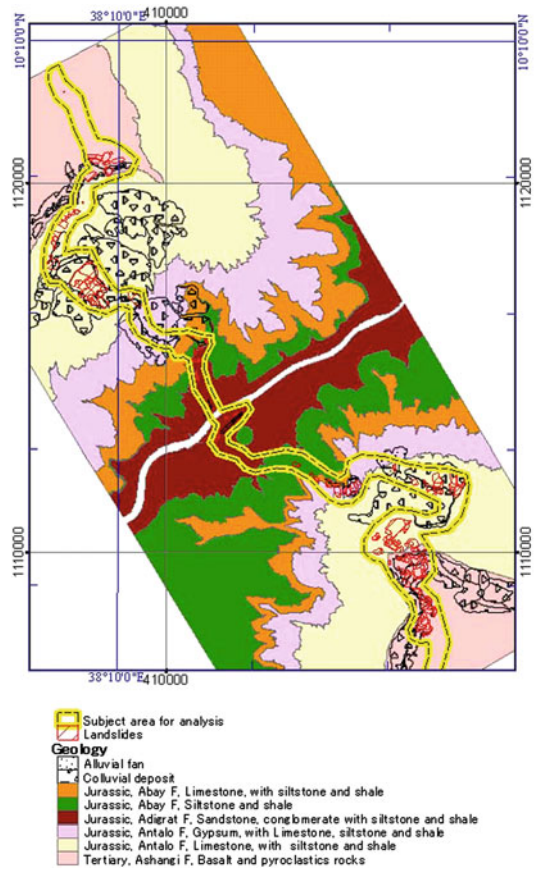
Table 76.3 Landslide density by Geology

Geology	Road length by geology (m)	Area of each geology (km^2)	Number of landslides (Landslides)	Density in each geology (Landslides/km^2)
Basalt and pyroclastic rocks	20659.56	5.39	69	12.81
Limestone, with siltstone and shale	9181.99	8.59	82	9.54
Gypsum, with Limestone, siltstone and shale	3827.89	1.74	7	4.03
Siltstone and shale	2023.25	1.08	3	2.77
Sandstone, conglomerate with siltstone and shale	5386.58	1.76	12	6.83

Colluvial deposits have been excluded because some colluvial deposits are themselves landslide mass

3.2 Analysis Example of the Relationship Between Landslide and Geology

In general, colluvial deposits are accumulated essentially under scarps and on gentle slopes. The data on landslide distribution and geology of the bedrock were combined by GIS to study the relationship between the number of landslides and the bedrock geological unit. In terms of the number of landslides per km^2 area, the landslide frequency is the highest (12.81 landslides per km^2) in the area of basalt and pyroclastic rock, followed by area covered with limestone, siltstone and shale of the Antalo Formation (9.54 landslides per km^2). The frequency is low in the area with gypsum, siltstone and shale in the Abay Formation and the area with sandstone and conglomerate in the Adigrat Formation. Both formations are located at low altitudes in Abay Gorge. Fig. 76.4 and Table 76.3 show the analysis result.

Fig. 76.5 The location of the high priority sites for countermeasures

3.3 Example of Sediment Disaster Hazard Mapping

The results of the landslide hazard assessment, combined with those of rockfall and debris flow hazard assessment, was used for a comprehensive "sediment disaster hazard map". With respect to the assessment method, the score rating system commonly used in Japan is adopted; the score rating of the system has been confirmed to make it suitable for the evaluation results by the experts, incorporating the characteristics of the landslides in the Abay Gorge area.

The sediment disaster hazard was mapped using GIS to explain the hazard as easily comprehensive as possible, so that the disaster hazard map can serve as a basic reference when

studying the priority of countermeasures and the road management in the future. The map was made by incorporating the results of not only the topographical survey but also the study of the landslide history, geological survey and two-year monitoring. As an example of the mapping result, the location of the high priority sites for countermeasure is shown in Fig. 76.5.

References

Japan Association for Slope Disaster Management (2012) Landslide survey, http://www.jisuberi-kyokai.or.jp /toha/chousa.html

Japan International Cooperation Agency (2012) The project for developing countermeasures against landslides in the Abay River Gorge, Final report

Kuwano et al (2012) Assessment of hazard and contributing factors of landslides in Abay Gorge in Ethiopia, in this proceedings

Road Maintenance Technology Center (2007) Guideline of inspection for road disaster prevention—torrential rain, heavy snow and etc

Features and Distribution of Landslides in the 2011 Earthquake of the Pacific Coast of Tohoku

Shoji Doshida and Shoichiro Uchiyama

Abstract

In the 2011 earthquake off the Pacific coast of Tohoku, the loss of human life resulted not only from the direct shaking of the earthquake and resulting tsunami, but also from many landslides that occurred in the region. However, these landslides were few and small, considering the magnitude of the Tohoku earthquake. Furthermore, many of the catastrophic landslides occurred inland instead of in coastal areas near the epicenter. In this research, we consider the underlying cause of this deviation of the landslide distribution by comparing the landslide distribution with various other parameters such as geomorphological features, geological features, and the peak ground acceleration and velocity of the seismic waves. We also compare the landslide distribution produced by the Tohoku earthquake with past landslide distributions. As a result, it is presumed that because of its geographical and geological features, catastrophic landslides do not occur easily in the Tohoku area along Pacific Ocean. This is thought to be one of the reasons why there were few reports of catastrophic landslides in spite of the of the Tohoku earthquake. The peak ground acceleration and velocity of the seismic waves of the Tohoku earthquake had greater values inland than in coastal areas. This is one of the factors that contributed to the large number of catastrophic landslides that occurred inland. An underground structure may have caused these high values in inland regions, although it is necessary to further research this hypothesis in the future.

Keywords

The 2011 earthquake off the Pacific coast of Tohoku · Landslide · Landslide map · GIS

1   Introduction

In the 2011 earthquake off the Pacific coast of Tohoku (M_W9.0, March 11, 2011, 14:46:27, Tohoku earthquake), the loss of human life resulted

S. Doshida (✉) · S. Uchiyama
National Research Institute for Earth Science and Disaster Prevention, 3-1, Tennodai, Tsukuba, Ibaraki, 305-0006, Japan
e-mail: sdoshida@bosai.go.jp

Table 77.1 Features of the earthquakes occurring after the 2011 earthquake off the Pacific coast of Tohoku

Day, Time	Earthquake	M	Type of earthquake	Type of fault
3/11, 14:46	The 2011 off the Pacific coast of Tohoku Eq.	9.0	Interplate	Reverse
3/12, 03:59	Sakae village, Nagano Pref. Eq.	6.6	Intraplate	Reverse
4/11, 17:16	Iwaki city, Fukushima pref. Eq.	7.1	Intraplate	Normal

not only from the direct shaking of the earthquake and resulting tsunami, but also from many landslides that occurred in the region. However, these landslides were few and small, considering the magnitude of the Tohoku earthquake as compared with other earthquakes that occurred in recent years, such as the 2004 Niigata Chuetsu earthquake and the 2008 Iwate-Miyagi inland earthquake. Furthermore, many of the catastrophic landslides occurred in inland areas such as Sirakawa city, Fukushima Pref., and Nasukarasuyama city, Tochigi Pref., instead of in coastal areas near the epicenter. In this research, we consider the underlying cause of the landslide distribution by comparing it with various parameters such as geomorphological features, geological features, and the peak ground acceleration and velocity of the seismic waves. Moreover, we also consider the features of the landslides caused by the Tohoku earthquake and compare them with those of the landslides produced by the Sakae village, Nogano Pref., earthquake (M_W6.6, March 12, 2011, 03:59, Sakae earthquake) and the Iwaki city, Fukushima Pref., earthquake (M_W7.1, April 11, 2011, 17:16, Iwate earthquake). Each earthquake had different features: the Tohoku earthquake was an interplate earthquake, while the Sakae earthquake and the Iwaki earthquake were intraplate earthquakes (Table 77.1). In addition, the Sakae earthquake occurred on a reverse fault, while the Iwate earthquake occurred on a normal fault, even though they were both intraplate earthquakes.

2   Creation of Landslide List

The landslide distribution data are some of the most important data in researching the cause underlying the landslide distribution. For the Tohoku earthquake, the collection of landslide distribution data was very difficult, because the damage occurred in a wide area, and the wide-range aerial photography surveys concentrated on the Tsunami damage along the shore. Thus, it was hard to obtain data on the mountainous areas.

We have created and made public a list of the landslides produced by the Tohoku earthquake and immediately following earthquakes by unifying various researchers' local field investigations (Fig. 77.1). Moreover, we are also continuing to add to and check the landside list by performing local field investigations. Although there is a danger that the landslide distribution data collected by these local field investigations could be overly focused on regions along major thoroughfares, we can check that the list covers most catastrophic landslides by considering subsequent reports, satellite photograph investigations, etc.

3   Comparison of Landslides and Various Data and Discussion Thereof

We compared the landslide distribution produced by the Tohoku earthquake with past landslide distributions (we used the "Landslide map" published by NIED) in Fig. 77.1. The red polygon show the locations of past landslides, and the red circles show the epicenters of earthquakes of more than M 6.5 that occurred after the Tohoku earthquake. It can be seen that almost no landslides have occurred along the Pacific coast, especially in the Kitakami Mountains and Abukuma highlands. The landslides produced by the Tohoku earthquake follow the same pattern. In the geological map (Fig. 77.2), it can be seen that this

Fig. 77.1 Epicenters (M6.5 or more), landslide distribution, and landslide map
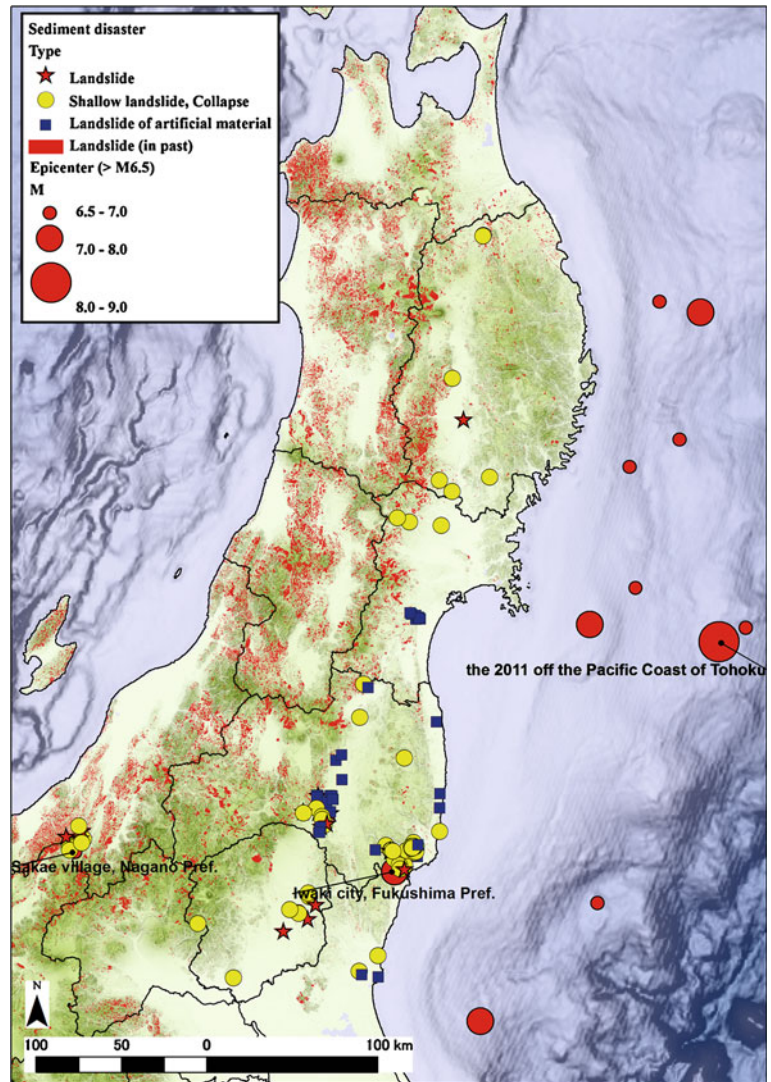
area is composed of granite rock (pink areas in the geological map).

As a result, it is presumed that the Tohoku area along Pacific Ocean has geographical and geological features that make it difficult for catastrophic landslides to occur. This is thought to be one of the reasons why few catastrophic landslides were reported, in spite of the size of the Tohoku earthquake. Thus, the reason that few catastrophic landslides resulted from the Tohoku earthquake is not only that it was an interplate earthquake. Therefore, it is still necessary to look for catastrophic landslides

generated by the interplate Tokai and Nankai earthquakes in future investigations.

Figures 77.3 and 77.4 present the landslide distribution overlaid on the peak ground acceleration (PGA) and the peak ground velocity (PGA) of the seismic waves of the Tohoku earthquake, respectively. The PGA and PGV data are interpolated from raster data based on a 5-km mesh that represents the interval between seismic observation points in the K-net and KiK-net of NIED. In these figures, the PGA and PGV of the Tohoku earthquake have lower values in coastal areas than in inland areas such as

Fig. 77.2 Landslide distribution and geological map
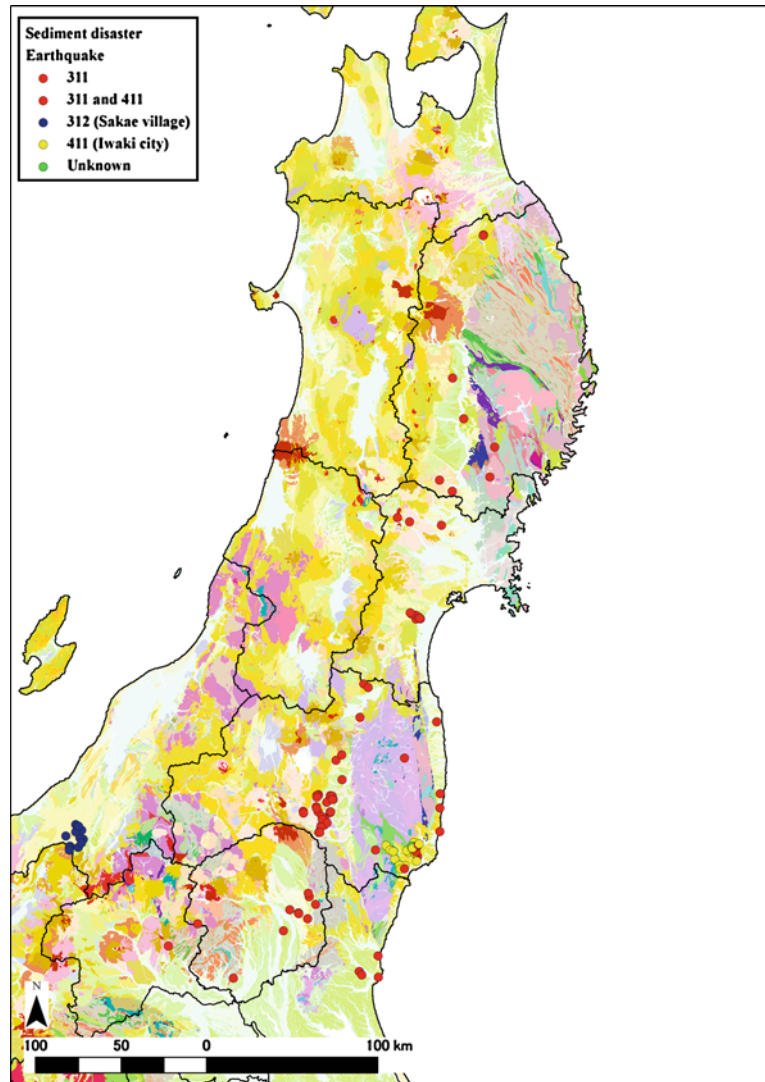
Sirakawa city, Fukushima Pref., and Nasukarasuyama city, Tochigi Pref. This is one of the factors that contributed to the many catastrophic landslides that occurred inland. The minimum PGA values producing the landslides in Sirakawa city and Nasukarasuyama city are about 400 gal, so it is assumed that the threshold PGA value for generating a landslide in this interplate earthquake was about 400 gal. Moreover, for comparison, we also checked the PGV values in these landslide areas and found that most had values of more than 22.30 cm/s (which is 5 or more on the JMA seismic intensity scale). However, discussion only in terms of PGA and PGV has many problems, and it is necessary to consider how these values should be compared

Fig. 77.3 Landslide distribution and peak ground acceleration (PGA)
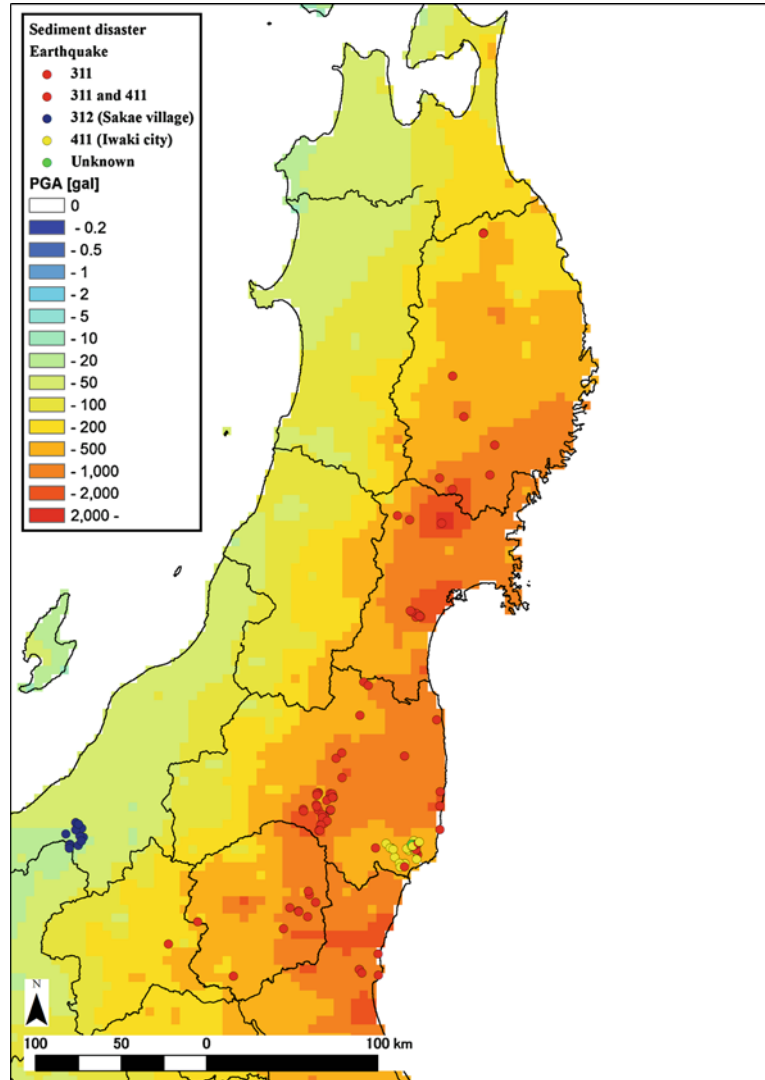
with other parameters, such as geology and geological structure data, the distance from the epicenter and the faults, etc.

The relation between the PGA and the PGV of each earthquake (Tohoku earthquake, Sakae earthquake, and Iwaki earthquake) at the various landslide sites is shown in Figs. 77.5 and 77.6.

The PGA is shown on the horizontal axis, and the PGV is on the vertical axis. The legend classifies the data by the kind of landslide (landside, collapse, and landslide of artificial material) in Fig. 77.5 and by earthquake, including the Tohoku earthquake (311), Sakae earthquake (312) and Iwaki earthquake (412), in

Fig. 77.4 Landslide distribution and peak ground velocity (PGV)
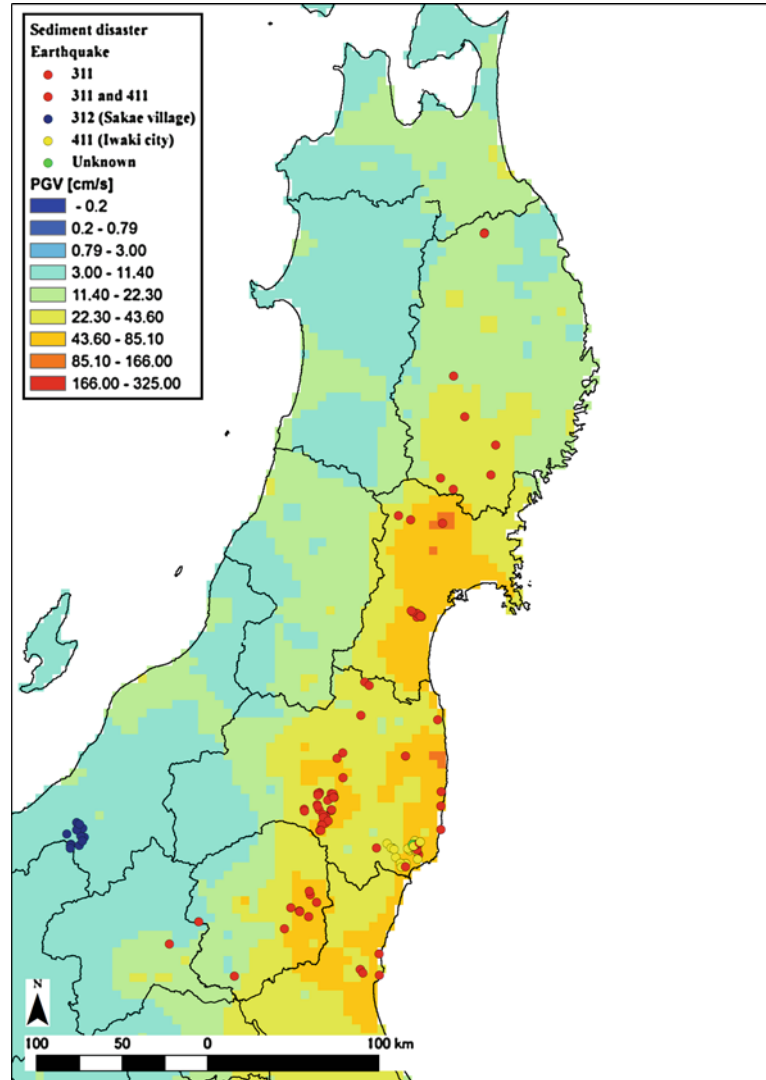
Fig. 77.6. No large difference was found in the relationship between PGA and PGV for different kinds of landslides in Fig. 77.5. On the other hand, it turned out that the short-period seismic waves were predominant in the Sakae earthquake, while long-period seismic waves were predominant in the Iwaki earthquake compared with the other earthquakes in Fig. 77.6. In general, it is thought that long-period seismic waves predominate in interplate earthquakes. However, it turned out that a long-period seismic wave occurred similarly in an earthquake on a normal fault. Moreover, the interplate earthquake affected a broad zone compared with the other earthquakes, which is the reason why landslides were generated in a wide area.

Fig. 77.5 Relationship between PGV and PGA for different types of landslide
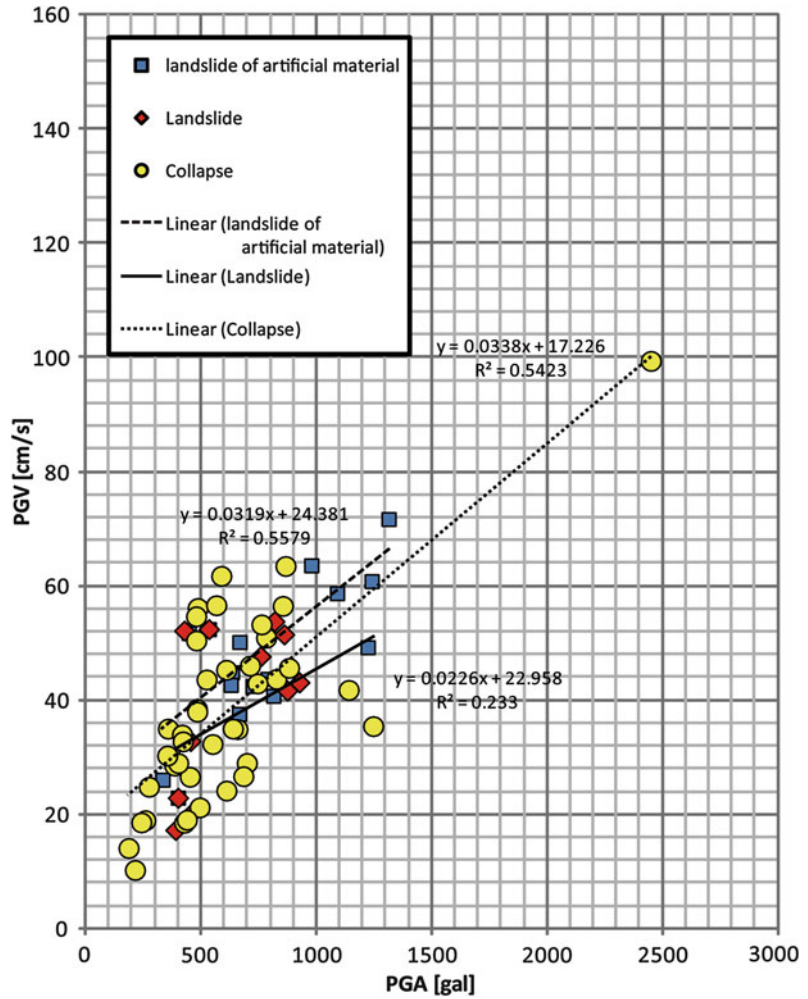
4   Conclusions

A spatial comparison of the landslide distribution in the Tohoku earthquake and the landslide map (past landslide distribution) provided by NIED indicated that the Tohoku area along Pacific Ocean has geographical and geological features that make it difficult for catastrophic landslides to occur. This is thought to be one of the reasons why few catastrophic landslides were reported, in spite of the magnitude of the Tohoku earthquake.

The PGA and PGV of the Tohoku earthquake were lower in coastal areas than in inland areas such as Sirakawa city, Fukushima Pref., and Nasukarasuyama city, Tochigi Pref. This is one reason why many of the catastrophic landslides occurred inland.

The relation between the PGA and the PGV of each earthquake (the Tohoku earthquake, Sakae earthquake and Iwaki earthquake) at the

Fig. 77.6 Relationship between PGV and PGA for each earthquake
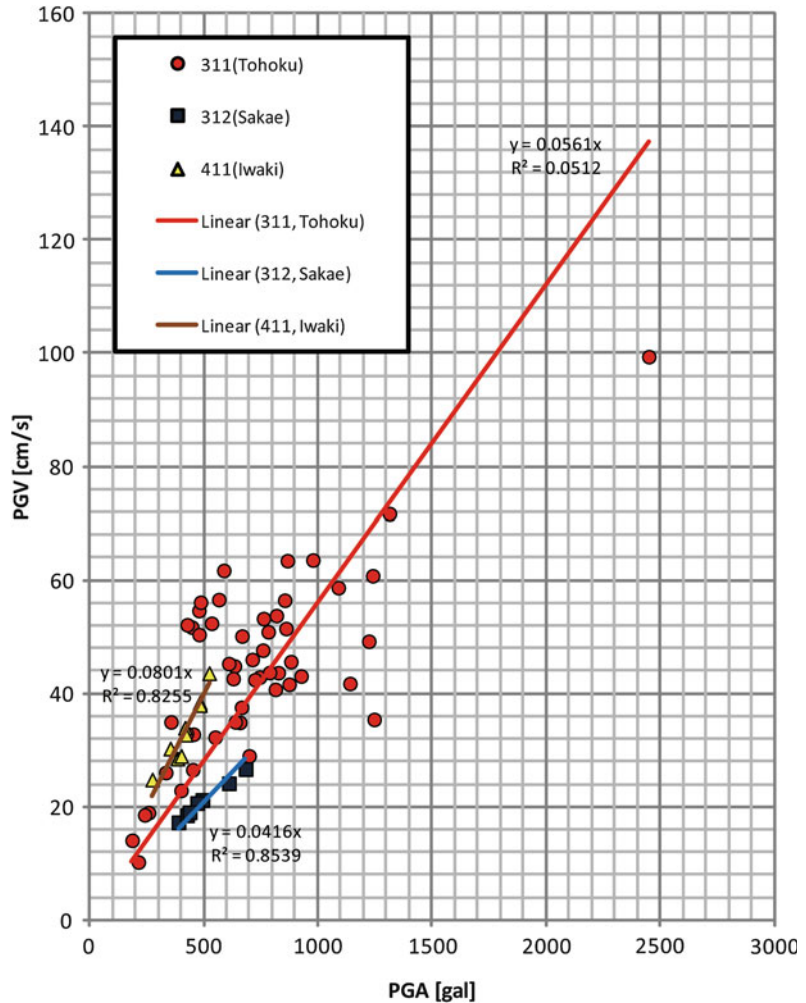
landslide sites indicated that short-period seismic waves predominated in the Sakae earthquake, while long-period seismic waves predominated in the Iwaki earthquake compared with the other earthquakes. Moreover, the interplate earthquake affected a broad zone compared with the other earthquakes, which is why landslides were generated in a wide area.

These results will help in the development of a risk assessment technique for the disasters following earthquakes by clarifying the features of the landslides caused by interplate and intraplate (normal fault and reverse fault) earthquakes. We would also like to clarify the detailed features of landslides by considering various other parameters in the future.

Quick Identification of Regional Earthquake-Induced Landslides Based on Sharp NDVI Change

78

Jiayuan Lin and Guiyun Zhou

Abstract

Landslides triggered by earthquake lead to substantial loss of life and damages to property. It was necessary and important to locate and plot out the landslides immediately after earthquake for quick victims rescuing. In addition, it is significant to map potential landslides for planning settlement and mitigating geological disaster. Landslide often results in sharp land cover changes in forested or bushed area, which can be easily detected by airborne or satellite-based remote sensing techniques. The region that landslide takes place is often inaccessible for field observation because of the accompanied temporary failure in transportation and communication. Therefore, remote sensing can be adopted to collect spatial information of landslide efficiently and quickly. By taking Wenchuan Earthquake as an example, this paper advanced one quick methodology to extract primary regional landslides with 8-day MODIS NDVI and terrain slope information. The threshold of temporal NDVI jump (value of 0.4) was introduced to discriminate landslide induced sharp NDVI decline from seasonal variations of vegetation cover, while slope information can be used to further confirm land cover change caused by landslide. In addition, the result emphasizes that region with slope over 15° is exposed to high landslide risk, which should be carefully taken into account in settlement and transportation planning.

J. Lin (✉)
Institute of Mountain Hazards and Environment, Chinese Academy of Sciences, Chengdu, China
e-mail: linjiayuan@gmail.com

G. Zhou
School of Resources and Environment, University of Electronic Science and Technology of China, Chengdu, China

1 Introduction

Landslides triggered by earthquake buried towns and village, leading to substantial loss of life and damages to property, infrastructure, and environment. It was necessary and important to locate and plot out the landslides immediately

after earthquake for quick victims rescuing. In addition, it is significant to map potential landslides for planning settlement and mitigating geological disasters.

Landslide related factors fall more within the environmental and human categories, and most research contribution of regional observation came from fields of visual/near infrared remote sensing and aerial photographs, which provide morphological, land use, and geological details to assist in analyzing relationships between landslides and causative factors (Metternicht et al. 2005). Landslide often results in sharp land cover changes, which can be easily detected by airborne or satellite-based remote sensing techniques. The region that landslide takes place is often inaccessible for field observation because of the accompanied temporary failure in transportation. Therefore, remote sensing can be adopted to collect spatial information of landslide efficiently and quickly. Remote sensing has gained increasing attentions for landslide evaluation and detection in recent decades (Tralli et al. 2005; Canuti et al. 2007; Hong et al. 2007). Cheng et al. (2004) discussed locating landslides induced by earthquake with multi-temporal satellite images, which was similar as the work of Hervas et al. (2003) who explored Tessina landslide of Italy with optical remotely sensed imagery. Spatial analysis provided by Geographical Information System (GIS) can synthetically assess the factors of landslide, so the techniques of GIS and remote sensing can be integrated to explore potential landslides in steep lands (Nagarajan et al. 1998; Perotto-Baldiviezo et al. 2004; Roessner et al. 2005). Temesgen et al. (2001) used GIS and remote sensing to evaluate the relationships of landslide with various controlling parameters in Ethiopia, which were used to develop the risk susceptibility index.

Change of land cover can be remotely sensed with methods of post-classification comparison, temporal image differencing, temporal image rationing, multi-fractal analysis, Bayesian probabilistic method, etc. (Zhang et al. 2010). Despite different behaviors of change detection algorithms, these methods share the idea of comparing multi-images to extract temporal difference in land cover. To extract and locate landslides induced by Wenchuan Earthquake, this paper explored how to quickly map landslides with 8-day MODIS products and terrain slope information, as well as to circumvent cloudy weather limit in remote sensing.

2 Study Area

Wenchuan Earthquake was triggered by thrust activities of two plates linked by Longmen Fault on May 12th, 2008, and the epicenter (31.0 °N, 103.4 °E) was on south end of the Fault. This geological event resulted in devastating disaster along the whole northeastward Longmen Fault Zone (LFZ), causing substantial loss of life and damages to property, infrastructure, and environment in many counties of the region (as shown in Fig. 78.1).

To focus on the serious earthquake influenced region, the southwestern half LFZ was selected as study area, totally about 30,000 km^2 (Fig. 78.1). Ranging 500 m to over 6,000 m in elevation, rugged terrain of the study area is the geographical transform zone from Tibetan Plateau to Sichuan Basin. It is the sharp variation in terrain that aggravated the damages of the Earthquake.

3 Data and Methodology

3.1 Data

In the last decade, Terra carried sensor of MODIS has been widely used in fields of land surface, ocean and atmosphere (NASA Terra 2008), as it makes a practical and successful trade-off between spatial and temporal resolution with an improved spectral schema (Qi et al. 1994; Huete et al. 2002; Wang et al. 2007). To overcome cloud influence in regional remote sensing, the 8-day MODIS composite product of land surface reflectance (MOD09Q1) was adopted to construct Normalized Difference Vegetation Index (NDVI) at scale of about 1:2,500,000, as this sensor can provide surface reflectances of red and near-infrared spectra with pixel resolution of

Fig. 78.1 The study area, southwestern half of the Longmen Fault Zone (based on SRTM-DEM)
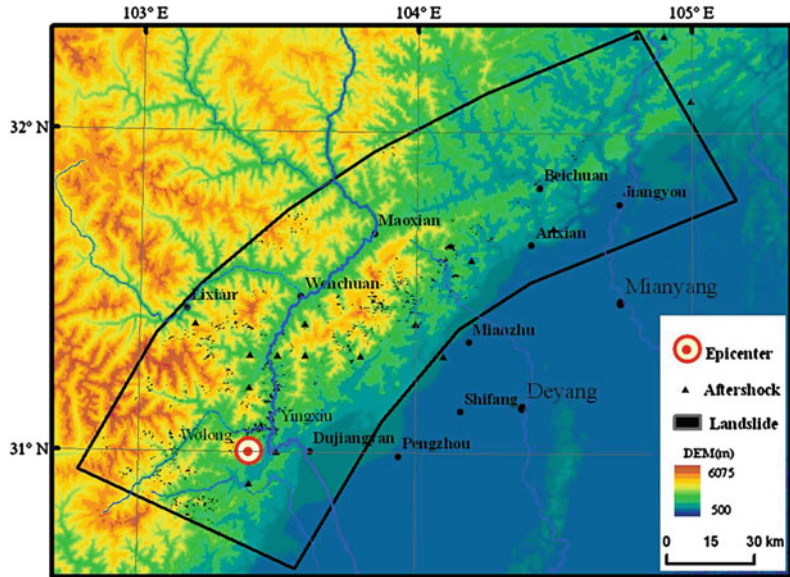
250 m. The product of MOD09Q1 can be accessed from the data gateway of NASA Earth Observation System (EOS) Data Gateway (NASA 2008). MODIS products are named with Julian Date (i.e. Day of Year, DOY), so MOD09Q1.2008121, for example, means the composite of MOD09Q1 during DOY 121–128 (i.e. 2008 April 30 to May 7). May 12 of 2008 (when Wenchan Earthquake erupted) corresponds with DOY 133, which is included in the 8-day MODIS composite product of DOY 129. The products of MOD09Q1 during DOY 105–161 of 2008 (ranging April 14–June 17) were all adopted to detect landslides in the study area. In addition, the MODIS product of land cover (MOD12Q1, in 1 km resolution) was used to provide surface cover types before landslide event, which were expressed with the land cover classification system of International Geosphere Biosphere Programme (IGBP) (GLCF 2008).

Data of another Terra carried sensor with higher spatial resolution (15 m for visual and near infrared bands), the Advanced Space-borne Thermal Emission and Reflection Radiometer (ASTER), was used to map detailed landslide of specific region in order to validate MODIS detecting results. NASA provided some free ASTER images of the earthquake region for rescue (USGS EROS Data Center 2008), from which

two scenes of AST_L1B images covering Wenchuan County with less cloud contamination were selected, respectively acquired on February 19 of 2003 and May 23 of 2008.

In addition, the elevation data collection of Shuttle Radar Topography Mission (SRTM) from NASA was used to provide information of terrain slope. The SRTM collected surface elevation data over 80 % of the landmass between 60 °N and 56 °S latitudes in February 2000 with Interferometric Synthetic Aperture Radar (Rabus et al. 2003). Elevation data of land surface outside United States was provided in the resolution of 3 arc-second, i.e. about 90 m (Rabus et al. 2003). NASA has released version 2 of the SRTM data (i.e. the "finished" version), which exhibits well-defined water bodies and coastlines and the absence of spikes and wells (single pixel errors) (Farr et al. 2007).

3.2 Methodology

Detect Land Cover Change

Land covers of the study area were extracted from MODIS products, as shown in Table 78.1. In this mountainous region, dominate cover types are forests, which totally consist up over 60 % area of the whole region, only with some

Table 78.1 Land covers of the study area

Land cover code	Type	Percentage (%)
1	Evergreen needleleaf forest	13.65
2	Evergreen broadleaf forest	0.46
3	Deciduous needleleaf forest	0.34
4	Deciduous broadleaf forest	11.24
5	Mixed forests	37.21
6	Closed shrublands	0.26
7	Open shrublands	4.63
8	Woody savannas	5.60
9	Savannas	1.17
10	Grasslands	7.76
11	Permanent wetlands	0.28
12	Croplands	14.29
13	Urban and built-up	0.28
14	Cropland/natural vegetation mosaic	2.08
16	Barren or sparsely vegetated	0.75
(Total)		100.00

settlement sparsely interspersed in valleys. Sharp elevation variation prevails in the areas over 2,000 m, which brings the distinct vertical zonality in land cover.

Grass mainly grows in the highlands above 4,000 m and some dry-hot valleys, but most valleys are agriculturally exploited, where towns and villages locate. The broad elevation belts between valleys and alpine grasslands are dominated by evergreen needle-leaf forest, deciduous broadleaf forest and mixed forest. Totally, over 98 % of land surface in this region is densely vegetated, and plants are nearly at growth peak on May 12 of 2008, when the Earthquake erupted. Therefore, landslide induced cover change would cause distinct vegetation fraction variation, which can be remotely sensed with vegetation index (VI).

Among different VIs, NDVI is a widely used one, which however shows the limits of easy saturation and atmospheric sensitivity (Qi et al. 1994; Park et al. 2004). To overcome the

weakness of NDVI, the Enhanced Vegetation Index (EVI) is gradually developed to substitute NDVI in most applications (Huete et al. 2002). With the spatial resolution limit of blue channel, MODIS provided EVI is coarser than 250-m resolution. However, a 250-m spatial resolution can be achieved by MODIS NDVI. For this reason, although EVI is a significant improvement, in this study NDVI is adopted to detect landslide triggered changes in vegetation coverage.

The reflectances of red and near infrared spectra were extracted and mosaicated with MODIS Reproject Tool (MRT), and NDVI was further derived by

$$\mathrm{NDVI} = (\rho_{nir} - \rho_r)/(\rho_{nir} + \rho_r) \qquad (78.1)$$

where ρ_r and ρ_{nir} are the MODIS-based red and NIR (near-infrared) reflectances respectively. Then, the difference ($Diff_{NDVI}$) between the NDVI before and after the Earthquake was estimated with

$$Diff_{NDVI} = \mathrm{NDVI}_{pre} - \mathrm{NDVI}_{post} \qquad (78.2)$$

where NDVI_{pre} and NDVI_{post} are respectively the NDVI before and after the event.

Variation of NDVI during certain period may result from change of land cover, vegetal and agricultural activities. As Table 78.1 indicated, the study area is dominated by natural forests, which excludes the possibility of harvest induced sharp NDVI variation. Within certain limited period, seasonal variations of NDVI can be discriminated out with critical threshold of NDVI variation. The NDVI of DOY121 (i.e. April 30–May 7) was used to represent vegetation cover before the Earthquake. As the study area is characteristic of cloud weather in early summer, even 8-day composite MODIS product with required quality immediately after the event was absent. For this reason, the NDVI of DOY153 (June 1–8) was adopted to describe vegetation fraction status after the event. Based on the landslides interpreted from ASTER images, variation of MODIS NDVI before and after the event was analyzed, and the jump threshold of MODIS NDVI was defined as 0.4 to detect the sharp land cover change induced by landslide.

Fig 78.2 MODIS NDVI map of the study area before the Earthquake (DOY121, April 30–May 7)
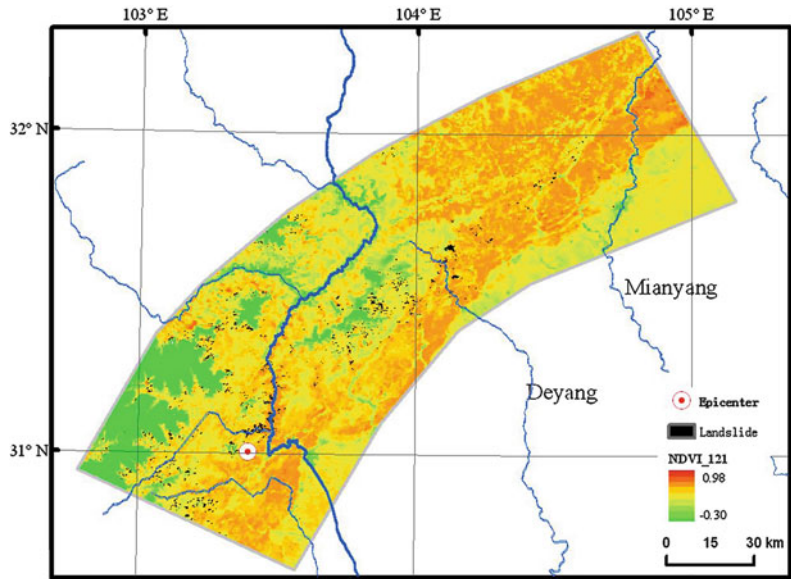
Detect Landslide

Miliaresis et al. (2005) analyzed relationship between terrain characteristics and landslide risk in western Greece, and suggested that the areas where mean slope is equal to or greater than 15 ° and mean elevation ranges 0–750 m show high landslide risk. Since the study areas of Miliaresis et al. (2005) and this proposed method were different in the elevation range (i.e. 0–2 333 m and 500–6,000 m, respectively), only their rule of slope over 15 ° was adopted to facilitate landslide detecting in the proposed method.

In general, NDVI jump can appear in three situations, i.e. a) source region of landslide with steep slope, b) accumulation region of landslide with moderate slope, and c) other non-landslide region, such as harvested fields and bare region as a result of logging. Therefore, land slope can be used to discriminate above situations of NDVI jump. Slope distribution of the study area was derived with SRTM elevation data. The areas with both the slope over 15° and the NDVI jump over 0.4 can be classified as landslide source region, while other area (with NDVI jump over 0.4 and falling within 500-m buffer of landslide source region) can be detected as landslide accumulation region. In addition, according to physical characteristics of landslide, the flat area

without sharp NDVI jump but within 500-m downslope buffer of landslide source region was also recognized as landslide accumulation region. The extracted source and accumulation regions constituted the whole landslide distribution to be detected with multi-temporal NDVI imagery. With this method, the jumps of NDVI and terrain were integrated to examine and locate landslides for the study area at regional scale. Though MODIS image with 250-m resolution may miss some landslide details, the proposed method is computation-efficient because of the middle resolution of MODIS data. For the study area, about 30,000 km^2, the landslides can be extracted in an hour with personal computer, which promises to offer timely landslide information.

4   Results of Landslide Detecting

In the study area, elevation ranging widely from 500 m to 6 000 m is the key element controlling vegetation cover. The inverse relationship between elevation and NDVI can be found in Figs. 78.1 and 78.2. In the LFZ, river valleys have relatively high NDVI value, such as the part of Minjiang River between Dujiangyan and
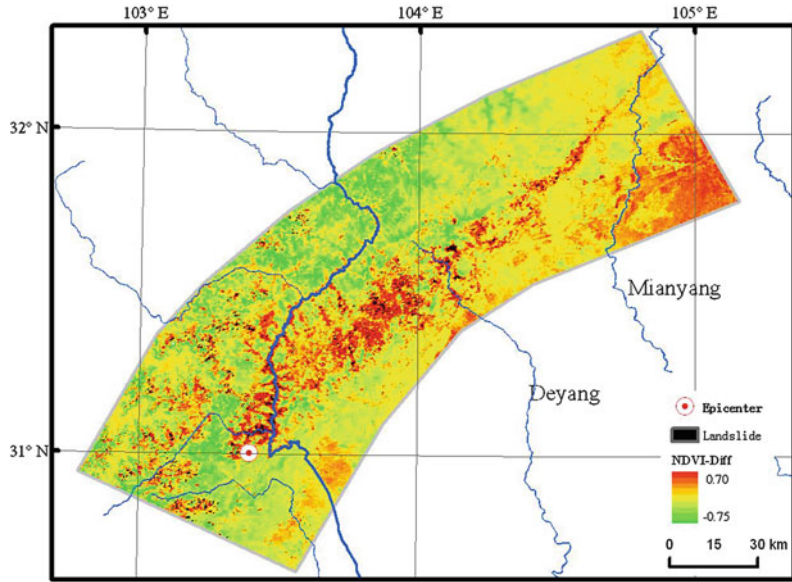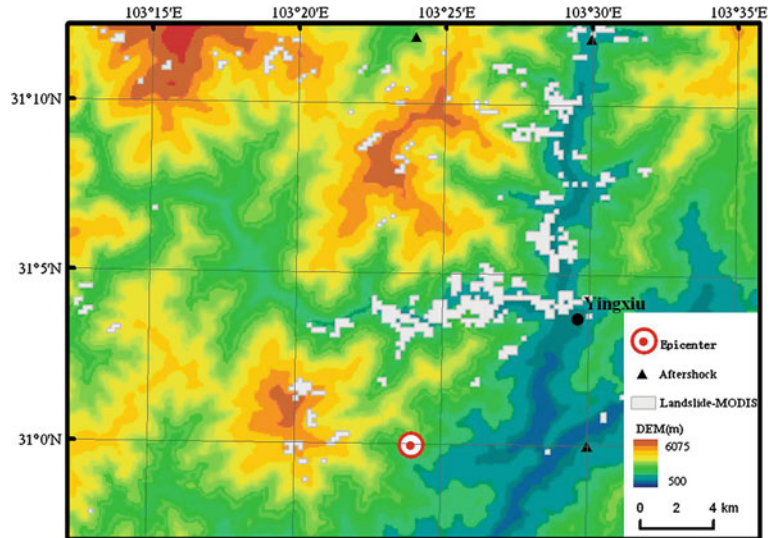
Maoxian (Fig. 78.4). Lowest NDVI value was found at upper mountains, which were permanently covered by snow. Though low as 600 m in elevation, plain of the eastern study area has smaller NDVI than that of some mountain region, where forest cover has a higher vegetation fraction.

The study area experienced sharp NDVI decline along the LFZ, i.e. from Dujiangyan northeastwardly to Wenchuan, Maoxian and Beichuan (Fig. 78.2), which all were seriously affected by the Earthquake. Using MODIS NDVI and terrain slope information, the Earthquake induced landslides were extracted, as shown in Fig. 78.3, and landslide distribution near the epicenter was further represented in detail by Fig. 78.4. The result indicated that these landslides mainly concentrated in areas of valley banks. Such result could be related to the fact that valley bank is often the steepest area

Fig 78.5 Slope of the landslides region in the study area
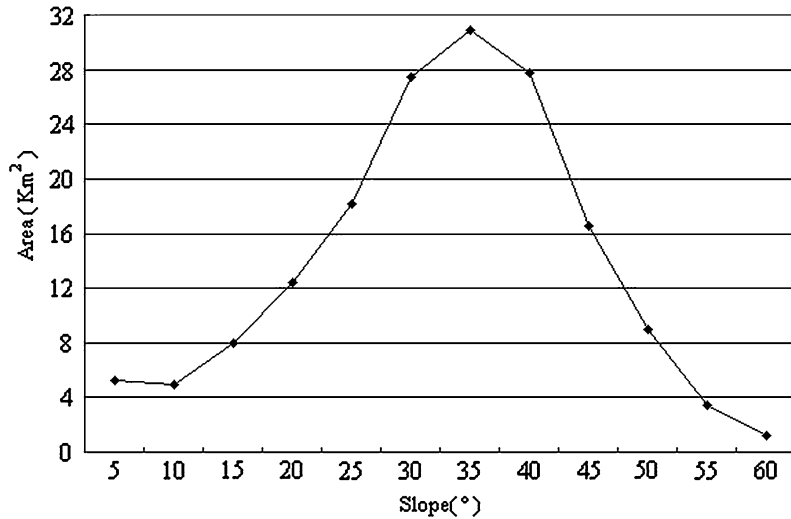
Table 78.2 Land covers of the regions where landslides took place in the study area

LAND COVER CODE	Type	Area (km^2)
1	Evergreen needleleaf forest	53.25
2	Evergreen broadleaf forest	1.25
4	Deciduous broadleaf forest	15.75
5	Mixed forests	75.00
7	Open shrublands	7.50
8	Woody savannas	3.25
9	Savannas	1.25
10	Grasslands	13.25
11	Permanent wetlands	2.75
12	Croplands	4.00

and therefore is more vulnerably affected by gravitational instability.

Land covers of the regions where landslides took place were summarized in Table 78.2. Total area of the landslides amounts to large as about 170 km^2, about 90 % of which was formerly covered with forest or shrub. This fact made it more difficult to ecologically restore these landslides resulted destruction. According to the MODIS result, there was totally about 4.00 km^2 of cropland area buried by landslides. Since cropland area in mountainous regions was often densely populated, the potential life losses could be extremely serious in landslides of cropland area.

Although slope of landslide regions ranges from 0 to 60°, the slope of about 90 % of landslide regions is larger than 20° (as the curve of Fig. 78.5). Slope is one important factor influencing landslide, so the constraint condition of terrain slope in the proposed method can efficiently discriminate landslide from other region with NDVI jump. In addition, this fact also suggested that areas with sharp terrain variation should be avoided in settlement planning and be carefully considered in building roads or bridges, so as to restrain landslide resulted damages.

Theoretical fundamentals underlying the proposed landslide detecting method are the NDVI jump and the slope threshold. Therefore, this method depends upon vegetation cover and related change, and it could fail to detect landslides in the region with sparse or without vegetation. As Table 78.2 indicated, the MODIS detected regions of landslide were almost all covered with dense vegetation before the Earthquake. In addition, though landslide risk itself is related with elevation and its variation (Miliaresis et al. 2005), this proposed method shows little dependence on elevation in the study area.

5   Conclusions

Earthquake induced landslide in mountainous region often results in substantial life loss and property damage. It is urgent to quickly and efficiently map landslides for victim rescuing immediately after the occurrence of earthquake. To conquer weather limits of remote sensing in the disaster area and to meet the requirements of regional quick observation, this paper proposed one landslide detecting method based on MODIS NDVI sharp change and terrain slope, which was used to extract the landslides induced by Wenchuan Earthquake.

With this method, about 170 km^2 of landslides was extracted in the study area of Wenchuan Earthquake, most of which was ever covered with forest and shrub. An ecological restoration of the areas affected by landslide would therefore be difficult. In addition, slope analysis upon these landslides suggests that region with high landside risk (i.e. with slope over 15°) should be carefully taken into account in settlement and transportation planning.

Though too coarse to examine specific landslides, this proposed method can locate and mark potential landslide regions for further observation with airplane or microwave narrow-scanning sensors. Landslide detecting based on NDVI jump requires that temporal span of multi-temporal images should be as short as possible, so that the NDVI variation resulted from factors other than landslide can possibly be avoided.

References

Canuti P, Casagli N, Catani F, Falorni G, Farina P (2007) Integration of remote Sensing techniques in different stages of landslide response. Progress in landslide science. Springer, Berlin, pp 251–260

Cheng KS, Wei C, Chang SC (2004) Locating landslides using multi-temporal satellite images. Adv Space Res 33:296–301

Farr TG, Rosen PA, Caro E, Crippen R, Duren R, Hensley S, Kobrick M (2007) The shuttle radar topography mission. Rev Geophys 45: . doi: 10.1029/2005RG000183

GLCF (2008) GLCF homepage. http://www.landcover.org/index.shtml. Cited on 25 Oct 2008

Hervas J, Barredo JI, Rosin PL, Pasuto A, Mantovani F, Silvano S (2003) Monitoring landslides from optical remotely sensed imagery: the case history of Tessina landslide, Italy. Geomorphology 54:63–75

Hong Y, Adler RF, Huffman G (2007) An experimental global prediction system for rainfall-triggered landslides using satellite remote sensing and geospatial datasets. IEEE Trans Geosci Remote Sens 45:1671–1680

Huete A, Didan K, Miura T, Rodriguez EP, Gao X, Ferreira LG (2002) Overview of the radiometric and biophysical performance of the MODIS vegetation indices. Remote Sens Environ 83:195–213

Metternicht G, Hurni L, Gogu R (2005) Remote sensing of landslides: an analysis of the potential contribution to geo-spatial systems for hazard assessment in mountainous environments. Remote Sens Environ 98:284–303

Miliaresis G, Sabatakakis N, Koukis G (2005) Terrain pattern recognition and spatial decision making for regional slope stability studies. Nat Resour Res 14:91–100

Nagarajan R, Mukherjee A, Roy A, Khire MV (1998) Temporal remote sensing data and GIS application in landslide hazard zonation of part of Western ghat, India. Int J Remote Sens 19:573–585

NASA (2008) EOS data gateway. http://delenn.gsfc.nasa.gov/~imswww/pub/imswelcome/. Cited on 15 June 2008

Park S, Feddema JJ, Egbert SL (2004) Impacts of hydrologic soil properties on drought detection with MODIS thermal data. Remote Sens Environ 89:53–62

Perotto-Baldiviezo HL, Thurow TL, Smith CT, Fisher RF, Wu XB (2004) GIS-based spatial analysis and modeling for landslide hazard assessment in steeplands, southern Honduras. Agric Ecosys Environ 103:165–176

Qi J, Chehbouni A, Huete AR (1994) A modified soil adjusted vegetation index. Remote Sens Environ 48:119–126

Rabus B, Eineder M, Roth A, Bamler R (2003) The shuttle radar topography mission–a new class of digital elevation models acquired by spaceborne radar. ISPRS J Photogram Rem Sens 57:241–262

Roessner S, Wetzel H-U, Kaufmann H, Sarnagoev A (2005) Potential of satellite remote sensing and GIS for landslide hazard assessment in Southern Kyrgyzstan (Central Asia). Nat Hazards 35:395–416

Temesgen B, Mohammed MU, Korne T (2001) Natural hazard assessment using GIS and remote sensing methods, with particular reference tot the landslides in the Wondogenet area, Ethiopia. Phys Chem Earth (C) 26:665–675

TERRA (2008). Terra project science. http://terra.nasa. gov. Cited on 30 Sept 2008

Tralli DM, Blom RG, Zlotnicki V, Donnellan A, Evans DL (2005) Satellite remote sensing of earthquake, volcano, flood, landslide and coastal inundation hazards. ISPRS J Photogram Rem Sens 59:185–198

USGS (2008) USGS EROS Data Center. http:// edcftp.cr.usgs.gov/pub/data/disaster/ 200805_Earth-quake_ China/data/. Cited on 10 Oct 2008

Wang X, Xie H, Guan H, Zhou X (2007) Different responses of MODIS-derived NDVI to root-zone soil moisture in semi-arid and humid regions. J Hydrol 340:12–24

Zhang W, Lin J, Peng J, Lu Q (2010) Estimating Wenchuan earthquake of China induced landslides based on remote sensing. Int J Remote Sens 31:3495–3508

Earthquake-Induced Landslide Hazard Zoning of the Island of Hawai'i

Peter Nicholson and Shailesh Namekar

Abstract

The purpose of this study is to develop earthquake induced landslide hazard zoning maps for the Island of Hawai'i using GIS tools. These potential hazard maps can be utilized to prioritize further investigation and to highlight where further recommendations of mitigation methodologies may be appropriate. Landslide analysis is a complex analysis, involving a multitude of factors and it needs to be studied systematically in order to locate the areas prone to landslides. Use of computer-based tools, namely Geographical Information Systems (GIS), has been found to be useful in hazard mapping schemes. Methodology for the current research consists of Qualitative Weight Analysis based on various causative factors and Quantitative Analysis (Slope failure analysis) based on slope stability models. In qualitative weight analysis, different causative factors are grouped according to their relative importance. Depending on the threat posed by each causative factor, the Landslide Susceptibility Index weights were assigned. The problem of missing data is common in any analysis and has certainly been an issue for this study with the lack of data for Hawai'i and Hawaiian soils/rock. One approach to deal with missing values is to delete the incomplete cases from the data set. This approach may disregard valuable information, especially in small samples. An alternative approach is to reconstruct the missing values using the information in the data set. In this analysis, missing data values of the landslide causative parameters, hardness and depth of the soil were obtained using an Artificial Neural Network. In quantitative analysis, the general approach to the landslide zoning method is based on

P. Nicholson (✉) · S. Namekar
Department of Civil and Environmental
Engineering, University of Hawai'i at Manoa, 2540
Dole Street, Holmes 383, Honolulu, HI 96822, USA
e-mail: pnichols@hawaii.edu

S. Namekar
e-mail: namekar@hawaii.edu

slope stability analyses to determine the Factor of Safety (FS) of the individual slopes based on profiles and specific geotechnical information. Factor of safety is obtained by dividing the forces resisting movement by the forces driving movement. Earthquake induced Landslide hazard zoning maps with ten zones viz., high (10) to low (1), have been developed from the data.

1 Introduction

Recent and continued population growth, development and the expansion of life-lines over hazardous areas are increasing the potential impact of natural disasters in both the developed and developing countries. Landslides are among the most deadly natural disasters as they can often cover a large area with little warning. Landslides can be triggered by many different processes such as rainfall, earthquakes, volcanic eruptions, groundwater change, river erosion, glaciers, ocean waves and human activity, etc. In seismically active regions such as Hawai'i, earthquake shaking is often the dominant cause of widespread landslides.

The term "landslide" refers to a wide variety of processes that result in the downward and outward movement of slope-forming materials, including in-place rock, soil, and/or "fill". The materials may move by falling, toppling, sliding, spreading, or flowing.

In Hawai'i, state efforts had previously focused on responding to landslides and rockfalls affecting State Department of Transportation responsible roadways and facilities. Recently, an effort was made to identify highway locations where landslides/rock falls may be potentially critical or likely. As this was a State Transportation Department project, surveys were generally limited to slopes adjacent to highway alignments or other state facilities. Many locations that may be prone to landslides were likely not identified. Given the deadly nature of earthquake-induced landslides, there is a need to develop techniques that aid in the assessment of such potential hazards.

2 Data Sources

The data required in this research includes topographical data, geotechnical data, geological data, geomorphologic data and historical landslide data. The digital elevation models (DEM) data (10 m) used for identification of slopes angles and heights, was obtained from the UH Coastal Geology Group website. Rainfall data, soil boring data and well water level data was previously collected as part of another study (Thomas 2005). Additional soil data was obtained from the Natural Resources Conservation Service (NRCS), which includes information about hardness, depth to the bedrock, unit weight of soil, clay fractions in percentage, liquid limit and plasticity index. Other geotechnical data was obtained from USGS open file reports prepared in cooperation with the City and County of Honolulu, Department of Public Works and from other available soil boring logs. Some historical earthquake-induced landslide data was obtained from post earthquake reconnaissance reports and personal communications with a State Geologist. Estimates of V_{s30} were extracted (Courtesy of Trevor Allen) from the Predefined V_{s30} map given at http://earthquake.usgs.gov/hazards/apps/vs30/predefined.php (Last accessed March 2012). Ground motion Database was obtained from G.M. Atkinson's website: (Atkinson 2010) http://www.seismotoolbox.ca/GMDatabases.html.

Table 79.1 Rating and weighting for different causative factors in qualitative analysis

Rating	Slope (angle in degrees)	Hardness	Drainage class	Depth to bedrock (inches)	Mean annual rainfall (inches)
1	0–9				0–40
2	9–18	Very strongly cemented	Excessively drained	0–15	41–80
3	19–27				81–120
4	28–36	Strongly cemented	Somewhat excessively drained	16–30	121–160
5	37–45		Well drained		161–200
6	46–54	Moderately cemented	Moderately well drained	31–45	201–240
7	55–63				241–280
8	64–72	Indurated	Somewhat poorly drained	46–60	281–320
9	73–81				321–360
10	82 and above	Weakly cemented	Poorly drained	61 and above	361–400
Weight (%)	30	15	20	15	20

3 Methodology

Landslide analysis is a complex analysis, involving a multitude of factors and needs to be studied systematically in order to locate the areas most prone for landslides. Fieldwork of detecting landslides by conventional methods can be expensive and time consuming. Computer-based tools namely Geographical Information Systems (GIS) may be more efficient in the hazard mapping of landslides by utilizing a variety of digital spatial data.

The Geographical Information System (GIS) has been described as a powerful set of tools for collecting, storing, retrieving at will, transforming and displaying spatial data from the real world for a particular set of purposes. Over the past three decades, GIS has attracted great attention in the assessment of natural disasters. Many scientists and engineers have attempted to assess landslide hazards and their spatial distributions using GIS. The literature on this subject is voluminous (Khazai and Sitar 2000; Van Westen 2000; Lee et al. 2003, etc.), but a review of the literature reveals that virtually no work

has been done on the Big Island of Hawai'i to assess landslide hazards.

Methodology for the current research consists of Qualitative Weight Analysis based on various causative factors and Quantitative Analysis based on slope stability models.

4 Qualitative Weight Analysis

In the qualitative weight analysis, different causative factors were listed, rated and given a weighting according to their presumed relative importance (given in Table 79.1). Depending on the threat posed by the culmination of all causative factors, the Landslide Susceptibility Index was generated.

The weight is a factor based on an assumed percentage of relative importance among factors such as slope, hardness, drainage class, depth to the bedrock, and rainfall. The rating is the "score" given to each factor according to the relative importance of site characteristics affecting each factor. For example, if slope is more important than drainage in landslide occurrence, more value is given to the slope factor. In this

study, weights and ratings were determined based on expert opinions, educated background and historical landslide data. A sensitivity analysis was carried out to characterize the relative importance of weights for each causative factor.

The input of factor weights and ratings, while somewhat subjective but based on research and education, can be varied for additional sets of 'results'. Based on sensitivity analyses using a wide range of 'reasonable' input parameters, it is not anticipated that results would be significantly different than those presented.

Landslides are essentially gravity-type, hence; the degree of slope was given a prime importance and hence 30 % weight was assigned. Rainfall and drainage were also considered of high importance since high rainfall and poor drainage are known to cause landslides by saturating soil (adding to its weight) and/or releasing debris sitting on bedrock on a 'lubricated' slide surface. Considering the importance of these two causative factors, each one was assigned with 20 % weight. The remaining causative factors included hardness, and the thickness of soil. Each of these were assigned with 15 % weight. The data layers were integrated into the GIS environment with the Weighted Overlay Analysis.

Weighted Overlay is a technique for applying a common measurement scale of values to dissimilar inputs to create an integrated analysis. In this study, input raster of each causative factor was reclassified into a common evaluation scale of 1–10. Then, the cell value of each input raster was multiplied with the raster's weight of importance (given in the last row of Table 79.1). The resulting cell values were added together to produce the final output raster with cell values in a range of 1–10. Results of the calculations (i.e. the cell values of final output raster), were then plotted with a color scheme in a final map with ten zones of landslide vulnerability (viz., Red (High) (10) to Green (Low) (1).

The problem of missing data is common in any analysis. One approach to deal with missing values is to delete the incomplete cases from the data set. This approach may disregard valuable information, especially in small samples. An alternative

approach is to reconstruct the missing values using the information in the data set. Gupta and Lam (1996) showed that an Artificial Neural Network (ANN) approach is a useful tool for reconstructing missing values in multivariate analysis. Kuligowski and Barros (1998) used ANN to estimate missing rainfall data. Abudu et al. (2010) used ANN to infill missing daily evapo-transpiration data. In this analysis, missing data values of the landslide causative parameters, hardness and depth of the soil were obtained using an Artificial Neural Network. The inputs to the neural network were the available causative factors while the output was the missing causative factor.

An ANN is a parallel-distributed information-processing system that resembles a function of the human brain by acquiring knowledge through learning by examples. It is composed of elements whose functions are analogous to the most elementary processes of biological neurons. A typical network consists of a number of neurons or nodes arranged in input, hidden, and output layers. There can be multiple hidden layers, which serve as the primary information repository and processing system. Each node sums up the information from an upper layer, activates a nonlinear data squashing process, and transmits a single signal to all the nodes in the next layer. Such a feed-forward network can be trained using a back-propagation algorithm (FFBP), which in its simplest form, involves minimization of the error between realized and target outputs. ANNs have been used to estimate complex cause–effect relationships in a number of geotechnical engineering applications (e.g., Goh et al. 1995; Juang et al. 1997; Kung et al. 2007, to name just a few).

The final hazard zoning map using this qualitative analysis is shown in Fig. 79.1.

5 Quantitative (Slope Stability Model) Analysis

In a quantitative analysis, the landslide zoning method is based on slope stability models. The general approach is to determine the Factor of Safety (FS) of the individual slopes based on
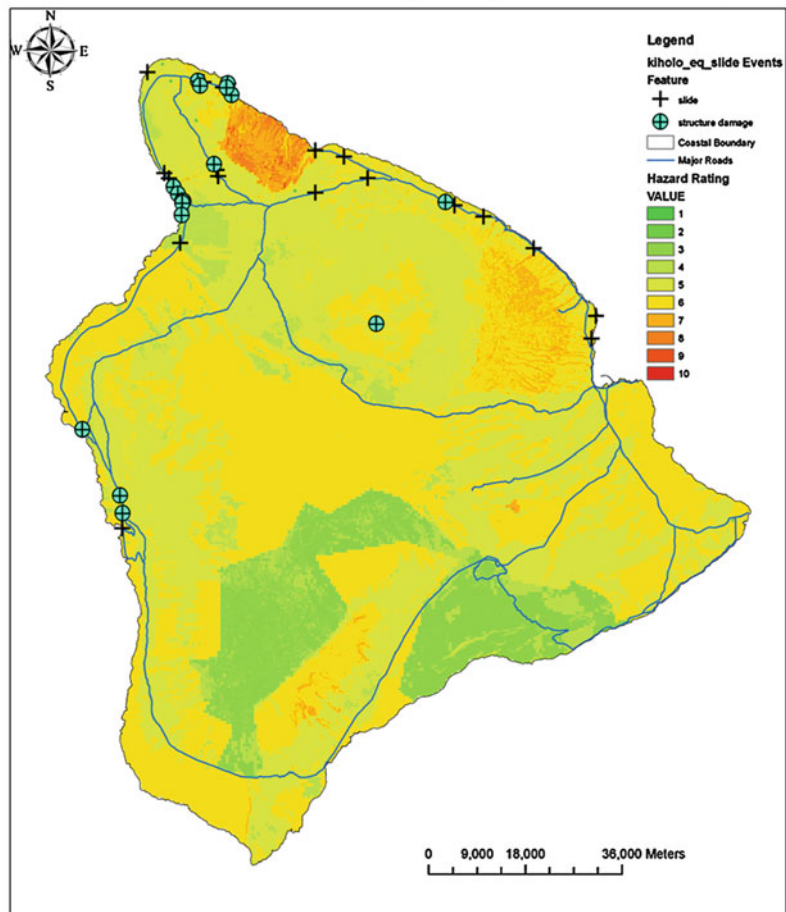
profiles and specific geotechnical information.
Factor of safety is obtained by dividing the
forces resisting movement by the forces driving
movement.

   In the current study, four regions were
selected for more detailed study; North Hawai'i,
Kona, Hamakua and Hilo, as shown in Fig. 79.2.
These regions were selected based on proximity
to developed property and lifelines along with
availability of data. A Quantitative analysis was
carried out on each of these four regions. The
availability of recent post-earthquake landslide/
rockfall data (2006 Kiholo Bay earthquake) was
also considered as another reason to select these
regions for development and verification of this
methodology.

5.1   Infinite Slope Model

The infinite slope model is frequently incorporated
in landslide hazard analysis (Christian and Urzua
1998; Luzi et al. 2000; Refice et al. 2002; Khazai
and Sitar 2002, Mahdavifar et al. 2008). It is a one-
dimensional model describing the stability of
slopes with an infinitely long failure plane. Failure
is assumed to occur by sliding of a slab of soil on a
planar slip surface, which is parallel to the ground
surface. It is typically only applicable to shallow
translational slides. It is frequently difficult to
obtain detailed geotechnical data on a large scale.
Infinite Slope model requires relatively little
geotechnical information. Hence, it is commonly
used for certain types of shallow slides.

Fig. 79.2 Region selection for quantitative (slope stability) analysis

Regions for Quantitative Analysis
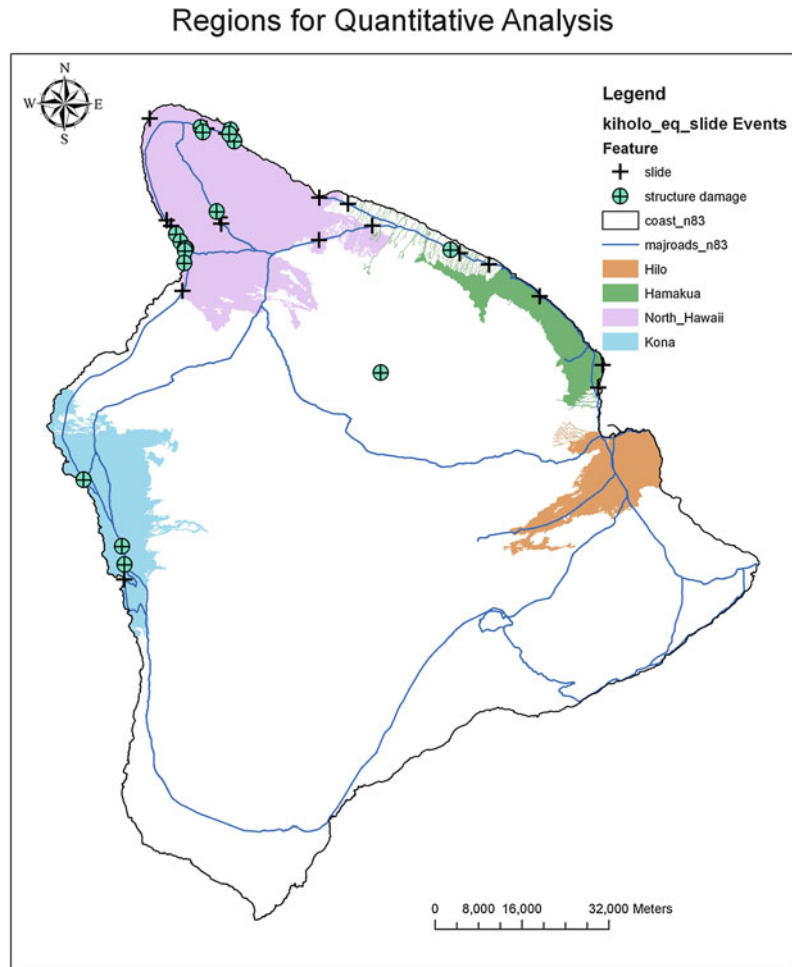
$$FS = \frac{c' + (\gamma - m\gamma_w)H\cos^2\alpha\tan\phi'}{\gamma H\sin\alpha\cos\alpha} \quad (79.1)$$

Where,

c' is effective cohesion (KPa)

γ is unit weight of sliding mass (KN/m^3)

m is groundwater saturation ratio

γ_w is unit weight of water (KN/m^3)

H is depth of failure surface below the ground surface (m)

α is slope surface angle (°)

ϕ' is effective friction angle (°)

The residual shear strength is primarily used to evaluate slope stability of existing landslides and the stability of deposits with preexisting shear surfaces or similar discontinuities. There

have been numerous landslides on the Island of Hawai'i. Since we do not have records of each of these slides, it is conservative to consider preexisting shear surfaces or similar discontinuities for the entire Island by considering the residual shear strength for evaluating slope stability for the entire region. While this may be considered overly conservative, it would provide an upper bound for the hazards, including consideration for soils with significant strength loss potential. It also allows for use of a much larger data set. The value of effective cohesion should be taken as zero when considering residual shear strength (Stark et al. 2005).

Hence, for residual shear strength, Eq. 79.1 can be rewritten as,

$$FS = \frac{(\gamma - m\gamma_w)H\cos^2\alpha\tan\phi'_r}{\gamma H\sin\alpha\cos\alpha} \qquad (79.2)$$

Equation (79.2) was used to determine factor of safety in the cases of cohesive soils while equation 79.1 was used to determine factor of safety in the cases of non-cohesive soils.

Extensive research and development was undertaken in the late 1960s through the 1970s regarding the measurement techniques for residual shear strength, and the correlation between the residual friction angle ϕ'_r and various index properties of the soil. Soil properties such as the liquid limit (LL), the plasticity index (PI), and the clay fraction (CF) were used to define residual values. Such correlations are very useful to estimate the residual shear strength of the soil when soil samples and funds are not available for soil testing (Tiwari and Marui 2005). Due to the lack of a significant amount of shear strength data for the entire Island of Hawai'i, it was decided to develop a prediction model using Adaptive Neuro Fuzzy Inference System (ANFIS) based upon available data pairs of residual friction angle and available soil parameters for various locations including Hawai'i. This derived residual friction angle data was then used in slope stability analyses. Other inputs to the infinite slope equation included, slope angle, which was derived from DEM data at 10 m resolution, water level data obtained from boring and well water level data previously collected, and soil thickness and soil unit weight collected from the NRCS reports. Analysis results showed a static factor of safety greater than or equal to one at most of the locations except a few. This may be due to selected geotechnical parameters being higher or lower than the actual parameters or to the fact that we are using a conservative approach by considering residual shear strength properties.

ANFIS incorporates use of fuzzy logic to process numerical input, fragmenting it into many components and combining these into values leading to the output. ANFIS was first introduced by Jang (1993). ANFIS models are now being employed in a wide variety of applications such as modeling, decision-making, and signal processing and control. The network paradigm used is a multi layer feed forward back propagation (FFBP) network.

6   Seismic Analysis

The Island of Hawai'i has one of the highest levels of seismic hazard in the US (Klein et al. 2001). In Hawai'i, earthquake shaking is often the dominant cause of widespread landslides. The 15 October 2006 moment magnitude (M) 6.7 Kiholo Bay earthquake, which caused more than $200 million in damage, is a recent example of the Big Island's seismic hazard. Hence, it is important to consider seismic analysis in landslide hazard zoning for the Island of Hawai'i.

Taking into account, the horizontal earthquake inertial force, kW, proportional to the weight of the body, W, by a critical acceleration k, the factor of safety becomes (Van Weste 1996; Luzi et al. 2000),

$$FS = $$
$$\frac{c' + (\gamma H\cos^2\alpha - \gamma Hk\cos\alpha\sin\alpha - \gamma_w h_w\cos^2\alpha)\tan\varphi'}{\gamma H\sin\alpha\cos\alpha + \gamma Hk\cos^2\alpha}$$
$$(79.3)$$

The critical acceleration can then be derived from the slope stability equation. Setting FS equal to unity for infinite slope analysis in Eq. (79.2), the corresponding critical acceleration (k value when FS = 1) can be calculated as

$$a_y = \frac{c'/\cos^2\alpha + (\gamma - m\gamma_w)H\tan\varphi' - \gamma H\tan\alpha}{\gamma H + \gamma H\tan\alpha\tan\varphi'}$$
$$(79.4)$$

When considering residual shear strength, Eq. (79.4) becomes,

$$a_y = \frac{(\gamma - m\gamma_w)H\tan\phi'_r - \gamma H\tan\alpha}{\gamma H + \gamma H\tan\alpha\tan\phi'_r} \qquad (79.5)$$

Table 79.2 Hazard rating scale for difference in peak ground acceleration and critical acceleration

(Difference in PGA and critical acceleration) (g)	Hazard rating
−0.6 to 0.5	1
−0.5 to 0.4	2
−0.4 to 0.3	3
−0.3 to 0.2	4
−0.2 to 0.1	5
−0.1 to 0	6
0 to 0.1	7
0.1 to 0.2	8
0.2 to 0.3	9
0.3 to 0.4	10

7 Peak Ground Acceleration

The peak ground acceleration (PGA) is the most commonly used ground motion parameter in seismic hazard assessment. A number of regression equations of attenuation relationships for different geographic and tectonic environments have been developed. For Hawai'i, a new PGA prediction model was developed using Adaptive Neuro Fuzzy Inference System (ANFIS). The available PGA values at various USGS strong motion stations during various earthquakes were used for model development. The model needs Earthquake magnitude, hypocentral distance and average shear wave velocity down to 30 m (V_{s30})

Fig. 79.3 Potential hazard map for North Hawai'i using quantitative analysis

North Hawaii Quantitative Analysis Hazard Rating
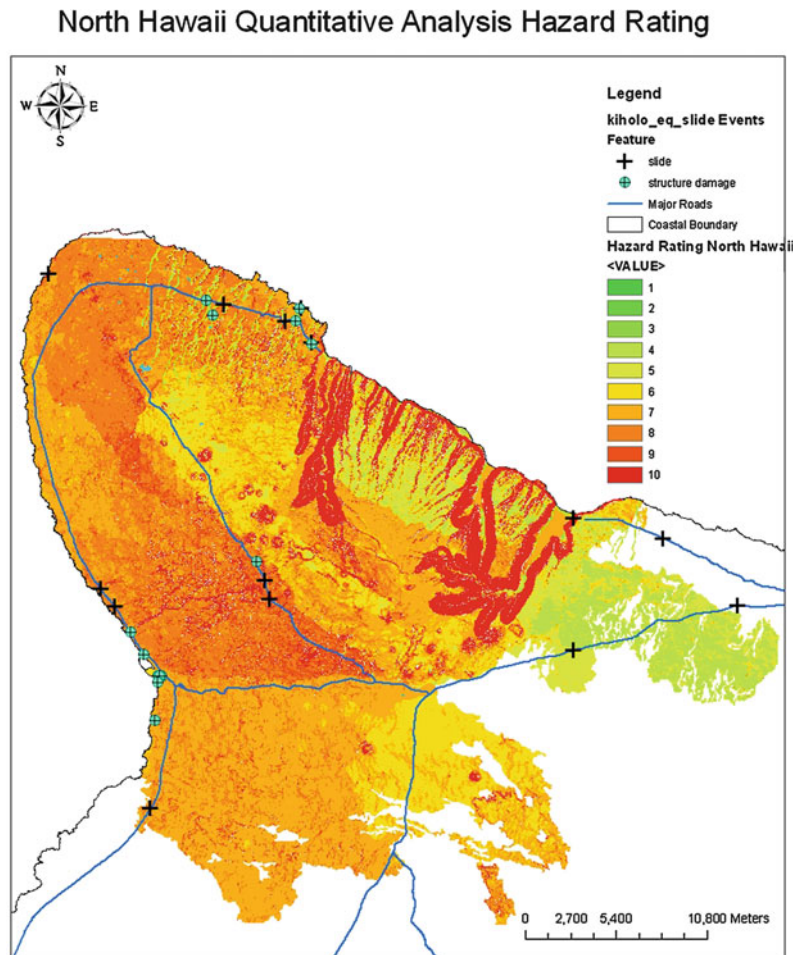
Fig. 79.4 Potential
hazard map for Kona using
quantitative analysis
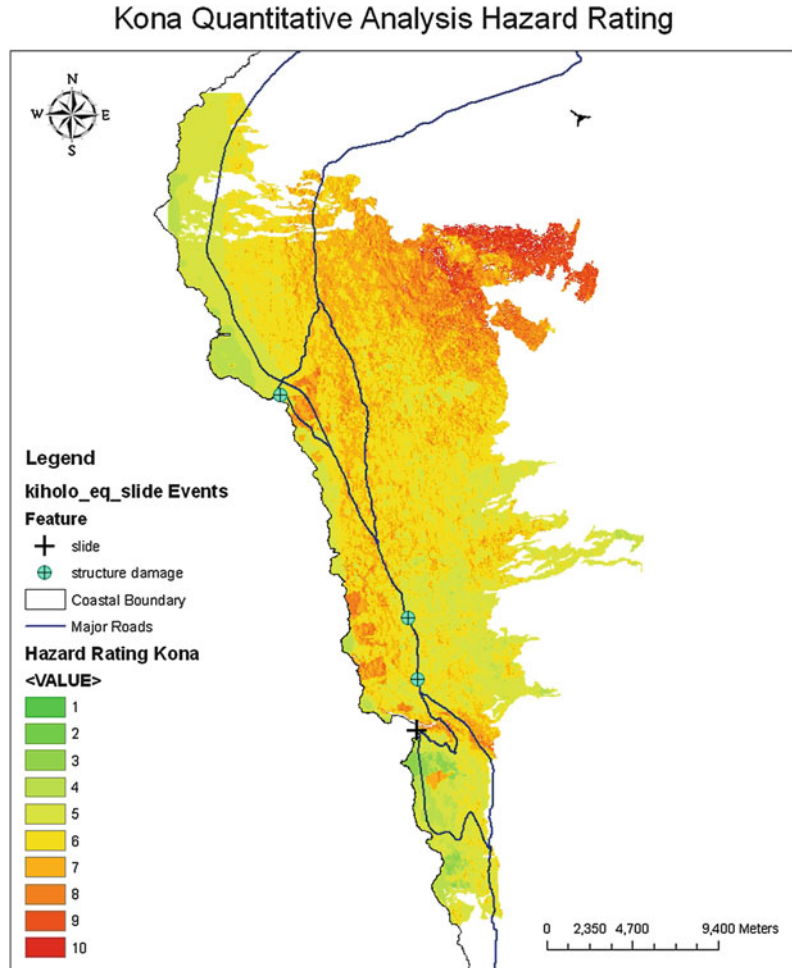
as input, and gives PGA as output. Shear wave
velocity (V_{s30}) for the entire island was obtained
from a USGS predefined V_{s30} map for Hawai'i.
Hence, for a given earthquake magnitude, loca-
tion and depth and V_{s30}, it is possible to calculate
a design PGA for entire Island. The PGA was
calculated for 2006 Kiholo Bay Earthquake event
for the example provided here.

This PGA was compared with critical accel-
eration a_y. Based on difference in PGA and
critical acceleration, a hazard rating scale was
then developed as Table 79.2. The first column
of the Table was obtained by subtracting critical
acceleration from PGA. Hence, when PGA was
smaller than the critical acceleration, the

difference was negative. This negative value of
difference was given a lower hazard rating while
positive difference (i.e., PGA higher than critical
acceleration) was given a higher hazard rating.
Based on this hazard rating scale, hazard maps
were developed for all four regions, North
Hawai'i, Kona, Hamakua and Hilo as shown in
Figs. 79.3, 79.4, 79.5, 79.6 respectively.

8   Validation

Validation is an important step whereby high
landslide susceptibility areas identified by the
analyses are consistent with past slope failure

Fig. 79.5 Potential hazard map for Hamakua using quantitative analysis

9   Conclusion
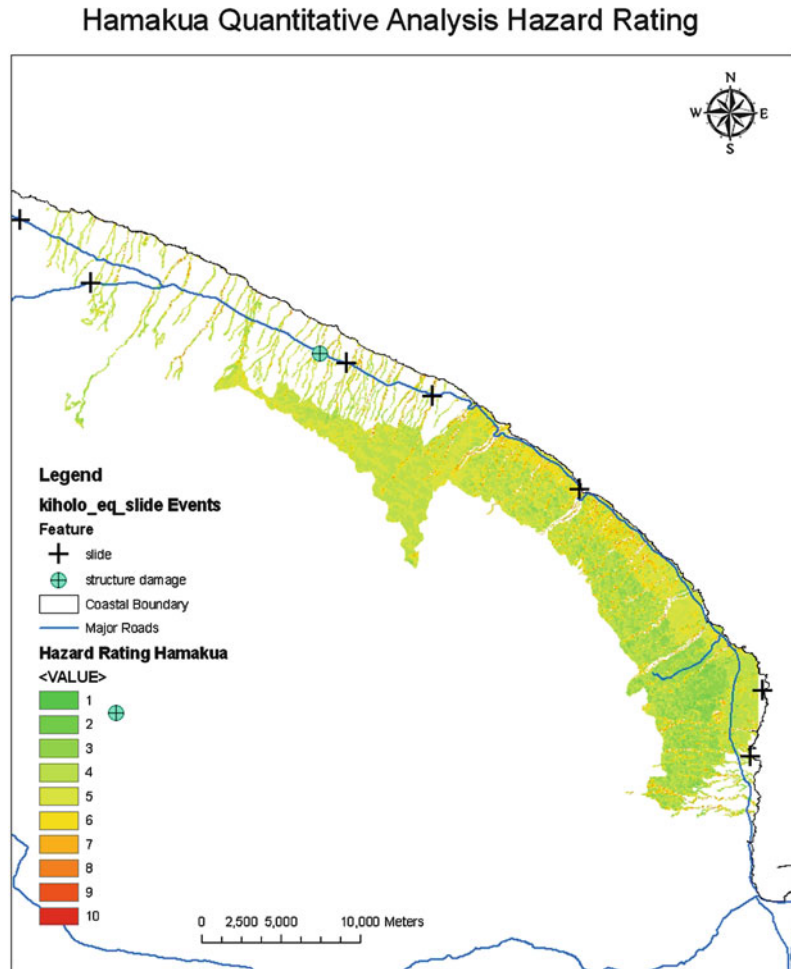
areas. Throughout history the island of Hawai'i has been struck by numerous earthquakes with magnitudes ranging up to 7.9. The recent Kiholo Bay Earthquake of 2006 caused various slides and structural damages which were reported in the literature. There were a few locations where various post-earthquake features such as slides and structural damages were noted. These are shown in the maps of Figs. 79.1, 79.2, 79.3, 79.4, 79.5, 79.6. Slide data obtained from post-earthquake reports was used for validation purposes in this project.

The Big Island of Hawai'i is located in an area of active seismicity where earthquake-induced landslides are typical. As very little mapping has been done to identify locations most susceptible to earthquake-induced landslides, a study was undertaken to map the potential landslide hazards using digitized data in a GIS format. Both qualitative and quantitative analyses were employed. The qualitative analysis was based on

Fig. 79.6 Potential hazard map for Hilo using quantitative analysis
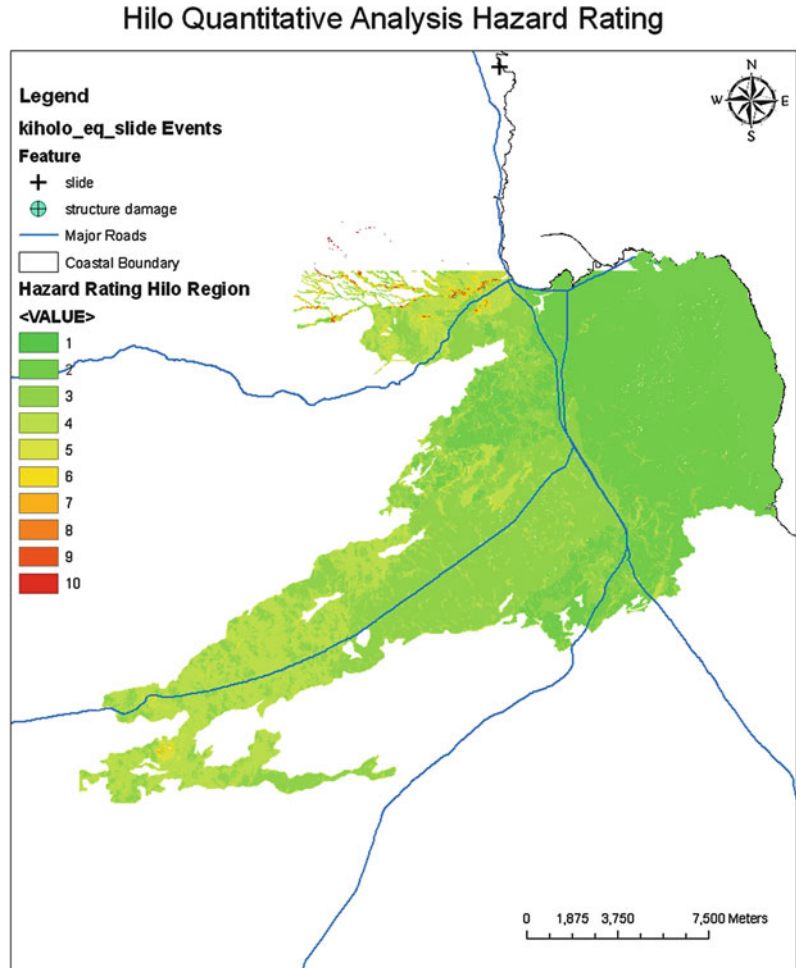
rating and weighing a number of factors considered to be most influential on landslide susceptibility. The quantitative analysis was based on conventional slope stability models. A number of tools were utilized in this study including the use of artificial neural networks (ANN) and adaptive Neuro Fuzzy Inference Systems (ANFIS) to aid in supplementing missing data. A decision was also made to use conservative residual soil strength parameters in the stability analyses as an upper bound for landslide susceptibility and to accommodate the much greater

and complete data set that could be inferred for these values.

To address seismic stability, pseudo-static parameters were incorporated into the model. As an example, the idealized ground motions from the recent 2006 Kiholo Bay earthquake were used in stability analyses. The results were validated in part by the recorded slides and damage assessments from that earthquake. The resulting potential landslide hazard maps based on the analyses employed in this study matched reasonably well with landslide occurrence and

damages following the 2006 Kiholo Bay earthquake for the zones studied.

Earthquake-induced landslide hazard zoning maps provide valuable information on the slope stability over a large area, which may be of interest for land use, infrastructure planning, engineering and hazard mitigation design. The methodologies formulated here could be easily transported to other regions where mapping of preliminary earthquake-induced landslide potential is desired, especially where the data is somewhat lacking and/or where this type of mapping has yet to be implemented.

References

Abudu S, Bawazir AS, King JP (2010) Infilling missing daily evapotranspiration data using neural networks. J Irrigation Drainage Eng 136(5):317–325

Atkinson G (2010) Ground-motion prediction equations for Hawai'i from a referenced empirical approach. Bull Seismol Soc Am 100(2):751–761

Christian JT, Urzua A (1998) Probabilistic evolution of earthquake induced slope failure. J Geotech Geoenviron Eng 124(11):1140–1143

Goh ATC, Wong KS, Broms BB (1995) Estimation of lateral wall movements in braced excavations using neural networks. Can Geotech J 32:1059–1064

Gupta A, Lam MS (1996) Estimating missing values using neural networks. J Oper Res Soc 47:229–238

Juang CH, Elton DJ (1997) Predicting collapse potential of soils with neural networks. Transp Res Rec 1582:22–28

Jang J-SR (1993) ANFIS: adaptive-Network-based Fuzzy Inference Systems. IEEE Trans Sys Man Cybern 23:665–685

Khazai B, Sitar N (2000) Assessment of seismic slope stability using GIS modeling. Geogr Inf Sci 6:2

Klein FW, Frankel AD, Mueller CS, Wesson RL, Okubo PG (2001) Seismic hazard in Hawai'i: high rate of large earthquakes and probabilistic ground-motion maps. Bull Seismol Soc Am 91:479–498

Kuligowski RJ, Barros AP (1998) Using artificial neural networks to estimate missing rainfall data. J Am Water Res Assoc 34(6):1437–1447

Kung TC, Hsiao CL, Schuster M, Juang CH (2007) A neural network approach to estimating excavation-induced wall deflection in soft clays. Comput Geotech 34:385–396

Lee S, Ryu J, Min K, Won J (2003) Landslide susceptibility analysis using G.I.S. and artificial neural network. Earth Surf Proc Land 28:1361–1376

Luzi L, Pergalani F, Terlien MTJ (2000) Slope vulnerability to earthquakes at subregional scale, using probabilistic techniques and GIS. Eng Geol 58:313–336

Mahdavifar M, Jafari MK, Zolfaghari MR (2008) GIS-based real time prediction of Arias intensity and earthquake-induced landslide hazards in Alborz and Central Iran. In: Proceedings of the 10th international symposium on landslides and engineered slopes, 30 June–4 July 2008, Xi'an, China

Refice A, Capolongo D (2002) Probabilistic modeling of uncertainties in earthquake induced landslide hazard assessment. Comput Geosci 28:735–748

Stark TD, Choi H, McCone S (2005) Drained shear strength parameters for analysis of landslides. J Geotech Geoenviron Eng 131(5):575–588

Thomas AE (2005) Application of GIS model to map liquefaction susceptibility on Maui, M.S. Thesis, University of Hawai'i

Tiwari B, Marui H (2005) A new method for the correlation of residual shear strength of the soil with mineralogical Composition. J Geotech Geoenviron Eng 131(9):1139–1150

Van Westen CJ (2000) The modeling of landslide using GIS. Surv Geophys 21:241–255 (Kluwer Academic Publishers)

Assessment of Hazard and Contributing Factors of Landslides in Abay Gorge in Ethiopia

80

Takeshi Kuwano, Mitsuya Enokida, Satoru Tsukamoto, Kensuke Ichikawa, Atsushi Nakagawa and Tomonari Takeuchi

Abstract

Main road 3, a major arterial road in Ethiopia, steeply climbs nearly 1,500 m over 40 km through the Abay Gorge. It is plagued by landslides in the rainy season from June to September. Some of these are up to 2-km wide and would jeopardize this vital link. To fundamentally solve this problem it is necessary to implement appropriate countermeasures after clarifying the mechanisms that trigger landslides in this stretch of road. In this paper, we discuss the hazard of each landslide and identified the factors to clarify the mechanisms. A quantification theory, which is a type of multivariate statistical analysis, is adopted as the assessment method in this paper. The theory assesses the hazard of each landslide according to disaster causes such as topographic features and geological conditions, and landslide history. The results are represented as a category score, which is a coefficient that correlates to the contribution of each item; and the score is directly influenced by the dependent variable. According to the results of the landslide hazard assessment, we have not only determined unique factors of landslides, but have also ranked them from A (extremely high hazard) to E

T. Kuwano (✉) · M. Enokida · S. Tsukamoto ·
K. Ichikawa · A. Nakagawa · T. Takeuchi
Disaster and Water Resources Management
Division, Overseas Operations Department, Kokusai
Kogyo Co., Ltd, Kamaishi, Japan
e-mail: kuwanota@gmail.com

M. Enokida
e-mail: enokida@jce.co.jp

S. Tsukamoto
e-mail: satoru_tsukamoto@kk-jrp.jp

K. Ichikawa
e-mail: kensuke_ichikawa@kk-grp.jp

A. Nakagawa
e-mail: nakagawa.atsushi@jica.go.jp

T. Takeuchi
e-mail: takeuchi.tomonari@jica.go.jp

(lowest hazard) in the Abay Gorge. As a result, fourteen landslides were assigned to rank A. Assessing hazards and identifying mechanisms of landslides enable the most appropriate countermeasures to be implemented.

Keywords

Hazard · Assessment · Multivariate statistical analysis · Quantification theory · Countermeasure

1   Introduction

In the Federal Democratic Republic of Ethiopia (hereinafter Ethiopia), serious landslides have been occurring along mountainous roads and affecting the road traffic in the rainy season. Therefore, it is necessary to implement appropriate countermeasures after clarifying the mechanisms that trigger landslides in this stretch of road. However it is difficult for engineers who have little experience on landslide investigation to clarify the mechanism and to evaluate the hazard. For such engineers in general, a road disaster inspection is suitable to identify easily the hazard on landslide.

In this paper, to prepare the inspection sheet in the Ethiopia where there are few engineers who little experience on landslide, we discussed the factors and their contributions that affect on each landslide and decide the item in the list on the road disaster inspection sheet in the Ethiopia using multivariate statistical analysis, namely Quantification Theory. The discussion helps us understand which feature and condition we should pay attention to identify accurately the hazard on landslide in the Ethiopia. Contents of this paper are mainly based on JICA (2011) and JICA (2012).

2   Study Area

Main road 3, a major arterial road in Ethiopia, through Abay Gorge has an elevation difference of 1,060 m over 40 km between Goha Tsiyon and Dejen villages (Fig. 80.1). The road that passes numerous steep cliffs is extremely windy in the gorge. The rainy season is from June to September, with July and August accounting for about 50 % of annual precipitation. Annual average rainfall is 1,394 mm/year (from 49 years of data) in Dejen and 1,195 mm/year (34 years) in Filiklik Village. The geology is characterized by stratified sedimentary rocks capped by a basaltic plateau. The area is plagued by landslides in the rainy season from June to September. Some of which are up to 2-km wide that would jeopardize this vital link.

3   Procedure of Analysis

3.1   Road Disaster Inspection

A road disaster inspection is used for first screening the priority of landslides. The high hazard landslide area determined by the inspection should be investigated and monitored in detail after the screening.

Inspection sheet that is composed of lists to check topographic features and geological condition at site is used for the inspection (Fig. 80.2). The check sheet of the inspection should be prepared for each site because the topographic features and geological condition is different for each site.

In this study, the road disaster inspection was carried out for 90 landslides in the Abay Gorge to identify the priority for countermeasures. The inspected items are topographic features, geological condition and history of landslide. The inspection results are compared with the hazard score of landslides determined by geotechnical experts with more than 20 years experience. The hazard score by the

Fig. 80.1 Location map
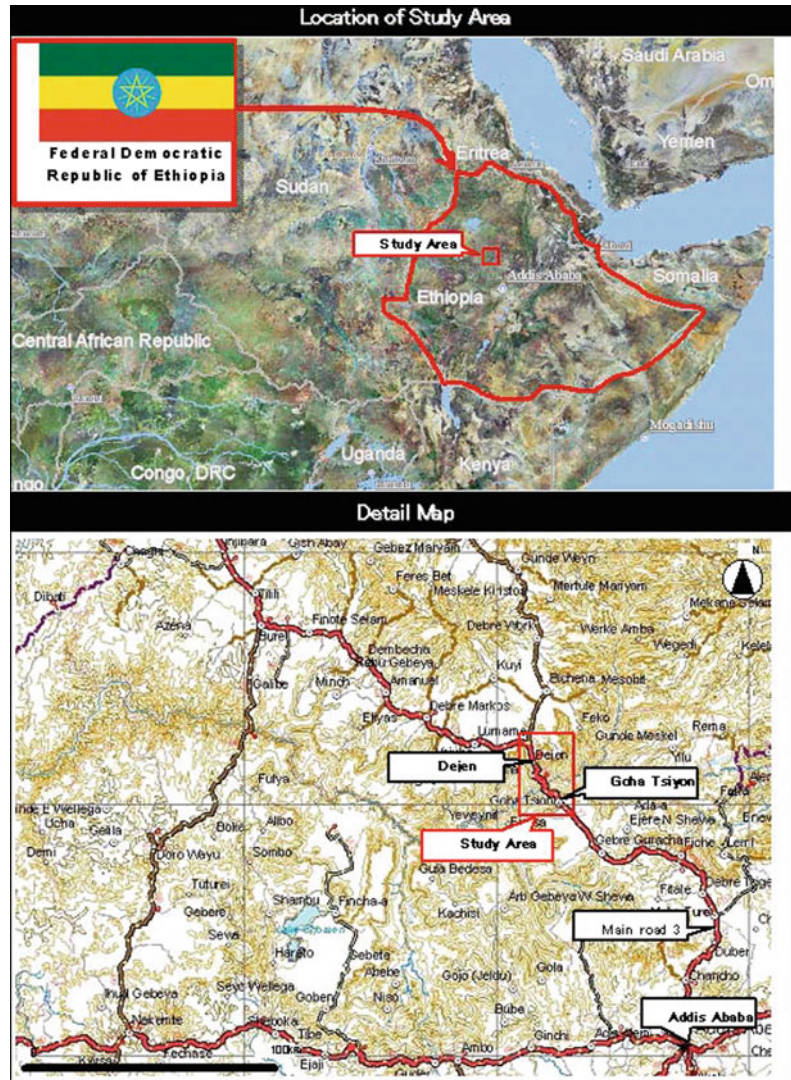
experienced experts is 0–20, that the high score means high hazard site. While the hazard score is considered as objective data, the comparison is made using multivariate statistical analysis, quantification theory type 1.

3.2 Quantification Theory Type 1

The basic factors of landslides do not only depend on topographic features and geological conditions, but also on water condition and landslide history. These items intricately affect the basic factors. The quantification theory facilitates analyses for intricate data.

In this study, we utilized type 1 quantification theory. This type enables quantitative dependent variable to be predicted based on various qualitative explanatory variables. Dependent variables are the desired result of analyses. Explanatory variables items affect dependent variables. Items and categories of qualitative explanatory variables in this study are shown in Table 80.1.

Fig. 80.2 Example of the road disaster inspection sheets

4 Results

Category score is indicated in Table 80.2. This is a coefficient that correlates to the contribution of the item, and it influences the dependent variable directly. The landslide hazard is large when the category score is high, and conversely is small when the category score is low.

Category range and partial correlation coefficient on each item are indicated in Table 80.3. Range is the difference between maximum and minimum values of category score, and indicates the contribution of the dependent variable. In other words, an item with a large range has a greater effect when predicting the dependent variable. Partial correlation coefficient is the index that shows the contribution of each item on the dependent variable, and can be considered to be a correlation coefficient that does not influence other items. The contribution becomes larger the closer the value comes to 1.

These analysis results lead to the conclusion that "main rock formation of landslide body" and "result of photo interpretation" affected the hazard of a landslide greatly, and the "geological structure" seldom affected it.

5 Discussion of High Priority Area

5.1 Prediction and Accuracy

Figure 80.3 indicates scattered plots of the actual measurement values and the prediction values that analyzed using the quantification theory. While the measurement value is the hazard score by the experienced experts that the score 0 is lowest and 20 is highest, the prediction value is calculated by adding all category scores on each item in Table 80.2. Coefficient of determination on the hazard on landslide is 0.74. The value indicates that regression formula has

Table 80.1 Items and categories in the type 1 quantification theory

Item	Category-1	Category-2	Category-3	Category-4	Category-5	Category-6	Category-7
Result of photo interpretation	Exist clearly	Exist but partial and not clear	Exist but not clear				
Surface anomalies	Large and new cracks, steps and subsidence	Small and old cracks, steps and subsidence	Slight deformation	No anomalies			
Geological structure	Fault, fracture zone, dip slope	Undip slope					
Main rock formation of landslide body	Colluvial deposit	Pyroclastic materials	Basalt	Limestone	Gypsum	Siltstone	Sandstone
Hydrological feature	Much springs/seepage	Little springs/little seepage	Surface water/ trace of water	No water observed			
Existing record (Documents or Patrimony)	Obvious	Slight	None				
Damage on road facilities and houses	Obvious	Slight	None				

Table 80.2 Category scores of the items

Item	Category	Category score
Result of photo interpretation	Exist clearly	2.567
	Exist but partial and not clear	−0.945
	Exist but not clear	−2.189
Surface anomalies	Large and new cracks, steps and Subsidence	0.958
	Small and old cracks, steps and subsidence	0.603
	Slight deformation	−0.381
	No anomalies	−1.625
Geological structure	Fault, fracture zone, dip slope	0.017
	Undip slope	−0.013
Main rock formation of landslide body	Colluvial deposit	0.100
	Pyroclastic materials	2.060
	Basalt	−0.673
	Limestone	0.007
	Gypsum	−2.562
	Siltstone	2.323
	Sandstone	−2.565
Hydrological feature	Much springs/seepage	−1.318
	Little springs/little seepage	0.995
	Surface water/trace of water	0.039
	No water observed	−0.163
Existing record (documents or patrimony)	Obvious	−0.199
	Slight	3.617
	None	−0.549
Damage on road facilities and houses	Obvious	1.569
	Slight	0.632
	None	−1.418
Constant		9.367

Table 80.3 Category range and correlation coefficient of the items

Item	Category range		Partial correlation coefficient	
Result of photo interpretation	4.756	2nd	0.675	1st
Surface anomalies	2.583	5th	0.307	6th
Geological structure	0.030	7th	0.006	7th
Main rock formation of landslide body	4.888	1st	0.526	2nd
Hydrological feature	2.313	6th	0.313	5th
Existing record (documents or patrimony)	4.166	3rd	0.490	3rd
Damage on road facilities and houses	2.987	4th	0.406	4th
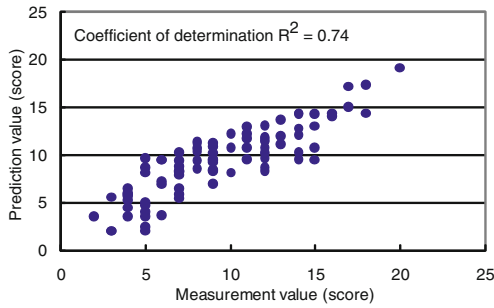
Fig. 80.3 Scattered plots of the score on road disaster inspection

Table 80.4 Results of the priority analysis for countermeasures

Priority rank	Score	Number
A: highest	13-	14
B: high	11–13	14
C: middle	9–11	25
D: low	7–9	14
E: lowest	−7	23

explained about 74 % among the total variation in this analysis. Although the analysis was done by calculating the category scores on all items in this study, the coefficient of determination could be increased by deleting the lower affected items such as "geological structure". However it is necessary to discuss carefully the deletion, addition and/or integration of items because the assortment and the combination of the items would highly affect the results on multivariate statistical analysis in general.

The prediction accuracy for the hazard on landslide is good because the coefficient of determination on the hazard on landslide is 0.74. Therefore scores by using the item and category in the statistical analysis in this study were calculated for each landslide. It is possible to consider the high hazard area on landslide if the score is high.

5.2   High Priority Areas for Countermeasures

The priority for landslide countermeasures has been discussed according to the statistical analysis. As mentioned before, the category score of each category is a coefficient that correlates to the contribution of the landslide. The sum of each score indicates the hazard of the landslide. The higher the score, the higher the hazard; that means the landslide has a higher priority for countermeasures. The hazard of the landslide area in the Abay Gorge were classified A to E, whereby A is highest hazard area and E is lowest, based on the summed scores in this study.

Table 80.4 shows the result of the priority analysis for countermeasures. The location of the high priority sites is referred a figure in Gonai et al. (2012). High rank A and B concentrate on the Tertiary basalt and Jurassic limestone with siltstone and shale. The basalt intercalates thin pyroclastic layers, which could be a trigger of landslide. The limestone is relatively soft and forms gentle slope with debris, which could be erosive materials.

However, the actual priority for landslide countermeasures should be finalized taking into consideration the difficulty and feasibility of design and construction, the budget and the request of the users.

6   Summary and Future Plans

This study is summarized as follows.
1) It turns out, using quantification theory, that "result of photo interpretation" and "main rock formation of landslide body" should be paid attention, which affect the hazard of landslide greatly, and "geological structure" has seldom affected it.
2) Coefficient of determination on the hazard of landslide is 0.74, utilizing significant items and categories. These coefficients indicate that it is good accuracy for the prediction.
3) The hazard on the landslide area in the Abay Gorge were classified A to E, based on the summed scores. The number of A that is highest hazard area is 14, B is 14, C is 25, D is 14, and E that is lowest hazard area is 23.

As the next step after the screening by the quantification theory type 1, it is necessary to investigate accurate hazard and risk condition by

drilling surveys and monitoring. The actual priority for the landslide countermeasures should be finalized taking into consideration the difficulty and feasibility of design and construction, the budget, and the request of the users.

References

JICA (2012) Final report, The project for developing countermeasures against landslides in the Abay River Gorge in the Federal Democratic Republic of Ethiopia

JICA (2011) Manual for survey and analysis on landslide, the project for developing countermeasures against landslides in the Abay River Gorge in the Federal Democratic Republic of Ethiopia

Gonai Y, Tsukamoto S, Enokida M, Ichikawa K, Nakagawa A, Takeuchi T (2012) Case example of GIS utilization on Abay Gorge's landslide survey in Ethiopia, in this proceedings

Risk Assessment for the Earthquake-Induced Slope Failures Using the Micro-Zoning Technique Applied for Mountain Area in Japan

81

Akio Yamamoto, Shun-ichi Azuma, Yoshiaki Inagaki, Katsuhiro Shirai and Tetsuro Kitahara

Abstract

Many prefectures in Japan have been provided the local disaster management plan for the future earthquake damage. The seismic micro-zoning technique has been used frequently to estimate the damages of earthquake and to make earthquake disaster reduction plans. This paper is specified the earthquake-induced slope failures and reviewed the risk assessment methods in the seismic micro-zoning technique. The new methods of risk assessment for earthquake-induced slope failures are introduced and indicate the validity for the earthquake disaster management plans.

1 Introduction

Every year there is a great loss of people's lives and property in Japan due to earthquake disasters. Especially Many people have been injured because of Tsunami at the 2011 off the Pacific coast of Tohoku Earthquake. In this earthquake, there are many types of damages, for example, liquefaction damage, slope failures and developed lands damage. So slope failures are frequently happened in earthquake because of mountainous area are very wide and there are many houses directly under the steep slopes in Japan.

There are many slope failures at Mid-Niigata Prefecture Earthquake in 2004, Iwate-Miyagi Nairiku Earthquake in 2008 and the 2011 off the Pacific coast of Tohoku Earthquake. The great loss of houses and lives are happened by these earthquakes.

For these earthquake disasters, the government in Japan and many local government have been provided the local disaster management plan for the future earthquake damage. The seismic micro-zoning technique has been used frequently to estimate the damages of earthquake and to make earthquake disaster reduction

A. Yamamoto (✉) · S. Azuma · Y. Inagaki · K. Shirai
Earthquake Disaster Prevention Department, Oyo Corporation, Tokyo, Japan

T. Kitahara
Sabo Consulting Department, Oyo Corporation, Tokyo, Japan

plans. These estimation of damages contains seismic motion (seismic intensity, PGA and PGV), liquefaction, slope failure, Tsunami flood, houses damage by earthquake and liquefaction, earthquake fire and loss of lifelines for countermeasures of future earthquakes. And more, the methods was developed for the reduction of people's lives-damage and houses-damage has been estimated if the earthquake-proof retrofit of houses will be achieve by 2015 for the effective earthquake management plans.

This paper is specified the earthquake-induced slope failures and reviewed the slope failure risk assessment methods in the seismic micro-zoning technique. The new methods of risk assessment for earthquake-induced slope failures are introduced and indicate the validity for the earthquake disaster management plans.

2 The Previous Method for Slope Failure Risk Assessment

The previous method for slope failure risk assessment by the seismic micro-zoning technique has been used mainly due to estimation methods of slope failure assessment by rain. This method developed by the Ministry of Land, Infrastructure, Transport(MLIT) as the inspection of steep slope failure maintenance by rain along the highway shown in Table 81.1a,b and c. The method of earthquake risk assessment is used frequently without factors of maintenance and weight in Table 81.1b. This earthquake risk assessment method basically used by the sum of scores of rain risk and added weight of estimated seismic intensity of the target earthquakes and established the slope failure risk by earthquake.

This slope failure assessment methods began to use in seismic hazard survey with the seismic micro-zoning technique by Saitama Prefecture(1982) and following Miyagi Prefecture(1986) and recently used by Tottori

Prefecture(2005), Cabinet Office(2005), Tokyo Metropolitan (2012). This method is shown in Tables 81.2a,b in Saitama Prefecture (1982). This method has been used many years until now to assess slope failure risk.

The advantage of this method as follows:

i. Location of slope is known because of using specified area of steep slope data.
ii. Available of slope basic data, such as height, slope, gradient of slope, and number of houses directly under the slope.
iii. Easily assessment of slope failure by earthquake because of the utilization of the slope failure risk assessment by rain.

The weak point of this method as follows:

a. There are many steep slope other than the specified area of steep slope data.
b. This method estimate only relative evaluation of slope failure risk and then there is no estimation of mechanism of slope failure.
c. Accuracy of the estimation of relative evaluation of slope failure risk is unknown as compared by the real slope failure damages.

Next chapter we will introduce the comparison by this method estimation and the real slope failure damage in 1978 Miyagi-ken-oki Earthquake in next chapter.

3 Assessment of Slope Failure Risk and Real Damages

The method of assessment of slope failure risk is the same as Chap. 2 in this paper. This method is shown in Table 81.3 as Miyagi Prefecture (1986). This table shows the (a), (b), (c) as the slope failure risk rank by rain and (a) is the most dangerous risk. Then the slope failure risk by earthquake is developed the estimated the seismic intensity to the target earthquake as the division of the 6 Upper, 5 Upper to 6 Lower, 4 Upper to 5 Lower and 4 Lower. The result of estimation of the slope failure risk rank are rank A, rank B and rank C.

Table 81.1 Slope failure factors by rain

No.	Item	Item2	Score	Remarks
(a) Slope failure factors and weights by rain.				
1	Height of slope (H)m	H < 10	3	–
		10 ≦ H < 30	7	
		30 ≦ H < 50	8	
		50 ≦ H	10	
2	Gradient of slope (α)	α < 1:1.0	1	–
		1:1.0 ≦ α < 1:0.6	4	
		1:0.6 ≦ α	7	
3	Overhang of slope	Overhang without slope stabilization	7	Overhanging of slope especially rock slope
		Overhang with slope stabilization	4	
		No Overhang	0	
4	Geomaterial of slope	A lot of rolling stones and unsteady stones at slope surface	10	Choice of worse item. A lot of rolling stones and unsteady stones of sandy ground chose score at 10
		A lot of rolling stones at cutting slope surface	7	
		Weathering rocks and cracked rocks	6	
		Sandy ground with gravel	5	
		Weathering rocks	4	
		Cracked rocks	4	
		Sandy ground	4	
		Clayey ground	1	
		Massive rocks	0	
5	Thickness of surface layer	More than 0.5 m	3	Thickness of surface layer means humus soil, very soft soil or very loose colluvium deposit.
		Less than 0.5 m	0	

(continued)

Table 81.1 (continued)

No.	Item	Item2	Score	Remarks
6	Spring water	Exist	2	Regularly appeared spring water.
		No exist	0	
7	Interval of rock fall	More than one time per year	5	Rock fall in its item means very slightly damage.
		Less than one time per year	3	
		No rock fall	0	
Sum of scores			–	–
(b) Slope failure factors of maintenance and weights by rain.				
8	Unusual deformation of slope	Exist	a	–
		No exist	c	
9	Unusual deformation of slope stabilization	Exist	a	–
		No exist	c	
10	Past rock fall damages of houses	Exist	a	
		No exist	c	
11	Harmful behavior to slope	Frequently	a	–
		Sometime	b	
		No exist	c	
12	Stability of slope due to slope stabilization	Low	a	–
		Medium	b	
		High	c	
(c) Slope failure criteria by rain.				
Sum of scores at Table 81.1a		–13	14–23	24 -
Table 81.1b 8–12	More than one in "a" at Table 81.2. score	(A)	(A)	(A)
	One "b" and the remaining "c" at Table 81.2. score	(B)	(A)	(A)
	All "c" at Table 81.2. score	(C)	(B)	(A)

Table 81.2 Slope failure criteria by earthquake

(a) Slope failure criteria No.1 by earthquake in the report of risk assessment of Saitama Prefecture (1982).

No.	Item	Item2	Score	Remarks
1	Height of slope (H)m	H < 10	3	–
		10 ≦ H < 30	7	
		30 ≦ H < 50	8	
		50 ≦ H	10	
2	Gradient of slope (α)	α < 1:1.0	1	–
		1:1.0 ≦ α < 1:0.6	4	
		1:0.6 ≦ α	7	
3	Overhang of slope	Overhang without slope stabilization	7	Overhanging of slope especially rock slope
		Overhang with slope stabilization	4	
		No overhang	0	
4	Geomaterial of slope	A lot of rolling stones and unsteady stones at slope surface	10	Choice of worse item. A lot of rolling stones and unsteady stones of sandy ground chose score at 10
		A lot of rolling stones at cutting slope surface	7	
		Weathering rocks and cracked rocks	6	
		Sandy ground with gravel	5	
		Weathering rocks	4	
		Cracked rocks	4	
		Sandy ground	4	
		Clayey ground	1	
		Massive rocks	0	
5	Thickness of surface layer	More than 0.5 m	3	Thickness of surface layer means humus soil, very soft soil or very loose colluvium deposit.
		Less than 0.5 m	0	
6	Spring water	Exist	2	Regularly appeared spring water.
		No exist	0	
7	Interval of rock fall	More than one time per year	5	Rock fall in its item means very slightly damage.
		Less than one time per year	3	
		No rock fall	0	

(continued)

Table 81.2 (continued)

No.	Item	Item2	Score	Remarks
Sum of scores			–	–
(b) Slope failure criteria No.2 by earthquake in the report of risk assessment of Saitama Prefecture (1982).				
Sum of scores at Table 81.2a Seismic Intensity in Japan		–13	14–23	24–
6		B	A	A
5		C	B	A
4		C	C	A

A Rock fall or slope failure risk high, *B* Rock fall or slope failure risk medium, *C* Rock fall or slope failure risk low

Table 81.3 Slope failure weights by earthquake (Miyagi Prefecture (1986))

| Failure risk rank by rain sum of scores at Table 81.2a Seismic Intensity in Japan | (c) | (b) | (a) |
	–13	14–23	24–
6 Upper	B	A	A
5 Upper ∼ 6 Lower	C	B	A
4 Upper ∼ 5 Lower	C	C	B
∼ 4 Lower	C	C	C

A Rock fall or slope failure risk high, *B* Rock fall or slope failure risk medium, *C* Rock fall or slope failure risk low

The slope failure risk rank in 1978 Miyagi-ken-oki Earthquake within the natural slope is shown in Fig. 81.1. The number of natural slope failures is 98 points in Miyagi Prefecture and assessment of slope failure risk rank A is 166 points. So assessment of slope failure risk is estimated more dangerous and hitting ratio of assessment result is about 60 %. Then the error range of assessment of slope failure risk is included about half to double of the real the number of slope failure damage.

4 New Methods of Slope Failure Risk Assessment

The slope failure mechanisms has been analyzed by the mainly 2D FEM analysis in every slope damage point. However there are few analysis in the wide area of mountainous district because of the need of 3D FEM analysis. 3D FEM analysis needs a lot of the capacity of the computer. Recently, the new method is developed by Wakai et al.(2008) to analyze the wide area concerning slope failure by earthquake.

This method by Wakai et al. (2008) is that the time history of the dynamic ground response during strong earthquake can be estimated by an effective constitutive model of soil with appropriate soil parameters. 3D FEM analysis is used but can be used by the 1 PC computer to divide the 3D structure with the 1D sub-structure and buffer dummy region to reduce the boundary effect of the reflective wave. The sub-structure in the 3D FEM structure is contained in Fig. 81.2a, b.
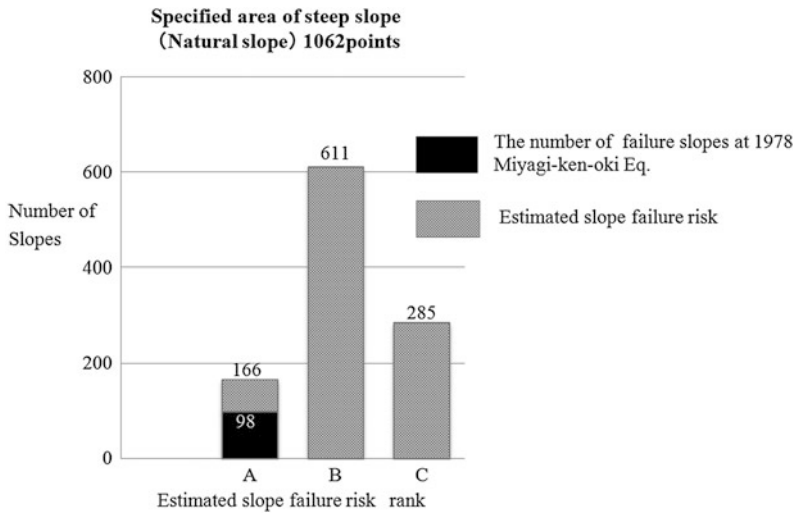
Fig. 81.1 Slope failures assessment and compared by the damage of slope failures in the 1978 Miyagi-ken-oki Earthquake (Miyagi Prefecture (1986)) (**a**) Simplified ground structure by Wakai et al. (2008) (**b**) Sub-structures for saving the computer memory by Wakai et al. (2008)
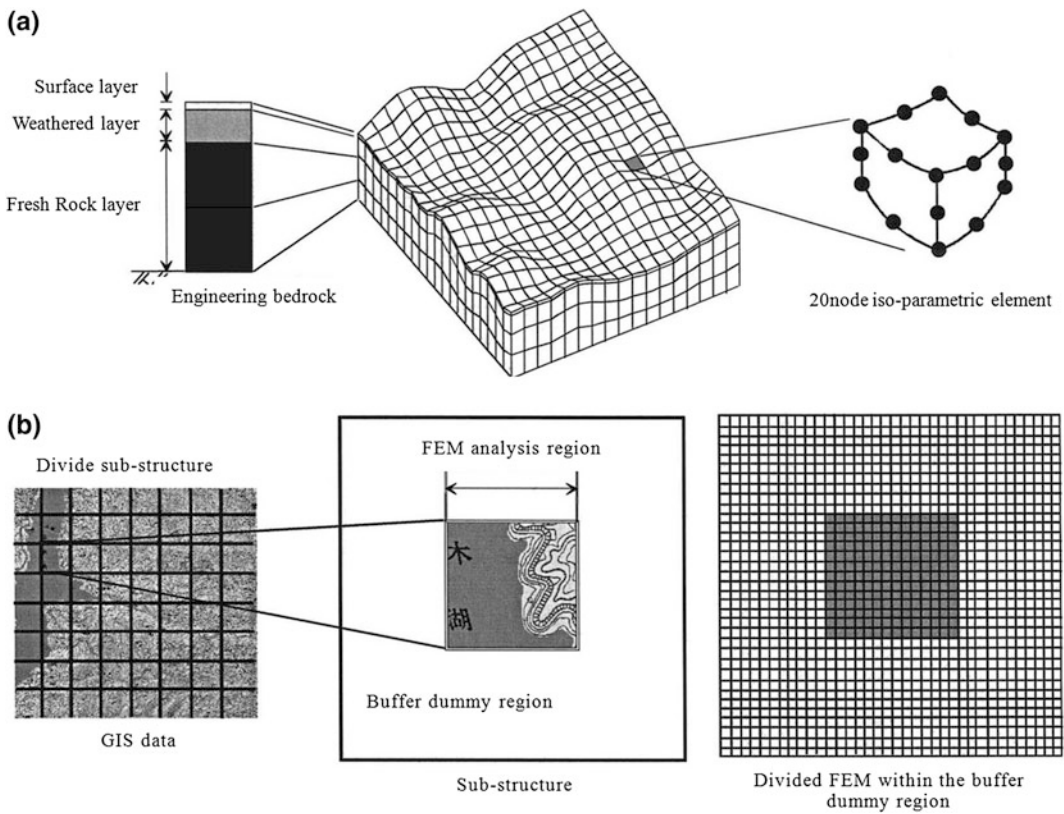
Fig. 81.2 Finite element model for the analyses by Wakai et al. (2008) (**a**) Analysis location map (**b**) Result of contour map in peak ground acceleration(m/sec²)
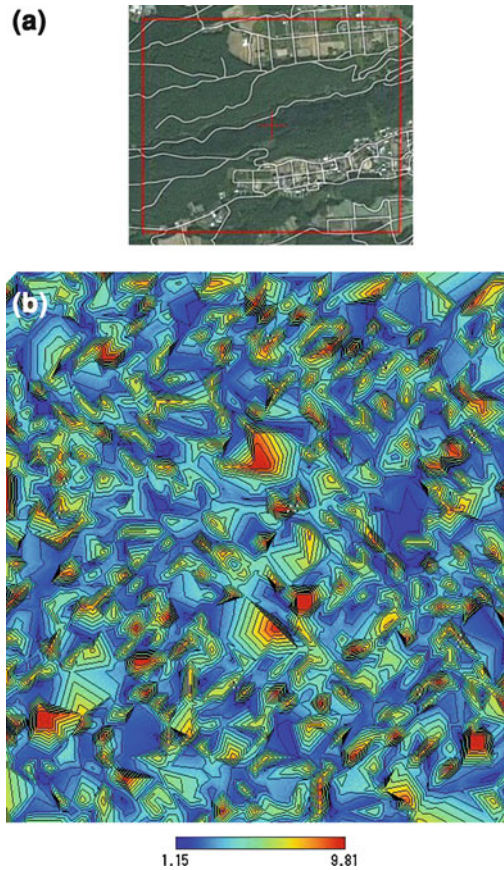
Fig. 81.3 Examples of the analytical assessment of slope failure after Wakai et al. (2008) approach

The example of analysis are shown in Fig. 81.3 at the south east part of Gunma Prefecture. The slope failure risk assessment in wide mountainous area due to the peak ground acceleration(PGA) and maximum shear stress at slope surface.

5   Conclusions

This paper is included the review of the method with the slope failure risk assessment using the seismic micro-zoning technique in the government and local government in Japan. This method is developed in the advantage and the weak point with the slope failure risk assessment. Then the recent new analytical method of wide areas of slope failure is introduced.

References

Cabinet Office (2005) Countermeasures against Tokyo inland Earthquakes (in Japanese), http://www.bousai.go.jp/jishin/chubou/shutochokka/15/shiryou3.pdf

Japan Road Association (1988) The book of countermeasures of earthquake damages before earthquake (in Japanese), pp 70–80

Miyagi Prefecture (1980) The instructions of 1978 Miyagi-ken-oki earthquake (in Japanese) pp 1–407

Miyagi Prefecture (1986) Miyagi prefecture earthquake hazard and risk assessment report (in Japanese) pp 1–239

Saitama Prefecture (1982) Saitama prefecture earthquake hazard and risk assessment report (in Japanese), pp 1–356

Tokyo Metropolitan (2012) Tokyo Metropolitan earthquake hazard and risk assessment report (in Japanese), pp 1–1, 3–94

Tottori Prefecture (2005) Tottori prefecture earthquake hazard and risk assessment report (in Japanese), pp 1–1, 14–12ty -30

Progressive Failure Cycles and Distributions of Earthquake-Triggered Landslides

Robert Parker, David Petley, Alexander Densmore, Nicholas Rosser, David Damby and Matthew Brain

Abstract

Advances in the collection and analysis of landslide inventory data have allowed for greater understanding of spatial distributions of landslides triggered by earthquakes. However, current approaches to analysing and modelling these phenomena do not account for the response of the individual potential landslide masses and their temporally evolving stability. This stems, in part, from the lack of a conceptual model describing the effect of seismic waves on the strength and stability of hillslopes, which can be applied at the regional scale and over long (multiple earthquake) time scales. Here we present such a conceptual model linking weakening via progressive failure, inertial displacements driven by seismic ground accelerations, and the repeating failure of sections of hillslopes through time. We explore the implications of the model for how various characteristics of earthquake-triggered landslide distributions are interpreted and understood. These include the apparently stochastic nature of spatial landslide occurrence, spatial patterns of landsliding, landslide magnitude-frequency distributions, global variability in numbers of landslides triggered by earthquakes, and in particular why in any earthquake smaller areas of hillslope fail than do not, even in regions of apparently high landslide susceptibility. Finally, we also propose means of testing the validity of this model relative to alternative hypotheses.

Keywords

Progressive failure · Newmark · Landslide distributions · Hysteresis

1 Introduction

Newmark analysis forms the basis of most currently available techniques for assessing the effect of seismic accelerations on hillslopes at the regional scale (e.g.: Jibson 2007). Here a potential landslide is modelled as a rigid

R. Parker (✉) · D. Petley · A. Densmore · Nicholas Rosser · D. Damby · M. Brain
Department of Geography, Institute of Hazard, Risk and Resilience, University of Durham, Durham, DH11PY, United Kingdom
e-mail: r.n.parker@durham.ac.uk

perfectly plastic block sat on an inclined surface. Deformation occurs along the shear plane in response to seismic accelerations that exceed the dynamic shearing resistance, which is assumed to be the same as the static shearing resistance. A key assumption of the Newmark approach is that the shearing resistance does not change in response to seismically-induced deformations. However, movement patterns in failing landslide masses and the results of stress-path triaxial tests have shown that cohesive hillslope materials undergo progressive weakening prior to full failure (Petley et al. 2005a, b). Logic also dictates that a stable section of hillslope must undergo weakening and a reduction in stability in order to reach the point of failure, and that once failed, in simplistic terms, a new more stable section of hillslope is produced. This means that the stability of individual locations in the landscape and therefore their sensitivity to earthquake-triggered landsliding is not temporally constant, but can be understood as evolving cyclically with the occurrence of seismic events.

In this paper, we present a conceptual model linking micro-scale deformation-weakening behaviour in hillslope materials and inertial displacements driven by seismic ground accelerations, in order to provide a physical approach to understanding the temporal evolution of hillslope stability in response to seismic events. We explore the implications of the model for understanding various observed characteristics of landslide distributions and propose means of testing the validity of this model relative to alternative hypotheses.

2 Temporal Model of Hillslope Weakening and Failure

2.1 Background

Failure in cohesive materials generally requires that the material that forms the eventual shear zone undergoes a transition from peak to residual strength (Bjerrum 1967). This requires the material to undergo progressive deformation, resulting in the formation and coalescence of

cracks that reduce the strength of the material. Based on observations of pre-failure landslide movement patterns (Petley et al. 2002; Kilburn and Petley 2002) and the results of stress path triaxial tests, Petley et al. (2005b) proposed a conceptual model for the development of progressive first-time failure in hillslopes formed from cohesive materials. The authors proposed that when a temporary reduction in factor of safety (FS) occurs due to elevated pore pressures, local stresses may exceed material strength in parts of the landslide, even though the global FS is still greater than unity. This allows deformation and micro-crack formation to take place in these segments, causing them to transition from peak to residual strength. The stress is then redistributed to other, unsheared, portions of the hillslope. This transfer process eventually reaches the point at which shear stress exceeds shear strength across the whole of the shear zone, such that failure becomes inevitable regardless of pore pressure state. However, it still takes time for the final sections of the shear zone to fail, such that collapse is not instantaneous. Hereafter we refer to this process of deformation, micro-crack formation and weakening by the term "deformation-weakening". Note also that whilst this model was developed for instability associated with hydrologically-triggered landslides, dynamic stresses from the passage of seismic waves may also serve to produce the temporary instabilities required for progressive failure.

2.2 Model Description

The Newmark sliding block model (Newmark 1965) provides a means of analysing the effect of seismic accelerations on hillslope stability in order to predict seismically-induced displacements in landslide masses (for a comprehensive review, see Jibson 2011). In this research we utilise the Newmark sliding block model as the basis for our conceptual model. We supplement the Newmark approach by changing two assumptions. First, we allow Newmark displacement to result in deformation-weakening, which breaks the assumption of perfectly plastic

stress–strain behaviour of Newmark sliding blocks (e.g.: Newmark 1965; Makdisi and Seed 1978; Chang et al. 1984; Ambraseys and Menu, 1988). Second, we theorise that the critical acceleration may be exceeded in segments of the landslide block and not the whole mass. This implies that the mass can deform internally, counter to the assumption that the landslide is a rigid block. Note also that we maintain the normal assumption in the Newmark approach of no change in pore pressure both under static and dynamic conditions. In this research we consider the response of multiple individual sections of hillslope at the spatial scale of mountain ranges (regional scale) to multiple earthquakes. While the effect of an earthquake on a section of hillslope is instantaneous, the return period of an earthquake may be hundreds to tens of thousands of years, depending on the large-scale rate of tectonic stress accumulation. This approach presupposes that over these periods of time hillslopes fail in the same location on multiple occasions in response to the multiple earthquakes that occur. Each time a section of hillslope fails, we assume that the material evacuates the shear surface, and the shear surface then forms the new hillslope surface. This new section of hillslope then becomes a new potential landslide. We assume that the geometry of sections of hillslopes does not change as they repeatedly fail— i.e. that the form of failure is that of a pseudo-infinite slope. As the majority of reported earthquake-triggered landslides take the form of shallow rockfalls, disrupted soil slides and rockslides (Keefer 2002), and occur across all parts of hillslope profiles, from toes to ridge crests (Densmore and Hovius 2000), this assumption is not unreasonable. Of course, as detachment and failure of material occurs, new hillslope surfaces are also formed from deposition of this material downslope, which in turn forms part of new potential landslide masses. We do not consider this process of mobilisation and deposition at this stage. These assumptions allow us to isolate the effect of material strength evolution without imposing ill constrained assumptions regarding material transport and surface modification from secondary aseismic processes.

The hillslopes of our model landscape are composed of a population of potential landslide masses, each of which is modelled as a Newmark sliding block. Hereafter we refer to these individual sections of hillslope as "blocks". Each block has a peak strength (at which the section of hillslope is at its maximum stability) and a residual strength (at which, if it has not already failed, the section of hillslope is at its minimum stability). Each block also has a surface gradient and a downslope length. A single ridge-to-stream hillslope profile may comprise of a single block or multiple blocks of different sizes, which will determine the size of landslides that occur on that hillslope. In Newmark analysis, sliding block displacement occurs when earthquake shaking exceeds the block's critical acceleration a_c—the horizontal component of acceleration required to overcome the shear strength of the material— thereby temporarily producing FS < 1.

$$a_c = (FS - 1)g \sin \alpha$$

$$FS = \frac{\tau_f}{\tau}$$

where a_c is the critical acceleration in terms of g (the acceleration due to Earth's gravity), FS is the static factor of safety (τ is the shear stress acting on the block and τ_f is the shear strength of the material), and α is the angle from the horizontal at which the centre of gravity of the slide mass moves when displacement occurs. The behaviour of a single section of hillslope is illustrated in Fig. 82.1. Initially τ_f at its peak is greater than τ such that the section of hillslope is stable (Fig. 82.1A). In our model, Newmark displacements result in deformation-weakening of the block material, causing a reduction in τ_f and therefore also in FS (Fig. 82.1B). The length of blocks determines the volume of material throughout which deformation-weakening is distributed. To generate the same net reduction in strength, longer blocks must therefore undergo larger displacements than shorter blocks; i.e. maintaining the same displacement-length ratio (strain, ε). If FS is reduced to <1, then failure of the block occurs (Fig. 82.1C), the weakened material evacuates the shear surface and a new hillslope

Fig. 82.1 Illustration of the failure cycle occurring in a single hillslope block. The hillslope experiences a time series of earthquakes that drive the failure cycle. Four stages in the cycle are highlighted. For each stage the following are provided: plots of shear strength (τ_f) against strain (ε), on which the static shear stress (τ) is indicated by the *red line*; illustrations of shear surface development and slope failure; time series of earthquake peak ground accelerations (PGA) on which the evolving value of a_c (proportional to FS) is indicated
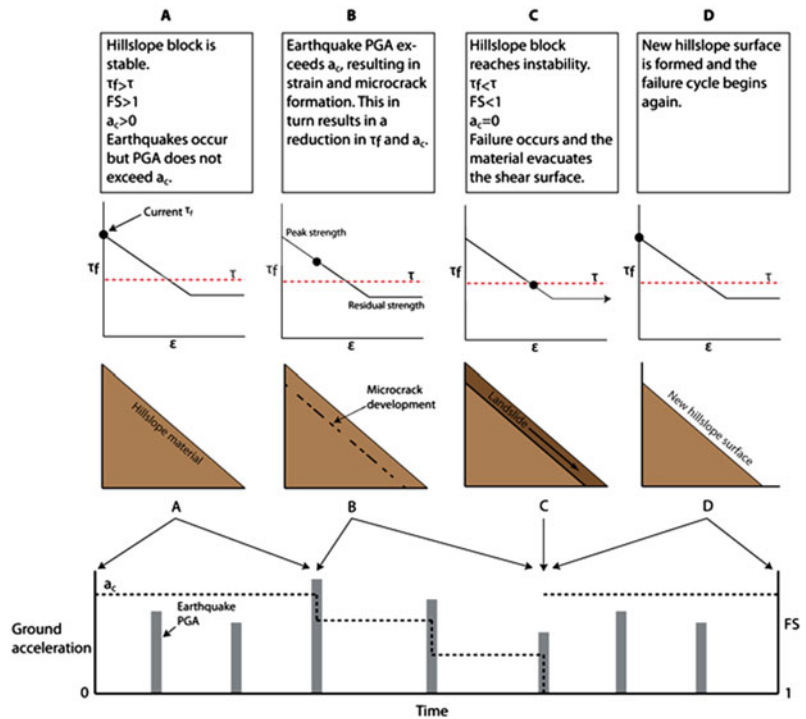
surface layer is formed (Fig. 82.1D). The new block retains the same gradient and length, whilst τ_f resets to its peak level. We term this cycle of weakening, failure and evacuation of material the "failure cycle". For simplicity we assume that blocks are spatially independent of one another.

Any earthquake in which a_c is exceeded will result in a reduction in *FS*. For a small earthquake generating weak ground accelerations, blocks have to have very low *FS* at the onset of shaking in order for a_c to be exceeded, and for failure to result from a small reduction in *FS*. For large earthquakes that generate strong ground accelerations, full transition to instability occurs in blocks that were more stable at the onset of shaking. As earthquakes occur, the weakest blocks reset and others weaken towards failure. An earthquake may reduce the population of potentially unstable blocks through complete failure and reset, but critically this net reduction is counteracted by other blocks that remain intact moving closer to failure, as a result of accumulating coseismic deformation-weakening. Note that, in theory, for blocks in which the residual strength is higher than the shear stress, complete

failure may never actually occur; once residual strength is reached these blocks will deform in a plastic manner each time a_c is exceeded.

3 The Failure Cycle and Characteristics of Landslide Distributions

A number of corollaries follow on from the basic assumptions of our conceptual model, which have implications for how observed characteristics of earthquake-triggered landslide distributions are interpreted. We outline these first, before exploring predictions that may be used to test the model relative to competing hypotheses.

3.1 Spatial Patterns of Landslide Probability

Over time, potential landslides progress through the failure cycle at different rates in response to ground accelerations and other factors that induce hillslope stress changes. For simplicity

we frame our discussion around the effect of earthquakes, although our arguments are also applicable to hydrologically-induced stress changes. Local factors controlling the rate of progression of blocks through the failure cycle, hereafter termed the "progression rate", can be broken down qualitatively into those pertaining to material rheology, static stresses governed by potential landslide geometry and the strength and duration of seismic accelerations.

In terms of block rheology, the peak strength and rate of strength decay with deformation control the progression rate. Blocks with lower peak strength must undergo less weakening to reach the point of failure than blocks with higher peak strength. Blocks with a higher rate at which strength decays with deformation progress through the failure cycle more rapidly than those with lower rates of strength decay. Different rates of landslide occurrence observed in different lithological units (e.g.:Parise and Jibson 2000) may be interpreted in terms of lithological variations in material stress–strain behaviour that define strength-decay due to deformation (e.g.: Plumb and Schlumberger Cambridge Research 1994; Hoek et al. 2005; Liang et al. 2007).

As blocks with steeper gradients have larger shear stresses the static FS is lower than for blocks with shallow gradients. In terms of the Newmark model this corresponds to a lower critical acceleration value, resulting in displacement occurring under weaker ground accelerations in general and larger displacements occurring under strong accelerations. Larger displacements result in a greater amount of deformation-weakening and subsequent decrease in FS. Thus for each earthquake, steeper blocks experience a greater reduction in relative strength (and thus stability) than do shallower blocks. Over time this translates to a higher progression rate for steeper blocks. Consequently a greater proportion of steeper blocks will fail with each event. This is reflected in observed patterns of increasing landslide probability with hillslope gradient (e.g.: Jibson and Keefer 1989; Keefer 2000; Lee et al. 2008; Parker et al. 2010; Parker 2010; Dai et al. 2011). Note that hillslope gradient and peak strength

are unlikely to be independent as higher shear strength is required to support steeper slopes. Observed relationships between landslide probability and hillslope gradient will therefore also reflect this interaction.

As the amplitude of seismic accelerations increases, critical acceleration thresholds are exceeded on a larger number of hillslopes. As amplitudes continue to increase above critical acceleration levels, the displacement produced by each seismic wave also increases. Furthermore, as the duration of seismic shaking increases, the cumulative displacement generated also increases. For each earthquake, blocks in regions experiencing seismic accelerations with higher amplitudes and longer durations progress through the failure cycle more rapidly, and thus experience a higher proportion of blocks that fail. This is reflected, for example, in observed patterns of increasing landslide probability with peak ground acceleration (e.g.: Meunier et al. 2007).

3.2   Landslide Size-Frequency Distributions

As the length of blocks determines the volume of material throughout which deformation-weakening is distributed, the progression rate decreases with increasing block length. To a reasonable first approximation landslide length, width and depth scale proportionally, and therefore landslide volumes increase with landslide length (e.g.: Larsen et al. 2010). Thus for any earthquake one would expect failure to occur in a greater proportion of small volume blocks than in large volume blocks. Even if the landscape was composed of equal numbers of small and large blocks, the frequency distribution of blocks experiencing failure would be skewed in favour of small sizes. Thus, we must distinguish between the size distribution of potential landslide masses—the distribution of blocks that makes up the landscape—and the size distribution of triggered landslide masses—the distribution of blocks that actually fail. Stark and Guzzetti (2009) have argued that the characteristic landslide size-probability distribution—

inverse power law decay for large landslides with rollover at small landslide sizes (e.g.: Hovius et al. 1997; Malamud et al. 2004a, b)—is rooted in a stochastic survival process of rupture growth. However, this process determines the probability of landslide rupture reaching a given area—the probability distribution of potential landslide masses—not the probability that a landslide with a given rupture area fails in any particular event—the probability distribution of triggered landslides. Our model suggests that the latter is a product of both the rupture-process-driven potential landslide size-probability distribution, and relative differences in rates at which potential landslides of different sizes progress through the failure cycle.

3.3 Stochastic Spatial Occurrence of Landslides

Whether or not a block actually fails depends on the state of the block in its failure cycle at the onset of shaking. The stochastic nature of spatial landslide occurrence therefore, in part, results from not knowing the seismic history of each block and therefore the position of each block in its failure cycle at the onset of shaking. This means that even for two identical successive earthquakes (with the same spatial pattern of ground accelerations), failure will occur for different populations of potential landslides. The fact that generally smaller areas of the landscape experience failure than do not, even in regions identified as having high landslide susceptibility, implies that the majority of blocks are not sufficiently close to failure prior to the earthquake to reach the point of failure as a result of the earthquake. These potential landslides may have experienced a large drop in their FS as a result of the earthquake, but still require further weakening to bring them to the point of failure.

3.4 Global Variability

A key output of this modelling is that the total proportion of blocks that actually fail in a particular earthquake depends on the population of blocks primed for failure—those sufficiently close to failure prior to the earthquake that they reach the point of failure as a result of the earthquake. Critically, this population may not necessarily be of a constant size. As blocks progress through the failure cycle, each at different rates, and as strong seismic events cause the simultaneous failure and reset of multiple blocks, there is potential for variability in block numbers primed for failure. The result of changes in this population is variability in landslide probability through time and therefore in the sensitivity of landscapes to earthquake-triggered landsliding. Global relationships between landslide frequency and earthquake magnitude (e.g.: Malamud et al. 2004b), and area affected by landslides and earthquake magnitude (e.g.: Keefer 1984; Rodríguez et al. 1999) exhibit unexplained variance of up to an order of magnitude. This has been attributed to variations in physiographic characteristics of different regions that are not taken into account in the analysis. However, this observed global variability may also be rooted in time-dependent variability in landscape sensitivity.

4 Tests for Model Validation

We have hypothesised the existence of an ordered system at the root of stochastic spatial patterns of earthquake-triggered landsliding. This hypothesis runs counter to ideas that the occurrence of earthquake-triggered landslides is rooted in a stochastic system resulting from (essentially unknowable) variability in ground accelerations and/or hillslope material properties. Both of these models are capable of generating stochastic spatial patterns of earthquake-triggered landsliding. A fundamental difference is that, according to our model, the system should exhibit memory or hysteresis. In this view, the response of a potential landslide mass to seismic accelerations is not only dependent on the current environment, but also the past environment (the history of seismic accelerations in the time since that section of hillslope last failed). Determining

which of these models provides a better representation of the system's behaviour requires tests for the presence or absence of this hysteresis. For instance, the strength of ground accelerations required for a potential landslide mass to progress to the point of failure becomes less as FS decreases. Therefore, sections of hillslopes that experience strong ground accelerations during one earthquake but do not fail, then have the potential to failure under weaker accelerations during a future earthquake. Where landslide inventories exist for multiple earthquakes with overlapping spatial extents, tests for this hysteresis may be formulated.

5   Conclusions

Current approaches to analysing earthquake-triggered landslide distributions and modelling the effect of earthquakes on hillslopes at the region scale do not consider changes in shearing resistance in response to seismically-induced deformations, and therefore cannot account for the temporally-evolving stability of individual potential landslide masses. The reduction in stability required for stable sections of hillslope to reach the point of failure can be understood by recognising that seismically-driven deformation in hillslopes results in the formation and coalescence of cracks, which reduce the strength of sections of hillslope until they fail. Over multiple-earthquake timescales, this process must repeat, such that sections of hillslopes experience a continual cycle of weakening and failure. The rate at which these potential landslide masses progress through the failure cycle determines the time-averaged probability of landsliding. The progression rate is dependent on the stress–strain behaviour of hillslope materials, the size and gradient of potential landslide masses and the strength and duration of seismic accelerations. Observed patterns of increasing landslide probability with hillslope gradient and peak ground acceleration, and variations in landslide probability among different lithological units, may therefore be interpreted as reflecting variations in progression

rates. Similarly, our model suggests that the size-probability distribution of triggered landslides is not only the product of the size-probability distribution of potential landslides, but also the scaling of progression rate with landslide size. Whether or not a hillslope fails as the result of an earthquake is dependent on both the amount of weakening produced by that earthquake and the history of seismic damage accumulated on the hillslope. The apparent stochastic nature of spatial landslide occurrence and variability in total numbers of landslides triggered by earthquakes of similar magnitudes can therefore be understood as the product of both the current earthquake and the seismic history of individual slopes. Further work to determine the validity of this model relative to competing hypotheses requires tests for evidence of this hysteresis in landslide datasets.

References

Ambraseys NN, Menu JM (1988) Earthquake-induced ground displacements. Earthquake Eng Struct Dyn 16:985–1006

Bjerrum L (1967) Progressive failure in slopes of overconsolidated plastic clay and clay shales. J Soil Mech Found Div Am Soc Civil Eng 93:1–49

Chang JC, Chen WF, Yao JTP (1984) Seismic displacements in slopes by limit analysis. J Geotech Eng 110:860–874

Dai FC, Xu C, Yao X, Xu L, Tu XB, Gong QM (2011) Spatial distribution of landslides triggered by the 2008 Ms 8.0 Wenchuan earthquake, China. J Asian Earth Sci 40:883–895

Densmore AL, Hovius N (2000) Topographic fingerprints of bedrock landslides. Geology 28:371–374

Hoek E, Marinos PG, Marinos VP (2005) Characterisation and engineering properties of tectonically undisturbed but lithologically varied sedimentary rock masses. Int J Rock Mech Min Sci 42:277–285

Hovius N, Stark CP, Allen PA (1997) Sediment flux from a mountain belt derived by landslide mapping. Geology 25:231–234

Jibson RW (2007) Regression models for estimating coseismic landslide displacement. Eng Geol 91:209–218

Jibson RW (2011) Methods for assessing the stability of slopes during earthquakes-A retrospective. Eng Geol 122:43–50

Jibson RW, Keefer DK (1989) Statistical-analysis of factors affecting landslide distribution in the New Madrid Seismic Zone, Tennessee and Kentucky. Eng Geol 27:509–542

Keefer DK (1984) Landslides caused by earthquakes. Geol Soc Am Bull 95:406–421

Keefer DK (2000) Statistical analysis of an earthquake-induced landslide distribution—the 1989 Loma Prieta, California event. Eng Geol 58:231–249

Keefer DK (2002) Investigating landslides caused by earthquakes—a historical review. Surv Geophys 23:473–510

Kilburn CRJ, Petley DN (2002) Forecasting giant, catastrophic slope collapse: lessons from Vajont, Northern Italy. Geomorphology 54:21–32

Larsen IJ, Montgomery DR, Korup O (2010) Landslide erosion controlled by hillslope material. Nat Geosci 3:247–251

Lee CT, Huang CC, Lee JF, Pan KL, Lin ML, Dong JJ (2008) Statistical approach to earthquake-induced landslide susceptibility. Eng Geol 100:43–58

Liang W, Yang C, Zhao Y, Dusseault MB, Liu J (2007) Experimental investigation of mechanical properties of bedded salt rock. Int J Rock Mech Min Sci 44:400–411

Makdisi FI, Seed HB (1978) Simplified procedure for estimating dam and embankment earthquake-induced deformations. J Geotech Eng Div 104:849–867

Malamud BD, Turcotte DL, Guzzetti F, Reichenbach P (2004a) Landslide inventories and their statistical properties. Earth Surf Proc Land 29:687–711

Malamud BD, Turcotte DL, Guzzetti F, Reichenbach P (2004b) Landslides, earthquakes, and erosion. Earth Planet Sci Lett 229:45–59

Meunier P, Hovius N, Haines J (2007) Regional patterns of earthquake-triggered landslides and their relation to ground motion. Geophys Res Lett 34:1–5

Newmark NM (1965) Effects of earthquakes on dams and embankments. Geotechnique 15:139–159

Parise M, Jibson RW (2000) A seismic landslide susceptibility rating of geologic units based on analysis of characteristics of landslides triggered by the 17 January, 1994 Northridge, California earthquake. Eng Geol 58:251–270

Parker R, Petley D, Rosser N, Densmore A, Whadcoat S (2010) Mapping and monitoring the spatial distribution of landslide hazards induced by the 2008 Wenchuan Earthquake, Sichuan Province, China. In: Geologically Active—11th International Association for Engineering Geology Congress. Aukland, New Zealand

Parker RN (2010) Controls on the distribution of landslides triggered by the 2008 Wenchuan earthquake, Sichuan Province, China. MSc, University of Durham

Petley DN, Bulmer MH, Murphy W (2002) Patterns of movement in rotational and translational landslides. Geology 30:719–722

Petley DN, Higuchi T, Dunning S, Rosser NJ, Petley DJ, Bulmer MH, Carey J (2005a) A new model for the development of movement in progressive landslides. In: Hungr O, Fell R Couture R, Eberhardt E (eds) Landslide risk management. A. T. Balkema, Amsterdam

Petley DN, Higuchi T, Petley DJ, Bulmer MH, Carey J (2005b) Development of progressive landslide failure in cohesive materials. Geology 33:201–204

Plumb RA, Schlumberger Cambridge Research U (1994) Influence of composition and texture on the failure properties of clastic rocks. Rock mechanics in petroleum engineering. Society of Petroleum Engineers, Delft

Rodríguez CE, Bommer JJ, Chandler RJ (1999) Earthquake-induced landslides: 1980–1997. Soil Dyn Earthq Eng 18:325–346

Stark CP, Guzzetti F (2009) Landslide rupture and the probability distribution of mobilized debris volumes. J Geophys Res-Earth Surf 114:1–16

Distribution of Landslides Induced in Iwaki City, Japan, by Two Large-scale Earthquakes in 2011

83

Go Sato, Kazunori Hayashi, Hiroshi Yagi and Daisuke Higaki

Abstract

Iwaki City in eastern Japan experienced two large-scale earthquakes in 2011: the Tohoku earthquake that occurred on March 11 and an active fault-type earthquake that occurred on April 11. We developed a landslide distribution map of Iwaki City using aerial images and show that the landslides induced by the April 11 aftershock alone account for 70 % of all landslides induced by March 11 and April 11 earthquakes. In particular, we show that the distribution of landslides caused by the April 11 earthquake was determined by fault structure and lithological character. Furthermore, the landslides occurred along mountain ridges and in regions that previously had convex slope profiles.

1 Introduction

Iwaki City is located in the coastal region of Fukushima Prefecture in eastern Japan (Fig. 83.1). In 2011, the city experienced two large-scale earthquakes, namely, the M9.0 Tohoku earthquake on March 11 and the M7.0 aftershock (related to the earthquake of March 11) on April 11, 2011. Both of these earthquakes registered in the lower 6 level of the Japanese earthquake scale. Although the earthquakes differed in that the Tohoku earthquake was a plate boundary-type earthquake, while the aftershock was an active fault-type earthquake, both caused many landslides. We developed a landslide distribution map using aerial images. In this paper, we explain the characteristics and distributions of the landslides induced by each earthquake and provide a brief description the sites of some landslides induced by the April 11 earthquake.

G. Sato (✉)
Teikyo Heisei University, 2-51-4 Higashi-Ikebukuro, Toshima, Tokyo, 170-8445, Japan
e-mail: gsato@thu.ac.jp

K. Hayashi
Okuyama Boring Co., Ltd, Yokote, Japan

H. Yagi
Yamagata University, Yamagata, Japan

D. Higaki
Hirosaki University, Hirosaki, Japan
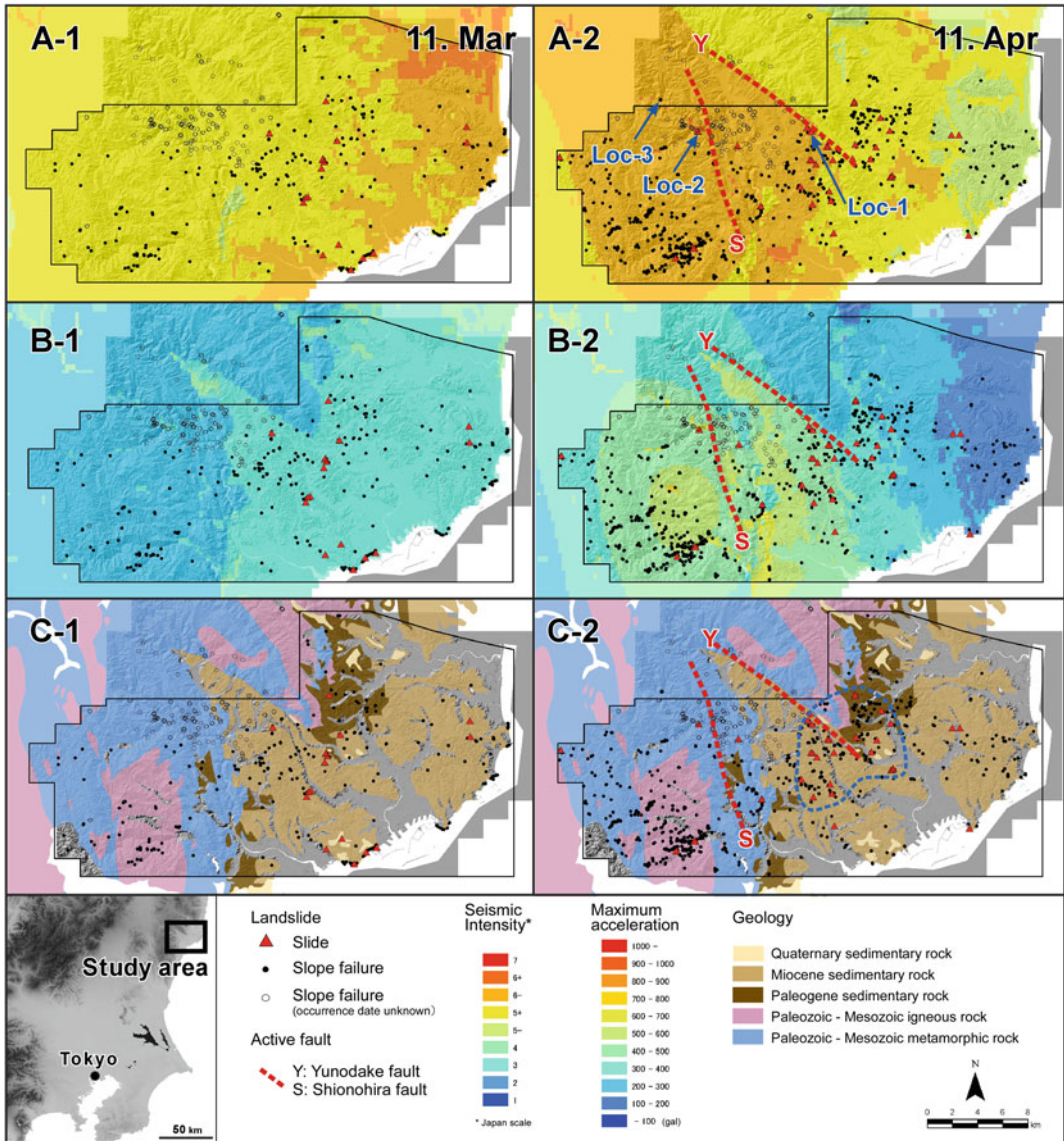
Fig. 83.1 The landslide distribution map of Iwaki City superposed on seismic intensity, maximum acceleration, and geological maps. The seismic intensity and maximum acceleration data are from the Geological Survey of Japan, and the geological information was obtained from the Digital Geological Map of Tohoku District published by the Tohoku Construction Association

2 Methods: Creating the Landslide Distribution Map

The study area (approximately 40×20 km) was mapped using aerial photographs taken by the Geospatial Information Authority of Japan after April 11. From these images, landslides induced by the March 11 and April 11 earthquakes were extracted on the basis of two criteria: (1) the landslide width is greater than 5 m, and (2) landslide activity has caused removal of vegetation. However, it is difficult to classify landslides according to the earthquake that

caused them. Therefore, we interpreted not only aerial photographs but also Google Earth images taken between March 11 and April 11. Further, the extracted landslides were classified into slide and slope-failure types.

3   Landslide Distribution

Landslides were superposed onto a seismic intensity map, a peak ground acceleration map, and a geological map using a geographical information system (GIS). We observed 52 slide-type landslides (17 related to the March 11 earthquake and 36 related to the April 11 earthquake) and 1,165 slope-failure-type landslides (82 related to the March 11 earthquake, 372 related to the April 11 earthquake; the remainder have unknown occurrence dates). Landslides induced by the April 11 earthquake account for 70 % of all landslides induced by March 11 and April 11 earthquakes. The landslides induced by the March 11 earthquake are widely dispersed in the study area. In contrast, the landslides induced by the April 11 earthquake appear to be concentrated in specific areas, namely, the area on the southwest side and western edge of the Yunodake Fault and the western side of the Shionohira Fault. Seismic intensity and peak acceleration (Fig. 83.1A-1,2 and B-1,2) were relatively high in these regions, except on the northeast side of the southeastern edge of the Yunodake Fault. Both Yunodake and Shionohira Faults are normal faults. As a result, the hanging wall side experienced higher intensity and peak ground acceleration than the footwall side; the landslides were concentrated on the hanging wall side. Past research has shown that landslides occurred on the hanging wall sides of the reverse faults that caused the Mid-Niigata Prefecture Earthquake of 2004, Iwate-Miyagi Nairiku Earthquake of 2008 in Japan, and the northern Pakistan Earthquake of 2005 (Yagi and Chigira 2006; Yagi et al. 2007; Yagi et al. 2007). This study shows that the hanging wall side can experience concentration of landslides not only for reverse faults but also for normal faults.

However, landslides were also observed to concentrate to a lesser extent in the footwall side around the southeastern part of the Yunodake Fault. This area experienced low intensity and low peak ground acceleration compared with the hanging wall area, but consists of pre-Tertiary sedimentary rock, which is prone to landslide activity. In particular, we focus on Miocene sedimentary rocks that are prone to slide-type movements, such as those in the area bounded by the dashed blue line in Fig. 83.1C-2.

Therefore, we suggest that the distribution of landslides caused by the April 11 earthquake is determined by fault structure and lithological character.

4   Landslide Case Studies

Large-scale landslides occurred along the Yuno-dake Fault and Shionohira Fault as a result of the April 11 earthquake (Sato et al. 2011). We examined three cases of landslides that occurred at Loc. 1, 2, and 3 in Fig. 83.1A-2. The common characteristic of these cases is that that the land-slides occurred in mountain ridges corresponding to areas that originally had convex slope profiles.

The Kamikamado landslide (Loc. 1) is the largest slide and extends more than 200 m in width and length (Pic. A); it is a lateral-spread type landslide, as indicated by the graben topography formed by sliding in the upper part of the landslide body. Fortunately, no fatality occur in this landslide, but the major road (Prefectural road 14) was severed (Fig. 83.2).

The Saibach landslide (Loc. 2) is of slide type and one fatality occur in this landslide. The landslide body is divided into three slide blocks (a, b, and c in Pic. B). Downhill-facing scarps are present above block c. These include fresh scarps (black line) resulting from the movement on April 11 and older scarps formed by previous landslide activity. From a geomorphological view, the area surrounded by the black dashed line in Pic. B could be interpreted to have formed as a result of deep-seated gravitational slope deformation. Therefore, this area may

Fig. 83.2 Photographs of
a Kamikamado landslide,
b Saibachi landslide, and
c Kaiya landslide (taken by
Miyagi in April 24, 2011)
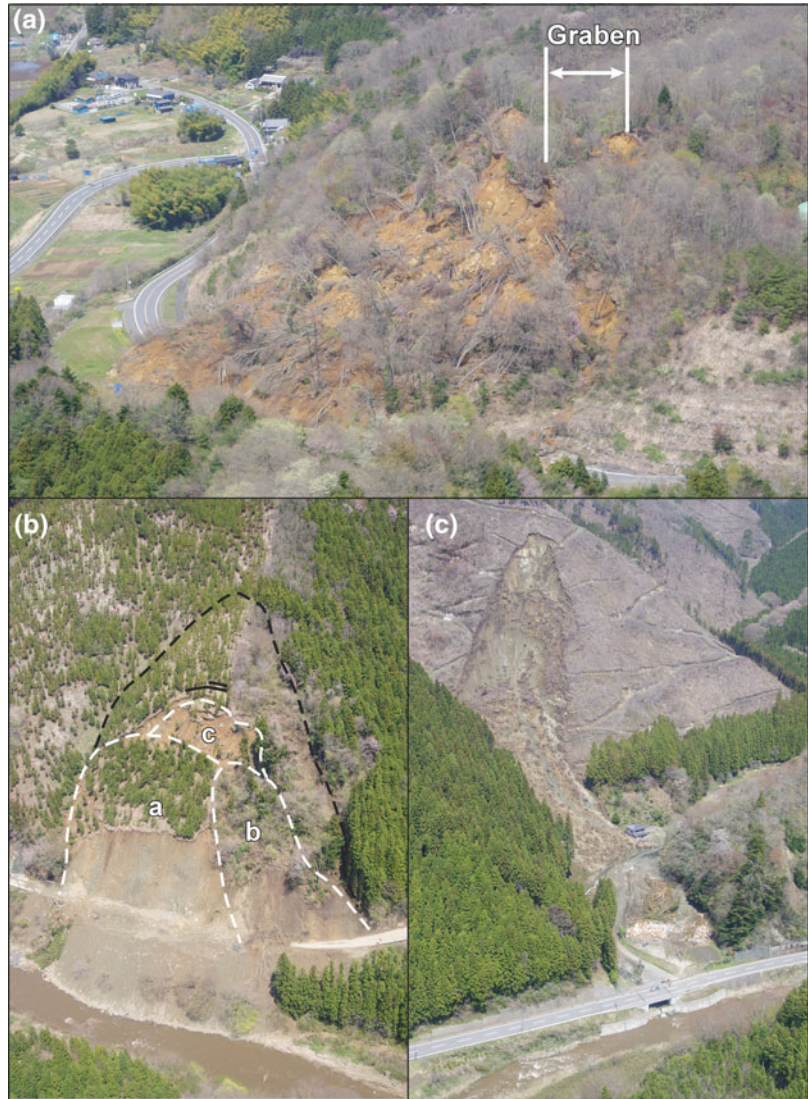
have been landslide-prone before the April 11 earthquake.

The Kaiya landslide (Loc. 3) is of slope-failure type. Houses were damage and three fatalities occurred in this landslide. The deposits formed as a result of this slope failure were removed in a mudslide caused by heavy rain after March 11, and one house was damaged in this incident.

Many other landslides in the study area also occurred along mountain ridges and occurred in regions that originally had a convex slope profile.

Therefore, such topography can be considered vulnerable to landslides caused by earthquakes.

5 Conclusions

The results of our study are summarized as follows.

(1) We observed 52 slide-type and 1,165 slope-failure-type landslides, respectively, in our study area, and the number of landslides induced

by the April 11 aftershock alone accounts for 70 % of all landslides.

(2) Two active surface faults appear to have caused the April 11 aftershock. The distribution of landslides was concentrated on the hanging wall sides of these faults and in area of landslide-prone geology.

(3) Most of the slide-type landslides were triggered by the April 11 earthquake. These landslides occurred in the ridge areas of mountains and in areas that previously exhibited convex slope profiles.

References

Sato G, Umemura J, Higaki D, Miyagi T, Yagi H (2011) Landslides induced by the earthquake in Iwaki City, Japan on April 11th -A preliminary report of the field survey along the Prefectural road No. 14. J Jpn Landslide Soc 48:173–175

Yagi H, Chigira M (2006) Outline of the slope disaster caused by 2005 North Pakistan Earthquake an example of Landslides and slope failures induced by earthquake. SABO 87:10–13

Yagi H, Yamasaki T, Atsumi M (2007) GIS analysis on geomorphological features and soil mechanical implication of landslides caused by 2004 Niigata Chuetsu earthquake. J Jpn Landslide Soc 43:294–360

Yagi H, Sato G, Higaki D, Yamamoto M, Yamasaki T (2009) Distribution and characteristics of landslides induced by the Iwate-Miyagi Nairiku earthquake in 2008 in Tohoku District, Northeast Japan. Landslides 6:335–344

Assessment of Earthquake-Induced Landslides Triggered by Roudbar-Manjil Earthquake in Rostamabad(Iran) Quadrangle Using Knowledge-Based Hazard Analysis Approach

84

Mohammadreza Mahdavifar and Parham Memarian

Abstract

In this paper earthquake-induced landslides hazard due to 1990 Roudbar-Manjil (Mw = 7.3) earthquake in the Rostamabad quadrangle (located in Gilan province of Iran) is assessed. For this purpose, a GIS-based software program for hazard zonation of earthquake-induced landslide is used. The basis of the program is knowledge-based landslide hazard analysis method which analyzes the hazard combining different effective parameters. In this program, landslides are classified in six groups and effect of different parameters on the occurrence of landslides of each group is assessed. The method utilizes digitized data using fuzzy logic to analyze input datasets and provide results. Firstly, in this study, earthquake-induced landslide inventory of the region is prepared by the study of aerial photographs; then input layers necessary for analysis are prepared and the program is applied for the region. The results are compared with the inventory of earthquake-induced landslides for the same quadrangle.

1 Introduction

Landslides are the most destructive of the geotechnical hazards (including liquefaction and the settlement of loose deposits) associated with earthquakes (Rodriguez et al. 1999); the important socioeconomic effect of landslides is sometimes downgraded because of tow reasons, firstly the losses of many kind of landslides occur during days, months or even years and secondly in the case of earthquake-induced landslides, the losses due to strong ground motion are highlighted upon landslide losses. One of the most deadly

M. Mahdavifar (✉)
Geotechnical Engineering Research Center,
International Institute of Earthquake Engineering
and Seismology (IIEES), Tehran, Iran
e-mail: mahdavif@iiees.ac.ir

P. Memarian
International Institute of Earthquake Engineering
and Seismology (IIEES), Tehran, Iran

earthquakes which caused a lot of fatalities in Iran was Roudbar-Manjil Earthquake of 1990. During Roudbar-Manjil earthquake several landslides were triggered, Fatalak village was completely ruined due to a huge rock avalanche and all 120 inhabitants were killed. Hazard analysis of slopes for areas prone to earthquakes can help to prevent or reduce the damages. Knowledge-based hazard analysis methods are very useful to analyze earthquake-induced landslide hazard in regional scale. Here the Roudbar-Manjil earthquake is selected as a case study for evaluating the approach for predicting the earthquake-induced landslides. Roudbar-Manjil earthquake occurred 30 min after midnight of June 21 1990 (local time) in province Gilan of Iran (Mw = 7.3). The study area is a 625 km^2 quadrangle, located at UTM zone 39S and between 49° 15′ and 49° 30′ Longitudes and 36° 45′ and 37° latitudes (containing Roudbar-Manjil earthquake epicenter at 49.3460 °N 36.9890 °E). The climate of the area is humid, being encompassed between Alborz Mountains and Caspian Sea, which affects the occurrence of landslides deeply. The geological properties of the region differ from hard limestone to very loose marl which is continually eroding. Also the area is mountainous (the height differs from 140 to 2,800 m above sea level); these properties all together besides the seismic potential of the region make it a landslide prone area.

2 Landslide Inventory

There were three main steps to derive landslide inventory of Roudbar-Manjil earthquake in Rostamabad quadrangle:

1. Stereoscopic study of the aerial photos of the area, taken before Roudbar-Manjil earthquake;
2. Stereoscopic study of the aerial photos of the area, taken after Roudbar-Manjil earthquake;
3. Comparing the results of two studies and creating inventory of earthquake-induced landslides in the region.

To make the inventory more precise, the aerial and satellite images of the area were studied, then all of the recognized landslides were determined and two landslide inventories, pre and post to the

Fig. 84.1 Rostamabad quadrangle index map and Roudbar-Manjil earthquake-induced landslide inventory

earthquake, were prepared using the ArcGIS. Finally two inventories were compared to find a database of probable earthquake-induced landslides and after rechecking the doubtful cases, the final earthquake-induced landslide inventory of Roudbar-Manjil earthquake was prepared.

The inventory was verified comparing with other studies done in parts of the region.

Totally 193 landslides have been founded, from which 24 landslides are due to 1990 Roudbar-Manjil earthquake (Fig. 84.1) and others are old landslides. Earthquake-induced landslides are divided to two groups of newly-occurred and reactivated landslides. Only 3 landslides are reactivated and all 21 others are triggered by the earthquake.

The biggest landslide in the region has an area of about 640,000 m^2 and there are five landslides with areas more than 240,000 m^2.

3   Layers Preparation

CAMEL (Comprehensive Areal Model of Earthquake-induced Landslides: Miles and Keefer 2007; Miles and Keefer 2009) is used to assess landslide hazard of the region. CAMEL is designed and implemented as a system based on fuzzy logic. Two types of knowledge found in the literature (knowledge about the possibility of landsliding and knowledge about the intensity or hazard of landsliding) forms the basis of CAMEL's design. CAMEL is comprised of two modules—the possibility and hazard modules—each of which are made up of several fuzzy IF–THEN rule-blocks and need several inputs. Inputs for possibility module are: Terrain Roughness, Earthquake Shaking Intensity, Soil Depth, Slope Height, Material Type, Moisture, and Slope Angle. The inputs for hazard module are: Disturbance Distance, Ground Class, Moisture, Shaking Intensity, Slope Angle, and Vegetation. CAMEL has been integrated with ESRI's ArcGIS so the input layers are made and implemented in ArcGIS for the region. All layers are raster type with cell size of 100 m.

Terrain Roughness is slope surface curvature; it is calculated as second derivative of elevation in the down-slope direction.

Modified Mercalli Intensity (MMI) is utilized by CAMEL for landslide hazard analysis. In current study Arias Intensity for each cell is calculated using attenuation relationship for Alborz region, converting it to MMI (Mahdavifar et al. 2008).

Soil Depth is assumed 3.5 m for all parts of the region, because of incomplete data, which allows the occurrence of soil slumps as the only landslide type related to soil depth.

Local slope height is one of the parameters affecting Rock avalanches occurrence. Slope Height is calculated using DEM and slope map of the region.

Material type is assumed to be both types of soil and rock for all parts.

Ground moisture content or water table depth affects the occurrence of different categories of landslides.

A range of slope angles is required for the occurrence of each landslide type assessed by CAMEL. Slope Angle is calculated using DEM of the region, as shown in Fig. 84.2.

Conceptually, Disturbance Distance facilitates representation of morphological factors contributing to slope failure, such as toe erosion by an undercutting stream or an over-steepened road cut. Specifically, it is the distance in meters between the slope (however defined) and the identified linear disturbance feature (Miles and Keefer 2007). Disturbance Distance is calculated according to rivers and roads maps.

Vegetation refers to the plant coverage (density) of a given area, expressed as a percent of the area. Vegetation is calculated as NDVI, using Landsat satellite images.

Ground Class is a parameter to determine ground strength of each part of the study area. Ground Class is prepared due to previous studies and 1:100,000 Geological map of the region, Ground Class was determined according to geology and age of alluviums and rocks. Ground Class was divided to five classes from high strength rocks of Permian (Ground ClassI) to quaternary alluviums (Ground ClassV). Ground Class map is shown in Fig. 84.3.

4   Landslide Hazard Analysis Results

In current landslide inventory map most rock falls are not mapped due to their small size on aerial photographs, only two big rock falls were determined and plotted. Comparing with slope angle map, parts of the study area with high rock fall hazard are located at areas with slopes more than 35° which complies with literature (Fig. 84.4).

Although no rock avalanches have been occurred in the study area during Roudbar-Manjil earthquake rock avalanche hazard map shows high hazard in parts of the study area. These parts have slope heights more than 150 m, comparing with slope height map, which is the threshold of rock avalanche occurrence in the literature. (Fig. 84.5).

Fig. 84.2 Slope angle of the study area
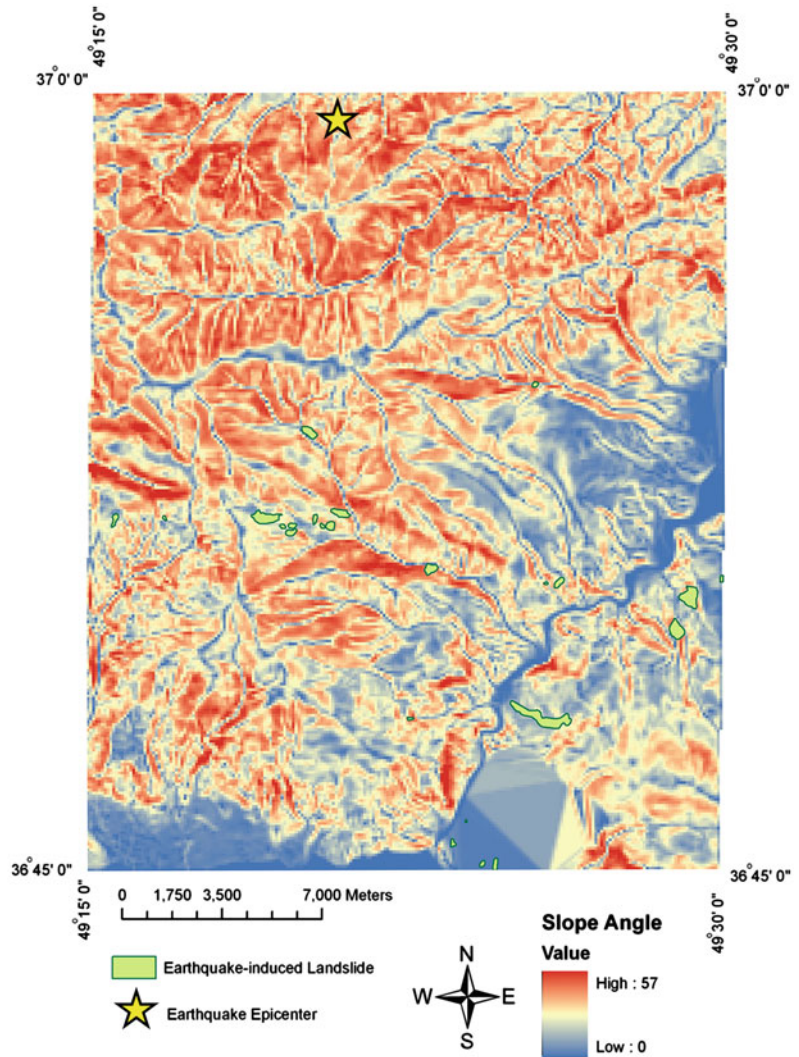
As mentioned before in eastern and southern parts of the region rock slump hazard is low due to low slopes, but in areas with steep slopes and with ground class of III and weaker, rock slump hazard is high. The rock slump hazard map shows good agreement with landslide inventory map (Fig. 84.6).

Soli flows occur in areas with loose soil and low slopes and this is in compliance with the soil flow hazard map which shows high hazard in eastern parts with quaternary alluviums and low slopes. Despite some high hazard areas in soil flow hazard map no soil flow has been occurred in the study area (Fig. 84.7).

Fig. 84.3 Ground class of the study area (from class 1 to class 5 strength decreases)
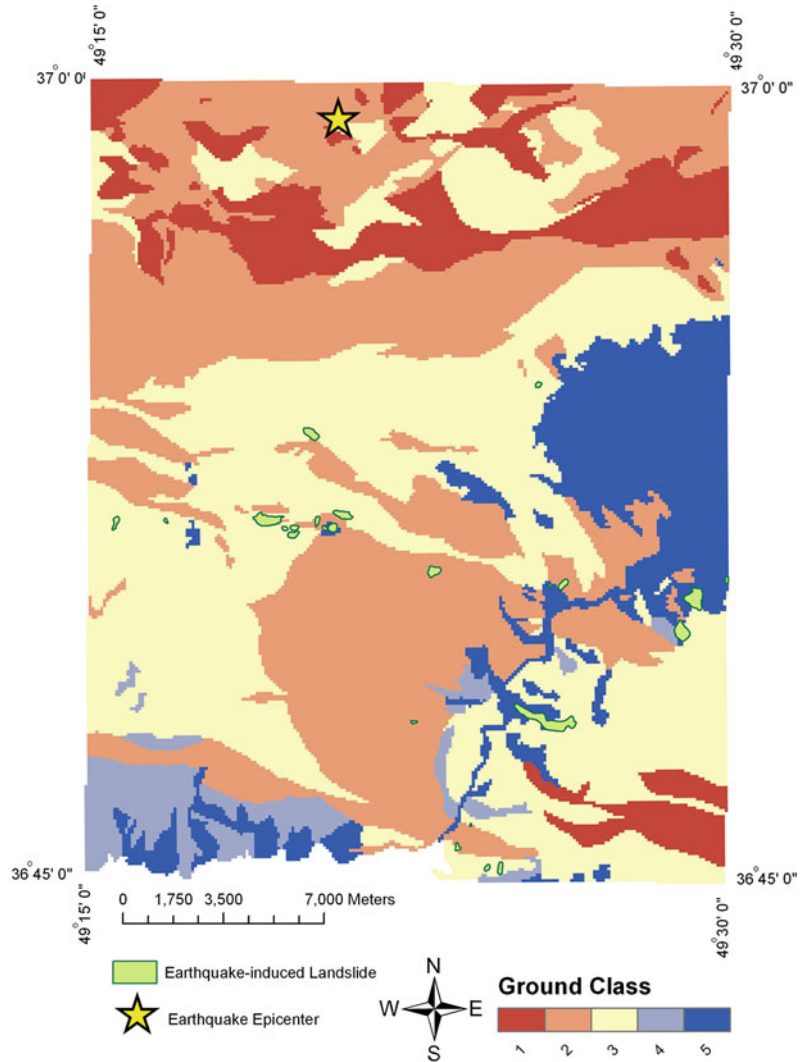
In current landslide inventory map soil falls are not mapped due to their small size on aerial photographs but probably several soil falls have been occurred in the region. Parts of the study area with high soil fall hazard are located at areas with slopes more than 15° which complies with literature (Fig. 84.8).

According to soil slumps inventory map, soil slumps and slides have mostly occurred in parts of the study area in which a weak ground type reaches a stronger one, this is in compliance with the soil slump hazard map which shows high hazard in such parts (Figs. 84.3 and 84.9). The soil slump hazard in eastern and northern parts of

Fig. 84.4 Rock fall hazard map
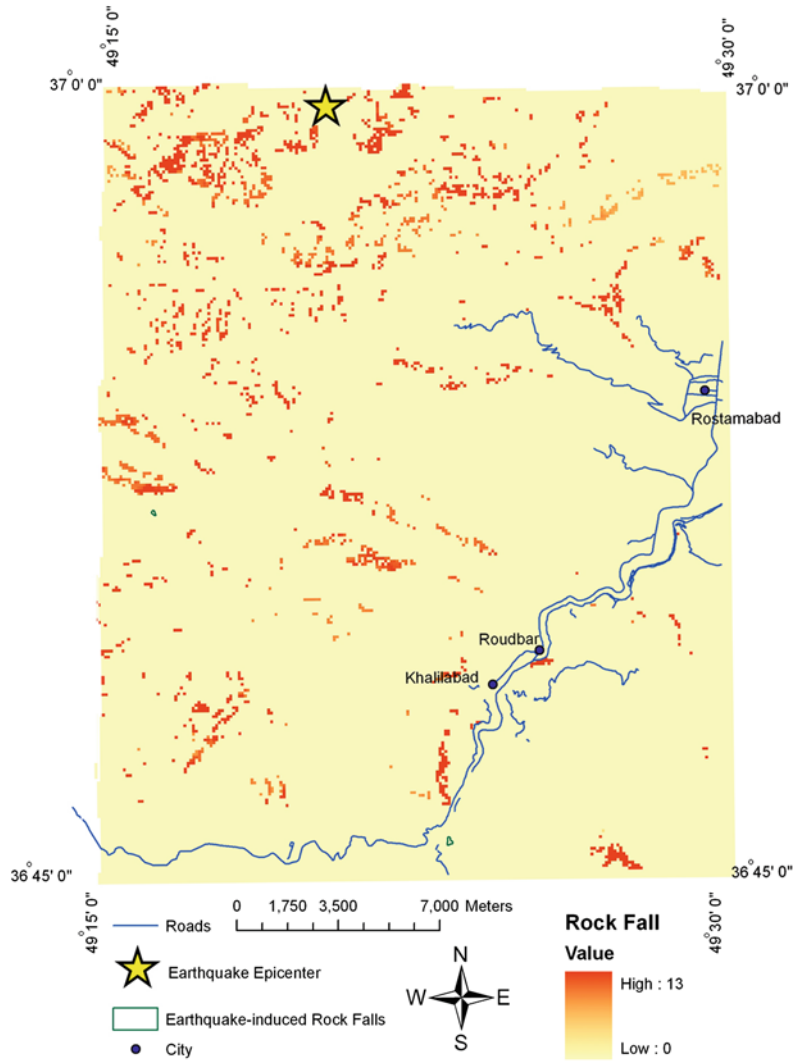
study area is assessed high which is not in compliance with soil slump inventory map. This, in eastern parts of the study area is because of extremely low slopes and low terrain roughness of quaternary alluviums of the region and in northern parts, because of high vegetation coverage and rock material type which is not provided in the Material Type input layer of the CAMEL.
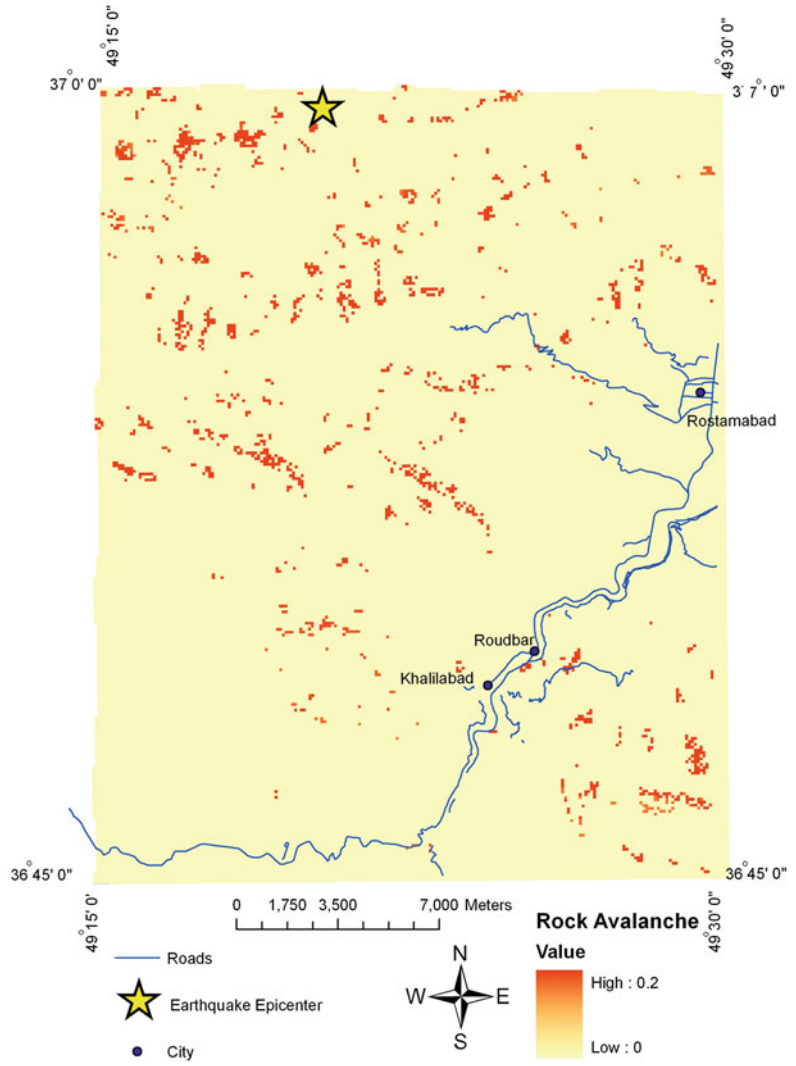
Fig. 84.5 Rock avalanche
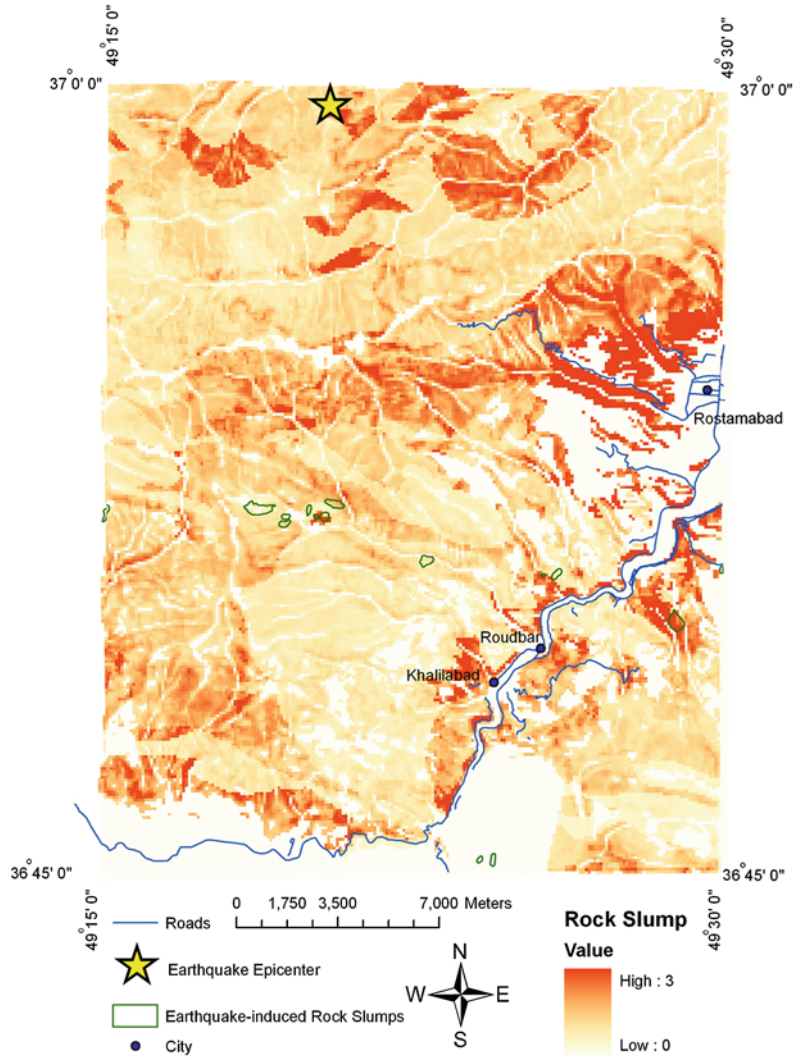hazard map

Fig. 84.6 Rock slump
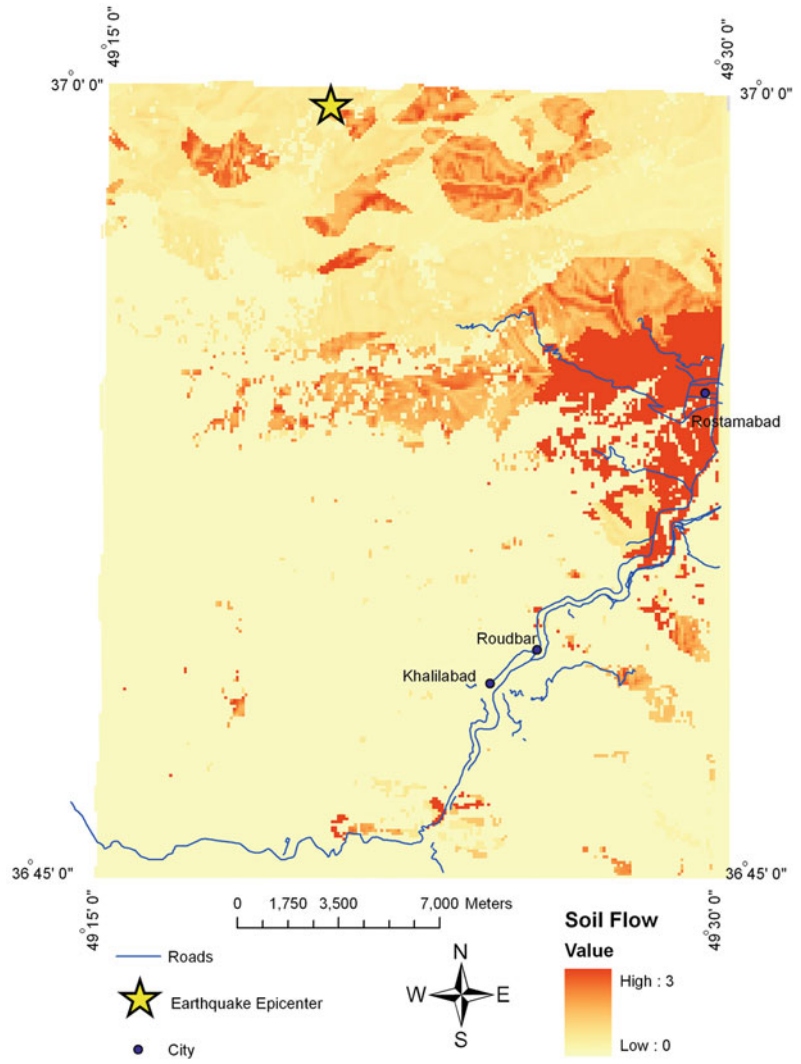hazard map

Fig. 84.7 Soil flow hazard map

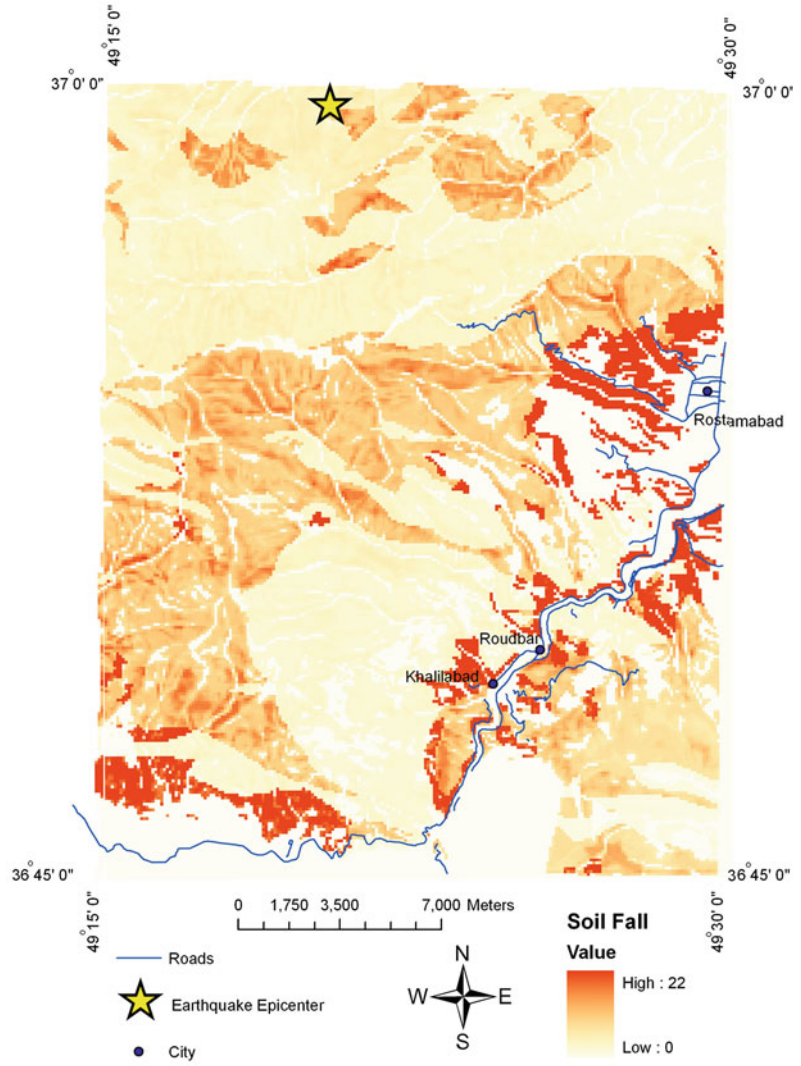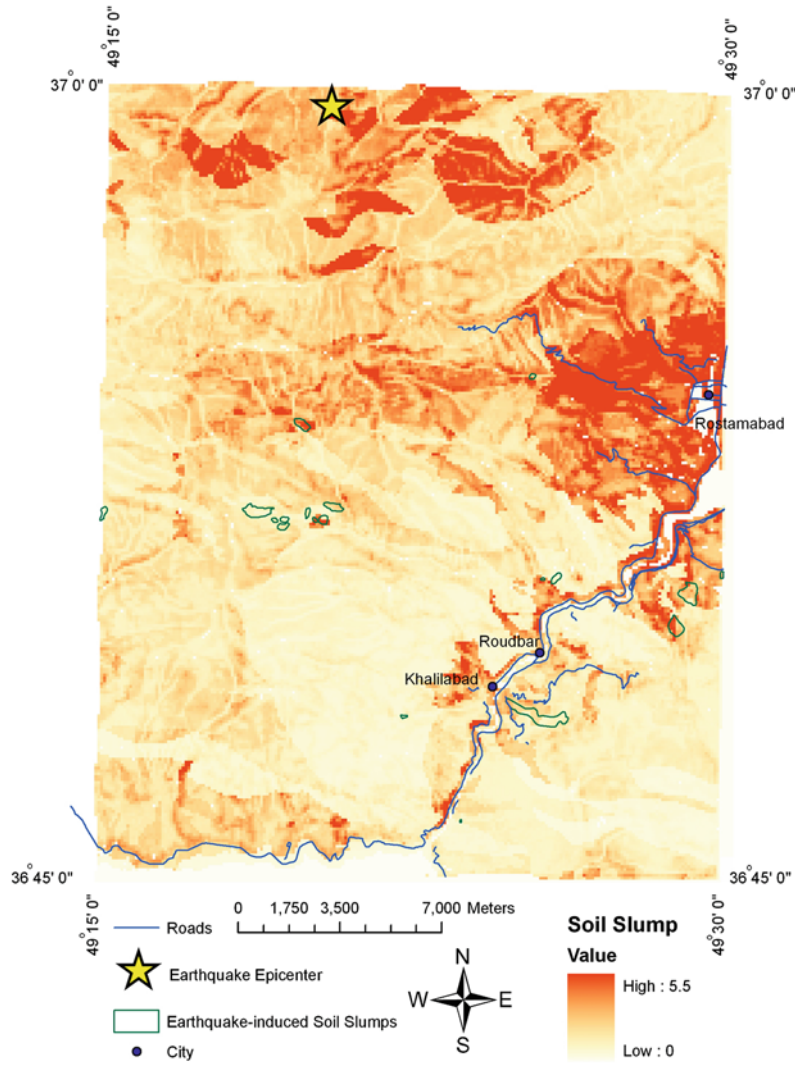**Fig. 84.8** Soil fall hazard map

Fig. 84.9 Soil slump
hazard map

5 Conclusions

Most of earthquake-induced landslides due to Roudbar-Manjil earthquake have occurred in areas with ground classes of I and III and few ones in areas with ground class of II and IV and almost no landslide has occurred in areas of Ground class I.

Because of strong ground class in northern parts of the region despite locating the epicenter of the earthquake in the same area, no considerable landslide has occurred, but in central and southern parts which contain weaker alluviums with steep slopes more landslides has occurred according to landslide inventory (Figs. 84.2 and 84.3).

Seismic landslides inventory map contains landslides of soil slump, rock slump and rock fall types which are in compliance with prepared landslide hazard maps of each type in the study area. Rock avalanche, soil flow and soil fall hazard maps are also consistent with literature thresholds and circumstances for occurrence of each type.

Most of the Rudbar-Manjil earthquake-induced landslides are located in the medium to high hazard areas of the hazard maps created by CAMEL.

References

Miles SB, Keefer DK (2009) Evaluation of CAMEL—comprehensive areal model of earthquake-induced landslides. Eng Geol 104:1–15

Miles SB, Keefer DK (2007) Comprehensive areal model of earthquake-induced landslides: technical specification and user guide. U.S. Geological Survey Open-File Report 2007-p1072. 69 pp

Mahdavifar M, Jafari MK, Zolfaghari MR (2008) Real-Time generation of Arias intensity and seismic landslides hazards maps using GIS. Journal of Seismology and Earthquake Eng (JSEE) 10(2):81–90

Rodriguez CE, Bommer JJ, Chandler RJ (1999) Earthquake-induced landslides: 1980–1997. Soil Dyn Earthq Eng 18:325–346

Identifying Landslides Using Binary Logistic Regression and Landslide Detection Index

Wentao Yang, Peijun Shi and Lianyou Liu

Abstract

Landslide mapping plays an essential role in landslide susceptibility, hazard and risk studies by providing landslide inventory. Although it is time-and labor-consuming, traditional manual interpretation of high resolution aerial images is still the most commonly used method. In this paper, a new automatic index-threshold method and two logistic regression models are developed to detect landslides triggered by the 2008 Wenchuan Earthquake with pre and post event SPOT5 (Systeme Pour l'Observation de la Terre 5) images. Both images are first pan sharpened, ortho-rectified, co-registered and relatively corrected for atmospheric influence. Then, layers of NDVI (Normalized Difference Vegetation Index) difference, image spectral angle change, principal components and independent components are obtained as candidate landslide identification layers. To pick up helpful layers for automatic landslide identification, usefulness index (*ui*) and landslides inventory in a training area are used to determine the importance of each layer. High *ui* layers are selected to calculate landslide detection index (*LSI*) over the full area and establish logistic models in the training area. Then, trained logistic models and the best threshold with the highest landslide detection accuracy found in the

W. Yang · P. Shi (✉) · L. Liu
Academy of Disaster Reduction and Emergency
Management, Beijing Normal University, Beijing,
100875, People's Republic of China
e-mail: spj@bnu.edu.cn

W. Yang · P. Shi · L. Liu
State Key Laboratory of Earth Surface Processes
and Resource Ecology, Beijing Normal University,
Beijing, 100875, People's Republic of China

W. Yang · P. Shi · L. Liu
Key Laboratory of Environmental Change and
Natural Disaster (MOE), Beijing Normal
University, Beijing, 100875, People's Republic of
China

training area are applied to the entire area, respectively. Accuracy comparisons are made among these techniques and results indicate that regression models and the index-threshold method can be independently used to map landslides with comparable high accuracy.

Keywords

Automatic landslides mapping · Index-threshold method · Logistic models

1 Introduction

Most commonly triggered by rainfall and earthquake, landslides are one of the most devastating geo-hazards in mountainous regions leading to great economic losses and heavy casualties around the world every year (Schuster and Highland 2007). Landslides also play an important role in the evolution of the landscapes, accelerating erosion and further contributing to the de-mountain building (Parker et al. 2011). With the changing climate, more extensive distributions of landslides triggered by extreme rainfalls pose great challenge for the quick disaster mitigation (Chiang and Chang 2011). Quick mapping of landslides after an event is an essential work for disaster relief, examination of the geo-hazard disaster chains (Shi 2002; Xu et al. 2012) as well as future development planning by landslide hazard, susceptibility and risk analysis (Fell et al. 2008; Mantovani et al. 1996; Metternicht et al. 2005). Landslide mapping (or landslide detection) is a term used to recognize or classify landslides in an remote sensing image and in this work it relates to distinguish landslides (surface denuded area) from their surrounding environments (Soeters and Westen 1996). Traditional work on landslide mapping is carried out on manual interpretation of high resolution aerial stereo images consuming much time and human power, so it is difficult to meet the requirement of high efficiency over vast regions (Gorum et al. 2011; Tang et al. 2011). The development of high resolution satellite sensors in recent years makes the auto mapping of landslides possible and more work has been carried out in this important field (Mondini et al. 2011b). Overall, all landslide

identification studies fall into two categories: either object oriented (Aksoy and Ercanoglu 2012; Lu et al. 2011; Martha et al. 2010) or pixel based (Mondini et al. 2011b) and the former is generally regarded as better than the latter because it does not generate isolated pixels as false landslides. However, there are drawbacks in object oriented methods, like the segmentation step does not fit all sizes of landslides leading to false landslide boundaries and decrease the accuracy of landslide mapping result, the classification of landslides relies heavily on the selection of features. Whereas, isolated false landslides resulted from using the pixel based methods can be further edited. In this sense, due to the relatively high automation, easy and quick advantages, pixel based methods are still very popular in automatic landslide mapping.

Based on previous work, this paper aims to develop an objective method to select useful layers for landslide detection models and a new landslide detection index to automatically identify landslides triggered by large magnitude earthquakes.

2 Methodology

The work is divided into two parts: (a) the first part is the initial processing of images in the study area, including pan-sharpening, ortho-rectification, co-registration, atmospheric correction, layers stacking, principal component analysis (PCA) and independent component analysis (ICA); and (b) layer selection using usefulness index (ui), model building and validations (Fig. 85.1). We used two SPOT (Systeme Pour l'Observation de la Terre) images (without
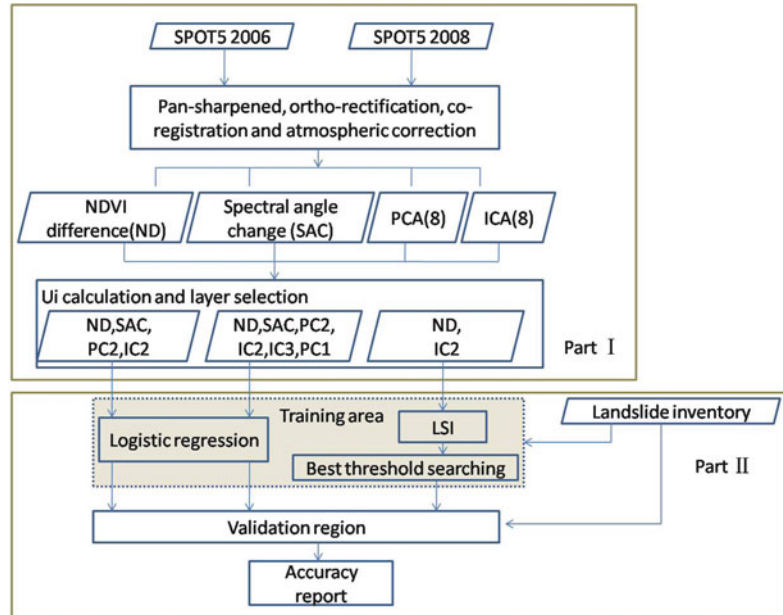
Fig. 85.1 Flowchart of the landslide detection

Table 85.1 Characteristics of the SPOT5 images used for mapping the earthquake induced landslides

	Pre-event image	Post-event image
Satellite operating altitude	832 km	832 km
Panchromatic band resolution (black and white)	2.5 m	2.5 m
Multispectral bands resolution (blue, green, red and near-infrared)	10 m	10 m
Acquisition date	5-Sep-2006	4-Jun-2008

cloud cover) with 2.5 m in panchromatic and 10 m in multi bands (shortwave infrared, near infrared, red and green) acquired on September 5, 2006 and June 24, 2008 of the southeast area of Pingwu County in Sichuan Province (Table 85.1). Besides, landslide inventory within the study area is manually interpreted by using stereo SPOT5 images overlaying DEM of the area and referring to (Xu et al. 2009). After the compilation of the landslide inventory, it is converted to a 30-m-resolution image file by assigning the value of one to landslide pixels whose center are located within the landslide region and zero to non-landslide pixels.

2.1 Initial Processing and Layer Selection

In the work, part of two SPOT5 images covering an area of approximately 86.1 km^2 pre and post the 2008 great Wenchuan Earthquake are used (Fig. 85.2). Both images are pan-sharpened using Pan Sharpening algorithm available in ENVI EX 4.8 version to improve the spatial resolution of multispectral bands to 2.5 m. 30-m-resolution ASTER GDEM in the region is used to ortho-rectify both images, which are later co-registered with an error of less than one pixel by using forty control points on turning points of roads, bridges and other objects which are easy to recognize. After that, relative atmospheric correction is implemented to eliminate atmospheric influence due to the time variance by correcting post image (Slave image) according to pre landslide image (Master image) using the following criterion (Hong and Zhang 2008; Mondini et al. 2011b):

$$N = (S - \mu_S) \times \frac{\sigma_M}{\sigma_S} + \mu_M \qquad (85.1)$$

where, N is pixel value of a certain band in Slave image (post landslides), S is the original value, μ_S and μ_M are mean values of the image in this

Fig. 85.2 SPOT5 image
of the study area, the
*smaller lower yellow
polygon* is the training
region and *upper yellow
polygon* is the validation
region for these models.
Blue polygons are
landslides triggered by
earthquake
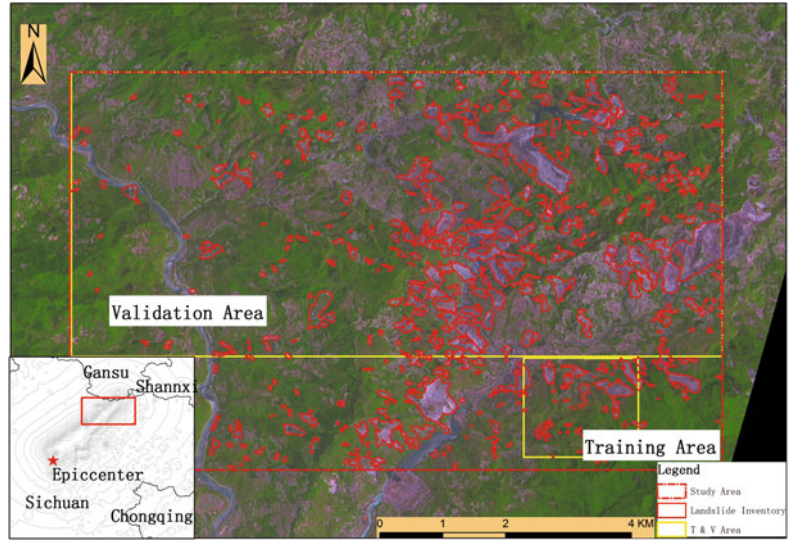
processing band of Slave and its corresponding
band in Master images, σ_M and σ_S are the standard
deviation of the image in this band of Slave and
Master images. After atmospheric correction,
every band in the post landslide image has the
same mean and standard deviation values with
their counterparts in the pre landslide image thus
reducing unnecessary noises in the image
introduced by different conditions of these two
time periods.

Based on these initial procedures, NDVI
(Normalized Difference Vegetation Index) differ-
ences (Mondini et al. 2011b) between both images
are calculated as a candidate layer for model
building in later works. Spectral angle change is a
measure of differences between two images on a
pixel by pixel base. Each pixel within an image has
a four dimensional vector corresponding to blue,
green, red and near-infrared band value and the
difference with another image from a different date
can be calculated as the changed angle ($\delta\theta$)
between both vectors (Chen et al. 2003; Masek
and Sun 2004; Mondini et al. 2011b).

$$\delta\theta = \arccos\left(\frac{\vec{u} \cdot \vec{v}}{|\vec{u}| \times |\vec{v}|}\right) \qquad (85.2)$$

where, $\vec{u} = (\rho_{green}, \rho_{red}, \rho_{nir}, \rho_{sir})_{pre}, \vec{v} = (\rho_{green}, \rho_{red}, \rho_{nir}, \rho_{sir})_{post}$ are the reflectance values
within each pixel vector.

More candidate layers, from Principal Com-
ponent Analysis and Independent Component
Analysis are generated using eight stacking
layers from both images, resulting in sixteen
more layers (eight layers for PCA and ICA
each).

Eighteen candidate layers are generated and
selection of helpful layers to develop landslide
detection models remains to be settled. It is
inappropriate to pick out highly correlated layers
by calculating the correlation coefficient
between the binary landslide inventory and
candidate layers. The relative importance of a
layer in landslide detection model is equivalent
to the separability of the pixel values within
landslide cells (in this work, pixels that is the
same location as in landslide inventory is named
landslide cells with an area of 2.5 × 2.5 m and
vice versa) and that in non landslide cells of the
layer. So, the usefulness of a layer can be
defined by employing the usefulness index (ui):

$$ui = \frac{|mean(C_{nls}) - mean(C_{ls})|}{std(C_{nls}) + std(C_{ls})} \qquad (85.3)$$

where, ui is the usefulness index to depict the
relative importance of the layer for landslide
detection, C_{ls} and C_{nls} are pixel values in the
landslide cells and non landslides cells, respec-
tively. Table 85.2 shows the ui ranking of all

Table 85.2 Usefulness index of each candidate layer

Layers	ui	Layers	ui	Layers	ui
ICA2	1.0660	ICA1	0.4221	PCA4	0.1425
NDVI difference	1.0017	PCA7	0.4043	PCA3	0.1294
PCA2	0.9280	ICA5	0.3806	ICA6	0.1024
PCA1	0.7482	ICA4	0.2956	PCA6	0.1020
ICA3	0.6002	PCA8	0.2855	ICA7	0.0469
Spectral angle changes	0.5240	PCA5	0.2477	ICA8	0.0468

candidate layers in the training area. High value for a layer denotes a high separability between values in landslide cells and non landslide cells, or in other terms, the close relation between the layer and landslide inventory.

Previous works show that NDVI difference and spectral angle changes between pre and post landslide images are two of the most commonly helpful layers for automatic landslide detection (Lin and Chou 2006; Mondini et al. 2011a, b; Zhang et al. 2010) and this is verified by their high *ui* ranks in Table 85.2.

2.2 Model Building and Validations

Binary logistic and other multiple regression models are important techniques for the automatic identification of landslides. Based on *ui* ranks, the first logistic model uses the first six high *ui* layers and the second logistic model uses four of them, i.e. NDVI difference, spectral angle changes, ICA2 and PCA2, which are among the highest *ui* ranks in ICA and PCA. Finally, after normalization, layers of top two *ui* ranks are selected to derive a landslide detection index (*LSI*).

$$LSI = \frac{C_1 - C_2}{C_2 + C_1} \qquad (85.4)$$

where, C_1 and C_2 are top two *ui* normalized layers, *LSI* is the landslide detection index and has a distribution from −1 to 1 with higher value for landslide pixels. Of all these models, to overcome the over-fit of the models by dominant landscape type, a balanced sample principle is applied, i.e. randomly select same number of

landslide pixels and non-landslide pixels (Mondini et al. 2011b).

To determine the best threshold for *LSI*, a threshold search techniques is used by gradually decreasing the search range till the best accuracy of landslide detection in the training area is reached. The initial search range is set from −1 to 1, which is the same range with *LSI* distribution. The search range and pace will gradually decrease until the best threshold *t* is found, when

$$L_i - L_{i-1} < \varepsilon. \qquad (5)$$

where, L_i and L_{i-1} are the landslide accuracy in two successive search loops, ε is a marginally small and acceptable value. The *i*th search pace is

$$p_i = (b_i - a_i)/m, \qquad (85.6)$$

where, b_i and a_i are the upper and lower boundaries in the *i*th search and *m* is an positive integer.

3 Results and Discussion

The usefulness index (*ui*) for landslide detection gives a relative importance of each layer by *ui* rankings (Table 85.2), which can be visually compared with landslide inventory (red polygon in Fig. 85.3).

Usually, it is much difficult and more subjective to manually decide which layer is more important than the other in landslide detection, while the *ui* gives an objective way on selecting important layers and in Fig. 85.3 with the decrease of *ui* values, the contrast of layer values between landslide cells (in red polygon) and non landslide cells becomes blur, which also demonstrates the effectiveness of the usefulness index.

Fig. 85.3 The comparison between landslide inventory (*red polygons*) and top six *ui* ranking layers (ICA2, NDVI difference, PCA2, PCA1, ICA3 and spectral angle changes and in a left to right, up to down order)
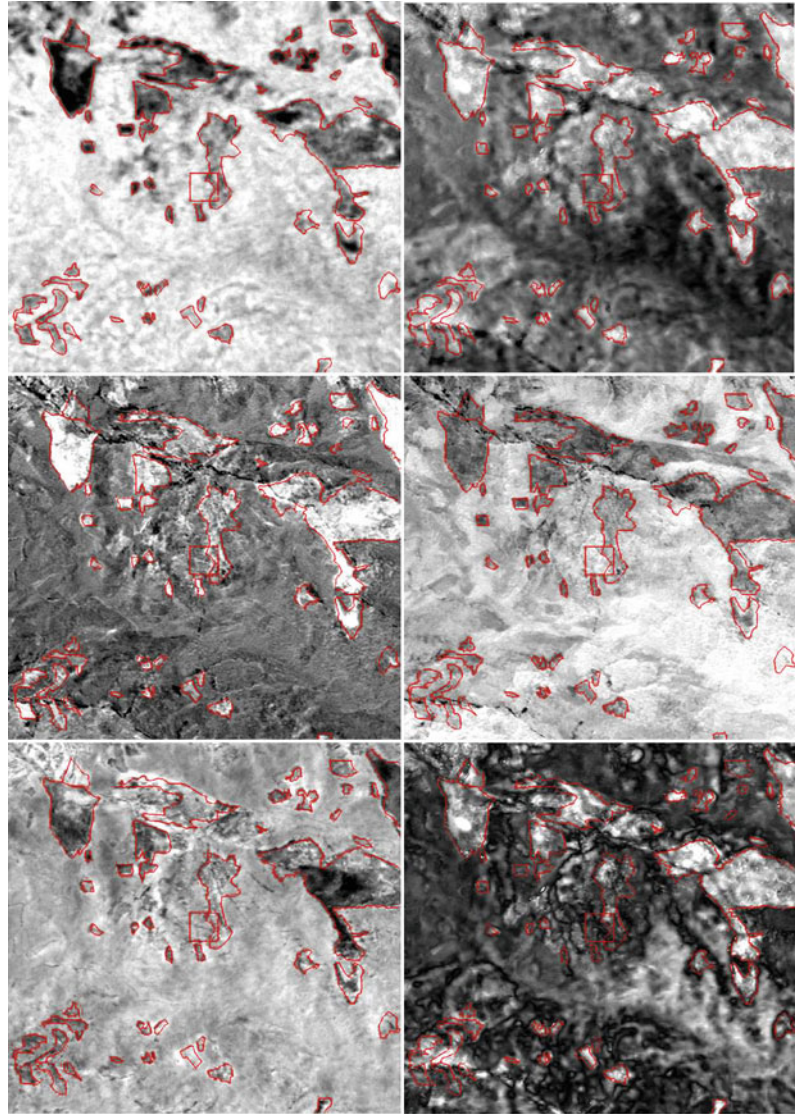
In the training area, the number of pixels within landslide cells, comprising 14.2285 % of all pixels, is far outstripped by non landslide pixels. In order to balance the regression model on the imbalanced training samples, all 86461 landslide pixels in the training area and the same number of non landslide pixels, which are randomly picked are used to train the two logistic models of the four and six layer variables, respectively. And without any modification, both calibrated logistic models are directly applied to the full region resulting landslide detection accuracies (Table 85.3).

Table 85.3 The accuracy report of the three models

Methods		Accuracy (%)
Logistic_6	Landslide	91.43
	Non landslide	72.48
Logistic_4	Landslide	86.29
	Non landslide	78.67
LSI	Landslide	88.08
	Non landslide	74.79

Layers with high *ui* value are more distinctive between landslide cells and non landslide cells, which is more consistent with the landslides
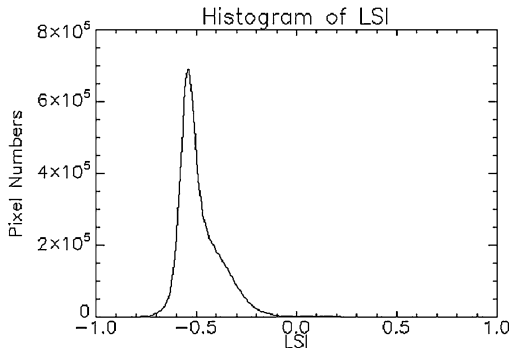
Fig. 85.4 *LSI* distributions of the entire area

inventory, while low *ui* ones have more noise and the contrast is not significant. What is more, values in landslide zones of ICA2 and NDVI difference have the opposite spectral pattern, i.e., low values in ICA2 and high values in NDVI difference denotes landslides. To enhance this contrast, landslide detection index (*LSI*) is used to magnify the differences between these two top layers. After the normalization of each candidate layer, the *LSI* has a range of −1 to 1 (Fig. 85.4), with high values in landslide pixels and low values in non landslide pixels. This landslide detection index (*LSI*) formula can be more flexible like

$$LSI = \frac{CL_1 + CL_2}{CL_2 - CL_1} \qquad (7)$$

to enhance the contrast, when the top two *ui* layers have a similar spectral pattern.

To find the best threshold to generate the highest accuracy for landslide and non landslide zones, the automatic threshold searching
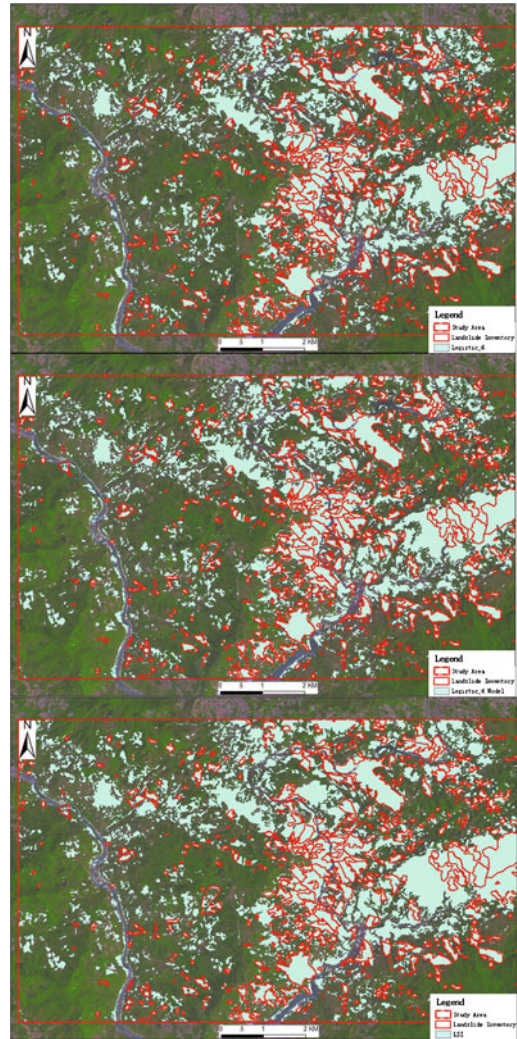

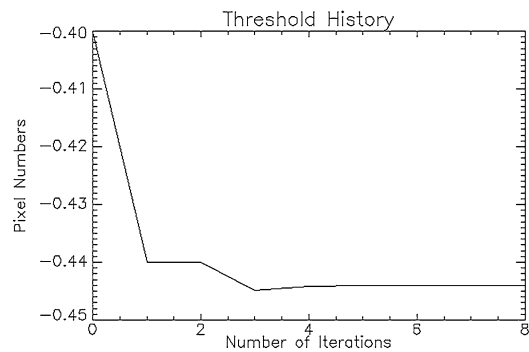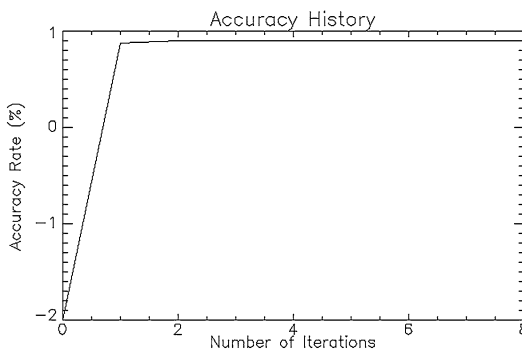Fig. 85.6 Comparisons of results from detection models with landslide inventory

Fig. 85.5 Left graph depicts accuracy history as the finding goes on and the right shows the corresponding thresholds and the best accuracy in the left is 92.98 % with the best threshold of −0.444083

technique is carried out in the training area as logistic regressions. An initial search pace of 0.2 is set and the maximum loop number is set at 8, finding the best threshold for the training region of −0.44 with a balanced accuracy of 92.98 % (Fig. 85.5). Then, the best threshold in the training area is applied directly in the entire region to calculate the accuracy (Table 85.3).

Results indicate that those three methods can all generate comparable accuracy of over 72 % both in true positive (TP) and true negative (TN). The highest TP reaches 91.43 % in the six-variable logistic regression, while the lowest TP of 86.29 % in the four-variable logistic regression model. However, the six-variable logistic regression has the lowest TN of 72.48 % and the four-variable logistic ranks the best with 78.67 %. Besides, all models show greater TP than TN (Fig. 85.6), which may be caused by the similar number of training samples (pixels) used from landslides areas and non-landslide areas and further work needs to be done to improve the problem. Among these three automatic landslide detection models, the index-threshold method has a medium, similar level but more robust accuracy compared to logistic regression models. To achieve a balance on accuracy between TP and NP, the index-threshold method is recommended as a fast and easy to use method to detect landslides.

4 Conclusion

Automatic identification of landslides provides an efficient way for landslide hazard, susceptibility and risk mapping. In this paper, a method to objectively select important layers for the establishment of multiple regression models in automatic landslide detection and a new index-threshold method with the best threshold searching technique are provided. Based on the rankings of *ui*, helpful layers for two logistic regression models are picked out and *LSI*, which takes full advantage of the most important layers and ignores low noisy *ui* layers, is calculated. The *LSI* has an explicit and concise form to depict landslides using transformations from pre and post landslide images. Combined with the best threshold search algorithm, the *LSI* technique has a similar level of good performance as achieved by those two logistic models and can be applied to other places with high landslide detection accuracy and robust results. Methods proposed in this paper are quicker, more objective and with less human interaction, so they can be used for fast automatic landslide mapping over a large region tortured by various types of landslides.

References

Aksoy B, Ercanoglu M (2012) Landslide identification and classification by object-based image analysis and fuzzy logic: an example from the Azdavay region (Kastamonu, Turkey). Comput Geosci 38:87–98

Chen J, Gong P, He C et al (2003) Land-use/land-cover change detection using improved change-vector analysis. Photogramm Eng Remote Sens 69(4):369–379

Chiang S, Chang K (2011) The potential impact of climate change on typhoon-triggered landslides in Taiwan, 2010–2099. Geomorphology 133:143–151

Fell R, Corominas J, Bonnard C et al (2008) Guidelines for landslide susceptibility, hazard and risk zoning for land use planning. Eng Geol 102:85–98

Gorum T, Fan X, Westen C et al (2011) Distribution pattern of earthquake-induced landslides triggered by the 12 May 2008 Wenchuan earthquake. Geomorphology 133:152–167

Hong G, Zhang Y (2008) A comparative study on radiometric normalization using high resolution satellite images. Int J Remote Sens 29(2):425–438

Lin W, Lin C, Chou W (2006) Assessment of vegetation recovery and soil erosion at landslides caused by a catastrophic earthquake: a case study in Central Taiwan. Ecol Eng 28:79–89

Lu P, Stumpf A, Kerle N et al (2011) Object-oriented change detection for landslide rapid mapping. IEEE Geosci Remote Sens Lett 8(4):701–705

Mantovani F, Soeters R, Westen V (1996) Remote sensing techniques for landslide studies and hazard zonation in Europe. Geomorphology 15(3–4):213–225

Martha T, Kerle N, Jetten V et al (2010) Characterising spectral, spatial and morphometric properties of landslides for semi-automatic detection using object-oriented methods. Geomorphology 116:24–36

Masek J, Sun G (2004) Technical note: a spectral-angle methodology for mapping net forest cover change in northeastern China. Int J Remote Sens 25(24):5629–5636

Metternicht G, Hurni L, Gogu R (2005) Remote sensing of landslides: an analysis of the potential contribution to geo-spatial systems for hazard assessment in mountainous environments. Remote Sens Environ 98(2–3):284–303

Mondini A, Chang K, Yin H (2011a) Combining multiple change detection indices for mapping landslides triggered by typhoons. Geomorphology 134:440–451

Mondini A, Guzzetti F, Reichenbach P et al (2011b) Semi-automatic recognition and mapping of rainfall induced shallow landslides using optical satellite images. Remote Sens Environ 115:1743–1757

Parke R, Densmore A, Rosser N et al (2011) Mass wasting triggered by the 2008 Wenchuan earthquake greater than orogenic growth. Nat Geosci 4:449–452

Schuster R, Highland L (2007) The third Hans Cloos lecture. urban landslides: socioeconomic impacts and overview of mitigative strategies. Bull Eng Geol Environ 66:1–27

Shi P (2002) Theory on disaster science and disaster dynamics. J Nat Disasters 11(3):1–9

Soeters R, Westen C (1996) Slope instability recognition, analysis and zonation. National Academy Press, Washington, DC

Tang C, Zhu J, Qi X et al (2011) Landslides induced by the Wenchuan earthquake and the subsequent strong rainfall event: a case study in the Beichuan area of China. Eng Geol 122:22–33

Xu C, Dai F, Chen J et al (2009) Identification and analysis of secondary geological hazards triggered by a magnitude 8.0 Wenchuan earthquake. J Remote Sens 13(4):742–762

Xu M, Wang Z, Qi L et al (2012) Disaster chains initiated by the Wenchuan earthquake. Environ Earth Sci 65:975–985

Zhang W, Lin J, Peng J et al (2010) Estimating Wenchuan earthquake induced landslides based on remote sensing. Int J Remote Sens 31(13):3495–3508

A Comparison of Predicted and Observed Slope Failures Due to the 2004 Niigata-Ken Chuetsu Earthquake

J.-C. Jiang and S. Nakano

Abstract

A GIS-based approach for regional assessment of seismic landslide displacements is represented. In this approach, a rigorous Newmark's analysis extended to a circular failure surface was integrated with a GIS to predict seismically induced slope displacements on the basis of rotation. More precise digital elevation model (DEM) with small size grid cells can be used to generate slope models and to extract the most critical slope section for each cell. In this paper, the proposed method is applied for a regional assessment of landslide displacements due to the 2004 Niigata-Ken Chuetsu Earthquake and the results obtained are compared with the observed slope failures during the earthquake.

Keywords

Slope · Failure · Earthquake · Newmark's displacements · GIS · Digital elevation model (DEM)

1 Introduction

Geographic information system (GIS) has become a common tool for regional assessment of geological and geotechnical hazard. This system has widely been used for static landslide hazard zonation. In recent years, increasing attentions are paid in application of GIS to hazard analysis of earthquake-induced landslides (Ho and Miles 1997; Jibson et al. 1998; Miles and Ho 1999; Jiang and Yamagami 2006). It has been shown that for such methods a rigorous algorithm should be employed to calculate the seismic displacements for each slope using Newmark's double integration (e.g. Miles and Ho 1999; Jibson et al. 1998).

Based on the same consideration, a GIS-based method was developed by Jiang and Yamagami (2006) for regional assessment of seismic displacements of slopes. In this method, a rigorous Newmark analysis extended to a circular failure surface was integrated with a GIS to predict seismic landslide displacements on the basis of rotation. A unique characteristic of the method by

J.-C. Jiang (✉) · S. Nakano
Department of Civil and Environmental Engineering, The University of Tokushima, Tokushima, Japan
e-mail: jiang@ce.tokushima-u.ac.jp

S. Nakano
e-mail: nakano@ce.tokushima-u.ac.jp

Jiang and Yamagami is to allow the use of more accurate digital elevation models (DEM) with small size grid cells to generate slope models and to extract the most critical slope section for each cell involved in a DEM coverage. In this paper, the method proposed by Jiang and Yamagami (2006) is applied for a regional assessment of landslide displacements due to the 2004 Niigata-Ken Chuetsu Earthquake and the results obtained are compared with the observed slope failures during the earthquake.
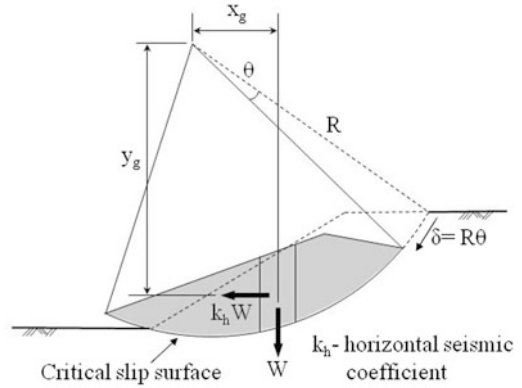
2   GIS-Based Newmark's Analysis

2.1   Newmark's Rotational Block Analysis

The original Newmark method (1965) assumes that the slope is rigid and perfectly elastic and permanent displacements occur along a well-defined planar slip surface when dynamic stress exceeds shear resistance during shaking. As rotational landslides along a curved slip surface often take place during earthquakes, it is preferable to compute seismic slope displacements on the basis of rotation. Sarma (1981) extended the Newmark's idea to a circular failure surface. The Sarma's procedure was slightly modified by Jiang and Yamagami (2006) for evaluating seismic displacements of slopes. This procedure is represented herein for the completeness.

Let us assume a rigid body on a circular slip surface, shown in Fig. 86.1, which is being acted upon by a horizontal earthquake load $K_h W$ (Note that K_h is a function of time). The equation of motion of the sliding body can be written as

$$
\begin{aligned}
J\ddot{\theta} = \sum WR\sin\alpha &+ K_h \sum Wy_g \\
&- R\sum W\cos\alpha\tan\varphi \\
&+ K_h R \sum W\sin\alpha\tan\varphi \\
&- R\sum c\cdot l
\end{aligned}
\tag{86.1}
$$

in which J = the mass moment of inertia; θ and $\ddot{\theta}$ = the angle of rotation and angular acceleration of the sliding body, respectively; W = total

Fig. 86.1 Rotational slope movements at failure

weight of the slice at the center of gravity; R = radius of the critical slip circle; α = angle of inclination of the slice base to the horizontal; K_h = horizontal seismic coefficient; y_g = vertical distance between the center of the critical slip circle and the center of gravity of the slice; l = length of the slice bottom; and c, $\varnothing$ = strength parameters of soil involved in the Mohr–Coulomb failure criterion.

The positive items of the right-hand side of Eq. (86.1) stand for the driving moment of the sliding mass, and the negative items express the resisting moment of the sliding mass. At the yield acceleration, F (the factor of safety) = 1.0, and therefore, the driving moment of the sliding mass is equal to the resisting moment. Let Kc to be the yield seismic coefficient, we obtain

$$
\begin{aligned}
\sum WR\sin\alpha &+ K_c\sum Wy_g - R\sum W\cos\alpha\tan\varphi \\
&+ K_c R\sum W\sin\alpha\tan\varphi - R\sum c\cdot l = 0.0
\end{aligned}
\tag{86.2}
$$

The yield seismic coefficient can be determined using the standard Bishop method while seeking the required K_c for $F = 1.0$. Once $K_h > K_c$ (or $F < 1.0$), the resisting moment remains constant while the driving moment increases according to K_h, and thus the relative angular acceleration, $\ddot{\theta}$, is induced in the failure mass. Combining Eqs. (86.1) and (86.2) yields the following equation.

$$\ddot{\theta} = (K_h - K_c)(\sum W y_g + R \sum W \sin\alpha \tan\varphi)/J$$
$$(\text{for } K_h > K_c)$$
$$(86.3)$$

The initial conditions of Eq. (86.3) are $\theta = 0$ and $\ddot{\theta} = 0$ at t = 0. Since K_h is a function of excitation time, solution of Eq. (86.3) in a closed form is not possible and numerical solutions may be obtained using Newmark's linear acceleration method. The angular velocity, $\dot{\theta}$ is determined by integrating Eq. (86.3). In the numerical procedure, the excitation time is divided into series of small increments, Δt, and a linear variation of acceleration within the time interval t and t + Δt is assumed to be

$$\dot{\theta}_{t+\Delta t} = \dot{\theta}_t + (\ddot{\theta}_t + \ddot{\theta}_{t+\Delta t})\Delta t/2.0. \qquad (86.4)$$

Similarly, integration of this equation leads to the rotation:

$$\theta_{t+\Delta t} = \theta_t + \dot{\theta}\Delta t + (2\ddot{\theta}_t + \ddot{\theta}_{t+\Delta t})\Delta t^2/6.0. \qquad (86.5)$$

The value of θ at the end of the excitation yields the permanent rotation of the rigid body. With reference to Fig. 86.1, when the movement is small, the total magnitude of rotational permanent displacement of the sliding mass can be approximated as $R\theta$.

It should be noted that the sliding-block model (Newmark 1965) was developed for analysing man-made dams and embankments subjected to earthquakes. The extended Newmark's analysis described above can be used only for rotational movements along a circular failure surface. It does not consider the mechanisms of failure for soil/rock falls, rock slides, and liquefaction induced landslides.

2.2 Creation of Surface Model and Extraction of Critical Slope Section

A digital surface topography coverage of a subject area is required for the slope instability analysis of this area. This is usually represented by digital elevation model (DEM). There are many kinds of DEM generation methods such as a stereo-matching from aerial photograph or satellite image, an interferometry technique with SAR data and an interpolation of topographic maps. Recently, DEM models with small size grid cells (e.g. 10×10 m) are available for many regions in Japan.

The creation of an accurate surface model is a first step to further analysis. The slope models greatly influence the calculated factor of safety and critical acceleration, which in turn directly control the amount of Newmark displacements. Existing methods for GIS-based landslide displacement assessment are to use an infinite slope stability model. Each grid cell derived from a surface model with large size grid cells (for instance, 50 m $\times$ 50 m) is treated as an infinitely long slope for computing seismic displacements. However, recent advancements in computer hardware and software allow the use of more precise DEM with small size grid cells for GIS-based regional hazard assessment. It is clear that an assumption of an infinitely long slope is not appropriate for small size grid cells. To overcome the shortcomings associated with the infinite slope assumption, the following procedure was devised (Jiang and Yamagami 2006). First, for a grid cell in the DEM coverage, we pick up 3×3 cells consisting of the cell under consideration and eight adjacent cells around it, as shown in Fig. 86.2a. Then, representative vertical sections in four different directions, a–b, c–d, e–f and g–h as shown in Fig. 86.2b, are formed using the elevations at the grid points,. For each slope in Fig. 86.2b, the critical slip surface is determined using the Bishop method, and the slope section with the lowest factor of safety is chosen as the most critical one. The permanent deformation calculated on this slip surface represents the Newmark displacement of the center cell of 3×3 grid cells. The above described procedure is in turn repeated for each cell of the grids derived from the DEM coverage. While the situations for 3×3 cells are described above, 5×5 or 7×7 cells (see Fig. 86.2a) can also be
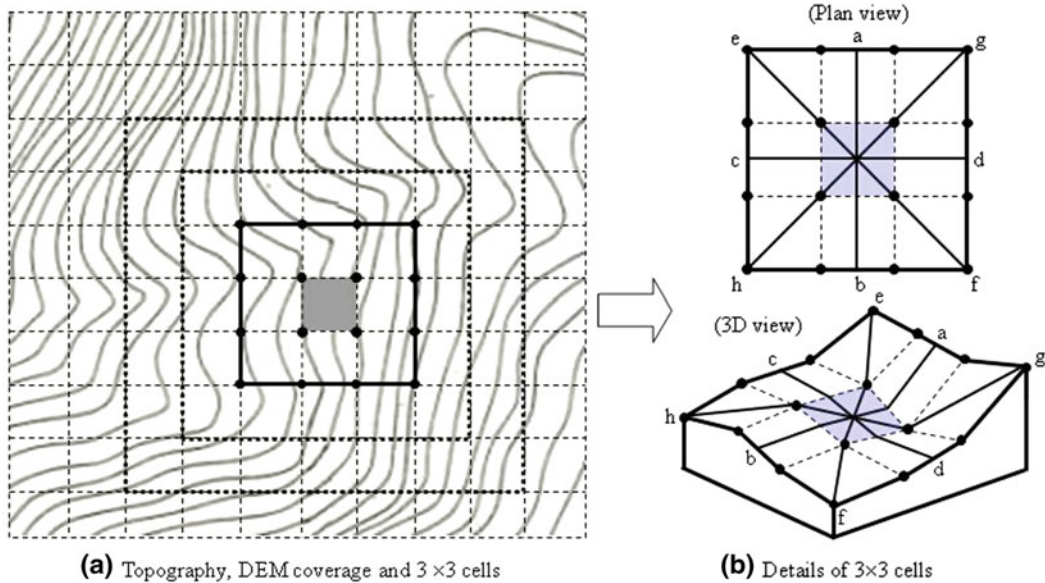
Fig. 86.2 Slope models and extraction of most critical slope section for a grid cell

used to generate slope models for each grid cell for Newmark displacement computations.

2.3 Selection of Strength Parameters

The selection of strength parameters is an important aspect of building a reliable seismic slope instability model. Generally, a digital geologic map forms the basis for assigning material properties over a wide area. Representative shear strength values are determined for each of geologic units by comprehensively considering all available data as those from field observations, stereoscopic inspection of high altitude aerial photo-graphs, and test results of published technical reports. Available empirical graphs and equations regarding the shear strength of local soils should also be incorporated into the procedure of selecting the strength parameters. The judgment of local practicing geotechnical engineers and geologists would be necessary for a reliable selection of the soil properties. When a geologic map is available, the strength parameters can individually be assigned to each of geologic units (Fig. 86.3).

2.4 Input Ground Motion

A ground motion can be obtained from an actual site acceleration record, scaling up or down an existing record for different source-to-site distances, and an artificial acceleration time history. A logical and practical choice is to use artificial acceleration data because it is usually difficult to obtain an appropriate site record.

By summarizing the steps 2.1–2.4, a simple flowchart was presented by Jiang and Yamagami (2006) to show the sequential steps of the GIS-based assessment of earthquake-induced slope displacements.

3 Prediction of Slope Failures Due to 2004 Niigata-Ken Chuetsu Earthquake

The 2004 Niigata Ken Chuetsu earthquake triggered a vast number of landslides that severely damaged roads and rail lines, destroyed houses and other structures, and dammed streams and rivers. Most of the triggered landslides were relatively shallow failures which were densely concentrated in a mountainous area in central
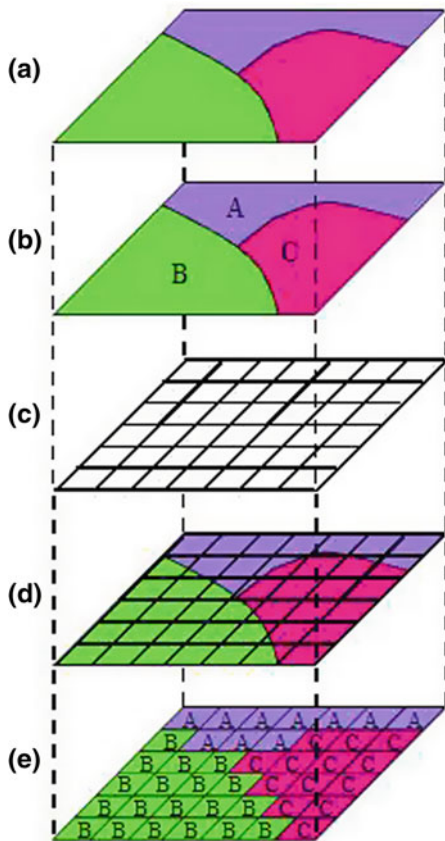
Fig. 86.3 Assignment of strength parameters of soil for each cell based on a digital geological map

Fig. 86.4 Distribution of landslides in the Yamakoshi village area triggered by the 2004 Niigata-ken Chuetsu earthquake (after The Geospatial Information Authority of Japan 2006)
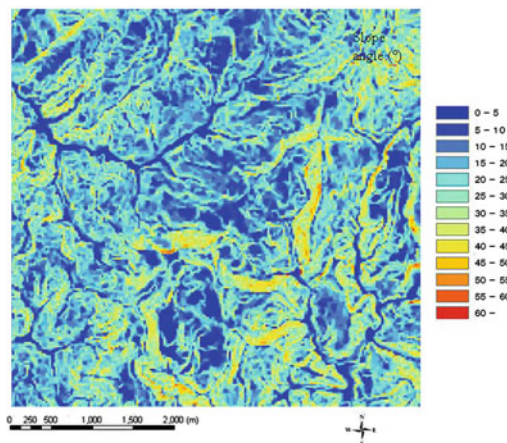
Fig. 86.5 Spatial distribution of slope angles in the Yamakoshi village area

Niigata Prefecture (Kieffer et al. 2006). High antecedent rainfall before the earthquake, very strong shaking and steep local topography in relatively weak geologic units were major factors contributed to the large concentrations and densities of landslides.

Figure 86.4 shows the distribution of landslides in the Yamakoshi village area triggered by the 2004 Niigata-ken Chuetsu Earthquake. The spatial distribution of slope angles in the Yamakoshi village area is illustrated in Fig. 86.5. In order to compute a distribution of seismic displacements of slopes using the method by Jiang and Yamagami (2006), a DEM coverage with 10 × 10 m cells is employed which is built from a 1:25000 contour line map. For simplicity, homogeneous soil properties with $c_u = 30.0$, $\phi = 0.0$ and $\gamma = 18.0$ kN/m^3 are used for the

whole study area. These values of shear strength were also used for a FEM analysis of the typical landslides in the same area (Ugai et al. 2005). An actual acceleration time history (Fig. 86.6) observed in the Yamakoshi village was adopted for displacement calculations. Since the sedimentary sequence of bedrock in the area of the main landslide concentration represents a shallow marginal facies (Yanagisawa et al. 1986) and the slides triggered by the earthquake are shallow, a limitation of the depth of 5.0 m was

set up for slip surfaces on which seismic displacements are computed.

The distribution of calculated displacements (>50.0 cm) of slopes in the Yamakoshi village area is shown in Fig. 86.7. It is shown that large displacements take place in relatively steep slopes (see Figs. 86.5, 86.7). In order to compare the obtained results with actual slope failures, the computed seismic displacements are presented by overlaying Figs. 86.4 and 86.7, as shown in Fig. 86.8. Although the magnitude of computed displacements may not directly reflect slope failures, it is meaningful to compare the results showed in Figs. 86.4 and 86.7 for a relative evaluation of instability of slopes. From Fig. 86.8 we can see that in the most parts the distribution of seismic displacements of slopes is in good agreement with the locations of actual landslides triggered by the earthquake. It is of interest to note that in Fig. 86.8 the areas of large seismic displacements (>100.0 cm) cover the most locations of large-scale landslides by the earthquake. This may suggest that not only the locations but also the scale of landslides can be predicted from the distribution of seismic displacements.

Fig. 86.8 Distribution of seismic displacements of slopes and actual landslides triggered by the earthquake

Seismic displacements > 50.0 cm
Large landslides   Small landslides

Seismic displacements > 100.0 cm
Large landslides   Small landslides
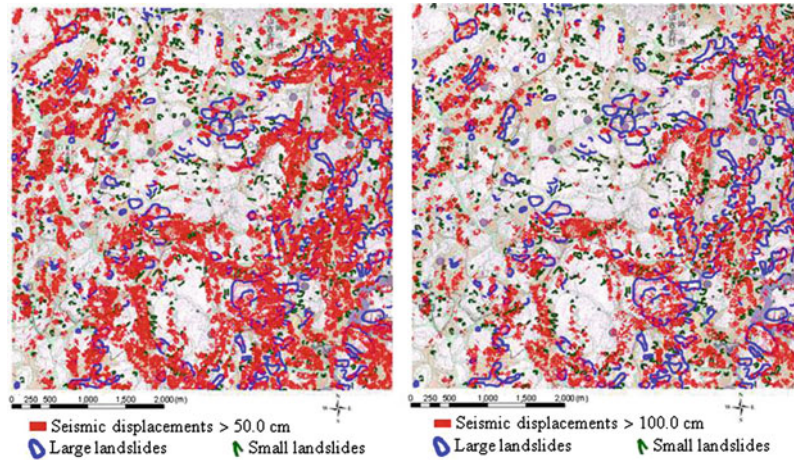
4   Summary

A GIS-based method for regional assessment of seismic displacements of slopes was represented. The method combines a rigorous Newmark model with GIS for computations of seismic displacements and allows the use of more accurate DEM with small size grid cells to generate slope models and to extract the most critical slope section for each cell. In this paper, the proposed method was applied for a regional assessment of landslide displacements due to the 2004 Niigata-Ken Chuetsu Earthquake and the obtained results were compared with the slope failures observed during the earthquake. It was shown that the distribution of seismic displacements of slopes may probably be used to predict not only the locations but also the scale of landslides triggered by earthquakes.

References

Ho CL, Miles SB (1997) Deterministic zonation of seismic slope instability: an application of GIS spatial analysis in soil dynamics. Spatial analysis in soil dynamics and earthquake engineering 1997:87–102

Jiang J-C, Yamagami T (2006) Regional seismic slope instability assessment using Newmark's method and geographical information system. In: Proceedings of the 4th Asian joint symposium on geotechnical and geo-environmental engineering, pp 247–252

Jibson RW, Harp EL, Michael JA (1998): A method for producing digital probabilistic seismic landslide hazard maps: an example from the Los Angeles, California area. U.S. Geological Survey Open-File Report, vol 98–113

Kieffer DS, Jibson R, Rathje J, Kelson K (2006) Landslides triggered by the 2004 Niigata Ken Chuetsu, Japan. Earthq Spectra 22(S1):S47–S73

Miles SB, Ho CL (1999) Rigorous landslide hazard zonation using Newmark's method and stochastic ground motion simulation. Soil Dyn Earthq Eng 18(4):305–323

Newmark NM (1965) Effects of earthquakes on dams and embankments. Geotechnique 15:139–160

Sarma SK (1981) Seismic displacement analysis of earth dams. J Geotech Eng ASCE 107(12):1735–1739

The Geospatial Information Authority of Japan (2006) 1:25,000 map of landslides triggered by the 2004 Niigata-ken Chuetsu earthquake (in Japanese)

Ugai K, Wakai A, Onoue A, Higuchi K (2005) Numerical analysis of slope failures subjected to earthquakes. In: Proceedings of the 40th annual conference in geotechnical engineering, pp 2291–2292 (in Japanese)

Yanagisawa Y, Kobayashi I, Takeuchi K, Tateishi M, Chihara K, Kato H (1986) Geology of Ojiya District, Geological Survey of Japan, Quadrangle Series, Niigata (7), no. 50, scale 1:50,000 (in Japanese, with English abstract)

Distribution Characteristics and Slope Structure Types of Landslide/Rock Fall Along the Roads in the 2010 Yushu Earthquake (Ms7.1) Disaster Area

87

Hongli Zhang, Honggang Wu, Daoyong Wu and Huimin Ma

Abstract

The earthquake often induces a large number of landslides or rock falls. During the 2010 Yushu earthquake (Ms7.1) in Qinghai province, landslides and rock falls were triggered at the slope of different degrees along National Highway G214 and Provincial Highways S308 and S309. After the earthquake, we conducted a lot of field surveys and referred related literatures, finally summarized the landslide/rock fall types and spatial distribution of their characteristics in the earthquake-damaged area. In advance, as focusing on the typical worksites, characteristics of the slope structure and slope deformation have been discussed. The results can provide suggestions for reconstruction engineering along the roads in the area, as well as for technological protection engineering against landslide/rock fall along the proposed highway of Xining to Yushu.

1 Introduction

Yushu is located in the southwestern hinterland of the Qinghai-Tibet Plateau, which is the source of three rivers such as Yangtze River, Yellow River and Lancang River. The terrain in general is higher in northwestern part, lower in southeastern and northeastern parts, with an average altitude more than 4,000 m. The terrain is towered and landform is complete. Alpine valleys and mountains are the major topography. There are many small basins and lake basins as well. The exposed lithological phasis is mainly fragmental rock, volcanic rock, clay rock and carbonate rock. The geological structures give priority to NW–WNW and NE–NS in lesser. Due to the special geological environmental conditions, it becomes one of the most severe geological hazard regions of collapse, landslide and debris flow in Qinghai province.

H. Zhang (✉) · H. Wu · D. Wu · H. Ma
Northwest Research Institute Co., Ltd. of CREC,
Lanzhou 730000, China
e-mail: ztxbywhg@yahoo.com.cn

D. Wu
Department of Civil Engineering, Lanzhou Jiaotong
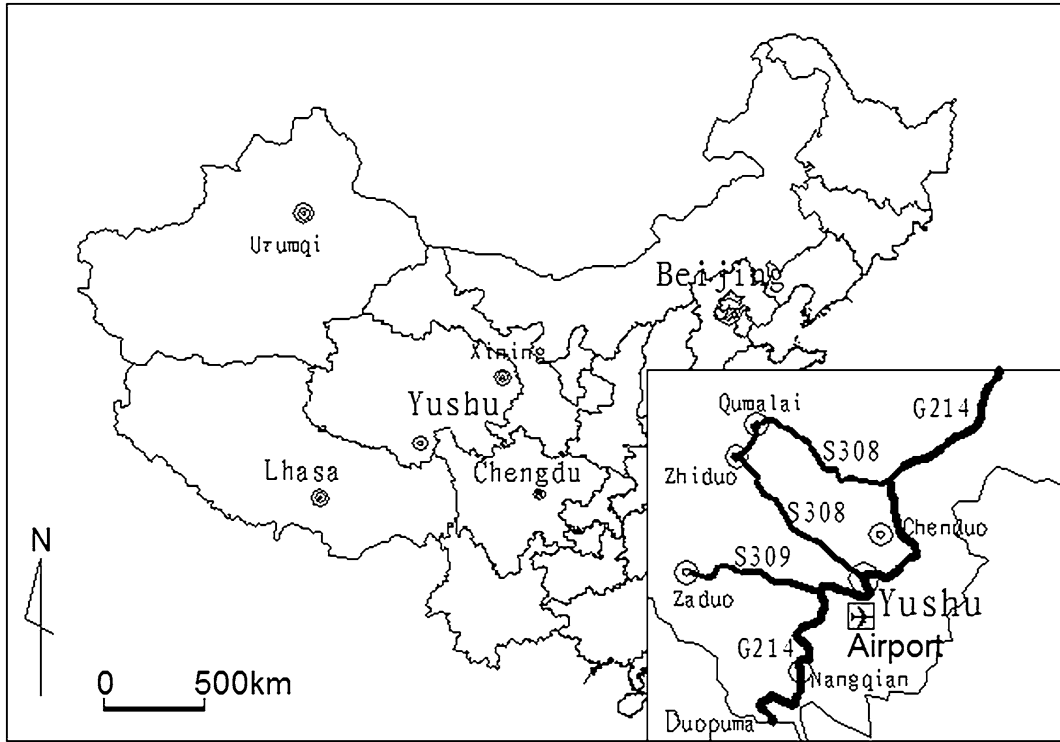University, Lanzhou 730070, China

Fig. 87.1 Road map of Yushu in Qinghai province

National Highway such as G214, Provincial Highway S308 and S309 are the main traffic route between Yushu and other cities and towns (Fig. 87.1). The 2010 Yushu earthquake (Ms7.1) on April 14 in Qinghai province gave not only minimal damage but also serious damage to the roads, and the damages on the Airport Road was most serious, that affected on the earthquake relief and reconstruction activities (Cornell 1968; Kumar and Manichandra 2007; Cui et al. 2011).

2 The Distribution Characteristics of Landslide/Rock Fall Along the Roads

After the earthquake, landslide/rock fall at 48 worksites were investigated along the roads (Table 87.1). There are 23 worksites related landslide in the valley and 20 worksites are related mainly rock fall (precursory rock fall is included) and five worksites related embankment deformation in plateau frozen soil region.

Table 87.1 Specifications of the worksites

Type road	Landslide	Rock fall	Embankment deformation	Total
G214	13	14	1	28
S308	4	1	4	9
S309	6	5	0	11
Total	23	20	5	48

In general, landslide/rock fall are concentrated near Yushu. It is mainly controlled by three factors such as lithological characteristics, faults of WNW–NW in strike and the Mediterranean-Himalayan-South Asia seismic belt.
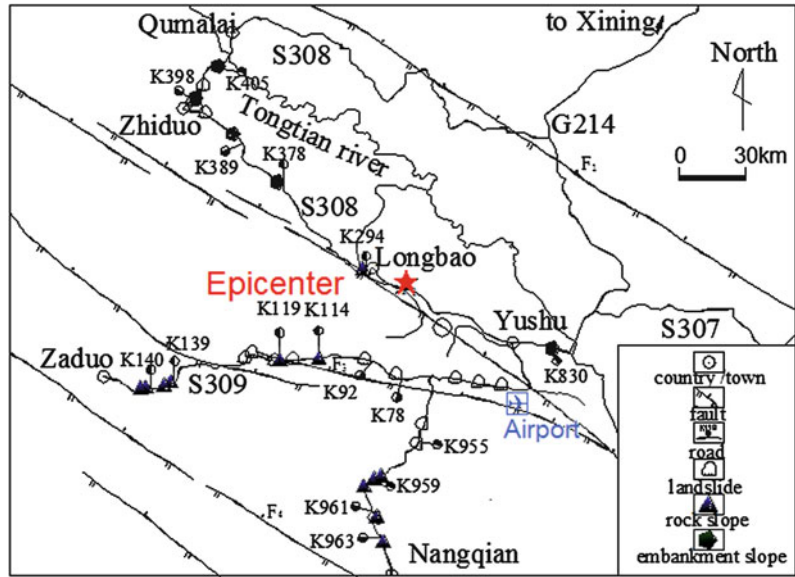
2.1 Relationship Between Landslide/Rock Fall and Lithological Characteristics

Carboniferous, Permian, Triassic, Tertiary rocks and Quaternary sediments covers this area. Among them, Triassic rock and Quaternary have

Fig. 87.2 Location of the worksites along the road and geological structure

been exposed widely. The exposed rocks and sediments facing on the roads are mainly fragmental rock, volcanic rock, clay rock and carbonate rock. The rocks are bedded and joints are developed notably. The rock dip angle is more than 50°, and part of them is close to upright. Judging from several group joints, the rock is not stable where is vulnerable for landslide/rock fall, including clayey soil, silty soil, sandy soil and fragmented rock. Such the unstable materials extend widely on the top of bedrock along the roads, which has important influence on the stability of slope. The embankment is mainly composed of artificial fills and debris depressed by strong shaking of the earthquake.

2.2 Relationship Between Landslide/Rock Fall and Geological Structure

Geological structure is an extremely important role to construct road in this area, where the arc faults of NNW–NW in strike are well developed. These faults are relatively long, stretching up to hundreds of kilometers to thousands of kilometers (Li et al. 1995). Our research shows that the spatial distribution of seismic-induced landslides/rock falls disasters is controlled obviously

by the active faults (as shown in Fig. 87.2). It can be seen that the faults are almost parallel to National Highway G214 and Provincial Highway S308 and S309. Damages caused by landslide/rock fall are serious. On the influence of fault belt, the distribution of high slope diseases and landslides along the roads are intensive.

2.3 Relationship Between Landslide/Rock Fall and Seismic Intensity

Landslide/rock fall damages induced by the earthquake mainly locate near the epicenter. As far away from the epicenter, the number of the damages reduces significantly.

The earthquake intensity was heavy in these areas closer to the epicenter. Because the seismic intensity exceeded more than 6°, many earthquake-induced landslide/rock falls occurred in the Airport—Nangqian section (Fig. 87.2) along National Highway G214, and Provincial Highway S308 and S309. The earthquake intensity was relatively small in the Nangqian–Duopuma section (Fig. 87.1) along National Highway G214, that is far away from the epicenter. Therefore the number of landslides/rock fall induced by the earthquake was quite less with scattered distribution.

Fig. 87.3 Slope structure classifications

$$\text{Structure type}\begin{cases} \text{Rock slope}\begin{cases} \textit{Dip bedded rock slope}\,(1a) \\ \textit{Anti}-\textit{dip bedded rock slope}\,(1b) \end{cases} \\ \text{Soil landslide}\begin{cases} \text{landslide}\begin{cases} \textit{Single layer}\,(2a) \\ \textit{Multi layer}\,(2b) \end{cases} \\ \text{Embankment slope}\begin{cases} \text{Filling - overlay - bedrock}(3a) \\ \text{Filling - bedrock}(3b) \end{cases} \end{cases} \end{cases}$$
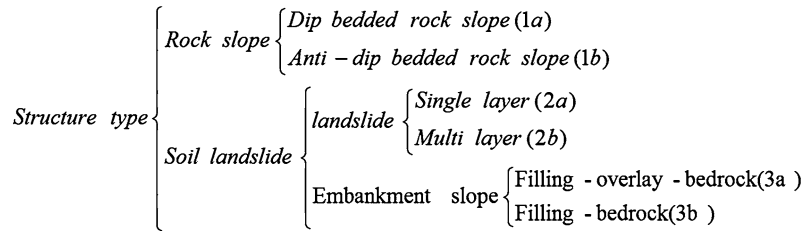
3 Slope Structure Related Landslide/Rock Fall

Similar characteristics in engineering and geological environment were observed and identified at the worksites. Therefore, to simply understand the damages, landslide/rock fall was classified according to lithological characteristics and slope structure. The classified results would provide a good reference for future disaster protection engineering and planning management on the roads.

Firstly, taking lithological characteristics into consideration, landslides/rock falls were divided into soil landslide and rock slope, and then more two items were categorized (Fig. 87.3).

In the light of relationship between slope structure and slope surface, stability of slope has a great of differences due to bedding plane obliquity. Inclination angle of rock bedding plane at the worksite is large in general, most in 50–80°; the inclination at some worksites was approximate vertical. According to the relation between bedding plane inclination and slope surface inclination, "rock slope" shown in Fig. 87.3 would be divided into dip bedded rock slope (1a) and anti-dip bedded rock slope (1b).

Soil landslides are divided into landslide and embankment slope in the light of artificial slope or not. The landslide has been already existed before excavation by road construction. Embankment slope is composed of artificial fill in recent, which is formed in road construction process. Landslides are also divided into single layer landslide (2a) and multi layer landslide (2b). Based on its local structure embankment slopes are further divided into filling-overlay-bedrock (3a) and filling-bedrock (3b).

4 Structure of Typical Landslide/Rock Fall

4.1 Dip Bedded Rock Slope

This kind of slope refers to the slip-downward slope with the angle less than 20° between strike of bedding plane and slope strike. The typical worksite is located in K958+880∼+975 segment of Airport—Nangqian along National Highway G214 (Fig. 87.4a). The valley is very narrow with steep rock slopes on both sides of the valley. Slope is mainly composed of gray limestone, with the occurrence of NE30°/NW∠70°. In the field survey, we found that the bedding plane inclination angle is in the range of 50–80°, and some is close to erect. The slope instability is controlled by the joints developed in the slope to collapse or formulate unstable rock. Once unstable rock mass was formed, it would be easily to collapse and have certain influence on the road traffic, i.e., it would threaten the road traffic by rainfall or earthquake.

4.2 Anti-Dip Bedded Rock Slope

This kind of slope refers to the slip-inward slope with the angle less than 20° between stratum strike and slope strike. The Typical worksite is located in K959+050∼+150 section of Airport—Nangqian along National Highway G214 (Fig. 87.4b). Once this kind of slope is collapsed, the remained slope appears to have fall cavity. The slope is mainly composed of thick bedded gray limestone, with the occurrence of NE30°/NW∠70°. There is a gentle inclination joints NW55°/NE∠42°, cutting off the rock to collapse.
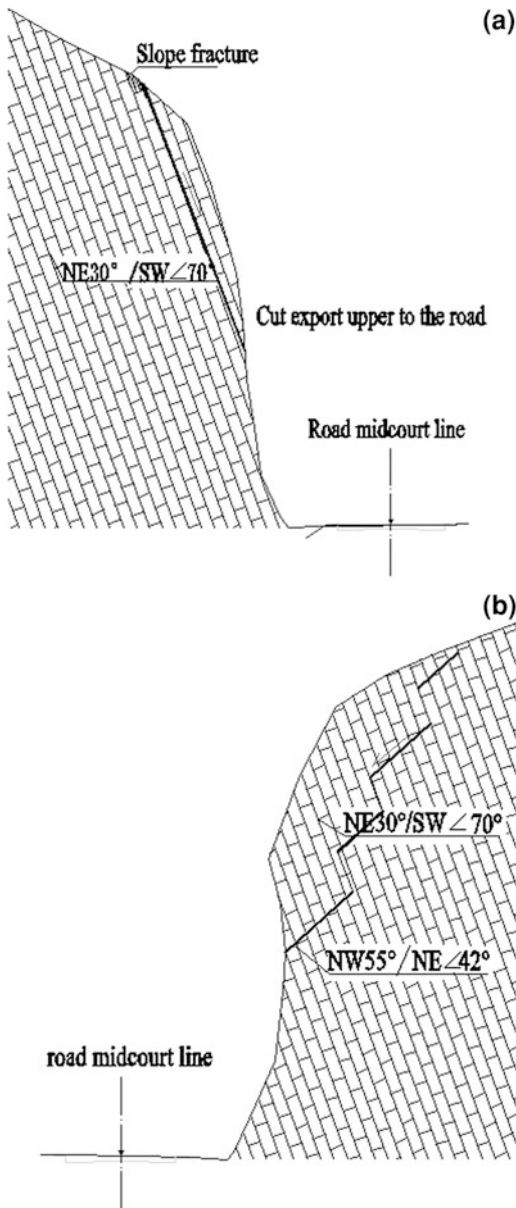
Fig. 87.4 Cross section of slope structure. **a** Dip bedded rock slope. **b** Anti-dip bedded rock slope

There are two kinds of the rock fall. (1) In case that joints have gentle inclination in the slope, the rock fall is mainly controlled by the group of joints and unstable rock mass are formulated. If not enough to resist against movement downward, the unstable rock mass would fall along the structure surface. (2) If the rock is relatively hard and less joint is developed, the slope could be mainly toppling over. In toppling over, rock bedding planes are bent in an arc, this bend develop gradually from the slope surface to deep layer and tensile cracks expand step by step. In the end, toppling would be transformed into deep rock slide.

4.3 Landslide

Based on the structure of surface and sliding zones, landslides are further divided into single layer landslide (2a) and multi layer landslide (2b).

(1) *Single layer landslide (2a)*

This refers to only one sliding layer. The typical worksite is Airport road landslide No.3 (Fig. 87.5). The angle of sliding zone is only about 3°. The most thickness of landslide body is estimated at 22.80 m, as well as average thickness of 19.8 m. The landslide is 317 m parallel to the road, and 482 m vertical to the road, with landslide volume estimated at 2.89×10^6 m^3. The sliding zone is mainly composed of silty clay and breccias soil. The landslide morphology is controlled by the broadside cracks and posterior discontinuous cracks.

(2) *Multi layer landslide (2b)*

This refers to multi sliding layer. The typical worksite is Airport road landslide No.1 (Fig. 87.7). The landslide is directed towards NE46°, with sliding surface inclination angle of 18–19°. The landslide is about 133 m parallel to the road, and 166 m vertical to the road, with landslide volume estimated at 3.82×10^5 m^3. The sliding zone is mainly composed of silty clay and breccias soil. The slided mass is mainly composed of breccias and gravel soils. This multi layer sliding zone is divided into two sliding zones. One is the shallow sliding zone and another is the deep sliding zone. The shallow sliding zone is less stable than the deep one (Fig. 87.6).

4.4 Embankment Slope

Comparing with other categories shown in Fig. 87.3, embankment slope has different characteristics about slope structure. The main
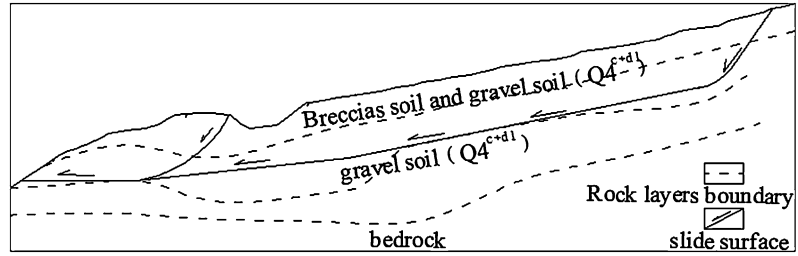
Fig. 87.5 Single layer landslide

Fig. 87.6 Multi layer landslide
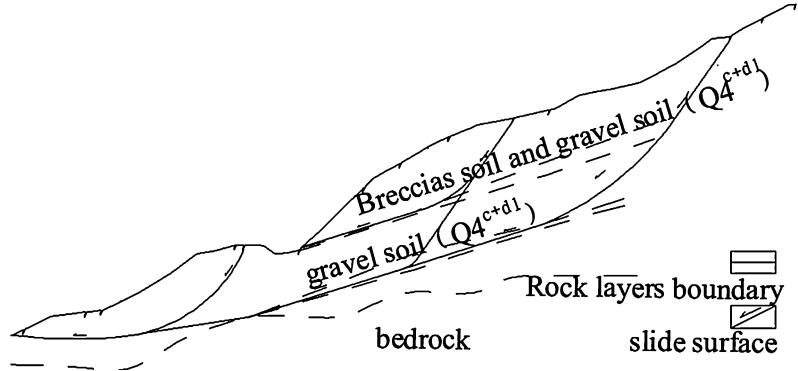
difference is reflected in lithological characteristics. Embankment slope is composed of artificial fills and original slope materials. The slopes can be divided into filling-overlay- bedrock embankment slope (3a) and filling-bedrock embankment slope (3b).

(1) *Filling-overlay-bedrock embankment slope (3a)*

This category refers to the thick overburden fills on the bedrock surface (Fig. 87.7a). The typical site is located in K389+800∼K39+060 along Provincial Highway S308. The water content is rich in the lower part of the embankment, only about 1 m in thickness. Therefore, this section of the overall embankment is depressed after the earthquake, and more than 100 m of cracks occur in inside of the embankment.

The upper part of the embankment is composed of artificial fills, mainly fragmental soils. The middle of the embankment is composed of silty clay. The bedrock is composed of limestone. The embankment is also located beside

Fig. 87.7 Two categories of embankment slope. **a** Filling-overlay-bedrock. **b** Filling-bedrock

the river and contacts with unconsolidated fluvial deposit. Because of the strong shaking by the earthquake, such the deposit was liquefied, and then the embankments were deformed and depressed in long segment.
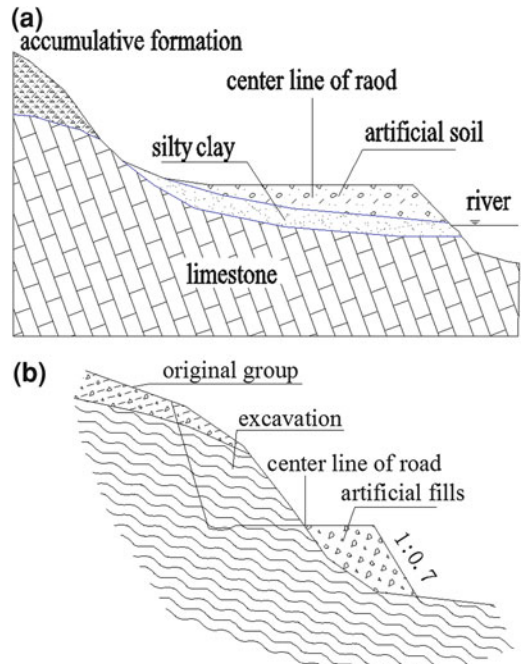
(2) *Filling—bedrock embankment slope* (3*b*)

This structure refers to embankment slopes that overlaid both on the fills and excavated bedrock (Fig. 87.7b). The typical worksite is embankment slope in K398+120∼+200 segment along Provincial Highway S308. The longitudinal length of the slope is 80 m, with the height of 10–20 m. Stability of the embankment is mainly controlled by the joints in the bedrock, with the occurrence of SE60°/NW∠63°. After the excavation, slope angle is much more than 63°, and then rock mass becomes unstable to collapse. Therefore, the possible instability also effects on the filled soil deformation along the interface between sliding zone and bedrock.

5   Conclusions

Relying on the post-disaster reconstruction projects along National Highway G214 and Provincial Highway S308 and S309, we collected and understood related literatures of the landslide/rock fall along the roads, and then summarized types of them and their characteristics of spatial distribution. The main conclusions are as follows:

Landslide/rock fall types were classified by lithological characteristics of rock mass. Landslide occurred mainly in the unconsolidated layer region. Rock fall occurs mainly in the exposed bedrock areas. When an earthquake occurs, the roadbed often deforms in floodplain areas on account of liquefaction.

(1) The spatial distribution of landslide/rock fall damages induced by the 2010 Yushu earthquake (Ms7.1) was quite obviously controlled by the active faults. On the influence of fault belt, landslides and serious rock fall damages located on the both sides of the road. The landslide/rock fall gave more serious damages in the region closer to the epicenter. The number of damaged worksites significantly decreases as far away from the epicenter.

(2) Based on the analysis of lithological characteristics and geological structure, landslides/rock falls occurred along the roads were divided into four categories, including dip bedded rock slope, anti-dip bedded rock slope, landslide and embankment slope. These examples illustrate that the deformation or failure condition is very different. Rock fall is controlled principally by the bedding planes and discontinuities. Landslide is controlled by weakness of resistibility between bedrock and landslide mass. Embankment slope may come into being liquefaction and sliding along original ground surface during earthquake.

References

Cornell CA (1968) Engineering seismic risk analysis. Bull Seismol Soc Am 58:1583–1606

Kumar A, Manichandra S (2007) Landslide studies along the National Highway (NH 39) in Manipur. Nat Hazards 40:603–614

Cui P, Chen X-Q, Zhu Y–Y, Su F-H, Wei F-Q, Han Y-S, Liu H-J, Zhuang J-Q (2011) The Wenchuan earthquake (May 12, 2008), Sichuan Province, China, and resulting geohazards. Nat Hazards 56:19–36

Li M-F, Xing C-Q, Cai C-X, Guo W-X, Wu S-X, Yuan Z-Z, Meng Y-Q, Tu D-L, Zhang R-B, Zhou R-J (1995) Research on activity of Yushu fault. Seismol Geol 17:218–224

Estimating the Strength Parameters of Geological Formations Using Fuzzy Sets and its Application in Generating Seismic–Landslide Hazard Maps

88

Reza Majidi Feijani, Mohammad Reza Mahdavifar and Mohammad Kashanchi

Abstract

Fuzzy sets are employed as a key tool in order to estimate strength parameters of soil. The strength parameters of geological formations can vary widely from one location to another, and definite values for strength parameters cannot be assigned to each formation. So, the fuzzy set can solve the problem by assigning a series of values to the parameters. The ultimate aim of this estimation is seismic–landslide hazard zonation using Jibson et al. (Eng Geol 57:271–289, 2000) method. The quadrangle of Tootkabon is selected for evaluating the ability of this method to predict the location of landslide occurred during 1990 Manjil earthquake (Mw = 7.3). Using a complete inventory map of the landslides occurred during the Manjil earthquake; the accuracy of the prepared seismic–landslide hazard zonation map and related strength parameters have been evaluated.

R. Majidi Feijani (✉)
Department of Geotechnical Engineering, Islamic Azad University, Central Tehran Branch (IAUCTB), Tehran, Iran
e-mail: reza.majidi.f@Gmail.com

M. R. Mahdavifar
Geotechnical Engineering Research Center, International Institute of Earthquake Engineering and Seismology (IIEES), Tehran, Iran

M. Kashanchi
Department of Geotechnical Engineering, Islamic Azad University, Arak Branch, Arak, Iran

1 Introduction

Landslides are one of the most damaging collateral hazards associated with earthquake. In fact, damage from triggered landslides has sometimes exceeds damage directly related to strong shaking and fault rupture (Jibson et al. 2000). Under such conditions, preparing seismic–landslide hazard maps in which landslide-prone areas are distinguished will play an important role in minimizing total damages of an earthquake.

On the other hand, the complexity of nature and its properties has been always a serious problem in geologic investigations. For instance,

material properties and their strength parameters is the most important factor in evaluation of slope stability. According to Goodman (1995) when the material is natural rock, the only thing known with certainty is that this material will never be known with certainty. Basically facing with uncertain conditions need special techniques in which wide range of uncertainty could be tolerated. The fuzzy logic is the most compatible technique with such uncertainty and complexity. It has been used widely in different sciences during last decades.

2   Study Area

Tootkabon (Estalkhjan) quadrangle has been selected as the study area. It is located in Gilan province and north of Iran.

From strong motion point of view, the Iranian territory can be divided into two tectonic provinces: (1) Zagros, (2) Alborz and Central of Iran (Mahdavifar et al. 2008).

In the Alborz and Central of Iran zones, the earthquakes are less frequent with relatively higher magnitude than those in Zagros (Mahdavifar et al. 2008). The 1990 Manjil earthquake (Mw = 7.3) has been one of the most severe earthquakes in this zone which induced 120 large landslides and many rock-falls in the epicentral area and vicinity of the earthquake fault. Figure 88.1 shows the quadrangle of the study. It has an area of about 309 km^2 and is a part of the whole area which was affected by Manjil earthquake (1990).

3   Methodology

3.1   Overview of Mapping

The main idea for generating seismic–landslide hazard maps is developed by Jibson et al. (1998, 2000; Jibson 1993)which is based on Newmark displacements of sliding blocks. Newmark's method models a landslide as a rigid friction block that slides on an inclined plane, the target is estimating displacements eventually; the quantity value of Newmark displacements will be a useful tool to categorize hazard into different intensities and levels.

Because fuzzy models can cope with the complexity of ill-defined systems in a flexible and consistent way.

As the flowchart shows (Fig. 88.2), in continuation, the critical acceleration could be determined according to safety factors, eventually, combination of critical acceleration and Arias intensity of slopes will be used for estimating Newark displacement and seismic–landslide hazard.

3.2   Geologic Map

Digital geologic map of the quadrangle forms the basis for assigning material properties. Figure 88.3 illustrates the geological units of the study area.

3.3   Strength Parameters

As Fig. 88.2 shows, determining the representative shear strengths values (friction angle and cohesion) for geological units is necessary to calculate factor of safety of slopes. Mahdavifar et al. (2008) determined strength parameters of the quadrangle during the field visit of the study area. He determined shear strength values for rock formations. Table 88.1 shows the values of strength parameters for all formations (rock and non-rock formations) in the quadrangle.

3.4   Fuzzy Inference System for Determining F$_s$

Static factor of safety in an infinite slope with material having both frictional and cohesive strength is calculated via Eq. 88.1:

$$F_s = \frac{c^{'}}{\gamma.t.\sin\alpha} + \frac{\tan\varphi^{'}}{\tan\alpha} - \frac{m.\gamma_w}{\gamma_{\text{sat}}}\frac{\tan\varphi^{'}}{\tan\alpha} \quad (88.1)$$

where $c^{'}$ is the effective cohesion, $\varphi^{'}$ is the effective friction angle, $\propto$ is the slope angle, γ is the material unit weight, γ_w is the unit weight of

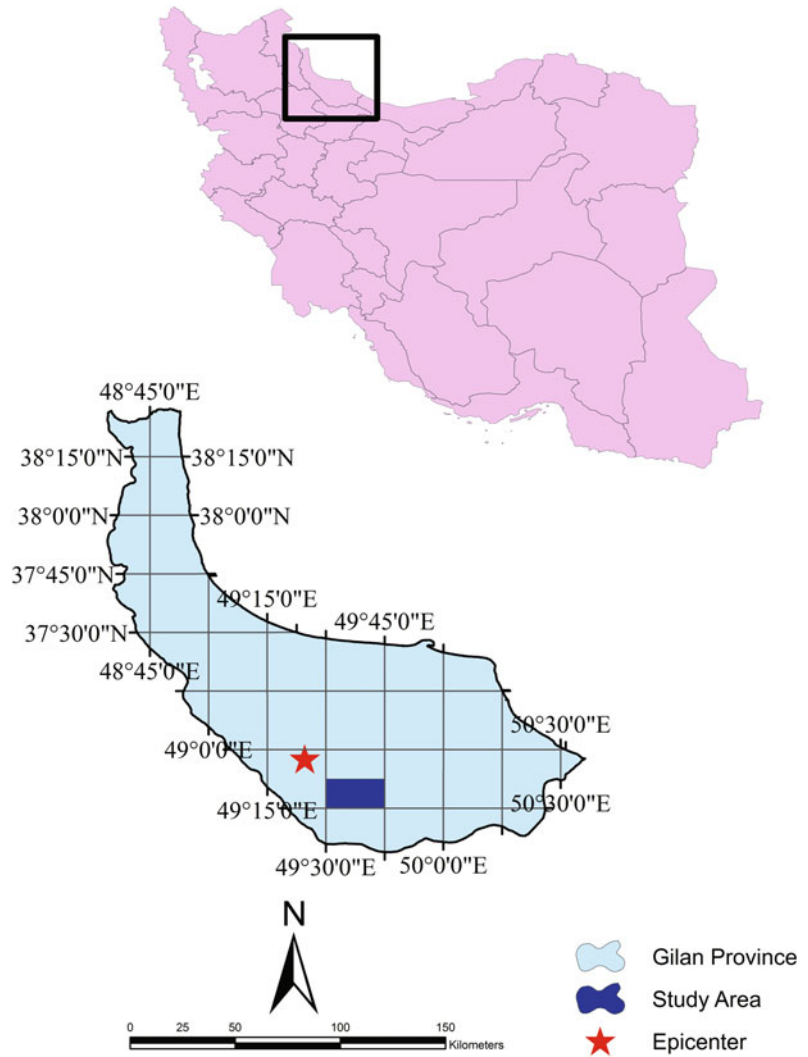Fig. 88.1 Epicenter of Manjil earthquake and the study area in Iran

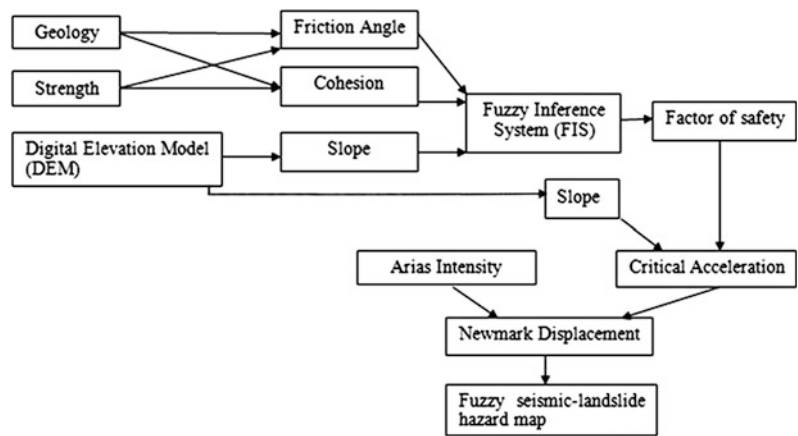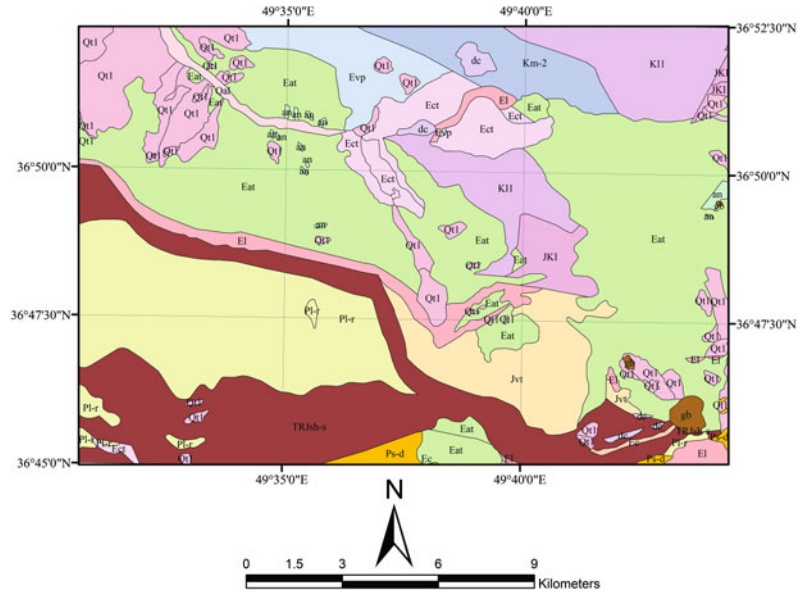Fig. 88.2 Steps for generating seismic–landslide hazard map

Fig. 88.3 Geologic map
of the study area

water, t is the slope-normal thickness of the failure, and m is the proportion of the slab thickness that is saturated.

t is estimated about 4 m; It represents the typical thickness of Manjil failures. Due to the climate and raining conditions of the study area m was considered as 0.5 for all of the slopes.

The problems related to rock masses are very complex and determination of the mechanical characteristics of the rock masses involves some uncertainties(Sonmez et al. 2003). For instance, the strength parameters of geological formations(used in Eq. 88.1) can vary widely from one location to another, and definite values for strength parameters cannot be assigned to each formation. Fuzzy set theory introduced by Zadeh (1965) is one of the tools to handle these uncertainties. Some uncertain parameters may be expressed as a fuzzy set, if there is some reason to believe that not all values in the intervals have the same degree of confidence (Juang et al. 1998).

In this study, the mamdani fuzzy algorithm is selected to calculate F_s by fuzzy sets. It is perhaps the most appealing fuzzy method to employ in engineering geological problems (Alvarez Grima 2000).

The basic elements of a fuzzy algorithm are the input and output sets and "If–Then" rules. In this study, the fuzzy inference system calculates the F_s values using antecedent of c' (effective cohesion), φ' (effective friction angle) and α (slope angle).

Fuzzy sets expand on the concept of crisp Boolean sets by representing the level of membership to a particular category—zero (0) indicating that membership is unambiguously false and one (1) indicating membership is unambiguously true, so, membership function for all variable ranges between 0 and 1.

As it is shown in Fig. 88.2, the three items which are important for determining factor of safety are friction angle, cohesion and slope angle. Therefore, we have used them as the main components of fuzzy inference system for inputs; also safety factor has been the output.

Membership function for all variables including inputs and the output are shown in Fig. 88.4. Defining membership function is an expert-base process which needs engineering judgment. Strength parameters has been categorized in three different levels; low, medium and high.

In comparison with steep slopes, There are much less landslides for slopes <10° which are deleted for next steps of analysis; that is why slope angles have been categorized in two levels named as moderate and high and slopes below 10° are not analyzed.

Table 88.1 Strength parameters and γ of the formations in the study area

| Unit name	Description	c'(Kpa)	φ'(degree)	γ (kN/m³)
an	Andesite-basaltic subvolcanic masses	150	52	25.51
dc	Dasite-andesitic subvolcanic masses	150	52	25.51
Eat	Red and dark grey dacitic-andesitic tuff	20	17	25.51
Ec	Red medium and well bedded conglomerate	70	39	24.53
Ect	Dark red and grey alternation of dacite-andesitic tuff with sandstone and coglomerate	20	20	25.51
EI	Creamy and grey, thin bedded limestone, tuffaceous limestone, numulite bearing	100	44	24.53
Evp	Brown, megaporphyritic-vesicular trachy andesitic lava	20	17	21.58
gb	Olivine gabbro-norite	250	59	27.47
Jkl	Grey, thick bedded to massive, fossiliferous limestone, locally chert bearing	300	48	
Jvt	Dark grey andesitic-basaltic lava, with intercalation of green dacitic tuff, shale and sand limestone	50	31	25.51
KL1	Grey, medium bedded to massive orbitolina bearing limestone	300	48	26.49
Km-2	Yellow alternation of limestone, marl, sandstone and sandy limestone, thin to medium bedded	30	22	26.49
P1r	Grey, thick to medium bedded limestone, locally chert bearing, and in some localities included thin-medium and well bedded, chert bearing limestone in upper part	30	22	24.53
Ps-d	Alternation of red–white quartzarenite and sandstone, siltstone and mudstone, with intercalation of limestone	30	22	21.58
Qal	Recent alluvium and river deposits	20	34	19.23
Qt1	Old terraces and lower gravel fans	20	34	19.23
Qt2	Young terraces and lower gravel fans	20	34	19.23
TrJsh-s	Alternation of dark grey shale and sandstone with intercalation of conglomerate	70	39	23.54
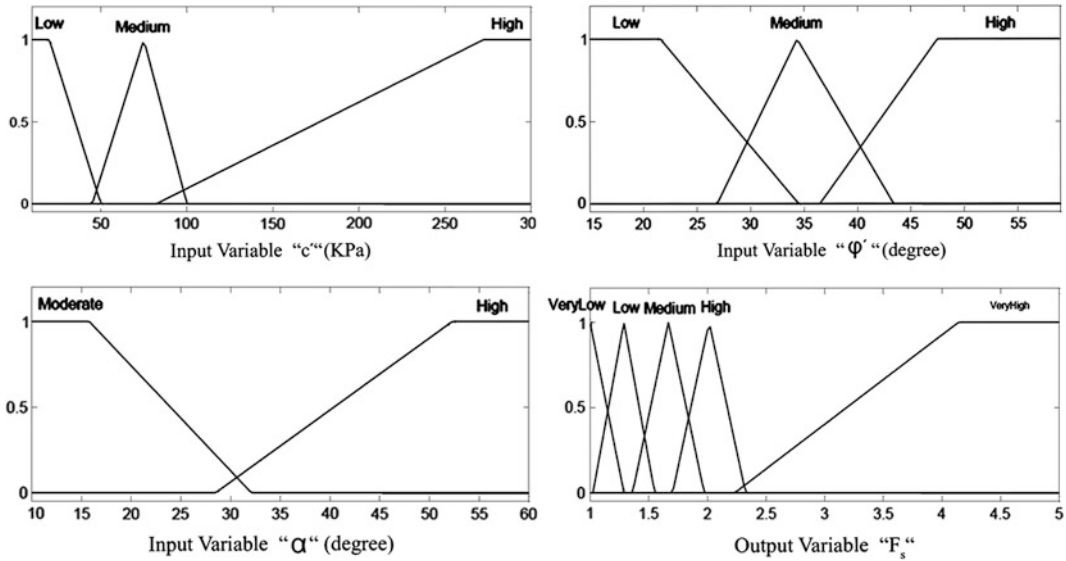
Fig. 88.4 Membership function of input and output fuzzy variables

As it was mentioned, safety factor has been the output of the fuzzy model. In order to get sufficient precision, factor of safety is defined in five levels which ranges from very low to very high.

The general "If–Then" rule structure of mamdani algorithm is given in the following equation:

$$\text{IF xi IS Ai and } \ldots, \text{ Then y IS Bi (for } i = 1, 2, \ldots, k)$$

(88.2)

where k is the number of rules, x_i is the input variable (antecedent variable) and y is the output variable (consequent variable).

As Fig. 88.4 illustrates, we have had three different input variables. "c'" and "φ'" are categorized in three different levels and "α" in two different levels; In order to consider all possible conditions, we have had 3*3*2 rules. Therefore 18 different fuzzy rules have been made ($k = 18$) which are given in Table 88.2.

It should be noted that each value of a variable has a truth value in each category, for instance, In the rule number 18:

*IF c' IS "High" and φ''IS "High" and α IS "High", Then F_s IS "Very High".*the statement "α IS High" indicates the variable α has a value of

"High". Considering the membership function used to define "High" shown in Fig. 88.4, it is true that a slope having an angle from the horizontal of 45° is "High" to a degree of about 0.7 (according to Fig. 88.4 in the α diagram). That is, the truth value associated with the statement "α IS High" is 0.75 for a slope angle of 45.

On the other hand, the truth value associated with the statement "α IS Moderate" is 0 for a slope angle of 45.

The last stage of fuzzy inference system is defuzzification. Aggregation of two or more fuzzy output sets gives a new fuzzy set in the basic fuzzy algorithm (Sonmez et al. 2004). In most cases, the result of a fuzzy set is converted into a crisp value by the defuzzification process (Berkan and Trubatch 1997). In this study, center of mass method is preferred for defuzzification due to its precision and computation simplicity.

3.5 Mapping Methodology

In the last part, we determined the fuzzy value of safety factors of slopes. In this section, the continuation of the process (according to Fig. 88.2) for generating seismic–landslide hazard map has been described briefly.

Table 88.2 Fuzzy rules for determining Fs

Rule no	If			Then
	Cohesion	Friction angle	Slope	Factor of safety
1	Low	Low	Moderate	Medium
2	Low	Low	High	Very low
3	Low	Medium	Moderate	Medium
4	Low	Medium	High	Very low
5	Low	High	Moderate	High
6	Low	High	High	Very low
7	Medium	Low	Moderate	Medium
8	Medium	Low	High	Low
9	Medium	Medium	Moderate	High
10	Medium	Medium	High	Medium
11	Medium	High	Moderate	High
12	Medium	High	High	High
13	High	Low	Moderate	High
14	High	Low	High	Medium
15	High	Medium	Moderate	Very high
16	High	Medium	High	High
17	High	High	Moderate	Very high
18	High	High	High	Very high

3.6 Critical Acceleration

Newmark (1965) showed that the critical acceleration of a potential landslide block is a simple function of the static factor of safety and the landslide geometry, expressed as:

$$a_c = (F_s - 1) \times g \times \sin \alpha \qquad (88.3)$$

where a_c is the critical acceleration in terms of g; F_s is the static factor of safety; and α is the slope angle.

We have determined a_c of each slope and assigned to them in ARCGIS Desktop software.

3.7 Arias Intensity

Mahdavifar et al. (2007) have suggested a predictive relationship for Arias intensity in Alborz and Central-Iran. The resulting regression equation is:

$$\log I_a = -3.880 + 0.810\,M - \log R - 0.002\,R \qquad (88.4)$$

where Ia is the Arias intensity in m/sec; M is the moment magnitude; and R is the closest distance from the slope to the surface trace of earthquake fault if the fault is known, otherwise R is the hypocentral distance. It should be in km for calculations.

We have calculated R of each slope in the software, also moment magnitude of Manjil earthquake (1990) has been 7.3. Therefore Ia for each slope has been calculated and assigned to it.
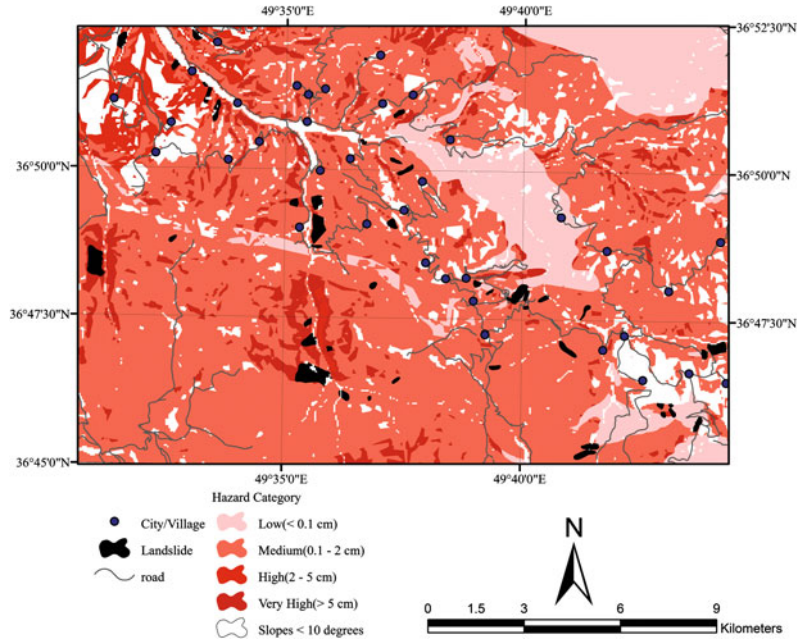
Newmark Displacement

Mahdavifar et al. (2007) have developed an empirical regression equation with which Newmark displacement was estimated as a function of shaking intensity and critical acceleration. It has been expressed as:

$$\log D_n = 1.207 \log I_a - 1.876 \log a_c + 1.608 \qquad (88.5)$$

where D_n is Newmark displacement in cm; Ia is the Arias intensity in m/sec; and ac is the critical acceleration in terms of g.

Fig. 88.5 Seismic–
landslide hazard zonation
map (Slopes <10° are not
analyzed)

Newmark displacement for each slope has been calculated and assigned.

Seismic–Landslide Hazard Map

As it was stated, we have categorized slide hazard, according to Newmark displacements. More displacement represent higher hazards and less displacement represent lower hazards, for instance, when displacement is more than 5 cm hazard level is very high (Fig. 88.5).

4   Evaluation of Results

In order to analyze the validity of seismic–landslide hazard map, Gee(1992) defined a quantitive value. It was called as 'density ratio' (*DR*), which was defined as:

$$DR = \frac{L}{A} \qquad (88.6)$$

where *L* is the number/area of landslides that occurred in real within each hazard category expressed as a percentage of the total number/area of landslides, and *A* is the areal extent of the hazard category expressed as a percentage of the total study area. A good hazard map is

considered to be one which provides the greatest separation into areas of high landslide density and area of low landslide density. Also a precise map is a map in which *DR* value is higher than 1 for high and very high hazard categories and lower than one for Low hazard category. In high and very high hazard categories, higher *DR* values, represents a more precise map because; It shows *L* is bigger than *A* which means the predicted landslide prone areas are more compatible with the real triggered landslides.

In contrast, in low hazard category, *DR* value should be <1 as much as possible, because it states that value of *L* is lower than *A* which means the total area of landslides is low in this category and is more compatible with real triggered landslides.

Also in a good map, medium hazard category should be about 1 which means total area of landslides is approximately equal to the area of the hazard category (medium).

Result of mapping for the study area and *DR* values is given in Table 88.3.

Values of *DR* in each category, indicates that the prepared seismic–landslide hazard zonation map is tolerable and precise. In the hazard zonation map prepared by Mahdavifar et al. (2008),

Table 88.3 DR values for each hazard category

Hazard category	Displacements (cm)	Area of category (km^2)	Area (A) (%)	Area of landslides (km^2)	Landslides (L) (%)	DR
Very high	>5	18.7	6.05	0.76	20.6	3.4
High	2–5	11.5	3.72	0.37	10.03	2.7
Medium	0.1–2	202.6	65.54	1.99	53.93	0.82
Low	<0.1	76.33	24.69	0.57	15.44	0.62
Sum	–	309.13	100	3.69	100	–

the values of density ratio in high and very high hazard categories were 0.8 and 1.48 respectively, which are 2.7 and 3.4 in the current map. Also density ratio in the other hazard categories shows that the prepared hazard zonation map has been more precise.

5   Conclusions

Due to recent advances in soft computing techniques, complex nature of different problems has transformed into a simple one. Fuzzy logic is one of these techniques which has developed so fast that the word "fuzzy" is perhaps no longer fuzzy to many engineers today.

At one level, fuzzy logic can be viewed as a language that allows one to translate sophisticated statements from natural language into mathematical formulas.

This research is an attempt in which fuzzy logic is used for generating seismic–landslide hazard map.

Comparing the results of maps generated by Mahdavifar et al. (2008) and the current study-which used fuzzy sets for creating seismic–landslide hazard map-, proved that application of fuzzy logic in generating seismic–landslide hazard map, is useful due to its flexibility.

References

Alvarez Grima M (2000) Neuro-Fuzzy modeling in engineering geology. A.A. Balkema, Rotterdam, p 244

Berkan RC, Trubatch SL (1997) Fuzzy system design principles, building fuzzy if-then rule bases. The institute of Electrical and Electronics Engineering, Inc., New York, p 496

Gee MD (1992) Classification of landslide hazard zonation methods and a test of predictive capability. In: Proceedings of 6th international symposium on landslides, Christchurch, New Zealand, pp 947–952

Goodman RE (1995) The 35th Rankine Lecture-Bloch theory and its application, Ge'technique, 45:381-423

Jibson RW (1993). Predicting earthquake-induced landslide displacement using Newmark's sliding block analysis. Transportation Research Record 1411, pp 9–17

Jibson RW, Harp EL, Michael JA (1998) A method for producing digital probabilistic seismic landslide hazard maps: an example from the Los Angeles, California, area, U.S. Geological Survey, Open-File Report, pp 98–113

Jibson RW, Harp EL, Michael JA (2000) A Method for Producing Digital Probabilistic Seismic Landslide Hazard Maps. Eng Geol 57:271–289

Juang CH, Jhi YY, Lee DH (1998) Stability analysis of existing slopes considering uncertainty. Eng Geol 49:111–122

Mahdavifar M, Jafari MK, Zolfaghari MR (2007) The attenuation of arias intensity in Alborz and Central Iran. International institute of earthquake engineering and seismology (IIEES), Tehran, pp 1–8

Mahdavifar M, Jafari MK, Zolfaghari MR (2008) Real-time generation of arias intensity and seismic landslides hazards maps using GIS. JSEE 10:81–89

Newmark NM (1965) Effects of earthquakes on dams and embankments. Geotechnique 15:139–160

Sonmez H, Gokceoglu C, Ulusay R (2003) An application of fuzzy sets to the geological strength index (GSI) system used in rock engineering. Eng Appl Artif Intell 16:251–269

Sonmez H, Gokceoglu C, Ulusay R (2004) A mamdani fuzzy inference system for the geological strength index (GSI) and its use in slope stability assessment. Int J Rock Mech Min Sci 41:1–6

Zadeh LA (1965) Fuzzy sets. Inf Control 8:338–353

Detection of 2011 off the Pacific Coast of Tohoku Earthquake-Induced Landslide Deformation Using InSAR

Hiroshi P. Sato, Basara Miyahara, Takaki Okatani, Masayuki Yamanaka, Akira Suzuki, Tatsuo Sekiguchi, Mamoru Koarai, Izumi Kamiya and Hiroshi Yagi

Abstract

Many researchers have reported the landslide triggered by the 2011 off the Pacific coast of Tohoku earthquake. However, these reports are mainly based on field surveys and interpretation of aerial photographs. In this study, we try to detect and analyze earthquake-induced landslide deformations from InSAR (synthetic aperture radar interferometry) images using Advanced Land Observing Satellite (ALOS)/Phased-array L band SAR (PALSAR) data. We explain this method of landslide detection and introduce examples of detected landslides. It is thought that these landslides do not cause serious, rapid damage because they caused only minor displacement. However, continual monitoring of detected landslides using InSAR is important to prepare for possible landslide reactivation caused not only by an earthquake but also by snowmelt and heavy rainfall.

1 Introduction

The 2011 off the Pacific coast of Tohoku earthquake (Mw 9.0) occurred on 11 March, 2011, with a hypocenter of $38°\,06.2'$ N, $142°\,51.6'$ E, ca. 24 km in depth (Japan Meteorological Agency 2011). This earthquake caused many landslides in the northeast (Tohoku) area of Japan, as reported by Miyagi et al. (2011). The reported landslides were accompanied by disrupted or fluidized debris. However, synthetic aperture radar interferometry (InSAR) helped researchers infer that the 2011 Tohoku earthquake also triggered low-displacement landslides. Surely such the low-displacement landslides do not give prompt harmful damages; however, such the landslides may show auspices of future landslide damages, triggered by coming future earthquake, heavy rain, or snowmelt. Therefore, this continued In-SAR monitoring is important as it can provide advanced notice of landslide reactivation. Purpose of this study is to develop the method of extracting local landslide deformation out of the

H. P. Sato (✉) · B. Miyahara · T. Okatani · M. Yamanaka · A. Suzuki · T. Sekiguchi · M. Koarai · I. Kamiya
Geospatial Information Authority of Japan, Tsukuba, Japan
e-mail: hsato@gsi.go.jp

H. Yagi
Yamagata University, Yamagata, Japan

Table 89.1 Specifications of InSAR images used in this study

| Master	Slave	Orbit	Path	$B_{PERP(m)}$
Sep 18, 2010	Mar 21, 2011	Descending	55	+1197
Nov 20, 2010	Apr 7, 2011	Descending	56	+998
Nov 25, 2010	Apr 12, 2011	Descending	59	+937
Jan 11, 2011	Apr 13, 2011	Ascending	400	+1125
Oct 28, 2010	Mar 15, 2011	Ascending	401	+1459
Sep 29, 2010	Apr 1, 2011	Ascending	402	+1212
Mar 3, 2011	Apr 18, 2011	Ascending	403	+358
Feb 2, 2011	Mar 20, 2011	Ascending	404	+847
Feb 19, 2011	Apr 6, 2011	Ascending	405	+406
Feb 24, 2011	Apr 11, 2011	Ascending	408	+522
Mar 1, 2011	Apr 16, 2011	Ascending	411	+508
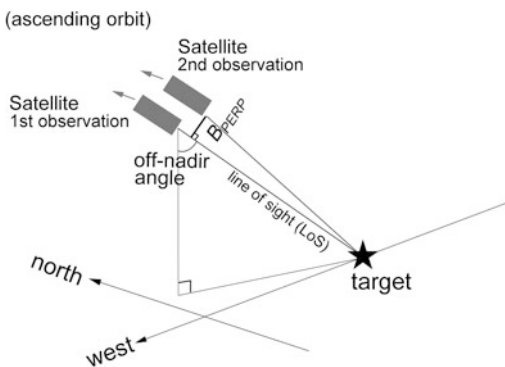
Fig. 89.1 Geometry of InSAR observation

deformation mainly caused by crustal deformation, and show the relation of the detected landslide deformation with existing landslide distribution map, as showing example of the result of the detection.

In this paper, we first explain the method used for detecting deformation caused by these landslides. Next, we introduce examples of detected landslides and discuss how InSAR monitoring provided useful information.

2   Method

SAR (synthetic aperture radar) is a microwave imaging system used to monitor Earth's surface. Using InSAR, we observe the same point on the ground twice (Fig. 89.1). Then, by measuring the distance between the radar and the ground through

atmosphere and ionosphere, we calculate displacement along line of sight (LoS) (Fig. 89.1).

In principle, the measurement precision can be of the order of millimeters. However, owing to various errors caused by meteorological, ionospherical, observational, and other conditions, each SAR interferogram varies in precision. The error caused by observational conditions is relatively easy to be removed, but it is difficult to fully remove errors caused by meteorological or ionospheric conditions. Typically, the measurement is precise of the order of a few centimeters.

InSAR data have been used to detect landslide deformation previously. For example, Peyret et al. (2008) used C-band microwave (ca. 6-cm wavelength) images captured by Environmental Satellite (ENVISAT)/Advanced SAR (ASAR). However, C-band microwaves are reflected by leaves in the upper part of trees and do not reach through to the ground. Because trees swing in the wind and grow taller, better coherence cannot be provided between two SAR observations in a vegetated area like Japan. In contrast, an L-band microwave (ca. 24-cm wavelength) can penetrate through vegetation. Therefore, an L-band radar such as Advanced Land Observing Satellite (ALOS)/Phased-array L band SAR (PALSAR) is suitable for observing landslide deformation in Japan.

The first and second images observed by SAR are called master and slave image, respectively. In this study, we used the combinations of master and slave images, as summarized in Table 89.1.
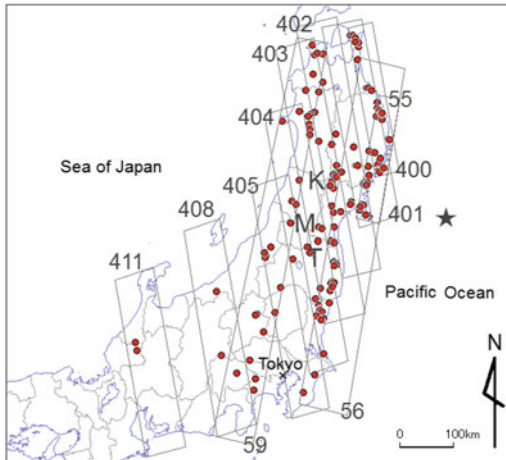
Fig. 89.2 Study area. Black star is epicenter of 2011 off the Pacific coast of Tohoku earthquake, Japan. The *numbers* correspond to the path numbers listed in Table 89.1. *Red circles* denote identified landslide deformation sites using InSAR images. *K* South Kurikoma, *M* Miyagi-zao, *T* Tsuchiyu, Fukushima

All InSAR images listed in Table 89.1 have the off-nadir angle (Fig. 89.1) of 34.3°.

As can be inferred from Table 89.1, B_{PERP} (Fig. 89.1) is the vertical component of the length from position of the second observation satellite to line of sight (LoS) of the first observation. In InSAR, the longer the B_{PERP}, the weaker the coherence, and, therefore, in this study, we selected a combination of images whose B_{PERP} was less than 1,500 m.

Table 89.1 also shows the path number (the strip of ALOS/PALSAR observation area, 70-km wide), and path locations are shown in Fig. 89.2. Figure 89.3a depicts path 403 InSAR image that was observed on an ascending (northward) orbit (Fig. 89.1). This means that the ALOS/PALSAR at 695 km above the ground observed the study area eastward and downward. Table 89.1 also assigns path 55 with a descending (southward) orbit. This means that ALOS/PALSAR from 695 km above the ground observed the study area westward and downward.

Figure 89.3a shows repeated fringe cycles, and these cycles are related to displacement from the 2011 Tohoku earthquake-induced crustal deformation. Referring to the color index given in Fig. 89.3, a color change from blue → red → yellow → blue constitutes one fringe cycle equivalent to ca.12 cm (half of the wavelength) displacement eastward or downward along the LoS; summation of the repeated fringes, shown in Fig. 89.3a, yielded a ca. 4 m eastward displacement along LoS (Geospatial Information Authority of Japan 2011).

Figure 89.3a′, that is enlarged part of Fig. 89.3a, shows the south Kurikoma site where was also affected by the 2008 Iwate-Miyagi Nairiku earthquake (M 7.2). Its location is shown as K in Fig. 89.2. However, the identification and detection of the local landslide deformation, shown in InSAR image of Fig. 89.3a′, is difficult because it is hidden in the nation-wide repeated fringe cycle. Therefore, we began extracting the nation-wide repeated fringe cycle, as shown in Fig. 89.3b, by 80-look processing, which averages over the original spatial resolution. Then, we removed the fringe only caused by crustal deformation in Fig. 89.3b from that in Fig. 89.3a, caused not only by crustal deformation but also by local landslide deformation and error. Therefore, Fig. 89.3c contains rest fringes caused by local landslide deformation and error. The error was ascribed primarily to meteorological and ionospherical conditions and notable ground surface changes. InSAR images of Fig. 89.3b′ and 3c′ show enlarged parts of Fig. 89.3b and 89.3c, respectively, and they also shows the same area of Fig. 89.3a′.

3 Result and Discussion

3.1 South Kurikoma Site

Murakami et al. (2011) have already reported on the local landslide deformation of the South Kurikoma site. Analyzing the same data as they used, the deformation is shown in Fig. 89.3c′. InSAR images of Fig. 89.4a, b (partially enlarged) are overlain on a topographic map provided by the Geospatial Information Authority of Japan (GSI) and a landslide distribution map provided by the National Research Institute for Earth Science (NIED) (National Research Institute for Earth Science and Disaster
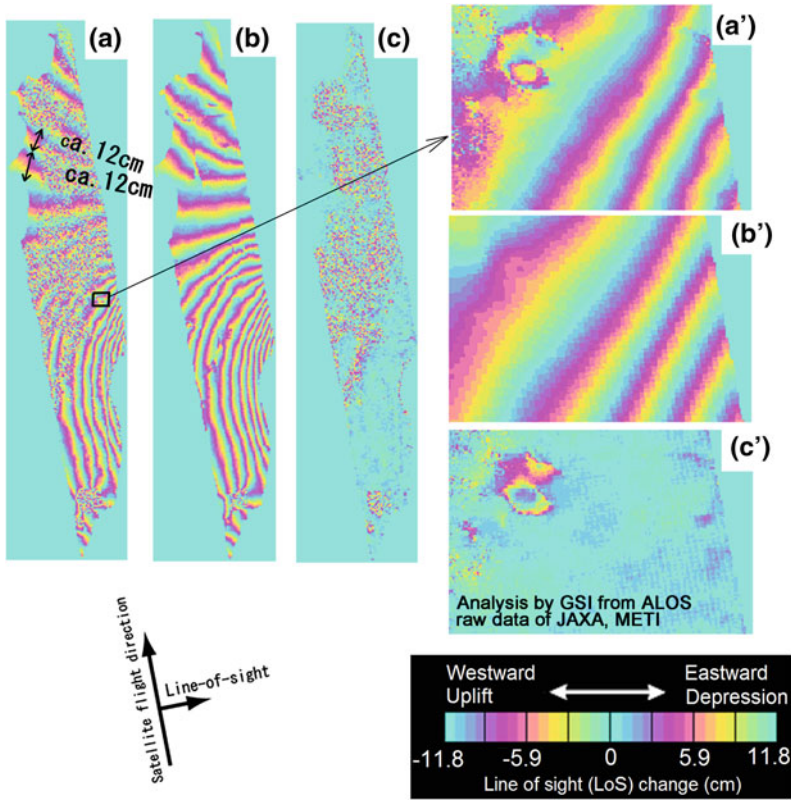
Fig. 89.3 Removal of crustal-deformation fringe Path 403 corresponding to Fig. 89.2 and Table 89.1. **a** Original InSAR image, **b** Fringe of crustal deformation. **c** Result of the removal. **a′**, **b′**, **c′** are the enlarged images of parts of **a**, **b**, and **c**, respectively

Fig. 89.4 Landslide deformation (South Kurikoma) Path 403 corresponding to Fig. 89.2 and Table 89.1. Base image is the topographic map by GSI and the NIED landslide distribution map. The photographs were taken by Prof.Yagi (Yamagata Univ)
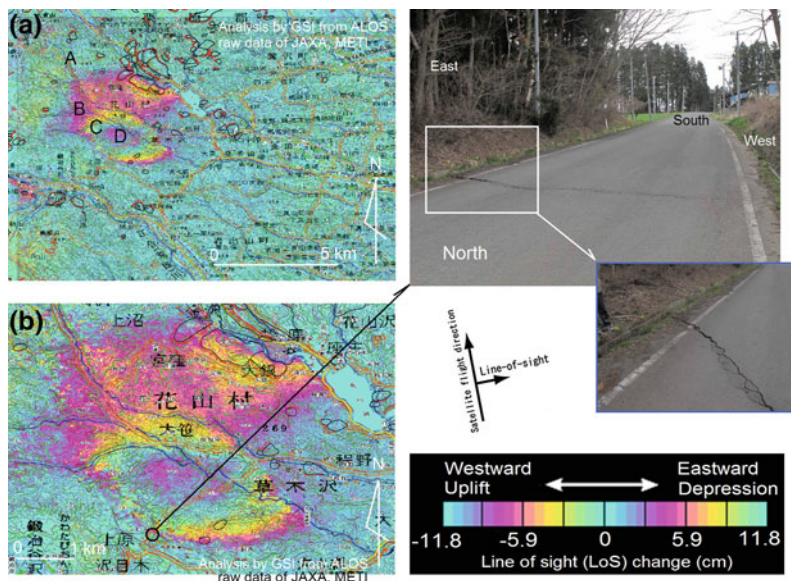
Prevention 2000). This site is at the southern foot of the volcano, Mt. Kurikoma (1,627 m in elevation), and overall, it has a gentle slope.

Figure 89.4a, the area from A (350 m in elevation) to B (300 m in elevation) shows a blue → red color change, which indicates a displacement of ca. 4 cm eastward or downward along the LoS at B. The area from A to C (220 m in elevation) shows a blue → red → yellow color change, indicating a displacement of ca. 8 cm at C. The area from A to D (300 m in elevation) shows a blue → red → yellow → blue → red color change, indicating a displacement of ca. 16 cm at D. Therefore, the magnitude of displacement increases from B to D.

Photographs in Fig. 89.4 were taken at the black hollow circle in Fig. 89.4b on April 28, 2011, after the 2011 Tohoku earthquake. The photograph of the road was taken from north to south; the left of this photograph shows the eastern direction. A fresh crack was identified on the road, and it indicates northeastward movement and depression at a few centimeters. This crack continues eastward through the forest to the shallow valley over the forest. Judging from observations of the crack, this site was displaced northeastward. It is important to note that the crack was at a right angle to the valley; this confirms that the local collapse of the valley-side slope did not cause the cracking.

Because both InSAR and the crack indicate the eastward component of the movement, we think that the crack is the evidence of the local landslide deformation detected by InSAR.

As shown in Fig. 89.4b, the detected landslide deformation has little correspondence with the overlapped NIED landslide distribution map and the size of this deformation is larger than the landslides described in the NIED map. Here, geological setting was investigated, and as shown in Fig. 89.5, InSAR image of Fig. 89.3c was overlain on the geological map (Geological Survey of Japan 1988).

Figure 89.5a also shows a contour from the Bouguer a gravity anomaly map. Welded tuff, originating mainly from the Onikobe Caldera (in west of Fig. 89.5), extends to the detected local landslide deformation area; welded tuff also covers Miocene pyroclastic rock (in central of Fig. 89.5a), and Pleistocene sandstone, siltstone, and acid tuff (in the southeast area of Fig. 89.5a).

Under geological settings, the area of the detected local landslide deformation falls on the old Hanayama Caldera (Agency for Natural Resources and Energy 1976), where low gravity has been observed (55 mGal). Because the caldera is filled with softer geological strata than the area outside, it is thought that the area inside the caldera was depressed by a strong jolt due to the 2011 Tohoku earthquake: the welded tuff layer spread slightly (Nagata 2012) similar to a lateral spread of bedrock (Varnes 1978); then, this spread caused the deformation.

3.2 Miyagi-Zao Site

After removal of the fringe caused by crustal deformation, local landslide deformation was interpreted as shown in Fig. 89.6 (location is shown as site M in Fig. 89.2). Figure 89.6 contains overlays of InSAR image on a topographic map by GSI as well as a landslide distribution map by the NIED. Elevation of the main ridge between A and B is 1,650–1,750 m, and weak coherence is seen in the case of the western-side slope of the main ridge; it is thought that this poor coherence is the effect of meteorological conditions or thick snow cover.

In Fig. 89.6a, the eastern-side slope of the main ridge generally shows no deformation except the enlarged site shown in Fig. 89.6b, which corresponds well with the landslides described in the NIED landslide distribution map. It is thought to be a reactivation of a landslide triggered by the 2011 Tohoku earthquake. The area from E (1,050 m in elevation) to C (1,250 m in elevation) shows a blue → red → yellow color change, indicating a displacement of ca. 7 cm eastward or downward along the LoS. The area from E (1,050 m in elevation) to D (1,100 m in elevation) shows a displacement of ca. 7 cm, eastward and downward along the LoS; These displacements also imply that the one landslide block shown in the NIED landslide distribution

Fig. 89.5 Geological map **a** 1:200,000 "Shinjo and Sakata" (Geological Survey of Japan 1980). **b** Overlay of Fig. 89.4b on the geological map
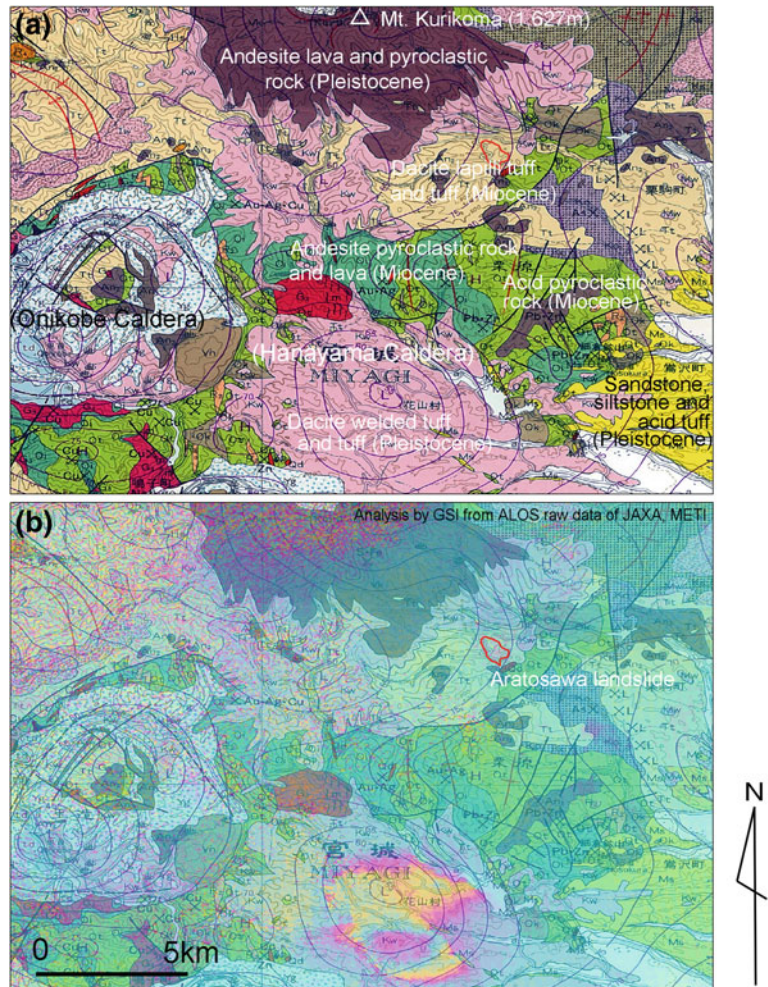
map are at least two separate blocks, and that each block shows different motion.

3.3 Tsuchiyu, Fukushima Site

After elimination of the fringe caused by the crustal deformation, local landslide deformation was interpreted as shown in Fig. 89.7 (location is shown as T in Fig. 89.2).

InSAR image of Fig. 89.7a shows no color change in the wide area; however, as shown in the enlarged area of Fig. 89.7b, one clear color change is identified. Furthermore, this color change roughly corresponds with the existing landslide described in the NIED landslide distribution map. It is thought that this deformation was triggered by the 2011 Tohoku earthquake.

Figure 89.7b shows the main block with the main scarp A and sub block with sub scarp B;

Fig. 89.6 Landslide deformation (Miyagi-Zao) Path 403 corresponding to Fig. 89.2 and Table 89.1. Base map is the 1:25,000 image by GSI and the NIED landslide distribution map
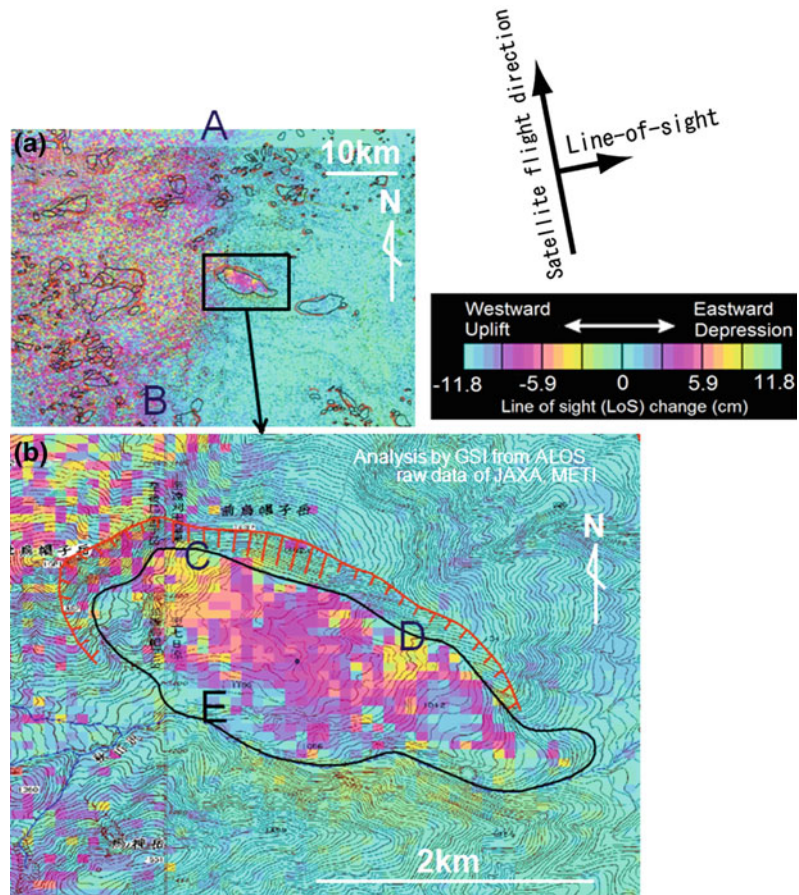
the main block is thought to have been deformed by the sub block. The area from A (bottom of the main scarp, 700 m in elevation) to B (bottom of the sub scarp, 580 m in elevation) shows a blue → red → yellow color change, indicating a displacement of ca. 7 cm eastward or downward along the LoS at B.
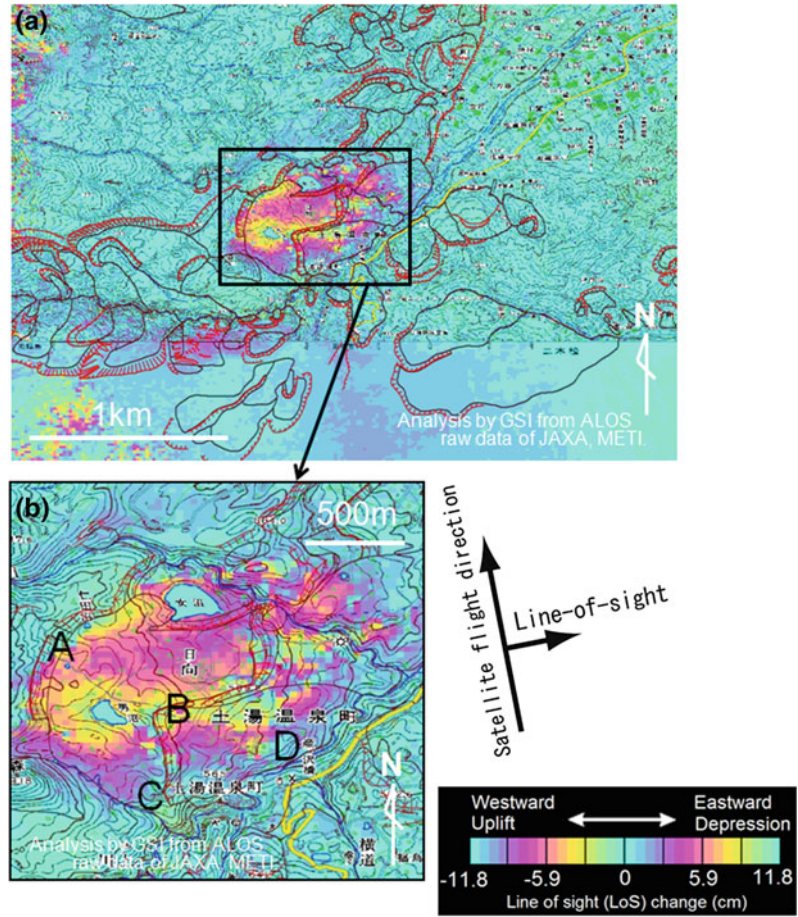
However, the color change does not completely correspond with the outer rims of the main block and sub block. For example, C and D are in the main and sub block, respectively, and no color change is identified at these points. Thus the

southern part of the main and sub blocks do not show displacement, which implies that simple landslide reactivation does not explain this displacement.

3.4   Entire East Japan Area

We interpreted local landslide deformation sites (slightly displaced sites) in hilly and mountainous areas, using all the InSAR images listed in Table 89.1. Next, we identified more than 100 sites, as shown by red dots in Fig. 89.2. Even if

field surveys are performed, it is not thought that these areas will reveal themselves to be accompanied by disrupted or fluidized debris. However, not only the next earthquake but also snowmelt or heavy rainfall may trigger a new landslide or induce landslide reactivation, which will give rise to a debris disaster. Therefore, continual monitoring using InSAR is important to prevent such disasters.

4 Conclusions

1. Removal of the fringe caused by nation-wide crustal deformation is an effective method for locating and interpreting local landslide deformation triggered by the 2011 Tohoku earthquake, and we developed the method.

2. We interpreted the InSAR images and found that in some sites, the color changes (local displacement) corresponded with the landslides described in the NIED landslide distribution map. This implies that landslide reactivation was caused by the 2011 Tohoku earthquake.

3. Field investigation revealed the landslide deformation at the South Kurikoma site; however, this landslide is more closely related with depression of the area inside the old varied caldera than reactivation of the existing landslides.

4. Analysis of InSAR images that cover the entire east Japan region confirm the existence of more than 100 landslide deformation sites.

5. Currently, we do not have the field observation or measurement data for most of the sites;

therefore, we have to carefully recognize the landslide deformations detected by InSAR.

References

Agency for Natural Resources and Energy (1976) Report of 1975 fiscal year on regional research "Kurikoma Area" (in Japanese)

Geological Survey of Japan (1988) 1/200,000 Geological Map "Shinjo and Sakata"

Geospatial Information Authority of Japan (2011) Crustal deformation detected by the combination analysis using SAR data and Nation-wide GPS observation data. http://www.gsi.go.jp/common/000060616.pdf (in Japanese, accessed on 15 June 2012)

Japan Meteorological Agency (2011) The 2011 off the Pacific coast of Tohoku Earthquake. Report of the Coordinating Committee for Earthquake Prediction, Japan 86:66-70. http://cais.gsi.go.jp/YOCHIREN/report/kaihou86/03_04.pdf (in Japanese, accessed June 15, 2012)

Miyagi T, Higaki D, Yagi H, Doshida S, Chiba N (2011) Reconnaissance report on landslide disasters in northeast Japan following the M 9 Tohoku earthquake. Landslides 8:339–342

Murakami M, Okuyama S, Furuya M, Abe T (2011): Ground deformation analysis using ALOS/PALSAR data—Consideration of application to detection of precursory sector collapse. In: Proceedings of 2011 fall meeting on Volcanological Society of Japan, p 55 (in Japanese)

Nagata H (2012): Spread topography in Japan. In: Proceedings of Japan geoscience union meeting 2012, HGM21-P01. http://www2.jpgu.org/meeting/2012/session/PDF_all/H-GM21/HGM21_P_e.pdf Accessed 15 June 2012

National Research Institute for Earth Science and Disaster Prevention (2000): Landslide distribution map. http://lsweb1.ess.bosai.go.jp (in Japanese, accessed 15 June 2012)

Peyret M, Djamour Y, Rizza M, Ritz J-F, Hurtrez J-E, Goudarzi MA, Nankali H, Chery J, Dortz KL, Uri F (2008) Monitoring of the large slow Kahrod landslide in Alborz mountain range (Iran) by GPS and SAR interferometry. Eng Geol 100:131–141

Varnes DJ (1978) Slope movement types and processes. In: Schuster RL, Krizek RJ (eds) Special report 176: landslides: analysis and control. Transportation and Road Research Board, National Academy of Science, Washington, DC, pp 11–33

Part VII

Monitoring and Countermeasure

Ground Anchor Structure for Seismic Resistance and Its Applications

90

Koji Takeya

Abstract

In Japan, ground anchors have been widely applied for stabilization of slopes and landslides, and the technology has advanced since its introduction in Japan in the 1950s. Success in prevention of landslides during earthquakes has shown that ground anchors have demonstrated effectiveness in resisting seismic forces. However, ground anchors may degrade when they are not maintained, and the stability of slopes that are reinforced by these anchors during earthquakes may be questionable. This report shows the importance of maintenance for assurance of seismic resistance. It also reports experimental results on the seismic resistance of ground anchors. The seismic resistance of nut-fixed anchors is certified by the technical examination and certification process of Sabo Technical Center (STC pp 3–6, 2009) and others. As a result, nut-fixed ground anchors have been applied in earthquake-resistant slope measure projects, and they have been used in many recovery efforts for quays in fishing ports damaged by the 2011 off the pacific coast of Tohoku Earthquake and other earthquakes. This report presents case studies of some of these applications.

1 Introduction

Ground anchors were introduced into Japan over 50 years ago, but for many years their seismic resistance was not a routine design criterion. However, since the Mid Niigata Prefecture Earthquake in 2004, when many slope failures followed the earthquake, ensuring the seismic resistance of slopes has been recognized as a

K. Takeya (✉)
Environment and Disaster Prevention Division, SE Corporation, 6-5-1, Nishi-Shinjuku, Shinjuku-ku, Tokyo, Japan
e-mail: koji_takeya@se-corp.com

requirement of structural designs. The 2004 earthquake yielded definitive evidence that slopes reinforced by ground anchors suffered less damage than slopes reinforced with rock bolts and unreinforced slopes (JAA 2004). Since that time, seismic resistance of the structure of the ground anchor became to be considered the required performance. Then earthquake resistance of nut-fixed structures has been experimentally confirmed (Takeya et al. 2009). As a result, ground anchors using nut-fixed systems of certified seismic resistance have been used for the seismic reinforcement of port quays and for disaster recovery of fishing port quays after the 2011 off the pacific coast of Tohoku Earthquake (Takeya 2011).

This report shows the importance of maintenance for assurance of seismic resistance and also shows experimental results on the seismic resistance of ground anchors. In addition this report presents case studies of some of these applications.

2 Maintenance to Ensure Seismic Resistance

2.1 Corrosion Protection

Maintaining the long-term performance and seismic resistance of ground anchors requires reliable corrosion protection. Double corrosion protection is considered to be effective for strands. Figure 90.1 and Table 90.1 show examples of double corrosion protection. However, because the anchor body grout in tension-type anchors will develop cracks under tension, the grout cannot rely on corrosion protection.

2.2 Load Adjustment

The possibility that the earthquake resistance of an anchor may decrease due to a decrease in the pre-stress tension force has been reported. Therefore, to ensure the seismic resistance of a ground anchor, management of the tension force is essential.

Table 90.1 Examples of double corrosion protection

Parts	Corrosion protection method of strands
Bond length	Polyethylene coatings and corrosion-inhibiting grease
Free anchor length	Polyethylene coatings and corrosion-inhibiting grease
Back of anchor head	Polyethylene sheath and corrosion-inhibiting grease
Anchor head	Head cap and corrosion-inhibiting grease

Tension adjustments require an anchor head structure that can accommodate either strand expansion or contraction due to changes in the anchor tension. The amount of expansion or contraction that corresponds to the load adjustment is represented by

$$\Delta L = \frac{\Delta T \times Lf}{As \times Es}, \qquad (90.1)$$

where ΔL is the amount of load adjustment, ΔT is the amount of change in the load on the anchor, Lf is the free tendon length, As is the cross-sectional area of the strand, and Es is the elastic modulus of the strand.

Figure 90.2 shows an example of the relationship between the free anchor length and the amount of adjustment necessary to respond to a change in the load. The adjustment is assumed to take place immediately when the load reaches the upper or lower limit. However, because the anchor load may continue to change, it is desirable for the anchor head structure to be adjustable in excess of the upper limit, and also to be capable of repeated adjustments. Considering the need for maintenance and repair, it is also desirable that the structure of the anchor head can be released from the load and repaired. For these purposes, it is effective to adopt anchor heads with a nut-fixed structure.
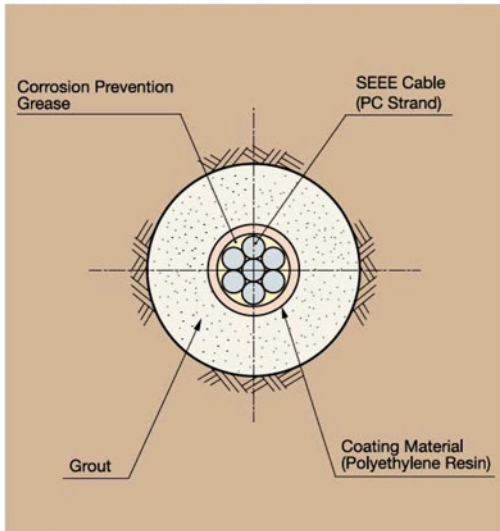
3 Seismic Resistance

Anchor heads may employ nut-fixed or wedge-fixed (Fig. 90.3). The superior seismic resistance

■ Cross Section of the Structures
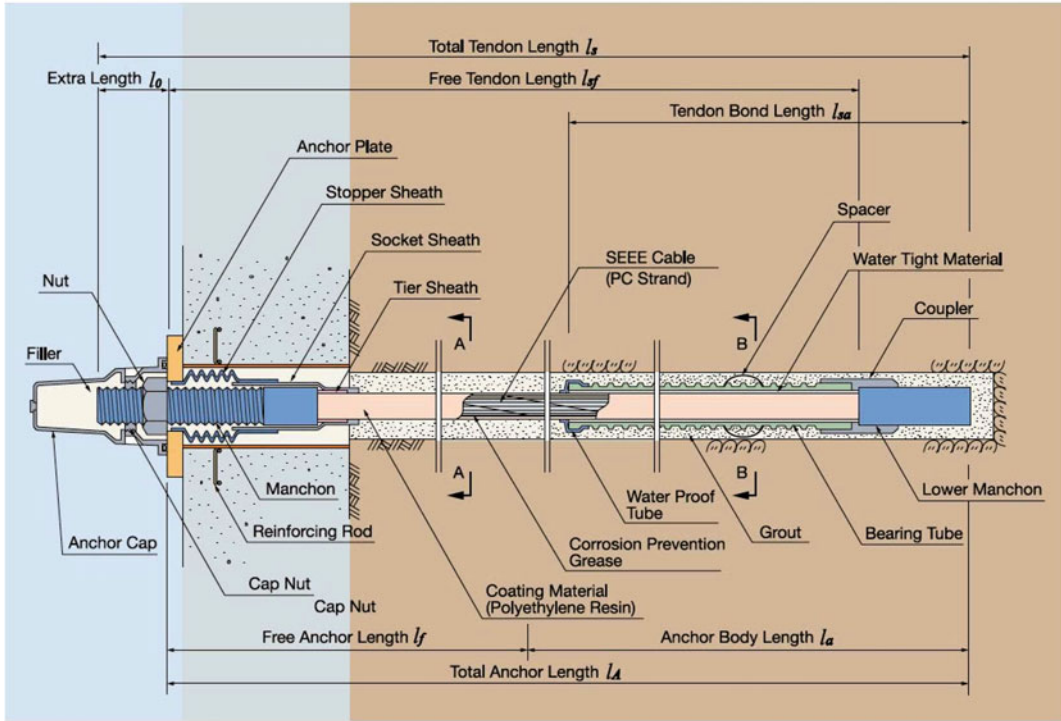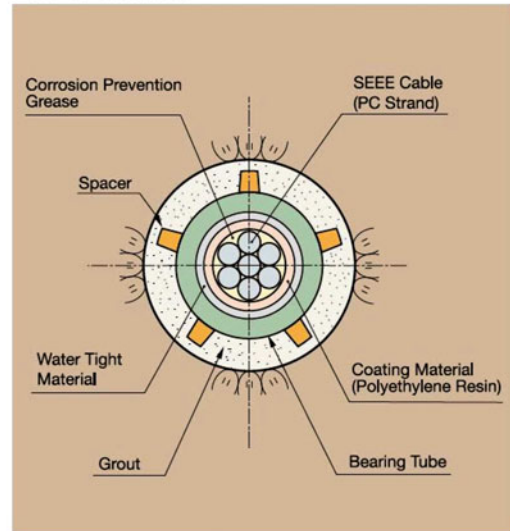

■ A-A Section

■ B-B Section

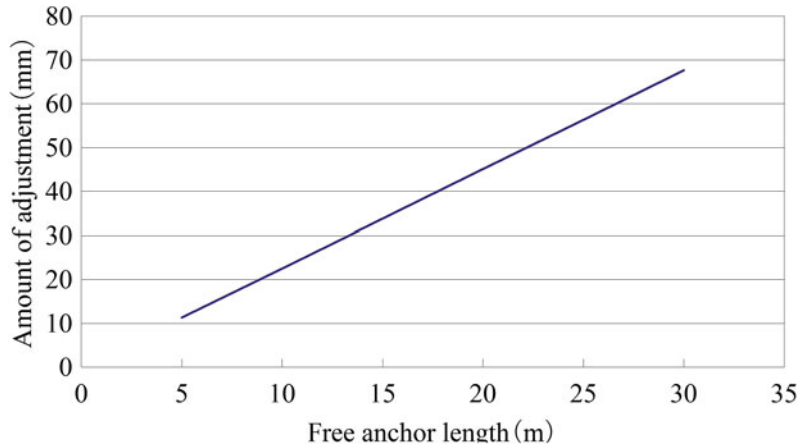**Fig. 90.1**

Fig. 90.2

Fig. 90.3
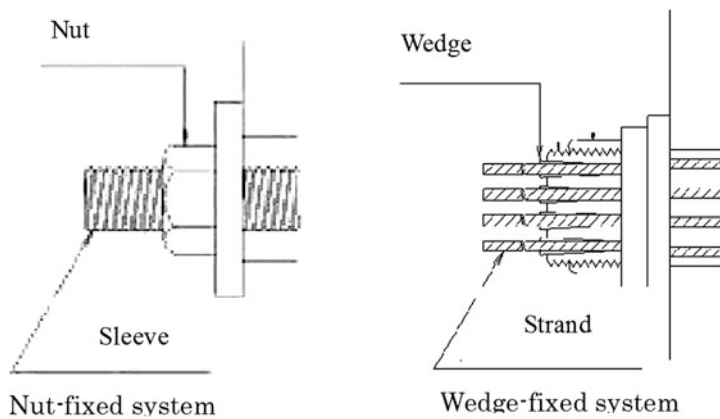
of the nut-fixed method has been confirmed by the following methods described in this section:

- Loading experiment with impact loads
- Impact tensile loading experiment on strands
- Surveys of anchors after earthquakes.

3.1 Impact Loading Experiments

An experiment was conducted to reproduce the impact load during an earthquake by dropping a weight multiple times to check the strength of the nut-fixed system against shock loading. The impact force to the fixing unit at the experimental apparatus (Figs. 90.4 and 90.5) was transmitted through the strand.

The results of the experiment (Fig. 90.6) confirmed the following:

- The load decreased minimally after repeated impacts.
- The nut-fixed system showed no scratches or damage after repeated impacts.

Fig. 90.4

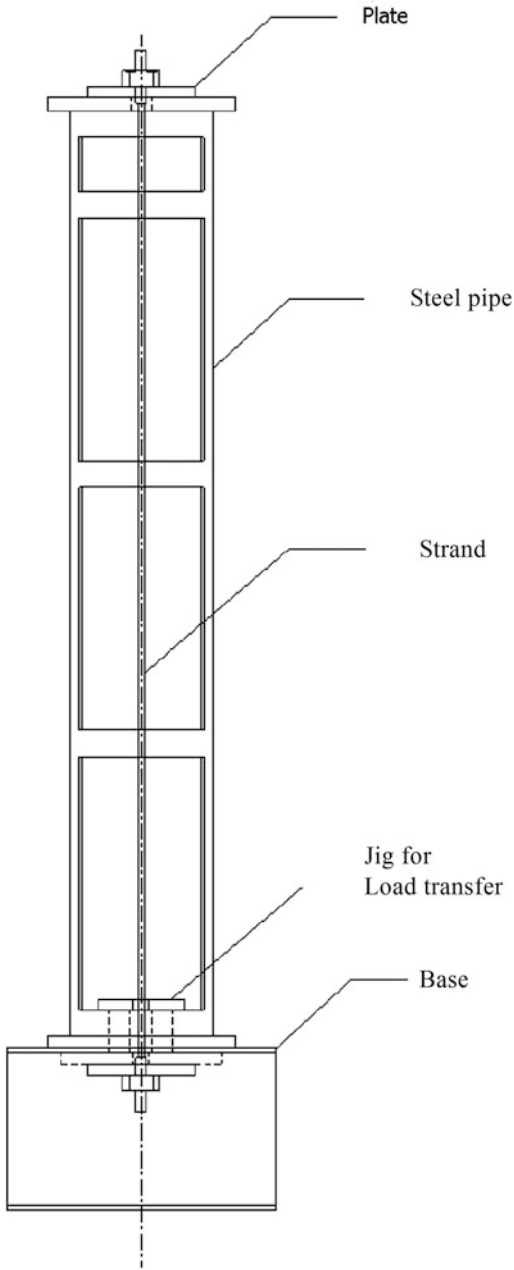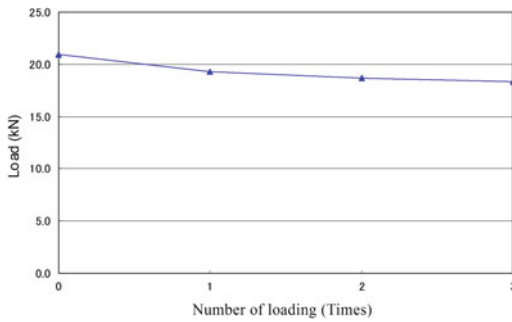

Fig. 90.5

Fig. 90.6

This experiment confirmed that the nut-fixed system performs satisfactorily even after repeated impact loads, as in an earthquake.

3.2 Impact Tensile Loading Experiment on Strands

A tensile loading experiment using impacts was carried out to verify the strength of the strand in the nut-fixed system. An experiment was conducted by dropping a weight of 4.8 kN from 10 m height to the beam connected strands (Fig. 90.7).

The results (Fig. 90.8) show that the impact load is greater than the static load. Therefore, the strand with nut-fixed system can resist dynamic seismic force as well as or better than static force.

3.3 Surveys of Anchors after Earthquakes

I investigated the performance of nut-fixed ground anchors that underwent shaking of seismic intensity six or more during four recent earthquakes (The Mid Niigata Prefecture Earthquake in 2004, The Noto Hanto Earthquake in 2007, The Niigataken Chuetsu-oki Earthquake in 2007, and The Iwate-Miyagi Nairiku Earthquake in 2008). In 86 instances, no damage was documented (STC 2009). Figure 90.9 shows a case in which slope failure was prevented during the Iwate-Miyagi Inland earthquake.

4 Application to Reinforcement of Structures

Ground anchors are increasingly used for reinforcing seawalls and quays to improve their stability against overturning and sliding and to suppress coseismic displacement. Compared with other conventional methods of reinforcing, the anchors typically require a small area for installation, helping to minimize the influence on existing facilities and work areas.

For reinforcing of caisson quays, anchors are fixed near the crest of the reinforcing concrete (Fig. 90.10).

For reinforcing of gravity quay walls by oblique anchors, anchor loads T are divided into a horizontal component ($T \cos \alpha$) and vertical component ($T \sin \alpha$), both of which contribute to the stabilization of the structure. Figure 90.11 and Table 90.2 show the components and effects of the anchor force.

For reinforcing a sheet-pile quay, anchors are fixed near the crest of the sheet piles using the base steel sheet pile and wale (Fig. 90.12).

The quay of the Funakoshi fishing port of Iwate Prefecture, damaged by the 2011 off the pacific coast of Tohoku Earthquake, was restored using ground anchors. The quay subsided by 0.26 m due to the earthquake, making it necessary to increase its height and adjust its reinforcement accordingly. After comparing several reinforcement methods, ground anchors were chosen as the most economical method requiring the shortest construction period.

Fig. 90.7
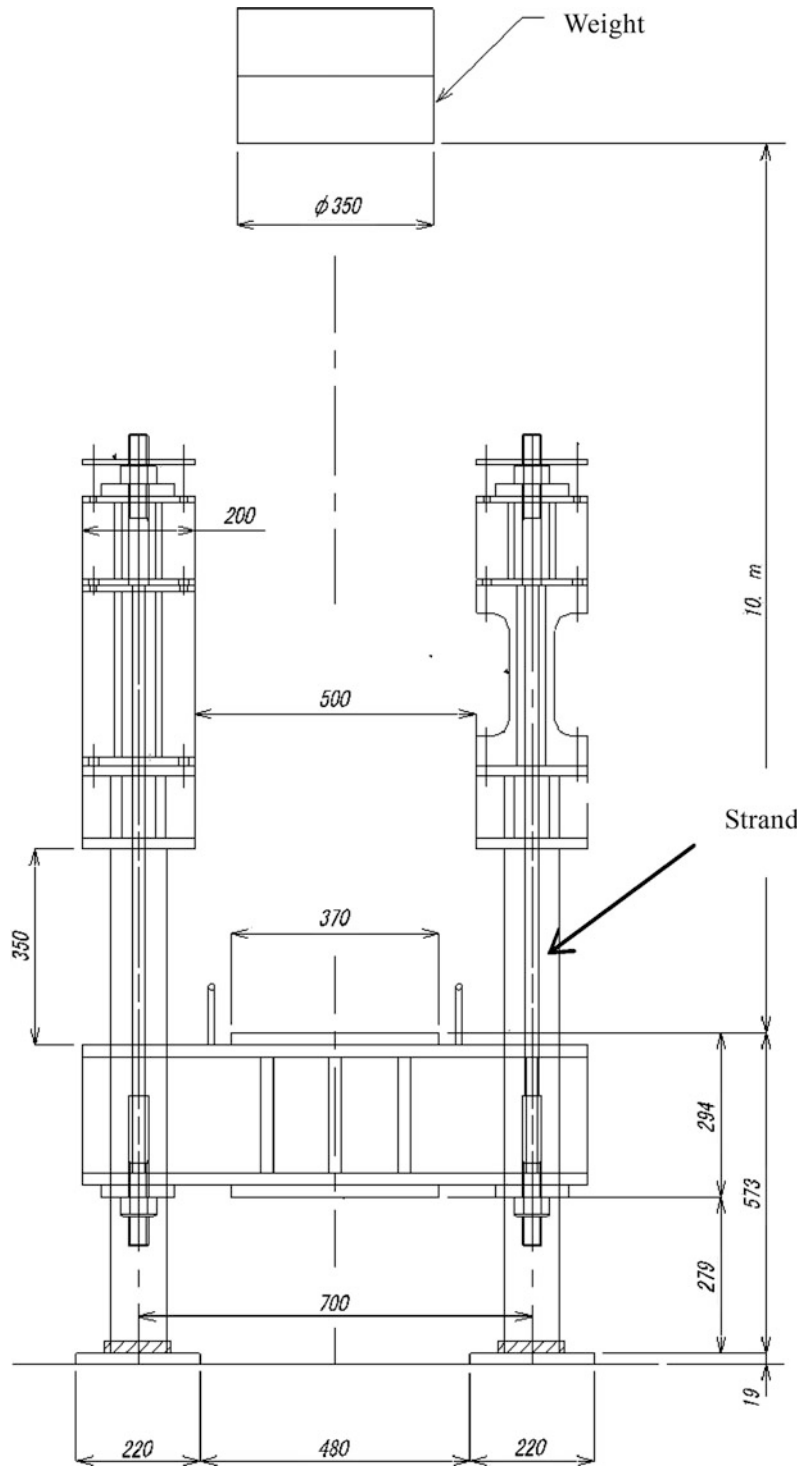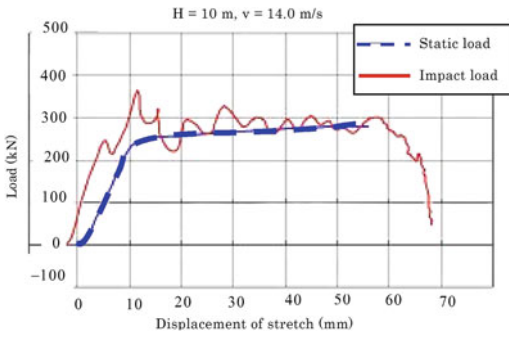
Fig. 90.11
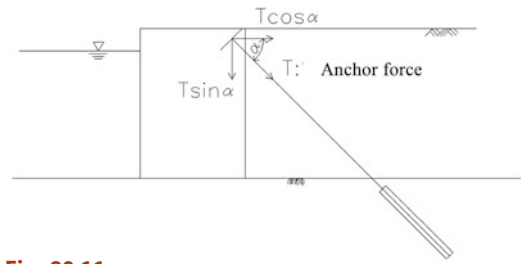
Fig. 90.8
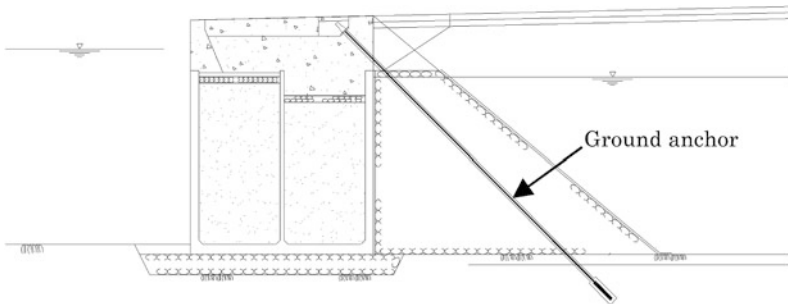
Fig. 90.9

Fig. 90.10

Fig. 90.12
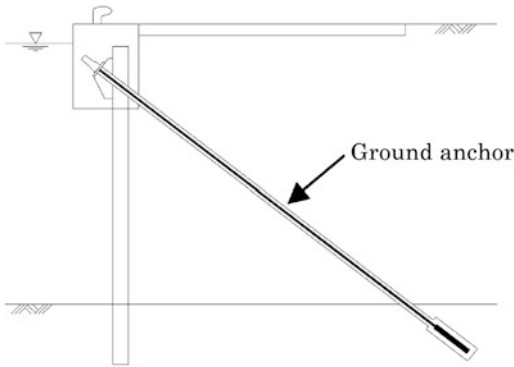
Table 90.2 Component and effect by anchor force

Type of anchor force	Formula	Effect
Horizontal component	$T \cos \alpha$	Resistance to soil pressure/water pressure/horizontal inertial force
Vertical component	$T \sin \alpha$	Increasing sliding resistance by increasing the weight of the structure
		Increasing overturning resistance
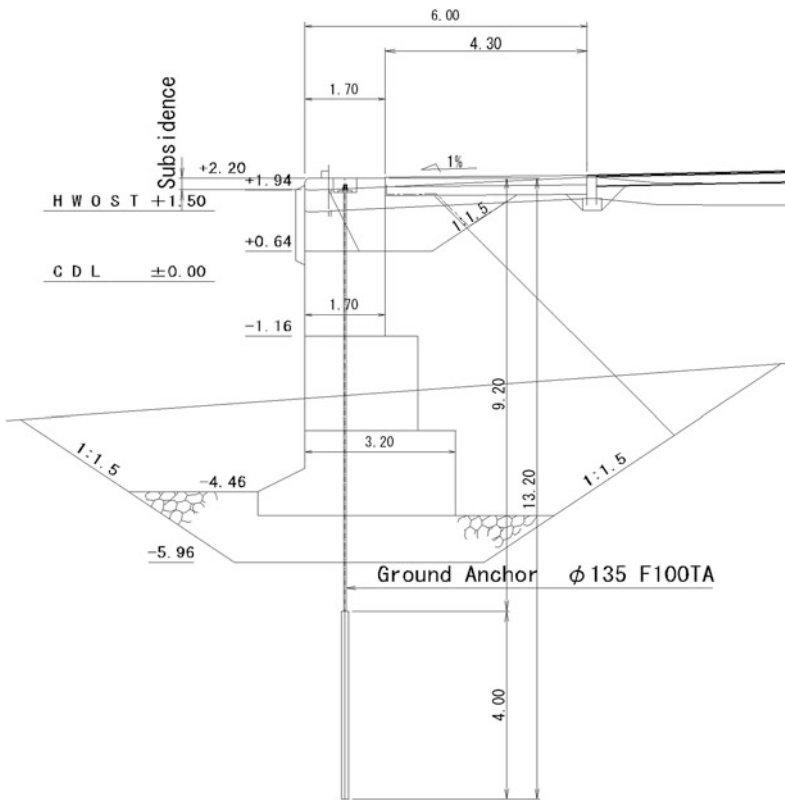
Fig. 90.13

Fig. 90.14

Reinforcement is the result of increased resistance to sliding and overturning due to tension in the vertical ground anchors (Fig. 90.13 and 90.14).

5   Conclusion

With the certification of ground anchors as effective for seismic resistance, their use is growing in reinforcing seawalls, quays, and other structures to improve their stability against overturning and sliding and to suppress coseismic displacement. As research on earthquake-induced landslides progresses, ground anchors with suitable seismic resistance will increasingly be required for stabilization of landslides.

References

JAA (2004) Newspaper of Kaiho No. 16. pp 1–2

STC (2009) Technical examination and certification reports of "SEEE permanent ground anchor method". SABO Technical Center. pp 3–6

Takeya K (2011) The current state of the ground anchor technology in Japan and the application to the seismic reinforcement construction. Geotec Hanoi 2011:175–180

Takeya K, Kiyomiya O, An T (2009) Experiments on the fixing performance of anchor head subjected to an impact load. In: Proceedings of the annual conference of the Japan society of civil engineers, Fukuoka, Japan, vol 64, III–065

Analysis on the Time-Dependent Rotational Displacement of Retaining Wall During the Process of Earthquake

91

H. Q. Yang, D. Huang, X. P. Zhou and Y. Chen

Abstract

A simple pseudo-dynamic method to predict the seismic rotational displacement of retaining wall is developed. The proposed method, which soil-structure interaction is considered, is a combination of the free-field seismic response of soil and pseudo-dynamic method. It is supposed that soil and structure is connected by a series of springs, the dynamic earth pressure is determined by the deformation of springs. So both active and passive conditions can be taken into account by means of different movement direction of retaining wall, no need to know whether active or passive earth pressure happens before analysis. A significant difference between this analysis and published method is that in the present analysis the time dependent process of earth pressure and displacement is obtained by iterative calculation. Although present analysis is limit to elastic state, comparisons with Mononobe–Okabe method show satisfactory agreement in the value of resultant forces acting on retaining wall. Moreover, it is revealed by numerical examples that the height of the resultant force from the base of the wall is underestimated by the Mononobe–Okabe method, this may cause unsafe factors. Furthermore, the effect of wide range of parameters like time, height of retaining wall, wall friction, horizontal and vertical seismic coefficients are taken into account to evaluate the seismic response of retaining wall. Apart from its intrinsic theoretical interest, the

H. Q. Yang (✉) · D. Huang · X. P. Zhou
School of Civil Engineering, Chongqing University,
400045, Chongqing, China,
e-mail: yanghaiqing06@163.com

H. Q. Yang · D. Huang · X. P. Zhou
Key Laboratory of New Technology for
Construction of Cities in Mountain Area, Chongqing
University, Ministry of Education, 400045,
Chongqing, China

Y. Chen
Zhejiang University, 310028, Hangzhou, Zhejiang,
China

proposed analysis can be used for the assessment of the safety of retaining wall under seismic condition.

1   Introduction

Seismic damage of highway system caused in seismic world wide indicated that modern highway system is still vulnerable, it may be damaged extensively and shut down the local traffic, which always makes big troubles for rescue in a past earthquake situation. The earthquake damage of highway system shows that the failure of retaining structures is one of the main causes of road damage. So it is key important to assess the reliability of retaining structure under seismic condition.

The seismic response of retaining structures is a complex soil-structure interaction problem. Wall movements and dynamic earth pressures depend on the response of the soil underlying the wall, the response of the backfill, the inertial and movement of the wall itself, and the nature of the input motions. Many efforts have been made in the field of seismic response of retaining wall, but it is not still sufficient. Most of the methods employed for the design of a retaining wall subjected to seismic loading are limit equilibrium. The pioneering work on earthquake induced lateral earth pressure under active and passive conditions acting on a retaining wall were published by Okabe (1926) and Mononobe and Matsuo (1929). The pseudo-static approach which is known as Mononobe–Okabe method, is widely used to calculate the dynamic earth pressure (either active or passive) on the back of retaining wall. The limit equilibrium method considers the response of the retaining wall as isolated from that of the soil. In other words, neither the interaction between the backfill and the retaining wall nor the displacement of retaining wall are considered in traditional limit equilibrium method. In order to take the soil-

structure interaction into account, elastic analysis of the seismic response of retaining structures is used by Scott (1973). Ortigosa and Musante (1991) proposed a simplified kinematic method to calculate the seismic earth pressure against retaining wall with restrained displacement. Futhermore, Richards (Richards et al. 1999) established an alternate analysis model, in which the soil supported by the retaining wall is modeled by springs in parallel. The fundamental solution to the free-field seismic response considering nonlinear, plastic behavior of soil is included in the retaining analysis. In previous approach, the dynamic loading induced by earthquake is considered as time-independent, which ultimately assumes that the magnitude and phase acceleration is uniform throughout the backfill. To overcome this constraint, Steedman and Zeng (1990) developed the pseudo-dynamic method to predict the seismic active earth pressure behind retaining wall. Later Munwar Basha and Sivakumar Babu (2010) extended pseudo-dynamic method to compute the rotational displacements of gravity retaining walls under passive condition when subjected to seismic loads. Similar alternatives have been made by Syed Mohd Ahmad and Deepankar Choudhury (2010) and Choudhury and Nimbalkar (2008). For pseudo-dynamic method, equilibrium equations of force or moment are still needed, and the soil structure interaction is ignored.

In light of the previous methods, it appears that the development of a new method for assessing seismically-induced earth pressure and rotational displacement would be desirable. The purpose of this paper is trying to combining the pseudo-dynamic method and free field solution, and then calculating the earth pressure and the rotational displacement of retaining wall under seismic loads. In this paper, not only the soil-

Fig. 91.1 Sketch of soil structure interaction model
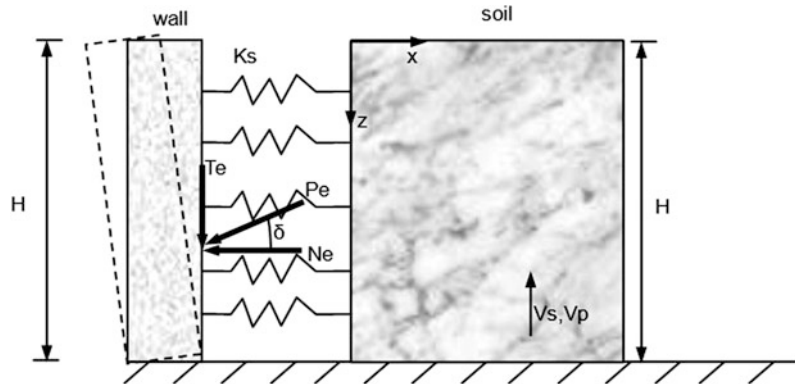
structure interaction is taken into account, but also the time and phase difference due to finite shear wave velocity is considered. One of the main features of this paper is the adoption of a new iterative program to evaluate the time-dependent seismic earth pressure and rotational displacement of retaining wall. The analysis of present is limit to cohesionless soil in elastic state.

2 Method of Analysis

The basic system studied is a semi-infinite layer of cohesionless soil of unit weight γ that is free at its upper surface, is bonded to a rigid base at bottom, and is retained on its vertical boundary by a rigid retaining wall. The soil is approximately considered as elastic body, the backfill is supposed to be never yield or fail under seismic load. In general it is not appropriate to simulate the seismic response of a retaining structure using elastic models because such models neither capture the static or cyclic elasto-plastic behavior of the soil, nor any failure state that may be reached. However, elastic models provide a first approximation to wall and soil response and, in some cases, they may be even acceptable. As shown in Fig. 91.1, the height of the wall and the stratum is considered to be the same and is denoted by H.

The free-field stress and deformation solutions are applied in the analysis of seismic response of retaining structures. The dynamic response of the soil-wall system can be analyzed using superposition for the particular case of

rotation about the base, soil in the free field has the horizontal displacement u_f and the wall has the horizontal displacement u_w. The response of this soil-wall system is the sum of two cases: (1) the wall has the same deformation as the free field under the inertia body force and (2) the wall is pushed back with some horizontal displacement Δu equal to the difference between the horizontal displacement of the free field u_f and horizontal displacement of wall. This superposition approach is applicable no matter how the wall moves (Huang et al. 1999; Huang 1996).

The pseudo-dynamic analysis, which considers shear and primary wave velocity, can be developed by assuming that the shear modulus G is constant with depth through the backfill and the phase not the magnitude of acceleration varies. It is assumed that the base of the retaining wall is subjected to harmonic horizontal and vertical earthquake accelerations with amplitude $k_h g$ and $k_v g$, the acceleration at any depth z below the ground surface and time t can be expressed as

$$a_h(z,t) = k_{hd}(z,t)g, \ k_{hd}(z,t)$$
$$= k_h \sin\left[\omega\left(t - \frac{H-z}{V_s}\right)\right] \quad (91.1)$$

$$a_v(z,t) = k_{vd}(z,t)g, \ k_{vd}(z,t)$$
$$= k_v \sin\left[\omega\left(t - \frac{H-z}{V_p}\right)\right] \quad (91.2)$$

where, ω is the angular frequency, V_s is the shear wave velocity, V_p is the primary wave velocity. k_h and k_v are horizontal and vertical seismic amplitude coefficients respectively.

The total horizontal stress σ_{xw} acting on the wall is the sum of horizontal stress σ_{xf} in the free field and the stress increment $\Delta\sigma_x$ due to the relative displacement between the wall and soil in the free field

$$\sigma_{xw} = \sigma_{xf} + \Delta\sigma_x \qquad (91.3)$$

The horizontal normal stress increment, $\Delta\sigma_x$, can be expressed as

$$\Delta\sigma_x = K_s[u_s(t) - u_w(t)] \qquad (91.4)$$

where, K_s is subgrade modulus of the backfill soil.

Since the springs in Fig. 91.1 can be thought of as bars with length proportional to the height of the wall (Scott 1973), their stiffness, defined as the subgrade modulus in Eq. (91.4) can be written as

$$K_s = C_2 G/H \qquad (91.5)$$

In most cases, a value of $C_2 = 1.35$ seems appropriate based on finite-element analysis (Huang 1996).

3   Free Field Deformation and Stress Solutions of Backfill Without Retaining Structures

The two dimensional differential equations of equilibrium can be written as

$$\frac{\partial\sigma_x}{\partial x} + \frac{\partial\tau_{xz}}{\partial z} = k_{hd}\gamma \qquad (91.6)$$

$$\frac{\partial\tau_{xz}}{\partial x} + \frac{\partial\sigma_z}{\partial z} = k_{vd}\gamma \qquad (91.7)$$

Since we are dealing with the half-space, all stress, strain and displacement components of backfill soil are independent on the x coordinate. Thus, this free-field problem is actually a one-dimensional problem, Eqs. (91.6) and (91.7) becomes

$$\frac{\partial\tau_{xz}}{\partial z} = k_{hd}\gamma \qquad (91.8)$$

$$\frac{\partial\sigma_z}{\partial z} = k_{vd}\gamma \qquad (91.9)$$

Stress components can be solved from Eq. (91.8), with the condition of when z = 0 and t = 0, $\tau_{xz} = 0, \sigma_z = 0$.

$$\tau_{xz} = \frac{2k_h v_s \gamma}{\omega}\left\{\sin\left[\frac{\omega(2tv_s + z - 2H)}{2v_s}\right]\sin\frac{z\omega}{2v_s}\right\} \qquad (91.10)$$

$$\sigma_z = \frac{2k_v v_p \gamma}{\omega}\left\{\sin\left[\frac{\omega(2tv_s + z - 2H)}{2v_p}\right]\sin\frac{z\omega}{2v_p}\right\} \qquad (91.11)$$

The horizontal stress is usually written as a lateral earth pressure coefficient K times the vertical stress σ_z. That is

$$\sigma_{xf} = K\sigma_z \qquad (91.12)$$

where, $K = K_0 = 1 - \sin\phi$ is the coefficient of lateral earth pressure in the elastic state.

For soil in the elastic state, the shear strain can be expressed as follow

$$\gamma_{xz} = \frac{\tau_{xz}}{G} \qquad (91.13)$$

According to elastic deformation theory, the horizontal displacement of soil in the free field is

$$u_s = -\int \gamma_{xz}dz = \frac{k_h v_s \gamma}{G\omega^2}$$
$$v_s \sin\left[\frac{\omega(tv_s + z - H)}{v_s} > -z\omega\cos\left[\omega\left(t - \frac{H}{v_s}\right)\right]\right] \qquad (91.14)$$

It is simply assumed that the rotational component of displacement can be ignored. The horizontal stress acting on the retaining wall can be expressed as

$$\sigma_{xw} = \sigma_{xf} + K_s[u_s(t) - u_w(t)] \qquad (91.15)$$

$$u_w(z, t) = \eta(H - z) \qquad (91.16)$$

where, $u_w(t)$ represents the displacement of retaining wall, η represents the rotating angle.

The total horizontal thrust acting on the retaining wall can be calculated by integrating the horizontal stress along the height of the retaining wall

$$N_e = \int_0^H \sigma_{xw}dz = \frac{1}{2G\omega^3}\{-GH^2K_s\eta\omega^3$$

$$-2k_hK_sv_s^3\gamma\cos(\omega t) + k_hK_sv_s\gamma(2v_s^2 - H^2\omega^2)$$

$$\times \cos m_1 + 2GKk_vv_p\gamma\omega[H\omega_2$$

$$+ v_p(\sin m_2 - \sin\omega t)]\} \tag{91.17}$$

where, $m_1 = \omega t - \frac{H\omega}{v_s}$; $m_2 = \omega t - \frac{H\omega}{v_p}$.

The vertical force acting on the retaining wall is determined with knowledge of the wall frictional angle

$$T_e = N_e\tan\delta \tag{91.18}$$

The total force acting on the retaining wall is expressed as

$$P_e = \sqrt{T_e^2 + N_e^2} \tag{91.19}$$

The moment of the acting earth pressure about the toe of the retaining wall is

$$M_e = \int_0^H (H - z)\sigma_{xw}dz$$

$$= \frac{1}{6G\omega^4}\{-2GH^3K_s\eta\omega^4$$

$$+ 6\gamma GKk_vv_p^3\omega\cos\omega t + 3\gamma GKk_vv_p\omega$$

$$\times (H^2\omega^2 - 2v_p^2)\cos m_3$$

$$- 6\gamma GHKk_vv_p^2\omega^2\sin m_3 + \gamma k_hK_sv_s[H\omega$$

$$\times (6v_s^2 - H^2\omega^2)\cos m_1$$

$$+ 6v_s^3(\sin m_1 - \sin\omega t)]\} \tag{91.20}$$

where, $m_3 = \frac{H\omega - \omega t v_p}{v_p}$.

So the height of the resultant forces P_{ae} from the base of the wall is

$$h = \frac{M_e}{N_e} \tag{91.21}$$

4 Rotational Displacement of Retaining Wall

The following equations of motion are presented to estimate the rotational displacements of gravity retaining wall, similar to equations reported in Zeng (Zeng and Steedman 2000) and Choudhury (Choudhury and Nimbalkar 2007).

The moment of the acting earth pressure about the toe of the retaining wall is

$$\sum M_0 = M_e + W_wx_c \tag{91.22}$$

where, W_w is the weight of the gravity wall, x_c is the horizontal distance from the center to toe of retaining wall.

Again, the motion equation of the retaining wall about its toe can be written as (Choudhury and Nimbalkar 2008)

$$\sum M_0 = -y_c(W_w/g)(a_c)_x + x_c(W_w/g)(a_c)_y + I_cA \tag{91.23}$$

$$(a_c)_x = a_g - Ay_c - \beta^2x_c \tag{91.24}$$

$$(a_c)_y = Ax_c - \beta^2y_c \tag{91.25}$$

where, $a_g = k_{hd}g$, y_c is the vertical distance from the center to toe of retaining wall, I_c is polar moment of inertia of the about the centroid, A is angular acceleration.

Substituting Eqs. (91.24) and (91.25) into Eq.(91.23), we have (Choudhury and Nimbalkar 2008)

$$\sum M_0 = (W_w/g)r_c^2A - (W_w/g)a_gy_c + I_cA \tag{91.26}$$

where, $r_c^2 = x_c^2 + y_c^2$.

Combining Eqs. (91.22) and (91.26), the rotating acceleration of retaining wall about its toe can be determined by

$$A = \frac{M_e + W_wx_c + (W_w/g)a_gy_c}{(W_w/g)r_c^2 + I_c} \tag{91.27}$$

The rotating angle velocity β is obtained by

Fig. 91.2 dynamic iterative strategy for the determination of rotating displacement

Initial state: t=0, u_s= u_w=0.

for each new time step n+1

    compute horizontal thrust force Ne by eq(17)

    compute the moment Me acting on retaining wall by eq(20)

    if Ne>0 and Me>0

        compute the height of the resultant force from the base of the wall by eq(21)

        compute the rotating angle velocity by eq (28)

        compute the rotating displacement by eq(29)

    endif

end for

$$\beta = \int A dt \qquad (91.28)$$

The tilting angle can be derived as

$$
\begin{aligned}
\eta_{(t_f)} &= \int_0^{t_f} \beta dt \\
&= \frac{W_w x_c + (W_w/g)a_g y_c}{2[(W_w/g)r_c^2 + I_c]} t_f^2 \\
&\quad + \frac{1}{(W_w/g)r_c^2 + I_c}\Big[-\frac{1}{6}H^3 K_s t_f^2 \eta_{(t_f-\Delta t)} \\
&\quad - \frac{K k_v v_p^3 \gamma}{\omega^5}(\cos \omega t_f - 1) \\
&\quad + \frac{K k_v v_p^3 \gamma}{\omega^5}(\cos m_6 - \cos m_7) \\
&\quad + \frac{H^2 K k_v v_p \gamma}{2\omega^3}(\cos m_7 - \cos m_6) \\
&\quad + \frac{H^2 K_s k_h v_s^3 \gamma}{G\omega^5}(\cos m_4 - \cos m_5) \\
&\quad + \frac{H^3 K_s k_h v_s \gamma}{6G\omega^3}(\cos m_5 - \cos m_4) \\
&\quad - \frac{K_s k_h v_s^4 \gamma}{G\omega^6}\sin \omega t_f\Big] \\
&\quad - \frac{H K k_v v_p^2 \gamma}{\omega^4}(\sin m_6 + \sin m_7) \\
&\quad + \frac{K_s k_h v_s^4 \gamma}{G\omega^6}(\sin m_4 + \sin m_5)
\end{aligned}
$$

$$(91.29)$$

where, η represents the cumulative rotating angle during the time from 0 to t_f. $m_4 = t_f \omega - \frac{H\omega}{v_s}$, $m_5 = \frac{H\omega}{v_s}$, $m_6 = t_f \omega - \frac{H\omega}{v_p}$, $m_7 = \frac{H\omega}{v_p}$.

It is revealed in Eq. (91.29) that the total rotational displacement is the summation of individual rotations during the entire earthquake motion. The above procedure is repeated for each cycle of vibration.

5 Implementation of Present Model

The algorithmic implementation of present model is based on an iterative strategy. The detailed iterative scheme is plotted in Fig. 91.2 .

Pseudo-dynamic method and free-field solution are coupled in this analysis. A simple iterative algorithmic is needed in present model and complex dynamic analysis as Newmark method is avoid. Although present method is still a pseudo-dynamic approximate one, the time-dependent seismic earth pressure and rotational displacement of retaining wall during the entire seismic process can be obtained conveniently by present model.

6 Results and Discussion

The results obtained from the numerical analyses, based on present method, are shown in this section. Comparisons have been made with the M–O

Fig. 91.3 Horizontal and vertical acceleration-time history response of backfill with $k_h = 0.1$, $\delta = 20°$, at $z = 0$
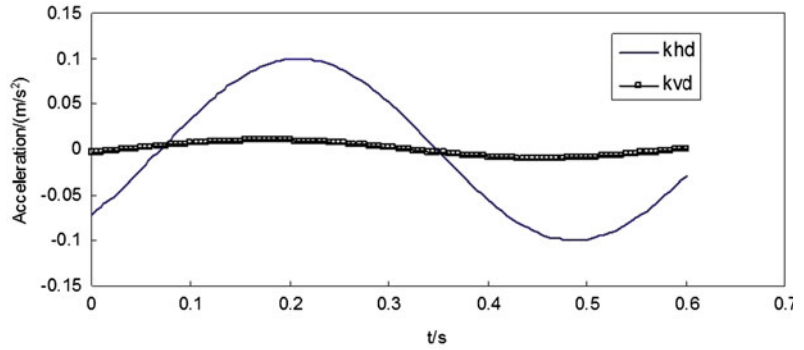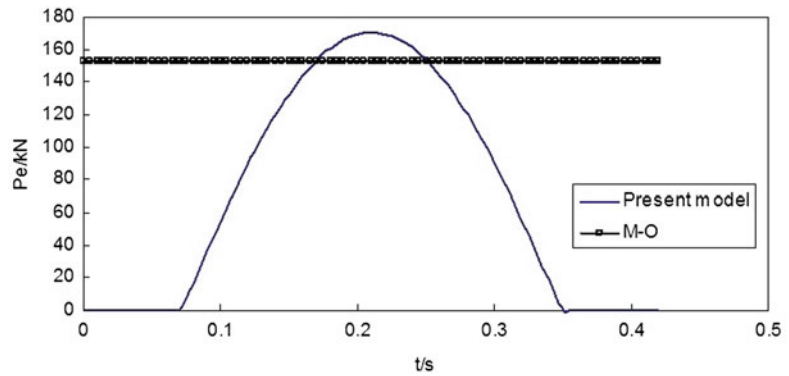

Fig. 91.4 Resultant force–time response which acting on the retaining wall with $k_h = 0.1$, $\delta = 20°$

method. The retaining wall is 7.0 m in height, made of concrete with a unit weight of 25 kN/m³. Moreover, the backfill is made of cohesionless soil with a unit weight of 17 kN/m³. The following parameters are used in the calculation: $G = 350$ MPa, $H = 7.0$ m, $b = 1.2$ m, $V_s = 100$ m/s, $V_p = 187$ m/s, $\phi = 25$ Deg.

Figure 91.3 shows horizontal and vertical acceleration-time history response of backfill during the entire seismic process. The acceleration is time dependent, which is different from pseudo-static method. Moreover, the horizontal and vertical acceleration is independent, and the phase difference due to finite shear wave velocity is considered.

Resultant force–time response is plotted in Fig. 91.4. It is revealed that before $t = 0.22$ s, as the time increases, the resultant force P_e acting on retaining wall also increases. But after $t = 0.22$ s, the resultant force P_e acting on retaining wall decreases with increase in the time. Because, after $t = 0.22$ s, the retaining

start to rotate about its toe and the relative displacement between retaining wall and backfill in the free-field decrease. Moreover, comparison between present and M–O method is carried out. It is obvious that M–O results are time-independent while present one is time-dependent. The maximum value of resultant force P_e is close to the results obtained by M–O method, with 6.25 % error.

The distribution of earth pressure is depicted in Fig. 91.5. It is revealed from Fig. 91.5 that non-linear seismic earth pressure distribution behind retaining wall in a more realistic manner compared to the pseudo-static method. It is also clear from Steedman and Zeng (1990) that the earth pressure distribution along the height is non-linear.

Figure 91.6 shows the time-dependent height of the resultant forces acting on retaining wall from the base of wall. It is well known that the height of the resultant forces obtained by pseudo-static method is time-independent, and is

Fig. 91.5 Distribution of earth pressure which varied with time
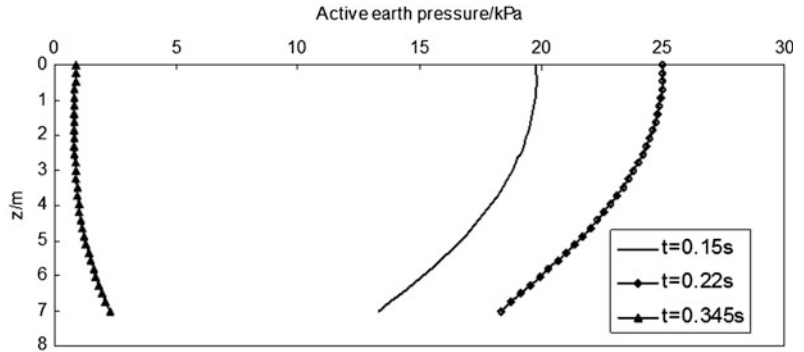
Fig. 91.6 The time-dependent height of the resultant forces acting on retaining wall from the base of wall
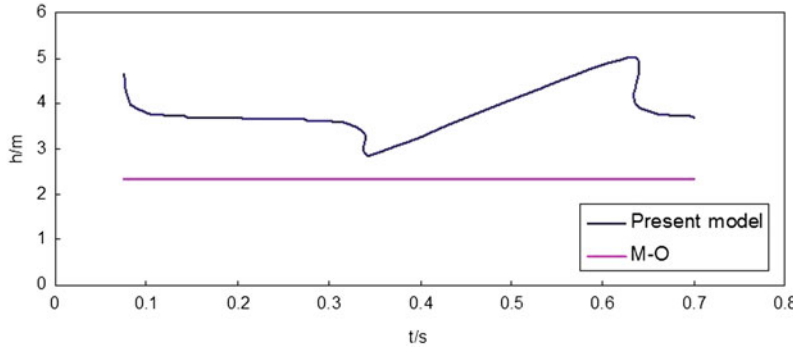
Fig. 91.7 Dependence of resultant force on the wall friction angle with $k_h = 0.1$, $\delta = 20°$
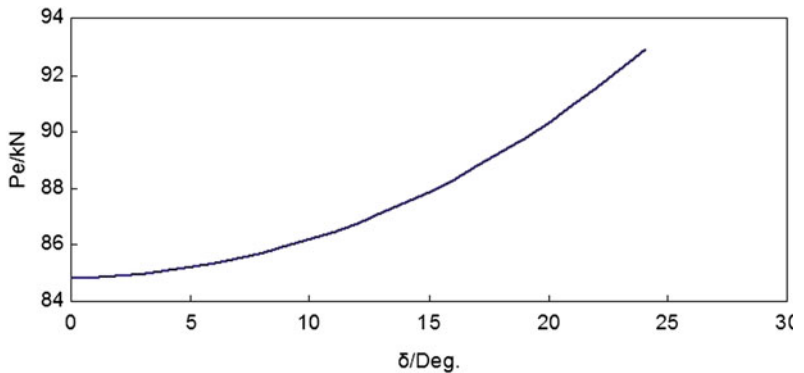
supposed to be one-third of the height of retaining wall. However, the height obtained by present method is time dependent, ranges from 3.0 m to 5.0 m. It is higher than the pseudo-static method, so the pseudo-static method may cause some unsafe factors when the retaining wall rotating.

Figure 91.7 shows the dependence of resultant force on the wall friction angle. It is obvious that the resultant force increases with the wall friction angle increases.

7   Conclusions

In this paper, by considering the time effect and phase changes in shear and primary waves propagating in the backfill, a simple method to determine the dynamic earth pressure and rotating displacement is established. Both active and passive earth pressure are considered and it is found that earth pressure may transfer from active to passive earth pressure as the seismic

intensity reach the critical value. Moreover, the rotational displacement, distribution of earth pressure along the height of retaining wall, resultant force and its height from the base of wall are time-dependent. Little iterative calculation is needed, but the time dependent process of earth pressure and displacement is obtained. Although assumptions are adopted in this paper, the proposed analysis can be used for the assessment of the safety of retaining wall under seismic condition.

In the present model only one ideal case, rotation about the toe of retaining wall, has been studied. Nevertheless, the cases for combined failure modes such as sliding and rotation can be easily extended by modify the kinetic equation. Although the method developed here is primarily for cohessionless soil, analysis for the soil with cohesion using this approach is straightforward extensions of this work.

References

Okabe S (1926) General theory of earth pressure. J Jpn Soc Civil Eng 12:1

Mononobe N, Matsuo H (1929) On the determination of earth pressure during earthquakes. In: Proceedings of the world engineering conference, 9:176

Scott RF (1973) Earthquake-induced pressures on retaining walls. In: Proceedings of the 5th world conference on earthquake engineering, International Association for Earthquake Engineering, Tokyo, vol 2, pp 1611–1620

Ortigosa P, Musante H (1991) Seismic earth pressures against structures with restrained displacements. In: Proceedings of the 2nd international conference on recent advances in geotechnical earthquake engineering and soil dynamics. pp 621–628

Richards RJ, Huang C, Fishman KL (1999) Seismic earth pressure on retaining structures. J Geotech Geoenviron Eng ASCE 125(9):771–778

Steedman RS, Zeng X (1990) The influence of phase on the calculation of pseudo static earth pressure on a retaining wall. Geotechnique 40(1):103–112

Munwar Basha B, Sivakumar Babu GL (2010) Seismic rotational displacements of gravity walls by pseudo dynamic method with curved rupture surface. Inter J Geomech 10(3):93–105

Ahmad SM, Choudhury D (2010) Seismic rotational stability of waterfront retaining wall using pseudodynamic method. Inter J Geomech 10(1):45–52

Choudhury D, Nimbalkar SS (2008) Seismic rotational displacement of gravity walls by pseudo dynamic method. Inter J Geomech 8(3):169–175

Huang C, Fishman KL, Richards R Jr (1999) Seismic plastic deformation in the free field. Int J Numer Anal Meth Geomech 23:45–60

Huang C (1996) Plastic analysis for seismic stress and deformation fields. PhD Dissertation, Department of Civil Engineering, SUNY at Buffalo, Buffalo, NY, USA

Zeng X, Steedman RS (2000) Rotating block method for seismic displacement of gravity walls. J Geotech Geoenviron Eng 126:709–717

Choudhury D, Nimbalkar S (2007) Seismic rotational displacement of gravity walls by pseudo-dynamic method: Passive case. Soil Dyn Earthq Eng 27:242–249

Prevention Works for 'Namasu landslide' in Gunma Prefecture and Behavior of the Landslide During the 2011 Earthquake off the Pacific Coast of Tohoku

Senro Kuraoka, Tamiaki Fujiwara and Tadashi Kudo

Abstract

A large ancient landside, called Namasu, is formed in North Western region of Gunma prefecture Japan. This landslide is 600 m wide, 600 m long, and the maximum thickness is 90 m. During 1982, the landslide mass moved and the bridge, that crosses the river along the toe of the landslide, deformed. The drainage works, as the main prevention measures, started in 1989 and have been completed in 2010. The drainage wells that have been installed during the last 5 years had been planned and designed by seepage analyses, using the FEA. This paper presents assessment of effectiveness of the drainage works by monitoring of the ground water and the seepage analysis. Effect of the drainage works on the behavior of the landslide, during the 2011 earthquake off the Pacific coast of Tohoku, is also examined.

1 Introduction

Namasu landslide, located in North West of Gunma prefecture, is an ancient type landslide. The marked distress was found with the bridge, which is indicated as the Ryugu bridge in Fig. 92.1, near the toe of the landslide mass after the heavy rainfall during August of 1985. The 91 m long bridge had shortened by 24 cm and deformed upward by 30 cm when the landslide moved and compressed the bridge in the longitudinal direction (Fujiwara et al. 2009). The prevention works, consisting of drainage tunnel and drainage wells, have started in 1982 and completed in the autumn of 2011.

The width and length of the main block are both 600 m, respectively. The maximum thickness of the landslide is 90 m. The prevention works have been carried out since 1985 in order to protect the schools, roads, and the bridge that is built near the toe of the landslide.

S. Kuraoka (✉) · T. Fujiwara · T. Kudo
Research and Development Center Nippon Koei
Co., Ltd, 2304 Inarihara, Tsukuba 300-1257, Ibaraki
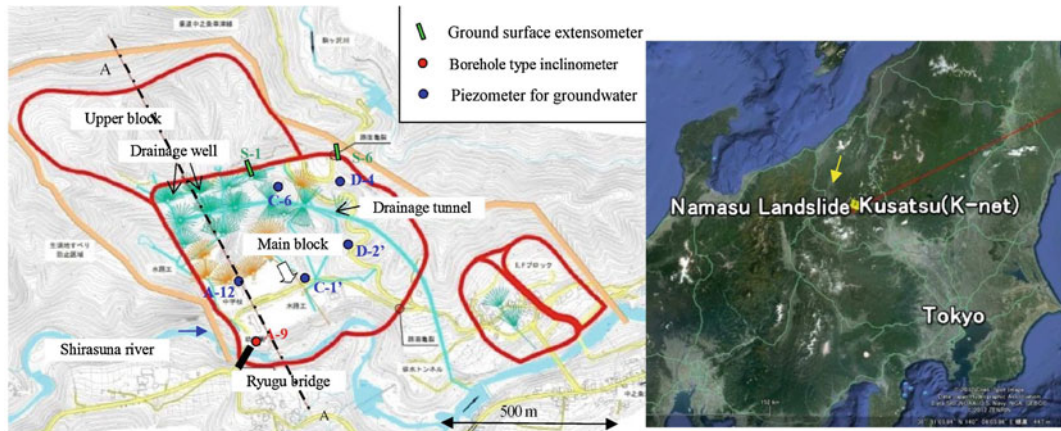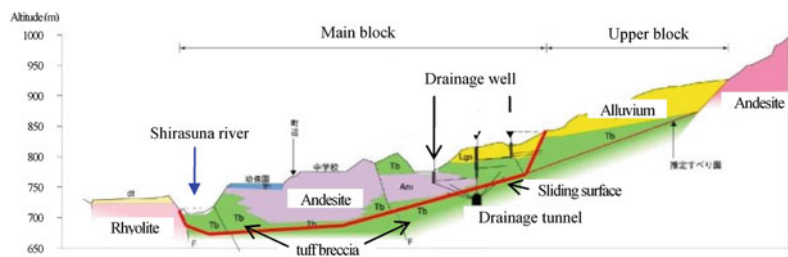Prefecture, Japan
e-mail: a4982@n-koei.co.jp

Fig. 92.1 Plan view and location of Namasu landslide

Fig. 92.2 Cross section A of Namasu landslide

This report presents the evaluation of the drainage works, using the seepage analysis, and also the behavior during the 2011 earthquake off the Pacific coast of Tōhoku and Nagano-ken Hokubu earthquake.

2 Sliding Mechanisms and the Main Distress

The representative geology of the area surrounding the landslide are andesite and tuff breccia of the Neogene period. The landslide mass consists of weak andesite and tuff breccia (Agatuma layer) that had undergone hydrothermal alteration (Fig. 92.2). The landslide shows typical topographical features such as the scarps, slumped blocks, and 20 m wide depression zones, resulting from the mass movement. The presence of the fault controlled the location of the 40 m high scarp at the head of the main block. Alluvium of the mid-Pleistocene period is

also present in the head region (Fig. 92.2). Near the toe of the landslide, river terrace is formed 50 m above the Shirasuna river. The sliding surface is formed within the weak tuff breccia.

Erosion of the toe region by the river and the supply of water to the sliding surface induced the sliding, which cause excessive deformation and damage to the Rygu bridge. As stated earlier, the Rygu bridge, shown in Fig. 92.1, had shortened by 24 cm and deformed upward by 30 cm, when it was compressed in the longitudinal direction due to the landslide movement which was triggered by the heavy rainfall in August of 1982. The cumulative rainfall depth was 340 mm. The hinge structure had been damaged and traffic was blocked. The bridge was repaired with new joints, between the two bridge segments, that can absorb longitudinal displacement. In May of 1989, however, the bridge deck shortened by 42 cm and heaved 52 cm at the center during the heavy rainfall.
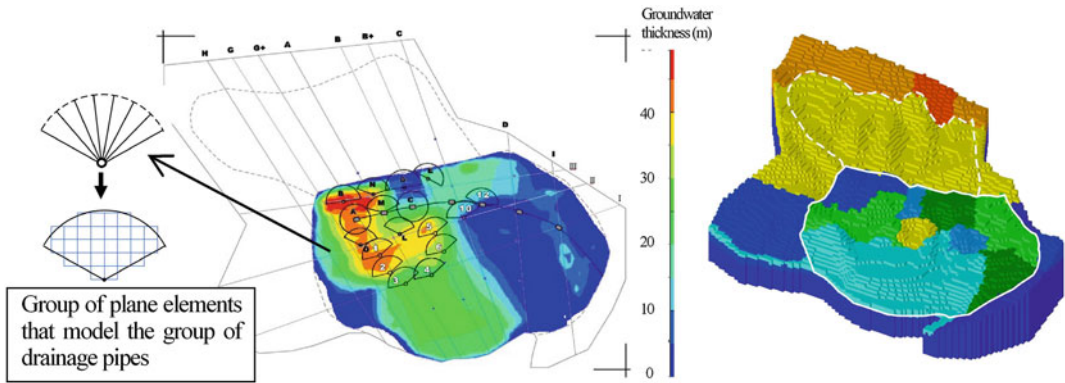
Fig. 92.3 An example of predicted groundwater level, location of the drainage work, and the finite element mesh

3 Prevention Works and Finite Element Analysis

It was decided to adopt the drainage works as the counter measures based on the size of the landslide and the mechanisms. The drainage works consist of the drainage tunnel, drainage wells, and surface drains. The construction of these drainage structures started in 1990 and completed in 2011. The main drainage structures that reduce the effect of the groundwater are the drainage tunnel and the drainage wells. The drainage tunnel was built below the sliding surface as shown in Fig. 92.2. The length of the tunnel is 1042 m and 7 halls were made to install drainage pipes which are directed towards the sliding surface. The total length of the drainage pipes installed in the tunnel is 3,239 m. In addition to the drainage tunnel, 21 drainage wells were constructed. Total length of 16,980 m drainage pipes are installed within the well. Boreholes were drilled inside the well in the radial direction to install drainage pipes that are typically 50 m long. A group of the drainage pipes per well are installed at the same depth, covering a fan shaped area as illustrated in Fig. 92.1 and 92.3.

Out of 21 drainage wells, 9 wells were built after 2004 and had been designed based on the results of saturated–unsaturated seepage finite element analysis (FEA) that can simulate the effects of the drainage wells on the groundwater.

The objective of FEA was to help determine the effective spatial layout and amount of the drainage wells. A group of the drainage pipes per well was modeled by a set of plane elements that are generated together to approximate the group of the pipes (Fig. 92.3). These plane elements are similar to planer joints, with high permeability, that collects water. A node, with prescribed zero pressure, is added at the end of the group of plane element to extract the water. The surface of the finite element mesh, shown in Fig. 92.3, was set as the inflow boundary condition, corresponding to the rainfall intensity with the specific return period.

Series of unsteady-state simulations were performed with the same rainfall intensity but with different layout and number of drainage wells. Factor of safety (FS) was also computed for each case by the three dimensional ordinary method of slices, using the simulated groundwater level. Consequently FS obtained from each case was compared and the most economical configuration, that meets the required FS, was selected for detail design of the wells. An example of the predicted ground water level is shown in Fig. 92.3.

Movement of Namasu landslide is correlated with the working rainfall which is a quantity that includes the effect of the antecedent rain. The previous rainfall depth is added to the current rainfall, while multiplying the reduction factor such that the rainfall depth at 30 days ago is halved. Before 2002, the sliding tended to occur when the working rainfall exceeded 200 mm.

Fig. 92.4 Time history of acceleration recorded at Kusatu station of K-net (Strong-motion seismograph networks) on March 11th
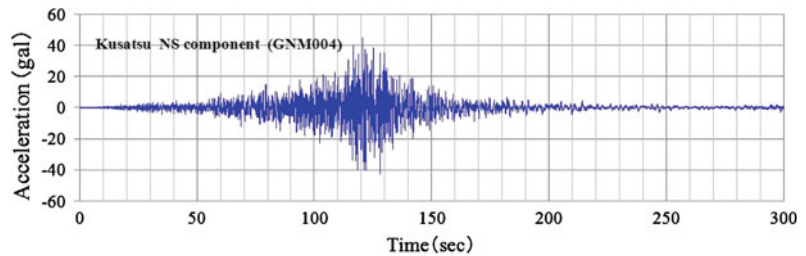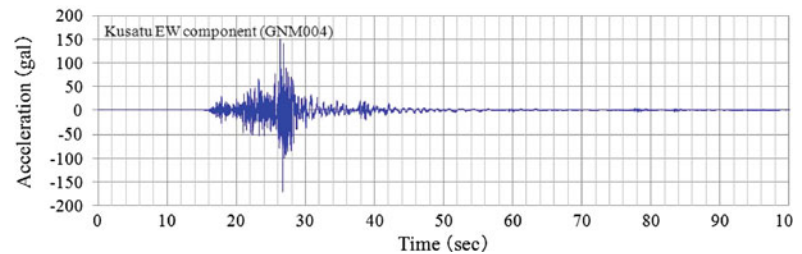

Fig. 92.5 Time history of acceleration recorded at Kusatu station of K-net (Strong-motion seismograph networks) on March 12th

After the completion of the drainage works, no movement was found when the working rainfall was 270 mm during the Typhoon in September of 2011. The factor of safety (FS) was 1.03. These assessments indicate that the drainage works have successfully stabilized the landslide.

4 Behavior of the Landslide During the Latest Earthquake

Displacements and change in groundwater level were recorded during the 2011 earthquake off the Pacific coast of Tohoku (referred to as 2011 Tohoku earthquake) and the Nagano-ken Hokubu earthquake. The landslide is 412 km away from the hypocenter of 2011 Tohoku earthquake. While the measured displacements of this landslide are relatively small, not many examples of monitored displacement have been published in the past. The trends of the measured displacements together with the groundwater levels are given herein to discuss the possible mechanisms.

The horizontal accelerations (NS component), measured at the seismograph 4 km away from the landslide, are shown as examples in Fig. 92.4 and 92.5, corresponding to the 2011 Tohoku earthquake and the Nagano-ken Hokubu earthquake, respectively. It is shown that maximum acceleration of the Nagano-ken Hokubu

earthquake is 3 times larger than that of the 2011 Tohoku earthquake, whereas the duration of the 2011 Tohoku earthquake is 5–6 times longer than the duration of the Nagano Hokubu earthquake.

It is noted that the magnitudes of the acceleration are significantly small compared to the estimated peak accelerations in the areas where slope failures occurred in Fukushima, Tochigi, and North Ibaraki (Kanto Branch of Japan Landslide Society 2012).

As shown in Fig. 92.6, the displacements were recorded by the two ground surface extensometers (S-1 and S-6) installed at the head of the landslide and one inclinometer installed near the toe of the landslide as shown in Fig. 92.6. The displacement of S-1 and the inclinometer started to increase on March 11th when 2011 Tohoku earthquake occurred. The displacement of S-6 started to increase on March 16th, which implies that the displacement may not be directly related to the earthquake. The displacement of S-1 and the inclinometer kept increasing for 4–5 days after March 11th and no obvious change in the trend can be seen on March 12th when the Nagano Hokubu earthquake occurred. There was no rainfall between March 8th and 14th. A small rainfall was recorded on March 15th and 16th. These results suggest that the recorded movement of S-1 and the inclinometer were induced by the earthquake.
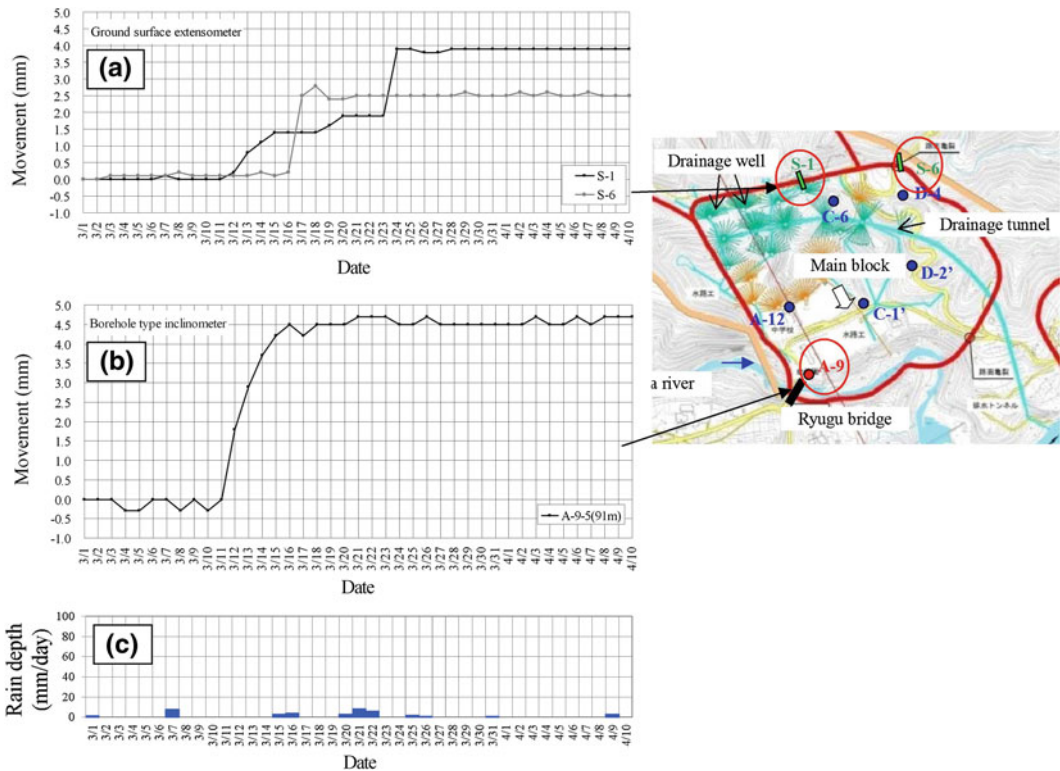
Fig. 92.6 (**a**) Displacements recorded by the ground surface extensometers (S-1 and S-6) (**b**) displacements recorded by the inclinometer (**c**) Daily rainfall depth

The increase in displacement after March 16th may be indicative of local failure, near the sensors, that was triggered by small rainfall as the surficial layer may have been weakened by the seismic loads.

Behavior of the groundwater level (GWL) was also examined. As shown in Fig. 92.7, the piezometer (A-12) in the left area of the landslide indicates increase in GWL by approximately 1 m on March 11th. The piezometer (C-6) near the head, on the other hand, recorded decrease in GWL by 1.5 m between March 11th and March 13th. The piezometer (D-2) in the right area showed increase in GWL on March 12th. Two piezometers (C-6 and D-4) showed slight increase in GWL on March 11th.

The change in GWL, recorded by A-12 and C-6 may be due to the earthquake, since there is no rainfall between March 11th and March 15th. The increase in GWL, recorded by A-12, may be related to compression of the landslide mass and the decrease, recorded by C-6, may be related to loosening of the landslide mass near the head region. The increase in GWL, recorded by D-2, may not be related to earthquake, since there is no change on March 11th followed by another increase on April 6th when there is no rainfall or earthquake. While the number of GWL data is limited, it is noted that the duration of the peak GWL of A-12 closely match with the duration of increase in the displacement recorded by the inclinometer as shown in Fig. 92.6b.

The magnitudes of the variation in GWL are compared with those measured during the strong rainfall on September 5th and 6th 2011. The piezometer, A-12, recorded 4 m increase, C-1 recorded 7 m, C-6 recorded 3 m, D-2 recorded 3 m, and D-4 recorded 3 m on September 6th. While there is scatter in the magnitudes, these piezometers show much larger increase in GWL than that measured on March 11th. However, no displacements were recorded on September 5th
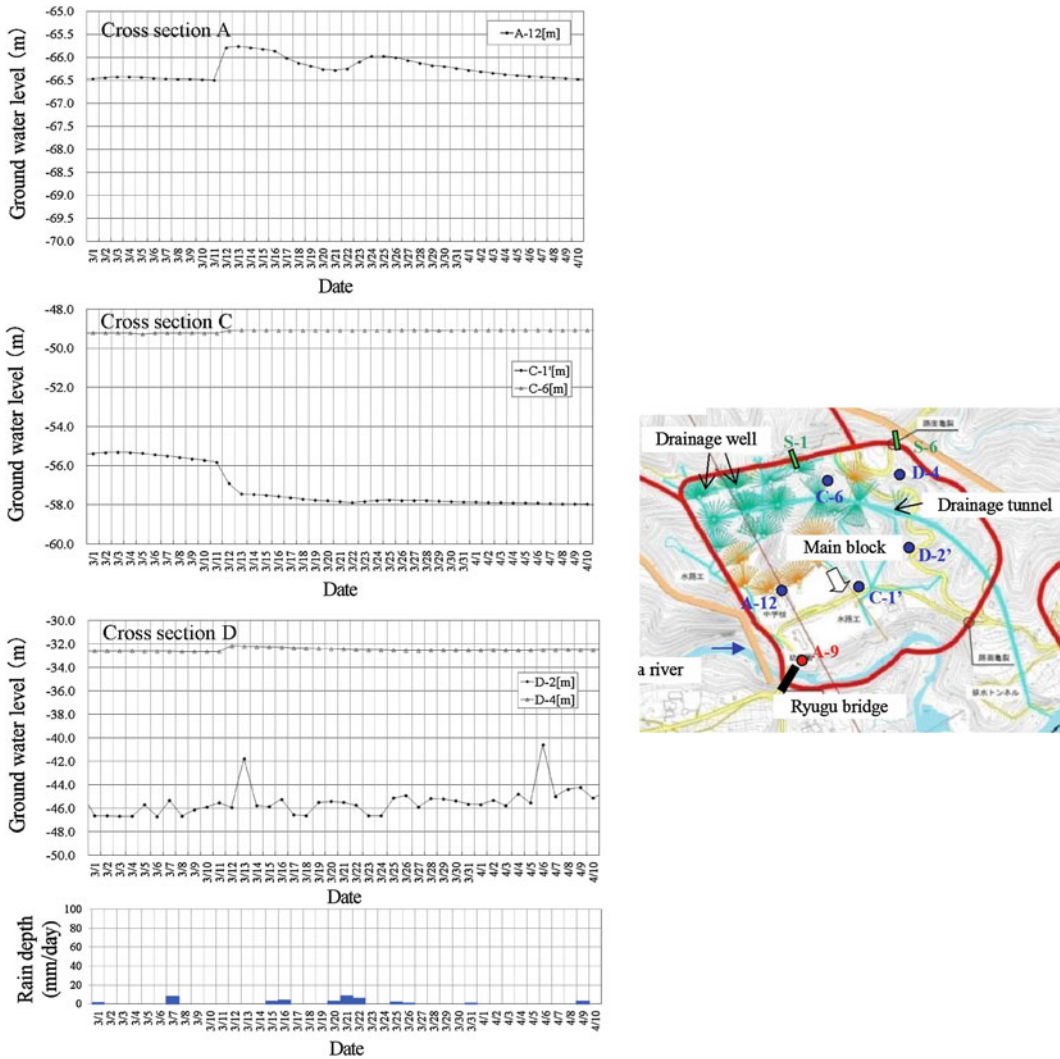
Fig. 92.7 Time history of groundwater measured with piezometers within landslide (A-12, D-2, D-4, C-1, and C-6)

or 6th. Therefore, it is implied that increase in the displacements that started on March 11th, may be due to the combined effects of seismic load and change in groundwater. It is unclear, as to why the displacement of the inclinometer kept increasing for 5 days, while the duration of the seismic load was approximately 2 min. Noting that the displacement increased with decelerating rate and converged to a constant value, the mechanism of the lasting deformation may be attributed to the time it takes for the kinetic energy to dissipate while the mass moved.

5 Concluding Remarks

(1) Comparison of monitored displacements before and after the drainage works, indicate that the landslide has been successfully stabilized against strong rainfall. No displacement was measured during the strong rainfall on September 5th of 2011.

(2) Some of the extensometers and the inclinometer indicated that the landslide mass may have been moved about 5 mm by the seismic load. The displacements are the

largest during the 1.5 years after the completion of the drainage works in the autumn of 2010. Noting that no displacements occurred during the strong rainfall on September 5th of 2011, it is implied that the seismic loads, applied on the landslide mass, were the main trigger of the movement, whereas the rise in the groundwater alone could not have induce the movement.

(3) The peak horizontal accelerations are 40 gal (cm/s^2) and 150 gal on March 11th, and March 12th, respectively. The fact that no obvious change in displacements or the groundwater level (GWL) occurred on March 12th, suggests that effect of the 2011 Tohoku earthquake on the stability was more significant than that of Nagano Hokubu earthquake. It is also implied that the duration of the earthquake may have more effects on stability than the magnitude of the acceleration.

(4) The displacement of the inclinometer kept increasing for 5 days, while the duration of

the seismic load was approximately 2 min. Noting that the displacement increased with decelerating rate and converged to a constant value, the mechanism of the lasting deformation may be attributed to the time it takes for the kinetic energy to dissipate while the mass moved.

References

Fujiwara T, Shinya H, Tomoda T, Kudou T (2009) The measures against the devastated bridge by the large-scale landslide and the effects on them. J Japan Landslide Soc 46(4):239–244 (In Japanese)

Kanto Branch of Japan Landslide Society (2012) Symposium on landslides, in the Kano region, induced by the 2011 earthquake off the Pacific coast of Tohoku, Kanto Branch of Japan Landslide Society, Proceeding (In Japanese)

Tunoda N, Ugai K, Wakai A, Cai F, Kuraoka S, Makino T, Fujiwara T, Shinya H (2004): Finite element analysis for landslide analysis No.11, J Japan Landslide Soc 41(4):103–107 (In Japanese)

Newly Developed Method of Predicting Slope Collapse Places Triggered by Faults Combined with γ-Ray and Magnetic Susceptibility Survey

Tatsuro Yoshimura and Naozo Fukuda

Abstract

After experiences of the east Japan huge earthquake catastrophe, prediction of disasters of earthquakes and/or heavy rainfalls are requested more and more for safety and security life for residents. Many slope collapses were induced by existence of fault in top area of slope zones from geological and topographical surveys. To find the places of fault from field survey are very difficult before disaster, because almost surfaces are covered by sediments, plants and trees. The easy and simple method to determine the size and direction of faults were developed by authors combined with γ-ray and magnetic susceptibility survey. The method is applied on mountain ridges without thick sediments or weathered layers to remove a shielding effect of γ-ray divergence from faults. Checking intervals points of γ-ray intensities on the survey line can be narrowed to 10 cm. From two survey lines the width and direction of the faults can be determined. Case studies of slope failed places induced by faults by the method are introduced from (1) large scale slope failure by extrapolate fault existence in near mountain area (2) middle scale slope failure 1 year after confirmed fault in small scale of surface failure and (3) slope failure along fault predicted by the proposed method. From those case studies to find slope-collapse places, the proposed method is applicable not only for heavy rainfalls, but also for earthquakes.

Keywords

Slope failure · Fault · γ-ray method · Magnetic susceptibility · Prediction of slope failure

1 Introduction

Slope instability by earthquakes has been induced from such conditions as follows; (1) inertia force increase, (2) pore-pressure increase in saturated slope and (3) differential settlement or displacement for structures on slopes.

T. Yoshimura (✉) · N. Fukuda
Fukken Co., ltd., Consulting Engineers, Kyushu Branch Office, 17-19, 2-Chome Hakata-ekimae, Hakata-Ku Fukuoka City 812-0011, Japan
e-mail: t-yoshimura@fukken.co.jp

N. Fukuda
e-mail: fukuda@fukken.co.jp

Additionally, slope collapses have been induced by heavy rainfall after damaged by earthquakes. The topics of paper are aimed to clarify the instability under heavy rainfalls weakened by the faults structures in slopes that were originated earthquakes.

Finding the places of faults in slopes is difficult in precision because of covering of soil deposits, vegetation of natural plants or slope protection works. The first author has been developed to find the existences of the place and direction of faults in 10 cm precision based on measuring γ-ray and magnetic susceptibility survey by simple method using scintillation measurement[1].

Case studies of determination of slope-collapse places related with the predicted faults by the method are introduced from (1) large scale slope failure by extrapolate fault existence in near mountain area (2) middle scale slope failure 1 year after confirmed fault in small scale of surface failure and (3) slope failure along fault predicted by the proposed method.

2 Determination of the Place of Faults

Intensity of γ-ray can be measured by scintillation survey meter TCS-151 (Aloka products). The intensity of γ-ray can be shown in the unit of $10^{-2} \mu Sv/h$ and the minimum error is less than 3 %. Measurement line (A) is set on about 90 ° against estimated fault direction that is determined from properties by topographical and geological maps. Interval of measuring points was set as 2–3 m in first stage as shown in Fig. 93.1. After finding abnormal intensity of γ-ray, the interval of measuring points are narrowed up to 10 cm and determined the boundary (pt. a1, a2) between normal and abnormal intensity of γ-ray as shown in Fig. 93.1. Same procedure is applied in parallel measurement line (B) apart about 1 m from measurement line (A) to determine the boundary pt. b1 and b2. The width and direction of abnormal intensity of γ-ray can be determined from extrapolation between pt.a1 to b1 and a2 to b2. The method should be applied on mountain ridge that the
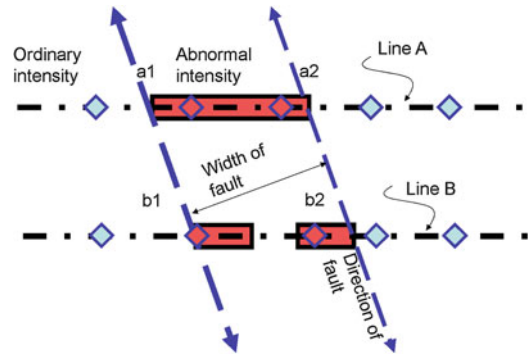
Fig. 93.1 Width and direction of fault detected by γ-ray survey

thickness of covered soil or weathered rock is estimated negligible thin. The width and direction of the faults are determined based on the method. However, three dimensional properties of the faults in slope should be determined by additional geological survey such as core boring survey or geophysical exploration and so on.

3 Preceision and Mechanism of Γ-Ray Intensity in Faults

γ-ray measurements were applied for the faults appeared on surface after earthquakes as Tanna, Satomura, Neodani and Nojima. The widths of faults were very narrow as about 10 cm from abnormal intensity of γ-ray just on fault appeared on surface[2]. From γ-ray and magnetic susceptibility measurement, abnormal low intensity of γ-ray intensity was measured in case of high magnetic susceptibility. The magnetic susceptibility is affected by the amount of magnetic mineral. Iron and lead of high atomic number are hard through γ-ray that means screening effect. From the point of view, low γ-ray intensity in the faults can be explained as the effect of shielding by containing materials of high magnetic susceptibility as shown in Fig. 93.2.

Figure 93.3 shows relationship between magnetic susceptibility and γ-ray absorption. γ ray is lower the higher the magnetic susceptibility. Fault activity makes fine-grained rocks and increase of magnetic minerals. In the

Fig. 93.2 Model of γ-ray screening effect
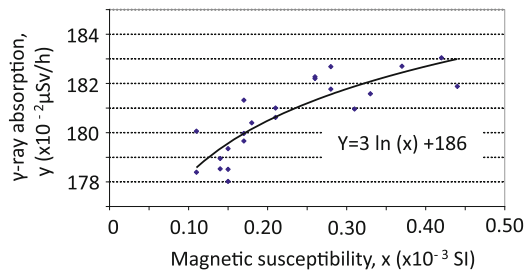
Fig. 93.3 γ-ray absorption compared with magnetic susceptibility (sedimentary rock)

condition, the intensity of γ-ray is shown as abnormally low value[3].

4   Evaluation of Slope Failure Induced by Faults

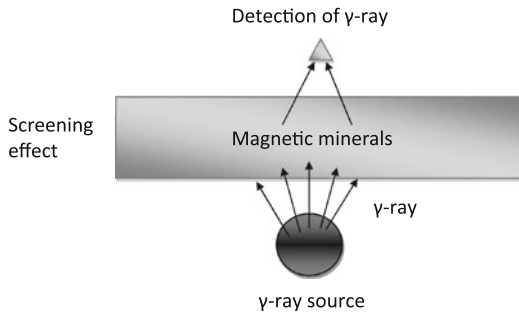Large landslide as about 60 m width and 100 m length had taken placed next to highway by heavy rainfall in July 2009 in Fukuoka Prefecture. Small scale of landslide next to the place had also taken place in 2003 in advance. Granite rock is distributed in this area and fault was estimated the direction of NNE east side of the failure place by geological map and NNE lineament structure was confirmed near failed place by topographic map. Therefore measurement lines of γ-ray were set on mountain ridge 700 m apart from southern direction of failed place as shown in Fig. 93.4.

Figure 93.5 shows the distribution of measured γ-ray intensity on the measure line as 9.3–9.2 in average in stable granite rock and 8.5 in fault zone. The direction and width of the fault
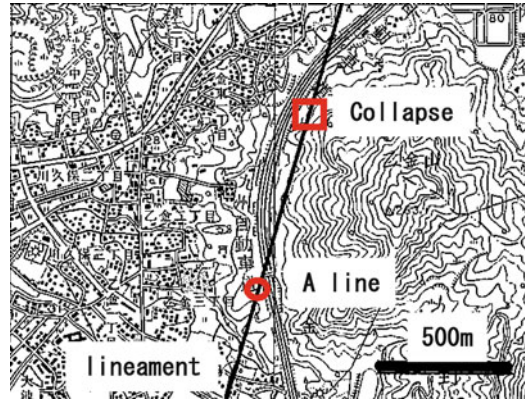
Fig. 93.4 Relationship between lineament direction measured by γ-ray and slope collapsed area in Onojo of Fukuoka prefecture
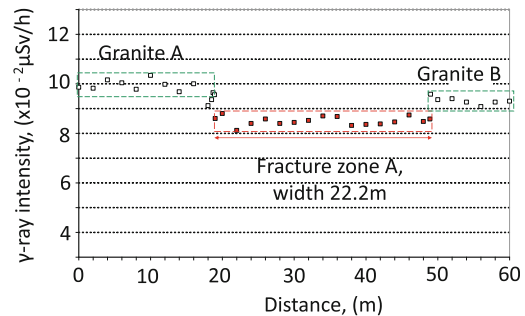
Fig. 93.5 Result of γ-ray survey in Onojo of Fukuoka prefecture

found to be N17°E and 22.2 m. Extrapolation of the measured fault was just coincided with failed place that means the slope failure was induced by heavy rainfall in the degraded fault zone.

5   Unstable Slope Extraporated from Active Fault

Active fault is defined as a fault that is expected to induce an earthquake on the order of 1000 years. In the geological survey on the active fault named Hinatatoge that was shown the direction WNW from geological map along the prefectural road No. 49 in Fukuoka. Two measurement lines of γ-ray was set 80 m length and 3 m space on the mountain ridge based on an aerial photo interpretation that was placed on the boundary of
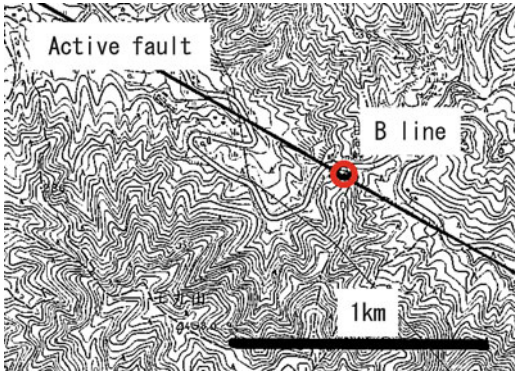
Fig. 93.6 γ-ray survey area in Hinatatoge fault

Fig. 93.7 γ-ray intensity measured in Hinatatohge fault

rocks between granite and granodiorite. The direction and the width of the active fault was found to be N60°W and 19.1 m, and intensity in average of γ-ray in the active fault was 6.86 in granite rock and 3.23 in granodiorite rock as shown in Figs. 93.6 and 93.7. Slope protection works were found to be applied just the extrapolation of the measured faults as shown in Fig. 93.8. It suggests slope instability was induced by the active fault named Hinatatoge.

6 Extension of Slope Failure Next to Non-Failed Slope Induced by Faults

Small size of slope failure neighboring a road in Kawara of Fukuoka prefecture was occurred in July 2009 as shown in Fig. 93.9. The width, length and outflow volume were 6, 7 and 33 m^3. γ-ray measurement lines of 60 m length and 3 m space were set on the mountain ridge in April 2010.

Fig. 93.8 Slope protection works on the end of extrapolation of active fault estimated γ-ray measurement

Fig. 93.9 Small slope failure in July 2009
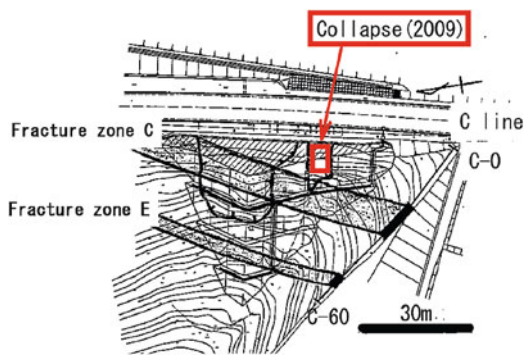
Fig. 93.10 γ-ray survey area in Kawara of Fukuoka prefecture

Three faults were measured in the failed slope and neighbored non-failed slope as shown in Figs. 93.10 and 93.11. Instability of non-
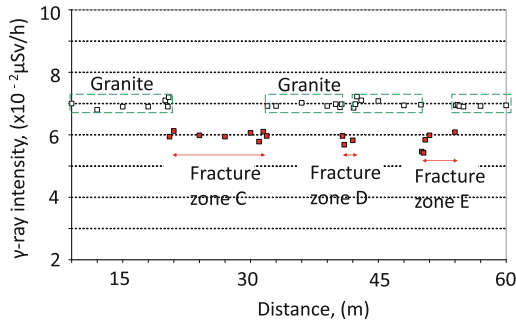
Fig. 93.11 Result of γ-ray survey in Kawara of Fukuoka prefecture

Table 93.1 Common conditions and functions for large and/or deep level slope failures induced by faults

Common conditions	Instability function induced by faults
(1) Deep layer of weathered material	Finalized rocks by crashing of faults, acceleration of weathering by ground water
(2) Gathering ground water	Formation of water flow trough faults
(3) Transition of the gradient in the gully head	Faults are often to be found in transition of gradient of slopes

Fig. 93.12 Occurrence of larger size of slope failure next to former small failure

failed slope under heavy rainfall was estimated, but middle size of slope failure was occurred in August 2010 before construction of slope protection works. This resulted that γ-ray survey after slope failure is effective to estimate and to prevent the followed occurrence of larger size of slope failure as shown in Fig. 93.12.

7 Procedure of Determine the Slope Instability Area Induced by Faults Using Gamma Ray Measurement

Slope failures were induced in many cases by the existence of faults. Causes of failures induced by faults were grand water shielding and following increase of water pressure inside

unstable rock mass[4]. Common conditions for large and/or deep level slope failures induced by faults were shown in Table 93.1 comparing with functions of faults.

The procedure of the proposed method to estimate of instable slope area is as follows.

Step-1: Confirm the linear structure formed as a line of small size of failed slopes from topographic map. And determine the potential sites of faults.

Step-2: Measure the directions and widths of faults.

Step-3: Choose hi-risk instable slopes from advanced survey of topographical, geological and spring water properties.

Figure 93.13 shows the linear relationship between fault width and fault length[5]. By measuring width of faults by γ-ray for previously
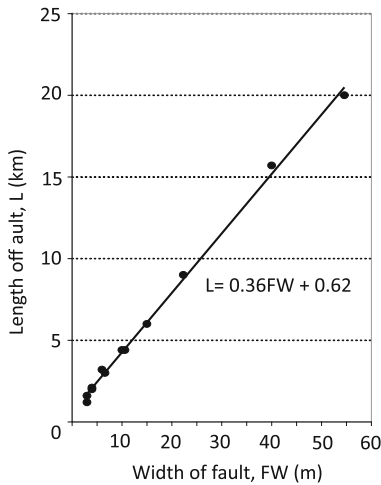
Fig. 93.13 Relationship between width and length for previously reported faults

remove a γ-ray divergence from faults. Checking intervals points of γ-ray intensities on the survey line can be narrowed to 10 cm. From two survey lines the width and direction of the faults can be determined.

Case studies of determination of slope-collapse places related with the predicted fault by the method are introduced from (1) large scale slope failure by extrapolate fault existence in near mountain area (2) middle scale slope failure 1 year after confirmed fault in small scale of surface failure and (3) slope failure along fault predicted by the proposed method.

From those case studies to find slope-collapse places, the proposed method is applicable not only for heavy rainfall, but also for earthquakes.

reported faults that can be obtain the length of faults. The width of fault can be determined by proposed γ-ray method. And hence, the effect of faults can be predict for any constructions as slope protection works or foundation works for structures by this linear relationship.

8 Conclusions

The easy and simple method to find the existences and determine the size of faults was developed by combining with γ-ray and magnetic susceptibility survey. The method is applied on mountain ridges without thick sediments or weathered layers to

References

Yoshimura T, Fukuda N (2011) Method of predicting slope collapse places combined by γ-ray and magnetic susceptibility survey. International symposium on advanced technology of preventive measures against landslides Fukuoka 2011: 273–277

Yoshimura T (1992) The method of γ-ray survey to investigate active fault. Active Fault Res 10:73–83 (in Japanese)

Yoshimura T (2012) Magnetic susceptibility affecting γ-ray around fault. GET Kyushu 33: in printing (in Japanese)

Chigira M (2007) Places of collapse. Kinmiraisha, Nagoya (in Japanese)

Yoshimura T (2010) Activity level evaluation of active fault by fracture width—relational expression of fracture width and fault length-. Active Fault Research 33:39–49 (in Japanese)

Observations on Earthquake Acceleration and Pore Water Pressure in a Hilly Region

94

Shiho Asano, Hirotaka Ochiai and Yasuhiko Okada

Abstract

Earthquake accelerations and pore water pressures were measured on a hill slope to constrain slope stability reduction caused by earthquakes. Acceleration responses were observed at various locations on and under the ground surface on a ridge slope and in neighboring valley fill units. Pore water pressure in the valley fill was also measured during earthquakes. The amplification of the acceleration response that was transmitted from underground to the ground surface was compared between sites. The acceleration responses became greater when an earthquake was transmitted from underground to the ground surface. Large earthquake accelerations on the ridge of the hill were amplified primarily in a direction perpendicular to the ridge crest. They were also amplified at specific frequencies by the topological effect. In contrast, earthquake accelerations in valley fill sediments were equally amplified in all directions and over a wide frequency band. Increases in the dynamic pore water pressure tended to be synchronized with increases in vertical acceleration.

1 Introduction

Seismic acceleration and groundwater pressure are important factors that need to be constrained for an earthquake slope stability analysis. Therefore, it is important to know the distribution and effects of seismic accelerations and dynamic pore water pressures in hilly regions to clearly understand the mechanisms of landslides occurring in conjunction with earthquakes.

S. Asano (✉)
Kyushu Research Center, Forestry and Forest Products Research Institute, 4-11-16 Kurokami, Kumamoto 860-0862, Japan
e-mail: shiho03@ffpri.affrc.go.jp

H. Ochiai · Y. Okada
Forestry and Forest Products Research Institute, 1 Matsunosato, Tsukuba, Ibaraki 305-8687, Japan

Table 94.1 List of considered earthquake event in Figs. 94.4 and 94.5

Start time of record at study site	Magnitude	Epicenteter	
2005/2/16 4:46	M5.4	36.035 N	139.895E
2005/7/23 16:35	M6.0	35.582 N	140.138E
2007/7/16 10:14	M6.8	37.557 N	138.608E
2008/5/8 1:45	M7.0	36.227 N	141.607E
2008/8/8 12:57	M4.6	35.630 N	139.537E
2009/8/11 5:07	M6.5	34.785 N	138.498E
2010/3/14 17:09	M6.7	37.723E	141.817E

Many seismically induced landslides occurred in the slopes and valleys of central Niigata Prefecture as a result of a 2004 earthquake (Yagi et al. 2005). One of the reasons for these landslides seems to be that large seismic accelerations tend to occur in both convex slopes (e.g., mountain ridge lines) and soft soil layers (e.g., valley fill sedimentary units). Also, in the valleys, dynamic water table variations seem to affect earthquake induced landslides. To identify the characteristics of earthquake and dynamic groundwater motions, observational and soil testing studies have been undertaken in conjunction with theoretical investigations.

Some observational studies of earthquake motion and dynamic groundwater in valley fill for earthquake-induced landslides in this region have previously been carried out (Mori et al. 2010; Kamai 2011). In these studies, the seismic responses of valley fill ground, cut ground and Table 94.1 and are compared, and some characteristics of the seismic response in the fill ground are identified. The observational study of seismic motion along the ridge of a hill was carried out, revealing that the seismic response was affected by topological effect (Ochiai et al. 1985).

In this study, observations of groundwater and seismic motion were carried out along a ridge and in the neighboring slope of a partially sediment-filled valley. Then, the differences in the amplification of seismic acceleration from underground to ground surface and the relationships of dynamic groundwater variations and seismic accelerations were examined.
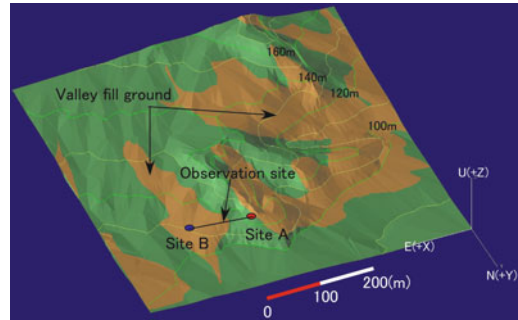
Fig. 94.1 Topological map in the study area

2 Study Site

Observations for this study were made in a hilly area in the western part of Tokyo, Japan. This is an area with gentle slopes at the edge of a region of Table 94.1 and, many short channels can be found here. The terrain in this region has been extensively modified by anthropogenic means in the 20th century, resulting in much hill degradation and valley fill. Topological maps of the study area from 1940 and 2007 were compared; the distribution of valley fill in 2007 can be seen in a 3D topological map (Fig. 94.1). In this figure, regions of valley fill are densely distributed.

Two observation Sites for earthquake motion and groundwater were established in this area. One Site was located on the ridge of a hill (Site A) and another Site was on sloping valley fill (Site B). Site A was located at an elevation of 127 m and Site B was at 112 m; and the horizontal distance between the stations was about 100 m.

Fig. 94.2 Cross section of the observation sites
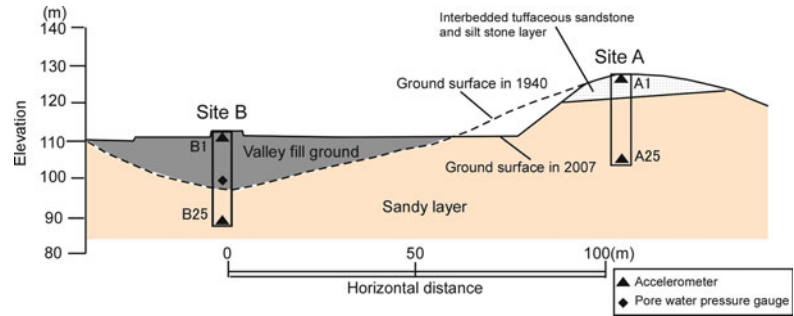
In this area, unconsolidated interbedded gravel, sand and mud strata accumulated during the Pleistocene epoch. At Site A, boring shows that loam developed on the ground surface down to a depth of 0.45 m depth, overlying interbedded tuffaceous sand and siltstone from 0.45 to 6.6 m, which in turn overlies unconsolidated fine sandstone. At Site B, the regolith extends from the surface to a depth of 0.4 m, overlying soil that consists of a mixture of loose sand and silt from 0.4 to 15.2 m, which in turn overlies unconsolidated fine-to-medium sized sand (Fig. 94.2).

3   Method

Earthquake acceleration was observed at Sites A and B and groundwater pore pressures at Site B. Borehole accelerometers were installed at depths of 1 m (A1, B1) and 25 m (A25, B25) at both Sites. A pore water gauge was installed at a depth of 13 m in the Site B borehole.

The accelerometers were servo type acceleration sensors that can make borehole measurements in three directions (model: SA-355CT, by Tokyo Sokushin Co). In this study, east is defined as the +X component, north is the +Y component, and vertical rise is the +Z component. The pore water gauge was a pressure transducer with a back pressure tube; it was buried with course sand in the borehole. The accelerometers and pore water gauge were connected to a signal conditioner (model: PSC-1025, by Tokyo Sokushin Co.) where signals were amplified. These signals were recorded in a

data logger (model: SAMTAC-700-16, by Tokyo Sokushin Co). The frequency response characteristics of this system consisted of a band from 0.05 to 35 Hz; the observational sampling rate was 100 Hz. The recording trigger level of the system was 6×10^{-4} m/s^2 and the recorded pre-trigger period was 10 s. The observation ran from October 2004 to March 2011, during which period 261 earthquake events were recorded. Full data sets have been obtained between 2005 and 2010 without sensor troubles.

Surface wave prospecting was carried out to investigate the distribution of underground strength at the study Site. Surface wave prospecting is a form of seismic prospecting in which data concerning the distribution of S-wave rock velocities is collected. A survey line was recorded between Sites A and B. A total of 24 geophones were used at a spacing of 2 m. Seismic data were collected by hammering at each geophone and then subsequently analyzed. These measurements were carried out using the McSEIS SXW (by Oyo Co.) and SeisImager/SW (by Oyo Co.) systems.

4   Results and Discussion

4.1   S-Wave Velocity Distribution in Soil

The distributions of S-wave velocities as determined by surface wave prospecting and geological structure as determined by boring and topological analysis along the survey line are shown in

Fig. 94.3 Distribution of S-wave velocities
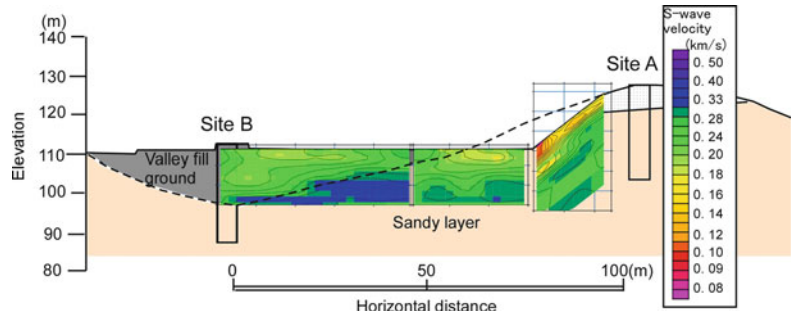
Fig. 94.3. In general, there is a positive correlation between S-wave velocity and the N value of standard penetration tests (Imai and Tonouchi 1982). The figure shows that the 3-m-deep surface layer of the steep slope is weaker and artificial fill in the valley is softer than naturally accumulated soil. The S-wave velocity of the valley fill material is occasionally lower than 0.1 km/s.

4.2   Amplification of Maximum Acceleration of Earthquake Events

The difference in the maximum acceleration observed at depths of 1 and 25 m was compared for each earthquake events (Figs. 94.4 and 94.5). Seven relatively large earthquake events recorded between 2005 and 2010 are shown (Table 94.1). The earthquake acceleration of each of the events was amplified when the wave was transmitted between depths of 25 and 1 m. The pattern of amplification was different between Sites A and B. At Site A, the X component of acceleration became larger than the Y component for large earthquake events (Fig. 94.4). At Site B, the X and Y components were amplified similarly (Fig. 94.5). The amplification of the Z component of acceleration at Site A was greater than at Site B.

4.3   Horizontal Motion of the Acceleration Response on a Hill Slope

Particle acceleration was analyzed to compare the time change of the acceleration response at
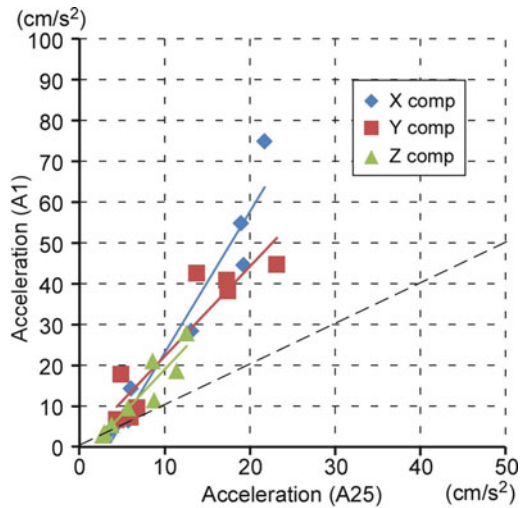
Fig. 94.4 Maximum acceleration response for each earthquake event at Site A
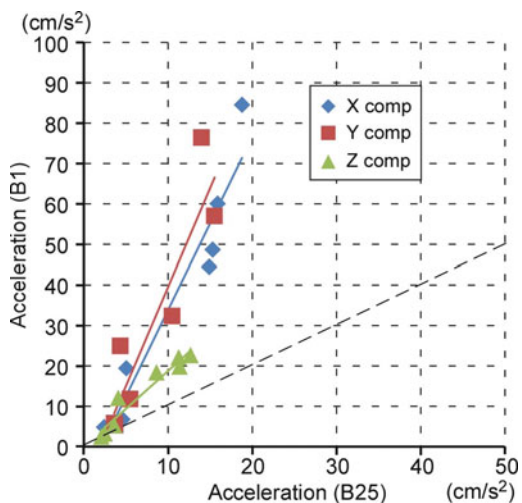
Fig. 94.5 Maximum acceleration response for each earthquake event at Site B
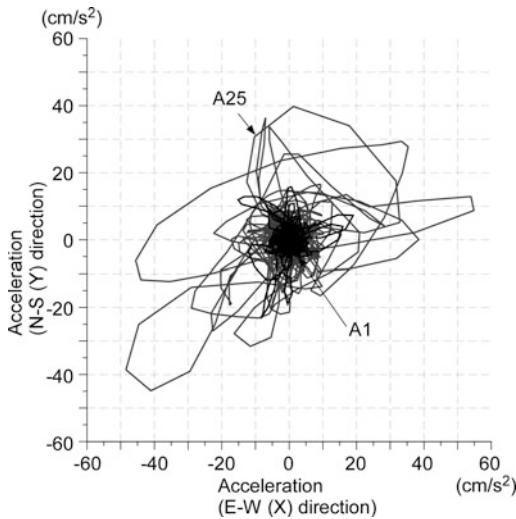
Fig. 94.6 Horizontal particle motion of the acceleration response at Site A
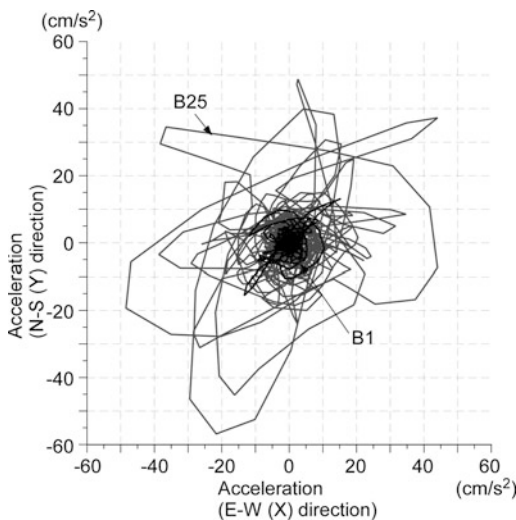
Fig. 94.7 Horizontal particle motion of the acceleration response at Site B

each Site. The results recorded on 8 August 2008 are shown in Figs. 94.6 and 94.7 because that earthquake has a relatively large acceleration at the recording Sites. These show the horizontal component of acceleration response. Acceleration of the ground surface (A1 and B1) was greater than the acceleration at depth (A25 and B25). For this seismic event, the acceleration at

A25 and B25 appeared to be almost the same size in all directions. The acceleration at A1 was amplified most in the X direction as accelerations increased (Fig. 94.6), which contrasts with the acceleration at B1 that was amplified equally in all direction (Fig. 94.7). The orientation of the ridge crest at Site A is in the Y direction and the slope at Site B faces the -X to Y direction. Therefore, the acceleration of the ground surface at Site A was amplified in a direction at right angles to the ridge crest when the acceleration became large. The amplification of acceleration at Site B seemed not to be influenced by topology, but rather was affected dominantly by the soil characteristics.

4.4   Spectral Characteristics of Each Site

The Fourier spectrum of the horizontal component of acceleration at each observation point was calculated using data from 11 August 2009 because this earthquake had a relatively large acceleration on the Site and pore water pressure data were obtained without error. Then, the increases in the acceleration amplitudes as energy was transmitted from a depth of 25 m to the ground surface were determined over a range of frequencies (Fig. 94.8). At Site A, the 6 Hz component of the acceleration response increased substantially, whereas the high frequency component was not increased as much. At Site B, the 4 Hz component of the acceleration, which was lower than at Site A, was increased in a similar way to Site A. However, in this case, the high frequency component was increased also. Therefore, the earthquake acceleration on the ridge crest can be considered to have been increased by topological influences that tend to amplify at a specific frequency range. In contrast, the acceleration in the slope fill units of the valley floor, which was increased in response to the soil characteristics there, tended to amplify a wide band of frequencies. These differences in acceleration response will have an effect upon the mechanism of landslide occurrences.
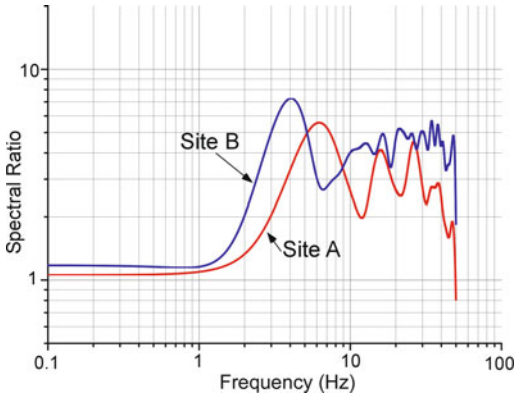
Fig. 94.8 Spectral ratio of the amplification of acceleration
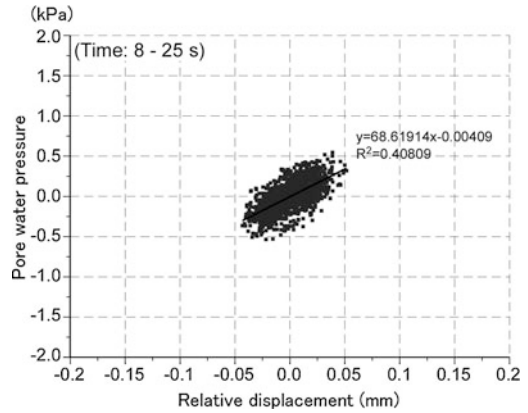
Fig. 94.10 Relationship between pore water pressure and relative displacement from 8 to 25 s
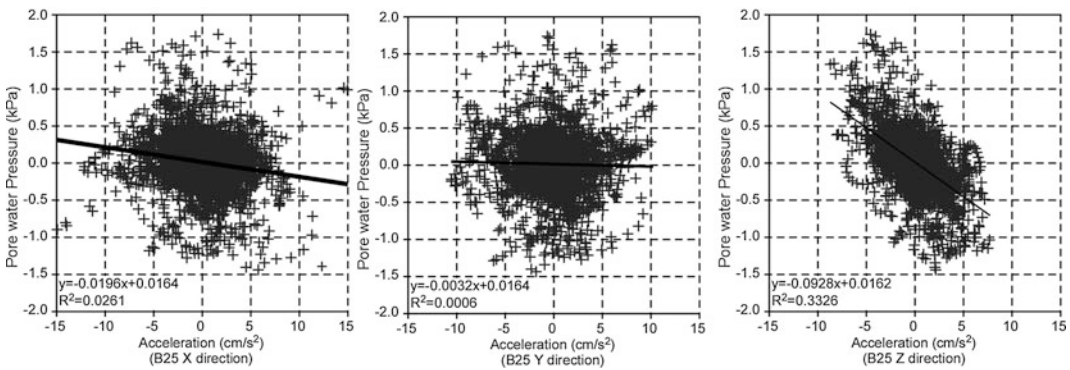
Fig. 94.9 Relationship between pore water pressure and acceleration response

4.5 Dynamic Groundwater Variations

The relationship between seismic acceleration and dynamic variations in pore water pressure, which may reduce slope stability, were examined for the earthquake of 11 August 2009. Pore water pressure was measured at a depth of 13 m at Site B, which has a groundwater table. The correlation was examined in conjunction with the time history change of the vertical (Z) component of earthquake acceleration and pore water pressure at B25 (Fig. 94.9). In this figure, the increase in pore water pressure tends to be synchronized with an increase in vertical acceleration. Horizontal acceleration, like X and Y, were not synchronized with pore water pressure variation.

The macroscopic vertical displacement of the ground was estimated from the observed acceleration response at B1 and B25 to examine the effect of ground deformation on pore water pressure variations. The vertical displacement of B1 and B25 was calculated by integrating the acceleration response. Then, the variation in the distance between B1 and B25 was obtained. This distance can be regarded as an index of deformation of the filled ground and compared with the variation of pore water pressure in the system. If the distance became longer, the ground was considered to be in extension mode in this study. On the other hand, if the distance became shorter, it was considered to be in compression mode. The phase difference between the deformation of ground and pore water pressure variation was small when the displacement was small (Fig. 94.10). However, when the
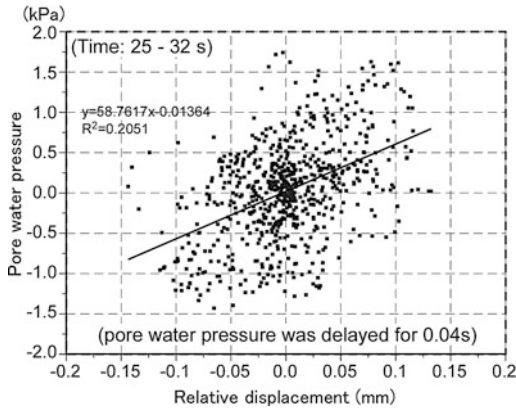
Fig. 94.11 Relationship between pore water pressure and relative displacement from 25 to 32 s

phase of pore water pressure variation was delayed from the ground deformation by 0.04 s, then the displacement changed to be large (Fig. 94.11). In this case, the absolute value of pore water pressures tended to increase. Also, an increase in positive pressure appeared in the ground extension mode. This might show that the effect of ground vibrations on the increasing pore water pressure is larger than the effect of ground compression.

5   Conclusions

Earthquake accelerations and pore water pressures were measured on a hill slope to clarify the effect of reducing the slope stability as a result of earthquake-induced ground accelerations. The acceleration response was observed both at the ground surface and at a depth of 25 m at Sites located at a ridge crest and in artificial valley fill. Pore water pressures were observed at a depth of 13 m at the latter location. Surface wave analysis showed that the severity of the deformation in the artificial fill was less than in soil that has accumulated naturally. The amplification of the acceleration response was transmitted from underground to the surface was examined at each site. The acceleration response from each observed earthquake event increased as it was transmitted from underground to the surface. At the ridge crest, large earthquake accelerations were amplified in a direction that was perpendicular to the ridge. This occurred at specific frequencies because of a topological effect. On the other hand, earthquake accelerations in valley fill units on the lower slopes of the hills were amplified to the same extent in all directions and over a wide frequency band. Increases in the dynamic pore water pressure tended to be synchronized with increases in the vertical acceleration.

References

Imai T, Tonouchi K (1982) Correlation of N value with S wave velocity. Proceedings of 2nd ESOPT, Vol 2. pp 67–72

Kamai T (2011) Seismic response of valley fills to strong earthquakes on residential region in Tokyo. J Jpn Landslide Soc 48(6):334–343 (in Japanese with English abstract)

Mori T, Chiba T, Uzuoka R, Kazama M (2010) The relationship between change of soil moisture resulted from rainfalls and seismic response characteristics in the valley fill ground. J Jpn Assoc Earthq Eng 10(4):1–13 (in Japanese with English abstract)

Ochiai H, Yanase H, Matsuura S, Shinagawa M (1985) Measurement of earthquake motion and pore water pressure at the Yui landslide area. Proceedings of IVth international conference and field workshop on landslides, pp 203–208

Yagi H, Yamasaki T, Moriiwa T, Atsumi K (2005) Landslides triggered by the Mid Niigata Prefecture Earthquake in 2004 and their characteristics based on a detail mapping. J Jpn Soc Eng Geol 46(3):145–152 (in Japanese with English abstract)

A Simplified Technique for Slope Stability Assessment Based on Insitu S-Wave Velocity Measurement

95

Mohsin Usman Qureshi, Suguru Yamada and Ikuo Towhata

Abstract

Natural disasters such as earthquakes or heavy rainfalls thwart the potential stability of weathered slopes which has significant effects on the safety of infrastructure in the vicinity. In the case of developing countries, this situation is inevitable and necessitates to develop a quick and economical technique for the overall progress in the assessment of safety. In dealing with the slope instability problems for such regions, at first it is important to identify the potentially unstable slopes and then decide the mitigation strategies. In this regard, in situ shear strength of weathered geo-material exposed on slopes should be carefully delineated which is a time consuming procedure. Therefore, a relation of in situ shear strength of weathered geo-material to the geophysically measured S-wave velocity is employed in the present study. Field experiments were conducted to evaluate the shear-wave velocity, depth and in situ shear strength of surface weathered layer which included seismic refraction, portable dynamic cone penetration and field direct shear tests. Field studies were conducted in Japan (Yokosuka, Nagano, Izu and Kobe), and Pakistan (Muzaffarabad and Taxila). The investigated sites were recently disturbed by strong earthquakes or heavy rainfalls. By using the depth

M. U. Qureshi (✉)
Department of Civil Engineering, Wah Engineering College, The University of Wah
Quaid Avenue, 47040 Wah Cantt, Pakistan
e-mail: mohsinqureshi81@gmail.com

S. Yamada
Department of Urban Engineering, Osaka City University, 3-3-138 Sugimoto, Sumiyoshi-ku, Osaka City, Osaka 558-8585, Japan
e-mail: yamada@urban.eng.osaka-cu.ac.jp

I. Towhata
Department of Civil Engineering, The University of Tokyo, 7-3-1, Hongo, Bunkyo-ku, 113-8656 Tokyo, Japan
e-mail: towhata@geot.t.u-tokyo.ac.jp

and in situ shear strength of surface weathered layer stability analysis (infinite slope) was carried out and correlated to S-wave velocity, which suggested that the safety factor of a weathered slope reduces to half during the rainfall event. Moreover a safety assessment matrix (SAM) is presented which by inputting the slope angle and the S-wave velocity of the weathered geo-material on slope surface categorizes the level of safety into, (a) stable, (b) Potentially unstable and, (c) Unstable. The authors envision using SAM for the direct evaluation of potential instability by a continuous monitoring of S-wave velocity and slope angle. Therefore, it is recommended that, monitoring of S-wave velocity of surface weathered layer for risk assessment is a quick and economical technique other than time consuming, local and expansive intrusive methods.

1   Introduction

A huge earthquake of magnitude Mw: 7.6 hit north-eastern part of Pakistan in Kashmir on October 8, 2005, which estimated to have killed up to 87,000 people, 26,500 died as a direct result of landslides and 2,424 landslides (most of them being shallow slides) took place during the earthquake affecting a large number of community and infrastructure (Aziz et al. 2009) (Fig. 95.1). The impending factors for expected instability of natural slopes were rainfalls, future earthquakes, human disturbances and environmental agents such as temporal change. More recently, post-earthquake risk to the seismically disturbed slopes was the potential instability during the rainy season and the effects of extreme environmental agents in the area such as temporal change, (below 0 °C in winter and more than 40 °C in summer). Close examination of disturbed slopes indicated that rock is highly weathered and lost its shear strength which could be inferred to in a huge number of slope failures. Those weathered slopes generate potential hazards to the transportation routes and community (Fig. 95.1).

According to Kausar et al. (2009), "after 2005 Kashmir earthquake deep seated landslides were far less numerous than shallow slides which were

as deep as the root zone of the vegetative cover, from several decimeters to a meter deep. Those landslides consisted of dry, highly weathered and fractured geo-material that cascade down-slope to flatter areas at or near the toe of the slope. Such shallow slides had a pervasive nature that significantly contributed to the damage".

In some cases, the stabilization of the entire distribution of weathered slopes may not be possible to improve the safety. In that case, identification of potentially unstable slopes will contribute to the safety improvements. So there is a need to develop a quick and economical technique for safety assessment which is envisaged in the present research. After the 2008 Wenchuan earthquake of magnitude Mw: 7.9 a similar situation was observed. The destruction to the natural slopes was small in size but may be of a huge number, which makes a huge cumulative geotechnical disaster. Recently, it has been reported that there is an increase in slope disasters during the rainy season in the areas shaken by the WenChuan Earthquake. The recent practice of stabilization of vulnerable slopes involves intrusive investigations such as borehole drilling and down-hole surveys to elucidate the mechanical properties, which are time-consuming and expensive, but accurate. With such technique, it is not possible to solve
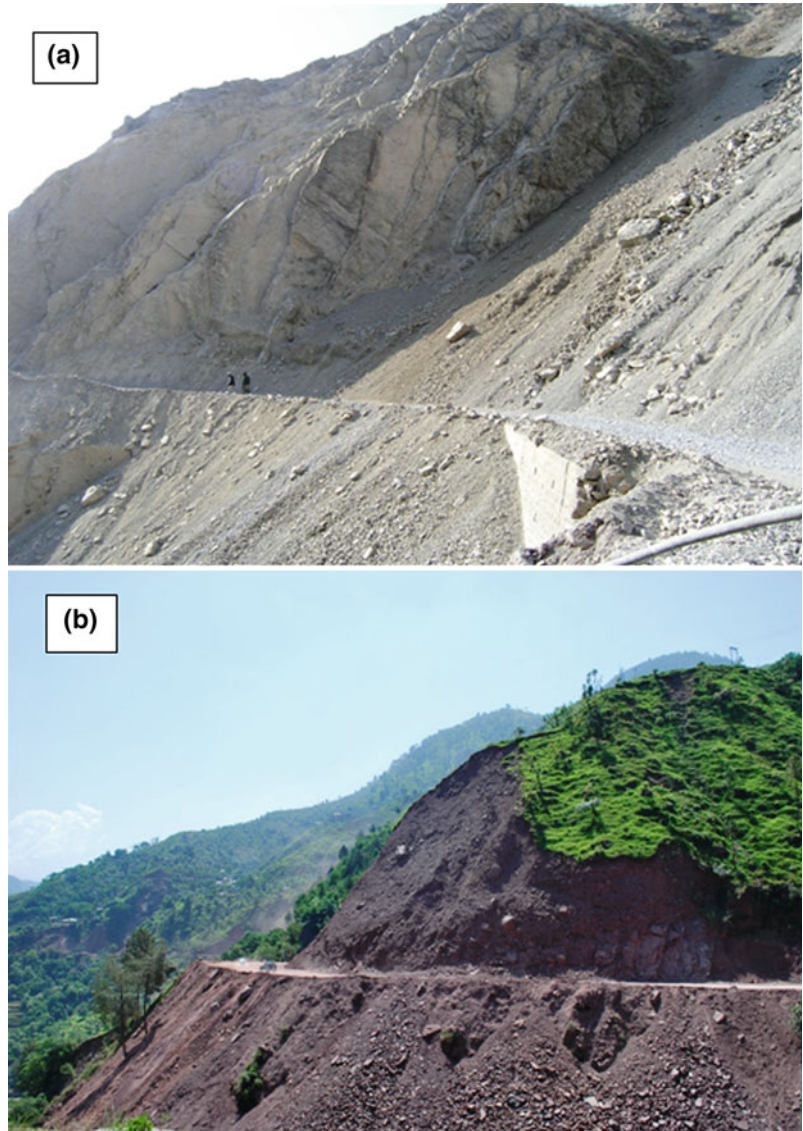
the geotechnical risk at the global scale. Because
of budgetary issues only the important slopes are
treated, leaving behind many vulnerable slopes.
Especially in the case of developing countries,
there is a need of an inexpensive as well as
reliable method, to deal with this problem.

In recent practice, many topographical stud-
ies were conducted, and hazard maps were
issued for the seismically disturbed areas. It is
noteworthy that the conventional approach relies
on topography and other empirical parameters,
which may not work well because change in the

property of geo-material cannot be incorporated.
Aerial photographs cannot represent the strength
of loosen soils and cracks visible through naked
eye; however, the slope failures can be cap-
tured. Borrelli et al. (2006) delimitated the
zones with different weathering conditions by
conducting the quantitative measurements of
weathering grade that included the analysis of
aerial photographs and index tests in the field.
Shang et al. (2004) estimated the weathering rate
to be 41.2–52.5 % of the volume loss per year in
Southeast of Tibet. Bhattarai et al. (2007)

reported that the physical weathering plays an important role to reduce the shear strength of mud rocks near the surface and in the ground water fluctuation zone. Kikuchi et al. (1986) related the slake durability index and content of montmorillonite to approximately evaluate the slope stability. Hachinohe et al. (1999) concluded that the mudstone withers faster than the sandstone by observing the needle penetration hardness, pore size distribution and mineralogical as well as change in chemical composition. The validity of existing hazard assessment methodologies concerning slope failures in Japan was comprehensively investigated by Mizuhashi et al. (2006) by using case histories of earthquake and rainfall-induced landslides. The studies concluded that the current risk assessment approach can be improved by incorporating the physical properties of soils with a focus on the effects of water on mechanical properties of soils. However, present research aims at the quick and economical technique of safety evaluation of weathered slopes that requires the elucidation of key parameter, i.e. shear strength.

In practice, the evaluation of in situ shear strength involves expansive and time-consuming techniques such as Vane-shear test, expansive boreholes and intrusive techniques such as pressure-meter tests. Many studies (Kawakami et al. 1983; Matsuoka and Liu 1998; Matsuoka et al. 2001; Liu and Matsuoka 2004) were conducted to determine the in situ shear strength by performing in situ shear tests. The key parameter controlling the slope disaster is in situ shear strength whose precise elucidation is vital for the risk assessment of slope failure.

The word "risk" covers a wide scope of social, economical, political and many other facts, so its full assessment is not possible, however in the sense of geotechnical engineering problems, risk is associated with the safety factor for any geotechnical structure during its life of operation. The weathering process influences the shear strength and threat a risk from the weathered slope to the infrastructure in the vicinity. In this sense, there is a need to estimate the shear strength by quick and economical technique, such as geophysical surveys.

1.1 Objectives

The present research was carried out for the evaluation of present safety of the jeopardizing slope and its correlation to the S-wave velocity measured at the slope surface. Following objectives were set for field studies;

1. Delineate the depth, S-wave velocity and shear strength of surface weathered layer from field experiments.
2. Propose a relationship between the factor of safety and shear wave velocity for practical application.

S-wave velocity can be measured on slopes to assess the corresponding safety factor. The continuous monitoring of S-wave velocity can warn of impending slope hazard and the overall scope of geotechnical risk assessment can be improved by the quick and economical assessment of safety by repeated (once a year) monitoring of S-wave velocity.

1.2 Methodology

The objective of field research is to elucidate the shear strength parameters and the geometry of surface weathered geo-materials for infinite stability analysis of weathered slopes and to relate it to the quickly and economically elucidated S-wave velocity. Field direct shear, portable dynamic cone penetration (PDCP) and seismic refraction tests were performed at each of the investigated sites (Figs. 95.2 and 95.3). The detailed description of the specification, procedures and data acquisition can be referred in Qureshi et al. 2009.

2 Test Results

The tests were performed on 11 sites in Japan and Pakistan (Fig. 95.3) to obtain the in situ shear strength, S-wave velocity and surface thickness of weather layer (Table 95.1). The profile of typical test results from the seismic refraction and portable dynamic cone penetration tests are presented in Fig. 95.4 which shows

(a) Investigated sites in Japan

(b) Investigated sites in Pakistan
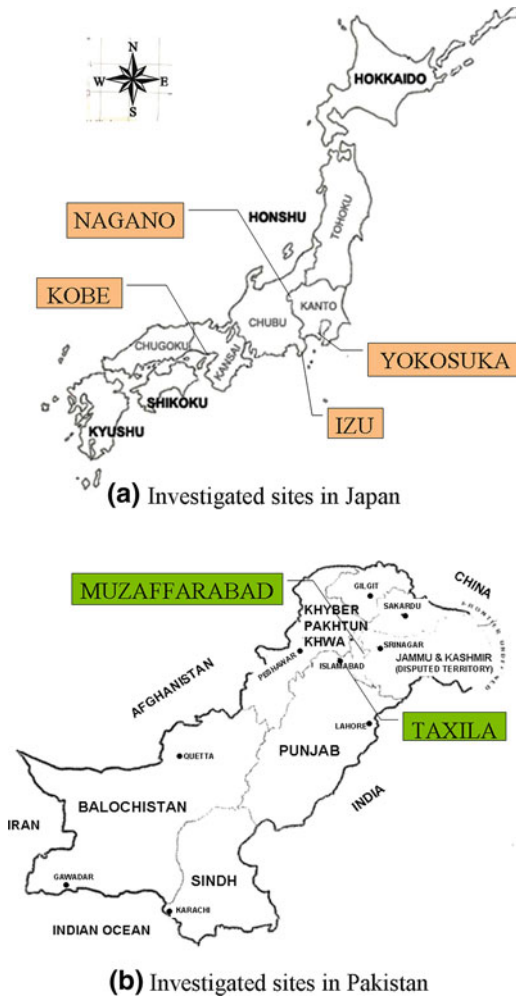
Fig. 95.2 Location map of field investigations

the delineated S-wave velocity of the weathered layer and its thickness along with the thickness elucidated by PDCP tests.

2.1 Depth of Surface Weathered Layer

The main aim of the present research is to promote a method which can estimate the mechanical properties and depth of surface layer quickly, economically and with a wide scope. One of the purposes of the combination of portable dynamic cone penetration tests and seismic refraction tests was to validate the depth calculated by seismic

refraction, whose reliability is still questionable in practice. So the depths of surface weathered layer on slopes calculated by seismic refraction (SR) and PDCP tests are compared in Fig. 95.5. It is interesting to note that the results somehow match up to a range of 2.5 m depth; however, 2 out of 3 results of deep extent differ by a fraction of 1–2 m. The interest of the authors is in shallow layers as represented by the 85 % of the test results, so the variation in depth measurement at a deeper extent is negligible.

2.2 Field Shear Strength

The direct shear tests were performed at five sites and the typical results of tests performed at the site of Muzaffarabad weathered mudstone is shown in Fig. 95.6. By utilizing the data obtained from the field direct shear tests performed at five sites, failure envelop was developed in Fig. 95.7. Linear curves were fitted on a set of 3 data points from each site to hit the ordinate which is apparent cohesion. It is interesting to note the presence of apparent cohesion in some of the investigated geo-materials. An exceptionally high value of internal friction angle was observed at Muzaffarabad limestone scree (63°). The high value of internal friction angle at the site of limestone scree in Muzaffarabad can be inferred to the big particle size and the cementation effects on the surface. However, in the case of silty clay high value of internal friction angle can be related to the fact that the roots of small grass have increased the shear resistance of soil near the surface. Moreover the highest value of cohesion was obtained in the silty clay tested at Taxila. By following the traditional approach, apparent cohesion is neglected and the angle of internal friction was considered as the representative of shear strength for such weathered surface layer whose stability is at potential risk during a heavy rainfall.

2.3 Correlating Shear Strength

In order to utilize the data of penetration N_d value for a given depth as the shear strength at

respective stress level, a suitable correlation is desired. After reviewing the literature (JGS 1433–1995), it was realized that in the case of loose-weathered geo-material a direct relationship which can correlate the N_d value with shear strength, does not exist. However, a relationship between SPT-N and the shear strength does exist. So, the author decided to correlate N_d with SPT-N first and then evaluate the shear strength from SPT-N value.

The correlation of N_d with SPT-N value is documented by JGS 1433–1995 and initially evaluated by Okubo (1971) suggests that, in the

case of mild slopes and plan ground, the SPT-N value relates to the portable dynamic cone penetration Nd in the form of following relation.

$$N_d = (1 \sim 3)N \tag{95.1}$$

So, the author decided to use the relation given by Okubo (1971) with its upper and lower bound limits. In the second step a suitable relationship has to be selected to correlate the SPT-N value with internal friction angle. Among the choice of relation between internal friction angle and SPT-N value, the relation given by Tanaka

Table 95.1 Lithologies and unit weights of geomaterials formed at the investigated sites

Sr. No.	γ_d (kN/m^3)	$\gamma_{sat} = \gamma_d(1 + e/G_s)$ (kN/m^3)	ID	Place	Type of geo-material
1.	18.2	21.8	YZ	Yokosuka, Japan	Sandy mudstone
2	19.5	23.4	MZDLS	Muzaffarabad, Pakistan	Limestone scree
3	16.8	20.2	MZDDS	Muzaffarabad, Pakistan	Dolomite scree
4	18.2	21.8	MZDWM	Muzaffarabad, Pakistan	Weathered mudstone
5	18.2	21.8	MZDWD	Muzaffarabad, Pakistan	Weathered dolomite
6	16.8	20.2	NGO	Nagano, Japan	Weathered sandstone
7	16.3	19.6	IZU	Izu, Japan	Volcanic ash
8	16.7	20.0	KOBE	Kobe, Japan	Weathered granite
9	16.7	20.0	TXLWL	Taxila, Pakistan	Weathered limestone
10	20.0	24.0	TXLLS	Taxila, Pakistan	Limestone scree
11	16.8	20.2	TXLSC	Taxila, Pakistan	Silty clay

Fig. 95.4 Seismic refraction profile along with the penetration test results on the weathered dolomite in Muzaffarabad, Pakistan
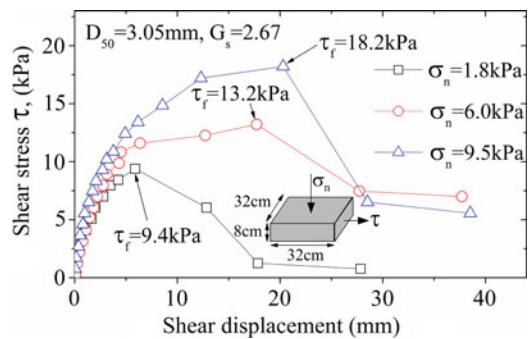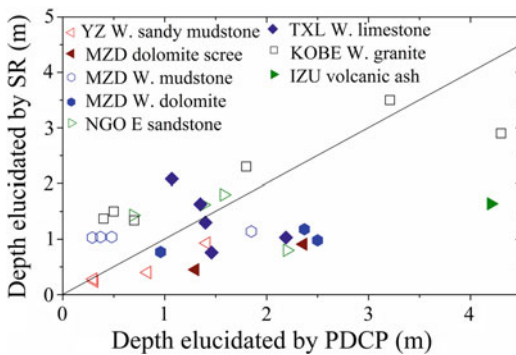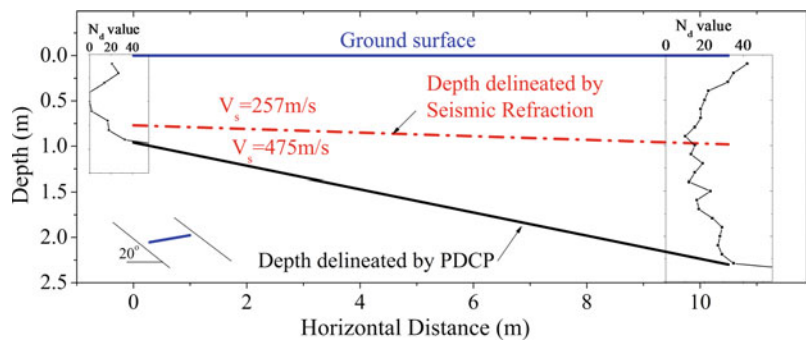
Fig. 95.5 Validation of the depth of surface weathered layer

Fig. 95.6 Field direct shear tests: Typical test results on weathered mudstone at Muzaffarabad, Pakistan

(1997) seems most relevant and also is a function of mean effective stress as well.

$$\phi = 25 + 31.2\left(\frac{N}{\sigma\prime + 68.65}\right)^{0.5} \quad (95.2)$$

where friction angle ϕ is measured in degree and σ' is the mean effective stress in kPa at any given depth for which the SPT-N value is selected. Equations 95.1 and 95.2 were used to calculate the internal friction angle from
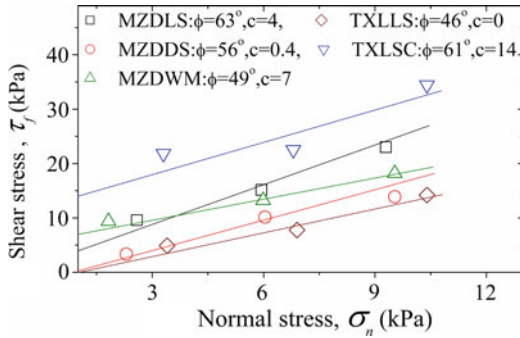
Fig. 95.7 Field direct shear tests: Failure envelop of investigated weathered geo-materials

Fig. 95.8 Plot between internal friction angle and S-wave velocity

portable dynamic cone penetration N_d value at a respective level of mean effective stress.

3 Data Analysis

3.1 Shear Strength and S-Wave Velocity

By using the Eqs. 95.1 and 95.2, internal friction angle is calculated for Nd values. Therefore, initially internal friction angle is plotted against the S-wave velocity in Fig. 95.8. The data-plot have two sets, one showing the upper and lower bound values of friction angle calculated by PDCP and the other group shows the internal friction angle calculated by field shear tests. The plot has a dispersion of data between the two groups. It is interesting to note that high friction angle values are reported by field shear tests performed at low effective stress levels which are even superseding the upper bound of internal friction angle values calculated by portable dynamic cone penetration. Shear strength is calculated by the relation $\sigma_n \tan\phi$ and plotted against the S-wave velocity in Fig. 95.9 to include the effects of effective stress in the ordinate of Fig. 95.8 which has reduced the scattering of data. The shear strength and S-wave velocity showed a general agreement with each other more sensibly in Fig. 95.9. The presented data is in the range of 2.4–29.6 kPa at the ordinate and 149–335 m/s on the abscissa,

Fig. 95.9 Plot between shear strength and S-wave velocity

which represents the general range of the mechanical properties of weathered geo-materials investigated at the sites.

4 Quick Assessment of Safety

An infinite slope is assumed which is covered with weathered layer (Fig. 95.10). The safety factors for dry and fully saturated cases were calculated at various slope angles and correlated to S-wave velocity. The direct values of the internal friction angle and S-wave velocity for the dry weathered geo-material are used here for the development of relationship between safety factor and S-wave velocity. The dry case represents the present situation in which the field investigations were conducted to obtain the
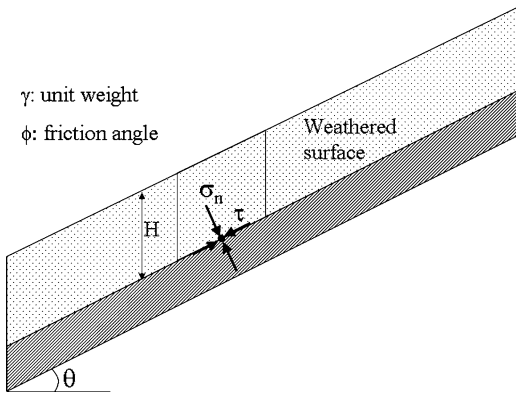
Fig. 95.10 Schematic illustration of infinite slope with surface weathered layer during dry season

Fig. 95.11 Schematic illustration of infinite slope with surface weathered layer during rainy season

shear strength parameters, S-wave velocity and the geometry of weathered slopes.

$$FOS(dry) = \frac{\tan \phi}{\tan \theta} \qquad (95.3)$$

Form Eq. 3, it is evident that in an infinite dry and cohesionless slope, FOS is independent of the thickness of surface weathered layer. The slope will remain stable as long as the internal friction angle ϕ remains higher than slope angle θ. By using the available data from the field shear tests and PDCP tests, FOS is calculated for the slope angles of 15, 30, 45 and 60°. For the delineation of internal friction angle ϕ from field shear or portable dynamic cone penetration tests for a particular slope angle, dry unit weight of the weathered geo-materials were used in calculating the normal stress levels. However this situation totally changes in the event of the rainfall which is dealt in the following wet case.

During rainfall, the surface of weathered slope gets saturated and jeopardizes the safety situation. To analyze such case, it is assumed that the weathered surface layer is fully saturated, with a streamline flow of seepage water and no excess pore water pressure is generated due to high permeability of the weathered geo-material (Fig. 95.11). FOS evaluated by infinite slope stability of weathered slope is given by Eq. 95.4.

$$FOS(wet) = \left(\frac{\gamma_{sat} - \gamma_w}{\gamma_{sat}}\right) \frac{\tan \phi}{\tan \theta} \qquad (95.4)$$

Fig. 95.12 Relationship between safety factor of infinite weathered slope and S-wave velocity at various slope angles

where ϕ is the friction angle of weathered layer, θ is the slope angle, γ_{sat} is the saturated unit weight of weathered geo-material and γ_w is the unit weight of water. The shear strength parameter ϕ is provided from the field test results and FOS is calculated for the slope angles of 15, 30, 45 and 60°. The relationship between the FOS and S-wave velocity for all the cases of slope angle is shown in Fig. 95.12. In the traditional practice safe slope is required to have a safety factor greater than unity. It is interesting to note that a considerably flat slope is stable, with a weathered geo-material of very low S-wave velocity, and vice versa. A decrease in FOS is rational with the increase of slope angle in the relationship of FOS with the measured S-wave velocity.
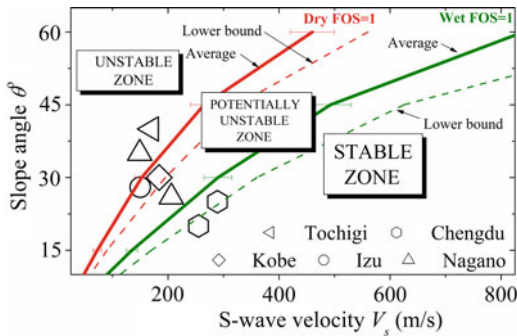
Fig. 95.13 Safety assessment matrix

4.1 Safety Assessment Matrix

The relationship between safety factor and S-wave velocity based on the infinite slope stability on weathered slopes is shown in Fig. 95.12. It is interesting to note that, for a particular slope angle there is twice the difference in the FOS for dry and wet cases for a given value of S-wave velocity of surface weathered layer measured in dry condition. Here is the need to select the suitable value of S-wave velocity and slope angle which can serve as a threshold between the safe or unstable weathered slope. With the aim to assess the safety of the weathered slope, only by measuring the S-wave velocity and slope angle at the site, Fig. 95.13 is extracted from Fig. 95.12 by picking up the values of slope angle and S-wave velocity for both dry and wet cases at a safety factor equal to unity. In the "Safety Assessment Matrix" (Fig. 95.13) the curves of dry and wet safety factors divided the safety in three zones, i.e. stable, potentially unstable and unstable zones, provided that the infinite slopes with shallow surface weathered layers is an assumption. So in the future, the risk of weathered slopes is aimed to be assessed only by measuring the slope angle and the S-wave velocity.

Stable zone means the weathered slope will remain stable both in dry and rainy season, potentially unstable zone indicates that the slope is stable during the dry season however potential hazards are imminent during the rainfall and the unstable zone engrosses the slopes with hazardous situation even in dry season and minor

disturbance, either human-induced or natural can trigger the slope failure. It is recommended to monitor those parameters periodically (annually) to warn the future risk from weathered slopes. Moreover the continuous monitoring of change in S-wave velocity can assess the time of future instability.

4.2 Practical Implementation of SAM

During the recent field investigations, S-wave velocity and slopes angles were measured at the site of slopes. For example, at the site of Nagano weathered sandstone which was under the monitoring of possible movement, measured S-wave velocity was 149 m/s at a slope angle of 35° which lies in unstable zone of SAM (Fig. 95.13). At another slope of weathered pumice which was failed by March 11, 2011, East Japan Earthquake (M. 9.0) at Tochigi, Japan, measured S-wave velocity and slope angle values lies in unstable zone. During an experiment of artificially reproduced rainfall induced slope failure on weathered slopes in Chengdu, China, the S-wave velocity and slope angles were measured, and their plot appear in the stable zone of Fig. 95.13. Later it was discovered that the slope did not fail as expected due to the artificial rainfall. With those cases a confidence is gained on the slope stability assessment in the practical implementation of "Safety Assessment Matrix".

5 Conclusions

In a general sense, risk assessment has a wide scope whose delineation involves many factors. However, in the present research risk is assessed from the weathered slopes by infinite slope stability analysis of dry and fully saturated cases. Infinite stability analysis of weathered slopes indicated that, during torrential rains factor of safety reduced to half of its value during the dry season. By the delineation of S-wave velocity of

surface weathered layer in the dry condition of a particular slope, safety is assessed for the extreme scenario of rainy season, by using the relationship between FOS and S-wave velocity. Moreover, with the measurement of slope angle and S-wave velocity on weathered slope, the level of safety is assessable by "SAM" which differentiates the geotechnical risk in three zones i.e. stable, potentially unstable and unstable. It is recommended that the periodic measurements of S-wave velocity should be conducted to warn any future instability which is the quickest and the most economical method to address the risk assessment of weathered slopes.

References

Aziz M, Qureshi MU, Towhata I, Yamada S, Saleem M (2009) "Geotechnical properties of weathered slopes in Muzaffarabad area after the 2005 Kashmir earthquake". J Harbin Inst Technol 16(S1):6–11

Bhattarai P, Marui H, Tiwari B, Watanabe N, Tuladhar GR (2007) Depth-wise variation of physical and mechanical properties of mudstone in relation to weathering-cases in several landslides in Niigata prefecture. Lanslides J Jpn Landslide Soc 44:79–89

Borrelli L, Greco R, Gulla G (2006) Weathering grade of rock masses as a predisposing factor to slope instabilities: reconnaissance and control procedures. Geomorphology 87:158–175

Hachinohe S, Hiraki N, Suzuki T (1999) Rates of weathering and temporal changes in strength of bedrock of marine terraces in Boso Peninsula. Jpn Eng Geol 55:29–43

JGS 1433–1995 (1995) Method of portable dynamic cone penetration test (in Japanese)

Kausar AB, Sadiq S, Alam A, Awais M, Ahmed Z (2009) 2005 Kashmir earthquake triggered major landslide problems in Muzaffarabad District, AJK and Mansehra, NWFP, Pakistan, Proceedings of symposium on mechanisms of large landslides, landslide society of Japan, pp 3–20

Kawakami H, Endou K, Saitou Y, Abe H (1983) The in situ direct shear test on gravely soils in a slope. Soils Found 31(2):27–31 In Japanese

Kikuchi K, Mimuro T, Susuki M (1986) Slake durability of rocks and its relation to slope instability, Proceedings of international symposium engineering in complex rock formations, Beijing, pp 3–7 Nov, 415–421

Liu SH, Matsuoka H (2004) Large-scale in situ direct shear test in Chinese dam construction field, Proceeding of 39th Japan national conference on geotechnical engineering, paper No. 272, D-06, pp 543–544

Matsuoka H, Liu SH, Sun D, Nishikata U (2001) A new in situ direct shear testing method for rockfill materials, sands and clays, Proceedings of XVth international conference of soil mechanics and geotechnical engineering, Istanbul, Turkey

Matsuoka H, Liu SH (1998) Simplified direct box shear test on granular materials and its application to rockfill materials. Soils Found 38(4):275–284

Mizuhashi M, Towhata I, Sato J, Tsujimura T (2006) Examination of slope hazard assessment by using case studies of earthquake- and rainfall-induced landslides. Soils Found 46(6):843–853

Okada K, Sugiyama T, Noguchi T, Moraishi H (1992) A correlation of soil strength between different sounding tests on embankment surface, Monthly magazine of Japanese geotechnical society, April 1992, 11–16, In Japanese

Okubo S (1971) Sub-surface investigation with cone penetration equipment: performance and testing of machine, reference of civil engineering technology, In Japanese

Qureshi MU, Towhata I, Yamada S, Aziz M, Kazmi AZ (2009) In situ direct shear tests on weathered rock materials for slope failure risk assessment, Proceedings of the international joint symposium on geodisaster prevention and geoenvironment in Asia (JS-Fukuoka 2009). Fukuoka, Japan, pp 84–89

Shang YJ, Park HD, Yang ZF, Zhang LQ (2004) Debris formation due to weathering, avalanching and rock falling, landsliding in Se Tibet, SINOROCK2004 symposium. Int J Rock Mech Min Sci 41(3), Paper 3B 12, CD-ROM © Elsevier Ltd

Tanaka H (1997) Approach and utilization cases of N-value-Harbour Structures, Kisoko Publications, In Japanese

Experimental and Analytical Studies of Landslides in the South of Ukraine Under the Action of Natural Seismic Impacts

96

O. M. Trofymchuk, I. I. Kaliukh, H. S. Hlebchuk and V. P. Berchun

Abstract

Activation of seismic activity in Vrancha area and in the Black Sea region as well as on the Planet as a whole lead to rising of the level of seismic hazard all over the territory of Ukraine and eventually to the growth of the corresponding landslide provoking factor. These events resulted in considerable activation of landsliding and in increasing of landslide hazard in earthquake-prone areas of Ukraine (Chernivetska and Odesska Oblasts/regions and Autonomous Republic of Crimea). Totally about 23 000 landslides were identified in the territory of Ukraine. Experimental and analytical studies of slumps in the Central Livadia landslide system *(natural seismic impacts)* were carried out with the aid of the *ZSUV* monitoring system. Theoretical and methodological principles for monitoring and experimental researches of landslides were developed. A provision was made for the use of an automated system of collection and accumulation of initial statistical information for analysis of fast changing factors. Measured were: ground water levels in boreholes determined by geologists, angles of slope of marked elements (determined by experts) inside the landslide slope being studied (angular deformations of the measuring boreholes drilled in the slope); other parameters characterizing the stress-deformed state and lithodynamics of the area being studied.

O. M. Trofymchuk (✉) · I. I. Kaliukh ·
H. S. Hlebchuk · V. P. Berchun
Institute of Telecommunications and Global
Information Space of National Academy of Sciences
of Ukraine, 13, Chokolivsky Blvd,
Kyiv 03186, Ukraine
e-mail: itelua@kv.ukrtel.net

I. I. Kaliukh
e-mail: kalyukh2002@yahoo.com

H. S. Hlebchuk
e-mail: glebchuk@i.ua

V. P. Berchun
e-mail: berchun2003@yahoo.com

1   Introduction

More than 90 % of the territory of Ukraine has complex ground conditions therefore unpredictable changes of natural geological and man-made factors governing ground conditions, may lead to dangerous deformation processes resulting in accidents and disasters. Among them, landslides are the first by the amount of the inflicted damage in Ukraine and the second only to earthquakes in the world. About 120,000 sq. km of the Ukrainian territory populated by almost 11 million people are located in the zone that has seismicity of natural origin with a magnitude varying from 6 to 9 (Kolisnichenko 2001) which requires additional protection measures. Activation of seismic activity in the Vrancha area and in the Black Sea region as well as on the Planet as a whole lead to rising of the level of seismic hazard all over the territory of Ukraine and eventually to the growth of the corresponding landslide provoking factor. These events resulted in considerable activation of landsliding and in increasing of landslide hazard in earthquake-prone areas of Ukraine (Chernivetska and Odesska Oblasts/regions and Autonomous Republic of Crimea). Totally about 23,000 landslides were identified in the territory of Ukraine (Ginzburg and Shvets 1999; Babich and Sedin 2010; Shuster 1981; Grishin and Snisarenko 2008; Svets 2001; Bileush 2009; Demchishin 1992). By the size of damage the landslides that occur on slopes of various inclinations (gradients) extend most often from 5–100 to 200–300 m laterally and from 15 to 200 m downdip and sometimes even more. The volumes of large landslides may amount to hundreds of thousands cubic meters of rocks (Shuster 1981; Bileush 2009; Demchishin 1992).

Natural slopes as well as earthwork structures which are located in the areas affected by the impact of earthquakes or by long-repeated vibrations caused by manmade sources require examination with regard to potential occurrence of destructive gravitational processes—landslides, landfalls, mudflows, and creeping. The analysis of macroseismic occurrences inside bodies of rocks adjacent to slopes, study of earthquake effect on the elements of relief provide a way to identify characteristic features of development of seismic deformations and seismic dislocations which occur in the slopes. Outgoing of seismic waves from the earthquake epicentre and their passage through various rock beds are accompanied by occurrences of diffractions, interferences, changes in the velocity of waves passage, and changes in the amplitude of vibrations. The most dangerous for structures are accelerations that occur in the rocks of beds. The effects of tremors on earth caused by bodies of rocks adjacent to slopes are intensified by the impact of the stress condition due to high incidences of slopes, presence of weakened zones and cracks. The amplitude and spectral content of vibrations are substantially influenced by geometrical parameters of slopes, their orientations relative to the directions of wave propagation, presence of projections, hollows, and benches on the slopes. The researches showed that in case of a lateral approach of impulses the resulting wave field on the opposite slopes of valleys (walls of canyons) is not a symmetrical one. The most sensitive to tremors are the upper parts of slopes in the presence of balmstones and the landslide deluvial deposits on slopes.

2   Earthquake Effect on Slopes

In areas with seismicity of magnitude exceeding 6 calculation of stability of slopes are made with due consideration of the seismic force. When doing so it is the most unfavourable direction of the force which is taken into account (Shvets et al. 1987; Sinitsyn 1982). The resultant force R of the gravity force P and the seismic force Q will be equal to:

$$R = \sqrt{Q^2 + P^2} \qquad (1)$$

Table 96.1 The earthquake effect on slopes

Magnitude according to MSK scale	Maximum acceleration MS^{-2}	Character of deformations and dislocations of slopes. Surface changes.	Dynamic seismic coefficient, μ	Relative increase of angle of slope ($\Delta\alpha$)
5	0,1–0,2	Rare landslide occurrences	0,01–0,02	1,0
6	0,2–0,3	Separate occurrences of landslides/slipouts	0,02–0,03	1,5
7	0,3–0,6	Landslides on steep slopes	0,03–0,06	2,0
8	0,6–1,0	Landslides of loose ground on medium steep slopes	0,06–0,10	3,0
9	1,0–2,0	Landslides and rockfalls on rock slopes	0,10–0,20	6,0
10	2,0–4,0	Substantial landslides on slopes of river valleys. Flowing sand and clay soil. Fountains on the valley slopes.	0,20–0,40	15,0
11	4,0–8,0	Landfalls and landslides on all slopes	0,40–0,80	30,0
12	≥ 8	Substantial reconstruction of landscape	$\geq 0,80$	≥ 30

$$Q = am = \mu P \qquad (2)$$

where m—the mass that experiences the action of the seismic wave acceleration; a—the magnitude of the seismic acceleration which is determined from the data given in Table 96.1 (Shvets et al. 1987; Sinitsyn 1982); μ—the dynamic seismic coefficient which is determined as the ratio of the earthquake acceleration a to the gravity force acceleration g.

3   Coastal Area of the Southern Crimea Affected by Landslides

Special consideration should be given to the condition of the landslide hazard areas in the Crimea. Lately considerable changes have taken place in the natural environment along the coast. The changes are mainly associated with intensive business activities which resulted in depletion of the fine natural beach material, washing away of depositional features, as well as in intensive development of landslide processes.

The coastal area of the Southern Crimea affected by landslides (Fig. 96.1) amounts to 30 %.

The growing number of landslides occurs mainly due to technogenic and natural technogenic causes with the latter occurring less frequently. As a result of technogenic causes alone about 600 technogenic landslides occurred in the entire Crimea and were registered in the Land Cadastre with the total number of landslides in the Crimea being 1,576 as of the end of 2009, that is about 38 % landslides are of technogenic origin. Landslide activation is associated with the periods of intensive fallouts on slopes as well as with technogenic activities (undercutting, weighing down, and watering of slopes with technogenic waters). The landslide activation had a catastrophic character during the winter-spring season 1996–1997 (anomalous period regarding the amount of atmospheric fallouts). Considerable damage was caused to highways and access roads along the entire Southern Coast of the Crimea (Fig. 96.2.).

It is well known that delayed construction of landslide and coastal shore protection structures leads not only to increase of expenses because of progressive character of landslide and abrasive processes but also to irretrievable losses of historical and architectural monuments (Fig. 96.3), to destruction of already existing expensive hydraulic engineering and landslide protection structures and also to residential buildings.

The above dictates the necessity to study the interaction of the natural environment and the engineering protection structures within the area

Fig. 96.1 Location of major landslides in the coastal area of the Southern Crimea
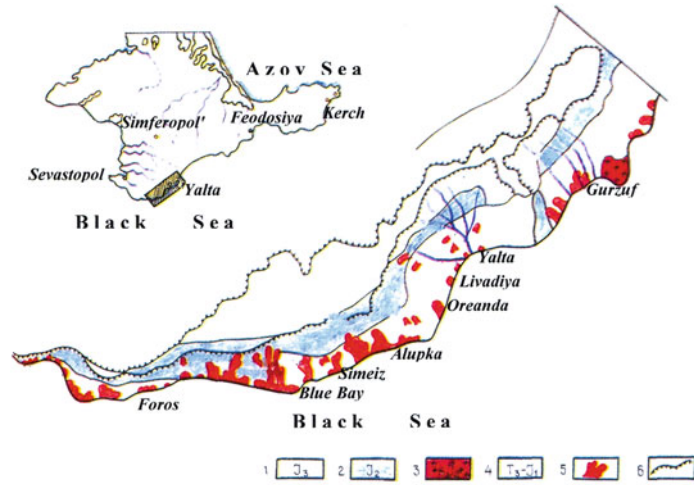
1 – Upper Jurassic carbonate rocks. 2 - Middle Jurassic rocks (claystones/argillites/, siltstones/aleurolites, sandstones). 3 - Middle Jurassic igneous/magmatic rocks. 4 –Tavria rocks (dislocated argillites, siltstones/aleurolites, sandstones). 5 – Major landslides. 6 – The edge of the Yailin cliff.

Fig. 96.2 Road to New Oreanda, Great Yalta, 2006

Fig. 96.3 Destroyed rotunda at the territory of the Livadia Palace and Park Complex, 2002

of the "dry land—sea" contact in the context of the most effective use of recreational and economic potential of the Crimea in the process of construction and implementation of measures regarding its engineering protection.

4 Computer System for Monitoring the Central Livadia Landslide System (*ZSUV* Program)

Objective information about destruction of structural elements of buildings and structures can be obtained by using nondestructive testing methods owing to high precision measurement of changes of their spatial position and of natural-vibration frequencies in the process of exploitation. One of the basic components of the equipment which was developed for solving problems of diagnosing the Central Livadia Landslide System (CLLS/ЦЛЗС) is the meter of slope angles and vibrations in which precision navigational accelerometers are used. The complex of instrumentation intended for formation and computer registering of the information about angles of deviation from the vertical of a place (horizontal plane) and about vibrations (linear accelerated ones) relative to two orthogonal directions of the load bearing

Fig. 96.4 ZSUV program
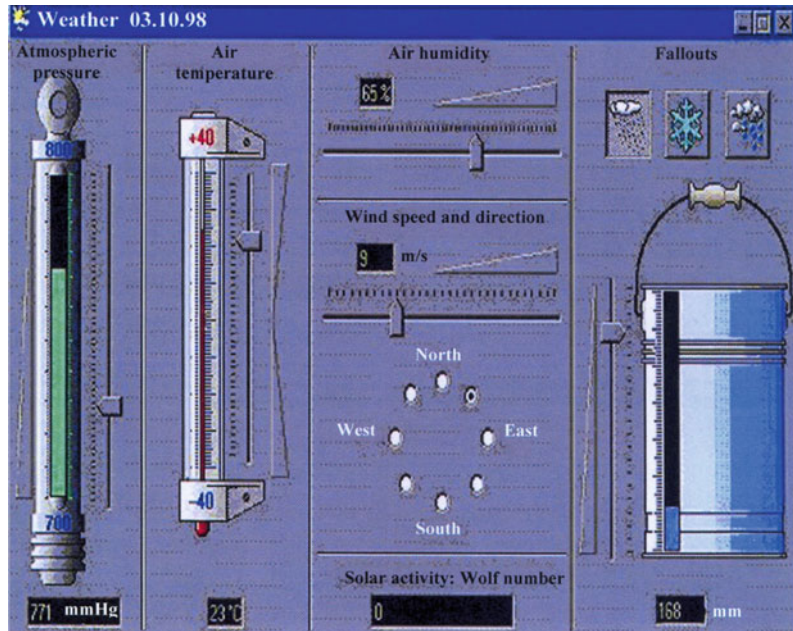
structures of the Livadia Palace was installed in 2002. The particular feature of the site under control consists in the fact that this historical and architectural complex is located in the zone of the active existing landslide. The boundaries of the present-day CLLS (Central Livadia Landslide System) are located in such a way that they envelope the southeastern part of the Livadia Palace and the lower steep part of the park zone. The long-term observations of the Livadia Palace have shown that landslide development resulted in deformation of the load bearing structures and formation of a great number of cracks. This trend of events may eventually lead to destruction of the Palace.

The instrumentation complex was designed according to the modular principle with the use of precision sensors of initial information, modern processing equipment and ADC (analog-to-digital converters), computers with realized optimal algorithms of digital processing of information. The complex operates on a real time basis. It allows maintaining control and carrying out diagnosis without disturbing normal functioning of the Livadia Palace and reception of sightseers and visitors. Experimental investigations were carried out with the aim of verifying compliance of the monitoring and recording equipment to the

basic requirements made to the equipment which was designed for monitoring landslide hazard processes.

For a real-time diagnosis of the lithodynamic condition an algorithm was developed and a computer system for monitoring the Central Livadia Landslide System (*ZSUV* program) was realized together with a real-time maintenance of the data base of geliogenic and lithogenic parameters of the Central Livadia Landslide System (CLLS), and manual updating of data by a high level programming language MS Visual Basic with the use of the function library wl1293g_.dll for controlling operation of the ADC et al. (2000). Together with the ADC the real-time program allows monitoring of the level of ground waters and of the deformation angles of landslide bodies; recording of the seismic activity, statistical processing of the obtained data, archiving of the obtained data and statistical processing results. The correlation dependence of the seismic activity of CLLS on the solar activity is analyzed by means of maintaining a data base of the geliogenic and lithogenic parameters. In this case the data are entered in the computer manually with the aid of the *ZSUV* program (Fig. 96.4.) because study of these processes does not require any automated system for gathering

Fig. 96.5 Analogue of
GIS of the ZSUV program

and accumulation of initial information (the solar
cycle of activity increase and decline has a period
of 11 years). The geliogenic parameters cover the
solar activity, changes of temperature and
humidity conditions, the character and intensity
of fallouts, wind, etc.

The lithogenic parameters—a complex of
conditions and factors characterizing the mech-
anism and dynamics of changes in the balanced
state of the CLLS slopes. Monitoring of dis-
placement of reference points of CLLS is exer-
cised by means of visual observations of the
landslide surface and subsequent manual entry
of data into computer with the aid of a specially
realized analogue of GIS (Fig. 96.5.) of the
ZSUV program (ADC et al. 2000).

Continuous real-time monitoring (Fig. 96.6.)
is exercised by means of the ZSUV program
according to the following sequence: recording
of the evolution of changes in the angle of
deviation of marked places and zones inside the
landslide body with the help of high-precision
electrical inclinometer sensors; filtration of
electrical signals after conversion of analogue
signals into digital codes with the aid of ADC,
and finally, real-time entry of digitized experi-
mental data into a computer.

With the aim of increasing reliability and
performance properties of equipment the open
architecture was used for building the hardware-
software system in the form of separate external
modules: high precision sensors of angle dis-
placements (movements), ADC, analogue filters
of lower frequencies, the power block, the
computer equipped with the WINDOWS oper-
ating system.

The south-eastern part of the Livadia Palace
was selected as a place for installation of the meter
of inclination angles and vibrations because it is
more subjected to landslides. The meter was
installed on the marble window sill outside the
corner room (Fig. 96.7) on the first floor (second
storey) of the building. The sensor was fixed to the
square base of the marble column with the help of
a clasping device. The firm adherence of the
sensor to the window sill and to the base is ensured
by the clasping device. At the place of installation
the meter is oriented along the longitudinal and
the transverse axes of the Livadia Palace. The
façade part of the Livadia Palace (from the
direction of Yalta city) was taken as the longitu-
dinal axis. The cable approximately 25 m long
was laid along the façade cornice of the Livadia
Palace. The signals about the angular location and

vibrations of the load-bearing structures of the
Livadia Palace are formed in the accelerometer
sensors installed in two mutually perpendicular
directions. The signals are created in the form of
alternating voltage proportional to the vibration
amplitude and frequency.

During the period from mid-December 2001
to December 2002 the vibrations of the Livadia
Palace (Fig. 96.8) caused by the action of

seismic impacts were measured with the use of
the BKП-2 M meter. The spatial position was
determined by measuring the inclination angle
of the building façade.

The results of the carried out monitoring
experimental examinations of dynamic charac-
teristics of the CLLS and Livadia Palace soils
were used as a base for calculation of the stress
state of a number of CLLS landslides (Polevet-
sky et al. 2005). In doing so the relevant geo-
detic and engineering- geological materials of
the CLLS structure provided by the CSTE "In-
zhzahyst" (Central Scientific and Technical
Enterprize "Engineering Protection") of Yalta
city were used as a basis for construction of
vertical sections of CLLS along with the use of
the dynamic characteristics of CLLS obtained in
the process of monitoring. Figure 96.9 sche-
matically shows one of the vertical sections of
CLLS including the Livadia Palace. From
Fig. 96.9 it follows that the CLLS landslide
system has a complex structure composed of a
number of separate landslides developing on the
surface which are located vertically above and
below in the cross-section.

On the basis of the experimental data of the
CSTE "Inzhzahyst" (Central Scientific and Tech-
nical Enterprize "Engineering Protection") it was
also found that the thickness of soils of separate
sections of the CLLS that were shifting downwards

Vibrations recorded during the Livadia Palace monitoring on the 1 channel of ADC during the period from 17.05.2002 to 13.09.2002 (part from 1 Hz to 10 Hz).
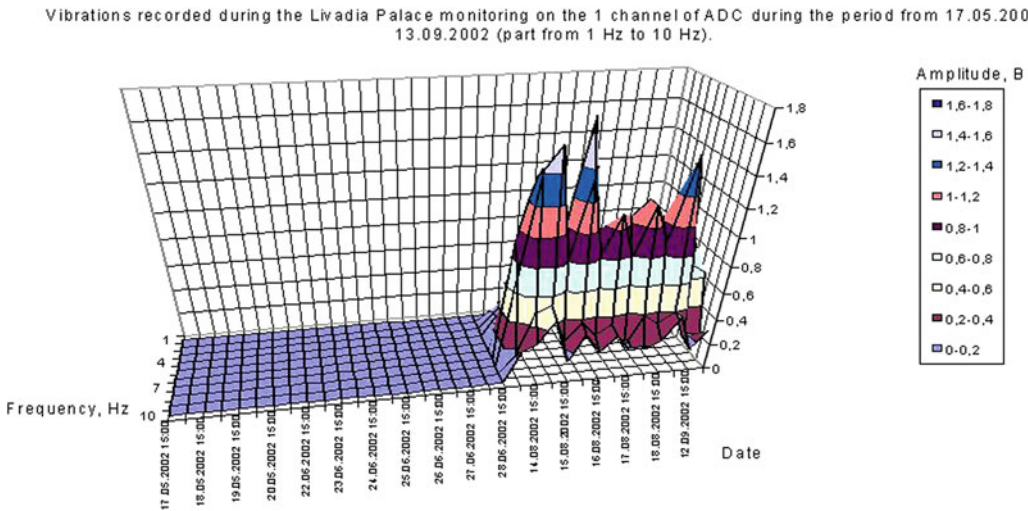
Fig. 96.8 The fragment of the instant information obtained from one of the numerous channels of high-precision sensors in 2002 during monitoring of the structural elements of the Livadia Palace

Fig. 96.9 Vertical section of the CLLS including the Livadia Palace
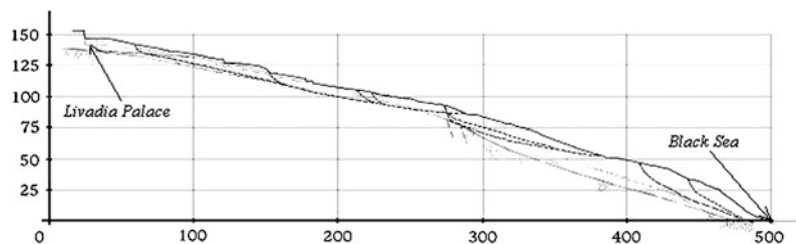
along the slope was as much as 10–15 m. On the one hand all this considerably complicates the task of correct mathematical modeling of the stress state of the CLLS, and on the other hand it strongly necessitates preliminary calculations of the CLLS on the basis of available simplified models for the purpose of identification of its lithodynamic mechanism. A landslide section 145 m long horizontally below the Livadia Palace was chosen for mathematical modeling taking into consideration the highest hazard to the structural elements of the Palace represented by soil displacements at this section. There is an underground sewage gallery in this section which was "cut up" by landslide displacements of the soil. It had been precisely the source of watering of the CLLS slope lying below the Palace up to the beginning of 2000th.

Three variants were considered: the landslide slope without the Livadia Palace and underground waters; the landslide slope with the

Livadia Palace but without underground waters; and the landslide slope with the Livadia Palace and underground waters one of the sources of which being the water income from the underground sewage gallery of the Livadia Palace. The analysis of the preliminary calculations based on the models of Maslov-Berer-Shakhunyants showed that in the first case the stability coefficient of the modeled landslide slope of the CLLS was 1.21, in the second case—1.30, and in the third case—0.87.

5   Conclusions

1. The theoretical and methodological principles were developed for monitoring experimental examination of the CLLS slopes. The fast changing factors were analyzed with the use of an automated system for gathering and

accumulation of initial statistical information. For a real-time diagnosis of the lithodynamic condition an algorithm was developed and a computer system for monitoring of the CLLS (*ZSUV* program) was realized along with a real-time maintenance of the data base of geliogenic and lithogenic parameters of the CLLS, and manual updating of data by a high level programming language MS Visual Basic with the use of the function library wl1293g_.dll for controlling operation of the (ADC et al. 2000).Together with the ADC the real-time *ZSUV* program allows monitoring of ground waters levels and deformation angles of landslide bodies; recording of the seismic activity, statistical processing of the obtained data, archiving of the obtained data and statistical processing results. Also measured were ground water levels in the wells defined by geologists; inclination angles of elements (defined by experts) inside the water hazard landslide slope under study (angle deformations of the measuring wells drilled in the slope); other parameters characterizing the stress-deformed state and the lithodynamics of the area under study.

2. The dynamic loads experienced by geological bodies in the wave fields during natural and technogenic earthquakes as well as during vibrations generated by operating mechanisms and transportation produce changes in physical and mechanical properties of soils and of the character of geological processes which define for the most part the changes of engineering and geological conditions of various sections. These changes occur either instantly (during the time of seismic waves passing) or with the due course of time after the waves damp out. Under the action of seismic waves the bearing capacity of soils in the bases of structures reduces sometimes to a critical level. This results in gravitational deformations and soil dislocations on the slopes. Severe earthquakes with the magnitude of more than 6 according to MSK scale are not infrequently the cause of landslides along the slopes where favourable conditions were created for such a process—available

amounts of movable material, sufficient height and steepness of the slope, earth overwatering and overloading, development of weakened surfaces and zones, loosened rocks and cracks.

3. The postdynamic deformations of slopes appear as a result of certain changes occurring in the rock body adjacent to the slope during passage of seismic waves. These changes eventually lead to development of weakened zones, accumulation of rock masses which can be engaged by landslides. Such cases most often cause disruption of the hydrogeological condition of the water-bearing horizons which are drained in the slopes, and destruction of regular filtration ways of ground waters. As a consequence the level of ground waters rises and the hydrostatic and hydrodynamic pressures increase.

4. It was found that the south eastern wing of the Livadia Palace executes continuous vibratory motions relative to a certain mid-position. These vibrations are obviously of a regular character. The amplitude of daily vibrations changes within 1.5 angular minutes, that is, about 45 angular seconds in each direction from the mid-position. The vibrations occur relative to the transverse axis of the building. Experimentally the seismicity coefficient of the Central Livadia Landslide System was defined more accurately—$\mu = 0.25$.

5. In some cases, such as, for example, on February 13–14 and 26–27, and March 22–23, 2002, abrupt increases of the angle of building inclinations were recorded. In these cases the amplitude increased up to 6 angular minutes. The calculations showed that usual daily vibratory motions were in the range of 1, 9 mm to each side from the mid-position while during the days mentioned in p.4 the vibratory motions were about 4, 2 mm to each side from the mid-position. The daily vibrations of the Livadia Palace can be primarily caused by differences between day and night temperatures due to warming and cooling of the building and the surrounding area. If the access of unauthorized persons to the ВКП-2 M meter is excluded then the

following factors and circumstances can cause an abrupt increase of the amplitude of deviation of the Livadia Palace façade from the mid-position: considerable amount of fallouts and associated rise of the ground water level, activation of the CLLS, local earthquakes, and other factors.

6. The mathematical modelling of the landslide activity of the CLLS showed that ground waters, which are one of the causes of landslide slope watering by inflow from the Livadia Palace through the sewage gallery, present a catastrophic hazard to both the Livadia Palace and the landslide slope located below. A substantial change of the landslide pressure is observed along the slope leading in the long run to the value of the stability coefficient much lower than the initial one ($\sim$ by 30 %). The risk of slope destruction is equal to 1. The stable slope gradually transforms into an unstable one. All this is supported by monitoring observations of the CLLS, the landslide shifts are correlated with the periods of active functioning of hydropathic establishments of "Livadia" and "Prykordonnyk" sanatoria located on the slope above the Livadia Palace.

References

Kolisnichenko Y.Y. (2001) Certain aspects of natural technogenic safety of Ukraine and the major directions to raise its level. Proceedings of the international workshop "Elements hazard—2001". pp 5–8

Ginzburg LK, Shvets VB (1999) The collapse of the slope in the residential microdistrict. Soil Mech Found Eng 3:28–30

Babich FV, Sedin VL (2010) Analysis of the collapse of the built-over slope (1971–2010). Collect Sci Pap 3(28):21–25

Shuster R, Kryzek R (eds.) (1981) Landslides. study and strengthening. Moscow Mir, 368 p

Grishin VA, Snisarenko VI (2008) Odessa slopes and landslides. Kyiv small business enterprise "Lessya", 300 p

Svets VB (2001) Ensuring stability of structures on landslide slopes composed of loess soils. Soil Mech Found Eng 6:11–15

Bileush AI (2009) Landslides and landslide protection measures. Kyiv Naukova Dumka, 330 p

Demchishin MG (1992) Present-day dynamics of slopes in the territory of Ukraine. Kyiv Naukova Dumka, 254 p

Shvets VB, Ginzburg LK, Goldstein VM et al. (1987) Reference book on soil mechanics and dynamics. Kyiv Budivelnyk, 232 p

Sinitsyn AP (1982) Assessment of stability of slopes and declivities during severe earthquakes. Probl Seismol 22:111–120

Kaliukh II, Dudarenko OO, Kaliukh TY et al. (2000) Modern information and analytical systems for providing support to making decisions of ensuring steady development of territories. Scientific-Methodical Manual. Kyiv Society "Znannia", 32 p

Polevetsky VV, Kaliukh TY, Ryzhiy MN et al. (2005) Analysis of stability of the landslide slope below the Livadia palace during watering. building structures. 63:248–256

Landslide Dam and Post-Earthquake Phenomena

Rainfall Patterns of Post-seismic Debris Flows in the Wenchuan Earthquake Area

97

Wei Zhou, Chuan Tang and Chun-hua Zhou

Abstract

Several giant debris flows occurred in southwestern China after the Wenchuan Earthquake, causing serious casualties and economic losses. Debris flows were frequently triggered after the earthquake. A relatively accurate prediction of these post-seismic debris flows can help to reduce the consequent damages. Existing debris flow prediction is almost based on the study of the relationship between occurrence of post-earthquake debris flows and cumulative rainfall. The authors collected rainfall data associated with the occurrence of representative debris flows in the Wenchuan Earthquake area and analyzed the rainfall data and obtained rainfall patterns of rainfall-induced debris flows in the Wenchuan Earthquake area. The critical rainfall patterns related to debris flows in the Wenchuan Earthquake area can be divided into three categories: (1) a rapid triggering response pattern, (2) an intermediate triggering response pattern and (3) a slow triggering response pattern. The difference among the three triggering patterns is the antecedent rainfall duration and intensity. These critical rainfall patterns influence soil mass failure and debris flow initiation significantly.

1 Introduction

Several giant debris flows occurred in southwestern China after the Wenchuan Earthquake, causing serious casualties and economic losses. Debris flows were frequently triggered after the earthquake. These post-earthquake disasters will still last for 5–10 years (Tang et al. 2009), or may last for 10–30 years (Cui et al. 2008; Xie et al. 2009).

W. Zhou (✉) · C. Tang
State Key Laboratory of Geo-Hazard Prevention and Geo-Environment Protection, Chengdu University of Technology, 610059, Chengdu, China
e-mail: chouvw@163.com

C. Zhou
Sichuan Provincial Meteorological Observatory, 610072, Chengdu, China

Table 97.1 Cumulative rainfall data of typical debris flows in Wenchuan Earthquake area

Study area	Location	Debris flow code	Date	Maximum rainfall intensity (mm/h)	Cumulative rainfall (mm)	Distance between rain gauge station and the gully (km)
Tangjiashan	Beichuan County	DFT1	23/09/2008	41.8	90.0	3
		DFT2	24/09/2008	61.8	226.5	3
Qingping	Mianzhu City	DFQ1	31/07/2010	50.4	89.5	5
		DFQ2	13/08/2010	38.7	163.9	5
		DFQ3	19/08/2010	31.9	176.0	5
Yingxiu	Wenchuan County	DFY1	14/08/2010	32	143.2	1
		DFY2	21/08/2011	56.5	131.6	1
Longchi	Dujiangyan City	DFL1	13/08/2010	75	123.5	1
		DFL2	19/08/2010	68.5	245.8	1

Typical debris flow events are the Tangjiashan debris flow (Hu et al. 2009), the Yingxiu debris flow, the Wenjia debris flow (Yu et al. 2010; Tang et al. 2012) and the Longchi debris flow. The critical rainfall thresholds for the triggering of debris flows have decreased after the Wenchuan Earthquake. Scientists are interested in this relationship between post-earthquake debris flows and critical rainfall because the research can help engineers to carry out relatively accurate predictions of post-earthquake debris flows. The typical study areas for these post-earthquake debris flows are the Kanto earthquake zone in Japan, the Chi–Chi earthquake area in Taiwan (e.g., Lin et al. 2006; Shieh et al. 2009; Chen and Hawkins 2009) and the Wenchuan Earthquake area (e.g., Tang et al. 2012).

A relatively accurate prediction of post-earthquake debris flows can help to reduce the casualties and economic losses. It is very difficult to predict debris flows on the basis of the initiation mechanisms. Therefore, it is the aim of this paper to assess the relationship between post-seismic debris flows and rainfall in order to increase the capacity of predicting possible future debris flow occurrences. To do so, rainfall records were collected to analyze the rainfall patterns for typical debris flows, which occurred in the Wenchuan Earthquake area. Finally, the differences between rainfall triggering patterns of debris flows and the controlling factors in the Wenchuan Earthquake area are discussed.

2 Data Collection

In order to obtain the rainfall pattern of post-seismic debris flows in the Wenchuan Earthquake area, rainfall data is needed prior to and after typical debris flow occurrences in the study area. In this study, we used a collection of published data of historical debris flow events (Table 97.1). Knowledge of the rainfall characteristics in a particular area requires well-recorded debris flows and corresponding rainfall-duration data. In the Wenchuan Earthquake area, however, systematically recorded debris flow data are rarely available because few giant debris flows occurred. Besides, precipitation gauging stations are not installed in all the debris flow gullies. In total nine rainfall data has been collected. Two debris flow events (DFT1 and DFT2) were selected as the typical cases in the Tangjianshan area. Three debris flow events (DFQ1, DFQ2 and DFQ3) were selected as the typical cases for Qingping area. Two debris flow events (DFY1 and DFY2) in Yingxiu area and two events (DFL1 and DFL2) in Longchi area were selected.

3 Methods

Rainfall data recorded at the station closest to the gully were chosen to represent the precipitation condition for the debris flows that
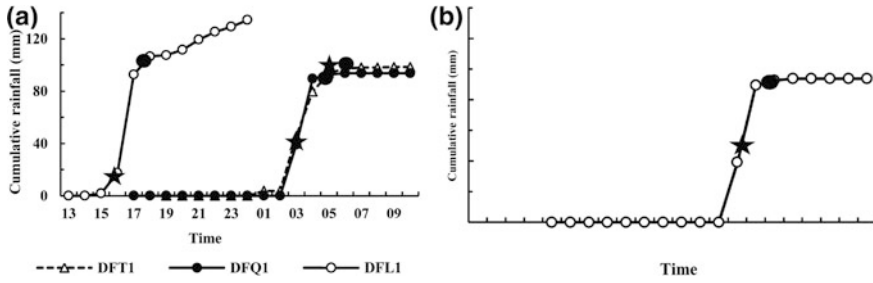
Fig. 97.1 Rapid triggering response patterns, for the Wenchuan Earthquake area. **a** Rapid triggering pattern of typical cases. **b** Schematic diagram of a rapid triggering pattern. ★ Represents the start of debris flow event. ● Represents the end of debris flow event

occurred there. The definition proposed by Jan and Lee (2004) is adopted to define the event of a continuous precipitation. The start of precipitation is defined when the rainfall intensity is >4 mm/h. The end of the precipitation event is defined when the rainfall intensity is <4 mm/h during 6 consecutive hours (Chang et al. 2011). The average rainfall intensity can be computed as the cumulative rainfall in this precipitation event divided by the duration of the event. Cumulative curves of the rainfall prior to and after the debris flow occurrence can be constructed. Given the starting time of the debris flow, the critical rainfall can be determined from these cumulative curves. One cumulative curve describes one rainfall pattern. Comparing those rainfall patterns, one can classify those rainfall patterns by the similar rainfall process.

4 Rainfall Patterns for Debris Flows in the Wenchuan Earthquake area

The rainfall triggering patterns in the Wenchuan Earthquake area can be divided into three categories, namely a rapid triggering response pattern, an intermediate triggering response pattern and a slow triggering response pattern.

(1) Rapid triggering response pattern

The rapid triggering response pattern is characterized by a small number of antecedent rainfall before triggering of the debris flow. The rainfall intensity usually increases rapidly from a small value to a maximum and then drops quickly to 0. The total rainfall duration is 4–8 h. Debris flows are not necessarily triggered when the rainfall intensity reaches its maximum. The debris flow will be induced prior to or after the maximum rainfall intensity. The cumulative rainfall is small and the debris flow will start shortly after the beginning of the rain event. A generalized diagram of a rapid triggering pattern for the Wenchuan Earthquake area is shown in Fig. 97.1b. DFT1, DFQ1 and DFL1 are the typical cases (Fig. 97.1a).

(2) Intermediate triggering response pattern

For an intermediate triggering response pattern, the rainfall duration before the triggering of the debris flow is longer (4–7 h) and the cumulative rainfall is large. The debris flows were triggered when the rainfall intensity reached its maximum. The rainfall intensity increases slowly from a small value to a maximum value and then decreases rapidly from the maximum value to 0. The total rainfall duration is 8–15 h. A generalized diagram of the medium triggering response pattern for the Wenchuan Earthquake area is shown in Fig. 97.2b. DFQ2, DFQ3 and DFY2 are the typical cases (Fig. 97.2a).

3) Slow triggering response pattern

One can speak of a slow *triggering* response pattern when the rainfall duration is long with multiple peaks. The rainfall intensity increases slowly from a small value to a large value and then decreases. This may happen two to three times. In general, the total rainfall duration is 12–17 h. Debris flows were triggered when the rainfall intensity reached the second or third peak intensity. The cumulative rainfall is large and
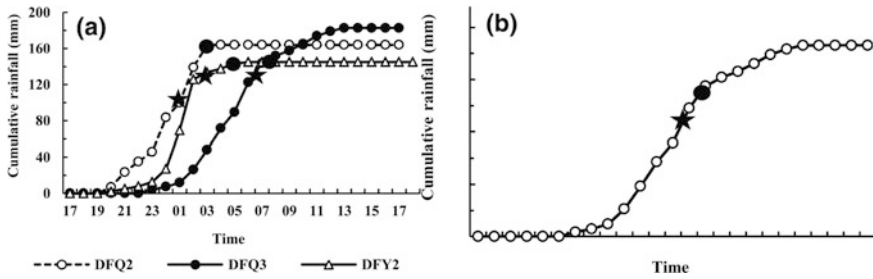
Fig. 97.2 Intermediate triggering response patterns for the Wenchuan Earthquake area. **a** Intermediate triggering response pattern of typical cases. **b** Schematic diagram of an intermediate triggering response pattern. ★ Represents the start of debris flow event. ● Represents the end of debris flow event
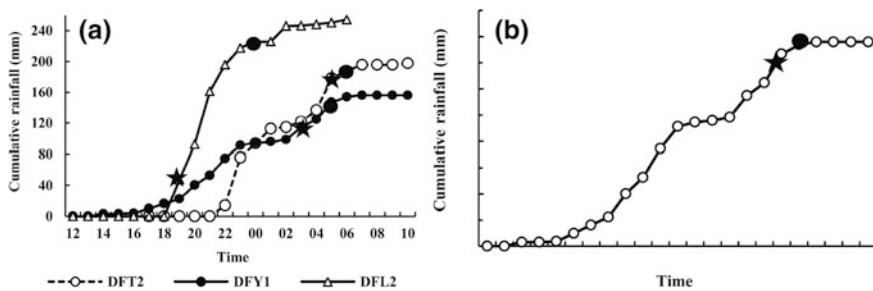
Fig. 97.3 Slow triggering response patterns for the Wenchuan Earthquake area. **a** Slow response pattern of typical cases. **b** Schematic diagram of slow triggering response pattern. ★ Represents the start of debris flow event. ● Represents the end of debris flow event

debris flows will occur after it rains for a long time. A generalized diagram of a slow triggering response pattern for the Wenchuan Earthquake area is shown in Fig. 97.3b. DFT2, DFY1 and DFL2 are the typical cases (Fig. 97.3a).

5 Discussion

In this paper, the initiation process of post-earthquake debris flows in the Wenchuan area was divided into four phases: (i) soil moisture increase and perched groundwater recharge, (ii) infiltration and excess runoff, (iii) soil slip failure, (iv) debris-flow triggering. The main difference in occurrence of debris flows under different rainfall pattern conditions is determined in the first phase, namely: the increase in soil moisture and groundwater recharge of the loose soil. So only the effect of these initial processes on the differences in triggering patterns is discussed in the following part. A current study (Zhu and Shao 2010; Mao et al. 2011) shows that the gravel content of the loose soil mass has little influence on the soil infiltration process. Therefore, the influence of the gravel content can be ignored.

Thus the infiltration and the recharge of perched groundwater in the loose soil materials are the determining factors for the different triggering rainfall patterns as described above.

In case of a rapid triggering response pattern, the rainfall duration prior to debris flow initiation is short and the amount of cumulative rainfall is small. At the beginning, rainfall intensity is low and does not exceed the soil infiltration capacity, resulting in infiltration of all the precipitation. The cumulative curve of a rapid triggering response pattern shows a sharp increase in precipitation. This results in a rapid decrease of the infiltration capacity. Once the rainfall intensity suddenly increased, the soil infiltration rate decreased rapidly, resulting in the time of loose
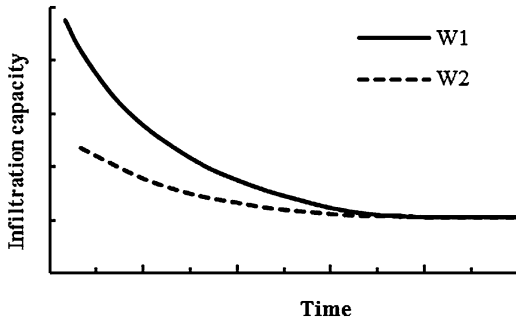
Fig. 97.4 Schematic diagram of changes in infiltration capacity during rainfall. The solidline curve is the infiltration capacity curve for an initial dry soil (W1). The dashed curve is the infiltration capacity curve for an initial wet soil (W2). The lower the initial moisture content (curve W1) the more the soil can absorb at the beginning of the rain and the more is available for the groundwater recharge

soil saturation cut down and debris flow induced soon after the rainfall occurrence.

For an intermediate triggering response pattern, the rainfall duration prior to debris flow occurrence is longer and cumulative rainfall is larger. The rainfall intensity increases from 0 to a maximum, and then decreases from the maximum down to 0. When the rainfall intensity does not exceed the soil infiltration capacity, all the precipitation will infiltrate into the soil. The soil water content increases in time and infiltration capacity decreases. The greater the initial water content of the soil the faster the infiltration rate of non-steady stage decreases (Fig. 97.4). And it needs less time to reach a steady infiltration rate. When the rainfall intensity reaches its maximum, the soil water content reaches the maximum value or becomes saturated. The soil infiltration rate has dropped to the lowest value or a constant value. Compared with the rapid triggering response pattern, the time of loose soil saturation is significantly prolonged. It is very easy to understand why debris flow occurrence under intermediate triggering response pattern conditions needs more time.

For a slow triggering response pattern, the rainfall duration prior to debris flow occurrence is longer and cumulative rainfall is larger. The rainfall intensity increases from a minimum to a maximum, and then decreases from this maximum down to another minimum. This pattern can be repeated several times. The infiltration rate of the loose soil in the debris flow source area decreases in time and becomes more and more constant (Zhang et al. 2010).

In general, for the entire scenario's that despite the initial moisture content, the faster the supply of rain, the faster the triggering of debris flow. But there is another very important factor, the thickness of the soil. The thicker the soil, the more water is needed to destabilize and the longer the time for the triggering of debris flow.

6   Conclusion

Debris flows were frequently triggered after the Wenchuan Earthquake, causing serious casualties and economic losses. A relatively accurate prediction of these post-seismic debris flows can help to reduce the consequent damages. In order to increase the capacity of predicting possible future debris flow occurrences, this paper assess the relationship between the occurrence of post-seismic debris flows and cumulative rainfall. The results shows the rainfall patterns related to the triggering of debris flows in Wenchuan Earthquake area can be divided into three categories, namely a rapid triggering response pattern, an intermediate triggering response pattern and slow triggering response pattern. Post-earthquake debris flows are caused by two main processes: slip failure of the soil and subsequent liquefaction and erosion of loose material on steep slopes by concentrated runoff water. The main difference in initiation mechanism of debris flow under different rainfall pattern conditions is loose soil saturation process. The difference among the three triggering patterns is the rainfall duration and intensity. The process of loose soil saturation is the difference for debris flow initiation under three triggering patterns conditions. The differences of rainfall pattern (i.e. rainfall duration and intensity) make the differences when the excess off formed and debris flow triggered.

References

Chang CW, Lin PS, Tsai CL (2011) Estimation of sediment volume of debris flow caused by extreme rainfall in Taiwan. Eng Geol 123(1–2):83–90

Chen H, Hawkins AB (2009) Relationship between earthquake disturbance, tropical rainstorms and debris movement: an overview from Taiwan. Bull Eng Geol Environ 68:161–186

Cui P, Wei FQ, He SM, You Y, Chen XQ, Li ZL, Dang C, Yang CL (2008) Mountain disasters induced by the earthquake of May 12 in Wenchuan and the disasters mitigation. J Mountain Sci 26(3):28–282, in Chinese

Hu XW, Lü XP, Huang RQ, Ren XM, Wang XR, Liu J (2009) Analyses of river-blocking and breaking mode of "9 × 24" debris flow near Tangjiashan barrier dam. J Southw Jiaotong Uni 44(3):312–320, in Chinese

Jan CD, Lee MH (2004) A debris flow rainfall-based warning model. J Chin Soil Water Conserv 35(3):275–285, in Chinese

Lin CW, Liu SH, Lee SY, Liu CC (2006) Impacts on the Chi–Chi earthquake on subsequent rain induced landslides in central Taiwan. Eng Geol 86(2–3):87–101

Mao TX, Zhu YJ, Shao MA, Wu B (2011) Characteristics of runoff and infiltration in stony soils under simulated rainfall conditions. Chin J Soil Sci 42(5):1214–1218, in Chinese

Shieh CL, Chen YS, Tsai YJ, Wu JH (2009) Variability in rainfall threshold for debris flow after the Chi–Chi earthquake in central Taiwan. China Int J Sediment Res 24(2):177–188

Tang C, Asch TWJ, Chang M, Chen GQ, Zhao XH, Huang XC (2012) Catastrophic debris flows on 13 August 2010 in the Qingping area, Southwestern China: the combined effects of a strong earthquake and subsequent rainstorms. Geomorphology 139–140:559–576

Tang C, Zhu J, Li WL (2009) Rainfall triggered debris flows after Wenchuan Earthquake. Bull Eng Geol Environ 68:187–194

Xie H, Zhong DL, Jiao Z, Zhang JS (2009) Debris flow in Wenchuan quake-hit area in 2008. J Mountain Sci 27(4):501–509, in Chinese

Yu B, Ma Y, Wu YF (2010) Investigation of severe debris flow hazards in Wenjia gully of sichuan province after the wenchuan earthquake. J Eng Geol 18(6):827–836, in Chinese

Zhang XY, Shi XZ, Yu DS, Wang HJ, Liu ZB, Zhang WT (2010) Effects of antecedent soil moisture on hillslope runoff-generation and soil erosion over red soil-mantled landscapes. Adv Water Sci 21(1):23–29, in Chinese

Zhu YJ, Shao MA (2010) Simulation of rainfall infiltration in stony soil. Adv Water Sci 21(6):779–787, in Chinese

The Future in the Tangjiashan Dammed-Lake Resulted from the M8.0 Wenchuan Earthquake: Discussion on Several Scientific Issues

Zhi-man Su, Peng Cui, Qing-qing Yang, Keizo Ugai and Fei Cai

Abstract

The Tangjiashan dammed-lake is the largest dammed-lake induced by the M8.0 Wenchuan Earthquake on May 12, 2008 in Sichuan Province, China. The highest water level in Tangjiasha dammed-lake once reached 743.10 m elevation, with a volume of about 2.466×10^8 m^3. After a spillway being evacuated on the debris dam, water level fell to about 713 m, with a volume of about 0.86×10^8 m^3. After that, the dam succeeded in withstanding the impacts from floods or debris flows in following 3 years. Till September 2011, many engineering countermeasures were adopted in strengthening the dam and a plan to transform the dammed-lake into an earthquake relic tourist spot was proposed. This paper discussed the influencing factors acting on the process of the Tangjiashan Dam breaching and pays special attention to the final stage when the erosion turned weaker and the water level got lower slowly. It was found that the slope of downstream face of dam and the river bed elevating in the site adjacent to the outlet during the process of breaching

Z. Su (✉) · P. Cui
Key Laboratory of Mountain Hazards and Surface
Process, CAS, Chengdu, 610041, China
e-mail: szmiyqq@imde.ac.cn

Z. Su · P. Cui
Institute of Moutain Hazards and Environment,
CAS, #.9, Block 4, Renminnanlu Road, Chengdu,
610041, China

Q. Yang · K. Ugai · F. Cai
Department of Civil Engineering and Environment,
Gunma University, Tenjin-cho 1-5-1, Kiryu,
3768515, Japan

Z. Su · P. Cui · Q. Yang · K. Ugai
Institute of Mountain Hazards and Environment,
CAS, #.9, Block 4, Renminnanlu Road, Chengdu,
China

play important roles in the cease of erosion. Recommendations in the future research in the Tangjishan dammed-lake are proposed.

Keywords

Dammed-lake · Tangjiashan landslide · Dam breaching · Wenchuan Earthquake

1   Introduction

Landslide dams are formed by various kinds of landslides, and occur in differing physiographic settings, ranging from rock slides and avalanches in steep-walled narrow valleys to slumps and flows of sensitive clays in flat river lowlands (Schuster 2000). Catastrophic outburst floods or debris flows following rapid dam failure usually causes a series of consequential off-site hazards. The world's worst landslie-dam disaster occurred when the 1786 Kangding-Luding Earthquake in Sichuan Province, China, triggered a huge landslide that dammed the Dadu River and finally resulted in an outburst flood that extended 1,400 km downstream and drowned 0.1 million people (Dai 2006). On the other hand, many landslide dams remained stable for centuries, which became scenic spots or were transformed into reservoirs for electric power or irrigation. A famous case about the beneficial aspect of landslide dams is the Lake Waikaremoana, the largest landslide-dammed lake (volume: 5.2 billion m^3) in New Zealand, which provides water and hydraulic head for production of hydropower (Read et al. 1992).

The Tangjiashan dammed-lake, which located in Beichuan County, Sichuan Province, China, was created in May 12, 2008 when a massive landslide, triggered by the Ms. 8.0 Wenchuan Earthquake, blocked the Tongkou River valley, creating a natural dammed-lake(Cui 2009, 2011, 2012; Chen 2011). It was the largest dammed-lake induced by the Wenchuan Earthquake, which caught a lot of attention from all over of the Country. The emergency response to the Tangjiashan Lake resulted in successful release of impounded water, and protecting lives, properties, and key infrastructures downstream. Till

September 2011, many engineering countermeasures were adopted to pursue a long term stability of the dam, including strengthening of the spillway and constructing a rock drainage tunnel. And then, a plan to build the dammed-lake as an earthquake relic tourist spot was proposed.

It is inclined to look forwards to a long-term stability of the Tangjiashan dam, which is hard to say so from the scientific point of view, however. We still have little knowledge in the field of dammed-lake. Nevertheless, it is believed that lessons can be learned by retrospections of the emergency response of the event. Several questions have been raised regarding the process of the artificial breaching of the dam.

2   Retrospections of Engineering Measures in Risk Reduction

The blockage of the Tangjiashan landslide dam consisted of 2.04×10^7 m^3 of landslide debris, 803 m in length along the river, 611 m in width across the river. The height of the dam above the original valley floor (669.5 m altitude) is $82.6 \sim 124.4$ m ($752.1 \sim 793.9$ m altitude). A lake quickly formed behind the dam, with 7.2 million m^3 daily increase in lake volume during the period between May 23 and May 28. Nearly 6 km^2 of upstream terrain was inundated then.

To reduce the risk of dam failure, a spillway was evacuated on the debris dam from May 26 to May 31, with elevation of inlet in 740.0; and 739.0 m in the outlet (Liu and Yang 2009). The water level was 735.53 m altitude at 8 am. Jun 2. It reached the inlet of the spillway at 7 am. Jan 7. At the beginning, the flow in the spillway was

Fig. 98.1 Looking downstream, shows flow in the channel of the Tangjiashan natural dam shortly after breaching (http://blog.gxnews.com.cn/u/4332/a/147392.html)

slow and small. It took 55 h to reach its highest elevation of the water level of 743.1 m, with the magnitude of flow in 497 m^3/s. At that time, the volume of the impounded water was about 2.466×10^8 m^3. In the following 7 h, with the spillway eroding (Fig. 98.1), the lake level had dropped to 742.8 m, but the discharge added to 940 m^3/s. 6 h later, Peak discharge of 6,500 m^3/s in the sluiceway occurred at 12:30 h June 10, with the water level reduced to 735.8 m. Thereafter, discharge fell rapidly, and by 20:00 h, the discharge was 290 m^3/s; the water level had dropped to 719 m, and the lake volume was reduced to 1.12×10^7 m^3. By 7:00 h on June 11, discharge had declined to 56 m^3/s, near the mean flow of the Tongkou River. Water level fell to about 710 m. The dam has succeeded in withstanding the impacts from floods or debris flows in the following 3 years.

To ensure a long term stability of the dam, a rock tunnel was constructed from April 12, 2010 and completed around May 31, 2011. The tunnel was designed to reduce the water level to about 705.00 m when it is necessary, such as in the case that a landslide or debris flow blocks the spillway. Besides, the inlet part of the spillway was strengthened to resist the erosion by the flow.

By artificial breaching of the dam, the total volume of discharge was as much as 1.34×10^8 m^3, and the elevation of the inlet part was lowered by 33.1 m. The spillway has enlarged from initial 475–800 m in length. The bottom of the spillway changed from initial 13 to $80 \sim 100$ m. The mean gradient of the channel increased from initial 0.2 to 2.5 %. The outflow deposited about 5×10^6 m^3 of sediment downstream from the dam, which resulted in the bed accretion of a river section in a few kilometer lengths downstream.

The data mentioned above implies significant erosion during the drainage process, resulted in widening and deepening of the spillway channel. Besides, there might be intensive headward erosion especially in the later stage of drainage, which increased the mean gradient of the channel.

The peak outflow discharge of 6,040 m^3/s, was larger than a flood of 1 % return period, of 6,040 m^3/s, and slightly less than the historical flood of record at Beichuan County of 6,720 m^3/s (Yang 2008). It means the new channel is able to convey future flows without a risk of dam failure in the same condition. The remaining portion of the natural dam, armored by significant proportions of boulder-size (>256 mm) debris, which is able to resist further erosion, and the channel cut through it will continue to stabilize by progressive engineering armoring. Risk of renewed blockage failure will also decline as the lake fills with sediment. Besides, the accretion of river bed

is believed to play a positive role in increasing the stability of the remained dam. Based on these qualitative analyses, it is safe to say that the stability of the Tangjiashan Dam has been significantly improved.

3 Scientific Issues About the Process of Dam Breaching

According to the variation of erosion effect of the flow acing on the spillway, the process of dam breaching was divided into three stages. In the initial stage of breaching, there was slight erosion and the water level increased. In the second stage, the erosion became intensive and the water level decreased sharply. In the final stage, the erosion turn weaker and the water level got lower slowly.

There are many statements towards the first two stages (Cui 2012). The designed gradient of the slope of the spillway was small, just one-third of the river gradient (0.6 %). In addition, high proportion of large boulders in the dam played a role as channel armored material which delayed erosion and retarded the initial drainage. Some of these boulders were mechanically disaggregated before discharge began and some were removed by flow during the initial stage. Partly because of the removal of large boulder-

size blocks, flow cut rapidly into the underlying layers, dramatically accelerating both lateral and vertical erosion.

The steep slope of the downstream face of the dam would be another important factor that accelerated the erosion. The slope of downstream face is 55° (Ma 2008). Therefore, surface erosion is easy to happen at the toe of the dam. Besides, the dam was formed of poorly consolidated earth material which was apt to be eroded by rapid surface flow. As a result, the elevation in outlet was 20 m lower than the one in inlet after breaching, while the difference was only 1 m before breaching.

Few attentions were paid to explain the final stage, especially the reason of the cease of erosion. Because of "self-armoring" of the eroding outlet (a process involving removal of fine material by the flowing water, leaving coarser, erosion-resistant blocks and fragments to line the channel), a breach often does not erode down to pre-dam channel level (Schuster 2000). It means the erosion of flow will cease when the flow meet an armoring layer which is strong enough to resist the flow erosion. An armoring layer with coarse material in the surface of spillway was found in the final stage of the Tangjiasha dam breaching (Fig. 98.2). It is an evidence of the "self- armoring". Owe to the armoring layer, only a part of the dam was
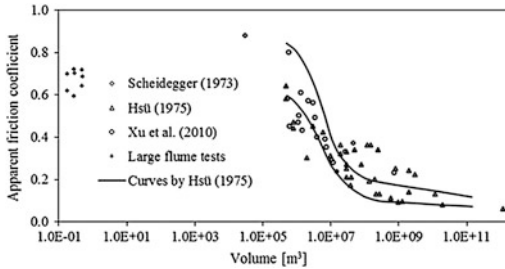
Fig. 98.3 Correlation between the volume and apparent friction coefficient (Yang 2012)

rushed away, and the water level was lowered by 33.1 m, approximately consistent with the case of 33 % collapse of the dam.

Why the armoring layer appeared in this position? In other words, why the coarser layer was covered by finer layer. The authors would like to relate it to the formation process of the blockage. The blockage occurred in a V-shape river valley with a right valley-side slope of about 60° and a left valley-side of about 30°, both of the slopes were steep. The apex of the landslide scar is 600 m above the pre-dammed river bed. The lateral movement was as much as 380 m. Generally speaking, the apparent friction coefficient of the Tangjiashan landside should be around 0.3 which is related with its mass volume (according to Fig. 98.3) In that case, the lateral movement should be about 2000 rather than 380 m. Therefore, when the front part of the landslide debris run to the opposite valley-side slope, it still has the strong tendency to run forwards, which resulted in a 140 m run up distance on the opposite valley-side slope. The middle part of the landslide debris stopped suddenly while the tail part of the debris kept moving and covered on the middle part. Usually, the size of the material of the tail part is smaller than the other parts. These deductions would be examined by numerical simulations in a near future.

Constructing an open-channel spillway across a landslide dam is the most common method of stabilizing the dam. An erosion-resistant spillway can control flow when overtopping occurs as is the case for emergency spillways on engineered dams. In addition, an excavated spillway lowers the elevation of the dam crest, thus reducing the extent of upstream flooding. In some cases, open-channel spillways constructed across landslide dams have not been successful because of retrogressive erosion (i. e. headward erosion from the spillway outlet to its intake). Subsequently, dam breaching and downstream flooding happened as in the case of the Tangjiashan Dam breaching. High amount of debris from the dam was conveyed with the flow and unloaded along the river downstream in a few kilometers long, resulting a hydropower station being buried 2 km away from the landslide site. In the Beichuan County, about 4 km away from the landslide site, the height of river bed accretion was near 6 m. Spillways that fail due to erosion may be partially successful because they have reduced both upstream and downstream flooding by limiting the amount of water impounded by limiting the total volume of the impoundment, thus reducing total discharge even if the dam breaches entirely.

In the case of the Tangjiashan Dam, partly failure of the dam resulted in the elevating of riverbed in the site of outlet to the similar elevation in the adjacent part of the dam, which actually enlarged the length of the dam along the river channel and played a positive role in improving the stability of the dam. Besides, the river bed accretion maybe another reason for the cease of erosion during breaching.

4   Recommendations in the Future Research in the Tangjishan Dammed-Lake

Based on the discussion on the scientific issues mentioned, recommendations for the future research were proposed as followings:

– Attentions should pay to the slope of downstream face of dam which plays a significant role in promoting the retrogressive erosion by high velocity outlet flow when overtopping occurs. The slope of downstream face of dam can be regarded as a key index of hazard assessment of landslide dam.
– The case of the Tangjiashan dam breaching provides an example of 33 % collapse of

landslide dam, which was under control initially by engineering measures and then by nature. It can be used to examine the physical model or empirical model. The role of the river bed elevating in the site adjacent to the outlet during the breaching should be considered, as well as the position of potential armoring layer in the landslide dam.

– In an emergency situation, it is difficult to collect the data of the structure of the landslide dam. Simulating the process of blockage may provide an approach in estimate the structure, especially the position of potential armoring layer.

References

Schuster R (2000) A worldwide perspective on landslide dams. In: UN International strategy for disaster reduction. USOI landslide dam and lake sarez: an assessment of hazard and risk in the Pamir Mountains, Tajikistan. New York

Dai FC, Lee CF, Deng JH, Tham LG (2006) The 1786 earthquake-triggered landslide dam and subsequent dam-break flood on the Dadu River, Southwestern China. Geomorphology 73:277–278

Read SAL, Beetham RD, Riley PB (1992) Lake Waika-remoana barrier: a large landslide dam in New Zealand. In: Bell DH (ed.), Landslides. Glissements de terrain. Proceedings of the sixth international symposium pp 10–14 (1992) Christchurch. Balkema, Rotterdam, pp 1481–1488

Cui P, Zhu YY, Han YS, Chen XQ, Zhuang JQ (2009) The 12 May 2008 Wenchuan landslide lakes: distribution and risk evaluation. Landslides 6:209–223

Cui P, Han YS, Chao D, Chen XQ (2011) Formation and treatment of landslide Dams Emplaced during the 2008 Wenchuan earthquake, Sichuan, China. In: Evans SG, Hermanns RL, Strom A, et al. Natural and artificial rockslide dams, Springer-Verlag, Berlin, Heidelberg, pp 295–321

Cui P, Dang C, Zhuang JQ, You Y, Chen XQ, Scott Kevin M (2012) Landslide-dammed lake at Tangjiashan, Sichuan province, China (triggered by the Wenchuan Earthquake, May 12, 2008): risk assessment, mitigation strategy, and lessons learned. Environ Earth Sci 65(4):1055–1065

Chen XQ, Cui P, Li Y, Zhao WY (2011) Emergency response to the Tangjiashan landslide-dammed lake resulting from the 2008 Wenchuan Earthquake, China. Landslides 8:91–98

Liu N, Yang QG (2009) The emergency handling technique and practice of Tangjiashan barrier lake. China Eng Sci 11(6):74–81 in Chinese

Yang QG (2008) Key technologies of emergency treatment of Tangjiashan dammed lake. China Water Resour 16:8–11 (in Chinese)

Ma GS, Luo XJ (2008) Formation mechanism of Tangjiashan landslide and engineer geological characters of the dam. Yangtze River 39(22):46–47 in Chinese

Yang QQ, Fei C, Ugai K, Su ZM, Huang RQ, Xu Q (2012) A simple lumped mass model to describe velocity of granular flows in a large flume. J Mountain Sci 9(2):221–231

Research on the Mechanism of Failure and Sediment Delivery of Landslide Dams in Debris Flow Channel

99

Zhu Xinghua, Cui Peng, Zhou Gongdan, Chen Huayong and Tang Jinbo

Abstract

Landslide dams, distributed in debris flow channel, may amplify the scale of debris flow in magnitude because of their block-failure process. Besides, the loose materials of landslide dams are important material source of debris flows. Therefore, research on the mechanism of failure and sediment delivery of landslide dams in debris flow channel has great significance in debris flow prevention and mitigation. In this paper, we designed large-scale flume experiments to explore the failure patterns and the mechanism of sediment transport of landslide dams in debris flow channel. The failure of incomplete -block landslide dams had two patterns: overtopping and downward erosion of spillway. Refer to the associated sediment delivery theory, we presented the formula of scour rate of dam materials and peak flow; the calculated results are found to be in good agreement with model test data.

Keywords

Debris flow · Landslide dam · Failure · Field flume experiments

Z. Xinghua (✉) · C. Peng · Z. Gongdan ·
C. Huayong · T. Jinbo
Chinese Academy of Sciences (CAS), Key
Laboratory for Mountain Hazards and Earth Surface
Process, Institute for Mountain Hazards and
Environment, CAS, Chengdu, China
e-mail: zhuxinghua09@163.com

Z. Xinghua
Graduate School, CAS, Beijing, China

Abbreviation

F_L	Uplift force acting on the sediment grain
F_d	Drag force acting on the sediment grain
a	Side slope angle
b	Angle between flow direction and horizontal axis of side slope
φ	Angle of repose of sediment
τ'_c	Critical shear stress of incipient motion of sediment
τ_c	Shear stress on the channel bed
h	The depth of debris flow
σ	Total stress of peak flow
ρ'	Debris flow density
g	Acceleration of gravity
γ	The volume weight of water
J	The flume gradient
g_T	The sediment carrying capacity of debris flow
U	The mean velocity of debris flow in cross-section
ω	Sediment settling velocity
e_b	The efficiency of bed load transport
D_{50}	Median size of sediment
U_*	Friction velocity of sediment
U_{*C}	Threshold friction velocity of sediment
S_r	Scour rate of dam materials
g_0	The amount of sediment from upper sections
γ_s	The volume weight of soil
ρ_s	Soil density
B	The width of the flume

1   Introduction

Debris flow is a common type of mountain hazards in western mountainous regions of China. The formation of debris flow requires abundant supply of loose materials, steep terrain and abundant surface runoff (Takahashi 1981). At present, many scholars and experts paid much attention to the relationship between rainfall and debris flow formation, but less attention to the relationship between loose material reserves and the scale of debris flow. There is a close relation to the loose material reserves and the frequency and scale of debris flow (Bovis and Jakob 1999; Jakob et al. 2005). The supply of loose materials may include bed erosion, landslide dams' failure and bank erosion in debris flow channel (Cannon

et al. 2001; Dong et al. 2009). There are two patterns of loose materials transport in debris flow channel: (1) Sediment transport type. A large amount of loose materials enter the channel, but cannot form landslide dams; mountain torrents transport these loose materials and form debris flow; (2) Landslide dams block-failure type. Landslides enter and block channel, forming landslide dams; after a period of rainfall, the landslide dams break and form debris flow. The block-failure process of landslide dams may amplify the scale of debris flow and cause significant loss of lives and property. For instance, there were at least 5 large landslide dams distributed in Sanyanyu Gully caused by Wenxian earthquake in 1879 before Zhouqu giant debris flow on August 7, 2000, in China. The peak flow of debris flow was amplified by 60 % as cascade

Fig. 99.1 The landslide dams in debris flow channel: **a** the residual body of a landslide dam in Luojiayu Gully; **b** a landslide dam in Yangxianger Gully in Wenchuan earthquake-stricken area
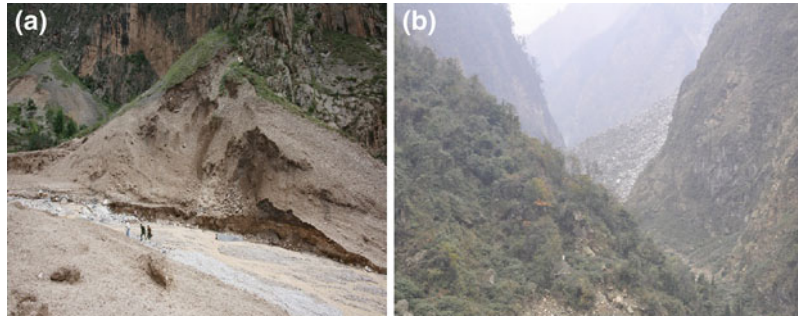
failure of these landslide dams (Tang et al. 2011; Yu et.al. 2010). Therefore, to explore the mechanism of sediment transport of landslide dams in debris flow channel has great significance in debris flow prevention and mitigation.

Due to the complexity of the structure and composition as well as capacity of landslide dams, rainfall and other conditions, the stability of landslide dams has been the focus and difficulty in this field of study (Ermini and Casagli 2003; Korup 2004; Dunning et al. 2005). Costa and Schuster (1988) classified the failure of landslide dams into overtopping, piping and slope failure, which laid the research basis of failure of landslide dams. With the improvement of numerical simulation theory and failure model of landslide dams (Singh 1996; Fread 1988; Bechteler and Broich 1991; Ralston 1987), numerical analysis about dammed lake outburst and flood routing has achieved significant progress, but few focus on the failure model of landslide dams in debris flow channel. The theory of sediment transport in channel can be summarized as empirical models, conceptual models and physical-based models (Aksoy and Kavvas 2005; Merritt et. al. 2003). Tang (2001) classified the ways of delivery of loose materials in debris flow channel into three types: rainfall erosion, attenuation of the soil shear strength, downward erosion of channel bed and channel bank erosion, but only carried out a preliminary analysis of the mechanism of sediment delivery; Berti and Simoni (2005) simulated the formulation of debris flow in channel based on the field observation data in Alps in northern Italy. However, landslides enter debris flow channel, either transported by debris flow directly, or blocking the channel and forming landslide dams,

and then transported to downstream by outburst flood when the dams broke (Brayshaw and Hassan 2009). The failure of landslide dams in debris flow channel is a complex issue, which has not been given due recognition.

In this paper, the mechanism of failure and loose materials transport in debris flow channel has been explored through field study of Zhouqu debris flow hazards and large-scale flume experiments. The formula of scour rate of dam materials and peak flow were also presented in this paper.

2 Field Study

We investigated the Sanyanyu Gully and Luojiayu Gully after Zhouqu "8.7" debris flow from March 21 to 26 in 2011. There were 20 residual bodies of landslide dams distributing along Luojiayu Gully, which amplified the scale of Zhouqu debris flow during this disaster. Figure 99.1a shows the residual body of a landslide dam after "8.7" debris flow in Luojiayu Gully. In addition, with the microtopography and the sediment yield conditions of watershed changed intensely by Wenchuan earthquake, a lot of loose material entered and blocked the channel, forming landslide dams (Cui et al. 2010). As Fig. 99.1b shows, during the field investigations of debris flow channels in Wenchuan Earthquake-stricken area, a lot of loosely structured landslide dams could be found beaded-distribution along debris flow channels.

As the dynamic process of failure of dams and loose materials transport can not be gotten according to field investigations, a large-scale

Fig. 99.2 Experimental installation: **a** the distribution of landslide dams in the experimental flume; **b** an instrument for measuring the depth of debris flow; **c** pore water pressure sensors and total stress sensors

model test was designed to explore the mechanism of sediment delivery of landslide dams.

3 Model Experiments

3.1 Experimental Design

The experiments were done in the Dongchuan Debris Flow Observation Station, Chinese Academy of Sciences, Yunnan, China. Figure 99.2 shows the experimental installation, which consists of water supply system, experimental flume and data acquisition system.

The water was supplied by a tank which stored water 2 m^3 in volume, 0.55 m in depth. The flume, with a gradient of 0.21, was 45 m in length, 0.7 m in width. In addition, 5 pieces of transparent glass, marked with accurate scale, were embedded on the right side of the flume for observation. The soil used in this test was prepared according to the sample of Zhouqu debris flow and excluded particles larger than 2 cm due to the limitations of the experimental conditions. Figure 99.3 shows the soil grading curve of the samples of Zhouqu debris flow and experimental soil. The distribution of landslide dams was shown in Fig. 99.2a: a section of loose soil, with 20 in length and 0.05 m thick, was laid in channel upstream; three incomplete-block landslide dams were followed with dimensions of 2.93 × 0.7 × 0.53 m (Length × Width × Height) and a clearance of 3.5 m. The pore water pressure
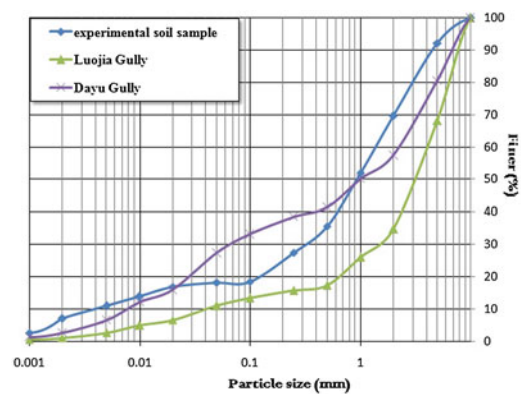
Fig. 99.3 The soil grading curve of the samples of Zhouqu debris flow and experimental soil

sensors and total stress sensors were arranged before and behind the dams. While opening the sluice gate, 2 m^3 of water poured out of the tank and rushed through the 20 m movable bed, forming hyper-concentration flow. The hyper-concentration flow eroded the landslide dams and transported the sediments of these dams, forming debris flow gradually. During the experiment, 6 HD cameras were arranged at the upper, middle and lower reaches of flume to record the experiment. The pore water pressure and total stress sensors arranged before and behind the dams to record the kinetic parameters of debris flow and the process of sediment transport. In addition, two instruments for measuring the depth of debris flow were arranged before No. 1 dam and behind No. 3 dam to record the depth of debris flow

during the experiment, which could be used to calculate the magnification times of the scale of debris flow when it rushed through 3 landslide dams. What's more, 4 samples were taken before No. 1 dam, behind No. 1, No. 2 dam and No. 3 dam to calibrate the density of debris flow.

3.2   Experimental Data Analysis

This experiment was designed to simulate the process of the failure and sediment transport of landslide dams. The dam break patterns, mechanism of dam materials transport and the amplification of peak flow of debris flow in flume were analyzed in this section.

Failure Patterns of Landslide Dams in Debris Flow Channel

In order to analyze failure patterns of landslide dams, we should make a force analysis on sediment particle at first. Figure 99.4 shows the forces acting on a sediment grain on an inclined plane: the uplift force F_L acting on the sediment particle is vertical with the slope; the drag force F_d is parallel to the flow direction; a is the side slope angle; b is the angle between flow direction and horizontal axis of side slope; Φ is angle of repose of sediment.

Based on the force analysis showing in Fig. 99.4, when the angle between flow direction and horizontal axis of side slope was 0 and the uplift force was ignored, the critical conditions of sediment starting can be determined by Eq. (99.1) (Qian and Wan 1983; Lane and Cartson 1953).

$$\frac{\tau_c'}{\tau_c} = \cos a \sqrt{1 - \frac{\tan^2 a}{\tan^2 \phi}} \qquad (99.1)$$

where τ_c' is critical shear stress of incipient motion of sediment, τ_c is shear stress on the channel bed. The shear stress on the channel bed can be calculated by Eq. (99.2).

$$\tau_c = \gamma h J \qquad (99.2)$$

where h is the depth of debris flow, γ is the volume weight of water, J is flume gradient. For
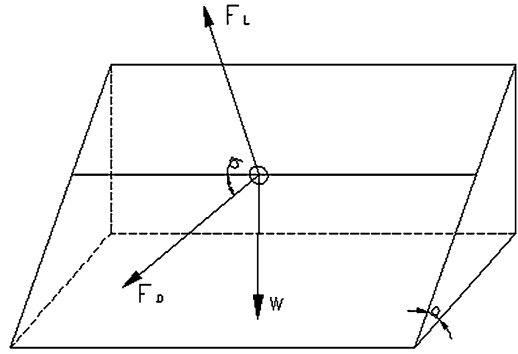
Fig. 99.4 Forces acting on sediment grain on an inclined plane

the loose soil above the water line, the stability index can be determined by Eq. (99.3).

$$N = \frac{w' \sin a}{C + w' \cos a \tan \phi} \qquad (99.3)$$

where C is soil cohesion, w' is the weight of soil mass. When N > 1,the soil mass collapse; when N ≤ 1, the soil mass will stay in quiescent state. The macro performance of patterns of soil mass starting was patterns of failure of landslide dams. Therefore, the two patterns of sediment starting determined two patterns of failure of landslide dams, which were shown in Fig. 99.5. Figure 99.5a shows the failure of landslide dam by overtopping when the upstream flow is large enough to submerge the dam and the dam materials was transported layer by layer. On the other hand, Fig. 99.5b shows the failure of landslide dam by downward erosion of spillway. The spillway formed when downward erosion of debris flow occurred on the lower side of the dam. When the soil mass on the higher side of the dam met N > 1 in Eq. (99.3), they collapsed and entered the spillway, transported to lower reaches of channel.

The Mechanism of Sediment Delivery of Landslide Dams

The pore water pressure and total stress sensors arranged before and behind the dams to record the kinetic parameters of debris flow and the process of dam materials transport. Besides,

Fig. 99.5 Failure patterns of landslide dams in debris flow channel: **a** overtopping; **b** downward erosion of spillway
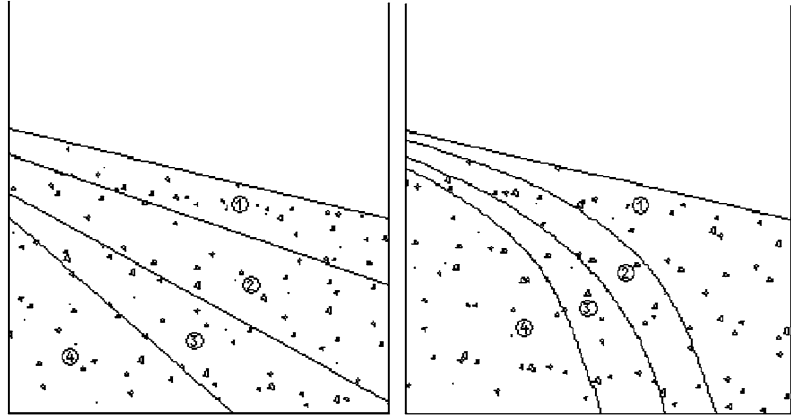
samples were taken before No. 1 dam, behind No. 1 dam, No. 2 dam and No. 3 dam to calibrate the density of debris flow (the sample behind No. 2 dam was not available due to operate miss). The depth of peak flow can be calculated by Eq. (99.4).

$$\sigma = \rho' g h \qquad (99.4)$$

Where σ is the total stress of peak flow (N/m^2), ρ' is debris flow density (kg/m^3), g is acceleration of gravity (m/s^2). The scour rate of landslide dam materials determined the magnification times of the scale of debris flow. The mechanism of sediment delivery of landslide dams' materials was analyzed as follows. The sediment carrying capacity of debris flow is calculated by the formula presented by Bagnold (1966):

$$g_T = \frac{\tau_c U}{\gamma_s} \cdot \left(\frac{e_b}{\tan \phi} + 0.01 \frac{U}{\omega} \right) \cdot B \qquad (99.5)$$

where g_T is the sediment carrying capacity of debris flow (m^3/s), U is the mean velocity of debris flow in cross-section (m/s), ω is sediment settling velocity, e_b is the efficiency of bed load transport. The sediment settling velocity can be calculated by Eq. (99.6).

$$\omega = -9 \frac{v}{D} + \sqrt{\left(9\frac{v}{D}\right)^2 + \frac{\gamma_s - \gamma}{\gamma} g D} \qquad (99.6)$$

where v is coefficient of kinematics viscosity, D is grain size of sediment. The efficiency of bed load transport can be calculated by Eq. (99.7) (Bagnold 1966).

$$e_b = \frac{U_* - U_{*C}}{U_*} \left[1 - \frac{5.75 U_* \log\left[\frac{0.4h}{D_{50}K} \left(\frac{U_{*C}}{U_*} \right)^{0.6} \right] + \omega}{U} \right] \qquad (99.7)$$

where k is modified coefficient of drag with the values range from 7.3 to 9.1, D_{50} is median size of sediment, U_* is friction velocity of sediment and U_{*C} is threshold friction velocity of sediment, which can be calculated by Eq. (99.8).

$$U_* = \sqrt{\tau/\rho_s} \ or \ U_* c = \sqrt{\tau_c/\rho_s} \qquad (99.8)$$

Then the sediment carrying capacity of debris flow can be calculated according to Eqs. (99.1), (99.2), (99.4), (99.5), (99.6), (99.7) and (99.8). However, the scour rate of dam materials depended on the sediment carrying capacity of debris flow and the amount of sediment from the upper section. In order to simplify this problem, we made three assumptions: (1) the scour rate will decrease more greatly with the decrease in amount of sediment from the upper section if the scour rate is higher as well as the sediment carrying capacity of debris flow is higher; (2) the scour rate will decrease more greatly with the decrease in amount of sediment from upper

Table 99.1 The measured scale of peak flow

Position	ρ' (kg/m³)	U (m/s)	h (m)	σ(KPa)	Q_{max} (m³/s)
Before No. 1 dam	1124.545	3.24	0.087	0.955	0.197
Behind No. 1 dam	1381.832	2.64	0.161	2.045	0.298
Behind No. 3 dam	1214.485	2.91	0.270	3.216	0.545

sections if the difference between the sediment carrying capacity of debris flow and the amount of sediment from upper sections is smaller (Wang et al. 1998); (3) the sediment is full supply during the dam materials transport process. Therefore, Eq. (99.9) can be elicited based on these three assumptions:

$$\frac{dS_r}{dg_0} = -\frac{g_T}{(g_T - g_0)^2} S_r \qquad (99.9)$$

where S_r is scour rate of dam materials (m³/s), g_0 is the amount of sediment from the upper section (m³/s). The solution of Eq. (99.10) was the relationship between the scour rate of dam materials, the amount of sediment from the upper section and the sediment carrying capacity of debris flow, which was shown as Eq. (99.9).

$$S_r = S_0 \cdot \exp(\frac{g_0}{g_0 - g_T}) \qquad (99.10)$$

where S_0 is scour rate of sediments by water per unit area (m³/(m²·s)), which can be calculated by Eq. (99.11) presented by Wang et al. (1998).

$$S_0 = 0.218 \frac{\gamma}{(\gamma_S - \gamma)\rho_s} \cdot \frac{J^{0.5}}{D_{50}^{0.25}} \qquad (99.11)$$
$$\cdot [\gamma hUJ - 0.1\frac{\gamma}{g}(\frac{\gamma_S - \gamma}{\gamma} gD_{50})^{1.5}]$$

where γ_s is the volume weight of soil and ρ_s is soil density ($\rho_s = 2{,}650$ kg/m³).

The Calculation of Magnification Times of Debris Flow Scale

The scale of peak flow can be calculated according to the theoretical analysis mentioned above when the landslide dams broken along the debris flow channel. The scale of peak flow Q_1 was the sum of upstream flow volume Q_0 and the scour rate of dam materials S_r, which can be expressed as Eq. (99.12).

$$Q_1 = Q_0 + S_r \qquad (99.12)$$

The magnification time of the scale of debris flow was the ratio of the peak flow behind and before the landslide dam, which can be expressed as Eq. (99.13).

$$k = Q_1/Q_0 = (Q_0 + S_r)/Q_0 \qquad (99.13)$$

where S_r can be calculate according to Eqs. (99.5), (99.6), (99.7), (99.9) and (99.10).

3.3 Calibrated by Experimental Data

The formula of scour rate of dam materials and peak flow were calibrated by experimental data in this section. The velocity of peak flow was calculated according to temporal difference of adjacent pore water pressure sensors; the depth of debris flow can be calculated by Eq. (99.4). The measured scale of peak flow was listed in Table 99.1 according to the measured data.

The scale of peak flow was calculated by Eq. (99.12) based on the experimental data. The values of parameters were as follows: $D_{50} = 0.003$ m, $\Phi = 35°$, J = 0.2126; the depth of debris flow before No. 1 dam was 0.087m, behind No.1 dam was 0.161m and behind No.3 dam was 0.270m; these three dams were 2.93m in length, 0.7m in width and 0.53m in height. In addition, the inclination of ridge of landslide dams were shown as follows: $a_1 = 28.955$, $a_2 = 33.557$, $a_3 = 31.388°$. The calculation results of the scale of peak flow were listed in Table 99.2.

Explanation: ① A_1 was scour area, which was multiplied 2.93 by 0.7 in this test; ②χ was the volume fraction of solid phase in debris flow; ③ the amount of sediment from the upper section can be calculated by Eq. (99.14).

Table 99.2 The predicted scale of peak flow

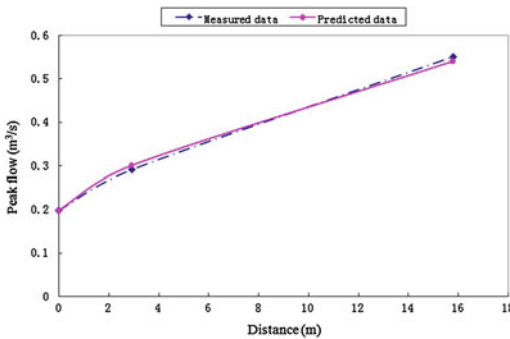| Parameters	In front of dam 1#	Behind dam 1#	Behind dam 3#
τ (N/m^2)	181.263	335.440	562.540
Tc (N/m^2)	97.207	87.536	235.638
U* (m/s)	0.402	0.493	0.638
U*c (m/s)	0.294	0.255	0.440
e_b	0.245	0.329	0.076
g_T (m3/s)	0.170	0.214	0.417
$S_0 \cdot A_1$ (m^3/s)	0.118	0.178	0.152
χ (%)	7.6	23.1	13.0
g_0 (m^3/s)	0.015	0.069	0.072
S_r (m^3/s)	0.107	0.111	0.123
Q_{max}(m^3/s)	0.197	0.304	0.538

Fig. 99.6 Verification of Eq. (12) for the scale of peak flow

$$g_0 = \chi \cdot U \cdot B \cdot h \qquad (14)$$

Figure 99.6 compared the calculated and measured scale of peak flow along the flume. It can be seen that the correlation is generally valid.

4 Conclusions

In this paper, the mechanism of failure and sediment transport of landslide dams was explored through large-scale flume experiment. The conclusions can be drawn as follows:

(1) The phenomenon that the scale of peak flow can be amplified by cascade failure of landslide dams did exist. The magnification times of peak flow was 2.73 after the debris flow rush through 3 landslide dams in this experiment.

(2) The failure of incomplete-block landslide dams contains two patterns: overtopping and downward erosion of spillway, which depends on the velocity and flow of the upstream flow.

(3) The formulas of scour rate of dam materials was presented refer to the associated sediment delivery theory. In addition, the predicted results were found to be in good agreement with measured data.

However, there were still several shortcomings in this paper: (1) the collapse of soil mass was random process during the failure of landslide dams, which was not considered in this paper; (2) Several semi-empirical formula were used in this paper, which affected the accuracy of calculation results; (3) The supply of solid materials included channel bed erosion, failure of landslide dams and channel bank erosion in debris flow channel. Therefore, we will pay more attention to channel bed erosion and channel bank erosion in debris flow channel in the future.

References

Aksoy H, Kavvas ML (2005) A review of hillslope and watershed scale erosion and sediment transport models, Catena. 64:247–271

Bagnold RA (1966) An approach to the sediment problem from general physics, US Geol Surv Prof Pap 422-I:37–38

Bechteler W, Broich K (1991) Effects in Dam-Break modeling. Proceeding 24th Congress IAHR [C], Madrid, Spain, pp 189–200

Berti M, Simoni A (2005) Experimental evidences and numerical modeling of debris flow initiated by channel runoff. Landslides 2:171–182

Bovis MJ, Jakob M (1999) The role of debris supply conditions in predicting debris flow activity. Earth Surf Process Land 24:1039–1054

Cannon SH, Kirkham RM, Parise M (2001) Wildfire-related debris flow initiation processes, Storm King Mountain, Colorado. Geomorphology 39:171–188

Costa JE, Schuster RL (1988) The formation and failure of natural dams. Geol Soc Am Bull 100:1054–1068

Cui P, Zhuang JQ, Chen XC, Zhang JQ, Zhou XJ (2010) Characteristics and countermeasures of debris flow in Wenchuan area after the earthquake. J Sichuan Uni (Eng Sci ed) 42(5):10–19 (in Chinese)

Dong JJ, Lee CT, Tung YH, Liu CN, Lin KP, Lee JJ (2009) The role of the sediment budget in understanding debris flow susceptibility. Earth Surf Process Landf 34:1612–1624

Drew B, Hassan MA (2009) Debris flow initiation and sediment recharge in gullies. Geomorphology 109:122–131

Dunning SA, Petley DN, Strom AL (2005) The morphologies and sedimentology of valley confined rock-avalanche deposits and their effect on potential dam hazard. In: Hungr O, Fell R, Couture R, Eberhardt E (eds) Proceeding of the international conference on landslide risk management. Balkema, London, pp 691–704

Ermini L, Casagli N (2003) Prediction of the behavior of landslide dams using a geomorphological dimensionless index. Earth Surf Process Landf 28:31–47

Fread DL (1988) BREACH: an erosion model for earth dam failures. National weather service (NWS) report, NOAA, Silver Spring, Maryland

Hafzullah AM, Levent K (2005) A review of hillslope and watershed scale erosion and sediment transport models. Catena 64:247–271

Jakob M, Bovis M, Oden M (2005) The significance of channel recharge rates for estimating debris-flow magnitude and frequency. Earth Surf Process Land 30:755–766

Korup O (2004) Geomorphometric characteristics of New Zealand landslide dams. Eng Geol 73:13–35

Lane EW, Cartson EJ (1953) Some factors affecting the stability of canals constructed in coarse granular material. Professional 5th congress international association hyderabad research

Merritt WS, Letcher RA, Jakeman AJ (2003) A review of erosion and sediment transport models. Environ Model Softw 18:764–799

Qian N, Wan ZH (1983) Mechanics of sediment movement. Science Press, Beijing, China, pp 256–257, in Chinese

Ralston DC (1987) Mechanics of embankment erosion during overflow. Proceedings of the 1987 ASCE national conference on hydraulic engineering, Williamsburg, Virginia, pp 733–738

Singh VP (1996) Dam breach modeling technology. Kluwer, Dordrecht, The Netherlands

Takahashi T (1981) Estimation of potential debris flows and their hazardous zones. J Nat Disaster Sci 3:57–89

Tang C, Rengers N, Van Asch Th WJ, Yang YH, Wang GF (2011a) Triggering conditions and depositional characteristics of a disastrous debris flow event in Zhouqu city, Gansu province, Northwestern China. Nat Hazards Earth Syst Sci 11:2903–2912

Tang HM, Weng QN, Wang K, Wang R, Yuan JY, Chen HK (2011b) Research on substances startup types and mechanisms of debris flows in impact-deposit deposit debris flow valleys. J Chongqing Jiaotong Univ 20(2):69–72 in Chinese

Tang HM, Weng QN, Wang K, Wang R, Yuan JY, Chen HK (2011b) Research on substances startup types and mechanisms of debris flows in impact-deposit deposit debris flow valleys. J Chongqing Jiaotong Univ 20(2):69–72 in Chinese

Zhaoyin W, Yongnian X, Xiaobo Su (1998) A study on channel scour rate of sediment laden flow and riverbed inertia. J Sediment Res 2:1–9 in Chinese

Wang ZY, Huang JC, Su DH (1998) River channel scour and scour rate of clear water flow. J Sediment Res 1:1–11 in Chinese

Yu B, Yang YH, Su YC, Huang WJ, Wang GF (2010) Research on the giant debris flow hazards in Zhouqu County, Gansu Province on August 7, 2010. J Eng Geol 18(4):437–444 in Chinese

Mechanism of Landslide-Debris Flow-Barrier Lake Disaster Chain After the Wenchuan Earthquake

Q. Zou, Z. M. Su and X. H. Zhu

Abstract

The Wenchuan earthquake of China has produced strong disturbance to ground surface, which made secondary mountain disasters to be extremely developed. As is well known, in the Wenchuan earthquake area, there are $3 \sim 4 \times 10^4$ landslides or collapses which provide abundant loose material for debris flow. With effect of heavy rainfall, it is common to see large-scale and simultaneously occurring debris flows. Due to the active occurrence of landslide and debris flow, disaster chain behaves strongly and its hazard to human environment is obviously represented. In this article, characteristics of some typical earthquake-induced disaster chains have been analyzed. And their relation rules are summarized. In an unbroken disaster chain, there are four key links: disaster formation phase, disaster triggered phase, disaster damaging phase, and chain-cutting phase. Moreover, the controlling factors in the process of disaster evolution have been analyzed. The induced factors mainly focus on complex geological and geomorphological conditions, rich loose earthquake-induced deposits, local special triggered

Q. Zou (✉) · Z. M. Su X. H. Zhu
Institute of Mountain Hazards and Environment,
CAS, 9#, Section 4, Renminnanlu Road, 610041,
Chengdu, Sichuan, People's Republic of China
e-mail: zouqiang@swust.edu.cn

Q. Zou
X. H. Zhu
Graduate University, CAS, Beijing, China

Q. Zou
College of Environmental and Resource, Southwest
University of Science and Technology, Mianyang,
China

Q. Zou
Key Laboratory of Mountain Hazards and Earth
Surface Process, CAS, Chengdu, China

conditions, post-earthquake hydrological conditions, and human factors. Also the analyzed result illustrates that, geological factors play a primary role in disaster formation and evolution, and other factors can induce or trigger disasters.

1   Introduction

On Monday, May 12, 2008, a devastating mega-earthquake of magnitude 8.0 struck the Wenchuan area, northwestern Sichuan Province, China. Numerous geo-hazards were triggered by the initial shock, including rock avalanches, landslides, and debris flows. According to investigation, $3 \sim 4 \times 10^4$ landslides or collapses have been triggered in the Wenchuan earthquake area, including more than 2×10^4 serious ones (Huang et al. 2009). Some experts pointed out that active period of collapses or landslides would last for $5 \sim 10$ years, and active period of debris flows would last for $10 \sim 20$ years. Due to strong active mountain hazards, the characteristic of chain reaction would be more outstanding in next 5–10 years (Cui et al. 2008, 2011).

After the Wenchuan earthquake, series of secondary disasters happened, and the disaster chain effect was comprehensively represented. Exactly, a large number of loose materials were deposited in gullies, which is helpful in the transformation process of landslide-debris flow chain. Moreover, earthquake also induced a large number of dangerous rocks and potential unstable slopes which become an important formation condition of disaster-chain. In addition, many landslides or debris flows block river, and then the barrier lake threatens downstream areas. In this situation, the stability of dam determines the potential hazard of barrier lake. Also, it turns to be a key link of mountain hazard chain. In this paper, according to investigation of mountain disasters after the Wenchuan earthquake, characteristics of some typical earthquake-induced disaster chains have been analyzed. Then important factors in the process of disaster evolution have been summarized.

2   Characteristics of Mountain Hazards After the Wenchuan Earthquake

Compared with the mountain hazards before the Wenchuan earthquake, collapses, landslides, debris flows and barrier lakes have obvious different characteristics in earthquake-affected areas. According to field investigation, test analysis and mechanism research, the activity characteristics of mountain hazards are discussed.

2.1   Collapse or Landslide

After the Wenchuan earthquake, numerous collapse or landslides with wide distribution are the most serious hazards which threaten the safety of earthquake-affected areas. During the hazard active period, the characteristics of collapses or landslides are as follows: (1) The types of hazard are various. (2) The scale of hazard is large, and the simultaneous occurring characteristic is obvious. (3) Sliding speed is large, and sliding distance is long. (4) The hazards are mainly triggered by rainfall. (5) The main components are changed from rolling stones and collapse bodies into shallow landslides. (6) The loose slumped masses are easy to be triggered to form debris flow with support of local intensive rainfall.

2.2   Debris Flow

Compared with debris flow before the earthquake, debris-flows have some especial characteristics after the earthquake. They are:
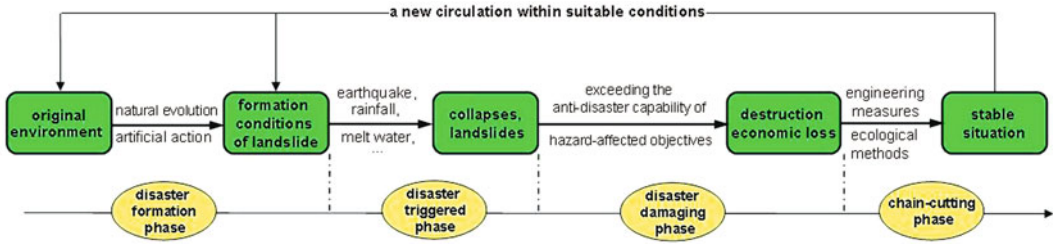
Fig. 100.1 Chain relations of collapse-landslide

(1) Density of debris flow universally increases, mainly with high-density viscous debris flows. (2) Critical starting condition reduces, and debris flows are often triggered by rainfall. (3) Ravines are seriously blocked, and the scale of debris flow obviously increases. (4) The characteristics of high-frequency and simultaneous occurring are significant in earthquake-affected areas. (5) Some non debris-flow gullies change into debris-flow gullies.

2.3   Barrier Lake

Barrier lake is the main secondary disaster in the Wenchuan earthquake areas, and the characteristics and development of barrier lakes have influence on reconstruction. According to field survey, there are hundreds of earthquake lakes induced by collapses, landslides and debris flows. And 256 large lakes exist more than 14 days and distribute like a string of beads. Moreover, these lakes have large potential risk for downstream areas. Eventually, the activity and evolution of earthquake lakes are threat the safety of earthquake areas.

3   Relation Rules of Typical Mountain Disaster Chain After the Wenchuan Earthquake

Disaster chain is a natural phenomenon in which a disaster triggers another disaster. Generally, the previous disaster is the activating link, while the successive disaster is the passive part of

hazard chain (Wen 2000). Moreover, disaster chain expresses the material, energy and information of each disaster which can be described by relationship graphics. As is well known, through analyzing relation rules of disaster chain and the disaster formation mechanism, disaster theoretical model can be easy to be built. Also, the qualitative or quantitative description for disaster can be achieved (Liu et al. 2006a; Wen 2000; Li et al. 2008).

3.1   Collapse-Landslide Disaster Chain

The formation conditions of landslides include geological factors, rock-soil nature and tectonic, artificial geotechnical engineering, heavy rainfall, and many other factors, of which, the weak rock belt is the internal and important factor. Generally, Landslides with the other geological hazards will form disaster chain. The chain relations are showing in Figure 100.1.

As is shown in Fig. 100.1, through natural evolution of geological environment and effects of human activities, the formation conditions are provided. With effects of heavy rains, earthquake, melt water, or collapse, landslides are triggered, and cause destruction for human and environment. Through controlling by engineering measures, landslides would be on a stable situation. From this chain process, it is well known that, if effective controlling measures are carried out before landslide formation, landslide disaster can be avoided or the loss would reduce to the lowest.
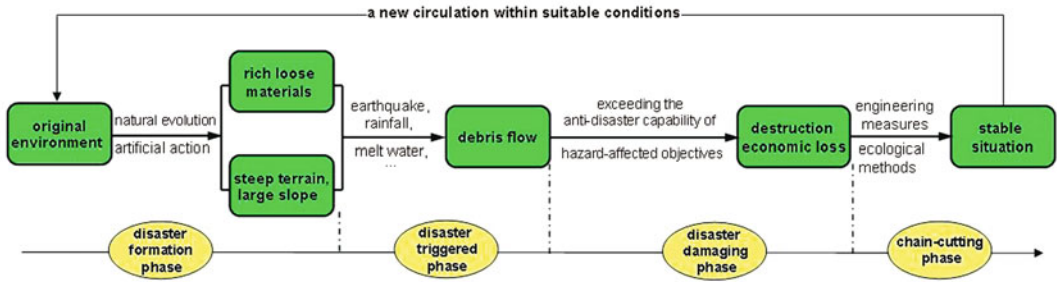
Fig. 100.2 Chain relations of debris flow

3.2 Debris Flow Disaster Chain

Debris flow is a solid–liquid two-phase migration process in mountain areas, which often causes huge damages for mountain ecological environment and mountain roads (Xie 2004). In small catchments, landslides and debris flows normally coexist. They are caused each other, and have strong destruction capability. The main relations of debris flow disaster chain are shown in Fig. 100.2. In the hazard formation stage, rich loose materials, steep terrain and large slope are important factors for debris flow. And the triggered factor is the heavy rain or abundant melt water of snow and ice. Eventually, debris flow would occur simultaneously and cause huge loss for human and environment (Chen et al. 2004; Liu et al. 2006).

The Wenchuan earthquake induced a large number of loose materials in main channel or slopes. With effect of local heavy rainfall, large-scale debris flows would occur. For instance, during August 13–14th, 2010, following heavy rainfall in the upper stream of Min River in Sichuan province, a debris flow broke out in Hongchun gully. Consequently, Min River was blocked and national road G213 was obstructed. The debris slumped into Min River causing a barrier lake to rise. Then the flooding of the barrier lake led to the inundation of Yingxiu Power Factory, Shaohuoping Bridge and a suspension bridge upstream. In addition, the debris dam changed watercourse of Min River, and flooding was forced to flow from the right side of Min River. The flood rushed into Yingxiu

town which was reconstructed on the first river terrace after the Wenchuan earthquake. It drowned the whole town, and destroyed civilian buildings and water supply facilities. The safety of the new town was greatly threatened (Fig. 100.3).

3.3 Barrier Lake Disaster Chain

Collapses and landslides slump into river and block watercourse. Then, a barrier dam is formed. If the dam is relative stability for a long time, the lake would become a natural lake called Haizi. Once the dam collapses, the rapid flood will cause serious hazards to the downstream areas.

After the Wenchuan earthquake, disasters chain of barrier lakes turns to be easy to form. Referring to the geo-hazards which induce disaster chain of barrier lakes, they include both a single disaster such as a collapse, a landslide and a debris flow, and the compound disasters. So, the disaster chain is complex and has various types. According to the chain length and evolution process, disaster chain of barrier lake have three categories: (1) earthquake—collapses (landslide)—barrier lake; (2) earthquake—collapse (landslide)—lake; (3) earthquake—collapse (landslide)—debris flow—dam—breaking flood (or larger debris flow). The third one which consists of five transformation links is the most complex and typical seismic chain form. The chain relations are shown in Fig. 100.4.

Fig. 100.3 Disaster chain induced by debris flow occurred in Hongchun gully (image from: Sichuan Bureau of Surveying, Mapping and Geoinfomation)
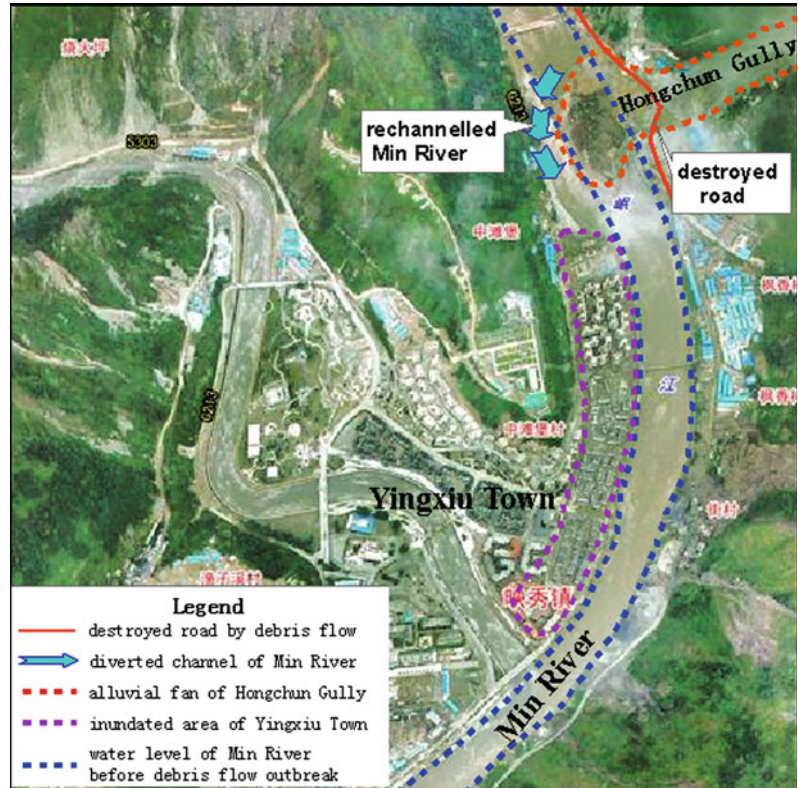
As is well known, barrier lake is mainly caused by rapid accumulation of collapses or debris. The structure of dam is much weak. And its components are loose and have poor cementation. With rising of lake level, the seepage pressure gradually increases. Eventually, the dam will be forced to breakdown. The water all together will directly discharge in a very short time, and the fierce flood will cause serious destruction for the inundated areas.

4 The Controlling Factors of Earthquake-Induced Disaster Chain

4.1 Complex Geological and Geomorphological Conditions

The Wenchuan earthquake area is located in the transition zone of Longmen Mountain and Sichuan Basin. The direction and width of Longmenshan fault not only determines the spatial distribution of the secondary mountain disasters, but also is the important factor for disaster chain formation (Yao 2007). Moreover, the Tibetan Plateau uplifting and fault activity control the development of rivers and cause strong erosion in the earthquake areas. Gradually, numerous meanders and scarps are formed. And large-scale landslides or collapses are liable to be triggered by earthquake. While rivers are blocked, the debris dam and barrier lake are formed.

In the West of earthquake-affected areas, altitude of mountain varies from 3,000 to 4,500 m, the slope is 20–45° or above. However, the altitude drops from 500–1,000 m in the West areas. In addition, rainfall is mainly concentrated in the period of late May to late July. And rainstorms or torrential rainfalls often appear in western mountain areas, especially concentrated only in one point sometimes. Based on the geological, terrain, hydrological condition above, the formation of collapse-slide-flow
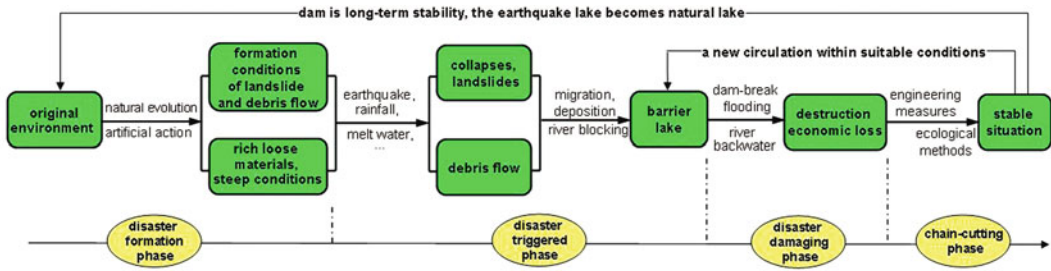
Fig. 100.4 Chain relations of barrier lake

disaster chain is liable to occur in earthquake areas.

4.2 Rich Loose Earthquake-Induced Detrituses

The Wenchuan earthquake induced a large number of collapses and landslides, which provide rich loose solid materials for debris flow. Moreover, earthquake also caused a lot of unstable slope bodies. These disasters threaten the safety of earthquake areas.

In addition, detrituses or deposits provide a formation precondition of barrier lakes and become the central link of conversion process of disaster chain. Due to the weak structure and poor cementation, the dam of earthquake lakes is easy to collapse. Then, a typical disaster chain, connecting with collapse, landslide, barrier lake and successive flooding hazard, is formed.

4.3 Micro-Topography Changed Obviously, Channel Blocked Seriously

The intensive collapses and landslides quite dramatically change micro-topography of earthquake basin. The Wenchuan earthquake resulted in bared rocks, steepened slopes and loose materials which are easy to enter into ravines and evenly block main channels. In earthquake areas, it is common to see that the residual objects of damaged forest or vegetation block main and branch ditches. Once a dam upstream collapses, the burst dam gradually impacts the lower blocking dams. The catenating effect will make the material and energy accumulating, and then all the accumulated material and energy instantly release to form large-scale debris flow disaster. This model can be described as "collapse, residual body of forest or vegetation → entering ravines → barrier dam → dam breaking → outburst step by step → large-scale debris flow".

4.4 Rainstorm and River

The rainstorm is the important motivational factor to trigger mountain disaster, also is the indirect factor to cause river blocking. In the Wenchuan earthquake-affected area, due to steep terrain and large longitudinal slope of gullies, loose solid materials can not safely stack on gully channel or channel wall. With effect of heavy rains, these loose materials are easily transported to form mountain disaster.

River system is the direct water source for inundation and flow discharge hazard. When rivers are blocked, barrier lakes can lead to an upstream inundation hazard. With supplement of upstream river water and rainfall water, the barrier dam becomes unstable. Once the dam collapses, it may result in flooding disasters.

4.5   Changed Hydrological Conditions

Due to disturbance of ground surface, destruction of vegetation and exposure of bare rock, ground lost its protective layer, which increases the erosion rate of surface loose material and the rate of flow from slope into channel. Moreover, it changed the original slope infiltration and runoff conditions. On one hand, earthquake-induced bedrock has large slope, smooth surface and small flow roughness. It basically lost the infiltration regulation of surface water. Consequently, the process of rainfall runoff and confluence is accelerated and rain erosion increases. On the other hand, because of loose structure, poor cementation and large infiltration rate, rich earthquake-induced deposits or debris will be rapidly infiltrated by rain. When soil is full filled with water, it not only reduces the accumulation of soil mechanics intensity, but also increases the weight of packing body. Eventually, deposits located on a steep slope start to slide.

4.6   Human Factors

With respect to the process of disaster chain formation or chain breaking, artificial action aggravates or delays the natural evolution of disaster chain to some extent. In order to reduce the hazard of earthquake-induced disaster chain, artificial judgment and disposal method play an important role in disaster controlling process. For example, the Tangjiashan barrier lake is the most serious earthquake lake after the Wenchuan earthquake. Through field investigation, some works such as artificial discharge, transferring threatened people are carried out. Consequently, the disaster chain was transformed into a normal process, and the downstream areas avoid suffering from flooding hazard.

5   Conclusions

In the Wenchuan earthquake area, the types of mountain secondary hazards are various, including collapse, landslide, debris flow and barrier lake. These mountain disasters have obviously presented chain-reaction characteristics. The Wenchuan earthquake has strong influence on the evolution of disaster chain. According to investigation and analysis of mountain disaster chain, the induced factors mainly focus on complex geological and geomorphological conditions, rich loose earthquake-induced deposits, local special triggered conditions, post-earthquake hydrological conditions, and human factors. The analyzed result illustrates that geological factors play a primary role in disaster formation and evolution, and other factors are very important that they can induce or trigger disasters outbreak.

Based on analysis of relation rules of typical geological disaster chain, the results show that an unbroken disaster chain process includes four key links: disaster formation phase, disaster triggered phase, disaster damaging phase, and chain-cutting phase. In the disaster formation phase, disaster formation conditions are formed through nature evolution or endogenetic geological process. In the disaster triggered phase, rainstorm, earthquake, and melt water are triggered factors which can cause disasters outbreak. In disaster chain-cutting phase, disaster can be controlled by engineering and ecological measures.

References

Chen HK, Tang HM, Ma YT (2004) Research and management of road debris flow. People's traffic press, Beijing

Cui P, Wei FQ, He SM et al (2008) Mountain disasters induced by the earthquake of May 12 in Wenchuan and the disasters mitigation. J Mountain Sci 26(3):280–282

Cui P, Chen XQ, Zhu YY et al (2011) The Wenchuan earthquake (May 12, 2008), Sichuan province, China, and resulting geohazards. Nat Hazards 56:19–36

Huang RQ, Tang C, Li Y et al (2009) Wenchuan earthquake geology disasters. Science Press, Beijing

Li M, Tang HM, Ye SQ (2008) Research on chain rule of typical geological disaster. J Catastrophol 23(1):1–5

Liu WF, Xiao SX, Sui YC et al (2006a) Analysis of natural disaster chain and chain2 cutting disaster mitigation mode. Chinese J Rock Mech Eng 25(Supp 1):2675–2680

Liu XL, Zhao Y, Ni HY et al (2006b) 2005 Investigation and assessment of group debris flows on June 30. J Catastrophol 21(4):58–65

Wen CJ (2000) Generalized disaster, disaster chain and their prevention and control. J Catastrophol 15(4):13–18

Xie H, Zhong DL, Li Y et al (2004) Features of debris flows in the upper reaches of the Changjia River. Res Environ Yangze Basin 13(1):94–98

Yao QL (2007) Field effect and regional conversion as the mechanism of natural hazards chains. Meteorol Disaster Reduct Res 30(3):31–36

Statistical Analysis of the Key Factors of Landslide Induced by Wenchuan Earthquake

Runqiu Huang, Guo Li, Nengpan Ju and Jianjun Zhao

Abstract

The distribution of landslides triggered by Wenchuan Earthquake is controlled by a variety of geological factors. Statistical results of 2,445 landslides of the four river basins show that all these factors, including the causative faults, slide direction, landform and the own properties of the slope have its contribution to the landslides distribution. In order to find out which factors have more significant influence on the landslide distribution, it is necessary to put all factors into consideration. Multivariate statistical analysis of these landslides shows that, in the near field of the causative fault during high intensity earthquake, landslides were affected distinctly by the strength of the seismic wave, instead of the properties of the slope itself such as slope structures and lithology. The factors can be generalized into five parts, which represent 76.15 % of the data set. In these factors, the first three are directly connected to the strength of the seismic wave, and the last two components involving the nature of the slope itself. Both the field investigation and statistic reveal that in the strong shock mountainous areas, the structure of the slope is not so important as usual.

1 Introduction

Longmenshan region is the transition zone between Tibet Plateau and Sichuan Basin, complex terrain and active fault motion are the two main characteristics. The two main fault belts of Longmenshan are also the causative tectonic of the Mw8.0 Wenchuan Earthquake: the Beichuan-Yinxiu fault (F2), and the

R. Huang (✉) · G. Li · N. Ju · J. Zhao
State Key Laboratory of Geohazards Prevention and Geoenvironment Protection, Chengdu University of Technology, Chengdu, 610059, Sichuan, People's Republic of China
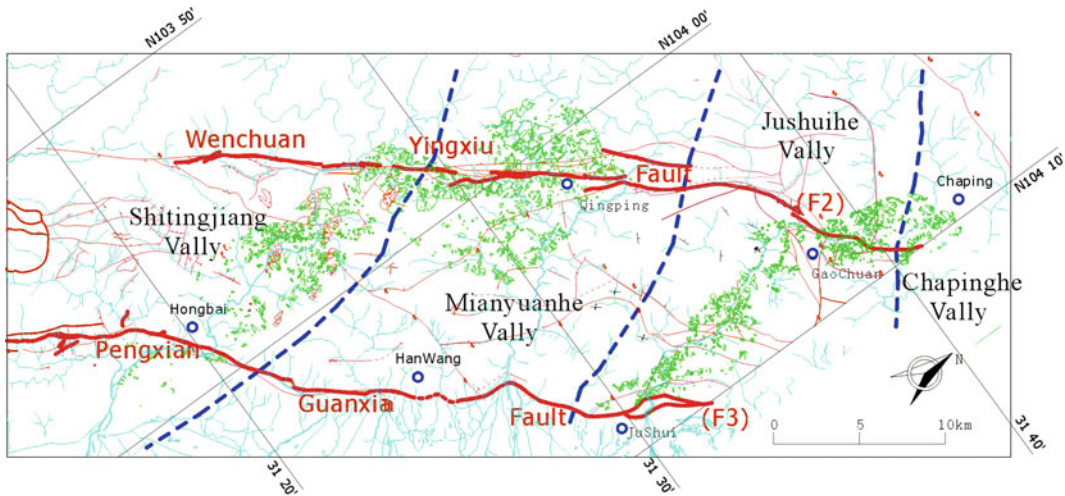e-mail: hrq@cdut.edu.cn

Fig. 101.1 Imagery interpretation results of the four basin (*Green color* represents landslides)

Pengxian-Guanxian fault (F3). The remote sensing interpretation reveals that more than 11,000 landslides are triggerd by the earthquake in this region (Huang and Li 2008). Most of which are located in the near field of these two fault belts, controlled by causative fault and the river systems. But field investigation also reveals that in the drainage area of a particular river, the distribution seems influenced by various other factors such as elevation, slope gradient, slope height, slope dip direction, the lithology and structure of the rock slope and, etc.

Previous studies on the relation between landslides and earthquake are usually concerned about landslide scale or quantity related with earthquake parameters such as magnitude, intensity and distance from the epicenter, even earthquake history (Keefer 1984; Papadonpoulous 2000). However, there are few exploring works about the relationship between landslide distribution and geological factors, due to limitation of landslides quantity and the radius of the earthquake impact. As Keefer has pointed out that: "The number of comprehensive post-earthquake studies of landslides is still relatively small, and one of the most pressing needs in this area of research is for the complete documentation of landslides triggered by many more

Table 101.1 Statistical table of landslides

Basin	JSH	CPH	MYH	STJ
Number of landslides	759	189	890	607

earthquakes in a wider variety of environments."(Keefer 2002). Wenchuan Earthquake deliver a great challenge to research how to mitigate losses caused by landslide, while a good opportunity to reveal co-seismic influential factors on landslide distribution.

2   Study Area and Data Collection

This article focused on four basins, that is Chapinghe (CPH) basin, Jushuihe (JSH) basin, Mianyuanhe (MYH) basin and Shitingjiang (STJ) basin (Fig. 101.1, Table 101.1). The study area locates along the two fault belts F2 and F3. Mainly about two major sections: from Hongbai to Qingping, and from Jushui to Chaping, including the most landslides developed area between the two faults and lateral 10 km. Such region is also the worst-hit area of Longmenshan (LMS) zone, and most of the large landslide developed with in this section (Xu and Li 2010). The investigation has acquired 2,445 data items

Fig. 101.2 Frequency distribution histogram related with distance from fault of the Longmenshan. *Data source*: Huang and Li (2008)
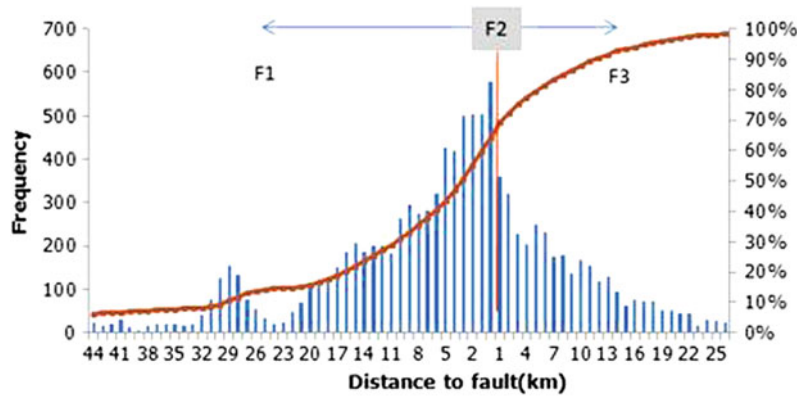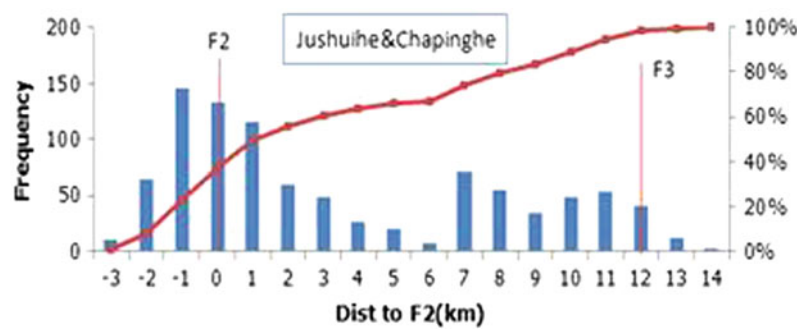

Fig. 101.3 Frequency distribution histogram related with distance from fault in Jushuihe–Chaping section

of landslide samples, each landslide parameter inventory contain following information: the distance from the epicenter, the distance from faults, elevation, slope gradient, slope height, dip direction of slope surface, the lithology and structure of the rock slope, etc.

3   Distribution Law Related to Each Influential Factor

Most landslides triggered by the earthquake are distributed along the causative faults and the river systems. This is the main distribution law of the landslides induced by the earthquake. Previous research about the whole earthquake region based on remote sensing data has revealed that most landslides occurred in the hanging wall section of 10 km along the fault belt, or developed in the valleys with 1500–2000 elevation (Huang and Li 2008). But in this paper, the study areas are four specific basins, mainly about the strong-

earthquake area, a finer description is needed and several influential factors are discussed.

3.1   Distance from the Fault

As a main causative fault, F2 has much more effect on landslide distribution regularity than other two faults (Fig. 101.2), and it is clear that the quantity of landslides on the hanging wall side is larger than that on the footwall side. Also we can found that on this side, there is a slight increase in the 15 and 30 km distance. Such distribution has a close relative to the F1 fault. That's a concrete proof of the connection between causative fault and the landslides distribution.

Reorganizing the data attribute in kilometers for each valley, using the shortest distance between landslides and the F2 fault belt, we got the frequency distribution histogram of the four valleys, as showed in Figs. 101.2, 101.3, 101.4, and 101.5.
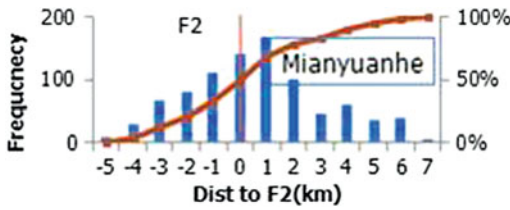
Fig. 101.4 Frequency distribution histogram related with distance from fault in Mianyuanhe
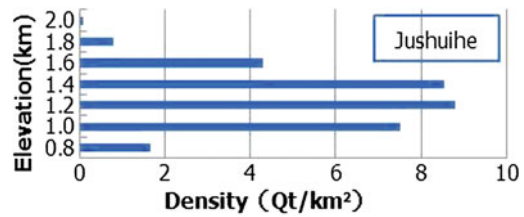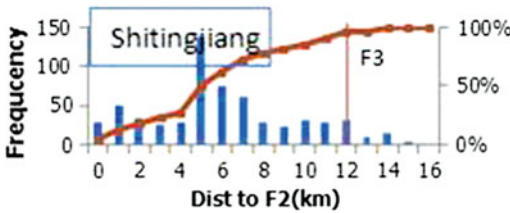

Fig. 101.5 frequency distribution histogram related with distance from fault in Shitingjiang

Fig. 101.6 Frequency distribution histogram related with elevation in Jushuihe

Fig. 101.7 Density distribution histogram related with elevation in Jushuihe

Fig. 101.8 Frequency distribution histogram related with elevation in Chapinghe

The statistical results suggest that the number of landslides in the study area decreases with the increment of distance, and mostly concentrate in the range of 3 km from the Yingxiu-Beichuan fault (F2).

As the study area of JSH and CPH is closely located and CPH is a relatively small area, these two are calculated together. The distribution law is just as the general law of the whole LMS area, the hanging wall side has more landslides developed (Fig. 101.3).

In JSH and STJ section, which is laying between F2 and F3 as a belt, the distance between F2 and F3 is approximately 12 km. Herein, if landslide is away from F2, it means close to F3. As a result of the influence of F3, landslide density re-increases after decrease with the distance from F2, as showed in Fig. 101.3

and 101.5). In STJ (Fig. 101.5), there is a peak value around 4–6 km from F2. In Fig. 101.3, a minor peak value in the 7–8 km range from F2, that is due to the STJ is closer to the epicenter and the main causative fault F2, also because there is a large fault branch of F2 goes through STJ basin. (Fig. 101.1)

3.2 Elevation and Relative Elevation

The LMS Mountains area is neighboring Sichuan Basin, which is a transition region from dale to canyon. The elevation around 1,500 m is a sensitive range to develop landslides (Huang and Li 2008). The statistical results of the study area came from 1:50,000 DEM data (Figs. 101.6, 101.7, 101.8, 101.9, 101.10, 101.11, 101.12, 101.13) shown that fewer landslides distributed in the valley which is laying below 1,000 m or above 1,600 m, but MYH is much higher than the other. Landslides in MYH Basin are mainly developed in the range of 1,200–2,000 elevation. By calculating the surface planar projection area of different elevation levels, landslide distribution density, expressed as number per square kilometers, was respectively obtained in each basin, as listed in Table 101.2. It reveals that the
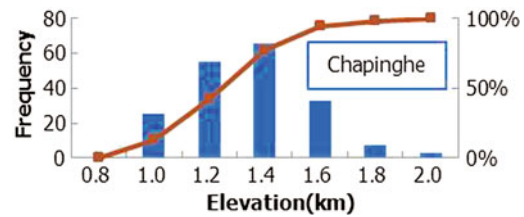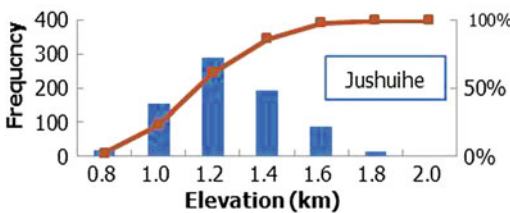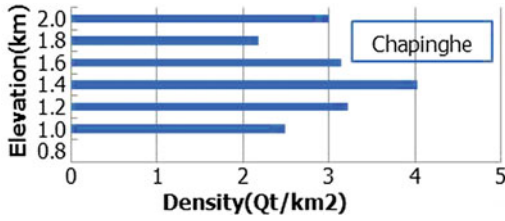
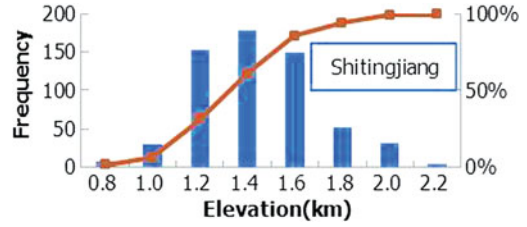**Fig. 101.9** Density distribution histogram related with elevation in Chapinghe

Fig. 101.10 Frequency distribution histogram related with elevation in Mianyuanhe

Fig. 101.11 Density distribution histogram related with elevation in Mianyuanhe

Fig. 101.12 Frequency distribution histogram related with elevation in Shitingjiang

Fig. 101.13 Density distribution histogram related with elevation in Shitingjiang

Table 101.2 Overall landslide distribution density in each basin

Basin	Elevation (m)	Area (km^2)	Density (Qt/km^2)
JSH	650–2320	133.2	5.2
CPH	740–2120	58.9	3.25
MYH	820–2880	87.4	10.18
STJ	650–2500	118.3	5.13

MYH and STJ section was induced more landslides per square kilometers than the others. Highest density of STJ is more than 10/km^2 (Fig. 101.11), while MYH is up to 13/km^2 (Fig. 101.13).

These data also show that the peak value of each chart is appearing at 300–500 m above the lowest elevation of the basin (Figs. 101.7, 101.9, 101.11, 101.13). As higher basin such as MYH, the highest density is between 1,400 and 1,600 m, while lowest elevation of this region is 800 m and JSH is 1200 m, the lowest elevation is 600–800 m. At the beginning 300–500 m which landslides distributed, the quantity and density of landslide increase rapidly, but after that, the attenuation seems slow. Fig. 101.14 shows the statistic of altitude difference, which is the relative elevation between landslides and the main ravine or larger branches. Above 100 m, the amount of landslides increased significantly, most landslides concentrated in the range of 100–300 elevation difference.

3.3 Dip Direction of Slope Surface

Due to the movement of sliding block was limited by the free space, the dip direction of the slope surface is regarded as landslide slip direction. The radar plots of the four basins (Fig. 101.15) revealed that the vulnerable slope dip direction is coincident with the mechanism of the earthquake and the terrain.

Fig. 101.14 frequency
distribution of landslides
related with altitude
difference
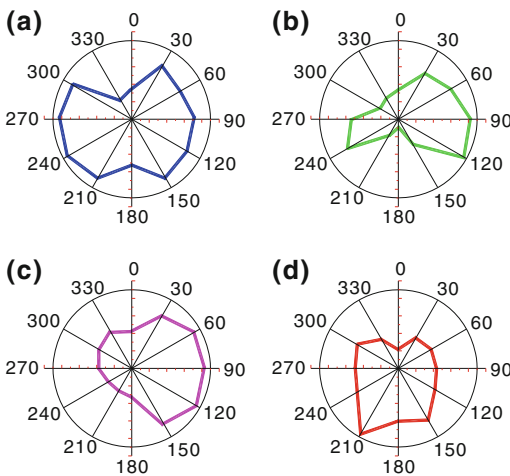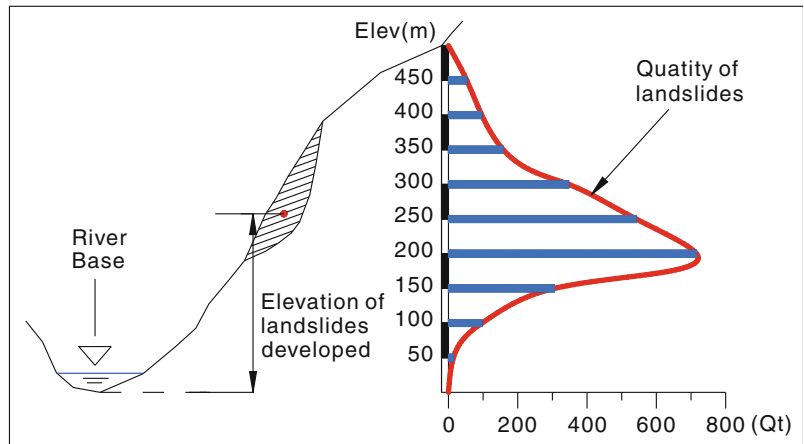
Fig. 101.15 Slip direction frequency radar plot

Table 101.3 Distribution of different gradients

Slope gradient (°)	Percentage of area (%)	Percentage of landslides count (%)
<20	12.87	2.29
20–30	19.85	9.4
30–40	33.31	34.73
40–50	23.89	43.19
>50	10.08	10.39

west to east, and the quantity of east towards always larger than the west. But in JSH (Fig. 101.15a), the distribution has been controlled by the flow direction of the main valley, it means in this section, there is little impact resulted from the fault's direction.

3.4 Gradient of Slope

The slope gradient in the study area varying mostly varies from 20 to 90°, but in general, most of the slope is around 40°, Table 101.3 lists the statistical result related to slope gradient, based on the data from DEM. It can be inferred that most landslides occurred in gradient range 40–50°, the percentage of the area is 23.89 %, but the percentage of quantity is 43.19 %.

As showed in the Table 101.3, the sensitive gradient is between 30 and 50°, which means the steeper slope does not lead to more landslides. In theory, it is easy to slip on the steep slope, but the result shows that when it's up to 60°, there are

Xu and Li (2010) has described the phenomenon of "Back-slope direction effect" of the large-scale landslide induced by Wenchuan Earthquake, with further explanation that which is directly relative to the rupture of the seismic fault. Such effect also can be found in the study area. From west to east, the STJ basin lies between the two faults and is much closer to the epicenter, so the direction distribution of landslides mainly controlled by the fault, merely influenced by the flow line of the river. As the landslide slides opposite to F2 (Fig. 101.15d), the impact can be considered as spreading from the northeast. In the MYH and CPH basin, the preferential direction is mainly along the rapture direction of the F2 (Figs. 101.15b,c,). The contour line spread from

fewer landslides in the study area. That is because the slope both has its gradient bigger than 60° and altitude higher than 300 m above the valley is rarely to be found in the field investigation.

3.5 Lithology of the Slope

Strata of the research area mainly includes following lithology: Pre-sinian, Devonian, Permian, Triassic, Silurian and Quaternary System. The major strata can be classified into five groups by its strength (Table 101.4). And the frequency distribution histogram reveals that the hard rock region, as group IV and V, was triggered relatively more landslides than the other groups, and the rock layer developed petrofabric, such as I and IV, the area density of landslides per square kilometers is also denser than the less developed gluternite group.

3.6 Structure of the Slope

Most of the slopes in the study area have a layer structure. Liu (1993) has classified stratified rock slope into five groups, based on the spatial relationship between bedding surface (α) and slope surface (β). Furthermore, five groups are classified into 11 sub-classifications (Fig. 101.16).

I: gentle stratified slope
  I_1: inward-dipping
  I_2: outward-dipping
II: crosswise slope
III: dip stratified slope
  III_1: gentle bedding dip
  III_2: middle bedding dip
  III_3: steep bedding dip
IV: Anti-dip stratified slope
  IV_1: gentle bedding anti-dip
  IV_2: middle bedding anti-dip
  IV_3: steep bedding anti-dip
V Inclined stratified slope
  V_1: inward-dipping
  V_2: outward-dipping

Table 101.4 Lithology of study area

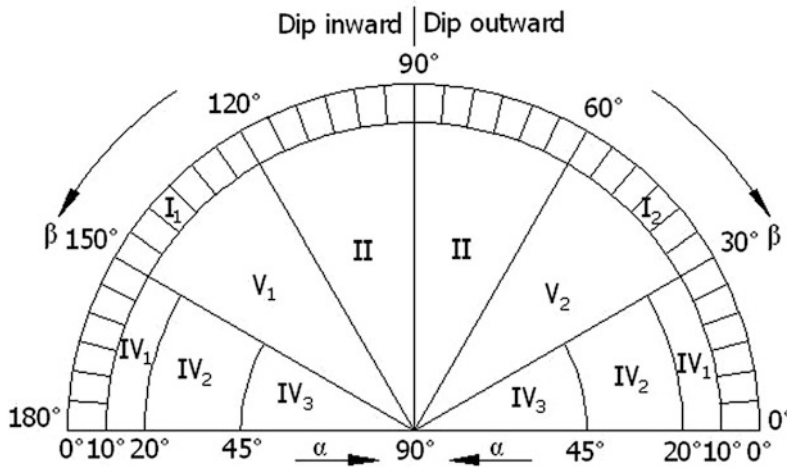| Group ID	Lithology	Representative strata	Landslides quantity		Area of lithology		Density (Qt/km²)
			Count (Qt)	PCT (%)	Area (km²)	PCT (%)	
I	Mudstone, shale	$T_1f,S_1ln,O_2b,$ Z_bq,Z_bw,J_2sn,J_3l	348	17.74	62.87	14.23	5.53
II	Sandy slate, phyllite	$S_{2-3}mx^1,$ $S_{2-3}mx^2,$	90	4.49	15.93	3.68	5.65
III	Gluternite	$\varepsilon_1c,T_3x,$	299	21.08	74.73	12.23	4.00
IV	Carbonatite	$T_2t,T_2j + 1,P_1,P_2,D_3tn,D_2gn,C_1zn,Z_bs,Z_bt$	1,401	49.06	173.96	57.30	8.00
V	Granite	$\gamma_{\delta2}^{(2)},\lambda_{\delta2}^{(2)},\beta_u$	307	7.61	26.96	12.56	11.38

Fig. 101.16 Classification of slope structure

Table 101.5 Statistical chart of geological structures

Structure		ID	JSH (Qt)	CPH (Qt)	MYH (Qt)	STJ (Qt)
Massive		0	0	0	278	0
Stratify	I_1	1	0	0	0	1
	I_2	2	0	0	0	0
	II	3	304	56	168	214
	III_1	4	10	0	0	16
	III_2	5	51	25	23	21
	III_3	6	19	18	67	27
	IV_1	7	7	0	0	34
	IV_2	8	61	16	61	40
	IV_3	9	71	7	92	53
	V_1	10	145	36	117	114
	V_2	11	91	31	84	87

Based on the mentioned geological structures classification standard, investigated landslides can be sorted as in Table 101.5. The statistical results suggest that the crosswise slope was the most widely induced landslide, while the second most vulnerable structures are inward-dipping inclined stratified slope and outward-dipping inclined stratified slope. As traditionally regarded unstable slope, dip stratified classification is easy to slide. But the

results show that whom have not produced more landslides. It means or that means influence of seismic wave intensity is more powerful than the structure of the rock slope in the strong earthquake region.

According to field investigation, in the crosswise slope, the joints perpendicular to bedding plane generally cut the slope into solid cubes, and all the cutting planes are not considered to be critical slide surface in the gravity environment, the dissected rock masses are usually just "placed" on the bedrock. So when the seismic inertia force acts on the slope, the loosening part was made to slide along the potential sliding surface. Besides, these kinds of landslides are always small in scale, but development intensively. For the same reason, the inclined stratified slope is also easier to slide than the others.

In the inclined stratified slope, the slide direction is not just along dip direction, also along trend direction. Beyond that, the anti-dip stratified slopes, as generally acknowledged, are more stable than the dip stratified slopes. But we can found in the statistics that the former was induced more landslides in the earthquake. The common sense of rock slope stability problem which based on rock structure is not operational under the circumstance of a strong shock.

Table 101.6 Correlative matrix of the 10 factors

Comp	Dist.EP	Elev	Grad	DD	R.Elev	Dist.F2	Dist.F3	BS	Lith	SS
Dist.EP	1.00	−0.20	0.02	−0.02	-0.14	0.35	0.11	−0.10	0.04	−0.03
Elev	−0.20	1.00	0.12	−0.11	0.27	0.51	0.61	0.24	0.39	0.36
Grad	0.02	0.12	1.00	0.01	0.20	0.05	0.07	−0.02	0.11	0.01
DD	−0.02	−0.11	0.01	1.00	0.01	−0.11	−0.13	−0.43	−0.07	−0.02
R.Elev	−0.14	0.27	0.20	0.01	1.00	0.03	0.07	0.03	0.09	0.08
Dist.F2	0.35	0.51	0.05	−0.11	0.03	1.00	0.88	0.32	0.29	0.26
Dist.F3	0.11	0.61	0.07	−0.13	0.07	0.88	1.00	0.38	0.40	0.31
BS	−0.10	0.24	-0.02	−0.43	0.03	0.32	0.38	1.00	0.19	0.15
Lith	0.04	0.39	0.11	−0.07	0.09	0.29	0.40	0.19	1.00	0.24
SS	−0.03	0.36	0.01	−0.02	0.08	0.26	0.31	0.15	0.24	1.00

Table 101.7 KMO and Bartlett's test

Test Indicator	KMO Measure	Bartlett test for sphericity		
		Approx. Chi-Square	Df	Sig
Value	0.636	7686.79	45	0.000

4   Analysis on Influential Factors

All the above geology factors have its own influences on the distribution of landslides while with each other. In order to figure out the key influential factors on landslide distribution, a multivariate statistical analysis is applied to combine and generalize these factors, namely, principal component analysis (PCA) (Pearson 1901; Miesch 1980). In order to give a detailed description of this case, the following 10 factors are selected:

1   Dist.EP: The distance between the landslide and the epicenter.
2   Elev: The elevation of the landslide.
3   Grad: Slope gradient where the landslide's located.
4   DD: Dip direction of the slope surface.
5   R.Elev: Slope height, elevation difference from the main ravine.
6   Dist.F2: The nearest distance to F2 on the horizontal projection surface.
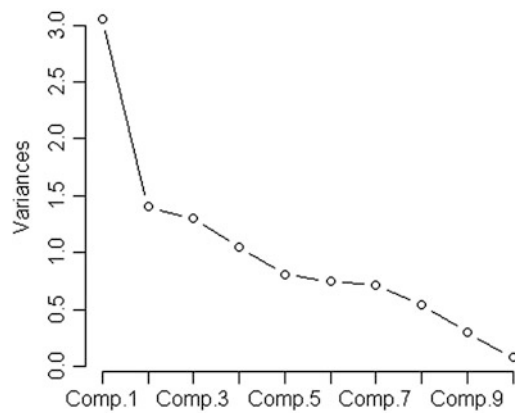
Fig. 101.17 Scree plot

7   Dist.F3: The nearest distance to F3 on the horizontal projection surface.
8   BS: Right bank of river or the left.
9   Lith: Lithology.
10 SS: Structure of rock slope.

The data set of 2,445 landslides was calculated, by using R statistical computing language (Ripley 2012).

The correlation matrix is the basis of PCA, it can be seen that a few factors have a better correlation to another (Table 101.6). And PCA analysis need the KMO and Bartlett test, as the KMO measure >0.5, and Sig 101.7), the data set is fit for analysis.

Fig. 101.18 Parallel analysis result

Table 101.8 Total variance explained

Component	Total	Variance (%)	Cumulative (%)
Comp 1	3.06	30.568	30.57
Comp 2	1.40	14.043	44.61
Comp 3	1.30	12.995	57.61
Comp 4	1.05	10.482	68.09
Comp 5	0.81	8.063	76.15

Table 101.9 Component score coefficient matrix

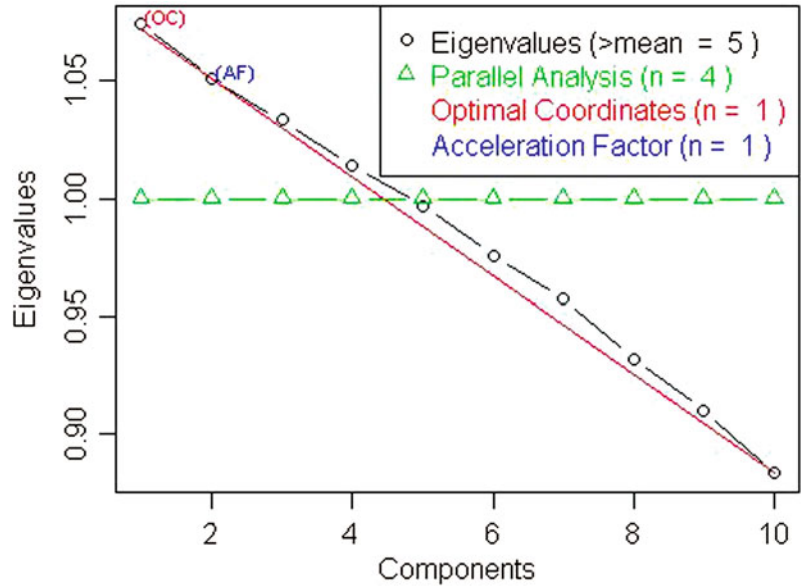| Comp	1	2	3	4	5
Dist.EP	0.09	−0.71	0.42	0.33	0.03
Elev	0.77	0.35	0.05	−0.15	−0.12
Grad	0.14	0.34	0.30	0.71	0.33
DD	−0.27	0.17	0.72	−0.36	−0.11
R.Elev	0.20	0.64	0.10	0.32	−0.43
Dist.F2	0.83	−0.36	0.22	0.04	−0.25
Dist.F3	0.90	−0.16	0.11	−0.05	−0.18
BS	0.52	−0.08	-0.64	0.12	0.01
Lith	0.57	0.11	0.13	−0.04	0.51
SS	0.49	0.18	0.10	−0.41	0.36

The number of component determination is the key step in the dimension reduction operation. Judging from scree plot (Venables 2006) in Fig. 101.17 and parallel analysis (Kong 2007) in Fig. 101.18, first five components are reasonable to represent all of the information, due to variance contribution is 76.15 % (Table 101.8). Though 80 % is better, in consideration of discreteness and randomness of the case, such value is difficult by some means. Current result is reasonable to represent most of the samples.

Using five factors to calculate, the results can be expressed as follows (Table 101.9, Fig. 101.19).

As the score coefficient stands for the relationship between ideal variables and the original variables, the coefficient has bigger weight means more contribution to the original variable. The variable has bigger absolute value in the table (Table 101.8), represents the bigger

influence. Combining Fig. 101.19 with previous analysis, the results can be concluded the following 5 components:

Comp 1: This component has biggest weight in the global variance contribution, over 30 %. In this component, elevation and distance from the faults is the two most important factor, play an important role in the seismic wave strength.

Comp 2: Represents the influence of the distance from the epicenter and elevation difference. Just as Comp 1, these factors are also close relative to seismic wave. The factor of distance from

Fig. 101.19 Plot of Correlation of main component
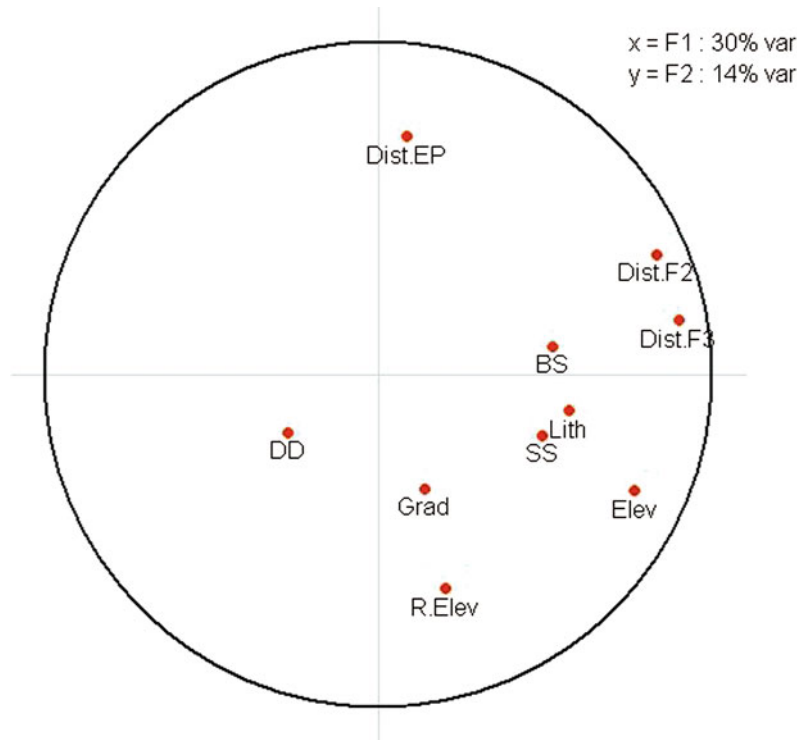
the epicenter is less effective than the distance from the fault. That is caused by the mechanism of Wenchuan Earthquake: a large scale linear rupture along the F2. The energy liberation source is not standstill. And relative elevation is also less effective than absolute elevation. Means the elevation is macroscopically more conclusiveness to the landslides. The relative elevation seems to be more specifically.

Comp 3 and 4: Dip direction of slope surface, the side of river bank and gradient of the slope represent the influence of orientation, a secondary level affects the seismic wave. Among them, the orientation seems to be more significantly.

Comp 5: Mainly about lithology, the relative elevation also has its influence.

5   Conclusions

The statistical analysis of the study area's landslides data set is helpful for understanding of the geology characteristic and its influence on the landslide distribution. These results had explained the geological phenomenon which has been seen in the field investigation. The main conclusions of this study are as follows:

(1) The distribution of the landslides in the study area is relative to the geological environment of the rock slope. 3 km along both sides of the causative fault region is a sensitive area to produce landslides during the earthquake, and the increasing number of landslides developed in the central section between F2 and F3 means the activity of F3 fault also affects the formation of landslides. The elevation amplification effect of the seismic waves will not increase without limitation, and the 200–300 m

above the main ravine is a concentrated landslides distribution area. These are key factors in the landslides distribution.

(2) The distance from the causative fault and elevation has more affection on the landslides than the others. The mechanism of the earthquake had determined the distribution of the landslides that directly triggered by the earthquake. Such fault rupture movement also means the movement of the energy liberation source, which leads to the preferred orientation of different section is different. Due to the seismic wave came from the epicenter has not been weakening significantly along the fault, the intensity of the whole study area is strong enough, which made the epicenter not so important.

(3) 30–50° is a sensitive range, especially the slope with a gradient 40–50° scale is easily damaged by the earthquake than the others.

(4) The harder rock slope seems more easily to be damaged by the seismic wave than the soft ones, and the bedding joints developed hard rocks are easier to produce landslides. Both the field investigation and the statistic reveal that in the strong shock mountainous areas, judging from space portfolio of joint plane. If there is a possibility of slide movement, it will lead to landslides in the end.

References

Huang R, Li W (2008) Research on development and distribution rules of geohazards induced by Wenchuan earthquake on 12th May, 2008. Chin J Rock Mech Eng 27(12):2585–2592

Karl Pearson FRS (1901) On lines and planes of closest fit to systems of points in space. J Philosophical Magazine 2(6):559–572

Keefer DK (1984) Landslides caused by earthquakes. J Geol Soc Am Bull 95(4):406–421

Keefer DK (2002) Investigating landslides caused by earthquakes–a historical review. Surv Geophys 23(6):473–510

Kong M, Bian R, Zhang H (2007) The application of parallel analysis in exploratory factor analysis. J Psychol Sci, Beijing

Liu H (1993) Evaluation studies of environmental geology in the reservoir area [M]. Chengdu University of Science and Technology Press, Chengdu

Miesch AT (1980) Scaling variables and interpretation of eigenvalues in principal component analysis of geologic data. J Math Geol 12(6):523–538

Papadopoulous GA, Plessa A (2000) Magnitude-distance relations for earthquake-induced landslide in Greece. J Eng Geol 58(3–4):377–386

Ripley D, Murdoch DJ (2012) R for windows FAQ & R language definition [C/OL]. http://CRAN. R-project. org/doc/FAQ/R-FAQ. html

Venables WN, Smith DM (2006) R-Guide[C/OL] The R development core team. V2. 03. 2006/04/24. http://cran. r-project. org/doc/

Xu Q, Pei X, Huang R (2009) Large-scale landslides induced by the Wenchuan Earthquake [M]. Science Press, Beijing

Xu Q, Li W (2010) Study on direction effects of landslides triggered by Wenchuan Earthquake. J of Sichuan University (Engineering science edition) 42(S1):7–14

Simultaneous Debris Flows of 13 August 2010 in the Mianyuan River Basin, China

102

Weile Li, Runqiu Huang, Chuan Tang and Qiang Xu

Abstract

The Wenchuan Earthquake triggered tens of thousands of landslides and many areas became susceptible to debris flow. From 12th to 14th, August 2010, heavy rain dropped in Wenchuan Earthquake disaster area, Sichuan province, China. The heavy rain triggered simultaneous occurrence of many debris flows in Qingping town in Mianzhu city, resulting in heavy casualty and property loss. Within the range of 4 km in Qingping Segment of Mianyuan River, 11 debris flows occurred simultaneously and the total runout deposits were about 600×10^4 m^3 mainly from Wenjia and Zoumaling gully. Field investigation indicated that the sediment supply was mainly derived from landslide deposits. The debris flows could be classified into three types, including gully erosion starting, branch gully starting and source area starting. It is suggested that Wenchuan earthquake areas are still prone to debris flows. Therefore it is important to regulate and restrict use of hazard areas as well as to arrange relocation of people currently living in areas susceptible to debris flows.

1 Introduction

Debris flow is a global phenomenon that plays an important role in the evolution of the landscape and can also cause enormous loss of life and damage to man-made structures (Jakob and Hungr 2005). Debris flows are triggered by a combination of three essential factors: sufficient available loose material, surface runoff, and steepness of the drainage channels on the slopes (Takahashi 1981). Strong earthquakes can play a major role in contributing to the accumulation of sediment supply on hillslope and in channels (Lin et al. 2006; Koi et al. 2008; Lin et al. 2008). The shaking associated with big earthquake triggers extensive landslides (Keefer 1984; Lin

W. Li (✉) · R. Huang · C. Tang · Q. Xu
State key Laboratory of Geohazard Prevention and Geoenvironment Protection, Chengdu University of Technology, 610059 Chengdu, China
e-mail: whylwl01@163.com

et al. 2006). Such co-seismic landslides produce massive loose material, accumulating in gullies, providing source material for the occurrence of debris flows. Thus, after a strong earthquake, the frequency and scale of debris flows triggered by rainfall events will increase markedly in an earthquake affected area.

The Wenchuan earthquake (Ms = 8.0; at 31.021°N, 103.367°E), with a focal depth of about 14 km, occurred beneath the steep eastern margin of the Tibetan plateau in Sichuan, China on May 12, 2008. The earthquake caused 69,227 deaths and 374,643 casualties, and also triggered over 56,000 landslides, with a total area of 811 km^2 (Dai et al. 2010), produced about 5–15 km^3 of loose material (Parker et al. 2011). The loose material caused by landslides accumulated in gullies or on the slope provided abundant material sources for the occurrence of debris flows. During the 3 years after the May 12, 2008 Wenchuan earthquake, heavy rain events have induced massive debris flows, resulting in many problems in the reconstruction of the earthquake-affected area (Tang et al. 2012). Examples of such events are the 24 September 2008 debris flows that buried the Beichuan town (Tang et al. 2008); the 7 August 2010 Zhouqu debris flows that buried the Zhouqu town, blocked the Bailongjiang river and killed over 1,400 people (Yu et al. 2010); the 13 August 2010 debris flows at Qingping that killed seven people (Xu et al. 2012); the 13 August 2010 landslides and debris flows near the epicentre that blocked the Min river and forced the river flow into the Yingxiu New Town (Tang et al. 2012). To better understand the spatial distribution and the characteristic features of debris flows triggered by the heavy rainfall on 13 August, 2010 in the Wenchuan earthquake disaster area, an intensive field investigation and a interpretation of multi-temporal images was undertaken in the Qingping section of Mianyuan river, Mianzhu County. Our primary purpose is to identify locations and distribution of debris flows that occurred in the Qingping area caused

by intense rainfall and to analyze the sediment supply condition in this area.

2 Study Area

As a branch of Tuo River, a tributary of the Yangzhe River, Mianyuan River was situated in Mianzhu County of Sichuan province. It is about 80 km far away from the northeast of epicenter (Fig. 102.1), with a length of 40 km and a basin area of 402 km^2. Its elevation difference reaches as high as 3,700 m for the highest elevation is 4,400 m, while the lowest is only 702 m. The three towns of this area including Hanwang Town, Tianchi Town and Qingping Town were all seriously damaged. The Qingping Town section of the Mianyuan river was selected as the study area. It is about 4 km long, which can be seen in Fig. 102.2.

The outcropping strata within the river basin included the strata of Sinan System, Cambrian System, Silurian System, Devonian System, Carboniferous System, Permian System, Triassic System, and loose accumulative strata of the Quaternary period in Cenozoic. The rocks included intermediate-acid granitoids; dolomites, conglomerates, sandstones, siltstones, and shales of Sinan System; sandstones, shales, phosphorite limestones and siltstones of Cambrian system; metamorphic sandstones, slates, and phyllites of Silurian system; Dolomites, quartz sandstones, and shales of Devonian system, micrite limestones and a few siltstones of Carboniferous system; limestones of Permian system; lithic sandstones and siltstones of Triassic system; and sandy clay, argillaceous sandy gravel strata of the Quaternary period (Fig. 102.2).

The central fault of Longmenshan, Yingxiu-Beichuan fault cut through the middle part of river, whereas the frontal fault, Jiangyou-Guanxian fault cut through the mountain's pass (Fig. 102.1). The study area is located in the front edge of tectonic belt in the northwest of
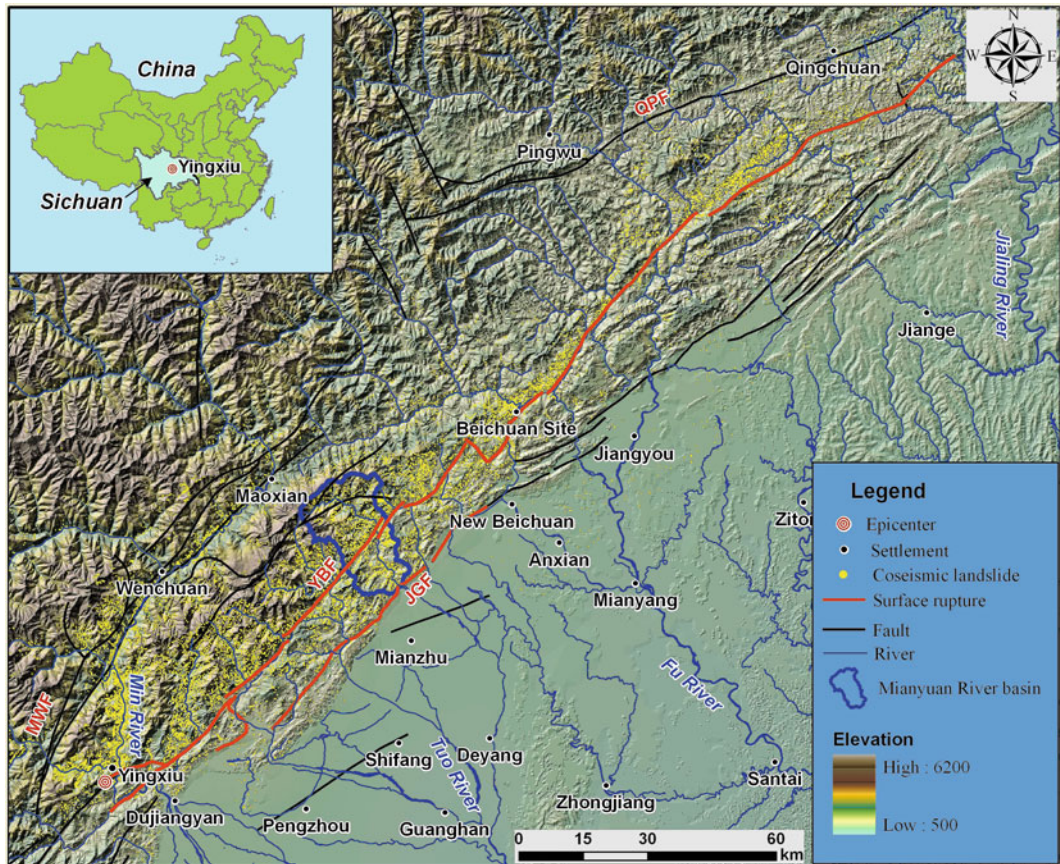
Fig. 102.1 Location map of study site, showing the faults and the landslides triggered by the Wenchuan earthquake

Sichuan basin, which is featured by intense tectonic action, developed fault, steep, straight or overturned rock strata, developed fracture and fragmental rock mass, constituting the favorable conditions for the development and occurrence of landslides.

3   The Debris Flow Event

3.1   General Characteristics of the Debris Flows

During 12th to 13th August, 2010, a storm swept over Mianyuan river basin. The accumulative rainfall was evaluated as 200 mm and the duration was 10 h (Xu et al. 2012). According to the interview, two debris flows happened firstly in Wenjia, Zoumaling gulley at 23:45 on 12 August. Subsequently, the other area surrounding the town also had another outbreak of debris flows. Finally, a deposits fan had formed and the Mianyuan river was blocked just in several seconds (see Figs 102.3b, 102.4).

During such a catastrophic debris flow event, seven people were killed, seven people missing and 33 people were injured. Subsequent survey showed that the massive amount of solid material generated by the 8.13 debris flows covered the whole town, with a covering area of 140×10^4 m^2, the length of about 4.3 km, width of 400–500 mm and average thickness of
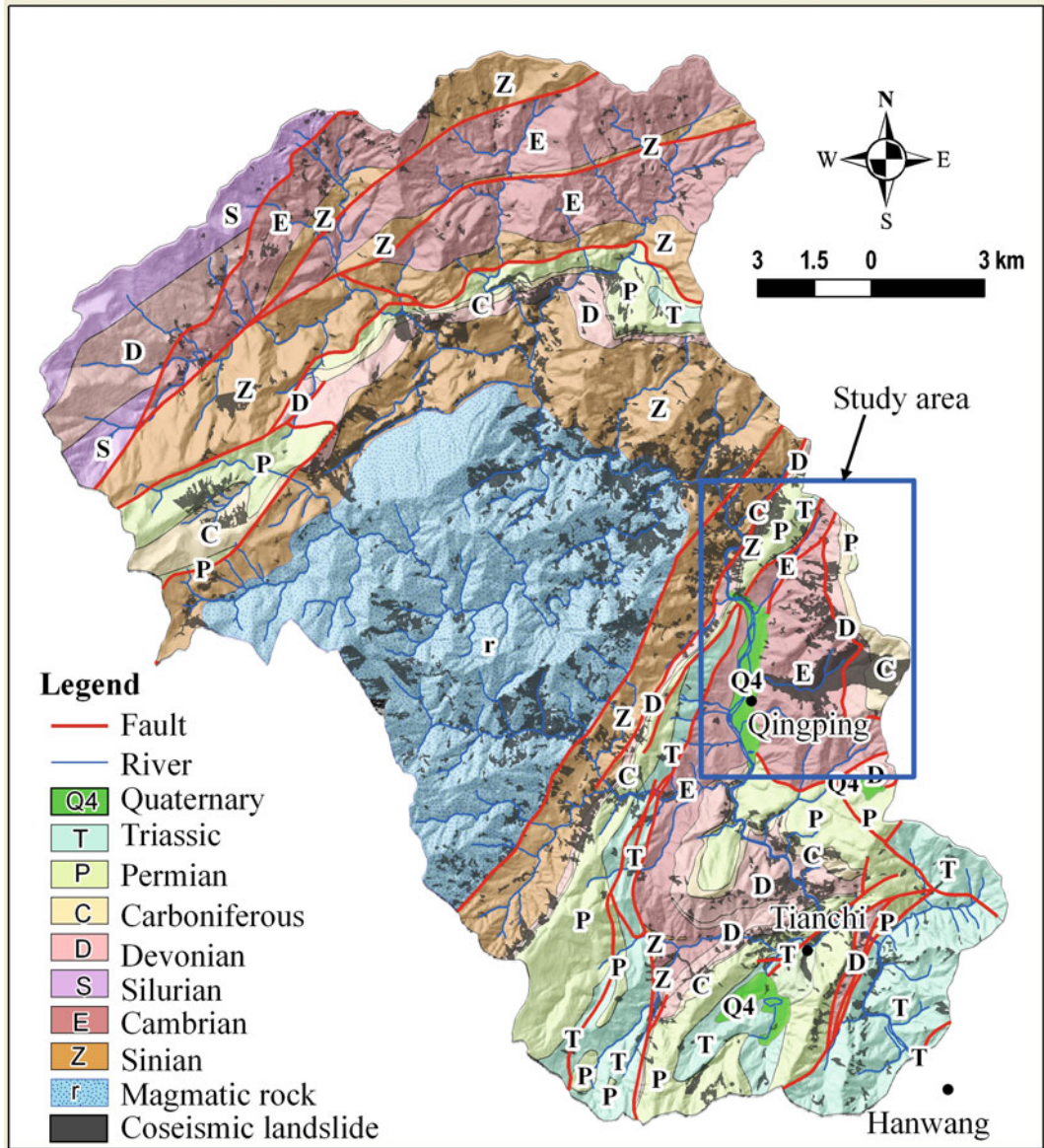
Fig. 102.2 Geological map of the Mianyuan river basin

5 m (as shown in Fig. 102.4). Three seventy nine Houses were destroyed which account for 20.9 % of the total number of households in Qingping Town.

The site survey and remote sensing interpretation results indicate that during the 8.13 heavy rainstorms, 11 debris flows in Qingping Town happened at same time (as shown in Figs. 102.3, 102.4). We had listed the specific parameters for

each debris flow gulley in Table 102.1, the total volume of loose deposit materials had reached to $564.6 \times 10^4 \ \text{m}^3$.

3.2 Wenjia Gully Debris Flow (DF06)

From Table 102.1, and Fig. 102.4, we know that Wenjia gully debris flow is the largest and
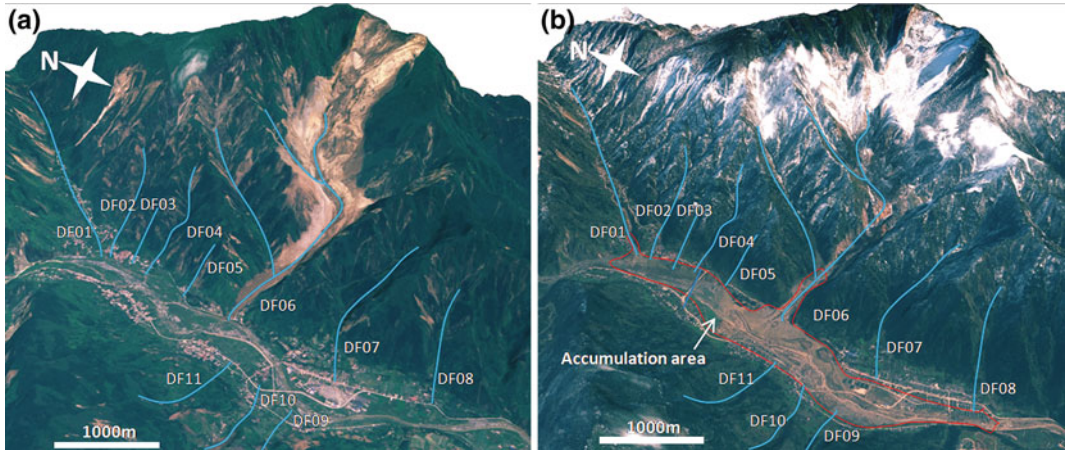
Fig. 102.3 Pre- and post- images of 13 August 2010 debris flow event in Qingping town (**a** Aerial photo taken on 18th May, 2008; **b** quickbird image taken on 13th Dec, 2010. DF01 is Zoumaling gully, DF06 is Wenjia gully and DF05 is Wawa gully)
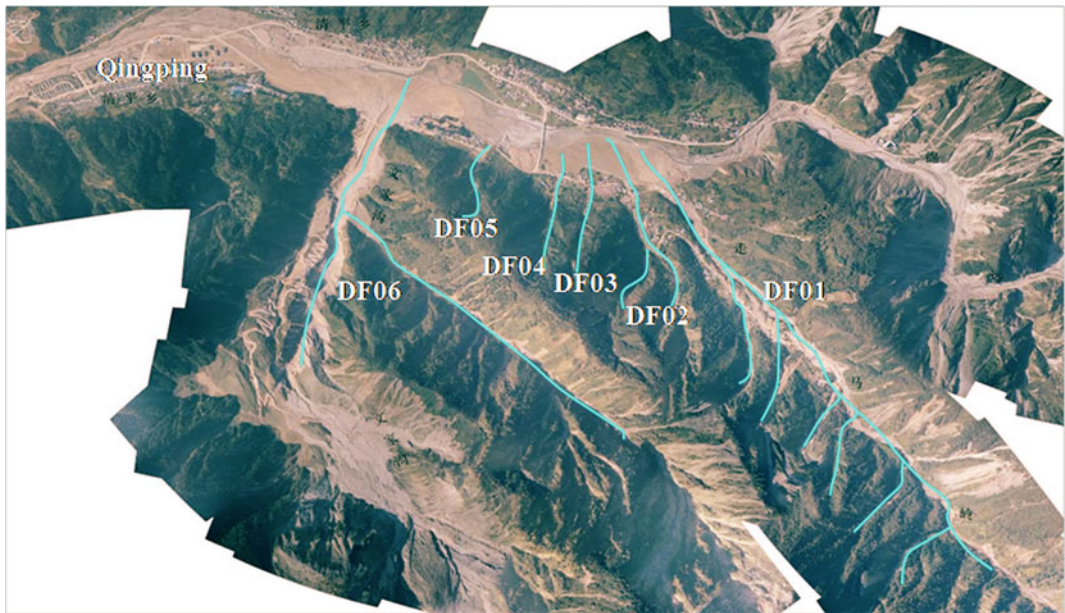
Fig. 102.4 Aerial photo of the study area taken by pilotless drones on 9 October, 2010

most serious one. Wenjia gully landslide is the second largest landslide induced by the Wenchuan earthquake (the largest landslide is Daguangbao landslide in Anxian country). When the Wenchuan earthquake happened, a limestone landslide mass with the volume of approximately $5,000 \times 10^4$ m^3 sliding from a height of 1,780–2,340 m at an extreme high speed. Subsequently, the huge amount of rock fragments reentried into the 1,300 m platform and moving along the SW direction (as shown in Fig. 102.5).

Massive deposits were mainly accumulated at the bottom of the slide source area, called Hanjia Plain ($2,260 \times 10^4$ m^3), and the 1,300 platform ($5,000 \times 10^4$ m^3) (as shown in Fig. 102.5).

Table 102.1 Feature parameter of 11 nos Qingping town debris flow gully

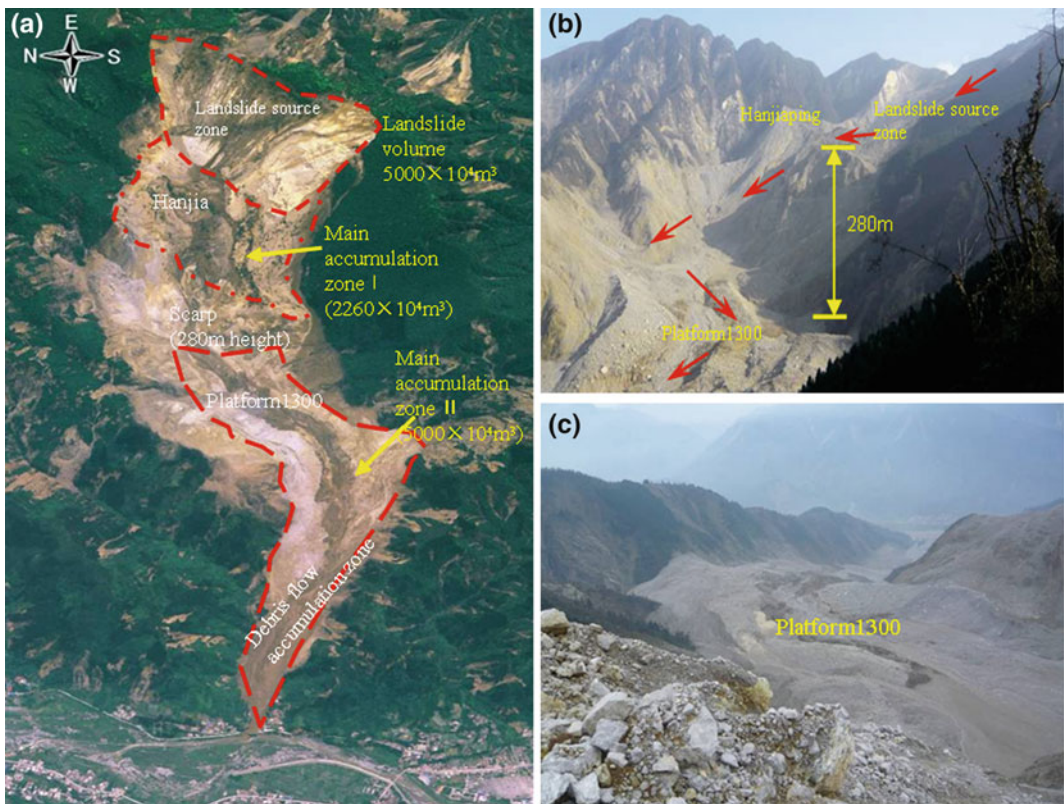| Gully code	Gully name	Basin area (km^2)	Channel length (km)	Basin relief (km)	Channel gradient (°)	Slope angle of initiation zones (°)	Debris supply (coseismic landslide) (10^4 m^3)	Volume of the 13 Aug. 2010 debris flow event (10^4 m^3)
DF01	Zoumaling	5.76	3.39	1.10	18.0	21.3	432.7	82.0
DF02	Luojia	1.64	2.91	1.40	25.7	28.0	130.8	16.0
DF03	Dongzi	0.12	0.64	0.38	30.7	33.1	4.4	1.2
DF04	Wawa	0.54	1.33	0.74	26.1	29.1	44.0	6.7
DF05	Didong	0.20	0.76	0.42	28.9	35.6	3.2	0.7
DF06	Wenjia	7.65	4.33	1.50	19.1	25.2	5000.0	450.0
DF07	Linjia	1.27	2.16	0.76	19.4	22.7	7.8	1.5
DF08	Taiyang	0.48	1.13	0.68	31.1	39.8	8.6	2.0
DF09	Maliuwan	1.01	2.06	0.80	21.2	27.4	8.3	1.3
DF10	Pujia	0.85	1.75	0.80	24.6	33.5	10.0	0.8
DF11	Caodun	0.29	1.31	0.68	27.4	34.0	10.3	2.4
Total	–	–	–	–	–	–	5656.3	564.6

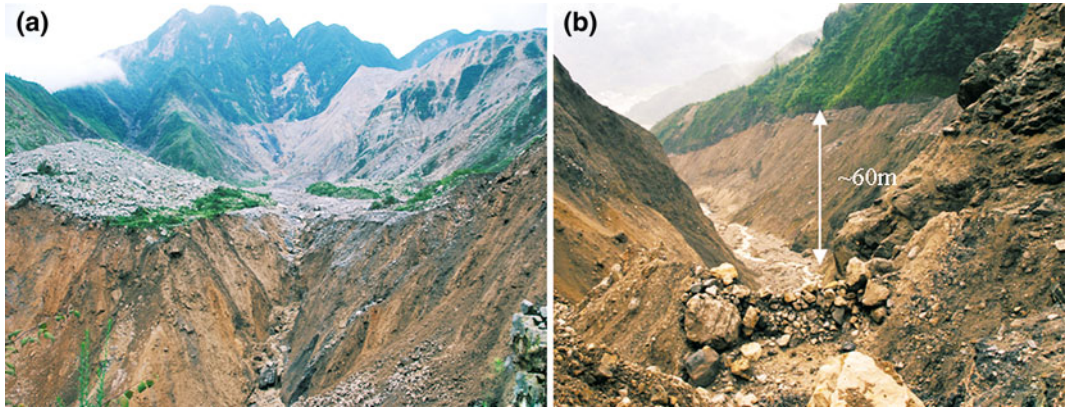**Fig. 102.5** Wenjia gully landslide triggered by the Wenchuan earthquake

Fig. 102.6 The source area **a** and the circulation area of **b** Wenjia debris flow

Field investigations show that, the loose material staying at Hanjia plain was mainly composed of large block rock, coupled with the flat terrain and its own stability even suffered several rainstorm events. Therefore, the main debris flow materials were from the 1300 platform.

Gulley gradient difference of Wenjiaogou is obviously large which ranges from 325 % at the debris accumulation area to 460 % at steep area. The catchment area is 7.8 km^2, a basin-shaped area above 1,300 platform had reached to 4 km^2. All special characteristic accompanied by the poor cemented material, which was composed by limestone powder, rock debris, breccia and chippings, made debris flow possible under rainstorm condition. The channel which developed in the landslide deposits reached a depth of 40–60 m and a width of 50–100 m caused by slope failures during the incision of the channel (Fig. 102.6).
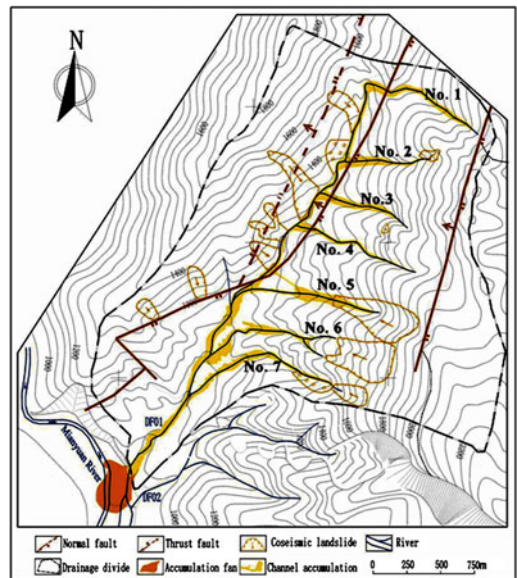
Fig. 102.7 The topographical and geological map of Zhoumalin gully

3.3   Zoumaling Gully Debris Flow (DF01)

Zoumaling gully was the second largest debris flow in the study area. The gulley gradient ranged from 85–361 %. Zoumaling gulley is composed of a main channel and seven branches (Fig. 102.7). Due to heavy rainfall on September 24, 2008, debris flows happened in the main channel and branches No. 5–7 as shown in Fig. 102.8a, while the other four branches (No. 1–4) were generated during the 8.13 debris flow events. The

preliminary investigations indicated that volume of solid debris material was about 83.5 × 10^4 m^3, and a debris fan with the length of 300 m, width of 50–400 m, thickness of 8 m was formed and blocked the Mianyang river (as shown in Fig. 102.8b.

With the characteristics of large catchment area and multi-branches, the total amount of debris deposits source from the seven branches of Zoumaling gulley had reach to 48.5 × 10^4 m^3, even surpass the material from main channel.

Fig. 102.8 The panorama pictures of Zhoumalin gully (**a** pre-8.13 debris flow event, **b** post-8.13 debris flow event)

Fig. 102.9 The panorama picture **a** and the deposition area of **b** Wawa gully debris flow

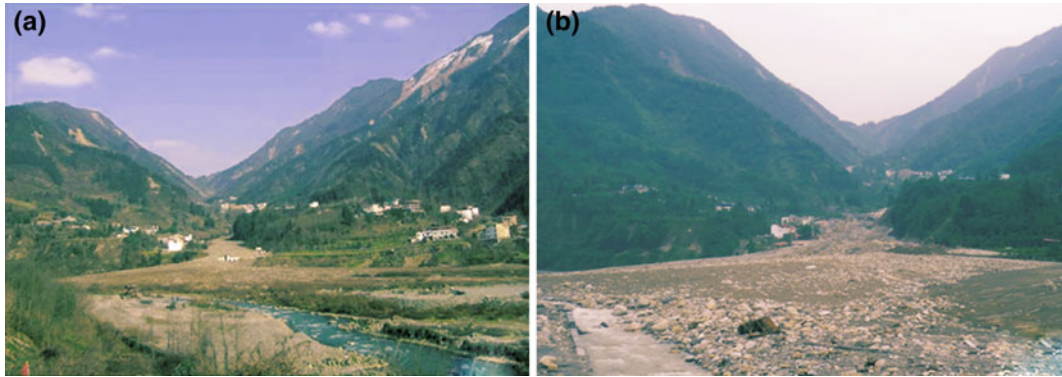Field survey results showed that, loose deposits existing at each end of branch was the primary reason of debris flow. Under the rainstorm condition, the deposits were reactivated and then transferred to the source material of debris flow. The loose deposits distributed in main gulley were seldom activated during 8.13 events. Thus, the source material was mainly generated from channel erosion. In the 8.13 rainstorm process, debris flows were triggered firstly in each branch, and then the debris material flowed into main gulley, the deposits in main gulley was activated. A "passive" debris flow occurred finally.

3.4 Wawa Gully Debris Flow (DF04)

The Wawa gully, located on the left bank of the Mianyuan River, has a catchment area of 0.67 km^2 and a channel length of 1.24 km. The upslope elevation of the gully is more than 1,630 m above sea level and the gully mouth is at 895 m ASL, its panorama can be seen clearly from Fig. 102.9(a). The investigations indicated that the volume of solid debris material transported to the deposition area by the 8.13 debris flow was about 6.7 × 10^4 m^3, with the thickness of about 4 m (Fig. 102.9b), resulting in the damage of more than ten houses and 300 m road.
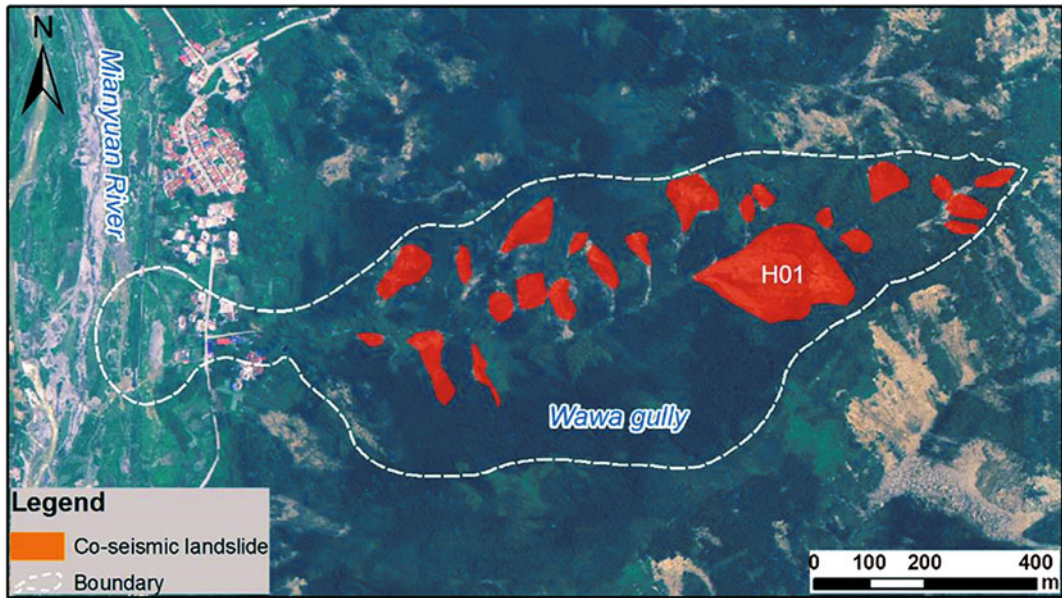
Fig. 102.10 The source area **a** and the circulation area of **b** Wawa gully debris flow
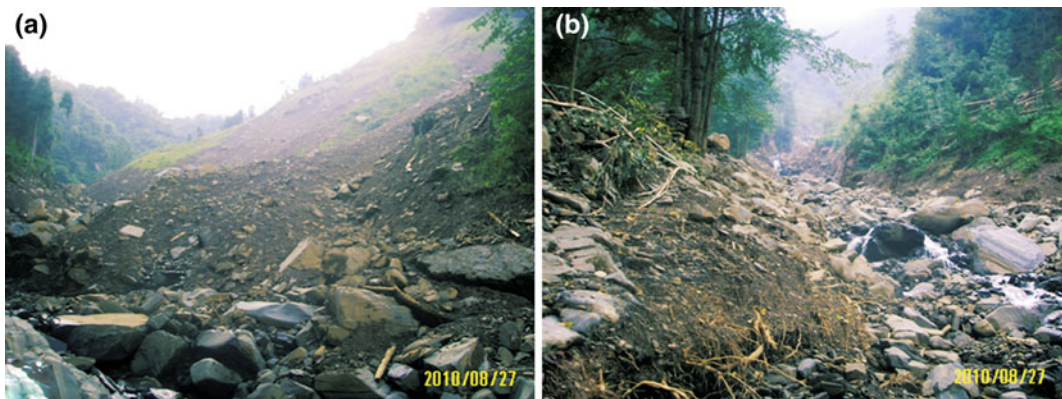
Fig. 102.11 The H01 landslide (**a**) and the circulation area of Wawa gully debris flow (**b**)

Using aerial photo taken on 23rd May, 2008, we identified 23 co-seismic landslides with a total surface area of 0.08 km^2 and the estimated total mass volume of 44×10^4 m^3 in the Wawa gully catchment area (Fig. 102.10). From Fig. 102.10, it can be seen that the largest landslide is H01 with a length of 150 m and a width of 180 m. The estimated average thickness is 11 m and the volume of H01 is estimated to be 33.7×10^4 m^3. This landslide moved downslope and blocked the drainage channel by the shaking of the Wenchuan earthquake, forming a 200 m long landslide-dam (Fig. 102.11a). In addition, the loose solid materials depositing in the gully also provided a large amount of source materials for the debris flow (Fig. 102.11b).

Field evidence showed that the 8.13 August debris flow was initiated in the erosive channel rills on the landslide deposits of H01 landslide. The overland flow of water induced by the intense rainfall eroded the loose sediment material and moved into the gully.

4   Conclusions

From observations of the debris-flow events on 13 August, 2010, the following conclusions can be drawn:

(1) The Wenchuan Earthquake triggered tens of thousands of landslides and a large number of loose soil were generated. Those loose debris caused by landslides accumulated in gullies or on the slope provided abundant material sources for the occurrence of debris flows. The intense rainfall on 13 August 2010 triggered 11 debris flows around Qingping Town and resulted in disastrous consequences to newly reconstructed communities or infrastructures. Field investigation indicates that the sediment supply was mainly derived from coseismic landslide loose materials accumulated in the gullies or on the slope.

(2) Judging by the starting mode, the debris flows could be classified into three types: the first type was gully erosion, such as Wenjia gully debris flow, which was started by undercutting the landslide accumulation in the gully of the middle and downstream area. The second type was branch gully starting. The debris flow occurred in the branch gullies first, and then merged into the main gully. The debris flow of Zoumaling gully was of this type and debris flows in the seven branch gullies on the left side occurred at the same time. The third type was source area starting, such as Wawa gully debris flow. The material sources of debris flows were distributed at the back edge of the gully. The debris flow started from the slope accumulation of back edge, the bottom tearing scouring happened at the downstream area, and then the debris flow was formed.

(3) The occurrence of debris flows triggered by the intense rainfall of 13 August indicates that the Wenchuan Earthquake areas are now still prone to debris flows. Many of the post-earthquake reconstruction projects had been done through landslide risk evaluation. However, traditional risk assessment approaches do not provide information on the magnitudes of slides or debris flows and their possible impact areas. As a result, many reconstruction works were buried repeatedly. So, it is necessary to reinforce the debris flow risk management. It is required to regulate and restrict use of hazard areas as well as to arrange relocation of people currently living in areas susceptible to debris flows and debris floods. Monitoring and early warning systems should be installed in the potentially high risk areas.

References

Dai FC, Xu C, Yao X, Lu L, Tu XB, Gong QM (2010) Spatial distribution of landslides triggered by the 2008 Ms 8.0 Wenchuan earthquake, China. J Asian Earth Sci 40(4):883–895

Jakob M, Hungr O (2005) Debris-flow hazards and related phenomena. Springer-Praxis, Chichester p 739

Keefer DK (1984) Landslides caused by earthquakes. Geol Soc Am Bull 95:406–421

Koi T, Hotta N, Ishigaki I, Matuzaki N, Uchiyama I, Suzuki M (2008) Prolonged impact of earthquake-induced landslides on sediment yield in a mountain watershed, the Tanzawa region, Japan. Geomorphology 101:692–702

Lin CW, Liu SH, Lee SY, Liu CC (2006) Impacts on the Chi-Chi earthquake on subsequent rain-induced landslides in central Taiwan. Eng Geol 86:87–101

Lin GW, Chen H, Chen YH, Horng MJ (2008) Influence of typhoons and earthquakes on rainfall-induced landslides and suspended sediments discharge. Eng Geol 97:32–41

Parker RN, Densmore AL, Rosser NJ, de Michele M, Li Y, Huang RQ et al (2011) Mass wasting triggered by the 2008 Wenchuan earthquake is greater than orogenic growth. Nat Geosci 4:449–452

Takahashi T (1981) Estimation of potential debris flows and their hazardous zones. J Nat Disaster Sci 3(1): 57–89

Tang C, Liang JT (2008) Characteristics of debris flows in Beichuan epicenter of the Wenchuan earthquake triggered by rainstorm on September 24, 2008. J Eng Geol 16(6):751–758 (in Chinese)

Tang C, Zhu J, Ding J et al (2012) An empirical estatistical model for predicting debris-flow runout zones in the Wenchuan earthquake area. Quat Int 250:63–73

Xu Q, Zhang S, Li WL (2012) The 13 August 2010 catastrophic debris flows after the 2008 Wenchuan earthquake, China[J]. Nat Hazards Earth Syst Sci 12:201–216

Yu B, Yang YH, Su YC, Huang WJ, Wang GF (2010). Investigation of the 7 (2010) Zhouqu debris flows. J Eng Geol 18(4):434–444 (in Chinese)

The Disaster Chain of Earthquake Induced Landslides

Guangqi Chen, Yange Li, Yingbin Zhang and Jian Wu

Abstract

A strong earthquake can cause a large number of landslides and avalanches, which can initiate causal disaster chains. A representative disaster chain is that a coseismic landslide can block a river and form a landslide dam, which may burst and cause a catastrophic flood. In order to disclose the serious impacts of the disaster chain induced by earthquake, this paper presented the form process of disaster chain and proposed some cutting measures. According to the developmenting process, the disaster chain from the 2008 Wenchuan earthquake was discussed. Firstly, the characteristics of both earthquake induced landslides and landslide dams are summarized in this paper. Secondly, four characteristics of debris flow also presented. Thirdly, two measures for cutting the chain are proposed, one is the landslide hazard map constructing on susceptibility analysis and the other is numerical simulation of debris flows for assessment of dangerous zone. The results of this study can help the authority make the right decision rapidly to take appropriate counter measures to reduce the risk of the disaster chain or cut it directly.

Keywords

Earthquake · Disaster chain · Landslide · Landslide dam · Debris flow

1 Introduction

Much more attention has been paid to the direct damages than the secondary disasters caused by an earthquake in studying on preventive measures against earthquake disaster. In fact, a strong earthquake can result in a series of natural disasters such as landslide, debris flow and flooding. These secondary disasters form a disaster chain as shown in Fig. 103.1.

The chain starts from earthquake induced landslides. A strong earthquake can induce a large number of landslides. Some of them can create landslide dams when their debris fill into and stop a river. When the water is impounded by a landslide dam and forms a dam reservoir

G. Chen (✉) · Y. Li · Y. Zhang · J. Wu
Department of Civil and Structure Engineering,
Kyushu University, 744 Motooka,
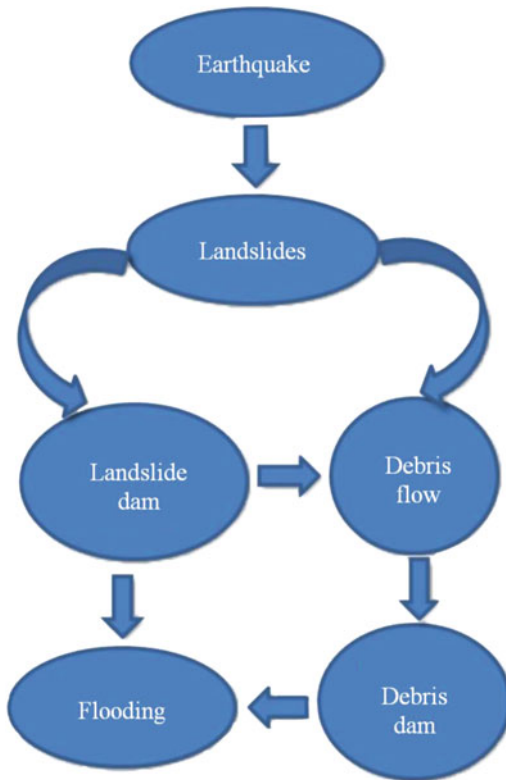Nishi-ku 819-0395, Fukuoka, Japan
e-mail: chen@civil.kyushu-u.ac.jp

Fig. 103.1 An earthquake induced disasters chain

(lake), the water level will rise. Then, the upriver district can be submerged and cause back-flooding (upstream flooding). Also, because of its rather loose nature and absence of controlled spillway, a landslide dam can easily burst catastropically. And then, the landslide dam induced debris flow can cause downstream flooding. Moreover, since the landslide deposit can be easily removed into a valley or a ravine by excessive precipitation, it is easy to form debris flows. Also, some of them can create debris dams sometimes.

Therefore, it is important to disclose the serious impacts from the disaster chain and cut the chain in an early stage. In this paper, the earthquake induced landslide disaster chain is clarified for the Wenchuan earthquake (Ms8.0). The characteristics of both earthquake induced landslide and debris flows are summarized. And some measures for cutting the chain are proposed.

2 The Characteristics of Earthquake Induced Landslides and Landslide Dams

A strong earthquake (Ms8.0) occurred at Wenchuan in Sichuan Province of China on 12 May 2008 (it is called the Wenchuan earthquake in this paper). It induced a large amount of landslides and landslide dams. It was reported that over one-third of the total lost arose from the earthquake induced landslides and their secondary disasters. Also, a lot of debris flows have occurred for a long time since the Wenchun earthquake, which caused very serious damages on the life and property in the epicenter area. We summarize the characteristics of these landslides and dams in order to mitigate the disasters in this chapter.

2.1 Characteristics of Earthquake Induced Landslides

The Wenchuan earthquake occurred in a mountainous region, where the geological and topographical features and climate conditions are very complex. The response to the ground shock was very strong. For this reason, as many as 60,104 landslides (Gorum et al. 2011) induced by the quake were identified. It has been found the following distinctive characteristics of these landslides:

(1) Large scale

Many large scale landslides were induced by the Wenchuan earthquake. More than tens of landslides with a volume are larger than 10^7 m^3 (Wu et al. 2010), and 113 landslides with the area are larger than 50,000 m^2. The largest one is the Daguangbao landslide in Anxian County, which has an area of 7,273,719 m^2 and the volume of about 8.4 × 10^8 m^3 (Chigira et al. 2010).

(2) The effect from the hanging and foot wall of the fault

It has been found that the number of landslides is quite different between the two sides of a fault. The majority of landslides are distributed in the side of the hanging wall of both the
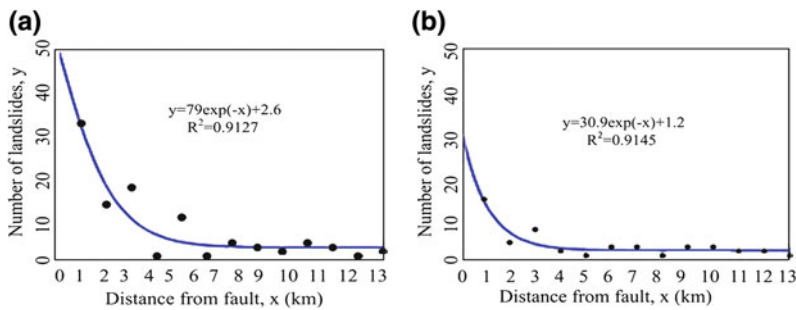
Fig. 103.2 Relationship between number of landslides and distance to fault. **a** Distance to fault for number of landslides located on hanging wall; **b** distance to fault for number of landslides located on foot wall

Yingxiu-Beichuan fault and Pengguan fault. For example, 70.8 % of the total 113 large-scale landslides occurred in the hanging wall while only 29.2 % were found in the foot wall. Therefore, there exists the so-called hanging/foot wall effect on earthquake induced landslides, which is also shown by some other studies (Xu et al. 2009a; Yin et al. 2009).

(3) The effect from the distance to the faults

Among the large scale landslides, about 70 % of landslides occured in the region of 3 km from the fault. It has been found that the number of landslides decreases by an exponential function with the distance to the fault in both hanging and foot wall (Fig. 103.2). The farthest landslide from the fault is about 12.6 km in the side of hanging wall and 13.35 km in the foot wall.

(4) Effect from the locking segment of the fault zone

The two largest scale landslides: Daguangbao landslide and Wenjiagou landslide with the area of 2,945,520 m^2 are found locating at a distance of 3.9 km from the end of the fault, although most of large-scale landslides are located in the region of less than 1 km from the fault. By examining the positions of the two landslides with the fault zone, it has be found that they are just located at the locking segment of the fault zone where high stress is believed to be concentrated and a lot of energy was absorbed by the locking of the rupture fault. Therefore, it should be notice that large scale landslides may occur at such kind of locking segment of the fault zone.

(5) Aspect effect

By examining the sliding directions of large-scale landslides along Hongshihe valley, it has been found that the aspect directions parallel to or perpendicular to the fault are dominated as shown by the rose diagram in Fig. 103.3. It is implied that the landslides are controlled by the earthquake wave propagation and the fault movement. The slopes parallel to or perpendicular to the fault are easy collapsed.

(6) The long run-out characteristic

Numerous landslides have been found with long run-out distances larger than 1000 m. This is quite different from rainfall induced landslides, which have the run-out distances mostly less than two times of the slope height (2H). For example, 95 % of the 19,035 landslides induced by rainfall are less than 50 m based on the records from 1972 to 2008 in Japan. Therefore, the long run-out characteristic should be studied in order to make the proper preventive measures in disaster prevention plan making.

2.2   Characteristics of Landslide Dams

It has reported that as much as more than 257 landslide dams were created by the Wenchuan earthquake (Cui et al. 2009). These landslide dams blocked the major large rivers. The water impounded by landslide dams created dam lakes. After the earthquake, one of the most important problems was how to evaluate the
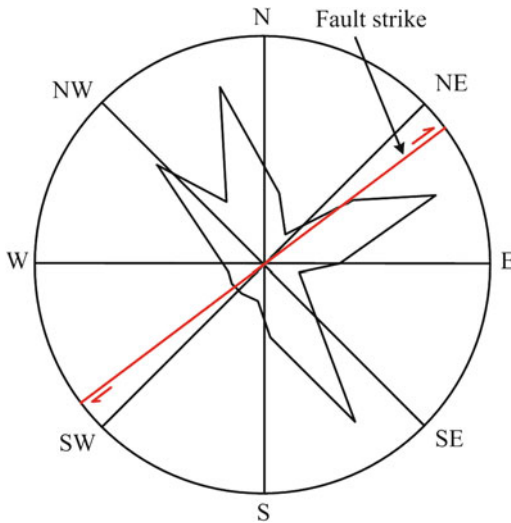
Fig. 103.3 Rose diagram showing the motion direction of large-scale landslides along the Hongshihe (after Xu et al. 2009a)

potential hazards of landslide dams in the densely populated region and rapidly to take appropriate counter measures to reduce the risk.

The largest scale landslide dam was formed by the Tangjiashan landslide. It blocked the upper portion of the Jianjiang river at a location of about 5 km from Beichuan County Town. The dam crest extended approximately 600 m across and 800 m along the valley (Xu et al. 2009b). The maximum height of the dam is about 124 m. The maximum capacity of the landslide lake was 2.4×10^8 m³, with the length of 20 km (Yin et al. 2009).

Because of its rather loose nature and absence of controlled spillway, it is feared that the landslide dam may fail catastrophically and lead to downstream flooding with high casualties. Hundreds of thousands of residents in downstream Mianyang City were evacuated to the higher locations out of the town before a temporary drainage channel was digged in the dam by Chinese government.

3 Characteristics of Debris Flows After the Earthquake

There have been many debris flows occured since the Wenchuan earthquake. The activity of

debris flows becomes obciously much higher than that before the quake. The characteristics of the debris flows caused by the quake can be summerized as the following four aspects.

(1) All the debris flows are clearly related to the earthquake. In the two years after the Wenchuan earthquake, a large number of debris flows have been occurred. For instance, in Beichuan area, there were 46 debris flows occured in range of 2869.18 km² . These debris flows were distributed along the rivers on the two sides of the earthquake fault. The sediments of landslides are the major sources of the debris flows.

(2) Most of these debris flows are of huge destructive because of their large surge peak discharge and huge volume. Since there are rich material sources after earthquake, it is easier to form a large scale debris flow. For example, the surge peak discharge of a debris flow reached to 260 m²/s, occurred in Beichuan Town on September 24th, 2008. Since the volume of the debris flow was so large to a basin with the area of 1.54 km² that the fourth floor of some buildings are covered by the deposit. Sanyanyu debris flow is another example. The volume reached to 144.20 million m³ . The debris flow carried many huge stones and destroyed houses and bridges (Tang et al. 2009).

Many preventive structures designed based on the standard of conventional debris flow were destroyed by these large scale debris flows after the earthquakes. For example, 19 check dams were destroyed by the Wenjiagou debris flow occurred in Mianzhu Qingping town area on August 13th, 2010. Figure 103.4a shows one of the check dam destroyed by the debris flow. The extreme large scale and destructive impact of the debris flow seemed beyond expectation.

(3) The critical precipitation level for triggering debris flow got decreased obviously after the earthquake. For example, the critical precipitation was identified as 37 mm before the quake, but it became lower after the earthquake in Zhouqu County areas. A 22 mm rainfall triggered a debris flow after the qauke. According to preliminary

Fig. 103.4 a The destroyed check dam in Qingping debris flow; **b** Ming river blocked at Yingxiu town by Hongchungou debris flow (photographs from Tang chuan)

analysis by Tang et al. (2009), the critical cumulative precipitation has been reduced about 14.8–22.1 %, the critical rainfall intensity per hour about 25.4–31.6 % in Beichuan County area.

(4) The debris flow dams were formed after the earthquake caused very serious disasters. The debris flows formed with the deposits of earthquake induced landslides blocked rivers, which caused flooding disasters. For example, Jianjiang river was blocked at three locations and half blocked at eight locations by debris flows during the rainstorm on September 24, 2008. Mianyuan river was blocked at two locations and half blocked at 11 locations by debris flows occurred on August 13, 2010. Ming river was blocked at one location and half blocked at five locations by debris flows occurred on August 14, 2010 (see Fig. 103.4b). Especially, the flood arisen from the debris flow dam hitted the reconstructed new Yinxiu town, the epicenter area of the quake, and caused 72 fatalities.

4   Some Measures for Cutting the Disaster Chain

In order to mitigate the disaster from earthquake, it is necessary to pay attention to the disaster chain shown in Fig. 103.1. How to cut the chain as early as possible becomes the key issue. Early detection and/or prevention is very significancy. From the view of this point, a detail hazard map of earthquake induced landslide in an area could be very helpful.

Since the landslide prone slopes are identified in the hazard map, they can be either inforced beforehand, or easily checked or confirmed whether collapsed or not immediately after an earthquake even for a wide area. Especially, if we can identify all the landslides, we can take some measures for the deposit and landslide dams at an early stage.

For a long term debris flow hazard after a strong earthquake, it is important to get all the landslides distributed in drainages, and estimate the potential debris flows as early as possible.

In this chapter, we propose a method of Landslide susceptibility analysis and making hazard map by using GIS and remote sensing technology. Also, we propose a numerical simulation method to estimate the movement behaviors of a potential debris flow.

4.1   Landslide Susceptibility Analysis and Hazard Map

A landslide susceptibility map showing the "likelihood that a phenomenon will occur in an area on the basis of the local terrain conditions" (Soeters and Westen 1996). One kind of landslide susceptibility analysis methods is so-called statistical method. It is based on landslide inventory map which provides the neccessary informations such as the spatial distribution, sizes, shapes of existing landslides. They can be obtained from field survey, air photo interpretation and literature search (Wieczorek 1984). However, it is difficult to obtain all the landslides by field investigation, especially in vastly inaccessible mountainous area.
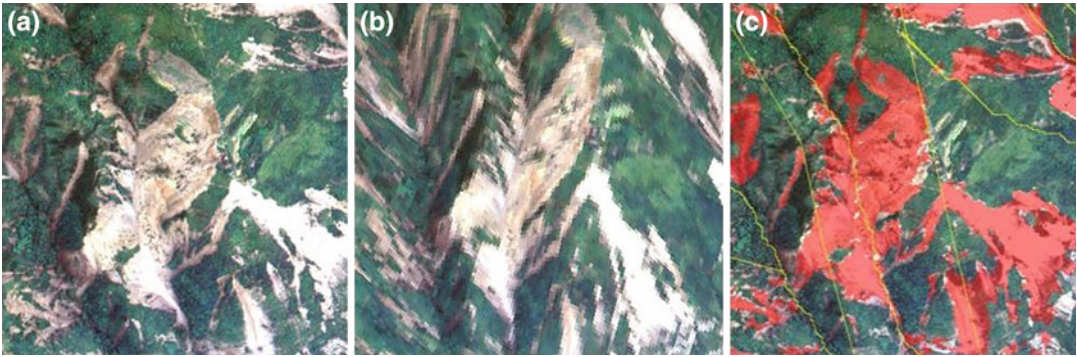
Fig. 103.5 **a** Conjoined landslides showed in the image; **b** tridimensional view of the landslides; **c** Landslide division by slope unit

Remote sensing technique,including visual and automatic interpretation, has been widely used recently to solve this problem (Cheng et al. 2004; Nichol and Wong 2005; Dymond et al. 2006; Mondini et al. 2011). However, up to now, most of the automatic method is pixel-based, which is ill-suited to detect landslides and give 'salt and pepper' noises in output. Moreover, the detection accuracy is usually suffering from mis-classification of landslides and bare ground. Therefore, we propose a new approach for automatic landslide detection combined by remote sensing (RS) and geographic information systems (GIS) technology in this study. The sub-process includes the following parts:

(1) Image segmentation

An important step before characterising diagnostic attributes of features is creation of objects that demarcate the boundary of features. This is done using image segmentation, which is a process of dividing the image into objects based on the homogeneity of the pixel values. Landslides pose a particular challenge to image segmentation because they often result in diverse spectral features due to land cover variability or illumination variations. Thus, it is impractical to attempt outlining landslides as single segments for only once. In our study, to ensure the image is rightly segmented, we suggest to select a small scale to avoid under-segmentation And then a merge procedure can be used to improve the delineation of feature boundaries based on a very fast edge-based segmentation algorithm.

(2) Image classification

Once objects have been divided and different attributes for each object have been calculated, next procedure is image classification. In order to classify the landslide candidates, training samples need to be assigned. Considering the identification accuracy is usually suffering from mis-classification of landslides and bare ground, we suggest not define the bare ground or residential areas category at first. This information can be removed later by expert-driven knowledge in GIS. For example, we can remove some plain ground by slope gradient and the residential area can be deleted by rectangular filter.

(3) Separation of detected conjoined landslides

A limitation of image interpretation need to be paid attention is, the widely used images are 2D and they cannot express certain individual landslides. As shown in Fig. 103.5a, several individual landslides are mis-detected as a single one. However, when presenting in a 3D scene supported by DEM data (Fig. 103.5b), this landslide area is supposed to be consisted of two individual landslides occurred on both sides of the valley. Therefore it is impossible to separate them only by using remote sensing technique. Slope unit (the division procedure can be seen in Xie et al. 2004) is proposed to resolve this problem (Fig. 103.5c).

Figure 103.6 is a recognition example for landslide detection using the above procedures in Hongchun gully of Wenchuan County, Sichuan Province, China. From the result, we can see almost all of the landslides are correctly

Fig. 103.6 Landslide recognition of Hongchun gully

detected. It indicates that the approach proposed in this study has ability for rapid preparation of landslide inventory maps, which is very vital to rescue and relief works after a disaster event happened, such as earthquake.

For landslide susceptibility analysis, artificial neural network (ANN) method is adapted. We successfully made the landslide susceptibility analysis in Qingchuan County of Sichuan Province, China.

The analysis was based on slope unit rather than the traditional grid units. Landslide susceptibility indexes are calculated by the following steps. (1) 885 landslides were identified by RS based on object-oriented aerial photographs interpretation in addition to field investigation. 55,899 slope units have been extracted from Arc Hydro tool and were used for the analysis. (2) The relationship of landslide distribution with selected individual causative factor is analyzed. (3) A landslide susceptibility map is made based on the ANN analysis results (Fig. 103.7).

By comparing the locations of landslides with high susceptibility zones, it can be concluded that 99 % of landslides can be predicated by the obtained ANN model, but 78.8 % of predictions would be false. On the other hand, 99.4 % of stable predications are correct and less than 0.2 % landslides would not be alarmed. In addition, the grey zone occupies 6 % of the whole area.

Therefore, the landslide susceptibility classification presented in this study is acceptable.

4.2   Numerical Simulations of Debris Flow

Prediction of a potential debris arisen from the deposits of earthquake induced landslides is an effective way to cut the earthquake induced disaster chain. It can be done by numerical simulation. Many studies on the simulation of debris flow have been done and a variety of numerical models have been proposed in the last few decades.

The forces driving the movement of debris flow depend on the collisions among the particles and plastic strength of the interstitial fluid. Different rheological schemes should be used for differrent type of flows. For examples, fluid effect can be negligible for granular flow but is dominant for mud flow. On the other hand, particle collisions are negligible for mud flow but should be considered for granular flow. Also, both particle interactions and the fluid effects should be considered in stony debris flow.

We have developed an effective tool for numerical simulation of debris flow based on GIS. The model of a catchment and sediments can be easily generated by using the powerful functions of GIS such as data collection, manipulation, visualization and analysis of the environmental data related to landslide, which makes the simulation much more efficiently and its cost more effectively (Carrara and Guzzetti 1999).

A model for muddy debris flow simulation is coupled with GIS. The depth-averaged model of debris flow as shown in Fig. 103.8 is used. The following govern equations are solved by finite difference method (FDM) using GIS gird.

$$\frac{\partial h}{\partial t} + \frac{\partial M}{\partial x} + \frac{\partial N}{\partial y} = 0 \qquad (103.1)$$

$$\begin{aligned}
\frac{\partial M}{\partial t} &+ \alpha \frac{\partial (MU)}{\partial x} + \alpha \frac{\partial (MV)}{\partial y} \\
&= -\frac{\partial H}{\partial x} gh + v\beta \left(\frac{\partial^2 M}{\partial x^2} + \frac{\partial^2 M}{\partial y^2} \right) \\
&- gh \cos \theta_x \tan \xi
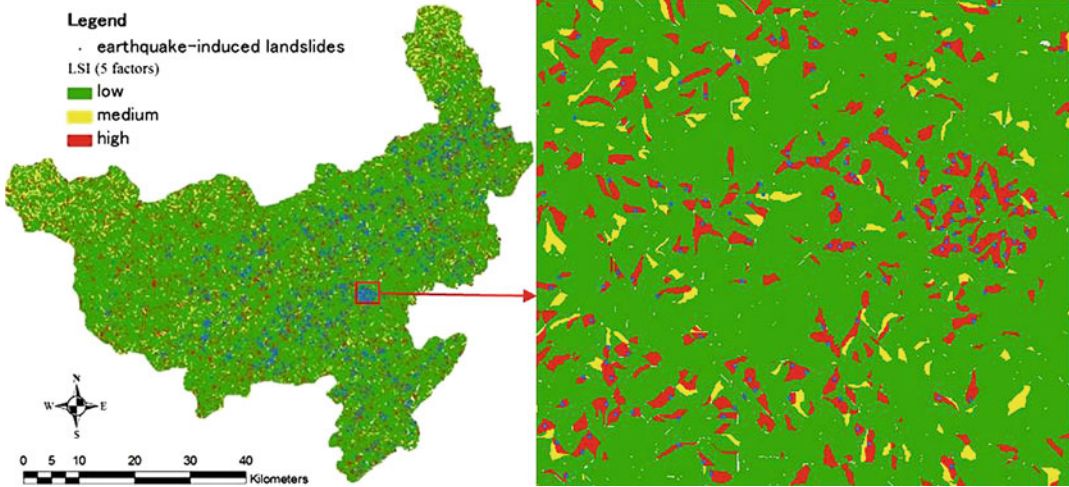\end{aligned} \qquad (103.2)$$

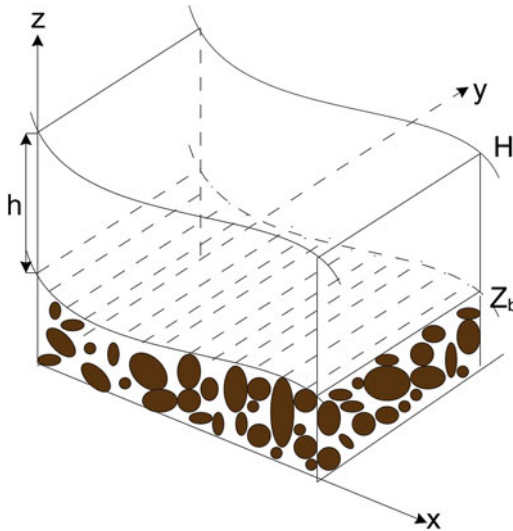**Fig. 103.7** Earthquake-induced landslide susceptibility map by using ANN analysis

Fig. 103.8 Definition sketch of coordinate systems

$$\frac{\partial N}{\partial t} + \alpha \frac{\partial (NU)}{\partial x} + \alpha \frac{\partial (NV)}{\partial y}$$
$$= -\frac{\partial H}{\partial y} gh + v\beta \left(\frac{\partial^2 N}{\partial x^2} + \frac{\partial^2 M}{\partial y^2} \right)$$
$$- gh \cos \theta_y \tan \xi \qquad (103.3)$$

where $M = Uh$ and $N = Vh$ are the x and y components of the flow flux; U and V are the x and y components of the depth-average velocity; H is the height of the free surface; h is the flow depth; θ_x and θ_y are the angle of inclination at the bed along the x and y directions, respectively; α and β are the momentum correction factors; $v = \mu/\rho_d$ is kinematic viscosity, ρ_d is the equivalent density of the debris mixture, and $\rho_d = \rho_s v_s + \rho_w v_w$, ρ_s and ρ_w are the densities of solid grains and water, v_s and v_w are the volumetric concentrations of solids particles and water in the mixture; and $\tan \xi$ is the dynamic friction coefficient.

The tool can be used to estimate the flow trajectory over the 3D complex topography, the potential runout distance and the extent of the hazard area. The results from FDM can be converted to GIS layers. Thus, The maximum flow depth, velocity distribution and inundation area can be identifed by GIS (see Fig. 103.9e). And the animation of debris flow can be easily made (see Figs. 103.9a–d). Comparing the simulated results with the actual event, it has been found there is a good agreement with each other. Therefore, the developed tool has been shown applicable and useful for predicting the movement of potential debris flow arisen from earthquake.
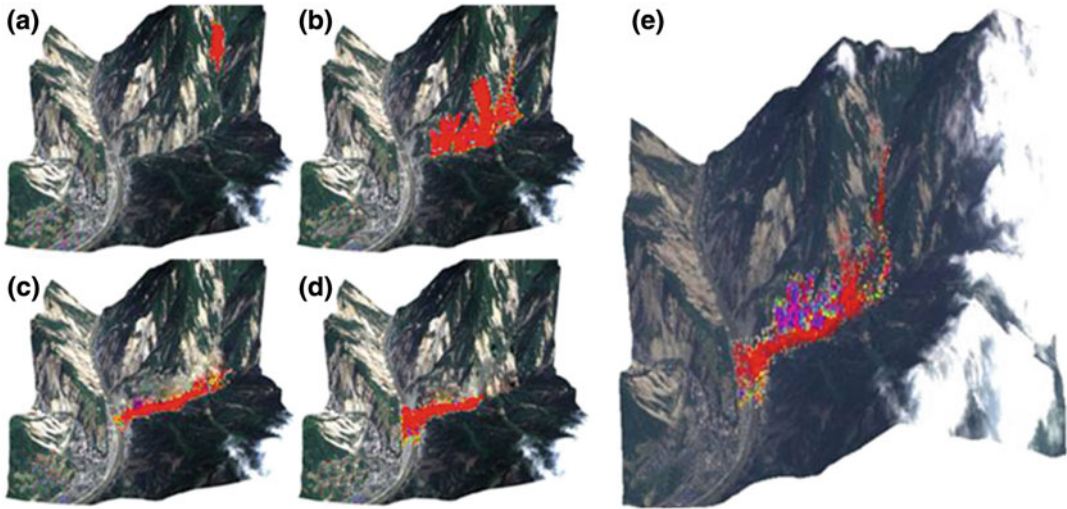
Fig. 103.9 The movement of the debris flow **a** for t = 10 s, **b** t = 76 s, **c** t = 120 s, **d** t = 150 s and **e** for the distribution of the maximum depth of Hongchungou debris flow

5   Conclusions

A strong earthquake can induce a chain of disasters. By discussing the disaster chain from the 2008 Wenchuan earthquake, we can obtain the following conclusions:

(1) A strong earthquake can induce (a) a huge number of landslides (e.g. 60,104 landslides induced by the quake) (b) many large-scale landslides (area larger than 50,000 m^2); (c) a large number of landslide dams.

(2) The major characteristics of earthquake induced landslides are (a) landslides in the hanging wall are more than the footing wall; (b) most landslides are located in the region of 3 km from the fault; (c) large-scale landslide can occur at the locking segment of the rupture fault; (d) there is a clear relationship between the sliding direction of landslides and the fault strike; (e) large quantities of long run-out landslides occurred; (f) regression formulas of run-out distance have been obtained based on the areas and volumes of landslides; and (g) a large

number of landslide dams (more than 257) was formed.

(3) The chance of debris flow occurence after a strong earthquake becomes much high. The characteristics of the debris flows arising from the 2008 Wenchuan earthquake can be summarized as: (a) most of debris flows have large surge peak discharges and huge volumes; (b) The critical precipitation for triggering debris flow became lower; and (c) many rivers were blocked by the debris flows and serious damages have been caused by the debris dams.

In order to cut the earthquake induced disaster chain in a early stage, the following two preventive measures have been proposed.

(1) The approach of susceptibility analysis has been proposed: (a) making a landslide inventor map by using RS techniques; (b) making susceptibility analysis by using ANN mothod. A new approach of RS with object-based analysis method has been developed for identifying landslides. The susceptibility analysis is carried out based on slope units rather than the traditional grids, which can be done by using

GIS. The relationship of landslide distribution with individual causative factor has been investigated. It has been found that slope gradient, elevation, slope range, the distances to the fault, the distances to a stream have contributed to landslides while specific catchment area, slope aspect and lithology have no clear relationship. A susceptibility map has been made for analysis of the earthquake induced landslides in Qingchuan County.

(2) An effective tool of simulating debris flow has been developed. The tool can be used to estimate the flow trajectory over the 3D complex topography, the potential runout distance and the extent of the hazard area. A practical simulation has been carried out and it has been shown that the developed tool is effective and useful for estimating the movement behaviours of a potential debris flow arising from a strong earthquake.

References

Carrara A, Guzzetti F (1999) Use of GIS technology in the prediction and monitoring of landslide hazard. Nat Hazards 20:117–135

Cheng KS, Wei C, Chang SC (2004) Locating landslides using multi-temporal satellite images. Adv Space Res 33:296–301

Chigira M, Yagi H (2006) Geological and geomorphological characteristics of landslides triggered by the 2004 Mid Niigta prefecture earthquake in Japan. Eng Geol 82(4):202–221

Cui P, Zhu Y, Han Y, Chen X, Zhuang J (2009) The 12 May Wenchuan earthquake-induced landslide lakes: distribution and preliminary risk evaluation. Landslides 6(3):209–223

Dymond JR, Ausseil AG, Shepherd JD, Buettner L (2006) Validation of a region-wide model of landslide susceptibility in the Manawatu-Wanganui region of New Zealand. Geomorphology 74:70–79

Gorum T, Fan X, Westen C, Huang R, Xu Q, Tang C, Wang G (2011) Distribution pattern of earthquake-induced landslides triggered by the 12 May 2008 Wenchuan earthquake. Geomorphology. doi: 10.1016/j.geomorph.2010.12.030X

Martha TR, Kerle N, Jetten V, van Westen Cees J, Kumar KV (2010) Characterising spectral, spatial and morphometric properties of landslides for semi-automatic detection using object-oriented methods. Geomorphology 116:24–36

Mondini AC, Chang KT, Yin HY (2011) Combining multiple change detection indices for mapping landslides triggered by typhoons. Geomorphology 134:440–451

Nichol J, Wong MS (2005) Satellite remote sensing for detailed landslide inventories using change detection and image fusion. Int J Remote Sens 26:1913–1926

Soeters R, Van Westen CJ (1996) Slope stability recognition, analysis, and zonation application of geographical information system to landslide hazard zonation. In: Turner AK, Schuster RL (eds) Landslides: investigation and mitigation. Sp.-Rep. 247, Transportation Research Board, National Research Council. National Academy Press, Washington, pp 129–177

Tang C, Zhu J, Li WL (2009) Rainfall triggered debris flows after Wenchuan earthquake. Bull Eng Geol Environ 68:187–194

Wieczorek GF (1984) Preparing a detailed landslide-inventory map for hazard evaluation and reduction. Bull Assoc of Eng Geologist 21:337–342

Wu S, Wang T, Shi L, Sun P, Shi J, Li B, Xin P, Wang H (2010) Study on catastrophic landlsides triggered by 2008 great Wenchuan earthquake, Sichuan, China. J Eng Geol 18(2):145–159 (in Chinese)

Xie MW, Esaki T, Zhou GY (2004) GIS-based probabilistic mapping of landslide hazard using a three-dimensional deterministic model. Nat Hazards 33:265–282

Xu Q, Fan X, Huang R, Westen C (2009a) Large-scale Landslides Induced by the Wenchuan earthquake. Science Press, Beijing (in Chinese). ISBN:978-7-03-026906-5

Xu Q, Fan X, Huang R, Westen C (2009b) Landslide dams triggered by the Wenchuan earthquake, Sichuan Province, south west China. Bull Eng Geol Environ 68(3):373–386

Yin Y, Wang F, Sun P (2009) Landslide hazards triggered by the 2008 Wenchuan earthquake, Sichuan, China. Landslides 6(2):139–151

Post-seismic Surface Processes in the Zoumaling Gully in the Qingping Area, Southwestern China: Landslide, Debris-flow and Sediment Delivery

104

Hong-zhi Chen, Zhi-man Su, Jian-zhong Wang
and Zhi-quan Chen

Abstract

The Zoumaling Gully locates about 80 km to the northeast of the epicenter of the M8.0 Wenchuan Earthquake, with the earthquake rupture, Yingxiu-Beichuan fault, running through the left bank of the gully. Huge amounts of co-seismic landslide debris were presented on the hillslopes and channels. The Zoumaling Gully was once a gingko scenic park where soil and water were conserved well and no large mass movement had occurred prior to the Wenchuan Earthquake in recent tens of years. Regarding that the surface processes in the Zoumaling Gully is totally different before and after the Wenchuan Earthquake, the Zoumaling Gully was selected as an example in this present study to examine the impact of earthquake on subsequent sediment yield and delivery. Field observations from May 2008 to May 2011 were conducted to record the post-seismic landslide and debris flow activities. The influencing factors of the erosion and deposition on the surface of the gully were analyzed, in order to provide evidences in supporting the reconstruction planning in the earthquake-affected area. Special attention was paid to the debris flow events occurred in the years of 2008 and 2010. Comparative analysis of the events revealed that the mean gradient of main channel and sub-channel and the rainfall intensity played important roles in the transportation of debris from sub-channel, which resulted in sediment storing in the main channel or sediment transporting to the inhabited alluvial fans and the Mianyuan River to form a debris dam and produce inundation.

H. Chen · J. Wang · Z. Chen
Chongqing Shutong Geotechnical Engineering
Co.Ltd, 610041 Chengdu, China

Z. Su
Key Laboratory of Mountain Hazards and Surface
Process, CAS, 610041, Chengdu, China

Z. Su (✉)
Institute of Mountain Hazards and Environment,
CAS, #0.9, Block 4, Renminnanlu Road,
610041 Chengdu, China
e-mail: szmiyqq@imde.ac.cn

1 Introduction

Intense seismic shaking can not only trigger co-seismic landslides but also subsequent rainfall-induced debris flows and frequent sediment delivery (Lin et al. 2003, 2006; Tang et al. 2009) because co-seismic landslides greatly increase the volume of sediment material available to be mobilized. However, few studies deal with the post-seismic mobilization of unstable geological materials that are frequently observed in the hillslopes after an earthquake (Chang et al. 2006). Thus, this paper mainly concerns with the study of post-seismic surface processes observed in the Zoumaling Gully area.

The Zoumaling Gully locates about 80 km to the northeast of the epicenter of the Ms 8.0 Wenchuan Earthquake, with the earthquake rupture Yingxiu-Beichuan fault running through the left bank of gully. Huge amounts of co-seismic landslides were triggered on the hillslopes and channels. After the Wenchuan earthquake, several debris flows have been triggered in the Zoumaling Gully. The two debris flows, happened on Sep. 24, 2008 and Aug. 13, 2010, rushed out the gully mouth, buried villages and roads, and extruded and rechanneled the Mianyuan River located at the gully mouth. Furthermore, several debris flows occurred on the tributary of the Zoumaling Gully. The debris accumulated, and raised the bed of the main gully.

The Zoumaling Gully was once a gingko scenic park where soil and water were conserved well and no large mass movement had occurred prior to the Wenchuan Earthquake in recent tens of years. After the earthquake, the mass movements frequently occurred, e.g., landslides, debris flows, and sediment transports, and the vegetation was destroyed heavily. Local residents suffer more and more critical threat on the survival and development. The largest debris flow with an volume of 8.0×10^5 m^3 happened on Aug. 13, 2010, blocking rivers and burying houses. Regarding that the surface processes in the Zoumaling Gully is totally different before and after the Wenchuan Earthquake, the Zoumaling Gully was selected as an example in this present study to examine the impact of earthquake on subsequent sediment yield and delivery.
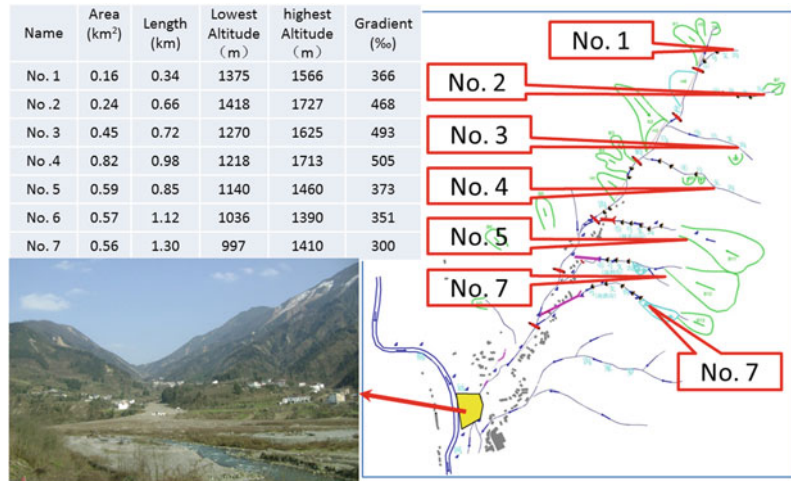
2 Summary of the Zoumaling Gully

The Zoumaling Gully is with a watershed area of 5.7 km^2, and a length of 3.5 km and a mean gradient of 145 ‰ of the main gully. From the gully mouth to source area, the change in the gully gradient can be separated into four parts: i.e., 90–140–210–620 ‰. The altitude difference is 1,140 m, from the top of the watershed (Alt. 2,044 m) to the estuary (Alt. 904 m) of the Mianyuan River. Cutting depth of the gully is general 10–30 m, or deeper in some places; the slope gradient of the gully bed is general 150–180 ‰, steeper than 400 ‰ near the source area. The inclination of the slope along the valley is 35–55°.

There are seven main tributaries in the Zoumaling Gully. The distribution and terrain parameter of each tributary are shown in Fig. 104.1. The mean slope gradient of the main gully is relative small; the area of the gully on left bank near the gully mouth is larger.

This region originally was natural forest conservation district with vegetation coverage of more than 85 %. The vegetation dominated by shrubs, firs, etc. Due to the earthquake, a number of slumped mass occurred along the Zoumaling Gully and its tributaries. These slumped mass rapidly moved down, and destroyed the vegetation on the region. They soon transformed into rock debris, filling the gully and destroying the vegetation along the gully.

Fig. 104.1 Distribution and terrain parameter of each tributary in the Zoumaling Gully

Name	Area (km²)	Length (km)	Lowest Altitude (m)	highest Altitude (m)	Gradient (‰)
No. 1	0.16	0.34	1375	1566	366
No .2	0.24	0.66	1418	1727	468
No. 3	0.45	0.72	1270	1625	493
No.4	0.82	0.98	1218	1713	505
No. 5	0.59	0.85	1140	1460	373
No. 6	0.57	1.12	1036	1390	351
No. 7	0.56	1.30	997	1410	300

3 Co-seismic Landslide and Post-seismic Landslide in the Zoumaling Gully

A number of collapses and landslides occurred along the Zoumaling Gully and its tributaries on May. 12, 2008. A great quantity of loose deposit accumulated on the gully and blocked the gully. The major landslides are listed in Table 104.1. Landslides on the left bank were larger in number and scale because the fault runs the left bank of the main gully. The landslides along the tributaries (No. 5–7) slid and deposited on the upper and middle parts of the gully. The thickness of loose deposits was in the range of 5–8 m, and thus the gully was buried. After the earthquake, the Zoumaling landslide further slid due to the rainfall, and some landslides were divided into several smaller ones.

4 Post-seismic Debris Flow and Sediment Delivery in the Zoumaling Gully

Debris flow has never occurred in the Zoumaling Gully and its tributaries before the Wenchuan earthquake. However, many debris flows events have successively occurred since the earthquake.

After a heavy rain on Jun. 24–25, 2008, loose deposits on the tributaries (No. 5, 6, and 7) were rushed out, and a debris flow formed.

On Jul. 24–25, a heavy rain occurred. The deposits on the main gully again transported, and accumulated on the gully mouth.

On Sep. 22–24, 2008, a large rainfall-induced debris flow occurred in the Zoumaling Gully. On Sep. 24, the precipitation on that day was up to 88 mm. The debris flow rushed out the gully mouth. The deposits with a volume of 3×10^5 m³ covered an area of 200 m × 400 m with a mean thickness of 4 m. The Mianyuan River changed its course due to the great quantity of deposits. A section of river valley with 250 m wide and 200 m long was wholly raised by 2–3 m, and the river way only 20–30 m wide was not buried. A three-floor building was completely buried (Fig. 104.2). A mass of materials existed on the main gully and its tributaries.

On Aug. 12–13, a heavy rain occurred in Qingping Village, Mianzhu City. The precipitation was 227.5 mm/day, and the maximum precipitation was up to 70 mm/h. Debris flows occurred along the Zoumaling Gully and its tributaries, especially for the middle and lower reaches of the main gully and tributaries (No. 5, 6, and 7). The existing loose deposit was cut deeply and transported with the flood, and a large debris flow occurred. This debris flow,

Table 104.1 Landslide sites in the Zoumaling Gully

Position	Amount of debris ($\times 10^4$ m^3)	Position	Amount of debris ($\times 10^4$ m^3)
Right bank of upstream in the main gully	18	Right bank of downstream in the main gully	4.3
Right bank of upstream in the main gully	32	Right bank of downstream in the main gully	2
Right bank of upstream in the main gully	18	Source area in tributary No. 1	3.5
Right bank of upstream in the main gully	16	Left bank in tributary No. 2	1.2
Right bank of mid-upstream in the main gully	22	Left bank in tributary No. 3	0.8
Right bank of midstream in the main gully	7	Left bank in tributary No. 4	0.4
Right bank of midstream in the main gully	9	Source area in tributary No. 5	43.5
Right bank of midstream in the main gully	7.6	Source area in tributary No. 6	18.5
Right bank of midstream in the main gully	24	Source area in tributary No. 7	6
Right bank of midstream in the main gully	18		
Subtotal	251.8		

Fig. 104.2 Debris flow in the Zoumaling Gully on Sep. 24, 2008

with a volume of 8.35×10^5 m^3, changed
again the course of the Mianzhu River and raised
the river bed, forming a fan with a length of
300 m, a width of 50–400 m, and a thickness of
8 m (Fig. 104.3). Houses located in the mouth of
the main gully and its tributaries were partly
buried, and a part of a road with 2.0 km was
destroyed.

After the 8.13 debris flow event, the channels
were eroded deeply, both in the main channel
and most of the tributaries.

- The Zoumagou Gully: The gully was cut by
  1–2 m along the upper and middle part,
  basically along the middle part of original
  river way.
- Tributaries No. 1–4: Debris flows have never
  occurred along the four tributaries. The heavy
  rain triggered collapses at each side of the
  gully. These collapses provided material
  source for debris flows. Few of them trans-
  ported into the main gully, and majority
  deposited on the gully.
- Tributary No. 5: After the event, the middle
  and lower part of the gully was eroded and cut
  by 5–7 m, and outcrop appeared locally. The
  diameter of the biggest boulder was up to
  3.5 m. A few of deposits accumulated on the
  gully mouth, with a thickness of $8 \sim 10$ m.
  The maximum thickness was as much as 15 m.
  Majority of the deposits transported into the
  main gully, and became one of the main
  material sources for the Zoumaling debris flow.

- Tributary No. 6: The width of the tributary was
  originally 5–8 m. After this event, the middle
  and lower part of the gully was widened to 12–
  20 m, and the depth was 3–5 m. A part of
  deposits accumulated on the gully mouth, and
  rest converged into the main gully and accu-
  mulated on the mouth of the main gully. These
  deposits were one of the main material sources
  for the Zoumaling debris flow.
- Tributary No. 7: The original gully was cut
  down by 2–3 m, and was widen by 5 m. Most
  of deposits accumulated on roads and part
  converged into the main gully.

5   Engineering Countermeasure in the Zoumaling Gully

As mentioned above, the three tributaries near
the gully mouth were the main active regions for
sediment yield and transport of the gully based
on activities of earthquake-induced landslides,
debris flows, and sediment transport. After the
Wenchuan earthquake, the three tributaries pro-
vided a loose materials with a volume of
6.8×10^5 m^3, accounting for 93 % of total mass
from the seven tributaries. If the intensity of the
rainfall was weak, the loose deposits was accu-
mulated on the main gully due to the gentle
gradient of the main gully, and further raised the
gully bed and reduced the gradient. In other
hand, if the intensity of the rainfall was strong,

debris flows along tributaries rushed out the gully mouth, and converged into the main gully. Then, the debris flows eroded and entrained the loose existing deposits accumulated on the main gully, and the scale of the debris flows was further enlarged.

To control sediment transport and mitigate disaster of debris flows on the Zoumaling Gully, an engineering measure was proposed. The measure, including four sandbars and five check dams on the upstream of the main gully, three sandbars on the middle stream, one resistant wall on the left bank of the downstream, and one debris flow silting ground on the mouth gully. To guarantee the safety of inhabitant on the right bank of the downstream, an embankment was built. A sandbar and five check dams were built on the upstream of the tributary (No. 5) for soil conservation, and a draining channel of 185.7 m was fixed on the outlet of the downstream. For the tributary (No. 7), four check dams were built on the upstream for soil conservation, and a drainage channel of 334.55 m was mounted on the outlet of the downstream. Furthermore, draining channel were fixed on the small gully of the downstream for the safety of inhabitants and farmland on both sides. The measure has been completed in 2011, and was successfully against torrential floods in 2011.

6   Conclusions

- The Zoumaling Gully is in a new active period of dynamic surface process after the Wenchuan earthquake, and landslides, debris flows, and sediment transport occurred frequently. Co-seismic landslides provided abundant material sources for dynamic surface process, and the seven tributaries on the left bank was an important material source because the fault passed through the left bank.

- If hydraulic conditions were not enough, the loose deposits firstly accumulated on the main gully due to the gentle gradient of the main gully, and thus further raised the gully bed and reduced the gradient. When the hydraulic conditions were sufficient, however, debris flows along tributaries rushed out the gully mouth, and converged into the main gully. Thus, the debris flows eroded and entrained the loose existing deposits accumulated on the main gully, and the scale of the debris flows was further enlarged.

- The Zoumaling Gully was once a gingko scenic park with well soil and water conservation condition. Therefore, it is reasonable to retain the debris and sediment in the gentle part of main gully by checking dams and the retained soil material which is believed to become consolidated in a near future.

References

Chang KJ, Taboada A, Chan YC, Dominguez S (2006) Post-seismic surface process in the Jiufengershan landslide area, 1999 Chi–Chi earthquake epicentral zone, Taiwan. Eng Geol 86:102–117

Lin CW, Shieh, CL, Yuan BD, Shieh YC, Liu SH, Lee SY (2003) Impact of Chi–Chi earthquake on the occurrence of landslides and debris flows: example from the Chenyulan River watershed, Nantou, Taiwan. Eng Geol 71:49–61

Lin CW, Liu SH, Lee SY, Liu CC (2006) Impacts on the Chi–Chi earthquake on subsequent rain-induced landslides in central Taiwan. Eng Geol 86:87–101

Tang C, Zhu J, Li WL (2009) Rainfall-triggered debris flows following the Wenchuan earthquake. Bull Eng Geol Environ 68:187–194

Study on the Breakage Mode and Risk Analysis of Tangjiashan Barrier Dam

Wen-jie Xu, Yu-xin Jie and Yu-zhen Yu

Abstract

The Wenchuan Earthquake (Ms 8.0), which happened in Sichuan, China on May 12, 2008, marked a major natural disaster in the human history. In the seismic disastrous area of Wenchuan Eearthquake, over 100 barrier dams were generated due to landslides and river blocking. Taking Tangjiashan barrier dam as an example, which had the most dangerous and the largest reservoir storage capacity of barrier lake in this earthquake event, this paper carries out a systematic study on the breakage mode and the disasters in this breakage process. Through the analysis, this paper concludes that the overflow and overtopping of Tangjiashan barrier dam is the most likely breakage mode. The analysis results may provide references to the implementation of disaster prevention and mitigation in the future similar ones.

1 Introduction

Earthquake is an important triggering factor of the landslides disasters. An earthquake of a higher magnitude may induce a huge number of geological hazards within the scope of 100,000 km^2 (Keefer 2000; Keefer and Larsen 2000). For example, Northridge earthquake (Ms 6.5), which happened in America in 1944 had triggered 11,000 landslide disasters within an area of more than 10,000 km^2 and caused the economic loss to \$30 billion (Parise and Jibson 2000). Luhuo Earthquake (Ms 7.9), which happened in Sichuan, China in 1973 triggered 137 landslides of various scales and caused a casualty of 2,175 (Yang 2002). Wenchuan Earthquake (Ms 8.0), which happened in Sichuan, China on May 12, 2008, marked a major natural disaster in the human history. It not only induced a large number of geological disasters, such as

W. Xu · Y. Jie · Y. Yu (✉)
State Key Laboratory of Hydroscience and Engineering, Tsinghua University, 100084, Beijing, China
e-mail: yuyuzhen@tsinghua.edu.cn

W. Xu
e-mail: wenjiexu@tsinghua.edu.cn

Y. Jie
e-mail: jieyx@tsinghua.edu.cn

Table 105.1 Physical and mechanical parameters of Tangjiashan barrier dam

Materials	Density (g/cm³)	Shear strength		Permeability (cm/s)	Allowable hydraulic gradient
		$\varphi(°)$	c (kPa)		
Gravel soil	1.9	32	30	5×10^{-4}	0.35–0.5
Block gravel soil	2.2	35	30	5×10^{-2}	0.4–0.6
Isolated gravel soil (quasi-layered structure rock)	2.4	43	50	5×10^{-3}	–
Grayish black silty gravel	1.8	30	10	1×10^{-5}	0.2–0.3

landslides and dilapidations, but also formed 104 barrier dams because of landslides and river blockings in the seismic disastrous areas. And so large quantity was rarely reported in history.

Landslide and river blocking hazards happen occasionally in the mountainous areas around the world and usually cause a great damage. This kind of landslides not only destroys nearby housing constructions, farmlands, highways, etc., but also blocks the river and forms barrier lakes. On the one hand, the formed barrier lakes have great potential threat to the residents downstream the reservoir area and the occurrence of geological disasters. On the other hand, the breakage of the barrier dam will bring a devastating destruction to the downstream residents. Taking Tangjiashan barrier dam as an example, which was the most dangerous in "5.12" Wenchuan Earthquake, this paper carries out a systematic study on the breakage mode and risk analysis from the stability characteristic of barrier dams in order to provide references to the implementation of the disaster prevention and mitigation in the future.

2   Stability Characteristics of Tangjiashan Barrier Dam

2.1   Engineering Geological Structure Characteristics of Tangjiashan Barrier Dam

The drilling and investigation data showed that the geotechnical materials constituting the Tangjiashan barrier dam has obvious layered characteristics (HydroChina Chengdu Engineering Corporation 2008a, b). And they can be divided into four layers from top to bottom: gravel soil layer, block gravel soil layer, isolated gravel soil layer (quasi-layered structure rock) and grayish black silty gravel layer. Among those layers, the gravel soil layer and the grayish black silty gravel layer can be classified into the soil-rock mixture layer. The block gravel soil layer is mainly composed of the broken rock mass that almost kept the original structure, and constitutes the principal component of Tangjiashan barrier dam.

2.2   Stability Analysis of Tangjiashan Barrier Dam

To analyze the breakage possibility of Tangjiashan barrier dam due to the instability of the dam slope, limit equilibrium method is used to analyze the stability of the dam slope of Tangjiashan barrier dam during the process of the reservoir water level rise. The main profile of Tangjiashan barrier dam along river direction is used as the analysis model, and the physical and mechanical parameters are shown in Table 105.1.

Stability of Tangjiashan Barrier Dam in the Natural Condition
The analysis of the stability of the slope adopted Janbu's method and the Morgenstern-Price method based on the limit equilibrium theory. And three conditions were taken into consideration, at 730, 745 and 752 m impounding elevation of the barrier lake, respectively. The local and overall stability characteristics of upstream and downstream dam slopes were analyzed. Table 105.2 lists the analysis results of each case and Fig. 105.1 shows the analysis results of

Table 105.2 Stability analysis results of the upstream and downstream dam slope of Tangjiashan barrier dam (under the natural condition)

Reservoir water level (m)	Safety factor of the upstream slope						Safety factor of the downstream slope				Unit width discharge $(1e^{-3}\ m^3/s)$
	Upper part		Lower part		Whole		Lower part		Whole		
	Janbu	M-P	Janbu	M-P	Janbu	M-P	Janbu	M-P	Janbu	M-P	
752		1.43		1.24		1.68		1.85		2.73	1.84
745	1.71	1.85	1.14	1.28	1.73	1.85	1.73	1.85	2.80	2.80	1.65
730	1.74	1.87	1.24	1.37	2.03	2.17	1.74	1.86	2.80	2.80	1.16

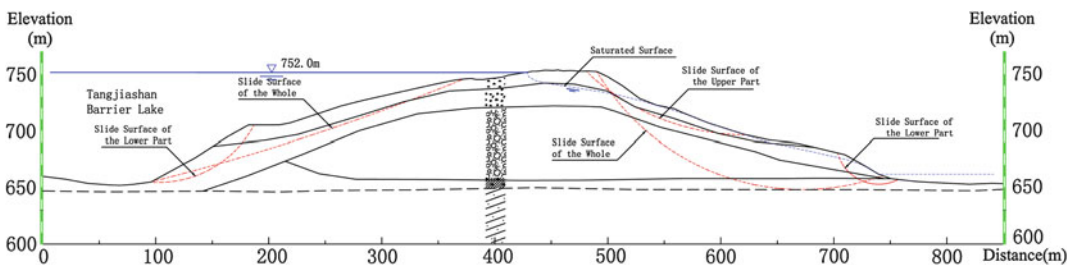*Note* M-P means Morgenstern-Price method

Fig. 105.1 Analysis results at 752 m impounding elevation of the barrier lake
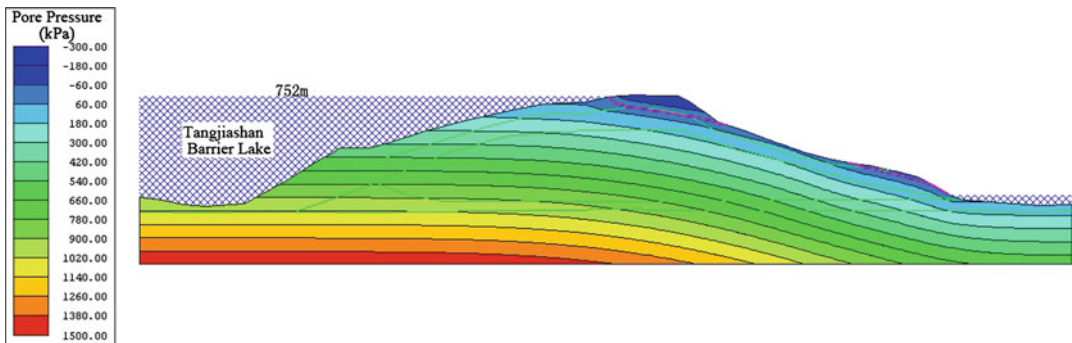

Fig. 105.2 Pore water pressure distributions at different impounding elevation of the barrier lake (at 752 m reservoir water level)

the seepage surface and sliding surface when the water level of the barrier lake is at 752 m.

From Table 105.2, it can be seen that the upstream slope of the barrier dam maintains a better stability in each impounding conditions and the factors of safety are all greater than 1.7. And the stability of the downstream slope is also stable enough. However, the stability at the slope toe is poor. When it is at 752 m impounding level, the factor of safety is only 1.1 by Janbu's method. In certain adverse conditions, local collapses may occur, but it will not influence the overall stability of the barrier dam.

Figures 105.2, 105.3, 105.4 are the seepage analysis results at 745 m impounding level and 752 m impounding level, respectively. It can be seen that, with the rising of reservoir water level, the overflow point of the downstream slope is around 670 m elevation. This finding is consistent with the fact observed on the spot that there are over 10 leakage points at 669 m elevation of the downstream dam toe. What's more, it can be

Table 105.3 Stability analysis results of upstream and downstream dam slope of Tangjiashan barrier dam (under the earthquake condition)

| Reservoir water level (m)	Safety factor of the upstream slope						Safety factor of the downstream slope			
	Upper part		Lower part		Whole		Lower part		Whole	
	Janbu	M-P	Janbu	M-P	Janbu	M-P	Janbu	M-P	Janbu	M-P
752	0.919	0.949	0.754	0.902	0.957	1.063	0.962	1.008	1.220	1.225
745	1.169	1.214	0.774	0.920	1.063	1.150	0.963	1.009	1.247	1.251
730	1.207	1.253	0.832	0.957	1.226	1.318	0.967	1.103	1.305	1.307

Note M-P means Morgenstern-Price method
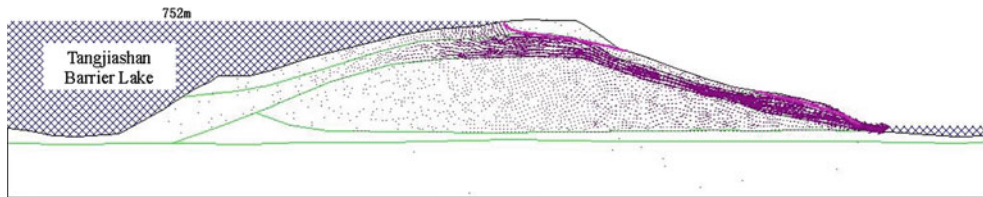
Fig. 105.3 Seepage velocity vector at different impounding levels in the barrier dam (at 752 m reservoir water level)

seen from the discharge per unit width of the cross section of the barrier dam in Table 105.2 that, with the rising of impounding level, the discharge tends to increase, which is also consistent with the actual observation.

The permeability of the block gravel soil layer of the barrier dam is larger than those of the upper gravel soil layer and lower isolated gravel soil layer (quasi-layered structure rock). Therefore, the flow velocity in this layer is greater (Fig. 105.3) and the downstream overflow points of the barrier dam are mainly located in this layer.

The permeability of the gravel soils distributed in the upper part of the barrier dam, especially the mud-siltstone that was in the alluvial river bed and uplifted to the dam surface during the landslide process, are very low. Because the thickness of this layer is thin and the permeability of the underlying block gravel soil layer is large, the hydraulic gradient is rather high in a certain range under the water level of the upstream slope surface (Fig. 105.4). However, as a whole, the hydraulic gradient in each layer of the barrier dam does not exceed the admissible value except in some local parts.

Even there are certain seepage failures in local parts, the interior flow can only take away a small amount of fine particles due to the larger grain size of interior rock blocks and the long seepage paths in the wide barrier dam. This finding is consistent with the fact that the water is clear and has no turbid phenomenon in over 10 leakage points observed in the downstream slope toe (Fig. 105.5). Therefore, the barrier dam may not be exposed to seepage failures. However, it does not exclude the possibility of the bracketed structure in local large rock blocks. When the water level rises high enough, it is likely to form the concentrated leakage and lead to small-scale collapses in the local area of the downstream, say the slope toe. It is expected that, this will not influence the overall stability characteristics of the barrier dam.

Stability of Tangjiashan Barrier Dam Under the Earthquake Condition

To study the stability characteristic of Tangjiashan barrier dam under earthquake condition, this paper takes into account the earthquake intensity of VIII with a 0.2 g horizontal
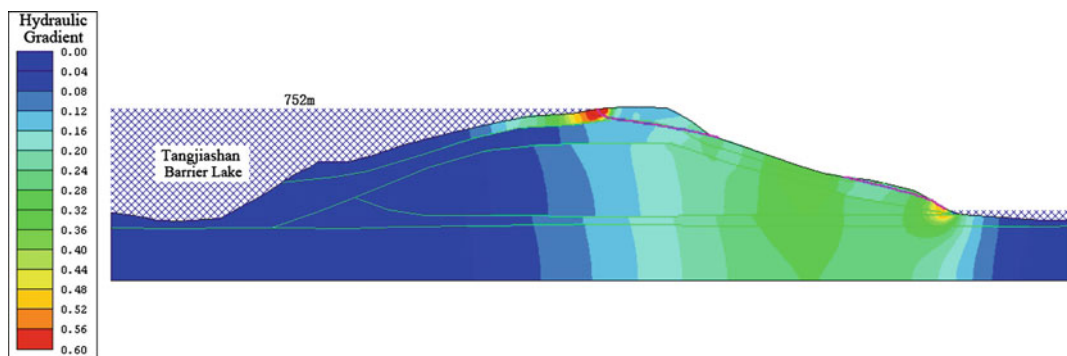
Fig. 105.4 Hydraulic gradient distribution at different impounding levels in the barrier dam (at 752 m reservoir water level)

Fig. 105.5 An overflow points at 669 m elevation of Tangjiashan barrier dam's downstream slope toe

earthquake acceleration and a vertical earthquake acceleration, which is 2/3 of the horizontal earthquake acceleration. Table 105.3 is the stability analysis results of the dam slope of Tangjiashan barrier dam at each impounding level under the earthquake condition.

From Table 105.3, it can be seen that the toes of the upstream and downstream slopes of the barrier dam may suffer local collapses if the earthquake intensity of VIII occurs again. However, in view of the overall stability, the slope is stable in other conditions except the downstream dam slope at high water levels (752 m).

3   Analysis of the Breakage Mode of Tangjiashan Barrier Dam

The two-dimensional stability analysis results of Tangjiashan barrier dam under the above mentioned different conditions indicate that, the overall stability of Tangjiashan barrier dam is good and only local collapses may take place under certain poor conditions. However, it will not influence the overall stability characteristics of the barrier dam. Besides, seen from the three-dimensional spatial structure (Fig. 105.6), Tangjiashan barrier dam along and across river directions present obvious shuttle-shapes with a broad middle and contractive ends, which greatly contributes to the stability. So, Tangjiashan barrier dam will not break due to dam slope instability.

However, from the seepage analysis (Table 105.2), the discharge of the barrier dam is far less than the inflow of the barrier lake(80 m^3/s), so the reservoir water level sharply increases after the formation of the barrier dam. In view of the geologic structure of Tangjiashan barrier dam, the gravel soil layer and the block gravel soil layer in the upper barrier dam have a poor erosion resistibility. When the barrier dam overtops, these two layers will be washed away immediately, which will

Fig. 105.6 Overview of Tangjiashan landslides: (a) Facing upstream; (b) aerial remote sensing image; (c) 3D contour of the Tangjiashan landslide dam
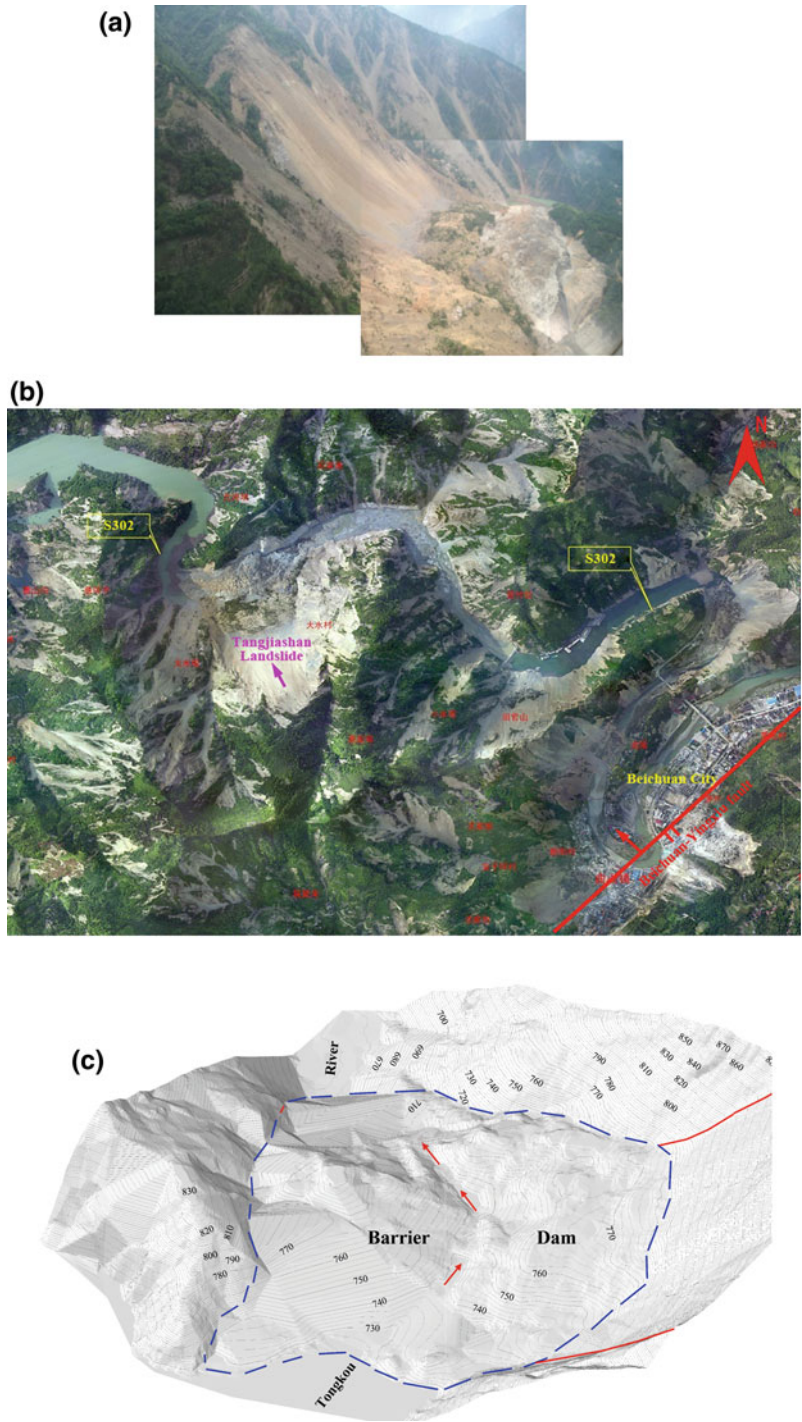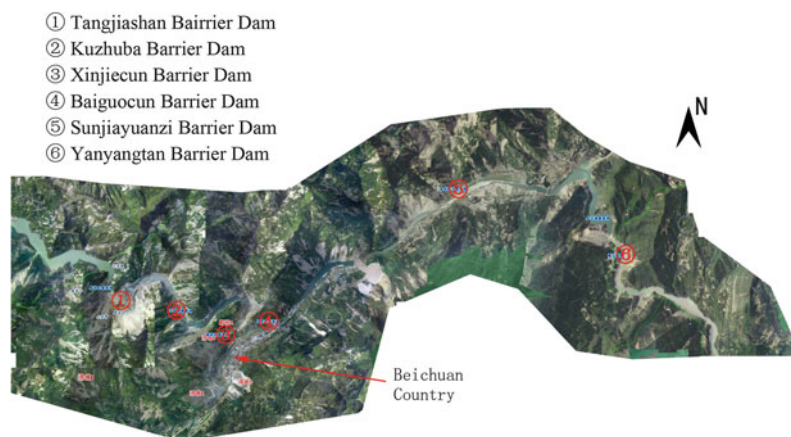
Fig. 105.7 Distribution of Tangjiashan barrier dam and its downstream barrier dams

① Tangjiashan Bairrier Dam
② Kuzhuba Barrier Dam
③ Xinjiecun Barrier Dam
④ Baiguocun Barrier Dam
⑤ Sunjiayuanzi Barrier Dam
⑥ Yanyangtan Barrier Dam

cause a quick breakage and destruction. Therefore, the overflow and overtopping of Tangjiashan barrier dam is the most likely breakage mode.

4   Risk Analysis on the Breakage of Tangjiashan Barrier Dam

4.1   Influences on the Downstream Barrier Dams

In the Wenchuan Earthquake, five barrier dams (Kuzhuba, Xinjiecun, Baiguocun, Sunjiayuanzi and Yanyangtan) formed at the downstream of Tangjiashan barrier dam along the main stream of Tongkou River (see Fig. 105.7). The breakage of Tangjiashan barrier dam is doomed to cause the succeeding breakages of these barrier dams at the downstream and further increase the water flow and aggravate the damage.

4.2   Influences on the Downstream Towns and Residents

The city of Beichuan County, 6 km away from the downstream of Tangjiashan barrier dam, had been destroyed in the earthquake. The whole city has been permanently kept as an earthquake museum and is of great value on the historical resources. Along Tongkou River, there are Jiangyou City and other small and medium cities

as well as the second largest city of Sichuan province -Mianyang City, with a population of about 1.3 million. What's more, along Tongkou River, there is the railway artery—Baoji to Chengdu Railway and the energy artery - Lanzhou to Chengdu to Chongqing refined oil pipeline at Tangjiashan downstream. Therefore, once the overtopping of the barrier dam occurs, it will bring a great calamity to the downstream towns and residents.

5   Restrictive Factors of the Breakage of Tangjiashan Barrier Dam

It can be seen from the above analyses that the dangerous conditions of Tangjiashan barrier dam are mainly caused by the factors as follows.

5.1   Large Catchment Area of the Barrier Lake and Quick Rise of the Water Level

Tongkou River is located at the north-western areas of Sichuan Basin and is a first grade tributary flowing into Fujiang River, with 4520 km^2 of the catchment area and 173 km of the main river length. According to the relevant statistics of meteorological station of Beichuan County from 1961 to 1990, 4 km away from the downstream, the mean annual rainfall in this

Fig. 105.8 Daily average flow curve of Tangjiashan barrier lake
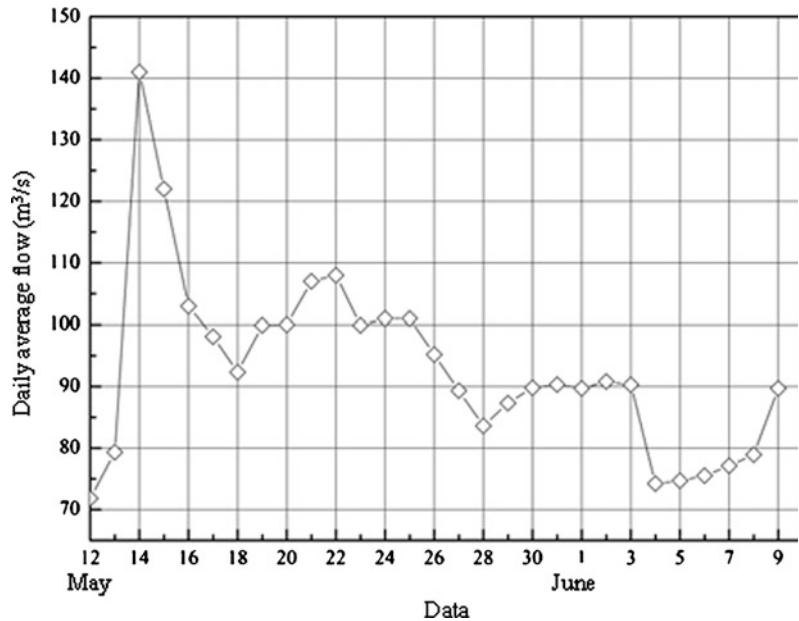
region is 1355.4 mm and the concentrated rainfall period is from May to September, occupying 86.3 % of the annual rainfall. Over the years, the largest amount of daily rainfall was 323.4 mm.

Figure 105.8 is the daily average flow curve of Tangjiashan barrier lake after the "5.12" Wenchuan Earthquake. It can be seen that in this period the average inflow is about 90 m³/s, far more than the seepage quantity of the barrier dam, which results in the quick rise of the water level in the barrier lake, with a daily rising velocity of 1.0–1.5 m.

## 5.2 Higher Barrier Dam, Large Reservoir Capacity and with Extreme Risk

The lowest elevation of the top of Tangjiashan barrier dam is 753 m and the river bed is 663 m. When the barrier lake fills up, the reservoir capacity will be up to 320 million m³ (Fig. 105.9) and the drop height of upstream and downstream will be up to 90 m. According to the analysis results in Sect. 4.2, if not taking emergency measures, the flood may ruin the small and medium cities along the river and

exceed the flood control criterion of Mianyang City with a return period of 100 years.

5.3 Geological Hazards in the Reservoir of the Barrier Lake

The length of the reservoir of Tangjiashan barrier lake from Tangjiashan to Zhicheng (a upstream city along Tongkou River) is about 15 km, and in this section there are 8 large-scale accumulation bodies along the river banks (HydroChina Chengdu Engineering Corporation 2008b). Especially Malingyan ancient landslide, 3.5 km away from the upstream of Tangjiashan barrier dam, has a volume of total 16.5 million m³. With the rise of the water level in the barrier lake, the slope toe will be immersed. The decreases of the toe weight and the mechanical parameters of the sliding surface will lead to the decrease of stability of the ancient landslide. In addition, the damage due to the strong shock of Wenchuan Earthquake and the actions of the aftershock and rainfalls, all are extremely harmful to the stability of these landslides. If these large-scale landslides rush into the

Fig. 105.9 Reservoir capacity-water level curve of Tangjiashan barrier lake
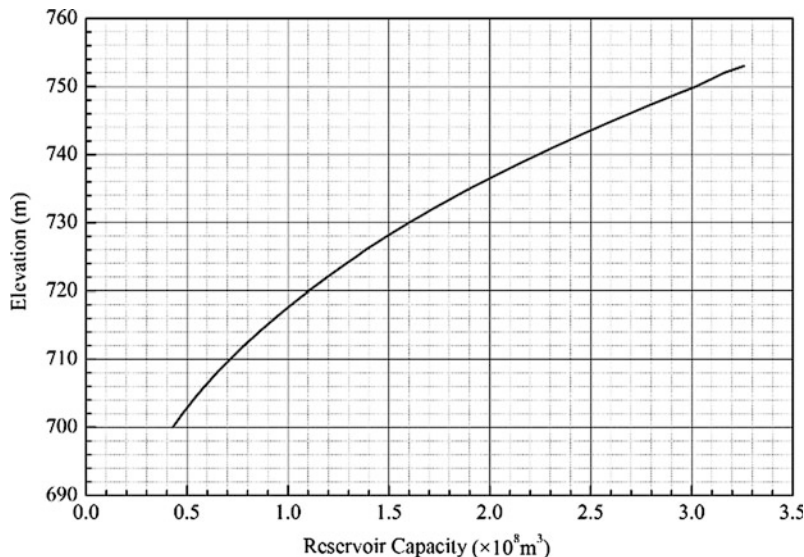
reservoir, it will form tremendous surges, which may cause breakage of Tangjiashan barrier dam or blocks the river again.

5.4   Totally Blocking the Ground Transportation

After the earthquake, the roads from Beichuan to Tangjiashan were totally blocked. Because of too many lake deposits and boulders in the upstream of the barrier dam as well as the complex underwater condition, large ships was not navigable. Therefore, constructers, equipments, materials and supplies, etc could only be transported by air.

6   Conclusions

Taking Tangjiashan barrier dam as an example, which was the most dangerous and the largest reservoir capacity of the barrier lakes formed in the "5.12" Wenchuan Earthquake, this paper carries out a systematic study on the breakage mode and the disasters in the breakage process. The following conclusions can be drawn.

 (1) The stability analysis of the formed barrier dam shows that Tangjiashan barrier dam is a typical broad crest dam with a width-hight ratio of about 9.8. Under the natural condition, its stability is good. Only in some poor conditions, local collapses may occur, but it will not influence the overall stability of the dam. The barrier dam may not have the risk of seepage failures.

 (2) The comprehensive analysis on the stability and the geological structure characteristics of the barrier dam indicates that the overflow and overtopping of Tangjiashan barrier dam is the most likely breakage mode.

 (3) Four main factors influencing the breakage of Tangjiashan barrier dam are: large catchment area and quick rise of water level; higher barrier dam, large reservoir capacity and with extreme risk; geological hazards in the reservoir of the barrier lake; and totally blocking of the ground transportation.

References

Keefer DK (2000) Statistical analysis of an earthquake-induced landslide distribution: the 1989 Loma Prieta, California event. Eng Geol 58(3–4):231–249

Keefer DK, Larsen M (2000) Assessing landslide hazards. Science 316:1136–1138

Parise M, Jibson RW (2000) A seismic landslide susceptibility rating of geologic units based on analysis of characteristics of landslides triggered by the 17 January, 1994 Northridge, California earthquake. Eng Geol 58:251–270

Yang Q (2002) Tibet Landslide Geologic Hazard and Countermeasures. J Geologic Hazards Control China 13(1):94–97

HydroChina Chengdu Engineering Corporation (2008a) Renovation plan-feasibility study report of Tangjiashan barrier dam. Chengdu

HydroChina Chengdu Engineering Corporation (2008b) Security evaluation report of Tangjiashan barrier dam and soil slope of upstream and downstream. Chengdu

Characteristics, Hazards and Mitigation of Debris Flows Along Min River after the Wenchuan Earthquake

Yonggang Ge, Peng Cui, Xingzhang Chen, Xinghua Zhu and Lingzhi Xiang

Abstract

After the Wenchuan Earthquake, debris flows frequently occurred and became the disastrous geo-hazard following this Earthquake at the seriously hit areas. This paper focused on characteristics,hazards, change and mitigation of the debris flows along Min River. The investigation and test data showed that debris flows were characterized by various types, low triggering rainfall with over 30 mm/24 h and over 10 mm/h, the density of 2.01–2.21 t/m^3, high frequency and large magnitude. Debris flow mainly appeared in the watersheds of which area and geomorphologic index (θ) was less than 10 km^2 and 6, respectively, accounting for 89 %, and the hazardous watersheds were featured with the area of 2–8 km^2 and the θ of 2–4. Moreover, debris flows occurred in simultaneity when rainfall reached 20 mm/h and produced step-dammed lakes. Debris flows and the following dammed lakes resulted in rapid change of river channel, endangered towns and frequently interrupted traffic. Debris flows, especially those from the watersheds with over 10 km^2,will continuously endanger reconstruction projects and local people in the future 10–15 years before they recover normal. After analyzing the loose materials amount and the potential destructed objects, the 23 hazardous watersheds are suggested to control and prevent. Finally, the mitigation

Y. Ge (✉) · P. Cui · X. Zhu · L. Xiang
Key Laboratory of Mountain Hazards and Earth
Surface Processes/Institute of Mountain Hazards
and Environment, Chinese Academy of Sciences,
Chengdu 610041, China
e-mail: gyg@imde.ac.cn

X. Chen
School of Environment and Resources, Southwest
University of Science and Technology,
Mianyang 621010, China

X. Zhu · L. Xiang
Graduate University of Chinese Academy of
Sciences, Beijing 100049, China

measures, including risk identification and zoning, hazards prediction, remote-monitoring and early-warning, emergency mitigation plan, integrated control and river channel dredging, are presented for debris flow hazards mitigation.

1   Introduction

Debris flow is an abrupt phenomenon of earth surface movement in mountainous areas. Abundant loose solid materials, steep geomorphology and intensive rainfall(rainstorm)prepare favorable conditions for debris flows. They generally format and distribute at active tectonic areas and intensive seismic areas (Tang et al. 2000). An intensive earthquake at mountainous areas usually result in the rise of frequency, flux, magnitude of debris flows and the increase of hazards, risks and losses, by virtue of the leaping rise of loose solid materials induced by seismic landslides and earth surface breach. After the catastrophic Wenchuan Earthquake, about 40–50 thousands landslides, rock falls and debris avalanches appeared in the seriously hit areas and 5–8 billions loose solid materials became the potential material sources. Debris flows become the most serious geo-hazard for the hit-areas and the reconstruction projects. The arresting debris flow hazards included coinstantaneous debris flows on Sept. 24, 2008 in Beichuan (Tang et al. 2009), on Jul. 17, 2009 in Wenchuan and Dujiangyan, on Aug. 13, 14 and 19, 2010 in Mianzhu, Dujiangyan and Wenchuan (Cui et al. 2011; Tang et al. 2011; Xu et al. 2012) and on Jul. 3 and Aug. 20, 2011 in Wenchuan. The section of Min River at the Wenchuan County, nearing the epicenter of this Earthquake (Yingxiu Town), had suffered intensive destruction by this Earthquake and is experiencing the damages of the following geo-hazards, especially debris flows. This paper aimed to analyze the characteristics, hazards, change of debris flow and give valuable suggestions and measures for mitigation.

2   Study Area

The study area is located at Wenchuan County, Sichuan Province, China, and composed of the valley of Min River and Yuzixi River, a tributary of Min River. It is dominated by mountains and steep gullies with the elevation difference of 2000 m and the average slope of 30–35° (Fig. 106.1). The granite, diorite and quartz diorite occupy the area where the altitude of 3500–5000 m, marble, phyllite, limestone and schist distribute at the area from 2000 to 3500 m, phyllite, schist, sandstone and mudstone mainly cover the area below 2000 m as well as the Quaternary terraces, alluvium and diluvia distribute the wide gully. The back fault and the centre fault of Longmen active faults run trough this region so that the earth surface is fractured and cracked due to the impacts of frequent tectonic movement. The humid of climate decrease from the southwest to the northeast. The south of Supodian of Yingxin Town, including Yingxing, Yingxiu, Gengda and Xuankou, is controlled by semitropical humid climate with the annual mean precipitation of over 1200 mm and the north, Mianchi and Weizhou, is characterized by drought-warm gully with the annual mean precipitation of about 500 mm. Before the Wenchuan Earthquake, this region is prone to debris flows and landslides.

The Wenchuan Earthquake originated from this region and the epicenter is located at the Niumian Watershed, Yingxiu Town. The study area was hit and destructed by the quakes and the following geo-hazards. Landslides, rock falls, debris avalanches and unstable slopes extensively distributed. The abundant loose solid
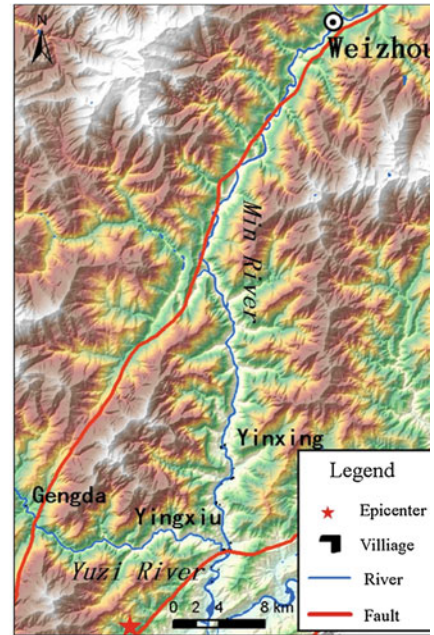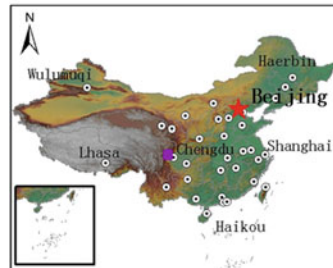
materials accumulated in slopes and gullies and prepare favorable conditions for debris flows. After this Earthquake, several decade debris flows occurred per years and has become the serious geo-hazards.

3   Debris Flow Formation and Distribution

3.1   Solid Material Sources

After the Wenchuan Earthquake, the landslides, rock falls and debris avalanches prepared abundant loose solid material for debris flows. The investigation and remote sense identification showed that about over 10000 geo-hazards distributed at the areas with the altitude from 1 000 m to 2 000 m and the slope is from 20 to 60° (Su et al. 2009). Geo-hazards destructed vegetation and the ratio of uncovered land reached 25 % of total, resulting in very intensive soil erosion and sediment transportation. Only in the Niumian Gully,the huge debris avalanche produced about 7.5 million debris and accumulated in the gullies,of which density reached 1.2 million m^3/km^2. The loose sediment density is about 0.60 million

m^3/km^2 in the Guanshan Watershed and the intensive erosion area occupy 26.7 %. The survey data from 44 watersheds along Min River and Yuzi River expressed that the density of loose material is more than 0.50 million m^3/km^2, the max reached 8.93 million m^3/km^2 and the average value was about 1.33 million m^3/km^2. As a result, all 55 watersheds along Min River from Wenchuan to Dujiangyan have the potential of debris flow and many have occurred after the Wenchuan Earthquake (Ge and Zhuang 2009), and the similar situation appeared in Yuzixi basin,especially at the section from Yingxiu to Gengda.

3.2   Debris Flow Types

Debris flows extensively developed and occurred in watersheds, gullies and slopes along Min River and Yuzi River due to quantity of loose sediment accumulation. Slope debris flows mainly occurred at the large-scale landslide body with the slope from 0.65 to 0.80, of which the middle and lower was transported into river and even blocked rivers. Gully debris flows occurred at the forming gullies with the channel slope of over 30 %, resulting in deep-cut gully and terraces
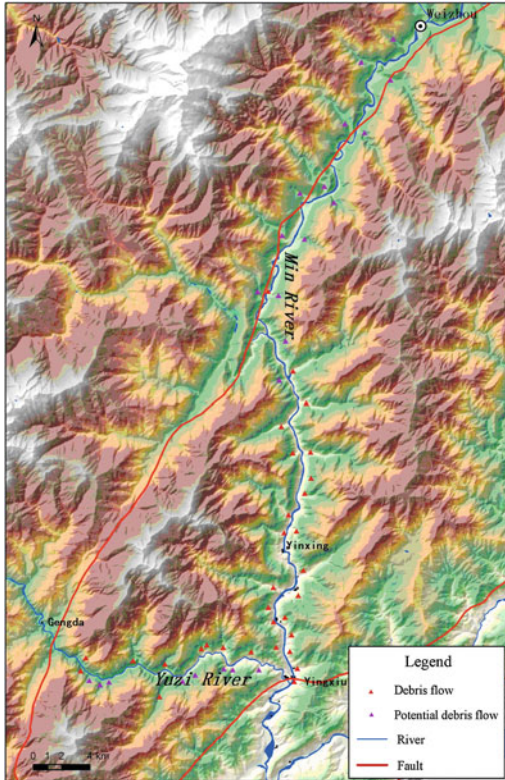
Fig. 106.2 Distribution of Debris flow watersheds along Min River and Yuzi River

Fig. 106.3 Geomorphologic features of debris flow watersheds. * the formula of watershed geomorphologic index (θ): $\theta = \frac{L}{J^{1/3}A^{1/4}}$, L, J and A is the channel length, the average slope of channel and the area of watershed, respectively

The low accumulated rainfall and few intensive rainfalls are not enough to trigger debris flows in many large scale watersheds until now (Fig. 106.3). The short-period intensive rainstorm probably initiates debris flow at drought valleys.

4 Characteristics of Debris Flows

Debris flows represent remarkable features after the Wenchuan Earthquake, which are different to those before this Earthquake.

4.1 High-Density and Low Viscosity

The debris flows are characterized by high-density and low viscous. The researches indicated that landslides, rock falls and debris avalanches induced by the Wenchuan Earthquakes mostly appeared in areas with the altitude from 1000 to 2000 m, accounting for 80 % of the total (Su et al. 2009). As the dominant solid materials, the majority came from the deep soil and the minority originated from surface weathered soil, which was composed by granite, limestone and phyllite and short of clay soil. The test data from 14 debris flow samples showed the density of debris flows was about 2.01–2.21 t/m^3 and the clay content was less than 3 %.

destruction. Watershed debris flows are the majority and occur at the watersheds with over 1 km^2 and sub-gullies,which had generated serous hazards on reconstruction and inhabitants.

3.3 Spatial Distribution

After the Wenchuan Earthquake, almost all the watersheds have the potential of debris flow occurrence along Min River from Yingxiu to Weizhou and Yuzi River from Yinxiu to Gengda. Debris flow watersheds and the potentials were showed in Fig. 106.2, which indicated that debris flows concentrated on humid areas including the regions from Yingxiu to Chediguan and from Yingxiu to Gengda, and only slope debris flows appeared the drought areas from Chediguan to Weizhou.
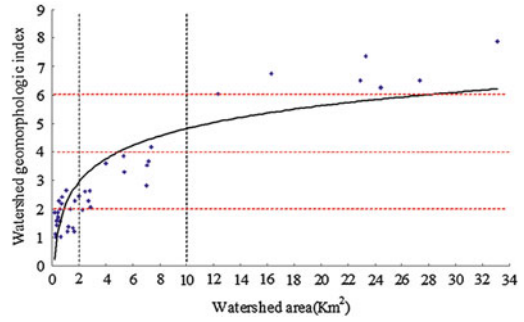
Table 106.1 Relationship between rainfall intensity and the magnitude of debris flows

Watershed name	Basin name	Rainfall (mm)		Probability (%)	Magnitude (million m^3)	Probability (%)
		24 h	1 h			
Hongchun Watershed	Min River	145.7	22.1	33	0.711	<0.1
Niumian Watershed					0.55	2
Shaofang Watershed					0.076	<0.1
Mozi-3 Watershed					0.158	2
Wangyimiao Watershed					0.104	<0.1
Mozi-1 Watershed		69.8	15.4	80	0.25	1
Gaojia Watershed		110.5/6	28.5	20	0.40	<0.1
Xiaojia Watershed	Yuzi River	145.7	22.1	33	0.35	1
Xiezi Watershed					0.461	<0.1
Yinchang Watershed					0.21	2
Wasi Watershed					0.23	<0.1

4.2 Low Triggering Precipitation and Large Magnitude

The triggering precipitation of debris flows significantly decreased after this Earthquake. Before the Wenchuan Earthquake, the threshold of rainfall intensity for triggering debris flow is 80–100 mm/24 h and 30–50 mm/h in this region (Tan 1996). The observation data showed debris flows occur once the rainfall intensity reaches 30 mm/24 h and 10 mm/h after 2008 and mass of debris flows appeared when the rainfall intensity exceeded 20 mm/h. Moreover, the magnitudes of debris flows are much larger than those before this Earthquake as showed in Table 106.1. These data indicted that the rainfall with the intensity of the probability from 33 to 20 % triggered the debris flow with the magnitude of the probability of 2 to 1 % and even less, and also proved that debris flow occurrence were controlled by rainfall but not loose solid materials.

## 4.3 High-Frequency and Group Debris Flows

Debris flows become very frequently due to the impacts of abundant loose sediments and lower triggering precipitation. Debris flow occurred in many watersheds every year and even several times in some watersheds. For example, debris flows ever appeared over 10 times, 6 times and 4 times in Niumian Watershed, Guanshan Watershed and Mozi Watershed, respectively, in 2008. They occurred at the three watersheds in the past 4 rain seasons. Moreover, when local intensive rainfall or rainstorm, debris flows generally occurred at many watersheds in simultaneity and produced huge disasters. The investigation showed that debris flows occurred at over 20 watersheds and 56 watersheds at this region on July, 17, 2009 and August, 13–14, 2010. This phenomena also occurred on July 3 and Aug. 20, 2011.

4.4 Watershed Features

The majority of debris flows occurred at the watersheds with less than 5 km^2, and a few in large watersheds. The statistical data showed that the watersheds with less 1 km^2, 2 km^2, 5 km^2 and 10 km^2 accounted for 36, 57, 77 and 89 %, respectively. Figure 106.3 showed that debris flows were very active in those watersheds with the geomorphologic index (θ) of less than 5, providing favorable formation and dynamic condition for debris flows. The observation data also proved that the hazardous watersheds are characterized with the area of 2–8 km^2 and the geomorphologic indexes of 2–4. Debris flows
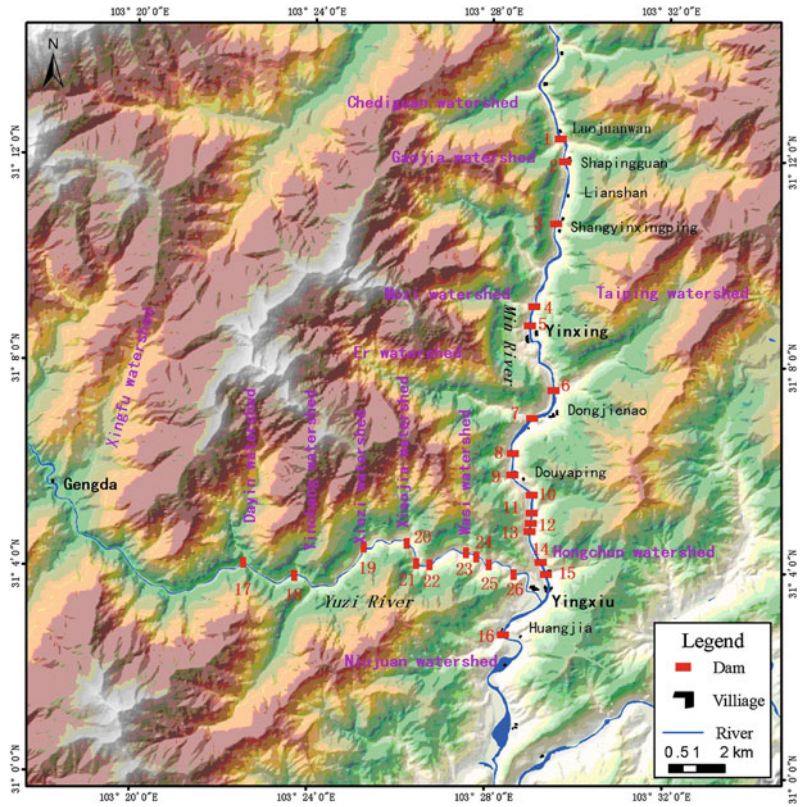
frequently and extensively occurred in the watersheds with less than 2 km^2 and $\theta < 2$, and were featured with low hazard. A few debris flows appeared in the watersheds with 10 km^2 and $\theta > 6$, but the large-scale and catastrophic debris flows would be potential when more intensive rainfall appeared, providing enough dynamic condition.

4.5 Debris Flow Hazard Chain

The increasing magnitude and flux of debris flows are favorable for blocking river. The assessment result showed that the debris flows from 19 watersheds are very easily to block Min River, accounting for 78 % of the total (Zhuang, et al. 2010). The research in Mozi Watershed proved that Min River could be completely blocked when debris flow magnitude reached 50 000 m^3 and most debris flows exceed this threshold. The large-scale debris flow from the Niumian Watershed, the epicenter of the Wenchuan Earthquake, ever blocked Min River on May 13, 2008, and the dam was always kept until now due to the accumulation impacts of the later frequent debris flows. From then on, 26 dammed lakes induced by debris flows had appeared in the Min River and Yuzi River (Fig. 106.4). The investigation also proved that the threshold of debris flow blocking river decreased. The debris flows from small watersheds and even slope debris flows could create dammed lakes by virtue of the impacts of step dam lakes along river. For example, the debris flows from the Mozi-3 and Shaofang Watershed. Furthermore, the dammed lakes generally outburst partly and rapidly along the front of debris flow deposition fan and produce flood. As a result, the only 1/4–1/3 part of the dam was destructed to be transported by flow and deposit in the lower dammed lake. Therefore, the hazards behave this model: debris flow, dammed lake and outburst flood.

Fig. 106.5 Debris flow and the following hazards change river channel (Yingxiu to Laohuzui). **a**. Hongchuan Watershed, **b**. Shaofang Watershed, **c**. Xiaojia Watershed, **d**. Wangyimiao Watershed, E. Mozi-3 Watershed, F. Laohuzui Landslide)

5 Hazards and Risks of Debris Flows

Debris flows have generated heavy impacts and hazards on river channel, highways, towns and villages,and will continuously endanger the security of the earthquake areas.

5.1 Change River Channel

Debris flows and the following dammed lakes resulted in the rapid change of river channel.The deposits of debris flow directly narrow river channel and rise river bed at the watershed mouth once debris flow move into river. The width of river channel only equaled to the 1/3 or 1/4 of that before the Earthquake and the river bed rise at the range from 8 to 15 m and even more in the watershed mouths. Moreover, debris flow dammed-lakes rise the river bed and wide river channel of the upper of debris flow dam due to the rapid deposition of quantity of sediments (Fig. 106.5). The step dams make river channel abrupt rise and fall along the flow direction and some step-dammed lakes even link with each other, which further decrease sediment delivery and facilitate deposition. As a result, the mountainous river become more curl and wander due to the impacts of the deposition fans and step dammed-lakes produced continuous abrupt sites (knick points), which increase the risks of catastrophic flash flood and improve the difficult of debris flow control due to the remarkable decrease of sediment transportation of mainstream.

5.2 Destruct Highways and Interrupt Traffic

Debris flows imposed serious hazards on mountainous highway and traffic by destroying bridge, burying highway, scouring roadbeds and depositing tunnel and inundating highway resulting from dam-lakes. The debris flows from Hongchun Watershed and Sahaofang Watershed ever buried the G213 highway about 800 m on Aug. 14, 2010. The debris flow from Gaojia Watershed seriously destructed highway bed and the bridge of G213 highway by debris flow deposits and the outburst flood of the dammed lake and also interrupted traffic about 15 days (Fig. 106.6). The debris flow and the following dammed lakes from Xiaojia Watershed, Xiezi Watershed and Xiangjia Watershed destroyed and inundated Yingxiu-Gengda Highway (S303) on Aug. 14, 2010. Moreover, group debris flows also destroyed highway at several sites and interrupt traffic by different means, producing
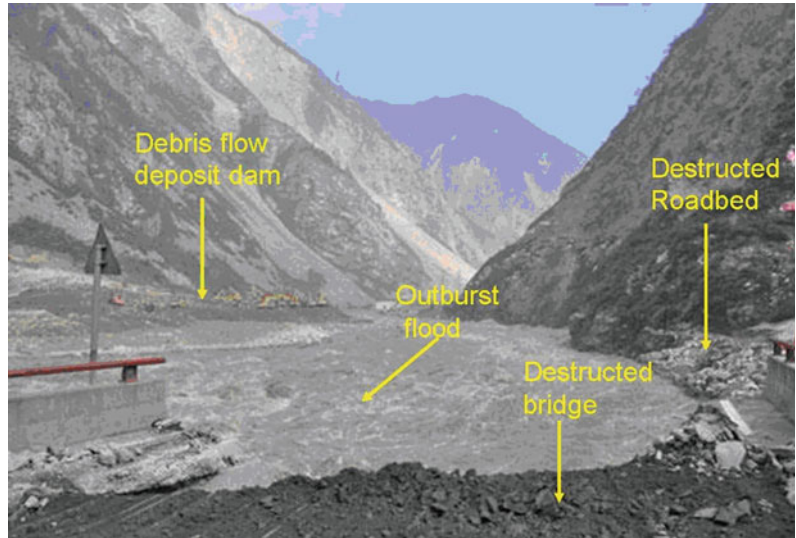
great difficulty for traffic recovery. The two highways (G213 and S303) are interrupted several times by debris flows and their resulting hazards from July to September every year.

5.3 Endanger Towns and Villages

Debris flow and it's following hazards has become the dominating threatens to inhabitants and reconstruction. Some inhabitants and reconstruction are encountering the hazards from debris flows by virtue of the shortage of safe area. The debris flow of Xiezi Gully and Xiangjia Watershed destroyed the reconstruction engineering for tourism on Aug. 14, 2010. The dammed lake induced by the debris flow of Mozi Watershed submerged Yiwanshui village in 2008, which was still in water until now. The outburst flood induced by debris flow dammed lake of Hongchun Watershed transported sediments into the newly town of Yingxiu in 2010. Flood and debris flow submerged and deposited the first floor and endangered the whole town and most local people (Fig. 106.7).
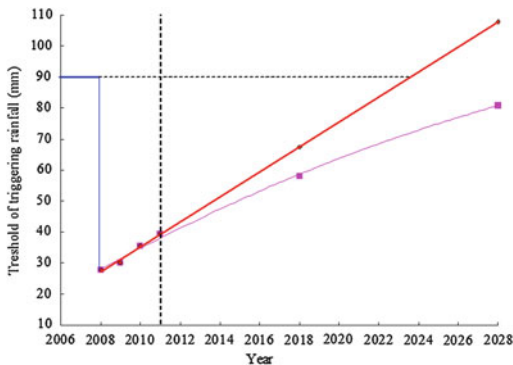
Fig. 106.8 Change trend of triggering precipitation of debris flow after the Wenchuan earthquake

6   Debris Flow Change Trend

6.1   Triggering Precipitation

With the gradual rise of stability and the decrease of amount of the loose solid materials, the threshold of triggering precipitation of debris flows will rise and recover. The data from Niumian Watershed and Mozi Watershed proved this fact. The change trend and prediction curve of triggering rainfall at Mozi Watershed was showed in the Fig. 106.8, which was made using the lowest triggering rainfall in 2008, 2009, 2010 and 2011 (Fig. 106.8). It expressed by the red line that this return process would cost about 15 years if this process followed the trend of the beginning 4 years. The return process mainly depended on the amount of loose materials in the initiation areas. The researches showed the recovery is a gradual,speed-down and abrupt process in the intensive Earthquake Areas (Chen 2011), and the accumulation rainfall threshold of triggering debris flow spent 7 years on recovering the 50 % of that before the Jiji Earthquake (Shieh et al. 2009) and debris flows occurred actively for 10–15 years after the Luhuo Earthquake. Therefore, this return process will cost 15–20 years at least which indicated by pink line and be in diversity in different watersheds with various loose solid materials,geomorphologic features,hydrologic condition,vegetation cover and rainfall.

6.2   Active Period

The mountainous intensive earthquake generally resulted in active geo-hazards in the special period. After comparing with the debris flows at the hit areas by Luhuo Earthquake and analyzing the triggering rainfall, it was estimated that debris flows and landslides will actively occurred in the future 10–20 years and 5–10 years, respectively (Cui et al. 2008). The abundant loose materials probably prepare favorable condition for debris flow in the future 15–20 years and even longer period, which will be probably in diversity at the different hit areas and the different climatic zones.

6.3   Magnitude and Frequency

The magnitude and frequency of debris flows will decrease with the reduction of loose materials amount and the rise of soil stability. It was proved by the data from the Nianjuan Watershed and Mozi Watershed. Debris flows occurred over 10 times (including 4 large-scale debris flows) at Niumian Watershed in 2008, and only 2 times in 2009, 2010 and 2011, respectively, as well as 4 times, 2 times, 1 time and 2 times in 2008, 2009, 2010 and 2011 at Mozi Watershed. This trend will continue until recover the situation before this Earthquake. Moreover, the magnitude of debris flow will also gradually decrease and recover the normal due to the decrease of the potential soil.

6.4   Spatial Scale

The debris flows will mainly occur at the lager watershed,especially those with over 10 km². The small watersheds are characterized by steep slope and channel so that loose sediments is very easily initiated and moved out even if the rainfall intensity is low and the normal. In the beginning years after the Earthquake, debris flows transported most loose sediment out of watersheds so that their frequency and magnitude gradually reduce by virtue of the decrease of loose materials, for example Mozi Watershed and Guanshan
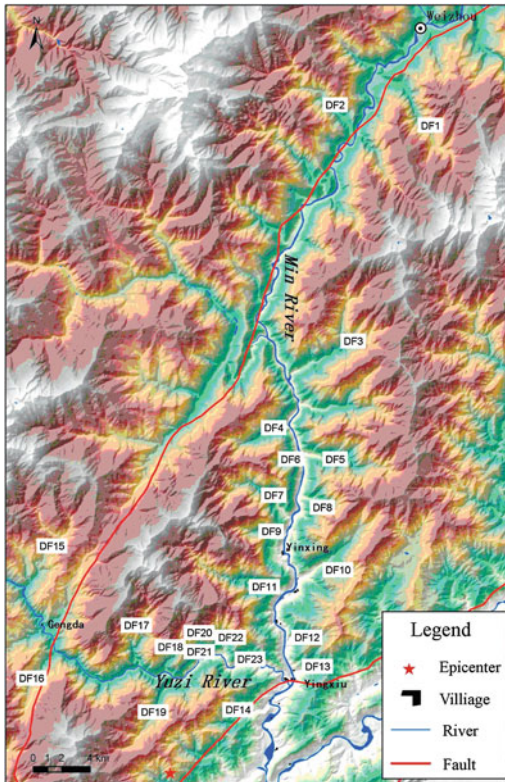
Fig. 106.9 Distribution of hazardous debris flow watersheds

Watershed. For the most large watersheds, debris flow generally deposited at sub-gullies and did not move out of the watershed until now, for example Taoguan Watershed. When higher intensive rainfall occur, the larger-scale debris flow will rush out of watershed and even block mainstream, for example Er Watershed and Ye-niu Watershed, of which debris flows were triggering the intensive rainfall with 20 % probability. The percent of debris flows from the large watersheds will gradually increase and those from small watersheds will decrease.

7 Mitigation Measures

7.1 Risk Identification and Zoning

For the over 70 debris flow watersheds, the hazard and risk assessment based on single-watershed

are strongly suggested to be made. The dangerous zones and the disastrous watersheds are ranked for the decision and plan of debris flow hazards mitigation. The potential hazard sites had better be found in advance to prevent and reduce losses. The hazard zoning based on debris flow watershed is carried out to serve for the relocation of inhabitants' resettlement, engineering construction and highway reconstruction. The following 23 watersheds, as showed in Fig. 106.9, will be the disastrous debris flow sites according to the formation conditions and the potential destructed objects, and are suggested to be controlled (Table 106.2).

7.2 Hazards Prediction

For the disastrous watersheds, the distribution and amount of loose solid materials should be known and calculated actually for predicting and controlling debris flows. The amount of loose solid materials and probable material sources for debris flows is estimated actually by the combination of field survey and remote sense identification. Moreover, the changed geomorphologic features of watershed and direct loose solid materials are strongly to be obtained by field investigation, aerial survey and high-resolution remote sense images, which will contribute to the computing of dynamic parameters of debris flow, the confirmation of control standard as well as the layout of control constructions and monitoring system and equipments.

7.3 Remote Monitoring and Early-Warning

The monitoring and early-warning system is very useful for the mitigation of disastrous debris flow watersheds. The appropriate methodology of early-warning including the threshold of rainfall, water content in soil and soil intensity, being adequately concerned for debris flow characteristics and change, is strongly researched, established and applied to guide debris flow forecast. According to the lessons from Zhouqu

Table 106.2 The potential disastrous debris flow watersheds

Watershed name	Basin name	No.	Area (km^2)	Geomorphologic index (θ)	Loose material (10^6 m^3)	Potential destructed objects
Qipan Watershed	Min River	DF1	50.61	8.90	31.7	Qipan village, highway, industrious areas
Banqiao Watershed		DF2	27.35	6.50	10.93	Banqiao village, highway
Taoguan Watershed		DF3	51.90	8.52	25.56	Taoguan village, water power station, bridges
Chediguan Watershed		DF4	16.97	6.87	20.44	Highway, tunnel, bridge and water power station
Luoquanwan Watershed		DF5	28.65	6.56	17.68	Highway, bridges
Gaojia Watershed		DF6	3.32	2.95	6.87	Highway, bridges
Yeniu Watershed		DF7	24.65	6.49	26.35	Highway, bridges
Yingxingping Watershed		DF8	7.00	3.50	10.85	Highway, bridge and villages
Mozi-1 Watershed		DF9	7.46	3.95	16.85	Highway, bridges, Yiwanshui village
Taiping Watershed		DF10	27.31	5.85	23.74	Highway, bridge, water power station
Er Watershed		DF11	39.1	7.04	34.61	Highway, water power station, Dongjienao village, tunnel,
Mozi-3 Watershed		DF12	5.33	3.8	6.90	Highway
Hongchun Watershed		DF13	5.35	3.30	3.84	Highway, bridge, Yingxiu town, water power station
Niujuan Watershed		DF14	12.7	5.55	22.10	Highway, epicenter heritage, Zhangjiaping village,
Xingfu Watershed	Yuzi River	DF15	33.3	7.92	32.17	Gengda town, Highway
Qicenglou Watershed		DF16	23.4	6.65	15.92	Highway, tunnel
Dayin Watershed		DF17	23.64	5.62	50.86	Highway, bridge
Yingchang Watershed		DF18	7.36	4.17	28.9	Highway, bridge, Gengda water power station
Huangliang Watershed		DF19	23.48	7.29	12.30	Highway, tunnel
Xiangjia Watershed		DF20	1.22	1.36	3.60	Highway, village
Xiezi Watershed		DF21	2.25	1.96	4.10	Highway, village
Xiaojia Watershed		DF22	6.999	2.83	3.57	Highway
Wasi Watershed		DF23	1.67	1.20	2.58	Highway, bridge

catastrophic debris flows,the remote monitoring equipments must be arranged in the initiation areas and material source areas for getting actual situation of debris flow activity immediately and providing enough time for evading and mitigating because the mountainous climate is various in different horizontal and vertical areas.

7.4 Emergency Mitigation Plans

The emergency plan is established for catastrophic debris flow watersheds,for example those of Gaojia Watershed, Yingchang Watershed and Hongchun Watershed. The catastrophic debris flows still probably occur at many watersheds in the future 10–15 years and will destruct highways, block river, interrupt traffic as well as isolate the local inhabitants and endanger their security. Moreover, the highways from Dujianyan to Wenchuan and from Yingxiu to Gengda are the key sections between the Tibet Plateau and Chengdu Plane. Therefore, the emergency plans, including early-warning, pre-practices, evading,emergency succor and reconstruction,for special debris flow watersheds are necessary for reducing the loss of property and lives and recovering the normal traffic as soon as possible.

7.5 Integrated Control

The disastrous debris flow watersheds may as well be controlled by integrating measures and modes, which are guided by the theory of the maximum transportation capability of mainstream and the regulation of debris flow process. The loose solid materials including landslides, rock falls, debris avalanches and unstable slope are prevent sliding and initiating debris flow by the optional configuration of protection walls, anchors, resistant stakes, check dams and sediment storage dams. The barrel-drains are constructed along the edge of landslides and debris avalanches to prevent debris flow initiating. The initiated debris flows are blocked in sub-gullies in priority to control debris flow conflux and reduce

the magnitude. The appropriate drainage slots, designed according to the sediment transportation capability of mainstream, are constructed in the main channel to adjust the flux and amount of debris flow into mainstream. Moreover, the local grass, shrubs and arbors are selected and planted to control surface runoff, prevent soil eroding and reduce debris flow initiation.

7.6 River Channel Dredging

It is a critical factor of debris flow hazard that the heavy sediment deposition in Min River and Yuzi River, particularly the impacts of step dam-lakes. Therefore, river channel dredging becomes a necessary measure to reduce the damages of debris flows and the following hazards. It not only staves the rapid change of river channel and mountainous geomorphology, reducing the hazards of debris flow on highways, but also keeps the transportation capability of river so that reduces the probability of blocking river of later debris flows. The dredging is also helpful for preserving the normal hydraulic condition.

8 Conclusions

This work concentrated on the characteristics, hazards, change and mitigation of debris flows along Min River. The investigation and test data showed that debris flows were characterized with various types, low triggering rainfall with over 30 mm/24 h and more than 10 mm/h, the density of 2.01–2.21 t/m^3, high frequency and large magnitude after the Wenchuan Earthquake. Debris flow mainly appeared in the watersheds of which area and θ was less than 10 km^2 and 6, respectively, accounting for 89 %, and the hazardous watersheds were featured with the area of 2–8 km^2 and the θ of 2–4. Moreover, many debris flows occurred in simultaneity when rainfall reached 20 mm/h and produced step-dammed lakes. Debris flows and their following geo-hazards resulted in rapid change of river channel, destructed farmlands, endangered towns and frequently interrupted

traffic. Debris flows will be active in the future 10–15 years and gradually recover the features before the Earthquake Debris flows, especially those from the watersheds with over 10 km^2,will continuously endanger reconstruction projects and local people. The 23 hazardous watersheds for highways, bridges and villages are identified and strongly suggested to be concerned and controlled. The mitigation measures, including risk identification and zoning, hazards prediction, remote-monitoring and early-warning, emergency mitigation plan, integrated control and river channel dredging, are presented for debris flow hazards mitigation.

References

Chen JC (2011) Variability of impact of earthquake on debris-flow triggering conditions: case study of Chen-Yu-Lan watershed, Taiwan [J]. Environ Earth Sci 64:1787–1794

Cui P, He SM, Yao LK et al (2011) Formation mechanism and risk control of mountain hazards induced by the Wenchuan earthquake [M]. Science Press, Beijing

Cui P, Wei FC, He SM et al (2008) Mountain disasters induced by the Earthquake of May 12 in Wenchuan and the disasters Mitigation [J]. J Mountain Sci 26(3):280–282

Ge YG, Zhuang JQ (2009) River channel change of the Upper of Minjiang River by 5. 12 Wenchuan Earthquake: a case study of the section of Dujiang-yan-Wenchuan [J]. Geol Sci Technol Inform 28(2):23–28

Shieh CL, Chen YS, Tsai YJ et al (2009) Variability in rainfall threshold for debris flow after the Chi–Chi earthquake in central Taiwan, China [J]. Int J Sedim Res 24:177–188

Su FH, Cui P, Han YS et al (2009) Distribution analysis of mountain hazards induced by 5. 12 Wenchuan Earthquake along Dujiangyan-Wenchuan highway using Remote Sensing [J]. Geol Sci Technol Inf 28(2):29–32

Tang BX, Zhou BF, Wu JS et al (2000) Debris flows in China [M]. Commercial Press, Beijing, pp 1–14

Tang C, Zhu J, Ding J et al (2011) Catastrophic debris flows triggered by a 14 August, 2010 rainfall at the epicenter of the Wenchuan Earthquake [J]. Landslides 8:485–497

Tan WP (1996) Basic theory and study situation of rainstorm debris flow forecast in China [J]. J Soil Eros Soil Conserv 2(1):88–95

Xu Q, Zhang S, Li WL et al (2012) The 13 August 2010 catastrophic debris flows after the 2008 Wenchuan earthquake. China Nat Hazards Earth Syst Sci 12:201–216

Zhuang JQ, Cui P, Ge YG et al (2010) Probability assessment of river blocking by debris flow associated with the Wenchuan Earthquake. Int J Remote Sens 31(13):3465–3478

Multiple Predict Landslides in Giant Earthquake Struck Region: A Case Study in Chengdu, China

107

Tian Hongling, Wang Meng, Yang Zongji and Qiao Jianping

Abstract

Many landslides are triggered by rainfall in mountain areas especially in earthquake struck regions. To forecast these landslides, three questions need to be answered. Where and when will landslides occur? And what kind of slopes will slide? An early warning method based on statistical model integrated with landslide monitoring is proposed. Landslide susceptibility zonation gives the potential landslide location. With historical landslide and rainfall records, the correlation between them can be worked out with statistics analysis. Thus, the temporal possibility can be calculated when an intensive rainfall is coming. As for the specific slopes in high risk area, through some sensors can we learn the changes of surface displacement, internal displacement and soil moisture. Alarm or prediction can be deduced from the data. With this idea, a well-organized warning and monitoring system began to be built in west Chengdu, China. The victims and loss declined in 2010, which proved this method is useful.

1 Introduction

When a giant earthquake occurs in mountain area, it usually triggers thousands landslides. Besides, the deposits and debris increase dramatically. Landslides easily occur on the slope covered by debris after rainfall or earthquake comes.

There are still thousands of people living in the earthquake struck area. Landslides will endanger their lives and properties. The public is anxious to know information about landslide development.

T. Hongling (✉) · W. Meng · Y. Zongji · Q. Jianping
Key Laboratory of Mountain Hazards and Surface Process, Institute of Mountain Hazards and Environment, Chinese Academy of Sciences, Chengdu, Sichuan, China
e-mail: tian@geot.t.u-tokyo.ac.jp

T. Hongling
Department of Civil Engineering, The University of Tokyo, 7-3-1 Hongo, Bunkyo-ku, Tokyo, 113-8656, Japan

2 Characteristics of Landslides After Earthquake

There are some common facts listed as follows.

- The post-quake landslides are mainly of small size and on shallow slope, according to statistics (Ayalew et al. 2011; Huang and Li 2009; Keefer 2002; Wang and Sassa 2007, Wang and Lin 2010).
- Both earthquake and rainfall can induce landslide. The seismic shaking is difficult to predict (Wang and Graham et al. 2001). However, the rainy weather is predictable (Reggiani and Weerts 2008).
- Landslides will occur with earthquake, but later than rainfall. Therefore it has enough time to predict a rainfall-induced landslide compared with an earthquake-induced one.
- Earthquake or aftershock is not so regular as rainfall. The frequency of earthquake-induced landslide is lower compared to rainfall. Statistics also show that a post-earthquake landslide has a close relation with rainfall (Shou et al. 2011).
- Rainstorm increases the total landslide area (Tang et al. 2011).

With these factors, the prediction will mainly focus on rainfall-induced landslides.

3 Prediction Method on Earthquake-Induced Landslides in Large Area

3.1 Predicting Landslide in Large Area

There are many models having been developed for landslide prediction. However, most models have many limitations and are difficult to apply in other area. Because of the data and people's understanding to landslide, the practical method for middle or large scale landslides are usually made up with space locating (landslide zonation) and temporal prediction(Van Westen et al. 2006).

3.2 Landslide Spatial Possibility

Landslide susceptibility and hazard zoning have been developed since the 1970s and has been widely accepted to the estimate of "where" landslides are expected (Cascini 2008; Guzzetti et al. 2005).

Among the susceptibility models, the statistical zoning method is good for assessing the spatial probability where there are enough historical landslide records.

3.3 Landslide Temporal Possibility

Information related to triggering factors generally has more temporal than spatial importance (Van Westen et al. 2008). To analyze the relationship between triggering factors and landslide historical records with occurrence time, and then construct a model is an effective way to know when the landslides are more likely to occur.

3.4 Landslide Simulation

The statistical model is a black-box model, and it is difficult to tell whether and how a factor contributes to landslide. A field experiment is a good way to test the reorganization on landslide acting factors and improve the prediction.

3.5 Small Size Landslide Monitoring

For local people, the landslide alarm must be specific so that they can learn what will happen and can make ready for it. However, the prediction is a trend for large area and not precise enough, which mean it is difficult to know the safety of a nearby specific slope. Therefore, a fast-install slope monitoring system is needed.
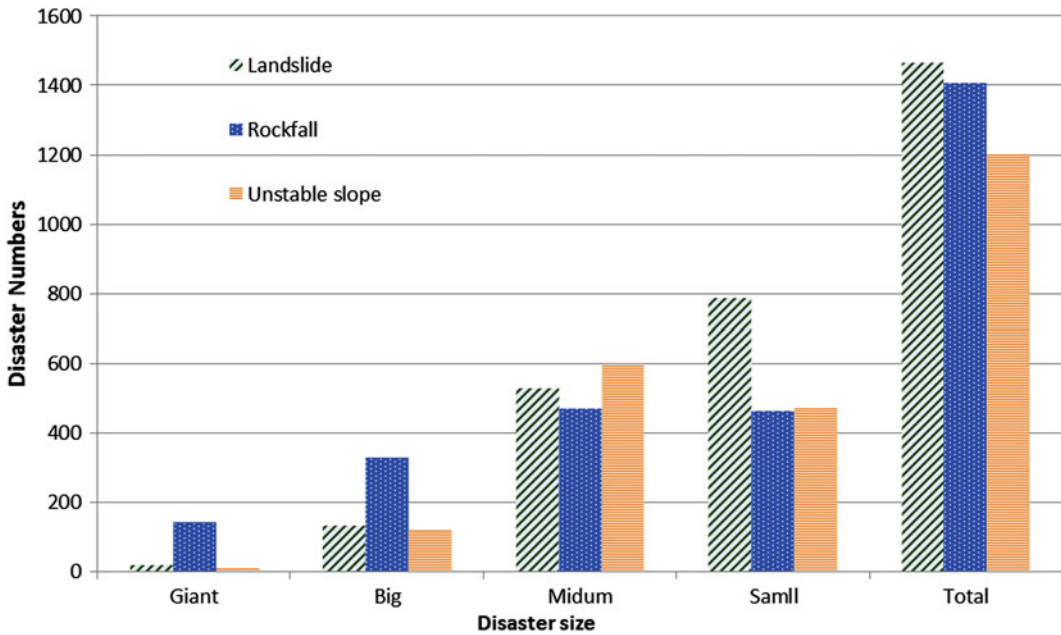
Fig. 107.1 Landslide style and its size

As the aforementioned distribution of landslide volume shows, the huge and large landslides are usually cared, it is the small to medium sized landslides that need a strategy for effective monitoring.

Because the small sized landslides are mainly shallow landslides and the deformation of the slope surface can be rather easily observed. In most cases, water content is related with the stability of a slope. Therefore, a few slope inclinometers and volumetric water content sensors can effectively give warning of a small slope landslide (Uchimura et al. 2010).

earthquake occurred in 2008 and directly caused more than 15,000 landslides. Chengdu is the capital of Sichuan province. Its population and economy is bigger than other earthquake struck area.

Before the earthquake, there are 240 landslide disasters in Chengdu area, but after the shock, the new disasters are 1315. The landslides are mainly small sized ones (Fig. 107.1) (Tian et al. 2010).

During 2008–2010 rainy seasons, the landslides broke out in Longmenshan hilly area, West Chengdu. These disasters bring continuous damages to local society, and the prediction is an urgent demand.

4 Application Example

4.1 After Shock Disasters in West Chengdu

Chengdu is located in west of the Sichuan province, China, where the Wenchuan M8.0

4.2 Landslide Susceptibility Zoning

Data collected for zoning include:
1) 1:50,000 DEM.
2) 1:200,000 digitalized geologic maps.
3) Digital Infrastructure map, include: road, river, resident settlement camp.

Table 107.1 Affecting factors and its weight

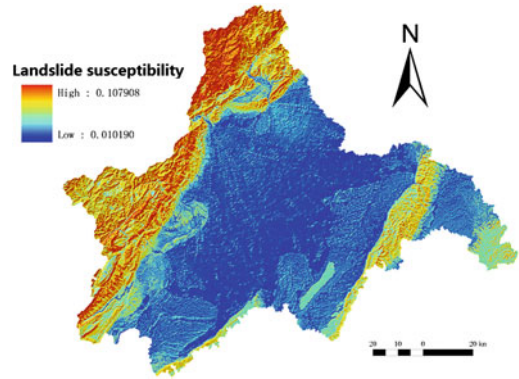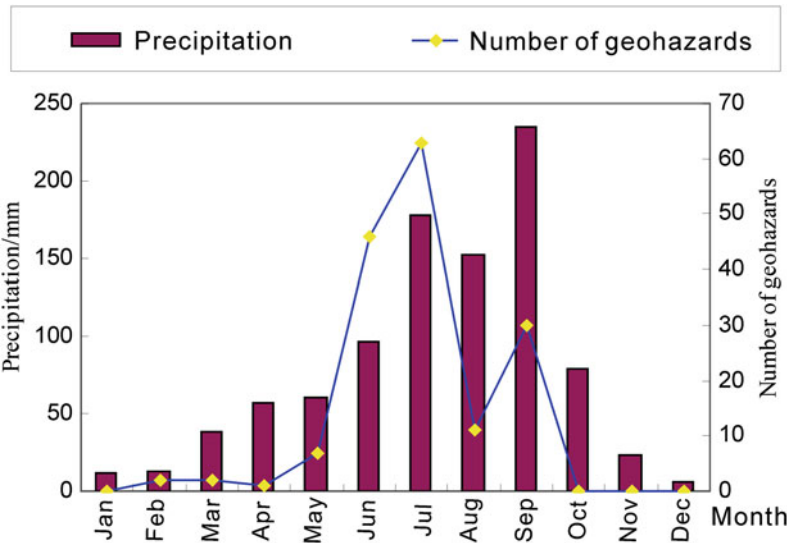| Affecting factor	Weight
Slope aspect	0.114
Distance to fault	0.111
Lithology	0.108
Water network density	0.107
Slope shape	0.099
Altitude	0.097
Land-use	0.096
Depth of river	0.092
Roughness of surface	0.089
Slope gradient	0.087

Fig. 107.2 Landslide susceptibility zoning map

Fig. 107.3 Relation of landslides and rainfall

4) Alos image with 2.5 m resolution.
5) Inventory of landslides (2,477 landslides from field investigation, 2,452 identified from satellite image) which includes: location of the landslide center, dimension, style of failure, triggering mechanisms, and the probable damage to infrastructure or private property.
6) Daily rainfall in research area from 2005 to 2010.

The zoning model adopted in this paper is the contributing weight model (Wang and Qiao et al. 2010).

After calculating the contribution of affecting factors, the main affecting factors are listed as Table 107.1.

With these, the zoning map is derived out (Fig. 107.2). A successive map and a 4 level-divided map is made for land planning and disaster mitigation.

4.3 Relation Between Rainfall and Landslide

After the Wenchuan earthquake, landslides usually came with rainfall (Fig. 107.3). The relation between landslide and rainfall of the same day and the antecedent precipitation was analyzed by logistic regression. The probability
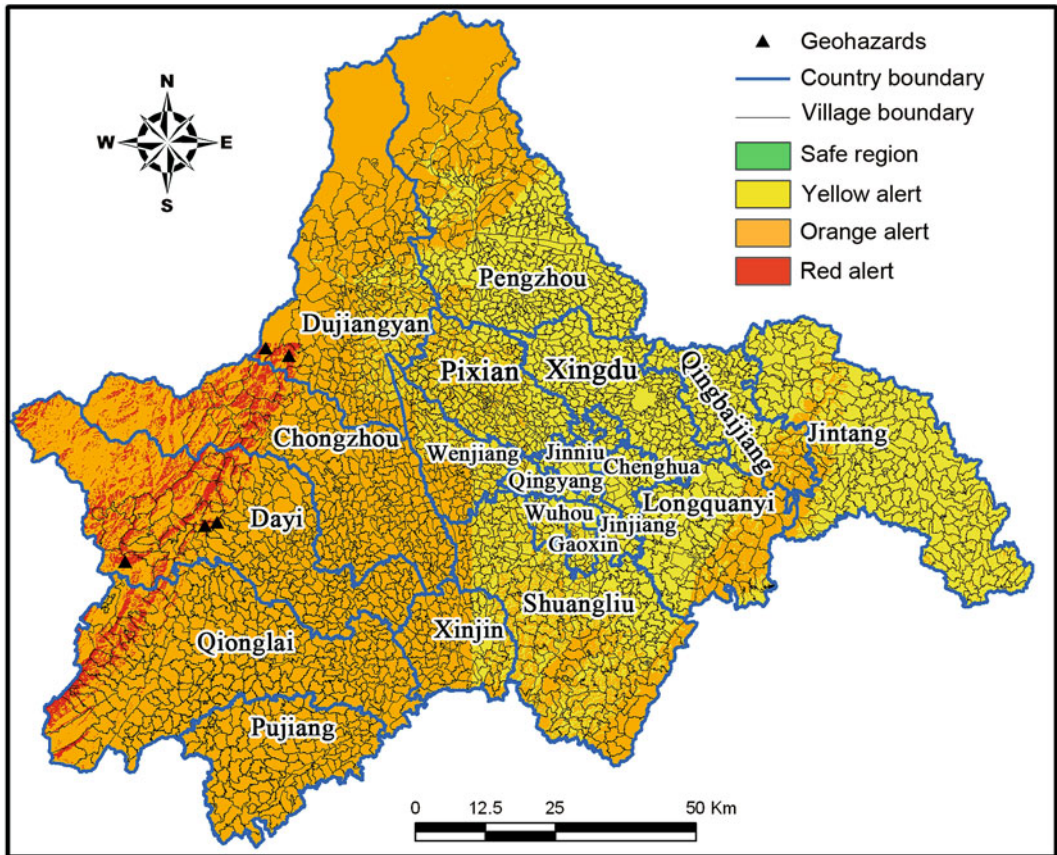
Fig. 107.4 Regional rainfall induced landslide prediction (*Red* means most possible, *orange* means middle possible, *yellow* means low possible, *green* means no possibility)

of rainfall-induced landslide is built as follows (Yang et al. 2010):

$$P_{AL} = P_{A(L/R)} * P_R \qquad (107.1)$$

$$P_{A(L/R)} = P_{(L/R)} * P_{DL} \qquad (107.2)$$

$$P_{(L/R)} = 1/(1 + e^{-p}) \qquad (107.3)$$

where P_{AL} is the possibility of regional landslide occurrence, $P_{A(L/R)}$ is the spatial possibility of rainfall landslide, P_{DL} is the possibility of landslide occurrence in different susceptibility levels, $P_{(L/R)}$ is the possibility of rainfall-induce landslides, P_R is the temporal possibility from weather service.

With this model, when the actual rainfall data is in, the disaster trend can be given as shown in Fig. 107.4.

4.4   Man-Made Rainfall Landslide Experiment

With the foregoing work, people will care about whether this model is accorded with the reality. Maybe the model is suited for the average conditions. So we choose a typical landslide and experiment to test if it will slide down in man-made rainstorm.

Taziping landslide located in northwest Chengdu, which adjoins to Baisha River and is the biggest landslide in Chengdu area (Fig. 107.5). Its surrounding area is the highest level in susceptibility map and sends out debris flow every year in post-earthquake time. The slope is made up with broke stones and debris and is also typical in earthquake struck area. The experiment is carried on the foot of Taziping slope.
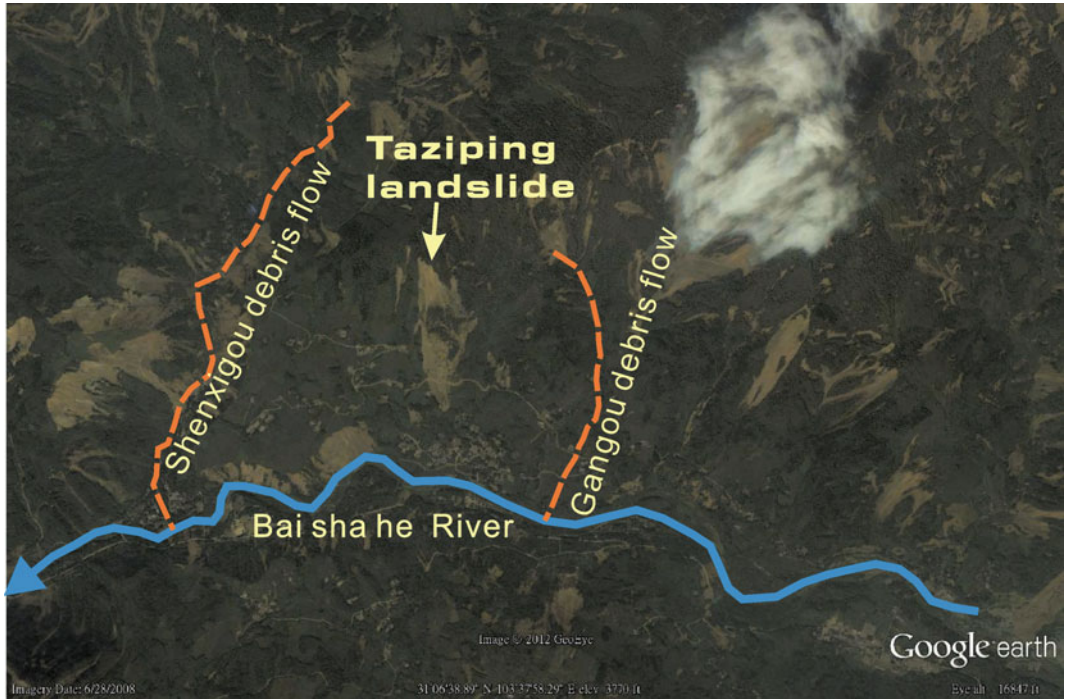
Fig. 107.5 Location of Taziping landslide (Snap from Google earth, the river flows from *right* to *left*)
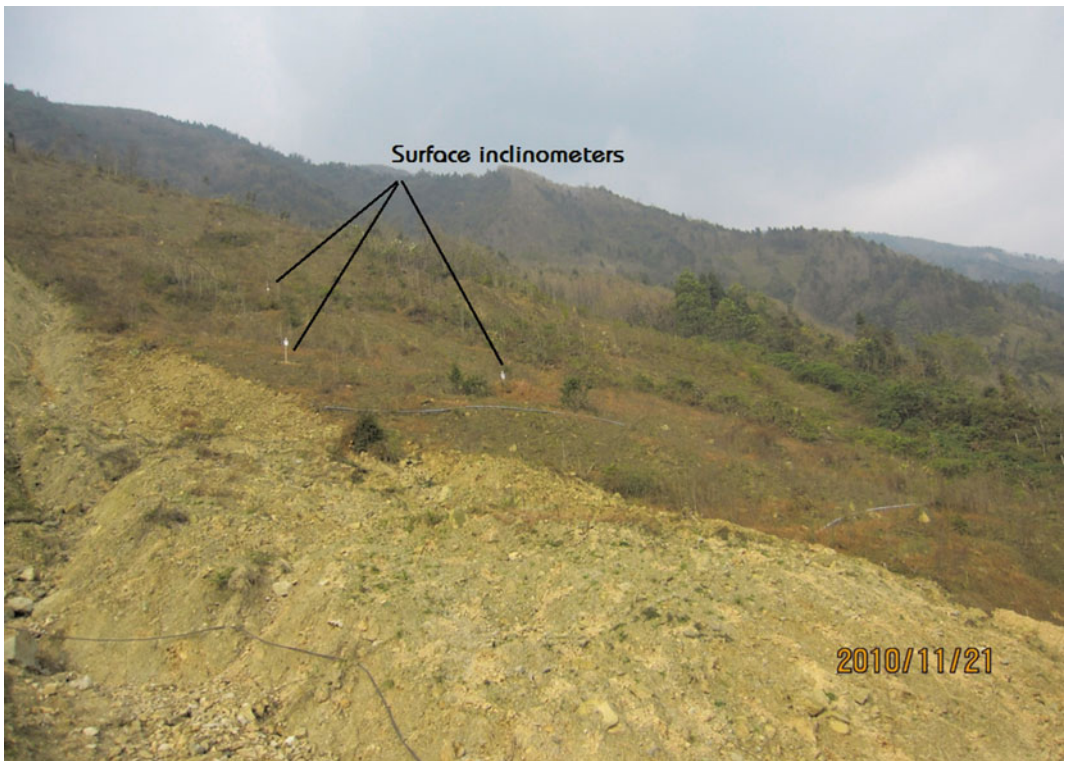

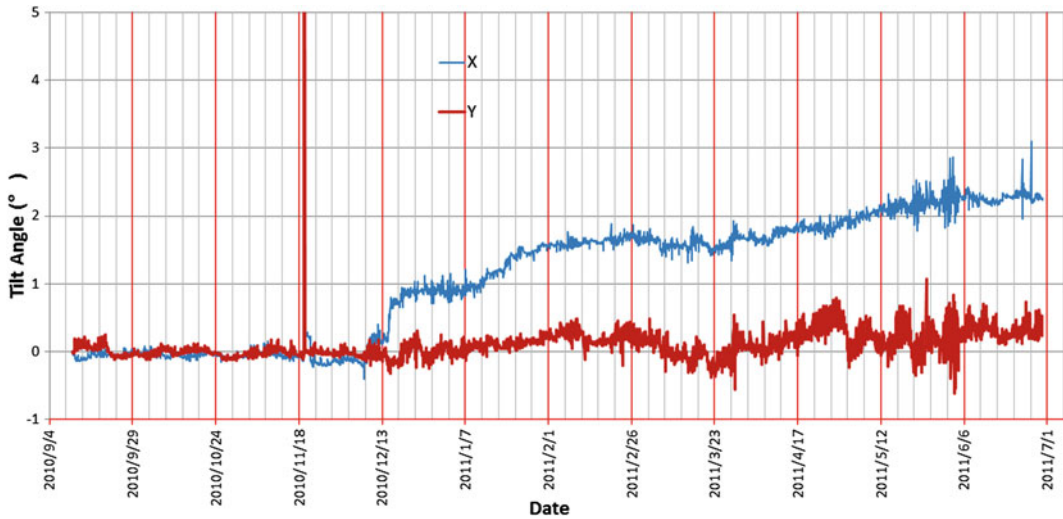**Fig. 107.6** Surface inclinometers for monitoring in Taziping landslide body

Fig. 107.7 Monitoring data of slope surface tilting

The experiment shows that without the prevention of big rocks, the slope will slide down when the rain intensity exceeds 100 mm/h. It is very close to the foregoing conclusions (Towhata et al. 2011).

4.5 Small (Shallow) Landslide Monitoring

In contrast with the experiment, the monitoring demonstration site is set up on Taziping landslide.

To monitoring large amounts of landslide, the monitoring sensors must be power-saving, easy to install and not expensive individually. Thereby, a MEMS inclinometer is selected as the main sensor. Other sensors include 3 surface clinometers, 2 tilt sensors, a rain-gauge and 3 soil moisture sensors (Huang et al. 2010) (Fig. 107.6). The monitoring curve (Fig. 107.7) shows the slope is sliding slightly.

5 Conclusions and Discussion

As earthquakes induce many shallow and small landslides, it is difficult to make an accurate prediction. On the basis of landslide susceptibility zoning and triggering factor analysis, the regional landslide prediction is successfully achieved. With the regional monitoring solution, the whole system not only can afford the disaster trend, but also can afford the specific slope's status.

Notwithstanding these achievements, the prediction data have not been merged with the monitoring data, and how to make a better monitoring for large areas still needs to be considered.

References

Ayalew L, Kasahara M, Yamagishi H (2011) The spatial correlation between earthquakes and landslides in Hokkaido (Japan), a GIS-based analysis of the past and the future. Landslides 8(4):433–448

Cascini L (2008) Applicability of landslide susceptibility and hazard zoning at different scales. Eng Geol 102(3–4):164–177

Guzzetti F, Reichenbach P, Cardinali M, Galli M et al (2005) Probabilistic landslide hazard assessment at the basin scale. Geomorphology 72:(1–4):272–299

Huang R, Li W (2009) Analysis on the number and density of landslides triggered by the 2008 wenchuan

earthquanke,china. J Geol Hazards Environ Preserv 03(20):1–7

Huang D, Qiao JP, Uchimura T, Wang L (2010) Research and application of landslide real-time monitoring system based on unsaturated soil mechanics. Disaster Adv 3(4):99–104

Keefer DK (2002). Investigating landslides caused by earthquakes—a historical review. Surv Geophys 23(6):473–510

Reggiani P, Weerts AH (2008) Probabilistic quantitative precipitation forecast for flood prediction: an application. J Hydrometeorol 9(1):76–95

Shou KJ, Hong CY, Wu CC, Hsu HY, et al (2011) Spatial and temporal analysis of landslides in Central Taiwan after 1999 Chi–Chi earthquake. Eng Geol 123(1–2):122–128

Tang C, Zhu J, Qi X, Ding J (2011) Landslides induced by the Wenchuan earthquake and the subsequent strong rainfall event: a case study in the Beichuan area of China. Eng Geol 122(1–2):22–33

Tian HL, Yang ZJ, Wang M (2010) Geological disaster characteristics and reconstruction suggestions for Pengzhou after "5–12" earthquake. J Sichuan Univ (Eng Sci Ed) 42(Compendex):33–37

Towhata I, Uchimura T, Wang L, Qiao J (2011). Validation and strategy of early warning instrument for mitigation of precipitation-induced slope failure. In: Proceedings of Indian geotechnical conference Kochi, p 2

Uchimura T, Towhata I, Lan Anh T, Fukuda J et al (2010) Simple monitoring method for precaution of landslides watching tilting and water contents on slopes surface. Landslides 7(3):351–357

Van Westen CJ, Van Asch TWJ, Soeters R (2006) Landslide hazard and risk zonation—why is it still so difficult? Bull Eng Geol Environ 65(2):167–184

Van Westen CJ, Castellanos E, Kuriakose SL (2008) Spatial data for landslide susceptibility, hazard, and vulnerability assessment: an overview. Eng Geol 102(3–4):112–131

Wang KL, Lin ML (2010) Development of shallow seismic landslide potential map based on Newmark's displacement: the case study of Chi–Chi earthquake, Taiwan. Environ Earth Sci 60(4):775–785

Wang Z, Graham GB, Madin IP, Industries ODOGaM (2001) Preliminary earthquake hazard and risk assessment and water-induced landslide hazard in Benton County, Oregon/by Zhenming Wang, Gregory B. Graham, and Ian P. Madin. [electronic resource]

Wang H, Sassa K, Xu W (2007). Analysis of a spatial distribution of landslides triggered by the 2004 Chuetsu earthquakes of Niigata Prefecture, Japan. Na Hazards 41(1):43–60

Wang M, Qiao JP, He SM (2010) GIS-based earthquake-triggered landslide hazard zoning using contributing weight model. J Mount Sci 7(4): 339–352

Yang ZJ, Qiao JP, Tian HL, Dong H et al (2010) Study on rainfall-induced regional geohazard prediction following Wenchuan earthquake. J Sichuan Univ (Eng Sci Ed), 42(supp1):38–42